

Eco-efficient Repair and Rehabilitation of Concrete Infrastructures

Edited by F. Pacheco-Torgal, Robert E.
Melchers, Xianming Shi, Nele De Belie,
Kim Van Tittelboom, Andrés Sáez

Eco-efficient Repair and Rehabilitation of Concrete Infrastructures

Related titles

Strengthening of Concrete Structures Using FRPs (ISBN 978-0-08-100636-8)

Principles for Evaluating Building Materials (ISBN 978-0-08-100707-5)

Woodhead Publishing Series in Civil
and Structural Engineering

Eco-efficient Repair and Rehabilitation of Concrete Infrastructures

Edited by

F. Pacheco-Torgal

Robert E. Melchers

Xianming Shi

Nele De Belie

Kim Van Tittelboom

Andrés Sáez



WP

WOODHEAD
PUBLISHING

An imprint of Elsevier

Woodhead Publishing is an imprint of Elsevier
The Officers' Mess Business Centre, Royston Road, Duxford, CB22 4QH, United Kingdom
50 Hampshire Street, 5th Floor, Cambridge, MA 02139, United States
The Boulevard, Langford Lane, Kidlington, OX5 1GB, United Kingdom

Copyright © 2018 Elsevier Ltd. All rights reserved.

No part of this publication may be reproduced or transmitted in any form or by any means, electronic or mechanical, including photocopying, recording, or any information storage and retrieval system, without permission in writing from the publisher. Details on how to seek permission, further information about the Publisher's permissions policies and our arrangements with organizations such as the Copyright Clearance Center and the Copyright Licensing Agency, can be found at our website: www.elsevier.com/permissions.

This book and the individual contributions contained in it are protected under copyright by the Publisher (other than as may be noted herein).

Notices

Knowledge and best practice in this field are constantly changing. As new research and experience broaden our understanding, changes in research methods, professional practices, or medical treatment may become necessary.

Practitioners and researchers must always rely on their own experience and knowledge in evaluating and using any information, methods, compounds, or experiments described herein. In using such information or methods they should be mindful of their own safety and the safety of others, including parties for whom they have a professional responsibility.

To the fullest extent of the law, neither the Publisher nor the authors, contributors, or editors, assume any liability for any injury and/or damage to persons or property as a matter of products liability, negligence or otherwise, or from any use or operation of any methods, products, instructions, or ideas contained in the material herein.

British Library Cataloguing-in-Publication Data

A catalogue record for this book is available from the British Library

Library of Congress Cataloguing-in-Publication Data

A catalog record for this book is available from the Library of Congress

ISBN: 978-0-08-102181-1 (print)

ISBN: 978-0-08-102182-8 (online)

For information on all Woodhead Publishing publications
visit our website at <https://www.elsevier.com/books-and-journals>



Working together
to grow libraries in
developing countries

www.elsevier.com • www.bookaid.org

Publisher: Jonathan Simpson

Acquisition Editor: Glyn Jones

Editorial Project Manager: Ashlie M. Jackman

Production Project Manager: Debasish Ghosh

Cover Designer: Vicky Pearson Esser

Typeset by MPS Limited, Chennai, India

Contents

List of contributors	xiii
Foreword	xvii
1 Introduction	1
<i>F. Pacheco-Torgal</i>	
1.1 Repair and rehabilitation of concrete infrastructures on the context of sustainable development	1
1.2 Outline of the book	7
References	10
Part I Deterioration assessment	13
2 Service life estimation of concrete infrastructures	15
<i>Robert E. Melchers and Igor A. Chaves</i>	
2.1 Introduction	15
2.2 Causes of reinforced concrete infrastructure deterioration	18
2.3 Carbonation-induced corrosion of reinforcement	22
2.4 Chloride-induced corrosion of reinforcement	25
2.5 Practical experience, observations and investigations	26
2.6 Recent research on the effects of chlorides	32
2.7 Practical implications for service life assessment	35
2.8 Closure and outlook	36
Acknowledgments	37
References	37
3 Impact of climate change on the service life of concrete structures	43
<i>Ronaldo A. Medeiros-Junior</i>	
3.1 Introduction	43
3.2 Effect of climate on the mechanisms of degradation of concrete structures	43
3.3 Climate change	49
3.4 Example of a numerical application—corrosion of reinforcements on the Brazilian coast	54
3.5 Final considerations	65
References	65

4	Monitoring of Reinforced Concrete Corrosion	69
	<i>Xianming Shi</i>	
4.1	Introduction	69
4.2	Online monitoring of rebar corrosion	70
4.3	Embeddable sensors for chloride concentration, pH, and other parameters	74
4.4	Accelerated testing of embeddable sensors: A case study	79
4.5	Future research needs	90
	Acknowledgments	91
	References	91
5	Monitoring of concrete structures with optical fiber sensors	97
	<i>Aghiad Khadour and Julien Waeytens</i>	
5.1	Introduction	97
5.2	Overview and classifications of optical fiber sensor technologies	98
5.3	Classifications of Structural Health Monitoring purposes	105
5.4	Use of distributed optical fiber sensors to monitor concrete structures: Some significant applications	107
5.5	Technical guide: from the identification of the SHM purpose to the selection of the appropriate optical fiber technology	114
5.6	Future trends	117
	References	118
6	Structural health monitoring through acoustic emission	123
	<i>Noorsuhada Md Nor</i>	
6.1	Introduction	123
6.2	Case study: Damage assessment of precast reinforced concrete beam subjected to fatigue loading	131
6.3	Experimental programme	132
6.4	Intensity analysis of AE signal	135
6.5	Results and discussion	135
6.6	Conclusions	142
	Acknowledgment	143
	References	143
7	Durability problems of concrete structures rehabilitated with FRP	147
	<i>Mariaenrica Frigione</i>	
7.1	Introduction	147
7.2	Application of fiber reinforced polymer composites for rehabilitation of concrete structures	148
7.3	Fiber reinforced polymer components	149
7.4	Durability of fiber reinforced polymer for rehabilitation of concrete structures	155
7.5	Standard tests, traditional and alternative methods of assessing durability of fiber reinforced polymer	163

7.6	Recommendations for further research and future trends	165
	References	166
	Further reading	170
8	Field assessment of concrete structures rehabilitated with FRP	171
	<i>Nur Yazdani, Eric Chavez Garcia and Mina Riad</i>	
8.1	Introduction	171
8.2	Types and benefits of fiber reinforced polymer rehabilitation systems for concrete structures	171
8.3	Destructive field assessment	173
8.4	Nondestructive assessment	176
8.5	Relative assessment of available techniques	190
8.6	Future trends	191
	References	192
	Further reading	194
9	Field assessment of a concrete bridge	195
	<i>Eva O.L. Lantsoght</i>	
9.1	Introduction	195
9.2	Description of the viaduct Zijlweg	196
9.3	Preparation of field assessment	200
9.4	Execution of field assessment	208
9.5	Postprocessing of field assessment	215
9.6	Cost of decision-making based on field assessment	223
9.7	Future trends	228
9.8	Summary and conclusions	229
	Acknowledgments	229
	References	230
10	Assessment of the deterioration of concrete structures using a finite element model	235
	<i>J.F. Jiménez-Alonso and A. Sáez</i>	
10.1	Introduction	235
10.2	Finite element models for concrete structures	237
10.3	Field tests and monitoring for deterioration assessment	238
10.4	Modal-based deterioration assessment methods	242
10.5	Finite element model updating	243
10.6	Application example: deterioration assessment of the Molinos Bridge	250
10.7	Conclusions	257
10.8	Future trends	258
	Acknowledgments	258
	References	258

Part II Innovative concrete repair and rehabilitation materials	261
11 Alkali activated repair mortars based on different precursors	263
<i>Wilma Ducman, Sabina Kramar and Aljoša Šajna</i>	
11.1 Introduction	263
11.2 Alternative repair mortars for concrete repair	264
11.3 Standard requirements for repair mortars	267
11.4 Performance of alkali-activated repair mortars based on different precursors	273
11.5 Future trends	285
References	286
Further reading	291
12 Geopolymeric repair mortars based on a low reactive clay	293
<i>Walid Tahri, Basma Samet, F. Pacheco-Torgal, José Aguiar and Samir Baklouti</i>	
12.1 Introduction	293
12.2 Experimental work	293
12.3 Results and discussion	301
12.4 Conclusions and future trends	311
References	311
Further reading	313
13 Assessment of corrosion protection methods for reinforced concrete	315
<i>Ana María Aguirre-Guerrero and Ruby Mejía de Gutiérrez</i>	
13.1 Introduction	315
13.2 Chloride-induced corrosion	317
13.3 Carbonation-induced corrosion	332
13.4 Conclusions and future trends	341
References	342
Further reading	353
14 Sulfoaluminate cement-based concrete	355
<i>Kedsarin Pimraksa and Prinya Chindapasirt</i>	
14.1 Introduction	355
14.2 Definition, type, and usages: sulfoaluminate cement	356
14.3 Production of sulfoaluminate cement	359
14.4 Hydration of sulfoaluminate cement	366
14.5 Usages of sulfoaluminate cement for repair	378
References	382
Further reading	385

15	Engineered cementitious composites-based concrete	387
	<i>Gürkan Yıldırım, Mustafa Şahmaran and Özgür Anıl</i>	
15.1	The need for sustainable repair of concrete infrastructures	387
15.2	Holistic model for the design of effective repair materials	389
15.3	Engineered cementitious composites: a potential repair material solution for sustainable infrastructures	392
15.4	Conclusions	421
	References	422
16	Self-healing concrete with encapsulated polyurethane	429
	<i>Kim Van Tittelboom, Philip Van den Heede and Nele De Belie</i>	
16.1	Encapsulation of polymeric healing agents	429
16.2	Suitable encapsulation materials and trigger mechanisms	430
16.3	Crack closure by encapsulated polyurethane	431
16.4	Regain in impermeability	440
16.5	Regain in mechanical properties	448
16.6	Regain in durability	457
16.7	Extension in service life	460
	References	464
17	Concrete with superabsorbent polymer	467
	<i>Hong Seong Wong</i>	
17.1	Introduction	467
17.2	Types of superabsorbent polymer	468
17.3	Properties of superabsorbent polymer	470
17.4	Superabsorbent polymers in concrete	471
17.5	Effects of superabsorbent polymer on properties of concrete	477
17.6	Applications of superabsorbent polymer in concrete	483
17.7	Summary and future research	491
	References	492
18	Concrete with self-sensing properties	501
	<i>Filippo Ubertini and Antonella D'Alessandro</i>	
18.1	Introduction	501
18.2	Composition and processing of self-sensing concrete	503
18.3	Measurement of sensing data and characterization of self-sensing concrete	508
18.4	Applications of self-sensing concrete	517
18.5	Trends and future developments	522
	Acknowledgments	523
	References	524

19	Bacteria-based concrete	531
	<i>Nele De Belie, Jianyun Wang, Zeynep B. Bundur and Kevin Paine</i>	
19.1	Introduction	531
19.2	Production of bacteria suitable for concrete applications	532
19.3	Direct addition of bacteria to concrete	537
19.4	Application of bacteria for surface protection and manual crack repair	540
19.5	Protection strategies for bacteria in concrete	545
19.6	Application of encapsulated bacteria for self-healing concrete	551
19.7	Future trends	560
	References	561
	Further reading	567
20	Bio-based admixture with substances derived from bacteria for the durability of concrete	569
	<i>Françoise Feugeas, Mai Tran and Sara Chakri</i>	
20.1	Introduction	569
20.2	Types of corrosion inhibitors in concrete	570
20.3	Case study: bio-based admixture from bacterial extracellular substances	572
20.4	Corrosion study	574
20.5	Conclusions	581
	References	582
	Further reading	587
	Part III Design, LCC, LCA, and case studies	589
21	Eco-efficient design of concrete repair and rehabilitation	591
	<i>Rachel Muigai</i>	
21.1	Introduction	591
21.2	Eco-efficient design of concrete structures	592
21.3	Conclusions	609
	References	609
	Further reading	611
22	Cost-effective design to address climate change impacts	613
	<i>Emilio Bastidas-Arteaga and Mark G. Stewart</i>	
22.1	Introduction	613
22.2	Adaptation of RC structures	614
22.3	Proposed adaptation framework	616
22.4	Considered repair and adaptation measures	622
22.5	Illustrative example: Adaptation of existing RC structures	625
22.6	Conclusions	633
	References	634

23	Lifecycle cost and performance analysis for repair of concrete tunnels	637
	<i>Jian Hong Wang</i>	
23.1	Introduction	637
23.2	Tunnel construction and structure	639
23.3	Tunnel degradation and maintenance practice	642
23.4	Tunnel repairs	649
23.5	Eco-efficient maintenance	654
23.6	Recommendations and future trends	667
	References	668
24	Life cycle analysis of strengthening concrete beams with FRP	673
	<i>Sebastian George Maxineasa and Nicolae Taranu</i>	
24.1	Introduction	673
24.2	Sustainability in civil engineering	674
24.3	Fiber-reinforced polymers for the rehabilitation of reinforced concrete members	685
24.4	Strengthening solutions for reinforced concrete beams	696
24.5	Life cycle analysis of carbon fiber-reinforced polymer strengthening solutions	699
24.6	Conclusions and future trends	716
	References	716
25	Life-cycle analysis of repair of concrete pavements	723
	<i>Hao Wang</i>	
25.1	Introduction	723
25.2	Lifecycle cost analysis of concrete pavement repair	724
25.3	Lifecycle assessment of concrete pavement repair options	727
25.4	Integration of economic and environmental analysis	733
25.5	Recommendations to future research	736
	References	736
	Further reading	738
	Index	739

This page intentionally left blank

List of contributors

José Aguiar University of Minho, Guimarães, Portugal

Ana María Aguirre-Guerrero Universidad del Valle, Cali, Colombia

Özgür Anıl Gazi University, Ankara, Turkey

Samir Baklouti University of Sfax, Sfax, Tunisie

Emilio Bastidas-Arteaga University of Nantes, Nantes, France

Zeynep B. Bundur Ozyegin University, Istanbul, Turkey

Sara Chakri Paris-Sorbonne University, Paris, France

Igor A. Chaves The University of Newcastle, Newcastle, NSW, Australia

Eric Chavez Garcia University of Texas at Arlington, Arlington, TX, United States

Prinya Chindaprasirt Khon Kaen University, Khon Kaen, Thailand

Antonella D'Alessandro University of Perugia, Perugia, Italy

Nele De Belie Ghent University, Ghent, Belgium

Vilma Ducman Slovenian National Building and Civil Engineering Institute, Ljubljana, Slovenia

Françoise Feugeas ICube, INSA Strasbourg, Strasbourg, France

Mariaenrica Frigione University of Salento, Lecce, Italy

J.F. Jiménez-Alonso Universidad de Sevilla, Sevilla, Spain

Aghiad Khadour Université Paris-Est, IFSTTAR, Marne-la-Vallée, France

Sabina Kramar Slovenian National Building and Civil Engineering Institute, Ljubljana, Slovenia

Eva O.L. Lantsoght Delft University of Technology, Delft, The Netherlands; Universidad San Francisco de Quito, Quito, Ecuador

Sebastian George Maxineasa “Gheorghe Asachi” Technical University of Iasi, Iasi, Romania

Ronaldo A. Medeiros-Junior Federal University of Parana (UFPR), Curitiba, Brazil

Ruby Mejía de Gutiérrez Universidad del Valle, Cali, Colombia

Robert E. Melchers The University of Newcastle, Newcastle, NSW, Australia

Rachel Muigai University of Johannesburg, Johannesburg, South Africa

Noorsuhada Md Nor Universiti Teknologi MARA (UiTM) Pulau Pinang Branch, Permatang Pauh, Penang, Malaysia

Fernando Pacheco-Torgal University of Minho, Guimarães, Portugal

Kevin Paine University of Bath, Bath, United Kingdom

Kedsarin Pimraksa Chiang Mai University, Chiang Mai, Thailand

Mina Riad University of Texas at Arlington, Arlington, TX, United States

A. Sáez Universidad de Sevilla, Sevilla, Spain

Mustafa Şahmaran Hacettepe University, Ankara, Turkey

Aljoša Šajna Slovenian National Building and Civil Engineering Institute, Ljubljana, Slovenia

Basma Samet University of Sfax, Sfax, Tunisie

Xianming Shi Washington State University, Pullman, WA, United States

Mark G. Stewart The University of Newcastle, Newcastle, NSW, Australia

Walid Tahri University of Sfax, Sfax, Tunisie

Nicolae Taranu “Gheorghe Asachi” Technical University of Iasi, Iasi, Romania

Mai Tran Paris-Sorbonne University, Paris, France

Filippo Ubertini University of Perugia, Perugia, Italy

Philip Van den Heede Ghent University, Ghent, Belgium

Kim Van Tittelboom Ghent University, Ghent, Belgium

Julien Waeytens Université Paris-Est, IFSTTAR, Marne-la-Vallée, France

Hao Wang Rutgers, The State University of New Jersey, Piscataway, NJ, United States

Jian Hong Wang Nippon Koei Co., Ltd, Tsukuba, Ibaraki, Japan

Jianyun Wang Ghent University, Ghent, Belgium

Hong Seong Wong Imperial College London, London, United Kingdom

Nur Yazdani University of Texas at Arlington, Arlington, TX, United States

Gürkan Yıldırım Adana Science and Technology University, Adana, Turkey

This page intentionally left blank

Foreword

Concrete infrastructures are of great importance to society. They provide the means to connect cities, transport people and goods, and protect land against flooding and erosion. Most concrete infrastructures were built in the past 50 years. In general they are designed to last for a period of 50–100 years, some even longer. This implies that more and more of these structures are approaching the end of their designed service life or that substantial maintenance is required to be able to reach their designed lifetime. A substantial part of these structures are still functioning relatively well at the end of their service life and could be given a second life with proper maintenance and rehabilitation. Certainly repair and upgrading of a structure will be more favorable than demolishing and newly building, because it will be a faster method, which causes less hindrance to traffic, it will make use of less material, which is better for the environment, and in most cases it is more economical. The importance of developing strategies for repair and rehabilitation of concrete structures is also illustrated by the budgets spent in Western countries on infrastructure. We have now reached the point where the annual budget for maintenance in most countries is higher than the budget for newly built structures.

This book with the title *Eco-efficient Repair and Rehabilitation of Concrete Infrastructures* gives the state of the art of all aspects dealing with the maintenance of infrastructures. It starts with methods to recognize, assess, and monitor damage in concrete structures. It discusses innovative strategies for the repair of damage, where it focuses on new eco-friendly materials like geopolymers, sustainable cements and concretes, and repair materials with improved properties, like strain-hardening behavior, low shrinkage, and self-healing and self-sensing properties. The last part of the book deals with case studies and how to perform a cost-effective design and maintenance strategy for concrete structures looking at the performance over the complete lifetime.

The editors have managed to compile a book which can be seen as a manual for proper repair and rehabilitation of concrete infrastructures. It is a must-have for all engineers and researchers dealing with the design and maintenance of concrete structures such as roads, bridges, tunnels, dams, and coastal defense works.

Prof. Erik Schlangen

Delft University of Technology, Delft, The Netherlands

This page intentionally left blank

Introduction

1

F. Pacheco-Torgal

University of Minho, Guimarães, Portugal

1.1 Repair and rehabilitation of concrete infrastructures on the context of sustainable development

[Rockström et al. \(2009\)](#) proposed an approach to global sustainability defining nine interdependent planetary boundaries within which they expect that humanity can operate safely. This include:

1. climate change (CO_2 concentration in the atmosphere < 350 ppm and/or a maximum change of $+1 \text{ W/m}^2$ in radiative forcing);
2. ocean acidification (mean surface seawater saturation state with respect to aragonite $\geq 80\%$ of pre-industrial levels);
3. stratospheric ozone ($< 5\%$ reduction in O_3 concentration from pre-industrial level of 290 Dobson Units);
4. biogeochemical nitrogen (N) cycle (limit industrial and agricultural fixation of N_2 to 35 Tg N/yr) and phosphorus (P) cycle (annual P inflow to oceans not to exceed 10 times the natural background weathering of P);
5. global freshwater use ($< 4000 \text{ km}^3/\text{yr}$ of consumptive use of runoff resources);
6. land system change ($< 15\%$ of the ice-free land surface under cropland);
7. the rate at which biological diversity is lost (annual rate of < 10 extinctions per million species).

Two additional planetary boundaries for which a boundary level was not yet determined are: chemical pollution and atmospheric aerosol loading. According to the authors, the “transgression one or more planetary boundaries may be deleterious or even catastrophic due to the risk of crossing thresholds that will trigger non-linear, abrupt environmental change within continental- to planetary-scale systems”. These authors estimated that humanity has already transgressed three planetary boundaries for changes to the global nitrogen cycle, the rate of biodiversity loss and, above all, climate change ([Hansen et al., 2013, 2016, 2017](#)). Most unfortunately, the repeated fiascos of the so-called Conference of Parties (COPs) in Warsaw (COP-19) in 2013, Lima (COP-20) in 2014, Paris (COP-21) in 2015 and, most recently, Marrakech (COP-22) in November of 2016 to agree on important reductions on greenhouse gas emissions only worsened the climate change scenario. The major problem being the fact that the major emission emitters: China, US and India, do not accept severe cuts. If the position of China and India is understandable from an economic view, the US is not, because it is a well-developed economy, and

on a per-capita historical basis, the U.S. is 10 times more accountable than China and 25 times more accountable than India for the increase of atmospheric CO₂ above its preindustrial level (Hansen and Sato, 2016).

As a consequence of this worrying status, it remains crucial to act in order to address those problems in a context in which urban human population is growing exponentially. Each day there are now about 200,000 new inhabitants on planet Earth and in the next decades human population will almost double, increasing from approximately 3.4 billion in 2009 to 6.4 billion in 2050 (WHO, 2014). As a consequence, recent estimates on urban expansion suggests that until 2030 a high probability exists (over 75%) that urban land cover will increase by 1.2 million square kilometer (Seto et al., 2012). This overpopulation will require new infrastructure and will put increase pressure on the existent infrastructures.

Concrete infrastructure encompasses bridges, piers, pipelines, dams, pavements, or buildings that are crucial to services and economic activities of modern civilization. Unfortunately, concrete deteriorates due to several causes including: mechanical deterioration from impact or excessive loading, or deterioration due to physical causes of erosion or shrinkage. More frequently, however, it deteriorates through chemical detrimental reactions when it is exposed to environmental conditions containing chlorides from seawater or from deicing salts, atmospheric carbon dioxide, or other aggressive media (Glasser et al., 2008).

The importance of concrete durability has been emphasized by Mora (2007), when he stated that increasing durability from 50 to 500 years would mean a reduction of its environmental impact by a factor of 10. Concrete infrastructure with low durability requires frequent maintenance and conservation operations and its integral replacement is associated with the consumption of huge amounts of raw materials and energy. Many of the degraded concrete infrastructures were built decades ago when little attention was given to durability issues (Hollaway, 2011). Deficient execution due to poor workmanship is also a relevant cause of premature degradation of concrete infrastructure and reinforcement corrosion (Costa and Appleton, 2002) and this cause is becoming increasingly relevant in recent decades (Elrakib and Arafa, 2012), relevant to the cost increase of workmanship. Additionally, the majority of technical standards and codes that deal with durability design and control of execution do not make any provisions for the assessment of concrete cover depth achieved in structures. This constitutes a serious gap, because failure to comply of the concrete cover depth with the specifications is one of the main causes of premature deterioration of reinforced concrete structures (Monteiro et al., 2015; de Medeiros et al., 2016).

Climate change is also increasingly responsible for the premature deterioration of concrete infrastructure. Not only due to occasional and extreme atmospheric events, but in a more frequent pattern due to concrete carbonation associated with the steady increase on CO₂ concentration (molecules of CO₂ for every one million molecules in the atmosphere) (Fig. 1.1). Its important to mention that 2016 was the first year with atmospheric CO₂ concentrations above 400 ppm all year round (Betts et al., 2016) and even if all the greenhouse gas emissions suddenly ceased, the amount already in the atmosphere would remain there for the next 100 years

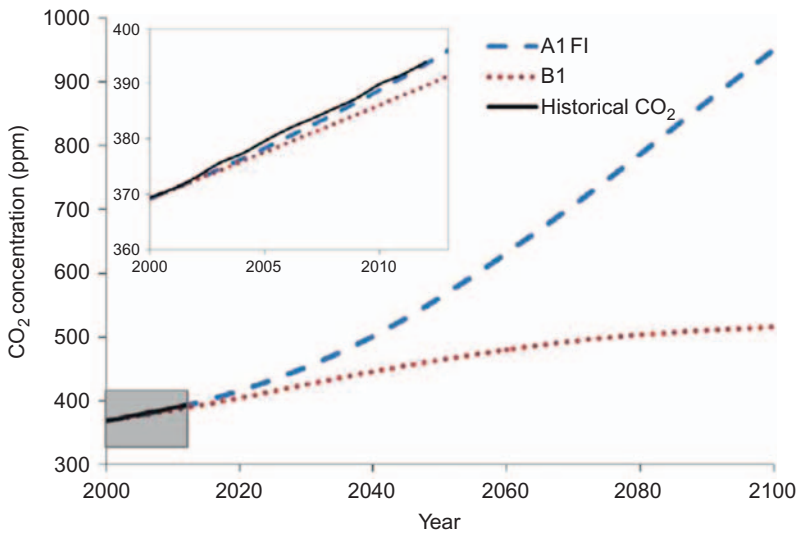


Figure 1.1 Predicted estimates of CO₂ concentrations. Actual atmospheric CO₂ concentration has been plotted side by side along with predicted concentrations for 2000–13 and shown in the inset panel.

Source: From Saha, M., Eckelman, M., 2014. Urban scale mapping of concrete degradation from projected climate change. *Urban Clim.* 9, 101–114. Copyright © 2014, with permission from Elsevier (Saha and Eckelman, 2014).

(Clayton, 2001). Wang et al. (2010) showed that additional carbonation-induced damage risks for the A1FI emission scenario (CO₂ concentrations increasing by more than 160% to 1000 ppm by 2100) are up to 16% higher if there are no changes to how concrete structures are designed or constructed.

Stewart et al. (2011) found that carbonation-induced corrosion can increase by over 400% by 2100 for inland arid or temperate climates in Australia. Bastidas-Arteaga et al. (2013) noticed that climate change might reduce the time to failure of reinforced concrete structures by up to 31%. Talukdar and Banthia (2013) found that concrete structures that will be constructed in the year 2030, in areas where carbonation induced corrosion would be a concern (moderate humidity, higher temperatures and for a dry exposure class), structures are expected to show a reduction in serviceable lifespan due to climate change of approximately 15–20 years, with signs of damage being apparent within 40–45 years of construction. Since, in urban settings, CO₂ concentrations can be much higher than in nearby rural environments, and that urban areas are subject to increase temperature levels due to urban heat island effects, this means that concrete infrastructure located in urban areas are subject to more intense carbonation-damaging actions. According to Saha and Eckelman (2014), climate change will accelerate corrosion and degradation of concrete structures in Boston. By the year 2055, the chlorination-induced corrosion depth in concrete structures built in year 2000 may exceed the code-recommended protected cover thickness of 38 mm. For carbonation-induced corrosion, the

threshold year is 2077. Rehabilitation of concrete infrastructures to address future carbonation-induced corrosion under much-higher CO₂ concentrations, or any other climate change related deterioration action, can be considered in the context of urban adaptation. Fig. 1.2 shows a world map concerning the status of urban adaptation to climate change in areas with over one million inhabitants, each covering a total of 1.3 billion people. Many of the existing infrastructures will still be in use by 2030 and even in 2050 when climate change might have far more substantial impacts than today, meaning that repair and rehabilitation action will be needed to prevent premature degradation (Giordano, 2012). Worldwide concrete infrastructure repair rehabilitation needs are therefore enormous. In US there are more than 60,000 structurally deficient bridges. For China this number exceeds more than 80,000 bridges. In Europe in the next 10 years some 1500 railway bridges are expected to be strengthened, 4500 have to be replaced, and the deck of other additional 3000 bridges has to be replaced (Casas, 2015). Consequently, its costs are staggering. According to OECD, improving the world's infrastructure will require an estimated \$7 trillion/year USD (Kennedy and Corfee-Morlot, 2013).

In the US, the corrosion deterioration cost due to deicing and sea salt effects is estimated at over 150 billion dollars and infrastructure repair rehabilitation overall needs are estimated to be over 1.6 trillion dollars over the next years (Davalos, 2012). A climate-change induced acceleration of the corrosion process by only a few percent can result in increased maintenance and repair costs of hundreds of

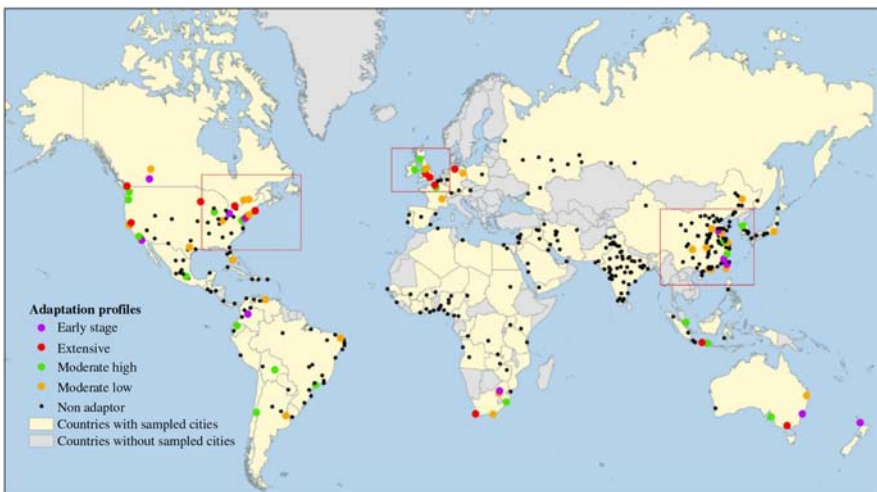


Figure 1.2 Map of global urban adaptation panel.

Source: From Araos, M., Berrang-Ford, L., Ford, J., Austin, S., Biesbroek, R., Lesnikowski, A., 2016. Climate change adaptation planning in large cities: a systematic assessment. *Environ. Sci. Policy* 66, 375–382. Copyright © 2016, with permission from Elsevier (Araos et al., 2016).

billions of dollars annually (Bastidas-Arteaga and Stewart, 2015). The annual cost of corrosion worldwide is already over 3% of the world's Gross Domestic Product (GDP) (Bossio et al., 2015). In Europe, bridge maintenance repair and strengthening requires an annual budget of £215M, and that estimate does not include traffic management cost (Yan and Chouw, 2012). In US, costs related to wasted fuel and time loss due to traffic congestion are estimated between 50 and 100 billion dollars (Report, 2012; Schlangen and Sangadji, 2013). In the in city of Hong Kong, more than 580,000 vehicles cross its 900 highway bridges on a daily basis (Pei et al., 2015). This traffic volume is expected to duplicate in the next decades. It can never be overemphasized that Earth's populations are growing at a very fast pace and as a consequence in 2014 there will be 12,000 million vehicles on the road and by 2035 this number will increase to 2000 million and 2500 million by 2050 (Navigant Research, 2014). This means that concrete highways bridges will be subject to increase use and will reach the end of their service life sooner than expected and repair and rehabilitation costs will increase even further. The "Law of Fives" states that \$1 spent on design and construction is equivalent to \$5 spent as damage initiates, before it propagates; \$25 once deterioration has begun to propagate, and \$125 after extensive damage has occurred (Delatte, 2009). This concept highlights the importance acting as soon as possible to prevent concrete infrastructure reaching a level where extensive damage has occurred and the rehabilitation costs grow exponentially. This action is related to the assessment of the infrastructure performance, but monitoring activities are also costly and not all countries can afford it. In the US, bridges are inspected every 2 years (Rehman et al., 2016). The lack of regular inspections worsens the problem and contributes to premature infrastructure deterioration, thus leading to possible bridge failure with an inevitable loss of human lives. Its worth remembering that the 1967 failure of the Silver Bridge in Ohio caused 46 deaths, in 1981 the failure of the Hyatt Regency walkway in Kansas City failure caused 114 deaths and 216 were injured, and in 2001 the Entre Rios bridge in Portugal caused 59 deaths.

The European Standard EN 1504 (2004) "Products and Systems for Protection and Repair of Concrete Structures-Definitions, Requirements, Quality Control and Evaluation of Conformity", consisting of 10 standards, is an interesting and important standard of great interest for construction companies involved in concrete repair, including: EN 1504-1:2005: Definitions; EN 1504-2:2005: Surface protection systems for Concrete; EN 1504-3:2006: Structural and non-structural repair; EN 1504-4:2005: Structural bonding; EN 1504-5:2005: Concrete injection; EN 1504-6:2007: Anchoring of reinforcing steel bar; EN 1504-7:2007: Reinforcement corrosion protection; EN 1504-8:2005: Quality control and certification of conformity; EN 1504-9:2008: General principles for the use of products and systems; EN 1504-10:2005: Site application of products and quality control of the works.

It is, by now, a standard that lags behind the state of the art on the field of repair and rehabilitation on concrete infrastructures. Bartuli et al. (2010) had already suggested an update of its content. Such an update is more necessary because a few years ago the European Union passed regulations concerning the

environmental performance of construction and building materials. On March 9, 2011, the European Union approved Regulation (EU) 305/2011, the Construction Products Regulation (CPR), that replaced Directive 89/106/EEC, already amended by Directive 1993/68/EEC, and known as the Construction Products Directive (CPD). When comparing the basic requirements of the CPR and CPD, one can see that the CPR has a new requirement: No. 7 (Sustainable use of natural resources), and also that No. 3 (Hygiene, health and the environment) and No. 4 (Safety and accessibility in use) have been refined. Meaning, since July 1, 2013, environmental assessment of construction materials in Europe it is mandatory for commercialization. Since some of the repair materials mentioned in the EN 1504 like polyurethane and epoxy have a high environmental impact (Pacheco-Torgal et al., 2012) the future revision of this standard will have to focus on more eco-efficient repair materials.

The methodology used to assess the environmental impacts of a given material or activity from cradle to grave is known as “Life Cycle Assessment” (LCA). It “includes the complete life cycle of the product, process or activity, i.e., the extraction and processing of raw materials, manufacturing, transportation and distribution, use, maintenance, recycling, reuse and final disposal”. The application of LCA has been regulated internationally since 1996 under International Standards Organization (ISO) which classifies the existing environmental labels into three typologies—types I (eco-labels, ISO 14024), II (product self-declarations, ISO 14021), and III (EPD’s, ISO 14025) (Pacheco-Torgal et al., 2013).

The concept of eco-efficiency was first coined in the book “Changing course” (Schmidheiny, 1992) in the context of 1992 Earth Summit process. This concept includes “the development of products and services at competitive prices that meet the needs of humankind with quality of life, while progressively reducing their environmental impact and consumption of raw materials throughout their life cycle, to a level compatible with the capacity of the planet”. The eco-efficient repair and rehabilitation means to increase the service life of concrete infrastructure, and to use eco-efficient materials when possible, to design accounting for damaging effects due to climate change and also by taking account LCC and LCA. Thus greater economic and environmental efficiency can be achieved by designing infrastructure that is simultaneously low carbon and climate resilient (Pacheco-Torgal, 2014; Kennedy et al., 2014).

The purpose of this book is to make a contribution in this area. Other books have already been written about repair and rehabilitation of concrete infrastructures, but some books focus only on strengthening and rehabilitation using fiber reinforced polymers (FRP)—a material that has some durability shortcomings as can be seen on a chapter of Part 1 of this book. Others rely only on practical advice, unsuitable to researchers. None have a strong cover of innovative materials, to which this book dedicates a relevant part, nor do they dedicate even a minimum attention to repair design, accounting to climate change design effects or to LCC and LCA of repair and rehabilitation of concrete infrastructure like this one does.

1.2 Outline of the book

This book provides an updated, state-of-the-art review on eco-efficient repair and rehabilitation of concrete infrastructures.

The first part encompasses materials and technologies (**Chapters 2–10**):

Chapter 2, Service life estimation of concrete infrastructures, concerns service life estimation of concrete structures and their main mechanisms. They are described and critically reviewed in the light of properly analyzed experience for, and behavior of, actual reinforced concrete structures.

Chapter 3, Impact of climate change on the service life of concrete structures, discusses some effects of climatic variables on concrete durability and some scenarios of climate change. An example of a numerical application about the corrosion of reinforcements on the Brazilian coast is presented.

Chapter 4, Monitoring of reinforced concrete corrosion, presents an overview of the state of the art in using sensors for online monitoring of rebar corrosion inside reinforced concrete (RC) structures. It includes: current technologies for online monitoring of those structures, embeddable sensors for chloride concentration, pH, humidity, reference electrode, and other parameters, and then a case study of accelerated testing of embeddable sensors.

Chapter 5, Monitoring with optical fiber sensors, deals with the use of distributed optic fiber for the monitoring of concrete structures. An overview on optic fiber technologies is given and then a practical guide in order to select the appropriate optic fiber system for a given monitoring purpose, such as the crack detection or the strain measurement is suggested.

Chapter 6, Structural health monitoring through acoustic emission, covers the use of acoustic emission as a structural health monitoring technique to monitor the performance and integrity of the structure when subjected to fatigue loading.

Chapter 7, Durability problems of concrete structures rehabilitated with FRP, provides a review of the use of Fiber Reinforced Polymer-FRP composites for the strengthening/reparation of concrete structures. Special attention is paid to the durability of FRP's in terms of their degradation causes and mechanisms; for resins, fibers, and the whole system.

Chapter 8, Field assessment of concrete structures rehabilitated with FRP, discusses several test methods to evaluate FRP, with a section to provide a relative assessment of each available test. The chapter closes by providing a section of the future of technology and application regarding FRP, with advice.

Chapter 9, Field assessment of a concrete bridge, presents a case study of the field assessment: visual inspection and load testing of a reinforced concrete bridge, with cracking caused by alkali-silica reaction. It encompasses the preparation, execution, and post-processing of the load test. It also includes a discussion of the cost-savings (economic, environmental, and social) that are obtained through this procedure compared to a replacement of the super-structure.

In **Chapter 10**, Assessment of the deterioration of concrete structures using a finite element model, finite element (FE) modeling is used to assess the deterioration of

concrete structures is discussed. In particular, focus is placed on reviewing the state of the art of FE model updating techniques. To illustrate the potential of the method, a case study is presented and discussed in detail.

Innovative materials for concrete repair and rehabilitation are the subject of Part II (Chapters 11–20).

Chapter 11, Geopolymer mortars based on different aluminosilicates, presents geopolymeric repair mortars based on metakaolin, fly ash and slag. This chapter also includes some comments about the EN 1504-3 requirements for the performance (including durability) and the safety of products and systems to be used for the structural and non-structural repair of concrete structures.

Chapter 12, Geopolymers mortars based on a low reactive clay, discloses results of an investigation concerning the development of geopolymeric repair mortars based on a low-reactive Tunisian clay. Geopolymeric mortars were studied for workability, compressive strength, adhesion, unrestrained shrinkage and modulus of elasticity. Several concrete beams, rehabilitated with a metallic grid and geopolymeric mortars were also tested for flexural strength.

Chapter 13, Assessment of corrosion protection methods for reinforced concrete, presents an evaluation of different prevention and control methods for the corrosion of reinforcing steel embedded in concrete after exposure to aggressive environments, including chlorides and/or carbonation. The methods include: the addition of permeation-reducing materials, the application of electrochemical methods, and the use of a geopolymer coating.

Chapter 14, Sulfoaluminate cement based concrete, concerns the synthesis of sulfoaluminate cement using primary and alternative raw materials, its hydration reaction with the presences of admixtures and OPC, its durability, and its usages for repairing in concrete infrastructures.

Chapter 15, Engineered cementitious composites based concrete, surveys Engineered Cementitious Composites (ECC) as new generation high-performance concrete repair and rehabilitation materials. Mechanical, dimensional stability, and durability properties of these High Performance Fiber Reinforced Cementitious Composites are discussed, along with a number of successful field applications.

Chapter 16, Self-healing concrete with encapsulated polyurethane, addresses the case of bacteria-based concrete. Production aspects of bacteria, suitable for concrete applications, are reviewed, including some cost-related comments. The cases of direct addition of bacteria to concrete and the application of bacteria for concrete surface protection are discussed in detail. Protection strategies, through encapsulation or immobilization of bacteria, are reviewed. Important data and discussion concerning the application of encapsulated bacteria for self-healing concrete are included.

Chapter 17, Concrete with super absorbent polymer, reviews self-healing concrete using encapsulated polyurethane. Its resulting crack closure efficiency, regain in impermeability, mechanical properties, and durability is demonstrated. The possible extension in service life which can be obtained through the use of this self-healing technique is described.

Chapter 18, Concrete with self-sensing properties, presents an overview of these properties and its effects on fresh and hardened concrete. It then discusses potential applications in concrete, including the use of SAP as an admixture for internal curing to mitigate autogenous shrinkage, improve freeze-thaw resistance, and induce self-sealing/healing of cracks. The focus is to review recent studies of SAP in concrete, identify gaps in knowledge and highlight future research needs.

Chapter 19, Bacteria based concrete, gives an overview on the current state of development of the technology of self-sensing concrete, also highlighting the most fruitful research, directions for the full development of its potential. Topics covered in the chapter include composition and processing of self-sensing concrete, strain sensing methods and models, main fields of applications, research trends and open problems.

Chapter 20, Bio based admixture with substances derived from bacteria for the durability of concrete, assesses the performance of bio-based admixture as corrosion inhibitor for steel bars used in concrete as reinforcement. Electrochemical methods, such as linear polarization and impedance spectrometry, were used to check the influence of the bioadmixture towards steel corrosion.

Finally, Part III presents Design, LCC, LCA and several case studies (**Chapters 21–25**).

Chapter 21, Eco-efficient design of concrete repair and rehabilitation, covers eco-efficient design of concrete repair and rehabilitation. A framework for eco-efficient design is presented and a case study concerning a concrete mix design for a reinforced concrete beam is included.

Chapter 22, Cost-effective design to address climate change impacts, poses the problem of adaptation for deteriorating RC structures, due to climate change actions. It describes a framework for evaluating the cost-effectiveness of adaptation measures that accounts for deterioration models, probabilistic methods, and cost-benefit analysis. The methodology is illustrated with an example focusing on cost-effective adaptation of existing RC structures placed in coastal French cities.

Chapter 23, Life cycle cost and performance analysis for repair of concrete tunnels, discusses concrete tunnel maintenance: from the tunnel structure, deteriorations and maintenance practice, to the eco-efficient maintenance. In order to realize the maximum utilization of the facility with the minimum LCC, a framework was proposed with the performance and LCC as the benchmarks for the decision-making, and was successfully applied to a tunnel.

Chapter 24, Life cycle analysis of strengthening concrete beams with FRP, analyses the implications, with respect to the environmental dimension of sustainable development, resulted from considering different carbon fiber reinforced polymers for strengthening reinforced concrete beams.

Chapter 25, Life cycle analysis of repair of concrete pavements, closes Part III with a chapter on the current state-of-practice in life-cycle cost analysis (LCCA) and life-cycle assessment (LCA) of concrete pavement as critical to developing eco-efficient concrete pavement repair solutions for overall sustainability.

References

- Araos, M., Berrang-Ford, L., Ford, J., Austin, S., Biesbroek, R., Lesnikowski, A., 2016. Climate change adaptation planning in large cities: a systematic assessment. *Environ. Sci. Policy*. 66, 375–382.
- Bartuli, C., Cigna, R., Fumei, O., Valente, T., 2010. Critical examination of European Standard EN 1504 for products and systems for concrete protection and repair. In: 2nd International Conference on Sustainable Construction Materials and Technologies, pp. 341–348.
- Bastidas-Arteaga, E., Stewart, M.G., 2015. Damage risks and economic assessment of climate adaptation strategies for design of new concrete structures subject to chloride-induced corrosion. *Struct. Saf.* 52, 40–53.
- Bastidas-Arteaga, E., Schoefs, F., Stewart, M., Wang, X., 2013. Influence of global warming on durability of corroding RC structures: a probabilistic approach. *Eng. Struct.* 51, 259–266.
- Betts, R., Jones, C., Knight, J., Keeling, R., Kennedy, J., 2016. El Niño and a record CO₂ rise. *Nat. Clim. Chang.* 6, 806–810.
- Bossio, A., Monetta, T., Bellucci, F., Lignola, G., Prota, A., 2015. Modeling of concrete cracking due to corrosion process of reinforcement bars. *Cem. Concr. Res.* 71, 78–92.
- Casas, J., 2015. The bridges of the future or the future of bridges. *Front. Built Environ.* Available from: <http://dx.doi.org/10.3389/fbuil.2015.00003>.
- Clayton, R., 2001. Editorial: is sustainable development an oxymoron? *Trans. Inst. Chem. Eng.* 79 (Part B), 327–328.
- Costa, A., Appleton, J., 2002. Cases studies of concrete deterioration in a marine environment in Portugal. *Cem. Concr. Compos.* 24, 169–179.
- Davalos, J.F., 2012. Advanced materials for civil infrastructure rehabilitation and protection. Seminar at The City College of New York, New York.
- Delatte, N., 2009. Introduction. In: Delatte, N. (Ed.), *Failure, Distress and Repair of Concrete Structure*. Woodhead Publishing Limited, Cambridge, UK.
- de Medeiros, M.H.F., Pereira, E., Quarcioni, V.A., Helene, P.R.L., 2016. Surface treatment systems for concrete in marine environment: effect of concrete cover thickness. *REM Int. Eng. J.* 69. Available from: <http://dx.doi.org/10.1590/0370-44672014690092>.
- Elrakib, T., Arafa, A., 2012. Experimental evaluation of the common defects in the execution of reinforced concrete beams under flexural loading. *HBRC J.* 8, 47–57.
- EN 1504, 2004. *Products and Systems for the Protection and Repair of Concrete Structures. Definitions, Requirements, Quality Control and Evaluation of Conformity*. European Committee for Standardization, Brussels.
- Giordano, T., 2012. Adaptive planning for climate resilient long-lived infrastructures. *Util. Policy*. 23, 80–89.
- Glasser, F., Marchand, J., Samson, E., 2008. Durability of concrete. Degradation phenomena involving detrimental chemical reactions. *Cem. Concr. Res.* 38, 226–246.
- Hansen, J., Sato, M., 2016. Regional climate change and national responsibilities. *Environ. Res. Lett.* 11. Available from: <http://dx.doi.org/10.1088/1748-9326/11/3/034009>.
- Hansen, J., et al., 2013. Assessing “dangerous climate change”: required reduction of carbon emissions to protect young people, future generations and nature. *PLoS One*. 8, e81648.
- Hansen, J., et al., 2016. Ice melt, sea level rise and superstorms: evidence from paleoclimate data, climate modeling, and modern observations that 2°C global warming could be dangerous. *Atmos. Chem. Phys.* 16, 3761–3812.

- Hansen, J., Sato, M., Kharecha, P., von Schuckmann, K., Beerling, D.J., Cao, J., et al., 2017. Young people's burden: requirement of negative CO₂ emissions. *Earth Syst. Dynam.* Discuss. Available from: <http://dx.doi.org/10.5194/esd-2016-42>.
- Holloway, L.C., 2011. Key issues in the use of fibre reinforced polymer (FRP) composites in the rehabilitation and retrofitting of concrete structure. In: Karbhari, V.M., Lee, L.S. (Eds.), *Service Life Estimation and Extension of Civil Engineering Structures*. Woodhead Publishing Limited, Cambridge, UK.
- Kennedy, C., Corfee-Morlot, J., 2013. Past performance and future needs for low carbon climate resilient infrastructure – an investment perspective. *Energy Policy*. 59, 773–783.
- Kennedy, C., Ibrahim, N., Hoornweg, D., 2014. Low-carbon infrastructure strategies for cities. *Nat. Clim. Chang*. 4, 343–346.
- Monteiro, A., Gonçalves, A., Gulikers, J., Jacobs, F., 2015. Basis for the statistical evaluation of measured cover depths in reinforced concrete structures. In: Beushausen, A., Luco, L. (Eds.), *Performance-Based Specifications and Control of Concrete Durability*. RILEM State-of-the-Art Reports, vol. 18. Springer, Dordrecht, Netherlands, pp. 267–299.
- Mora, E., 2007. Life cycle, sustainability and the transcendent quality of building materials. *Build. Environ*. 42, 1329–1334.
- Navigant Research, 2014. *Transportation forecast: light duty vehicles*. <<http://www.navigantresearch.com/research/transportation-forecast-light-duty-vehicles>>.
- Pacheco-Torgal, F., 2014. Eco-efficient construction and building materials research under the EU Framework Programme Horizon 2020. *Constr. Build. Mater*. 51 (1), 151–162.
- Pacheco-Torgal, F., Jalali, S., Fucic, A. (Eds.), 2012. *Toxicity of Building Materials*. Woodhead Publishing Limited, Elsevier Science and Technology, Cambridge, UK.
- Pacheco-Torgal, F., Cabeza, L.F., Labrincha, J.A., de Magalhães, A. (Eds.), 2013. *Eco-efficient Construction and Building Materials: Life Cycle Assessment (LCA), Eco-labelling and Case Studies*. Woodhead Publishing Limited, Elsevier Science and Technology, Cambridge, UK.
- Pei, H., Li, Z., Zhang, J., Wang, Q., 2015. Performance investigations of reinforced magnesium phosphate concrete beams under accelerated corrosion conditions by multi techniques. *Constr. Build. Mater*. 93, 989–994.
- Rehman, S., Ibrahim, Z., Memon, S., Jameel, M., 2016. Nondestructive test methods for concrete bridges: a review. *Constr. Build. Mater*. 107, 58–86.
- Report, 2012. *A new economic analysis of infrastructure investment*. Prepared by the department of the Treasury with the council of economic advisers. <<http://www.treasury.gov/resource-center/economic-policy/Documents/20120323InfrastructureReport.pdf>>.
- Rockström, J., Steffen, W., Noone, K., Persson, Å., Chapin III, F.S., Lambin, E., et al., 2009. Planetary boundaries: exploring the safe operating space for humanity. *Ecol. Soc*. 14 (2), 32.
- Saha, M., Eckelman, M., 2014. Urban scale mapping of concrete degradation from projected climate change. *Urban Clim*. 9, 101–114.
- Schlangen, E., Sangadji, S., 2013. Addressing infrastructure durability and sustainability by self healing mechanisms-Recent advances in self healing concrete and asphalt. *Procedia Eng*. 54, 39–57.
- Schmidheiny, S., 1992. *Changing Course: A Global Perspective on Development and the Environment*. MIT Press, Cambridge, MA.
- Seto, K.C., Guneralp, B., Hutyra, L.R., 2012. Global forecasts of urban expansion to 2030 and impacts on biodiversity and carbon pools. *PNAS*. 109 (40), 16083–16088.

- Stewart, M., Wang, X., Nguyen, M., 2011. Climate change impact and risks of concrete infrastructure deterioration. *Eng. Struct.* 33 (4), 1326–1337.
- Talukdar, S., Banthia, N., 2013. Carbonation in concrete infrastructure in the context of global climate change: development of a service lifespan model. *Constr. Build. Mater.* 40, 775–782.
- Wang, X., Nguyen, M., Stewart, M.G., Syme, M., Leitch, A., 2010. Analysis of Climate Change Impacts on the Deterioration of Concrete Infrastructure – Part 2: Modelling and Simulation of Deterioration and Adaptation Options. CSIRO, Canberra, 444 p.
- WHO, 2014. Urban population growth. Global Health Observatory. <http://www.who.int/gho/urban_health/situation_trends/urban_population_growth_text/en/>.
- Yan, L., Chouw, N., 2012. Behavior and analytical modeling of natural flax fibre reinforced polymer tube confined plain concrete and coir fibre reinforced concrete. *J. Compos. Mater.* 47, 2133–2148.

Part I

Deterioration assessment

This page intentionally left blank

Service life estimation of concrete infrastructures

2

Robert E. Melchers and Igor A. Chaves
The University of Newcastle, Newcastle, NSW, Australia

2.1 Introduction

Reinforced concrete (RC) can be a wonderful material for infrastructure applications, able to provide high structural strength and long-term durability, even in severe exposure environments. More than 100 years of practical experience supports its use (Broomfield, 1999; Gjorv, 2009). It can, however, also behave quite poorly in similar environments, with deterioration of the concrete itself and—significantly for infrastructure applications—the faster-than-expected rate of corrosion of its reinforcement (Gjorv, 1971, 1994). Reinforced concrete structures prone to deterioration are usually those not protected from the environment. Sometimes they are prone to material degradation or damage from loading that may cause concrete cover to crack. Examples include: RC bridges, reinforced concrete road decks, RC railway sleepers, concrete-lined water channels and retaining walls, harborside piers and other structures, and offshore oil and gas platforms.

If the concrete surfaces of a RC structure are protected by a physical barrier such as ceramic or other low-permeability tiles, protective coatings of durable paints or bituminous materials, or enclosed within the weather-proof skin of a building, long-term durability is unlikely to be a design consideration or a problem for asset owners. Local failures of such protective systems, however, can cause serious problems, for the same underlying reasons as those to unprotected RC structures. To be adequate, protective systems must be well-designed and properly applied. They also require adequate (and periodic) maintenance.

To protect steel reinforcement against corrosion, it is possible for some types of RC structures to use cathodic protection. The electrons required to keep the steel from corroding are supplied from another source, either a sacrificial metal (such as zinc or aluminum) or by a direct current through a so-called “impressed current” system. Both these methods can work only for steels that are wet. They also require maintenance and usually are relatively expensive with an on-going annual cost. These techniques do not work to protect the concrete matrix.

For modern infrastructures, the decision whether to protect or not, and the form the protection might take may hinge on the expected life with and without protection, and on overall economics. Many older RC structures are not protected. This chapter deals with unprotected concrete structures and the estimation of their expected service life.

Estimating the expected life of an item of infrastructure, or the expected safety over a defined lifetime, may be considered a problem in structural reliability. In its simplest form it considers just one stochastic loading process $Q(t)$ applied to a structure. The strength or resistance capability of that structure is then considered to have an uncertain strength, defined, at any time t , by the random variable $R(t)$ (Melchers, 1999). Fig. 2.1 shows these variables and their corresponding probability density functions at time t , as well as the notion that the strength deteriorates as a function of time. This may include deterioration factors like fatigue. The expected life t_L for a given, acceptable level of the probability of failure, p_{fA} is the matter of most concern to structural engineers and asset owners, even though it is seldom presented to them in the way shown here. Equally, the expected probability of failure p_f for a defined lifetime is of interest. Furthermore, for more complex systems, both $Q(t)$ and $R(t)$ are made up of multiple components and may be stated as $\mathbf{Q}(t)$ and $\mathbf{R}(t)$.

The probability of failure $p_f(t)$ can be estimated or predicted using conventional structural systems reliability analysis (Melchers, 1999):

$$p_f|t = \iint_{D_f} f_Q(x) f_R(x) dx \quad (2.1)$$

where $f_Q(t)$ is the (conditional) probability density function for Q at time t and similarly for R at t . The failure domain D_f conventionally is defined by a performance function (or Limit State function) that may be stated as $G(\mathbf{X}) = G(\mathbf{R}, \mathbf{Q}) = R - Q < 0$, where \mathbf{X} collects all the relevant random and other variables which, for the simplest case shown here, are simply Q and R . Of course $G(\mathbf{X})$ is time dependent if one or more of the components of \mathbf{X} is time-dependent. Stochastic variables may be included in a variety of ways but often the simplest approach is to consider them using a simple combination rule (Melchers, 1999). It is now clear that to estimate the probability of failure $p_f(t)$ as a function of time t requires knowledge of

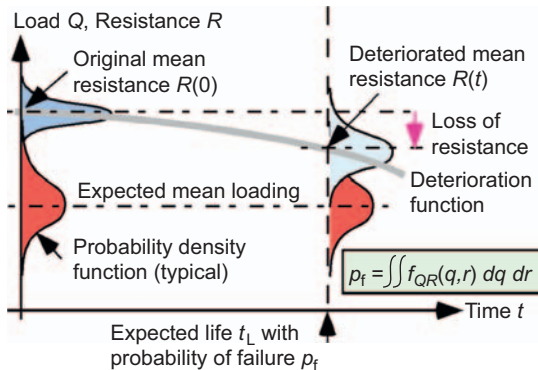


Figure 2.1 Schematic relationship between loading process $Q(t)$, deteriorating resistance $R(t)$ and probability of failure p_f .

the functional form of the decrease in $R(t)$, that is, of the deterioration function. This is the subject of much of the present chapter, although, as will be seen, for most practical situations that function is relatively complex and itself influenced by a considerable number of potential variables. Once that function is known, the actual estimation of service life, or probability of failure, according to Eq. (2.1) can be performed using techniques described elsewhere (Melchers, 1999; Paik and Melchers, 2008).

Before proceeding, it should be noted that increasingly there is interest in “whole of life” or “life-cycle cost” analysis. This considers not just the probability of violating some defined probability limit, or a defined minimum lifetime, but the total expected cost C_E , including allowances for renovation, repair and maintenance costs and their probability of occurrence as well as the cost(s) of failure and the probability of failure:

$$C_E = \sum p_i C_i \quad (2.2)$$

where p_i is the (conditional) probability for the occurrence of event i that has corresponding cost C_i , and the i ranges over the full range of possible scenarios (maintenance possibilities, repair scenarios, failure scenarios, etc.). The p_i values may be obtained, if enough information is available, from estimates such as given by Eq. (2.1), or, more generally may be estimated subjectively or based on historical data (Bakker et al., 2017).

The concept of adding steel bars to concrete to produce structures dates back to the late-1800s but its commercial use did not commence until the early 1900s. Much of the early efforts were devoted to making the concept feasible, practical, and economic. Most attention was given to structural strength issues and the development of fundamental theory for design purposes. Much of this is now mature, and increasing practical and research attention is being given to the production of higher-strength RC structures with less cement, in part because of economics and in part because of the environmental impacts, notably the production of carbon dioxide associated with the making of cement. As will be seen, this trend has implications for durability.

Early in the history of reinforced concrete structures, some concern was expressed about their durability, particularly in marine environments but it appears experiences varied widely (Wig and Ferguson, 1917; Wakeman et al., 1958; Lewis and Copenhagen 1959; Lewis, 1962). Development of understanding of the causes of deterioration and of the processes involved has progressed since, but as described in Section 2.2, is still not complete. One of the difficulties is the correlation between actual experience under realistic (field) conditions, perhaps over many decades, and what can be learnt from laboratory testing, usually under conditions designed to accelerate the processes. As described in the rest of this chapter, efforts to increase understanding is the subject of on-going research, increasingly focussed on building models for predicting the amount or rate of deterioration, both for use in lifetime estimation and for specifications in design codes. Section 2.3 deals with one form of deterioration potentially leading to reinforcement corrosion, namely

“carbonation,” while [Section 2.4](#) considers the important problem of “chloride-induced” reinforcement corrosion. How this relates to actual field experience is discussed in [Section 2.5](#). It includes a small number of case studies to illustrate the point that well-made reinforced concrete structures can survive many decades with no apparent (and usually no actual) evidence of reinforcement corrosion. How these data should be reconciled with some of the conventional thinking about chloride-induced corrosion alongside fundamentals in corrosion mechanics is considered in [Section 2.6](#). This section also brings the discussion to the cutting edge of current research understanding the processes involved in leading up to reinforcement corrosion and to its quantitative modeling. [Section 2.7](#) deals with implications for practical structures—many of these are entirely consistent with what is considered good practice based on empirical experience. The new research findings, however, also suggest new ways of increasing long-term durability.

2.2 Causes of reinforced concrete infrastructure deterioration

2.2.1 Overview

The causes of deterioration of a RC structure fall in two broad categories: deterioration of the concrete itself, and deterioration (i.e., corrosion) of the steel reinforcement. One may lead to the other if, for example, the concrete cover to the reinforcement is damaged, providing little, if any, protection and the reinforcement might as well be exposed directly to the environment. Unfortunately, the cases of reinforcement corrosion in practice have not always taken this possibility into consideration.

2.2.2 Physical damage

Physical damage of concrete, such as damage to the concrete cover of the reinforcement and the cracking of concrete, should be considered. Careful analysis of the corrosion of reinforcement for concrete highway bridges in Germany ([Volkswein and Dörner, 1986](#)), Austria ([Lukas, 1985](#)), and the US ([Beaton and Stratfull, 1963](#)) showed that the prime cause of extensive reinforcement corrosion was the damage done by motor vehicles and lorries to the bridge deck concrete cover, and that this was particularly bad where no bituminous wearing or riding course had been applied. The blame for the aggressive corrosion is usually placed on the use of calcium and sodium chlorides during frost periods, but it is clear that severe corrosion would have occurred in any case.

Cracks in concrete have always provided a source of concern. If the cracking is along the direction of reinforcement bars, it is highly likely that the bars underneath are undergoing active corrosion. Cracks transverse to the reinforcement that did not intersect them have been considered to have no influence on the initiation of

reinforcement corrosion, provided the cracks were of moderate size (Beeby, 1978). This was based on the results of relatively short-term testing of concrete specimens with longitudinal bars and pre-formed cracks, using sodium chloride (NaCl) solutions and in laboratory conditions. This led to cracks up to 0.3 mm crack-opening size to be considered acceptable, including for observations of existing structures. More recently, however, it has been found that even hairline cracking, barely visible to the naked eye, can cause very severe localized corrosion of reinforcement if the crack intersects the reinforcement (e.g., Melchers and Li, 2006). In many cases, there are tell-tale rust marks on the surface, but not always. The reasons for such severe, and dangerous reinforcement corrosion will become clear in Section 2.6.

2.2.3 Material-related deterioration

The making of concrete has varied little since the early 1900, except for tighter controls on mix proportions and a tendency to use less cement if possible, by the use of various additives. These are, however, a relatively recent phenomenon. During the 1960s, there was a gradual change in the making of cement. It involved the use of higher clinkering temperatures and finer grinding. There have been claims that this change has had an effect on the durability of concretes, but objective evidence for this claim is difficult to find and it did not appear as a critical issue in a wide-ranging survey of the reinforcement durability of many structures (Melchers and Li, 2009). Comparisons of the older and newer cements show relatively little change in the critical components (Cornish and Jackson, 1982; Nixon and Spooner, 1993). There are many other variables that can influence durability (Hewlett, 1988).

The setting reaction when cement is mixed with water and aggregates produces a material with a high pH—typically 13.5–14. The higher pH values are imparted by the alkalis NaOH and KOH, while the principal alkali, $\text{Ca}(\text{OH})_2$ imparts a pH of about 12. In contrast, solutions of the almost-insoluble calcium carbonate (CaCO_3) have a pH of around 10.

Probably the most important aspect for the durability of concretes is the “alkalinity” of the concrete, perhaps more easily visualized as its “acid-buffering capacity.” Good quality concretes have a high alkalinity and thus can absorb a large amount of acid attack and still retain useful pH values. As usual, the alkalinity of concrete can be considered in terms of the concentration of hydroxide ions, i.e., $[\text{OH}^-]$.

Since concretes are made from aggregates and the highly alkaline cement, it is possible for certain reactions to occur between these components. This can give rise to alkali-aggregate reactions (AAR) and alkali-silica reactions (ASR) that damage the concrete matrix (Jensen, 1996; Richardson, 2002; Gjorv, 2009).

2.2.4 Atmosphere-related deterioration

Atmospheric deterioration is mainly through the physical effect of weather wearing away the finer particles of a concrete surface, and, in polluted atmospheres, the possibility of chemical attack, particularly from airborne sulfur. In moist conditions these form sulfuric acid that attacks the alkaline surfaces of the concrete.

Another, indirect deterioration mechanism is that of carbonation (Parrott, 1987; Richardson, 2002). Particularly for concrete surfaces which are only occasionally or periodically wet, atmospheric carbon dioxide (“acid rain”) can diffuse into the concrete and convert the critical alkali, calcium hydroxide ($\text{Ca}(\text{OH})_2$), to calcium carbonate (CaCO_3). This lowers the pH of the concrete—in particular its surface—and thus its resistance to chemical attack. If sufficiently aggressive, carbonation also has an effect on reinforcement corrosion (see below).

2.2.5 Effect of seawater

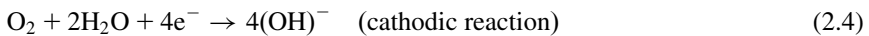
Surprisingly, unpolluted seawater tends to have a protective effect on concrete. This is as a result of the high carbonate content (calcium and magnesium carbonates) of natural seawater, and the tendency for these carbonates to deposit as solid species on the high pH surfaces, particularly of new concrete. The deposits provide a layer of carbonates that help reduce diffusion of gasses such as oxygen into the concrete, even if such diffusion is very slow in water-saturated concretes.

2.2.6 Reinforcement corrosion

Like all other forms of wet corrosion, the corrosion of steel reinforcement involves chemical reactions. Some are known as electrochemical reactions because they may occur at slightly different locations and thus transportation of electrons is required to balance the equations. Typically, one part of the reaction is the oxidation of ferrous iron (at anodic sites) (Jones, 1996):



This releases ferrous ions into the adjacent water and allows electrons (e^-) to move through the metal to other locations. Typically, these are the cathodic site(s), where the electrons combine with (i.e., reduce) oxygen dissolved in water to form a hydroxide:



This reaction (2.4) is then followed by a purely chemical reaction, at these cathodic sites, to produce the usual first form of hydrated iron oxide (i.e., rust):



In practice the $\text{Fe}(\text{OH})_2$ may oxidize further to other forms of rust such as magnetite, but this does not change the basic scenario. Note that Eqs. (2.3) and (2.4) are inter-connected through the transfer of electrons between anodic and cathodic sites. (It is noted that cathodic protection works through interrupting this flow of electrons or obtaining it from another metal rather than from Fe in Eq. (2.3). In both

cases this reduces the demand for electrons from the anodic reaction, and thus the metal loss.)

Like all chemical reactions, Reactions (2.3–2.5) can occur only if the relevant thermodynamic requirements are met. These are the Gibbs free energy requirements in chemistry. In corrosion theory, it is more common to employ the equivalent electrochemical form given by the well-known Pourbaix diagram for the metal and liquid being considered (Jones, 1996). In both cases, the criterion depends on the pH of the solution. Whether the reaction occurs also depends on the available electrochemical potentials. These are either imposed (such as by an applied voltage, as in electrochemical tests (Huet et al., 2005)) or are those freely available from the metal and the liquid compositions. This means that in pure water, general corrosion of ferrous iron can occur only for $\text{pH} < \text{approximately } 9$ (Jones, 1996; Chitty et al., 2005). For waters containing chlorides, however, the electrochemical potentials (free energies) are higher and it has been observed that pitting corrosion (but not much general corrosion) can occur at much higher pH values—up to ~ 13 (Pourbaix, 1970). It is important to note that all these conditions refer to whether corrosion can actually occur. They say nothing about the rate of corrosion and thus about its severity in practice.

Corrosion can continue to occur only if the thermodynamic requirements continue to be met. The rate of the inter-connected reactions (2.3) and (2.4) is controlled, in most cases, by the rate at which electrons can transfer between them. For most metals, and slightly less so for water, the conductivity for electron flow is very high and not limiting. Often, the limiting condition is the rate at which gaseous oxygen can accept electrons to become ionized oxygen as in Reaction (2.4). Usually, this is limited by the rate of oxygen availability and, in turn, this is limited by diffusion considerations. In drier conditions, the rate of the reaction may be limited also by the availability of water to combine with oxygen to allow (2.4) to proceed.

Consequently, if oxygen is not available, corrosion should not occur. Even small amounts of oxygen, however, permit some corrosion and, if combined with other conditions, could cause severe corrosion—particularly localized corrosion. One of these is the presence of species of very low pH. For example, for $\text{pH} < 4$, corrosion can be severe (Jones, 1996). The other is the presence of chlorides or similarly aggressive species (e.g., other halides). These have always been recognized as particularly aggressive—shown to be so in laboratory experiments as well as in, say, coastal atmospheric exposures of steels. But care is required in translating observations from one environment to another. In studying the corrosive effect of various salts, including NaCl, on immersed strips of steel, Heyn and Bauer (1908) observed almost no difference in corrosion mass loss over an extended period of time. The observations caused considerable controversy, particularly since the electrochemical nature of corrosion was at that time still not well-understood (Evans, 1960). Subsequently, however, Brasher (1967) and Mercer and Lumbard (1995) have provided both explanations and supporting evidence that the critical aspect of the 1908 experiments was that the solutions were stagnant. Under these conditions even a small availability of oxygen was sufficient to create an oxidation layer sufficient to

out-compete the chlorides. In fact, [Mercer and Lumbard \(1995\)](#) have shown clearly, using rotating specimens in chlorinated water, that chlorides become progressively more important on corrosion mass loss as the speed of rotation is increased. At zero water velocity, the concentration of chlorides had no effect on corrosion mass loss. These observations are important because inside well-made concretes, conditions will be stagnant, but they apply only to general corrosion such as measured by mass loss. For pitting, the above observations about pitting in aerated chloride solutions, apply. Once the pitting process has been established, however, pitting can continue under almost-anoxic conditions and can become very severe ([Wranglen, 1974](#); [Jones, 1996](#)).

2.2.7 Summary

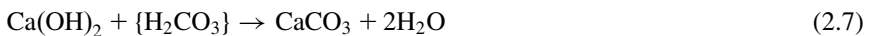
In practice, usually the most critical factor in the service life of RC structures is reinforcement corrosion. Its causes must be separated from damage to the concrete cover. Whether from externally applied loadings such as traffic loads, from environmental factors such as thermal cracking, or from internal stresses caused by AAR or ASR. In the following two sections, the two major causes of reinforcement corrosion are considered: carbonation-induced corrosion and chloride-induced corrosion. They draw on the summary of the basic mechanics and reactions for corrosion reviewed above.

2.3 Carbonation-induced corrosion of reinforcement

Carbonation is the process in which the alkaline calcium hydroxide Ca(OH)_2 in the concrete reacts with carbon dioxide (CO_2) to produce calcium carbonate (CaCO_3) (and also a limited amount of calcium bicarbonate) within the concrete matrix ([Hunkeler, 2005](#)). The reaction is at least a two-step process:



where the { } is used to indicate that product, carbonic acid, usually exists mainly as a solution of the low solubility CO_2 in water. It is a weak acid with, at atmospheric pressure, a pH around 5.5–6 and thus will react with the Ca(OH)_2 in the concrete to form CaCO_3 :



Carbonation also may be the result of carbon dioxide reacting with the hydrated silicon and aluminum oxides and the sodium and potassium hydroxides (NaOH and KOH) in the cement.

Typically, the gaseous CO_2 diffuses from the atmosphere through the concrete cover. Considering its large molecular size, typically the diffusion is slow—much

slower than that of oxygen or water, and for most good quality high density low permeability concretes carbonation is not of practical concern (Parrott, 1987). Furthermore, the diffusion of CO₂ through water, as might be present in the pores of concretes, is very slow. This means that carbonation is very unlikely for wet concretes or concretes under water.

There is a long history of inferring that there is a causal relationship between the pH of ~ 10 resulting from the carbonation process (Reactions 2.6 and 2.7), and the initiation of reinforcement corrosion. This follows observations that, in concretes carbonated as far as the reinforcing bars, the bars usually are corroded. Additionally, laboratory tests using alkaline solutions or accelerated testing appeared to support the inference (Parrott, 1987). Although this simple correlation has been widely accepted, it is simplistic and there are some problems with it. Some texts refrain from mentioning pH values in their discussion of carbonation (e.g., Bertolini et al., 2004).

As noted above, corrosion theory and controlled experiments have shown that, under normal oxygenated conditions, steel in immersion exposures requires the pH to be below ~ 9 for general corrosion to occur. The pH can be higher only in the presence of halides such as chlorides, and then pitting is dominant. Since carbonation does not involve chlorides, a pH of ~ 10 should be protective. In fact, this is one of the mechanisms for corrosion protection set up by impressed current protection for steels in seawater (Jones, 1996). In a classic field trial (Humble, 1949), when the current was applied, there was a gradual build-up of calcium carbonates on the metal surface and no corrosion. When subsequently the current was turned off, no corrosion took place until such time as the calcium carbonate layers fell off, months later, due to wave action. This demonstrates that calcium carbonate is protective and does not directly cause corrosion. Similar findings are available for concretes that retained their pH above 10 for more than 60 years, and only where the pH had fallen below 9, such as at cracks in the concrete permitting entry of sea and rain water, was corrosion observed (Melchers et al., 2009). And, as discussed further below, there is field evidence that concretes made with limestones or non-reactive dolomites take much longer to show signs of reinforcement corrosion.

A closer examination is required of the carbonation process to explain these apparent contradictions. One of the earliest descriptions of observations of concretes that were considered to have suffered carbonation noted a miss-match between the apparent front of the carbonated zone, as measured by pH tests, and whether the reinforcement showed corrosion (Hamada, 1969). The explanation is not difficult to find. As CO₂ diffuses into the concrete it will be neutralized by the alkalinity of the concrete, and as further CO₂ enters, the neutralization front will move further into the concrete, leaving behind CaCO₃ (Fig. 2.2). Also, under high CO₂ concentrations inside the concrete, calcium bicarbonate (Ca(HCO₃)₂) may result, and this has some additional alkaline buffering capacity (Hunkeler, 2005). The level to which the concrete pH then falls is an interesting question since it is generally assumed that it will fall low enough for corrosion to initiate, that is to pH < 9.

Because the measurement of pH inside concretes is difficult, many of the experiments have used solutions to simulate concrete pore waters. Even then, for

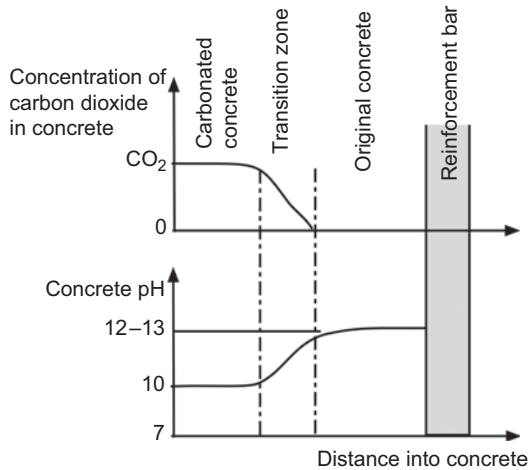


Figure 2.2 Migration of CO₂ into concrete showing progressive loss of pH and the transition zone between carbonated concrete and the original concrete with high pH.

carbonates in solution and for rock samples, the measurement of pH is known to be difficult and liable to give different results, depending on the environmental conditions. Under anaerobic conditions, the pH for a saturated solution with calcium carbonate is ~ 9.9 . As air is introduced the pH falls slowly to around 8.4 at standard temperature and pressure (Garrels and Christ, 1965). This is one reason why concrete structures, broken open, eventually show much worse corrosion than when first broken open. It demonstrates the importance of the permeability (mainly to oxygen) of the concrete. High quality concretes are far more likely to have close to anaerobic conditions next to the reinforcement bars (as discussed further in Sections 2.4 and 2.5).

As the CO₂ continues to diffuse into the concrete, the carbonation front will move further into the concrete. Depending on the rate at which neutralization can occur, relative to the rate of ingress of CO₂, some CO₂ is likely to precede the carbonation front (Fig. 2.2). This means that, when all local alkalinity has been consumed, such as at the reinforcement bar, any further ingress of CO₂ will not be neutralized. It is this carbonic acid at the reinforcement bar that must be responsible for corrosion attack.

Carbon dioxide in water, as carbonic acid, is, although a weak acid, well-known in the oil and gas industry to be very aggressive in terms of corrosion attack of unprotected steels (Jones, 1996). Thus, the net result of the carbonic acid preceding the carbonation front once alkalis have been exhausted is that it causes reinforcement corrosion ahead of the carbonation front reaching reinforcing bars. This corresponds to the observations recorded by Hamada (1969) for many of the RC structures he examined in detail. In summary, it is not necessarily the lower pH of the CaCO₃ (and bicarbonate) produced by the ingress of CO₂, but the eventual

un-neutralized carbonic acid, at pH ~ 6 in normal atmospheric temperature and pressure conditions, that causes initiation of reinforcement corrosion.

Extensive literature exists for estimating the rate of inward diffusion of CO_2 and hence the “depth of carbonation” $x(t)$ as a function of exposure time t . It uses Fick’s second law (of diffusion) to obtain a relationship:

$$c_2(x, t) = c_1 \operatorname{erfc} [x/2 (D t)^{-1/2}] \quad (2.8)$$

where c_1 and c_2 are the concentrations of CO_2 in the exterior atmosphere and at the carbonation front, the latter a function of distance into the concrete x , and time t , and D = the diffusion coefficient of CO_2 in carbonated concrete (i.e., that on the left side of the transition zone in Fig. 2.2). A simplification for Eq. (2.8) is obtained using the first two terms of the approximation for the complementary error function “erfc”:

$$c_2(x, t) = c_1 [1 - (x/a)(D t)^{-1/2}] \quad (2.9)$$

where a is a constant. In the case of complete carbonation c_2 in Eq. (2.9) will be zero. Extracting x produces

$$x = Kt^{-1/2} \quad (2.10)$$

where the so-called “carbonation constant” K includes c_1 and D and is known from observations to have a wide range of typical values, varying from 2 to 6 for low permeability (high-quality) concretes to $K > 9$ for highly porous, poor-quality concretes. Various modifications to these relationships have been proposed to better fit some experimental data (e.g., Bertolini et al., 2004; Hunkeler, 2005). However, the variability in predicted carbonation depth x for defined conditions and concrete properties remains very high, typically some two orders of magnitude (Glass and Buenfeld, 1997).

Fortunately, practical experience indicates that carbonation is not a critical issue for well-made, dense, low-permeability concretes. Industry experience is that good quality concretes permit only a few millimeters of carbonation depth, even over extended periods of exposure (Parrott, 1987). Nevertheless, carbonation receives considerable discussion in reinforcement corrosion texts.

2.4 Chloride-induced corrosion of reinforcement

It has long been thought that the build-up of aggressive ions such as chlorides on the surface of the reinforcement in concrete structures will cause the reinforcement to corrode once a sufficient chloride ion concentration has been reached (e.g., Richardson, 2002; Hunkeler, 2005; Gjorv, 2009). In modern RC construction, the use of seawater has been banned for many years. It follows that the chlorides must come

from outside the concrete structure, for example from surrounding seawater or from seawater spray in coastal regions. To assist in estimating service life for such RC structures, much research attention has been given to the rate at which chloride ions can reach the reinforcement. Principally, the transport phenomenon has been taken to be diffusion, expressible through Fick's second law of diffusion (see Eqs. 2.8–2.10 above) but now with chloride concentrations. Again, the actual transport phenomenon is not purely diffusion and thus (Eq. 2.10) is an approximation. Various modifications have been proposed also in this case (e.g., Hunkeler, 2005).

The situation is complicated by the effect of environmental conditions. In the atmosphere, rain may allow chlorides close to the surface to leach out again, but leaving higher internal concentrations. This may occur also as a result of wet-dry cycling, including in tidal conditions. In fully-immersed conditions, inward chloride diffusion is usually assumed to be low as a result of the known build-up of calcium and magnesium carbonates on the concrete surface (see above). These carbonate layers are also a diffusion barrier for oxygen transport and diffusion. Overall quantification of these effects has been difficult, in part attributed to wide variations in concrete properties (Hunkeler, 2005). Practical experience supports measures to reduce chloride diffusion and other forms of transportation for RC structures directly exposed to the environment, including thick concrete cover, high density concrete, permeability-reducing additives such as protective coatings and waterproofing agents and “good-quality” workmanship. In some cases, cathodic protection may be useful.

The actual effect of chlorides was, for a long time, attributed to their direct attack on the steel reinforcement. Much research effort has focused on ascertaining the “chloride threshold” at which corrosion commences. Other investigations have focused on the ratio $[Cl^-]/[OH^-]$, i.e., ratio of the concentration of chloride ions to the concentration of hydroxide ions, following Hausmann (1988). Despite the extensive investigations, both criteria still suffer from wide variability and problems with repeatability (Bentur et al., 1997, p. 31; Angst et al., 2009). This may be due in part to the “stochastic nature of initiation of pitting corrosion. . .” (e.g., Bertolini et al., 2004) but it has been increasingly recognized that the situation is more complex. Specifically, it has become clear that the action of chlorides is not necessarily a direct attack of the steel reinforcement, although the precise mechanisms involved have remained elusive. The terminology “chloride-induced” corrosion is now current. As described in Section 2.6, some recent progress has been made, but it is first necessary to learn something from the observations of actual structures exposed to realistic environments.

2.5 Practical experience, observations and investigations

2.5.1 Introduction

By definition, durability studies require long-term observations. They cannot be replicated with confidence in laboratory trials. Although accelerated testing, for

example, can be done using salt sprays, higher temperatures, impressed current on the reinforcement, etc., the relationship of the results obtained to actual in-service behavior remains tenuous, as well as in fields other than reinforcement corrosion (Poursae and Hansen, 2009; Lee et al., 2010). An alternative is to try learning something from actual operational experience with real structures. The usual drawback is that there are few structures available for investigation, they tend to be one-off so that investigation of causative parameters is difficult, and typically they are not well-documented (or the documentation no longer exists or cannot be found). Nevertheless, the approach does have merits and can be considered an archeological one, such that with care useful observations can be made. Several investigations along these lines have been described for reinforced concrete structures (e.g., Melchers et al., 2009) as well as for materials of potential use in nuclear waste storage facilities (Chitty et al., 2005). In the following sections, the corrosion performance of a number of reinforced concrete structures exposed to marine environments is described, admittedly briefly, and a summary is given of a much wider overview of cases reported in the literature.

2.5.2 Hornibrook Bridge, Brisbane

In 2010 the 2.7 km long reinforced concrete substructure supporting the timber superstructure of a narrow bridge at Bramble Bay, Brisbane and immediately adjacent to the Pacific Ocean was demolished after some 80 years service. The substructure consisted of 879 reinforced concrete driven piles, each 400×400 mm in cross-section with (in most cases) only 4 reinforcing bars of 32 mm (1-1/4") diam. with 40 mm cover. The piles extended through the tidal and atmospheric zones, but they showed, when removed, little or no visible evidence of reinforcement corrosion and certainly no longitudinal cracking along the reinforcement (Fig. 2.3).



Figure 2.3 Piles in storage after demolition, showing no exterior evidence of internal corrosion. Even after the extended period (80+ years) of exposure in the marine atmosphere, the tidal zone and immersed, there were no signs of longitudinal cracking along the lines of reinforcement.

Several samples of the piles were taken for detailed investigation (Pape and Melchers, 2013). Some samples were cut across with a concrete saw and the pH sampled over the cross-sections. Fig. 2.4 gives one example. It shows, as did all others examined, that, even after 80 years, almost all the concrete still has a pH of at least 9 and predominantly ~ 12 . The cross-sections mostly showed no sign of reinforcement corrosion around the perimeters of the bars. The chloride levels in the concrete at the reinforcing bars were very high, up to 3% by weight of cement. This is significantly higher than any permitted by conventional design requirements (typically 0.4% by weight of cement). Steel reinforcing bars, when extracted (with considerable difficulty) from the very high strength concrete (around 60 MPa) showed almost no signs of corrosion. The few rust products were identified as those associated with corrosion under very low oxygen conditions, such as the “green” rusts.

Further investigations revealed that the bridge designer and constructor demanded high quality workmanship and always erred on the side of adding more, rather than less, cement. The likely sources of cement, sand and aggregate were identified, but no inference could be made that the materials had any significant influence on the durability performance of the piles.

Of the nearly 900 RC piles extracted from the seabed, only one was removed with any incident. That pile was found to be cracked, transversely, about half way along and about halfway through the thickness of the pile. Of the four reinforcing bars, those intersected by the transverse crack had corroded right through and some way back along the reinforcement itself. Almost no visible evidence of rust products on the exterior pile surface was noted, however, and on the cross-sectional

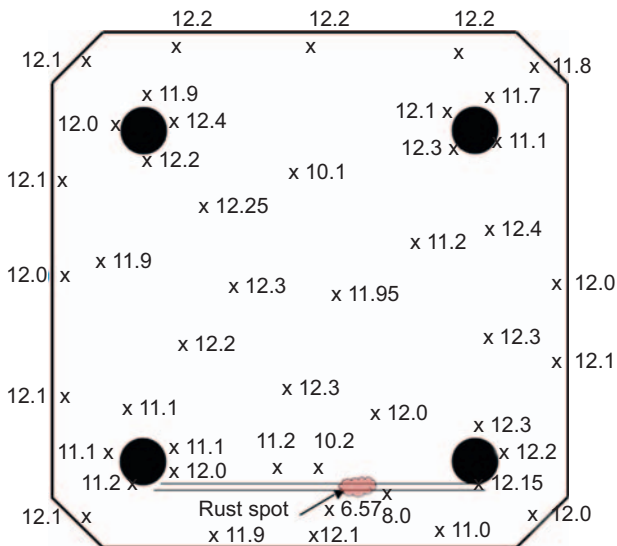


Figure 2.4 pH map of typical pile cross-section, showing pH predominantly 12, except at the one small rust spot where the pH is ~ 7 .

cracked zone there were only “watery-looking” rust stains. The likely reasons for this behavior have been described elsewhere (Melchers, 2015).

2.5.3 Handrails at Arbroath, Scotland

Immediately next to the North Sea at Arbroath on the East coast of Scotland there is a 1.6 km-long reinforced concrete balustrade constructed during 1943. It runs along and above the beach and consists of almost 1000 precast concrete handrail elements each about 2 m long and 130×150 mm in cross-section, with four 6 mm diam. steel reinforcing bars. 90% of the elements dating from 1943 were still in place in 2006, when the whole system was inspected in detail. The other 10% had been replaced in 1968 and in 1993. Remarkably, when inspected in 2006, all replacements were badly damaged by longitudinal cracking from reinforcement corrosion (Melchers et al., 2009). The 1943 concretes, however, had no longitudinal cracking.

Samples of the 1943 elements were selected at random by local Council staff and used for detailed investigation. When cut with a saw, the concrete samples showed the presence of seashells inside the concrete. This can be taken as implying the concrete was made using the local beach sands and perhaps also seawater. All samples showed very high concentrations of chlorides in the concrete, much higher than the accepted thresholds for corrosion initiation. Concrete cover and aggregate size showed wide variations in amount and size. Almost no evidence of external rust staining was observed for the whole structure, except the 1968 and 1993 elements. This may be because of the high rainfall in the area washing away soluble ferrous chloride rust products (Melchers and Li, 2009). Almost all the cross-sections of the 1943 concrete elements examined showed pH of 9–10 or more. Most notably, where rusts were observed on the cross-sections, and this was rare, the local concrete pH at reinforcement in all cases was <9 . No cases of corrosion were observed for higher concrete pH values.

When a number of lengths selected at random from the 1943 concrete handrails were broken open, they almost always revealed reinforcement that appeared to be in “as-new” condition. One section, however, revealed extremely severe corrosion at a transverse crack, with almost complete loss of the reinforcing bars. Similar to the Hornibrook Bridge, on the cracked concrete surface and inside the concrete locally, where the bars had corroded away, light watery rust staining was observed (Melchers and Li, 2009).

2.5.4 Other cases

Several other cases with features generally similar to those above include:

1. Maria Island cement works silos (1922) (Melchers et al., 2014),
2. Newcastle Harbour fortifications (1941) (Melchers, 2010a)
3. Thames Estuary forts (British Navy, Airforce) (1943) (Melchers, 2011),

4. U-Boat bunkers along the East Atlantic coast (1940s) (Melchers, 2011; Melchers and Pape, 2012),
5. Mulberry Harbour Phoenix caissons (1944) (Melchers, 2010b)
6. Concrete lighters (Severn Estuary, Sydney Harbour) (Melchers, 2010b; Melchers and Pape, 2010)
7. German highway bridges (Lukas, 1985)
8. Cylindrical bridge piers in the Gulf of Mexico (Lau et al., 2007).
9. Progreso Piers, Yucatan, Mexico (Melchers, 2015).

These cases all showed long-term durability, despite some—such as the Mulberry Harbour caissons, having been made quickly and under difficult conditions such as a shortage of skilled labor. In this case, it is clear from the records that all design efforts were concentrated on simplicity and resistance to storm conditions (Wood, 1948). No attention was given to durability. Many of the caissons are still largely intact off the Normandy coast, where they are almost entirely under water. Some caissons were not used at Normandy, however, and are in the UK, exposed for many years to primarily marine atmospheres (Fig. 2.5). Nearly all show some corrosion, but it is modest considering the length of exposure and the exposure conditions.

2.5.5 Synthesis of observations

Before all the above cases were examined, it was already proposed that there should be revision of the notion that corrosion initiation was also the beginning of serious longer-term corrosion, expressed in the well-known Tuuti (1982) model (Fig. 2.6A). This model for the progression of corrosion with time assumes that there is negligible or no corrosion in the period prior to the initiation time t_i after which corrosion becomes serious (Richardson, 2002; Hunkeler, 2005; Gjorv, 2009).



Figure 2.5 End view in 2009 of one of the two Phoenix caissons used as breakwaters in Portland Harbour, UK, showing typical condition of the concrete. Both caissons were constructed in 1943 and intended for use with the Mulberry harbours, but not used.

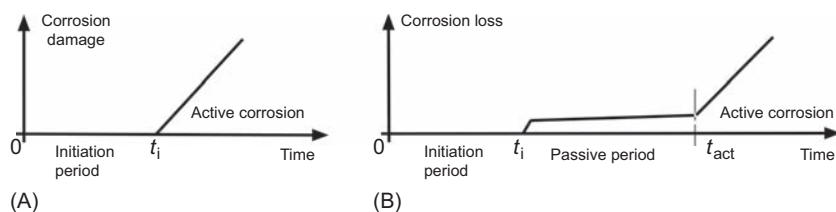


Figure 2.6 (A) Classical [Tuutti \(1982\)](#) model showing no corrosion (damage) until t_i followed immediately by progressive serious corrosion (damage), (B) modified model with separation between initiation at t_i and start of active corrosion at t_{act} .

Working with corrosion damage rather than corrosion, [Weyers \(1997\)](#) and [Bentur et al. \(1997\)](#) have proposed that serious corrosion might occur at a time later than t_i , to allow for minor cracking to facilitate chloride diffusion, such that when the chloride threshold was reached, significant and damaging corrosion could begin. A similar idea was proposed for bending cracks in beams ([Francois and Arliguie, 1999](#)).

Working with corrosion loss rather than damage, [Melchers and Li \(2006\)](#) proposed there should be separation in time between the time to initiation (t_i) and the time to active reinforcement corrosion (t_{act}) ([Fig. 2.6B](#)). The rationale for this proposal was that initiation of corrosion involves a different set of physico-chemical mechanisms to those responsible for active reinforcement corrosion. Support of this concept can be seen in the analyses of reinforced concrete structures in field situations as described below ([Melchers and Li, 2009](#)). Other support includes long-term laboratory exposures of pre-cracked beams which showed corrosion commencing soon after first exposure that “practically halted” after a short time, before increasing again much later ([Yu et al., 2015](#)).

The separation of t_i and t_{act} was used to review and analyze the reported observation given in almost 30 reports, extracted from the literature, covering around 300 individual reinforced concrete structures and compared with chloride content and with type of aggregates (fine and coarse) ([Melchers and Li, 2009](#)). Cases suspected of AAR or ASR were removed. The results are shown in [Fig. 2.7](#). It is seen that there is a difference of 10–20 years between t_i and t_{act} and that, overall, chloride concentration is not a major influencing factor. There is also a considerable difference in the trends, depending on the type of aggregate used in the concrete—limestone and non-reactive dolomites on the one hand, and igneous aggregates on the other. The concentration of chlorides next to the reinforcing bars was estimated, and in some cases showed a large degree of uncertainty, but as seen in [Fig. 2.7](#), this has little effect on the overall trends. In this regard, it is of interest that a number of (more historical) papers have described cases of good quality, apparently-durable concrete being made with seawater (and in some cases also with alkaline materials such as coral) ([Wig and Ferguson, 1917](#); [Narver, 1954](#); [Wakeman et al., 1958](#); [Dewar, 1963](#); [Mather, 1964](#); [Boqi et al. 1983](#); [Burnside and Pomerening, 1984](#)). It is noted that the use of seawater as mixing water for making concrete was not prohibited in most countries until the 1960s, apparently in part as a result of tests

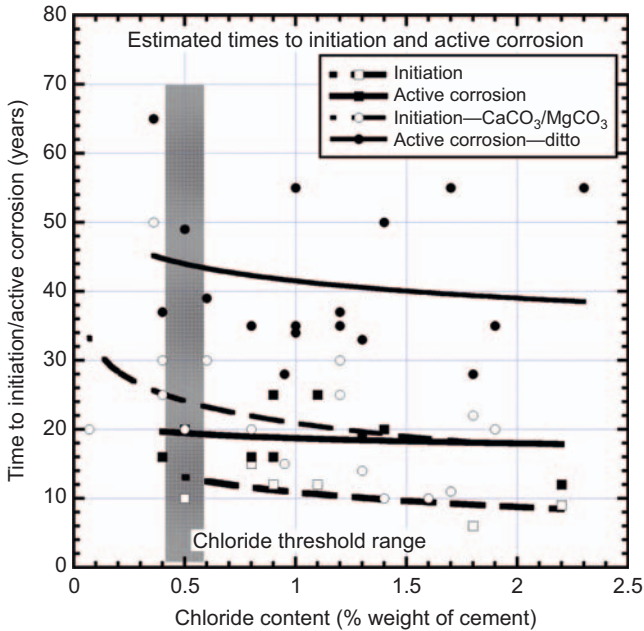


Figure 2.7 Times to initiation (t_i) or active corrosion (t_{act}) as a function of concentration of chlorides estimated to be next to the reinforcement and of the type of aggregate used for the concrete. The typical range of threshold values in chloride concentration for corrosion initiation also is shown.

reported by [Shalon and Raphael \(1959\)](#) (see [Richardson, 2002](#); [Gjorv, 2009](#)). However, as discussed further in [Section 2.6](#), these tests are unlikely to be representative of concrete industry practice.

2.6 Recent research on the effects of chlorides

The summary results ([Fig. 2.7](#)) show that, contrary to the conventional wisdom, the concentration of chlorides estimated to exist adjacent to reinforcing bars in real concrete structures has little effect on the times t_i and t_{act} . This is consistent with the laboratory results discussed in [Section 2.2](#) for corrosion of steel in stagnant solutions showing little general corrosion, although pitting may occur. [Fig. 2.7](#) also shows a substantial difference, on average, between t_i and t_{act} and this reinforces the notion that they are governed by different mechanisms ([Melchers and Li, 2006](#)). This possibility is under investigation in a long-term exposure trial, having commenced in 2004, in which several series of model concrete specimens each $40 \times 40 \times 160$ mm long, with a central 6 mm diameter steel reinforcing bar, are exposed continuously to a 25°C high-humidity environment. The high humidity of the environment ensures carbonation can be discounted. Most of the specimens were made with (Pacific

Ocean) seawater as mixing water, some with additional salt and some with soft tap water. Almost-yearly recoveries and detailed examinations are being made. Although the tests are on-going, some observations are of interest.

After 10 years exposure, the most striking observation was that, irrespective of water/cement and aggregate/cement ratio, the amount of general corrosion was extremely low, and was only slighter greater for higher chloride content at the reinforcing bars. This is entirely consistent with the observations reported in Fig. 2.7. The high density, low permeability concretes showed higher pH values for the concrete nearer the reinforcement, usually around pH 12. This was consistent with observations of no corrosion for the corresponding reinforcing bars.

Where corrosion had occurred on the reinforcing bars, it was predominantly pitting—often on an otherwise un-corroded bar (Fig. 2.8A). In most of these cases there were multiple pits, and primarily along one side of the reinforcing bars. This side corresponded to the lower horizontal part of the bar surfaces relative to the casting direction and the shaking table used for compaction of the concrete. Closer examination revealed the presence of air-voids in the concrete at the steel interface. These were significantly larger and more frequent along the lower side of the reinforcing bars. They were also larger for the less-dense concretes. From this, it can be

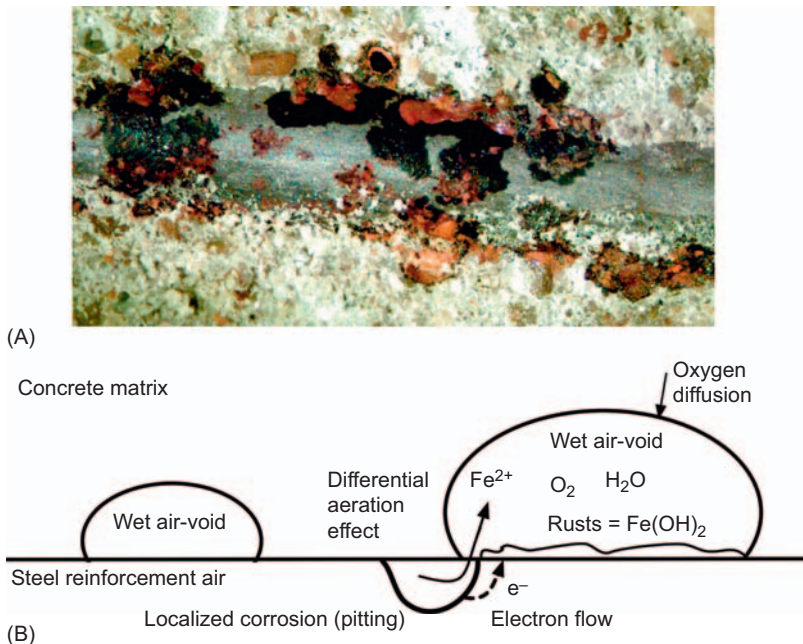


Figure 2.8 (A) Reinforcement bar (6 mm diameter) with part of the surrounding concrete removed showing rust products at isolated points. The rust products would have had to be within voids in the concrete matrix removed from the steel surface. A little of this can be seen at lower right. (B) Model for localized corrosion (pitting) showing the importance of air-voids in creating cathodic areas.

concluded that the air-voids provide pockets of oxygen necessary for the cathodic reaction (Jones, 1996). The pitting is the result of differential aeration at the edges of the air-voids (Fig. 2.8B), consistent with basic corrosion theory (see Section 2.2). It also is consistent with observations that corrosion pits on reinforcing bars do not always align closely with air-voids (Verbeek, 1975; Angst, 2011).

The scenario shown in Fig. 2.8 does not accord with the representation common in text books and some literature. Typically, these show a cathodic reaction on the un-pitted, un-corroded parts of a reinforcing bar, without air-voids. It is assumed that the resulting reaction corresponds to active corrosion. This, however, requires a rate of oxygen supply sufficient to sustain the corrosion reaction and, while this may be realistic for poor quality concretes that permit oxygen diffusion far enough inward to reach the reinforcing bar surface, it is unlikely for high quality concretes with very low permeability. As noted in Section 2.5, field observations show clearly that, for high quality concretes, rusts, if any, are of the extremely low oxygen type, including “green”-rusts (Gilberg and Seeley, 1981).

One of the series of specimens (series C) was made with sulfate-resistant cement rather than the standard, commercial, blended cement used for all the other series. An interesting feature of this cement is that it produces a concrete of a dark color that becomes lighter soon after exposure to the atmosphere (Hanson, 2015). In the present test program, it was noticed after just 2–3 years that, when the specimens were broken open, the concrete was dark in color around the reinforcing bar but much lighter in color around the outside (Fig. 2.9). Examination of the interiors of the concrete specimens in the other series, not made with sulfate resistant cement, showed a similar, but less clear pattern. In the series examined the outer lighter zone was wider in width for the more permeable concretes.

Detailed investigation, using scanning electron microscopy and energy dispersive spectroscopy (SEM/EDS), X-ray diffraction (XRD) and pH examination, showed that the light-colored concrete was essentially devoid of $\text{Ca}(\text{OH})_2$, contained little or no C (and thus no calcium carbonate as would be caused by carbonation) and had relatively low pH readings, typically 8.7–9.5 (Melchers and Chaves, 2016). In contrast, the dark colored concretes showed much higher pH readings (11–12) and the clear presence of $\text{Ca}(\text{OH})_2$. The concrete from the lighter zones showed a much more open, and presumably more permeable structure, compared with the dark



Figure 2.9 Specimen C4, made with seawater after 10 years continuous exposure, after breaking open, showing dark interior, typical of concrete made with sulfate resistant cement and the light outer zone found to be devoid of alkalis such as calcium hydroxide.

inner zone. From these observations, it was concluded that calcium hydroxide is lost from the concrete by leaching from the concrete after dissolution in water, noting that the dissolution is accelerated by a greater concentration of NaCl (Johnston and Grove, 1931) and that the more permeable concretes are likely to present a greater area of material for dissolution.

The loss of calcium hydroxide from the outside inwards can be seen as a “front” that penetrates from the outer surface into the concrete, along the way lowering the local pH to ~ 9 (unless calcium carbonates are present in the concrete in which case the pH may be somewhat higher—see Section 2.2). When the pH 9 front reaches a reinforcing bar, the stage is set for that part of the bar to commence active corrosion, since the thermodynamic conditions are now satisfied (see Section 2.2).

The mechanisms outlined above are considered to be those primarily responsible for what has been termed “chloride-induced corrosion” of reinforcement. Of course, for concretes in current practice not made with seawater, the overall process also includes the inward diffusion of chlorides. In this case, the effect on calcium hydroxide dissolution will be more gradual as the concentration of chlorides builds up, but the principle remains the same. It follows that, taken together, the total time to the commencement of active reinforcement corrosion must include the rate of inward diffusion of chlorides relative to the location of the reinforcing bars and the outward rate of loss of alkalis, governed in most cases not by diffusion but by the much slower rate of calcium hydroxide dissolution.

2.7 Practical implications for service life assessment

Much of the laboratory work directed at durability issues, including that in Section 2.6, has focused on un-cracked, unstressed concretes, although there has been some interest in the effect of cracking on reinforcement corrosion. That earlier work came to the conclusion that cracks transverse to reinforcement bars were of little importance, at least for carbonation, and that, even if the cracks penetrated to the reinforcement, the severity of corrosion was directly proportional to crack width and that, in any case, autogenous healing of the concrete tended to reduce any long-term effect, a view supported by observations of high concrete pH values adjacent to cracks (Beeby, 1978; Bentur et al., 1997, p.50). Unfortunately, these findings were derived from relatively short-term experiments and also from field observations on structures such as the British Navy and Air Force forts constructed in the Thames Estuary during the Second World War. These forts have shown good durability overall, but most likely this is because their aggregates were local limestone. As discussed above, this tends to impart greater alkalinity (or acid-neutralizing buffering capacity) to the concrete.

There is now strong evidence from field observations that transverse cracking, even if only hairline, and particularly if it intersects the reinforcement bars, can be very destructive of reinforcement in longer-term marine exposures (Section 2.5). This should not be surprising in view of the observations of alkali leaching in

seawaters (Section 2.6). The cracks would facilitate the earlier entry of seawater to the bars and thus facilitate dissolution and leaching out of the concrete alkalis. In cases of wide-spread cracking and for quite-permeable concretes, the concrete itself provides little protection and the bars can be expected to corrode at a rate and in a manner similar to that of bare steel in seawater. It follows that, in addition to high alkalinity (pH buffering, or acid-neutralization buffering capacity), the concrete for structures particularly in marine atmospheric environments must be of high density, very low permeability, and possibly have significant (and practically feasible) cover. Simply increasing cover thickness by itself is unlikely to be sufficient (Lau et al., 2007). Similarly, deeper cracking, of whatever crack size, should be avoided. The interaction of these measures remains a matter for further research, but at least the underlying mechanisms involved have now been identified.

For reinforced concrete permanently submerged or wet, in unpolluted seawater, corrosion of reinforcement bars is known to be very low for long periods of exposure, even for relatively poor-quality concretes. In most texts and papers, this is attributed to the low oxygen content of seawater inhibiting corrosion (e.g., Richardson, 2002). This does not, however, correspond to the significant corrosion of bare steels in seawaters, even if submerged. For these, the oxygen dissolved in seawater is more than enough to permit corrosion. From the above discussion, it can now be seen that the critical factor is the development, in a reasonably short time, of layers of calcium and magnesium carbonates on the exterior surfaces of immersed concrete. This will occur even if the concrete is of poor quality and may even penetrate some way into porous concrete. These carbonate layers reduce the rate at which O_2 (and NaCl) can migrate into the concrete. In principle, these layers might also reduce the rate at which outward transport of alkalis could occur, thereby retaining the concrete alkalinity at a higher level for longer. Yet, rather than rate of transport or diffusion, the rate-limiting step most likely is the rate of dissolution of $Ca(OH)_2$ and this is known to be slow, even with NaCl present. It follows that for concretes permanently immersed or wet with seawater, increasing the thickness of concrete cover, as often advocated, is not likely to be particularly effective (cf. Lau et al., 2007). Other measures, such as reducing the permeability through waterproofing agents, addition of fines, or more effort in grading of the aggregates to produce a denser concrete are all likely to be beneficial—not just in reducing the rate of ingress of chlorides, as conventionally assumed to be the critical step, but in reducing the surface area of calcium hydroxide available for dissolution within the concrete matrix. In addition, keeping the depth of transverse cracking as low as possible to reduce the pathways for faster inward and outward transport of species relative to the reinforcing bars is also likely to be beneficial.

2.8 Closure and outlook

The above results are largely derived, directly or indirectly, from observations on actual structures or surrogates for actual structures, rather than from laboratory

studies on highly artificial samples, in solutions, and (for electrochemical tests) under artificially accelerated conditions. While the limitations of these various techniques are well-recognized in some circles (Lee et al., 2010; Poursaee and Hansen, 2009), the limitations currently appear to not be reflected in most texts, and, unfortunately, not in many technical papers. Much more care needs to be taken to ensure that surrogate testing replicates the conditions inside real concretes. Once this is done, it should be possible to verify (or disprove) the inferences described above, as obtained from long-term testing and from observations on real structures. Such testing should also enable a more refined approach to be developed in quantifying the parameters involved—in particular to develop models for t_i and t_{act} . In practice, it is the latter that is of most significance. Once reinforcement corrosion has commenced in a serious way (such as at t_{act}), the end of effective service life has been reached. After that, remedial action is expensive. It is far better to try and find ways of extending the time t_{act} . The discussion given herein provides a basis for finding such research. In all such investigation, attention should be given to the degree of uncertainty involved, including the variability in corrosion studies.

The results described herein are consistent with fundamental notions and results in corrosion science, yet the overall mechanisms differ from the conventional wisdom in some important ways. This is particularly the case for the idea that reinforcement corrosion initiation in a concrete is governed by mechanisms that differ from those that govern the commencement of serious, active, corrosion (i.e., Fig. 2.6). The present results also bring a degree of unity to the mechanisms involved—for both carbonation-induced corrosion and for chloride-induced corrosion, it is ultimately the loss of protective alkalinity that permits initiation at a local level and then eventually, active corrosion.

Acknowledgments

The authors acknowledge the financial support of the Australian Research Council for facilitating some of the work reported herein. They also acknowledge the support of the Civil Engineering laboratories at the University of Newcastle, in particular Ian Jeanes and Goran Simundic, the suggestion of (the late) Dr. Dick van der Molen to try sulfate-resistant cement, the early support of Dr. Torill Pape in sample analysis, and the assistance of the Harbour Master at Portland Harbour, UK, to inspect the Phoenix caissons. The support from the Central Scientific Services at the University of Newcastle with SEM/EDS and XRD observations is also much appreciated.

Some parts of this chapter have appeared earlier as parts of conference papers, with Section 2.5 drawn, in part, from Melchers (2015) and parts of Section 2.6 from Melchers and Chaves (2016).

References

- Angst, U., 2011. Chloride induced reinforcement corrosion in concrete. PhD Thesis, Norwegian University of Science and Technology, Trondheim.

- Angst, U., Elsener, B., Larsen, C.K., Vennesland, O., 2009. Critical chloride content in reinforced concrete – a review. *Cem. Concr. Res.* 39, 1122–1138.
- Bakker, J., Frangopol, D.M., van Breugel, K., 2017. *Life-Cycle of Engineering Systems: Emphasis on Sustainable Civil Infrastructure*. CRC Press, Taylor and Francis, London.
- Beaton, J.L., Stratfull, R.F., 1963. Environmental influence on corrosion of reinforcing in concrete bridge substructures. *Highw. Res. Rec.* 14, 60–78.
- Beeby, A.W., 1978. Corrosion of reinforcing steel in concrete and its relation to cracking. *Struct. Eng.* 56A (3), 77–80.
- Bentur, A., Diamond, S., Berke, N., 1997. *Steel Corrosion in Concrete: Fundamental and Civil Engineering Practice*. E&FN Spon, London.
- Bertolini, L., Elsener, B., Pedeferri, P., Polder, R., 2004. *Corrosion of Steel in Concrete*. Wiley-VCH, Weinheim.
- Boqi, C., Dinghai, H., Hengquan, G., Yinghao, Z., 1983. Ten-year field exposure tests on the endurance of reinforced concrete in harbor works. *Cem. Concr. Res.* 13, 603–610.
- Brasher, D.M., 1967. Stability of the oxide film on metals in relation to inhibition of corrosion. I. Mild steel in the presence of aggressive ions. *Br. Corros. J.* 2, 95–103.
- Broomfield, J.P., 1999. *Corrosion of Steel in Concrete*. E&FN Spon, London.
- Burnside, O.H., Pomeroy, D.J., 1984. Survey of experience using reinforced concrete in floating marine structures. Report SSC-321, Ships Structures Committee, US Coast Guard Headquarters, Washington, DC.
- Chitty, W.-J., Dillmann, P., L'Hostis, V., Lombard, C., 2005. Long-term corrosion resistance of metallic reinforcements in concrete: a study of corrosion mechanisms based on archaeological artefacts. *Corros. Sci.* 47, 1555–1581.
- Cornish, A.T., Jackson, P.J., 1982. Portland cement properties: past and present. *Concrete*. 16 (7), 16–18.
- Dewar, J.D., 1963. *The Workability and Compressive Strength of Concrete Made With Seawater*, Technical Report, TRA/374. C&CA, London.
- Evans, U.R., 1960. *The Corrosion and Oxidation of Metals: Scientific Principles and Practical Applications*. E. Arnold, London.
- Francois, R., Arliguie, G., 1999. Effect of microcracking and cracking on the development of corrosion in reinforced concrete members. *Mag. Concr. Res.* 51 (2), 143–150.
- Garrels, R.M., Christ, C.L., 1965. *Solutions, Minerals, and Equilibria*. Harper & Row, New York.
- Gilberg, M.R., Seeley, N.J., 1981. The identity of compounds containing chloride ions in marine iron corrosion products: a critical review. *Stud. Conserv.* 26 (2), 50–56.
- Gjorv, O.E., 1971. Long-time durability of concrete in seawater. *ACI J.* 68 (1), 60–67.
- Gjorv, O.E., 1994. Steel corrosion in concrete structures exposed to Norwegian marine environment. *Concr. Int.* 16 (4), 35–39.
- Gjorv, O.E., 2009. *Durability Design of Concrete Structures in Severe Environments*. Taylor & Francis, London.
- Glass, G.K., Buenfeld, N.R., 1997. The presentation of the chloride threshold level for corrosion of steel in concrete. *Corros. Sci.* 39 (5), 1001–1013.
- Hamada, M., 1969. Neutralization (carbonation) of concrete and corrosion of reinforcing steel. In: *Proceedings, International Symposium on Chemistry of Concrete*, Vol. 3, Part 3 Carbonation of Concrete, pp. 343–369.
- Hanson, 2015. *Sulphate-Resisting Cement: Technical Data Sheet, Version 3.3*, November 2015. Hanson Heidelberg Cement, Ketton, UK.
- Hausmann, D.A., 1988. A probability model of steel corrosion in concrete. *Mater. Prot.* 37 (10), 64–68.

- Hewlett, P.C. (Ed.), 1988. *Lea's Chemistry of Cement and Concrete*. fourth ed. Butterworth, Oxford.
- Heyn, E., Bauer, O., 1908. Ueber den Angriff des Eisens durch Wasser und wässrige Lösungen. *Stahl Eisen*. 28 (44), 1564–1573.
- Huet, B., L'Hostis, V., Miserique, F., Idrissi, H., 2005. Electrochemical behavior of mild steel in concrete: influence of pH and the carbonate content of the pore solution. *Electrochim. Acta*. 51 (1), 172–180.
- Humble, H.A., 1949. The cathodic protection of steel piling in sea water. *Corrosion*. 3 (September), 292–300.
- Hunkeler, F., 2005. Corrosion in reinforced concrete: processes and mechanisms. In: Bohni, H. (Ed.), *Corrosion in Reinforced Concrete Structures*. Woodhead Publishing Limited, Cambridge, pp. 1–45.
- Jensen, V., 1996. Present experience with aggregate testing in Norway. In: *Proceeding of the 10th International Conference on Alkali-Aggregate Reaction in Concrete*, Melbourne, VIC, Australia, pp. 133–142.
- Johnston, J., Grove, C., 1931. The solubility of calcium hydroxide in aqueous salt solutions. *J. Am. Chem. Soc.* 53 (11), 3976–3991.
- Jones, D.A., 1996. *Principles and Prevention of Corrosion*. second ed. Prentice-Hall, Upper Saddle River, NJ.
- Lau, K., Sagues, A.A., Yao, L., Powers, R.G., 2007. Corrosion performance of concrete cylinder piles. *Corrosion*. 63 (4), 366–378.
- Lee, J.S., Ray, R.I., Little, B.J., 2010. The influence of experimental conditions on the outcome of laboratory investigations using natural coastal seawaters. *Corrosion*. 66 (1), 105001-1-6.
- Lewis, D.A., 1962. Some aspects of the corrosion of steel in concrete. In: *Proceeding of the First International Congress on Metallic Corrosion*, London, pp. 547–555.
- Lewis, D.A., Copenhagen, W.J., 1959. The corrosion of reinforcing steel in concrete in marine atmospheres. *Corrosion*. 15 (7), 382t–388t.
- Lukas, W., 1985. Relationship between chloride content in concrete and corrosion in unseasoned reinforcement on Austrian bridges and concrete road surfacings. *Betonwerk Fertigteil-Technik*. 51 (11), 730–734.
- Mather, B., 1964. The effects of sea water on concrete. Misc Paper 6-690, US Army Engineering Waterways Experimental Station, Vicksburg, MI.
- Melchers, R.E., 1999. *Structural Reliability Analysis and Prediction*. second ed. John Wiley & Sons, Ltd, Chichester, UK.
- Melchers, R.E., 2010a. Carbonates, carbonation and the durability of reinforced concrete marine structures. *Aust. J. Struct. Eng.* 10 (3), 215–226.
- Melchers, R.E., 2010b. Observations about the time to commencement of reinforcement corrosion for concrete structures in marine environments. In: Castro-Borges, P., Moreno, E.I., Sakai, K., Gjørsv, O.E., Banthia, N. (Eds.), *CONSEC'10, Concrete Under Severe Conditions*. CRC Press, Boca Raton, FL, pp. 617–624.
- Melchers, R.E., 2011. Observations about the corrosion of reinforcement in marine environments. In: *Proc. XII DBMC, International Conference on Durability of Building Materials and Components*, Porto, Portugal, April 12–15, CD Rom, paper 6.59.
- Melchers, R.E., 2015. Field experience and the long-term durability of reinforced concrete structures. In: *Proc. Second International Conference on Performance-Based and Life-Cycle Structural Engineering (PLSE 2015)*, University of Queensland, Brisbane, QLD, Australia, December 9–12.
- Melchers, R.E., Chaves, I.A., 2016. Long-term durability of reinforced concrete structures in marine environments. In: *Proc. Eurocor2016*, Montpellier, France, September 11–15.

- Melchers, R.E., Li, C.Q., 2006. Phenomenological modelling of corrosion loss of steel reinforcement in marine environments. *ACI Mater. J.* 103 (1), 25–32.
- Melchers, R.E., Li, C.Q., 2009. Reinforcement corrosion initiation and activation times in concrete structures exposed to severe marine environments. *Cem. Concr. Res.* 39, 1068–1076.
- Melchers, R.E., Pape, T.M., 2010. Aspects of long-term durability of reinforced concrete structures in marine environments. In: *Medachs2010*, La Rochelle, France, April 28–30.
- Melchers, R.E., Pape, T.M., 2012. The durability of reinforced concrete structures in marine environments. In: *Proc. Australasian Structural Engineering Conference*, Sydney, NSW, Australia, July 11–13, paper 094.
- Melchers, R.E., Li, C.Q., Davison, M.A., 2009. Observations and analysis of a 63-year old reinforced concrete promenade railing exposed to the North Sea. *Mag. Concr. Res.* 61 (4), 233–243.
- Melchers, R.E., Papè, T.M., Chaves I.A., 2014. The long-term durability of reinforced concrete structures exposed to aggressive marine environments. In: *Proc. First International Conference on Infrastructure Failures and Consequences*, Melbourne, VIC, Australia, July 16–20, paper No. SFC 103.
- Mercer, A.D., Lumbard, E.A., 1995. Corrosion of mild steel in water. *Br. Corros. J.* 30 (1), 43–55.
- Narver, D.L., 1954. Good concrete made with coral and seawater. *Civ. Eng.* 24 (11), 49–52.
- Nixon, P.J., Spooner, D.C., 1993. Concrete proof for British cement. *Concrete.* 27 (5), 41–44.
- Paik, J.K., Melchers, R.E. (Eds.), 2008. *Condition Assessment of Aged Structures*. Woodhead Publishing, Cambridge.
- Pape, T.M., Melchers, R.E., 2013. A study of reinforced concrete piles from the Hornibrook Highway Bridge (1935–2011). In: *Proc. ACA Conference, Corrosion & Prevention 2013*, Brisbane, QLD, Australia, November 10–13, CD ROM, paper 086.
- Parrott, L.J., 1987. *A Review of Carbonation in Reinforced Concrete*. Building Research Establishment, Department of the Environment, Crowthorne, Berks, UK.
- Pourbaix, M., 1970. Significance of protection potential in pitting and intergranular corrosion. *Corrosion.* 26 (10), 431–438.
- Poursae, A., Hansen, C.M., 2009. Potential pitfalls in assessing chloride-induced corrosion of steel in concrete. *Cem. Concr. Res.* 39, 391–400.
- Richardson, M.G., 2002. *Fundamentals of Durable Reinforced Concrete*. SponPress, London.
- Shalon, R., Raphael, M., 1959. Influence of seawater on corrosion of reinforcement. *J. ACI.* 30 (12), 1251–1268.
- Tuuti, K., 1982. *Corrosion of Steel in Concrete*, Swedish Cement and Concrete Research Institute, Stockholm, Research Report No. 4. see also (1984) Service life of structures with regard to corrosion of embedded steel. In: *Performance of Concrete in Marine Environment*, ACI SP-65, American Concrete Institute, Detroit, MI, pp. 223–236.
- Verbeek, G.J., 1975. *Mechanisms of Corrosion of Steel in Concrete*, Publication SP-49. American Concrete Institute, Farringham, MI, pp. 21–38.
- Volkswain, A., Dorner, H., 1986. *Untersuchungen zur Chloridkorrosion der Bewehrung von Autobahn-Brücken aus Stahl-oder Spannbeton*, Forschung Strassenbau und Strassenverkehrstechnik, Heft 460. Bundesminister für Verkehr, Abteilung Strassenbau, Bonn-Bad Godesberg, Germany.
- Wakeman, C.M., Dockweiler, E.V., Stover, H.E., Whiteneck, L.L., 1958. Use of concrete in marine environments. *Proc. ACI.* 54 (4), 841–856.

- Weyers, R.E., 1997. Corrosion service life model concrete structures. In: Silva-Araya, W.F., De Rincon, O.T., O'Neill, L.P. (Eds.), *Repair and Rehabilitation of Reinforced Concrete Structures: The State of the Art*. ASCE, Reston, VA, pp. 105–119.
- Wig, R.J., Ferguson, L.R., 1917. Reinforced concrete in sea water fails from corroded steel. *Eng. News-Rec.* 79, 689–693.
- Wood, C.R.J., 1948. Phoenix. *The Civil Engineer at War, a Symposium of Papers on War-Time Engineering Problems*, Vol. 2. Docks and Harbours. The Institution of Civil Engineers, London, pp. 336–368.
- Wranglen, G., 1974. Pitting and sulphide inclusions in steel. *Corros. Sci.* 14, 331–349.
- Yu, L., Francois, R., Dang, V.H., Gagne, R., 2015. Development of chloride-induced corrosion in pre-cracked RC beams under sustained loading: effect of oad-induced cracks, concrete cove, and exposure conditions. *Cem. Concr. Res.* 67, 246–258.

This page intentionally left blank

Impact of climate change on the service life of concrete structures

3

Ronaldo A. Medeiros-Junior

Federal University of Parana (UFPR), Curitiba, Brazil

3.1 Introduction

The study of the durability of concrete structures (reinforced and prestressed) is fundamental to evaluate the behavior of the material in the long term. Knowledge regarding the degradation processes of concrete structures is essential for the design of optimized projects and the execution of more-durable structures. This science also contributes to the projection of a rational recovery program, as well as helping in the responsible management of social, economic and environmental resources.

According to [Mehta and Monteiro \(2014\)](#), concrete is not an eternally durable material, since the microstructure and, consequently, the characteristics of the material are changed over time, as a result of the interaction with the environment. Thus, the useful time of a material in a safe and economically viable way is limited, resulting in the concept of “service life.”

Most concrete degradation processes are related to climate variables, and data collected over the years has shown that climate change is a reality on planet Earth. Several sectors of society are concerned about the effects of climate changes. These effects are emerging as a response of the environment to the often disordered interventions caused by human action in nature ([Cortekar et al., 2016](#); [Freeman and Yearworth, 2017](#)).

Works and research are developed worldwide to deepen knowledge on this subject, as well as propose preventive actions as the negative impacts caused by climate change are increasingly visible ([Talukdar and Banthia, 2013](#)). In the same way, international agreements are motivated in order to minimize these effects, aiming to achieve satisfactory environmental, economic and social consequences.

Increasing planet temperature, melting polar ice caps and raising seawater levels are just a few examples of phenomena that are linked to climate changes that may interfere with the durability of concrete structures.

3.2 Effect of climate on the mechanisms of degradation of concrete structures

Aggressive agents acting on concrete structures are usually grouped into three agent types (chemical, physical and biological). However, the action of these agents

happens simultaneously, which makes it difficult in some situations to fully understand and reproduce this degradation under controlled conditions (Medeiros-Junior and Lima, 2016). In general, the mechanisms of degradation of concrete structures are complex and are influenced by the interaction between the environment and the material. The importance of the different climatic parameters in this interaction is quite diverse depending on the different processes of degradation.

The degradation mechanisms can be divided into three types: (1) degradation of the concrete itself; (2) degradation of the reinforcement; and (3) degradation of the structure itself. The main causes for the decrease in concrete performance are leaching, expansion by sulfate attack, and alkali-silica reaction (ASR). Regarding the reinforcement, the main mechanisms are related to corrosion by chloride attack and carbonation. Finally, the structure itself may undergo mechanisms of degradation from mechanical actions, thermal origin movements, impacts, cyclic actions, shrinkage, and creep (Mehta and Monteiro, 2014).

The classification and dimension of the climate where a concrete structure is exposed gives an idea of how to estimate the behavior of this structure in service. These dimensions also give an idea of the accuracy of mathematical models for predicting the service life. Studies related only to the macroclimate may favor a trend of less accuracy. On the other hand, studies that consider the microclimate generally produce more accurate results that are more consistent with reality, since these studies consider environmental factors in the surroundings of the structure.

According to DuraCrete (1999), the local climate is the result of the transformation of the regional climate, with the influence of the geometry and the orientation of the considered structure. For example, it is not common to have large differences between the air temperature near a structure and the air temperature measured at a nearby weather station. However, the microclimate has been shown to be a parameter of great influence on the durability of concrete structures mainly in marine environment (Medeiros-Junior et al., 2015a; Ekolu, 2016).

The microclimate can be defined as the interaction between the climatic conditions and the surface (or very close to it) of the material. This interaction has a decisive effect, in most cases, on the internal conditions of the concrete. The study of microclimate conditions, however, is more laborious and expensive, mainly due to the lack of available data and sensors installed in the structures. Different environmental variables can be influence factors in the processes of concrete degradation. The main ones are: temperature, relative humidity (RH), precipitation, wind, waves and tides.

3.2.1 Temperature

Temperature plays an important role in some degradation processes of concrete structures, such as in the penetration of chlorides, for example. Temperature also interferes in different corrosion parameters. For instance, in the electrical resistivity, in the corrosion potential, and in the corrosion rate.

Another effect is the physical action on the structures due to the temperature variation. This variation can cause thermal tensions and shrinkage that generate cracks

in the structural elements. These cracks, in conjunction with other variables (winds, humidity), may facilitate the entry of aggressive agents into concrete (Mehta and Monteiro, 2014).

In most chemical processes, temperature increases the kinetics of reactions. This fact explains why certain structures located in hot regions degrade faster than structures inserted in cold and temperate regions, although rainfall is a decisive condition for such behavior.

Raising the temperature may help propagate or reduce a particular mechanism of degradation. For example, increasing the temperature during the concrete cure process can minimize the chloride diffusion coefficient (steam cure). This is due to the acceleration of the hydration reactions occurring into the concrete and, consequently, the improvements provided in the microstructure conditions (Nie et al., 2016).

However, the increase of the external and internal temperature after a more-advanced degree of hydration of the concrete may cause greater ionic mobility of the chlorides, thus increasing the penetration of these ions (Medeiros-Junior et al., 2015a).

In short, two distinct situations are identified: In the concrete curing step, the chloride ingress, which usually is verified in accelerated penetration tests, tends to be smaller for concretes cured at higher temperatures (steam cure). The other situation concerns the concrete exposed in the external environment and tested later, in which the increase in temperature leads to an increase in ionic mobility, resulting in higher kinetic of the reactions.

The sulfate attack with a formation of delayed ettringite is also influenced by elevated temperatures, usually above 65°C. On the other hand, the ingress of external sulfates combined with the presence of carbonates and water at low temperatures (below 15°C) may lead to the transformation of hydrated calcium silicates to taumasite (Cefis and Comi, 2017). Therefore, the effect of temperature is varied and depends on the degradation process analyzed.

3.2.2 Relative humidity

RH is very important for the degradation processes of concrete structures. Most of the degradation processes do not occur without the presence of moisture inside the concrete. The RH influences the concrete properties both in the curing and hardening phases, as well as in their performance stage, when the structure is put into service. This variable can be considered as the most significant parameter when it comes to concrete durability.

Data on moisture in real-size structures are scarce, in contrast to studies involving laboratory testing in specimens. According to Andrade and Castillo (2003), the majority of laboratory tests are performed in chambers with a controlled hydrothermal regime to allow the concrete to reach steady state and equilibrium. However, the natural and real exposure of the concrete induces permanent situations of non-stationary state, due to the evolution of temperature and climatic events such as precipitation.

Another point to be observed is that the RH condition governs the degree of saturation in the pores of the concrete and provides a decisive effect on the paths available for the diffusion of aggressive agents (Cl^- , CO_2 , sulfates). Generally, there is a balance between the relative humidity of the environment and the humidity inside the concrete structure. However, concrete easily absorbs moisture from the environment and tends to lose that absorbed water more slowly.

The corrosion risk factor decreases in extreme values of relative humidity. For extremely high values of RH, the concrete may be completely saturated, so that the oxygen must first be dissolved in the water in order to reach the reinforcement, even at low resistivity.

In this way, the corrosion rates under these conditions will not be the highest, but moderate, or even very low. At the other extreme, in the case of low relative humidity, the resistivity is very high and the corrosion process becomes very difficult. In this case, the corrosion rate is low (Mehta and Monteiro, 2014).

Therefore, there is an ideal range of relative humidity that favors the entry of aggressive agents, usually around 80%. The highest carbonation rates are observed for RH values between 55% and 75% (Ta et al., 2016).

Moisture plays an important role in the occurrence of both the ASR and in the expansion of the silica gel. The ASR presents damages to the concrete in relative humidity above 80%. Below this value, the formation of the gel can also occur, but the expansion is not significant. This explains why the ASR occurs mainly in hydraulic works, such as dams and foundations. These structures are in constant contact with humidity (Guthrie and Carey, 2015).

3.2.3 Precipitation

Precipitation on the concrete confers higher moisture compared to a simple increase in relative humidity. Therefore, the amount and duration of precipitation should be considered.

In addition to being related to relative humidity, precipitation can also be linked to wetting and drying cycles. These cycles can contribute to the development of some aggressive processes to the reinforced concrete structures, such as chloride ingress. Considering a structure exposed to the marine environment, rainwater contributes to the chlorides available on the surface of the concrete penetrate by capillary absorption. During the drying period, the chlorides remain inside the pores of the concrete. The ingress preferably proceeds by diffusion, even in the drying period, but with lower speed. However, in the next rain, the penetration process is intensified (Medeiros-Junior et al., 2015a).

The surface washing effect due to precipitation is another relevant aspect of concrete durability. Surface washing tends to provide a leaching in the outer layer of the concrete, reducing the surface concentration of aggressive agents (example: CO_2) (Köliö et al., 2014).

Andrade and Castillo (2003) studied the influence of the shelter on concrete structures regarding the aggressiveness caused by precipitation. Unprotected concrete behaves as a porous material under natural exposure conditions. Under these

conditions, concrete works like a sponge: holding water inside it and losing water by evaporation, mainly as a result of increases in temperature. Conversely, concrete protected from precipitation usually absorbs small amounts of liquid water and its internal relative humidity is influenced mainly by the external relative humidity.

While temperature and relative humidity are the main factors that influence the degree of saturation in sheltered structures, precipitation and snow (in countries with strong winters) represent a more important part on exposed structures (Andrade and Castillo, 2003).

3.2.4 Wind

Winds have great importance as a degradation agent and act by transporting ions in the forms of solid particles and drops of saline solution. In the case of the marine environment, the wind is essential for the formation of the marine aerosol (Castro-Borges et al., 2013). Even structures inserted out of the sea, but in the zone of marine atmosphere, continue to receive the action of the chlorides transported by the winds. This is most important along the first few hundred meters beyond the coast (Meira et al., 2010).

Winds also act as a catalyst in the wetting and drying cycles, favoring the precipitation and formation of salts (Medeiros-Junior et al., 2015a).

Regarding the forms of measures, the wind is usually observed by its speed and direction. However, these variables can change very quickly due to different factors, such as the effect caused by the surrounding terrain.

The wind-driven rain is the result of a simultaneous action of precipitation and wind. This event in the built environment is a complex multiscale phenomenon. According to Derome et al. (2017), different rain deposition distributions within the city can be associated with wind flows and rain events in complex urban environment. Thus, this climatic variable also interferes with the environment-built durability mainly on the building facade. Due to the predicted increase in precipitation, facades will receive more wind-driven rain in the future. This parameter can also be related to the freeze-thaw cycles and frost attack (Pakkala et al., 2014).

3.2.5 Waves and tides

Waves and tides are related to the movement of seawater and have direct effects on the degradation of reinforced concrete structures. They influence the concentration of chemical compounds and the amount of material carried in suspension, which cause erosion or chemical attack on structures.

Oceans make up 80% of the surface of the Earth. In addition, several countries have large territory along the coastline and cities with significant urban occupation in these regions. Therefore, several concrete structures (coastal or offshore structures) are exposed—directly or indirectly—to seawater in a marine environment (Seleem et al., 2010).

The seawater usually has an irregular chemical composition, but about 3.5% by weight is made of soluble salts. The main aggressive agents to concrete structures

and to reinforcement found in the seawater are the Cl^- , Na^+ , Mg^{2+} and SO_4^{2-} (Seleem et al., 2010; Mehta and Monteiro, 2014).

Besides the chemical attack caused by seawater, the waves act in the degradation of the concrete structures through the superficial wear caused by its continuous impact. The tide variation influences wetting and drying cycles, being one of the zones more aggressive to the concrete (Mehta and Monteiro, 2014; Medeiros-Junior et al., 2015a). The tides range from 0.5 m in some locations to more than 15 m in others. The amplitude of the tides in the oceans is often quite small, usually less than 1 m, but when approaching the coast this variation can increase to 4–5 m (DuraCrete, 1999).

The tidal variation can also affect parts of the structures that are subject to variations in groundwater level, which has very peculiar chemical characteristics.

3.2.6 Chloride deposition

The chloride deposition has an important effect in the time of corrosion initiation of the reinforced concrete structures. The service life of structures decreases when there is an increase in the surface concentration of chlorides. The chloride deposition is strongly influenced by environmental conditions. An average behavior is expected to prevail over time as a consequence of the availability of chlorides in the environment and its interaction with the concrete matrix (DuraCrete, 1999).

The surface concentration of the chlorides in the structure depends mainly on the proximity of the sea. McGee (2000) found on bridges in Tasmania (Australia) that the surface concentration of chloride in a concrete structure varies according to the height above the mean sea level. According to Polder and Rooij (2005), a single mean plus standard deviation can be adopted for concretes up to 7 m above mean sea level. However, above 7 m, the influence of the local microclimate is decisive for increasing or reducing the chloride deposition. Rincón et al. (2006) comment that there is a decrease in the concentration of chloride with the increase of the altitude in relation to the level of the sea. These authors analyzed a concrete bridge located in Venezuela and clearly verified the effect of height in the chloride ingress in the concrete structure, observing a significant reduction from 6 m in height.

The concentration of chlorides on the surface of a reinforced concrete element is highly dependent on parameters such as wetting and drying cycles, preferential wind direction, and local topography. All these variables define a rate of deposition of chlorides, resulting in a higher or lower deposition of these ions according to the distance of the sea. According to DuraCrete (1999), the salt concentration is almost constant immediately above the sea. However, the concentration is dependent on the wind speed, especially in the coastal zone.

Regarding the horizontal distance of the sea, as the distance to the coast increases, the deposition of the saline particles occurs in a marked way in the first hundreds of meters from the interface with the sea. Jaegermann (1990) noted that, in the first 400 m of soil from the coast, there is a marked reduction in the concentration of chlorides in the marine aerosol to the Mediterranean region. In Brazil, Meira et al. (2010) found a clear reduction in the concentration of chloride ions in

the first 200 m from the coastline. After the initial 200 m, the reduction in chloride concentration is less pronounced, reaching minimum values after the first kilometer of distance. [Pontes \(2006\)](#) and [Romano \(2009\)](#) also identified that chloride deposition is most important in the earliest ranges of land. According to [Pontes \(2006\)](#), this occurs mainly in the first 400 m and, according to [Romano \(2009\)](#), in the first 100–200 m from coastline.

This behavior is due to a deposition process that occurs, mainly, through the gravitational effect and the shock of the particles with the obstacles in the land. Thus, it should be noted, this behavior is characteristic of each region and may fluctuate throughout the seasons.

The gravimetric effect is responsible for the deposition of the particles. Larger particles of the marine aerosol soon settle on the first meters of the land due to gravity. With the action of the wind, these particles can reach further, but the effect of gravity is still important. Thus, the deposition of salts particles from the aerosol is attenuated with the distance from the sea ([DuraCrete, 1999](#); [Meira et al., 2010](#); [Romano, 2009](#)).

According to [DuraCrete \(1999\)](#), the atmospheric salinity content usually declines rapidly with the distance from the coast. However, in dry regions, where precipitation is rare, fine salt particles can be transported hundreds of meters into the continent.

3.3 Climate change

According to the [Intergovernmental Panel on Climate Change \(IPCC\) \(2013\)](#), climate changes are changes in the mean and/or in the variability of the climate that remain for a long time (decades or longer). Therefore, climate changes are any changes in weather over time, whether due to natural variability or as a result of human activity.

Environmental variables to describe the climate are usually measured in a network of weather stations positioned around the world or at least in the inhabited part of the world. The weather stations must be positioned so that their location does not have a significant influence of other near objects. From these data, climate change can be identified, for instance, using statistical tests and forecasting models.

Conferences, congresses, publications, and reports on climate change are developed in various locations around the world. The issue has become of great concern in practically all sectors of society, not just those called environmentalists. The consequences of climate changes are already present on the planet Earth, regardless of the causes and attribution of blame for this phenomenon. The reason for this is that the negative effects of climate change are becoming more intense and visible ([Kölliö et al., 2014](#); [Saha and Eckelman, 2014](#); [Bastidas-Arteaga and Stewart, 2015](#)).

Planned human interference may result in changes in radiation, hydrological balances, and in local wind flow. This interference is known as an intentional modification of the climate. Human interference in the natural climate system may also be

unplanned. This type of intervention can result in surface changes or atmospheric pollution, for example. In practice, the dividing line between intentional and accidental climate change is unclear (DuraCrete, 1999).

Most climatic events do not occur singly in space, but are linked to other parameters that contribute to their formation and/or intensification. Therefore, only study with details of these events can reveal essential information concerning their genesis and development (Bastidas-Arteaga et al., 2010).

The seasonal cycle depends on the dynamic environments and should also be discussed in climate change studies. According to Donohoe and Battisti (2013), the seasonal input of energy into the atmosphere is not subject to the same constraints imposed on the annual average.

Some mechanisms have been suggested to explain variability in the phase of the annual cycle of surface temperature. Some studies suggest that changes in temperature seasonality occur due to changes in the relative sensitivity of surface temperature to annual insolation. Changes in the relative influences of land and ocean at different locations resulting from variability in ocean and atmosphere circulation may also contribute to the variability in the seasons (Thompson, 1995; Stine and Huybers, 2012).

The heating source governs the phase of the seasonal cycle of temperature within the atmosphere. The seasonal cycle of heating is usually divided into two components: (1) a component due to direct solar absorption in the atmosphere; and (2) a component due to the flux of energy from the surface to the atmosphere. The large seasonal variations in shortwave radiation at the top of the atmosphere are primarily balanced by an energy flux into the ocean (Donohoe and Battisti, 2013).

According to Stine and Huybers (2012), the strong relationship between atmospheric circulation and the structure of the seasonal cycle suggests that physical explanations for changes in atmospheric circulation also extend to explaining changes in the structure of the seasonal cycle.

The division of seasonal atmospheric heating into upward surface fluxes and shortwave atmospheric absorption has implications for the vertical structure of the seasonal temperature response, the temporal phasing of the seasonal cycle, and the change in seasonality (Donohoe and Battisti, 2013).

According to Erickson et al. (1996) and Donohoe and Battisti (2013), the increase in CO₂ will have a direct impact on the seasonal cycle of atmospheric temperatures. In parallel, according to Peixoto and Oort (1996), an increase in temperature generally would lead to an increase of the amount of water vapor in the atmosphere and an increased absorption of thermal radiation.

Seefeldt et al. (2012) studied the variation in relative humidity cycles across West Africa during the dry season—occurring from approximately December to May. The results show distinctly different frequency and sequencing of relative humidity patterns from year to year and there is some indication of a larger, possibly decadal, pattern of the year-to-year changes in the variation of relative humidity over the course of the dry season.

Concerning the seasonal cycle of the sea ice, according to Eisenman et al. (2011), Arctic sea ice has been rapidly retreating during recent decades. The

year-to-year retreat of sea ice extent has been more rapid at summer minimum than at winter maximum. This behavior is associated with an increase in the amplitude of the seasonal cycle.

3.3.1 Climate projection

It is not possible to predict the exact climate for a distant future, but it is possible to evaluate the relative probability of different long-term trends. For that, the restrictions and limitations imposed by the observations and knowledge available today must be considered.

The Intergovernmental Panel of Climatic Change (IPCC, 2013) was created in 1988 by the World Meteorological Organization (WMO) and the United Nations Environment Programme (UNEP). The IPCC is an organization responsible for discussing and monitoring climate change and proposing mitigating solutions. Since the 1990s, the IPCC has released series of IPCC Assessment Reports, Special Reports, Technical Papers, Methodology Reports and other products. According to IPCC, most of the temperature increase observed in the last 50 years was caused by human activities, assuming more than 90% reliability. The globally-averaged combined land and ocean surface temperature data show a warming of 0.85°C ($0.65\text{--}1.06^{\circ}\text{C}$) over the period from 1880 to 2012. These values are calculated by a linear trend (IPCC, 2013).

IPCC (2013) discusses a projected increase of the global mean surface temperatures for 2081–2100 relative to 1986–2005 between $0.3\text{--}1.7^{\circ}\text{C}$ (RCP2.6), $1.1\text{--}2.6^{\circ}\text{C}$ (RCP4.5), $1.4\text{--}3.1^{\circ}\text{C}$ (RCP6.0), and $2.6\text{--}4.8^{\circ}\text{C}$ (RCP8.5), where RCP2.6, RCP4.5, RCP6.0, and RCP8.5 are the Representative Concentration Pathway scenarios. The increase of global mean surface temperatures for 2100 can be represented on average within the range of $1.0\text{--}3.7^{\circ}\text{C}$, depending on the population growth, economy, and the consumption of fossil fuels. A reliable estimate proposes an average increase of 3.0°C , taking into account projections for the expected carbon dioxide (CO_2) levels in the year 2100.

Thus, the emission of carbon dioxide into the atmosphere has a strong influence on climate change. According to DuraCrete (1999), the stabilization of CO_2 at concentrations around 450, 650, and 1000 ppm can lead to an increase in the air temperature of 1°C (range from 0.5 to 1.5°C), 2°C (range from 1.5 to 4°C), and 3.5°C (range from 2 to 7°C), respectively. According to Talukdar and Banthia (2013), increasing atmospheric CO_2 emissions will likely increase the rates of carbonation in reinforced concrete structures.

In addition to carbon dioxide, methane (CH_4) and nitrous oxide (N_2O) also contribute to climate change. These agents may come from human activities, especially in the agricultural sector.

According to IPCC (2007), considering the period 1850–2006, 11 of the last 12 years are among the twelve warmer years. The rate of increase between 1850 and 1899 was 0.57°C , whereas between 2001 and 2005 this rate went up to 0.95°C , corresponding to an average increase in the period of 0.76°C .

This increase in temperature may influence the durability of the concrete. For instance, the formation of the marine aerosol, which is a great source of chloride, can be facilitated by the increase in temperature. Global warming boosts evaporation in the oceans, which leads to an increase in the water vapor content in the atmosphere. Since chlorides are arranged in the aerosol from seawater, there is greater availability of these ions in the atmosphere in the marine environment.

Another point to consider is the sea level rise. In temperature records, [IPCC \(2007\)](#) also noted an increase in the global mean sea level over the years from 1970 to 2000. [IPCC \(2013\)](#) shows a projected increase of the global mean sea level for 2081–2100 between 0.26–0.55 m (RCP2.6), 0.32–0.63 m (RCP4.5), 0.33–0.63 m (RCP6.0), and 0.45–0.82 m (RCP8.5). This will also impact the durability of concrete structures.

Changes in precipitation are also predicted in [IPCC \(2013\)](#). These changes are strongly influenced by the region considered. For instance, increases in the amount of precipitation are more likely in regions of high latitudes, while reductions are expected in most subtropical terrestrial regions. This behavior may occur if trends observed in recent years have been maintained and considering projections for the period from 2090 to 2099 ([IPCC, 2007](#)).

The aerosol is a function of air-mass history and origin, and is strongly influenced by cloud and precipitation processes ([IPCC, 2013](#)). Other environmental parameters are susceptible to climate change, such as winds, relative humidity, frost, and salinity. It is emphasized that winds act as a means of transport for aggressive agents to the concrete. These relationships are still the focus of several studies for a better understanding of the interconnection of these phenomena.

3.3.2 Impact on concrete durability

Climatic conditions have a considerable influence on the behavior of concrete structures over time. The reinforcement corrosion induced by the ingress of chlorides (Cl^-) has been recognized as a factor of extreme importance for the reduction of the service life of reinforced concrete structures. The penetration of Cl^- into reinforced concrete structures is the major concern regarding to the durability of structures located in the marine environment. Thus, from now on, this chapter will mainly deal with this process of degradation.

[Bastidas-Arteaga et al. \(2010\)](#) presented a study about the influence of global warming on the degradation of concrete structures located in the marine environment through stochastic approaches. The study points out that global warming interference is closely related to the distancing of concrete structures into the sea. There are some uncertainties related to the consequences of climate change, since these events are influenced by several factors. However, these uncertainties can be reduced as more data and reliable studies are available ([Bastidas-Arteaga et al., 2010](#)).

According to [Bastidas-Arteaga et al. \(2010\)](#), global warming can reduce service life by 6–14 years for structures located 3 km away from the seashore. The conditions of global warming were considered by the authors according to [IPCC's \(2007\)](#) predictions for a period of 100 years.

Stewart et al. (2011) conducted a study to determine impacts on concrete infrastructures due to predicted climate change for various CO₂ emission scenarios. The study was conducted for the cities of Sydney and Darwin, both located in Australia. Some of the aspects considered in Stewart et al. (2011) are: uncertainties in CO₂ concentrations in the atmosphere, degradation processes (carbonation and chloride attack), and property of materials. In the case of the corrosion of the reinforcement due to chloride ions, the variation in the probabilities of corrosion was verified. The probability of corrosion is defined as the chances of a critical concentration reaching a depth at least equal to the concrete cover. These probabilities behaved in different ways for selected climate scenarios.

Stewart et al. (2011) analyzed the impacts on concrete infrastructures due to the expected climate change for various CO₂ emission scenarios. According to the researchers, the alterations in the evaluated scenarios, in relation to projections for 2100, caused an increase in the probability of corrosion in the range of 6%–15%.

Medeiros-Junior et al. (2015b) studied the effect of climate change on the service life of concrete structures, considering the effects of temperature and relative humidity on chloride transport. Among the results, Medeiros-Junior et al. (2015b) found that changes in temperature and relative humidity identified in a period of 100 years were responsible for a reduction of 7.8–10.2 years of service life.

The carbonation in concrete infrastructure will probably be affected by climate changes too. According to Talukdar and Banthia (2013), climate changes modify the progression of carbonation process, and structures being constructed in 2020–30 may have to begin taking into account such degradation during design. Concrete structures constructed in the year 2030 (worst case scenario) in areas where carbonation-induced corrosion has appropriate environmental conditions (moderate humidity, higher temperatures and dry exposure class) may have a reduction in service life due to climate change of approximately 15–20 years (Talukdar and Banthia, 2013). According to Stewart et al. (2012), a detailed spatial and time-dependent probabilistic analysis showed that additional carbonation-induced damage risks may increase in 2100 by 16%.

Saha and Eckelman (2014) used high and low scenarios of climate change in combination with downscaled temperature projections and code-recommended material specifications to model carbonation and chloride-induced corrosion. The study was focused on concrete structures in the north-east of the United States. According to Saha and Eckelman (2014), current concrete construction projects will experience carbonation and chloride ingress that exceed the current code-recommended cover thickness by 2077 and 2055, respectively.

Frost attack (Pakkala et al., 2014) and carbonation induced corrosion (Köliö et al., 2014) were studied for concrete buildings in a changing climate expected for Finland. These studies show that facades will get more wind-driven rain in the future because of increasing precipitation and windiness. According to Köliö et al. (2014), the increase of precipitation in the future will have a small effect on the corrosion rate during propagation time, since the active corrosion period is rather short even now, only 6–8 years. It's expected that this period will accelerate to 5–6 years in the beginning of century in southern and middle Finland (Köliö et al., 2014).

According to Bastidas-Arteaga and Stewart (2015), among the possible alternatives to mitigate the effects of climate change on the durability of concrete, increasing concrete strength grade is more cost-effective than increasing design cover. The cost-effectiveness of a certain adaptation strategy also depends of factors such as the type of structural component, exposure conditions, and climate change scenarios.

3.4 Example of a numerical application—corrosion of reinforcements on the Brazilian coast

The influence of climate changes on the penetration of chloride ions into concrete structures located in the marine environment will be studied from a numerical application below. In this example, climate changes are represented by measured and projected variations in temperature and relative humidity for different scenarios of marine environments (past, current and future). Subsequently, prediction models of chloride penetration will be applied to the different environmental scenarios.

3.4.1 Hypotheses

Some hypotheses and limitations were assumed to apply this numerical example. Therefore, the methods, analyses and results that will be presented were made with the following considerations:

1. The study area selected for this numerical application is the North Coast of Sao Paulo (Brazil). Thus, the results refer to the type of environment studied, that is, a marine environment with characteristics similar to the North Coast of Sao Paulo.
2. The chloride ions considered are solely derived from seawater.
3. Possible errors in the measurements of the environmental data available by weather stations are insignificant and do not interfere in the results.
4. The choice of the environmental variables temperature (T) and relative humidity (RH) are sufficient to translate the influence of climate changes in the penetration of chlorides in the concrete, since most of the literature considers these (T and RH) as the main environmental factors that interfere in the mechanism of Cl^- ingress.
5. The models used for the prediction of the service life have some limitations. However, these limitations will not be discussed, so it has been assumed that such models satisfactorily reproduce the penetration of chlorides into concrete structures under natural conditions.

3.4.2 Study area

The study area (North Coast of Sao Paulo, Brazil—Fig. 3.1) selected for this numerical application has an economy characterized by seasonality due to the predominance of vacationer tourism. The economic activities are fundamentally linked to the natural resources due to high tourism present in these regions. According to

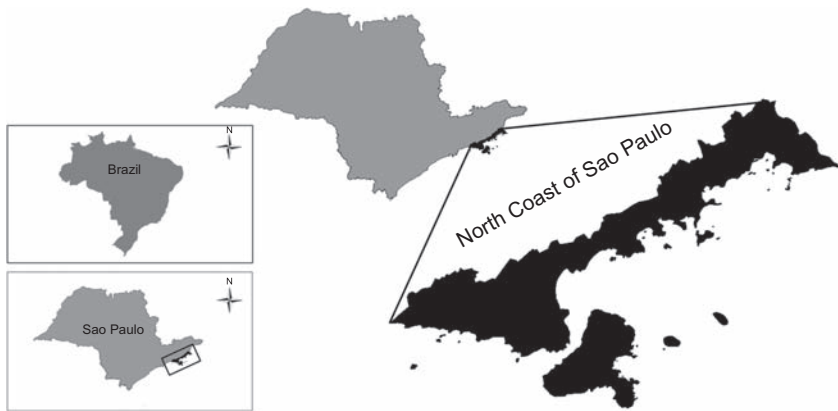


Figure 3.1 Study area.

the latest data published, the estimated population in 2010 is 281,779 inhabitants in an area of 1956 km² (Medeiros-Junior et al., 2015b).

Although this numerical application is focused in the North Coast of São Paulo, the methods and results processed for this area of study can be carefully extrapolated to a marine environment with characteristics similar to the North Coast of São Paulo, since there are reinforced concrete structures in coastal areas in many other areas in the world.

3.4.3 Data and scenario definition—temperature

Temperature data were obtained from weather stations. The methodology for obtaining this data is presented in Medeiros-Junior et al. (2015b). The data of temperature available for the North Coast of São Paulo corresponds to the period from 1961 to 2002 (42 years of data). It was not possible to get a longer continuous series of data for this area.

The 42 years of the environmental variables data was equally split in two scenarios. The first one (scenario A) is related to the oldest environmental conditions (first 21 years, 1961–81). Scenario B was set to the most current environmental conditions: the 21 most recent years available (1982–2002).

A third scenario (scenario C) was defined. For that, 2100 was assumed as the year of interest for future projections of environmental variables (temperature and relative humidity). The B2 scenario proposed by IPCC (2007) was used—this scenario assumes low emission of greenhouse gases into the atmosphere (optimistic scenario).

The average temperature was used for each period. Weather stations provide a large amount of data. These data were treated in a statistical way for practical use and to improve their reliability. This statistical treatment can be performed in two ways: using the mean values and/or approximations with periodic variations. The calculation of the mean values is a practical mathematical device to make the meteorological data useful (DuraCrete, 1999).

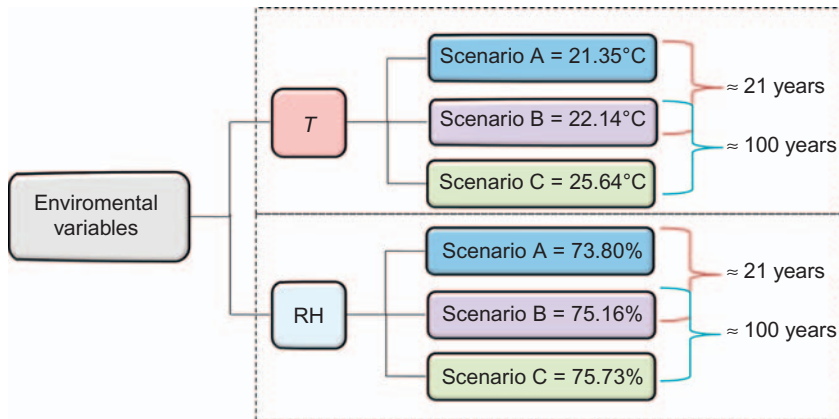


Figure 3.2 Temperature (T) and Relative Humidity (RH) data for all scenarios.

As mentioned before, the climate near or on the surface of a structure is a result of the local climate, affected by the details of the geometry of the structure and the properties of the constituent materials. Thus, the most practical way of expressing temperature conditions near or on a surface is to use the air temperature.

After a statistical treatment of the temperature data obtained from the weather stations, Fig. 3.2 shows the annual average temperatures (T_a) for 1961–81 (scenario A) and 1982–2002 (scenario B).

Projections of T_a for scenario C (2100) were obtained through results available in Marengo et al. (2010) for future environmental variables predictions. Marengo et al. (2010) used the HadCM3 model to simulate future trends for different projections of scenarios available in IPCC (2007). The HadCM3 model was developed at the Hadley Center (England) and has a horizontal resolution of 2.5167 degrees of latitude and 3.75 degrees of longitude, producing a global grid of 96×73 cells.

The prediction models of climatic variables are important for studies that require environmental data for future. Numerical weather forecasts can be made with the help of powerful computers, since the computers are periodically supplied with various observations on which the weather predictions are based. As the climate variables are not constant in time, the dynamics of the atmosphere must be modeled for reliable forecasts. In this chapter, the results from the North Coast of Sao Paulo were used from Marengo et al. (2010), assuming scenario B2 proposed by IPCC (2007) and projections for 2100.

Fig. 3.2 shows the annual average temperatures (T_a) for 2100 (scenario C). Thus, these temperatures were used in the models for predicting the chloride ingress at each scenario.

3.4.4 Data and scenario definition—relative humidity

A series of uninterrupted data of RH was not available on the weather stations in the study area within the period of analysis. Therefore, this variable was estimated using the model presented by Castellví et al. (1996). This model (Eq. 3.1) was

validated and used in different studies to estimate the RH (Vuille et al. 2003; Delgado et al. 2009; Medeiros-Junior et al., 2015b).

$$\text{RH (\%)} = 100 \frac{e_s(T_{\text{po}})}{e_s(T_{\text{m}})} \quad (3.1)$$

where $e_s(T_{\text{po}})$ is the saturation vapor pressure (hPa), determined from the dew point temperature ($^{\circ}\text{C}$), and it may be replaced by the minimum temperature (T_{n}) (Dyer and Brown 1977; Castellví et al. 1996; McVicar and Jupp 1999); and $e_s(T_{\text{m}})$ is the saturation vapor pressure (hPa), calculated from the hourly average temperature ($^{\circ}\text{C}$).

Therefore, the RH data were obtained using pre-measured temperature data. The chloride penetration in concrete is influenced directly by the internal T and RH of concrete. Therefore, the differences between T and RH in the environment and inside concrete should be discussed.

According to DuraCrete (1999) and Medeiros-Junior et al. (2015b), the temperature of concrete cover (T_{Xc}) is near to the air temperature (T). Thus, for the sake of approximation, they were considered equal in this example.

According to Bazant and Thonguthai (1978), the humidity flux from the external environment to the concrete surface can be determined by Eq. (3.2), where the flux is assumed linearly dependent on the difference between the air relative humidity (RH) and the relative humidity in surface (RH_{Xc}).

$$n \times J_{\text{h}} = B_{\text{h}} \cdot (\text{RH}_{\text{Xc}} - \text{RH}) \quad (3.2)$$

where J_{h} is the humidity flux ($\text{m}^2 \cdot \text{s}^{-1}$); $n \times J_{\text{h}}$ it the scalar product of n , vector normal to surface; B_{h} is the surface mass transfer coefficient ($\text{m}^2 \cdot \text{s}^{-1}$).

Two conditions can be assumed to B_{h} value (Saetta et al., 1993): (1) $B_{\text{h}} = 0$, perfectly sealed surface ($J_{\text{h}} = 0$); and (2) B_{h} tending to infinity—perfect superficial transmission. The better fit of the numerical results with the experimental data from drying tests of concrete specimens has been verified by using the second condition: B_{h} approaching infinite (Bazant and Thonguthai, 1978; Saetta et al., 1993). Therefore, a perfect superficial transmission was assumed in this numerical example and the relative humidity inner concrete cover (RH_{Xc}) was assumed the same as the air relative humidity (RH), for the sake of approach. It should be noted that only the first layers of concrete are the focus of this example (concrete cover), because the greatest interest is to verify the chloride ingress to a depth equal to reinforcement/concrete interface. This fact supports the simplification made here.

Fig. 3.2 shows the annual average relative humidity for 1961–81 (scenario A), 1982–2002 (scenario B) and 2100 (scenario C).

3.4.5 Models for predicting the chloride penetration

Some models for predicting chloride penetration into the concrete were applied with the environment data of scenarios A, B, and C. The following models were used: Saetta et al. (1993), Bob (1996), Amey et al. (1998), Andrade (2001), and

Mazer (2009). These models will be briefly presented below. For more detailed information concerning their applications, the original reference should be consulted. These models were chosen because they have in their formulation the presence of at least one of the selected environmental variables in this example (T and RH). However, many other models may also be appropriate for application.

Saetta et al. (1993) applied a numerical method based on the finite element formulation to analyze the chloride ingress in concrete (Eq. 3.3).

$$D_{c2} = D_{c1} \cdot f_1(T) \cdot f_2(t_e) \cdot f_3(RH) \quad (3.3)$$

where: D_{c1} and D_{c2} (cm^2/s) are the reference and corrected chloride diffusion coefficient, respectively; $f_1(T)$ is the factor that represents the influence of temperature, according to the Arrhenius' law (Eq. 3.4); $f_2(t_e)$ is the factor that represents the influence of the equivalent maturation time (Eq. 3.5); and $f_3(RH)$ is the factor that represents the influence of relative humidity (Eq. 3.6).

$$f_1(T) = \exp \left[\frac{E_a}{R} \left(\frac{1}{T_1} - \frac{1}{T_2} \right) \right] \quad (3.4)$$

$$f_2(t_e) = \zeta + (1 - \zeta) \cdot \left(\frac{28}{t_e} \right)^{1/2} \quad (3.5)$$

$$f_3(RH) = \left[1 + \frac{(1 - RH)^4}{(1 - RH_c)^4} \right]^{-1} \quad (3.6)$$

where: T_1 is the reference temperature ($=296\text{K}$) and T_2 (K) the desired temperature; E_a is the activation energy of diffusion (kJ/mol), relative to the water/cement ratio of the concrete ($=44.6 \text{ kJ/mol}$, $w/c = 0.5$), according to (Collepardi et al. 1972; Goto and Roy 1981; Page et al. 1981); and R is the universal gas constant (8.314 J/mol K).

In Eq. (3.5), ζ measures how much the diffusivity decreases with time and varies from 0 to 1, and t_e is the time of exposure to chloride (days), according to Saetta et al. (1993). In Eq. (3.6), RH_c is the humidity at which D_{c1} drops halfway between its maximum and minimum values ($=75\%$, according to Bazant and Najjar 1971), and RH is the current relative humidity considered (%).

Bob (1996) shows Eq. (3.7) to modeling the chloride penetration, based on data from long-term experiments.

$$x_c = 150 \left(\frac{ck_1k_2d}{f_c} \right) \sqrt{t_{ic}} \quad (3.7)$$

where: x_c is the concrete cover (mm); f_c is the compressive strength of the concrete (N/mm^2); c is the fixing ability of chlorides, tabulated depending on the type of cement; k_1 and k_2 are constants that represent the influence of temperature and

relative humidity, respectively (tabulated in [Bob, 1996](#)); and d is a parameter tabulated in [Bob \(1996\)](#) and depends on the ratio between the surface and the critical concentration of chlorides in the concrete.

[Amey et al. \(1998\)](#) shows a model (Eq. 3.8) based on the Nernst-Einstein theory.

$$D_{c2} = D_{c1} \left(\frac{T_2}{T_1} \right) \exp \left[q \left(\frac{1}{T_1} - \frac{1}{T_2} \right) \right] \quad (3.8)$$

where: D_{c1} and D_{c2} (cm²/s) are the reference and corrected chloride diffusion coefficient, respectively; T_1 is the reference temperature (=296K) and T_2 (K) is the desired temperature; and q is an experimental constant of the model (=5450, $w/c = 0.5$; according to [Amey et al. \(1998\)](#)).

Some studies have shown that the attempt to relate the chloride penetration profiles of buildings with advanced age (older than 20 years) with deterministic models based exclusively on Fick's laws, in some cases, may result in significant differences between the depth predicted by models and the values effectively measured in the structures within different zones of marine environment, such as tidal, splash or atmosphere zones ([Andrade, 2001](#)).

Some formulations resulting from the resolution of Fick's laws have a high degree of complexity, whereby obtaining certain parameters requires a long exposure time. In this way, other models not necessarily based on Fick's laws are elaborated to predict the penetration of chlorides in the concrete. [Andrade \(2001\)](#) developed an empirical model for predicting the chloride ingress in concrete. The model involves parameters related to concrete characteristics and environmental conditions (Eq. 3.9).

$$x = 7.35 \cdot \frac{RH^{0.7} \cdot T^{0.1} \cdot Cl^{0.7}}{k_1 \cdot f_{ck} \cdot (1 + Ad)^{0.2}} \cdot \sqrt{t} \quad (3.9)$$

where: x , depth of chloride ions penetration (equivalent to a chlorine content equal to 0.4% by the weight of cement); RH, average relative humidity of the environment (%); T , average environment temperature (°C); Cl, surface chlorides concentration, in % by the weight of cement; K_1 , factor that varies according to the type of cement (tabulated in [Andrade, 2001](#)); f_{ck} , compressive strength (MPa); K_2 , factor that varies according to the type of mineral addition (tabulated in [Andrade, 2001](#)); and Ad, mineral addition content in concrete (% by the weight of cement).

According to [Andrade \(2001\)](#), Eq. (3.9) presents general trends of behavior that are quite coherent concerning the expected effect of the intervening variables on the ingress of chlorides into concrete. Using an example of the application of Eq. (3.9) in real field data, [Andrade \(2001\)](#) comments that the model presented results very close to the values obtained in the concrete structure, with differences between the results (predicted and measured) in the range of 0.2–0.4 cm for points located in the atmospheric zone.

For points where the structure was under the action of the splash and tide, an approximate difference of 1.0 cm was found between the value obtained by the model

and the measurements in situ, representing a difference between 26.7% and 36.8%. This difference may be related to some particularities of the analyzed structure, such as the type of construction. In the splash and tidal zone the structure was made of precast concrete, differently from the atmospheric zone (conventional concrete). The extraction position of the chloride samples was also important to influence the results. The samples at the points of the atmospheric zone were drawn perpendicular to the direction of casting, while the samples at the points of the splash and tidal zone were obtained parallel to the direction of casting (Andrade, 2001).

The Mazer's model (2009) used a methodology for the determination of the chloride diffusion coefficient based on fuzzy logic. The model considers parameters inherent to the concrete and the environment to which the structure is inserted, in addition to a database with values for the chloride diffusion coefficient obtained through the use of Fick's laws. The methodology adopted for this model involves intelligent systems (artificial intelligence), applied by a large number of computational systems.

The Mazer's model (2009) considers three factors: water/cement ratio (w/c), compressive strength, and concrete casting temperature. To define the membership functions and the amplitude range of the values of water/cement ratio (w/c) and compressive strength, Mazer (2009) used the Brazilian standard NBR 6118 (2014). This standard is the most frequently used for concrete design in Brazil, and sets the limit values of the w/c ratio and compressive strength as a function of the environmental aggression class to which the structure is exposed.

The output variables were defined based on the input variables of the system (w/c ratio, compressive strength, and temperature) and the possible combinations between them, as well as the fuzzy rules base and membership functions. In order to define the inference rules, the conjunctive operation "and" was adopted, because the w/c ratio and the compressive strength are defined for dimensioning the concrete and it is also possible to determinate the temperature during the concrete pouring (Mazer, 2009).

In summary, the application of the Mazer's (2009) model can be performed from the following steps:

- The fuzzy vectors for the input variables are determined.
- The possible mathematical rules are identified to be applied, according to the map of rules exposed in Mazer (2009).
- Considering that the fuzzy operators used are the conjunction "and", the MAX-MIN inference is used to get the composition of the output variable of the fuzzy system;
- The value of the chloride diffusion coefficient is determined by the Center of Maximum defuzzification method, which consists of a weighted average of the maximum values of the membership functions of the fuzzy system.

Mazer and Lima (2011) applied the Mazer's (2009) model to different situations studied in laboratory to evaluate the performance of the model. The parameters adopted for the validation were: water/cement ratio = 0.55; compressive strength = 30 MPa; and temperature = 22°C. When using the model, Mazer and Lima (2011) analyzed several possible combinations with variations in

environmental parameters, resulting in a total of 180 simulations. According to the authors, the model presented good results and has potential to be used, with prediction errors of less than 40%, on average.

Once the five models were selected, environmental data were used (T_a and/or RH) for each scenario of climate change studied (scenario A, B, and C). In order to find only the influence of climate change (T_a and RH), all other variables in the models were kept constant (i.e., D_{c1} , $f_2(t_c)$, water/cement ratio = 0.5, E_a , T_1 , RH_c, x_c , c , d , f_c and q). Therefore, the percentage changes between chloride diffusion coefficient (D_c) and/or service life (t_{ic})—depending on the model analyzed—were found. These variations were solely the result from changes in environmental variables between each scenario, since the other variables were kept constant and did not interfere in the results.

It is worth noting that, according to the type of approach used, the models did not provide specific values of D_c or t_{ic} , but percentage changes of these values from one evaluated scenario to the other, according to changes in T_a and RH, regarding the scenarios A, B, and C.

The results of all models in terms of percentage changes in t_{ic} were evaluated to allow a comparative analysis between models. However, the [Saetta et al. \(1993\)](#), [Amey et al. \(1998\)](#), and [Mazer \(2009\)](#) models do not provide a direct determination of t_{ic} . For that, the variations of D_c resulting from these models were performed by the relation so called “square root of time” (Eq. 3.10). This procedure has shown how much the differences in D_c changed t_{ic} in percentage.

$$t_{ic} = \frac{x_c^2}{2D_c} \quad (3.10)$$

Finally, according to Brazilian Association of Technical Standards [NBR 6118 \(2014\)](#), the reinforced concrete structures must be designed and constructed so that, under the expected environmental conditions at the time of the design, and keeping its use as recommended in the project, they preserve their safe, stability and suitability in service for a minimum period of 50 years, without requiring extra measures for maintenance and repair.

This numerical example assumed that 50 years is the period in which the concrete structures should remain without any extra maintenance and repair. In other words, the initial service life of concrete structures (t_{ic}) should be 50 years. This step quantify the percentage changes of results obtained from the models and Eq. (3.10). [Fig. 3.3](#) shows a summary (flowchart) of the main steps followed in this example application.

The models for predicting chloride penetration were applied in order to verify the changes in the service life due to changes in temperature and relative humidity resulting from climate changes identified between the established scenarios. As expected, the service life (t) was reduced due to the climate change.

The beginning of reinforcement corrosion was anticipated due to the climate changes. According to [Fig. 3.4](#), temperature and relative humidity changes occurring in a period of approximately 21 years (scenario A × scenario B) resulted in a

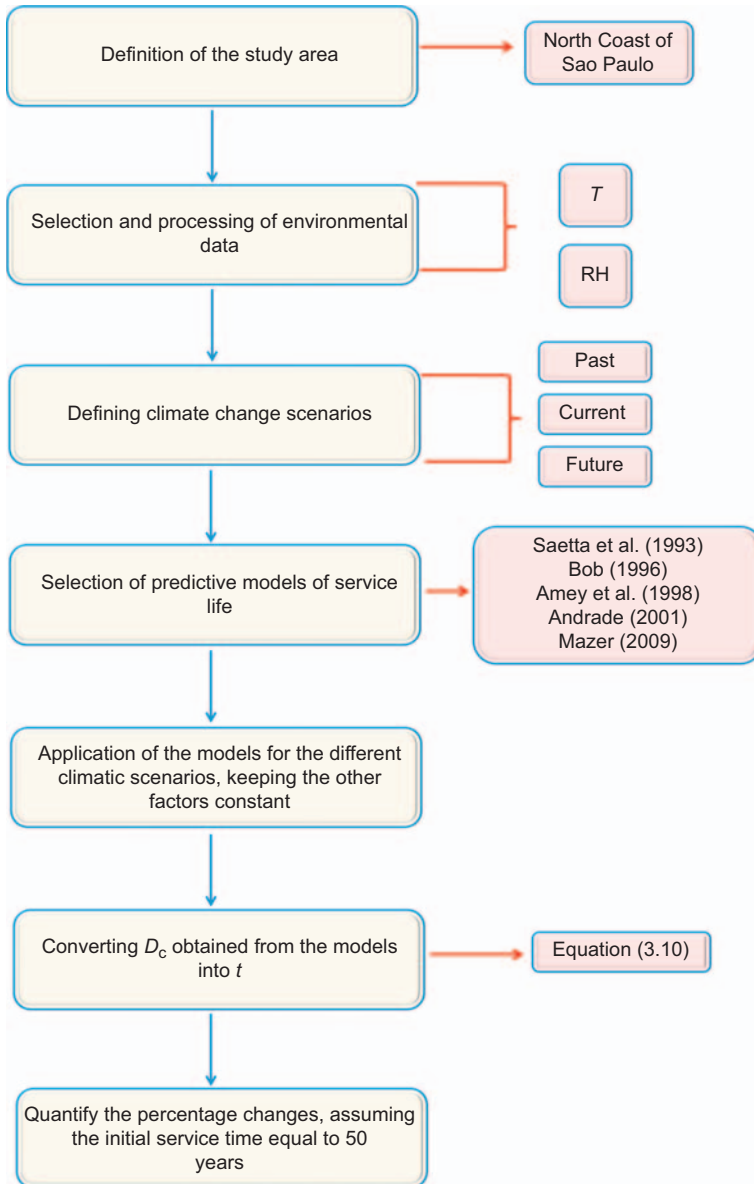


Figure 3.3 Summary of the main steps.

reduction in t from 0.2 to 2.9 years. The mean for the period is 1.4 ± 1.2 years. Therefore, the penetration of chlorides in concrete structures was accelerated and the reinforcement corrosion will no longer occur in the previewed 50 years, but in about 48.6 years.

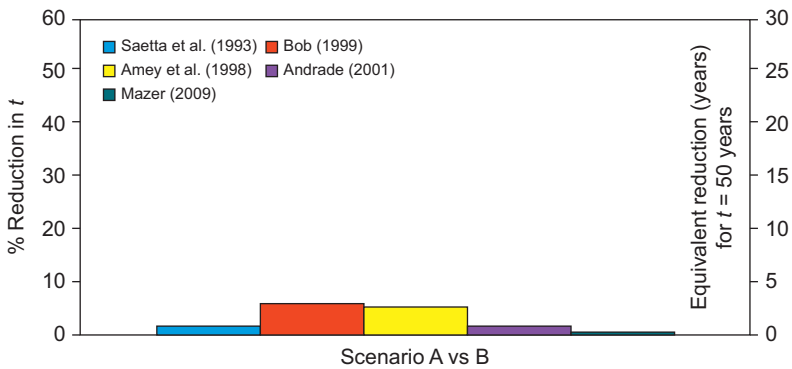


Figure 3.4 Results of climate change in chloride penetration: scenario A versus B.

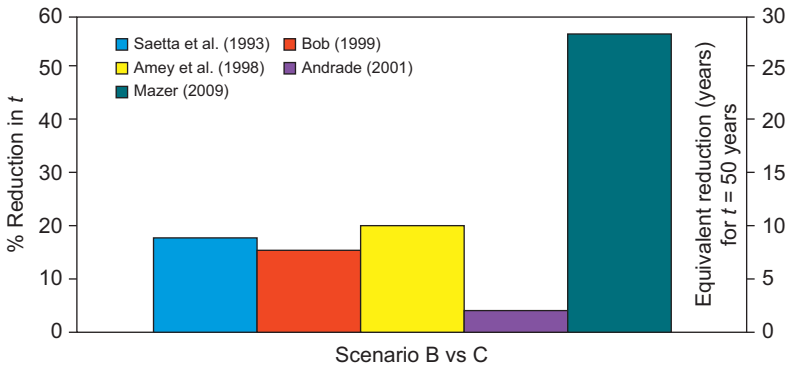


Figure 3.5 Results of climate change in chloride penetration: scenario B versus C.

In a period of 100 years (scenario B \times scenario C), the service life was reduced by 2.0–28.3 years (Fig. 3.5). Eliminating the Andrade (2001) and Mazer (2009) models (extreme results) of the analyses, this represents a mean for the period of 9.0 ± 1.2 years. Thus, t will be reduced to 41.0 years.

The service life was reduced by 2.7–28.4 years comparing the past scenario with the future scenario (Fig. 3.6). Table 3.1 shows the numerical results of climate change impact in chloride penetration for all models and scenarios studied.

This example of a numerical application reinforces the importance of making changes in the standards alongside the time to adapt them to the trend of climate change in the Earth. The models' errors must be taken into account when predicting chloride penetration. For instance, the chloride penetration may be accelerated in the hottest period of the year (summer), and in a cooler period, usually the penetration is slower. However, the proposal of this example was to seek trends and not an absolute value.

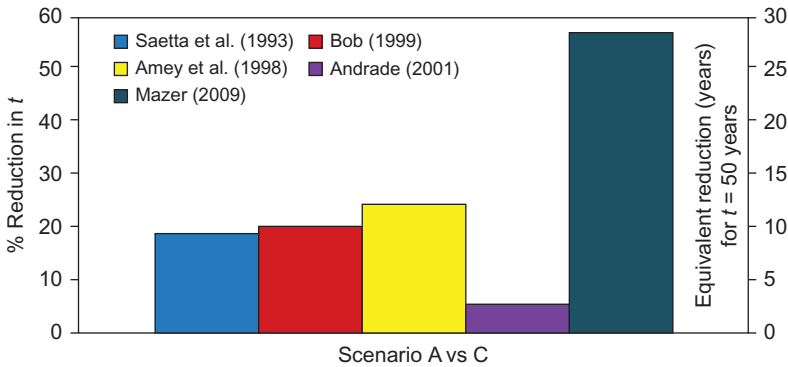


Figure 3.6 Results of climate change in chloride penetration: scenario A versus C.

Table 3.1 Results of climate change in chloride penetration for all models studied—changes in the service life (t)

Scenarios	Models	% Reduction in t	Equivalent reduction (years) for $t = 50$ years
Scenario A \times scenario B (~ 21 years)	Saetta et al. (1993)	1.22	0.6
	Bob (1996)	5.72	2.9
	Amey et al. (1998)	5.09	2.5
	Andrade (2001)	1.56	0.8
	Mazer (2009)	0.36	0.2
Scenario B \times scenario C (~ 100 years)	Saetta et al. (1993)	17.91	9.0
	Bob (1996)	15.49	7.7
	Amey et al. (1998)	20.39	10.2
	Andrade (2001)	3.92	2.0
	Mazer (2009)	56.68	28.3
Scenario A \times scenario C (~ 121 years)	Saetta et al. (1993)	18.90	9.5
	Bob (1996)	20.32	10.2
	Amey et al. (1998)	24.43	12.2
	Andrade (2001)	5.42	2.7
	Mazer (2009)	56.83	28.4

Another important point is that this example did not consider the technological evolution developed over the years in civil construction (evolution of concrete strength, for example). But the question is whether these technological developments are enough to counter the effect of increased aggressiveness of environmental variables due to climate change. The effect of other environmental variables (wind, precipitation, waves) was also not considered in this example, which can further worsen this behavior.

3.5 Final considerations

Most concrete degradation processes are related to climate variables. Data collected over the years has shown that climate change is happening in planet Earth. Global warming and the increase in the global mean sea level over the years are just a few examples of climate change phenomena that can interfere with the durability of concrete. Some studies have already demonstrated impacts on the service life of concrete structures due to climate change.

A numerical example was applied to verify the influence of climate changes on the penetration of chloride into concrete structures exposed in the marine environment. The results indicate that measures should be taken, either in developing studies that may mitigate the effects provided by climate changes, or in considering this worsening in the development of new studies. For instance, the same concrete structure built in three different scenarios of climate change (A, B, and C) has differing service life. Thus, adaptations may be necessary in standards over time to consider the effect of climatic variables changes.

References

- Amey, S.L., Johnson, D.A., Miltenberger, M.A., 1998. Predicting the service life of concrete marine structures: an environmental methodology. *ACI Struct. J.* 95, 205–214.
- Andrade, C., Castillo, A., 2003. Evolution of reinforcement corrosion due to climatic variations. *Mater. Corros.* 54, 379–386.
- Andrade, J.J.O., 2001. Contribution to the service life prediction of reinforced concrete structures attacked by reinforcement corrosion: chloride initiation (only in Portuguese: Contribuição à previsão da vida útil das estruturas de concreto armado atacadas pela corrosão de armaduras: iniciação por cloretos). Thesis (PhD), Federal University of Rio Grande do Sul, Porto Alegre, Brazil.
- Bastidas-Arteaga, E., Chateauneuf, A., Sánchez-Silva, M., Bressolette, P., Schoefs, F., 2010. Influence of weather and global warming in chloride ingress into concrete: a stochastic approach. *Struct. Saf.* 32, 238–249.
- Bastidas-Arteaga, E., Stewart, M.G., 2015. Damage risks and economic assessment of climate adaptation strategies for design of new concrete structures subject to chloride-induced corrosion. *Struct. Saf.* 52, 40–53.
- Bazant, Z.P., Najjar, L.J., 1971. Drying of concrete as a nonlinear diffusion problem. *Cem. Concr. Res.* 1, 461–473.
- Bazant, Z.P., Thonguthai, W., 1978. Pore pressure and drying of concrete at high temperatures. *J. Eng. Mech. Div.* 104, 1059–1079.
- Bob, C., 1996. Probabilistic assessment of reinforcement corrosion in existing structures. In: Dhir, R.K., Jones, M.R. (Eds.), *Concrete in the Service of Mankind: Concrete Repair, Rehabilitation and Protection*. E & FN Spon, London, pp. 17–28.
- Castellví, F., Perez, P.J., Villar, J.M., Rosell, J.L., 1996. Analysis of methods for estimating vapor pressure deficits and relative humidity. *Agric. For. Meteorol.* 82, 29–45.
- Castro-Borges, P., Balancán-Zapata, M., López-González, A., 2013. Analysis of tools to evaluate chloride threshold for corrosion on set of reinforced concrete in tropical marine environment of Yucatán, México. *J. Chem.* 2013, 1–8.

- Cefis, N., Comi, C., 2017. Chemo-mechanical modelling of the external sulfate attack in concrete. *Cem. Concr. Res.* 93, 57–70.
- Colleparidi, M., Marcialis, A., Turriziani, R., 1972. Penetration of chloride ions in cement pastes and in concretes. *J. Am. Ceram. Soc.* 55, 534–535.
- Cortekar, J., Bender, S., Brune, M., Groth, M., 2016. Why climate change adaptation in cities needs customised and flexible climate services. *Clim. Serv.* 4, 42–51.
- Delgado, R.C., Sedyama, G.C., Zolnier, S., Costa, M.H., 2009. Physical-mathematical models for estimating the relative humidity of air from temperature data (*only in Portuguese: modelos físico-matemáticos para estimativa da umidade relativa do ar a partir de dados de temperatura*). *Rev. Ceres.* 56, 256–265.
- Derome, D., Kubilay, A., Defraeye, T., Blocken, B., Carmeliet, J., 2017. Ten questions concerning modeling of wind-driven rain in the built environment. *Build. Environ.* 114, 495–506.
- Donohoe, A., Battisti, D.S., 2013. The seasonal cycle of atmospheric heating and temperature. *J. Clim.* 26, 4962–4980.
- DuraCrete, 1999. Models for environmental actions on concrete structures. In: Lindvall, A., Nilsson, L.O. (Eds.), *Probabilistic Performance Based Durability Design of Concrete Structure*. The European Union – Brite EuRam III, Europe.
- Dyer, J.A., Brown, D.M., 1977. A climatic simulator for field-drying hay. *Agric. Meteorol.* 18, 37–48.
- Eisenman, I., Schneider, T., Battisti, D.S., Bitz, C.M., 2011. Consistent changes in the sea ice seasonal cycle in response to global warming. *J. Clim.* 24, 5325–5335.
- Ekolu, S.O., 2016. A review on effects of curing, sheltering, and CO₂ concentration upon natural carbonation of concrete. *Constr. Build. Mater.* 127, 306–320.
- Erickson III, D.J., Rasch, P.J., Tans, P.P., Friedlingstein, P., Ciais, P., Maier-Reimer, E., et al., 1996. The seasonal cycle of atmospheric CO₂: a study based on the NCAR Community Climate Model (CCM2). *J. Geophys. Res.* 101, 15079–15097.
- Freeman, R., Yearworth, M., 2017. Climate change and cities: problem structuring methods and critical perspectives on low-carbon districts. *Energy Res. Soc. Sci.* 25, 48–64.
- Goto, S., Roy, D.M., 1981. Diffusion of ions through hardened cement pastes. *Cem. Concr. Res.* 11, 751–757.
- Guthrie, G.D., Carey, J.W., 2015. A thermodynamic and kinetic model for paste–aggregate interactions and the alkali–silica reaction. *Cem. Concr. Res.* 76, 107–120.
- IPCC, 2007. *Climate Change 2007: synthesis report*. Intergovernmental Panel on Climate Change. Cambridge University Press, Cambridge, UK.
- IPCC, 2013. *Climate Change 2013: the physical science basis*. Intergovernmental Panel on Climate Change. Cambridge University Press, Cambridge, UK.
- Jaegermann, C., 1990. Effect of water-cement ratio and curing on chloride penetration into concrete exposed to mediterranean sea climate. *ACI Mater. J.* 97, 333–339.
- Kölliö, A., Pakkala, T.A., Lahdensivu, J., Kiviste, M., 2014. Durability demands related to carbonation induced corrosion for Finnish concrete buildings in changing climate. *Eng. Struct.* 62–63, 42–52.
- Marengo, J.A., Ambrizzi, T., da Rocha, R.P., Alves, L.M., Cuadra, S.V., Valverde, M.C., et al., 2010. Future change of climate in South America in the late twenty-first century: inter-comparison of scenarios from three regional climate models. *Clim. Dyn.* 35, 1073–1097.
- Mazer, W., 2009. Method for predicting the penetration of chloride ions into reinforced concrete structures using diffuse logic (*only in Portuguese: metodologia para a previsão da penetração de íons cloreto em estruturas de concreto armado utilizando lógica difusa*). Thesis (PhD), Aeronautics Institute of Technology, Sao Jose dos Campos, Brazil.

- Mazer, W., Lima, M.G., 2011. Numerical model based on Fuzzy Logic for predicting penetration of chloride ions into the reinforced concrete structures – first estimates. In: International Conference on Durability of Building Materials and Components – XII DBMC, Porto, Portugal.
- McGee, R., 2000. Modelling of chloride ingress in Tasmanian bridges. In: Second International RILEM Workshop on Testing and Modelling the Chloride Ingress Into Concrete, UNESCO, Paris, France.
- McVicar, T.R., Jupp, D.L.B., 1999. Estimating one-time-of-day meteorological data from standard daily data as inputs to thermal remote sensing based energy balance models. *Agric. For. Meteorol.* 96, 219–238.
- Medeiros-Junior, R.A., Lima, M.G., 2016. Electrical resistivity of unsaturated concrete using different types of cement. *Constr. Build. Mater.* 107, 11–16.
- Medeiros-Junior, R.A., Lima, M.G., Brito, P.C., Medeiros, M.H.F., 2015a. Chloride penetration into concrete in an offshore platform-analysis of exposure conditions. *Ocean Eng.* 103, 78–87.
- Medeiros-Junior, R.A., Lima, M.G., Medeiros, M.H.F., 2015b. Service life of concrete structures considering the effects of temperature and relative humidity on chloride transport. *Environ. Dev. Sustain.* 17, 1103–1119.
- Mehta, P.K., Monteiro, P.J.M., 2014. *Concrete: Structures, Properties and Materials*. fourth ed. McGraw-Hill Education, New York.
- Meira, G.R., Andrade, C., Alonso, C., Borba Jr, J.C., Padilha Jr, M., 2010. Durability of concrete structures in marine atmosphere zones: the use of chloride deposition rate on the wet candle as an environmental indicator. *Cem. Concr. Compos.* 32, 427–435.
- NBR 6118, 2014. *Projects of Concrete Structures* (in Portuguese). Brazilian Association of Technical Standards—ABNT, Rio de Janeiro, Brazil.
- Nie, S., Hu, S., Wang, F., Yuan, P., Zhu, Y., Ye, J., et al., 2016. Internal curing: a suitable method for improving the performance of heat-cured concrete. *Constr. Build. Mater.* 122, 294–301.
- Page, C.L., Short, N.R., El Tarras, A., 1981. Diffusion of chloride ions in hardened cement pastes. *Cem. Concr. Res.* 11, 395–406.
- Pakkala, T.A., Köliö, A., Lahdensivu, J., Kiviste, M., 2014. Durability demands related to frost attack for Finnish concrete buildings in changing climate. *Build. Environ.* 82, 27–41.
- Peixoto, J.P., Oort, A.H., 1996. The climatology of relative humidity in the atmosphere. *J. Clim.* 9, 3443–3463.
- Polder, R.B., Rooij, M.R., 2005. Durability of marine concrete structures – field investigations and modeling. *HERON.* 50, 133–153.
- Pontes, R.B., 2006. Dissemination of chloride ions on the seafront of the Boa Viagem district (*only in Portuguese: disseminação de íons cloreto na orla marítima do bairro de Boa Viagem, Recife-PE*). Dissertation (Master's degree), Catholic University of Pernambuco, Recife, Brazil.
- Rincón, O.T., Contreras, D., Sánchez, M., Romero, M.F., Bravo, J., Bravo, O.M., et al., 2006. Evaluation/rehabilitation of structures in marine environments. Historical case: Maracaibo bridge (*only in Spanish: evaluación/rehabilitación de estructuras en ambientes marinos. Caso histórico: puente de Maracaibo*). *Corros. Prot. Mater.* 25, 74–91.
- Romano, F.S., 2009. Study of the chloride ingress in concretes located in the North Coast of Rio Grande do Sul (*only in Portuguese: estudo do ingresso de cloretos em concretos localizados no Litoral Norte do Rio Grande do Sul*). Dissertation (Master's degree), Federal University of Rio Grande do Sul, Porto Alegre, Brazil.

- Saetta, A.V., Scotta, R.V., Vitaliani, R.V., 1993. Analysis of chloride diffusion into partially saturated concrete. *ACI Mater. J.* 90, 441–451.
- Saha, M., Eckelman, M.J., 2014. Urban scale mapping of concrete degradation from projected climate change. *Urban Clim.* 9, 101–114.
- Seefeldt, M.W., Hopson, T.M., Warner, T.T., 2012. A characterization of the variation in relative humidity across West Africa during the dry season. *J. Appl. Meteorol. Climatol.* 51, 2077–2089.
- Seleem, H. El-D. H., Rashad, A.M., El-Sabbagh, B.A., 2010. Durability and strength evaluation of high-performance concrete in marine structures. *Constr. Build. Mater.* 24, 878–884.
- Stewart, M.G., Wang, X., Nguyen, M.N., 2011. Climate change impact and risks of concrete infrastructure deterioration. *Eng. Struct.* 33, 1326–1337.
- Stewart, M.G., Wang, X., Nguyen, M.N., 2012. Climate change adaptation for corrosion control of concrete infrastructure. *Struct. Saf.* 35, 29–39.
- Stine, A.R., Huybers, P., 2012. Changes in the seasonal cycle of temperature and atmospheric circulation. *J. Clim.* 25, 7362–7380.
- Ta, V.-L., Bonnet, S., Kiese, T.S., Ventura, A., 2016. A new meta-model to calculate carbonation front depth within concrete structures. *Constr. Build. Mater.* 129, 172–181.
- Talukdar, S., Banthia, N., 2013. Carbonation in concrete infrastructure in the context of global climate change: development of a service lifespan model. *Constr. Build. Mater.* 40, 775–782.
- Thompson, R., 1995. Complex demodulation and the estimation of the changing continentality of Europe's climate. *Int. J. Climatol.* 15, 175–185.
- Vuille, M., Bradley, R.S., Werner, M., Keimig, F., 2003. 20th century climate change in the tropical Andes: observations and model results. *Clim. Change.* 59, 75–99.

Monitoring of Reinforced Concrete Corrosion

4

Xianming Shi

Washington State University, Pullman, WA, United States

4.1 Introduction

Reinforcement corrosion induced by chloride contamination is a leading cause of structural damage and premature degradation in reinforced concrete (RC) structures, with significant implications for safety, reliability, economics, and environmental performance. According to the American Society of Civil Engineers (ASCE), approximately 56,007 bridges built in the United States are classified as structurally deficient in 2016, representing approximately 9.1% of the total number of bridges in the country (ASCE, 2016). Remediation projects for concrete bridges undertaken as a direct result of chloride-induced rebar corrosion was estimated to cost U.S. highway departments \$5 billion per year (Glass and Buenfield, 2000), aside from other economic, social, and environmental implications. Concern is the greatest in coastal and northern states where these structures are exposed to marine environments and deicing salts, respectively, such as in the States of California, Oregon and Massachusetts.

Many agencies are faced with the difficult and expensive task of more-frequent, routine corrosion inspection of aging infrastructure to enhance on-time maintenance decision-making. For instance, the Oregon Department of Transportation (ODOT) has historic RC bridges along the Pacific coast that experience serious corrosion and degradation. ODOT currently conducts labor-intensive corrosion surveys of its coastal bridges to determine the timing and type of remedial action they require. Fig. 4.1 shows a typical corrosion damage pattern for ODOT coastal bridges. Consequently, ODOT tends to focus on obtaining chloride content profiles and rebar corrosion status on the side of the girder near the bottom where corrosion damage is most likely. This would be a likely location to embed corrosion sensors. A method of obtaining frequent corrosion information would provide better condition assessment at much lower cost than the periodic hands-on surveys.

Considering the aging infrastructure and dwindling maintenance budget, it is necessary to develop a small, reliable, embedded, multi-parameter sensor system to be deployed at distributed locations of the existing RC structure, which can capture the critical data indicative of chloride ingress, corrosion initiation, and possibly early-age corrosion propagation. Such an effective, adaptive, field-deployable system can meet the urgent agency needs for corrosion monitoring, detection, and diagnosis, for the assessment of the remaining life of RC structures, and for the capability of timely intervention based on early warning.



Figure 4.1 Two photos of the same reinforced concrete girder showing no concrete damage on the ocean-facing side (left) and corrosion damage on the face of the beam opposite the ocean (right).

In this context, this chapter will provide a brief overview on the state of the art in online monitoring of rebar corrosion, followed by recent advances in embeddable sensors that help assess the corrosion-relevant parameters in concrete. Subsequently, this chapter will present a case study of testing embeddable sensors in an accelerated manner, and conclude with a discussion of future research needs. Note that the focus of this chapter is on technologies enabling *online* and *in situ* monitoring of rebar corrosion, instead of those enabling periodic, non-destructive testing and evaluation of the RC structure itself (e.g., radiography, acoustic emission, and ground penetrating radar). Yet, both groups of technologies are vital to condition assessment, health monitoring, reliability engineering, and resilience preservation of RC structures.

4.2 Online monitoring of rebar corrosion

The inherent drawbacks of current corrosion sensors are their inability to effectively monitor the overall evolution of corrosion in RC structures, and to detect or quantify the corrosion risk prior to the corrosion initiation. Currently available commercial or laboratory prototype sensors for rebar corrosion (Schuessl and Raupach, 1992; Raupach and Schießl, 2001; Reis and Gallaher, 2006; Watters et al., 2003; Song et al., 2008; Qiao et al., 2011) are typically placed in new structures during casting. Thus, they are not suitable for corrosion sensing of existing RC structures. Arguably, the corrosion sensors are most needed for existing structures which have endured decades of environmental exposure conditions (e.g., high humidity/wetness and chloride contents) and faced with an imminent risk of rebar corrosion and concrete cracking.

Some technologies of assessing rebar corrosion are of an indirect nature, since they are based on the ability to assess the condition and damage of the concrete embedding the rebar. Among them, the use of piezoelectric sensors has shown great promise. Li et al. (2016) demonstrated the feasibility of coupling the embedded piezoceramic lead zirconate (PZT) transducer with acoustic emission (AE) technique for health monitoring of concrete structures, which may find its application in

corrosion monitoring of RC structures. [Qin et al. \(2015\)](#) demonstrated the feasibility of using PZT material as an embedded corrosion sensor able to differentiate between stages of rebar corrosion during an accelerated corrosion test. Specifically, the PZT sensor embedded in concrete was designed to generate and receive ultrasonic waves, and the amplitude of the received waves indicated the accumulation of corrosion product(s) or formation of cracks at the rebar/concrete interface. [Talakokula and Bhalla \(2015\)](#) conducted accelerated corrosion tests on RC specimens and measured the conductance signature of both embedded and surface-bonded embedded PZT sensors. They found that the embedded PZT sensor to be highly sensitive in detecting the changes inside the concrete due to chloride ingress, i.e., during the initiation stage of rebar corrosion, whereas the surface bonded PZT sensor was more effective during the propagation stage of rebar corrosion. [Talakokula et al. \(2014\)](#) conducted accelerated corrosion tests on RC specimens with PZT patches bonded onto the rebar surface. Using the electro-mechanical impedance (EMI) technique, they were able to correlate the corrosion rates using PZT-identified mass loss with those using actual mass loss of the rebar. The PZT sensor was sensitive enough to detect significant levels of rebar corrosion, based on the extracted structural parameters, mainly the percent stiffness loss.

Some technologies of assessing rebar corrosion are of a direct nature, since they are based on the ability to quantitatively measure the instantaneous corrosion rate of the embedded rebar or closely related parameter(s). For instance, a three-electrode configuration can be embedded into concrete, with the working electrode being a probe made of material similar to the rebar; as such, its corrosion rate can be evaluated using electrochemical techniques such as linear polarization resistance—LPR ([Andrade and González, 1978](#)), or galvanic pulse method—GPM ([Elsener et al., 1997](#)). For chloride-induced corrosion of bare rebar or coated rebar, however, these techniques fail to provide a realistic evaluation of corrosion rate, as they assume that the rebar corrosion is uniform. [Karthick et al. \(2014\)](#) investigated the performance of a corrosion rate monitoring probe sensor which was embeddable in concrete, relative to the conventional guard ring system which was mounted on the surface of the RC specimen. This corrosion rate sensor was based on the LPR technique, with the rebar, 316 L stainless steel, and MnO_2 as its working, counter, and reference electrode, respectively. The authors reported that the embedded LPR sensor provided more reliable corrosion rate measurements than its surface-mounted counterpart, but they did not provide details on the dimensions of the LPR sensor or comment on its possible limitations (e.g., assuming that corrosion was uniform across the entire embedded rebar). Alternatively, electrochemical impedance spectroscopy (EIS) is a more powerful technique that can obtain mechanistic details of the rebar corrosion behavior ([Song and Saraswathy, 2007](#); [Dong et al., 2011](#)), but more difficult to implement for *in situ* monitoring. [Xu et al. \(2013\)](#) proposed a new spatial arrangement of the three-electrode system in concrete alongside an anodic polarization current (weak polarization) method, which effectively monitored chloride ingress into the concrete despite fluctuations in its relative humidity.

Another sensor configuration uses galvanic couples typically consisting of an anode/cathode macrocell, sometimes using the embedded rebar as the anode. The corrosion rate of the rebar or the corrosivity of its embedding concrete is evaluated by the macrocell current measurements (Schiesl and Raupach, 1992; Raupach and Schießl, 2001; Yoo et al., 2003). Park et al. (2005) reported that the embedded steel/copper galvanic sensor correlated well with the corrosion rate of the steel bar in concrete. Pereira et al. (2009) conducted laboratory tests in various simulated concrete pore solutions and then established the relationship between the galvanic current density measured by a carbon steel/stainless steel galvanic sensor (I_{gal}) and the corrosion current density estimated from a LPR sensor (I_{corr}), i.e., $I_{corr} \cong 10^{9/2} I_{gal}^{6/5}$. As such, the macrocell current density (corrosion current density) values indicative of passive and active corrosion condition were established as $I_{gal} < 0.14 \text{ nA/cm}^2$ ($I_{corr} < 0.1 \text{ }\mu\text{A/cm}^2$) and $I_{gal} > 1 \text{ nA/cm}^2$ ($I_{corr} > 1 \text{ }\mu\text{A/cm}^2$), respectively. For monitoring rebar corrosion in field concrete, however, the macrocell measurements are known to be prone to interference by wet/dry cycles and electrical resistance of the concrete.

Yet another sensor configuration simply uses a steel wire (Andringa et al., 2005). This passive, low-cost sensor prototype enables interrogation by inductively coupled magnetic fields to detect the corrosion status inside the concrete through the resonant frequency. Similarly, Perveen et al. (2013) demonstrated the use of a printed circuit board (PCB)-based corrosion potential sensor, which “uses a coupled coil resonator whose resonant frequency varies” as a result of change of potential difference between a rebar-sensing electrode and a stainless steel reference electrode. Such change in resonant frequency can be wirelessly interrogated. This passive sensor features a corrosion potential detection resolution of less than 10 mV and “allows for the unimpeded transport of reactants in the surrounding media”. Bhadra et al. (2013a,b) reported that this type of passive, wireless sensor can be very effective in monitoring early stages of corrosion, as the formation of corrosion product is indicated by a shift in the resonant frequency.

Recent years have seen continued research and development of multi-parameter corrosion sensors intended for implementation in RC structures. Duffó et al. (2013) reported the development of a prototype of integrated corrosion sensor which features sensing elements for temperature, oxygen concentration, chloride ion concentration, electrical resistivity of the concrete, as well as corrosion potential and corrosion current density of the rebar. The long-term performance of the sensing elements in concrete, however, remain to be reported. The schematic diagram and appearance of the sensor are shown in Fig. 4.2, and the sensor is embedded in a porous mortar before its deployment in new or existing concrete structure. Dong et al. (2011) reported the development and evaluation of a multifunctional sensor capable of monitoring the rebar potential, corrosion current density, as well as the pH and Cl^- concentration of concrete. This laboratory study confirmed that the chemical environment in the concrete, particularly *pH* and *Cl⁻ concentration*, are the most crucial factors defining the “corrosion tendency and corrosion rate of reinforcing steel”. Lu and Ba (2010) reported on an integrated corrosion sensor consisting of a reference probe, an electrical resistance probe, and a LPR unit. This

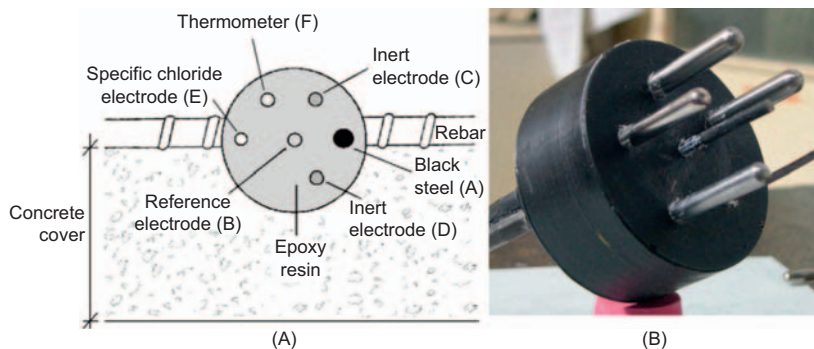


Figure 4.2 Schematic diagram of the sensor design and its location in concrete (a) and appearance of the sensor before embedded in porous mortar (b) (Duffó and Farina, 2009).

laboratory study revealed a strong correlation between the *electrical resistance* of the embedding cement mortar and the LPR of the embedded steel. Qiao et al. (2011) reported the development of a prototype five-electrode electrochemical corrosion sensor, which consists of one all-solid-state reference electrode, one counter electrode (graphite rod), and three identical working electrodes made of carbon steel. Galvanostatic step measurements and electrochemical noise measurements were enabled by this sensor configuration, and used to “extract the characteristics of general corrosion and pitting” of RC beams. The aforementioned prototype sensors were embeddable in concrete, but they were rather large in dimensions and thus would not provide the level of spatial resolution needed for service life prediction of RC structures. Yu and Caseres (2012) and Shi et al. (2015) reported the working technology of another integrated corrosion sensor prototype. The sensing elements include a patented 9-pin Multielectrode Array Sensor (MAS) probe at rebar depth, custom-made silver/silver chloride (Ag/AgCl) probes as chloride sensors at various depths in concrete, along with a graphite rod as the pseudo-reference probe. Instead of directly measuring the corrosion rate of the actual rebar embedded in concrete, the MAS measures the instantaneous corrosion rate of multiple miniature electrodes (~ 1 mm in diameter) made of the rebar material. In other words, the use of MAS sensors is intended to capture dramatic changes in the instantaneous corrosion rate, instead of incremental changes. The MAS sensor was less than 1 cm in diameter, with 9-pin electrodes sealed in an inert epoxy matrix, with careful fabrication to eliminate the risk of crevice corrosion. Corrosion current measurements are conducted using the coupled MAS pins and reading the voltage difference over the precision $100\ \Omega$ resistor between them. Conceptually, in a more corroding environment, both the maximum and the average current flowing between different pins would increase; as such, these parameters are used to quantitatively assess the corrosivity of the environment in which the MAS probe is embedded. As discussed later, this corrosion sensor prototype has its advantages as well as limitations.

4.3 Embeddable sensors for chloride concentration, pH, and other parameters

If deployed at strategic locations within an RC structure, embeddable sensors for online monitoring of multiple concrete state variables present a great opportunity for the structural health monitoring of RC structures. Such sensors would greatly improve the ability to assess the conditions inside the concrete, in real time or near real time, and with better spatial resolution, enabling more informed decisions for inspection, maintenance, rehabilitation, etc.

Considering the abundance of data available for referencing, these sensors will also enable better prediction of the remaining service life of RC structures in various environments. In addition, sensors that detect upsets in the chloride concentration or pH may provide early-warning capability for imminent risk of rebar corrosion. This section is thus devoted to the overview of recent advances in the sensors embeddable in concrete to detect the temporal or spatial evolutions of chloride concentration, pH, and other parameters relevant to the corrosion of the embedded rebar.

4.3.1 Embeddable chloride sensors

Chlorides play a critical role in the initiation and propagation of rebar corrosion inside the concrete. As such, it is vital to be able to monitor the temporal and spatial evolutions of chloride concentration inside RC structures, despite the lack of consensus on a specific chloride threshold value to depassivate the rebar and initiate its active corrosion (Alonso et al., 2000; Ann and Song, 2007; Shi et al., 2012).

Some technologies of assessing chloride ingress into concrete are based on the measurements of a parameter closely related to chloride concentration, such as electrical resistivity. Lecieux et al. (2015) reported the use of an integrated resistivity sensor compatible with Geoelectrical Imaging methods and assessed the detection threshold of this sensor using concrete beams with different levels of admixed chlorides. This embeddable sensor showed great promise for monitoring chloride gradients in concrete, despite the inherently stochastic variability of electricity readings, as it featured “a detection threshold of $37.85 \Omega \cdot \text{cm}$ [and a] 85.5% probability to detect a chloride content in concrete at 28 days higher than 30 g/l ”. Jin et al. (2017) reported the development of a graphene/cement composite as embeddable sensor to monitor chloride ion penetration in concrete structure, as the electrical conductivity of this sensor is directly correlated with the chloride ion content and insensitive to changes in the relative humidity of the concrete.

Another technology of interest to rebar corrosion monitoring is based on the highly affordable radio frequency identification (RFID) tags. Myers and Hernandez (2014) reported that these RFID-based corrosion sensors were as small as a coin and demonstrated as able to detect the arrival of sufficient amount of chlorides inside the concrete to initiate rebar corrosion. In other words, this technology serves as a way to indirectly assess the corrosion risk of embedded reinforcing or

prestressing steel, by detecting the chloride concentration at a given depth of concrete. Murthy (2015) reported the development and evaluation of a batteryless RFID-based embeddable sensor which showed great promise for long-term structural health monitoring. Specifically, the embedded sensor consists of a corrosion potential sensor or humidity sensor, temperature sensor, and interface electronics that can be remotely queried in a few seconds using “a few microwatts of power harvested from the interrogating RF signal”.

Torres-Luque et al. (2014) presented a review of the techniques developed in the last two decades for measuring chloride ingress into concrete structures, including those based on electrical resistivity (ER), ion selective electrode (ISE), and optical fiber sensors (OFSs). The embedded ER sensors are prone to interference by the moisture saturation level of the concrete, external electric fields, temperature fluctuations, etc. The embedded ISE sensors (e.g., Ag/AgCl) are prone to interference by the alkalinity of the concrete, presence of other ionic species, temperature fluctuations, the durability and reliability of the embedded reference electrode, etc. Embeddable OFSs are considered as the most promising techniques, as they are immune to interference by “environmental factors, ions presences or electromagnetic fields”. Yet, very few practical implementations of embeddable OFSs have been reported, likely due to the high cost of interrogating sensor signals and the extra protection needed for the fiber during construction and deployment (Mendez et al., 1990; Torres-Luque et al., 2014).

4.3.2 Embeddable pH sensors

In addition to chloride concentration, the pH value also plays a critical role in the initiation and propagation of rebar corrosion inside the concrete (Shi et al., 2011, 2012; Moreno et al., 2004). In general, the chloride anions work to catalyze and facilitate localized disruption of passive film on the rebar surface, whereas the hydroxyl ions work to repassivate the rebar surface or mitigate pH drop induced by rebar corrosion. As such, the chloride threshold to initiate rebar corrosion is sometimes characterized by the $[\text{Cl}^-]/[\text{OH}^-]$ ratio and it is desirable to monitor the temporal and spatial evolutions of pH inside RC structures subject to the risk of carbonation, acid attack, or rebar corrosion.

Some embeddable pH sensors are based on the measurement of optical properties. Srinivasan et al. (2000) reported an affordable solid-state pH sensor that features the use of a sol-gel/ trinitrobenzenesulfonic acid (TNBS) composite film that changes its optical properties in the pH range of 12–14, i.e., the range of most interest to concrete health monitoring. They reported the use of “a simple LED/filter/photodiode transducer”, along with the encapsulation and embedment of “the optical window, the light-source and sensor”. Dantan et al. (2005) also reported the development of a fiber-optic pH sensor that holds the promise for long-term, online monitoring in concrete structures. Nguyen et al. (2014) reported the development and evaluation of an optical fiber pH sensor that changes its fluorescence intensity in the pH range of 10.0–13.2. This embeddable sensor exhibited “an acceptable response rate of around 50 minutes, . . . a very good stability over more

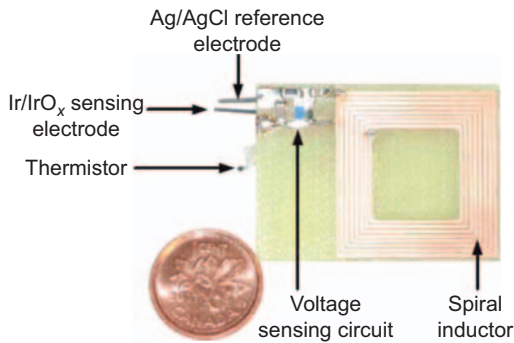


Figure 4.3 Photos of the 18 MHz wireless passive temperature and pH sensor (Bhadra et al., 2013a,b).

than 20 months, . . . and little cross-sensitivity to ionic strength”, making it a promising candidate for long-term online monitoring.

Other commonly-used embeddable pH sensors are based on an ion selective electrode (ISE), coupled with a reference probe—the potential difference of which features a strong correlation with pH of the embedding concrete (McCarter and Vennesland, 2004; Ha et al., 2004). Du et al. (2006) reported the use of Ag/AgCl electrode (fabricated by electrochemical anodization) and Ir/IrO₂ electrode (fabricated by thermal oxidation) as embeddable Cl and pH sensors, respectively. Both sensors exhibited robust and sensitive performance in quantifying the Cl⁻ concentration and pH inside the concrete specimens. Bhadra et al. (2013a,b) reported the development of an integrated wireless passive sensor as shown in Fig. 4.3, which provides the ability for online monitoring of both pH and temperature inside concrete. This sensor consists of an interrogator coil inductively coupled to the sensor inductor, a voltage sensing circuit, a thermistor, a pH probe (Ir/IrO_x), and a reference probe (Ag/AgCl). It is “calibrated for temperature over a range of 25–55°C and pH over a 1.5–12 dynamic range”, and features a response time of less than 1 second for a measurement accuracy of less than 0.1 pH (with the use of temperature compensation). However, this sensor is not immune to interference by the presence of other ionic species or cross-sensitivity to ionic strength.

4.3.3 Other embeddable sensors

In addition to chloride concentration, pH, and temperature, there are other parameters indicative of conditions inside concrete that may affect the level of rebar corrosion or corrosion risk. For instance, one essential embeddable sensor is the reference probe, as it is often needed to enable potential readings out of the ISE for chloride or pH. In addition, the reference probe is also known as a half-cell potential sensor, as it enables the potential reading of the embedded rebar or embedded working electrode, thus revealing the thermodynamic probability of active corrosion (Myrdal, 2007). Once the potential of the working electrode or rebar drops below a

given threshold (e.g., -276 mV vs SCE or saturated calomel electrode), it is known to indicate a high probability of active corrosion (e.g., 90%) even though this does not provide any information on the rate of corrosion (ASTM C876-15, 2015). Karthick et al. (2014) reported that a MnO_2 reference probe embedded in concrete exhibited excellent stability during an exposure period of 24 months, with an average potential of 198.5 ± 3.5 mV despite the presence of chloride ions. Muralidharan et al. (2007) and Ha et al. (2004) also reported the use of an alkaline MnO_2 sensor as reference electrode for concrete monitoring. Other reference or pseudo-reference probes reported in literature include: Ag/AgCl electrode (Bhadra et al., 2013a,b), metal–metal oxide (MMO)-activated titanium (Pease et al., 2011), and graphite rod (Shi et al., 2015).

An embeddable moisture sensor is another important type of sensor for concrete health monitoring. It is known that the risk of rebar corrosion would be minimized if the moisture level (or relative humidity) inside the concrete drops below a certain threshold. Furthermore, moisture presence also plays a crucial role in many other types of concrete durability distresses, such as freeze/thaw damage, salt scaling, sulfate attack, and alkali-aggregate reactions. Raupach et al. (2006) reported the extensive use of multiring-electrode (MRE) in the last two decades for monitoring the distribution of the moisture content profile along the concrete depth. The MRE sensor works by firstly establishing the relationship between moisture content of the concrete and its electrical resistivity at ambient temperature. As illustrated in Fig. 4.4, the embedded MRE was able to detect the moisture content profile along the concrete depth, as well as moisture content upsets induced by rainfall events (Raupach et al., 2013). Correia et al. (2012) developed a relative humidity (RH) sensor “based on a Bragg grating written in an optical fiber”, featuring the

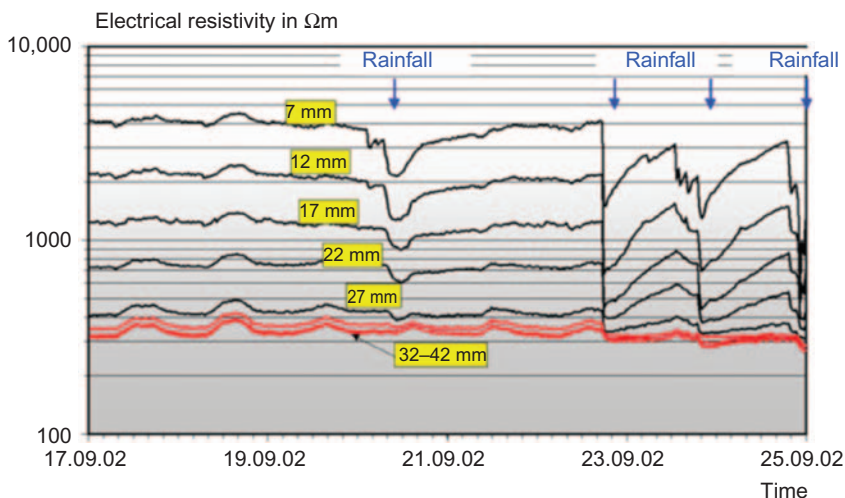


Figure 4.4 Readings from a MRE installed in outdoor concrete, at different depths from the concrete surface (Raupach et al., 2013).

use of an organo-silica diureasil hybrid sol-gel coating. The coating serves as a transducer layer as it adheres well to the fiber and expands reversibly with an increase in RH of the embedding environment. This RH sensor exhibited an outstanding sensitivity (22.2 pm/%RH) in the RH range of 15%–95%. Embedded in concrete blocks for 1 year, this optical sensor showed great promise for applications in monitoring of large structures. Zhou et al. (2016) developed a passive wireless RH sensor based on Ultra-High Frequency (UHF) RFID technology, featuring the use of interdigitated metal electrodes filled with polyimide for humidity sensing. With the transmission of electromagnetic wave in concrete, the sensing layer works by converting “the humidity capacitance into a digital signal in the frequency domain”. This RH sensor exhibited “a high linearity with a normalized sensitivity of 0.55% %RH at 20°C”, and a reliable communication distance of 0.52 m when embedded 8 cm deep into the concrete. The authors reported that “the measured results are highly consistent with the results measured by traditional methods”.

Electrical resistivity of concrete is known to indicate its chloride permeability (Shi, 2004) and also affects the rate of rebar corrosion propagation (Otieno et al., 2011). McCarter et al. (2005) reported an embeddable electrical conductivity sensor, consisting of 10 stainless steel electrode pairs mounted on a small Plexiglas, along with four thermistors. This sensor was able to monitor *in situ* the temporal and spatial evolutions of electrical conductivity inside the cover zone of concrete specimens exposed to natural conditions.

Embeddable oxygen sensors are yet another type of sensor important for concrete health monitoring, since the availability of oxygen in concrete is known to affect the level of rebar corrosion risk (Shi et al., 2011). Correia et al. (2006) developed an oxygen sensor that features the use of platinum and stainless steel as working electrodes, activated titanium as reference electrode, and graphite as counter electrode. The sensor works by establishing a linear relationship between the limiting currents of oxygen reduction (cathodic half-reaction) with the oxygen concentration in the concrete pore solution. The authors reported that “this sensor detects oxygen content variations in the interstitial solution of the concrete, providing qualitative information about the evolution of oxygen availability in concrete”.

4.3.4 Concluding remarks

The vast majority of currently-available corrosion sensors have their limitations. For example, some are too large to be embeddable in existing structures, or they have an insufficient number of sensor types to illustrate the full picture of the rebar-concrete interfacial environment and associated corrosion risk. The longevity and reliability of these sensors are questionable inside concrete over extended periods within aggressive environments, in light of possible issues due to chemical instability or interference by other environmental conditions—such as wet/dry and temperature cycling (Abbas, 2015). Furthermore, corrosion damage inside concrete is difficult to detect, particularly at the initiation stage. The use of real-time data for corrosion diagnosis and prognosis is still relatively unexplored and the ability to intelligently interrogate the multi-parameter, time-series, noise-containing sensor

data is currently lacking. A significant challenge for infrastructure managers and maintenance personnel is the ability to analyze sensor data and make informed maintenance decisions. Finally, interrogation of sensor systems requiring manual connection or wireless communication (but with limited range) makes it difficult to collect sensor data, which is especially true for hidden or hard-to-inspect locations.

Promising advances are being made in the domains of sensor technology, ICT (information and communications technology), data mining, and Internet of Things (IoT), all of which will contribute to advances in the monitoring of rebar corrosion and health monitoring of RC structures. For instance, [Leon-Salas et al. \(2011\)](#) reported the development of an RFID-based corrosion sensor which enables open circuit potential, linear polarization, and temperature measurements. Specifically, the sensor's electronic circuit consists of "a RFID modem, a low-power microcontroller and a three-electrode low-power potentiostat" housed in a 3D-printed case. With the decreases in cost and size of sensors, it is increasingly feasible to deploy a multiple sensor array at distributed, critical locations in RC structures, providing sensor data with enhanced temporal and spatial resolutions.

4.4 Accelerated testing of embeddable sensors: A case study

This section describes a case study that was conducted to test the longevity and reliability of the critical sensing elements in an embeddable, multi-parameter corrosion sensor along with those of customized chloride sensors, in an accelerated manner.

4.4.1 Sensors and sensing units tested

The prototype corrosion sensor consists of an array of sensing units, based on the corrosion sensor developed and patented by the Southwest Research Institute (SwRI), in which a 9-pin multi-electrode array sensor (MAS) corrosion current sensor, a Ag/AgCl chloride probe, a mixed metallic oxide (MMO) pH probe, and a four-point concrete resistivity probe are included in each sensor unit. Per the suggestion of the sponsoring agency, the fluctuations in the pH and electrical resistivity along the concrete depth of bridge structures are not very significant and these two types of probes were thus excluded from the prototype corrosion sensor ([Shi et al., 2015](#)).

The chloride probe in the prototype sensor was also improved as below, in order to enhance its stability in concrete over time. The existing research indicates that while Ag/AgCl remains sensitive to chloride content variation in a highly alkaline concrete environment, its long-term durability as a chloride probe can be compromised as the sensing surface layer gets oxidized by the hydroxyls in the concrete pore solution ([Montemor et al., 2006](#); [De Vera et al., 2010](#); [Jin et al., 2014](#)). The conventional Ag/AgCl probe fabrication process involves dipping a Ag rod into a molten bath of AgCl to develop a thick AgCl coating. In the prototype corrosion sensor, after dipping the Ag rod into molten AgCl twice, a #20 Ag mesh (diameter: 0.04 in.)

was wrapped on the AgCl coating surface. Subsequently, the whole probe pack was dipped into the molten AgCl to promote a light AgCl coating on the surface of the mesh. Subsequently, the electrical connection between the Ag wire and mesh was checked. This new process can partially re-melt the AgCl packed between the Ag mesh and rod and result in a more compact bond between the Ag/AgCl mesh and Ag/AgCl wire with a larger contact area.

Fig. 4.5A presents a photograph of the fabricated Ag/AgCl probes and high-density graphite rod probes made for the prototype sensor. The geometry of both probes is $\frac{1}{4}$ " (6.35 mm) in diameter with a length of $\frac{1}{2}$ " (12.7 mm). Fig. 4.5B presents a photograph showing the rear wire connection (which was spot welded or glued by conductive coating before sealing), and the epoxy seal in the polypropylene tube (D 2" by L 6", or 51 mm by 152 mm). The top-view photograph of the sensor prototype and the overview of the wired sensor are shown in Fig. 4.5C and D, respectively. The material used for the MAS sensing probes was a 1018 carbon steel wire with a diameter and length of 0.05 and $\frac{1}{4}$ " (1.27 and 6.35 mm), respectively. The sensing surfaces of the MAS and graphite probes were polished to a #600 grit surface finish. The surface of the Ag/AgCl probes were indented 0.05" (1.27 mm) into the matrix. A 24-pin standard serial cable was used to electrically connect the MAS probes and ribbon cables were used to connect the graphite and Ag/AgCl probes to the electrical platform. Note that one of the MAS probes had some of the pins short-circuited, thus turned into a 6-pin differential MAS, with 3 small pins and 3 pins with doubled exposed surface area.

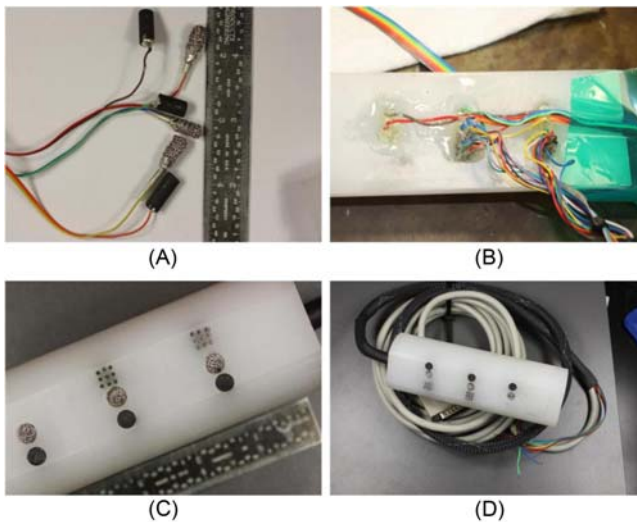


Figure 4.5 (A) Ag/AgCl and graphite probes, (B) wire connection inside the sensor tube, (C) top-view photograph of the sensor prototype, and (D) sensor and wired cable (Shi et al., 2015).

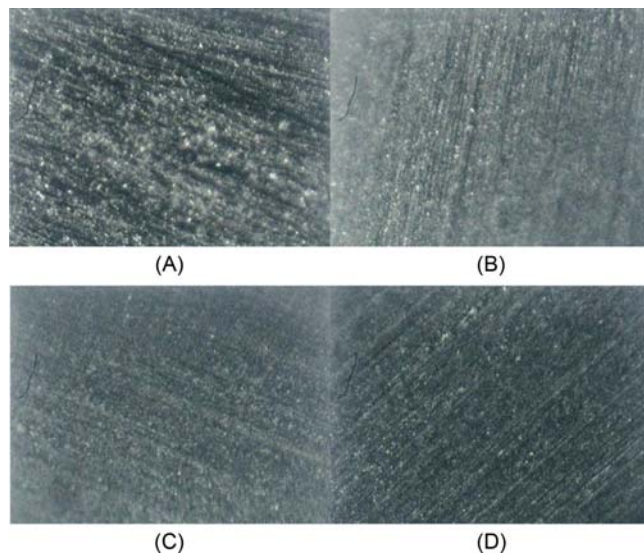


Figure 4.6 Micrograph ($230\ \mu\text{m} \times 310\ \mu\text{m}$) of Ag/AgCl probe surface after various stages of (A) to (C): electrodeposition using various current densities and (D): dip-coating in a polymeric solution.

Furthermore, laboratory experiments were conducted at the Western Transportation Institute (WTI) to fabricate 18 different Ag/AgCl probes. These were designed to explore the best method to fabricate a more-durable Ag/AgCl sensing layer, by first electrodepositing AgCl onto Ag rods and then soaking the Ag/AgCl into a certain polymeric solution for 10 minutes once or twice. At each step of the fabrication process, an Olympus BX61 optical microscope was employed to examine the surface morphology of the prepared sensing surface, as illustrated in Fig. 4.6. Once each probe was made, its potentiometric response was measured in five simulated concrete pore solutions with known chloride concentrations; and the data all showed very strong linear correlation between the open circuit potential of the probe and the logarithm of chloride concentration (with R-square no < 0.96). A conventional Ag/AgCl probe made with electrodeposition, but without the subsequent dip-coating, was used as a control for the probe longevity testing described in the next section.

4.4.2 Procedure of accelerated weathering test

The long-term integrity and stability of the MAS probes, chloride probes and reference probes integrated into one sensor are critical to the success of the corrosion monitoring system. As such, they were evaluated in an accelerated manner, by regulating the critical environmental variables (e.g., alkalinity, chloride concentration, heat, and moisture) during controlled “weathering tests”. The weathering tests subjected each sensing element (or probe) to a cyclic procedure of immersion in

simulated concrete pore solutions (0.6 M KOH + 0.2 M NaOH + 0.001 M Ca (OH)₂) with a given NaCl concentration for 2 weeks at 104°F (40°C) and subsequent drying by air for 3 days at room temperature (20°C). In the first four cycles, the hours of wetness featured the NaCl concentration increases from 0.001 M, to 0.01 M, 0.02 M, and ultimately 0.03 M. This was followed by another four cycles, where the hours of wetness featured the NaCl concentration increases from 0.04 M, to 0.06 M, 0.08 M, and ultimately 0.10 M. During the hours of wetness, the sensing elements were connected to the data acquisition system and their readings were taken, at least, on an hourly basis to monitor their stability during the immersion time and as a function of wetting cycle. The sensitivity and error levels of each sensing element were analyzed as data became available. Before and after each weathering cycle, the potentiometric response of the Ag/AgCl electrodes were measured in saturated Ca(OH)₂ solutions simulating the concrete pore solution, contaminated by free Cl⁻ concentration ranging from 1×10^{-7} to 2 M to see whether they still maintained good linearity with the logarithm of Cl⁻ concentration. Similarly, the potentiometric response of each reference probe in the sensing system was measured against that of a reference electrode that did not undergo the weathering tests. The purpose of this test was to determine whether they were prone to interference by the exposure to various solutions, heating, or wet/dry cycling. The corrosion rate estimated from the MAS probes was compared against that of three rust-free, bare steel #4 rebars that also underwent the weathering tests. The rebars were immersed 2" (50.8 mm) into the solution and their corrosion rate was measured using the EIS method.

4.4.3 Results and discussion

As shown in Table 4.1, only 6 of the 18 WTI custom-made chloride probes (WTI C11a, WTI C11b, WTI C12a, WTI C12b, WTI C11c, and WTI C13) can be considered stable after the eight cycles of weathering (consisting of wet-dry and chloride concentration changes). This is based on the fact that the open circuit potential reading of these six probes during the eight exposure cycles exhibited no coefficients of variance (COVs) higher than 20%. In other words, these six probes featured a stable potential reading during each cycle, which is vital for their practical application as a sensor.

As shown in Table 4.2, the control Cl⁻ probe (Ag/AgCl via electrodeposition only) failed to remain stable after the fourth cycle, likely due to the degradation of AgCl surface layer by alkaline oxidation and wet-dry cycling. The second SwRI chloride probe failed to remain stable after the sixth cycle, whereas the other two SwRI chloride probes remained stable after the eight weathering cycles. All three SwRI graphite probes remained stable after the eight weathering cycles. Note that: after the fourth cycle (Cl⁻ concentration increased from 0.03 to 0.04 M), the third rebar exhibited great variability in its potential readings during each cycle, which is attributable to its active corrosion.

The accelerated laboratory testing results should indicate whether the critical sensing elements can retain their sensing properties and integrity after being

Table 4.1 Potentiometric responses of WTI custom-made Ag/AgCl probes during the weathering cycles, in mV_{SCE}^a

Name of the chloride probe	Cycle 1		Cycle 2		Cycle 3		Cycle 4		Cycle 5		Cycle 6		Cycle 7		Cycle 8	
	Average	COV (%)	Average	COV (%)	Average	COV (%)	Average	COV (%)	Average	COV (%)	Average	COV (%)	Average	COV (%)	Average	COV (%)
Amberlite IRA—400 chloride	-722.4	-45	-323.7	-9	-378.9	-13	-569.8	-40	-896.1	-14	-1001.2	-24	-1033.1	-8	-895.9	-6
Polyethylene oxide	-310.1	-6	-328.1	-5	-331.9	-11	-342.1	-9	-365.2	-31	-356.5	-10	-314.3	-18	-376.7	-19
WTI CI1a	-159.2	-5	-170.0	-4	-156.7	-8	-155.5	-6	-170.0	-3	-171.1	-6	-157.3	-5	-178.3	-4
Polytetrafluoroethylene	-416.1	-17	-409.1	-24	-411.7	-19	-484.4	-34	-973.2	-12	-951.1	-6	-876.2	-9	-914.7	-11
Poly vinyl alcohol	-721.8	-42	-763.0	-44	-679.8	-42	-649.7	-47	-934.3	-29						
Dextrose (glucose) anhydrous	-378.8	-11	-426.7	-37	-499.2	-44	-454.7	-42	-924.6	-10						
WTI CI1b	-158.1	-6	-172.4	-5	-171.2	-3	-167.9	-4	-185.8	-3	-207.6	-5	-220.4	-8	-252.7	-5
Chitosan	-368.1	-7	-820.9	-39	-1068.7	-9	-1055.8	-9	-1111.2	-6	-984.9	-13	-774.7	-6	-925.5	-13
WTI CI2a	-163.1	-6	-174.4	-6	-180.5	-3	-181.0	-6	-216.9	-5	-252.3	-6	-271.9	-12	-321.8	-9
Chitosan	-352.4	-5	-370.2	-10	-400.6	-24	-360.6	-16	-567.0	-51	-1001.7	-10	-709.3	-29	-861.9	-15
Polyethylene glycol	-305.2	-5	-343.1	-14	-412.7	-25	-342.2	-34	-874.2	-21	-737.1	-32	-832.3	-21	-890.0	-11
Chitosan	-1047.4	-13	-1067.6	-7	-988.6	-13	-815.8	-28	-992.9	-13	-867.6	-11	-893.0	-14	-907.0	-11\$
Poly vinyl alcohol	-344.9	-9	-369.6	-17	-477.7	-41	-511.9	-44	-1022.8	-12						
Poly acrylic acid	-354.4	-6	-399.8	-14	-467.4	-28	-502.3	-44	-1094.1	-12						
Poly vinyl alcohol	-1036.8	-15	-896.9	-26	-934.8	-15	-979.4	-8	-1041.5	-9	-775.0	-2	-916.2	-14	-1077.2	-5
WTI CI2b	-167.2	-8	-179.3	-4	-174.3	-5	-172.0	-4	-197.3	-3	-220.2	-4	-216.9	-4	-241.9	-3
WTI CI1c	-266.4	-5	-266.1	-5	-281.9	-6	-269.3	-6	-287.2	-6	-304.7	-8	-276.9	-9	-303.5	-3
WTI CI3	-330.2	-9	-374.3	-10	-358.8	-7	-341.5	-6	-370.9	-7	-367.0	-6	-348.2	-6	-406.4	-13

Note: The potential of chloride probes was measured against an SCE.

*The gray color indicates sensors being removed from the test due to poor linearity, measured in proceeding cycles.

Table 4.2 Potentiometric responses of the rebars, control Cl⁻ probe, and SwRI sensing probes during the weathering cycles, in mV_{SCE}

Sensors	Cycle 1		Cycle 2		Cycle 3		Cycle 4		Cycle 5		Cycle 6		Cycle 7		Cycle 8	
	Average	COV (%)	Average	COV (%)	Average	COV (%)	Average	COV (%)	Average	COV (%)	Average	COV (%)	Average	COV (%)	Average	COV (%)
REBAR (1)	-161.9	-11	-136.6	-5	-151.9	-13	-115.1	-8	-118.7	-6	-125.1	-9	-107.9	-31	-121.1	-26
REBAR (2)	-155.9	-7	-141.9	-8	-134.9	-2	-166.6	-35	-131.3	-20	-123.3	-8	-100.0	-10	-124.6	-7
REBAR (3)	-184.0	-23	-159.4	-25	-124.1	-17	-161.9	-19	-116.4	-660	-142.9	-74	-324.9	-21	-159.6	-534
Control Cl	-203.8	-6	-202.3	-9	-188.0	-9	-278.3	-17	-495.8	-49	-526.5	-56	-297.9	-14	-478.4	-44
SWRI_CL (1)	-282.7	1	283.8	2	261.0	7	261.9	1	259.7	2	235.5	2	206.2	11	224.5	9
SWRI_CL (2)	271.5	4	275.4	10	245.7	11	227.1	14	217.6	16	145.7	33	146.9	50	126.3	39
SWRI_CL (3)	267.1	3	269.6	6	261.4	5	272.0	6	297.6	6	306.2	9	335.1	11	311.3	14
GTE_SCE (1)	-186.5	-2	-183.2	-5	-156.5	-14	-167.8	-6	-174.3	-4	-179.0	-2	-164.8	-8	-187.3	-4
GTE_SCE (2)	-177.1	-6	-193.3	-7	-180.9	-8	-194.1	-8	-243.9	-4	-256.5	-2	-212.1	-8	-244.1	-2
GTE_SCE (3)	-174.8	-3	-180.9	-8	-173.8	-11	-199.5	-7	-228.2	-5	-267.4	-6	-293.2	-14	-274.9	-15

Note: The potential of rebars, control chloride probe, and graphite probes (GTE_SCE) was measured against an SCE, whereas that of the SwRI chloride probes (SWRI_CL) was measured against their closest graphite probe.

subjected to aggressive service environments. It is noteworthy that the temperature in existing concrete structures would rarely (if ever) reach as high as 104°F and the use of this relatively high temperature aimed to accelerate the possible oxidation and degradation of the sensing elements once they are embedded in concrete. Similarly, the sensing elements in field concrete would rarely be completely dry. The alternated wetting and drying aimed to capture the effects of moisture fluctuations experienced by field concrete on the stability of the embedded sensing elements.

During the testing of sensor longevity, instead of periodically measuring the anodic current flowing between the MAS pins (i.e., ΔI_{ij}), we periodically measured the potential difference between the MAS pins (i.e., ΔE_{ic} , with the central pin as reference). The potential difference between certain MAS pins (e.g., ΔE_{ij}) was not directly measured but was calculated using the following equation:

$$\Delta E_{ij} = \Delta E_{ic} - \Delta E_{jc}$$

All the ΔE values were taken at their absolute values. Subsequently the maximum and average ΔE of each MAS probe in a given test solution was monitored on an hourly basis during the weathering cycles (except the drying periods).

For the 9-pin MAS, even the “best” parameter derived from MAS readings exhibited only a relatively good correlation with the average rebar corrosion rate during each weathering cycle (R-square of 0.79, as shown in Fig. 4.7A). Nonetheless, the 9-pin MAS served as a very effective chloride ion sensor, as there existed a very strong one-to-one correlation between the chloride concentration of simulated pore solution and the following parameter derived from MAS readings: $stdev(t)Max(p)/Avg(t)Avg(p)$, with R-square of 0.91 (Fig. 4.7B). For each exposure cycle, the numerator term is calculated from the standard deviation of maximum pin ΔE_{ij} over time, and the denominator term is calculated from the average of average pin ΔE_{ij} over time.

For the 6-pin differential MAS, there existed a very strong correlation between the average rebar corrosion rate during each weathering cycle and the following parameter derived from MAS readings: $stdev(t)Max(p)/Avg(t)Avg(p)$, with R-square of 0.92 (Fig. 4.8B). However, these two did not exhibit a one-to-one relationship; as such, the 6-pin differential MAS may not serve as an effective corrosion sensor, unless augmented by other sensing elements. Nonetheless, the 6-pin differential MAS served as a very effective chloride ion sensor, as there existed a very strong one-to-one correlation between the chloride concentration of simulated pore solution and the following parameter derived from MAS readings: $max(t)Max(p)/Avg(t)Avg(p)$, with R-square of 0.91 (Fig. 4.8B). For each exposure cycle, the numerator term is calculated from the maximum of maximum pin ΔE_{ij} over time, and the denominator term is calculated from the average of average pin ΔE_{ij} over time.

As shown in Fig. 4.9, only three of the eighteen WTI custom-made chloride probes (WTI C11b, WTI C12a, and WTI C13) can be considered reliable chloride probes after the eight cycles of weathering. This is based on the fact that their

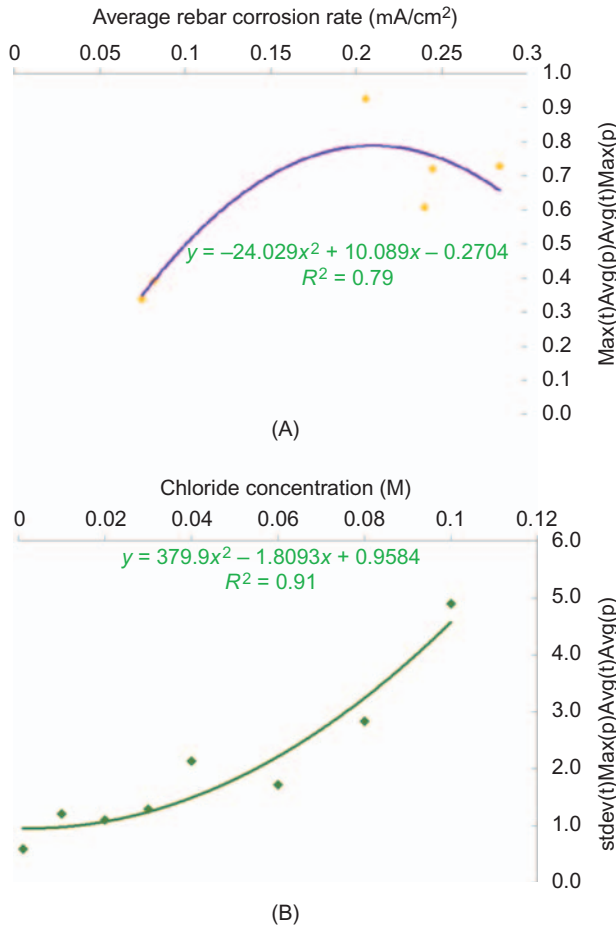


Figure 4.7 Correlation between (A) average rebar corrosion rate and (B) chloride concentration of each weathering cycle, with a certain parameter derived from the 9-pin MAS.

average potential reading maintained a high second-order polynomial correlation (R-square of 0.90 or above) with the chloride concentration of simulated pore solution, over the eight weathering cycles. In contrast, only one of the SwRI chloride probes (SwRI Cl2) exhibited this level of high correlation, yet it failed to remain reliable after the sixth cycle (Table 4.2). Furthermore, the control Cl^- probe (Ag/AgCl via electrodeposition only) failed to exhibit a good correlation between its average potential reading with the chloride concentration of simulated pore solution, over the eight weathering cycles. The R-square in this case was only 0.562, indirectly confirming the superior longevity of custom-made WTI chloride probes. The three reliable chloride probes, WTI Cl1b, WTI Cl2a, and WTI Cl3 were

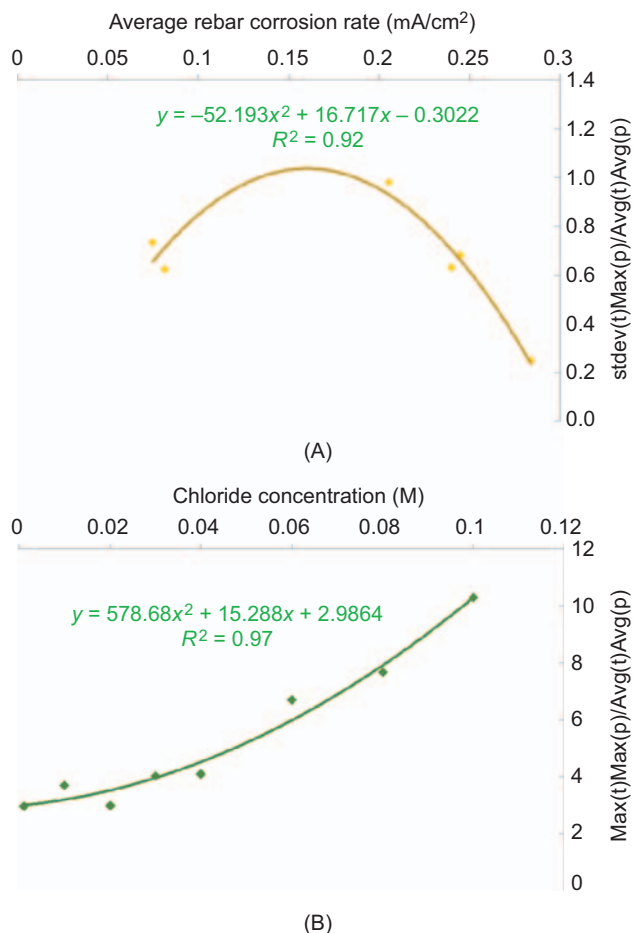


Figure 4.8 Correlation between (A) average rebar corrosion rate and (B) chloride concentration of each weathering cycle, with a certain parameter derived from the 6-pin differential MAS.

fabricated by the same stepwise electrodeposition of AgCl on Ag rod, followed by dip-coating in 0.05 wt.% poly(vinyl alcohol) twice, 0.05 wt.% chitosan twice, and 0.05 wt.% poly(ethylene oxide) once, respectively.

Table 4.3 reveals that, over the eight weathering cycles, only one of the SwRI graphite probes (GTE_SCE(1)) remained relatively stable, with its potential showing a standard deviation of 11 mV and a COV of -6% . Interestingly, a few of the WTI custom-made Ag/AgCl probes showed good potential to serve as reliable reference electrodes in concrete. The most reliable reference probe, WTI C11a, was fabricated by the same stepwise electrodeposition of AgCl on Ag rod followed by dip-coating in 0.05 wt.% poly(tetrafluoroethylene) once.

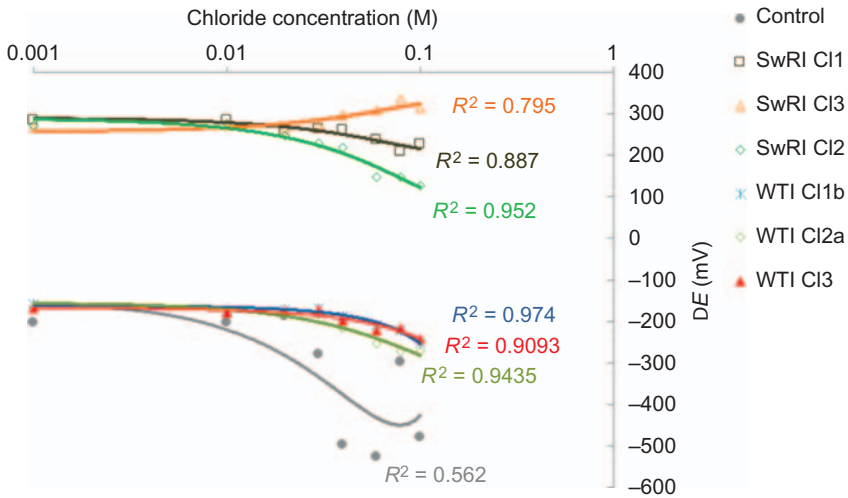


Figure 4.9 Potential reading of selected chloride probes as a function of chloride concentration of simulated pore solution over the eight weathering cycles.

Table 4.3 Potentiometric responses of the SwRI reference probes and WTI reference probes during the weathering cycles

Cycle	Solution (Cl ⁻ , M)	WTI Cl1a	WTI Cl2b	WTI Cl1c	WTI Cl3	GTE_SCE (1)	GTE_SCE (2)	GTE_SCE (3)
1	0.001	-159.2	-167.2	-266.4	-330.2	-186.5	-177.1	-174.8
2	0.01	-170.0	-179.3	-266.1	-374.3	-183.2	-193.3	-180.9
3	0.02	-156.7	-174.3	-281.9	-358.8	-156.5	-180.9	-173.8
4	0.03	-155.5	-172.0	-269.3	-341.5	-167.8	-194.1	-199.5
5	0.04	-170.0	-197.3	-287.2	-370.9	-174.3	-243.9	-228.2
6	0.06	-171.1	-220.2	-304.7	-367.0	-179.0	-256.5	-267.4
7	0.08	-157.3	-216.9	-276.9	-348.2	-164.8	-212.1	-293.2
8	0.1	-178.3	-241.9	-303.5	-406.4	-187.3	-244.1	-274.9
	COV (%)	-5	-14	-6	-6	-6	-15	-22
	Average	-165	-196	-282	-362	-175	-213	-224
	Standard dev.	9	27	16	23	11	31	49

Table 4.4 shows the variability of potential readings of various sensing probes within 60 seconds of immersion into a simulated pore solution with 0.03 M NaCl, with readings taken every 10 seconds. This sheds light on the response time of the sensing probes. The vast majority of WTI custom-made Ag/AgCl probes (except WTI Cl1b) exhibited rapid response time as their potential quickly stabilized in the test solution. In comparison, the SwRI sensing probes featured a slightly higher variability in their 60 seconds potential readings. Nonetheless, the vast majority of the sensing probes featured a response time of less than 60 seconds.

Table 4.4 Response time of various sensing probes, measured by the potential variability within 60 s of immersion into a simulated pore solution with 0.03 M NaCl

Name of the WTI CI sensor	Average	Standard dev.	COV (%)	Name of the SwRI sensor	Average	Standard dev.	COV (%)
Amberlite IRA—400 chloride	-826.8	0.4	-0.05	Surface sensor 1-1	-61.5	0.9	-1.5
Polyethylene oxide	-266.5	0.2	-0.09	Surface sensor 1-2	-59.7	0.5	-0.9
WTI CI1a	-123.7	0.3	-0.22	Surface sensor 1-3	-57.7	0.7	-1.3
Polytetrafluoroethylene	-821.8	0.4	-0.05	Surface sensor 1-4	-55.7	0.6	-1.0
				Surface sensor 1-5	-54.0	0.7	-1.2
				Surface sensor 1-6	-52.1	0.7	-1.3
WTI CI1b	-19.3	16.2	-83.88	Surface sensor 1-7	-50.4	0.7	-1.3
Chitosan	-97.6	0.9	-0.90	Surface sensor 1-8	-48.8	0.7	-1.4
WTI CI2a	-95.0	0.7	-0.72				
Chitosan	-92.0	0.7	-0.77	Surface sensor 2-1	-47.2	0.7	-1.6
Polyethylene glycol	-89.3	0.7	-0.78	Surface sensor 2-2	-45.6	0.6	-1.3
Chitosan	-86.8	0.6	-0.70	Surface sensor 2-3	-43.9	0.7	-1.5
				Surface sensor 2-4	-42.4	0.9	-2.1
				Surface sensor 2-5	-40.9	0.8	-2.1
Poly vinyl alcohol	-78.9	0.8	-1.03	SWRI-1	-39.5	0.9	-2.3
WTI CI2b	-76.8	1.0	-1.27	SWRI-2	-38.0	0.8	-2.0
WTI CI1c	-74.5	0.6	-0.76	SWRI-3	-36.7	0.8	-2.2
WTI CI3	-72.0	0.6	-0.82	Control CI sensor	-63.7	0.5	-0.8

4.4.4 Conclusions

Eighteen custom-made chloride probes, along with the SwRI sensors, a conventional Ag/AgCl probe (as control), and three bare steel #4 rebars went through a cyclic immersion in simulated concrete pore solutions. Only 6 out of the 18 WTI custom-made chloride probes can be considered stable after the eight cycles of weathering (consisting of wet-dry and chloride concentration changes). All three SwRI graphite probes remained stable after the eight weathering cycles. The three reliable chloride probes, WTI C11b, WTI C12a, and WTI C13, were fabricated by the same stepwise electrodeposition of AgCl on Ag rod followed by dip-coating in 0.05 wt.% poly(vinyl alcohol) twice, 0.05 wt.% chitosan twice, and 0.05 wt.% poly(ethylene oxide) once, respectively. All three SwRI chloride probes and the conventional Ag/AgCl probe failed the accelerated weathering test. Over the eight weathering cycles, only one of the three SwRI graphite probes remained relatively stable. The most reliable reference probe, WTI C11a, was fabricated by the same stepwise electrodeposition of AgCl on Ag rod followed by dip-coating in 0.05 wt.% poly(tetrafluoroethylene) once. The vast majority of the sensing probes featured a response time of less than 60 seconds.

4.5 Future research needs

In light of findings from the published literature and the case study, the following research needs are identified:

- Additional research should further explore the use of differential MAS as corrosion rate sensors, with either potential or current readings from individual pins. It is envisioned that such sensor design can be coupled with electrochemical noise analysis to derive average corrosion rate and localized corrosion index, and this may help address the challenges for sensing in cases of active corrosion and high chloride concentration. Sensing elements for other parameters, such as corrosion potential, temperature, moisture, and pH may be incorporated in an advanced version of the multi-parameter corrosion sensor. The goal is to deploy a user-friendly, maintainable, rugged (durable and stable), sensitive, accurate, and cost-effective sensor that can be easily embedded into both new and existing RC structures, and *in situ* monitoring of localized corrosion risk and corrosion rate of the reinforcing steel.
- Research is needed to enhance and evaluate the long-term durability and stability of sensing elements in the multi-parameter sensor and to improve the system reliability, usability and cost-effectiveness. The ideal corrosion monitoring system should provide high-quality corrosion condition information at reduced cost; be able to detect corrosion initiation and propagation in RC structures at the earliest possible time, and enable condition-based or reliability-centered maintenance strategies. Furthermore, it should provide increased reliability and remote-sensing capability for condition assessment and service life prognosis of RC structures, enabling lifecycle performance assessment of corrosion-affected RC structures. The use of low-power wireless data acquisition hardware and alternative power source will facilitate the implementation of such corrosion monitoring systems.
- Research is warranted in evaluating the combined use of the corrosion monitoring system, with impressed current cathodic protection (ICCP) to automatically adjust the protective

current in a way that maximizes anode life and optimizes corrosion control. This may also entail the strategic placement of the sensor at distributed locations of the RC structure.

- The multivariate data obtained from the online monitoring system will present a great opportunity for data mining, which can be applied for recognizing corrosion patterns as they unfold in real time, providing valuable insights on corrosion initiation, and propagation and structural degradation. Advances need to be made in developing algorithms to filter and interrogate the collected sensor data, producing actionable corrosion condition information, and presenting such information through an intuitive interface to facilitate asset management and decision-making. A possible methodology for corrosion health monitoring could adopt the approach of statistical pattern recognition enabled by time series modeling, similar to identification of damage-sensitive features or outliers (Gul and Catbas, 2009; Qiao, 2009; Cudney et al., 2007). Ultimately, one can expect that the numerous periodical measurements of corrosion and environmental parameters inside concrete will provide: (1) abundant data to develop the algorithms for data display and quality control; (2) capability of an evolving predictive model that can capture the near-real-time condition of the structure being monitored and enable early-warning of sudden degradation of rebar and/or service conditions during extreme events.

Acknowledgments

The research reported herein was financially supported by the Oregon Department of Transportation (ODOT) as well as U.S. Department of Transportation (USDOT) through Alaska University Transportation Center (AUTC) and Western Transportation Institute (WTI). The author is indebted to the AUTC project manager Billy Connor, ODOT project manager Steve Soltesz, and other technical panel members for their support throughout this project. The author also extends his appreciation to Anburaj Muthumani and Nirap Sanju for their assistance in the laboratory testing.

References

- Abbas, Y., 2015. In-situ measurement of chloride ion concentration in concrete. Doctoral Dissertation, University of Twente.
- Alonso, C., Andrade, C., Castellote, M., Castro, P., 2000. Chloride threshold values to depassivate reinforcing bars embedded in a standardized OPC mortar. *Cem. Concr. Res.* 30 (7), 1047–1055.
- Andrade, C., González, J.A., 1978. Quantitative measurements of corrosion rate of reinforcing steels embedded in concrete using polarization resistance measurements. *Mater. Corros.* 29 (8), 515–519.
- Andringa, M.M., Neikrik, D.P., Dickerson, N.P., Wood, S.L., 2005. Unpowered wireless corrosion sensor for steel reinforced concrete. *IEEE Sens.* 155–158. Available from: <http://dx.doi.org/10.1109/ICSENS.2005.1597659>.
- Ann, K.Y., Song, H.W., 2007. Chloride threshold level for corrosion of steel in concrete. *Corros. Sci.* 49 (11), 4113–4133.
- ASCE, 2016. 2016 Report Card for America's Infrastructure. <<http://www.infrastructurereportcard.org>> (accessed March 2017).

- ASTM C876-15, 2015. Standard test method for corrosion potentials of uncoated reinforcing steel in concrete. American Society for Testing and Materials, ASTM International.
- Bhadra, S., Tan, D.S., Thomson, D.J., Freund, M.S., Bridges, G.E., 2013a. A wireless passive sensor for temperature compensated remote pH monitoring. *IEEE Sens. J.* 13 (6), 2428–2436.
- Bhadra, S., Thomson, D.J., Bridges, G.E., 2013b. A wireless embedded passive sensor for monitoring the corrosion potential of reinforcing steel. *Smart Mater. Struct.* 22 (7), 075019.
- Correia, M.J., Pereira, E.V., Salta, M.M., Fonseca, I.T.E., 2006. Sensor for oxygen evaluation in concrete. *Cem. Concr. Compos.* 28 (3), 226–232.
- Correia, S.F., Antunes, P., Pecoraro, E., Lima, P.P., Varum, H., Carlos, L.D., et al., 2012. Optical fiber relative humidity sensor based on a FBG with a di-ureasil coating. *Sensors.* 12 (7), 8847–8860.
- Cudney, E.A., Hong, J., Jugulum, R., Paryani, K., Ragsdell, K.M., 2007. An evaluation of Mahalanobis-Taguchi system and neural network for multivariate pattern recognition. *J. Ind. Syst. Eng.* 1 (2), 139–150.
- Dantan, N., Habel, W.R., Wolfbeis, O.S., 2005. Fiber optic pH sensor for early detection of danger of corrosion in steel-reinforced concrete structures. *Smart Structures and Materials. International Society for Optics and Photonics, Bellingham, WA*, pp. 274–284.
- De Vera, G., Climent, M.A., Antón, C., Hidalgo, A., Andrade, C., 2010. Determination of the selectivity coefficient of a chloride ion selective electrode in alkaline media simulating the cement paste pore solution. *J. Electroanal. Chem.* 639 (1), 43–49.
- Dong, S.G., Lin, C.J., Hu, R.G., Li, L.Q., Du, R.G., 2011. Effective monitoring of corrosion in reinforcing steel in concrete constructions by a multifunctional sensor. *Electrochim. Acta.* 56 (4), 1881–1888.
- Du, R.G., Hu, R.G., Huang, R.S., Lin, C.J., 2006. *In situ* measurement of Cl^- concentrations and pH at the reinforcing steel/concrete interface by combination sensors. *Anal. Chem.* 78 (9), 3179–3185.
- Duffó, G.S., Farina, S.B., 2009. Development of an embeddable sensor to monitor the corrosion process of new and existing reinforced concrete structures. *Constr. Build. Mater.* 23 (8), 2746–2751.
- Duffó, G.S., Farina, S.B., Arva, E.A., Giordano, C.M., Lafont, C.J., 2013. Development of an integrated sensor to monitor the corrosion process of reinforced concrete structures. In: Ferreira, R.M., Gulikers, J., Andrade, C. (Eds.), *Proceedings of the International RILEM Workshop on Integral Service Life Modelling of Concrete Structures. RILEM, Bagneux*, pp. 167–174.
- Elsener, B., Klinghoffer, O., Frolund, T., Rislund, E., Schiegg, Y., Böhni, H., 1997. Assessment of reinforcement corrosion by means of galvanostatic pulse technique. In: Blankvoll, A. (Ed.), *Repair of Concrete Structures: From Theory to Practice in a Marine Environment, Svolvær, Norway, 28–30 May, 1997. Norwegian Road Research Laboratory, Oslo*, pp. 391–400.
- Glass, G.K., Buenfield, N.R., 2000. Chloride-induced corrosion of steel in concrete. *Prog. Struct. Eng. Mater.* 2 (4), 448–458.
- Gul, M., Catbas, F.N., 2009. Statistical pattern recognition for structural health monitoring using time series modeling: theory and experimental verifications. *Mech. Syst. Signal Process.* 23, 2192–2204.
- Ha, T.H., Muralidharan, S., Bae, J.H., Ha, Y.C., Lee, H.G., Park, K.W., et al., 2004. Role of sensors in corrosion monitoring and durability assessment in concrete structures: the state of the art. *Sens. Mater.* 16 (3), 133–158.

- Jin, M., Jiang, L., Lu, M., Bai, S., 2017. Monitoring chloride ion penetration in concrete structure based on the conductivity of graphene/cement composite. *Constr. Build. Mater.* 2017 (136), 394–404.
- Jin, M., Xu, J., Jiang, L., Gao, G., Chu, H., Xiong, C., et al., 2014. Electrochemical characterization of a solid embeddable Ag/AgCl reference electrode for corrosion monitoring in reinforced concrete. *Electrochemistry*, 82 (12), 1040–1046.
- Karthick, S.P., Muralidharan, S., Saraswathy, V., Thangavel, K., 2014. Long-term relative performance of embedded sensor and surface mounted electrode for corrosion monitoring of steel in concrete structures. *Sens. Actuators, B*, 192, 303–309.
- Lecieux, Y., Schoefs, F., Bonnet, S., Lecieux, T., Lopes, S.P., 2015. Quantification and uncertainty analysis of a structural monitoring device: detection of chloride in concrete using DC electrical resistivity measurement. *Nondestr. Test. Eval.* 30 (3), 216–232.
- Leon-Salas, W., Kanneganti, S., Halmen, C., 2011. Development of a smart RFID-based corrosion sensor. *IEEE Sens. J.* 534–537. Available from: <http://dx.doi.org/10.1109/ICSENS.2011.6127274>.
- Li, W., Kong, Q., Ho, S.C.M., Mo, Y.L., Song, G., 2016. Feasibility study of using smart aggregates as embedded acoustic emission sensors for health monitoring of concrete structures. *Smart Mater. Struct.* 25 (11), 115031.
- Lu, S., Ba, H.J., 2010. Corrosion sensor for monitoring the service condition of chloride-contaminated cement mortar. *Sensors*, 10 (4), 4145–4158.
- McCarter, W.J., Vennesland, Ø., 2004. Sensor systems for use in reinforced concrete structures. *Constr. Build. Mater.* 18 (6), 351–358.
- McCarter, W.J., Chrisp, T.M., Starrs, G., Basheer, P.A.M., Blewett, J., 2005. Field monitoring of electrical conductivity of cover-zone concrete. *Cem. Concr. Compos.* 27 (7), 809–817.
- Mendez, A., Morse, T.F., Mendez, F., 1990. Applications of embedded optical fiber sensors in reinforced concrete buildings and structures. In: *OE/FIBERS'89*. International Society for Optics and Photonics, pp. 60–69.
- Montemor, M.F., Alves, J.H., Simoes, A.M., Fernandes, J.C.S., Lourenço, Z., Costa, A.J.S., et al., 2006. Multiprobe chloride sensor for in situ monitoring of reinforced concrete structures. *Cem. Concr. Compos.* 28 (3), 233–236.
- Moreno, M., Morris, W., Alvarez, M.G., Duffó, G.S., 2004. Corrosion of reinforcing steel in simulated concrete pore solutions: effect of carbonation and chloride content. *Corros. Sci.* 46 (11), 2681–2699.
- Muralidharan, S., Ha, T.H., Bae, J.H., Ha, Y.C., Lee, H.G., Kim, D.K., 2007. A promising potential embeddable sensor for corrosion monitoring application in concrete structures. *Measurement*, 40 (6), 600–606.
- Murthy, S.G.N., 2015. Batteryless Wireless RFID based embedded sensors for long term monitoring of reinforced concrete structures. In: *2015 International Symposium Non-Destructive Testing in Civil Engineering*, pp. 1–8.
- Myers, J.J., Hernandez, E., 2014. Implementation of radio frequency identification (RFID) sensors for monitoring of bridge deck corrosion in Missouri. Final Report for the Center for Transportation Infrastructure and Safety/NUTC Program, Missouri University of Science and Technology, Rolla, MO.
- Myrdal, R., 2007. *The Electrochemistry and Characteristics of Embeddable Reference Electrodes for Concrete*, Structural Engineering. Woodhead, Cambridge.
- Nguyen, T.H., Venugopala, T., Chen, S., Sun, T., Grattan, K.T., Taylor, S.E., et al., 2014. Fluorescence based fibre optic pH sensor for the pH 10–13 range suitable for corrosion monitoring in concrete structures. *Sens. Actuators, B*, 191, 498–507.
- Otieno, M.B., Beushausen, H.D., Alexander, M.G., 2011. Modelling corrosion propagation in reinforced concrete structures: a critical review. *Cem. Concr. Compos.* 33 (2), 240–245.

- Park, Z.T., Choi, Y.S., Kim, J.G., Chung, L., 2005. Development of a galvanic sensor system for detecting the corrosion damage of the steel embedded in concrete structure: Part 2. Laboratory electrochemical testing of sensors in concrete. *Cement Concrete Res.* 35 (9), 1814–1819.
- Pease, B., Geiker, M., Stang, H., Weiss, J., 2011. The design of an instrumented rebar for assessment of corrosion in cracked reinforced concrete. *Mater. Struct.* 44 (7), 1259–1271.
- Pereira, E.V., Figueira, R.B., Salta, M.M.L., Da Fonseca, I.T.E., 2009. A galvanic sensor for monitoring the corrosion condition of the concrete reinforcing steel: relationship between the galvanic and the corrosion currents. *Sensors.* 9 (11), 8391–8398.
- Perveen, K., Bridges, G.E., Bhadra, S., Thomson, D.J., 2013. An embedded inductively coupled printed circuit board based corrosion potential sensor. *Instrumentation and Measurement Technology Conference (I2MTC), 2013 IEEE International.* IEEE, Piscataway, NJ, pp. 22–26.
- Qiao, G., Xiao, H., Sun, G., 2011. Identification of the reinforcing steel's corrosion state in RC beams based on electrochemical sensor. *Sens. Rev.* 31 (3), 218–227.
- Qiao, L., 2009. Structural damage and detection using signal-based pattern recognition. A Doctoral Dissertation for the Department of Civil Engineering, Kansas State University, Manhattan, KS.
- Qin, L., Ren, H., Dong, B., Xing, F., 2015. Development of technique capable of identifying different corrosion stages in reinforced concrete. *Appl. Acoust.* 94, 53–56.
- Raupach, M., Dauberschmidt, C., Wolff, L., 2006. Monitoring the moisture distribution in concrete structures. In: Alexander, M.G., Beushausen, H.-D., Dehn, F., Moyo, P. (Eds.), *Proceedings of the International Conference on Concrete Repair, Rehabilitation and Retrofitting (ICR2006)*, Cape Town, South Africa, 21–23 2005. Taylor & Francis Group, London, p. 166.
- Raupach, M., Gulikers, J., Reichling, K., 2013. Condition survey with embedded sensors regarding reinforcement corrosion. *Mater. Corros.* 64 (2), 141–146.
- Raupach, M., Schießl, P., 2001. Macrocell sensor system for monitoring of the corrosion risk of the reinforcement in concrete structures. *NDT&E Int.* 34, 435–442.
- Reis, R.A., Gallaher, M., 2006. Evaluation of the VTI ECI-1 embedded corrosion instrument. Final Report, FHWA/CA/TL-2003/07/ECI-1, January 2006.
- Schiessl, P., Raupach, M., 1992. Monitor system for the corrosion risk for steel in concrete. *Concr. Int.* 14 (7), 52–55.
- Shi, C., 2004. Effect of mixing proportions of concrete on its electrical conductivity and the rapid chloride permeability test (ASTM C1202 or ASSHTO T277) results. *Cem. Concr. Res.* 34 (3), 537–545.
- Shi, X., Nguyen, T.A., Kumar, P., Liu, Y., 2011. A phenomenological model for the chloride threshold of pitting corrosion of steel in simulated concrete pore solutions. *Anti-Corros. Methods Mater.* 58 (4), 179–189.
- Shi, X., Xie, N., Fortune, K., Gong, J., 2012. Durability of steel reinforced concrete in chloride environments: an overview. *Constr. Build. Mater.* 30, 125–138.
- Shi, X., Ye, Z., Muthumani, A., Zhang, Y., Dante, J.F., Yu, H., 2015. A corrosion monitoring system for existing reinforced concrete structures. Final Report for the Oregon Department of Transportation, Salem, OR, May 2015.
- Song, G., Gu, H., Mo, Y.-L., 2008. Smart aggregates: multi-functional sensors for concrete structures a tutorial and a review. *Smart Mater. Struct.* 17 (3), 033001.
- Song, H.W., Saraswathy, V., 2007. Corrosion monitoring of reinforced concrete structures: a review. *Int. J. Electrochem. Sci.* 2, 1–28.

- Srinivasan, R., Phillips, T.E., Barger, C.B., Carlson, M.A., Schemm, E.R., Saffarian, H.M., 2000. Embedded micro-sensor for monitoring pH in concrete structures. In: SPIE's 7th Annual International Symposium on Smart Structures and Materials. International Society for Optics and Photonics, pp. 40–44.
- Talakokula, V., Bhalla, S., 2015. Reinforcement corrosion assessment capability of surface bonded and embedded piezo sensors for reinforced concrete structures. *J. Intell. Mater. Syst. Struct.* 26 (17), 2304–2313.
- Talakokula, V., Bhalla, S., Gupta, A., 2014. Corrosion assessment of reinforced concrete structures based on equivalent structural parameters using electro-mechanical impedance technique. *J. Intell. Mater. Syst. Struct.* 25 (4), 484–500.
- Torres-Luque, M., Bastidas-Arteaga, E., Schoefs, F., Sánchez-Silva, M., Osma, J.F., 2014. Non-destructive methods for measuring chloride ingress into concrete: state-of-the-art and future challenges. *Constr. Build. Mater.* 68, 68–81.
- Watters, D.G., Bahr, A.J., Jayaweera, P., Huestis, D.L., 2003. SMART PEBBLES: passive embeddable wireless sensors for chloride ingress monitoring in bridge decks. Final Report, FHWA/CA/TL-2003/07, June 2003.
- Xu, C., Li, Z., Jin, W., 2013. A new corrosion sensor to determine the start and development of embedded rebar corrosion process at coastal concrete. *Sensors*. 13 (10), 13258–13275.
- Yoo, J.H., Park, Z.T., Kim, J.G., Chung, L., 2003. Development of a galvanic sensor system for detecting the corrosion damage of the steel embedded in concrete structures: Part 1. Laboratory tests to correlate galvanic current with actual damage. *Cem. Concr. Res.* 33 (12), 2057–2062.
- Yu, H., Caseres, L., 2012. An embedded multi-parameter corrosion sensor for reinforced concrete structures. *Mater. Corros.* 63 (11), 1011–1016.
- Zhou, S., Deng, F., Yu, L., Li, B., Wu, X., Yin, B., 2016. A novel passive wireless sensor for concrete humidity monitoring. *Sensors*. 16 (9), 1535–1549.

This page intentionally left blank

Monitoring of concrete structures with optical fiber sensors

5

Aghiad Khadour and Julien Waeytens

Université Paris-Est, IFSTTAR, Marne-la-Vallée, France

5.1 Introduction

The monitoring of civil engineering structures is becoming an increasingly important issue. The maintenance and safe operation of existing structures, as well as new regulations regarding Structural Health Monitoring (SHM) of new buildings, has led to a growing demand for cost-efficient and reliable measurement systems. Historically, visual inspection is the most popular technique to monitor concrete structures. Thanks to the experience of experts, visual inspection allows the detection of structure pathologies, water infiltrations, cracks, spalling and corrosion of the reinforcing steels. Nevertheless, visual inspection can be insufficient to unravel the root cause of the distress or damage. Moreover, the general frequency of visual inspections is low; In France, for example, concrete bridges are inspected approximately once per year. Additionally, some parts of the structure may be difficult to access. Thus, specific and expensive equipment and strategies can be required to visually inspect these areas. With the development of sensor technologies and numerical simulations, structures can be monitored and assessed in real time. Many pointwise sensors, such as accelerometers and extensometers, have already been deployed for structural monitoring. A vast amount of literature addresses vibration-based damage identification methods, and a detailed review is presented in [Doebling et al. \(1996\)](#). Hence, sensor-based strategies can be strategically used to complement visual inspections.

The emergence of optical fiber sensors and their commercial availability during recent years presents new options for SHM engineers. Using an optical fiber as a sensor element presents numerous and distinct advantages over traditional sensing principles. Fiber optic sensors can be multiplexed and are immune to electromagnetic interference; non-conducting, relatively small in size, reliable, relatively low cost, lightweight, and non-corrosive. They can be used in flammable or explosive environments and can endure high temperatures ([Brown and Hartog, 2013](#); [Jackson, 1995](#); [Grattan and Sun, 2000](#); [Leung, 2001](#); [Tennyson et al., 2000](#); [Ye et al., 2014](#)).

Based on the spatial distribution of the quantity to be measured, optical fiber sensors can be classified into one of the following four categories:

1. Point sensors: the measurement is carried out at a single point in space, but possible multiple channels are used to address multiple points. Examples such as Fabry-Perot sensors and single Fiber Bragg Grating (FBG) sensors.

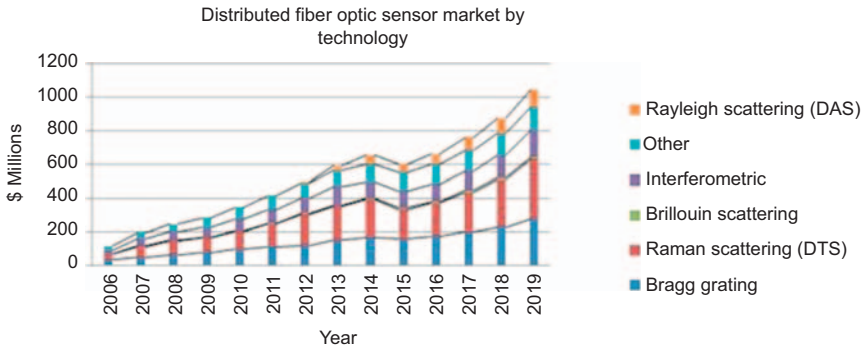


Figure 5.1 Photonic Sensor Consortium Market Survey Report (http://www.igigroup.com/st/pages/photonic_sensor_report.html).

2. Quasi-distributed or multiplexed sensors: the measured quantity is determined at a number of fixed, discrete points along a single fiber optical cable. The most common example is multiplexed FBGs.
3. Integrated sensors: the measurement averages a physical parameter over a certain spatial section and provides a single value. An example is a deformation sensor, measuring strain over a long base length.
4. Distributed sensors: the parameter of interest is measured with a certain spatial resolution at any point along a single optical cable.

As shown in Figs. 5.1 and 5.2, the market of distributed fiber sensors is growing each year due to their wide range of applications. The market is dominated by distributed temperature sensors (DTS) based on Raman Scattering and FBGs.

Based on their unique characteristics, optical fiber sensors find their place in a wide spectrum of applications. Here, we present the main applications for infrastructure monitoring.

5.2 Overview and classifications of optical fiber sensor technologies

In the last few decades, telecommunication industries have accelerated the optical fibers deployment using their major performance in light guidance (Giallorenzi et al., 1982; Grattan and Sun, 2000). The development of optoelectronic technology has pushed optical fibers to be widely investigated for sensing applications thanks to their unique characteristics of low fabrication cost, low propagation loss, high flexibility, small form factor, high sensitivity, high accuracy, multiplexing capability, remote sensing capability, simultaneous sensing capability, and immunity to electromagnetic interference.

A distributed optical sensor should deliver information regarding the temperature, strain and vibrations from any point along the optical fiber through light

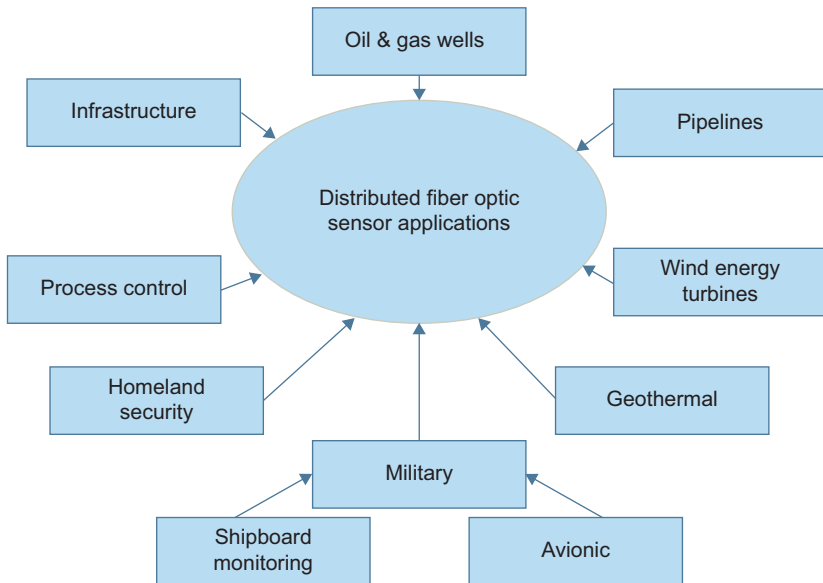


Figure 5.2 Distributed fiber optic sensor applications (http://www.igigroup.com/st/pages/photonic_sensor_report.html).

scattering phenomena (Rogers, 1986a; Giles, 1987; Dakin, 1993). The main challenge was to find a mechanism that measures the key structural parameters along the optical fiber with acceptable spatial resolution and good sensitivity in a reasonable measurement time. The performance of distributed strain or temperature fiber sensors are adequate for many applications that require a large area coverage with high location accuracy using standard communication fibers, which can be imbedded in different structures such as bridges, buildings, dams, power generators, and other civil works, to report their internal status in real time (Tennyson et al., 2000; Li et al., 2004; Barrias et al., 2016).

The sensing capabilities of optical fibers based on scattering phenomena (Rayleigh, Brillouin, and Raman) have been considerably enhanced by using innovative detection solutions (Barrias et al., 2016), as they better satisfy the end-user requests and field needs. In the following, we briefly describe the scattering phenomena inside the optical fibers and the main technologies used to investigate them.

When light propagates along an optical fiber, several mechanisms scatter photons back toward the light source as well as forward. The different observed backscattered light spectra are schematically illustrated in Fig. 5.3.

- Rayleigh scattering: It is an elastic scattering process in optical fibers due to the fluctuation in the refractive index profile along the fiber. Therefore, the scattered light has the same wavelength as the incident light. In the majority of these types of systems, the detected signal is the time-varying power intensity or the state of polarization of the backscattered light.

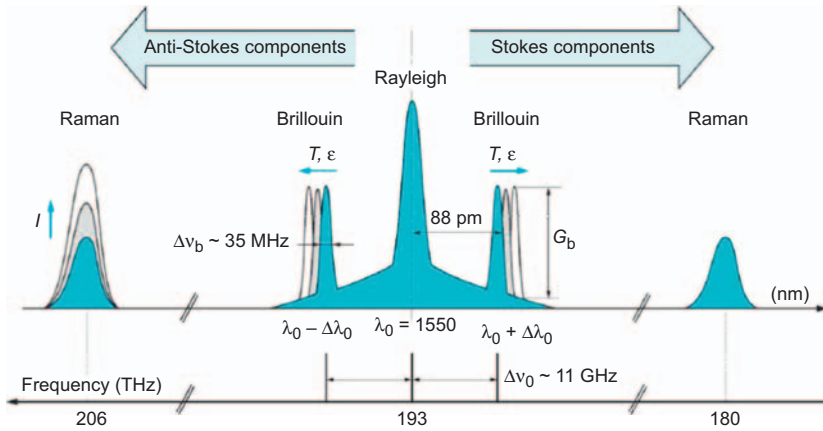


Figure 5.3 The optical spectrum of the scattering phenomena in silica (SiO_2) optical fibers, used in distributed sensing, for an injected laser wavelength of 1550 nm (Alan, 1999; Motil et al., 2016).

- Brillouin scattering: It is an inelastic (nonlinear) scattering process in which a frequency shift occurs due to an interaction between the light wave and acoustic waves (Stokes ray). The frequency shift is in the range of 11 GHz and typically depends on the temperature and stress in the fiber. A large range of optical sensors have been designed using this phenomenon to measure spectra or absorption. Dynamic and distributed sensors can be done using the time modulation of the acoustic wave.
- Raman scattering: It is an inelastic (nonlinear) scattering process in which the electromagnetic and acoustic energies are exchanged. Stokes rays with frequencies smaller than the source and anti-Stokes rays with frequencies higher than the source appear. Only the anti-Stokes rays depend on the temperature, which is of interest for metrology.

5.2.1 Intrinsic distributed optical fiber sensors

Based on the location of the fiber sensing element, it is possible to distinguish between two fiber sensor categories: extrinsic and intrinsic.

On the one hand, extrinsic optical fiber sensors are used as information carriers and not in sensing (Rogers, 1986b; Tracey, 1991). They generate a light signal that depends on the information arriving at the sensing element. The sensing element may be composed of mirrors, gas or any other mechanism that generates an optical signal. This type of sensor is used to measure rotation, vibration velocity, displacement, twisting, torque and acceleration. The major benefit of these sensors is their ability to reach places which are otherwise unreachable.

On the other hand, intrinsic optical fiber sensors use the internal property of the optical fiber to convert the physical or environmental change into a modulation of the optical signal in the form of intensity, phase and frequency (Loayssa, 2011). Distributed sensors are considered to be the optimal configuration of intrinsic optical sensors, as presented in Fig. 5.4.

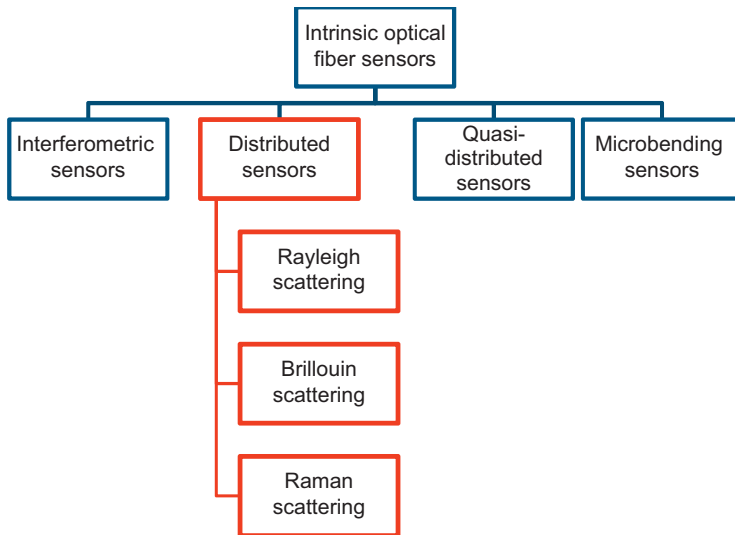


Figure 5.4 Simplified schematic classification of intrinsic optical fiber sensors.

Based on the types of the scattering mechanisms: Rayleigh, Raman, and Brillouin scattering, the demodulation techniques used in actual systems can be divided into three associated classes: optical time domain reflectometry (OTDR), optical frequency domain reflectometry (OFDR) and polarization optical time domain reflectometry (P-OTDR). The measured parameters include temperature, strain and pressure.

5.2.2 *Optical Time-Domain Reflectometry (OTDR) based distributed sensor*

OTDR was initially developed for telecommunication applications. The sensors for this technique have been the starting point of distributed sensing techniques and are still the most commonly used device in distributed sensing applications (Aoyama et al., 1981; Philen et al., 1982; Rogers, 1986a; Barnoski and Jensen, 1976).

In general, Rayleigh scattered light has been used to measure the attenuation profiles of long-optical fiber optics. In the OTDR technique, an optical pulse from a pulsed laser is launched into the fiber, and the light is continuously backscattered as it propagates through the fiber, caused by the small inhomogeneities and impurities in the amorphous silica fiber material. The backscattered light power is detected at the launching end (Danielson, 1985). The detected signal shows an exponential decay with time, which is directly related to the linear attenuation in the fiber. Similar to radar signal detection techniques, the time information is converted into distance information using the speed of light in the fiber core. A simplified schematic presentation of an OTDR system is presented in Fig. 5.5 and contains a modulated laser, a fast detector, an optical coupler, a data acquisition system, and a signal processor.

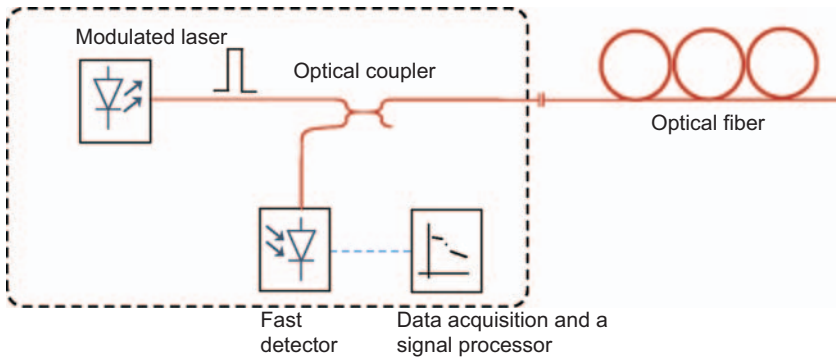


Figure 5.5 Schematic presentation of an OTDR system (Aoyama et al., 1981; Philen et al., 1982; Rogers, 1986a; Barnoski and Jensen, 1976).

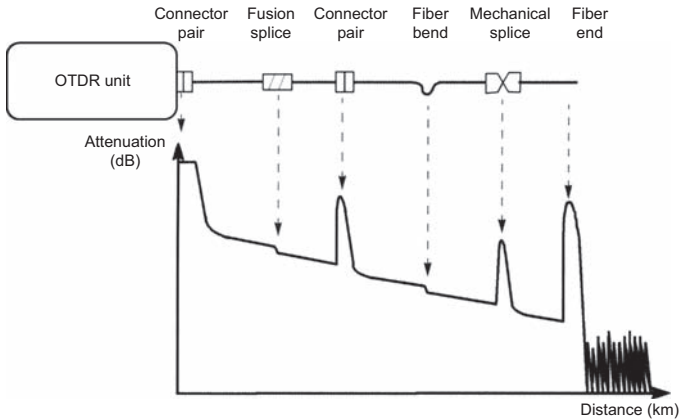


Figure 5.6 A typical OTDR trace (Aoyama et al., 1981; Philen et al., 1982; Rogers, 1986a; Barnoski and Jensen, 1976).

In addition to the information on fiber losses, the measured OTDR profiles can be used to localize breaks, bendings, connectors; to evaluate splices; and in general to evaluate the overall quality of an optical fiber link. Fig. 5.6 shows a typical OTDR return trace. Considering that the time at which the backscattered light is received can be precisely measured, the fiber section from which the backscattering occurred can be identified by the distance from the launching end.

Since the power of the received light decays as time increases, at the signal processor, the power of the backscattered light can be measured as a function of distance by analyzing the time delay of the received light pulse compared with the reference point in the fiber.

The OTDR techniques for distributed sensing applications using Raman and Brillouin scattering phenomena have been developed over the past few decades. Raman scattering was first proposed for sensing applications in the 1980s (Dakin

et al., 1985), whereas Brillouin scattering was introduced later, initially as a way to enhance the range of OTDR and then eventually for strain and/or temperature monitoring applications.

Brillouin OTDR is the most powerful tool for distributed strain sensing. Since the Brillouin frequency shift depends on both the local strain and temperature of the fiber, the sensor configuration will determine the actual sensitivity of the system. The sensor configuration should be designed to ensure proper mechanical coupling between the sensor and the host structure along the entire length of the fiber. To resolve the cross-sensitivity to temperature variations, it is also necessary to install a reference fiber along the strain sensor. Knowing the frequency shift of the unstrained fiber allows an absolute strain measurement. To measure the temperature, it is sufficient to use a standard telecommunication cable that shields the optical fibers from mechanical strain. The fiber will therefore remain in its unstrained state, and the frequency shifts can be unambiguously assigned to temperature variations.

There are two configurations based on the type of Brillouin scattering. The first is based on spontaneous Brillouin scattering, which is induced by the acoustical noise generated by the Brownian motion of the molecules in the silica fiber and is usually ~ 20 dB weaker than the Rayleigh scattering. The other configuration is based on the stimulated Brillouin scattering, which is the process that follows the spontaneous scattering due to the electrostriction effect of the silica fiber material (Horiguchi et al., 1995; Bao et al., 1999; Boyd et al., 1990).

The Brillouin optical time domain reflectometry (B-OTDR) technique was demonstrated in the 1990s (Motil et al., 2016; Bao and Chen, 2011); this technique can be further divided into two other methods:

1. Coherent detection, which is based on the measurement of the Brillouin frequency shift.
2. Direct detection, which is focused on the intensity measurement.

The coherent detection method, still the most attractive and the most developed in current B-OTDR systems.

During the same period, the first distributed Brillouin scattering sensing system, based on stimulated Brillouin scattering, was demonstrated by researchers in the NTT Communication Lab in Japan and is called Brillouin optical time domain analysis (B-OTDA). Distributed temperature measurement with a 3°C temperature resolution and a 100 m spatial resolution over a 1.2 km sensing length was demonstrated in 1990 (Tateda et al., 1990; Kurashima et al., 1990; Horiguchi and Tateda, 1989). In 1993, the sensing range was extended to 22 km using a similar measurement technique, in which a temperature resolution of 1°C and a spatial resolution of 10 m were reported (Bao et al., 1993). Fig. 5.7 shows typical schematics of the B-OTDR and B-OTDA systems.

For the Raman OTDR used for distributed temperature sensing (Dakin et al., 1985; Rogers, 1986a; Wait et al., 1997; Farahani and Gogolla, 1999), the magnitude of the spontaneous Raman backscattered light is relatively low, so high numerical aperture multimode fibers are used to increase the guided intensity of the backscattered optical light wave. The range of Raman-OTDR based systems is limited to approximately 30 km because of the relatively high attenuation characteristics of the multimode optical fibers.

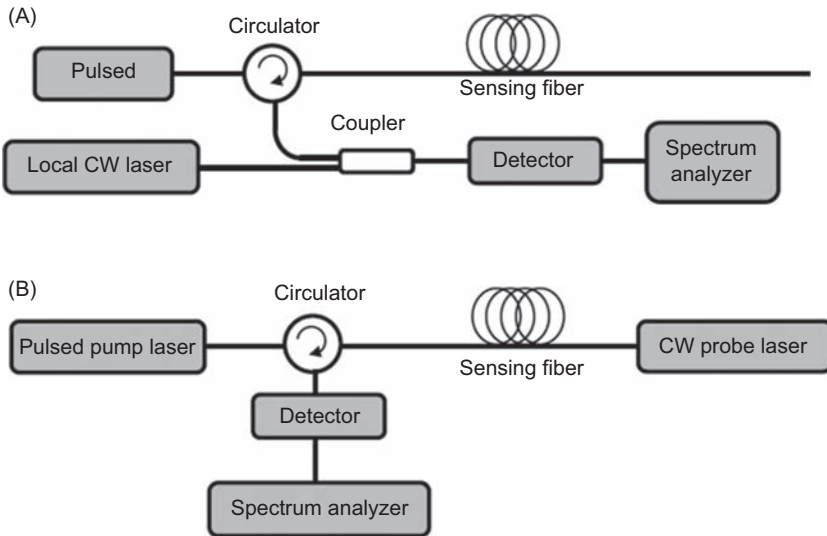


Figure 5.7 Schematic diagram of (A) a B-OTDR system and (B) a B-OTDA system (Motil et al., 2016; Bao and Chen, 2011; Tateda et al., 1990; Kurashima et al., 1990; Horiguchi and Tateda, 1989).

5.2.3 Optical Frequency-Domain Reflectometry (OFDR) based distributed sensor

The OFDR technology in a single-mode fiber was reported in 1981 for the first time (Eickhoff and Ulrich, 1981) as a method to measure the spatial distribution of the Rayleigh scattering and optical losses along the optical fiber. However, it has recently been investigated and commercialized for numerous monitoring applications. The OFDR technology has significantly higher spatial resolution and exponentially more sensing locations than the OTDR technology solutions (Bao et al., 2014). The combination of a high spatial resolution, a quick refresh rate, an additional number of sensors, and full distribution set the OFDR apart as the most sophisticated technology on the market today. Fig. 5.8 shows the general schema of the OFDR based distributed sensor.

OFDR uses a variable frequency laser beam that is coupled to an optical interferometer. The output of a tunable laser source (TLS) is split between the reference and measurement arms of an interferometer. In the measurement path, the light is further split to interrogate a length of fiber under test (FUT) and return the scattered light. Since the laser is linearly tuned in the optical frequency, the interference between the measurement and reference field is recorded using optical detectors. The auxiliary interferometer used to trigger the data acquisition in equal optical frequency increments and a portion of the network where a gas cell is used to monitor the absolute wavelength of the tunable laser are not shown in the figure.

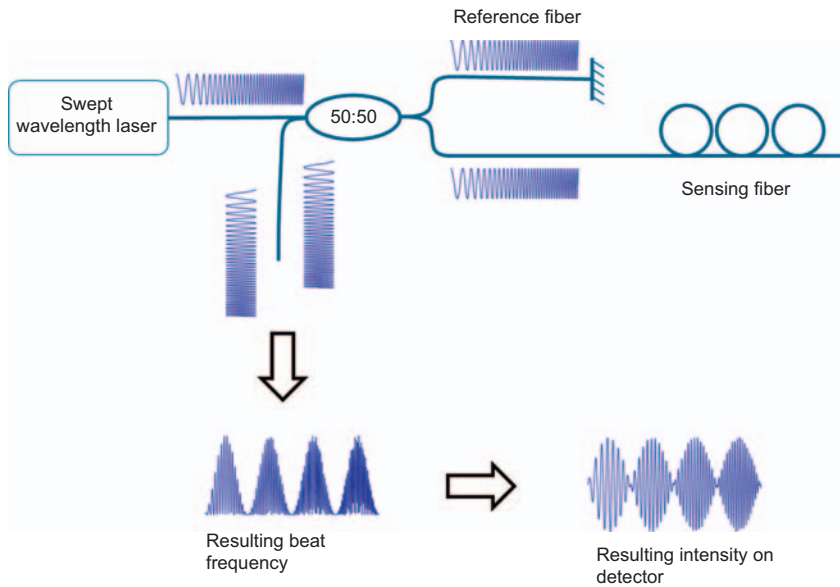


Figure 5.8 Diagram of the operating principle behind OFDR: from the laser pulse to the analyzed signal (Eickhoff and Ulrich, 1981).

Actual OFDR systems are classified in two main classes: coherent and incoherent OFDR. Most OFDR systems based on Rayleigh scattering are classified as coherent OFDR, while incoherent OFDR is mainly used for systems based on Raman or Brillouin scattering.

The OFDR configuration is used to detect temperature, strain, beat length and high order mode coupling in optical fibers. It is an excellent choice for short sensing lengths (<100 m), while longer measurement distances (5 km) are possible at the cost of both spatial resolution and temperature and strain resolution (Koshikiya et al., 2007).

5.3 Classifications of Structural Health Monitoring purposes

As defined in Balageas (2010), SHM aims to diagnose the “state” of a structure at each moment during its life. SHM is found in a wide variety of fields, including mechanics, civil engineering, and aerospace. In civil engineering applications, SHM helps the supervisor to plan and adjust the interventions for maintenance and repair, allowing a reduction in the maintenance costs while ensuring the safety of the users. It has been applied to various structures, such as bridges, buildings, nuclear installations, and tunnels. A full description can be found in the review article (Brownjohn, 2007).

Regardless of the application, SHM embraces sensor technologies, the communication systems, damage-identification methods, information representation, etc.

This chapter is limited to structural damage identification. Physically, the damage can be interpreted as a structural modification that leads to a deterioration in the structural behavior. A classification of damage monitoring purposes has been proposed in [Rytter \(1993\)](#). The four levels are defined as follows:

1. Damage detection, i.e., the presence of damage in the structure
2. Damage localization, i.e., the determination of the geometric location of the damage
3. Damage quantification, i.e., the quantification of the severity of the damage
4. Damage prognosis, i.e., the prediction of the remaining service life of the structure

The choice in instrumentation and in the damage identification method depends on the level of interest. Consequently, the structure supervisor has to select the appropriated level in the classification detailed above as the first step.

Only the damage identification methods related to Levels 1, 2, and 3 are discussed here. More information concerning the damage prognosis involved in level 4 can be found in [Farrar and Lieven \(2007\)](#). Generally, data driven methods can reach Levels 1 and 2, which statistical approaches are a part of. When information is available for both damaged and undamaged states of the structure, supervised learning can be used. Unsupervised learning is considered when monitored data are compared to the undamaged structure responses. Non-exhaustively, the reader can referred to [Farrar and Worden \(2007\)](#), [Santos et al. \(2013\)](#), [Laory et al. \(2013\)](#), [Posenato et al. \(2010\)](#), and [Dohler et al. \(2014\)](#). Damage identification approaches which combine sensor outputs and models ([Mottershead and Friswell, 1993](#); [Waeytens et al., 2016](#)) allow for damage assessment up to Level 3. The starting point of these approaches is to consider a physical model (generally solved by the Finite Element Method) that is sufficiently accurate to represent the behavior of the structure. Model parameters associated with damage phenomena such as stiffness, are sought to ensure the best compatibility between the model and the measurements. Hence, these approaches allow the localization and quantification of the structural damage.

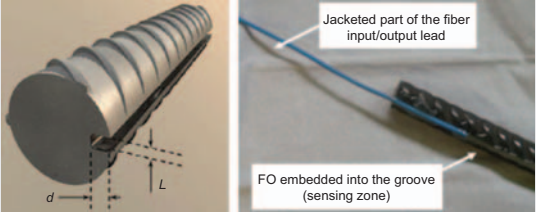
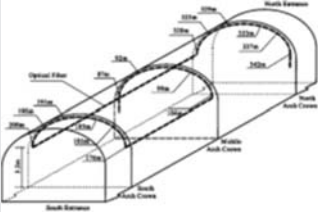
A significant amount of literature exists on damage identification methods based on vibration responses, which has been studied since the early 1980s. A review is given in [Doebling et al. \(1996\)](#). Of note, damages in the structure can affect its dynamic behavior. The most popular monitored quantities are the frequencies, the mode shape (displacement) and the derivative mode shape (strain). Static responses are also used for damage identification while generally considering the temperature, displacement and strain. As mentioned previously, the wide range of optical fiber technologies allows the assessment of strain and temperature measurements.

Finally, it is noted that damage identification methods have been integrated in smart infrastructure monitoring system for structures such as bridges in British Columbia, Canada ([Kaya et al., 2014](#)).

In the next section, we address applications of data driven methods based on optical fiber devices and model-based approaches for monitoring concrete structures.

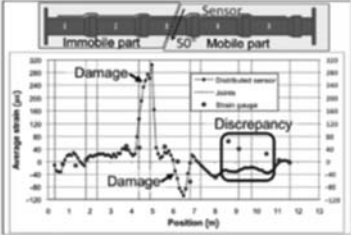
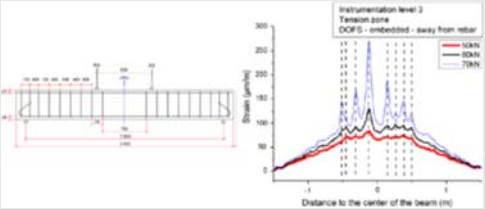
5.4 Use of distributed optical fiber sensors to monitor concrete structures: Some significant applications

5.4.1 Data driven monitoring using only optical fibers

Type of monitoring	Objective, description, illustration and reference	Optical fiber scattering	Test or Real	Year	Type of structures
Strain	<p>Measurement of strain in a reinforced concrete beam after cracking. Fiber optic embedded in a groove in the rebar using adhesive. (Quiertant et al., 2012)</p> 	Rayleigh	T	2012	Reinforced concrete samples
	<p>Measurement of mechanical strain. Use of Raman scattering to filter out temperature influence. Comparison of measurements from Raman, Brillouin and Rayleigh. (Henault et al., 2010)</p>	Raman Brillouin Rayleigh	T	2010	Concrete slab
	<p>Structural Health Monitoring of Nanjing Gulou tunnel by measuring the strain in the arch. Use of measured strain to calculate arch displacement. (Shi et al., 2003)</p> 	Brillouin	R	2002	Tunnel

(Continued)

(Continued)

Type of monitoring	Objective, description, illustration and reference	Optical fiber scattering	Test or Real	Year	Type of structures
	<p>Real-time damage localization in buried pipelines due to earthquake ground movement. (Glisic and Yao, 2012)</p> 	Brillouin	T	2012	Pipelines
	<p>High resolution strain monitoring during load tests applied to a newly built viaduct in Barcelona. (Villalba et al., 2012)</p>	Rayleigh	R	2012	Viaduct
	<p>Monitoring of bridge deflection using high accuracy and spatial resolution of the strain measured by optical fiber. Optical fiber also allows examination of the bridge support conditions and the load distribution between beams. (Regier and Hoult, 2014)</p>	Rayleigh	R	2014	Reinforced concrete bridge
Crack	<p>Crack detected earlier by optical fiber than visual inspection (peaks in figure at right). Different placements of the optical fiber (embedded bonded, embedded near and far) allows detection of the cracks. (Henault et al., 2012)</p> 	Rayleigh	T	2012	Reinforced concrete beam

5.4.2 Model-based monitoring by coupling optical fiber measurements and physical models

Optical fibers can be used to localize early stage damage, which may be difficult to detect during a visual inspection. To establish efficient maintenance plans for structures, a manager can be interested to know the time evolution of structural damages. Hence, the damage must be quantified. A strategy to obtain damage quantification is to couple an optical fiber measurement and a mechanical model. In the following, we review some representative applications of concrete structures that use both optical fiber measurements and physical models. In each application, its objective, measurement technology, mechanical model, and interactions between the measurements and the model are concisely detailed.

5.4.2.1 Case #1: Reinforced concrete beam in the laboratory

In this first case presented in [Waeys et al. \(2016\)](#), the goal was to localize and to quantify damages in an 8-m reinforced concrete beam.

Optical fiber measurement: Optical fibers were placed on the steel reinforcements before pouring the concrete. As shown in [Fig. 5.9](#), the optical fibers are in regions where potential damage is likely to occur, i.e., at the vicinity of the lower fiber and the upper fiber of the beam.

The beam was simply supported, and a static load of 10 kN was applied to the middle of the beam. Since the temperature of the laboratory was kept constant during the test, the Rayleigh sensor was able to only monitor the mechanical strain along the fiber with the high spatial resolution of approximately 1 cm. The measured strain at the lower part of the concrete along the length of the beam is presented in [Fig. 5.10](#). It is noted that the peak on the optical fiber signal indicates the position of a crack at $x = 0.7$ m. As mentioned previously, optical fiber devices are sufficient to locate damage, but the coupling of the measurement and a physical model is generally required to quantify the damage.

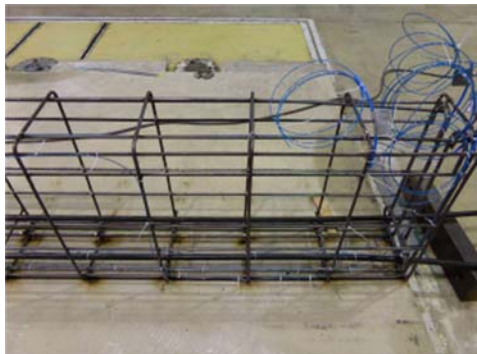


Figure 5.9 Steel reinforcement of the concrete beam and the optical fiber (in blue)—CASE #1.

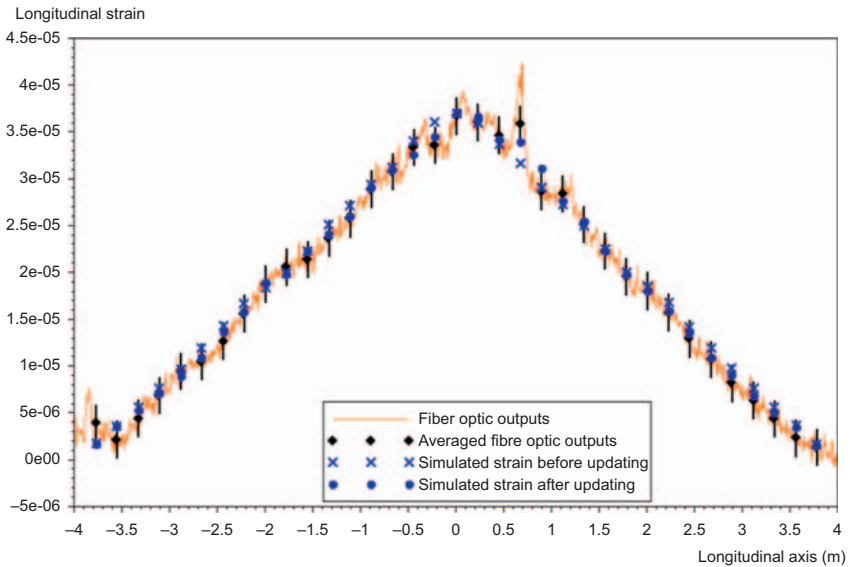


Figure 5.10 Measured strain from the optical fiber (in brown) and simulated strain before (x) and after (circles) the model updating process—CASE #1.

Mechanical model: The simple mechanical model used to represent the damage phenomena at a reasonable computation cost is the 3D linear elastic model. The damage is modeled in a continuous way by reducing the Young's modulus. The potential damaged area of the beam is decomposed into subdomains. The Young's modulus of the subdomains is then adjusted by a model updating process to obtain good agreement between the sensor outputs and the simulation. More details are given in the next paragraph.

Interaction between the optical fiber and the model: The damage parameters, i.e., the Young's modulus in each subdomain, is sought to minimize the data misfit function. It leads towards solving an inverse problem. To obtain a unique solution that is relatively insensitive to the measurement error, a regularization term is added to the data misfit function. In this application, three model-updating strategies that consider different kinds of regularization were tested and compared. The Tikhonov and Constitutive Relation Error-based techniques give a deterministic identification of the damaged parameters, while a Bayesian framework is probabilistic. The advantages and the drawbacks of the deterministic and probabilistic approaches are summarized in [Table 5.1](#).

In [Waeytens et al. \(2016\)](#), it is shown that the Constitutive Relation Error-based technique ([Ladeveze and Chouaki, 1999](#)) was the most adapted for early damage localization and quantification. The outlines of the method are summarized in [Fig. 5.11](#). First, we propose decomposing the potential damaged area into 21 subdomains. Then, a damage indicator named the Constitutive Relation Error (CRE) is computed in each subdomain. The Young's modulus is updated in the subdomain that has the highest CRE. This corresponds to subdomain #13. Hence, Step B in the

Table 5.1 Deterministic and probabilistic model updating techniques for damage quantification purposes

Model updating strategies	Deterministic	Probabilistic
Advantages	<ul style="list-style-type: none"> Reasonable computation cost 	<ul style="list-style-type: none"> Confidence interval for the model parameters
Drawbacks	<ul style="list-style-type: none"> Deterministic value for the model parameters 	<ul style="list-style-type: none"> Time consuming Requirement of an a priori probability law for the model parameters Dedicated computing codes

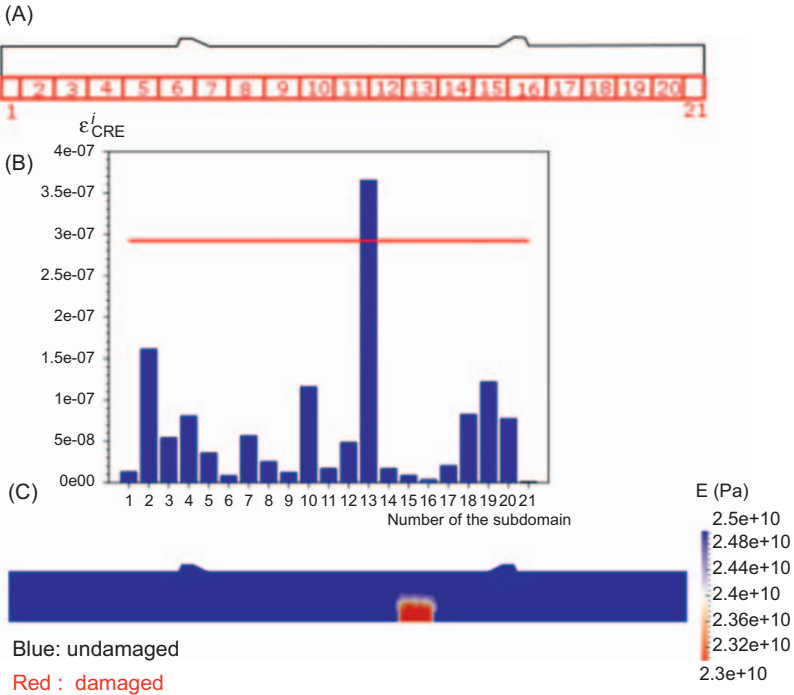


Figure 5.11 Model updating strategy to localize and to quantify structural damages—CASE #1. (A) Decomposition of the potential damaged area into 21 subdomains, (B) localization of damaged subdomain using Constitutive Relation Error, and (C) damaged quantification given by Young modulus reduction from model updating.

figure is associated with the damage localization. Lastly, the Young’s modulus is updated in the selected subdomain to minimize the data misfit.

This process gives a Young’s modulus in subdomain #13 that is 8% less, compared to the undamaged value of 25 GPa. The 8% reduction corresponds to the damage quantification.

5.4.2.2 Case #2: Pre-stressed concrete beams in a viaduct

The second case describes the monitoring of pre-stressed concrete beams and piers on a 110 m viaduct constructed in Bary, Italy (Uva et al., 2014). The objective was to obtain real-time acquisition of the mechanical strain during the construction phases of the structure and to evaluate the instant and deferred pre-stressed losses.

Optical fiber measurement: Optical fibers were placed before the concrete was cast. Since the purpose was not to detect local cracks, a long-based measurement of a few meters, using the French based Surveillance des Ouvrages par Fibres Optiques (SOFO) technology, was selected. This technology is composed of one reference fiber free of movement and one measurement fiber. It allows the removal of the thermal effects and to only obtain the mechanical strain.

Mechanical model: In the first step, a physical mechanical model was used to optimally place the optical fibers in the piers. Even though distributed optical fiber sensors can measure the strain along the fiber over more than 100 m, only the most critical parts of the structure are generally monitored. Therefore, a physical model allowed identification of the critical piers of the viaduct and the potentially damaged areas. In the second step, an empirical model was considered for the pre-stressed beams. The objective was to verify that the measured strain induced by the pre-stress losses and loadings did not exceed the upper theoretical values established by the manufacturers.

This case shows that the model must be selected in agreement with the sought objectives.

Interaction between the optical fiber and the model: Only a simple comparison between the strain sensor outputs and the theoretical values is performed, and the theoretical values are considered to be an upper limit. If the measured strain is higher than the limit, an alert may be launched due to an abnormal structural response.

5.4.2.3 Case #3: Reinforced concrete slab in the laboratory

The third case addresses the detection, localization and quantification of cracks in a reinforced concrete slab of $5.6 \text{ m} \times 1.6 \text{ m} \times 0.285 \text{ m}$.

The laboratory study detailed in Rodriguez et al. (2014) aims for the early detection of cracks in a reinforced concrete slab of $5.6 \text{ m} \times 1.6 \text{ m} \times 0.285 \text{ m}$, which may be difficult to see by visual inspection. So, for durability purposes, the objective is to estimate the crack widths, associated with the third level: damage quantification, mentioned in Section 5.3. For the experiment, the slab is simply supported, and an increasing load is applied at the mid-span.

Optical fiber measurement: To detect and localize the cracks, a high resolution of $\sim 1 \text{ mm}$ is required. Consequently, Rayleigh scattering—which belongs to optical backscattered reflectometry (OBR) measuring technology, was selected. This measuring system is often used on existing structures to detect cracks. The optical fiber sensor outputs were validated by comparing the results with other standard sensors. Contrary to previous cases, the fibers were not embedded in the structure but were positioned on the top and bottom faces of the concrete slab. The first strain peaks due to the cracks appearing close to the mid-span for a loading of 50 kN, which was confirmed by visual inspection.

Mechanical model: A non-linear mechanical model was considered to represent the crack phenomena and was solved with the standard finite element method. Although a crack is associated with a discontinuity, a non-discrete model named the “smeared crack model” was used. This kind of continuous model is easy to use and not time consuming. More details about damage and smeared crack models can be found in [Jirásek \(2011\)](#).

Interaction between the optical fiber and the model: As mentioned in [Section 5.3](#), coupling between the sensor outputs and a physical model is needed to quantify the damage, i.e., the third level defined in [Rytter \(1993\)](#). In Case #3, a model calibration is performed as a first step. Then, once the strain simulations are in agreement with strain sensor outputs, the model is used to estimate the crack width.

To conclude, we can see that optical fibers can be used on both new and existing structures. The measurement technology must be selected depending on the objective, e.g., local crack detection or verification of pre-stress losses. Optical fibers can be sufficient to detect and localize damages, but coupling between the measurement and a physical model is required to obtain the damage quantification.

5.5 Technical guide: from the identification of the SHM purpose to the selection of the appropriate optical fiber technology

In general, optical fiber sensors for SHM are embedded into civil engineering structures. For this reason, optical fibers should be mechanically protected ([Merzbacher et al., 1999](#)). From a mechanical point of view, the strain of the structure is transferred to the optical fiber sensor through the protective and adhesive layers, which mainly deform under shear stress.

Due to this shear mechanism, the stress level is lower in the fiber than in the structure, so the fiber is protected against high stress concentrations arising from cracks. As the measured strain in the optical fiber sensor can be different from the real strain in the structure, measurements in the fiber are not directly quantitative.

For example, in a linear stress transfer, the relationship between the real strain of the structure ε_{St} and the strain measured in the fiber ε_{Op} for any position along the optical fiber x can be written as:

$$\varepsilon_{Op}(x) = (MTF * \varepsilon_{St})(x)$$

where $*$ is the convolution operator and MTF is the Mechanical Transfer Function that is equal to the strain profile along the fiber when the strain of the structure is a Dirac delta function. In other words, this function is the impulsive response of the system formed by the fiber optic sensor embedded in the structure.

The variety of realized analytical studies to identify the MTF are based on Volkersen’s theory ([Volkersen, 1938](#)). These studies have been used for Bragg grating sensors and distributed sensors ([Ansari and Libo, 1998](#); [Li et al., 2009](#); [Xihao and Junhua, 2008](#); [Her and Huang, 2011](#); [Wang and Zhou, 2012](#)). It is important to

Table 5.2 Some distributed fiber sensing units commercially available today include the following: B-OTDR—Yokogawa AQ8603 (left), Sensornet DTSS (middle), and Febus optics (right); B-OTDA—Omnisens DITEST STAR (left), Neubrex Neubrescope (middle), and OZ Optics Foresight DSTS (right); B-OFDA—fibrisTerre fTB 2505; R-OTDR—Silixa ULTIMA DTS; R-OFDA—LIOS DTS200SM; and C-OFDR—LUNA OBR4600.

B-OTDR	
B-OTDA	
B-OFDA	
R-OTDR	
R-OFDA	
Rayleigh-OFDR	

find the best configuration between the optical fiber sensing cable and the optoelectronic system to measure the Brillouin, Raman or Rayleigh scattering.

In [Table 5.2](#), we present some distributed fiber sensing units that are currently commercially available.

To make the best choice for a distributed fiber sensing system, it is important to identify the primary parameters to measure. Mainly, the maximum fiber length and the spatial resolution are the two parameters to be specified before acquiring a distributed fiber sensor for strain measurements. A simplified graph presents these two

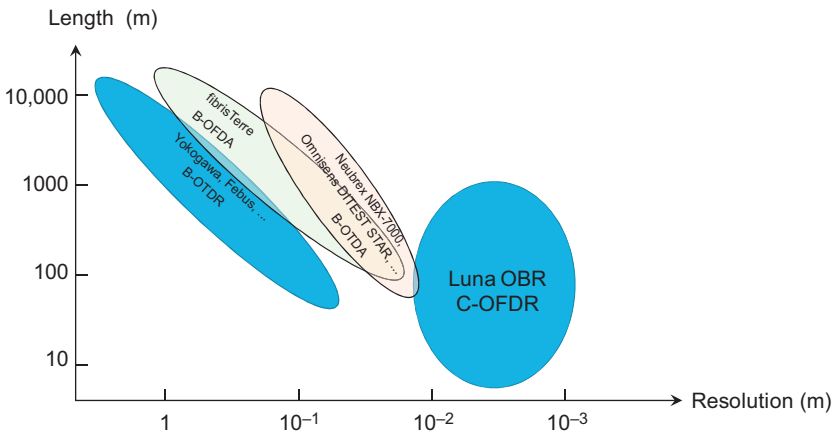


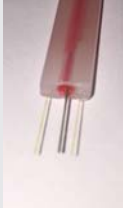
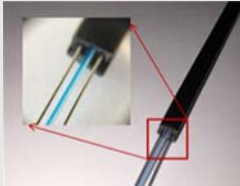


Figure 5.12 Scope for sensing length and spatial resolution of the most common commercially available distributed fiber sensors.

parameters for distributed fiber sensors currently available in the market, leading to a better choice of sensing length and spatial resolution (Fig. 5.12).

The best choice of optical fiber cable to be used depends on the purpose: for alarms for cracks or fire, or for strain/temperature profile measurement.

There are many optical fiber cables currently available in the market, as shown in the following table:

AFL (Sensornet)	
BruSteel (Brugg)	
DiTeSt SMARTprofile (SMARTEC)	
FN-SILL-2 (Neubrx)	

Finally, installing fiber optic sensors in civil engineering structures is a critical task. The following remarks are based on our experience installing fiber optic sensors in civil structural monitoring. A optical fiber sensor must respond to different requirements, both from the optical point of view regarding its mechanical solidity, and for the transmission of the displacements from the structure to the fiber.

Therefore, from a mechanical point of view:

- avoid bending the optical fiber cables, and ensure that the entire fiber is continuously in contact with the concrete or any other host material.
- avoid high pressures on the fiber to maintain its mechanical characteristics.
- avoid any unwanted optical losses.

5.6 Future trends

The use of optical fiber technologies is not limited to laboratory tests. As shown before, many operational concrete structures are monitored using them. Nevertheless, some research concerning the optical fiber technologies and the coupling with physical models remain. Let us emphasize a few major fields of interest:

- Increasing the sensing length of the optical fiber with a high spatial resolution while maintaining acceptable costs is one of the main problems to solve. An actual system delivers massive quantities of information over time, so one challenge is to find the best algorithm to estimate the lifetime and performance of a civil engineering structure by using accumulated data over a limited time (<5 years for example).
- Optical fiber outputs can be used to detect and localize damages. To quantify the damage, one can solve an inverse problem by coupling sensor outputs and a physical model. Two subjects of study in current academic research can be highlighted: the improvement of the physical model and the real-time strategies for coupling the sensor outputs and the models.

Concerning the physical model, damage phenomena can, on the one hand, be modeled in a continuous way. This is the most convenient way for practical use in terms of computation time, ease of use and existing numerical software. Nevertheless, it is noted that research is still undergoing to improve the damage mechanical models (Giry et al., 2011). On the other hand, fracture-based models exist to represent cracks and their propagation. Some numerical strategies, such as the Extended Finite Element Method (X-FEM) (Sukumar et al., 2000) introduce singularities at the crack front through analytical formulae in a finite element framework. Consequently, there is no remeshing required during the propagation of the crack. This method shows significant promise for application to concrete structures.

To quantify the damage by an inverse modeling strategy that couples the physical model and sensor outputs, one may need many finite element solutions. Thus, this process can be highly time consuming when dealing with concrete structures. In view of advanced real-time monitoring, a numerical strategy called “reduced basis” (Prud’Homme et al., 2002; Taddei, 2017) can be set up. For a given structure, this strategy consists of performing many finite element solutions in an offline stage and then computing the numerical solution in real time in an online stage. The damage information can be rapidly provided to the structure manager.

- Finally, using systems to realize multi-parameter measurements, such as physical and chemical characteristics, will be the ultimate objective for distributed fiber sensing. For civil engineering structures, it is very important to measure the strain and the evolution of the pH during the lifetime of the structure. The research activities in this domain are focused on real acceleration, since the first systems have used Bragg gratings or titled Bragg gratings (Norris, 2000; Guo et al., 2016; Lieberman, 1992).

References

- Alan, R., 1999. Distributed optical-fibre sensing. *Meas. Sci. Technol.* 10, R75.
- Ansari, F., Libo, Y., 1998. Mechanics of bond and interface shear transfer in optical fiber sensors. *J. Eng. Mech.* 124, 385–394.
- Aoyama, K.I., Nakagawa, K., Itoh, T., 1981. Optical-time domain reflectometry in a single-mode fiber. *IEEE J. Quantum Electron.* 17, 862–868.
- Balageas, D., 2010. Introduction to structural health monitoring. In: Balageas, D., Fritzen, C. P., Güemes, A. (Eds.), *Structural Health Monitoring*. ISTE, London, pp. 13–43.
- Bao, X., Brown, A., DeMerchant, M., Smith, J., 1999. Characterization of the Brillouin-loss spectrum of single-mode fibers by use of very short (<10-ns) pulses. *Opt. Lett.* 24, 510–512.
- Bao, X., Chen, L., 2011. Recent progress in Brillouin scattering based fiber sensors. *Sensors (Basel)*. 11, 4152–4187.
- Bao, X., Webb, D.J., Jackson, D.A., 1993. 22-km distributed temperature sensor using Brillouin gain in an optical fiber. *Opt. Lett.* 18, 552–554.
- Bao, X., Li, W., Qin, Z., Chen, L., 2014. OTDR and OFDR for distributed multi-parameter sensing. *Proc. SPIE*. 9062, 11 pp.
- Barnoski, M.K., Jensen, S.M., 1976. Fiber waveguides: a novel technique for investigating attenuation characteristics. *Appl. Opt.* 15, 2112–2115.
- Barrias, A., Casas, J.R., Villalba, S., 2016. A review of distributed optical fiber sensors for civil engineering applications. *Sensors (Basel)*. 16, 1–35, <http://europemc.org/abstract/MED/27223289>; <http://europemc.org/articles/PMC4883438?pdf=render>; <http://europemc.org/articles/PMC4883438>; <http://dx.doi.org/10.3390/s16050748> (last accessed 2016).
- Boyd, R.W., Rzaewski, K., Narum, P., 1990. Noise initiation of stimulated Brillouin scattering. *Phys. Rev. A*. 42, 5514–5521.
- Brown, G.A., Hartog, A., 2013. Optical fiber sensors in upstream oil & gas. *J. Pet. Technol.* 54, 63–65.
- Brownjohn, J.M.W., 2007. Structural health monitoring of civil infrastructure. *Philos. Trans. R. Soc., A*. 365, 589–622.
- Dakin, J.P., 1993. Distributed optical fiber sensors. *Proc. SPIE*. 1797, 76–108.
- Dakin, J.P., Pratt, D.J., Bibby, G.W., Ross, J.N., 1985. Distributed optical fiber Raman temperature sensor using a semiconductor light-source and detector. *Electron. Lett.* 21, 569–570.
- Danielson, B.L., 1985. Optical time-domain reflectometer specifications and performance testing. *Appl. Opt.* 24, 2313–2322.
- Doebbling, S.W., Farrar, C.R., Prime, M.B., Shevitz, D.W., 1996. *Damage Identification and Health Monitoring of Structural and Mechanical Systems From Changes in Their*

- Vibration Characteristics: A Literature Review. United States Department of Energy, Washington, DC, 127 pp.
- Dohler, M., Hille, F., Mevel, L., Rucker, W., 2014. Structural health monitoring with statistical methods during progressive damage test of S101 Bridge. *Eng. Struct.* 69, 183–193.
- Eickhoff, W., Ulrich, R., 1981. Optical frequency domain reflectometry in single-mode fiber. *Appl. Phys. Lett.* 39, 693–695.
- Farahani, M.A., Gogolla, T., 1999. Spontaneous Raman scattering in optical fibers with modulated probe light for distributed temperature Raman remote sensing. *J. Lightwave Technol.* 17, 1379–1391.
- Farrar, C.R., Lieven, N.A.J., 2007. Damage prognosis: the future of structural health monitoring. *Philos. Trans. R. Soc., A.* 365, 623–632.
- Farrar, C.R., Worden, K., 2007. An introduction to structural health monitoring. *Philos. Trans. R. Soc., A.* 365, 303–315.
- Giallonenzi, T.G., Bucaro, J.A., Dandridge, A., Sigel, J.G.H., Cole, J.H., Rashleigh, S.C., et al., 1982. Optical fiber sensor technology. *IEEE J. Quant. Electr.* 18, 626–665.
- Giles, I.P., 1987. Distributed optical fibre sensors. *Phys. Technol.* 18, 153.
- Giry, C., Dufour, F., Mazars, J., 2011. Stress-based nonlocal damage model. *Int. J. Solids Struct.* 48, 3431–3443.
- Glisic, B., Yao, Y., 2012. Fiber optic method for health assessment of pipelines subjected to earthquake-induced ground movement. *Struct. Health Monit.* 11, 696–711.
- Grattan, K.T.V., Sun, T., 2000. Fiber optic sensor technology: an overview. *Sens. Actuators A Phys.* 82, 40–61.
- Guo, T., Liu, F., Guan, B.-O., Albert, J., 2016. [INVITED] Tilted fiber grating mechanical and biochemical sensors. *Opt. Laser Technol.* 78, 19–33.
- Henault, J.-M., Moreau, G., Blairon, S., Salin, J., Courivaud, J.-R., Taillade, F., et al., 2010. Truly distributed optical fiber sensors for structural health monitoring: from the telecommunication optical fiber drawing tower to water leakage detection in dikes and concrete structure strain monitoring. *Adv. Civ. Eng.* 2010, 13.
- Henault, J.M., Quiertant, M., Delepine-Lesoille, S., Salin, J., Moreau, G., Taillade, F., et al., 2012. Quantitative strain measurement and crack detection in RC structures using a truly distributed fiber optic sensing system. *Constr. Build. Mater.* 37, 916–923.
- Her, S.C., Huang, C.Y., 2011. Effect of coating on the strain transfer of optical fiber sensors. *Sensors (Basel)*. 11, 6926–6941.
- Horiguchi, T., Tateda, M., 1989. BOTDA-nondestructive measurement of single-mode optical fiber attenuation characteristics using Brillouin interaction: theory. *J. Lightwave Technol.* 7, 1170–1176.
- Horiguchi, T., Shimizu, K., Kurashima, T., Tateda, M., Koyamada, Y., 1995. Development of a distributed sensing technique using Brillouin scattering. *J. Lightwave Technol.* 13, 1296–1302.
- Hubbell, D., Glisic, B., 2013. Detection and characterization of early-age thermal cracks in high-performance concrete. *ACI Mater. J.* 110, 323–330.
- Jackson, D.A., 1995. Overview of fiber sensor developments. In: Grattan, K.T.V., Meggitt, B.T. (Eds.), *Optical Fiber Sensor Technology*. Springer Netherlands, Dordrecht, pp. 1–9.
- Jirásek, M., 2011. Damage and smeared crack models. In: Hofstetter, G., Meschke, G. (Eds.), *Numerical Modeling of Concrete Cracking*. Springer, Vienna, pp. 1–49.
- Kaya, Y., Ventura, C., Turek, M., Huffman, S., 2014. British Columbia Smart Infrastructure Monitoring System. In: EWSHM—7th European Workshop on Structural Health Monitoring. Nantes, France.

- Koshikiya, Y., Fan, X., Ito, F., 2007. Highly sensitive coherent optical frequency-domain reflectometry employing SSB-modulator with cm-level spatial resolution over 5 km. In: 33rd European Conference and Exhibition of Optical Communication, pp. 1–2.
- Kurashima, T., Horiguchi, T., Tateda, M., 1990. Distributed-temperature sensing using stimulated Brillouin-scattering in optical silica fibers. *Opt. Lett.* 15, 1038–1040.
- Kwon, I.B., Kim, C.Y., Choi, M.Y., 2002. Continuous measurement of temperature distributed on a building construction. In: Smart Structures and Materials 2002 Conference. San Diego, CA, pp. 273–283.
- Ladeveze, P., Chouaki, A., 1999. Application of a posteriori error estimation for structural model updating. *Inverse. Probl.* 15, 49–58.
- Laory, I., Trinh, T.N., Posenato, D., Smith, I.F.C., 2013. Combined model-free data-interpretation methodologies for damage detection during continuous monitoring of structures. *J. Comput. Civ. Eng.* 27, 657–666.
- Leung, C.K.Y., 2001. Fiber optic sensors in concrete: the future? *NDT&E Int.* 34, 85–94.
- Li, H.-N., Li, D.-S., Song, G.-B., 2004. Recent applications of fiber optic sensors to health monitoring in civil engineering. *Eng. Struct.* 26, 1647–1657.
- Li, H.N., Zhou, G.D., Ren, L., Li, D.S., 2009. Strain transfer coefficient analyses for embedded fiber bragg grating sensors in different host materials. *J. Eng. Mech.* 135, 1343–1353.
- Lieberman, R.A., 1992. Distributed and multiplexed chemical fiber optic sensors. *Proc. SPIE.* 1586, 80–91.
- Loayssa, A., 2011. Optical fiber sensors for structural health monitoring. In: Mukhopadhyay, S.C. (Ed.), *New Developments in Sensing Technology for Structural Health Monitoring*. Springer Berlin Heidelberg, Berlin, Heidelberg, pp. 335–358.
- Merzbacher, C.I., Kersey, A.D., Friebele, E.J., 1999. Fiber optic sensors in concrete structures: a review. In: Grattan, K.T.V., Meggitt, B.T. (Eds.), *Optical Fiber Sensor Technology: Applications and Systems*. Springer US, Boston, MA, pp. 1–24.
- Motil, A., Bergman, A., Tur, M., 2016. [INVITED] State of the art of Brillouin fiber-optic distributed sensing. *Opt. Laser Technol.* 78, 81–103.
- Mottershead, J.E., Friswell, M.I., 1993. Model updating in structural dynamics: a survey. *J. Sound Vib.* 167, 347–375.
- Norris, J.O.W., 2000. Optical fiber chemical sensors: fundamentals and applications. In: Grattan, K.T.V., Meggitt, B.T. (Eds.), *Optical Fiber Sensor Technology: Advanced Applications—Bragg Gratings and Distributed Sensors*. Springer US, Boston, MA, pp. 337–378.
- Philen, D.L., White, I.A., Kuhl, J.F., Mettler, S.C., 1982. Single-mode fiber OTDR: experiment and theory. *IEEE J. Quantum Electron.* 18, 1499–1508.
- Posenato, D., Kripakaran, P., Inaudi, D., Smith, I.F.C., 2010. Methodologies for model-free data interpretation of civil engineering structures. *Comput. Struct.* 88, 467–482.
- Prud'Homme, C., Rovas, D.V., Veroy, K., Machiels, L., Maday, Y., Patera, A.T., et al., 2002. Reliable real-time solution of parametrized partial differential equations: reduced-basis output bound methods. *J. Fluids Eng.* 124, 70–80.
- Quiertant, M., Baby, F., Khadour, A., Marchand, P., Rivillon, P., Billo, J., et al., 2012. Deformation monitoring of reinforcement bars with a distributed fiber optic sensor for the SHM of reinforced concrete structures. In: NDE. Seattle, WA, 10 p.
- Regier, R., Hoult, N.A., 2014. Distributed strain behavior of a reinforced concrete bridge: case study. *J. Bridge Eng.* 19, doi:10.1061/(ASCE)BE.1943-5592.0000637.
- Rodriguez, G., Casas, J.R., Villalba, S., 2014. Assessing cracking characteristics of concrete structures by distributed optical fiber and non-linear finite element modelling. In: EWSHM—7th European Workshop on Structural Health Monitoring. Nantes, France.

- Rogers, A.J., 1986a. Distributed optical-fibre sensors. *J. Phys. D. Appl. Phys.* 19, 2237.
- Rogers, A.J., 1986b. Intrinsic and extrinsic distributed optical-fibre sensors. *Proc. SPIE.* 0566, 234–242.
- Rytter, A., 1993. Vibrational based inspection of civil engineering structures. Ph.D. Thesis, Department of Building Technology and Structural Engineering, University of Aalborg, Denmark, 206 p.
- Sang, A.K., Froggatt, M.E., Gifford, D.K., Kreger, S.T., Dickerson, B.D., 2008. One centimeter spatial resolution temperature measurements in a nuclear reactor using Rayleigh scatter in optical fiber. *IEEE Sens. J.* 8, 1375–1380.
- Santos, J.P., Cr mona, C., Orcesi, A.D., Silveira, P., 2013. Multivariate statistical analysis for early damage detection. *Eng. Struct.* 56, 273–285.
- Shi, B., Xu, H.Z., Chen, B., Zhang, D., Ding, Y., Cui, H.L., et al., 2003. A feasibility study on the application of fiber-optic distributed sensors for strain measurement in the Taiwan Strait Tunnel project. *Mar. Georesour. Geotechnol.* 21, 333–343.
- Sukumar, N., Moes, N., Moran, B., Belytschko, T., 2000. Extended finite element method for three-dimensional crack modelling. *Int. J. Numer. Methods Eng.* 48, 1549–1570.
- Taddei, T., 2017. Model order reduction methods for data assimilation; state estimation and structural health monitoring. Ph.D. Thesis, Department of Mechanical Engineering, Center for Computational Engineering, Massachusetts Institute of Technology, 258 p.
- Tateda, M., Horiguchi, T., Kurashima, T., Ishihara, K., 1990. First measurement of strain distribution along field-installed optical fibers using Brillouin spectroscopy. *J. Lightwave Technol.* 8, 1269–1272.
- Tennyson, R.C., Coroy, T., Duck, G., Manuelpillai, G., Mulvihill, P., Cooper, D.J.F., et al., 2000. Fibre optic sensors in civil engineering structures. *Can. J. Civ. Eng.* 27, 880–889.
- Thevenaz, L., Facchini, M., Fellay, A., Robert, P., Inaudi, D., Dardel, B., 1999. Monitoring of large structure using distributed Brillouin fibre sensing. In: 13th International Conference on Optical Fiber Sensors and Workshop on Device and System Technology Toward Future Optical Fiber Communication and Sensing. Kyongju, South Korea, pp. 345–348.
- Tracey, P.M., 1991. Intrinsic fiber-optic sensors. *IEEE Trans. Ind. Appl.* 27, 96–98.
- Uva, G., Porco, F., Fiore, A., Porco, G., 2014. Structural monitoring using fiber optic sensors of a pre-stressed concrete viaduct during construction phases. *Case Stud. Nondestr. Test. Eval.* 2, 27–37.
- Villalba, V., Villalba, S., Casas, J.R., 2012. Application of OBR fiber optic technology in the Structural Health Monitoring of the Can Fatjo Viaduct (Cerdanyola del Valles, Spain). In: *Bridge Maintenance, Safety, Management, Resilience and Sustainability*, pp. 498–501.
- Volkersen, O., 1938. Die Nietkraftverteilung in zugbeanspruchten Nietverbindungen mit konstanten Laschenquerschnitten. *Luftfahrtforschung.* 15, 41–47.
- Waeysens, J., Rosic, B., Charbonnel, P.E., Merliot, E., Siegert, D., Chapeleau, X., et al., 2016. Model updating techniques for damage detection in concrete beam using optical fiber strain measurement device. *Eng. Struct.* 129, 2–10.
- Wait, P.C., DeSouza, K., Newson, T.P., 1997. A theoretical comparison of spontaneous Raman and Brillouin based fibre optic distributed temperature sensors. *Opt. Commun.* 144, 17–23.
- Wang, H., Zhou, Z., 2012. A review on strain transfer mechanism of optical fiber sensors. *Pac. Sci. Rev.* 14, 248–252.
- Xihao, C., Junhua, H., 2008. Strain transfer capability of strain sensing optical fiber cable and its measurement method. In: *International Wire & Cable Symposium*, pp. 424–428.
- Ye, X.W., Su, Y.H., Han, J.P., 2014. Structural health monitoring of civil infrastructure using optical fiber sensing technology: a comprehensive review. *Sci. World J.* 2014, 652329.

This page intentionally left blank

Structural health monitoring through acoustic emission

6

Noorsuhada Md Nor

Universiti Teknologi MARA (UiTM) Pulau Pinang Branch, Permatang Pauh, Penang, Malaysia

6.1 Introduction

Structural health monitoring (SHM) is a useful system that functions to assess the integrity, health condition and durability of various types of structures. Its usage is mainly targeted at implementing damage identification strategies (Farrar and Worden, 2007). By utilizing tools to assess changes in a structure, SHM is also a promising system for real time structural damage assessment. The information generated by this system allows the engineers appointed by the asset owners to improve the safety, serviceability, and operational cost of structures through their life cycle. In turn, SHM systems would potentially increase life-safety and ease the economic impact (Farrar and Worden, 2007) as it helps to reduce the maintenance cost and prevent irreparable damage (Abbasnia and Farsaei, 2013; Surre et al., 2013; Annamdas et al., 2016).

In the context of civil engineering structures, the SHM has become an essential system to be taken into account, as there is no maintenance-free condition for existing reinforced concrete structure. The system allows detection and location of damage presence in structures through the utilization of suitable tools as an alternative to scheduled inspection. This enables condition-based maintenance where there will be savings in the through-life costs and increased reliability of the structures (Gagar et al., 2014). The development of reliable techniques for monitoring and damage-evaluation of reinforced concrete structures has demanded more attention due to aging factor and increasing of load application to the structure. This situation occurs because most reinforced concrete structures start to show signs of deterioration or impairment, such as cracks, after several years of servicing. These impairments constitute 90% catastrophic damage caused by fatigue loading (Puskar and Golovin, 1985). Fatigue is a process of progressive structural damage in a material when it is subjected to repetitive loading. Since repetitive loading is a common occurrence in the field, fatigue damage has now become a serious problem in reinforced concrete structures. It usually starts with a small crack and gets bigger as the fatigue load is continuously applied. Thus, the inspection and assessment of fatigue damage needs to be carried out in order to maintain the integrity of the reinforced concrete structures.

To date, visual inspection is commonly used in SHM to inspect the condition of structures when subjected to repetitive loading as 80% of the defects can be found using this technique (Roberts, 1992). This visual inspection is inspector-dependant,

quick, convenient and periodical as it is based on condition. It is also very economical since it is a form of surface inspection which acts as a good indicator of larger defects. In the application of visual inspection on concrete, visual cracks and spalled concrete are normally inspected. However, visual inspection is less prominent in assessing the condition of larger structures and the structures which are at a location which is difficult to access. Besides, its inspection accuracy for real time monitoring is still inaudible apart from the difficulty faced in detecting small or hidden damages (Noorsuhada, 2016). The defects can be identified only when the reinforced concrete structure has attained the dangerous and perilous size. It makes visual inspection and identification of possible small damage unattainable. This becomes the main weakness of this form of inspection. Early detection of damage as a warning to the reinforced concrete structural integrity is extremely crucial; another technique for SHM is required.

Considerable efforts have been made for practical SHM systems, such as the use of acoustic emission (AE), which is one of the non-destructive testing (NDT) techniques. Since the SHM aims to diagnose the condition at every moment during the life of a structure, the use of AE sounds assuring. AE technique can be exploited to detect cracks, as it is very effective in identifying micro and macro defects. The AE technique also can be used to detect, locate and assess damage that occurs in the structure caused by fatigue loading. Hence, the conditions that are close to the integrity risk of the structure under fatigue loading can be diagnosed using AE technique. This study concentrated on the SHM through AE technique in assessing the integrity of civil engineering structure when subjected to fatigue loading.

6.1.1 Background and general application of acoustic emission technique

AE is defined as the class of phenomena whereby elastic waves are generated by the rapid release of energy from the localized source or sources within a material, or the transient elastic waves generated (ASTM E976-10, 2010). As reported by Evans et al. (2000), AE was first used commercially in the late 1960s in the testing of pressurized systems for the chemical and aerospace industries. The history of AE started in 1950 by Joseph Kaiser has been then verified by Ohtsu and Watanabe (2001). However, the fundamentals of AE measurement has been reported earlier by Kishinoue (1990), Drouillard (1994), and Ohtsu (2008). Meanwhile, AE related to environmental noises has been addressed by Kishinoue (1990). In 1972, Liptai reviewed the material properties and defect for composite material using AE. Earlier information about material properties of plain concrete using AE technique has been reported by Nielsen and Griffin (1977). Later, the advanced AE analysis related to the determination of crack location, type of cracks, and orientation of cracks in concrete structures has been reported by Ohtsu et al. (1991). A new method for the determination of microcrack kinematics generated in concrete has been proposed. Recently, the application of AE has received more attention as a real-time monitoring technique in civil engineering structures. It has been used extensively for damage detection and damage assessment of various types of

structures such as bridges, dams and buildings. The localization of damage that occurred in the structures can be identified. From this damage assessment through AE monitoring, the structural integrity and performance can be recognized.

AE has been used worldwide for various applications, inclusive of the monitoring of structures and infrastructures. It has been utilized for damage identification, location and assessment. The knowledge of the damage identification mechanisms is valuable in maintaining the performance and integrity of the structures. Thus, the service life of the structures can be maintained and the structures safety can be managed. It is cost effective and economical for long term monitoring.

As mentioned earlier, in the context of civil engineering, the AE has been utilized for monitoring of bridge structures such as steel bridges (Holford et al., 2001) and concrete bridges (Yuyama et al., 2007). It has also been used for the monitoring of reinforced concrete slabs (Yuyama et al., 2001; Degala et al., 2009) and reinforced concrete beams (Md Nor and Mat Saliah, 2016; Md Nor et al., 2013a, 2014). The monitoring of masonry towers has also been carried out by Carpinteri and Lacidogna (2007) using AE. Its application for monitoring the reinforced concrete strengthened with carbon fiber-reinforced polymer on the soffit (Wan Ahmad and Md Nor, 2016; Muhamad et al., 2016). The AE has been used for monitoring the behavior of rubberized concrete (Wang et al., 2011), concrete beam strengthened with engineered cementitious composites (ECC) layer (Leung et al., 2007) and carbon fiber reinforced vessel (Ziehl, 2000). Reviews on the application of AE closely related to the damage assessment in concrete have been carried out by Basri et al. (2012), Behnia et al. (2014), and Noorsuhada (2016). This indicates that the AE is a powerful tool for SHM in evaluating damage of reinforced concrete structural systems and materials. It has also been used in detecting crack formation and growth in the structure without damaging it.

Concerning damage assessment, AE has been utilized for the monitoring of crack propagation and development in reinforced concrete structures. For instance, the development of crack progression in the reinforced concrete from microcrack to macrocrack has been assessed by Md Nor et al. (2011). Based on the AE signal strength, the occurrence of crack nucleation can be characterized (Md Nor and Mat Saliah, 2016; Md Nor et al., 2015). The AE parameter also has been used to investigate the damage classification of reinforced concrete beams when subjected to monotonic loading to failure (Md Nor et al., 2012) and fatigue loading at various fatigue amplitudes (Md Nor et al., 2013a). A clear trend of the relationship between average frequency and RA value obtained from the AE signal—with respect to crack progression—has been observed. The next investigation was concentrated on the fatigue damage severity of a reinforced concrete beam when constant fatigue amplitude was applied (Md Nor et al., 2014). The bath-tub curve for diagnostic the fatigue damage severity using severity analysis of AE signal was then presented. It is found that the curve was closely related to the service life of the beam. AE is also useful in detection and evaluation of failures, as reported by Yuyama et al. (2007). A study on damage assessment of the high strength tendon of prestressed concrete bridges has been performed and the researchers have concluded that the AE is a reliable technique for detection of failures.

Instead of the application stated above, AE has many advantages—predominantly for monitoring purposes through its parameters. The AE parameters play an important role on the determination and assessment of damage in the structures. The main AE parameters are: amplitude, energy, duration, threshold, frequency, count, and rise time as shown in Fig. 6.1. Such AE parameters can be used as valuable information for SHM.

Each parameter is constructive in the determination of the AE characteristic which relates to the AE source such as a crack. Threshold is “a voltage level on an electronic comparator such that signals with amplitudes larger than this level will be recognized. The voltage threshold may be user adjustable, fixed, or automatic floating” (ASTM E1316, 2006). Threshold is useful in filtering the noise intervention in the AE signal during monitoring process. In doing so, a suitable threshold level must be set up in order to obtain the required signal. The threshold is measured in decibel (dB) or volts (V). It can be set at a certain level such as 40 dB. Normally, the identification of a suitable threshold for monitoring is based on the noise test (ASTM E1316, 2006). During monitoring, only AE parameters above the threshold level would be captured and stored. Amplitude is defined as “the peak voltage magnitude of the largest excursion attained by the signal waveform from an emission event” (ASTM E1316, 2006). It is the maximum (positive or negative) AE signal excursion during an AE hit and expressed in dB (Physical Acoustic Corporation, 2005). The amplitude is measured, however, in dB or V.

Duration is “the time between AE signal start and AE signal end” (ASTM E1316, 2006). The duration is the length between the first and the last threshold crossing of the signal. It is measured in microseconds. Xu (2008) stated that various AE sources may produce different signal durations. Pollock (1995) added that long duration and less duration ($<10 \mu\text{s}$) signals are normally generated due to

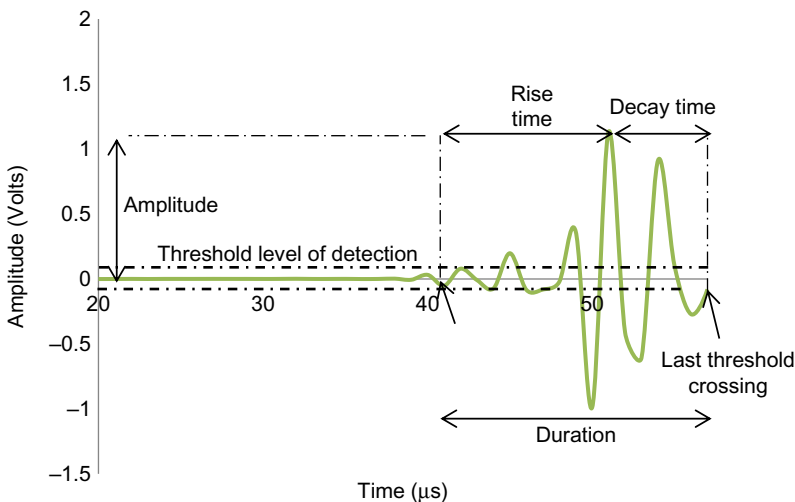


Figure 6.1 Simple waveform parameter (Md Nor et al. 2013b).

mechanical noise sources and electrical pulses. The duration is useful for crack characterization as well as the nucleation and growth. One of the AE energies is signal strength. It is defined as “the measured area of the rectified AE signal with units proportional to volt-seconds” (ASTM E1316, 2006). It includes the absolute area of positive and negative envelopes (Ziehl, 2000). It is related to the amount of energy released by the specimen as the crack grows.

Count is “the number of times the AE signal exceeds a pre-set threshold during any selected portion of a test” (ASTM E1316, 2006). The count which has been used in classification of damage is one of the AE parameters. Frequency is defined as the number of cycles per second of the pressure variation in a wave and an AE wave comprises of several frequency components (Xu, 2008). In many types of AE analysis, average frequency is always used. Average frequency is defined as count divided by duration and measured in kilohertz (kHz) (RILEM, 2010). Rise time is the time between the first threshold crossing and peak amplitude (relate to source-time function). It is also related to the wave propagation in the material.

6.1.2 Acoustic emission monitoring and AE analysis

For the monitoring of structural damage, the AE can be utilized to locate, detect and evaluate any local deformation. Fig. 6.2 illustrates the generation of AE source owing to occurrence of cracks, where the crack causes a stimulus in a structure and travels in a form of stress wave. The stress wave travels from the AE source to the surface and then is captured by the sensor, which is used to detect the acoustic wave at the surface of a structure. Typically, the propagation of waves in a structure can be categorized into three different types: the dilatation wave (compression waves or longitudinal wave, P-wave), the distortion wave (shear waves, S-wave) and the Rayleigh wave (surface wave, R-wave) (Md Nor et al., 2013b; Lovejoy, 2006). The wave is then amplified before transmitted to the AE instrument and transmitted to AE data acquisition, where it would be recorded, stored and analyzed.

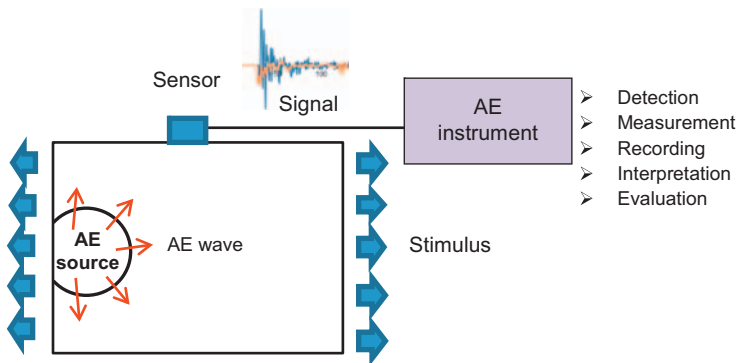


Figure 6.2 Principles of AE technique.

Source: Adaptation from Pollock, A., 1995. Inspecting Bridges With Acoustic Emission-Inspection Details About in Service Steel Bridges and Monitoring Weld Operations: Application Guidelines. Physical Acoustic Corporation.

Prior to the monitoring of a structure, three main verifications must be performed. The first is verification of sensor mounting, the second is noise test and the third is pulsing table. Sensor verification is carried out to identify the sensitivity of the sensor and the structure's surface. It is generally based on the pencil lead fracture (PLF) to simulate the acoustic wave against the surface of the structure using a magnetic pencil with a Nielson shoe (Teflon shoe) (ASTM E976-10, 2010). The breaking of the lead would generate a short-duration, localized impulse which is quite similar to the natural AE source, for instance a crack (ASNT, 2005). For this purpose, three or more replicates of PLFs are required. The sensor is considerably coupled if the wave produced by the PLF is high amplitude of 99 dB or when the sensitivity is within ± 3 dB in difference (Ziehl, 2000; Md Nor et al., 2013b).

Noise test that is carried out to determine the suitable threshold level can be set in the AE hardware to be used throughout the monitoring process. The noise intervention in the signal can be reduced if it uses the suitable threshold level. It is dependent upon the noise in the vicinity of the tested structure and the constant threshold that is generally used. The noise test is normally performed with a low threshold level that is set in the AE hardware and runs for at least 20 minutes. Threshold level of 40 dB (Schumacher, 2009; Md Nor et al., 2013a) to 45 dB (Liu, 2007) is normally utilized for reinforced concrete testing. In order to ensure good communication between sensors, the pulsing table is used. It depends on the number of sensors fixed on the structure surface. The pulsing table results are influenced by the location of the sensors. It is auto-calibration, which is carried out in a particular short duration. The magnitude of the results can be in amplitude or in wave velocity depending on the threshold level set in the AE system.

After the three main verifications, the AE monitoring can be conducted. During AE monitoring, all AE data are displayed immediately in AE visual with various parameter options. The analysis can be visualized in AE visual and stored in data acquisition.

There are various approaches of AE analyses which have been used for the assessment of reinforced concrete structure. For example: the analysis based on the AE parameter (Chotickai, 2001; Wan Ahmad and Md Nor, 2016; Md Nor et al., 2015), the relationship between average frequency and RA value (Md Nor et al., 2013a; Aggelis et al., 2013), the intensity analysis (Degala et al., 2009; Md Nor et al., 2012), b-value, and so forth. Each analysis has its own ability to diagnose the occurrence of damage in the structure for SHM implementation. At the same time, the damage is also required to be characterized and classified. In doing so, an appropriate AE analysis can be exploited. One of the AE analyses is intensity analysis. The intensity analysis is a useful method for the identification of structural damage level. The structures can be zoned according to the damage level, whereby appropriate action can be taken into account based on the recommended action for each zone. This analysis can give useful information for further action on SHM. The identification of damage level with respect to its location—especially at high crack concentration—can be used for the determination of structural intensity as a whole.

The intensity analysis involves two indices: historical index, *HI* and Severity index, S_r (Fowler and Gray, 1979) and these indices are based on the strength of the

AE signal. They are also based on the intensity chart as shown in Fig. 6.3 which are divided into five zone intensities namely Zone A, Zone B, Zone C, Zone D, and Zone E as represented in Table 6.1. HI is generally based on the Eq. (6.1), where N is the number of hits up to and including time t ; S_{oi} is the signal strength of the i th hits (Liu, 2007) and events (Lovejoy, 2006), and K is a parameter that depends on the number of AE hits. The K parameter for reinforced concrete structures based on ASTM (2006) is used as depicted in Table 6.2. S_r is the “average signal strength of J hits having the maximum numerical value of signal strength” (Carey, 2008) as defined in Eq. (6.2). Where, J is an empirically-derived constant as presented in Table 6.3 for reinforced concrete structures.

$$H(I) = \frac{N}{N - K} \frac{\sum_{i=K+1}^N S_{oi}}{\sum_{i=1}^N S_{oi}} \quad (6.1)$$

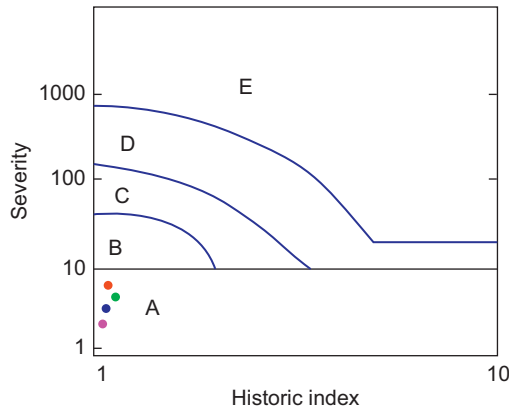


Figure 6.3 Typical intensity chart for concrete (Golaski et al., 2002).

Table 6.1 Significant of intensity zones (Gostautas et al., 2005)

Zone intensity	Recommended action
A—No significant emission	Insignificant acoustic emission. No follow up recommended.
B—Minor	Note for reference in future tests. Typically minor surface defects such as corrosion, pitting, gouges, or cracked attachment welds.
C—Intermediate	Defect requiring follow-up evaluation. Evaluation may be based on further data analysis or complementary non-destructive examination.
D—Follow up	Significant defect requiring follow up inspection.
E—Major	Major defect requiring immediate shut-down and follow-up.

Table 6.2 *K*-parameter for reinforced concrete structure (ASTM E1316, 2006)

Number of hits, <i>N</i>	<i>K</i>
≤50	Not applicable
51–200	$N - 30$
201–500	$0.85N$
≥501	$N - 75$

Table 6.3 *J* value for reinforced concrete structures (Nair, 2006)

Number of hits or events	<i>J</i>
<50	Not applicable
>50	50

$$S_r = \frac{1}{J} \sum_{i=1}^J S_{oi} \quad (6.2)$$

The intensity analysis has been used extensively in SHM to characterize damage of a fiber-reinforced composite bridge deck (Gostautas et al., 2005), a reinforced concrete member (Nair, 2006; Md Nor et al., 2012; Nair and Cai, 2009), a reinforced concrete slab retrofitted with carbon fiber reinforced polymer (CFRP) (Degala et al., 2009), reinforced concrete bridges (Golaski et al., 2002; Lovejoy, 2006), and fiber reinforced vessel specimen (Ziehl, 2000). Gostautas et al. (2005) have utilized this analysis to categories the damage of six glass fiber-reinforced composite bridge decks. The bridge decks were tested under increasing static load to failure. The intensity analysis was performed on channel basis to categories damage level. They found that the results are promising to measure structural integrity and the onset of permanent damage can be identified. Degala et al. (2009) conveyed that the intensity analysis chart offers quantitative information on the identification of damage for large area and are able to categories different sources of damage. Nine small-scale reinforced concrete slab retrofitted with carbon fiber reinforced polymer (CFRP) strips were tested under static load to failure. The intensity plots signify different damage occurrences on the slab mainly the disbond of CFRP strip from the soffit and shear failure. Golaski et al. (2002) conducted testing for pre-stressed concrete beams. The beams were statically loaded to fracture under repeated loading. The IA was carried out at different percentage of failure load, based on AE signal captured from the channel basis. From intensity analysis, the damage of the beams can be classified.

From the review, it is found that the intensity analysis can be used for quantification of damage severity, detection of crack development, determination of onset of cracking, identification of failure and classification of cracking. Hence, the intensity

analysis based on AE signal is convenient to be used for the implementation of SHM. In the following subsections, a case study related to damage assessment of reinforced concrete beam subjected to fatigue loading, with the aids of AE technique is discussed. The intensity analysis collected from AE signal would be utilized for assessing the fatigue damage.

6.2 Case study: Damage assessment of precast reinforced concrete beam subjected to fatigue loading

Fatigue is a process of progressive, localized, permanent structural change in a material subjected to repetitive loading (Md Nor et al., 2015; Noorsuhada, 2016). Many structures experience repetitive loads as well as bridges due to traffic. Exposure of repetitive loads from time to time may result in fatigue failure. Before reaching fatigue failure, structures need to undergo the inspection of the fatigue behavior, such as fatigue crack starting from the nucleation of crack to the failure stage.

Fatigue damage evaluation of reinforced concrete beams subjected to increasing fatigue loading has been performed by Md Nor et al. (2013a). The relationship between average frequency and RA value collected from AE signal has been utilized to evaluate the progression of damage in the beam. Two crack modes were identified, namely tensile crack and shear crack. They found that the relationship corresponds well with the crack pattern appears on the beam surface.

Fatigue damage assessment of an RC slab using AE technique has been investigated by Yuyama et al. (2001). From the AE analysis, four stages of fatigue damage have been identified. The first stage is crack initiated and grew rapidly. It induced very high AE activities in the initiation of crack and reduced rapidly, then increased again as the crack density increased. The second stage showed no significant crack growth was observed as in stable state. However, the AE activity increased slowly and seems some instability occurred in the slab. In the third stage, the crack density increased almost linearly: at a constant rate and AE activity was stable. The fourth stage is: crack density increased rapidly leading to the final failure and AE activity increased rapidly just before the final failure. They found that AE signal was generated near the minimum loading phase in the final stage of the fracture process. Hence, fatigue damage can be predicted and evaluated by monitoring the AE signal.

The AE signal distribution during the fatigue process in the rubberized concrete and plain concrete beam has been investigated by Wang et al. (2011). They found that AE monitoring can assess the health of concrete beam under repetitive loading. Meanwhile, Shield (1997) has investigated the AE activity of reinforced and pre-stressed concrete beam under fatigue loading. It was found that the AE is able to determine the active crack growth in RC structures.

In order to assess damage of RC specimen under fatigue, fatigue testing in laboratory with constant fatigue amplitude is generally used. For instance, Md Nor et al.

(2015) have performed a laboratory testing on RC beam subjected to constant fatigue amplitude and frequency. The testing required a long period of testing for determination of fatigue damage from the initiation of crack to failure of the specimen. When looking back to real phenomena, the fatigue loading is unpredictable. For instance, on a bridge the loading increases from time to time due to the increasing traffic. Related to this case, only few researchers have attempted to account for the effect of increasing fatigue amplitude loading in relation to AE: for carbon fiber-reinforced plastic composites laminates by Burchak et al. (2007) and for crane shaft by Fowler and Berkowitz (1995). However, the study conducted on the application of increasing fatigue loading in relation to AE to assess fatigue damage on RC specimen is still limited.

Hence, this study presents the damage assessment of RC beam subjected to increasing fatigue loading with the aids of AE technique. This study is mainly to assess the fatigue damage of RC beam from the crack nucleation to fatigue failure using AE parameter analysis and intensity analysis. In doing so, the AE signal collected from located event and channel basis were used. For the AE parameter analysis, the signal strength captured on Channel 4 (CH4) and Channel 5 (CH5) was analyzed. Meanwhile, for the intensity analysis, AE signal collected from Section A (SEC A) and CH4 was analyzed and compared. Then, the intensity analysis was compared with the crack patterns that mapped on the beam surface.

6.3 Experimental programme

6.3.1 Preparation of sample and experimental set up

A series of experiments were conducted in a laboratory. The experiments were performed on the precast reinforced concrete beams sized 300 mm width, 600 mm depth and 4050 mm length. The concrete was designed using grade 40 and its strength as collected from the compressive strength test was 42.74 N/mm². The same proportion of the concrete by weight of cement: water: fine aggregate: coarse aggregate was 1.00: 0.45: 2.07: 2.74, respectively. Coarse aggregate of 20 mm was the maximum size used in this study. The admixture (superplasticizer) of 0.8% of the cement weight was added into the fresh concrete. Figs. 6.4 and 6.5 show the dimensions of the beam used in this study. The reinforcement of the beam was designed using the high strength steel of 460 N/mm². Yield stress for the steel bar size T20, T12, and T10 were 636.23 N/mm², 595.90 N/mm², and 622.30 N/mm², respectively.

The fatigue test was conducted using force-controlled mode in conjunction with AE monitoring. The test set-up is shown in Fig. 6.6. An AE monitoring system supplied by Vallen Systeme was used to monitor the reinforced concrete beam during the crack growth, and a fatigue test with sine wave load cycle of 1Hz frequency was used. Twelve phases of maximum fatigue loads, P_{\max} were applied to the beam specimens, as depicted in Fig. 6.7. Table 6.4 depicts the summary of the maximum fatigue loading that was used in this study. The P_{\max} was based on first load crack,

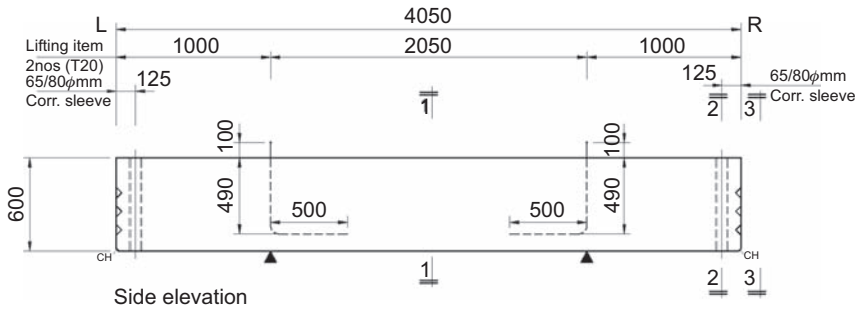


Figure 6.4 Dimensions of the actual size of the reinforced concrete beam. Note: All dimensions in millimeter.

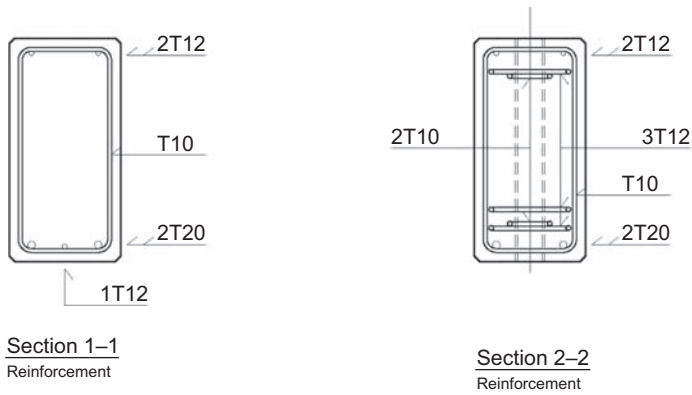


Figure 6.5 Cross section of the reinforced concrete beam. Note: All dimensions in millimeter.

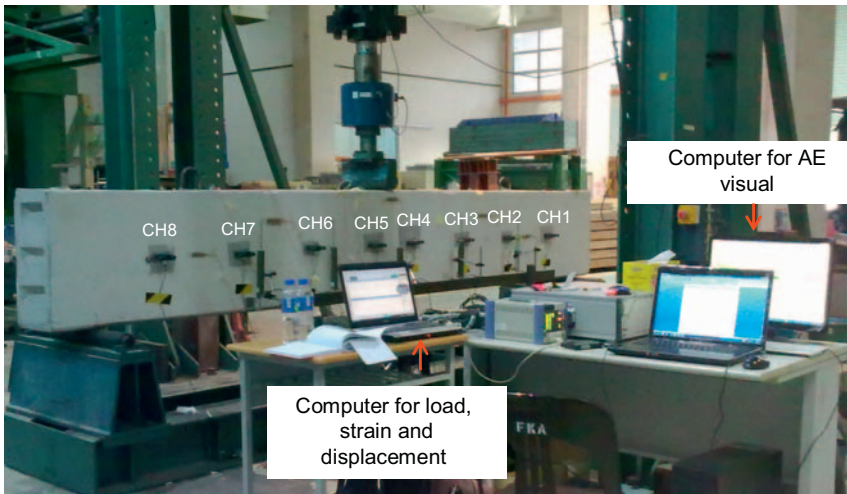


Figure 6.6 Test setup instrumented with AE system and other instruments.

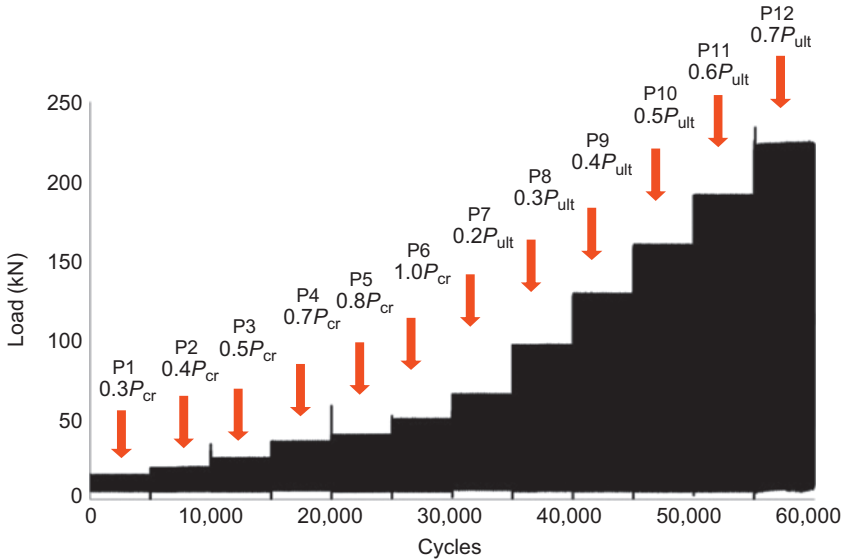


Figure 6.7 Load versus load cycle for reinforced concrete subjected to 12 phases of maximum fatigue load.

Table 6.4 The summary of 12 phases of maximum fatigue load applied to the precast reinforced concrete beam

Based on P_{cr}						
Load phases	P1	P2	P3	P4	P5	P6
Load ratio	0.3 P_{cr}	0.4 P_{cr}	0.5 P_{cr}	0.7 P_{cr}	0.8 P_{cr}	1.0 P_{cr}
P_{max} (kN)	15	20	26	36	41	51
Based on P_{ult}						
Load phases	P7	P8	P9	P10	P11	P12
Load ratio	0.2 P_{ult}	0.3 P_{ult}	0.4 P_{ult}	0.5 P_{ult}	0.6 P_{ult}	0.7 P_{ult}
P_{max} (kN)	66	99	133	166	199	233

P_{cr} of 51 kN and ultimate static load, P_{ult} of 332.31 kN. Those values were identified from the results of a static test of one reinforced concrete beam. 5000 fatigue cycles were applied for each load phase. The minimum fatigue load, P_{min} of 5 kN was applied throughout the testing.

For SHM, the AE with eight sensors was used. The sensors were set in linear array arrangement and coupled to the selected location of the beam specimen as shown in Fig. 6.6. The threshold level was set at 45 dB with the wave velocity of 4000 m/s, rearm time of 1.62 ms, duration discrimination time of 400 μ s, pre-trigger samples of 200 and sample rate of 10 MHz (Md Nor et al., 2013a).

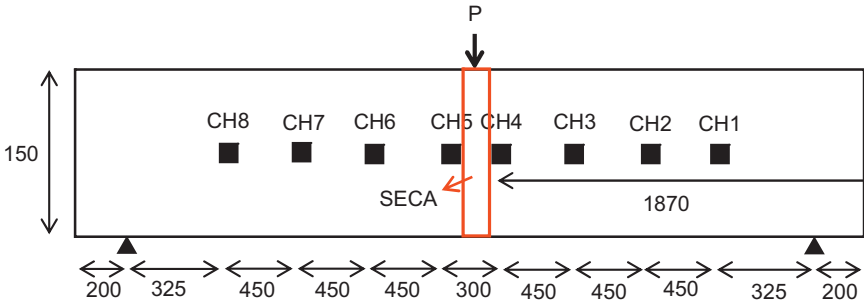


Figure 6.8 Schematic diagram for selection of located event location and channel basis.
Note: All dimensions in millimeter.

6.4 Intensity analysis of AE signal

The intensity analysis was based on Eqs. (6.1) and (6.2) for historic index, HI and severity analysis, S_r , respectively. K and J parameters were based on Tables 6.2 and 6.3, respectively. The intensity analysis plot of S_r - HI was calculated from the AE signals recorded on the located event and compared with that from the channel basis. A typical intensity chart of S_r versus HI is depicted in Fig. 6.3.

The intensity analysis was carried out based on the four zones in which the intensity for each load phase was compared to the physical crack pattern of the beam. The located event analysis was concentrated at a critical crack region, as well as flexural crack locations, namely SEC A. Meanwhile, for the channel basis, the intensity of AE signal was collected from CH4. CH4 has received high AE activity corresponding to the propagation of fatigue crack during loading and unloading process in the beam specimens. The located event was used to identify damage of the small part of the beam at where the flexural crack occurred along the distance of 1.92–2.12 m from the edge of the beam as shown in Fig. 6.8. The selection of SEC A was due to the bending crack concentration which normally occurs at the mid-span of the beam, when the beam is subjected to the three-point loading. Hence, the analysis in SEC A was used to assign bending crack characteristic of the reinforced concrete beam.

6.5 Results and discussion

6.5.1 AE parameter analysis based on the signal strength

Fig. 6.9 shows the signal strength generated, corresponding to the different phases of fatigue load with respect to load cycles. The signal strength was collected from CH4 and CH5, since both channels have received higher AE signal than other channels. In Fig. 6.9, the signal strength for CH4 and CH5 are designated as SS CH4 and SS CH5, respectively. It is surprising that when the maximum fatigue load based on P_{cr}

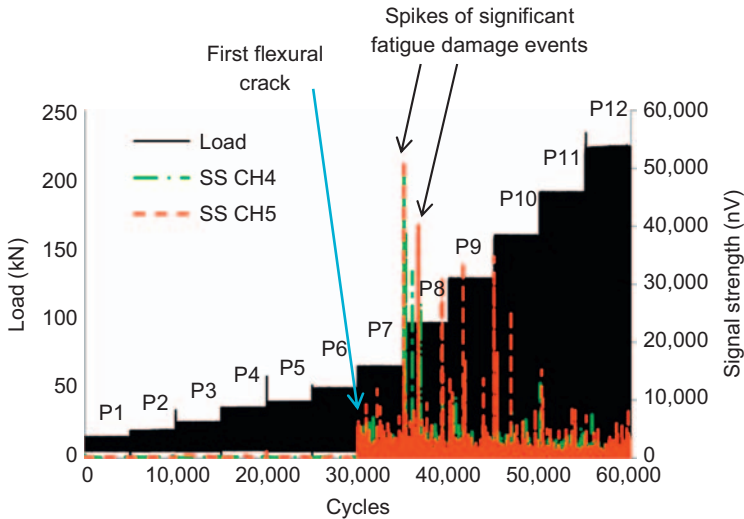


Figure 6.9 The relationship between load, signal strength and load cycle under increasing fatigue loading.

was applied onto the beam, no crack was visually observed. It can be seen in Fig. 6.9, from the relationship between signal strength and cycles, when $0.3P_{cr}$ to $1.0P_{cr}$ were applied onto the beam, it created very low AE activities represented by signal strength. It indicates that the load of $0.3P_{cr}$ (15 kN) to $1.0P_{cr}$ (51 kN) does not generate high stress concentration to the beam. This is supported by Lovejoy (2006) and Watanabe et al. (2007) who found that low load cycle generates low level of stress and hence produces little AE activity. Moreover, Hsu (1984) stated that in stress-strain curve under static load, the increase of crack is negligible at load below 30% of the P_{ult} —which corresponds to the nearly linear portion of the stress-strain curve. It shows that the beam at the phase of loading $0.3P_{cr}$ to $1.0P_{cr}$ experiences invisible tensile crack modes. It is considered as micro-crack since the crack is unable to be visualized. According to Balazs et al. (1996), the crack is assumed as micro-crack because the crack did not appear on the beam surface.

The first single crack, as shown in Fig. 6.10A, is noted to have appeared shortly after the fatigue test was run under the load $0.2P_{ult}$ (P7) or 66 kN. The crack propagated from the bottom part, to beyond neutral-axis or mid-depth of the reinforced concrete beam. From this phenomenon under fatigue load, it is unreasonable to neglect the occurrence of crack below 30% of P_{ult} . From Fig. 6.9, it can be depicted that the flexural crack occurred at 30,732 load cycles, with the signal strength of 9210 nVs. This finding corroborates with that of Wang et al. (2011) who found that, under the fatigue loading, cracks are initiated shortly after the load is applied on the specimen.

Then, the spike of the highest signal strength of 51,700 nV was recorded at the load of $0.3P_{ult}$ (P8) or 99 kN obtained from CH5. The spike occurred when the load

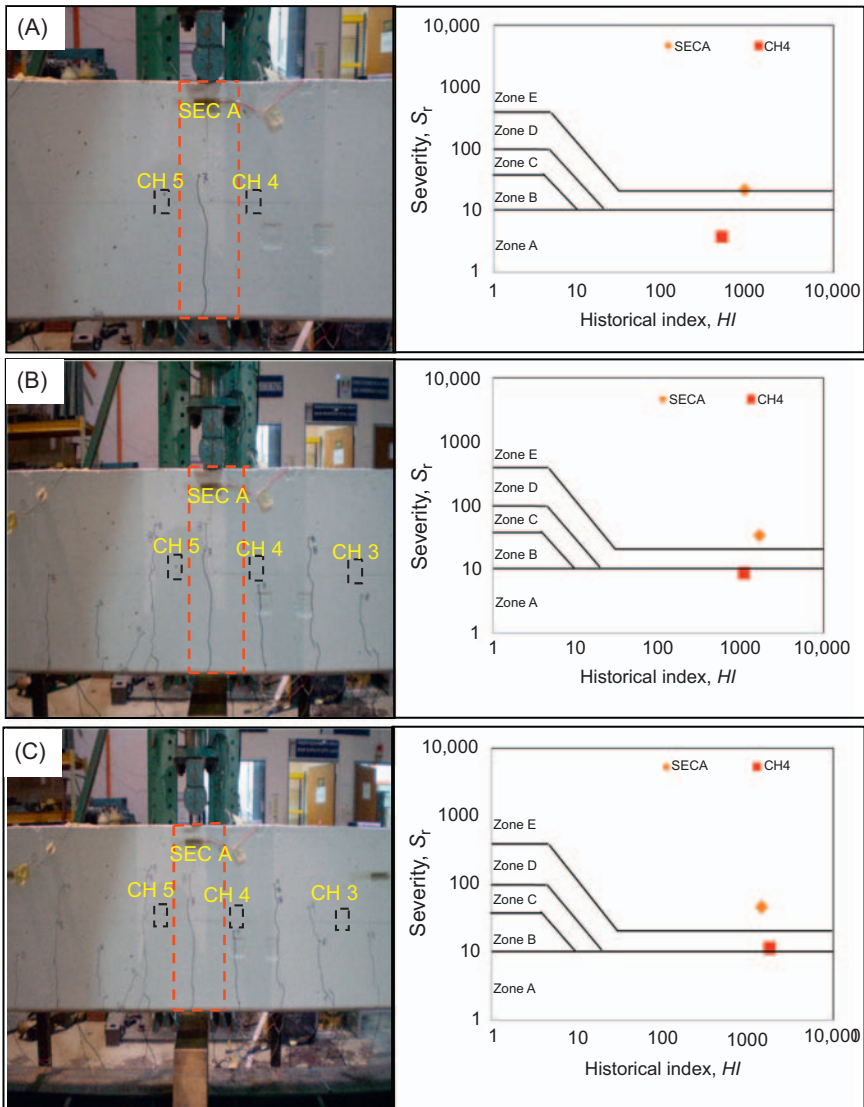


Figure 6.10 Crack modes and intensity chart of precast reinforced concrete beam subjected to (A) $0.2P_{ult}$ (P7) (B) $0.3P_{ult}$ (P8) (C) $0.4P_{ult}$ (P9) (D) $0.5P_{ult}$ (P10) (E) $0.6P_{ult}$ (P11) (F) $0.7P_{ult}$ (P12).

was applied onto the beam specimen for this load phase. Fig. 6.9 shows that the highest signal strength occurred at the load cycle of 35,085. It is found that the flexural cracks in the beam progressed as the load reached $0.3P_{ult}$ (P8). Therefore, the spike of the highest signal strength reflects the occurrence of damage such as the progression of flexural cracks in the beam. The highest signal strength of

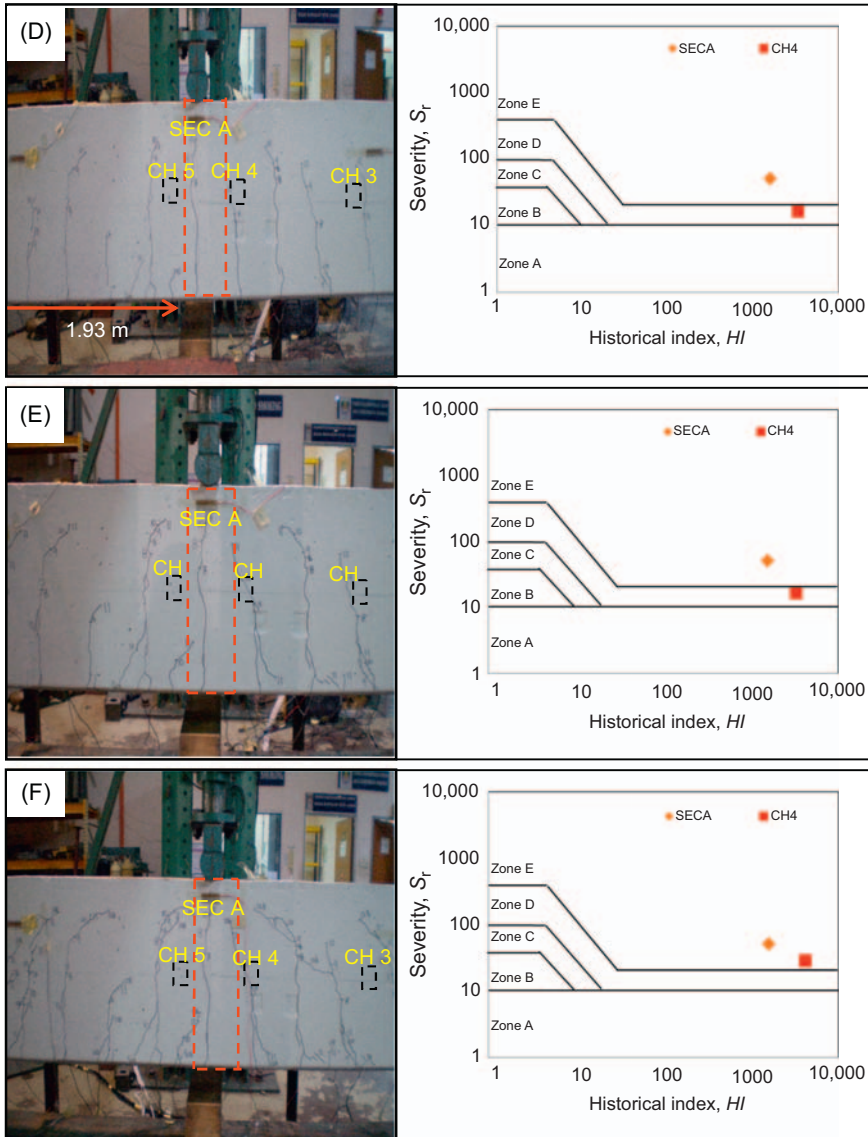


Figure 6.10 Continued

48,900 nV was recorded by CH4 at the same load cycle. This high jump of signal strength corresponds to the damage that happened in the specimen (Chotickai, 2001; Bourchak et al., 2007; Md Nor and Mat Saliah, 2016). Xu (2008) stated that the high signal strength is related to the amount of energy released by the specimen. If the location is considered, it indicates that there is an extension of flexural crack at the mid-span of the beam. After the load $0.3P_{ult}$ was applied, the signal strength

gradually decreased as shear crack started to take place until the last phase of loading. It indicates that the progression of new crack does not generate high AE signal.

6.5.2 Intensity of the precast beam specimen under various phases of fatigue load range

Fig. 6.10A–F show the crack modes and intensity chart of precast reinforced concrete beam subjected to $0.2P_{ult}$ (P7) to $0.7P_{ult}$ (P12). When maximum fatigue load, which is based on P_{cr} , was applied on the beam, no crack was visually observed. This implies that low load level does not generate crack on the beam surface and hence produces low AE activity as well as signal strength. Signal strength is analyzed to determine HI and S_r . For instance, when the beam was subjected to maximum fatigue load $0.3P_{cr}$ (P1) to $0.5P_{cr}$ (P3), very low AE activities were detected from the sensors mounted on SEC A and CH4. The AE signal strengths captured were mostly below 50 events, which were insufficient in calculation of HI and S_r . However, when the load reached to $0.7P_{cr}$ (P4) to $1.0P_{cr}$ (P6) loadings, the intersection HI - S_r plots of SEC A was below 1.0 and was not considered in the intensity chart. Similar to those obtained by Nair and Cai (2009), the plots below 1.0 are not presented in the chart. However, for those collected from CH4, the AE signal captured were similar to those of previous series of load application of $0.3P_{cr}$ (P1) to $0.5P_{cr}$ (P3). These plots correspond well to the low activity such as signal strength as presented in Fig. 6.9.

At load phase $0.2P_{ult}$ (P7), a vertical bending crack was observed and the intensity of the beam can be plotted as shown in Fig. 6.10A. At this load phase, the crack has propagated beyond the mid-depth of the beam at both sides. As the crack increased beyond the mid-depth of both sides of the beam, the plot of intensity zone falls in Zone E. It identifies that the major defect is related to severe damage of the structure, implying the inferiority of concrete in resisting tensile crack (McCormac and Nelson, 2006). Otherwise, with reference to fatigue, the stress within the material may cause higher damage, even though it is not capable to be visibly measured (Alliche, 2004). Indeed, if the crack which is beyond the neutral axis or mid-depth of the beam is taken into account, it means that the severe crack has occurred. If the AE intensity obtained from SEC A is used for fatigue damage assessment of the beam, it reflects that the beam requires immediate shut down and a follow-up inspection. The verification was made by those plots detected at CH4 which was the closest sensor to SEC A. However, the plot computed from CH4 indicates that the plot falls under Zone A which indicates that no significant AE is detected. The plot collected from CH4 seems to be a mismatch with the actual crack patterns.

As expected, when the load increased to $0.3P_{ult}$ (P8), more cracks were observed as shown in Fig. 6.10B. The previous single crack spotted on SEC A was extended to slightly higher than the mid-upward of the beam. However, two vertical cracks were observed beside SEC A beyond the mid-depth of the beam, where they matched the intensity plot as shown in Fig. 6.10B, and this beam was categorized

under Zone D. This is because the increase of load results in the progressive crack propagation from the beam specimen produced high AE activity such as signal strength. Most of the cracks were propagated almost vertically to the mid-depth of the beam specimen. At the mid-span, the length of previous single crack was extended to a slightly higher than the mid upward of the beam. The crack formation in this beam is found to be similar to the typical crack formation for beam under three-point bending (Shield, 1997). Consequently, the plots for high intensity are more to the upper right of the chart (Gostautas et al., 2005). In the following phase, these vertical cracks indicate that the beam was in Zone E (major defect) as represented by intensity plot in Fig. 6.10C. Hence, it is confirmed that the intensity plot of located event in the previous load phase can be used as a precaution to predict the condition if the next phase would be applied. Since CH4 is in the region of extensive cracks, more AE activities are recorded. It can be seen in Fig. 6.9 that at this load phase, the highest signal strength was produced. However, the S_r and HI calculation did not represent those activities. The intensity plot collected from CH4 shows that the beam is in Zone A, which indicates insignificant emission. It is found that the plots do not represent the actual condition of the beam that experiences extensive crack occurrences.

When the maximum load increased from $0.4P_{ult}$ to $0.7P_{ult}$, the AE signal obtained from the located event presents a constant plot and the beam condition falls under Zone E which is shown in Fig. 6.10C–F. When the load of $0.4P_{ult}$ was applied, the plot that derived from CH4 implies that the beam condition falls under category Zone D. It indicates the plot is in reasonable intensity when compared with the actual crack pattern that appeared on the beam surface.

The plot obtained from CH4 constantly falls under Zone D when the load increased from $0.5P_{ult}$ to $0.6P_{ult}$ as depicted in Fig. 6.10D,E. However, the plot moves to Zone E as the result of increased load. The plots obtained from CH4 show that the beam condition is in Zone E when maximum fatigue load of $0.7P_{ult}$ was applied as depicted in Fig. 6.10F. Hence, the plots in Fig. 6.10A–F portray the beam behavior under increasing fatigue load range corresponding to fatigue crack classification. From the figures, it can be deduced that the plots based on the located event produce better prediction of reinforced concrete behavior under fatigue load than of the channel basis.

6.5.3 Summary of intensity category of the beam under various phases of fatigue load range

Fig. 6.11 shows the crack map produced from the application of all fatigue load phases. Figs. 6.12 and 6.13 show the intensity chart corresponding to SEC A and CH4 under various phases of fatigue load range, respectively. The summary of intensity category that corresponds to AE signal collected from SEC A and CH4 is depicted in Table 6.5. When loads of $0.3P_{cr}$ to $1.0P_{cr}$ were applied, it is visualized that the beam was intact and no crack was generated. However, the AE activities in SEC A depict an early warning, placing the beam under insignificant emission

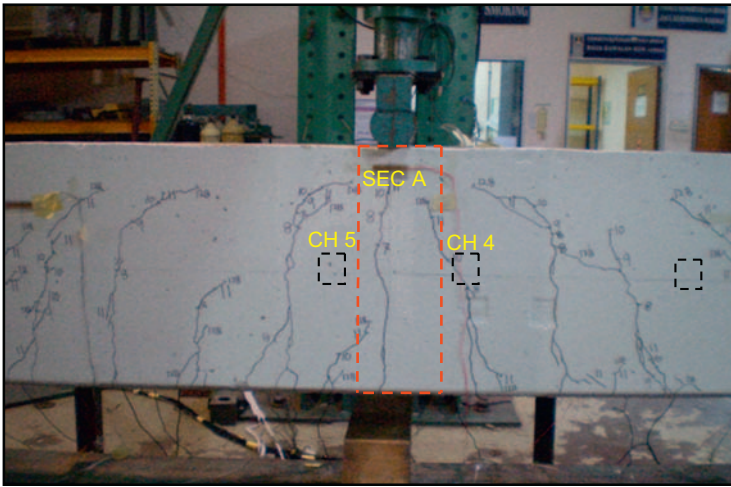


Figure 6.11 Mapped cracks produced from the application of all fatigue load phases.

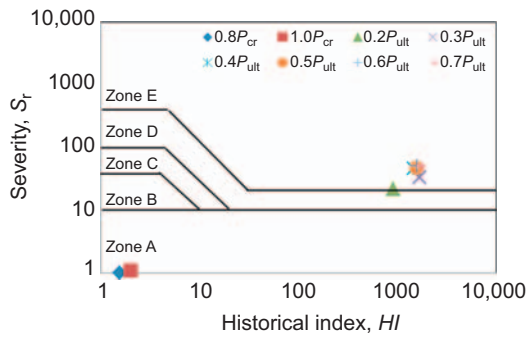


Figure 6.12 Intensity chart corresponding to SEC A under various phases of fatigue load range.

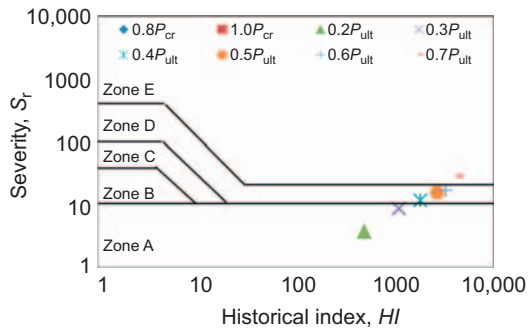


Figure 6.13 Intensity chart corresponding to CH4 under various phases of fatigue load range.

Table 6.5 Summary of intensity category for beam under various phases of fatigue load range derived from SEC A and CH4

Phase	Load (kN)	Intensity zone	
		Located event SEC A	Channel basis CH4
$0.3P_{cr}$	15	Intact	Intact
$0.4P_{cr}$	20	Intact	Intact
$0.5P_{cr}$	26	Intact	Intact
$0.7P_{cr}$	36	Insignificant emission	Intact
$0.8P_{cr}$	41	Insignificant emission	Intact
$1.0P_{cr}$	51	Insignificant emission	Intact
$0.2P_{ult}$	66	Major	Insignificant emission
$0.3P_{ult}$	99	Major	Insignificant emission
$0.4P_{ult}$	133	Major	Follow-up
$0.5P_{ult}$	166	Major	Follow-up
$0.6P_{ult}$	199	Major	Follow-up
$0.7P_{ult}$	233	Major	Major

zone. It could be a precaution before the damage due to the next higher loading takes place. It is proven that when load $0.2P_{ult}$ was applied, the beam was in the category of major defect. However, in this study, the plots that derived from the channel basis CH4 are unable to predict the similar defect. It shows that the plot of intensity category at the critical damage area corresponding to AE signal collected from SEC A is useful on the determination of active fatigue crack classification of the beam specimen. It gives a prompt indication of the beam performance and can be used as a reference for future inspection. The plot of intensity zone on a channel can be confirmed by those obtained from the located event. It is due to the fact that the located event receives the first hit of AE signal when the crack occurred in the beam. Besides, the signals in a located event at a concentrated particular location are captured by many sensors. When the load increased to $0.4P_{ult}$ to $0.7P_{ult}$, all plots show that the beam is in the intensity category of follow-up, due to major crack caused by high load application. In the real situation, the reinforced concrete structure is considered unsafe.

6.6 Conclusions

From the review of AE application, AE monitoring and AE analysis, it is indicated that AE is a reliable technique for SHM of RC structure. This was then enhanced by the case study that relates to the use of AE for SHM of RC beam under fatigue loading. From the case study, it was found that the AE analyses through signal

strength and intensity analysis show reasonable fatigue damage classification of the beams with respect to the actual physical crack pattern.

Acknowledgment

The author would like to acknowledge the Prof. Dr. Azmi Ibrahim, Assoc. Prof. Dr. Norazura Muhamad Bunnori, Prof. Dr. Hamidah Mohd Saman and Mr. Soffian Noor Mat Saliah for their encouragement and support throughout the research. The author would also like to acknowledge the Minister of Higher Education (Malaysia) and RMI, Universiti Teknologi MARA (UiTM) for providing the financial support for this research.

References

- Abbasnia, R., Farsaei, A., 2013. Corrosion detection of reinforced concrete beams with wavelet analysis. *Int. J. Civ. Eng.* 11 (3), 160–169.
- Aggelis, D.G., Mpalaskas, A.C., Matikas, T.E., 2013. Investigation of different fracture modes in cement-based materials by acoustic emission. *Cem. Concr. Res.* 48, 1–8.
- Allische, A., 2004. Damage model for fatigue loading of concrete. *Int. J. Fatigue.* 26, 915–921.
- Annamdas, V.G.M., Bhalla, S., Soh, C.K., 2016. Applications of structural health monitoring technology in Asia. In: *Structural Health Monitoring*, pp. 1–23.
- ASNT, 2005. third ed. *Nondestructive Testing Handbook: Acoustic Emission Testing*, vol. 6. American Society for Nondestructive Testing (ASNT).
- ASTM E1316, 2006. *Standard Terminology for Nondestructive Examinations*. ASTM International.
- ASTM E976-10. (2010). *Standard Guide for Determining the Reproducibility of Acoustic Emission Sensor Response*. ASTM International, 5.
- Balazs, G.L., Grosse, C.U., Koch, R., Reinhardt, H.W., 1996. Damage accumulation on deformed steel bar to concrete interaction detected by acoustic emission technique. *Mag. Concr. Res.* 48 (177), 311–320.
- Basri, S.R., Muhamad Bunnori, N., Abdul Kudus, S., Shahidan, S., Md Jamil, M.N., Md Nor, N., 2012. Applications of acoustic emission technique associated with the fracture process zone in concrete beam: a review. *Adv. Mater. Res.* 626, 147–151.
- Behnia, A., Chai, H.K., Shiotani, T., 2014. Advanced structural health monitoring of concrete structures with the aid of acoustic emission. *Constr. Build. Mater.* 65, 282–302.
- Bourchak, M., Farrow, I.R., Bond, I.P., Rowland, C.W., Menan, F., 2007. Acoustic emission energy as a fatigue damage parameter for CFRP composites. *Int. J. Fatigue.* 29, 457–470.
- Carey, S.A., 2008. *Acoustic emission and acousto-ultrasonic signature analysis of failure mechanisms in carbon fiber reinforced polymer materials*. PhD Thesis, University of South Carolina.
- Carpinteri, A., Lacidogna, G., 2007. Damage evaluation of three masonry towers by acoustic emission. *Eng. Struct.* 29, 1569–1579.
- Chotickai, P., 2001. *Acoustic emission monitoring of prestressed bridge girders with premature concrete deterioration*. Master of Science in Engineering, The University of Texas.

- Degala, S., Rizzo, P., Ramanathan, K., Harries, K.A., 2009. Acoustic emission monitoring of CFRP reinforced concrete slabs. *Constr. Build. Mater.* 23, 2016–2026.
- Drouillard, T.F., 1994. Acoustic Emission: The First Half Century. CONF-9410182-1. USDOE.
- Evans, M.J., Webster, J.R., Cawley, P., 2000. Design of a self-calibrating simulated acoustic emission source. *Ultrasonics*. 37 (8), 589–594.
- Farrar, C.R., Worden, K., 2007. An introduction to structural health monitoring. *Philos. Trans. R. Soc. A*. 365 (1851), 303–315.
- Fowler, T.J., Berkowitz, P.C., 1995. Crack detection in naval crane shafts using acoustic emission. The University of Texas.
- Fowler, T.J., Gray, E., 1979. Development of an acoustic emission test for FRP equipment. American Society of Civil Engineers Convention and Exposition.
- Gagar, D., Martinez, M., Foote, P., 2014. Development of generic methodology for designing a structural health monitoring installation based on the acoustic emission technique. *Procedia CIRP*. 22, 103–108.
- Golaski, L., Gebiski, P., Ono, K., 2002. Diagnostics of reinforced concrete bridges by acoustic emission. *J. Acoust. Emiss.* 20, 83–98.
- Gostautas, R.S., Ramirez, G., Peterman, R.J., Meggers, D., 2005. Acoustic emission monitoring and analysis of glass fiber-reinforced composites bridge decks. *J. Bridge Eng.* 10 (6), 713–721.
- Holford, K.M., Davies, A.W., Pullin, R., Carter, D.C., 2001. Damage location in steel bridges by acoustic emission. *J. Intell. Mater. Syst. Struct.* 12 (8), 567–576.
- Hsu, T.T.C., 1984. Fatigue and microcracking of concrete. *Mater. Constr.* 17, 51–54.
- Kishinoue, F., 1990. An experiment on the progression of fracture (a preliminary report). *Jisin*. 6, 24–31 (1934) translated and published by Ono, K., *Journal of AE* 9 (3), 177–180.
- Leung, C.K.Y., Cheung, Y.N., Zhang, J., 2007. Fatigue enhancement of concrete beam with ECC layer. *Cem. Concr. Res.* 37, 743–750.
- Liptai, R.G., 1972. Acoustic emission from composite materials. In: *Composite Material: Testing and Design*, ASTM-497, pp. 285–298.
- Liu, Z., 2007. Evaluation of reinforced concrete beams using cyclic load test, acoustic emission and acousto-ultrasonics. PhD Thesis, University of South Carolina, ProQuest LLC.
- Lovejoy, S.C., 2006. Development of acoustic emissions testing procedures applicable to conventionally reinforced concrete deck girder bridges subjected to diagonal tension cracking. PhD Thesis, Oregon State University.
- McCormac, J.C., Nelson, J.K., 2006. *Design of Reinforced Concrete: ACI 318-05 Code Edition*. John Wiley & Sons.
- Md Nor, N., Mat Saliah, S.N., 2016. Acoustic signal strength for damage evaluation of reinforced concrete beam. *ARPN J. Eng. Appl. Sci.* 11 (4), 2622–2626.
- Md Nor, N., Muhamad Bunnori, N., Ibrahim, A., Shahidan, S., Basri, S.R., Mat Saliah, S.N., 2011. B-value analysis of AE signal subjected to stepwise loading. *Adv. Mater. Res.* 403–408, 4126–4131.
- Md Nor, N., Ibrahim, A., Muhamad Bunnori, N., Mat Saliah, S.N., Mohd Saman, H., Shahidan, S., 2012. Classification of damage mode of reinforced concrete beams using acoustic emission technique. *Adv. Mater. Res.* 626, 953–957.
- Md Nor, N., Ibrahim, A., Muhamad Bunnori, N., Mohd Saman, H., 2013a. Acoustic emission signal for fatigue crack classification on reinforced concrete beam. *Constr. Build. Mater.* 49, 583–590.
- Md Nor, N., Muhamad Bunnori, N., Ibrahim, A., Mohd Saman, H., Shahidan, S., Mat Saliah, S.N., 2013b. An investigation of an acoustic wave velocity in a reinforced concrete

- beam from out-of plane and in plane source. *Modeling and Measurement Methods for Acoustic Waves and for Acoustic Microdevices*. INTECH, pp. 171–188.
- Md Nor, N., Ibrahim, A., Muhamad Bunnori, N., Mohd Saman, H., Mat Saliah, S.N., Shahidan, S., 2014. Diagnostic of fatigue damage severity on reinforced concrete beam using acoustic emission technique. *Eng. Fail. Anal.* 41, 1–9.
- Md Nor, N., Ibrahim, A., Muhamad Bunnori, N., Mohd Saman, H., Mat Saliah, S.N., Shahidan, S., 2015. Fatigue crack inspection and acoustic emission characteristics of precast RC beam under repetition loading. *Appl. Mech. Mater.* 773–774, 1022–1026.
- Mohamad, M.Z., Md Nor, N., Wan Ahmad, W.N.A., 2016. Average frequency-RA value for reinforced concrete beam strengthened with carbon fibre sheet. *MATEC Web Conf.* 47, 1–6.
- Nair, A., 2006. Acoustic emission monitoring and quantitative evaluation of damage in reinforced concrete members and bridges. Master of Science in Civil Engineering, Kerala University.
- Nair, A., Cai, C.S., 2009. Damage detection of concrete structures using acoustic emission. *Key Eng. Mater.* 400–402, 101–106.
- Nielsen, J., Griffin, D.F., 1977. Acoustic emission of plain concrete. *J. Test. Eval.* 5 (6), 476–483.
- Noorsuhada, M.N., 2016. An overview on fatigue damage assessment of reinforced concrete structures with the aid of acoustic emission technique. *Constr. Build. Mater.* 112, 424–439.
- Ohtsu, M., 2008. History and fundamentals. In: Grosse, C.U., Ohtsu, M. (Eds.), *Acoustic Emission Testing*. Springer, pp. 11–18.
- Ohtsu, M., Watanabe, H., 2001. Quantitative damage estimation of concrete by acoustic emission. *Constr. Build. Mater.* 15 (5–6), 217–224.
- Ohtsu, M., Shigeishi, M., Iwase, H., Koyanagi, W., 1991. Determination of crack location, type and orientation in concrete structures by acoustic emission. *Mag. Concr. Res.* 43 (155), 127–134.
- Physical Acoustic Corporation, 2005. User's Manual for Samos AE System. Physical Acoustic Corporation.
- Pollock, A., 1995. *Inspecting Bridges With Acoustic Emission-Inspection Details About in Service Steel Bridges and Monitoring Weld Operations: Application Guidelines*. Physical Acoustic Corporation.
- Puskar, A., Golovin, S.A., 1985. *Fatigue in Materials: Cumulative Damage Processes*. Materials Science Monographs, vol. 24. Elsevier.
- RILEM, 2010. Recommendation of RILEM TC 212-ACD: acoustic emission and related NDE techniques for crack detection and damage evaluation in concrete. *Mater. Struct.* 43, 1187–1189.
- Roberts, P.M., 1992. *Visual Inspection*. John Wiley & Sons, Inc.
- Schumacher, T., 2009. New acoustic emission applications in civil engineering. PhD Thesis, Oregon State University.
- Shield, C.K., 1997. Comparison of acoustic emission activity in reinforced and prestressed concrete beams under bending. *Constr. Build. Mater.* 11 (3), 189–194.
- Surre, F., Sun, T., Grattan, K.T., 2013. Fibre optic strain monitoring for long term evaluation of a concrete footbridge under extended test conditions. *IEEE Sens. J.* 13 (3), 1036–1043.
- Wan Ahmad, W.N.A., Md Nor, N., 2016. A study on damage assessment of RC beam wrapped with carbon fibre sheets using parameters of acoustic emission signal. *ARPN J. Eng. Appl. Sci.* 11 (4), 5391–5396.
- Wang, C., Zhang, Y., Ma, A., 2011. Investigation into the fatigue damage process of rubberized concrete and plain concrete by AE analysis. *J. Mater. Civ. Eng.* 23 (7), 953–960.

- Watanabe, T., Nishibata, S., Hashimoto, C., Ohtsu, M., 2007. Compressive failure in concrete of recycled aggregate by acoustic emission. *Constr. Build. Mater.* 21, 470–476.
- Xu, J., 2008. Nondestructive evaluation of prestressed concrete structures by means of acoustic emissions monitoring. PhD Thesis, Auburn University.
- Yuyama, S., Li, Z.-W., Yoshizawa, M., Tomokiyo, T., Uomoto, T., 2001. Evaluation of fatigue damage in reinforced concrete slab by acoustic emission. *NDT&E Int.* 34, 381–387.
- Yuyama, S., Yokoyama, K., Niitani, K., Ohtsu, M., Uomoto, T., 2007. Detection and evaluation of failures in high-strength tendon of prestressed concrete bridges by using acoustic emission. *Constr. Build. Mater.* 21, 491–500.
- Ziehl, P.H., 2000. Development of a damage based design criterion for fiber reinforced vessels. PhD Thesis, The University of Texas.

Durability problems of concrete structures rehabilitated with FRP

7

Mariaenrica Frigione
University of Salento, Lecce, Italy

7.1 Introduction

Application of externally-bonded fiber reinforced polymer (FRP) composite reinforcement is becoming one of the most popular repair techniques for aged concrete structures exposed to harsh environments, due to their high-strength, low weight, ease of installation, and cost-effectiveness.

There are, however, several aspects of this technology still needing further research and development. Probably the most critical is the scarce, often-contradictory, information on the long-term performance of FRP's subjected to weathering, the so-called "durability."

It is generally accepted that polymer composites are very durable materials, particularly those designed for aeronautical/aerospace applications. However, FRP's used in civil engineering applications are significantly different from those developed in a much more demanding industry, especially for the techniques used to manufacture the composite. In the construction industry, in fact, large surfaces must be strengthened by an FRP often formed on field (i.e., in situ), without the possibility to effectively control the manufacturing procedures as well as the conditions for the processing (hardening) of the adhesive/matrix resin.

The durability of a rehabilitated concrete structure depends on the material chosen and the processing techniques used for this operation, the load regime, and the kind and level of environmental exposure. FRPs typically employed as reinforcement for concrete are composed by thermosetting (often epoxy) resins with the addition of (carbon, glass or rarely aramidic) fibers. The durability of the FRP, then, depends on the durability of any single component of the composite and on its production techniques, in addition to the service conditions in which the system operates.

While the long-term performance of the traditional solutions employed for the strengthening and repair of concrete structures has been long ago assessed, the use on FRP in this field is relatively recent, thus the service life prediction of structures that use FRP is still a knotty problem.

Although the research on this topic became very active in recent years, durability data available in literature for FRP employed in constructions are still limited and not organically collected. The studies are often presented devoid of details on the materials and the processing conditions used (for instance, the chemical formulation of the matrix resin, the processing parameters, the time elapsed before the execution

of durability tests). The observed discrepancies between results obtained by different durability studies could be, then, attributed to different materials, processing or conditions employed for conditioning—all fundamental information for the understanding of the effects of the external environment on properties of materials, and for an accurate prediction of their behavior over a lifespan.

The limited understanding and confidence in the long-term performance of externally-bonded FRP composites to concrete structures inhibits their wider application in the construction industry, forcing engineers to employ greater safety factors; increasing the cost and the weight of the composites, partially nullifying their advantages, and reducing the capability of tailoring their properties for the specific application.

In this chapter, the peculiarity of FRP's available for rehabilitation of concrete structures will be illustrated, along with an overview of their durability—highlighting some issues not yet assessed or addressed.

7.2 Application of fiber reinforced polymer composites for rehabilitation of concrete structures

The need for structural interventions on concrete constructions is increasing in the recent years for several reasons: the continued aging of civil infrastructure, the low sustainability of demolition and reconstruction instead of repairing, the high vulnerability to seismic actions experienced during earthquakes, the changed usage that requires structural upgrading.

Traditional techniques for both global and local interventions are generally based on the use of steel and reinforced concrete: they evidence some weakness, such as durability aspects when using steel and the increased mass when concrete or reinforced concrete is applied. Other drawbacks are related to long times of interventions and, consequently, of activities interruption.

The problems associated with the corrosion and deterioration of reinforcing steel in concrete structures, and the high costs connected with the disruption of traffic, have lead the engineering community to look for innovative solutions.

Externally-bonded FRP (pre-cured) plates and in situ-cured sheets are considered as an effective, reliable alternative for the strengthening of deteriorated structures due to the ease with which they can be applied to the concrete substrate.

The attractiveness of polymeric composites, that which makes them often preferred to traditional construction materials, resides in their lower weights and adaptability to any specific application. FRP display outstanding performance in terms of high strength-to-weight and stiffness-to-weight ratios and excellent durability against corrosion. A wide choice of materials (polymeric resins and fibers) is commercially available. From their combinations, different structures/components can be shaped with tailored anisotropy and geometry able to satisfy the project requirements.

Several studies have been performed since the 1980s on the use of FRP as concrete reinforcement, mainly in Japan, where FRP have been largely applied to

existing structures, North America and Europe (Bakis et al., 2002). Different codes or guidelines devoted to the use of FRP on existing concrete structures have been released in many countries from more than 10 years (Fédération International du Béton (fib) Bulletin, 2001; JSCE, 2001; Fédération International du Béton (fib) Bulletin, 2006; ACI 440.2R-08, 2008; ISIS Design Manual, 2001; TR55, 2004; CNR-DT_200/2004, 2004).

The retrofit technique of concrete structures by means of FRP composites is applied to improve the flexural and/or shear strength and stiffness of beams, and to provide confinement to concrete elements (columns) under compression actions (Mirmiran and Shahawy, 1997; Norris et al., 1997). The external installation of FRP sheets can provide the required additional strength for an existing bridge superstructure to accommodate additional live loads or to restore the designed load capacity of a damaged structure (Jeong et al., 2016).

Additional advantages in the use of FRP reside in the capacity to speed the time of repairing structures, thus reducing the overall costs. Maintenance operations are also cut when FRP are applied in substitution of traditional construction materials.

Furthermore, externally-bonded FRP applied on the concrete surface using (thermosetting) adhesive materials, isolates concrete element from the environment, serves as a barrier against diffusion of harsh agents, and protects concrete elements from environmental effects. They can even represent a solution to improve the durability of concrete.

On the negative side, FRP's are generally more expansive compared to traditional materials. However, the low weight of materials and ease of construction provide large labor and traffic control cost savings. Transportation costs for FRP components are lower, in comparison to the traditional materials, due to their low specific weight. Furthermore, if appropriately selected, designed and fabricated, FRP composites can provide longer service life and greater reduced maintenance costs than equivalent structures fabricated from conventional materials. Thus, whole life cycle cost savings have been shown to more than offset the relatively high initial cost of the FRP materials compared to conventional ones (Hollaway, 2010).

7.3 Fiber reinforced polymer components

The FRP composites used in repair and strengthening of concrete structures applications are typically composed of continuous fibers (carbon, glass, aramid) embedded in a thermosetting resin matrix (epoxy, vinyl ester, and polyester resins) that holds together the fibers and transfers the load between them. A thermosetting resin (the same composing the matrix of FRP or a different one) is also employed to act as adhesive between the FRP and the concrete substrate.

The behavior and integrity of an FRP-reinforced concrete element depends on the properties of the individual materials, and on the performance of the FRP-adhesive and adhesive-concrete interface bonds. That is to say, the reliability of the strengthening technique by using externally-bonded reinforcement made by FRP

materials depends, to a large extent, on the bond between the reinforcement and the substrate and, therefore, on the ability of stresses transfer at the interface.

Among the polymeric resins able to accomplish this task, epoxy resins are known to exert a strong interfacial bond between cement concrete and a broad range of reinforcing materials. Epoxies, assuring good performance in terms of flexibility and effectiveness of repairing technique and moderate costs, are the most-used resins. They can be formulated as low viscosity systems which “cure” (i.e., form cross-links throughout the structure and, as a consequence, harden) at room temperature with minimal shrinkage and no, or very little, release of volatile products. When correctly formulated and cured, they exhibit a good combination of mechanical properties and chemical resistance towards environmental agents.

For strengthening/repairing applications with FRP, epoxies are frequently preferred to both vinyl ester and unsaturated polyester resins, characterized by excessive shrinkage during curing, with the possible formation of micro-cracks or micro-gels in the bulk, resulting in micro-inhomogeneities and incomplete polymerization (Mays and Hutchinson, 1992). Unsaturated polyester resins, in addition, display a high susceptibility to moisture and low bonding efficiency in damp or wet conditions, and when exposed to alkaline environments.

Referring to the fibers: although carbon fibers are generally considered to be inert to most environmental influences likely faced in civil infrastructure applications, the inertness does not apply to the fiber-matrix bond. Glass fibers are well known to undergo “corrosion,” a phenomenon occurring in ordinary glasses in presence of moisture/alkaline environment. Nevertheless, their durability upon exposure to typical outdoor applications is still satisfactory.

7.3.1 Peculiarities of fiber reinforced polymer used in constructions

FRP can be applied to concrete structures following two different procedures: (1) the precured FRP elements are adhesively bonded as precured (often pultruded) laminates to the concrete substrate; (2) the composite is applied through a wet lay-up of fabrics, directly onto the substrate.

In the pultrusion process, the fibers undergo impregnation by thermosetting resin and are pulled through a heated stationary die which allows for epoxy polymerization. The application of precured materials, produced in factories through industrially-controlled processes, permits achieving a high level of uniformity in the final product and better performance in a desired, functional, shape. On the negative side, prefabricated FRP is less flexible and adaptable for unpredicted configurations that can be found in true application (as few examples: the confinement of cylindrical columns, the strengthening of arches and vaults). Moreover, the application of a precured FRP to a concrete substrate is carried out by means of another thermosetting, often epoxy, adhesive applied and hardened on site. This, therefore, implies the introduction of an adhesive interphase between the already-cured matrix

of the composite and the substrate. In addition, their elevated costs are not always justified for these low-technology applications (Karbhari, 2002).

“Wet lay-up” FRP application (with the FRP formed in situ) is performed by saturating a dry fiber fabric with resin. The wet fabric is, then, placed on the concrete surface. Primers are sometimes used to facilitate adhesion to the concrete substrate. A putty can be also employed in order to adequately finish the surface of the substrate. Primers and putty are both generally composed by epoxy resins, very fluid (unfilled) the first, containing (inorganic) fillers the second. The use of the wet lay-up technique provides enormous flexibility, since the preimpregnated fabric can closely follow the geometrical configuration of the structure to be rehabilitated. Moreover, the bond between the FRP and the concrete substrate is achieved with an adhesive resin which is very similar, if not the same, to the matrix of the composite, i.e., it is able to form a continuum between the FRP and the concrete substrate. The lack of careful control of curing, however, leads to a significant higher level of variation in performance.

Figs. 7.1 and 7.2 illustrate the application of pultruded FRP laminates and wet lay-up composites, respectively, for the strengthening of internal ceilings.

In both the described techniques, the weakest link is represented by a cold-cured resin, used as adhesive in the first case and as matrix/adhesive in the second one. While the resin is responsible for the overall integrity of the rehabilitate of structure, since it must assure an effective stress transfer among the concrete structure and the FRP reinforcement, it can undergo both chemical and physical degradation by environmental conditions and mechanical stresses.

The choice of the first technique, i.e., employing precured (plane) FRP, or the second one, i.e., (the more flexible and cheaper) wet lay-up configuration, is made on the basis of the scheme and geometry of the concrete structure to rehabilitate (flat vs irregular, vaulted or cylindrical surfaces); on the accessibility of the intervention area; on the available time for the intervention vs. the curing time required



Figure 7.1 Adhesively bonded pultruded strips.

Source: Reprinted from: Karbhari, V.M., 2005. Building materials for the renewal of civil infrastructures. *Reinf. Plast.* 49 (1) 14–25, with permission from Elsevier.



Figure 7.2 Wet lay-up of fabric on soffit affords efficient strengthening.

Source: Reprinted from: Karbhari, V.M., 2005. Building materials for the renewal of civil infrastructures. *Reinf. Plast.* 49 (1) 14–25, with permission from Elsevier.

to the cold-cured adhesive, in the first case, or to the matrix-adhesive cold-cured resins, in the second one (Karbhari et al., 1997; Karbhari and Zhao, 1998). As already underlined, precured FRP's generally present higher values of the in-service properties (and strength and stiffness values) compared to wet lay-up produced FRP, and therefore a more robust resistance to hostile environments; thus they are preferred when the civil infrastructures are required to withstand harsh and varying environmental exposure for long periods of time (Hollaway, 2010). Precured FRP's are often employed as efficient substitutes of beton-plaque techniques. The deterioration mechanism experienced by the concrete structure has a minor effect on the choice of the most appropriate strengthening systems based on FRP.

7.3.2 Cold-cured thermosetting (epoxy) resins

Epoxy resins, from a chemical point of view, are cross-linked polymers in which their molecular structure is a network. Generally speaking, the polymerization (curing) reaction of an epoxy occurs in the presence of a suitable curing agent (hardener) and is favored by heat/radiation, depending on the curing mechanism. The kind and amount of hardener are selected on the basis of the resin and curing conditions, and have both an appreciable influence on the final performances of the cured epoxy.

During the curing of the epoxy, the cross-linking of the resin progressively proceeds with a decrease in free volume and molecular mobility of the polymer network, leading to the development of mechanical properties and the increase of the glass transition temperature of the resin. The mean value of the temperature range below which the typical properties of a cured thermosetting resin vary in a manner similar to that of a solid (glassy) phase, and above which it behaves in a manner similar to that of rubber, is known as glass transition temperature, T_g . The T_g establishes the service environment for the resin usage. When the resin is exposed to

greater temperatures than its glass transition temperature, its behavior drastically changes from solid to that of a soft material. Approaching the T_g , a dramatic decrease (up to 70%) in stiffness and strength is experienced by the resin (Frigione et al., 2000; Shin et al., 2011); above T_g , both properties become almost zero. The detrimental effects of moderate temperatures on the performance of a resin are reproduced in its behavior as adhesive. When an adhesively-bonded joint is tested below the T_g of the adhesive, the latter will behave like a low-strain rigid material, able to effectively bond two different materials, while above this temperature it will have a rubber-like behavior, unable to guarantee the required stress transfer between the same materials (Banea et al., 2011). As a consequence, in most applications, the epoxy is used at a temperature well below T_g (i.e., in the glassy state).

For economic and practical reasons, the resins used as matrix and/or adhesive for FRP in constructions are “cold-cured” types, typically based on bisphenolic epoxies and cured at ambient temperatures on site with the addition of aliphatic amines (Hollaway, 2010). Providing any kind of heat sources, over the large areas required for the described applications, is very difficult and prohibitively expensive. Furthermore, the process (outdoor) conditions in which the resins set and harden are not sufficiently controlled and kept constant, unlike the factory fabrication conditions used for aeronautical/aerospace products.

The main consequences of a cure at ambient (uncontrolled) temperature of epoxy resins are: (1) long curing times (even months) are necessary to achieve sufficient mechanical properties, the lower the curing temperature, the longer the curing time (Moussa et al., 2012; Maljaee et al., 2017)—this observation is incompatible with the short periods suggested in the technical datasheets for complete curing of epoxy resins (Sciolti et al., 2010); (2) the curing (cross-linking) reactions, taking place at ambient temperatures, are often not completed because of kinetic restraints (Karbhari, 2007), that is to say: a full degree of curing may never be achieved when the epoxy is cured in natural environmental conditions; (3) a moderate glass transition temperature (T_g), in practice never greater than 65°C–70°C, is attainable by these systems, particularly if the curing of the resin occurs at low winter temperatures (see, for instance, Fig. 7.3) (Frigione et al., 2001; Frigione et al., 2006; Frigione et al., 2006; Frigione and Lettieri, 2008; Sciolti et al., 2010; Moussa et al., 2012). In addition, the absorption of external water (as atmospheric moisture or rain), produces a decrease in the T_g of the resin (as illustrated in Fig. 7.4), which in turn negatively affects its mechanical and adhesive properties (Shin et al., 2011), as the data reported in Table 7.1.

The incomplete cure attained by the cold-cured epoxy resins at short/medium times (even after 1 year) is testified by the presence of unreacted epoxy groups in the cured resin and a glass transition temperature lower than that achievable by the same fully-cured resin (Savvilotidou et al., 2017a). When the T_g is surpassed by even mild external temperature, the adhesion between FRP and concrete is likely to be reduced. Furthermore, in thermosets which are not fully cross-linked, exposure to moderate temperatures (above the T_g) can promote the postcure of the matrix/adhesive. The postcuring is usually reflected in increment of T_g and of stiffness of the resin (Silva et al., 2016); the T_g of the fully cured epoxy resin ($T_{g\infty}$) may be

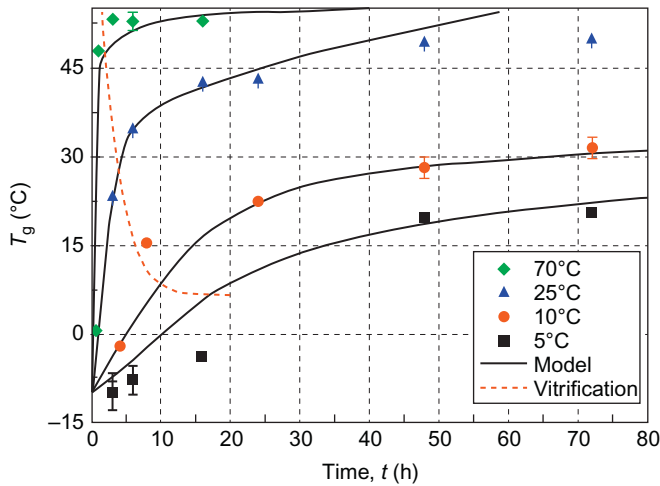


Figure 7.3 Glass transition temperature versus time of partially cured commercially epoxy adhesive samples at different isothermal temperatures.

Source: Reprinted from: Moussa, O., Vassilopoulos, A.P., Keller, T., 2012. Effects of low-temperature curing on physical behavior of cold-curing epoxy adhesives in bridge construction. *Int. J. Adhes. Adhes.* 32, 15–22, with permission from Elsevier.

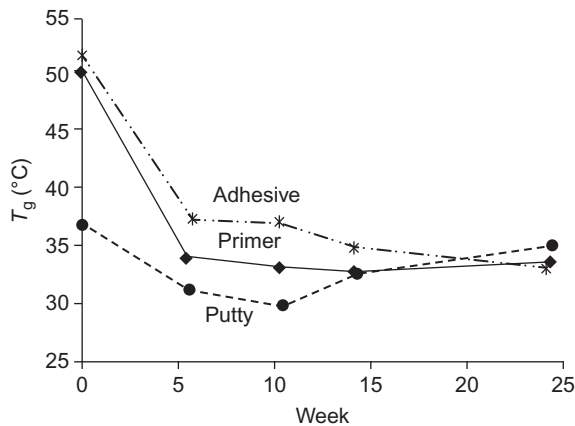


Figure 7.4 Glass transition temperature (T_g) versus immersion time measured on commercial primer, putty, and adhesive employed for the manufacturing of wet lay-up FRP systems.

Source: With permission from ASCE of: Sciolti, M.S., Frigione, M., Aiello, M.A., 2010. Wet lay-up manufactured frps for concrete and masonry repair: influence of water on the properties of composites and on their epoxy components, *J. Compos. Constr.* 14, 823–833.

Table 7.1 Results of adhesion tests performed on joints obtained with f_{ck} 50 concrete and commercial (S50) epoxy adhesive after different immersion time in distilled water

Days of immersion	Adhesive thickness (mm)	F_u (kN)	S_{F_u} (kN)	COV (%)	σ_b (MPa)	S_{σ_b} (MPa)	COV (%)	$\Delta\sigma_b$ (%)
0	0.5	164.96	1.61	1	19.56	0.12	1	—
	2.0	152.20	0.97	1	17.62	0.03	0	—
	5.0	146.32	17.98	12	16.51	2.00	12	—
2	0.5	153.34	0.53	1	18.02	0.02	1	-8
	2.0	169.20	7.51	4	19.68	1.01	5	+12
	5.0	135.82	22.78	17	15.65	2.30	15	-5
7	0.5	138.33	3.06	2	15.78	0.33	2	-19
	2.0	118.59	5.12	4	14.04	0.62	4	-20
	5.0	—	—	—	—	—	—	—
14	0.5	105.59	11.38	11	12.52	1.30	10	-36
	2.0	96.09	11.22	12	11.49	1.34	12	-35
	5.0	94.83	7.1	7	11.15	0.75	7	-32
28	0.5	104.38	15.65	15	12.41	1.76	14	-36
	2.0	92.37	15.87	17	10.81	1.90	18	-39
	5.0	92.65	9.71	10	10.73	1.26	12	-35

Source: Reprinted from: Frigione, M., Aiello, M.A., Naddeo, C., 2006. Water effects on the bond strength of concrete/concrete adhesive joints. *Constr. Build. Mater.* 20, 957–970, with permission from Elsevier.

even achieved. These systems, therefore, operate in a nonequilibrium state, with the properties evolving in time and as a consequence of the variable external conditions.

Nevertheless, the effect of a long curing time on the mechanical properties of FRP produced with a cold-cured epoxy matrix mainly depends on the disposition of fibers in the composite, and on the direction of application of the load. Mechanical in-plane tensile tests performed on unidirectional single-ply FRP during the curing stage of the resin demonstrated that the curing time has no influence on FRP performance, irrespective of the kind (carbon or glass) of fibers (Sciolti et al., 2010). Conversely, it is expected that the adhesion strength developed between FRP and the substrate during the curing of the matrix (for wet lay-up systems) and the adhesive (for all systems) is appreciably influenced by the progress of curing. It must be emphasized that only a few systematic studies focalized on this critical topic have appeared only recently in literature (Jeong et al., 2016).

7.4 Durability of fiber reinforced polymer for rehabilitation of concrete structures

Most of the literature on durability studies on FRP refers to applications limited to aerospace and automotive industries (hot-cured matrices, controlled processes

carried on in industrial plants). As already underlined, these applications display significant differences from the infrastructure field, in terms of manufacturing and installation processes, exposure environments, and load regimes. Only recently the academic efforts were more systematically devoted to the study of long-term performance of FRP's exposed to the environmental agents typically encountered in infrastructure and building applications. However, although the knowledge on FRP degradation mechanisms is rapidly growing, not all the studies present in literature can be truly useful for the assessment of the FRP's durability and their remaining service-life in such "new" applications.

As already pointed out, different results are often found in studies carried out by different researchers. In some published papers, generic "FRP" laminates are reported, without specifying whether the composite was previously produced by an industrial process employing controlled high-temperature curing cycles or manually applied by wet lay-up at "uncontrolled" ambient temperature. In other studies, insufficient details are reported on the kind of matrix used (often commercial with a proprietary composition) and on the curing conditions (time, temperature, relative humidity) used before any environmental exposure of the specimens. Yet, it is perhaps almost inevitable that companies change the composition of their products as a result of drivers such as material developments, economics and sustainability, and still maintaining the same trade name (Lees et al., 2017). On the other hand, all the cited parameters have an appreciable influence on the durability performance of the FRP: a different (not declared) choice of resin or curing/conditioning conditions can partly justify the observed discrepancies. Thus, once carefully established at the design stage of the experimental campaign, any parameter must be specified as much as possible when illustrating the experimental procedure.

In addition, it must be emphasized once again that the behavior of the cold-cured resins during natural exposure or laboratory experiments can be appreciably influenced by the progress of curing reactions if these are not completed before the beginning of the exposure and/or the experiments. Any change in properties should be properly considered in interpretation of the experimental results, as the measurements are usually conducted at relatively early curing ages (e.g., 2 months) (Maljaee et al., 2017). Ideally, one should ensure the attainment of a "stable" system, i.e., a system that has achieved the maximum degree of cure (even if not necessarily fully cured) at the same temperature of the aging experiments (i.e., with steady values of properties at the specific environmental conditions under analysis), in order to separate and analyze the effects that can be totally attributed to the aging conditions.

Generally speaking, the performance and the long-term behavior of polymer composites based on thermosetting resins depend intrinsically on the choice of constituent materials (i.e., primer, adhesive, fibers), on the conditions in which the matrix resin sets and hardens, on the process used to manufacture and to apply the composite, and on the surrounding environmental conditions over its entire service life. The environmental conditions to which FRP's for strengthening and rehabilitation of concrete structures are more frequently exposed during their application and service life are neither constant nor predictable, and they depend on several

parameters such as the latitude of the site, the season, the distance from sea, the local weather, etc. (Wypych, 1995). Environmental factors can severely affect the performance in service of each element composing FRP and of the whole FRP, even after a short time since installation, due to specific processes—either reversible or permanent—taking place between the external agents and the materials composing the FRP.

An environment can be defined as the sum of all factors acting on a material. For indoor applications, the influence of humidity, small variations in temperature, and their combinations on the properties of FRP's must be taken into account. For the more common outdoor applications, it can be hypothesized that, during its service life, a polymeric composite will come in contact with atmospheric humidity, rain, solar (UV) radiations, large variations in temperature, freeze–thaw regimes, acid rain, sea-water, deicing chemicals, and alkaline environment when in the proximity of Portland cement concrete. Finally, polymer composites can be accidentally exposed to extreme environments, such as: fire, earthquake, explosive blasts.

Referring to the resins, concerns arise from the behavior of cold-cured epoxies used as matrices and adhesives in FRP. The experimental studies present in current literature on the effect of environmental agents on the properties of FRP highlight the crucial role of the adhesive/matrix resin on the behavior of the whole system. Due to the peculiarity of cold-cured epoxy resins, there are environmental conditions frequently encountered in civil infrastructures that may severely affect the performance of wet lay-up type FRP as well as the integrity of FRP-to-FRP and FRP-to-concrete bonds. Many other parameters (i.e., direction and disposition of fibers, direction of load application) are involved in the assessment of the durability of an FRP.

7.4.1 Durability of matrix/adhesive resins

The performance and the long-term behavior of cold-cured thermosetting matrix/adhesive resins depends on the chemical nature of the base materials (resin/hardener couple), on the curing conditions and, above all, on the environmental service conditions (temperature, presence of water/moisture, chemicals and other harsh agents).

The most common exposure conditions in civil engineering structures are simultaneous moisture and temperature variations, known as “hygrothermal” aging. The properties modification of epoxy resins in hygrothermal conditions is the result of several complex and interrelated mechanisms, which are even more complicated in the case of not-fully cured epoxy, employed in such applications. Many studies have recently focused on the effect of moisture and temperature (in an uncoupled or coupled manner) on the cold-cured epoxy resins (Lettieri and Frigione, 2012; Moussa et al., 2012; Blackburn et al., 2015), highlighting the concurrence of different physical (reversible) or chemical (not reversible) phenomena.

Starting with the influence of the service temperature, as already underlined, the mechanical/adhesive properties of epoxy resins reduce significantly at temperatures near or above T_g , which can lead to failure of structural components. A moderate service temperature (such as that measured inside a concrete element with the surface irradiated by sun), is able to appreciably reduce the adhesion strength to

concrete (by over 80% at 50°C) and the fatigue resistance (Aiello et al., 2002; Shin et al., 2011). Therefore, several design codes established limitations for the minimum acceptable T_g with respect to the environment's temperature: under working conditions, the latter should be 20°C below the glass transition temperature of the resin (Hollaway, 2010).

It is worth noting that exposure to temperatures above the T_g of the fully cured system, i.e., $T_{g\infty}$, can cause a thermal degradation of the resin, with reductions in T_g and mechanical characteristics (Stewart et al., 2007; Carbas et al., 2013). Most of the effects of moderate/high temperatures on thermosetting (adhesive and matrix) resins are permanent and irreversible.

Water, either in the form of moisture or actual water through rain, or even in immersion, is another harmful external agent frequently encountered by matrices and adhesives employed in FRP for civil engineering applications. The ingress of water/moisture over time is particularly significant if the polymer is permanently immersed in water.

The high vulnerability of unsaturated polyester resins to moisture has been already mentioned.

Epoxy resins are prompt to absorb substantial amounts of water due to the presence in their macromolecules of polar groups able to attract water molecules. Moisture absorption can cause reversible (plasticization) and irreversible (hydrolysis, cracking and crazing) changes in physical, chemical and mechanical properties of epoxy resins. At short-time exposures, moisture leads to increments of free volume in cross-link chain, with a depression of T_g . This process, termed plasticization, is a physically reversible process and its effects can be mostly reversed upon drying (Frigione and Lettieri, 2008; Zhang et al., 2014). An excessive penetration of water is generally considered harmful, since it leads to a reduction (even halved) in stiffness and strength of the resin with a consequently marked, unsuitable decrease of its load-bearing capacity (Frigione et al., 2006; Frigione et al., 2006; Silva et al., 2016). The absorbed moisture is able to modify the type of failure mode of the epoxy from brittle, for the not-aged, to ductile, for the saturated specimens (Lin and Chen, 2005). Long-term exposure to moisture can lead to chemical changes in the polymeric ester linkage (chemical process), and in some cases produces further cross-linking when the epoxy resin is not-fully cured (with an increase in T_g). Most of the effects on the physical properties of resins exposed for longer times to moisture are permanent.

Immersion at moderate temperatures (i.e., 60°C) caused further degradation with significant decreases in strength and stiffness, much higher than those measured under other conditions, such as in salt-water at 23°C (Yang et al., 2008; Cabral-Fonseca et al., 2009). Increases in temperature lead to increment of moisture absorption rate and thus, faster plasticization—amplifying the degradation caused by the immersion conditions (Bao and Yee, 2002). Depending on the degree of cure of the (not-fully cross-linked) resin, the combination of temperature and moisture exposure can even cause an increase in T_g and in mechanical properties of the resin (Sciolti et al., 2015; Maljaee et al., 2017).

The bond between the concrete elements and the FRP material plays an important role on the success and efficiency of a strengthened system. Therefore, the

effect of temperature, moisture and hygrothermal conditions on the adhesive bond between the FRP sheet and the concrete surface has been under investigation. When the service temperature approaches and exceeds the T_g of the matrix/adhesive, for wet lay-up FRP, and of the adhesive, for precured FRP (both applied to concrete elements), an appreciable decrease in bond strength occurs (Almusallam and Al-Salloum, 2006; Leone et al., 2009). The effect of temperature on the adhesive strength depends on the strength of the concrete in relation to that of the adhesive and on the thickness of the adhesive layer. Exposure to a moderate temperature (i.e., 40°C) can even increase the bond strength developed with concrete, due to the postcuring of the resin. However, the combination of sustained loading and elevated temperatures hampers any strengthening effect (Gullapalli et al., 2009).

The bond strength is also severely affected by the presence of water at the concrete substrate level (Wan et al., 2006; Karbhari and Navada, 2008). In the presence of appreciable water-moisture amounts or at medium-high temperatures, mechanism of failure occurring in concrete-adhesive elements changed from predominantly concrete failure to mixed failure of epoxy and at the interface (Aiello et al., 2002; Frigione et al., 2006; Jeong et al., 2016), which further supports the hypothesis of the adhesion bond degradation due to hygrothermal conditioning.

The presence of salts in water does not greatly affect the properties of resins, and their bond strength with concrete, with respect to the immersion in pure water (Grace and Grace, 2005; Silva et al., 2016).

The effect of alkaline water exposure on physical and mechanical properties of cold-cured epoxy resin has been widely investigated with contradictory results. After 24 months of exposure to pure water and alkaline solutions at different temperatures, a higher decrease of tensile strength and stiffness was measured in the case of alkaline exposure with respect to pure water (Yang et al., 2008; Cabral-Fonseca et al., 2009). In other studies, however, it was found that the water uptake in pure and alkaline water were the same and the immersion in alkaline water resulted in reductions of physical and mechanical properties of cold-cured epoxy resins similar to those obtained after immersion in demineralized water (Wolff et al., 2006; Savvilotidou et al., 2017b). Epoxies, however, have shown to be more resistant to alkaline environments than vinyl esters and polyesters.

Finally, ultraviolet radiations mainly affect the surface of the resin and, consequently, can degrade only the matrix of an FRP, possibly causing a decomposition of the resin molecules. The possible embrittlement of the matrix produces micro-cracks at the surface, which, in presence of other environmental agents, can accelerate the degradation process by allowing easier penetration of fluids into the laminates. In some cases, the exposure to radiations can even slightly increase the stiffness and strength of laminates through the post-cure of the not-fully cured matrix resin.

7.4.2 Durability of fibers

Carbon is the most commonly-used fiber in FRP systems for repair and strengthening where exposure to aggressive environments is expected. Carbon fibers are, in fact, generally considered to be inert to most environmental influences likely to be

faced in civil infrastructure applications. The mechanical properties of carbon fibers remained totally unaffected by thermo-hygro-metric treatments. In addition, carbon fibers did not show weakness towards alkaline solutions.

Glass fibers, on the other hand, are well known to undergo stress corrosion in presence of moisture (Mascia and Allavena, 1976). Moreover, when alkaline solution penetrates the composite, it can severely damage glass fibers through loss in toughness, strength, and embrittlement. When in close contact with Portland cement concrete, glass fibers are damaged due to the combination of two processes: (1) chemical attack of the glass fibers by the alkaline cement environment, and (2) concentration and growth of hydration products between individual filaments (Murphy et al., 1999). The embrittlement of fibers is due to the nucleation of calcium hydroxide on their surface. The hydroxylation can cause fiber surface pitting and roughness, which act as flaws severely reducing the properties of fibers in the presence of moisture. In addition, found in the concrete pore solution are also aggressive towards glass fibers (Benmokrane et al., 2002). Therefore, the degradation of glass fibers not only depends on the high pH level, but also on the combination of alkali salts, pH, and moisture.

Carbon-reinforced FRP's are reported to be generally not affected by ultraviolet rays. Aramidic and glass fiber-reinforced composites, on the other hand, show reductions in impact tensile strength as a consequence of exposures to radiations, resulting in the loss of performance of the strengthened system (Larsson, 1986; Tomosawa et al., 1998).

It can be concluded that carbon-based composites are better suited for applications involving harsh exposures while glass fiber laminates show the lowest durability in chemical solutions, especially alkaline ones. Both ultimate strength and strain-at-break of Glass Fiber Reinforced Polymers (GFRP) are significantly reduced by exposure to either water or simulated seawater and acidic and alkaline solutions. In order to provide adequate protection to the glass fibers, the use of appropriate, tailored sizings able to significantly reduce the level of degradation through development of a protective coating on the fiber—which also served to enhance bonding—has been recommended. GFRP durability can be also improved by using hybrid glass-carbon fabrics.

7.4.3 Durability of the whole system

As underlined, the experimental durability studies performed on FRP's intended for civil engineering applications highlight the crucial role of adhesive/matrix resin, especially if cold-cured, on the behavior of the whole system. However, many other parameters (i.e., number of plies, direction and disposition of fibers and weave pattern, direction of load application) must be taken into account when assessing the durability of an FRP applied on a concrete surface (Hollaway, 2010).

Although FRP composites do not corrode, they do undergo physical and chemical changes, including oxidation and hydrolysis of the matrix/adhesive resin. While synergistic effects of multiple exposure conditions can be severe, it is generally agreed that the most significant issue with externally-bonded FRP composites is

their susceptibility to degradation when exposed to water/moisture, subjected at high temperatures and under mechanical stresses (Karbhari et al., 2002). Generally speaking, the matrix is more affected by environmental agents than do fabrics.

Referring to the influence of water/moisture, apart from the kind of matrix resin (being epoxy and vinyl ester resins generally more resistant to the action of water than polyester) and fibers used (carbon vs glass), the performance of FRP mainly depends on configuration of fabrics (number and disposition of plies) and on the direction of application of the load.

The tensile properties of an FRP composed by a single-ply in the direction of fibers are highly dependent on the properties of the fibers. In the case of in-plane tensile tests performed on unidirectional single-ply wet layup carbon-based FRP (i.e., CFRP), only a negligible influence of presence of water is observed (Saadatmanesh et al., 2010; Sciolti et al., 2010), as illustrated in Fig. 7.5. Water, on the other hand, can cause a deterioration of the mechanical properties (stiffness and strength) of laminates manufactured with glass fibers (i.e., GFRP) (Saadatmanesh et al., 2010; Ghiassi et al., 2013). Moisture can easily penetrate along the fiber-matrix interface causing deleterious effects to the fiber-matrix bond (Rinaldi and Maura 1993; Karbhari, 2002).

In laminates composed of several plies, the presence of water at the interface between the adjacent layers is likely to be severely harmful. Since the matrix resin is responsible for the adhesion between plies, and is generally very susceptible to degradation by water, greater reductions in tensile strength are found for thicker specimens composed by a large number of plies (Abanilla et al., 2006; Abanilla et al., 2006). Interlaminar properties are also intrinsically dependent on the resin characteristics, and undergo similar deteriorations. An increase in the interlaminar fracture toughness, however, can take place as a result of the immersion in pure water, which causes plasticization of the matrix resin with a consequent reduction in its stiffness.

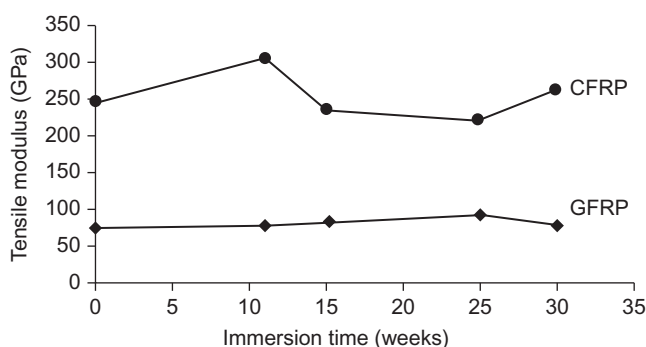


Figure 7.5 Tensile elastic modulus versus immersion time measured on commercial carbon-based fiber reinforced polymer (CFRP) and Glass fiber reinforced polymer (GFRP) specimens.

Source: With permission from ASCE of: Sciolti, M.S., Frigione, M., Aiello, M.A., 2010. Wet lay-up manufactured FRPs for concrete and masonry repair: influence of water on the properties of composites and on their epoxy components. *J. Compos. Constr.* 14, 823–833.

As already underlined, the presence of water/moisture at the adhesive/fibers/substrate interfaces is particularly detrimental when the FRP is applied to a concrete substrate (Dai et al., 2010). Moisture plays an important role in the durability of the bond between FRP and concrete, affecting the whole structural response of the strengthened elements. Moisture, in fact, reduces the fracture energy up to debonding; it often causes the failure mode to change from cohesive, within the concrete substrate, to adhesive, at the interface (Tatar and Hamilton, 2016); it involves a decrease of the ultimate capacity of FRP-strengthened reinforced concrete beams (Sciolti et al., 2012). Other parameters affect the fracture energy displayed by an FRP-concrete structural element, namely the environmental relative humidity, the specimen dimension and configuration, the material diffusion properties, the test approach, and the surface treatment of the specimens. As a consequence, the assessment of a model of general validity, defining its durability in presence of water/moisture, is still a complex task.

Wide temperature variations possibly encountered under normal service conditions can also adversely affect the performance of an FRP applied to a concrete substrate, since the coefficient of thermal expansion of epoxy resin is of about one order of magnitude greater than that of concrete. Similarly, in many cold climates, such as those found in Canada and in the Northern U.S., seasonal and daily temperature variations have the potential to cause numerous freezing–thawing cycles than can, again, result in different thermal expansion in the FRP reinforce and the concrete substrate (Bisby and Green, 2002). The bond strength at FRP-concrete interface reduces with increasing freeze–thaw cycles (Kolluru et al., 2008; Yun and Wu, 2011).

Cyclic variations in temperature in conjunction with presence of moisture may lead to even more severe effects. This is the case of concrete columns strengthened with GFRP warps that experienced an appreciable decrease in axial tensile stiffness (Silva, 2007).

Freeze–thaw exposure generally causes a severe degradation of FRP properties, also attributed to the stiffening and embrittlement of the matrix resin at temperatures below its T_g , with the consequential formation of micro-cracks. Reductions in tensile strength and interlaminar fracture toughness are generally observed after freeze–thaw repeated cycles. The loss in strength is even more severe when the thaw regime is performed in saline environments. All the mentioned effects are generally magnified by increasing the number of freeze–thaw cycles and are almost independent of the kind of matrix resin and fibers used. The permanence at a sub-zero temperature has only a limited influence on the mechanical properties of an FRP.

Potential synergies can exist between individual physical and environmental factors when the structural element is also subjected to a sustained load. As an example, GFRP externally-bonded to concrete prisms and subjected to a sustained load experienced severe decreases in interfacial fracture energy when exposed to either moderate temperatures (50°C–60°C) or freeze–thaw conditions during sustained loading (Jia et al., 2005). On the other hand, relatively moderate decreases in fracture energy were observed for the same specimens subjected to indoor laboratory conditions during the same loading.

The durability of a composite material, also in conjunction with concrete, in saline or acid solutions depends on the resistance of both the matrix and the reinforcing fibers to these agents. Seawater, deicing salts, alkaline and acid solutions are

particularly harmful for Aramidic Fiber Reinforced Polymers (AFRP) and GFRP, producing in both composites damage at the fiber/resin interface and the degradation of the glass fibers for GFRP. Exposure to alkaline solution also severely affects the integrity of the bond developed with concrete (Cromwell et al., 2011). The tensile properties of GFRP are scarcely influenced by immersion in alkaline and acid solutions, while their flexural and interlaminar characteristics are affected by both chemicals (Karbhari and Ghosh, 2009).

A major concern for the construction engineer using polymer-based composites is their vulnerability against fire, since resins are organic materials mainly composed of carbon and hydrogen, both highly flammable. However, the most important health hazard derived from polymer and composites in a fire accident is generated from the toxic combustion products produced during burning of materials. In order to reduce the fire hazards in FRP, it is recommended (Hollaway, 2010) to provide thermal protection for structures on site (Ludovico et al., 2012); to introduce flame retardant (halogen based) additives into resin formulations; or to apply a protective intumescent coating on the surface of the manufactured composite (Keller et al., 2006).

Finally, natural exposure of FRPs generally has the following effects: (1) a reduction in mechanical properties of FRP caused by plasticization of the matrix resin by atmospheric water uptake; (2) severe degradation of the surface in the resin-rich areas, mainly attributed to UV exposure, which creates cracks and provide an easy path for ingress of moisture, which can, in turn, cause degradation of the fibers; (3) possible slight increases in T_g of the matrix resin, due to postcure. Comparison of properties measured on samples naturally weathered with those measured after (possibly more severe) laboratory exposures, generally indicates that levels and rates of degradation of outdoor exposed samples are significantly lower than those recorded for specimens exposed to simulated environments (Jia et al., 2005). In addition, outdoor exposure tests have demonstrated that deterioration of the bond between FRP and concrete substrate is usually marginal.

7.5 Standard tests, traditional and alternative methods of assessing durability of fiber reinforced polymer

Due to the lack of specifically designed standards for polymers used in civil engineering applications, many of the experiments on durability aspects are conducted according to standard procedures which are not appropriate for the particular systems. Although standards referring to FRP based on hot-cured thermosetting adhesives and matrices employed in many areas (aeronautical, aerospace, automotive, etc.) can be useful, they are not directly applicable to FRP materials employed for strengthening and upgrading concrete structures for the reasons previously illustrated.

As an example, the standard code frequently employed for water absorption tests (ASTM D 570) recommends a conditioning procedure, able to assure the complete dryness to samples before their immersion in water, in which each sample is dried in vacuum oven for 24 h at 50°C and then cooled in a desiccator. The described

conditioning procedure performed on cold-cured resins, which are not fully cross-linked, can be regarded as a thermal treatment (possibly postcure) that can influence the properties of the resins (Frigione and Lettieri, 2008), i.e., the behavior upon immersion will be assessed on a system different from that employed on field. Thus, to overcome this inconvenience, a new procedure to completely dry the specimens of FRP, based on cold-curing resins, before the water-immersion tests has been proposed and successfully experimented in different studies (Frigione and Lettieri, 2008; Sciolti et al., 2010; Sciolti et al., 2012).

As illustrated in the previous example, there is an urgent need to develop durability standards and guidelines pertinent to these specific applications and exposure conditions.

Another issue relates to the applicability of durability studies carried out in laboratory to the true (on field) behavior of the materials.

Current knowledge concerning the long-term performance of FRP's used for external reinforcement of concrete exposed to different environments is mainly based on laboratory investigations aimed at assessing the effect of any single environmental agent on the FRP. It is performed for a very limited duration, generally not exceeding two years, while reliable durability studies would require periods of natural exposure longer than 2 years. In the field monitoring, on the other hand, the combined effects of environmental factors and the variability of conditions often result in different rates, and mechanisms, of degradation with respect to laboratory experiments. This makes it difficult, therefore, to obtain good correlations with controlled laboratory exposures. In addition, as illustrated so far, one of the strengths of FRP's is that there are a multitude of variables that can be modified in order to achieve on-demand material properties. Thus, considering the enormous number of different composites that can be manufactured and applied (type of matrices and fibers, presence of surface finishes or coatings, curing and processing conditions, technology of application) and the wide variability of climatic conditions that can be encountered during natural weathering, field exposure is too expensive and time consuming to be considered the only reliable method to estimate the durability of composite materials.

Accelerated laboratory tests are, then, continuously under investigation in order to assess if they can be regarded as a meaningful and effective method in replicating the real environmental conditions, able to predict the long-term behavior of the materials subjected to weathering.

In standardized accelerated procedures, one or more weather-like conditions are intensified to levels greater than those occurring naturally. For example, one of the frequently applied methods to accelerate the effect of exposition to water is immersion in boiling water. Another possible method is to employ significantly increased levels of radiation and temperature for testing under simulated conditions in weathering cabinets. None of these standards, moreover, imposes rigid conditions on how an accelerated test should be performed, which is basically left to the experimenter, despite some guidelines for choosing the test parameters. These procedures, whilst reducing test time, may give unrealistic failure modes which may not take place under true service conditions (Zhou et al., 2011; Eldridge and Fam, 2014). Furthermore, a rationale prediction through accelerated procedures must include, for each specific material (matrix/resin, fiber, configuration of plies, etc.), a precise

correlation between the results obtained under natural and under artificial weathering conditions. This would require, in turn, a huge number of carefully selected procedures based on both natural and artificial exposures.

Starting from the matrix/adhesive resins, the few studies performed on cold-cured resins demonstrated that substantially poor correlations exist between the results found for accelerated tests and those obtained from on field exposure (Lettieri and Frigione, 2011). In particular, more severe effects were produced by an accelerated aging, attributed to the improved influence of any single environmental agent amplified for the purpose: a higher amount of water absorbed, which was able to produce the plasticization of the resins; a high temperature of exposure, which caused a more rapid post-cure of the resin; thermo-oxidative processes; and the erasure of “physical aging” in the resins (a well-known process taking place in cold-cured resins that are in an unstable thermodynamic state due to their incomplete cure at ambient temperature). Furthermore, the condition levels remained constant during the accelerated weathering treatment and were, therefore, more harsh and not even able to reproduce the fluctuations of external agents.

Similar uncertainty on the soundness and effectiveness of accelerated weathering tests can be extended to the prevision of durability for composites employed to strengthen a concrete structure outdoor located (Wu and Yan, 2013). Whether FRP's are formed in situ through wet layup technique, using a cold-cured matrix/adhesive, or applied as precured laminates using a cold-cured adhesive, the unpredictable behavior of the cold-cured resin will affect the durability in service of the FRP. Accelerated weathering procedures, as well as Time-temperature superposition principle, employ values of temperature possibly able to postcure the resin and must be, therefore, avoided as possible. As an example, it has been established that aging of GFRP in seawater at 50°C is 12 times as severe as that in seawater at 23°C without any real evidence for the accuracy of this rule (Silva, 2007).

In conclusion, at the present time the field monitoring of properties of FRP and its components still seems to be the only reliable and realistic method to assess the durability of the composite employed for concrete strengthening technique and the accelerated procedures can only supply qualitative indications, i.e., reference limit values never achievable in true service conditions.

7.6 Recommendations for further research and future trends

It is expected that the already well-esteemed FRP strengthening techniques will increasingly continue to be the preferred choice for many rehabilitation and repair projects involving buildings, bridges, historic monuments, and other aged concrete structures; when their demolition and reconstruction is restricted by sustainability and economic considerations. Therefore, one of the main challenges of the researchers in this area for the forthcoming years is to determine a more complete understanding of the degradation process taking place in FRP-concrete structural elements in different environments, collecting and organizing rationally the

numerous available studies in order to accomplish an adequate reliability of the proposed solutions, i.e., comparable to that achieved in aeronautical and aerospace industries.

The development of proper codes and standards is strongly suggested, including considerations for safety, short-term development of properties (it has been underlined, for instance, the essential lack of information concerning the adhesion strength developed between FRP and the substrate during the curing of the matrix/adhesive resin in dependence of the curing conditions, i.e., temperature and time), long-term performance and durability. As already pointed out, experiments are often conducted according to standard procedures that are not appropriate for these particular systems. Another challenge is the development of suitable predictive models able to supply reliable previsions for the service life of composites or bonded structures. The poor suitability of accelerated aging tests in replicating the real environmental conditions has been mentioned. In addition, there is a urgent need to transfer the results of research from laboratory to the market.

In terms of implementing materials, the development of improved cold-cured resins is compulsory. The adhesives/matrices for FRP employed in concrete structures must set and harden in different environmental conditions, possibly at very low temperatures, and perform, even after short curing times, at a sufficient level irrespective to the exposure regimes. To this regard, the use of nano-structured polymers, such as nano-composites, based on preformed nano-sized inorganic (silica, clay, carbon nanotubes) particles dispersed into the resin, or organic–inorganic hybrid materials, is expected to become a realistic alternative to traditional polymeric products due to their superior properties—especially in terms of higher durability against moisture, temperatures, harsh environments, fire. The formulation strategy of these systems must be aimed at increasing T_g and the elastic modulus in the rubbery region of the resin, as well as at improving their performances under different environmental regimes. At the present time, the development processes of such nano-structured polymers are still complicated and expensive to be conveniently applied in the construction industry. And, in fact, none of the mentioned systems are commercially available at the present time.

In conclusion, the efforts of academic and industrial research in this field must be mainly devoted to the development of more durable thermosetting matrix/adhesive resins at affordable costs, also able to achieve a stable thermodynamic state after short curing times; an improvement in the long-term performance of FRP's and a reliable assessment of their service life; a standardization of procedures and tests.

References

- ACI 440.2R-08, 2008. *Guide for the Design and Construction of Externally Bonded FRP Systems for Strengthening Concrete Structures*. American Concrete Institute, Farmington Hills, MI.
- Abanilla, M.A., Karbhari, V.M., Li, Y., 2006. Interlaminar and intralaminar durability characterization of wet layup carbon/epoxy used in external strengthening. *Composites, Part B*. 37, 650–661.

- Abanilla, M.A., Li, Y., Karbhari, V.M., 2006. Durability characterization of wet lay-up graphite/epoxy composites used in external strengthening. *Composites, Part B*. 37, 200–212.
- Aiello, M.A., Frigione, M., Acierno, D., 2002. Effects of environmental conditions on performance of polymeric adhesives for restoration of concrete structures. *ASCE J. Mater. Civil Eng.* 14, 185–189.
- Almusallam, T., Al-Salloum, Y., 2006. Durability of GFRP Rebars in concrete beams under sustained loads at severe environments. *J. Compos. Mater.* 40, 623–637.
- Bakis, C.E., Bank, L.C., Brown, W.L., Cosenza, E., Davalos, J.F., Lesko, J.J., et al., 2002. Fiber-reinforced polymer composites for construction-state-of-the-art review. *J. Compos. Constr.* 6, 73–87.
- Banea, M.D., de Sousa, F.S.M., da Silva, L.F.M., Campilho, R.D.S.G., de Bastos Pereira, A. M., 2011. Effects of temperature and loading rate on the mechanical properties of a high temperature epoxy adhesive. *J. Adhes. Sci. Technol.* 25, 2461–2474.
- Bao, L.-R., Yee, A.F., 2002. Effect of temperature on moisture absorption in a bismaleimide resin and its carbon fiber composites. *Polymer*. 43, 3987–3997.
- Benmokrane, B., Wang, P., Ton-That, T., Rahman, H., Robert, J., 2002. Durability of glass fibre reinforced polymer reinforcing bars in concrete environment. *J. Compos. Constr.* 6, 143–153.
- Bisby, L.A., Green, M.F., 2002. Resistance to freezing and thawing of fiber-reinforced polymer-concrete bond. *ACI Struct. J.* 99, 215–223.
- Blackburn, B.P., Tatar, J., Douglas, E.P., Hamilton, H.R., 2015. Effects of hygrothermal conditioning on epoxy adhesives used in FRP composites. *Constr. Build. Mater.* 96, 679–689.
- Cabral-Fonseca, S., Nunes, J.P., Rodrigues, M.P., Eusébio, M.I., 2009. Durability of epoxy adhesives used to bond CFRP laminates to concrete structures. *Proceedings of the 17th International Conference on Composite Materials (ICCM 17) U.K.*
- Carbas, R.J.C., da Silva, L.F.M., Marques, E.A.S., Lopes, A.M., 2013. Effect of post-cure on the glass transition temperature and mechanical properties of epoxy adhesives. *J. Adhes. Sci. Technol.* 27, 2542–2557.
- CNR-DT_200/2004, 2004. English, Guide for the design and construction of externally bonded FRP systems for strengthening existing structures.
- Cromwell, J.R., Harries, K.A., Shahrooz, B.M., 2011. Environmental durability of externally bonded FRP materials intended for repair of concrete structures. *Constr. Build. Mater.* 25, 2528–2539.
- Dai, J.-G., Yokota, H., Iwanami, M., Kato, E., 2010. Experimental investigation of the influence of moisture on the bond behavior of Fibre Reinforced Polymer (FRP) to concrete interfaces. *ASCE J. Compos. Constr.* 14, 834–844.
- Di Ludovico, M., Piscitelli, F., Prota, A., Lavorgna, M., Mensitieri, G., Manfredi, G., 2012. Improved mechanical properties of CFRP laminates at elevated temperatures and freeze-thaw cycling. *Constr. Build. Mater.* 31, 273–283.
- Eldridge, A., Fam, A., 2014. Environmental aging effect on tensile properties of GFRP made of furfuryl alcohol bioresin compared to epoxy. *J. Compos. Constr.* 18 (5), 1–10, 04014010. DOI:10.1061/(ASCE)CC.1943-5614.0000467.
- Fédération International du Béton (fib) Bulletin No. 14. 2001. Externally bonded FRP reinforcement for RC structures, p. 138; ISBN 2-88394-054-1.
- Fédération International du Béton (fib) Bulletin No. 35. 2006. Retrofitting of concrete structures by externally bonded FRPs, with emphasis on seismic applications, pp. 220, ISBN 978-2-88394-075-8.

- Frigione, M., Naddeo, C., Acierno, D., 2000. Epoxy resins employed in civil engineering applications: effects of exposure to mild temperatures. *Mater. Eng.* 11, 59–80.
- Frigione, M., Naddeo, C., Acierno, D., 2001. Cold-curing epoxy resins: aging and environmental effects. I - thermal properties. *J. Polym. Eng.* 21, 23–51.
- Frigione, M., Aiello, M.A., Naddeo, C., 2006. Water effects on the bond strength of concrete/concrete adhesive joints. *Constr. Build. Mater.* 20, 957–970.
- Frigione, M., Lettieri, M., Mecchi, A.M., 2006. Environmental effects on epoxy adhesives employed for restoration of historical buildings. *ASCE J. Mater. Civil Eng.* 18, 715–722.
- Frigione, M., Lettieri, M., 2008. Procedures conditioning the absorption/desorption behavior of cold-cured epoxy resins. *J. Polym. Sci. Part B: Polym. Phys.* 46, 1320–1336.
- Ghiassi, B., Marcari, G., Oliveira, D., Lourenço, P., 2013. Water degrading effects on the bond behavior in FRP-strengthened masonry. *Compos. Part B: Eng.* 54, 11–19.
- Grace, N.F., Grace, M., 2005. 3rd International Conference Composites in Constructions, CCC, Lyon, France, pp. 391–396.
- Gullapalli, A., Lee, J., Lopez, M.M., Bakis, C.E., 2009. Sustained loading and temperature response of fiber-reinforced polymer-concrete bond. *Transp. Res. Rec.* 2131, 155–162.
- Hollaway, L.C., 2010. A review of the present and future utilization of FRP composites in the civil infrastructure with reference to their important in-service properties. *Constr. Build. Mater.* 24, 2419–2445.
- ISIS Design Manual No. 4, 2001. Strengthening Reinforced Concrete Structures with Externally—Bonded Fibre Reinforced Polymers (FRPs), ISIS Canada.
- Jeong, Y., Lopez, M.M., Bakis, C.E., 2016. Effects of temperature and sustained loading on the mechanical response of CFRP bonded to concrete. *Constr. Build. Mater.* 124, 442–452.
- Jia, J., Boothby, T.E., Bakis, C.E., Brown, T.L., 2005. Durability evaluation of glass fiber reinforced-polymer-concrete bonded interfaces. *J. Compos. Constr.* 9, 348–359.
- JSCE, 2001. Recommendation for upgrading of concrete structures with use of continuous fiber sheets. Concrete Engineering Series 41, Japan Society of Civil Engineers, Tokyo, Japan.
- Karbhari, V.M., 2002. Durability of FRP composites for civil infrastructure—Myth, mystery or reality. In: Shenoi, R.A., Moy, S.S., Hollaway, L.C. (Eds.), *Proc., 1st Int. Conf. of Advanced Polymer Composites for Structural Applications in Construction*, Southampton Univ., Thomas Telford, U.K., pp. 33–43.
- Karbhari, V.M., 2007. *Durability of Composites for Civil Structural Applications*. Woodland, Cambridge, England.
- Karbhari, V.M., Engineer, M., Eckel II, D.A., 1997. On the durability of composite rehabilitation schemes for concrete: use of a peel test. *J. Mater. Sci.* 32, 147–156.
- Karbhari, V.M., Ghosh, K., 2009. Comparative durability evaluation of ambient temperature cured externally bonded CFRP and GFRP composite system for repair of bridges. *Compos. Part A: Appl. Sci. Manuf.* 40, 1353–1363.
- Karbhari, V.M., Navada, R., 2008. Investigation of durability and surface preparation associated defect criticality of composites bonded to concrete. *Compos. Part A: Appl. Sci. Manuf.* 39, 997–1006.
- Karbhari, V.M., Riviera, J., Zhang, S., 2002. Low-temperature hygrothermal degradation of ambient cured E-glass/vinylester composites. *J. Appl. Polym. Sci.* 86, 2255–2260.
- Karbhari, V.M., Zhao, L., 1998. Issues related to composite plating and environmental exposure effects on composite-concrete interface in external strengthening. *Compos. Struct.* 40, 293–304.

- Keller, T., Tracy, C., Hüge, E., 2006. Fire endurance of loaded and liquid-cooled GFRP slabs for construction. *Compos. Part A: Appl. Sci. Manuf.* 37, 1055–1067.
- Kolluru, V.S., Mohamad, A.A., Michel, G., 2008. Freeze-thaw degradation of FRP–concrete interface: impact on cohesive fracture response. *Eng. Fract. Mech.* 75, 3924–3940.
- Larsson, F., 1986. The effect of ultraviolet light on mechanical properties of Kevlar 49 composites. *J. Reinf. Plast. Compos.* 5, 19–22.
- Lees, J.M., Toumpanaki, E., Barbezat, M., Terrasi, G.P., 2017. Mechanical/durability screening test methods for cylindrical CFRP prestressing tendons. *J. Compos. Constr.* 21 (2), DOI:10.1061/(ASCE)CC.1943-5614.0000727.
- Leone, M., Stijn, M., Aiello, M.A., 2009. Effect of elevated service temperature on bond between FRP EBR systems and concrete. *Compos. Part B: Eng.* 40, 85–93.
- Lettieri, M., Frigione, M., 2011. Natural and artificial weathering effects on cold-cured epoxy resins. *J. Appl. Polym. Sci.* 119, 1635–1645.
- Lettieri, M., Frigione, M., 2012. Effects of humid environment on thermal and mechanical properties of a cold-curing structural epoxy adhesive. *Constr. Build. Mater.* 30, 753–760.
- Lin, Y., Chen, X., 2005. Moisture sorption—desorption—resorption characteristics and its effect on the mechanical behavior of the epoxy system. *Polymer*. 46, 11994–12003.
- Maljaee, H., Ghiassi, B., Lourenço, P.B., 2017. Effect of synergistic environmental conditions on thermal properties of a cold curing epoxy resin. *Compos. Part B: Eng.* 113, 152–163.
- Mays, G.C., Hutchinson, A.R., 1992. *Adhesives in Civil Engineering*. Cambridge University Press, Cambridge, U.K.
- Mascia, L., Allavena, A., *Reinforced Plastics Congress Brighton, U.K.*, pp. 175–182 (1976).
- Mirmiran, A., Shahawy, M., 1997. Behavior of concrete columns by fiber composites. *ASCE J. Struct. Eng.* 123, 583–590.
- Moussa, O., Vassilopoulos, A.P., Keller, T., 2012. Effects of low-temperature curing on physical behavior of cold-curing epoxy adhesives in bridge construction. *Int. J. Adhes. Adhes.* 32, 15–22.
- Moussa, O., Vassilopoulos, A.P., de Castro, J., Keller, T., 2012. Early-age tensile properties of structural epoxy adhesives subjected to low-temperature curing. *Int. J. Adhes. Adhes.* 35, 9–16.
- Murphy, K., Zhang, S., Karbhari, V.M., 1999. Effect of concrete based alkaline solutions on short term response of composites. In: Cohen, L.J., Bauer, J.L., Davis, W.E., (Eds.), *Proc., 44th Int. SAMPE Symposium and Exhibition, Society for the Advancement of Material and Process Engineering, Long Beach, California*, pp. 2222–2230.
- Norris, T., Saadatmanesh, H., Ehsani, M.R., 1997. Shear and flexural strengthening of R/C beams with carbon fiber sheets. *ASCE J. Struct. Eng.* 123, 903–911.
- Rinaldi, G., Maura, G., 1993. Durable glass-epoxy composites cured at low temperatures—effects of thermal cycling, UV irradiation and wet environment. *Polym. Int.* 31, 339–345.
- Saadatmanesh, H., Tavakkolizade, M., Mostofinejad, D., 2010. Environmental effects on mechanical properties of wet lay-up fiber-reinforced polymer. *ACI Mater. J.* 107, 267–274.
- Savvilitidou, M., Vassilopoulos, A.P., Frigione, M., Keller, T., 2017a. Effects of aging in dry environment on physical and mechanical properties of a cold-curing structural epoxy adhesive for bridge construction. *Constr. Build. Mater.* 140, 552–561.
- Savvilitidou, M., Vassilopoulos, A.P., Frigione, M., Keller, T., 2017b. Development of physical and mechanical properties of a cold-curing structural adhesive in a wet bridge environment. *Constr. Build. Mater.* 144, 115–124.

- Sciolti, M.S., Frigione, M., Aiello, M.A., 2010. Wet lay-up manufactured FRP's for concrete and masonry repair. Influence of water on the properties of composites and of their epoxy components. *ASCE J. Compos. Constr.* 14, 823–833.
- Sciolti, M.S., Aiello, M.A., Frigione, M., 2012. Influence of water on bond behavior between CFRP sheet and natural calcareous stones. *Compos. Part B: Eng.* 43, 3239–3250.
- Sciolti, M.S., Aiello, M.A., Frigione, M., 2015. Effect of thermo-hygro-metric exposure on FRP, natural stone and their adhesive interface. *Compos. Part B: Eng.* 80, 162–176.
- Shin, H.-C., Miyauchi, H., Tanaka, K., 2011. An experimental study of fatigue resistance in epoxy injection for cracked mortar and concrete considering the temperature effect. *Constr. Build. Mater.* 25, 1316–1324.
- Silva, M.A.G., 2007. Aging of GFRP laminates and confinement of concrete columns. *Compos. Struct.* 79, 97–106.
- Silva, P., Fernandes, P., Sena-Cruz, J., Xavier, J., Castro, F., Soares, D., et al., 2016. Effects of different environmental conditions on the mechanical characteristics of a structural epoxy. *Compos. Part B.* 88, 55–63.
- Stewart, I., Chambers, A., Gordon, T., 2007. The cohesive mechanical properties of a toughened epoxy adhesive as a function of cure level. *Int. J. Adhes. Adhes.* 27, 277–287.
- Tatar, J., Hamilton, H.R., 2016. Bond durability factor for externally bonded CFRP systems in concrete structures. *J. Compos. Constr.* 20 (1), <[http://dx.doi.org/10.1061/\(ASCE\)CC.1943-5614.0000587](http://dx.doi.org/10.1061/(ASCE)CC.1943-5614.0000587)>.
- Tomosawa, F., Nakatsuji, T., Kimura, K., Saka, K., Kawaguchi, H., 1998. Evaluation of the ACM reinforcement durability by exposure test. New York, N.Y.: American Society of Mechanical Engineers, Proceedings of 17th International Conference on Offshore Mechanics and Arctic Engineering, Lisbon, Portugal, p. 4361.
- TR55, 2004. Design guidance for Strengthening Concrete Structures Using Fibre Composite Materials. The Concrete Society, UK.
- Yang, Q., Xian, G., Karbhari, V.M., 2008. Hygrothermal ageing of an epoxy adhesive used in FRP strengthening of concrete. *J. Appl. Polym. Sci.* 107, 2607–2617.
- Yun, Y.C., Wu, Y.F., 2011. Durability of CFRP-concrete joints under freeze-thaw cycling. *Cold Reg. Sci. Technol.* 65, 401–412.
- Wan, B., Petrou, M.F., Harries, K.A., 2006. The effects of the presence of water on the durability of bond between CFRP and concrete. *J. Reinf. Plast. Compos.* 25, 875–890.
- Wolff, L., Hailu, K., Raupach, M., Mechanisms of blistering of coatings on concrete. International Symposium Polymers in Concrete, Portugal, 2006.
- Wu, H.-C., Yan, A., 2013. Durability simulation of FRP bridge decks subject to weathering. *Compos. Part B: Eng.* 51, 162–168.
- Wypych, G., 1995. Handbook of Material Weathering. ChemTec Publishing, Toronto, Canada.
- Zhang, Y., Adams, R.D., da Silva, L.F.M., 2014. Absorption and glass transition temperature of adhesives exposed to water and toluene. *Int. J. Adhes. Adhes.* 50, 85–92.
- Zhou, J., Chen, X., Chen, S., 2011. Durability and service life prediction of GFRP bars embedded in concrete under acid environment. *Nucl. Eng. Des.* 241, 4095–4102.

Further Reading

- Kahraman, R., Al-Harathi, M., 2005. Moisture diffusion into aluminum powder-filled epoxy adhesive in sodium chloride solutions. *Int. J. Adhes. Adhes.* 25, 337–341.

Field assessment of concrete structures rehabilitated with FRP

8

*Nur Yazdani**, *Eric Chavez Garcia* and *Mina Riad*
University of Texas at Arlington, Arlington, TX, United States

8.1 Introduction

Repair and rehabilitation methods for civil infrastructure have become a topic of great interest to engineers. Fiber Reinforced Polymer (FRP) is considered one of the most popular and practical solutions for strengthening and retrofitting civil infrastructure. Several past studies indicated that significant increase in strength and stiffness can be achieved by using this technology. The FRP–concrete interface bond is critical in transferring stresses from the concrete substrate to the FRP. However, the evaluation of the bond strength is still a challenging issue.

8.2 Types and benefits of fiber reinforced polymer rehabilitation systems for concrete structures

The two dominant materials for infrastructure construction today continue to be steel and concrete. While they maintain their relative importance in infrastructure, there has been an increasing need for advanced techniques, especially for the rehabilitation of aging infrastructure. FRP has emerged as a potential strengthening agent for deteriorating and/or under-designed concrete infrastructures. FRP is a composite material made of a polymer matrix reinforced with fibers. The fibers are usually glass, carbon, or basalt. There are two main types of FRP rehabilitation methods: embedded FRP rebars and externally applied FRP laminates. Examples of retrofitted structures using FRP laminates are shown in [Fig. 8.1](#).

Embedded FRP rebars are highly corrosion-resistant and, unlike steel, will not rust when exposed to harsh weather and chemicals. They are also nonconductive, impact resistant, and have higher strength than steel. Externally-applied FRP laminates are being effectively used for their high strength to weight ratio, fast and easy application, confinement of concrete elements, very small thickness and excellent corrosion resistance. They can be used whenever there is a change in use of the structure, construction defect, code change, seismic retrofit, or deterioration of an existing structure.

* Profile: <http://www.uta.edu/faculty/yazdani/>

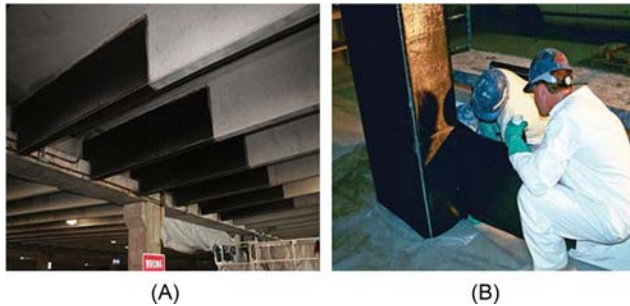


Figure 8.1 (A) fiber reinforced polymer (FRP) laminate applied to exterior of bridge beam; (B) FRP laminate applied to typical canopy column (Alkhrdaji, 2015).

Source: Reprinted with permission, STRUCTURE magazine, June 2015.

FRP composite materials can acquire higher strength and stiffness characteristics with the use of less material to achieve a similar performance to other available techniques, thus resulting in less resource use and waste production. FRP is also a lightweight composite that can lower construction costs and increase the speed of construction, resulting in minimal environmental impacts (Lee and Jain, 2009). FRP provides many benefits, with the most promising being the development of structural systems with greater service lives exceeding that of traditional materials due to its physical characteristics. Subsequently, the promise of FRP composites is to extend service life of existing structures while protecting new structures from ageing, weathering, and degradation in severe environments. The durability for FRP composites in harsh and changing environments, however, has not yet been fully understood. The critical factor is the quantification of material durability in comparison to conventional materials. This will provide designers with the knowledge to select the best material for achieving a sustainable environment. While some advantages are well known for the FRP composites, challenges in developing and implementing the technology still exist. In addition to durability, new developments are needed to minimize costs of production and environmental impacts. The implementation in codes and standards are needed to bring this product to the market and include safety, performance, and sustainability. Equally important is the education of designers and architects is a paramount component for the use of composites in a built environment (Lee and Jain, 2009).

8.2.1 Rehabilitation with embedded fiber reinforced polymer rebars

Steel rebar in reinforced concrete has one underlying weakness; susceptibility to corrosion (oxidation) when exposed to salts, chemicals, or moisture. As the steel corrodes the concrete begins to crack and spall due to the swelling and increase of the tensile load on the rebar. This, in turn, creates openings that lead to faster deterioration of the concrete that can be mitigated with embedded FRP rebars in

concrete structures. First and foremost, composite rebar will not corrode, meaning it is ideal for periodic and long-term immersion in fresh water for applications such as retaining walls, piers, decks, and canals. It is also resistant to road salt and other chemicals, making it more durable while providing less maintenance for structures such as roadways and bridges. Another advantage is that the tensile strength of FRP rebar is typically 1.5–2 times higher than steel. This provides a good counterbalance to concrete's high compressive strength. Although the initial cost of composite rebar is generally higher than standard steel rebar and is roughly comparable to epoxy-coated steel rebar, when considered on a lifecycle cost (LCC) basis, it can be quite economical (Malnati, 2011). In contrast to steel, however, there is yet no standardization for the surface characteristics of FRP bars. Therefore, determining the bond characteristics of nonstandardized commercial rebars is a fundamental requirement for their practical use, as this influences the mechanism of load transfer between reinforcement and concrete.

8.2.2 Rehabilitation with external fiber reinforced polymer fabric wrapping

External application of FRP (also known as FRP wrapping) is a technique whereby FRP fabric is saturated in a polymeric epoxy and the fabric is applied to the desired surface of a structure. This wrapping technique is known as the wet layup or prefabricated systems using cold-cured adhesive bonding, and is the most widely-used method due to its fast and easy application without a significant change in the dimensions of the original structure. The main and important feature of this technique is that the fibers of externally-bonded FRP composites are in parallel, as practicable with the direction of principle tensile stresses. The basic technique of the FRP-strengthening described refers to the manual application of FRP reinforcement to an existing member. A two-part cold-cured bonding agent is used to achieve bonding (Setunge, 2002). One of the keys to assuring proper bonding comes in the surface preparation of the structure. Because FRP relies heavily on the bond between the FRP system and the existing concrete, any existing deterioration and corrosion of the internal reinforcing must be taken care of prior to installation. Strengthening can only be applied after all such problems have been determined and resolved using appropriate procedures (Alkhrdaji, 2015).

8.3 Destructive field assessment

One of the main drawbacks to using FRP rehabilitation is the cost. Because of this aspect, it is important to properly evaluate the structure and assess which tests are most suitable for the given conditions. Destructive field assessments give the inspector the ability to determine the areas of deficiency by testing the FRP conditions in situ. Due to the nature of the tests, careful analysis must be completed in order to ensure the test is suitable and will give useful results to the engineers.

This section will talk about some of the major destructive tests performed on FRP enhanced structures.

8.3.1 ASTM pull-off test

American Society of Testing and Materials (ASTM) FRP pull-off testing determines the greatest tension force (applied perpendicular to the surface) that the FRP–epoxy–concrete bond can resist. The method consists of adhesively bonding a metallic circular loading fixture (dolly) normal to the testing surface (Fig. 8.2). The instruments and materials needed consist of: the pull-off tester, loading fixtures (dollies), epoxy to attach the dollies to the surface, and a core drill or circular hole cutter. The circular hole cutter is used to isolate the area being tested from the rest of the surface. This hole must be the same diameter as the loading fixture, commonly taken as 50 mm for concrete elements. The dolly contains a threaded hole in the center that allows for attachment of the fixed-alignment adhesion testing device (pull-off tester shown in Fig. 8.3). After attaching the tester, a tension force is applied gradually to the dolly until a partial or full detachment of the dolly is witnessed. This load at the time of rupture is regarded as the maximum bond force (ASTM, 2009). The observed modes of failure can shed light on the condition of the epoxy–FRP–concrete interface, the long-term performance, and the quality of

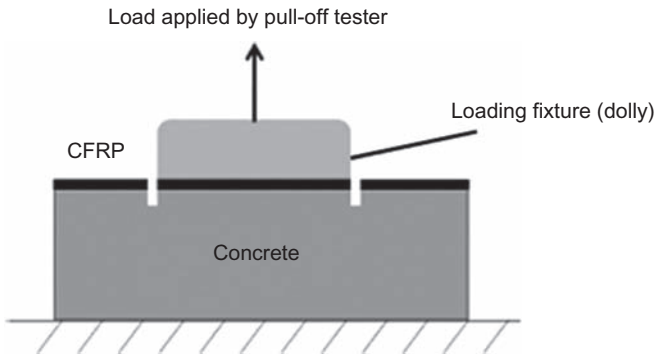


Figure 8.2 Pull-off test mechanisms (Pallempati et al., 2016).



Figure 8.3 ASTM pull-off testing apparatus: (A) testing dollies (B) pull-off adhesion tester (Pallempati et al., 2016).

the initial FRP installation. The ASTM pull-off test method has the following advantages: quick and economic, on-site testing with only minimal damage to the FRP, and immediate test results. A field assessment of the FRP-strengthening and the evaluation of the long-term behavior of FRP is helpful in better understanding of FRP as a concrete strengthening material. The ASTM pull-off test results are used to evaluate the performance of FRP as a strengthening material (Pallempati et al., 2016).

8.3.2 Differential scanning calorimetry

FRP materials are combustible and susceptible to deterioration of mechanical and bond properties at elevated temperatures. Therefore, the concrete members strengthened with FRP must be evaluated in the case of a fire before the system can be used with confidence in buildings. The overall goal of the calorimetric study is to elucidate the high temperature performance of specific FRP systems currently in use, in such a way that fire recommendations can be made with confidence and regarding the conservative fire design of a structure (Foster and Bisby, 2005). The Differential Scanning Calorimetry (DSC) test is used to determine the glass transition temperature (GTT, T_g) of the polymer matrix used. This value allows for the evaluation of the behavior of FRP at elevated temperatures. At elevated temperatures, externally-bonded FRP materials can be expected to display severe reduction in strength, stiffness, and bond properties. This is most likely due to reductions in mechanical properties of the polymer matrix at the given temperatures, which leads to a reduction in the bonding stress between the fibers. Consequently, for unidirectional composites, the major properties of the matrix such as shear strength and bond strength are expected to be affected by the rise in temperature. DSC studies were conducted according to ASTM D3418 (ASTM, 2003) using a TA Instruments DSC Q100 differential scanning calorimeter (Foster and Bisby, 2005).

8.3.3 Witness panel test

Witness panel tests, also known as coupon tests, are used to evaluate tensile strength and modulus, lap splice strength, hardness, and GTT of the FRP system (ACI, 2008). These panels are flat and fabricated on site using the installation process similar to those used for the typical FRP system. Once cured, the panels are sent to a laboratory where they undergo testing. For small projects, it is common to select one panel for each new roll of material for each new batch of epoxy, or one per day. Randomly selected material (around 15%) is sent to the laboratory for testing. For large projects, one panel for each new roll of material or for each new batch of epoxy or three per area are selected. Randomly selected material (around 10%) is to be sent for testing (Chen et al., 2009). Once the specimen has been properly prepared, aligned, measured, gripped and tested, the witness panel test follows the ASTM 2008 standard and provides the true tensile properties of the FRP, such as modulus, rupture strain, and rupture strength. Because the FRP composites are linear elastic brittle, meaning there is no strain hardening, the failure occurs when

the fiber reaches the rupture strain. Reasons for failure occurring prior to the strain reaching the rupture strain point could be due to the existence of bending or local stress concentration, arising from factors such as misalignment and improper gripping. It is because of this reasoning that the rupture strain obtained from the witness panel represents the lower bound of the actual rupture strain if no flaws exist in the procedure (Chen et al., 2009).

8.4 Nondestructive assessment

The reliability of nondestructive testing (NDT) techniques to detect and assess defects in FRP-rehabilitated concrete structures is highly dependent upon their ability to detect critical defect types and on the practicality of the method. Whereas some methods require very little equipment that could lead to the defect size, depth, and type being questionable, other methods are extremely powerful but have requirements such as power supply, experience, and ample space which are impractical in the field. The following sections discuss different types of applicable NDT techniques along with the advantages and disadvantages.

8.4.1 Visual inspection

Visual inspection is used in all fields of construction, making it the most versatile and simple technique. In this technique, personnel use their own judgment to determine whether a procedure was followed correctly (Karbhari et al., 2005). Visual inspection can be categorized in two ways: either by overall visual appearance or by inspection for localized visual defects. These defects can be in the form of chips, cracks, delamination, burns, or even fractures. The Standard Practice for Classifying Visual Defects in Glass Reinforced Plastic Laminate Parts (ASTM D 2563, 2015) provides the specifier with an important resource for managing the quality of corrosion-resistant FRP. It is the specifier's responsibility to assure that the requirements of the specifications are realistic—from both the technical and the economic points of view (Reichhold, 2009). Advantages to visual inspection include instantaneous data results, economy, and low equipment cost. Disadvantages include the limitation of the human eye, mistakes made by human misinterpretation, and inspection only of the structure's surface. Anything as simple as illumination can provide a major restriction for the NDT method, thus make it a cheap yet unreliable method.

8.4.2 Mechanical and acoustic vibration

One of the most common types of mechanical vibration evaluation is the tap test. Tap testing is an NDE practice used on bridge decks that is fast, low cost and effective for inspecting composites. To perform the test, an inspector taps the surface of the area of interest with a coin or hammer and then listens for any distinctive change in frequency which marks where a void or delamination exists (Fig. 8.4). A clear, sharp ringing indicates a well bonded structure, whereas a dull sound

indicates a delamination or void (Groenier et al., 2006). Although the tap test is basic, changes within the structure can also produce a distinctive change in frequency; therefore, the inspector must be familiar with the features of the structure. Tap testing is fast, low cost, and provides an effective way to inspect composites for delamination. Drawbacks to this test include the presence of ambient noise which could result in the erroneous interpretation of the defects.

8.4.3 Acoustic emission

Acoustic Emission (AE) is defined as the transient elastic wave generated by a sudden redistribution of stress from a localized source or sources within a material (Degala et al., 2008). When a structure is subjected to an external stimulus, the elastic energy propagates as a stress wave (AE event) in the structure and is detected by one or more AE sensors. AE events may be generated by moving dislocations, crack onset, growth and propagation, fiber breaks, disbonds, and plastic deformation, among others. This detection can serve as a valuable tool as it pertains to the origin of the discontinuity of a material. Fig. 8.5 displays the basic test set up for the AE test. Due to the versatility of the test, AE differs from other NDT methods

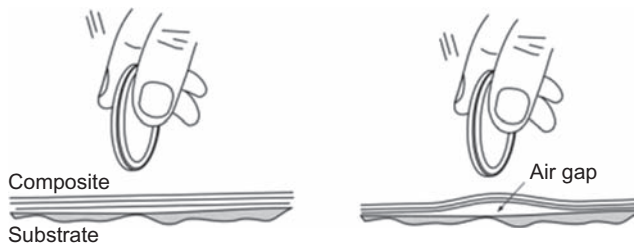


Figure 8.4 Coin tap test demonstration (Karbhari et al., 2005).
Source: Image courtesy of the Oregon Dept. of Transportation.

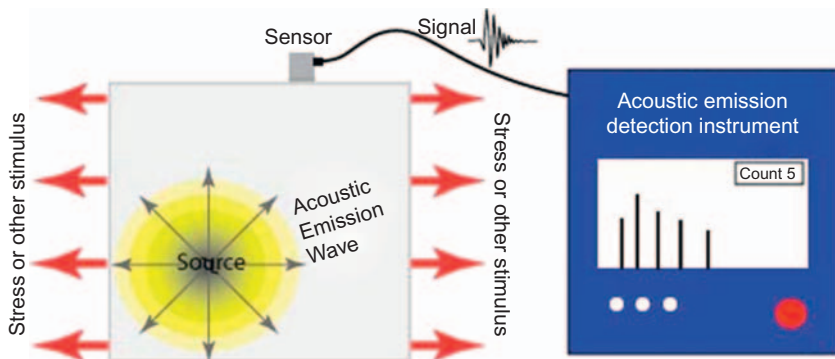


Figure 8.5 Acoustic Emission test equipment (NSF, 2009).

Source: Reproduced with permission from the NDT Resource Center and Center for NDE, Iowa State University.

in two key aspects. First, the signal has its origin in the material itself and is not introduced from an external source. Due to this advantage, AE tests are often performed on operating structures due to proper loading placed on the structure for triggering these AEs. Second, AE detects dynamic processes such as movement or strain, whereas most other methods detect existing geometric discontinuities or breaks (NSF, 2009). Other advantages of AE include: fast and complete volumetric inspection using multiple sensors, permanent sensor mounting for process control, and no need to disassemble and clean a specimen. Drawbacks of AE testing include the possibility of flaws remaining undetected due to insufficient loading—resulting in a value not high enough to cause an acoustic event. Another drawback of AE comes from environments that have load and noisy natures, which contribute extraneous noise to the signals. For successful applications, signal discrimination and noise reduction are crucial.

8.4.4 Ultrasonic methods

In contrast to the AE tests where elastic waves are generated through existing loading, in the ultrasonic pulse velocity (UPV) tests, a pulse signal of high frequency sound energy is sent traveling through the structure to evaluate its condition. This inspection can be used for assessment of cracks, delamination, flaw detection and more. Because wave propagation depends on the extent of the cracks, damage assessment tools may be developed based on the variation of UPV (Mirmiran and Wei, 2001). A typical ultrasonic testing inspection system consists of several functional units, such as the pulser/receiver, transducer, and display devices. Fig. 8.6 displays typical inspection materials to run the test. The pulser/receiver produces high voltage electrical pulses and drives the transducer, which generates high



Figure 8.6 Ultrasonic Pulse Velocity test equipment (Controls Group, 2016).

frequency ultrasonic energy. From here, the sound energy propagates through the material as a wave. Discontinuities in the structure (such as cracks) will cause the wave path to be reflected back. This energy is then transformed into an electrical signal by the transducer and displayed on the screen (NSF, 2009). The signal travel time can then provide information about the reflector size, location, and orientation. Advantages of the UPV test include; instantaneous results, minimal preparation, the production of detailed results, and high accuracy. Limitations to the UPV test include accessibility to transmit ultrasound, proper required training, and only suitably for homogenous materials.

Impact echo is another ultrasonic method for NDT. This method is based on the use of impact-generated stress waves that propagate through concrete and are reflected by internal flaws and external surfaces (Sansalone and Streett, 1998). A short impact, produced by tapping a steel ball against the concrete surface, is used to generate low-frequency stress waves that propagate in the structure and get reflected by flaws or other discontinuities. These surface displacements caused by wave reflections are recorded by a transducer that produces a voltage proportional to displacement, resulting in a voltage-time signal. This is then transformed by a computer into a spectrum of amplitude versus frequency (Sansalone and Streett, 2003). These variations in reflections are then used to identify and evaluate the integrity of the structure and to determine the location of flaws. Impact echo can be used to determine the severity and location of discontinuity in concrete structures, such as voids, cracks, delaminations, and debonding. Principal components include: a cylindrical handheld transducer unit, a set of spherical impactors, a portable computer, a high-speed analog-to-digital data acquisition system, and a software program that controls and monitors the test—displaying the results in numerical and graphical forms. Impact echo should not be confused with ultrasonic methods, such as pulse velocity and pulse echo. Unlike ultrasonic methods, impact echo utilizes lower frequency signals (2–20 kHz, typically). This low frequency allows the impact echo to overcome high-signal attenuation encountered with ultrasonic methods.

Another technique used for NDT is the Ultrasonic Tomography method. This technique consists of exciting an elastic wave within the concrete structure in order to determine location and size of defects, such as cracks, air voids, or inclusions. Instrumentation features a multihead antenna that generates 50 kHz ultrasonic pulses and is used for receiving and processing ultrasonic signals. Fig. 8.7 shows a schematic of the tomograph with three perpendicular cross sections of the tested object and the coordinate system connected with the antenna. Each head is mounted on the antenna and, due to the dry point contact, means of coupling and special preparation of the surface for testing are not required (Schabowicz, 2013). The methodology has been geared to locate defects in unilaterally accessible concrete members, determining their size and estimating the thickness of the members. Fig. 8.8 further explains the sequence of the technique.

Nonlinear ultrasonic is a newer approach for NDE of material degradation that is helpful in detecting cracks at early stages. When there is presence of micro-cracks in an elastic medium, the proportionality between an impinging ultrasonic wave and the corresponding elastic response of the medium occurs. Due to an increase of

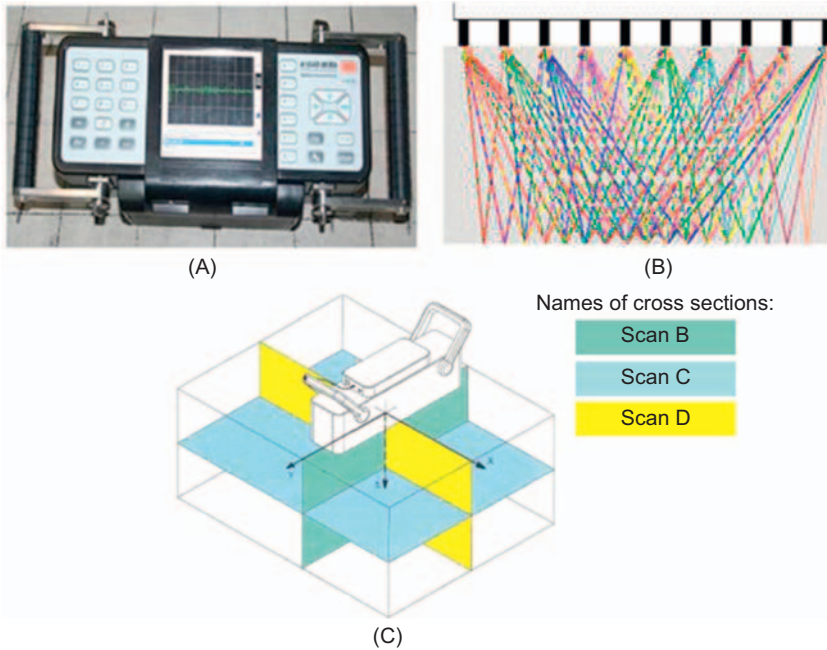


Figure 8.7 Ultrasonic tomograph: (A) top view, (B) ultrasonic pulses, and (c) three mutually perpendicular cross sections (scans) of investigated object and coordinate system connected with tomograph antenna (Schabowicz, 2013).

nonlinearity associated with increased damage, the goal of nonlinear ultrasonic methods is to extract the signature of the nonlinearity from the elastic response of the tested element in order to characterize damage progression (Antonaci et al., 2009). Scaling Subtraction Method (SSM) is a type of nonlinear ultrasonic method for the detection of nonlinear terms in the elastic response of a solid to a linear ultrasonic wave excitation. The method compares the recorded nonlinear signal, which represents the elastic nonlinear response of a damaged element, and the reference signal. It has been found to be more efficient than traditional linear and other nonlinear techniques, due to its ability to distinct between initial stages of degradation and latter damage propagation (Bruno et al., 2010). Another type of nonlinear test includes spectral analysis – that uses a filtering technique, allowing for the study of frequency content of the elastic response and to evaluate the amplitude of the generated high order frequencies, along with their dependence on the amplitude of the fundamental frequency of the excitation (Bruno et al., 2010).

8.4.5 Radiographic imaging

Real time radiography (RTR) is an NDT whereby an image is produced electronically, rather than filming, so that limited lag time occurs between the item being exposed to radiation and the image. The image comes from the radiation passing

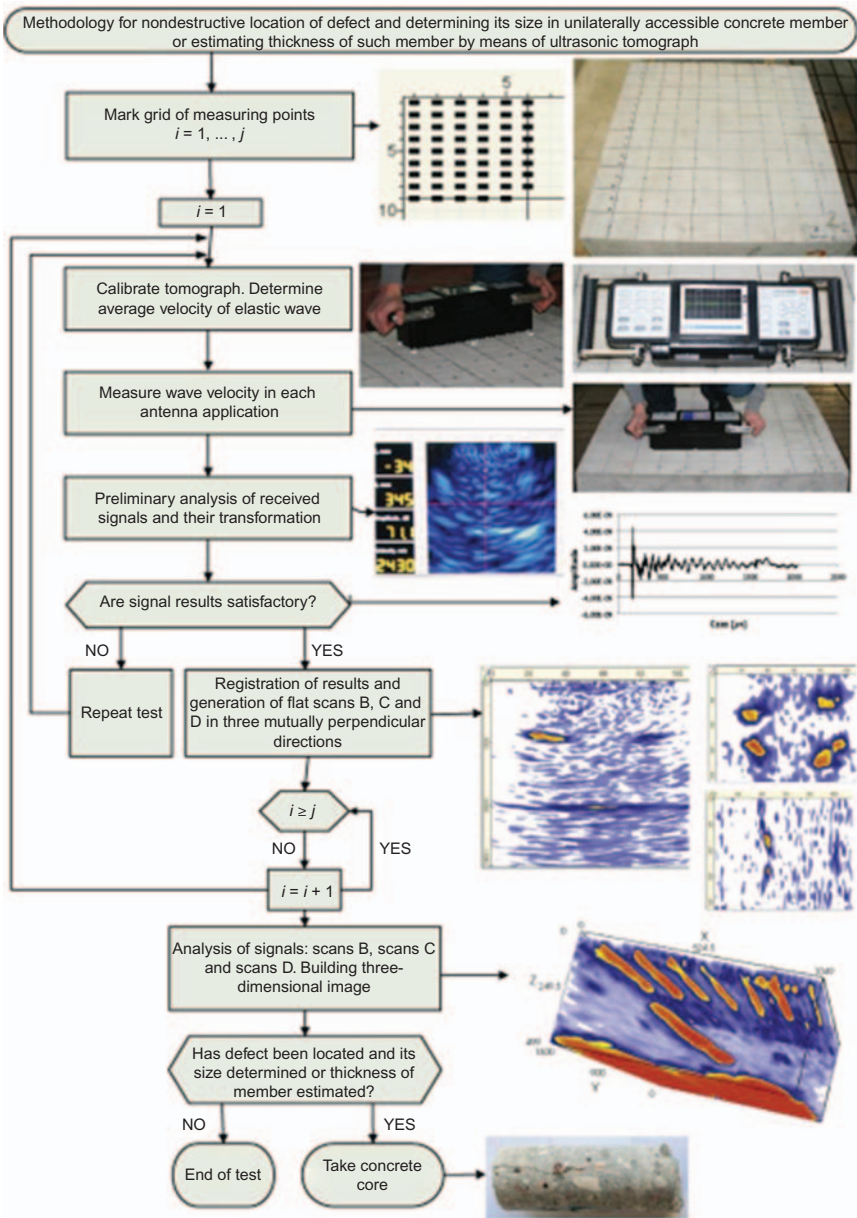


Figure 8.8 Methodology for nondestructive testing (NDT) of defects in or estimating thickness of such members by ultrasonic tomography technique (Schabowicz, 2013).

through the object, resulting in a light emitted from the interaction. These lights or fluorescent elements form the image that is seen in the film radiography. The positive image is formed showing where the higher levels of radiation were transmitted.

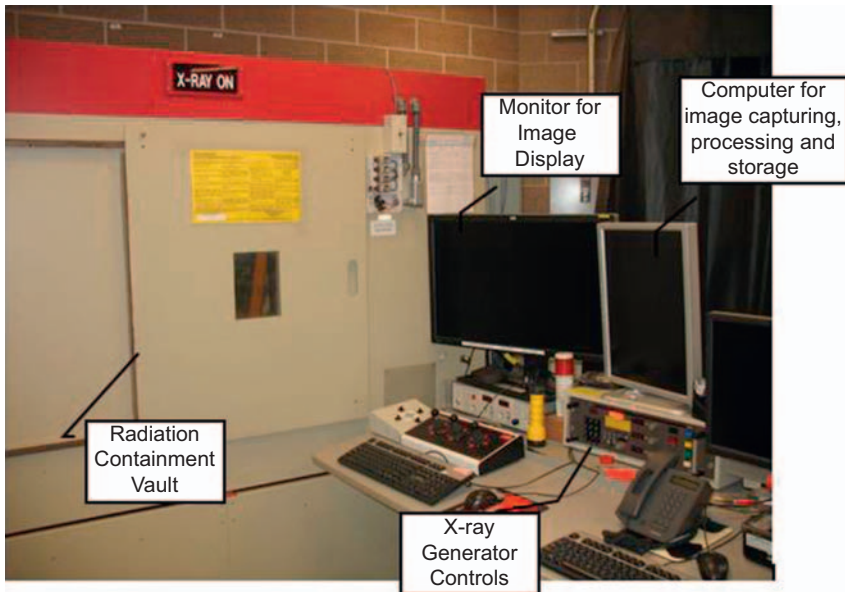


Figure 8.9 Equipment for real time radiography (RTR) system (NSF, 2009).

Source: Reproduced with permission from the NDT Resource Center and Center for NDE, Iowa State University.

Lighter and brighter images mean a thinner, or less dense, section. Most types of defects can be detected, including porosity and matrix cracks. Fig. 8.9 shows the equipment set up for the RTR test. One of the main features of the radiographic imaging is the sensitivity of the test. Accurate results largely depend on the orientation of internal material. For long cracks, for example, the best desired orientation must be in a position such that the photon ray will penetrate the maximum distance of the crack. If the orientation is perpendicular to the crack, the penetration region would be very small and the result of the recorded image would likely reveal no vital information (NSF, 2009). RTR offers plenty of advantages, especially during in situ testing. For starters, the test produces instantaneous and extremely accurate images of the radiographed section. It also works with any form of radiation including X-ray, gamma, or neutron radiation. The electronic signal from the RTR test can also be digitally processed to enhance image quality, and eliminate noise and other unnecessary information. Additionally, no surface contact is required; almost any geometric shape can be inspected. Disadvantages to RTR include sensitivity, the need for high energy sources, and safety precautions due to radiation.

8.4.6 Electromagnetic techniques

One of the popular electromagnetic techniques is the Eddy Current Test (ET). The eddy currents are created through electromagnetic induction. When alternating

current is applied to the conductor, such as a coil or copper wire, a magnetic field is developed around the conductor. The magnetic field propagates as the current rises to a maximum level, and collapses until the current is reduced to zero. When another electric conductor is brought close to the original one, a change in magnetic field occurs and current will induce in the second conductor (Laight et al., 1997). As a result, electrons in the material under investigation are forced to circulate in an “eddy-like” pattern (Fig. 8.10). The Eddy name comes from eddies that form when a liquid or gas flows in a circular path around obstacles under the proper conditions. Simultaneously, the circular currents form a magnetic flux field that can be detected by the driving coil or a second, separately-placed coil. When a flaw is introduced to the conductive material, the eddy currents are disrupted (NSF, 2009). ET poses many advantages as an NDT tool due to its wide range of variety in inspections and measurements. Advantages include: detection of near-surface defects, instantaneous results, portable equipment, minimal preparation, no surface contact needed, and the ability to inspect irregular shapes. Some limitations include: characteristics that only allow inspections in regions of high fiber density due to the magnetic flux, the skill and training needed to operate equipment, limited depth of penetration, and undetectable flaws—such as delamination that lie parallel to the probe coil winding direction. The Eddy Current method requires a conductive material. The Glass FRP (GFRP) is not conductive, therefore this method has limited application for GFRP testing.

Another popular Electromagnetic technique is microwave-based. It uses high frequency electromagnetic energy, ranging from a few hundred megahertz to a few hundred gigahertz (Dong and Ansari, 2011). Here, the material is tested by measuring various properties of the electromagnetic waves scattered by or transmitted through the test material. The imaging capabilities are based on transmitting directed electromagnetic waves into a dielectric material, using the information of magnitude and phase to create images of the specimen (Karbhari et al., 2005). This test poses advantages with thick composites as the microwaves have the ability to penetrate inside the mentioned dielectric materials. This test can be used to detect

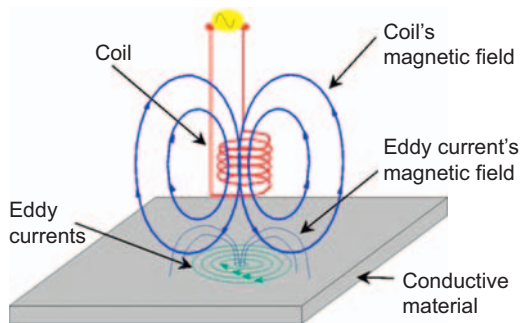


Figure 8.10 Alternating current source and coil wire for Eddy Current testing (NSF, 2009). Source: Reproduced with permission from the NDT Resource Center and Center for NDE, Iowa State University.

delamination, voids, and debonding, along with their depth in FRP reinforced concrete. Location and geometry of the debonded regions can also be identified.

Dielectric spectroscopy is a fundamental technique that measures the dielectric properties of a medium, as a function of frequency. The application allows for the prediction of parameters such as porosity and pore connectivity, based on the interaction of an external field with the electric dipole moment, often expressed by permittivity (Sanchez-Fajardo, 2013). The permittivity represents the electrical polarization. Equipment set up for dielectric test can be seen in Fig. 8.11. The dielectric spectroscopy technique could be used to measure moisture penetration in adhesively-bonded composite structures and to monitor the degradation of adhesive joints.

Nuclear Magnetic Resonance (NMR) is a technique that studies the properties of water storage and transport. They also provide information about the porosity and water tightness of structures which allows for the determination of environmental durability problems at an early stage. Solving these problems can prevent unexpected fatal damage due to moisture entrance. NMR is a spectroscopic technique that uses the resonance interaction between electromagnetic waves and hydrogen nuclei placed in an external magnetic field (Dobman et al., 2002). With one-sided access (OSA) NMR, a moisture content profile can be measured non-destructively. This offers the possibility of monitoring water absorption/desorption and moisture migration during drying and wetting processes. Using the OSA method, successful aquametric applications have been performed for concrete and polymers (Wolter



Figure 8.11 Dielectric spectroscopy measurement set up (Raihan, 2014).

et al., 2003). With this instrumentation, it is possible to recognize the risk for a reduced residual life time of building materials at very early ages.

8.4.7 Ground penetrating radar

Ground Penetrating Radar (GPR) is a real-time NDT technique that uses high frequency radio waves, yielding data with very high resolution in a short amount of time. This technique uses electromagnetic waves that travel at a specific velocity determined by the permittivity of the material. Velocities will differ based on the kind of material, due to difference in electrical properties and will thus provide responses at different times. As antennae move along the survey line, a series of traces are collected at specific points along the line (Fig. 8.12). The scans are then positioned side by side to form a profile of the area (Ekes, 2007). The main components that make up the GPR include a waveform generator, a single transducer comprised of an emitting and receiving antenna, a signal processor, and a data storage/display unit. Various approaches have been used for structural applications, such as frequency modulation, synthetic pulse-radar, and pulse systems. Although all are accepted methods, the pulsed system method has been found to be the most accepted and used in most available equipment (Bungey and Millard, 1993). GPR is most-commonly used for locating spacing and depth for reinforcing steel, post-tensioning cables or anchors, measuring rebar cover, and mapping voids (Fig. 8.13). With the growing availability and improvement of GPR processing software, research has found that it can be used as a subsurface condition assessment for FRP composites. GPR waveforms can now help detect voids inside the concrete. Compared to other nondestructive techniques, such as infrared thermography,



Figure 8.12 Ground penetrating radar equipment.

ultrasonic or microwave, GPR offers more penetrating power and so can detect concrete defects or deteriorations at greater depths (Dong and Ansari, 2011).

8.4.8 Optical methods

Optical field testing has a large variety of methodologies that allow for the detection of surface deflections, through the formation of fringe patterns on the surface of an object. These methods measure the change in strain which requires the application of loads on the structure. The most common methods are interferometry, holography and shearography. These methods use a geometrical moire (large scale interference patterns) which uses superposition of two gratings to cause formation of fringe patterns (Parks, 1998). These patterns correspond to the displacement relative to a fixed reference point. Depending on the number of fringes in a region, it corresponds to the strain in the material as well as the magnitude of displacement. Moire interferometry (Fig. 8.14) uses a more complex geometrical moire that

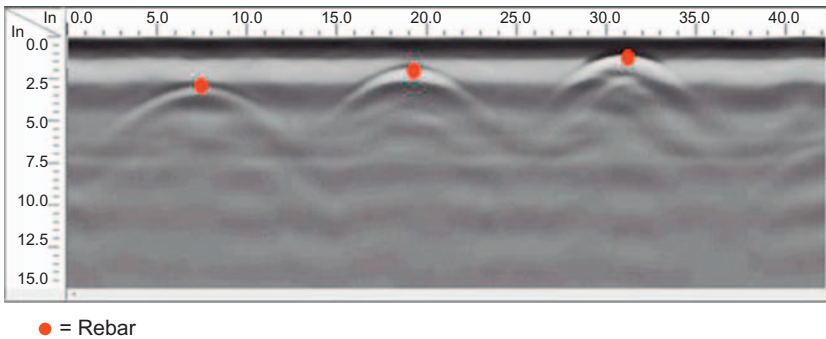


Figure 8.13 Ground penetrating radar waves for locating rebar.

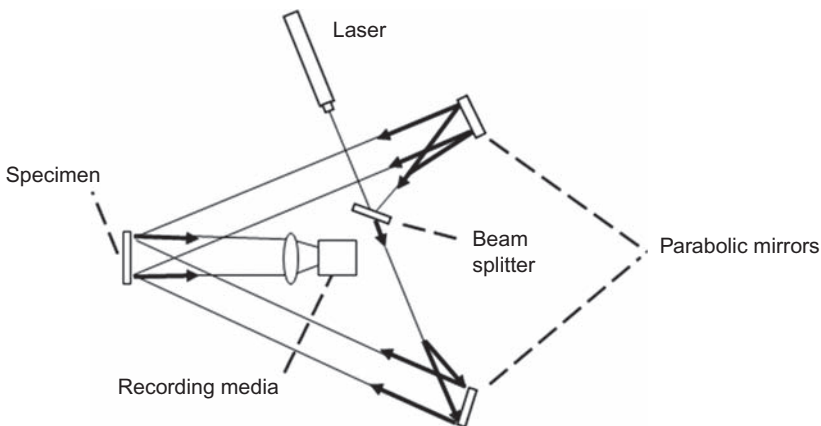


Figure 8.14 Test set up for moire interferometry (Karbhari et al., 2005).

Source: Image courtesy of the Oregon Dept. of Transportation.

provides high flexibility and resolution. Here, the grating is formed by interference of two coherent light beams illuminating the specimen at two complimentary angles. Due to coherence, the beams generate walls of constructive and destructive interference, which result in a virtual grating in the zone of their intersection (Post et al., 1994). For holographic interferometry (Fig. 8.15), a three dimensional image is created from a body. Rather than interference of two beams to form grating, a reference beam is aimed directly at the recording media, and the second illuminates the test object. The white surface of the object causes a reflection of the scattered light waves towards the recording device, where interference of the two beams occurs. An advantage of this test is that it does not require specimen grating, while a disadvantage is the need to perform this test in a laboratory due to stability requirements. For shearography (Fig. 8.16) the key to the study is the birefringent crystal that serves as a shearing device. This crystal brings two non-parallel beams scattered from two separate points onto the object surface to become almost collinear (Hung, 1998). Flaw detection is based on the comparison of two states of

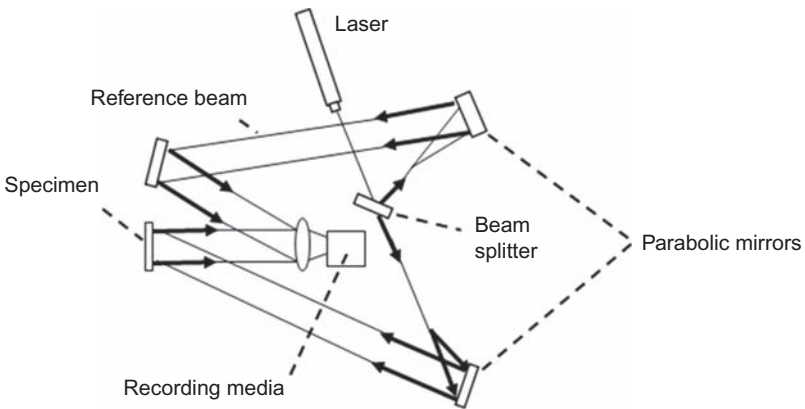


Figure 8.15 Test set up for holographic interferometry (Karbhari et al., 2005).

Source: Image courtesy of the Oregon Dept. of Transportation.

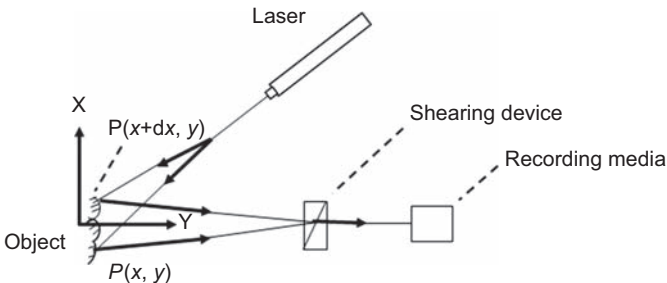


Figure 8.16 Test set up for shearographic imaging (Karbhari et al., 2005).

Source: Image courtesy of the Oregon Dept. of Transportation.

deformation in the test object. The differences in light emitted can be related to surface strains through the use of image subtraction. All these optical methods are limited to the surface inspection. This puts a limitation on the detectability of the defects that are of insufficient size, creating a huge drawback in the inspection of thick composites.

8.4.9 Thermographic imaging

Thermal NDT methods involve the measurement of surface temperatures as heat flows to and from an object. These tests range from simple thermal measurements, such as point measuring with a thermal couple to locate hot spots like worn out bearings, to more advanced testing such as thermal imaging systems that have thermal information rapidly available through a vast area (NDT). The Infrared Thermography technique is one method that has been used for many years to scan aerospace structures, particularly to detect and characterize delamination in carbon/epoxy composites (Maldague, 2001). This technique involves heating the surface of a structure during a period and measuring the temperature distribution of the sample with the use of an infrared camera (Fig. 8.17). There, the infrared camera will produce images of pixels composed of uncooled microbolometer detectors allowing to see temperature differences. The principle is that the camera monitors the flow of heat from the surface, which is affected by internal flaws such as disbands, cracks or voids. Solid bonds will cause rapid heat dissipation throughout the material, while areas with defects will retain the heat for longer periods of time. A basic test set up is shown in Fig. 8.18. The method behind this principle is that the presence of subsurface anomalies will alter the rate of diffusion with respect to the surrounding area. As such, entrapped pockets or air will retain heat longer and serve as hot spots. This phenomenon is due to the low thermal conductivity of air as well as the high heat flow rate in the surrounding material (Karbhari et al., 2005). Advantages of this test include ease of accessibility due to in situ testing and short inspection time. Difficulties include the differentiation in thermal contrast between the good and defective regions.



Figure 8.17 Infrared camera.

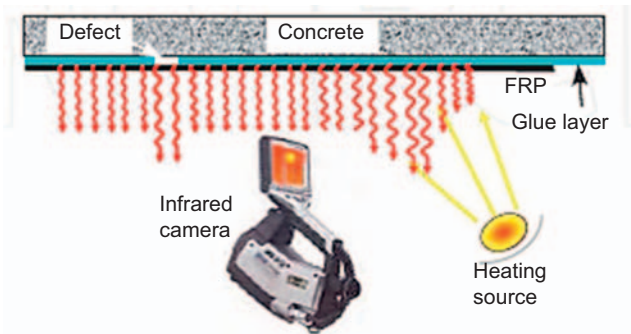


Figure 8.18 Infrared Thermography test set up (Taillade, 2012).

Source: © 2012 Taillade, F., Quiertant, M., Benzarti, K., Dumoulin, J., Aubagnac, C.

Published in [short citation] under CC BY 3.0 license. Available from: <http://dx.doi.org/10.5772/27488>

8.4.10 Load testing

The main principle of design is based on the maximum permissible level of loading and deflection. Structures are considered to be in good service as long as they meet the loading criteria and do not surpass their service load levels. When aging occurs, these structures are likely to experience some sort of degradation including fatigue, cracking, moisture absorption, or creep. Diagnostic load tests can be performed to monitor a structure's response to known loading conditions. If linear–elastic behavior is exhibited during the load test, meaning the load below the elastic load limit is observed, the results can be used for model calibration and load rating (AASHTO, 2011). Strain or deflection measurements are taken at strategic locations to determine the load distribution or stiffness characteristics of the bridge. Strain gauges are typically installed near the location of maximum moment in the girder, while deflection is measured using linear variable differential transformer (LVDT). After the test is performed, the results are compared to the analytical response to better estimate the capacity. Generally, the measured strains during the live load test are smaller than the theoretical due to increased live load distribution previously unaccounted for (Sanayei et al., 2015). Since the load testing rating is based on the structure's response to loading, it is widely considered a more accurate load rating reflecting the actual capacity of the bridge at the time of testing (Jauregui and Barr, 2004). Problems of the load testing method can include: concrete cracking, debonding of concrete composite interface, and fiber rupture. The load testing method is effective where the defects in composites have already exceeded the acceptable limits. This means defects in CFRP composites or in the interfacial region may not be of enough magnitude to change the load deflection response acquired during the load test. To sum up, this method is likely to lack sensitivity to small defects or capability to provide information about size, location and magnitude of individual flaws.

8.4.11 Embedded sensors for real time structure health monitoring

There has been a large demand for in-service structural health monitoring (SHM) in response to the need for safety, security and lower LCCs. SHM assesses the state of the structural health and, through appropriate data processing and interpretation, predicts the remaining life of the structure. An SHM program involves selection and placement of sensors suitable for measurement of key parameters that influence the performance and health of the structural system. There are two popular types of sensors used for monitoring the structure performance.

The first is optical fiber sensors. These are emerging as a superior non-destructive means for evaluating the condition of concrete structures. Optical fibers are able to detect minute variations in structural conditions through remote measurements. Structures fully integrated with optical fibers will be able to monitor the initiation and progress of various mechanical or environmentally-induced degradations in concrete elements (Ansari, 1997). The optical fibers sense the physical and ambient perturbations based on intensity, wavelength, and interference of the light wave. Fiber-optic sensors have been developed and effectively employed in civil engineering applications (Yuan and Ansari, 1997; Gu et al., 2004; Wu and Xu, 2002; Zeng et al., 2002). Advantages of fiber-optic sensors include dimensional and material compatibility. The fibers will not corrode or degrade during curing and will bond strongly to the matrix.

The second type is ultrasonic sensors. This is an NDE method that relies on elastic wave propagation and reflection within a material (Giurgiutiu and Cuc, 2005). Using measurements such as: time of flight, path length, frequency, phase angle, amplitude, acoustic impedance, and angle of wave deflection, the purpose of the test is to try to identify the wave field disturbance due to local damage and flaws. Through a network of sensors embedded into the structure, real time monitoring can be achieved for loads, stress, and environmental conditions. Another method employs piezoelectric wafer active sensors (PWAS) that send and receive ultrasonic Lamb waves and determine the presence of cracks, delaminations, disbands, and corrosion. This method is enabled by embeddable ultrasonic transducers, consisting of thin piezoelectric wafers that can be permanently attached to metallic and composite structures.

8.5 Relative assessment of available techniques

While FRP-retrofitted concrete members may be evaluated by a large number of NDT techniques, most methods are not yet fully developed for field application. Currently there is not a single method capable of comprehensively assessing the response of FRP rehabilitated concrete structures at the global as well as local levels. Visual inspection is the primary method that is still utilized; it is convenient, inexpensive and fast, but results are not quantitative and are subjective. It is unable to detect internal cracks and delamination.

Acoustic impact methods are usually used for large near-surface voids and delamination. This is in contrast to ultrasonic techniques which provide a viable methodology capable of assessing both surface and subsurface discontinuities, but can be restricted by thickness and material interface. The latter two are the most-used techniques after visual inspection. Methods such as AE allow for the monitoring of the entire structure, but the test objects need to be loaded and is often difficult to identify the type of defect present and its location. Radiographic techniques provide detailed and sensitive results and can be used for point detection of defects, but due to their health hazards and cost, are considered in a small number of cases. Most of the popular electromagnetic techniques (e.g., Eddy current) have limited application in the case of concrete repaired with FRP, due to the low conductivity of the surface. Optical methods are effective for thin composite materials, and they require the application of load. Most of these methods are suitable for laboratory environment because of their complexity and sensitivity to external noise and vibration. Inhomogeneity of composites used in civil engineering limits the application of optical techniques. Advances in thermography have allowed for rapid inspection, but is typically used for periodic monitoring and not real time monitoring. They are effective to detect near-surface defects, fast, accurate, reliable and cost effective. GPR offers good penetration but is less sensitive to cracks and small voids. Due to the development of embedded sensing systems, health monitoring of FRP-repaired concrete structures is now possible. Embedded at the FRP–concrete interface, fiber-optic sensors provide the ability to measure strain remotely. The use of embedded sensors in FRP-rehabilitated concrete structures for real-time structural monitoring can greatly improve the durability and safety of the structure.

Generally speaking, there is no single method that provides all the inspection requirements. Combinations of different methods are necessary to properly evaluate a structure. The results of NDE, accompanied by analytical simulation of structural performance with proper damage models, will ideally provide a comprehensive evaluation tool for assessment of the structural condition and service life.

8.6 Future trends

FRP applications in civil engineering have advanced significantly since their introduction. As the knowledge-base on the material continues to grow, so does the potential of addressing the challenges for ageing infrastructure. Engineers will hopefully become more comfortable with the behavior of FRP-repaired concrete structures, with standards that provide detailed procedures for quality control and assurance of the FRP repaired structures.

The progress in developing embedded sensor technology is arguably one of the most exciting developments for the future of civil engineering. This technology allows for a better understanding of the actual performance of the repaired structure and will pave the way for the development of smart composites. A composite structure embedded with intelligent sensors that monitor and respond to the structural

health is forthcoming. This developing idea is likely to grow rapidly in the near future, resulting in more efficient and sustainable structures. On the other hand, there is still a great amount of room for further NDT research in an effort to improve current techniques and capabilities, and their combined use of strategies for better material characterization and damage assessment. These fast and noncontact NDT methods will soon become an essential tool for damage assessment and for condition evaluation of existing structures.

References

- AASHTO, 2011. Manual for Bridge Evaluation, second ed. Farmington Hills, MI.
- ACI, 2008. Guide for the Design and Construction of Externally Bonded FRP Systems for Strengthening Concrete Structures. ACI 440.2R-0 American Concrete Institute, Detroit.
- Alkhrdaji, T., June 2015. Strengthening of Concrete Structures Using FRP Composites. N.p.: STRUCTURE Magazine.
- Ansari, F., 1997. State-of-the-Art in the Applications of Fiber-Optic Sensors to Cementitious Composites. Elsevier.
- Antonaci, P., et al., 2009. Nonlinear Ultrasonic Evaluation of Load Effects on Discontinuities in Concrete. Elsevier.
- ASTM, 2003. Standard Test Method for Transition Temperatures of Polymers by Differential Scanning Calorimetry, Test Method D3418-03. American Society for Testing and Materials 7 pp.
- ASTM, 2009. Standard Test Method for Pull-off Strength for FRP Bonded to Concrete Structures. ASTM D7522M, Reston, VA.
- ASTM, 2015. Standard Practice for Classifying Visual Defects in Glass-Reinforced Plastic Laminate Parts. ASTM D2563-0.
- Bruno, C.L.E., et al., 2010. Monitoring Evolution of Compressive Damage in Concrete with Linear and Nonlinear Ultrasonic Methods. Elsevier.
- Bungey, J.H., Millard, S.G., 1993. Radar inspection of structures. Proc. Inst. Civ. Eng.: Struct. Build. 99 (2), 173–186.
- Chen, J.F., Li, S.Q., Ai, J., 2009. Relationship Between FRP Fracture Strains in Flat Coupon Tests, Split Disk Tests and FRP Wrapped Columns. APFIS.
- Controls Group, 2016. Ultrasonic Pulse Velocity Tester, Concrete Testing Equipment.
- Degala, S., et al., 2008. Acoustic Emission Monitoring of CFRP Reinforced Concrete Slabs. Elsevier.
- Dobman, G., et al., 2002. The Potential of Nuclear Magnetic Resonance (NMR) to Non-Destructively Characterize Early-Age Concrete by a One-Sided Access (OSA) Technique. ISNT.
- Dong, Y., Ansari, F., 2011. Non-Destructive Testing and Evaluation of Civil Structures Rehabilitated Using Fiber Reinforced Polymer (FRP) Composites. Woodhead Publishing Limited.
- Ekes, C., 2007. GPR: A New Tool for Structural Health Monitoring of Infrastructure. Sewervue.
- Foster, S.K., Bisby, L.A., 2005. High Temperature Residual Properties of Externally-Bonded FRP Systems. Research Gate.

- Giurgiutiu, V., Cuc, A., 2005. Embedded Non-Destructive Evaluation for Structural Health Monitoring, Damage Detection, and Failure Prevention. The Shock and Vibration Digest.
- Groenier, J., Eriksson, M., Kosmalski, S., 2006. A Guide to Fiber-Reinforced Polymer Trial Bridges. United States Forest Service.
- Gu, X., Chen, Z., Ansari, F., 2004. Fiber Optic Distributed Crack Sensor for Concrete Structures. ASCE.
- Hung, Y.Y., 1998. Computerized shearography and its application for nondestructive evaluation of composites. In: Jenkins, C.H. (Ed.), Manual on Experimental Methods for Mechanical Testing of Composites. The Fairmont Press, Lilburn.
- Jauregui, D., Barr, P., 2004. Nondestructive Evaluation of the I-40 Bridge over the Rio Grande River. ASCE.
- Karbhari, V., et al., 2005. Methods for Detecting Defects in Composite Rehabilitated Structures. Oregon Department of Transportation.
- Laight, A., Court, R., Treen, A., 1997. Measurement of the Electromagnetic Shielding Properties of Mechanically Loaded Composites. Polymer Composites.
- Lee, L., Jain, R., 2009. The Role of FRP Composites in a Sustainable World. Springer-Verlag.
- Maldague, X.P.V., 2001. Theory and Practice of Infrared Technology for Non-destructive Testing. John Wiley and sons Inc.
- Malnati, P., 2011. A Hidden Revolution: FRP Rebar Gains Strength. Composites Technology.
- Mirmiran, A., Wei, Y., 2001. Damage assessment of frp-encased concrete using ultrasonic pulse velocity. J. Eng. Mech. 127 (2) .
- NSF (National Science Foundation), 2009. NDT course material. Non Destruction Test Resource Center.
- Pallempati, H., Beneberu, E., Yazdani, N., Patel, S., 2016. Condition Assessment of Fiber-Reinforced Polymer Strengthening of Concrete Bridge Components. ASCE.
- Parks, V.J., 1998. Geometric Moiré. In: Jenkins, C.H. (Ed.), Manual on Experimental Methods for Mechanical Testing of Composites. The Fairmont Press, Inc., Lilburn.
- Post, D., Han, B., Ifju, P., 1994. High Sensitivity Moiré: Experimental Analysis for Mechanics and Materials. Springer Verlag, New York.
- Raihan, R., 2014. Dielectric Properties of Composite Materials During Damage Accumulation and Fracture. University of South Carolina.
- Reichhold, 2009. FRP Inspection Guide. Reichhold.
- Sanayei, M., Reiff, A., Brenner, B., 2015. Load Rating of a Fully Instrumented Bridge: Comparison of LRFR Approaches. ASCE.
- Sanchez-Fajardo, V.M., 2013. Study of the Pore Structure of the Lightweight Concrete Block with Lapilli as an Aggregate to Predict the Liquid Permeability by Dielectric Spectroscopy. Elsevier.
- Sansalone, M., Streett, W., 1998. The Impact-Echo Method. NDTnet.
- Sansalone, M., Streett, W., 2003. Impact Echo: Nondestructive Evaluation of Concrete and Masonry. Bullbrier Press.
- Schabowicz, K., 2013. Ultrasonic Tomography—The Latest Nondestructive Technique for Testing Concrete Members—Description, Test Methodology, Application Example. Elsevier.
- Setunge, S., 2002. Review of Strengthening Techniques Using Externally Bonded Fiber Reinforced Polymer Composites. CRC.

- Taillade, F., et al., 2012. Nondestructive Evaluation of FRP Strengthening Systems Bonded On RC Structures Using Pulsed Stimulated Infrared Thermography. InTech.
- Wolter, B., Kohl, F., Surkowa, N., Sept. 2003. Practical Applications of NMR in Civil Engineering.
- Wu, Z., Xu, B., 2002. Infrstructural Health Monitoring with BOTDR Optic Fiber Sensing Technique. Elsevier.
- Yuan, L., Ansari, F., 1997. White-Light Interferometric Fiber-Optic Distributed Strain-Sensing System. Elsevier.
- Zeng, X., et al., 2002. Strain Measurement in a Concrete Beam by Use of the Brillouin-Scattering-Based Distributed Fiber Sensor with Single-Mode Fibers Embedded in Glass Fiber Reinforced Polymer Rods and Bonded to Steel Reinforcing Bars. OSA publishing.

Further reading

- ASTM, 2008. Standard Test Method for Tensile Properties of Polymer Matrix Composite Materials, D3039/D3039M-08 Annual Book of ASTM Standards, Vol. 15.03. 200, American Society for Testing Materials.

Field assessment of a concrete bridge

9

Eva O.L. Lantsoght^{1,2}

¹Delft University of Technology, Delft, the Netherlands,

²Universidad San Francisco de Quito, Quito, Ecuador

9.1 Introduction

Field assessment of concrete bridges can be carried out in different ways. One way is the traditional visual inspection. To see beyond the surface of the structure, non-destructive techniques can be used. With these techniques, regions of corrosion, delamination, cracking, and other structural faults can be identified (ASCE/SEI-AASHTO Ad-Hoc Group On Bridge Inspection Rating Rehabilitation and Replacement, 2009; Ryan et al., 2012). In some cases, samples need to be taken from the bridge to know the concrete compressive strength, the level of carbonation, the amount of chlorides, and/or the steel quality that was used. To know more about the structural behavior of a bridge, a nondestructive load test can be carried out (Schacht et al., 2016b).

Two types of load tests can be distinguished. The first type consists of diagnostic load tests (Sanayei et al., 2016; Olaszek et al., 2014; Matta et al., 2008; Velázquez et al., 2000), which are carried out at a lower load. These types of tests can be used for comparison to an analytical model. By studying the differences between the analytical model and the field response, it can be identified which elements differ from the assumptions in the analytical model. Examples of such differences, which can occur separately or combined, depending on the bridge type, are (Barker, 2001):

- the actual impact factors compared to the impact factor from the code,
- the actual section dimensions,
- the unaccounted stiffness of secondary elements such as curbs and railings,
- the actual transverse load distribution,
- the level of restraint at the bearings,
- the actual longitudinal load distribution,
- unintended composite action with the deck.

The second type of load testing is proof load testing (Lantsoght et al., 2016c; Liu et al., 2014; Faber et al., 2000; Lin and Nowak, 1984; Koekkoek et al., 2016). Proof load testing is chosen when there are large uncertainties that make an analytical determination of the structural response difficult. Such uncertainties include: the effect of material degradation, uncertainties from a lack of information when structural plans are missing, and uncertainties with regard to the load path at higher load

levels. In a proof load test, a load that corresponds to the factored live load is applied to the bridge. If the bridge can withstand the applied load without signs of distress, it is shown that the bridge can carry the prescribed loads to a satisfactory level. None of the nondestructive load tests give insight into the ultimate capacity of the tested structure. If the ultimate capacity needs to be known, and the bridge is decommissioned, a collapse test can be considered (Lantsoght et al., 2016a,b, 2017; Bagge et al., 2015; Nilimaa et al., 2015; Puurula et al., 2014, 2015).

One type of material degradation that makes an analytical assessment of a bridge difficult is the effect of damage caused by alkali-silica reaction (ASR). ASR takes place when the alkali in the cement reacts with silica that is present in some aggregates. The result of this reaction is a gel. When this gel comes in contact with moisture, the gel will expand. This expansion causes internal stresses in the concrete. If these stresses exceed the tensile strength of the concrete, cracking will result. In particular, the shear capacity of elements with ASR-damage is subject to discussion, as the cracking reduces the tensile strength of the concrete (Siemes et al., 2002). Experimental research has shown that ASR-damage has a limited effect on the bending moment capacity, unless the level of expansion caused by the ASR-gel is high (Talley, 2009). For reinforced concrete members, the expansion is partially counteracted by the reinforcement, and a prestressing effect takes place. This idea is confirmed by testing reinforced concrete members with and without ASR-damage, in which it is found that the cracking moment for the specimens with ASR is higher than for the specimens without, as a result of this prestressing effect (Haddad et al., 2008). For the shear capacity, some authors report that laboratory testing leads to higher shear capacities (attributed to the beneficial prestressing effect) (Ahmed et al., 1999; Ahmed et al., 1998), whereas testing of beams (den Uijl and Kaptijn, 2004) taken from ASR-affected viaducts resulted in a reduction of the shear capacity by 25% when compared to Rafla's formula (Rafla, 1971). Additionally, a number of reported load tests on ASR-affected viaducts (Talley, 2009) in Japan, France, South Africa, and Denmark (Schmidt et al., 2014) showed that the effect of ASR on the overall structural response is limited. However, these few studies are not sufficient to declare all ASR-affected viaducts as structurally safe. Specific cases can be analyzed with proof load testing. In this chapter, the proof load testing of the ASR-affected viaduct Zijlweg is discussed.

9.2 Description of the viaduct Zijlweg

9.2.1 History of viaduct

The viaduct Zijlweg is located in the road Zijlweg near Raamsdonksveer and Waspik, and crosses the highway A59. The bridge was built in 1965 for the Province of Noord Brabant in the Netherlands. The originally-devised service life was 80 years, and the original live loads were determined for traffic class B, which used a distributed lane load of 400 kg/m^2 and a design truck with two axles of 10 ton and one axle of 20 ton. The current bridge owner is Rijkswaterstaat, the



Figure 9.1 Photograph of viaduct Zijlweg: (A) top view; (B) bottom view.

Ministry of Infrastructure and the Environment, Direction Noord Brabant. A photograph of the viaduct is given in [Fig. 9.1](#).

Viaduct Zijlweg is a reinforced concrete, solid slab bridge with four continuous spans under a skew angle of 14.4 degrees. The span lengths are 10.32 m for the end spans and 14.71 m for the central spans. An overview of the geometry of viaduct Zijlweg is given in [Fig. 9.2](#). The total width of the cross-section is 6.6 m, whereas the width of the carriageway equals 4 m. The thickness varies parabolically between 550 and 850 mm. The spans are supported by concrete piers at the central supports and by an abutment at the end supports, and elastomeric bearing pads are used at the supports.

In terms of documentation of the bridge, the original calculation report ([Provincie Noord Brabant, 1965](#)) is available. Repair activities were carried out in 2002, and a report of these activities with a plan for management and maintenance is available ([Rijkswaterstaat, 2002](#)). An inspection report from 2008 ([Gielen et al., 2008](#)) is available as well, and inspections are programmed to take place every five years. During the repairs in 2002, a waterproofing layer was added on the top side of the slab, to prevent further ingress of moisture. The inspection of 2008 concluded that the viaduct is in moderate conditions. The possibly insufficient capacity of the main superstructure was identified as a considerable risk. As such, it was noted that the viaduct does not fulfill all the performance requirements and has an increased risk with respect to safety in fulfilling its required functions.

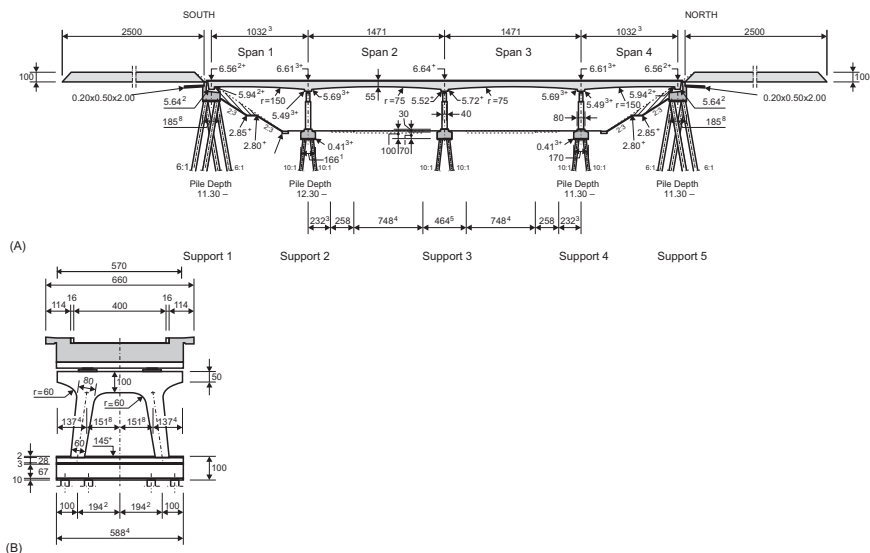


Figure 9.2 Structural system of viaduct Zijlweg: (A) longitudinal section; (B) cross-section. Units: centimeter (cm).

9.2.2 Alkali-silica reaction monitoring

The presence of ASR was detected in 1997 in a large number of bridges over the highway A59 in the Province of Noord Brabant, including the viaduct Zijlweg (Projectteam RWS/TNO Bouw, 1997). All these bridges were built around the same time, using the same materials. For the viaduct Zijlweg, cracking had occurred as a result of the ASR-damage. When taking concrete cores from the viaduct, many of the cores would be completely intersected by cracks, and thus had a uniaxial tensile strength of 0 MPa. Other cores still had some uniaxial tensile strength, but much smaller than expected from the concrete compressive strength. At that time, the small uniaxial tensile strength of the concrete in bridges with ASR-damage caused concerns with regard to the shear capacity of these bridges. Besides the low uniaxial tensile strength, these bridges were also showing large cracking and were not provided with shear reinforcement. Moreover, the bridges were designed for lower live loads and larger shear capacities than prescribed by the current governing codes.

A structural assessment was carried out in 1997. In a firsthand calculation, the Unity Check (UC) for shear at the end support was found to be $UC = 5.4$ and at the mid support as $UC = 4.7$ (Projectteam RWS/TNO Bouw, 1997). The Unity Check is the ratio of the shear stress caused by the considered load combination to the shear capacity. The load combination for assessment is the combination of the self-weight, superimposed dead load, and live loads consisting of distributed lane loads and concentrated loads for the design tandem as prescribed by Load Model 1 from NEN-EN 1991-2:2003 (CEN, 2003). A Unity Check larger than 1 thus means

that the structure does not fulfill the requirements. The extremely large values for the Unity Check found in the first calculations raised serious concerns with regard to the shear capacity. Prior to deciding that the structure should be strengthened or replaced, however, it was decided to carry out refined calculations. In these calculations, the value of the tensile strength was determined from the combination of 51 specimens tested in uniaxial tension and 10 specimens in splitting tension. The shear stress caused by the considered load combination was determined by using a linear finite element program. From these calculations, the results were $UC = 1.29$ at the end supports and $UC = 1.31$ at the mid supports (Projectteam RWS/TNO Bouw, 1997). These results still indicate that the structural capacity of the viaduct Zijlweg is insufficient, and that further studies are required to determine if the bridge should be strengthened or replaced. It was then decided that the viaduct Zijlweg would be a good candidate for assessment through proof load testing.

In 2003, monitoring of the viaduct for ASR was applied (Koenders Instruments, 2015). The temperature, deck thickness, moisture in the concrete, and longitudinal expansion of the deck are monitored, see Fig. 9.3. Measurement locations 3–7 were installed in 2003, and additional sensors on locations 8–10 were installed in mid-2007. The measurements are taken hourly, and were started on April 1, 2003.

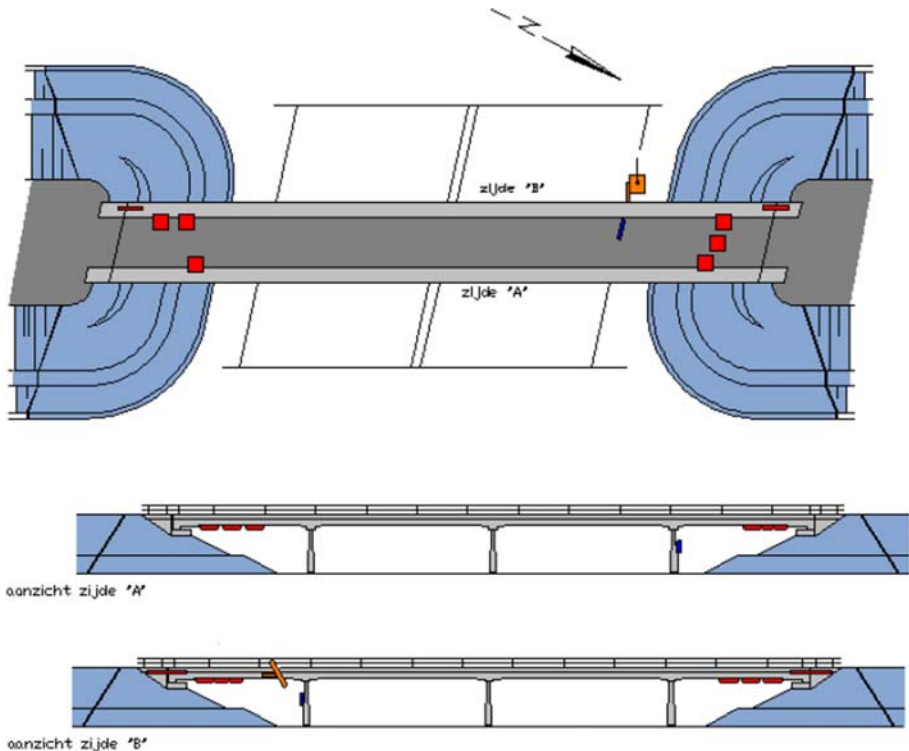


Figure 9.3 Monitoring system for alkali-silica reaction (ASR) on viaduct Zijlweg.

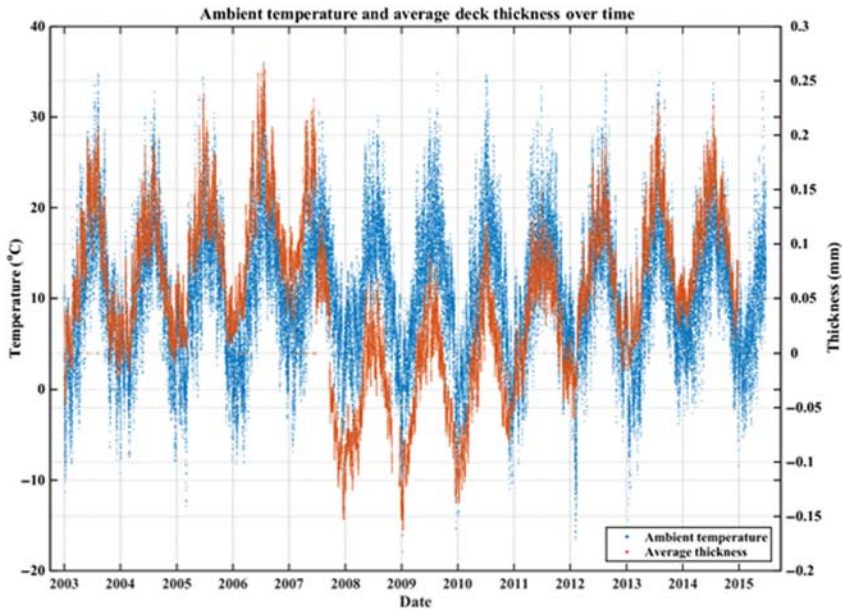


Figure 9.4 Relation between ambient temperature from Dutch meteorological institute and the average thickness of the deck over time.

The inspection report of [Gielen et al. \(2008\)](#) also evaluated the results of the ASR-monitoring. It was noted that the expansion in the longitudinal direction of the viaduct was reaching the maximum value. The measurements of the monitoring system can be compared to the ambient temperature from the official Dutch meteorological institute. The selected location is Gilze-Rijen, 14 km south of the viaduct Zijlweg. The full analysis of the data can be found in the experimental report ([Koekkoek et al., 2015](#)). In all plots, a clear correlation between the ambient temperature and the thickness, joint size, and moisture content can be seen. The average deck thickness follows the trend of the ambient temperature (see [Fig. 9.4](#)), whereas the joint size is inversely correlated to the temperature. The joint size decreases when the expansion in the longitudinal direction of the deck increases as a result of increasing temperatures. As such, the observed data follow the expectations. From the data, it is also seen that the moisture increase is only observed at one measurement point, and that this increase is limited.

9.3 Preparation of field assessment

9.3.1 Damage identification

The material properties were determined in the same period as when the field test was carried out. The concrete properties were determined based on six

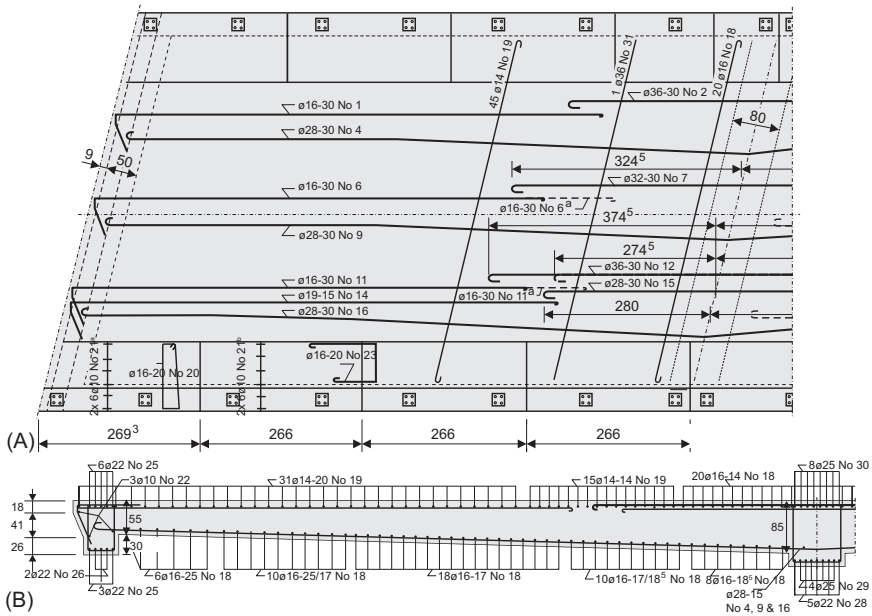


Figure 9.5 Reinforcement drawing: (A) top view; (B) side view. Bar diameters in (mm), all other dimensions in (cm).

core tests (Witteveen + Bos, 2014), resulting in a characteristic cylinder concrete compressive strength of 24.5 MPa and an average cube compressive strength of 44.4 MPa. The properties of the reinforcement steel were not determined based on sample tests. However, the symbols on the drawings indicate that plain reinforcement bars were used. These bars could be steel grade QR22 (with a characteristic yield strength of 220 MPa) or QR24 (with a characteristic yield strength of 240 MPa), and it is not specified in the drawings which grade was used. An overview of the reinforcement in viaduct Zijlweg is given in Fig. 9.5.

Prior to the field test, a visual inspection of the bridge was carried out. In this inspection, deterioration of the top deck was observed, which was limited to the edge of the sidewalk (see Fig. 9.6). As a result of the longitudinal expansion, the expansion joint between the deck and the abutment has become very small, as can be seen in Fig. 9.7. Given this problem with the expansion joint, it was decided to monitor the joint opening and closing during the proof load test. As a result of the ASR-damage, a typical cracking pattern (map cracking) was observed on the bottom of the slab bridge. Additionally, cracking on the side faces was detected. The drawing showing all detected cracking is given in Fig. 9.8.



Figure 9.6 Concrete deterioration of the sidewalk.



Figure 9.7 Closing of the expansion joint between the slab and the abutment.

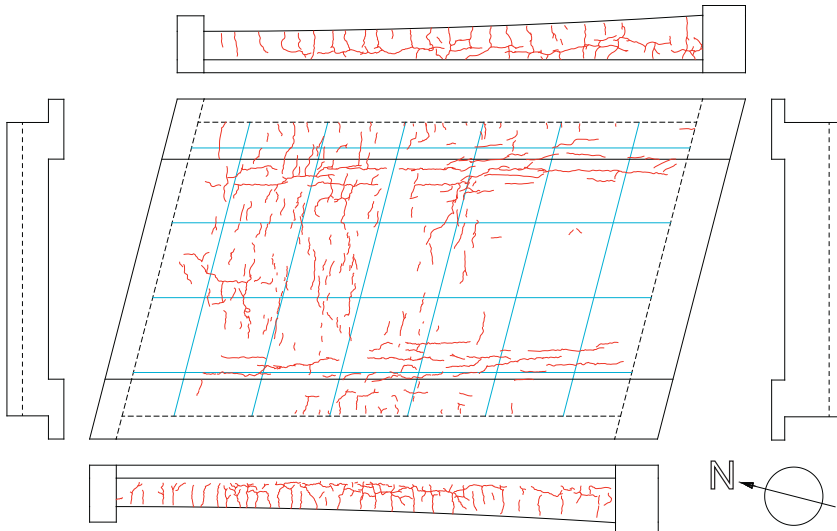


Figure 9.8 Map of cracks, showing bottom of slab and side faces.

9.3.2 Preparation of proof load test: shear and bending moment positions

The northernmost span, span 4 in Fig. 9.2, is used for a proof load test. The reason why the end span is used, is that this span is not directly above the highway, so that closing off the highway during the execution of the test is not required and no obstruction for the traveling public occurs. Span 4 has a varying thickness over the length. At the end support, the thickness is 550 mm. The thickness increases parabolically to 850 mm near the mid support. The parabola has a curvature radius of 150 m.

To define the positions at which the proof load should be applied, a linear finite element model is used. In this model, the sectional forces and moments are determined. The model is developed in TNO DIANA (TNO DIANA, 2012). The thickness of the slab in the transverse direction was considered to be uniform; the larger depth of the sidewalk was not modeled. Instead, an additional load was applied to represent the additional self-weight from the sidewalk. Shell elements were used in the model (eight-node quadrilateral isoparametric flat shell elements). The slab is modeled as 5.7 m wide instead of the full 6.6 m (see Fig. 9.2 for geometry). Elements with a height of 500 mm and a width of 483.15 mm were used in the model. The crossbeams at the intermediate supports have an element width of 410 mm and the crossbeams at the end supports have an element width of 250 mm. All crossbeams have elements of 500 mm height. The final mesh contains 106 elements in the longitudinal direction and 12 elements in the transverse direction. The two elastomeric bearing pads supporting the crossbeams are modeled as supports in the finite element model. Full details of the finite element model can be found in the analysis report of the proof load test (Koekkoek et al., 2015).

For an assessment of reinforced concrete slab bridges, a load combination containing the self-weight, superimposed dead load, and loads from the live load model (distributed lane loads, and concentrated live loads) is used. These loads are also applied to the finite element model. The self-weight (permanent dead weight) is automatically derived from the geometry modeled in the finite element model, using a load of 25 kN/m^3 . The load at the edge, resulting from the difference between the modeled 5.7 m and the real 6.6 m width, is applied as 2.3 kN/m . Additionally, the wearing surface of 46 mm of concrete is modeled by applying a distributed load of 1.15 kN/m^2 . The superimposed dead load (variable dead weight) is modeled as an asphalt layer of 110 mm with a load of 23 kN/m^3 .

For the live loads, Load Model 1 from NEN-EN 1991-2:2003 (CEN, 2003) is used, consisting of a distributed lane load and concentrated wheel load pertaining to a design tandem in each lane, as shown in Fig. 9.9. The wheel print of the design tandem is $400 \text{ mm} \times 400 \text{ mm}$ (see Fig. 9.9). An axle load of $\alpha_{Q1} \times 300 \text{ kN}$ is applied in the first lane, of $\alpha_{Q2} \times 200 \text{ kN}$ in the second lane, and of $\alpha_{Q3} \times 100 \text{ kN}$ in the third lane. Since the viaduct Zijlweg only has one lane, only $\alpha_{Q1} \times 300 \text{ kN}$ is applied. The values of α_{Qi} are nationally-determined parameters, which, for the Netherlands, all take the recommended value of $\alpha_{Qi} = 1$. The lane load equals $\alpha_{q1} \times 9 \text{ kN/m}^2$ for the first lane, and $\alpha_{qi} \times 2.5 \text{ kN/m}^2$ for all lanes with $i > 1$.

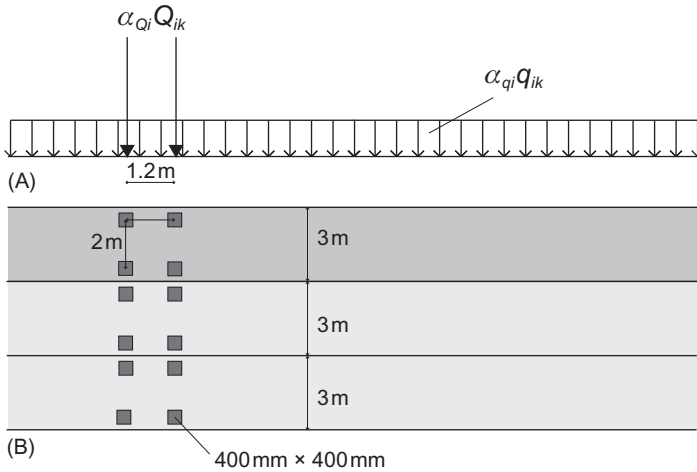


Figure 9.9 Live Load Model 1 from NEN-EN 1991-2:2003: (A) side view, (B) top view.

Again, the values of α_{qi} are nationally determined parameters, which, for the Netherlands, take the value of $\alpha_{qi} = 1$ when only one lane is present. The distributed lane load is applied over the width of the notional lane of 3 m, and pattern loading is used to find the most unfavorable loading arrangement. On the remaining width, $\alpha_{qr} q_{rk} = 2.5 \text{ kN/m}^2$ is applied with $\alpha_{qr} = 1$ and q_{rk} the distributed load on the remaining width of the viaduct. On the sidewalk, a pedestrian load of 5 kN/m^2 is applied. Additionally, since the viaduct has less than 250,000 vehicles per year, the reduction factors from NEN-EN 1991-2/NA:2011 (Code Committee 351001, 2011b) are used: 0.97 on the live loads from Load Model 1, and 0.90 on the remaining area. The reduction does not apply to the pedestrian load on the sidewalk.

The wheel print from Load Model 1, in Fig. 9.9, is $400 \text{ mm} \times 400 \text{ mm}$. Since the finite element model uses shell elements, the loads are applied at mid-depth. It is assumed that the load is distributed under 45 degrees over the height, (Fig. 9.10) so that the load is distributed over $950 \text{ mm} \times 950 \text{ mm}$ in the finite element model, or 2 by 2 elements. The load per wheel of 150 kN becomes a distributed load of 0.155 N/mm^2 . The tandem is centered in the notional lane of 3 m, so that distance between the edge of the lane and the face of the first wheel in the transverse direction equals 500 mm. The wheel print of the proof load tandem is $230 \text{ mm} \times 300 \text{ mm}$, which better corresponds to the actual wheel print of a vehicle. The same distribution, as shown in Fig. 9.10, leads to a contact area in the finite element model of $780 \text{ mm} \times 850 \text{ mm}$.

The viaduct Zijlweg has a skew angle of 14.4 degrees. Therefore, in the finite element model the position of the wheel prints is applied in two ways: parallel to the driving direction, and following the width direction. The analysis showed that, for bending moment, applying the loads parallel to the driving direction is more unfavorable and that, for shear, the position along the width is more critical (Fig. 9.11).

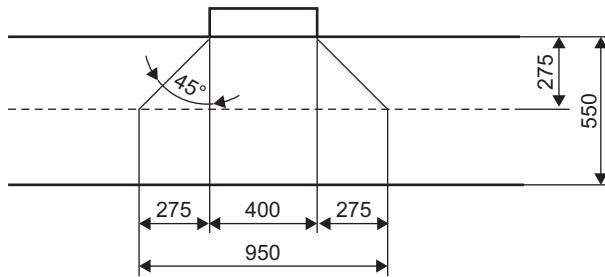


Figure 9.10 Distribution of wheel print over the depth.

Table 9.1 Overview of safety levels for new and existing structures in the Netherlands, with their respective load factors

Safety level	β	Reference period	γ_{sw}	γ_{sd}	γ_{LL}
ULS Eurocode	4.3	100 years	1.35	1.35	1.50
RBK design	4.3	100 years	1.25	1.25	1.50
RBK reconstruction	3.6	30 years	1.15	1.15	1.30
RBK usage	3.3	30 years	1.15	1.15	1.25
RBK disapproval	3.1	15 years	1.10	1.10	1.25
SLS Eurocode	1.5	50 years	1.00	1.00	1.00

with β the associated reliability index; γ_{sw} the load factor on the self-weight; γ_{sd} the load factor on the superimposed load; γ_{LL} the load factor on the live load.

The different safety levels that are used in the Netherlands are described in NEN-EN 1990:2002 (CEN, 2002) for new structures, in NEN 8700:2011 (Code Committee 351001, 2011a) for existing structures, with additional requirements for existing bridges in the Guidelines for the Assessment of Bridges (RBK) (Rijkswaterstaat, 2013). An overview of these safety levels, their corresponding reliability index, and reference period is given in Table 9.1. For a bridge assessed with a proof load test, a different load combination, see Table 9.2 is used. For this load combination, the load factor for the self-weight becomes 1.10. For an existing structure, the self-weight can be considered a deterministic value. Only the model factor remains, which equals 1.07 in NEN-EN 1991-2 + C1:2011 (CEN, 2011). This value can be rounded off to 1.10. So, for an assessment using the load combination with the Eurocode live loads, the load factors γ_{sw} , γ_{sd} , and γ_{LL} from Table 9.2 are used, whereas for preparations for a proof load test, the load factors γ_{sw} , γ_{sd} , and γ_{proof} from Table 9.2 are used.

To find the required load on the proof load tandem for the bending moment test, first the critical position is sought. For this purpose, the design tandem of the Eurocode is moved along the span (parallel to the driving direction as discussed previously) until the position that results in the largest sectional moment is found. Then, the Eurocode live loads are removed, and the proof load tandem is applied at the critical position. The load on the proof load tandem is then increased until the same sectional moment

Table 9.2 Load factors used in combination with a proof load test at the different safety levels

Safety level	γ_{sw}	γ_{sd}	γ_{LL}	γ_{proof}
ULS Eurocode	1.10	1.35	1.50	1.00
RBK design	1.10	1.25	1.50	1.00
RBK reconstruction	1.10	1.15	1.30	1.00
RBK usage	1.10	1.15	1.25	1.00
RBK disapproval	1.10	1.10	1.25	1.00
SLS Eurocode	1.00	1.00	1.00	1.00

with γ_{sw} the load factor on the self-weight; γ_{sd} the load factor on the superimposed load; γ_{LL} the load factor on the live load; γ_{proof} the load factor for the proof load tandem.

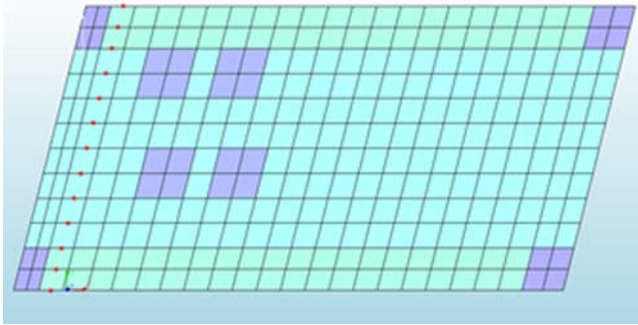


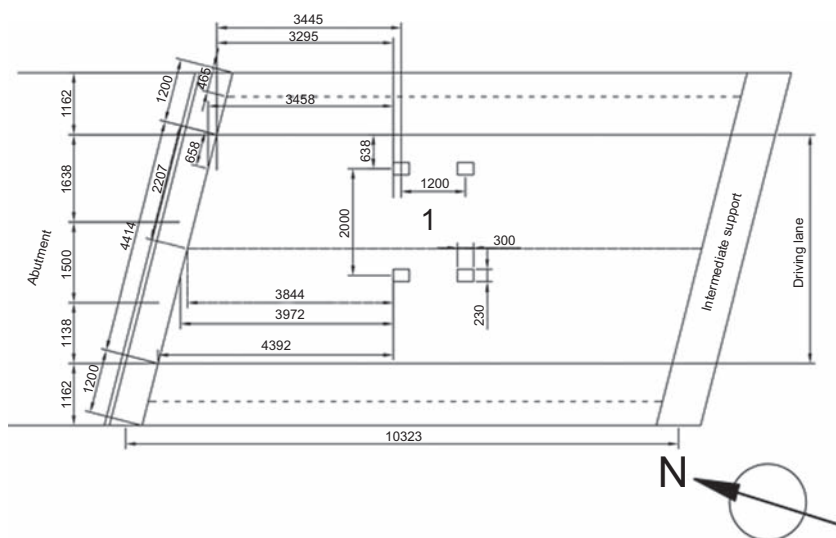
Figure 9.11 Overview of finite element model with critical position for shear.

is found for the load combination with the proof load tandem as with the Eurocode load combination. For bending moment, the critical position in span 4 of the viaduct Zijlweg is found at a face-to-face distance between the support and the tandem of 3382 mm (7 elements). The magnitude of the target proof load depends on the considered safety level. The resulting values for the required target proof loads are given in Table 9.3 as $P_{tor, bending}$.

For shear, the critical position is known to be at a face-to-face distance of $2.5 d_l$ between the load and the support (Lantsoght et al., 2013b), with d_l the effective depth to the longitudinal reinforcement. An overview of the finite element model is given in Fig. 9.12. This critical distance is derived from slab shear experiments in the laboratory (Lantsoght et al., 2013c, 2014, 2015a,b,c). This distance, however, has been derived for straight slabs, and the behavior of skewed reinforced concrete slabs in shear requires further research. Limited testing showed that the behavior of skewed slabs in shear is complex and that the failure mode changes as the skew angle changes (Cope et al., 1983; Cope, 1985). It is known that the obtuse corner results in the largest concentrations of shear stresses, so that the critical position is with the tandem in the obtuse corner. The peak shear stress in the linear finite

Table 9.3 Required target proof loads for different safety levels, for bending moment and shear

Safety level	$P_{tot, bending}$ (kN)	$P_{tot, shear}$ (kN)
ULS Eurocode	1259	1228
RBK design	1257	1228
RBK reconstruction	1091	1066
RBK usage	1050	1027
RBK disapproval	1049	1025
SLS Eurocode	815	791

**Figure 9.12** Position of proof load tandem for the bending moment test.

element model can be distributed over $4 d_f$, as was derived based on the comparison between linear finite element models and measurements of the support reaction for slabs (Lantsoght et al., 2013a). This averaged shear stress is then used for the analysis and for comparison between the shear stress caused by the load combination prescribed by the code, and the load combination with the proof load tandem. Both the design tandem and the proof load tandem are placed at a face-to-face distance of $2.5 d_f$ from the support. First, the sectional shear (averaged over $4 d_f$) is determined as caused by the load combination prescribed by the code. Then, the required proof load to get the same sectional shear (averaged over $4 d_f$) for the load combination that includes the proof load is determined. The proof load tandem is placed in the obtuse corner, which is known from the literature (Cope, 1985) to lead to the largest concentrations of shear stresses. Finite element models were made to study the difference for the viaduct Zijlweg between loading at the acute

and obtuse corner. It was confirmed that the critical position is in the obtuse corner (Koekkoek et al., 2015). Finally, the results of the target proof loads for shear $P_{tot, shear}$ for the different safety levels are determined, as shown in Table 9.3. It must be mentioned that proof load testing for shear is generally not permitted by the existing codes and guidelines, and that the development of stop criteria for a proof load test for shear is still the subject of research (Schacht et al., 2016a).

For practical reasons during the execution of the proof load test, the position of the load is slightly moved from the critical position determined based on the finite element models. The same centerline is kept for the test for bending moment as for the test for shear, so that the loading setup can be partially kept in place. This means that, during the execution, the supports can remain in place, but that the load spreader beams, jacks, and load cells need to be moved between the two experiments.

9.4 Execution of field assessment

9.4.1 Load testing procedures

The field tests on the viaduct Zijlweg were carried out on Wednesday, June 17, 2015. On Sunday, June 14th, all measurement equipment was brought to the test site. On Monday and Tuesday morning, all sensors were applied, and on Tuesday afternoon, all sensors were tested.

For the proof load tests at the shear- and flexure-critical positions, a cyclic loading protocol was used. According to the German guideline for load testing of buildings (Deutscher Ausschuss für Stahlbeton, 2000), each load test should be carried out in at least three steps, during which the maximum load in each step is kept constant for at least two minutes. The advantage of a cyclic loading protocol (Koekkoek et al., 2016) is that reproducibility, symmetry, and linearity of the measurements can be verified. For testing of the viaduct Zijlweg, four load levels were selected:

1. A low load level of about 40 ton, to verify if all sensors are functioning properly. If sensor malfunctioning is detected, it is possible to make corrections prior to continuing with the proof load test. In the bending moment test, corrections were necessary for the load cells at the first load level, and in the shear test, one linear variable differential transformer (LVDT) had to be placed within its measurement range.
2. The Serviceability Limit State load level. For this load level, large deflections or cracks are not expected to occur, and the behavior should be linear elastic. Prior to continuing to the next load level, the measurements are interpreted to see if it is safe to load to the next load level.
3. An intermediate load level, to build up to the target proof load. The measurements are followed closely, and based on the observed structural response, it is determined if the testing can be continued.
4. The target proof load, the RBK design level from Table 9.3, plus 5%. This load level does not require cycles, as the stop criteria and linearity of the measurements need not be interpreted to decide if further loading is allowed. The 5% additional loading is applied to cover the local variations in the material, and to take into account the fact that only two positions are tested.

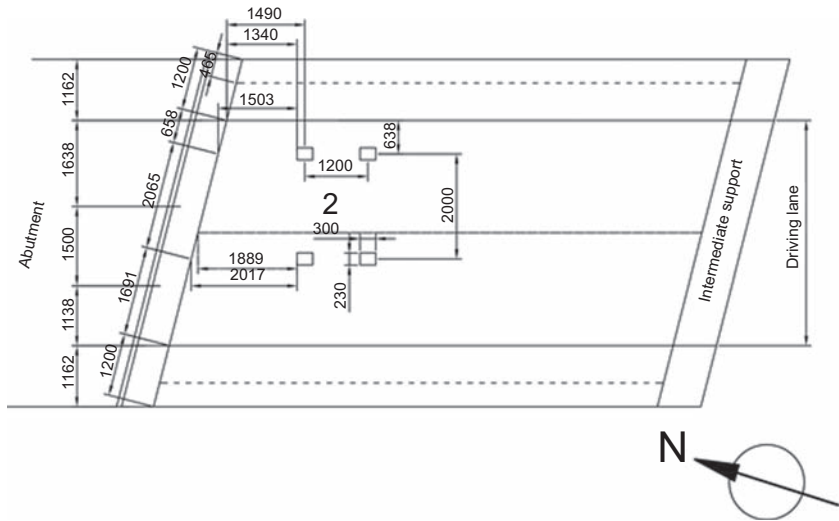


Figure 9.13 Position of proof load tandem for the shear test.

After each load cycle, the load is not returned to the level of 0 ton, but instead a lower threshold value of 10 ton is used. This minimum load level ensures that all sensors and the loading jacks remain activated, and avoids the occurrence of noise on the acoustic emission measurements, which are sensitive to full unloading. The aim was to keep the loading speed constant during the load test. However, the speed was determined by a manual operation, so that some deviations occurred. The position of the proof load tandem in the bending moment test is shown in [Fig. 9.12](#), and the position in the shear test in [Fig. 9.13](#).

9.4.2 Sensor plan

At various locations on the bottom of the slab, side faces of the slab, and at the joint, sensors are placed to follow different responses of the bridge during the proof load test. An overview is given in [Fig. 9.14](#). All data are measured in real time and shown on the measurement computer in the control center. These results are used after every load cycle to determine if further loading can be permitted. The following structural responses are followed during the proof load tests:

- deflections of the slab
- deflections of the crossbeams
- crack widths
- strains on the bottom of the slab
- rotation of the end support
- acoustic emission signals
- opening of the joint
- opening of cracks on the side face

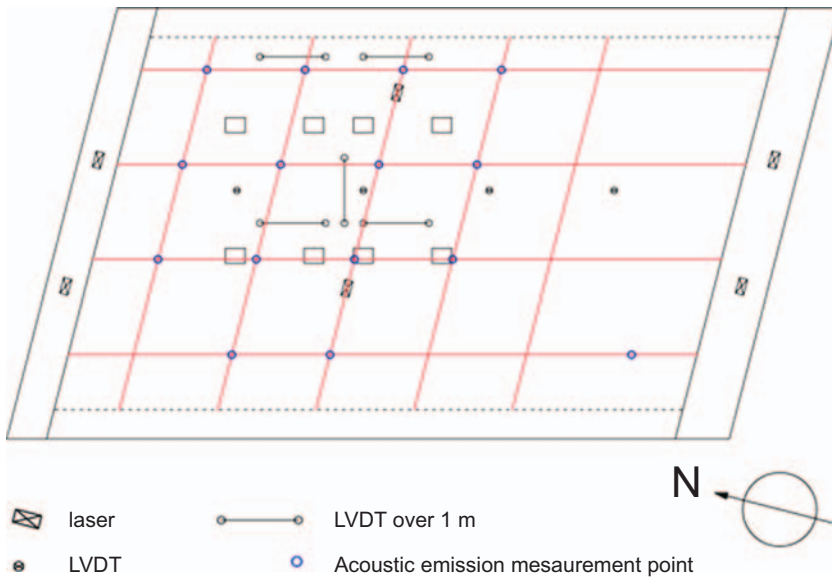


Figure 9.14 Overview of applied sensors.

These responses are measured with LVDTs and laser distance finders (lasers). The opening of cracks on the side face is monitored by applying gypsum over the crack and then checking after the test if the gypsum has cracked, which would mean that the crack was activated during the test. An overview of the applied sensors is given in [Table 9.4](#). In this chapter, the results of the acoustic emission signals are not discussed, as they are a topic of further research. The first analysis of the acoustic emission measurements is given elsewhere ([Yang and Hordijk, 2015](#)).

The vertical displacement of the deck is determined with measurements taken by laser distance finders and LVDTs. At the center of the notional lane, a row of four LVDTs is placed to determine the longitudinal deformation profiles. An additional LVDT is used to correct for the way the measurement frame is applied: it is attached to the slab at the mid support, but resting on the abutment at the end support. For the transverse deformation profiles, two lasers are used, at a location between the position of the wheel prints for the bending moment test and the shear test. The goal of measuring the deflections is to set up the deformation profiles in the transverse and longitudinal directions, to follow the load-displacement diagram in real time during the experiment, and to calculate residual deformations after each load step. The load-displacement diagram is used to detect non-linearity, and existing codes ([Deutscher Ausschuss für Stahlbeton, 2000](#), [ACI Committee 437, 2013](#)) give limits to the residual deformation as a stop criterion. An overview of the applied lasers and LVDTs for measuring the displacements is given in [Fig. 9.15](#). The vertical displacement of the crossbeams at the end support

Table 9.4 Overview of applied sensors, measurement range, and their application

Name	Range (mm)	Application
LVDT1	10	Strain over 1 m
LVDT2	10	Strain over 1 m
LVDT3	10	Strain over 1 m
LVDT4	10	Reference for change in temperature
LVDT5	20	Deflection of the slab (on a longitudinal line)
LVDT6	20	Deflection of the slab (on a longitudinal line)
LVDT7	20	Deflection of the slab (on a longitudinal line)
LVDT8	20	Deflection of the slab (on a longitudinal line)
LVDT9	10	Displacement of the joint
LVDT10	10	Displacement of the joint
LVDT11	10	Displacement of the joint
LVDT12	10	Displacement of the joint
LVDT13	10	Deflection of the slab (on a longitudinal line)
LVDT14	10	Crack width
LVDT15	10	Crack width
LVDT16	10	Crack width
Laser1	100	Deflection of the slab (on a transverse line)
Laser2	20	Deflection of the slab (on a transverse line)
Laser3	20	Deformation of support (N)
Laser4	20	Deformation of support (N)
Laser5	100	Deformation of support (S)
Laser6	100	Deformation of support (S)

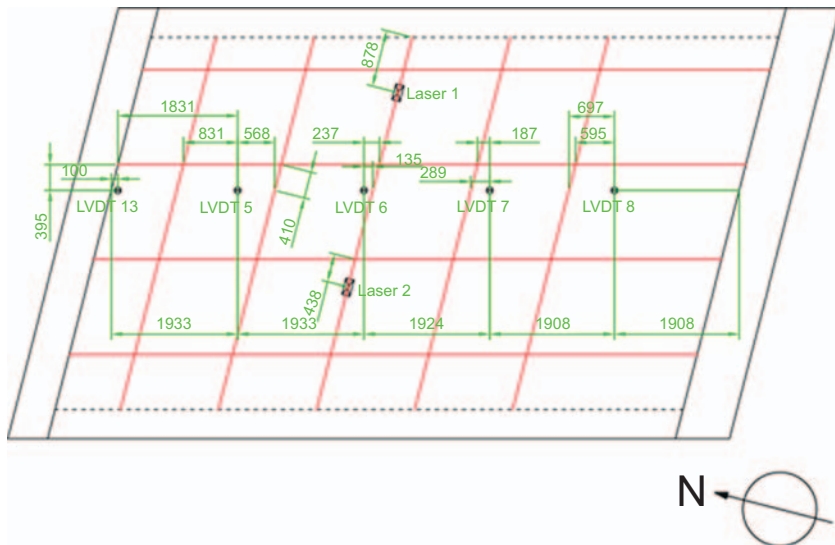


Figure 9.15 Applied sensors for measuring deflections of the slab.

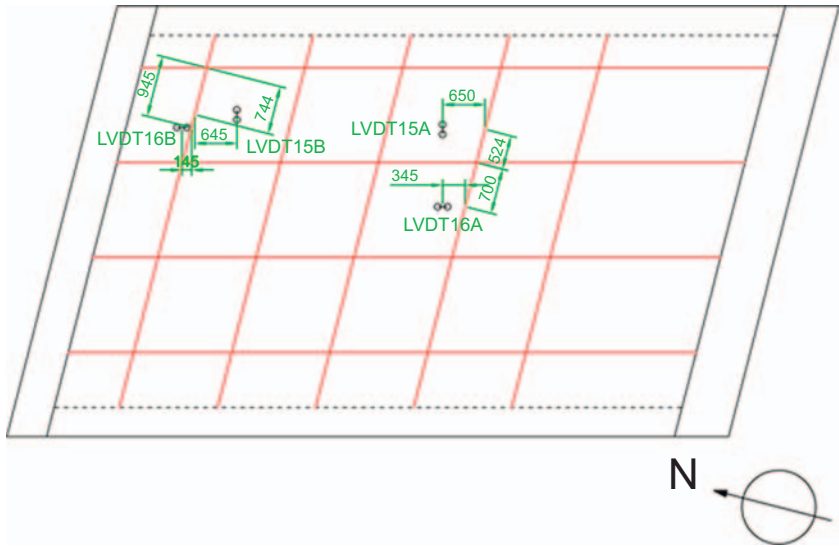


Figure 9.17 Applied linear variable differential transformers (LVDTs) for measuring the crack widths during the test. Position “A” is the bending moment test, and position “B” is the shear test.

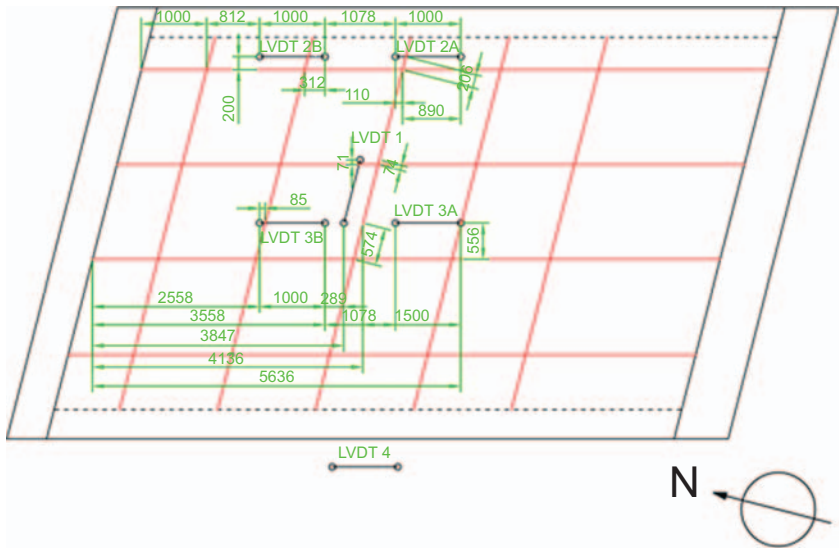


Figure 9.18 Applied linear variable differential transformers (LVDTs) for measuring strains during the test (not showing the reference LVDT). Position “A” is the bending moment test, and position “B” is the shear test.

The expansion caused by ASR resulted in a clear expansion of the viaduct in the longitudinal direction, leaving less space for the joint. To measure the movement in the joint and the rotation of the end support, and to check if, at some point, insufficient space is left in the expansion joint, and/or if the required rotation of the bridge deck during the proof load tests becomes restrained, two LVDTs are placed on both sides of the viaduct. The LVDTs measure the joint horizontally. One end of the LVDT is connected to the abutment and the other end to the slab. The layout of the LVDTs on the joint at the west side of support 5 is shown in Fig. 9.19. For the east side, LVDTs are applied at the same positions as for the west side; the only difference then is the numbering of the LVDTs, which are LVDT11 and 12 for the east side.

A final measurement is the measurement of the applied load during the proof load test at the four different wheel prints by four separate load cells. The load cells have a capacity of 1000 kN and an accuracy of 1% (10 kN). The measurements of the load are important during the proof load test, as they are used to follow the load-displacement diagram in real time. When the load-displacement diagram ceases to be linear, one of the stop criteria is exceeded.

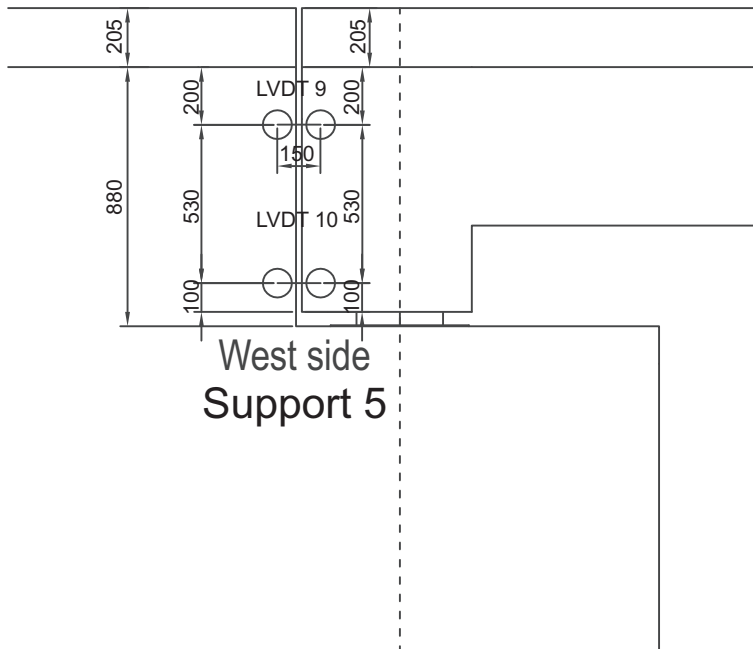


Figure 9.19 Position of linear variable differential transformers (LVDTs) that measure joint opening and rotation, on the west side of the support. The east side is symmetric.

9.5 Postprocessing of field assessment

9.5.1 Test results

First, the results of the proof load test at the flexure-critical position are studied. The maximum measured load in the proof load tandem was 1332 kN. Adding the weight of the steel plate and jacks results in a total load of 1368 kN. Nonlinearity is studied, based on the envelope of the load-displacement diagram, in which the measured load on the four jacks is used. The envelope of the load-displacement diagram is given in Fig. 9.20. The straight lines indicate the tangent to the load-displacement diagram, or the stiffness. If the angle of the straight lines changes significantly, nonlinear behavior is observed. In the third straight line, the stiffness has decreased mildly, whereas for the last loading and unloading step, stiffening occurred in the unloading branch. This stiffening could be caused by redistribution of stresses at the higher loads, interaction between the applied loading frame and the structural behavior of the bridge, or the lower loading speed in the last loading step.

The LVDTs in the longitudinal direction are used to plot the deflection in the span direction at the different load steps. The results show behavior as expected, (see Fig. 9.21 in which the axles of the proof load tandem are indicated as well). As expected, the LVDT under the proof load tandem measures the largest deflections. A similar plot, seen in Fig. 9.22, can be made for the transverse direction. In the

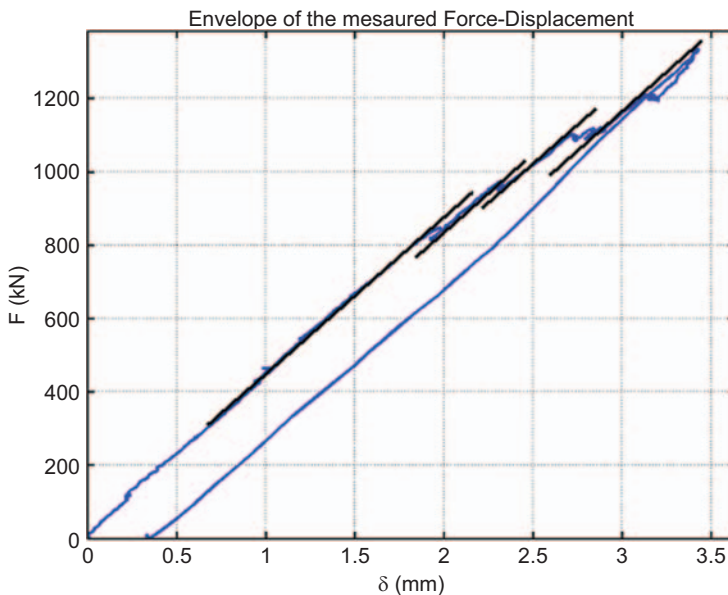


Figure 9.20 Envelope of load-displacement diagram for the bending moment test. The straight black lines indicate the tangent to the diagram, i.e., the stiffness.

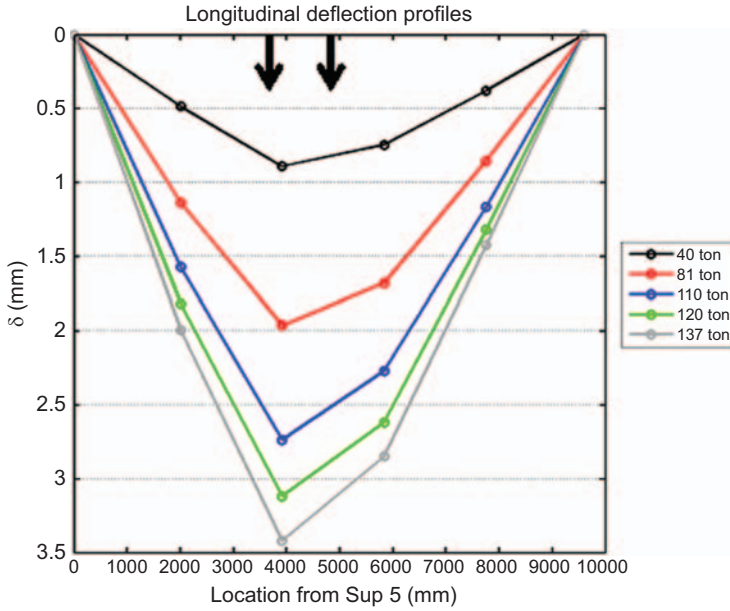


Figure 9.21 Deflection plots in the longitudinal direction for the bending moment test, indicating the position of the proof load tandem.

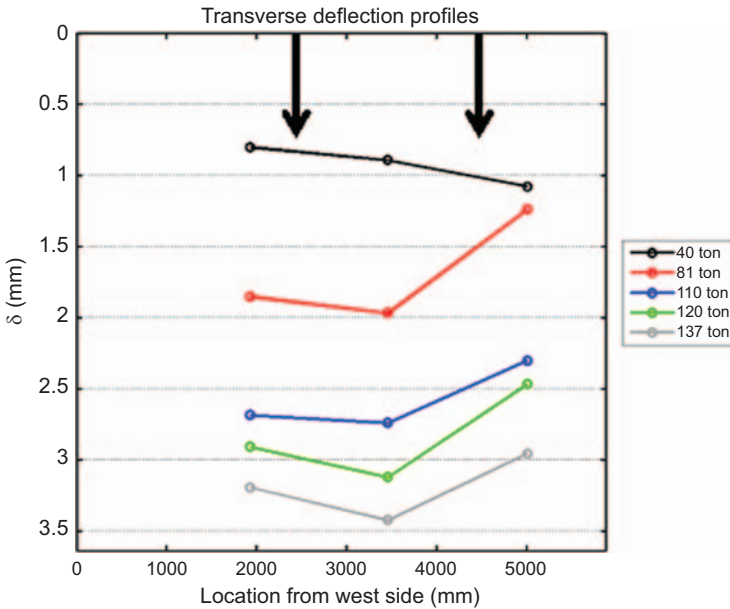


Figure 9.22 Deflection plots in the transverse direction for the bending moment test, indicating the position of the proof load tandem.

transverse direction, the measurement point closer to the sidewalk is deflecting more at lower load levels, and less at higher load levels. A possible explanation for this observation is that, at low load levels, the behavior is less stiff because of the observed cracking on the side of the slab with the sidewalk. The larger stiffness at higher loads can be explained by the presence of stirrups in the sidewalk. The measured strains are fully linear.

Three cracks were followed during the proof load test. LVDT14 measures a possibly critical shear crack, LVDT15 measures a longitudinal crack on the bottom of the slab, and LVDT16 a transverse crack. The results of the crack width for different load levels during the test was plotted (see Fig. 9.23). From this plot, it can be seen that the possible shear crack was not activated by the test. The longitudinal crack was activated and the behavior was mostly linear. The transverse crack was more activated than the longitudinal crack. Note that the maximum increase in crack width for all measured cracks was very small, and that no signs of nonlinearity are observed. Finally, the results of the measurements of the reference LVDT are shown in Fig. 9.24. These strains are compared to the ambient temperature, taken from the published measurements of the Dutch Royal Meteorological Institute (KNMI, 2015) for a location 14 km south of the load testing location, as well as to the average temperature of the bridge deck, which is measured as a part of the ASR-monitoring system. It can be seen that the behavior of the temperature of the bridge deck and the ambient temperature is similar. The behavior of the strain is inversely proportional to the temperature. A negative strain represents compression of the LVDT, or elongation of the aluminum strip, which is caused by the

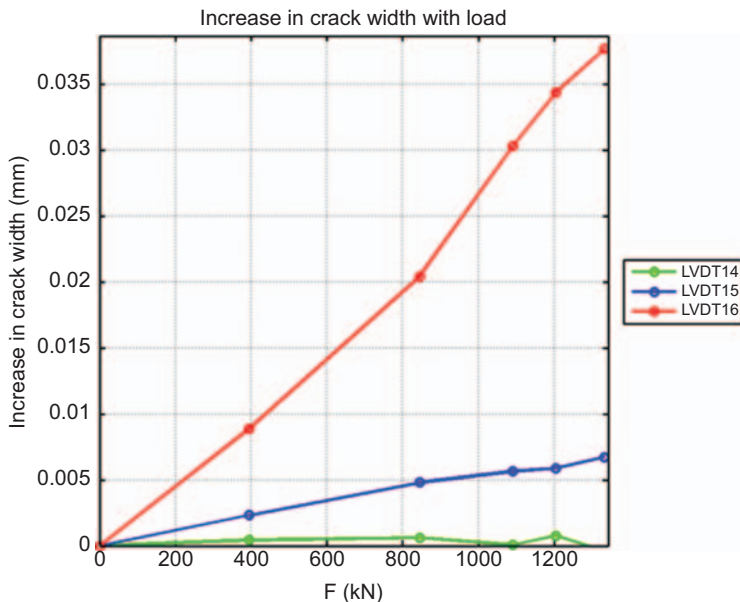


Figure 9.23 Measured crack width for selected load levels during the bending moment test.

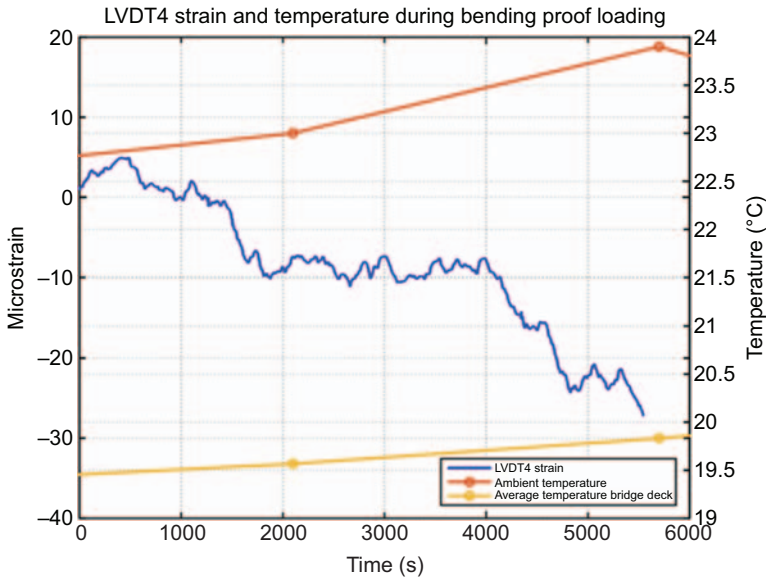


Figure 9.24 Strain measured by LVDT4 during the bending moment test, compared to ambient temperature and average temperature of bridge deck.

increasing temperature. The measured strains thus are as expected, and they are used to correct the strains measured on the bottom of the slab.

Now the results of the proof load test at a shear-critical position can be revised. The load-displacement diagram is shown in Fig. 9.25. The maximum applied load during the proof load test for shear was 1342 kN, which leads to a maximum load of 1377 kN, taking into account the weight of the jacks and the steel plate. From the load-displacement diagram (Fig. 9.25), it can be seen that the behavior is fully linear and that no signs of nonlinearity are observed. Next, the deflection plots in the longitudinal direction are shown in Fig. 9.26. All results are as expected, except for the last measurement point. A more detailed study of the output of this LVDT showed that the results were suddenly shifted to larger strains between 600 and 1100 kN, and then shifted back to smaller strains afterwards. This observation is explained by the fact that the LVDT was possibly out of its measurement range, resulting in it being fully compressed, and only being able to move slightly as result of changes in the aluminum measurement frame due to temperature. The deflection plot in the transverse direction is as expected, see Fig. 9.27. The deflection under the sidewalk is slightly less than the deflection in the span, which is expected since the sidewalk is provided with shear reinforcement and thus has slightly stiffer behavior. The measured strains are fully linear. Again, the opening of three cracks was followed with LVDT14 over a possible shear crack at the same position as during the bending moment test, LVDT15 over a longitudinal crack on the bottom face and LVDT16 over a transverse crack on the bottom face. The increase in crack width with the applied load is shown in Fig. 9.28. It can be seen that all monitored

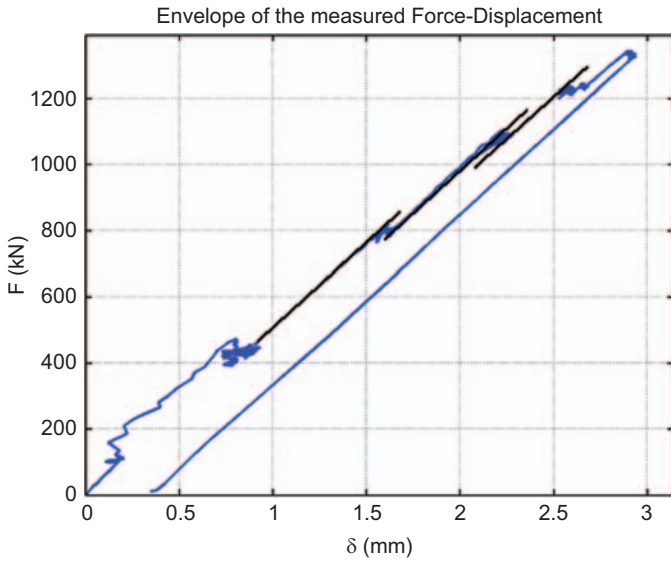


Figure 9.25 Envelope of load-displacement diagram for the shear test. The straight black lines indicate the tangent to the diagram, i.e., the stiffness.

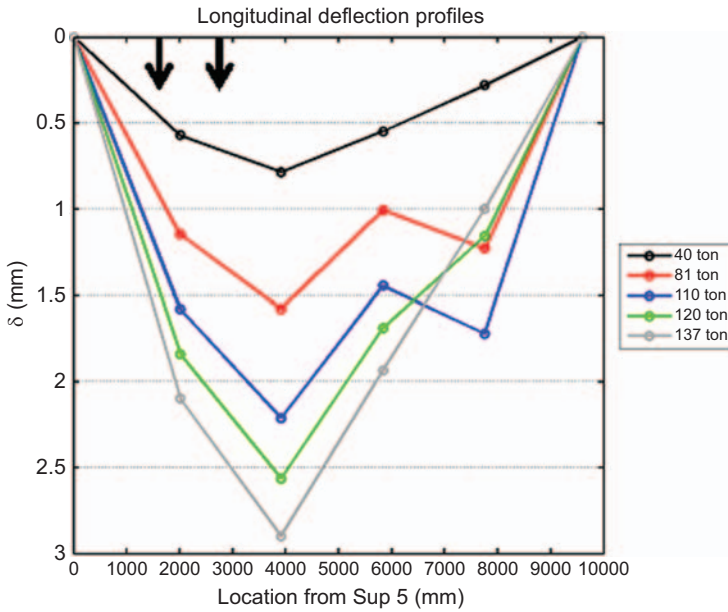


Figure 9.26 Deflection plots in the longitudinal direction for the shear test, also indicating the position of the proof load tandem.

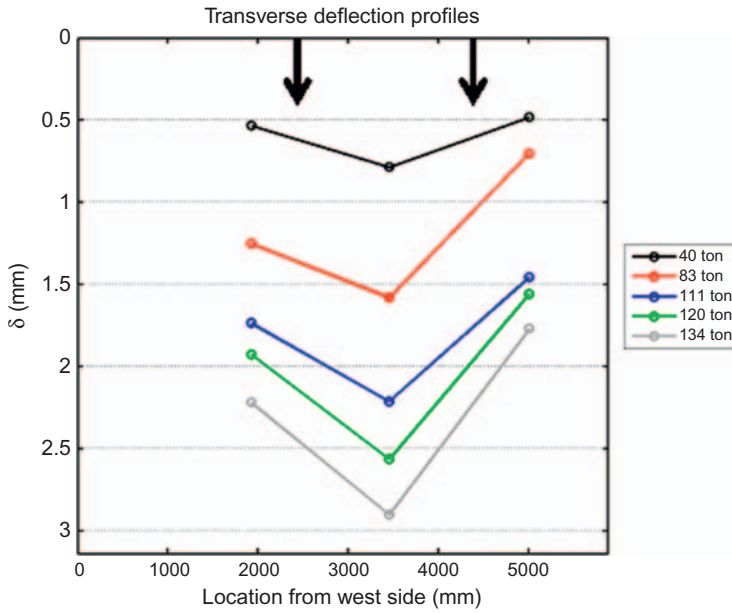


Figure 9.27 Deflection plots in the transverse direction for the shear test, also indicating the position of the proof load tandem.

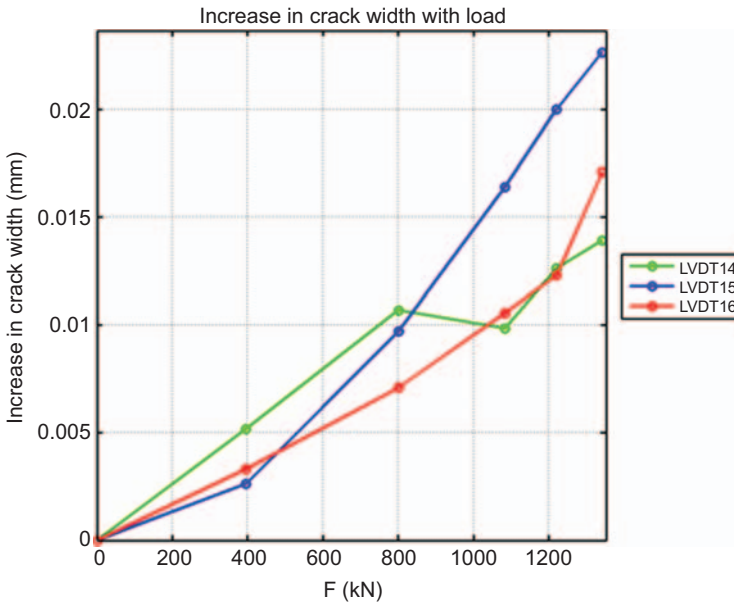


Figure 9.28 Measured crack width for selected load levels during the shear test.

cracks are slightly activated (note that the maximum crack width is less than 0.025 mm). The increase in crack width in the possible shear crack was small and linear, and did not cause concerns about the structural safety of the tested bridge. The joint did not fully close or cause rotation during the experiment, and the effect of temperature was as discussed for the bending moment test.

9.5.2 Discussion and comparison to international guidelines

In the German guideline ([Deutscher Ausschuss für Stahlbeton, 2000](#)), stop criteria are defined. These criteria are derived from the output of the sensors, and indicate when further loading is not permitted. The stop criteria from the German guideline can be used for bending moment. For shear, currently no stop criteria are defined, but research on this topic has been carried out ([Schacht et al., 2016a](#)). Since shear is a brittle failure mechanism, this failure mode needs to be avoided, and adequate stop criteria need to be defined. For this purpose, the acoustic emission measurements are used as well, to gain more insight in the internal cracking occurring in the slab during the load test. As no stop criteria for shear are defined, the acoustic emission signals were followed closely to capture signs of increased cracking activity and instable crack development, and the output of all sensors was closely followed to capture signs of changes to the structure and nonlinearity. Moreover, the effect of ASR-damage on the shear capacity is unknown. On one hand, the cracking caused by ASR reduces the uniaxial tensile strength, which is expected to reduce the shear capacity. On the other hand, the restraint of expansion in the direction of the reinforcement creates a prestressing effect on the cross-section, which increases the shear capacity. As such, one has to be extra careful when proof loading a shear-critical viaduct with ASR-damage.

In this section, the stop criteria from the German guideline are analyzed ([Deutscher Ausschuss für Stahlbeton, 2000](#)). These stop criteria are derived for buildings, and only consider flexure. Further research on stop criteria is necessary for the application to proof load testing of existing concrete bridges that are shear-critical. The first stop criterion from the German guideline says that the ratio of the residual to maximum deformation is limited to 10%. For the bending moment test, this ratio was 9.7% and for the shear test 9.7%. For both proof load tests, the first stop criterion is thus fulfilled. It must be remarked here that the residual deformation during the proof load test is measured at the moment when the base load level is still acting on the bridge. Unloading to 0 kN is not used during the bridge to keep all sensors activated. Therefore, a recommendation for the development of stop criteria that can be used during a proof load test would be to express the stop criterion for the residual deformation differently. The new expression then would take into account the fact that no full unloading occurs after each load cycle. Moreover, it should be defined if the residual deformation after the i -th load cycle is based on the difference between the start of the test and load cycle i , or based on the difference between load cycles $i-1$ and i .

The second stop criterion from the German guideline considers the strains in the steel. Typically, a bridge owner might not allow the removal of the concrete cover

to measure the steel strains. Therefore, this stop criterion is considered as not practical for the load testing of bridges. The third stop criterion considers the strains measured in the concrete. This stop criterion is formulated as follows:

$$\varepsilon_c < \varepsilon_{c,lim} - \varepsilon_{c0} \quad (7.1)$$

with ε_c the measured strain in the concrete, $\varepsilon_{c,lim}$ the limiting strain of $800 \mu\varepsilon$, and ε_{c0} the strain caused by the permanent loads. The maximum strain observed in the bending moment experiment is $240 \mu\varepsilon$ at LVDT2. The value of ε_{c0} is determined from the linear finite element program. As a result, the maximum measured strain has to be smaller than $800 \mu\varepsilon - 38 \mu\varepsilon = 762 \mu\varepsilon$, and this requirement is fulfilled. The maximum strain in the shear experiment was $224 \mu\varepsilon$ at LVDT2, and the strain caused by the permanent loads is taken from the finite element model as $45 \mu\varepsilon$. The requirement now becomes that $224 \mu\varepsilon$ has to be smaller than $800 \mu\varepsilon - 45 \mu\varepsilon = 755 \mu\varepsilon$, and this requirement is fulfilled.

The last stop criterion from the German guideline is related to crack width. The guideline has different requirements for existing cracks and newly developed cracks. Since the two proof load tests only monitored existing cracks, only the stop criteria for existing cracks need to be verified. The first requirement is that the maximum crack width increase during the proof load test, $\Delta w \leq 0.3$ mm. The second requirement considers the residual crack width, after a load cycle, for which it holds that the value of the residual crack width $\leq 0.2 \times \Delta w$. An overview of these results is given in Table 9.5 for the bending moment test and in Table 9.6 for the shear test. For both cases, it can be seen that the studied crack widths are extremely small. In general, crack widths smaller than 0.05 mm can be neglected (Koekkoek et al., 2016). When neglecting the small crack widths, the conclusion is that none of the cracks was activated nor needs to be considered. When following the German guideline for crack widths, regardless of how small they are, it is found that all requirements are fulfilled in the bending moment test. For the shear test, the requirement for the residual crack width is not fulfilled. However, no signs of distress were observed during the proof load test, and it can be recommended to add the requirement that crack widths smaller than 0.05 mm be neglected to the prescribed requirements for maximum and residual crack width. The physical significance of cracks smaller than 0.05 mm is almost nonexistent.

Table 9.5 Overview of maximum and residual crack width, and the limitation to the residual crack width during bending moment test

	Measured Δw (mm)		$0.2 \times \Delta w$ (mm)
	During proof loading	After proof loading	
LVDT14	0.0163	0.0147	0.00326
LVDT15	0.0248	0.0117	0.00496
LVDT16	0.0183	0.0061	0.00366

Table 9.6 Overview of maximum and residual crack width, and the limitation to the residual crack width during shear test

	Measured Δw (mm)		$0.2 \times \Delta w$ (mm)
	During proof loading	After proof loading	
LVDT14	0.0163	0.0147	0.00326
LVDT15	0.0248	0.0117	0.00496
LVDT16	0.0183	0.0061	0.00366

9.5.3 Repair recommendations

Both proof load tests on the viaduct Zijlweg were carried out successfully. It was shown experimentally that the viaduct can carry the loads prescribed by the code, using the load factors of the RBK Design load level with an additional 5%. This means that the structure fulfills the same requirements as a designed and newly built structure. The viaduct was monitored closely with a large number of sensors during the experiments, and no signs of distress were found. The final conclusion is that it is safe to keep the viaduct open to all traffic, and that load restrictions and posting are not necessary. This conclusion is important, because the very low uniaxial strength of the concrete with ASR-damage led to discussions about the shear capacity of the viaduct. To prevent durability problems resulting from further cracking caused by ASR, a waterproofing layer on top of the slab was added in 2002. Since moisture is necessary for the ASR gel to expand and cause cracking, providing waterproofing and preventing the ingress of moisture are a good solution to prevent further cracking and future durability problems. Moreover, regular inspections and continued monitoring of the effects of ASR are necessary. Special attention should be paid to the space in the expansion joints, which has become small as a result of the longitudinal expansion of the slab caused by ASR.

9.6 Cost of decision-making based on field assessment

9.6.1 Replacement cost: economic, environmental, and social

In the field of bridge engineering, the current trend is to consider the lifecycle cost of the structure (Frangopol et al., 2016). From the past concept of only considering the cost of design and construction, bridge engineering is moving towards a concept of determining the cost of design, construction, inspection, maintenance, strengthening, demolition, and the salvage value (Kim and Frangopol, 2011). These costs are the so-called economic costs. For a full sustainability analysis of a bridge, the environmental and social cost need to be determined as well (Gervasio et al., 2012, Beck et al., 2012). For buildings, rating for sustainability is a common practice. For

bridges on the other hand, sustainability analyses are still the topic of research. In the majority of the cases, when tendering a bridge project, it is the offer with the lowest initial cost that is most successful (Beck et al., 2012). In some countries, such as the United Kingdom where the Sustainability Index for Bridges is developed (Hendy and Petty, 2012), bridge authorities are trying to turn the tide. In general, five stages are considered during the life of a structure (Beck et al., 2012):

1. the product stage,
2. the construction process,
3. the usage stage,
4. the end-of-life stage, and
5. the stage identified as “supplementary information beyond the building life cycle”, which contains benefit and loads beyond the system boundary.

In bridges, the operation phase plays a much less important role than in buildings. As a result, the relative importance of the construction stage and end-of-life stage increases. During the end-of-life stage, the total sustainability impact is determined by the demolition processes, transportation of materials, and finally waste processing for reuse, recovery, and recycling.

To assess the sustainability impact of field testing, the economic, environmental, and social impact should be addressed. The Sustainability Index for Bridges from the United Kingdom (Hendy and Petty, 2012) pays attention to the influence on climate change and the use of resources as well. The analysis will be carried out assuming that the superstructure of the viaduct Zijlweg should be replaced, and will then be compared to the result of the field test, which shows that the viaduct still fulfills all requirements. The difficulty in determining the impact on sustainability, is that a number of parameters must be combined. Not all of these parameters can be determined in quantitative terms. Moreover, combining elements from the fields that study the effect on the environment and on society require a basic insight in concepts that are generally not covered in engineering education. An additional challenge is to determine how to weigh the different elements that form part of the full assessment. These different problems should be thought through and analyzed before a certain repair or replacement scheme is selected.

9.6.2 Cost savings through field assessment

To determine the cost savings obtained from the field testing of the bridge, the sustainability cost of replacing the ASR-affected superstructure of the viaduct Zijlweg is studied and compared to the cost of field testing. It must be noted here that the structure that is found to be sufficient in a field test can still require replacement later during its service life. Moreover, since the topic of the application of proof load testing to shear-critical structures is still under development, it is expected that the cost of proof load testing will decrease significantly once standardization of the procedures is obtained.

First, the economic cost of replacing the superstructure is determined. This cost can be calculated based on the assumption of a cost of 800–1000 €/m², which is the construction cost for slab bridges in the Netherlands. The viaduct Zijlweg has four spans: two end spans of 10.32 m and two mid spans of 14.71 m. The width is 6.6 m, so that the total area equals 330.4 m². The economic cost of replacing the superstructure would thus lie in between 264300 and 330400 €, assuming that the geometry is not altered. If a bridge that facilitates more than one lane of traffic should be built, then the cost increases, and an additional complication becomes that the existing substructure might not be sufficient to carry the additional loading.

To assess the environmental impact of replacing the superstructure, the Carbon Calculator for Construction Activities is used (Environment Agency, 2016). First, the total volume of concrete needs to be determined. Since the thickness of the slab varies between 550 and 850 mm, the average value of 700 mm is used for these exploratory calculations. Multiplying this value with the area of 330.4 m² gives a volume of 232 m³ of concrete, assuming that the design of the replacement bridge will be very similar to the existing bridge. Then, the amount of reinforcement steel needs to be determined. Using the assumption of 120 kg of steel per 1 m³ of concrete leads to an approximate value of 28 ton. If the distance between reinforcement steel producer and construction site is 75 km, the footprint of the reinforcement steel becomes 41 ton CO₂. Then, for 232 m³ of concrete with an exposure class of XC4, and assuming a distance of 20 km between the plant and the construction site, the estimated carbon footprint becomes 67 ton CO₂. The effect of transportation of fewer than 8 people on site for 48 weeks gives a footprint of 15 ton CO₂ for the transportation of personnel. The total footprint then becomes 109 ton CO₂. A breakdown of the contributions is shown in Fig. 9.29. In this calculation, a few elements are not considered. The lifecycle conversion factors for waste disposal are not considered. The emissions from plant and equipment, which is the fuel consumption on site and the distance over which this fuel is transported, is not considered. The choice of fuel depends on the contractor, and is difficult to estimate a priori. This fuel consumption needs to be split between the plant and equipment used on site, and the site accommodations. For example, a diesel generator can be used to power a mobile plant as well as site offices. For the considered small project, only site offices would be powered. The choice of fuel, and the amount of water used on site, can then be used to calculate this additional contribution to the carbon footprint.

The breakdown shown in Fig. 9.29 is based on Portland cement. Since the largest contribution to the carbon footprint of the construction of the superstructure comes from the concrete, it is interesting to explore the effect of using different types of cement. The types of cement that are analyzed here are: Portland cement (with 6% limestone), Portland fly ash cement (with 28% of fly ash), Portland slag cement (with 35% of ggbs), blastfurnace slag (with 80% of ggbs), and Pozzolanic cement (with fly ash and 45.5% of ggbs). The results of this analysis, and the resulting reduction on the total CO₂ footprint are shown in Table 9.7. These calculations are based on the assumption that 14% of the weight of the total concrete is the weight of cement. For 232 m³ of concrete, assuming 2.4 ton/m³, a weight of

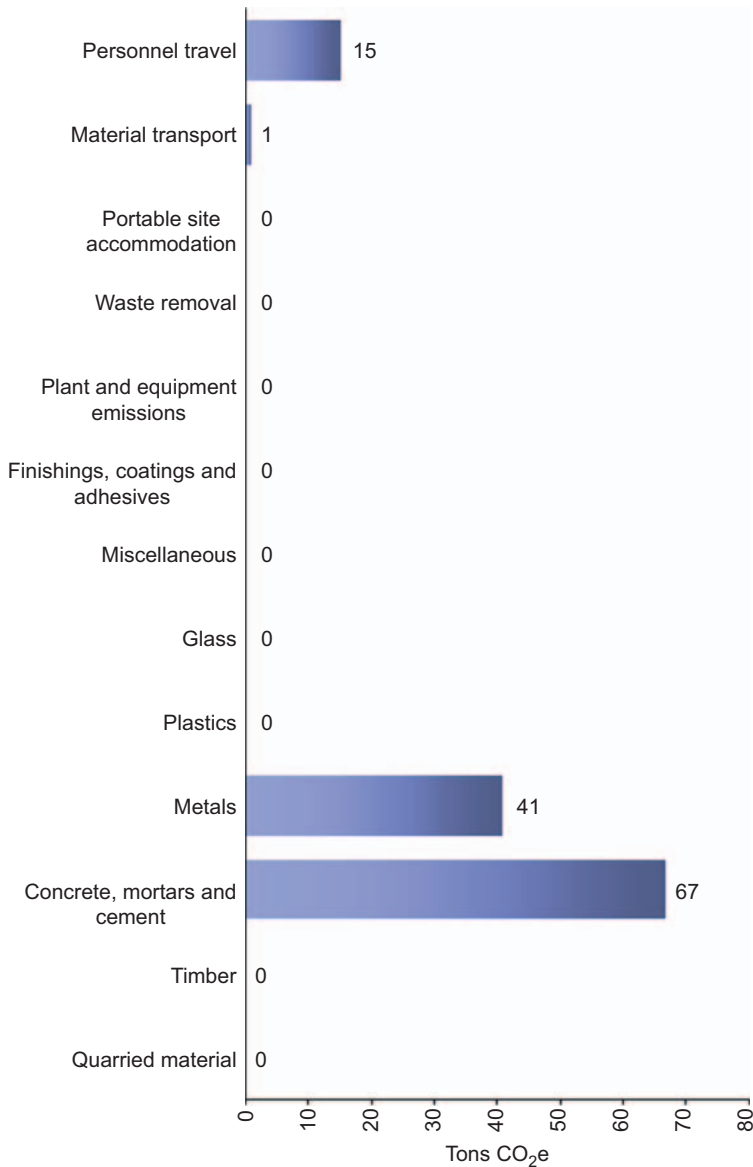


Figure 9.29 Breakdown of contributions of construction materials and transportation on total carbon footprint of replacement of superstructure.

556.8 ton of concrete is found, which equals 78 ton of cement. The effect of this amount of cement is studied in [Table 9.7](#). The effect of improved concrete mixtures with reduced amounts of cement is not considered here. In [Table 9.7](#), it becomes clear that significant reductions of the carbon footprint can be achieved

Table 9.7 Effect of choice of type of cement on total carbon footprint of replacement of superstructure

Type of cement	CO ₂ emission (tCO ₂ e/ton)	Total CO ₂ cement (ton)	Total CO ₂ superstructure (ton)	Saving (%)
Portland cement	0.88	68.60	110.2	–
Portland fly ash cement	0.67	52.23	93.83	14.9
Portland slag cement	0.62	48.33	89.93	18.4
Blastfurnace slag	0.23	17.93	59.53	46.0
Pozzolanic cement	0.51	39.76	81.36	26.2

when blastfurnace slag (with 80% ggbs) is used: 46% of the carbon emissions can then be saved as compared to the case with Portland cement (with 6% limestone). In the Netherlands, blastfurnace slag is the most common choice for cementitious material, for reasons of availability. The environmental impact of this standard choice is large, and positive.

Finally, the social dimension depends on a large number of aspects, such as visual impact, time delays, job opportunities, and more (Zinke et al., 2012). Currently, the social impact is most often calculated based on the driver delay costs. These driver delay costs are caused by delays resulting from the obstruction of traffic at the construction site, and the need for drivers to use another route, where more congestion is created. These costs depend, by and large, on the location of the structure. It is important to study these costs, as it has been shown that for bridges in densely-populated areas, the delay costs can be about 9 times higher than the direct economic costs (Zinke et al., 2012). The viaduct Zijlweg serves less than 250,000 vehicles per year. If a driver delay cost of 10 €/vehicle/hour is assumed, and a reroute to the next bridge creates a 20-minute delay, the total driver delay cost for a year of demolition and replacement can be estimated at 833,000 €, which is 2.8 times larger than the direct economic cost. This first estimate already shows that even for a bridge that is subjected to only local traffic, the social impact caused by driver delays is significant.

For the proof load testing, similar calculations can be carried out. Again, it must be stressed that further standardization and implementation of proof load testing will reduce the costs. Moreover, the practice of proof load testing of shear-critical structures is still in the stage of research, which makes the cost of the minimum required instrumentation and other minimal requirements difficult to estimate.

The economic cost includes the cost of the load application, the cost of material research, the cost of scaffolding and site provisions, and a budget for research on the topic of proof load testing related to this pilot. As such, the economic cost of about 80,000 € is a cost that can be reduced once standardization of the procedures is in place. It must be noted as well that this cost includes a budget for research to achieve

standardization and optimization, whereas no research budget is required for the option of replacement of the superstructure. The environmental impact is now only caused by the transportation of people to the construction site, and is about 0.3 ton CO₂. For the social cost, the driver delays are calculated assuming a price of 10 €/vehicle/hour and a detour of 20 minutes. The bridge was closed for 5 days, so an estimated 3425 vehicles were affected, resulting in 11,415 € in driver delays. This value is most likely even lower, as the testing was carried out during the summer holidays.

The presented calculation of the sustainability cost shows the important economic, environmental, and social savings that result from an improved assessment of reinforced concrete slab bridges through the use of proof load testing. A replacement of the ASR-affected superstructure would cost on average 297,000 €, create carbon emissions of at least 60 ton CO₂ if blastfurnace slag with 80% ggbs is used, and would create significant additional costs caused by driver delays. The successful proof load tests showed that the ASR-affected superstructure still fulfills the requirements with regard to strength, and can carry the prescribed loads without signs of distress. The replacement costs can thus be avoided. The remaining costs of the service life of the existing structure are as determined in the maintenance plan, and these have been budgeted for. A field test (including a research budget) currently costs about 27% of a replacement, results in negligible CO₂ emissions, and leads to only 1% of the driver delay costs of a replacement scheme. Finalization of the research will lead to standardization and optimization, so that a cost of 5%–10 % of the replacement cost (for the economic cost) is hoped to be achieved in the future. It can thus be seen that the economic savings of field testing are considerable, but that the positive impact on the environment and the social costs is much larger than on the economic cost. When taking into account a full sustainability analysis, the option of field testing thus becomes even more attractive than when only economic costs are considered.

One final remark with regard to the previous calculations is that the major savings obtained by proof load testing are only valid when the proof load test is successful, i.e., when it can be proven through a proof load test that the tested structure can carry the prescribed live loads, and that replacement is not necessary. For this reason, it is of the utmost importance to identify which bridge structures are good candidates for proof load testing. Especially structures with large uncertainties are interesting in this regard: bridges without plans, bridges that are expected to have large redistribution capacity beyond the codified calculation methods, and bridges where the effect of material degradation on the structural capacity is unknown. Further research to develop clear guidelines on how to select good candidate structures for proof load testing is recommended.

9.7 Future trends

Future research on the topic of field assessment through load testing will focus on the reliability aspects of the determined target proof load, and on determining stop

criteria for shear. Currently, several countries (Germany, United States, the Netherlands) are working towards the development or updating of the guidelines for field testing of bridges. Load testing will become more and more important for existing structures, as it is an excellent method to assess the structure in its real conditions. As more of the existing bridges are ageing and the traffic loads and volumes are increasing, more accurate methods for the assessment of existing bridges are necessary.

In the Netherlands, the goal is to develop guidelines for proof load testing of existing bridges that can be followed by the industry. To achieve this goal, more research on the stop criteria for shear is necessary, so that a safe execution of a proof load test when using the guideline is guaranteed. Moreover, faster methods to determine the target proof load and the minimum required number of sensors need to be developed. These actions are necessary to develop a cheap and fast method for proof load testing, through which an existing bridge can quickly be assessed by the industry.

9.8 Summary and conclusions

As a result of the aging bridge stock, assessment of existing bridges becomes increasingly important. Research is carried out to determine if proof load testing can be a cost-effective method for a direct field assessment of an existing bridge. The viaduct Zijlweg was selected as a pilot project, as large cracking caused by ASR-damage raised concerns with regard to the shear capacity of the viaduct. This viaduct is also monitored to study the effect of ASR, and to find out when the elongation has become so large that the functioning of the expansion joint is endangered. A visual inspection of the bridge was also carried out prior to the proof load test.

The first goal for proof load testing of the viaduct Zijlweg was to gain more experience in the technique of proof load testing. An extensive sensor plan was developed to monitor the structural response during the proof load tests, and to verify the usefulness of the existing stop criteria from the German guideline. These stop criteria are only valid for flexure, and new stop criteria for shear need to be developed. Moreover, the stop criteria from the German guideline do not take into account the effect of existing cracking on the structure. A second goal of proof load testing of the viaduct Zijlweg was to experimentally show that the viaduct can carry the prescribed loads without signs of distress. This goal was successful, and the cost savings from a sustainability perspective can be calculated and are significant when compared to the cost of replacement of the superstructure.

Acknowledgments

I'd like to express my gratitude and sincere appreciation to the Dutch Ministry of Infrastructure and the Environment (Rijkswaterstaat) and the Province of Noord Brabant for financing this research work. I'd also like to thank Rutger Koekkoek from Delft University

of Technology for all his contributions to the preparation of the test, the finite element modeling, the planning, the on-site work, and the evaluation of the experiment. Thanks to Prof. Dick Hordijk from Delft University of Technology for the coordination of the project and the photographs from the visual inspection he did. I'd also like to acknowledge Dr. Ane de Boer from Rijkswaterstaat for all his input and the fruitful discussions on this topic. Credit also goes to former MSc student Werner Vos of Delft University of Technology, who analyzed the data of the ASR-monitoring and patiently drew the map of cracks. The contributions and help of our colleagues Albert Bosman, Dr. Cor van der Veen, and Dr. Yuguang Yang, and of student Arthur Ennouri from Delft University of Technology during planning, execution, and analysis of this proof load test have been of great value and help, and are gratefully acknowledged. I'm also thankful for the fruitful discussions with Frank Linthorst and Danny den Boef of Witteveen + Bos, responsible for the logistics and safety, and with Otto Illing and the late Chris Huissen of Mammoet, responsible for applying the load.

References

- ACI Committee 437, 2013. Code Requirements for Load Testing of Existing Concrete Structures (ACI437.2M-13) and Commentary Farmington Hills, MA.
- Ahmed, T., Burley, E., Rigden, S., 1998. The static and fatigue strength of reinforced concrete beams affected by alkali-silica reaction. *ACI Mater. J.* 95, 376–388.
- Ahmed, T., Burley, E., Rigden, S., 1999. Effect of alkali-silica reaction on tensile bond strength of reinforcement in concrete tested under static and fatigue loading. *ACI Mater. J.* 96, 419–428.
- ASCE/SEI-AASHTO Ad-Hoc Group On Bridge Inspection Rating Rehabilitation And Replacement, 2009. White paper on bridge inspection and rating. *J. Bridge Eng.* 14, 1–5.
- Bagge, N., Sas, G., Nilimaa, J., Blanksvard, T., Elfgren, L., Tu, Y. et al., 2015. Loading to failure of a 55 year old prestressed concrete bridge. *IABSE Workshop*. Helsinki, Finland.
- Barker, M.G., 2001. Quantifying field-test behavior for rating steel girder bridges. *J. Bridge Eng.* 6, 254–261.
- Beck, T., Fischer, M., Pfaffinger, M., 2012. Life Cycle Assessment for representative steel and composite bridges. In: Biondini, F., Frangopol, D.M. (Eds.), *Proceedings of the Sixth International Conference on Bridge Maintenance, Safety and Management*. Taylor & Francis Group, Stresa, Lake Maggiore, Italy.
- CEN, 2002. Eurocode – Basis of Structural Design, NEN-EN 1990:2002. Comité Européen de Normalisation, Brussels, Belgium.
- CEN, 2003. Eurocode 1: Actions on structures—Part 2: Traffic loads on bridges, NEN-EN 1991-2:2003. Comité Européen de Normalisation, Brussels, Belgium.
- CEN, 2011. Eurocode 2: Design of concrete structures—Concrete bridges—Design and detailing rules, NEN-EN 1992-2 + C1:2011. Comité Européen de Normalisation, Brussels, Belgium.
- Code Committee 351001, 2011a. Assessment of Structural Safety of an Existing Structure at Repair or Unfit for use—Basic Requirements, NEN 8700:2011 (in Dutch). Civil center for the execution of research and standards, Dutch Normalisation Institute, Delft, The Netherlands.
- Code Committee 351001, 2011b. Eurocode 1—Actions on Structures—Part 2: Traffic Loads on Bridges, EN 1991-2/NA:2011. Civil engineering center for research and regulation, Dutch Normalization Institute, Delft, The Netherlands.

- Cope, R.J., 1985. Flexural shear failure of reinforced-concrete slab bridges. *Proc. Inst.Civ. Eng.Part 2: Res. Theory.* 79, 559–583.
- Cope, R.J., Rao, P.V., Edwards, K.R., 1983. Shear in Skew Reinforced Concrete Slab Bridges—Analytical and Experimental Studies—A Report to the Department of Transport. University of Liverpool, Liverpool.
- den Uijl, J.A., Kaptijn, N., 2004. Structural consequences of ASR: an example on shear capacity. *Heron.* 47, 1–13.
- Deutscher Ausschuss Für Stahlbeton, 2000. DAFStb-Guideline: Load Tests on Concrete Structures. Deutscher Ausschuss für Stahlbeton.
- Environment Agency, 2016. *Carbon Calculator for Construction Activities* [Online]. Available: <<https://www.ice.org.uk/disciplines-and-resources/best-practice/environment-agency-carbon-calculator-tool>>.
- Faber, M.H., Val, D.V., Stewart, M.G., 2000. Proof load testing for bridge assessment and upgrading. *Eng. Struct.* 22, 1677–1689.
- Frangopol, D.M., Sabatino, S., Dong, Y., 2016. Bridge life-cycle performance and cost: analysis, prediction, optimization and decision making. In: Bittencourt, T.N., Frangopol, D. M., Beck, A.T. (Eds.), *Maintenance, Monitoring, Safety, Risk and Resilience of Bridges and Bridge Networks*. IABMAS, Foz do Iguacu, Brazil.
- Gervasio, H., Silva, L.S.D., Perdigao, V., Barros, P., Orcesi, A., Nielsen, K., 2012. Life cycle analysis of highway composite bridges. In: Biondini, F., Frangopol, D.M. (Eds.), *Proceedings of the Sixth International Conference on Bridge Maintenance, Safety and Management*. Taylor & Francis Group, Stresa, Lake Maggiore, Italy.
- Gielen, C., Kolkman, M., Veldhuizen, A.C., 2008. Inspection Report Object 44G-113-01: Bridge Over Highway—Zijlweg (in Dutch), Rijkswaterstaat Noord Brabant.
- Haddad, R.H., Shannag, M.J., Al-Hambouth, M.T., 2008. Repair of reinforced concrete beams damaged by alkali-silica reaction. *ACI Struct. J.* 105, 145–153.
- Hendy, C., Petty, R., 2012. Quantification of sustainability principles in bridge projects. In: Biondini, F., Frangopol, D.M. (Eds.), *Proceedings of the Sixth International Conference on Bridge Maintenance, Safety and Management*. Taylor & Francis Group, Stresa, Lake Maggiore, Italy.
- Kim, S., Frangopol, D.M., 2011. Cost-effective lifetime structural health monitoring based on availability. *J. Struct. Eng.-ASCE.* 137, 22–33.
- KNMI, 2015. Uurgegevens van het weer in Nederland [Online]. Available: <http://www.knmi.nl/klimatologie/uurgegevens/datafiles/350/uurgeg_350_2011-2020.zip>. [Accessed 26.06.15].
- Koekkoek, R.T., Lantsoght, E.O.L., Hordijk, D.A., 2015. Proof Loading of the ASR-Affected Viaduct Zijlweg Over Highway A59. Delft University of Technology, Delft, The Netherlands.
- Koekkoek, R.T., Lantsoght, E.O.L., Yang, Y., de Boer, A., Hordijk, D.A., 2016. Defining loading criteria for proof loading of existing reinforced concrete bridges. *fib Symposium 2016: Performance-Based Approaches for Concrete Structures*. H. Beushausen (Ed.) Cape Town, South Africa.
- Koenders Instruments, 2015. Zijlweg Monitoring System (in Dutch).
- Lantsoght, E.O.L., de Boer, A., van der Veen, C., Walraven, J.C., 2013a. Peak shear stress distribution in finite element models of concrete slabs. In: Zingoni, A. (Ed.), *Research and Applications in Structural Engineering, Mechanics and Computation*. Taylor and Francis, Cape Town, South Africa.
- Lantsoght, E.O.L., van der Veen, C., de Boer, A., Walraven, J.C., 2013b. Recommendations for the shear assessment of reinforced concrete slab bridges from experiments. *Struct. Eng. Int.* 23, 418–426.

- Lantsoght, E.O.L., van der Veen, C., Walraven, J.C., 2013c. Shear in one-way slabs under a concentrated load close to the support. *ACI Struct. J.* 110, 275–284.
- Lantsoght, E.O.L., van der Veen, C., de Boer, A., Walraven, J., 2014. Influence of width on shear capacity of reinforced concrete members. *ACI Struct. J.* 111, 1441–1450.
- Lantsoght, E.O.L., van der Veen, C., de Boer, A., Walraven, J., 2015a. One-way slabs subjected to combination of loads failing in shear. *ACI Struct. J.* 112, 417–426.
- Lantsoght, E.O.L., van der Veen, C., de Boer, A., Walraven, J.C., 2015b. Proposal for the extension of the Eurocode shear formula for one-way slabs under concentrated loads. *Eng. Struct.* 95, 16–24.
- Lantsoght, E.O.L., van der Veen, C., Walraven, J., de Boer, A., 2015c. Experimental investigation on shear capacity of reinforced concrete slabs with plain bars and slabs on elastomeric bearings. *Eng. Struct.* 103, 1–14.
- Lantsoght, E.O.L., Yang, Y., van der Veen, C., de Boer, A., Hordijk, D., 2016a. Ruytenschildt Bridge: field and laboratory testing. *Eng. Struct.* 128, 111–123.
- Lantsoght, E.O.L., van der Veen, C., de Boer, A., Hordijk, D.A., 2016b. Probabilistic prediction of the failure mode of the Ruytenschildt Bridge. *Eng. Struct.* 127, 549–558.
- Lantsoght, E.O.L., Yang, Y., Tersteeg, R.H.D., van der Veen, C., de Boer, A., 2016c. Development of Stop Criteria for Proof Loading. IALCCE 2016, Delft, The Netherlands.
- Lantsoght, E.O.L., van der Veen, C., de Boer, A., Hordijk, D.A., 2017. Collapse test and moment capacity of the Ruytenschildt reinforced concrete slab bridge. *Struct. Infrastruct. Eng.* 13, 1130–1145.
- Lin, T.S., Nowak, A.S., 1984. Proof loading and structural reliability. *Reliab. Eng.* 8, 85–100.
- Liu, Y., Lu, D., Fan, X., 2014. Reliability updating and prediction of bridge structures based on proof loads and monitored data. *Constr. Build. Mater.* 66, 795–804.
- Matta, F., Bastianini, F., Galati, N., Casadei, P., Nanni, A., 2008. Distributed strain measurement in steel bridge with fiber optic sensors: validation through diagnostic load test. *J. Perform. Constr. Facil.* 22, 264–273.
- Nilimaa, J., Blanksvärd, T., Taljsten, B., 2015. Assessment of concrete double-trough bridges. *J. Civil Struct. Health Monit.* 2015, 29–36.
- Olaszek, P., Lagoda, M., Ramon Casas, J., 2014. Diagnostic load testing and assessment of existing bridges: examples of application. *Struct. Infrastruct. Eng.* 10, 834–842.
- Projectteam RWS/TNO Bouw, 1997. Safety Evaluation Existing Structures: Reinforced Concrete Bridges, Ministry of Infrastructure and the Environment, Utrecht, the Netherlands, (in Dutch).
- Provincie Noord Brabant, 1965. Viadukt in de Zijlweg, Ministry of Infrastructure and the Environment, the Netherlands (in Dutch).
- Puurula, A.M., Enochsson, O., Sas, G., Blanksvärd, T., Ohlsson, U., Bernspång, L., et al., 2014. Loading to failure and 3D nonlinear FE modelling of a strengthened RC bridge. *Struct. Infrastruct. Eng.* 10, 1606–1619.
- Puurula, A.M., Enochsson, O., Sas, G., Blanksvärd, T., Ohlsson, U., Bernspång, L., et al., 2015. Assessment of the strengthening of an RC railway bridge with CFRP utilizing a full-scale failure test and finite-element analysis. *J. Struct. Eng.* 141, 1–11, D4014008.
- Rafla, K., 1971. Empirical formula for calculation of shear capacity of reinforced concrete beams (in German). *Strasse Brücke Tunnel.* 23, 311–320.
- Rijkswaterstaat, 2002. Management and Maintenance Plan Viaduct Zijlweg Over Highway A59, Ministry of Infrastructure and the Environment, Utrecht, the Netherlands, (in Dutch).

- Rijkswaterstaat, 2013. Guidelines Assessment Bridges—Assessment of Structural Safety of an Existing Bridge at Reconstruction, Usage and Disapproval (in Dutch), Ministry of Infrastructure and the Environment, Utrecht, the Netherlands.
- Ryan, T.W., Mann, E., Zachary, E., Chill, M., Ott, B.T., 2012. Bridge Inspector's Reference Manual. In: US Department of Transportation, Federal Highway Administration, Washington DC.
- Sanayei, M., Reiff, A.J., Brenner, B.R., Imbaro, G.R., 2016. Load rating of a fully instrumented bridge: comparison of LRFR approaches. *J. Perform. Constr. Facil.* 2016, 2.
- Schacht, G., Bolle, G., Curbach, M., Marx, S., 2016a. Experimental evaluation of the shear bearing safety (in German). *Beton- und Stahlbetonbau*. 111, 343–354.
- Schacht, G., Bolle, G., Marx, S., 2016b. Load testing—International state of the art (in German). *Bautechnik*. 93, 85–97.
- Schmidt, J.W., Hansen, S.G., Barbosa, R.A., Henriksen, A., 2014. Novel shear capacity testing of ASR damaged full scale concrete bridge. *Eng. Struct.* 79, 365–374.
- Siemes, T., Han, N., Visser, J., 2002. Unexpectedly low tensile strength in concrete structures. *Heron*. 47, 111–124.
- Talley, K.G., 2009. Assessment and Strengthening of ASR and DEF Affected Concrete Bridge Columns. Ph.D. Thesis, The University of Texas at Austin.
- TNO DIANA, 2012. User's Manual of DIANA, Release 9.4.4. Delft, The Netherlands.
- Velázquez, B.M., Yura, J.A., Frank, K.H., Kreger, M.E., Wood, S.L., 2000. Diagnostic Load Tests of a Reinforced Concrete Pan-girder Bridge. The University of Texas at Austin, Austin, TX.
- Witteveen + Bos, 2014. Material Research Bridges, Case 31084913: 44G-113-01: viaduct Zijlweg (in Dutch). Deventer.
- Yang, Y., Hordijk, D.A., 2015. Acoustic Emission Measurement and Analysis on Zijlwegbrug. Delft University of Technology, Delft, The Netherlands.
- Zinke, T., Ummenhofer, T., Pfaffinger, M., Mensinger, M., 2012. The social dimension of bridge sustainability assessment—impacts on users and the public. In: Biondini, F., Frangopol, D.M. (Eds.), *Proceedings of the Sixth International Conference on Bridge Maintenance, Safety and Management*. Taylor & Francis Group, Stresa, Lake Maggiore, Italy.

This page intentionally left blank

Assessment of the deterioration of concrete structures using a finite element model

10

J.F. Jiménez-Alonso and A. Sáez
Universidad de Sevilla, Sevilla, Spain

10.1 Introduction

In a context of aging civil infrastructures, it is of key importance to characterize and validate the deterioration state of concrete structures during their overall life cycle. The reliability and functionality of concrete structures may be assessed via the numerical simulation of their behavior, based on finite element (FE) models (Wenzel, 2009). Frequently, these numerical models do not accurately reflect the actual state of concrete structures, so they need to be improved based on the results obtained from field tests and continuous monitoring (Friswell and Mottershead, 1995). After the numerical model is adjusted, the behavior of the concrete structure is better known, being possible to establish a more accurate basis for the subsequent management operations (Doebeling et al., 1996). The tuning of the numerical model may be achieved via the modification of the value of several physical parameters of the structure, in order to reduce the differences between the numerical and experimental behavior of the structure. Results obtained from field tests and continuous monitoring are normally used as reference for the adjusting process. This procedure may even allow for the further establishment of a strategy for damage detection or deterioration assessment: The comparison of physical parameters of the finite element model adjusted during the life cycle of the structure permits detecting the existence of damage or deterioration and its location on the structure (Peeters, 2000). The adoption of this type of strategy is crucial to extending the life cycle of the concrete structures, thus improving their maintenance, reducing the environmental impact, and reducing their life cycle cost (Wenzel, 2009).

In general terms, after a concrete structure is built, four types of actions are performed for its management: inspection, assessment, maintenance, and repair (Wenzel, 2009). The inspection, which encompasses visual inspection, field testing, and monitoring, is performed according to a periodic plan in order to check the evolution of some physical parameters of the structure over time. The structural assessment is performed for a definite requirement in order to validate the safety, the functionality or the condition of a concrete structure. The structural assessment is usually based on both a FE model and the results of preliminary inspections of the structure. Finally, measures of maintenance and repair are undertaken based on the results of a previous structural assessment (Fib, 2003).

Among the main causes for conducting the structural assessment of a concrete structure, one may cite the following: (1) the change of the requirements that the structure must fulfill, due to a modification of the service conditions or standards; (2) the repair or retrofit of the structure; (3) the damage induced on the structure by an extreme event; and (4) the deterioration of the structure due to environmental effects. The activities required for structural assessment depend on the results of the previous inspections and they can be summarized as: (1) numerically simulate the behavior of the structure in order to evaluate its safety, functionality or condition; (2) increase the number and accuracy of the inspections to better characterize the causes of damage and deterioration; (3) conduct field testing and monitoring to characterize the actual behavior of the structure and (4) perform a more detailed evaluation of the safety of the structure based on both the results of the previous activities and the use of probabilistic methods (Wenzel, 2009).

Depending on the outcome of the structural assessment, the following scenarios may be adopted: (1) maintain the structure in use; (2) increase the number of inspections; (3) establish a continuous monitoring system; (4) reduce the service loads on the structure; (5) retrofit the structure; (6) repair the structure; or (7) replace the structure.

In order to guarantee the adequate management of a concrete structure during its overall life cycle, a strategy to perform its structural assessment is necessary. As part of this strategy, the use of numerical models is currently employed during the design phase of the structure and during its management stage. Nevertheless, the FEs models used for this second stage need to be improved in order to adequately characterize the current state of the structure. The process of adjusting an initial FE model of a structure to match the results of experimental tests is called model updating (Friswell and Mottershead, 1995). The updating process is usually a fundamental part of the strategy for structural assessment, as the updated model may be useful to make decisions about subsequent inspections, to assess the safety and functionality of the structure, and to further adopt decisions of maintenance, repair and retrofit.

In this chapter, a strategy to assess the deterioration state of concrete structures based on the FE model updating approach is presented (Marwala, 2010). As the key point of the strategy is the performance of the updating process, the content of the chapter is focused on this topic. Nevertheless, additional information, such as recommendations on how to create FE models for structural assessment, experimental tests, and data used as basis for the updating process have been included to facilitate the reading of the chapter. The updating process is formulated as a global optimization problem (Brownjohn et al., 2001). In this way, some physical parameters of the FE model, considered as design variables, are modified in order to minimize the relative difference between the numerical and experimental behavior of the structure. The comparison between the updated physical parameters during the life cycle of the structure allows characterizing its deterioration state (Peeters, 2000). In order to illustrate the potential of the method a case study is presented: the deterioration assessment of an ancient reinforced concrete bridge, to select the most appropriate retrofit method.

The chapter is organized as follows: First, some general recommendations on how to elaborate adequate FE models of concrete structures and facilitate their subsequent model updating, are presented in Section 10.2. Second, a summary of the main field tests that may be conducted on structures to record the experimental data considered in the updating process is presented in Section 10.3. Later, a strategy for deterioration assessment of concrete structures based on the FE model updating method is presented in Section 10.4. An introduction to the FE model updating process is presented in Section 10.5. Then, a case study—the deterioration assessment of an ancient reinforced concrete bridge—is presented in Section 10.6. The study shows the potential of this strategy for structural assessment. Finally, Sections 10.7 and 10.8 present the main conclusions obtained from the chapter and future research lines to be explored, respectively.

10.2 Finite element models for concrete structures

Structural assessment of concrete structures may be conducted with the assistance of numerical FE models that approximate the actual response of the structure (Brownjohn et al., 2001). The level of detail of these models may vary depending on the objectives of the study, the geometrical representation of the structure, and the constitutive material laws considered for the simulation (Rombach, 2011).

The numerical models elaborated during the design phase of the structure are usually not adequate to assess the state of the structure during its entire life cycle, being necessary to develop more detailed numerical models for this latter purpose.

Three levels of detail may be considered for the geometrical representation of the FE models in terms of their complexity: The first level—the most simplified—corresponds to the use of 2D elements based on the beam or frame theory. The main objective of these models is to obtain the response of the structure and subsequently to determine the cross-section forces and moments. The second level—for more complicated geometries—corresponds to the use of 3D elements based on beam, plate or shell theories. For instance, these elements become indispensable when analyzing a geometrically curved structure, where the spatial configuration significantly influences its behavior. The last level corresponds to continuum solid element models that must be used when the above-mentioned beam/shell theories are not valid. For example, this would be the case when analyzing the structural response of a concrete gravity dam.

Regarding the constitutive material law implemented with the FE model, one of the following four approaches is normally adopted (Wenzel, 2009): (1) linear elastic analysis; (2) linear analysis with limited re-distribution; (3) plastic analysis; or (4) nonlinear analysis. The more advanced the analysis is, the better it may reflect the actual response of the structure. Nevertheless, the more advanced the analysis is, the more demanding and computation time-consuming it is. In particular, nonlinear analyses with advanced constitutive material laws are suitable to assist in taking decisions about the assessment, the maintenance, and the retrofitting of the structure.

The development of FE models for structural assessment is normally carried out using either commercial FE packages, for instance ANSYS (ANSYS, 2017), or programming directly the FE method in any computational language package (see, e.g., Kwon and Bang, 2000). Alternatively, a combination of both approaches may be implemented by exploiting the capabilities of commercial programs in conjunction with user-programmed subroutines.

Although it is possible to create detailed FE models to simulate accurately the behavior of concrete structures—intended at even assessing their deterioration or damage state, great differences may still be observed between the numerical simulations provided by these initial FE models and the actual behavior of the structure. Experimental tests (field tests and continuous monitoring) are normally used to validate and calibrate these FE models (Fib, 2003). Therefore, if the difference between the numerical and experimental responses is significant, the FE models may be adjusted in order to match the results of the experimental tests. In this way, the tuning of the numerical model provides a tool to better characterize the actual behavior of concrete structures.

The updating process may be achieved via the modification of some physical parameters of the structure within an optimization scheme aimed at minimizing the discrepancies between the numerical model and the experimental observations. In this way, this procedure allows identifying indirectly the values of these parameters that better adjust to the measured data. As it is possible to perform the model updating of the concrete structure during its overall life cycle, the evolution of the value of these physical parameters over time may be easily obtained. The comparison of the values of these parameters at two different instants enables the establishment of strategies for damage detection or deterioration assessment (Marwala, 2010). Additionally, the updated model may be used as a starting point for the development of further, more sophisticated analyses (Compán et al., 2017).

A final recommendation in this section: It is of key importance to design the initial FE model intended for structural assessment bearing in mind the needs of the subsequent updating process. In particular, the physical parameters of the model with greater influence in the actual behavior of the structure must be included and should be easily identified in the model.

In next section, a brief description of the experimental tests usually conducted to improve FE models of structures will be summarized.

10.3 Field tests and monitoring for deterioration assessment

Field-testing and monitoring have been historically used to improve FE models of concrete structures in order to better reflect their actual behavior (Fib, 2003). Field-testing refers to the measure of the response of the structure under a controlled load scenario during a limited time interval. Monitoring is associated with the continuous measure of the structural response under service conditions over a long period of time.

Among field-testing, diagnostic tests are normally used to experimentally assess the state of the structure. Additionally, the results of these tests may be further employed to improve numerical models, by adjusting the numerical response to the observed experimental behavior via an updating process. During these tests, the structure is exposed to load scenarios which simulate the service conditions. Diagnostic tests may be classified, depending on the velocity of the application of the load, in static and dynamic tests. The physical magnitudes normally obtained in diagnostic tests, which are useful for the development of the updating process, include displacements, strains, accelerations, and forces (Fib, 2003).

In a static test, the displacements and strains at different points of the structure under a predefined load scenario (location and magnitude of the load) are measured. The results of these tests have been traditionally used to check the performance of real structures and, more recently, to help improving FE models (Schlune et al., 2009).

In a dynamic test, the identification of the experimental modal parameters of the structure (natural frequencies, vibration modes and modal damping ratios) is performed, based on measuring the dynamic response of the structure. Conventional modal analysis may be classified in experimental (EMA) and operational (OMA) modal analysis, depending on whether the input force and the resulting response can both be measured (EMA), or only the response can be recorded experimentally (OMA) (Ewins, 2000; Rainieri and Fabbrocino, 2014). In this way, forced vibration tests under controlled excitation are conducted in EMA, while ambient or free vibration tests are used for this purpose using OMA algorithms (Caetano et al., 2009). The resulting modal characteristics of the structure may be used to improve the FE model of concrete structures (Gentile, 2006).

In order to experimentally identify the modal parameters of the structure based on a forced vibration test, an EMA algorithm has to be used (Ewins, 2000; Maia et al., 1997). For the estimation of the frequency response function, the most commonly used identification methods utilize a spectral description of the input and the response of the structure. For its practical implementation, two alternatives may be used: either implement an EMA algorithm in a programming package (e.g., Matlab, 2017) or employ an experimental identification commercial software (e.g., ME'scope, 2017; Pulse, 2017).

In a forced vibration test, the structure is commonly excited by three types of actuators: hammers, hydraulic-, or electrodynamic vibrators. Consequently, the method used to identify the modal parameters of the structure depends on the excitation source. It is recommended to excite the structure in a wide-band of frequencies; taking care that the energy associated with the low natural frequencies is great enough to guarantee an adequate signal-to-noise ratio (Caetano et al., 2009).

In case an impulsive hammer is used to excite the structure, a wide range of natural frequencies, such as DC-200 Hz (according to the precision of the sensors) may be identified experimentally. However, due to the limited energy introduced by the hammer, the length of the signal under forced vibration is normally not long enough to allow an adequate identification of the natural frequencies and vibrations modes at very low frequencies (Caetano et al., 2009). In this case, the use of other types of excitation sources, like hydraulic or electrodynamic shakers, exhibit better

performance. Two forms of excitation can be generated with these latter devices: a wide-band excitation or a sinusoidal excitation. The wide-band excitation can be either transient or continuous. The modal identification based on the response measured under a transient excitation has the same treatment as that generated by hammer excitation. The continuous excitation requires the filtering of both the input and the response in order to reduce the leakage effects and the contribution of the edge samples. The application of this excitation source provides a more accurate definition of the frequency response functions, which allows the experimental identification of vibration modes with low natural frequencies. Nevertheless, if the shaker has enough power, the sinusoidal excitation provides better results. For the development of the sinusoidal test, a preliminary estimation of the natural frequencies based on the measurement of the ambient response is performed. Subsequently, the frequency response function is obtained partially around the previously estimated values. Additionally, the sinusoidal test provides better estimations of damping, when obtained from the signal processing of the free vibration response, after the sudden interruption of the excitation applied at resonance frequency (Caetano et al., 2009).

Alternatively, the high sensitivity and precision of the current sensors (Fig. 10.1A) enables using ambient vibration as excitation source in an OMA test context (Fig. 10.1B). In such cases, the response of the structure is measured under operational conditions. In these tests, it is assumed that the input excitation—the ambient vibration—may be idealized as a white-noise, thus ensuring that all the vibration modes are excited at constant amplitude. As the magnitude of the applied force during the test is unknown, it is not possible to scale the frequency response functions, so the identification algorithms lead to operational deflection shapes instead of vibrations modes. In order to obtain a good estimation of the vibration modes from the deflection shapes, different approaches have been proposed, in both frequency and time domains (see, for instance, Rainieri and Fabbrocino, 2014 for details). There are currently several commercial software packages that implement the different OMA algorithms (e.g., Artemis, 2017; LMS 2017; MACEC, 2017) to facilitate its application to practical case studies. However, despite the use of the

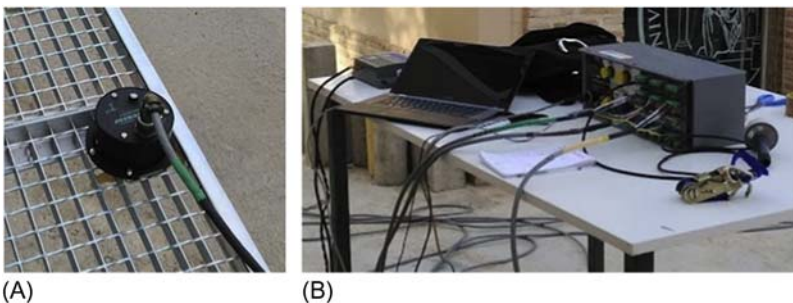


Figure 10.1 (A) Force balance accelerometer and (B) Acquisition equipment for ambient vibration test.

more advanced, output-only algorithms, the modal parameters estimated by these algorithms are still less accurate than the estimates obtained from EMA methods. This is particularly remarkable in the case of modal damping, whose results should be used carefully (Magalhães and Cunha, 2011).

Furthermore, free vibration tests may be conducted in order to estimate the experimental modal parameters of the structure. In these tests, the structure is excited by the drop of a weight, or the release of a tensioned cable. The effect of these actions is equivalent to the application of an impulse. The identification of the modal parameters of the structure may be accomplished by either using EMA algorithms or OMA techniques. In the first method, it is assumed that the input is constant for the frequency range under study. For the second method, the same assumptions previously mentioned are considered. The modal characteristics obtained from a free vibration test are, in general terms, more accurate than the estimates from an ambient vibration test.

Finally, the evolution of the modal parameters of the structure over time may be determined if a long-term monitoring system is installed (Caetano et al., 2009). Long-term continuous monitoring is a useful tool to determine experimentally the behavior of the structure as it evolves along time, since its construction and during its overall life cycle. Combining continuous monitoring of the structure and model updating allows for the establishment of strategies to assess its damage or deterioration state: The continuous updating of the FE model based on the results obtained from long-term monitoring facilitates finding the causes that originate the changes of the modal parameters of the structure along its life cycle (Wenzel, 2009). The main limitation that this approach presents lies in the quantification of the environmental effects on the change of the modal parameters of the structure. To remove these effects, the scientific community has conducted large efforts during the last decade (Rainieri and Fabbrocino, 2014). Statistical correlations have been proposed between the change of the natural frequencies and the environmental effects (Hu et al., 2013). These results allow for establishing thresholds that determine when the modifications of the modal parameters of the structure are caused by damage or deterioration rather than by environmental causes. Nevertheless, further studies are still required to better characterize such effects and overcome these limitations.

Field tests and long-term monitoring must be carefully designed so their results can be easily employed to improve the numerical models, by reducing the uncertainties associated with the most sensitive physical parameters of the model (Rainieri and Fabbrocino, 2014). It is advisable to develop an initial FE model of the structure, in order to perform preliminary numerical analyses which results may be used to help in designing the experimental set-ups. In a static test, for example, the selection of sensors, their location on the structure, and the definition of the load scenario (position, configuration and magnitude) are the main design parameters to be determined before the performance of the test. In a dynamic test, the first decision focuses on selecting the type of test (forced vibration, free vibration or ambient vibration test). Subsequently, the design of the test has to concentrate on establishing other design parameters such as, the selection of the excitation source, the type of sensors, the sensitivity of the sensors, the optimal location of the sensors

on the structure, the sample frequency, the duration of the measures, the improvement of the signal-to-noise ratio, the amplification and filtering of the signal and finally the selection of the most adequate modal analysis algorithm for the signal processing (Ewins, 2000; Maia et al., 1997; Rainieri and Fabbrocino, 2014).

In conclusion, the results of dynamic tests and long-term monitoring can be used to calibrate FE models in order to match the actual behavior of real concrete structures during their overall life cycle. Based on these ideas, a strategy for deterioration assessment is presented in next section.

10.4 Modal-based deterioration assessment methods

Vibration data may be used for damage detection or deterioration assessment of concrete structures (Teughels et al., 2002; Teughels and De Roeck, 2004). Regardless of the type of vibration data considered, any vibration-based deterioration assessment method can be organized into four steps: (1) obtain the vibration data; (2) improve the vibration data via filtering and de-noising of the signal; (3) build or improve a numerical model based on the previous collected vibration data; and (4) assess the deterioration state of the structure.

In general terms, two types of algorithms are considered to assess the deterioration state of structures, depending on whether a numerical model is directly created from the measured vibration data (e.g., using neural networks, support vector machines, fuzzy logic, or rough sets), or an initial FE model is calibrated (model updating) based on the vibration data (Marwala, 2010). In any of these two cases, the resulting numerical model, as well as the physical parameters that characterize it, will adequately resemble the actual dynamic behaviour of the structure at the time the vibration data has been obtained. Therefore, if vibration data is recorded at different time instants –and the associated numerical models are constructed–, the variation of the resulting physical parameters of the models at those time instants will allow estimating the deterioration state of the structure along time.

Data may be handled in four alternative domains: time domain, frequency domain, time-frequency domain and modal domain. A brief description of each domain is next included for the sake of clarification, although the interested reader is referred to the bibliography for a complete review on the topic (Jaishi and Ren, 2006; Marwala, 2010; Teughels and De Roeck, 2004; Wenzel, 2009). In time domain methods, the deterioration of the structure is detected via the direct analysis of the changes in the measured signal. These methods are especially effective if the structure is time-dependent or it exhibits a nonlinear behavior. In frequency domain methods, the measured data is transformed to the frequency domain using the Fourier transform (Maia et al., 1997). Auto-regressive models and deterioration ratios, based on the change of the frequency response functions, are considered to assess the deterioration of the structure. In time-frequency domain methods, it is equally necessary to transform the measured data into the frequency-time domain using transformation techniques like wavelet transform, short-time Fourier transform, Gabor distribution or Wigner-Ville distribution (Marwala, 2010). The main

advantage of this transformation is that both time and frequency are analyzed at once. The use of this domain is especially useful for structural responses whose characteristics change with time. Finally, in modal domain methods, the assessment of the deterioration state of the structure is based on the change of its modal parameters (natural frequencies, damping, and vibration modes). As modal parameters are sensitive to the changes of the physical parameters of the structure, they can be used for deterioration detection. The modal parameters of the structure can be identified experimentally from the results of field tests or continuous monitoring using experimental or OMA, as described in the previous section.

In building and civil engineering, two domains have historically been used, depending on whether frequency response functions or modal data were used for the correlation between the numerical and experimental results (Peeters, 2000). Recently, however, the modal domain is applied more often, since the frequency response functions of large buildings and civil engineering structures are not available over a wide frequency range (Caetano et al., 2009). For this reason, currently the most common way to establish a strategy for deterioration assessment is based on a model updating process, adopting as reference the modal parameters of the structure estimated from an ambient vibration tests via OMA algorithms.

The assessment of the deterioration state of a structure based on such model updating approach may be organized as follows:

1. build an initial FE model of the structure;
2. determine the experimental modal data of the structure;
3. update the initial FE model to ensure it matches the experimental modal data of the structure, by tuning some physical parameters of the model;
4. determine the experimental modal data again after the deterioration happened, by repeating steps (2) and (3);
5. utilize the updated physical parameters as an indicator of the presence and location of the deterioration.

As one of the key points of the detection procedure is the updating process, next section is devoted to summarize some fundamentals of this technique.

10.5 Finite element model updating

In order to establish the correlation between the numerical and experimental modal parameters, several ratios have been proposed (Ewins, 2000). Among the different proposals, the relative difference between the numerical and experimental natural frequencies, $\Delta f_j(\theta)$, and the modal assurance criterion, $MAC_j(\theta)$, are widely used (Friswell and Mottershead, 1995). The relative difference between frequencies, $\Delta f_j(\theta)$, is defined as:

$$\Delta f_j(\theta) = \frac{f_{num,j}(\theta) - f_{exp,j}}{f_{exp,j}} 100[\%] \quad (10.1)$$

where $f_{num,j}(\theta)$ and $f_{exp,j}$ are the numerical and experimental j natural frequency of the structure, and θ is the physical parameter vector. The modal assurance criterion, $MAC_j(\theta)$, is defined as:

$$MAC_j(\theta) = \frac{\left(\Phi_{num,j}^T(\theta)\Phi_{exp,j}\right)^2}{\left(\Phi_{num,j}^T(\theta)\Phi_{num,j}(\theta)\right)\left(\Phi_{exp,j}^T\Phi_{exp,j}\right)} \quad (10.2)$$

where $\Phi_{num,j}(\theta)$ and $\Phi_{exp,j}$ are the numerical and experimental j vibration mode, and T denotes transpose.

A good correlation between a numerical and experimental vibration mode is achieved when their relative difference is below 5.00 % and their MAC ratio is above 0.90 (Zivanovic et al., 2007). In case the mentioned ratios do not achieve the adequate correlation level, it is necessary to calibrate the FE model of the structure via the application of an updating process.

10.5.1 Basics of finite element model updating

The FE model updating based on modal-domain data (natural frequencies and vibration modes) may follow either a direct or an indirect approach (Friswell and Mottershead, 1995). In the early years of this technique, the adjustment of the FE model was performed directly through the introduction of changes in the mass and stiffness matrices of the structure, which has the advantage of allowing an adjustment between the numerical model and the experimental data through a direct algorithm. However, this method has as its main disadvantage the updating process is performed without necessarily involving the physical knowledge of the problem. This drawback caused the later appearance of another family of methods, indirect methods (Brownjohn et al., 2001), where the model updating arises from the changes applied on some well-defined structural physical parameters selected by the users. In this case, the modified parameters are not linearly related to the modal parameters so the adjustment process requires the use of iterative techniques (Mottershead et al., 2011). The most widely used iterative techniques are based on optimization algorithms for nonlinear problems (Levin and Lieven, 1998), machine-learning algorithms (Marwala, 2010), or Bayesian approaches (Marwala et al., 2016).

Among the different possible approaches, a straightforward manner to perform the FE model updating consists of minimizing an objective function, defined as a least square problem between the numerical and experimental modal parameters (Jin et al., 2014), and considering as design variables the physical parameters of the structure with a greater influence on its dynamic behavior. The relative differences between the numerical and experimental modal parameters are called residuals. Several types of residuals may be considered in the updating process. In order to evaluate the influence of the different residuals in the objective function, two different approaches are usually employed: single-objective function and multiobjective function.

In the single-objective function approach, the residuals must be weighted in order to account for the relative contribution of each modal parameter to the objective function and to account for the uncertainty associated with its experimental estimation. There are several proposals for estimating the value of the weighting variables, based on the statistical properties of the measures (Teughels et al., 2002). Alternatively, these weights may be determined based on the experience and engineering judgement of the user (Zivanovic et al., 2007).

Normally, because the natural frequencies provide global information of the structure—they are very sensitive with respect to its stiffness and can be accurately identified experimentally, they are indispensable magnitudes to be considered in the model updating process, so that higher values of their weighting factors are assigned (Zivanovic et al., 2007). On the other hand, because the vibration modes provide spatial information of the structure, which is only necessary to identify local parameters, they are less sensitive to the stiffness of the structure and are more difficult to identify experimentally, it is necessary to analyze their weighting factors in order to find the values that achieve the best adjustment between the numerical and experimental modal parameters (Teughels et al., 2002). To establish the most adequate value for the weighting factors of the different residuals, a search range, (0,1), is considered (Zivanovic et al., 2007; Jin et al., 2014). In this way, the value of the weighting factors associated with the different residuals is determined by a trial and error procedure to guarantee the best correlation between the numerical and experimental modal parameters.

The general formulation of the single-objective function approach may be stated as follows:

$$\min f(\theta) = \min \frac{1}{2} \sum_{j=1}^m w_j r_j(\theta)^2 = \min \frac{1}{2} \sum_{j=1}^{m_f} w_j^f r_j^f(\theta)^2 + \frac{1}{2} \sum_{j=1}^{m_m} w_j^m r_j^m(\theta)^2 \quad (10.3)$$

$$\theta_l \leq \theta \leq \theta_u \quad \sum w_j = \sum w_j^f + w_j^m = 1 \quad w_j \geq 0$$

where $f(\theta)$ is the objective function for the single-objective function approach; m_f is the size of the residuals vector related to the natural frequencies, $r^f(\theta)$; m_m is the size of the residuals vector related to the vibration modes, $r^m(\theta)$; m is the size of the residuals vector, $r(\theta)$; w_j is the weighting factor of the element j of the residuals vector; $r_j(\theta)$ is the element j of the residuals vector; w_j^f is the weighting factor of the element j of the residuals vector related to the natural frequencies; $r_j^f(\theta)$ is the element j of the residuals vector related to the natural frequencies; w_j^m is the weighting factor of the element j of the residuals vector related to the vibration modes; $r_j^m(\theta)$ is the element j of the residuals vector related to the vibration modes; θ_l is the lower constraint vector of the physical parameter vector; θ_u is the upper constraint vector of the physical parameter vector.

In the multiobjective function approach, all objective functions are explored independently, without assigning weighting factors (Kim and Park, 2004). The main objective of this approach is to find the best solution among a set of optimal solutions, called the Pareto optimal front. Since the alternative solutions on the

Pareto optimal front are nondominated, a reasonable criterion must be established to determine the best solution. For bi-criteria problems (two subobjective functions), the application of an additional condition is generally employed. This condition is usually based on a decision-making strategy, where the trade-off between the two objective functions is considered (Jin et al., 2014). A widely-used criterion in model updating is to consider the so-called edge-knee point (Jin et al., 2014) as the best solution of the Pareto optimal front. According to this criterion, the best solution is defined by the point of the Pareto optimal front such that a movement to any alternative solution in the Pareto optimal front gives rise to a small reduction of one subobjective function and a large increase in the other subobjective function.

The multiobjective function approach can be formulated as follows (for bi-criteria problems):

$$\min(f_1(\theta) \quad f_2(\theta)) = \min \left(\frac{1}{2} \sum_{j=1}^{m_f} r_j^f(\theta)^2 \quad \frac{1}{2} \sum_{j=1}^{m_m} r_j^m(\theta)^2 \right) \quad (10.4)$$

$$\theta_l \leq \theta \leq \theta_u$$

where $f_1(\theta)$ is the first subobjective function for the multiobjective function approach and $f_2(\theta)$ is the second subobjective function for the multiobjective function approach.

The election of one of these two alternative approaches depends on experience, expertise, and engineering judgement. The single-objective function approach requires multiple runs of optimization, in order to find the best updated model among the candidates originated by the different values of the considered weighting factors. However, this approach may be simplified by directly adopting the weighting factors provided by the results of previous studies (Zivanovic et al., 2007). On the other hand, the multiple-objective function approach directly searches the overall set of updated models. Subsequently, the best solution is selected on the Pareto optimal front. In the case of inexperienced users, this second approach can reduce the computational time for the selection of the best updated numerical model, since the application of a trial and error scheme is not necessary to establish the value of the weighting factors of the residuals.

In building and civil engineering, it is usual to formulate the objective function, for both approaches, in terms of the differences between the numerical and experimental modal data (see Subsection 10.5.2). The previously defined objective function—considering any of the two alternative approaches—must be minimized by the application of an optimization algorithm. Local and global optimization algorithms have been considered in the past for this purpose (Nocedal and Wright, 1999). Currently, global algorithms are widely implemented due to their robustness and controlled dependence on the initial value of the parameters selected to initiate the search process. In particular, genetic algorithms will be used for the application example described later in this chapter.

10.5.2 Residual selection

In building and civil structures, modal parameters are usually considered to define the residual vector that configures the objective function. In this way, the residual vector is defined in terms of the differences between the numerical and experimental modal data, such as natural frequencies, vibration modes, modal curvatures, etc. However, additional inaccuracies are introduced due to the experimental and operational modal extraction operations. In order to pair the numerical and experimental data correctly, some precautions should be taken to avoid convergence problems during the iterative process: First, the experimental vibration modes inaccurately defined must be rejected. Second, the numerical and experimental vibration modes must be sorted. Subsequently, the numerical and experimental vibration modes are paired based on their $MAC_j(\theta)$ ratio.

Two types of residuals are normally considered: $r_j^f(\theta)$, in relation to the natural frequencies, and $r_j^m(\theta)$, in relation to the vibration modes. The first term, $r_j^f(\theta)$, is defined as the relative differences between the numerical, $f_{num,j}(\theta)$, and experimental, $f_{exp,j}$, natural frequencies of the structure. As previously indicated, the natural frequencies are indispensable magnitudes to be used in the updating process, since they provide information of the overall structural behavior, they are very sensitive to structural stiffness and, they are easily identified experimentally (Caetano et al., 2009). Regarding $r_j^m(\theta)$, there are different proposals in the literature on how to determine the vibration mode residuals (Moller and Friberg, 1998) that relate the numerical, $\phi_{num,j}(\theta)$, and experimental, $\phi_{exp,j}$, vibration modes (Teughels et al., 2002). The authors recommend the use of the average differences between the numerical and experimental vibration modes. Although the vibration modes are not as sensitive as the natural frequencies with respect to structural stiffness, and their experimental determination is more affected by noise (so their accurate identification is more difficult), they provide spatial information of the structure necessary to identify local parameters (Teughels et al., 2002). For this reason, their residuals should be included in the updating process.

In order to guarantee that the two types of residuals are well-balanced, the residuals may be normalized as follows (Jin et al., 2014):

$$r_j^f(\theta) = \frac{f_{num,j}(\theta) - f_{exp,j}}{f_{exp,j}} \quad j = 1, 2, \dots, m_f \quad (10.5)$$

$$r_j^m(\theta) = \sqrt{\left(\frac{(1 - \sqrt{MAC_j(\theta)})^2}{MAC_j(\theta)} \right)} \quad j = 1, 2, \dots, m_m \quad (10.6)$$

where by only the translational degrees of freedom are considered for the definition of the numerical and experimental vibration modes. Furthermore, the grid of measuring points in the experimental set-ups must be sufficiently dense to avoid spatial aliasing problems associated with the determination of the $MAC_j(\theta)$ ratio (Brownjohn et al., 2001). Additionally, the experimental vibration modes can be smoothed to reduce the effect of the noise associated with the identification method.

It is also recommended that the number of residuals, $m = m_f + m_m$, is greater than the number of the considered physical parameters, θ , in order to avoid ill-conditioned problems (Nocedal and Wright, 1999).

10.5.3 Sensitivity analysis and parameter selection

In order to pose a well-conditioned updating process, it is recommended to select those updating parameters that will be most effective in reducing the differences between the numerical and experimental modal data (Mottershead et al., 2011). The number of parameters should be kept small enough, in order to avoid losing the physical knowledge of the problem while ensuring the sensitivity of the model to their variation. Parameter selection may be accomplished based on a sensitivity analysis, where the modal sensitivities are obtained following the method proposed by Fox and Kapoor (Fox and Kapoor, 1968). If only stiffness parameters are to be modified, Fox and Kapoor's approach may be summarized in terms of the following equations:

$$\frac{\partial \lambda_{num,j}(\theta)}{\partial \theta} = \Phi_{num,j}^T(\theta) \frac{\partial K(\theta)}{\partial \theta} \Phi_{num,j}(\theta) \quad (10.7)$$

$$\frac{\partial \Phi_{num,j}(\theta)}{\partial \theta} = \sum_{i=1; i \neq j}^{m_f} \frac{\Phi_{num,i}(\theta)}{\lambda_{num,j}(\theta) - \lambda_{num,i}(\theta)} \left(\Phi_{num,i}^T(\theta) \frac{\partial K(\theta)}{\partial \theta} \Phi_{num,j}(\theta) \right) \quad (10.8)$$

with $\lambda_{num,j}(\theta) = (2\pi f_{num,j}(\theta))^2$ being the numerical eigenvalue j and $K(\theta)$ the stiffness matrix of the structure. The solution to Eqs. (10.7) and (10.8) may be obtained using commercial software like FEMtools (FEMtools, 2017) or ANSYS (ANSYS, 2017).

In this sense, although the stiffness matrices are not directly available in much commercial FE software, these magnitudes may be obtained from the nodal forces generated by the deflection of the structure associated with the considered vibration modes (Teughels et al., 2002).

The result of the sensitivity analysis, together with the engineering judgement of the user allows for determining the most adequate physical parameter that will be adjusted during the updating process. A typical choice of physical parameters may include: (1) geometrical parameters, such as the dimensions of the different elements of the structure and the imperfections; (2) material parameters, such as the modulus of elasticity and the shear modulus; (3) boundary conditions; (4) effects of interaction elements; (5) dynamic parameters, such as mass and damping; (6) durability parameters, such as corrosion rate and carbonation rate; or (7) force-dependent elements, as cables (Mottershead et al., 2011).

10.5.4 Preliminary manual tuning and establishing a search domain

Independent of the global optimization algorithm selected, it is always recommended to perform an initial manual tuning of the FE model before initiating the updating process, in order to determine a reasonable starting point for the selected

parameters (Brownjohn et al., 2001). This step reduces the computational time and favors solutions with physical significance.

It is also of key importance to establish reasonable lower and upper limits for parameter variation. For this purpose, it is a common practice to resort to the results of nondestructive tests, in particular when these parameters are related to the material properties of the structure (Fib, 2003).

10.5.5 Model updating process

The FE model updating process is sketched in the flowchart of Fig. 10.2. The unknown model parameters, θ , are adjusted, in an iterative process, in order to reduce the differences between the numerical and experimental modal parameters. The numerical modal parameters are obtained from a FE model of the structure. The experimental modal parameters are estimated through the signal processing of the measurements recorded during the development of a dynamic field tests. The process allows improving the FE model, such that it better reflects the actual behavior of the structure. On the other hand, an estimation of the parameters is obtained as a result of the updating. In order to perform the updating process the common practice is to either use commercial software that develops all the process (e.g., FEMtools, 2017) or to implement a code linking a global optimization package (e.g., Matlab, 2017) to a commercial FE package (e.g., ANSYS, 2017). The first

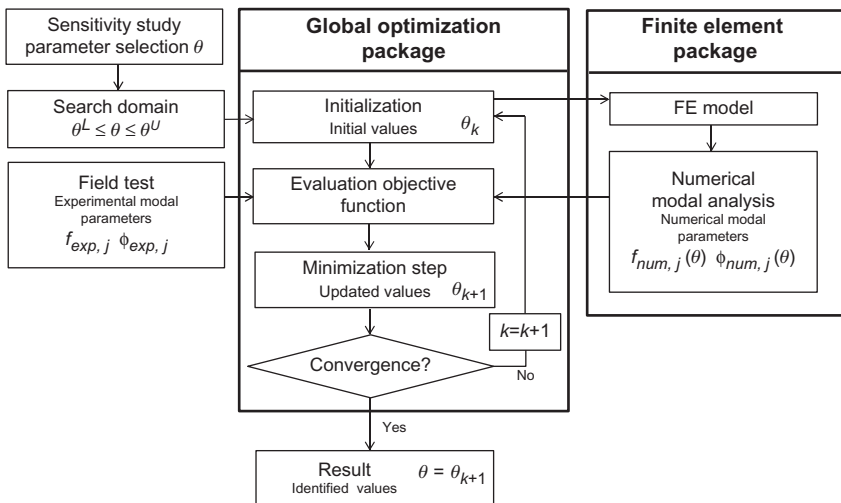


Figure 10.2 Flowchart of the iterative updating method based on global optimization. *Source:* From Costa, C., Ribeiro, D., Jorge, P., Silva, R., Arêde, A., Calçada, R., 2016. Calibration of the numerical model of a stone masonry railway bridge. *Eng. Struct.* 123 345–371; Jiménez-Alonso, J.F., Sáez, A., Caetano, E., Magalhães, F., 2016. Vertical crowd-structure interaction model to analyse the change of the modal properties of a footbridge. *J. Bridge Eng.* ASCE 21 C4015004.

option has as its main advantage the provision of a compact solution to the model updating, allowing inexperienced users to perform the process. The second option, reserved for users with a deeper theoretical knowledge on the subject, allows more freedom in the selection of the different options related to the development of the updating process (Jiménez-Alonso et al., 2016; Costa et al., 2016).

Summarizing, the updating process consists of the following seven steps: (1) create an initial FE model of the structure; (2) perform a preliminary modal analysis to obtain the numerical modal parameters; (3) design the field test based on the results of this preliminary modal analysis; (4) perform the field test; (5) identify the modal parameters via the signal processing of the measurement data; (6) modify the value of some physical parameters of the FE model based on the differences between the numerical and experimental modal parameters (model updating); and (7) use the updated model for decision making, structural assessment and other management activities.

The updated numerical model constitutes a good approximation to the real structure and it may be used for any structural evaluation under service conditions. Additionally, the updated FE model may be used as the starting point to perform further nonlinear FE analyses (Wenzel, 2009).

10.6 Application example: deterioration assessment of the Molinos Bridge

Finally, in order to illustrate the potential of the proposed approach, a case study is presented next. In this study, the deterioration assessment of an ancient reinforced concrete bridge was performed by FE model updating, based on its experimental modal parameters. These experimental modal parameters were obtained from an ambient vibration test using OMA. The study focused on estimating the deterioration state of the structure via the comparison of the results for two load scenarios: (i) a numerical load test performed on the updated FE model and (ii) the available original experimental load test of the bridge. The conclusions of this study were later used to select the most adequate retrofitting method for the reinforcement of the bridge, before undertaking the planned widening of its deck. A more detailed description of this case study may be found in Jiménez-Alonso and Sáez (2016).

The Molinos Bridge (Almería, Spain), originally built in 1927, is an isostatic truss structure with five spans (32.64, 32.72, 32.72, 32.68, and 32.78 m) and a total length of 163.54 m (Fig. 10.3A). The structure of each span is configured by two reinforced concrete truss girders separated transversally (2.70 m) and braced at the top by a reinforced concrete slab of variable depth (between 0.18 and 0.54 m). The depth of the structure is ~ 2.66 m and its width ~ 6.20 m.

The planning department of the city of Almeria decided, for economic reasons, to rehabilitate this ancient bridge in order to improve the road access to the neighborhoods located at the east of the town. A public contest was held, and six proposals were presented. One of the provisions that the rehabilitation project should

meet was the retrofitting of the main girders, in order to ensure an adequate bearing capacity under the new loading conditions. Regarding this issue, the alternatives proposed by the different engineering firms could be grouped into two retrofitting methods: (1) use external prestressing or (2) use carbon fiber reinforced polymer (CFRP) laminates. In order to decide which retrofitting method was better suited to the structural needs, the deterioration state of the structure and its influence on the structural stiffness had to be characterized. In this way, if the structure was seriously damaged, the retrofitting method should focus on controlling both the stress level and the deflection of the structure, so the alternatives based on the external prestressing technique would become the most adequate. On the contrary, if the deterioration state was limited, the CFRP reinforcement would be the appropriate solution.

Therefore, a detailed study was performed to assess the deterioration state of the bridge. Due to its monumental character, the evaluation should be performed by nondestructive methods. First, the deterioration state of the structure was analyzed through visual inspection. Detachment of the reinforced concrete along the truss girders and cracking in the lower chord were observed during this preliminary inspection (Fig. 10.3B).

In order to assess the influence of the detected cracks on the structural stiffness of the bridge, the authors decided to compare the results of the original load test at the time of construction with the same load test replicated on the current structure. However, due to the impossibility of reproducing this original experimental load test on the bridge at present, due both to its monumental character and to deterioration, we decided to numerically simulate its current response with the assistance of a calibrated FE model of the bridge. To ensure that the numerical model adequately reflected the current deterioration state of the structure, the FE model was updated based on the results of two different field tests: an ambient vibration and a rebound-hammer test.



Figure 10.3 (A) Elevation of the Molinos Bridge and (B) Detail of the cracking of its lower chord.

Source: From Jiménez-Alonso, J.F., Sáez, A., 2016. Model updating for the selection of an ancient bridge retrofitting method. *Struct. Eng. Int.* 26 (1), 17–26.

The FE model updating of this structure followed the flowchart in Fig. 10.2:

First, an initial FE model of the fifth span (east abutment) of the structure was made using the commercial software ANSYS (ANSYS, 2017). Only this span was analyzed due to the isostatic configuration of the structure, its greater length, and accessibility reasons. For the purpose of this study, reinforced concrete was considered homogenous and the resulting model consisted of 870,945 3D solid-brick elements. The pavement and barriers of the bridge were accounted for by adding an additional mass of 275 kg/m^2 and 75 kg/m , respectively. The effect of the supports in longitudinal direction was simulated by spring elements, with the other two displacement degrees of freedom constrained.

Second, a preliminary FE static analysis of the structure under permanent loads was performed. The results of this analysis, together with a subsequent sensitivity study, were later used to select the physical parameters to be calibrated during the updating process.

Third, a numerical modal analysis was completed in order to obtain the first three vertical vibration modes of the structure, as Fig. 10.4 illustrates.

Fourth, the modal parameters of the considered span were identified experimentally by the signal processing of the measurements recorded during an ambient vibration test, via the application of an OMA algorithm in the frequency domain (Magalhães and Cunha, 2011), namely the Enhanced Frequency Domain Decomposition method, as implemented in the commercial software Artemis (Artemis, 2017). The numerical and experimental first three vertical natural frequencies and vibration modes are compared in Table 10.1. To correlate the numerical and experimental modal parameters, Table 10.1 includes the values of the relative differences between natural frequencies,

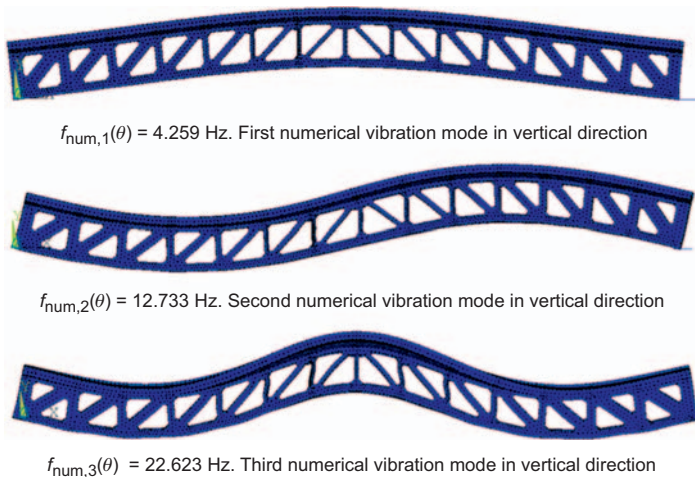


Figure 10.4 First three vertical numerical vibration modes of the initial finite element (FE) model.

Source: From Jiménez-Alonso, J.F., Sáez, A., 2016. Model updating for the selection of an ancient bridge retrofitting method. *Struct. Eng. Int.* 26 (1), 17–26.

Table 10.1 Correlation between the first three vertical numerical, $f_{num,j}(\theta)$, and experimental, $f_{exp,j}$, natural frequencies of the Molinos Bridge

Mode	$f_{num,j}(\theta)$ [Hz]	$f_{exp,j}$ [Hz]	$\Delta f_j(\theta)$ [%]	$MAC_j(\theta)$	Description
1	4.259	4.320	- 1.412	0.992	First bending
2	12.733	10.100	26.069	0.985	Second bending
3	22.623	17.840	26.810	0.961	Third bending

Source: From Jiménez-Alonso, J.F., Sáez, A., 2016. Model Updating for the Selection of an Ancient Bridge Retrofitting Method. Struct. Eng. Int., 26 (1), 17–26.

$\Delta f_j(\theta)$, and the modal assurance criterion values, $MAC_j(\theta)$. Although the $MAC_j(\theta)$ values for the three considered vertical vibration modes were adequate (with $MAC_j(\theta)$ above 0.95), the relative differences in terms of frequencies were still large (with $\Delta f_j(\theta)$ greater than 25% for modes 2 and 3). Therefore, it was necessary to adjust the FE model of the structure to better reflect the current structural behavior occasioned by the deterioration state of the bridge.

Subsequently, the model updating was conducted by implementing an indirect approach (Mottershead et al., 2011), as a single-objective optimization problem. Genetic algorithms were adopted in this study as an optimization method. The objective function was defined in terms of the weighted least square residuals between the numerical and experimental modal parameters. As residuals, the first three vertical natural frequencies and associated vibration modes were considered, due to the good quality of the experimental data. The lower reliability of the experimental vibration modes in comparison to the experimental natural frequencies is reflected in the considered values of the weighting factors, $\sum w_j^f = 0.90$ and $\sum w_j^m = 0.10$ respectively, according to the recommendations of several authors (Teughels et al., 2002; Zivanovic et al., 2007).

The definition of each term (θ_j) of the physical parameter vector (θ), which are the design variables of the optimization problem, was made—based on the trade-offs among the results of three independent analyses: (1) the preliminary visual inspection of the structure; (2) the resultant stresses distribution of the previously mentioned static analysis of the structure; and (3) a sensitivity analysis of the considered modal parameters to the stiffness of the different structural elements in the numerical model. Ten parameters were considered, namely: (1) the Young's modulus of the concrete in different parts of the structure, $\theta_1 - \theta_9$, and (2) the stiffness of the longitudinal spring elements that simulates the deck–pier interaction, θ_{10} , as Fig. 10.5 illustrates.

Finally, in order to increase the efficiency of the optimization method yet maintain the physical meaning of the updating process, a search domain for each term of the considered physical parameter vector was established. The results obtained from the rebound-hammer test were used to determine the range of variation of the parameters associated with the Young's modulus of the concrete. The uncertainty associated with the high friction of the steel bearings under low vibration levels is

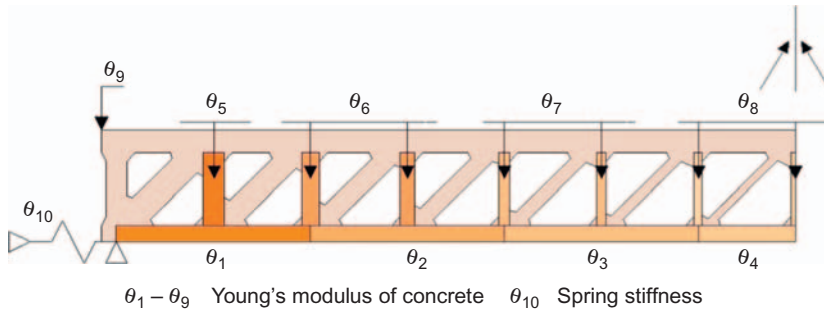


Figure 10.5 Parameter selection for the updating process (see Table 10.2).

Source: From Jiménez-Alonso, J.F., Sáez, A., 2016. Model updating for the selection of an ancient bridge retrofitting method. *Struct. Eng. Int.* 26 (1), 17–26.

Table 10.2 Initial value, range of variation and updated value of the considered physical parameter vector (see Fig. 10.5)

θ	Description	Initial (θ_k)	Lower (θ_l)	Upper (θ_u)	Updated (θ_{k+1})
θ_1	Young's modulus lower chord (GPa)	30.00	3.00	38.00	25.38
θ_2	Young's modulus lower chord (GPa)	30.00	3.00	38.00	17.21
θ_3	Young's modulus lower chord (GPa)	30.00	3.00	38.00	12.32
θ_4	Young's modulus lower chord (GPa)	30.00	3.00	38.00	10.69
θ_5	Young's modulus strut (GPa)	30.00	3.00	38.00	28.71
θ_6	Young's modulus strut (GPa)	30.00	3.00	38.00	29.02
θ_7	Young's modulus strut (GPa)	30.00	3.00	38.00	29.32
θ_8	Young's modulus strut (GPa)	30.00	3.00	38.00	29.63
θ_9	Young's modulus remaining structure (GPa)	30.00	3.00	38.00	30.15
θ_{10}	Longitudinal stiffness of spring (MN/m)	265.00	100.00	700.00	345.00

Source: From Jiménez-Alonso, J.F., Sáez, A., 2016. Model Updating for the Selection of an Ancient Bridge Retrofitting Method. *Struct. Eng. Int.*, 26 (1), 17–26.

considered, establishing a search domain for this parameter whose lower and upper terms reduce and increase respectively 2.5 times its initial value. The range of variation for each component of the physical parameter vector is given in Table 10.2.

The model updating process was conducted implementing the previously described algorithm with the aid of: (1) a global optimization software, Matlab[®] (Matlab, 2017) and (2) a FE software, ANSYS (ANSYS, 2017). A population of

1000 vectors was considered for the genetic algorithm optimization. Such genetic algorithms are based on the analogy with the natural evolution, whereby the members of a population compete to survive and reproduce, presenting the best individuals a genetic code that allows them to take advantage over the rest of the population. The algorithm acts on a population of design variables (chromosomes) whose fitness value is given by the objective function value. The algorithm generates a new population of design variables from the old population using three randomized operators that mimic the natural evolution: reproduction (selection), crossover, and mutation. According to these operators, each subsequent generation tends to have an average fitness level higher than the previous generation (Nocedal and Wright, 1999). In Table 10.2, the initial value, the range of variation, and the updated value of the considered physical parameter vector are shown.

After the updating process, the differences between the numerical and experimental modal data are really small. The correlation between the updated and experimental modal data are shown in Table 10.3 and Fig. 10.6. The improvement of the updated model with respect to the initial one is clear, with differences in the natural frequencies values below 0.15 % and MAC_j values above 0.990.

Furthermore, the updated values of the physical parameter vector (Table 10.2) show that the visually-observed cracking of the lower chord affects the stiffness of this element, exhibiting a good correlation between the inertia reduction predicted by the model, and the localization and size of the observed cracks. Additionally, the estimated medium value of the Young's modulus of the reinforced concrete presents a reasonable value with reference to the value considered in the original project of the structure.

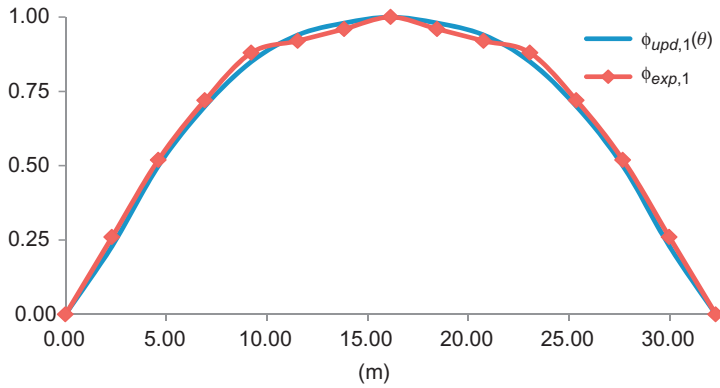
In this way, the updated FE model adequately reflects the structural behavior of the actual bridge, with an excellent agreement between the numerical and experimental modal data.

Finally, the updated model was used to numerically simulate the original experimental load test of the bridge on the current structure. According to the published results of this experimental test, the maximum vertical deflection at the mid-span was 8 mm. The maximum deflection predicted by the updated model under the same load conditions was around 7.2 mm. From these results, it was concluded that the inertial reduction of the lower chord had not caused deflection problems in the

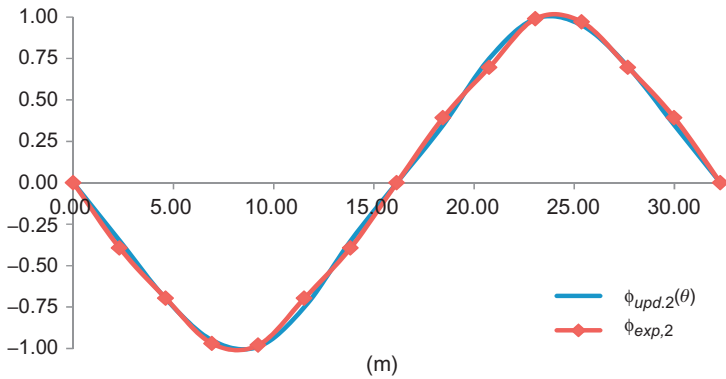
Table 10.3 Correlation between the first three vertical updated, $f_{upd,j}(\theta)$, and experimental, $f_{exp,j}$, natural frequencies of the Molinos Bridge

Mode	$f_{upd,j}(\theta)$ (Hz)	$f_{exp,j}$ (Hz)	$\Delta f_j(\theta)$ (%)	$MAC_j(\theta)$	Description
1	4.323	4.320	0.069	0.999	First bending
2	10.114	10.100	0.138	0.997	Second bending
3	17.853	17.840	0.072	0.996	Third bending

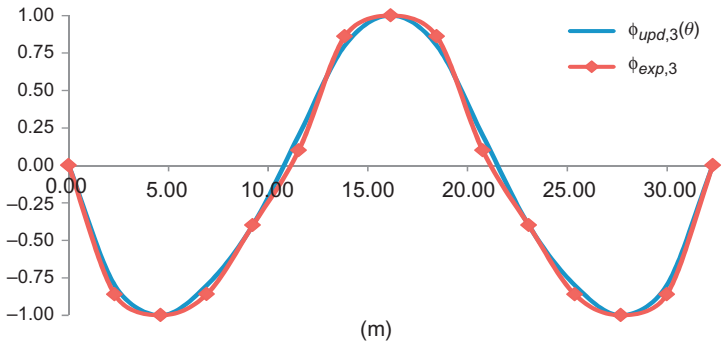
Source: From Jiménez-Alonso, J.F., Sáez, A., 2016. Model Updating for the Selection of an Ancient Bridge Retrofitting Method. Struct. Eng. Int., 26 (1), 17–26.



First updated numerical ($\phi_{upt,1}(\theta)$) and experimental ($\phi_{exp,1}$) vertical vibration mode



Second updated ($\phi_{upt,2}(\theta)$) and experimental ($\phi_{exp,2}$) vertical vibration mode



Third updated ($\phi_{upt,3}(\theta)$) and experimental ($\phi_{exp,3}$) vertical vibration mode

Figure 10.6 First three vertical updated, $\phi_{upd,j}(\theta)$, versus experimental vibration modes, $\phi_{exp,j}$.

Source: From Jiménez-Alonso, J.F., Sáez, A., 2016. Model updating for the selection of an ancient bridge retrofitting method. Struct. Eng. Int. 26 (1), 17–26.

structure. Therefore, the retrofitting of this ancient bridge should be performed using CFRP laminates.

After the completion of the rehabilitation works using CFRP, the Molinos Bridge is currently in service showing adequate structural behavior.

10.7 Conclusions

FE models may be a useful tool to assess the deterioration state of concrete structures and make further decisions about the best strategy for their maintenance and reinforcement. In this sense, it is necessary that the structural response predicted by these numerical models adequately reflects the actual behavior of the structure. To guarantee it, the FE models must be checked and updated based on the results of field tests and/or continuous monitoring conducted on the structure. On the other hand, adequate FE models are necessary in order to interpret both the results provided from field tests and the structural changes detected by the continuous monitoring of structures.

The FE model updating of concrete structures is usually based on the results of two types of experimental diagnosis tests: (1) static and (2) dynamic tests. Static tests are normally used to provide only secondary information for the updating process. Dynamic tests are used mainly to identify the modal parameters of the structure. Among the identified modal parameters, natural frequencies and vibration modes are commonly adopted as reference for the model updating process.

The updating process is usually formulated as an optimization problem whereby some physical parameters of the structure are modified in order to minimize the relative differences between the numerical and experimental modal parameters. Such an updating process usually follows the following scheme: (1) create an initial FE model of the structure; (2) perform a preliminary modal analysis; (3) design the field test based on the results of this preliminary modal analysis; (4) perform the field test; (5) identify the modal parameters via the signal processing of the measured data; (6) adjust some previously selected physical parameters of the numerical model based on the experimental modal data; and (7) use the updated model for decision making or structural assessment.

In particular, this model updating approach may be used, due to its similarity to damage detection, to establish a strategy for deterioration assessment of concrete structures. The process may be organized in five steps: (1) create an initial FE model of the structure; (2) identify the experimental modal parameters; (3) update the initial FE model based on the experimental modal parameters; (4) repeat steps (2) and (3) again after the deterioration has happened; and (5) use the updated parameters as an indicator of the deterioration.

The potential of the model updating approach has been illustrated with a case study, the deterioration assessment of the Molinos Bridge (Almeria, Spain). The main objective of this study focused on assessing the deterioration state of this ancient bridge in order to select the best retrofitting method for its reinforcement, before a planned modification of its service conditions.

10.8 Future trends

Although the FE model updating process is a mature technique, further studies are being conducted in order to improve the numerical simulation of the actual behavior of concrete structures through calibrated FE models. Among others, the following research lines may be cited:

1. The model selection, the process of choosing the best updated FE model among all the plausible updated models, has been performed here by solving an optimization problem. Other alternatives, as for example those based on Bayesian approaches need to be further explored.
2. The parameter selection is, principally, an arbitrary process based on the engineering judgement of the user. The inclusion in the updating process of computational intelligence techniques for the automatic parameter selection deserves additional research efforts.
3. The data used as reference for the model updating and deterioration assessment are commonly the modal parameters (natural frequencies and vibration modes). The effective use of other types of data, like time-frequency domain data (wavelet data), modal strain or modal strain energy is another active area of research.
4. The difficulty in modeling damping has meant that the current updating methods do not include this parameter in the identification process. As there is a direct relationship between damping and deterioration, the proposal and implementation of appropriate models considering this modal parameter should be further explored.

Acknowledgments

This work was supported by the Ministerio de Economía y Competitividad of Spain, the European Regional Development Fund and the Consejería de Economía, Innovación, Ciencia y Empleo of Andalucía (Spain) under projects DPI2014-53947-R and P12-TEP-2546. The financial support is gratefully acknowledged. The authors also acknowledge the Planning Department of the City of Almería (Spain) for their support during the development of the experimental field test. Some of the figures in Section 10.6 were reprinted from [Jiménez-Alonso and Sáez \(2016\)](#)—Structural Engineering International (SEI), 26 (1), 17–26—with permission from SEI journal (published by IABSE—International Association for Bridge and Structural Engineering).

References

- ANSYS Mechanical Release (2017), <<http://www.ansys.com/>>.
- ARTEMIS Modal (2017), <<http://www.svibs.com/>>.
- Brownjohn, J.M.W., Xia, P.-Q., Hao, H., Sia, Y., 2001. Civil structure condition assessment by FE model updating: methodology and case studies. *Finite Elem. Anal. Des.* 37, 761–775.
- Caetano, E., Cunha, A., Hoopah, W., Raoul, J., 2009. *Footbridge vibration design*. CRC Press. Taylor and Francis Group, London.

- Compán, V., Pachón, P., Cámara, M., Lourenço, P.B., Sáez, A., 2017. Structural safety assessment of geometrically complex masonry vaults by non-linear analysis. The Chapel of the Würzburg Residence (Germany). *Eng. Struct.* 140, 1–13.
- Costa, C., Ribeiro, D., Jorge, P., Silva, R., Arêde, A., Calçada, R., 2016. Calibration of the numerical model of a stone masonry railway bridge. *Eng. Struct.* 123, 345–371.
- Doebling, S.W., Farrar, C.R., Prime, M.B., Shevolsz, D.W., 1996. Damage Identification and Health Monitoring of Structural and Mechanical Systems From Changes in Their Vibration Characteristics: A Literature Review. Los Alamos National Laboratory Report LA-13070-MS.
- EWINS, D.J., 2000. *Modal Testing, Theory, Practice and Application*. John Wiley & Sons.
- FEMtools v3.8 Dynamic Design Solutions, 2017. <<http://www.femtools.com/>>.
- Fib Bulletin 22, 2003. Monitoring and Safety Evaluation of Existing Concrete Structures. International Federation for Structural Concrete.
- Fox, R., Kapoor, M., 1968. Rate of change of eigenvalues and eigenvectors. *AIAA J.* 6, 2426–2429.
- Friswell, M.I., Mottershead, J.E., 1995. *Finite Element Model Updating in Structural Dynamics*. Kluwer Academic Publishers.
- Gentile, C., 2006. Modal and structural identification of a R.C. arch bridge. *Struct.Eng. Mech.* 22, 53–70.
- Hu, W.H., Caetano, E., Cunha, A., 2013. Structural health monitoring of a stress-ribbon foot-bridge. *Eng. Struct.* 57, 578–593.
- Jaishi, B., Ren, W.X., 2006. Damage detection by finite element model updating using modal flexibility residual. *J. Sound Vib.* 290, 369–387.
- Jiménez-Alonso, J.F., Sáez, A., 2016. Model updating for the selection of an ancient bridge retrofitting method. *Struct. Eng. Int.* 26 (1), 17–26.
- Jiménez-Alonso, J.F., Sáez, A., Caetano, E., Magalhães, F., 2016. Vertical crowd-structure interaction model to analyse the change of the modal properties of a footbridge. *J. Bridge Eng. ASCE.* 21, C4015004.
- Jin, S.-S., Cho, S., Jung, H.-J., Lee, J.-J., Yun, C.-B., 2014. A new multi-objective approach to finite element model updating. *J. Sound Vib.* 333, 2323–2338.
- Kim, G.-H., Park, Y.-S., 2004. An improved updating parameter selection method and finite element model update using multi-objective optimisation technique. *Mech. Syst. Signal Process.* 18, 59–78.
- Kwon, Y.W., Bang, H., 2000. *The Finite Element Method using MATLAB*. CRC Press LCC.
- Levin, R.I., Lieven, N.A.J., 1998. Dynamic finite element model updating using simulated annealing and genetic algorithms. *Mech. Syst. Signal Process.* 12, 91–120.
- LMS Testlab, 2017. <https://www.plm.automation.siemens.com/es_es/products/lms/testing/test-lab/>.
- MACEC 3.3 released, 2017. <<http://bwk.kuleuven.be/bwm/macec>>.
- Magalhães, F., Cunha, A., 2011. Explaining Operational Modal Analysis with data from an arch bridge. *Mech. Sys. Signal Process.* Invited Tutorial Paper 25 1431–1450.
- Maia, N.M.M., Silva, J.M.M., He, J., et al., 1997. *Theoretical and Experimental Modal Analysis*. Research studies Press Ltd, Somerset.
- Marwala, T., 2010. *Finite-Element-Model Updating Using Computational Intelligence Techniques. Applications to Structural Dynamics*. Springer.
- Marwala, T., Boulkaibet, I., Adhikar, S., 2016. *Probabilistic Finite Element Model Updating Using Bayesian Statistics: Applications to Aeronautical and Mechanical Engineering*. John Wiley & Sons.
- Matlab R2016b, 2017. <<http://www.mathworks.com/>>.

- ME' scope, 2017. <<https://www.vibetech.com/mescope/>>.
- Moller, P.W., Friberg, O., 1998. Updating large finite element models in structural dynamics. *AIAA J.* 36, 1861–1868.
- Mottershead, J.E., Link, M., Friswell, M.I., 2011. The sensitivity method in finite element model updating: a tutorial. *Mech. Syst. Signal Process.* 25, 2275–2296.
- Nocedal, J., Wright, S.J., 1999. *Numerical Optimization*. Springer, New York.
- Peeters, B., 2000. *System Identification and Damage Detection in Civil Engineering*. Ph.D. Thesis, Katholieke Universiteit Leuven.
- Pulse Analysis Software, 2017. <<https://www.bksv.com/en/products/PULSE-analysis-software>>.
- Rainieri, C., Fabbrocino, G., 2014. *Operational Modal Analysis of Civil Engineering Structures. An introduction and Guide for Applications*. Springer Science + Business Media, New York.
- Rombach, G.A., 2011. *Finite-Element Design of Concrete Structures: Practical Problems and Their Solutions*. Institution of Civil Engineers, London.
- Schlune, H., Plos, M., Gylltoft, K., 2009. Improved bridge evaluation through finite element model updating using static and dynamic measurements. *Eng. Struct.* 31, 1477–1485.
- Teughels, A., Maeck, J., De Roeck, G., 2002. Damage assessment by FE model updating using damage functions. *Comp. Struct.* 80, 1869–1879.
- Teughels, A., Roeck, G., 2004. Structural damage identification of the highway bridge Z24 by FE model updating. *J. Sound Vib.* 278, 589–610.
- Wenzel, H., 2009. *Health Monitoring of Bridges*. John Wiley & Sons, Ltd, West Sussex.
- Zivanovic, S., Pavic, A., Reynolds, P., 2007. Finite element modelling and updating of a lively footbridge: the complete process. *Eng. Struct.* 301 (1-2), 126–145.

Part II

Innovative concrete repair and rehabilitation materials

This page intentionally left blank

Alkali activated repair mortars based on different precursors

11

Vilma Ducman, Sabina Kramar and Aljoša Šajna

Slovenian National Building and Civil Engineering Institute, Ljubljana, Slovenia

11.1 Introduction

Repair works in the construction sector present a huge part of all the construction work carried out; namely, with the aging of the existing infrastructure there is an increased need for its repair, maintenance and protection (Raupach, 2006). It is estimated that infrastructure rehabilitation costs go into trillions of dollars; for the 84,000 concrete bridges in the European Union alone, the annual cost for maintenance and repair is £215 million (Pacheco-Torgal, 2012b), while in the United States, the annual cost of repair, protection, and strengthening is estimated to be between \$15 and \$22 billion (Emmons, 2012).

Repair mortars need to fulfill many specific requirements for the intended uses that are described in more detail in the next subchapter (11.3), but—to mention only a few, such as freezing resistance, high compressive strength, rapid setting, and good adhesion to substrate—it is clear that they belong to the group of demanding construction products, both from the technical point of view and from the perspective of cost.

The first repair mortars, which are still sometimes used, were based on cement alone, but were not satisfactory mainly because they did not harden fast enough, their tensile and adhesion strength was low, and they were not suitable for thin section repair. Thus, the most commonly used repair mortars nowadays are based on Portland or blended cements, to which different polymers are added, such as polyurethane, epoxy and acrylic resins, or thermosetting vinyl. These additives are used in order to achieve the required properties, such as high early compressive strength, good adhesion, and impermeability (Chatterjee, 2012). To achieve high tensile strength, fibers are also often used in repair systems, such as High Performance Fiber-Reinforced Cement Based Composites (HPFRCC) and Textile Reinforced Concrete (TRC) (Bruhwiler, 2012, Mechterine, 2012).

Magnesia–phosphate cement has also been used as repair mortar, because, if properly ground and mixed with additives, it can be hardened within one hour, even at -10°C . The addition of fly ash in such systems is also common. Such rapid repair systems are especially welcome for airport runways, highways and other places where longer interruptions that can cause service delays, are unwanted (Yang and We 1999; Yang et al., 2000).

Even bacteria are being used for repair purposes; a specific group of spore-forming bacteria from the *Bacillus* group and a nutrient for bacteria

(e.g., calcium lactate) are added to the repair mortar. Through the bacterial metabolisms, this nutrient is transformed into carbonates which fill the present cracks (Jonkers, 2011).

Because of the market demand for an environmentally friendly, yet technically suitable and cost-competitive repair mortar, the development of other alternative mortars has been on the rise (Pacheco-Torgal et al., 2014). Recently, many attempts have been made to make repair mortars out of waste, such as fly ash and slag, precursors for geopolymers or alkali-activated materials (AAM).

11.2 Alternative repair mortars for concrete repair

According to Imbabi et al. (2012), it is to be expected that, by 2030, the cost of cement will double due to the increase in energy costs and green taxes. Even though significant improvements in cement production have been made so far, its production still accounts for 6% of all man-made CO₂ emissions. Therefore, an alternative to cement binder is needed as an environmentally friendly replacement. Here, different waste materials come to light. Some of them (fly ash, slag) have already been successfully implemented in blended cements and/or as supplementary cementitious materials (SCM) added to concrete. However, the focus has been placed on “cement-free” binders; alkali-activated binder is one such type. Alkali-activated binders are produced by the reaction of aluminosilicate materials (also containing calcium)—preferably from waste or industrial by-products, with an alkaline activator, consisting of an aqueous solution of alkali hydroxide, silicate, carbonate, or sulfate. The term “geopolymer” is often used as a synonym, but according to the Davidovits definition, in geopolymers in the binding phase there are almost exclusively highly-coordinated aluminosilicates and the content of calcium is usually low; during the alkali-activation process, a zeolite-like structure is formed (Provis and van Deventer, 2013). Calcined clays and low-calcium fly ash are typical precursors in geopolymer synthesis, while in alkali activation processes—which is a broader term—slag, natural pozzolan, fly ash or bottom ash are also included (Provis and van Deventer, 2013).

Metakaolin has been extensively studied as a precursor for AAM. It is environmentally-beneficial if it can be obtained as waste (Dembovska et al., 2017), but metakaolin is usually obtained through the calcination of kaolin between 600°C and 900°C (Zuhua et al., 2009), which is still a significantly lower temperature than that in cement production. Hundreds of papers have been published related to this precursor for different applications, among them the use as repair mortars. Vasconcelos et al. (2011) studied the use of metakaolin-based geopolymer as a repair layer and as an adhesive between carbon-fiber reinforced polymer (CFRP) sheets and concrete substrate. They used a different sand-to-binder mass ratio (30%, 60%, and 90%), and they also varied the sodium hydroxide concentration (12, 14, and 16 M), and Ca(OH)₂ content (5% or 10%). In most of the cases the adhesion was too low (recommended minimum given by the Concrete Society is 0.8 MPa)

and it is assumed that if the sand-to-binder ratio is low, then high shrinkage causes microcracks on the contact surface, which decreases the bond strength. The bond strength mechanism proposed by Zhang et al. (2010b) is chemical bonding, whereby the dissolution of hydrated cement takes place and a new geopolymer gel containing calcium is formed. Since zeolite-like compounds are formed in the metakaolin-based geopolymer, which tend to crystallize (at hydrothermal curing conditions), reorganization on a micro level takes place—which causes a reconstruction of the gel and loss of compressive strength. Such phenomenon, however, has not been noticed in fly ash-based geopolymer. Zhu et al. (2013) reported that they have prepared metakaolin-based repair mortars that were cured at 20°C in air and 95 ± 5% relative humidity (AC), sealed in a plastic bag and cured at 80°C (SC), and cured in a water bath at 80°C (WC). An identical cement-based mortar was also cured. For the cement-based mortars, it was confirmed that, where high humidity was present (AS, WC), compressive strength from 7 to 28 days' value increased, while in the sealed conditions it decreased (likely because of water evaporation from the sample at the elevated temperature). For geopolymer samples, in both cases of elevated temperature (SC, WC), the compressive strength dropped from 7 to 28 days, which was ascribed to the formation of zeolite. A similar drop is also noticed in bond/adhesion strength after 28 days in elevated temperature conditions. The X-ray diffraction (XRD) analyses have confirmed the formation of zeolite for geopolymer repair mortars exposed to elevated curing. This presents a question about the kinetics of zeolite formation at lower temperatures, because this is related to the durability aspects.

Slag is rarely used as a single material for repair mortar, but more often in combination with other precursors, mostly metakaolin, which can contribute to improved properties of the final product (Dufka et al., 2015; Zhang et al., 2010a; Hu et al., 2008; Tamburini et al., 2017). Slag does not need thermal pretreatment; often only grinding to obtain a fine, reactive powder. The study by Dufka has confirmed that such alkali-activated mortars (the slag-to-metakaolin mass ratio was 4.3:0.5) when exposed to sulfate and chloride solutions did not cause changes in the mechanical properties, while selected polymer cement-based mortar exhibited a strong decrease (50%) after exposure to sulfate solution. Zhang et al. (2010a) also noted that the addition of 10% (and up to 30%) of granulated blast furnace slag-to-metakaolin reduced the permeability of the prepared geopolymers. He has also proposed a bonding mechanism, supposedly of a chemical nature, caused by the dissolution of Ca (in fact breaking of the Ca–O bond in C–S–H gel in strong alkali conditions), which then reacts with the alkali activator and forms another C–S–H gel. This interfacial-formed C–S–H gel makes the transition zone more homogeneous, providing a strong bonding. Also, portlandite from ordinary Portland cement (OPC) can react with Al and Si-containing specimens and contribute to the stronger bond (Pacheco-Torgal et al., 2008a). Hu et al. (2008) also reported a much higher bond strength for the geopolymer based on metakaolin (calcined at 750°C for 6 hours) than for the cement-based one; the 28-day bond strength for the geopolymer sample was 2.91 MPa, while for the cement repair material it was 1.95 MPa. An additional slight increase in bond strength was observed when 20% of

metakaolin was replaced with steel slag. Geopolymer mortar exhibited better abrasion resistance than cement mortar; when steel slag was added, this characteristic also improved.

Contrary to (meta)kaolin, fly ash is waste that does not need any pretreatment prior to alkali activation. Fly ash, if it fulfils the requirements of EN 197-1: 2011 and EN 450-1: 2012, can be used as an additive for cement to make blended cement, or added directly to the concrete as a mineral additive. There is still a lot of available fly ash, while biomass ash could also serve as a precursor for alkali-activated mortars with high compressive strengths (Temuujin et al., 2010), which makes it a candidate for use as repair mortar. Wanchai (2014) reported that he applied lignin-arising fly ash for the repair material in reinforced-concrete structures. The basic properties of geopolymer mortar were similar to those of cement-based mortars, e.g., the 28-day compressive strength of all three investigated mixtures amounted to ~ 40 MPa and the load carrying capacity of the optimal alkali-activated sample was similar to the conventional cement-based repair mortar. However, the corrosion of steel-reinforcements of fly ash geopolymer reinforced concrete was higher than in the cement-based case; the weight loss of the rebar was higher when a geopolymer was used. Consequently, the durability is lowered. In the paper, there is no data about the microstructure properties, but looking at other studies of fly ash geopolymer mortars (Natali et al., 2014) it can be observed that geopolymer mortars, when compared to cement mortars, have a more open structure. Using mercury-intrusion porosimetry (MIP), they have confirmed that a more compact microstructure is found in cement mortars. In this study, a better corrosion performance was detected when measured after one week of exposure (in the samples where the nominal molar ratio $\text{Na}_2\text{O}/\text{SiO}_2$ was equal to 0.12 and 0.14), but after 3 months, the geopolymer and the OPC mortars exhibited similar corrosion behavior. It should be noted, however, that OPC mortar was prepared with a w/c factor of 0.52. If they had compared mortars with a lower w/c factor (with the addition of superplasticizers) it is very likely that the cement mortar would have exhibited a lower corrosion rate, due to the more compact structure.

Tungsten mine waste, previously heat-treated at 950°C to increase the amorphous phase, was also tested as a geopolymeric binder. Alkali precursors in different ratios and $\text{Ca}(\text{OH})_2$ were added to tungsten mine waste, resulting in the highest compressive strength when 10% of $\text{Ca}(\text{OH})_2$ was added. A correlation between $\text{H}_2\text{O}/\text{Na}_2\text{O}$ and compressive strength was also found; the lower the $\text{H}_2\text{O}/\text{Na}_2\text{O}$ molar ratio, the higher compressive strength was obtained, where the maximum compressive strength was around 70 MPa (Pacheco-Torgal et al., 2008b). The authors also report very good adhesion strength of such binder, even at early ages, and it was also shown that adhesion was not affected by the surface roughness of the substrate, which was not the case with commercially available cement-based repair mortars. By using scanning electron microscopy (SEM) analysis they confirmed that the geopolymer binder is chemically bound to the concrete substrate (Pacheco-Torgal et al., 2008a).

The benefits of combining alkali activation and classic cement-based bonding materials have been explored in the research on so-called hybrid systems, where part

of the cement is replaced by fly ash or other precursors (up to 80%) and activated by alkali activators. Researchers ([Garcia-Lodeiro et al., 2016](#)) reported that in such systems N-A-S-H and C-S-H gels coexist. With a highly alkaline activator (e.g., 12 M NaOH) the dissolution of ash is faster than clinker dissolution, but with a moderate alkaline activator (e.g., 5 M NaOH), then clinker hydration is favored and ash dissolution is retarded. With time, the thermodynamically most stable state is established, which in such systems is the coexistence of C-A-S-H and (N,C)-A-S-H. With such a combination, the benefits of both systems can be harvested in the reduced CO₂ emissions.

Like in cement-based repair mortars, the addition of fibers in AAM can contribute to mechanical improvements. [Lin et al. \(2009\)](#) reported that the addition of short carbon fibers to the metakaolin-based mortar—when added in the amount of 3.5 and 4.5 vol. %—significantly contribute to the strengthening and toughening effect. Flexural strength, e.g., increased by a factor of nearly 5. With higher amounts of additional fiber, the strengthening effect was reduced, attributed to the fiber damage and formation of high shear stress at intersections between fibers and matrix.

Alkali-activated mortars are emerging as prospective materials for concrete repair which, in spite of some shortcomings and sometimes contradictory reports, have so far been successfully used for rapid road repair ([Hawa et al., 2013](#)), for marine concrete protection ([Zhang et al., 2010a,b, 2012](#)), and stone repair and protection ([Pinto, 2010](#)), etc.

Due to the environmental constraints that promote the use of more environmentally-friendly materials with a lower CO₂ footprint, and due to cost restraints, it is very likely that alternative repair mortars—which AAM belong to—will find their market share, provided they guarantee the compliance with the standards' requirements. Although alkali-activated mortars nowadays may still be more expensive than cement-based ones because alkaline activators are costly, when taxes are applied to the cement due to CO₂ emissions (based on European Emission Trading Scheme), then the AAM can also become a cost-competitive solution ([Pacheco-Torgal et al., 2008a,b](#)).

11.3 Standard requirements for repair mortars

11.3.1 Introduction

In Europe, the provisions for the repair and protection of concrete structures are given in a series of European standards (EN 1504 Products and systems for the protection and repair of concrete structures). The series consist of 10 parts. Part 1 ([EN 1504-1:2005](#)) gives the definitions used in the standards. Part 8 ([EN 1504-8:2016](#)) sets forth the provisions for the quality control and evaluation of conformity. Part 9 ([EN 1504-9:2008](#)) is on the general principles for the use of products and systems. Part 10 ([EN 1504-10:2003](#) and [EN 1504-10:2003/AC:2005](#)) gives guidelines for the site application of the products and systems, and quality control of the work. Parts

2–7 are harmonized standards giving definitions and requirements for different types of products and systems for the protection and repair of concrete structures as follows: Part 2 (EN 1504-2:2002) for surface protection systems, Part 3 (EN 1504-3:2005) for structural and nonstructural repair, Part 4 (EN 1504-4:2004) for structural bonding, Part 5 (EN 1504-5:2013) for concrete injection, Part 6 (EN 1504-6:2006) for anchoring of reinforcing steel bars and Part 7 (EN 1504-7:2006) for reinforcement corrosion protection. In this chapter, the emphasis is on Part 3 which provides the requirements for structural and nonstructural repair of concrete structures using repair mortars and concretes. At the time of the preparation of this chapter, EN 1504-3:2005 was still valid, but a new edition was to be issued. The provisions summarized in the next chapters are taken from draft of EN 1504-3:2015.

11.3.2 Basic requirements

The standard EN 1504-3 specifies the requirements for the identification, performance (including durability), and safety of products and systems to be used for the structural and non-structural repair of concrete structures. The standard covers repair mortars and concretes based on cementitious and polymer binders, containing additions, admixtures or fibers, the addition of standardized binders such as calcium aluminate cement, and the addition of hydraulic or latent hydraulic or pozzolanic binders and aggregates.

Even though the standard is meant for the repair mortars based on cement and polymer binders, the methodology can be of help in the assessment of alkali-activated repair mortars; it can also serve as the basis for the eventual technical assessment.

Possible fields of application (the principles and methods) of mortars and concretes, as defined in the standard EN 1504-9, are listed in Table 11.1.

The European standard EN 1504-3 classifies mortars and concretes according to their constituent materials (product classes) and essential characteristics related to physical properties (performance classes). According to the standard, dependent on the constituent materials the following product classes apply (Chapter 4 of draft of EN 1504-3:2015):

- CM 1: Repair mortar product or system containing constituents according to EN 197-1:2011, EN 12620:2013, type I or II additions, admixtures or fibers;
- CM 2: Repair mortar product or system containing constituents according to CM 1 allowing the addition of standardized binders (e.g., according to EN 14647:2005);
- CM 3: Repair mortar product or system containing constituents according to CM 2 allowing the addition of hydraulic or latent hydraulic or pozzolanic binder and aggregates;
- CM 4: Repair mortar product or system containing polymer binder.

Generally, constituent materials for repair mortar/concrete shall not contain harmful ingredients in such quantities as may be detrimental to the durability of the concrete or cause corrosion of the reinforcement and shall be suitable for the intended use as repair mortars/concretes or repair mortar systems for concrete structures.

Table 11.1 Fields of application of mortars and concretes (EN 1504-3)

Principle	Method
Principle 3 (CR) Concrete restoration	3.1 Hand applied mortar
	3.2 Recasting with concrete or mortar
	3.3 Spraying concrete or mortar
Principle 4 (StS) Structural strengthening	4.4 Adding mortar or concrete
Principle 5 (PR) Increasing physical resistance	5.3 Adding mortar or concrete
Principle 6 (RC) Resistance to chemicals	6.3 Adding mortar or concrete
Principle 7 (PRP) Preserving or restoring passivity	7.1 Increasing cover with additional mortar or concrete
	7.2 Replacing contaminated or carbonated concrete

Primarily repair mortars and concretes are classified as structural and nonstructural repair mortars and furthermore as high- and low-strength (or high and high E-modulus) mortars (Chapter 5 of EN 1504-3:2015). The repair mortars of class R4 are high-class mortars intended to be used for structural repairs, i.e., those applications where load transfer must be considered in the design of the repair. Class R3 mortars are also intended to be used for structural repairs, but exceed lower strengths. Class R2 and Class R1 are high- and low-strength mortars intended to be used for non-structural and cosmetic repair. The required mechanical properties are listed in Table 11.2.

In addition to minimum compressive strength, the standard defines the minimum performance requirements related to durability (Chapter 6.2 of EN 1504-3:2015). The repair mortars of class R4 are high-class mortars intended to be used for structural repairs in harsh environments. Class R3 mortars are also intended to be used for structural repairs in severe environments, but exceed lower durability. Class R2 and Class R1 are intended to be used for nonstructural and cosmetic repair in mild environments. Dependent on the intended repair principle, the following characteristics related to physical properties are defined: compressive strength, adhesive bond, elastic modulus, flexural strength, thermal compatibility after dry cycles, thunder showers or freezing-thawing, shrinkage, and swelling or creep in compression. Dependent on the intended repair principle, the following characteristics related to durability are defined as: chloride ion content, carbonation resistance, coefficient of thermal expansion, capillary absorption, frost resistance, corrosion behavior, and skid resistance. In test methods, the minimum requirement is given

Table 11.2 Required mechanical properties of repair mortars

Characteristic	Compressive strength	Adhesive bond	Elastic modulus	Flexural strength
Reference substrate (EN 1766)	None	MC (0.40)	None	None
Test method	EN 12190	EN 1542	EN 13412	EN 1015–11
Class R1	≥10 MPa	≥0.5 MPa	None	Measured value ^a
Class R2	≥15 MPa	≥0.8 MPa	≥10 GPa	Measured value ^a
Class R3	≥25 MPa	≥1.5 MPa	≥15 GPa	Measured value ^a
Class R4	≥45 MPa	≥2.0 MPa	≥20 GPa	≥8 MPa

^aNo strength-loss at increasing age.

for individual class from R1 to R4 (Table 11.3). Compressive strength, chloride ion content and adhesive bond are performance characteristics which are required for all repair principles and methods listed in Table 11.1. Carbonation resistance is required for all intended uses of principles 3, 4, 6, and 7, and for certain intended uses of principle 5. Elastic modulus is required for all intended uses of principle 4, and for certain intended uses of principles 3, 5, 6, and 7. All other performance characteristics are only required for certain intended uses.

11.3.3 Special requirements

For special applications like high or low temperature, exposure to sea water, or other sources of high chemical concentration, additional requirements may be necessary—such as, chloride ingress, chloride migration, chemical resistance, sulfate resistance, restrained shrinkage, bond strength after dynamic load, and durability in water cycling or calcium hydroxide solution (Annex B of draft of EN 1504-3:2015). For some of these characteristics, no harmonized European test methods are available, national regulations shall be applied, and the producer has to give the declared value.

In the case of products which contain ≤1% of organic material by weight or volume, depending on which fraction is the less advantageous, it is assumed that—in accordance with the provisions of EC Decision 96/603/EC, including changes—they fulfill the requirements of the performance classes A1 or A1_f respectively on the characteristics in respect of fire behavior without the necessity of a test.

Other products shall be tested and classified in accordance with EN 13501-1:2007. Where fire resistance is required, this is to be tested in accordance with EN 13501-2:2016. Prior to the commencement of a fire resistance test, the manufacturer should check that the intended test(s) is/are in accordance with the execution requirements for the intended application in the country of destination.

Table 11.3 Required properties of repair mortars related to durability

Characteristic	Thermal compatibility, Part 1 De-icing salt immersion Bond strength after 50 cycles	Thermal compatibility, Part 2 Thunder showers Bond strength after 30 cycles	Thermal compatibility, Part 4 Dry cycling Bond strength after 30 cycles	Shrinkage	Swelling	Creep in compression
Reference substrate (EN 1766)	MC (0.40)	MC (0.40)	MC (0.40)	None	None	None
Test method	EN 13687-1	EN 13687-2	EN 13687-4	EN 12617-4	EN 12617-4	EN 13584
Class R1	No cracking or delamination			None		Value declaration
Class R2	≥ 0.8 MPa			$\leq 0.60\%$ at 28 days if E-Modul ≤ 25 GPa $\leq 0.80\%$ at 28 days if E-Modul ≤ 20 GPa	$\leq 0.30\%$ after 28 days	
Class R3	≥ 1.5 MPa					
Class R4	≥ 2.0 MPa			$\leq 0.90\%$		

The electrical resistivity of cementitious repair materials to be used in combination with all types of electrochemical applications shall be as close to the properties of the parent concrete as possible (see [EN ISO 12696:2012](#), 05, 5.10.4, Note).

Surprisingly the standard does not provide any requirements for fresh mortars/concretes such as stiffening time, thixotropy, workability, and pot life. They are to be defined by the manufacturer and are to be used for identification purposes only.

Although no requirements for fresh mortars/concretes are given in the standard, they are extremely important for the execution of repair and protection work. Characteristics like pot life, thixotropy, workability, consistency, etc. must be selected in accordance with the intended use and adjusted to the application method selected.

11.3.4 Application of repair mortars and concretes

Site application of products and systems and quality control of the works is defined in the standard [EN 1504-10:2003](#). As a new edition is pending, the provisions summarized in this chapter are taken from [EN 1504-10:2015](#).

During preparation, protection, and repair work, consideration shall be given to safety structural stability, chemical, electrochemical, and physical condition of the substrate to any contaminants, to the ability of the structure to accept loading, movement, and vibration during protection and repair, to ambient conditions, to the characteristics of the materials contained in the structure, to the characteristics of the protection and repair products and systems, and to the time required to gain the strength of the repair product and system (curing time).

General requirements on substrate and reinforcement preparation given in [EN 1504-10:2015](#) also apply to AAM based repair mortars.

The provisions for the application of repair mortars are given in [Chapter 8](#) of [EN 1504-10:2015](#). They also apply for the AAMs. Some of them are summed up as follows:

The application of the products and systems shall be suitable for the substrate and structure to which it is applied. Protection shall be provided so that the preparation, application, and subsequent curing shall be carried out in accordance with this standard. Before and during the application of the products and systems, the substrate temperature and moisture content, and the characteristics of the environment—e.g., temperature, relative humidity, dew point, rate of change of moisture content as influenced by precipitation and wind, shall be considered. If mortar or concrete is hand-applied, it shall be decided whether the repair mortar or concrete is to be built up in layers to prevent sagging or slumping. The layer thickness, time between application of layers and other requirements shall be specified. Sprayed concrete and sprayed mortar used as repair material shall comply with the standard for sprayed concrete, i.e., [EN 14487-1](#) and [EN 14487-2](#). When mortar or concrete is cast, work shall comply with [EN 13670](#). The method and period of any curing shall be specified, taking into account the nature of the products and systems, the thickness of the repair and environmental conditions.

11.4 Performance of alkali-activated repair mortars based on different precursors

11.4.1 Slag-based repair mortars

Despite the recent increase in research on slag-based mortars (Fernandez-Jimenez et al., 1999; Brought and Atkinson, 2002; Rovnanik et al., 2016), there is only limited research on the performance of ground-granulated blast furnace slag (GGBFS) mortars as repair materials (Kramar et al., 2016).

The main chemical components of GGBFS are represented by the CaO-SiO₂-MgO-Al₂O₃ system, where the key glass network-forming cations are Si⁴⁺ and Al³⁺, and the divalent Ca²⁺ and Mg²⁺. They act as network modifiers, along with other alkalis present (Li et al., 2010). The reactivity of different slags in AAM mostly depends on their phase composition and glass structure (Mostafa et al., 2001). The major phases of alkali-activated GGBFS are C-S-H, which are the main hydration products, regardless of the activator used (Wang and Scrivener, 1995), and three-dimensional zeolite-like polymers, sometimes also the hydrotalcite, calcite, and AFm phases are present (Li et al., 2010). The products are controlled by the composition of the slag, the type of activator, and pH environment.

The most commonly used types of activators are sodium hydroxide (NaOH), sodium silicate of various moduli n (Na₂SiO₃ · n H₂O), or mixes of both alkalis. When the cementitious material contains a large amount of calcium oxide (CaO), as in the case of GGBFS, the alkali-silicates are, in general, more effective activators than the alkali hydroxides (Ravikumar and Neithalath, 2012).

The chemical composition of the slag used as the precursor for alkali-activated mortars in our study is given in Table 11.4.

Regarding the fresh properties of the mortars studied, problems were encountered when applying alkali-activated GGBFS mortars on vertical surfaces of concrete slabs (Table 11.5). In particular, it was difficult to apply the mortars in thicknesses exceeding 0.5 cm, since the mortars did not apply smoothly, and the mass was rolling under the trowel during application. In addition, the adhesion to the surface was very poor, which consequently led to the delamination of the mortar layer from the surface. The mortar with higher workability had crept down along the vertical surface. Some mixtures showed a very short workability time, as after 10 minutes the mortar was already stiff. Our previous study showed that the flow decreased by about 30% of the initial value (Kramar et al., 2016) after 30 minutes. Furthermore, the setting times, which are of practical importance since they define the times required for initial hardening and the time interval after which we could deal with the formed product, are much shorter in comparison to traditional OPC mortars. Among other precursors, the slag mixtures usually showed the shortest setting times due to the introduction of calcium in the alkali-activated system (Diaz et al., 2010). The results of studies show that the initial setting time of GGBFS can be designed and controlled by controlling the characteristics of the activating solution (Jansson and Tang, 2015). For instance, the initial setting time of GGBFS, alkali-activated by water glass of various moduli, is dependent on the particle size

Table 11.4 Chemical composition of precursors for alkali-activated repair mortars *b.d.l.* = below detection limit

	Slag	Fly ash	Metakaolin
SiO ₂	36.28	51.74	68.82
Al ₂ O ₃	11.30	22.92	24.27
Fe ₂ O ₃	0.35	7.40	2.31
CaO	41.39	6.02	0.47
P ₂ O ₅	b.d.l.	0.68	b.d.l.
MgO	6.38	2.44	0.19
K ₂ O	0.37	2.21	0.18
Na ₂ O	0.26	0.79	b.d.l.
TiO ₂	0.45	0.91	1.14
Cr ₂ O ₃	b.d.l.	0.02	0.02
MnO	0.32	0.07	0.01
SO ₃	1.08	0.49	b.d.l.
LOI	b.d.l.	2.3	1.5

b.d.l., below detection limit.

of the GGBFS material and the specific modulus of the water glass, which are both parameters that have an influence on the viscosity of the activated mixture.

The compressive strength of GGBFS mortars, which increased gradually over time, usually exceeded 40 MPa after 28 days, as also seen from [Table 11.8](#). The alkali-activated slag mortars have high early strength, which exceeded 30 MPa after 7 days ([Kramar et al., 2016](#)). Thus, it fulfils the requirements of [EN 1504-3](#) standards for all classes, which prescribe the minimum compressive strength ≥ 15 MPa. In any case, for a repair material to be considered excellent, a good bond between the repair material and the concrete substrate is essential ([Gorst and Clark, 2003](#)). This represents the largest obstacle in the case of alkali-activated slag repair mortars, since, in our experience, the adhesion-to-surface of the tested mortar mixture was very poor. Among the studied precursors, the shrinkage was probably not the cause for its delamination, but rather chemical incompatibility. On the other hand, the modulus of elasticity was very high, even above the requirements for structural repair products of the highest class (Class R4) given in the standard [EN 1504-3](#).

Another significant phenomenon, which is potentially harmful to the repaired structure, is the crystallization of soluble salts. The crystallization of soluble salts is one of the most significant factors affecting the degradation of materials, damaging

Table 11.5 Compositions of alkali-activated mortars

Mortar	Si/Al	Na/Al	Slag (g)	Fly ash (g)	Na-water glass ^a (g)	NaOH flakes (g)	Water (g)	Calcite powder (g)	Aggregate (g)
M0	2.82	0.84	557.4	—	22.4	33.4	232.3	—	1350
M1	2.83	0.93	501.6	—	22.4	33.4	232.4	55.7	1350
M2	2.93	1.78	501.6	—	44.8	66.8	232.4	—	1350
M3	2.66	0.79	501.6	55.7	22.4	33.4	322.4	—	1350
M4	2.65	0.86	445.9	55.7	22.4	33.4	232.4	55.7	1350
M5	2.66	0.79	501.6	55.7	22.4	33.4	256.7	135.0	1215
M6	2.70	0.63	501.6	55.7	33.4	22.4	247.7	135.0	1215
M7	2.70	0.63	501.6	55.7	33.4	22.4	244.3	135.0	1215
M8	2.70	0.63	616.1	68.5	40.7	27.9	240.3	110.0	1100
M9	2.84	1.27	445.9	55.7	66.8	44.8	232.3	135.0	1215
M10 ^b	2.70	0.63	501.6	55.7	33.4	22.4	232.3	135.0	1215
M11	2.36	0.56	334.4	222.9	33.4	22.4	232.3	135.0	1215
M12	2.20	0.53	222.9	334.4	33.4	22.4	232.3	135.0	1215

^aComposition of water glass: Na₂O, 15.5%; SiO₂, 30.6%.

^bAddition of 2.5 g of polypropylene fibers.

porous materials through a range of mechanisms, including the generation of physical stress derived from the crystallization of salts from the solution in pores, thermal expansion differences, hydration pressure, and enhanced wet/dry cycling caused by deliquescent salts (Charola, 2000). AAM contain higher soluble alkali metal concentrations, and so efflorescence could be a significant issue when the products are exposed to humid air or in contact with water (Škvára et al., 2009, Zhang et al., 2014, Pacheco-Torgal et al., 2016). Efflorescence is the result of the leaching of sodium from the alkali-activated matrix, which is only weakly bonded in the structure of the N–A–S–H gel (Škvára et al., 2012). Efflorescence was already observed on the surface of the applied alkali-activated slag repair mortar 1 day after application and was also extensive after the water absorption test (Fig. 11.1). In addition to various sodium carbonates, sodium sulfates were also observed for slag mortar (Kramar et al., 2016). The most extensive crystallization of soluble salts was observed for the metakaolin mortar, for which besides the porosity the alkali content introduction was also the highest. Depending on the different absorption rate of the mortars, either the crust or fluffy efflorescence was formed. The porosity of mortars was between 11.1% and 15.2%. There was a bimodal distribution of pores with the first intrusion peak at 0.02 μm and the second at 10 μm . Also, the values of capillary absorption of GGBFS repair mortar were much higher with respect to cement-based mortars and strongly exceeded the requirement of EN 1504-3.

Concerning durability, a rapid progress of carbonation of the slag mortar was observed. Fig. 11.2 shows the progress of the natural carbonation of the alkali-activated mortar after 7 and 28 days of curing in laboratory conditions. As seen from the SEM/BSE microphotographs (Fig. 11.2B and C), the matrix of the carbonated area of alkali-activated binder is densified with respect to the noncarbonated area. FTIR spectra clearly indicated enhanced vibrational bands in the region associated with the stretching vibration of O–C–O bonds in the carbonate group (CO_3^{2-})



Figure 11.1 Efflorescence of alkali-activated repair mortars based on different precursors (up-metakaolin based mortar, in the middle-slag based mortar, bottom-fly ash based mortar) after water absorption test.

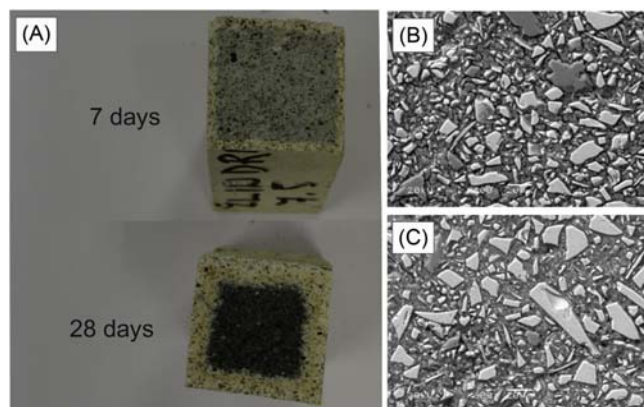


Figure 11.2 (A) Carbonation depths of GGBFS repair mortar, (B) SEM/BSE photomicrograph of noncarbonated area, (C) SEM/BSE photomicrograph of carbonated area.

for the carbonated area (Fig. 11.3). The commonly reported carbonation products of slag activated by sodium hydroxide or silicate are calcium (polymorphs of CaCO_3) and sodium carbonates (Puertas et al., 2006; Bernal et al., 2010; Song et al., 2014). The asymmetric stretching vibration representing the Si–O bond, characteristic of silicon tetrahedral (SiO_4) in the chain structure of C-S-H, shifted from 995 to 1036 cm^{-1} after carbonation, indicating the decomposition of C-S-H by carbonation and a higher degree of polymerization and lengthening of silicates within the remaining gel. That is, the carbonation of C-S-H makes the structure of silica gel amorphous such that this band shift signifies the existence of C-S-H before carbonation (Puertas et al., 2006). However, among the alkali-activated precursors, the slag showed a relatively slow carbonation. According to the literature, an increase in the activator amount leads to a higher amount of C-S-H and a slower rate of carbonation in the microstructure (Song et al., 2014).

The sulfate resistance of mortar specimens (Table 11.6) was evaluated, based on the length change of the specimens after exposure to sodium sulfate solution for 1 year according to the ASTM C 1012 standard for cement-based materials. The specimens were cured in lime water and then exposed to the sulfate solution when they reached the compressive strength of 20 N/mm^2 , and length change was measured regularly for 1 year. Immersion of alkali-activated slag mortars in sodium sulfate solutions showed shrinkage in the first weeks of exposure, but after a few weeks it promoted expansion as the length of the specimens gradually increased (Fig. 11.4). The early age shrinkage of the S1 mortar was slightly higher compared to the S2 mortar. However, after 2 weeks the S1 mortar started to expand, thus compensating for the shrinkage. On the other hand, the S2 mortar started to expand after 4 weeks and after 1 year it had expanded by 0.02%, which is still well below the 0.10% expansion limit after 1 year as given by ASTM C 1157. In specimen, after 356 days of immersion in 5% sodium sulfate solution there was no loss of mass or cracking observed. An SEM/BSE microphotograph of the mortar showed densification of its

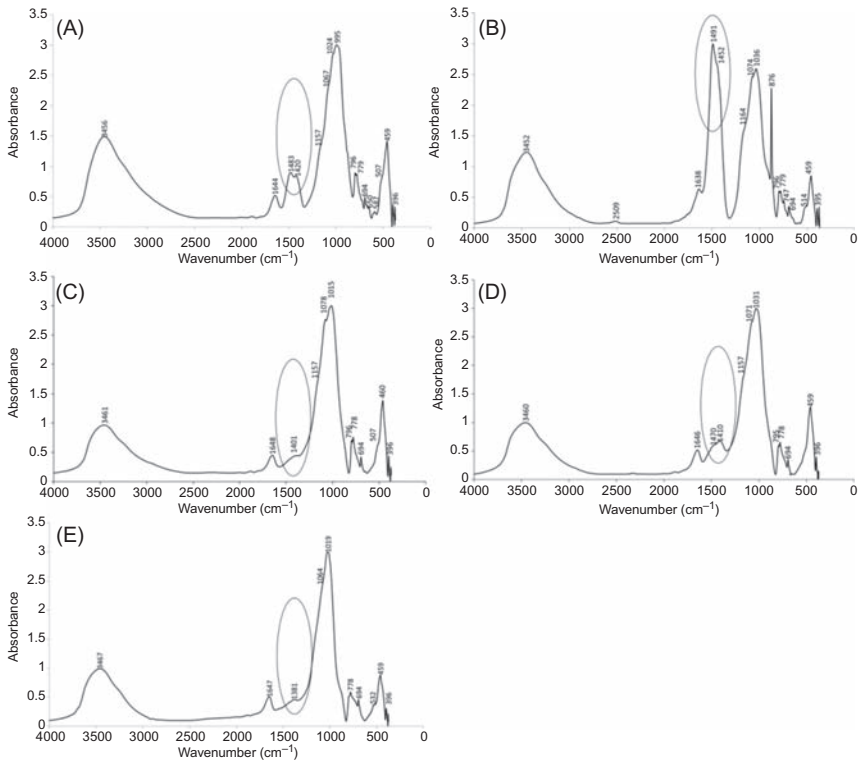


Figure 11.3 (A) FTIR spectrum of noncarbonated area of alkali-activated slag. (B) FTIR spectrum of carbonated area of alkali-activated slag. (C) FTIR spectrum of noncarbonated area of alkali-activated fly ash. (D) FTIR spectrum of carbonated area of alkali-activated fly ash; (E) FTIR spectrum of carbonated area of alkali-activated metakaolin.

structure after exposure to the sulfate solution with angular particles corresponding to the unreacted slag (Fig. 11.5). As seen from the Hg-porosimetry results, the porosity of the mortar and average pore size diameter decreased after the sulfate resistance test (Table 11.6). Therefore, exposure to Na_2SO_4 seems to favor the structural evolution of the binding phases and densification of the system, which is consistent with the known role of Na_2SO_4 as an activator in some higher Ca alkali-activated and hybrid binders (Donatello et al., 2013). Studies report that the key factor controlling the degradation mechanisms of AAM is not the sulfate itself, as tends to be the case in Portland cement systems, but rather it is the nature of the cation accompanying the sulfate anions (Ismail et al., 2013).

11.4.2 Fly ash-based repair mortars

Fly ash can be, based on the CaO content, divided into siliceous or low-calcium, and calcareous or high-calcium fly ash. The chemical composition consisted mainly

Table 11.6 Compositions of the alkali-activated mortars for the sulfate resistance experiment

Mortar	Curing time ≥20 N/mm² (days)	Slag (g)	Na-water glass (g)^a	NaOH flakes (g)	NaOH solution (41.7 wt.%) (g)	Water (g)	Aggregate (g)
S1 mortar	6	570.9	17.1	17.1	–	358.6	1983
S2 mortar	3	557.4	22.4	33.4	–	232.3	1350
FA2 mortar	16	478.8	177.0	–	67.7	–	1350
FA8 mortar	13	455.9	168.5	–	64.4	17.7	1350
MK2 mortar	2	450.0	372.0	37.8	–	5.0	1350

^aComposition of water glass for slag and fly ash mortar: Na₂O, 15.5%; SiO₂, 30.6%; composition of water glass for metakaolin mortar: Na₂O, 8.3%; SiO₂, 27.5%.

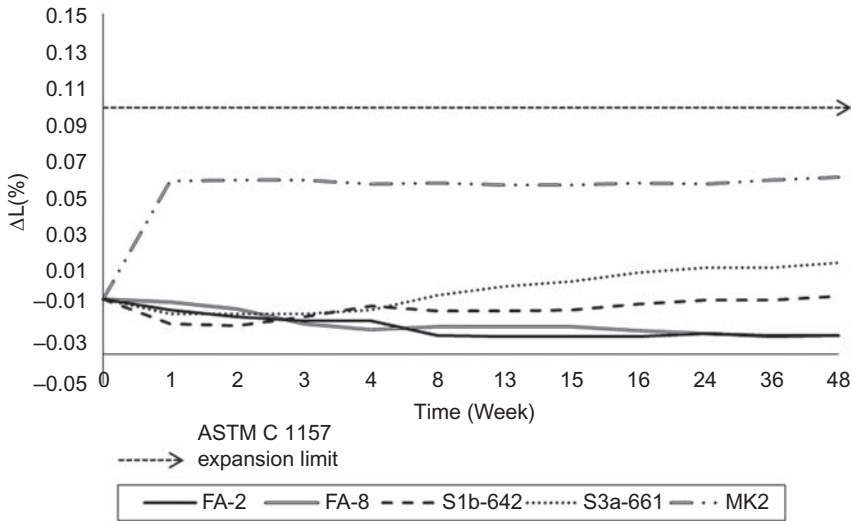


Figure 11.4 Length change of AAM mortars over a 1-year period exposure to sulfate solution according to the standard [ASTM C1012/C1012C](#).

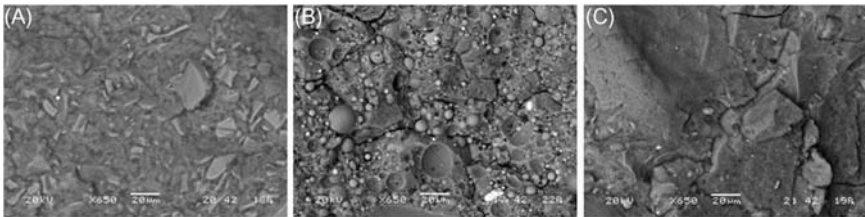


Figure 11.5 SEM/BSE microphotographs of the mixtures of (A) slag based, (B) fly ash based, and (C) metakaolin-based mortars after the exposure to the sulfate solution.

of $\text{SiO}_2\text{-Al}_2\text{O}_3\text{-Fe}_2\text{O}_3\text{-CaO-MgO}$ with a higher introduction of Ca in the calcareous fly ash. The primary reaction product of the alkali activation of fly ash is a three-dimensional alkaline aluminosilicate gel (alkaline aluminosilicate hydrate, N–A–S–H gel). Crystalline zeolites such as herschelite and hydroxysodalite are obtained as secondary products (Fernandez-Jimenez *et al.*, 2005).

There is a limited number of studies related to the use of alkali-activated fly ash as a repair mortar (Warid Wazien *et al.*, 2016). The activators used are most frequently sodium hydroxide, (NaOH), sodium silicate of various moduli n ($\text{Na}_2\text{SiO}_3 \cdot n\text{H}_2\text{O}$) or mixes of both alkalis.

In our study, siliceous fly ash was used as a precursor for repair mortars (Table 11.4) and activated with sodium silicate (Kramar *et al.*, 2016). When applying the alkali-activated siliceous fly ash mortar onto a vertical concrete surface, the mortar sagged down the surface during application, and the application of the mortar in a thicker layer was not possible. The workability remained unchanged for

30 minutes. On the other hand, the initial and final setting times of the alkali-activated fly ash mortar were very long, i.e., more than 40 hours, which in practice would require accelerators to speed up the setting time of the mortar and to increase the rate of the hydration process for early strength gain. The longer setting time of the alkali-activated fly ash binder is due to the slow rate of the chemical reaction at low ambient temperatures. In literature, however, a reduction in the setting time was observed as the CaO content increased (Fernandez-Jimenez et al., 2006; Diaz et al., 2010).

With the most commonly used precursors for AAM, the compressive strength gain is the slowest for fly ash binder. Specifically, after 7 days the mortars exhibited $\sim 20\%$ of the 90th day strength, which exceeded 70 MPa (Kramar et al., 2016). The bond strength of the fly ash mortar is very good and was above the requirements for both structural and nonstructural repair products of the EN 1504-3 standard. A 100% cohesion failure, which was attributed to the weak tensile strength of the alkali-activated repair mortar, was observed. The fly ash mortar shows large shrinkage (gradually increased up to around -4 mm/m after 56 days) when exposed to air conditions, and expansion in water was significant (up to 0.5 mm/m after 56 days), which could have contributed to weak bonding. The modulus of elasticity was above the requirements for structural repair products of the highest class (Class R4) given in the standard EN 1504-3.

Efflorescence appeared soon after the application of the mortar on the concrete surface and was also extensive after the water absorption test (Fig. 11.1). It consisted of crystals of various sodium carbonates (Kramar et al., 2016). Zhang et al. (2014) reported that the efflorescence behavior of fly ash-based AAM is strongly dependent on the alkali-activator solution type, curing temperature, and slag addition, as the composition and microstructure change when these factors are varied. At the same alkali content (in terms of Na_2O -to-solid-precursor mass ratio), soluble silica present in the activator restricts the early age efflorescence of AAM cured at room temperature. Sodium is bound weakly in the nanostructure of the N–A–S–H gel and is almost entirely leachable, which causes AAM to be prone to efflorescence with excessive remnants of alkalis in the system (Škvara et al., 2012). The same authors reported that almost all Na can be leached out of the gel without compromising compressive strength. The porosity of fly ash mortar was $\sim 13\%$ and a unimodal distribution of pores with peak at $0.2 \mu\text{m}$ was observed. The values of capillary absorption of fly ash repair mortar were much higher (3–7 times) with respect to cement-based mortars, and strongly exceed the requirement of EN 1504-3, which should not exceed $0.5 \text{ kg/m}^2\text{h}^{0.5}$. Other researchers, however, reported that capillary water absorption was low for fly ash mortars activated with different M of NaOH, i.e., in the range from 0.1 to $0.45 \text{ kg/m}^2\text{h}^{0.5}$ (Tahri et al., 2015).

Carbonation testing has shown that, in comparison to slag-based mortars, the fourier transform infrared (FTIR) spectra of the alkali-activated fly ash mortars showed only slightly enhanced intensities of vibrational bands in the region corresponding to the carbonates, which were insignificant in the noncarbonated area (Fig. 11.3). With respect to the slag base mortars, the formation of carbonates is not so intense in this case. This is most probably related to the low-calcium content in the system. Thus, sodium bicarbonates were reported as reaction products after the

carbonation (Criado et al., 2005). The asymmetric stretching vibration representing the Si–O bond characteristic of the silicon tetrahedral (SiO_4) in the chain structure of C–S–H shifted from 1015 to 1031 cm^{-1} after carbonation, indicating a higher degree of polymerization and the lengthening of silicates within the remaining gel. In alkali-activated concrete, the carbonation is hypothesized as the reaction of the sodium hydroxide with CO_2 -forming sodium carbonate hydrates (Low et al., 2015; Criado et al., 2005). The OPC produce $\text{Ca}(\text{OH})_2$ and C–S–H gel, while the geopolymers produced $[\text{Mz}(\text{AlO}_2)_x(\text{SiO}_2)_y \cdot n\text{MOH} \cdot m\text{H}_2\text{O}]$ gel (Law et al., 2015).

When alkali-activated siliceous fly ash mortars (Table 11.6) were exposed to sodium sulfate solution for 1 year, a slight shrinkage was observed after 4 weeks (Fig. 11.4). After that period, the shrinkage remained constant; the change in length was in general very small and less than 0.02% for both studied mixtures. This could be related to the migration of alkalis from the specimens into the solution. In our study, mechanical properties before and after sulfate exposure were not determined, but according to Bakharev (2005), the loss of compressive strength of mortars was noticed and was ascribed to the leaching. On the contrary, other authors (Škvara et al., 2005; Fernandez-Jimenez et al., 2007) reported the increase of the compressive strength in the later stages of exposure. The appearance of the pastes exposed to Na_2SO_4 showed no significant physical change after 1 year of exposure, however, a slight dusting of the surface can be observed. The porosity of the mortar increased slightly after the end of the sulfate resistance test, but average pore size decreased (Table 11.7).

11.4.3 Metakaolin-based repair mortars

The two major components of metakaolin precursor for the alkali-activated binder are SiO_2 and Al_2O_3 . Many authors (Granizo et al., 2002) have found that the product of metakaolin activation with NaOH solutions is N–A–S–H gel with good mechanical properties. In addition, the amorphous N–A–S–H gel has a similar

Table 11.7 Results of the MIP after sulfate resistance test

Mixture	Porosity (%)	Average pore diameter (μm)	Median pore diameter by volume (μm)	Bulk density (g/mL)	Apparent density (g/mL)
S2	11.2	0.02	0.2	2.14	2.41
S2 sulfate	9.4	0.01	0.03	2.13	2.45
FA2	13.1	0.08	0.83	2.14	2.46
FA2 sulfate	15.0	0.02	0.03	2.14	2.36
MK2	17.3	0.05	0.06	2.02	2.44
MK2 sulfate	16.9	0.01	0.01	2.04	2.45

chemical composition to natural zeolitic materials, but without the extensive crystalline zeolitic structure (Barbosa et al., 2000).

Among the precursors, the majority of studies use the metakaolin precursor as repair mortars with sodium silicates or hydroxide as the activator (Alanazi et al., 2016; Zanotti et al., 2016, Moura et al., Kramar et al., 2016).

The composition of the metakaolin used in our study is given in Table 11.4. Regarding the fresh properties of the mortars, problems were encountered with the application of the mortar mixture on the vertical surface of the concrete as the mortar mass crept down the surface. The flow also remained equal after the 30 minutes indicating the stability of the metakaolin mortar (Kramar et al., 2016). Workability of mortar is usually reduced with the molar concentration of hydroxide, as high sodium hydroxide concentrations reduce the flow (Pacheco-Torgal et al., 2011). Some studies showed that the addition of up to 10% of CaOH_2 reduced the flow of the mortar (Pacheco-Torgal et al., 2011). On the other hand, the initial and final setting times were between 7 and 8 hours respectively, which is much longer in comparison to the OPC, but much shorter than for the studied fly ash mortar. The setting time is also dependent on the $\text{SiO}_2/\text{Al}_2\text{O}$ ratio and $\text{Na}_2\text{O}/\text{SiO}_2$ ratio (Silva and Sagoe Crenstil, 2008; Chindaprasirt et al., 2012).

The gain in the compressive strength of the alkali-activated binders using metakaolin as a precursor is very fast, as after 7 days they have already reached their final strength. It is usually reported to be more than 30 MPa (Vasconcelos et al., 2011) or even 70 MPa after 7 days (Kramar et al., 2016). Studies showed that a higher NaOH concentration leads to a compressive strength increase (Vasconcelos et al., 2011). In our study, the reported bond strength (2.0 N/mm^2) to the concrete substrate was also above the requirement, with an observed cohesion failure in the concrete substrate, as well as in the mortar layer and adhesion failure. The metakaolin mortar shows a small air shrinkage (up to around -0.5 mm/m), and a high expansion in water (up to 0.5 mm/m after 56 days). The modulus of elasticity is above the requirement for structural repair products of the highest class (Class R4) given in EN 1504-3.

The efflorescence appeared soon after the application of the metakaolin mortar on the concrete surface (Fig. 11.1) and consisted of various sodium carbonate hydrates (Kramar et al., 2016). The porosity of fly ash mortar was 16%, with bimodal distribution of pores, with an intrusion peak at $0.03 \mu\text{m}$ and the second at $1 \mu\text{m}$. The values of capillary absorption of metakaolin repair mortar were much higher with respect to cement-based mortars and strongly exceeded the requirement of EN 1504-3.

Carbonation of metakaolin mortars is relatively fast. However, it is interesting to note that there was no significant vibrational band attributed to the carbonates observed on the FTIR spectrum after the carbonation (Fig. 11.3). In metakaolin-based geopolymer activated by sodium silicate, in which calcium is barely detectable, the presence of CO_2 will lead to the formation of sodium carbonates (Pouhet and Cyr, 2014).

As seen in Fig. 11.4, the metakaolin mortar (Table 11.6) showed a rapid expansion (up to 0.06%) immediately at the beginning of the exposure period, which did not change with the exposure after 1 year. The expansion was found to be well below the 0.10% expansion limit at 1 year, as indicated by ASTM C 1157, but still

the highest among the tested precursors. This could be related to the previous curing in lime water and high porosity, as it was the highest for metakaolin mortar among the investigated mortars (Kramar et al., 2016). Chareerat (2008) reported that the particle size of raw materials was essential to the expansion of the submerged geopolymer in sulfate solution. There was no significant change observed in porosity after the sulfate resistance test (Table 11.7).

11.4.4 Repair mortars based on mixtures of different precursors

Due to the issues raised in our previous study (Kramar et al., 2016), we tested a series of slag/fly ash-based mortars, as the substitution of fly ash by slag is reported to reduce the efflorescence rate (Zhang et al., 2014).

The first series of mortar mixtures (M1-M6) was applied to verify the influence of the alkali/precursor ratio, replacements of the precursor with calcite powder, slag with fly ash, slag with fly ash and calcite, and aggregate with calcite, with respect to the M0 mortar, which was tested in our previous studies, showed poor adhesion, high efflorescence, and was quite stiff to apply (Table 11.8).

The application of all those mortars to the vertical concrete surface was difficult because of the mortar mass “roll,” since the grip on the surface was very poor consequently leading to the delamination of the mortar layer or, with mixtures with a higher alkalis/binder ratio, creeping down the surface. The water retention of some mortars was low, and the mortar mixtures had already lost their workability (densified) after 10-15 minutes, which obstructed further handling of the mass. The addition of fly ash contributed to a better grip to the concrete surface, with the mortar not immediately falling off. When replacing a part of the aggregate with calcite powder, the application of those mixtures (M5, M6) was smoother and the texture of the mortar was favorable due to the higher amount of fine fraction. In addition, the grip to the surface was better. However, M5 stiffened quite quickly, thus we increased the water glass/NaOH ratio for the M6 mortar.

None of the mortar mixtures developed a good adhesion to the concrete surface after 28 days. However, the mixture M6 showed a very low efflorescence rate when applied to the vertical surface of a concrete slab. After 28 days of curing, all the mixtures were exposure to water and showed efflorescence. The optimal properties, such as application behavior, mortar texture and the amount of the efflorescence, have been found for the M6 mortar, which was then optimized.

For the next 6 mortar mixtures (M7-M12) the following parameters: binder/aggregate ratio, activator/precursor ratio, influence of PP fibers, and slag/fly ash ratio were varied. In the mixture with the higher binder/aggregate ratio problems arose related to fast stiffening and it had a poor grip on the concrete surface. The replacement of slag with fly ash contributed to the higher workability, as the flow was increased at a constant w/b ratio (Table 11.8).

After the application of the mortar to the surface, a significant reduction of the efflorescence was observed with respect to the first series. Also, after the water absorption, the efflorescence did not appear on the surface of the mixtures that had a Na/Al ratio of less than 0.7 (Table 11.1). The introduction of the fly ash reduced the Na/Al ratio. The Si/Al ratio was reduced as well. When slag is used to partially

Table 11.8 Properties of alkali-activated mortars

Mortar	Flow (mm)	Flexural strength (N/mm ²)	Compressive strength (N/mm ²)	Porosity (%)
M0	160	4.7	48.1	11.1
M1	157	6.7	45.4	13.3
M2	173	7.7	34.4	14.3
M3	191	7.1	54.2	15.2
M4	202	5.0	46.3	16.4
M5	184	4.1	47.2	17.5
M6	210	7.9	52.6	17.7
M7	195	6.4	52.1	19.9
M8	165	8.2	65.5	14.3
M9	200	7.0	53.8	30.6
M10	172	8.6	57.3	17.4
M11	210	6.6	47.1	17.2
M12	236	5.2	37.2	20.5

substitute fly ash in alkali activation as a source of Ca, the pore sizes and porosities are smaller than those in nonslag-containing samples with either room temperature or hydrothermal curing, which leads to a much lower efflorescence rate (Zhang et al., 2014). Other authors also reported that the effect of slag-blending on the efflorescence of geopolymers is more related to reduction in permeability rather than the chemical binding of alkalis (Najafi Kani et al., 2011).

With the exception of mixture M9 (bond strength was 0.95 N/mm²), which had a higher activator/precursor ratio, there was, however, practically no adhesion between the mortars and concrete surface for the investigated mortars.

In general, the replacement of slag with fly ash reduced the 28-day compressive strengths, due to the slower reaction of the fly ash. A larger binder/aggregate and activator/precursor ratio increased the compressive strength.

11.5 Future trends

So far, many researchers succeeded in obtaining AAM with good workability and high compressive strength, which are the prerequisite for considering the potential of such material to be used as repair mortars for concrete. But, as can be seen from literature, as well as from our own experience, there is still room for progress in the development of repair mortar.

The most researched system is that with metakaolin as the precursor material. For this system, there are also reports about its successful use as repair mortar in real conditions (Zhang et al., 2010 a,b). Attempts have also been made with many other (waste) materials and their combinations to be used as repair mortars, but mostly at a laboratory level. For such precursors, there is still no definite answer as to which activators are the most adequate and what their ratio to the precursors should be in order to develop repair mortars that would meet all the criteria prescribed in the standard for concrete repair mortars. It seems that, due to the complexity of the systems, the most common approach is still that of trial and error, which can be time consuming and usually does not give complete insight into the mechanisms of bonding.

Furthermore, there are some other open issues. Among them, the urgent one is the development of commercially available superplasticizers for such alkali-activated systems. These systems certainly need effective superplasticizers that will make structure denser. It is often reported (Natali et al., 2014; Zhang et al., 2010a,b) through determination of water absorption, capillary uptake, and/or mercury intrusion porosimetry (MIP), that such systems are rather open on a microstructural level, in comparison to cement-based mortars, and consequently prone to the ingress of different chemicals. Chloride, sulfate, and water can easily penetrate the structure, which can cause different types of deterioration.

Having a denser structure might also hinder the problem with efflorescence, which is also one of the major issues when using alkali-activated repair mortars. Some successful attempts have been made to decrease efflorescence by application of potassium activators instead of sodium ones, or by adding calcium aluminate admixture, which reduces the mobility of alkalis, or even by application of hydrothermal curing (Pacheco-Torgal et al., 2012a). As apparently from recent research, some of the shortcomings might be overcome by the application of hybrid systems (Garcia-Lodeiro et al., 2016).

The last, but not the least important, factor that needs further investigation is the adherence of alkali-activated mortars to different substrates. In some publications (Vasconcelos et al., 2011) it is reported that the adherence of alkali-activated mortars to the cement-based substrate is poor. The influential parameters are chemical bonding between AAM layer and substrate, shrinkage/expansion matching, and also mechanical interlocking (usually improved if the surface is rough).

For market penetration and technical acceptance, some more successful demonstrated cases (not only laboratory ones) which will give certainty about compatibility, durability, and long service life, will be of the utmost importance.

References

- Alanazi, H., Yang, M., Zhang, D., Gao, Z.J., 2016. Bond strength of PVC pavement repairs using metakaolin-based geopolymer mortar. *Cem. Concr. Compos.* 65, 75–82.

- ASTM C1012, 2004/C1012C, 2015. Standard Test Method for Length Change of Hydraulic-Cement Mortars Exposed to a Sulfate Solution. ASTM International, West Conshohocken, PA, 2015, www.astm.org.
- ASTM C 1157, 2008/C1157, 2017. Performance Specification for Hydraulic Cement. ASTM International, West Conshohocken, PA, 2017, www.astm.org.
- Bakharev, T., 2005. Durability of geopolymer materials in sodium and magnesium sulfate solutions. *Cem. Concr. Res.* 35, 1233–1246.
- Barbosa, V.F.F., Mackensie, K.J.D., Thaumaturgo, C., 2000. Synthesis and characterisation of materials based on inorganic polymers of alumina and silica: sodium polysialate polymers. *Int. J. Inorg. Mater.* 2, 309–317.
- Bernal, S.A., de Gutierrez, R.M., Provis, J.L., Rose, V., 2010. Effect of silicate modulus and metakaolin incorporation on the carbonation of alkali silicate-activated slags. *Cem. Concr. Res.* 40 (6), 898–907.
- Brough, A.R., Atkinson, A., 2002. Sodium silicate-based, alkali-activated slag mortars: Part I. Strength, hydration and microstructure. *Cem. Concr. Res.* 32, 865–879.
- Bruhwyler, E., 2012. Rehabilitation and strengthening of concrete structures using Ultra High Performance Fiber Reinforced Concrete. In: Alexander, M., Beushausen, H.D., Dehn, F., Moyo, P. (Eds.), *Concrete Repair, Rehabilitation and Retrofitting III*. Taylor & Francis group, London, pp. 30–31.
- Chareerat, T., 2008. A study of compressive strength and durability of mae moh fly ash geopolymer. A thesis of Degree of Doctor of Philosophy in Civil Engineering, Khon Kaen University.
- Charola, E.A., 2000. Salts in the deterioration of porous materials: an overview. *J. Am. Inst. Conserv.* 39, 327–343.
- Chatterjee, A.K., 2012. Concrete repair materials, polymers and green chemistry—how far synergistic are they? In: Alexander, M., Beushausen, H.D., Dehn, F., Moyo, P. (Eds.), *Concrete Repair, Rehabilitation and Retrofitting III*. Taylor & Francis group, London, pp. 315–316.
- Chindapasirt, P., de Silva, P., Sagoe-Crenstil, K., Hanjitsuwan, S., 2012. Effect of SiO₂ and Al₂O₃ on the setting and hardening of high calcium fly ash-based geopolymer systems. *J. Mater. Sci.* 47, 4876–4883.
- Criado, M., Palomo, A., Fernández-Jiménez, A., 2005. Alkali activation of fly ashes. Part I: effect of curing conditions on the carbonation of the reaction products. *Fuel*. 84, 2048–2054.
- Dembovska, L., Bajare, D., Ducman, V., Korat, L., Bumanis, G., 2017. The use of different by-products in the production of lightweight alkali activated building materials. *Constr. Build. Mater.* ISSN 0950-0618. [Print ed.], 135, 315–322.
- Diaz, E.I., Allouche, N., Eklund, S., 2010. Factors affecting the suitability of fly ash as source material for geopolymers. *Fuel*. 89, 992–996.
- Donatello, S., Fernández-Jiménez, A., Palomo, A., 2013. Very high volume fly ash cements, early age hydration study using Na₂SO₄ as an activator. *J. Am. Ceram. Soc.* 96, 900–906.
- Dufka, A., Brožovský, J., Melichar, T., 2015. Development of repair mortars based on alkali activated materials for application in chemically aggressive surroundings. *Adv. Mater. Res.* 1122, 98–104.
- Emmons, P.H., 2012. The concrete repair industry, actions for improvements. In: Alexander, M., Beushausen, H.D., Dehn, F., Moyo, P. (Eds.), *Concrete Repair, Rehabilitation and Retrofitting III*. Taylor & Francis group, London, pp. 13–14.
- EN 197-1, 2011. Cement. Composition, specifications and conformity criteria for common cements.

- EN 450-1, 2012. Fly ash for concrete. Definition, specifications and conformity criteria.
- EN 1504-1, 2005. Products and systems for the protection and repair of concrete structures. Definitions, requirements, quality control and evaluation of conformity. Definitions.
- EN 1504-2, 2004. Products and systems for the protection and repair of concrete structures. Definitions, requirements, quality control and evaluation of conformity. Surface protection systems for concrete.
- EN 1504-3, 2005. Products and systems for the protection and repair of concrete structures. Definitions, requirements, quality control and evaluation of conformity. Structural and non-structural repair.
- Pr EN 1504-3, 2015. Products and systems for the protection and repair of concrete structures. Definitions, requirements, quality control and evaluation of conformity. structural and non-structural repair.
- EN 1504-4, 2004. Products and systems for the protection and repair of concrete structures. Definitions, requirements, quality control and evaluation of conformity. Structural bonding.
- EN 1504-5, 2013. Products and systems for the protection and repair of concrete structures. Definitions, requirements, quality control and evaluation of conformity. Concrete injection.
- EN 1504-6, 2006. Products and systems for the protection and repair of concrete structures. Definitions, requirements, quality control and evaluation of conformity. Anchoring of reinforcing steel bar.
- EN 1504-7, 2006. Products and systems for the protection and repair of concrete structures. Definitions, requirements, quality control and evaluation of conformity. Reinforcement corrosion protection.
- EN 1504-8, 2016. Products and systems for the protection and repair of concrete structures—Definitions, requirements, quality control and AVCP—Part 8: quality control and assessment and verification of the constancy of performance (AVCP).
- EN 1504-9, 2008. Products and systems for the protection and repair of concrete structures. Definitions, requirements, quality control and evaluation of conformity. General principles for use of products and systems.
- EN 1504-10, 2003. Products and systems for the protection and repair of concrete structures. Definitions, Requirements, Quality control and evaluation of conformity. Site application of products and systems and quality control of the works.
- EN 1504-10, 2015. Products and systems for the protection and repair of concrete structures. Definitions, Requirements, Quality control and evaluation of conformity. Part 10: site application of products and systems and quality control of the works.
- EN 12620, 2013. Aggregates for concrete.
- EN ISO 12696, 2012. Cathodic protection of steel in concrete.
- EN 13501-1, 2007 + A1:2009 Fire classification of construction products and building elements. Part1: Classification using data from reaction to fire tests.
- EN 13501-2, 2016. Fire classification of construction products and building elements. Part 2: Classification using data from fire resistance tests, excluding ventilation services.
- EN 14647, 2005. Calcium aluminate cement. Composition, specifications and conformity criteria.
- Fernández-Jiménez, A., Palomo, J.G., Puertas, F., 1999. Alkali-activated slag mortars: Mechanical strength behavior. *Cem. Concr. Res.* 29, 1313–1329.
- Fernández-Jiménez, A., Palomo, A., Criado, M., 2005. Microstructure development of alkali-activated fly ash cement: a descriptive model. *Cem. Concr. Res.* 35, 1204–1209.
- Fernández-Jiménez, A., Palomo, A., López-Hombradoc, C., 2006. Engineering properties of alkali-activated fly ash concrete. *ACI Mater. J.* 103, 106–112.

- Fernández-Jiménez, A., Garcia-Lodeiro, I., Palomo, A., 2007. Durability of alkali activated fly ash cementitious materials. *J. Mater. Sci.* 42, 3055–3065.
- Garcia-Lodeiro, I., Donatello, S., Fernández-Jiménez, A., Palomo, A., 2016. Hydration of hybrid alkaline cement containing a very large proportion of fly ash: a descriptive model. *Materials*. 2016 (9), 605. Available from: <http://dx.doi.org/10.3390/ma9070605>.
- Gorst, N., Clark, L., 2003. Effects of thaumasite on bond strength of reinforcement in concrete. *Cem. Concr. Res.* 25, 1089–1094.
- Granizo, M.L., Alonso, S., Blanco-Varela, M.T., Palomo, A., 2002. Alkaline activation of metakaolin: effect of calcium hydroxide in the products of reaction. *J. Am. Ceram. Soc.* 85, 225–231.
- Hawa, A., Tonnayopas, D., Prachasaree, W., Taneerananon, P., 2013. Development and performance evaluation of very high early strength geopolymer for rapid road repair., *Adv. Mater. Sci. Eng.* 13, 1–9.
- Hu, S., Wang, H., Zhang, G., Ding, Q., 2008. Bonding and abrasion resistance of geopolymeric repair material made with steel slag. *Cem. Concr. Compos.* 30, 239–244.
- Imbabi, M.S., Carrigan, C., McKenna, S., 2012. Trends and developments in green cement and concrete technology. *Int. J. Sustainable Built Environ.* 1 (2), 194–216.
- Ismail, I., Bernal, A., Provis, J.L., Hamdan, S., Deventer, J.S.J., 2013. Microstructural changes in alkali activated fly ash/slag geopolymers with sulfate exposure. *Mater. Struct.* 46, 361–373.
- Jansson, H., Tang, J., 2015. Parameters Influencing the Initial Setting Time of Alkali-Activated Ground Granulated Blast furnace Slag Materials, <http://publications.lib.chalmers.se/records/fulltext/230879/local_230879.pdf>.
- Jonkers, H.M., 2011. Bacteria-based self-healing concrete. *HERON*. 56 (1/2), 1–12.
- Kramar, S., Šajna, A., Ducman, V., 2016. Assessment of alkali activated mortars based on different precursors with regard to their suitability for concrete repair. *Constr. Build. Mater.* 124, 937–944.
- Law, D.W., Adam, A.A., Molyneaux, T.K., Patnaikuni, I., Wardhono, A., 2015. Long term durability properties of class F fly ash geopolymer concrete. *Mater. Struct.* 48, 721–731.
- Li, C., Sun, H., Li, L., 2010. A review: the comparison between alkali-activated slag (Si + Ca) and metakaolin (Si + Al) cements. *Cem. Concr. Res.* 40, 1341–1349.
- Lin, T., Jia, D., Wang, M., He, P., Liang, D., 2009. Effects of fibre content on mechanical properties and fracture behavior of short carbon fibre reinforced geopolymer matrix composites. *Bull. Mater. Sci.* 32 (1), 77–81.
- Mechterine, V., 2012. Novel cement-based composites for strengthening and repair of concrete structure. In: Alexander, M., Beushausen, H.D., Dehn, F., Moyo, P. (Eds.), *Concrete Repair, Rehabilitation and Retrofitting III*. Taylor & Francis group, London, pp. 27–29.
- Mostafa, N.Y., El-Hemaly, S.A.S., Al-Wakeel, E.I., El-Korashy, S.A., Brown, P.W., 2001. Characterization and evaluation of the hydraulic activity of water-cooled slag and air-cooled slag. *Cem. Concr. Res.* 31, 899–904.
- Najafi Kani, E., Allahverdi, A., Provis, J.L., 2011. Efflorescence control in geopolymer binders based on natural pozzolan. *Cem. Concr. Res.* 34, 25–33.
- Natali, M.E., Manzi, S., Carabba, L., Chiavari, C., Bignozzi, M.C., Abbottoni, M., et al., 2014. Mechanical performance and corrosion resistance of reinforced fly ash geopolymer mortars. *Adv. Sci. Technol.* 92, 50–55.
- Pacheco-Torgal, F., Castro-Gomes, J.P., Jalali, S., 2008a. Adhesion characterization of tungsten mine waste geopolymeric binder. Influence of OPC concrete substrate surface treatment. *Constr. Build. Mater.* 22, 154–161.

- Pacheco-Torgal, F., Castro-Gomes, J.P., Jalali, S., 2008b. Investigations on mix design of tungsten mine waste geopolameric binder. *Constr. Build. Mater.* 22, 154–161.
- Pacheco-Torgal, F., Moura, D., Ding, Y., Jalali, S., 2011. Composition, strength and workability of alkali-activated metakaolin based mortars. *Constr. Build. Mater.* 25, 3732–3745.
- Pacheco-Torgal, F., Abdollahnejad, Z., Camoes, A.F., Jamshidi, M., Ding, Y., 2012a. Durability of alkali activated binders: a clear advantage over Portland cement or an unproven issue? *Constr. Build. Mater.* 30, 404–405.
- Pacheco-Torgal, F., Abdollahnejad, Z., Miraldo, S., Baklouti, S., Ding, Y., 2012b. An overview on the potential of geopolymers for concrete infrastructure rehabilitation. *Constr. Build. Mater.* 36, 1053–1058.
- Pacheco-Torgal, F., Barroso de Aguiar, J., Ding, Y., Tahri, W., Baklouti, S., 2014. Performance of alkali-activated mortars for the repair and strengthening of OPC concrete. In: Pacheco-Torgal, F., Labrincha, J., Leonelli, C., Palomo, A., Chindaprasit, P. (Eds.), *Handbook of Alkali-activated Cements, Mortars and Concretes*. Woodhead Publishing Limited- Elsevier Science and Technology, Abington Hall, Cambridge, UK, pp. 627–641.
- Pacheco-Torgal, F., Abdollahnejad, Z., Mirlado, S., Kheradmand, M., 2016. Alkali-activated cement-based binders (AACB) as durable and cost competitive low CO₂ binders: some shortcomings that need to be addressed. In: Nazari, Sanjayan (Eds.), *Handbook of Low Carbon Concrete*. Elsevier Science and Technology, Waltham, pp. 195–216.
- Pinto, A.T., 2010. Repairing of damaged stone in monuments and stone buildings. *Adv. Sci. Technol.* 69, 164–173.
- Pouchet, R., Cyr, M., 2014. Studies of natural and accelerated carbonation in metakaolin-based geopolymer. *Adv. Sci. Technol.* 92, 38–42.
- Provis, J.L., van Deventer, J.S.J., 2013. *Alkali-activated materials: State-of-the-Art Report*, RILEM TC 224-AAM. Springer/RILEM, Berlin.
- Puertas, F., Palacios, M., Vázquez, T., 2006. Carbonation process of alkali-activated slag mortars. *J. Mater. Sci.* 41, 3071–3082.
- Ravikumar, D., Neithalath, N., 2012. Reaction kinetics in sodium silicate powder and liquid activated slag binders evaluated using isothermal calorimetry. *Thermochimica Acta.* 546, 32–43.
- Raupach, M., 2006. Concrete repair according to the new European standard EN 1504. In: Alexander, M., Beushausen, H.D., Dehn, F., Moyo, P. (Eds.), *Concrete Repair, Rehabilitation and Retrofitting*. Taylor & Francis group, London, pp. 6–8.
- Rovnaník, P., Šimonová, H., Topolář, L., Bayer, P., Schmid, P., Keršner, Z., 2016. Carbon nanotube reinforced alkali-activated slag mortars. *Constr. Build. Mater.* 119, 223–229.
- de Silva, P., Sagoe-Crenstil, K., 2008. The effect of Al₂O₃ and SiO₂ on setting and hardening of Na₂O-Al₂O₃-SiO₂-H₂O geopolymer systems. *J. Aust. Soc.* 44 (1), 39–46.
- Song, K.-I., Song, J.-K., Lee, B.Y., Yang, K.-H., 2014. Carbonation characteristics of alkali-activated blast-furnace slag mortar. *Adv. Mater. Sci. Eng.* 2014(2014) 11 pages (Open Access). <<http://dx.doi.org/10.1155/2014/326458>>.
- Škvára, F., Jilek, T., Kopecký, L., 2005. Geopolymer materials based on fly ash. *Ceram-Silik.* 49, 195–204.
- Škvára, F., Kopecký, L., Šmilauer, V., Alberovská, L., Vinšová, L., 2009. Aluminosilicate polymers—influence of elevated temperatures, efflorescence. *Ceram-Silik.* 53, 276–282.
- Škvára, F., Šmilauer, V., Hlaváček, P., Kopecký, L., Cílová, Z., 2012. A weak alkali bond in (N, K)–A–S–H gels: evidence from leaching and modelling. *Ceram-Silik.* 56, 374–382.

- Tahri, W., Abdollahnejad, Z., Mendes, J., Pacheco-Torgal, F., de Aguiar, J.B., 2015. Performance of fly ash Geopolymeric mortar for coating of ordinary Portland cement concrete exposed to harsh chemical environments. *Adv. Mater. Res.* 1129, 573–580.
- Tamburini, S., Natali, M., Garbin, E., Panizza, M., Favaro, M., Valluzzi, M.R., 2017. Geopolymer matrix for fiber reinforced composites aimed at strengthening masonry structures. *Constr. Build. Mater.* 141, 542–552.
- Temuujin, J., van Riessen, A., MacKenzie, K.J.D., 2010. Preparation and characterization of fly ash based geopolymer mortars. *Constr. Build. Mater.* 24, 1906–1910.
- Vasconcelos, E., Fernandes, S., Barroso de Aguiar, J.L., Pacheco Torgal, F., 2011. Concrete retrofitting using metakaolin geopolymer mortars and CFRP. *Constr. Build. Mater.* 25, 3213–3221.
- Wanchai, Y., 2014. Application of fly ash based geopolymer for structural member and repair materials. *Adv. Sci. Technol.* 92, 74–83.
- Wang, S.-D., Scrivener, K.L., 1995. Hydration products of alkali activated slag cement. *Cem. Concr. Res.* 25, 561–571.
- Warid Wazien, A.Z., Al Bakri Abdullah, M.M., Abd Razak, R., Mohd Remy Rozainy, M.A. Z., Mohd Tahir, M.F., Hussin, K., 2016. Potential of geopolymer mortar as concrete repairing materials. *Mater. Sci. Forum.* 857, 382–387.
- Yang, Q., Wu, X., 1999. Factors influencing properties of phosphate cement-based binder for rapid repair of concrete. *Cem. Concr. Res.* 29 (3), 389–396.
- Yang, Q., Zhu, B., Zhang, S., Wu, X., 2000. Properties and applications of magnesia-phosphate cement mortar for rapid repair of concrete. *Cem. Concr. Res.* 30 (11), 1807–1813.
- Zanotti, C., Borges, P.H.R., Bhuta, A., Du, Y., Banthia, N., 2016. Bond strength of PVA fiber reinforced geopolymer repair to Portland cement concrete substrate. 9th RILEM International Symposium on Fiber Reinforced Concrete-BEFIB, Vancouver, Canada, pp. 90–100.
- Zhang, Z., Yao, X., Zu, H., 2010a. Potential application of geopolymers as protection coatings for marine concrete I. Basic properties. *Appl. Clay Sci.* 49, 1–6.
- Zhang, Z., Yao, X., Zu, H., 2010b. Potential application of geopolymers as protection coatings for marine concrete II. Microstructure and anticorrosion mechanism. *Appl. Clay Sci.* 49, 7–12.
- Zhang, Z., Yao, X., Wang, H., 2012. Potential application of geopolymers as protection coatings for marine concrete III. Field experiment. *Appl. Clay Sci.* 67–68, 57–60.
- Zhang, Z., Provis, J.L., Reid, A., Wang, H., 2014. Fly ash-based geopolymers: the relationship between composition, pore structure and efflorescence. *Cem. Concr. Res.* 64, 30–41.
- Zhu, H., Zhang, Z., Deng, F., Cao, Y., 2013. The effects of phase changes on the bonding property of geopolymer to hydrated cement. *Constr. Build. Mater.* 48, 124–130.
- Zuhua, Z., Xiao, Y., Huajun, Z., Yue, C., 2009. Role of water in the synthesis of calcined kaolin-based geopolymer. *Appl. Clay Sci.* 48, 218–223.

Further reading

- Colangelo, F., Roviello, G., Ricciotti, L., Ferone, C., Cioffi, R., 2013. Preparation and characterization of new geopolymer-epoxy resin hybrid mortars. *Materials.* 6, 289–3006.

- Huseien, G.F., Mirza, J., Ismail, M., Ghoshal, S.K., Mohd Azreen, Mohd Ariffin, 2016. Effect of metakaolin replaced granulated blast furnace slag on fresh and early strength properties of geopolymer mortar. *Ain Shams Eng. J.* <<http://dx.doi.org/10.1016/j.asej.2016.11.011>> (Open Access).
- Phoo-ngernkham, T., Sata, V., Hanjitsuwan, S., Ridthirud, C., Hatanaka, S., Chindaprasirt, P., 2015. High calcium fly ash geopolymer mortar containing Portland cement for use as repair material. *Constr. Build. Mater.* 98, 482–488.
- Wardhone, A., Law, D.W., Strano, A., 2015. The strength of alkali-activated slag/fly ash mortar blends at ambient temperature. *Procedia Eng.* 125, 650–656.

Geopolymeric repair mortars based on a low reactive clay

12

Walid Tahri¹, Basma Samet¹, Fernando Pacheco-Torgal², José Aguiar² and Samir Baklouti¹

¹University of Sfax, Sfax, Tunisie, ²University of Minho, Guimarães, Portugal

12.1 Introduction

Worldwide infrastructure rehabilitation costs are staggering. The patch repair method is widely used to restore the original conditions of the concrete structures (Emmons and Vaysburd, 1994, 1996). Most patch repair mortars fall into two categories: mortars based on organic binders (epoxy resin or polyester) or those based on inorganic binders, like Portland cement (PC). The former are associated with toxic side effects (Pacheco-Torgal et al., 2012b) while the latter are known for their high embodied carbon (Pacheco-Torgal et al., 2013). Geopolymers are novel inorganic binders with a high potential to replace PC-based ones (van Deventer et al., 2012). The geopolymerization of alumino-silicate materials is a complex chemical process involving the dissolution of raw materials, transportation or orientation, and polycondensation of the reaction products (Li et al., 2010; Van Deventer et al., 2010; Provis, 2014; Pacheco-Torgal et al., 2016). Investigations in the field of geopolymers reveal a third category of mortars with potential to be used in the field of concrete patch repair (Pacheco-Torgal et al., 2012a). Some authors (Pacheco-Torgal et al., 2008a) have shown that concrete specimens repaired with geopolymeric mortar and one day curing have higher bond strength than specimens repaired with current commercial repair products after 28 days curing. This is a promising performance because adhesion to the concrete substrate is a crucial property of the repair mortars (Khan et al., 2012). This chapter presents results of an investigation concerning the development of geopolymeric repair mortars based on a low reactive, calcined clay. The influence of replacing small amounts of calcined clay with fly ash (FA) and metakaolin (MK) was also studied.

12.2 Experimental work

12.2.1 Materials

The clay materials used originate from Medenine Region of Tunisia. Previous studies performed on many clay materials showed that kaolinite is the major mineral and quartz the major impurity. The dried clay fractions were crushed in

a mortar and then sieved to 100 μm . The clay fractions were calcined in a programmable electric furnace (Nabertherm, Mod.LH 60/14) for 6 hours at a heating rate of 11.33°C/min at a temperature of 700°C (Essaïdi et al., 2014). Results of the chemical composition of the clay fractions are given in Table 12.1. Fig. 12.1 presents the X-ray diffractograms (XRD) of the natural clay (NC). The basic clay mineral in the clay fractions is kaolinite, associated to quartz and illite. Minor amounts of gypsum and hematite can be considered as impurities. Quantitatively, the diffractogram confirms that this clay has lower kaolinite content. The characteristic peaks of illite (8.8, 18.8, and 19.9°C) can be observed. The overall result shows that the thermal treatment of the clay fractions at 700°C is enough to transform kaolinite into metakaolinite. This is in agreement with the thermal analyses—differential scanning calorimetry (DSC) and thermogravimetric (TG)—results, which show that the dehydroxylation of kaolinite starts from around 480°C. In the X-ray diffraction patterns of the calcined clay, the disappearance of the kaolin peaks and their change to metakaolinite was observed. After calcination, the kaolinite disappeared but some traces of illite remained almost intact. However, after calcination gypsum was transformed into anhydrite. Fig. 12.2, presents DSC and TG curves of the clay fractions of NC. The thermal behavior, typical of kaolinite clays is displayed (Mackenzie, 1957; Bouaziz and Rollet, 1972). The interval (20–120°C) showed the period of drying the raw material, which consisted of the disappearance of the water molecules. From 400 to 500°C, the kaolinite changed into the new metakaolinite phase. Between 600 and 800°C, calcite also decomposed, generating CO₂. The SEM analysis (Fig. 12.3) shows the morphology of the raw material, which consisted of major mineral clay kaolinite layers. This transformation of kaolinite into metakaolinite produces a more reactive material. This result was confirmed by the infrared spectra of the raw material NC (Fig. 12.4), in which some absorption bands characteristic of kaolinite are present (3693–3619cm⁻¹) (Kakali et al., 2001).

Table 12.1 Chemical composition of the natural clay (NC) fractions

Raw material (clay, NC)	
Oxides	Weight (%)
SiO ₂	60.80
Al ₂ O ₃	16.20
CaO	2.15
F ₂ O ₃	5.87
SO ₃	0.08
K ₂ O ₃	2.71
MgO	2.38
Na ₂ O ₃	0.003
PF	9.16

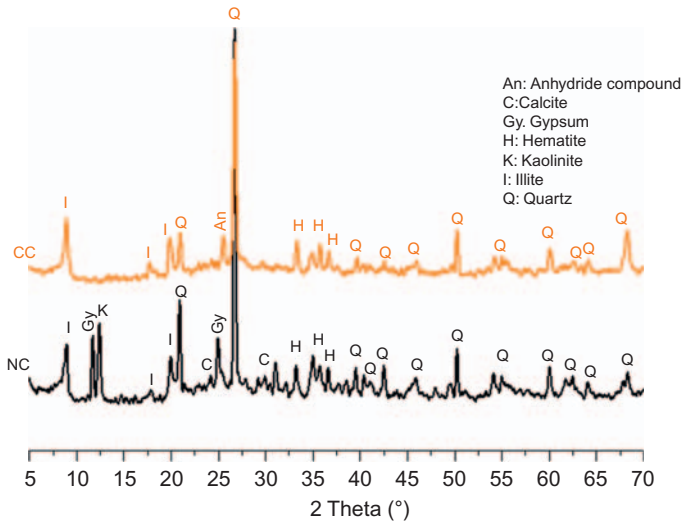


Figure 12.1 X-ray diffractograms of the raw material natural clay (NC) and calcined clay at 700°C (CC).

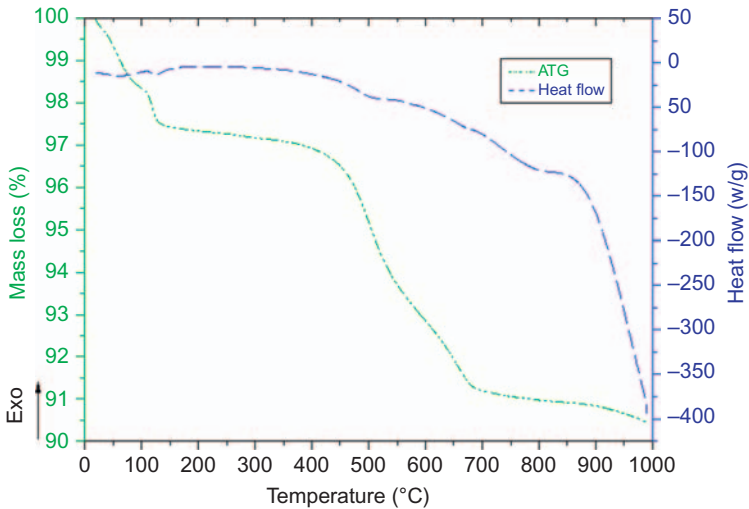


Figure 12.2 Thermo-gravimetric analysis/differential scanning calorimetry (TGA/DSC) of natural clay (NC).

12.2.2 Mix proportioning and synthesis

The alkaline solution used was a mixture of an aqueous solution of sodium hydroxide 12 M and sodium silicate, with a bulk density of 1350 kg/m³ and

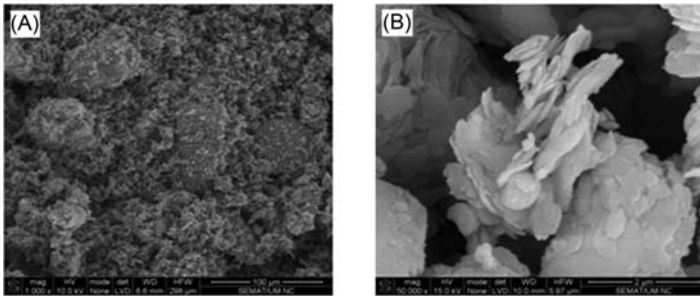


Figure 12.3 Morphology of the natural clay (NC): (A) Before calcination; (B) After calcination.

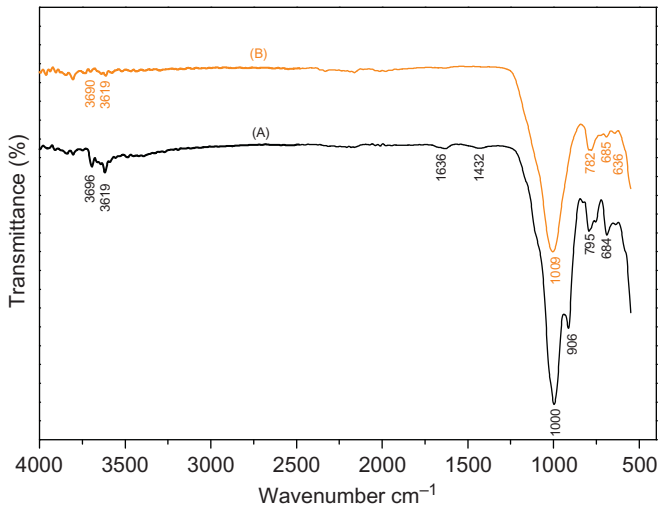


Figure 12.4 Fourier transform infrared (FTIR) spectra of raw material: (A) to natural clay (NC) and (B) calcined clay (CC).

ratio: $\text{Na}_2\text{SiO}_3/\text{NaOH} = 2.5$. The sodium hydroxide solution was obtained by dissolving dried pellets of 99% purity in distilled water. The sodium silicate solution had a composition by weight of $\text{Na}_2(\text{SiO}_2)_x \cdot y(\text{H}_2\text{O})$ in which $3.19 \leq x \leq 3.53$ and $50\% \leq y \leq 60\%$. The geopolymer mortar consisted of a mixture of the alkaline solution, powdered calcined clay, calcium hydroxide and sand. The sand has a maximum dimension of 4 mm and a density of 2660 kg/m^3 . The calcium hydroxide had more than 70% of CaO and a density of 460 kg/m^3 . Several authors have shown that the use of minor amounts of calcium hydroxide is crucial for the strength and durability of geopolymers (Lee and Van Deventer, 2002; Yip et al., 2005; Pacheco-Torgal et al., 2008b; van Deventer et al., 2012). The assembly was mixed in a Hobart mixer (M & O, model N50-G) for 3 minutes. The sample of geopolymer mortar was vibrated in the vibrating table to remove entrapped air bubbles. During

the hardening of the geopolymer samples, the molds were covered with a thin plastic film to avoid water evaporation and then kept for 24 hours at the ambient atmosphere of the laboratory (24–26°C). After measurement of the compressive strength, certain fragments of geopolymer mortar samples were kept for XRD, FTIR, TGA, DSC, and SEM analyses. Table 12.2 shows the composition of the geopolymeric mortars. In a second phase, a new set of six mixtures was prepared, based on G1R3, containing 80% of the initial activator/binder ratio and with a partial replacement of Tunisian clay by FA and MK (Table 12.3). The compositions of MK and FA are presented in Table 12.4.

12.2.3 Workability

The workability assessment has been conducted with a truncated conical mold and a jolting table, according to the standard EN 1015-3.

12.2.4 Unrestrained shrinkage

Unrestrained shrinkage was determined according to LNEC E398-1993 standard. The specimens were removed from the molds 24 hours after being mixed and placed, then were wrapped with Perspex paper. Other authors used aluminum paper, having reported the formation of hydrogen gas bubbles due to a reaction between the aluminum and the alkalis from the mortar (Pacheco-Torgal et al., 2008c). The measurement of shrinkage was carried out on hardened geopolymer mortar samples aged at 1, 7, 14, and 18 days respectively.

12.2.5 Compressive strength testing

Compressive strength data was obtained according to EN 1015-11 standard. The fresh mortar was cast and allowed to set at room temperature for 24 hours before being removed from the molds and kept at room temperature (20°C) until being tested. Compressive strength for each mortar mixture was obtained from an average of three specimens. The compressive strength was determined on the hardened geopolymer mortar samples, aged of 28 days using an electrohydraulic press (M & O, type 11.50, N°21) at an average rate of 3 mm/min.

Table 12.2 Mixture quantities—first phase

Materials						
Mixtures	Calcined clay (g)	Lime (g)	Sand (g)	Activator (g)		(Lime + Calcined clay)/sand
				Na ₂ SiO ₃	NaOH	
G1R2	674	74.8	1496	535	213	1:2
G1R3	674	74.8	2250	535	213	1:3
G1R4	674	74.8	2992	535	213	1:4

Table 12.3 Mixture quantities—second phase

Mixtures	Calcined clay (g)	Lime (g)	Sand (g)	Activator (g)		FA (g)	FA (%)	Mk (g)	Mk (%)	Mass ratio _{Agr} = (Lime + Clay)/sand	Mass ratio _{Act} = Na ₂ SiO ₃ /NaOH
				Na ₂ SiO ₃	NaOH						
G1R.3_80%_REF	1264.79	140.53	4215.97	801.97	322.29	0	—	0	—	1: 3	2, 5
G1R3_80%_10%FA	1138.31	140.53	4215.97	801.97	322.29	126.48	10	0	—		
G1R3_80%_15%FA	1075.07	140.53	4215.97	801.97	322.29	189.72	15	0	—		
G1R3_80%_10%Mk	1138,31	140.53	4215.97	801.97	322.29	0	—	126.48	10		
G1R3_80%_15%Mk	1075.07	140.53	4215.97	801.97	322.29	0	—	189.72	15		
G1R3_80%_30%Mk	885.35	140.53	4215.97	801.97	322.29	0	—	379.44	30		

MK, metakaolin; FA, fly ash.

Table 12.4 Chemical composition of metakaolin (MK) and fly ash (FA)

Constituents (%)	MK	FA
SiO ₂	61.26	49.12
Al ₂ O ₃	27.0	27.3
Fe ₂ O ₃	3.08	8.19
CaO	0.159	2.36
MgO	0.161	1.42
Na ₂ O	0.096	0.99
K ₂ O	6.622	3.34
SO ₃	0.048	—
TiO ₂	0.994	2.32
P ₂ O ₅	0.325	—
Zn	0.005	—
ZrO ₂	0.056	—
Other oxides	0.255	—

12.2.6 Modulus of elasticity

The modulus of elasticity was determined using cylindrical samples with a diameter of 50 mm and a length of 100 mm. These specimens were tested after the established curing time of 28 days. The values of the modulus of elasticity were obtained from the average of the three specimens.

12.2.7 Adhesion strength and flexural strength of Portland cement concrete rehabilitated beams

Bond strength is one of the most important properties of concrete repair materials. Bond strength depends on the repair material characteristics and on the roughness of the concrete substrate surface. In this investigation, the Pull-off test was used to assess this property. This test was done according to the standard [BS EN 1542 \(1999\)](#). A 20 MPa compressive strength was used as substrate ([Table 12.5](#)) and a geopolymeric mortar layer was cast over the concrete substrate. A circular hole (50 mm diameter and 60 mm in depth) was then cut through the mortar layer. Afterwards, several metallic discs were glued with epoxy resin to the geopolymeric mortar. The Pull-off machine (Proceq Dyna Z15 device) was attached to the metallic discs, allowing for the assessment of the adhesion strength until rupture. Additionally, several concrete beams, with the same composition of the Pull-Off substrates ([Table 12.5](#)) and with dimensions of 100 × 100 × 1000 mm³, were water-cured during 28 days until they were tested for flexural strength.

Table 12.5 Composition of the Portland cement (PC) concrete substrate used in the Pull-off test (kg/m^3)

Components	Mix
Cement II 32.5	400 kg
Fine river sand	578 kg
Coarse aggregate	1066 kg
W/C ratio	0.53 kg
Fc 28 days (MPa)	20.3

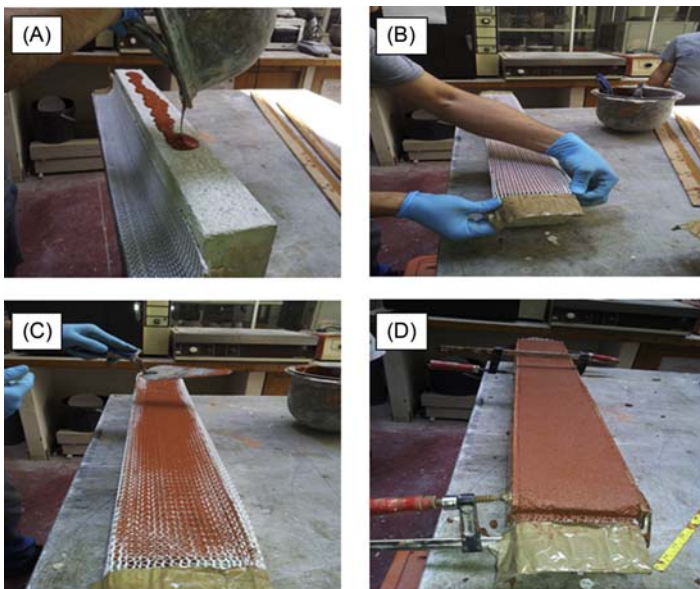


Figure 12.5 Portland cement (PC) concrete rehabilitated beams preparation: (A) placement of a geopolymeric primer; (B) placement of the metallic grid; (C) covering the metallic grid with geopolymeric mortar; (D) concluded beam.

The concrete beams were rehabilitated with a metallic grid and geopolymeric mortars (Fig. 12.5).

12.2.8 Fourier transform infrared

The FTIR spectra were acquired in the attenuated total reflectance (ATR) mode, between 4000 and 550 cm^{-1} , using a Perkin Elmer FTIR Spectrum BX with an ATR PIKE MIRacle. The specimens for FTIR study were prepared by mixing 1 mg of sample in 100 mg of KBr. Spectral analysis was performed over the range $4000\text{--}400\text{ cm}^{-1}$ at a resolution of 4 cm^{-1} .

12.2.9 Scanning electron microscopy

Scanning electron microscopy (SEM) was carried out using a Phillip XL 30 on pellets from hardened geopolymer samples aged at 28 days.

12.3 Results and discussion

12.3.1 Workability

The investigations showed that the flow diameter for the three mixtures decreases when the sand mass increases. The mixture with a binder/sand ratio of 1:2 has an excessive flow (23 cm), while the mixture with a binder/sand ratio of 1:3 has a flow currently found in most mortars (180 mm). The mixture with a binder/sand ratio of 1:4 seems to have a low flow diameter. However, it is acceptable when using the hand placement technique in which higher flows are not desirable, in order to avoid detachment risks.

12.3.2 Unrestrained shrinkage

The results of this test are shown in Fig. 12.6. In the first 2 days, the shrinkage increases very rapidly. Since the tests have been carried out with the isolation of specimens under a perspex film to avoid the evaporation of water, the measured shrinkage is due to the hydration reaction (autogenous shrinkage). Consequently, the rapid increase in the first two days is relative to the capillary tensions within the gel framework during geopolymerization (Brinker and Scherrer 1990). Other authors (Teixeira-Pinto, 2004) that used alkali-activated MK-based binders in similar experimental conditions reported shrinkage results between 500 and 840 microstrain. Since mortars used in PC patch repair require very low shrinkage (Cusson, 2009) this means that those geopolymeric mortar mixtures show an unacceptable performance. Fig. 12.7 shows the unrestrained shrinkage of the second

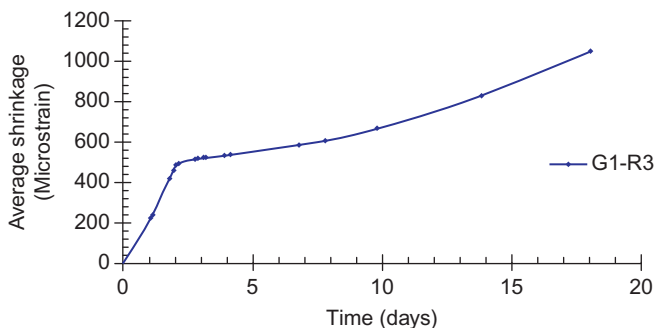


Figure 12.6 Shrinkage of the mixture with a binder/sand ratio of 1:3 as function of curing time (days).

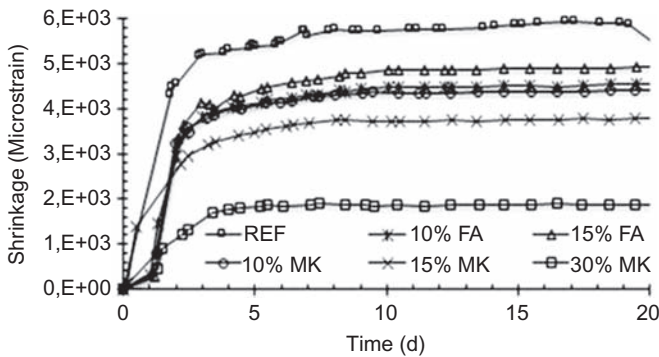


Figure 12.7 Unrestrained shrinkage of the modified G1R3 geopolymer mixture as function of curing time (days).

set of mixtures. The maximum unrestrained shrinkage is of $\sim 500\text{--}600$ microstrain and is due to the reduction of the alkaline activator. The partial replacement of Tunisian clay by FA also leads to a lower unrestrained shrinkage performance than the reference mixture. Partial replacement by MK outperforms FA-based mixtures. The comparison of the unrestrained shrinkage in 15% FA mortar and in 15% MK shows a very relevant difference. When 30% MK is used, the observed unrestrained shrinkage is very low. This means that the new geopolymeric mortar mixtures based on the partial replacement of Tunisian clay by MK have an acceptable performance concerning this parameter.

12.3.3 Compressive strength

Fig. 12.8 shows the compressive strength results at 28 days curing. Although it seems that the compressive strength is influenced by the sand/binder mass ratio, the differences are very slight and fall within the standard deviation interval. The compressive strength at 28 days curing is below typical compressive strength of old PC reinforced concrete structures, in which 20–30 MPa can be expected, thus meaning that repair mortars should have a strength of at least 30 MPa. Other authors (Pacheco-Torgal et al., 2011) analyzed mortars with the same activator/binder ratio and the same 12 M sodium hydroxide concentration obtaining a 40 MPa compressive strength just after 7 days curing. However, they used MK as a binder, which is much more reactive than the calcined Tunisian clay used in this investigation. Mixtures with a small replacement of calcined Tunisian clay by MK should also be analyzed for compressive strength. Fig. 12.9 shows the compressive strength of the second set of mixtures. The results show that the partial replacement of Tunisian clay by 10% or even 15% of FA is not advantageous for 28 days compressive strength. The same occurs for flexural strength, although the 15% FA mixture shows a minor increase when compared to the reference mixture. This behavior is related to the low reactivity of FA. In the geopolymeric mixtures in which the Tunisian clay was partially replaced by MK, an increase in compressive strength is

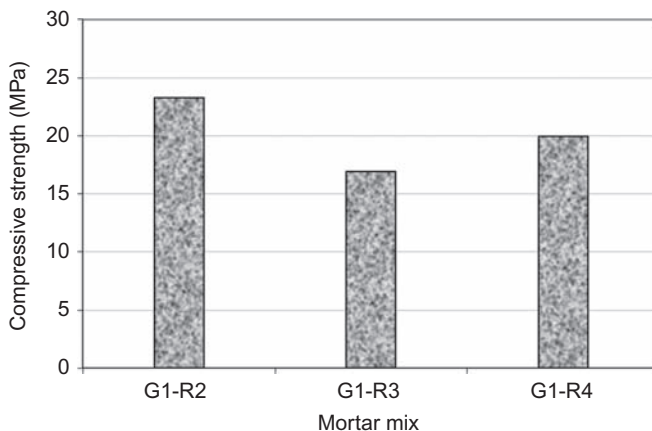


Figure 12.8 Compressive strength for geopolymeric mortar mixtures with sodium hydroxide concentrations (12 M) and sand/binder mass ratios ($R = 2$; $R = 3$, $R = 4$).

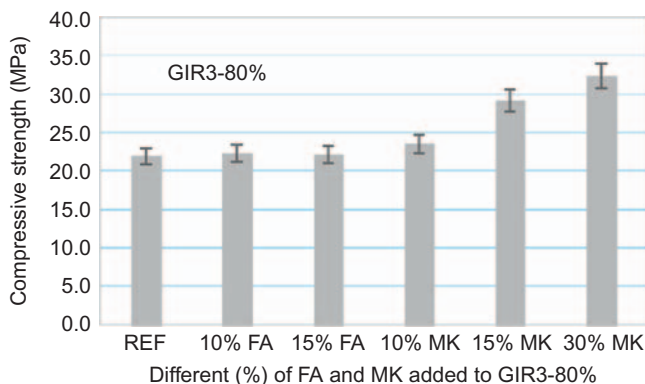


Figure 12.9 Compressive strength of the modified G1R3 geopolymer mixture.

visible only for 15% and 30%. The replacement of Tunisian clays by 15% and 30% MK allows for compressive strengths around 30 MPa, which are typical of old PC reinforced concrete structures and constitute an important compressive strength requirement for repair mortars.

12.3.4 Modulus of elasticity

The modulus of elasticity of the mixtures with a binder/sand ratios of 1:3 and 1:4 are 1 and 0.82 GPa, respectively. Although these values are very different from typical PC-based binders, they bear some resemblance with the ones reported by other authors for the same compressive strength (Duxson et al., 2005, 2006). The modulus of elasticity at 28 days curing is below the typical modulus of elasticity of

Ordinary Portland Cement (OPC) reinforced concrete structures. For a concrete substrate with 25 MPa compressive strength at 28 days and using the EN 1992-1-1 (2004) European code expression $E_{cm} = 22[(f_{cm})/10]^{0.3}$ to predict modulus elasticity, one obtains a value of 29 GPa. Therefore, in order to meet structural compatibility requirements (Table 12.6) new mixtures with a modulus of elasticity around 29 GPa are needed. Fig. 12.10 shows the modulus of elasticity of the second set of mixtures. The results show that the modulus of elasticity increases slightly with the replacement of Tunisian clay by FA. This behavior is not influenced when the FA percentage increase from 10% to 15%. A higher modulus of elasticity is associated with the replacement of Tunisian clay by MK. This behavior is partially related to the increase in the compressive strength.

12.3.5 Adhesion strength and flexural strength of rehabilitated beams

The results of the adhesion strength in the Pull-off test show that the geopolymeric mortar which contain 15% FA replacement led to an increase of the adhesion strength by $\sim 40\%$. The replacement of 30% calcined clay by MK leads to an adhesion strength increase of almost 80%. Furthermore, experimental tests have shown that it takes a 40% replacement of the Tunisian clay by MK to reach the 0.8 MPa threshold of adhesion strength for patch repair of reinforced concrete (Concrete Society, 1991). The flexural strength of the PC concrete beams rehabilitated with geopolymeric mortars is shown in Fig. 12.11. The concrete beams repaired with the

Table 12.6 Structural compatibility—general requisites for repair mortars

Properties	Relation between the repair mortar (Rp) and the concrete substrate (Cs)
Strength in compression, tension, and flexure	$R_p \geq C_s$
Modulus in compression, tension, and flexure	$R_p \sim C_s$
Poisson's ratio	Dependent on modulus and type of repair
Coefficient of thermal expansion	$R_p \sim C_s$
Adhesion in tension and in shear	$R_p \geq C_s$
Curing and long-term shrinkage	$R_p \geq C_s$
Strain capacity	$R_p \geq C_s$
Creep	Dependent on whether creep causes desirable or undesirable effects
Fatigue performance	$R_p \geq C_s$

Source: From Morgan, D., 1996. Compatibility of concrete repair materials and systems. Constr. Build. Mater. 10 57–67.

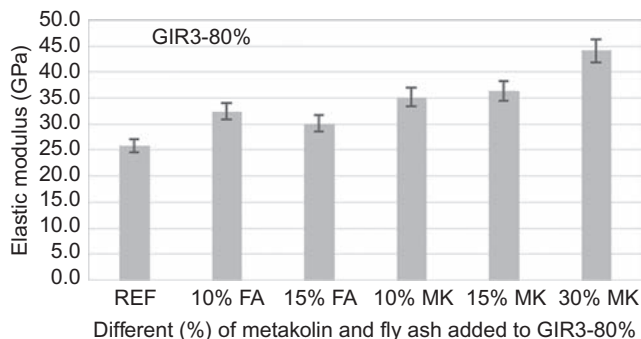


Figure 12.10 Modulus of elasticity of the modified GIR3 geopolymer mixtures.

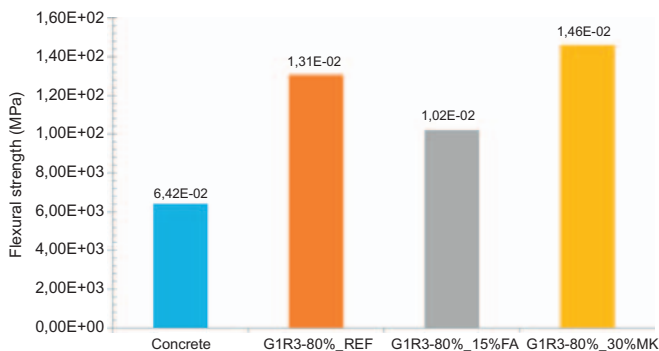


Figure 12.11 Flexural strength of the Portland cement (PC) concrete rehabilitated beams.

calcined clay and 30% MK mortars show a flexural strength around 230% higher than plain concrete beams.

12.3.6 Hydration products of mortars

12.3.6.1 Thermal analysis (TGA/DSC)

Simultaneous thermo-gravimetric analysis (TGA) and DSC analyses were performed on three geopolymeric mortars (Fig. 12.12). In a temperature interval between 0 and 120°C, the three TGA curves showed three similar weight losses. In this case, the phenomenon presented was the evaporation of the molecular water. These results were confirmed by the DSC curves, as the three endothermic peaks indicated the release of H₂O in the mixture.

12.3.6.2 X-ray diffractograms

The XRD of the hardened geopolymer mortar are presented in Fig. 12.13. The XRDs show the presence of characteristic peaks of quartz and calcite CaCO₃, which

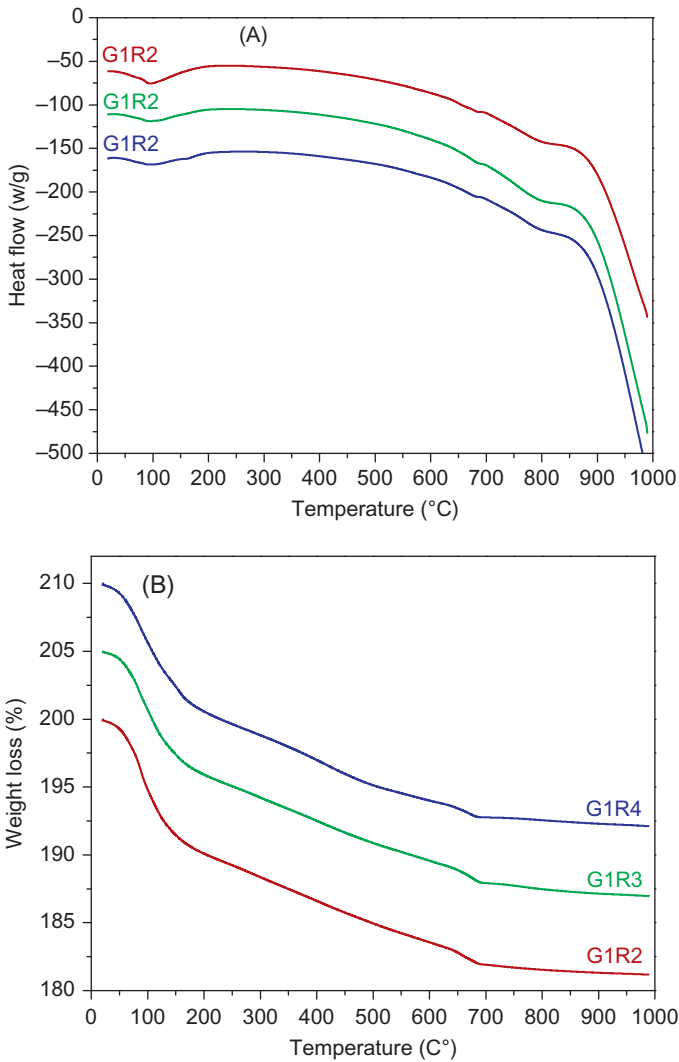


Figure 12.12 Thermo-gravimetric analysis/differential scanning calorimetry (TGA/DSC) data of geopolymer mortars: (A) DSC; (B) TGA.

means that these minerals are not dissolved during geopolymerization. In addition, a weak zeolite (analcime) appeared at 31°C in the spectrogram of the three geopolymeric mortars. This occurs in the same position of two theta with a small modification of intensity. These phases usually appear in geopolymer systems with a high water content. Too little or too much water content can hinder zeolite formation (Wang et al., 2005). Fig. 12.14 shows the XRD of geopolymers of G1R3 modified

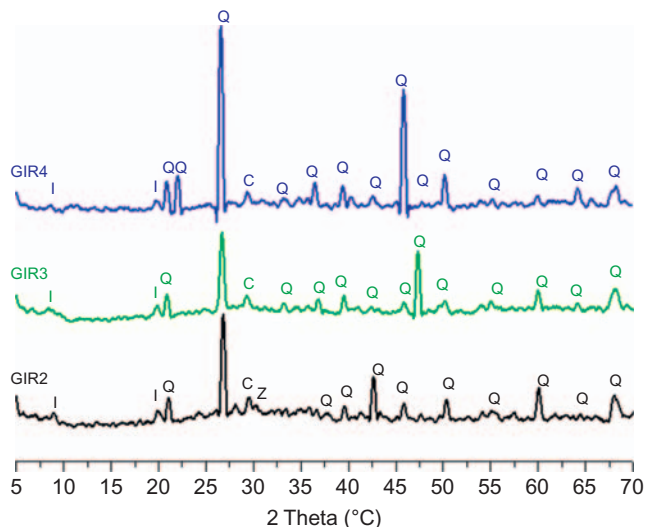


Figure 12.13 X-ray diffractograms of geopolymers I-Illite, Q-Quartz, C-Calcite, Z-Zeolite (G1R2, G1R3, G1R4).

mixtures. The mullite in the FA samples appears to have reacted entirely under the alkaline conditions.

12.3.6.3 Fourier transform infrared spectra

The Fourier transform infrared (FTIR) spectra of the hardened geopolymer mortar are presented in Fig. 12.15. Strong vibrations, typical of aluminosilicates can be observed. The peak centered around 975 cm^{-1} , shifts to a lower value and this shift is characteristic of a geopolymerization reaction corresponding to the Si–O–Al and Si–O–Si vibration bands. The band at $\sim 870\text{ cm}^{-1}$ is assigned to Si–OH bending vibration. Al–O–Si vibrations correspond to the absorption bands $600\text{--}800\text{ cm}^{-1}$. The absorption peak of 782 cm^{-1} was an indication of the presence of quartz (Lin et al., 2003). The absorption band around 1413 and 1433 cm^{-1} is attributed to stretching vibrations of CO_3^{2-} ions, confirming the existence of carbonate species (Fernandez-Jimenez and Palomo, 2005). The decreasing in the OH bond may be also be due to the zeolites structure (crystalline phase) needing more water molecules than the minerals polymers (amorphous phase). Fig. 12.16 shows the FTIR spectra of geopolymers belonging to the G1R3 modified mixtures. All FTIR spectra developed in a single band located at 1000 and 1004 cm^{-1} , corresponding to a region assigned for Si–O–Si (Lazarer, 1972; Nakamoto, 1997; Phair and van Deventer, 2002). The presence of the bands located at 776 and at 692 cm^{-1} are due to the quartz (Criado et al., 2007). The small bands appearing at ~ 1420 , 1422 , and at 1489 cm^{-1} are related to the asymmetric stretching of the O–C–O bonds of CO_3^{2-} due to atmospheric carbonation for all geopolymers mortars.

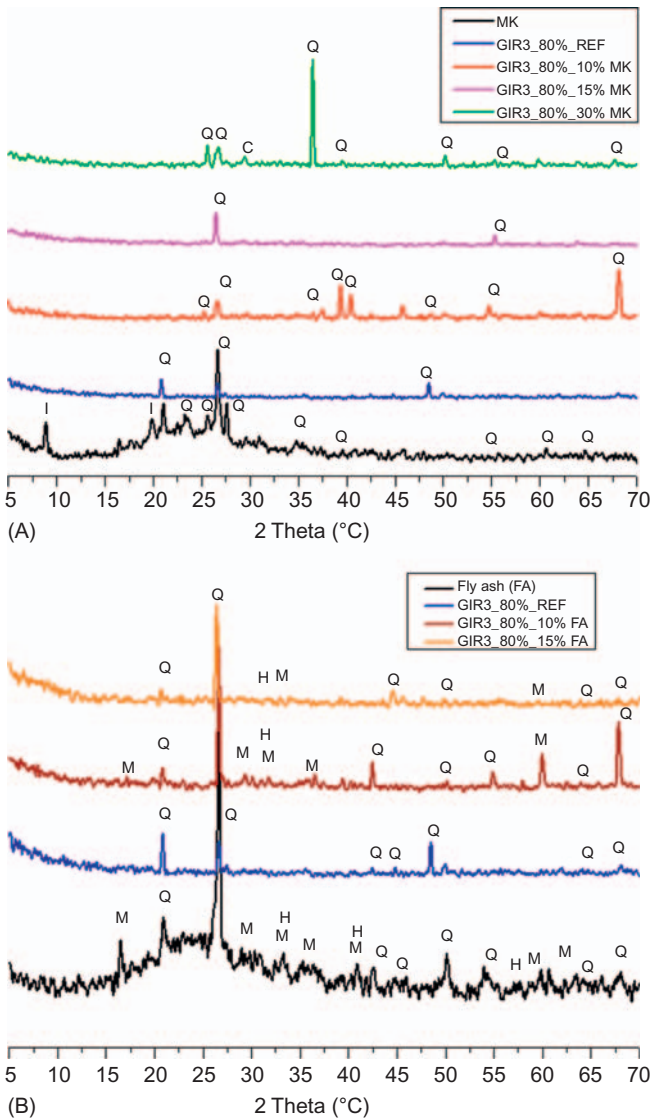


Figure 12.14 X-ray diffractograms of GIR3 modified geopolymeric mixtures: (Above) Metakaolin (MK) based; (Below) Fly ash (FA) based.

12.3.6.4 Scanning Electron Microscopy

SEM micrographs of the first-phase geopolymeric mortars are shown in [Fig. 12.17](#). A homogeneous microstructure appears in all samples. Some visible cracks can be associated to the high autogenous shrinkage. [Fig. 12.18](#) shows the microstructure of GIR3-modified mixtures. Several microcracks can be noticed, with the exception

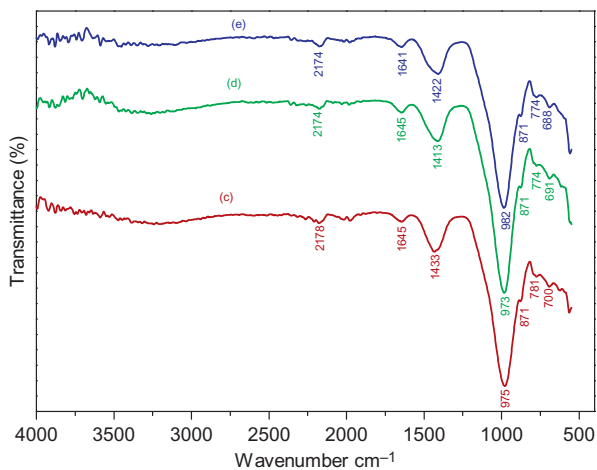


Figure 12.15 Fourier transform infrared (FTIR) spectra of the geopolymeric mortars (A) GIR2, (B) GIR3 and (C) GIR4.

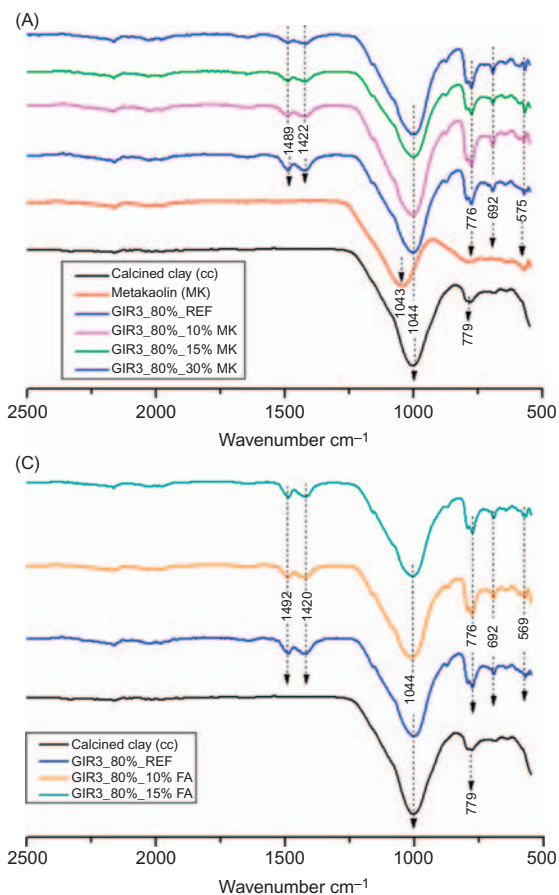


Figure 12.16 Fourier transform infrared (FTIR) spectra of GIR3 modified geopolymeric mixtures: (Above) metakaolin (MK) based; (Below) Fly ash (FA) based.

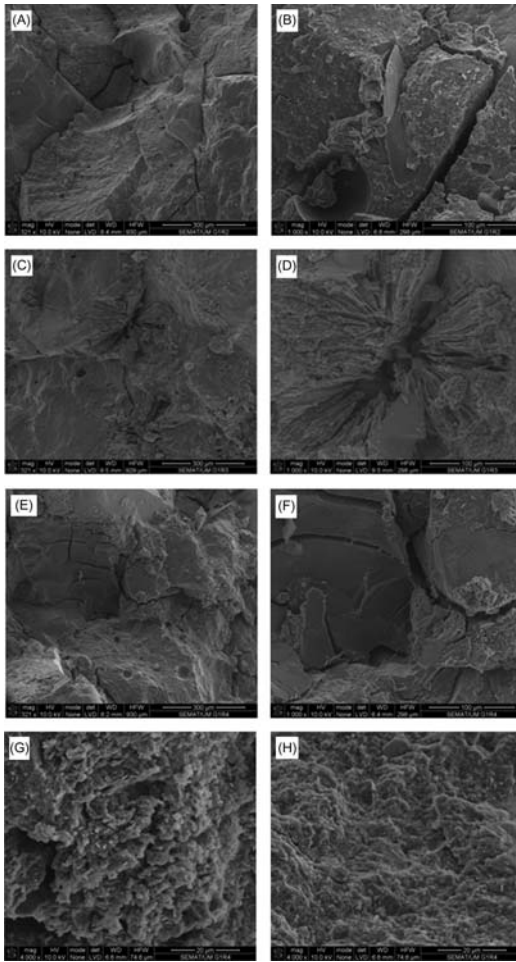


Figure 12.17 SEM micrographs of geopolymeric mortars: G1R2 (A),(B); G1R3 (C),(D); G1R4(E),(F),(G),(H).

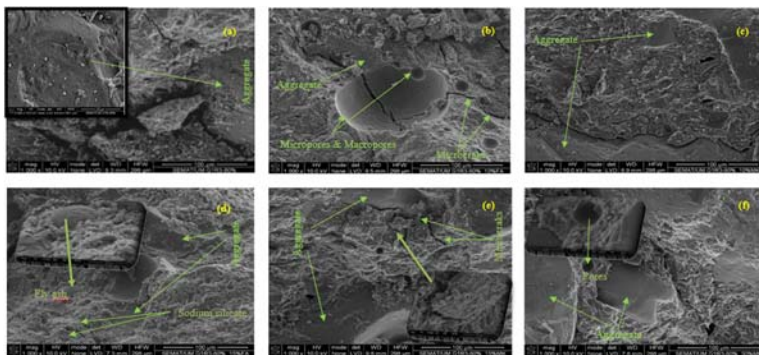


Figure 12.18 SEM images of geopolymeric mortar G1R3-80% with different (%) Metakaolin (MK) and fly ash (FA): (A) (G1R3-80%_ REF); (B) G1R3-80%–10%FA; (C) G1R3-80%–10%MK; (D) G1R3-80%–15% FA; (E) G1R3-80%–15% MK; (F) G1R3-80%–30% MK.

of the mixture with 30% MK content (f), which has the lowest shrinkage performance. The SEM analysis also revealed the existence of unreacted elements as aggregates, and some micropores and macropores with different shapes (b) inside the geopolymeric sample. The alkaline solution contacts with the smaller particles housed inside the larger spheres and forms a dense geopolymer matrix: (Photo (d)). Thus, the microstructures in all geopolymer mortar samples confirmed that the crystalline phases are generally nonreactive, and that these are present in the form of inactive fillers as the particle of sand (aggregate). Additionally, the dissolution of FA under the conditions prevailing during geopolymerization is much slower than the dissolution of MK. From these results, it appears that increasing the amount of MK increases the amount of reactive phase.

12.4 Conclusions and future trends

This chapter presents some experimental results of an investigation concerning the development of geopolymeric repair mortars based on low reactive Tunisian clay. The following conclusions can be made upon it. The mineralogical analysis shows that the Tunisian clay is composed of kaolinite associated to quartz and illite, with minor amounts of gypsum and hematite. The use of a geopolymeric mortar with a binder/sand ratio of 1:4 meets minimum workability conditions for patch repair using the hand placement technique. The geopolymeric mortar shows a high unrestrained shrinkage behavior. However, the reduction of the alkaline activator/binder mass ratio to 80% of the former mixtures led to a relevant reduction in the shrinkage performance. The partial replacement of Tunisian clay by FA also leads to a lower shrinkage performance when compared to that of the reference mixture. Partial replacement by MK outperforms FA-based mixtures. The compressive strength at 28 days curing is below typical compressive strength of reinforced concrete structures, although the replacement of the Tunisian clay by 15% and 30% MK allows for compressive strengths of around 30 MPa, typical of old PC reinforced concrete structures and constitute an important compressive strength requirement for repair mortars. The modulus of elasticity increases slightly with the replacement of Tunisian clay by FA and in a higher extension when MK is used. The concrete beams repaired with the calcined clay and 30% MK mortars show a flexural strength around 230% higher than the plain concrete beams. The hydration products show typical geopolymeric phases. Further investigations regarding compatibility issues are still needed.

References

- Bouaziz, R., Rollet, A.P., 1972. Tome 2 Paris .L'analyse thermique L'examen des processus chimiques. Gautier-Villars.
- Brinker, C.J., Scherrer, G.W., 1990. Sol Science. The physics and chemistry of sol-gel processing. Academic Press, San Diego.

- BS EN 1542, 1999. Products and Systems for the Protection and Repair of Concrete Structures. Test Methods. Measurement of Bond Strength by Pull-off, first ed. IPQ, Portugal.
- Criado, M., Fernandez-Jimenez, A., Palomo, A., 2007. Alkali activation of fly ash: effect of the $\text{SiO}_2/\text{Na}_2\text{O}$ ratio: Part I: FTIR study. *Microporous Mesoporous Mater.* 106 180–191.
- Concrete Society, 1991. Patch Repair of Reinforced Concrete. Model Specification and Method of Measurement. Concrete Society Technical Report no. 38.
- Cusson, D., 2009. Durability of concrete repaired concrete structures. In: Delatte, N. (Ed.), *Failure, Distress and Repair of Concrete Structure*. Woodhead Publishing Limited, Abington Hall, Cambridge, pp. 297–321.
- Duxson, P., Mallicoat, S., Grant, L., Kriven, W., Deventer, J., 2006. The effect of alkali and Si/Al ratio on the development of the properties of metakaolin-based geopolymers. *Colloids Surf.* 292, 8–20.
- Duxson, P., Provis, J., Grant, L., Mallicoat, S., Kriven, W., van Deventer, J.S.J., 2005. Understanding the relationship between geopolymer composition, microstructure and mechanical properties. *Colloids Surf.* 269, 347–358.
- Emmons, P., Vaysburd, A., 1994. Factors affecting the durability of concrete repair: the contractor's viewpoint. *Constr. Build. Mater.* 8, 5–16.
- Emmons, P., Vaysburd, A., 1996. Total system concept—necessary for improving the performance of repaired structures. *Constr. Build. Mater.* 10, 69–75.
- EN 1992-1-1, 2004. Eurocode 2: Design of Concrete Structures – Part 1-1: General Rules and Rules for Buildings. 225 p.
- Essaidi, N., Samet, B., Baklouti, S., Rossignol, S., 2014. Feasibility of producing geopolymers from two different Tunisian clays before and after calcination at various temperatures. *Appl. Clay Sci.* 88–89, 221–227.
- Kakali, G., Perraki, T., Tsvilis, S., Badogiannis, E., 2001. Thermal treatment of kaolin: the effect of mineralogy on the pozzolanic activity. *Appl. Clay Sci.* 20 (1–2), 73–80.
- Khan, M.I., Almusallam, T.H., Alsayed, S.H., Al-Salloum, Y.A., Almosa, A.A., 2012. Bond characteristics of substrate concrete and repair materials. *Concrete Repair, Rehabilitation and Retrofitting III—Proceedings of the 3rd International Conference on Concrete Repair, Rehabilitation and Retrofitting, ICCRRR 2012*, pp. 1041–1045.
- Lazarer, A.N., 1972. *Vibrational Spectra and Structure of silicates*. Consultants Bureau, New York/London.
- Lee, W.K.W., van Deventer, J.S.J., 2002. The effects of inorganic salt contamination on the strength and durability of geopolymers. *Colloids Surf.* 211, 115–126, 2002.
- Li, C., Sun, H., Li, L., 2010. A review: the comparison between alkali-activated slag (Si + Ca) and metakaolin (Si + Al) cements. *Cem. Concr. Res.* 40, 1341–1349.
- Lin, X., et al., 2003. In-situ synthesis of NaY zeolite with coal-based kaolin. *J. Nat. Gas Chem.* 12, 63–70.
- Mackenzie, R.C., 1957. *The Differential Thermal Investigation of Clays*. Mineralogical Society, London.
- Morgan, D., 1996. Compatibility of concrete repair materials and systems. *Constr. Build. Mater.* 10, 57–67.
- Nakamoto, K., 1997. *Infrared and Raman Spectra of Inorganic and Coordination Compounds*. Wiley, Chichester.
- Pacheco-Torgal, F., Gomes, J., Jalali, S., 2008a. Adhesion characterization of tungsten mine waste geopolymeric binder. Influence of OPC concrete substrate surface treatment. *Constr. Build. Mater.* 22, 154–161.

- Pacheco-Torgal, F., Gomes, J.P., Jalali, S., 2008b. Investigations on mix design of tungsten mine waste geopolymeric binders. *Constr. Build. Mater.* 22, 1939–1949.
- Pacheco-Torgal, F., Castro-Gomes, J., Jalali, S., 2008c. Properties of tungsten mine waste geopolymeric binder. *Constr. Build. Mater.* 22, 1201–1211.
- Pacheco-Torgal, F., Domingos, M., Ding, Y., Jalali, S., 2011. Composition, strength and workability of alkali-activated metakaolin based mortars. *Constr. Build. Mater.* 25, 3732–3745.
- Pacheco-Torgal, F., Abdollahnejad, Z., Miraldo, S., Baklouti, S., Ding, Y., 2012a. An overview on the potential of geopolymers for concrete infrastructure rehabilitation. *Constr. Build. Mater.* 36, 1053–1058.
- Pacheco-Torgal, F., Fucic, A., Jalali, S., 2012b. *Toxicity of Building Materials*. Woodhead Publishing Limited, Abington Hall, Cambridge, 512 p.
- Pacheco-Torgal, F., Labrincha, J.A., Jalali, S., John, V.M., 2013. *Eco-Efficient Concrete*. Woodhead Publishing Limited, Abington Hall, Cambridge, 592 p.
- Pacheco-Torgal, F., Abdollahnejad, Z., Miraldo, S., Kheradmand, M., 2016. Alkali-activated cement-based binders (AACB) as durable and cost competitive low CO₂ binders: some shortcomings that need to be addressed. In: Nazari, A., Sanjayan, J. (Eds.), *Handbook of Low Carbon Concrete*, first ed., Elsevier Science and Tech, Waltham, pp.195–216.
- Phair, J.W., van Deventer, J.S.J., 2002. Effect of the silicate activator pH on the microstructural characteristics of waste-based geopolymers. *Int. J. Min. Process.* 66 (1–4), 121–143.
- Provis, J.L., 2014. Geopolymers and other alkali activated materials: why, how, and what? *Mater. Struct.* 47, 11–25.
- Teixeira-Pinto, A., 2004. *Metakaolin Alkali-Activated Based Binders*. PhD Thesis, University of Minho, Portugal.
- Van Deventer, J., Provis, J., Duxson, P., Brice, D., 2010. Chemical research and climate change as drivers in the commercial adoption of alkali activated materials. *Waste Biomass Valor.* 1, 145–155.
- Van Deventer, J., Provis, J., Duxson, P., 2012. Technical and commercial progress in the adoption of geopolymer cement. *Miner. Eng.* 29, 89–104.
- Yip, C.K., Lukey, G.C., Deventer, S.J.S., 2005. The coexistence of geopolymeric gel and calcium silicate hydrate gel at the early stage of alkaline activation. *Cem. Concr. Res.* 35 (9), 1688–1697.
- Wang, H., Li, H., Yan, F., 2005. Synthesis and mechanical properties of metakaolin-based geopolymer. *Colloids Surf. A: Phys. Chem. Eng. Aspects.* 268 (1–3), 1–6.

Further reading

- Davalos, J.F., 2012. *Advanced Materials for Civil Infrastructure Rehabilitation and Protection*. Seminar at The City College of New York, New York.
- Fernandez-Jimenez, A., Palomo, A., 2005. Mid-infrared spectroscopic studies of alkali activated fly ash structure. *Microporous Mesoporous.* 86, 207–214.
- Holloway, L.C., 2011. Key issues in the use of fibre reinforced polymer (FRP) composites in the rehabilitation and retrofitting of concrete structure. In: Karbhari, V.M., Lee, L.S. (Eds.), *Service Life Estimation and Extension of Civil Engineering Structures*. Woodhead Publishing Limited, Abington Hall, Cambridge.

This page intentionally left blank

Assessment of corrosion protection methods for reinforced concrete

13

Ana María Aguirre-Guerrero and Ruby Mejía de Gutiérrez
Universidad del Valle, Cali, Colombia

13.1 Introduction

In recent decades, reinforced concrete has been one of the most used materials in the construction sector, especially in the construction of bridges, buildings, skyscrapers, and tunnels (Shi et al., 2012). Reinforced concrete is a composite material that is characterized by the combination of the high compressive strength of Portland cement concrete, and the ductility and high tensile strength properties of steel, which make it an ideal construction material (Bertolini et al., 2004). The variety of environments that reinforced concrete structures are exposed to make it necessary to consider the durability of the concrete as an additional property to the mechanical strength because the useful life of the structure depends on its durability (Neville, 2001).

The main problem with reinforced concrete's durability is the corrosion of the reinforcing steel, which diminishes the mechanical and structural properties (Bertolini et al., 2004). The corrosion of the reinforcing steel is mainly caused by exposure to aggressive environments, mostly the presence of chloride ions and/or carbonation (Ahmad, 2003). Noncarbonated concrete is an alkaline material with a pH between 12.6 and 13.6 (Alonso and Andrade, 1987). Under these pH conditions, the steel spontaneously forms a protective passive layer; the layer, however, can be destroyed by aggressive agents (chloride ions and/or carbon dioxide), which results in depassivation (Bertolini et al., 2004; Fajardo et al., 2009). Chloride attack is one of the most aggressive causes that leads to corrosion of the steel reinforcement. In this case, the chloride ions are spread through the concrete until they reach the steel, where they accumulate and reach a critical concentration. This accumulation destroys the passive layer of steel and begins the corrosive process (Angst et al., 2009). Carbonation is a process in which CO₂ from the environment enters concrete. CO₂ decreases the concrete alkalinity by reducing the pH to approximately 9. Therefore, the passive layer is destabilized, which causes corrosion in the reinforcing steel (Baccay et al., 2006; Han et al., 2013).

There are several ways to prevent this deterioration, beginning with the design stage and considering structural calculations, material selection, concrete mix design, proper compaction and correct curing (El-Reedy, 2008). Despite these considerations, complementary methods are required, such as the use of pozzolanic additions,

the application of coatings, and electrochemical techniques among others (Bertolini et al., 2004; El-Reedy, 2008). A good protection extends the time before the chloride or carbonation front reaches the reinforcing steel (El-Reedy, 2008).

The incorporation of mineral additions (pozzolanic and steel-based) to concrete modifies the porosity and reduces the permeability, which can extend the useful life of structures (Cyr, 2013). The most used additions are silica fume (SF), metakaolin (MK), blast-furnace steel slag, and fly ash (FA).

Conversely, coatings have been widely used as an economically profitable option; they can be applied on the steel or on the surface of the concrete, depending on the case. There are three types of coatings: metallic, organic, and inorganic. Organic coatings are the most used and are mainly used on the surface of concrete because of their easy application, flexibility, and adherent properties (Brenna et al., 2013; Criado et al., 2015; Criado et al., 2014; Keßler et al., 2015; Pour-Ali et al., 2015; Saravanan et al., 2007; Selvaraj et al., 2009). The different types of coatings that fall within this category are paints, acrylic dispersions, polyurethanes, epoxy resins, waterproof coatings and penetrating sealers, among others (Al-Zahrani et al., 2002; Almusallam et al., 2003; Batis and Pantazopoulou, 2000; Christodoulou et al., 2013; Dang et al., 2014; de Vries and Polder, 1997; Medeiros and Helene, 2009; Pacheco-Torgal and Jalali, 2009; Sadati et al., 2015; Swamy and Tanikawa, 1993; Tittarelli and Moriconi, 2010; Vaidya and Allouche, 2010; Zhu et al., 2013). Recent studies have proposed the application of geopolymers as a viable coating alternative for concrete, because they have a low permeability and excellent adhesion and anticorrosive properties (Zhang et al., 2012, 2010a,b).

Electrochemical techniques, such as cathodic protection, cathodic prevention, electrochemical chloride extraction (ECE), electrochemical realkalisation (RE), and electrical injection of corrosion inhibitors or nanoparticles are used to prevent, avoid, or rehabilitate reinforced concrete structures (Bertolini et al., 2004; Cardenas et al., 2010; Karthick et al., 2016; Kupwade-Patil et al., 2012; Pan et al., 2008). Among these techniques, cathodic protection is the oldest. It has been widely used in steel structures submerged in water, and its application in concrete began around 1955 for submerged and buried structures. Since the mid-1970s, this technique has been used in structures such as bridges, buildings, tunnels, etc. Therefore, cathodic protection is the standardized electrochemical technique in different countries. ECE and realkalisation are recent techniques (from the last 20 years) still in the research and development stage (Martínez et al., 2009). The three techniques are similar. They are based on using the metal to be protected as the cathode and inducing several electrochemical phenomena on its surface (Bertolini et al., 1996, 2004; Martínez et al., 2009). These methods increase the durability of deteriorated concrete structures; ECE and realkalisation are temporary protection techniques, while cathodic protection is permanent.

This chapter includes a review of published literature and laboratory investigations related to the chloride and carbonation-induced corrosion of reinforced concrete, some of which have been reported by the authors (Aguirre and Gutiérrez, 2013; Aguirre-Guerrero et al., 2016, 2017). The laboratory investigations include

the addition of pozzolans, the application of electrochemical methods (ECE and RE), and the use of a type of geopolymer coating for concrete surface. To produce the concrete specimens, the raw materials available in the Colombian market were selected, including general use ordinary Portland cement (OPC), reinforcing Steel, and natural aggregates (sand and gravel). A water/cement (w/c) ratio of 0.55 and 10% replacement of cement with commercial MK Metamax and commercial SF from Sika each. The concrete thickness was 35.2 mm.

13.2 Chloride-induced corrosion

The presence of chlorides inside concrete comes from two main sources. First, chloride ions are in the concrete mixture (contaminated aggregates, sea water, or contaminated water, additives with high chloride content). Second, chloride ions come from the environment (coastal or deicing environments).

The penetration of the chloride ion (Cl^-) produces a profile in the concrete, and the profile is characterized by a high chloride content near the external surface and a reduction in the content towards the interior. The diffusion process is governed by Fick's 2nd Law (Bertolini et al., 2004). When concrete is subjected to wetting and drying cycles, chloride ions enter via capillary absorption and are transported through the concrete via convection in the liquid phase. The chloride ions can then migrate via diffusion into the saturated zones. This penetration mode allows for the rapid entry of chloride ions, which explains why concrete subjected to wetting and drying cycles often degrades more quickly than fully submerged concrete (Cyr, 2013). Another chloride ingress mechanism into concrete is the water flow due to pressure gradient.

Once the chloride ions penetrate the concrete, they are distributed as bound chloride ions and free chloride ions. The former correspond to chloride ions that react with the tricalcium aluminate (C_3A) which exists in cement, to form calcium chloroaluminates. This compound is known as "Friedel's salt," and it is not considered expansive (Torres et al., 2007). For this reason, it is advisable to use cements with a high C_3A content for concrete that is exposed to chloride ions. In addition, other cement hydrates (e.g. C-S-H gel) can bind chloride ions by physical action (Florea and Brouwers, 2012; Yuan et al., 2009). On the other hand, free chloride ions reach the steel, which causes a localized dissolution of the passive layer and generates localized attacks that can drastically reduce the structural properties of concrete (Angst et al., 2009; El-Reedy, 2008).

There are many factors that affect the mobility of chloride ions within concrete. A less permeable concrete will have better resistance against attack, and for this reason, concrete design parameters are important. The most influential factor is the w/c ratio. A smaller ratio means a lower porosity and higher resistance to attack. Other mixture factors to consider are the type of cement (with a high C_3A content) and the proportion of cement by mass of concrete (El-Reedy, 2008; Güneysi et al., 2007; Song et al., 2008). In addition, the use of pozzolans into concrete contributes

to refinement of the pore size distribution and decrease the open porosity; the main consequence is a decrease in the diffusivity of chloride ions (Andrade and Buják, 2013; Cyr, 2013).

13.2.1 *Supplementary cementitious materials*

The durability of cementitious materials depends on transport properties because of the difficulty that aggressive agents have in penetrating the porous concrete network. The mineral additions used in concrete reduce the porosity and refine the pores, especially for concretes with low w/c ratios and suitable curing processes (Cyr, 2013; Hossain and Lachemi, 2004; Özbay et al., 2016; Ramezaniapour and Malhotra, 1995; Song and Saraswathy, 2006). Mineral additions perform an important role in concrete durability and its mechanical properties and reduce cement consumption, which helps mitigate the environmental impact of Portland cement production (Damineli et al., 2013).

There are different types of minerals used as supplementary cement materials, including pozzolanic additions and ground-granulated blast-furnace slag (GGBFS). The slag content with respect to the cement mass plays a very important role. If the slag content is greater than or equal to 50%, an adequate curing process is required because adverse effects on the permeability may occur, which would lead to a reduction in the corrosion resistance (Shi et al., 2012; Zhang and Ba, 2012). Different authors agree that GGBFS offers a significant resistance to chloride ion access and a high resistance to corrosion (Aghaeipour and Madhkhan, 2017; Chen et al., 2012; Polder, 2012; Topçu and Boğa, 2010; Wang et al., 2014; Yeau and Kim, 2005). With high slag replacement levels (45%–65%) and a w/c ratio of 0.40, the penetration resistance to the chloride ion has been confirmed for blocks exposed to tidal zones for 25 years (Thomas et al., 2008). This effect on chloride ion penetration is attributed to the capacity of GGBFS to bind chloride ions (Friedel's salt formation), thus reducing their diffusion coefficient (Chen et al., 2012; Luo et al., 2003; Yiğiter et al., 2007). Moreover, it has been found that the addition of GGBFS decreases the pH of the pore solution, but it does not have any adverse effects on steel corrosion (Cheng et al., 2005; Song and Saraswathy, 2006).

FA, an aluminosilicate-type pozzolan, is a by-product of coal combustion that is generated by boilers, plants, or power stations. Good quality FA generally has a high amorphous material content and a spherical shape with particle sizes ranging from 10 to 100 μm (Shi et al., 2012). The addition of FA as cement replacement is beneficial for the rheology and mechanical properties of concrete. In addition, FA decreases the permeability of concrete, which reduces the diffusion coefficient of the chloride ions and enhances the resistance of the concrete to chloride ion attack (Ampadu et al., 1999; Boğa and Topçu, 2012; Dhir and Jones, 1999; Choi et al., 2006; Chousidis et al., 2016; Montemor et al., 2000, 2002; Simčič et al., 2015). Moreover, as in the case of slag, the effect is attributed to the capacity of FA to bind chloride ions because of its high alumina content (Dhir and Jones, 1999). Chloride permeability can be reduced with 15% FA (Aponte et al., 2012; Boğa and Topçu, 2012; Nath and Sarker, 2011). Concretes with high FA content may have

higher absorption and permeable voids, but they have a high resistance to chloride ion penetration because of the binding capacity (Güneyisi et al., 2013a). However, the use of FA as replacement of cement may or may not improve the chloride binding capacity of concrete, depending on the specific type of FA used and the replacement dosage as reported by Shi et al. (2011b). It should be noted that, even using low-quality FA with an unburned content of 19% results in a high corrosion resistance in reinforced steel, in the presence of chloride ions (Burgos et al., 2012).

SF is a siliceous-type pozzolan with an amorphous silica content of at least 85%. It is available as a powder, densified powder, or liquid mixture. SF is a highly effective pozzolan because of its high reactivity, small particle size (0.1–0.5 μm), and large specific surface area (Shi et al., 2012). Its small particles plug the existing pores to produce a less permeable concrete (Song et al., 2010). In turn, it accelerates the hydration process of cement because the pozzolanic action is active in the first few hours of hydration (Khan and Siddique, 2011). SF percentages above 10% affect the rheology of the mixture and increase the costs because of the requirement of special additives. Between 6% and 8% of the cement mass is the suggested usage (Kepler et al., 2000). The partial replacement of cement content in concrete by SF reduces the diffusion coefficient of chloride ions (Shekarchi et al., 2009; Farahani et al., 2015). Nevertheless, unlike other aluminum pozzolans, SF reduces the ability to bind chloride ions (Thomas et al., 2012). Increases of up to 88% in the linear polarization resistance have been reported in reinforced concrete, and this further increases for specimens with 5% SF relative to concrete without additions (Chao and Lin, 2013). Dotto et al. (2004) studied the influence of SF on corrosion behavior. Different w/c ratios and percentages of SF addition were evaluated, and it was determined that the corrosion time for concrete with the addition was much higher. Kayali and Zhu (2005) observed that concrete with a 10% SF addition had excellent corrosion resistance.

MK is also an aluminosilicate-type pozzolan and a material obtained from the calcination of kaolinite clay at temperatures between 500°C and 800°C (Badogiannis et al., 2005). Its particle size is finer than cement but not as fine as SF (Shi et al., 2012; Siddique and Iqbal Khan, 2011). Its main characteristics are: a high reactivity with the calcium hydroxide in cement, and its ability to accelerate cement hydration (Badogiannis et al., 2015). Because it is a highly reactive pozzolan, its addition contributes to increased compressive and flexural strength, reduced permeability, and increased resistance to chemical attack (Badogiannis et al., 2015; Dinakar et al., 2013; Güneyisi et al., 2008; Keleştemur and Demirel, 2015; Ramezaniapour and Bahrami Jovein, 2012). The corrosion resistance of the reinforcing steel increases with MK additions in the range of 10%–15% (Batis et al., 2005; Parande et al., 2008). The presence of MK in concrete greatly reduces the diffusion of chloride ions in the cementitious matrix by restricting access via Friedel's salt formation, thus extending the useful life of the structures (Abo-El-Enin et al., 2010; Courard et al., 2003; Poon et al., 2006; Siddique and Klaus, 2009). Güneyisi et al. (2013b) reported that the corrosion rate was reduced by 50% for MK-concrete exposed to chloride ions. Keleştemur and Demirel (2015) concluded that a 15% MK replacement of the cement content increased the

compressive and tensile strength, and improved the corrosion resistance of the reinforcing steel.

As mentioned above, the formation of “Friedel’s salt” contributes to better performance in concrete exposed to chloride ions. Fig. 13.1 shows the X-ray diffraction results for the formation of Friedel’s salt ($C_4Al_2O_4Cl_2 \cdot 10H_2O$) in cement pastes with 10% MK and 10% SF (based on cement weight) and the reference, OPC without any additions, exposed to an aqueous solution of 3.5% NaCl for 365 days. This compound shows the highest peak at $d = 7.9 \text{ \AA}$ ($2\theta = 11.2$). The highest peak intensity was observed for the sample with the MK addition. This result indicated that the addition of MK promotes the formation of Friedel’s salt.

Fig. 13.2 shows the curves for the current intensity versus time, measured using the impressed-voltage (IV) technique, to determine the corrosion performance of reinforcing steel in blended concrete with MK and SF at 10% replacement of cement weight. The increase in the current is related to the progression of corrosion in the concrete. The corrosion products contribute to concrete deterioration by increasing the volume of the reinforcing steel, generating tensile stresses in the concrete matrix (El-Reedy, 2008), and producing cracking—which is related to a significant increase in the current (Güneyisi et al., 2005). As shown in Fig. 13.2, the sudden increase in current coincides with cracking and/or visualization of the corrosion products. The maximum current for the OPC concretes was 25.26 mA, 6.9 mA for MK, and 11.12 mA for SF.

The OPC specimen exhibited a much higher current, which indicated that it is more susceptible to chloride ion penetration. The appearance of the first crack for

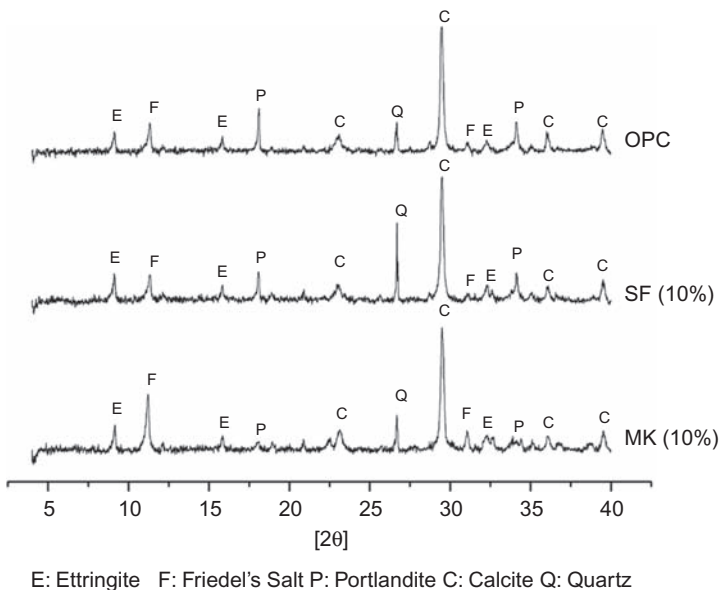


Figure 13.1 X-ray diffractogram of ordinary Portland cement (OPC), metakaolin (MK) (10%), and silica fume (SF) (10%) exposed to NaCl 3.5% for 365 days.

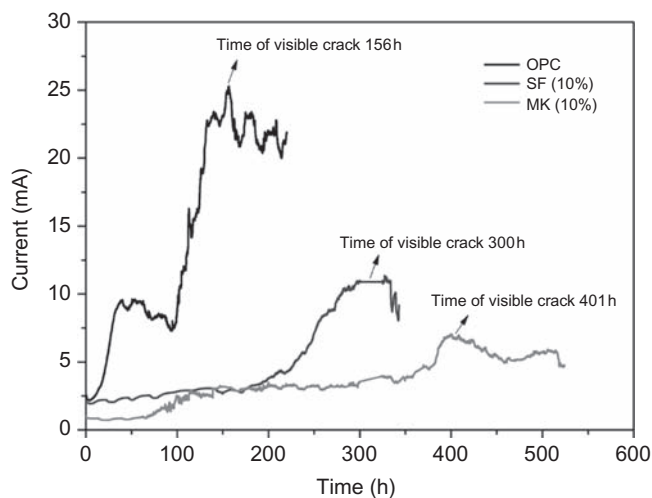


Figure 13.2 Current intensity versus time for ordinary Portland cement (OPC), metakaolin (MK) (10%), and silica fume (SF) (10%) concretes.

OPC was at approximately 156 hours. For the MK concrete, it was at 401 hours and at 300 hours for the SF concrete. The appearance time for the first crack significantly increased for the MK-concrete, 61% longer with respect to OPC. The SF concrete time increased by 48% with respect to OPC.

In other investigations, Güneysi et al. (2013b) observed that concrete with 15% MK had a cracking time of 132 hours, which was much higher than the 5 hours reported for the concrete without additions. Parande et al. (2008) performed a study on MK incorporation as a cement replacement at 5%, 10%, 15%, and 20%. The study showed that the crack initiation time was the longest for specimens with 15% MK, and the time was much longer with respect to the concrete without any additions. Khedr and Idriss (1995) studied the effectiveness of adding SF as a cement replacement using IV.

Fig. 13.3 shows the evolution of the open circuit potential (OCP) of blended concretes with MK and SF and OPC without additions. The IV technique was performed in combination with wetting/drying cycles (w/d). In the initial condition, the three specimens were in a passive state. After applying the accelerated IV technique, the three specimens were in the range where the corrosion probability was greater than 90%, which indicated that corrosion was active. The blended concrete had a better performance. Nevertheless, from cycle 1 to cycle 6, no significant changes were observed among the specimens. However, after cycle 7, the effect of the modified concrete against chloride ions was evident.

Fig. 13.4 shows the evolution of the corrosion current, i_{corr} , calculated using the linear polarization resistance technique, R_p , for specimens with MK and SF and OPC without additions. After the application of IV, the corrosion current drastically increased. The OPC and SF specimens were in the high corrosion range, and MK

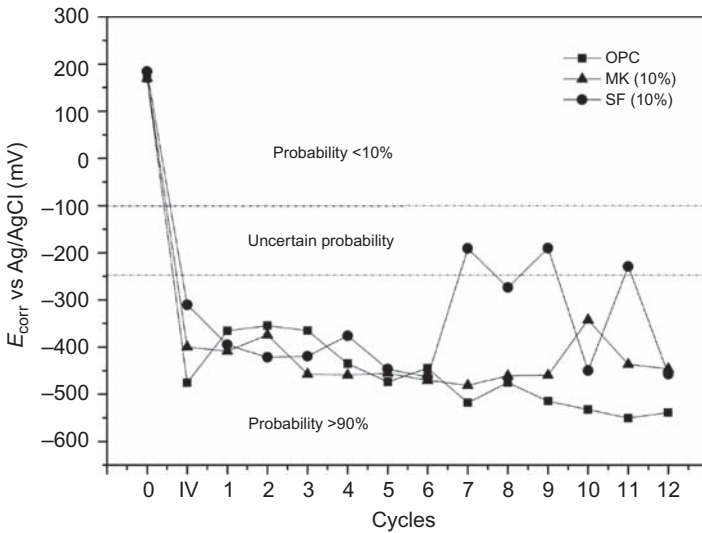


Figure 13.3 Corrosion potential (E_{corr}) for ordinary Portland cement (OPC), metakaolin (MK) (10%) and silica fume (SF) (10%) concretes exposed to chlorides.

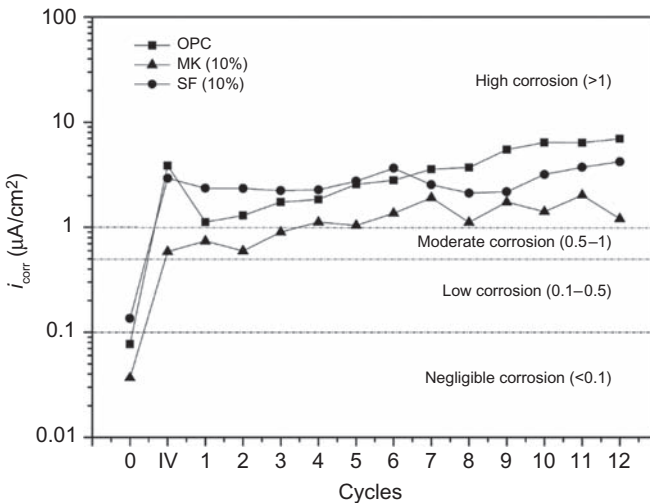


Figure 13.4 Corrosion current density (i_{corr}) for ordinary Portland cement (OPC), metakaolin (MK) (10%) and silica fume (SF) (10%) concretes exposed to chlorides using Rp technique.

was in the moderate corrosion range. During the w/d cycles, a slight increase in the corrosion rate was observed for all specimens, but MK had a better performance throughout the exposure time. After cycle 7, the beneficial effect of the pozzolanic additions was observed. At the end of the exposure in cycle 12, the MK-concrete

had an 82% reduction in the corrosion rate with respect to OPC. At the end of the exposure, the SF concrete had an i_{corr} reduction of 39.6% with respect to OPC. MK concrete exposed to chloride ions had a superior performance, which was attributed to the formation of Friedel's salt.

There are other types of pozzolanic additions, but their studies are limited. These types of pozzolanic additions include rice husk ash (RHA), sugar cane bagasse, palm oil fuel ash (POFA), and fluid catalytic cracking (FCC). In general, a good performance in the presence of chloride ions has been reported in different studies (Bahurudeen et al., 2015; Chao-Lung et al., 2011; Gastaldini et al., 2010; Madandoust et al., 2011; Megat Johari et al., 2012; Morozov et al., 2013; Saraswathy and Song, 2007; Torres-Castellanos et al., 2014; Zeyad et al., 2017).

13.2.2 Geopolymer coatings

Geopolymers, also known as inorganic polymers, are aluminum-silica, three-dimensional products of the chemical interactions between a strongly alkaline dissolution and an aluminosilicate source (Komnitsas and Zaharaki, 2007; Shi et al. 2011a). The results have demonstrated that the geopolymers possess excellent mechanical properties, high resistance to chemical attack, and high resistance to fire (Abdulkareem et al., 2014; Davidovits, 2002; Duan et al., 2016; Kong and Sanjayan, 2010; Pacheco-Torgal et al., 2008a; Zhuang et al., 2016). MK and FA are commonly used as aluminosilicate sources (Shi et al. 2011a).

In recent studies, these types of materials have been proposed as protective coatings for steel exposed to high temperatures (Irfan Khan et al., 2015; Kaloari et al., 2016; Mohd Basri et al., 2016; Temuujin et al., 2009, 2011), reflective coatings, thermal insulation (Zhang et al., 2015), fire protection coatings on concrete tunnels (Sakkas et al., 2015), and chemical attack protection coatings for cement pipes (Chindaprasirt and Rattanasak, 2016), among others. Applying a geopolymer coating on the surface of embedded steel (Kriven et al., 2009; Rostami et al., 2015) and/or on the concrete surface has been proposed as a method of protecting reinforced concrete, which can be an alternative for concrete exposed to marine environments (Zhang et al., 2012, 2010a,b). To ensure the geopolymer coating performs well on reinforced concrete exposed to chloride ions, it is important to consider different factors: low permeability of the GP material, low contraction, coating adhesion strength to concrete, adequate setting time, chloride ion penetration resistance, and corrosion resistance of the reinforcing steel (Aguirre-Guerrero et al., 2017; Zhang and Wang, 2015).

Zhang et al. (2010a) developed a coating based on a binary type geopolymer (90% MK–10% GBFS), reinforced with short polypropylene fibers to protect marine structures. It was incorporated during the setting time to mitigate cracking from contraction. The results demonstrated the low permeability, high adhesion, and excellent anticorrosion properties provided by the coating, which supports its use as a protective barrier for marine structures. In a later study, Zhang et al. (2010b) attributed the protective performance of the geopolymer coating to its high mesoporosity: 22.3% total porosity and 94% of pores ≤ 20 nm. When Zhang et al.

(2010b) compared the results to a Portland cement paste (OPC) (29.5% total porosity and 73.7% pores ≥ 50 nm), the cause of its low permeability was reflected. They also observed that the geopolymerization products were stable when immersed in sea water or exposed to air. These results reaffirmed that geopolymers based on 90% MK–10% GBFS can be used as a coating for marine structures.

Regarding adhesion strength, two hybrid-type geopolymer mortars—based on the alkaline activation of FA and MK with a 10% addition of Portland cement—were applied as a coating on the surface of concrete. A very similar adhesion strength—in the range of 1.5–2.5 MPa after 7 days of curing, was determined using Elcometer 106 equipment off the Dolly attached to the surface of the two coatings (Fig. 13.5) (Aguirre-Guerrero et al., 2017). Other researchers observed very similar adhesion strengths for geopolymer-type coatings applied to concrete (Hu et al., 2008; Zhang et al., 2010a, 2016). The hybrid-type geopolymer coatings form C–A–S–H gels, which are similar to the C–S–H gels formed by cementitious paste but include Al in their structure. These gels favor the homogeneity of the interface between the substrate (OPC concrete) and the GP mortar, which results in a strong interface zone between the two materials. In addition, the calcium hydroxide in the OPC substrate can react with the Al and Si in the geopolymeric paste because of the Ca^{2+} balance effect (Pacheco-Torgal et al., 2008b). The increase in these reaction products improves the interface zone between the GP coating and the concrete substrate. Therefore, the geopolymer coating has a strong adhesion to the OPC substrates.

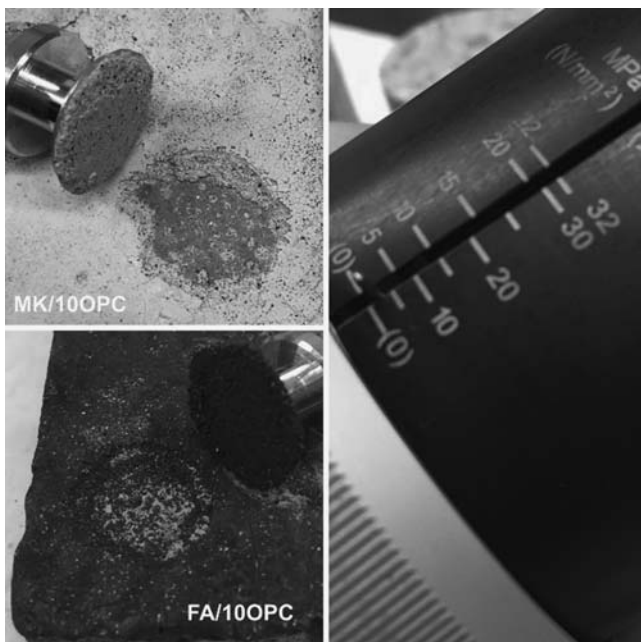


Figure 13.5 Adhesion test for coated ordinary Portland cement (OPC) concrete.

GP materials show a reduction in the permeability of the chloride ions, compared to OPC concrete (Bernal et al., 2012; Ismail et al., 2013; Zhu et al., 2014), because of a smaller pore size and increase in tortuosity. The latter is due to the dense structure of the (C, N)—A—S—H gel (Ismail et al., 2013). However, these studies were performed for bulk materials. Fig. 13.6 presents the permeability of chloride ions for uncoated OPC concrete and concrete coated with two types of hybrid coatings: GP mortar based on MK (MK/10OPC), and GP mortar based on FA (FA/10OPC). The uncoated concrete had the highest values for the passing charge, compared to the coated concrete. In contrast, the FA/10OPC coating showed the lowest passing charge of the two evaluated coatings (less than 1000 coulomb), which indicated a “very low” permeability to chloride ions. The MK/10OPC coated concretes also demonstrated a good performance against chloride ions and fell within the “low” permeability range.

Regarding the corrosion performance of the reinforcing steel, the current versus time curve, obtained from the accelerated IV test, is shown in Fig. 13.7. Here, the coated concrete shows a much lower initial current compared to the uncoated concrete. The current remained constant until approximately 3.5 hours of accelerated chloride exposure, at which point a significant increase in the current was observed. The appearance time for the first crack was similar for all specimens: FA/10OPC 161.7h, MK/10OPC 157.4h, and without a coating 156.2h. This suggests that the coatings protect the material against chloride corrosion when the chloride ions are slowly passing through the coating, and this was observed in the initial stage of the test. In the first three hours of the accelerated test, very low currents were observed for the coated concrete.

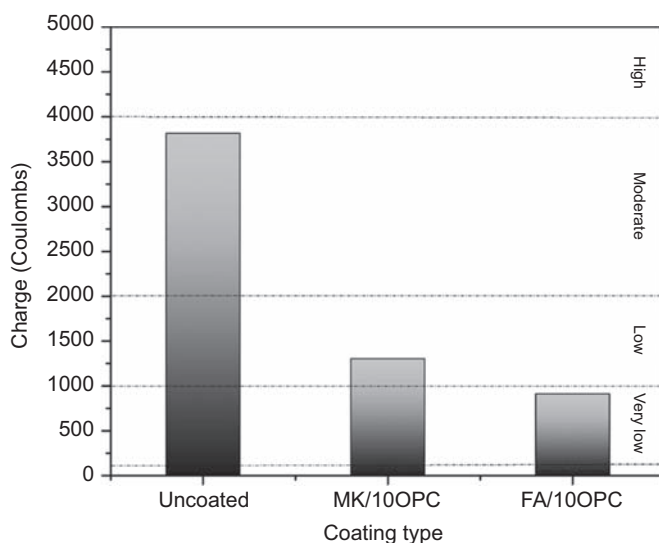


Figure 13.6 Chloride permeability based on ASTM C 1202. Passing charge of concretes uncoated and coated specimens.

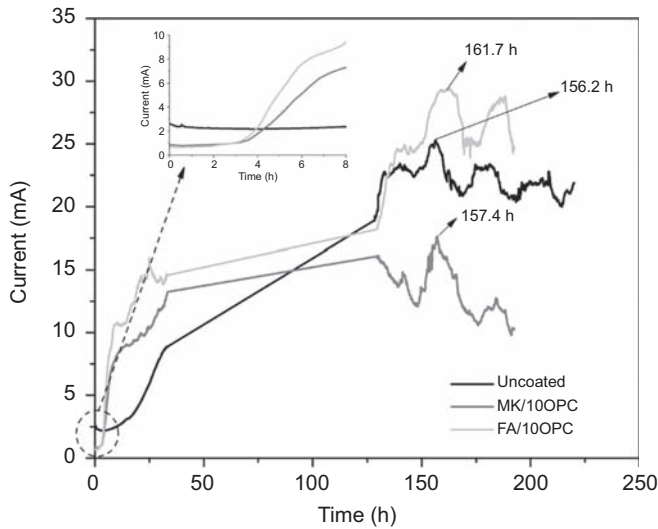


Figure 13.7 Current intensity versus time for uncoated and coated specimens.

Once the chloride ions move through the coating barrier, they continue their diffusion process through the cementitious matrix. This is why similar values for the appearance time of the first crack were seen for all specimens. It is important to mention that this method is an accelerated test for chloride ions entering the system, and it far exceeds any real exposure conditions because the reinforcing steel behaves as an anode in the test assembly. The MK/10OPC coated concrete had the lowest current value, which suggested it had a higher electrical resistance (Reddy et al., 2011) than the other specimens. The concrete with the geopolymer coating based on MK had the best corrosion behavior for the reinforcing steel.

Fig. 13.8 shows the evolution of an OCP for coated and uncoated specimens. For the initial time (0 cycles), the concrete with and without a coating had a 10% corrosion probability, which corresponded to the passive state of the steel rebar. After cycle 2, the potentials were much more negative for the specimens, a result of the exposure to chloride ions. However, for the specimen with the MK/10OPC coating, the potential was more positive than that of FA/10OPC and the uncoated concrete. This behavior was displayed from cycle 2 to cycle 4, which is the zone of uncertain corrosion probability. From cycle 5 until the end of the exposure, all specimens had similar behaviors with more negative potentials and a 90% corrosion probability. This technique indicates the corrosive state of rebar, but it is not a quantification of the corrosion.

Fig. 13.9 shows the current densities for the coated and uncoated specimens exposed to w/d cycles. The i_{corr} for the MK/10OPC coated specimens from cycles 1 to 4 was lower compared to the uncoated specimen with steel in its passive state. For the specimen with the FA/10OPC coating, the i_{corr} was smaller compared to the uncoated specimen from cycle 1 to cycle 2; nevertheless, after cycle 3, the i_{corr} was

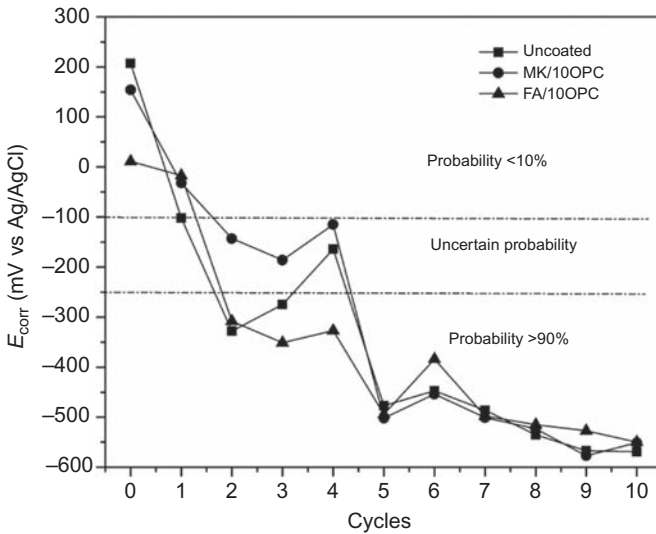


Figure 13.8 Corrosion potential (E_{corr}) versus wetting/drying (w/d) cycles for uncoated and coated specimens.

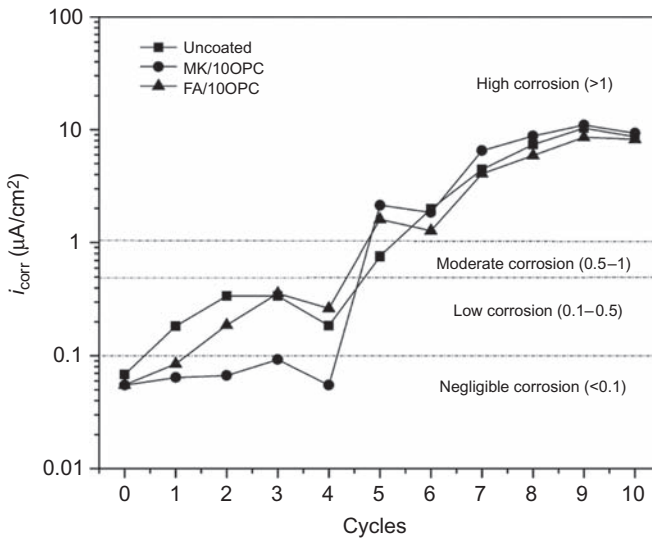


Figure 13.9 Corrosion current density (i_{corr}) versus wetting/drying (w/d) cycles for uncoated and coated specimens.

similar to the uncoated specimen. The application of the geopolymer coating significantly improved the corrosion performance of the reinforcing steel in the first cycles. The results presented suggest that the chloride ions manage to diffuse through the coating after the initial cycles (MK/10OPC up to cycle 4, FA/10OPC

up to cycle 2) and reach the OPC cementitious matrix, where the diffusion is very similar. The application of geopolymeric coatings to concrete can reduce the penetration of chloride ions, improving the durability properties of concrete (Wiyono et al., 2015) until the chloride ions cross the coating.

13.2.3 Electrochemical chloride extraction on blended concretes

To extend the useful life of structures affected by chloride-induced corrosion, the ECE technique can be used to extract chloride ions present in the concrete structure by applying a direct current to the reinforcing steel. This acts as a cathode and an external anode located on the surface of the concrete, in contact with an electrolyte (saturated solution of sodium hydroxide or potable water). Applying the current generates the necessary electric field for the chloride ions to migrate to the external anode, and the negatively charged ions (OH^-) to enter the cathode. The applied current density fluctuates between 1 and 5 A/m^2 , and its application is for a short time—approximately 6–10 weeks (Bertolini et al., 1996, 2004; Cañon et al., 2013; Elsener and Angst, 2007; Liu and Shi, 2012; Sánchez and Alonso, 2011; Yeih et al., 2016). Higher current densities have undesirable consequences for structural properties of reinforced concrete, a significant reduction in bond strength, hydrogen embrittlement, alkali-aggregate reaction, among others (Bertolini et al., 2004; Guo and Gong, 2011; Orellan et al., 2004).

The possibility of extracting chloride ions using this technique emerged in the 1970s, and the process was patented in Europe by NORCURE in 1986 (Bertolini et al., 2004). There are numerous investigations that have been reported on this technique (Abdelaziz et al., 2009; Arya et al., 1996; Carmona et al., 2015; Castellote et al., 2000; Chang et al., 2014; Elsener and Angst, 2007; Fajardo et al., 2006; Garcés et al., 2006; Liu et al., 2014; Miranda et al., 2007; Orellan Herrera et al., 2006; Orellan et al., 2004; Pérez et al., 2010; Rodríguez Reyna et al., 2010; Sánchez and Alonso, 2011; Swamy and McHugh, 2006; Toumi et al., 2007; Tritthart, 1995; Ueda et al., 2012; Yeih et al., 2006; Zhang and Gong, 2014); however, the use of the technique for blended concrete has not been extensively evaluated.

13.2.3.1 Electrochemical chloride extraction application

To evaluate the efficiency of the technique, the total chloride content is usually determined before and after applying ECE. The extraction was applied over a period of 6 weeks using calcium hydroxide as the electrolyte and a current density of 1 A/m^2 . Fig. 13.10 shows the percentage of chloride ions removed after applying ECE to blended concretes, with MK and SF at 10% replacement of cement weight and OPC concrete without additions. The evaluation was performed at depths of 11 and 17 mm from the concrete surface. The OPC concrete showed the highest extraction percentage for the two depths, 52% at 11 mm and 37% at 17 mm. The figure shows that, at greater depths, the extraction percentages decrease. Tritthart (1995) stated that the ECE is more efficient in the areas where the chloride

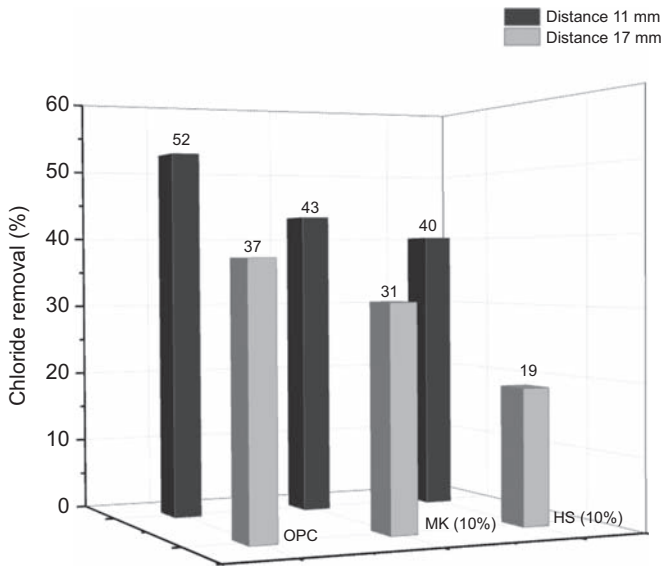


Figure 13.10 Percentage of chlorides removal in ordinary Portland cement (OPC), metakaolin (MK), and silica fume (SF) concretes at distances 11 and 17 mm from the concrete surface.

contamination is higher, such as the area closest to the concrete surface, and as the depth increases, the extraction process becomes less efficient. Blended concrete had lower rates of chloride extraction, and the SF-concrete had the lowest effectiveness. As mentioned above, the addition of MK into concrete in the presence of chloride ions promotes the formation of Friedel's salt, and in the ECE process, the bound chloride ions are more difficult to remove than the free chloride ions in the matrix (Elsener and Angst, 2007; Orellan Herrera et al., 2006; Toumi et al., 2007). Elsener and Angst (2007) observed that it is possible to remove bound chloride ions by performing a system disconnection and reconnecting the system, which promotes a greater ECE efficiency. The disconnection period allows the system to re-establish equilibrium between the bound and free chloride ions. The re-stabilization time can be 24–48 hours.

Ismail and Muhammad (2011) studied the application of ECE (AE) in blended cements with ground-granulated blast slag (GGBS) and pulverized fuel ash by applying a current density of 5 A/m^2 for 12 weeks, and they observed that the concentrations of the total chloride ions and free chloride ions were higher for the reference material based on OPC. Moreover, they stated that the pozzolanic additions limited the diffusion of chloride ions. Therefore, incorporating SF in concrete, even though it does not bind chloride ions, densifies the matrix, generates pore refinement, and obstructs chloride ion diffusion; the efficiency of the ECE process decreases.

Fig. 13.11 shows the evolution of E_{corr} for concrete types prior to the AE, immediately after disconnection of the ECE (ID) system, and for measurements at 30, 60, 90, 335, 425, and 575 days after ECE (OPC, MK (10%), SF (10%)). Before the treatment, the OPC and MK specimens were below -500mV , indicating that they had a high corrosion probability; however, SF-concrete was in the uncertain corrosion probability zone. At the end of the ECE period, the potential values were below -700mV and reached values around -900mV . At this point (ID), it was not possible to determine the corrosive state of the reinforcement steel because it was necessary to allow a depolarization time for the potentials to stabilize. The steel polarization can be attributed to the energy loads supplied during the treatment (Abdelaziz et al., 2009; Rodríguez Reyna et al., 2010). At 335 days, the potentials of the specimens with treatment were in the corrosion probability range of less than 10%. These values suggested that the reinforcement steel was in a passive state. Nevertheless, the potential measurements correspond to a qualitative technique, and it is necessary to complement the results with R_p to demonstrate if the passive state is reached after treatment (Miranda et al., 2007).

Fig. 13.12 shows the evolution of i_{corr} . The current density immediately after the system disconnection (ID) was higher than the current density before the application of the treatment (AE). This behavior has also been observed by other researchers (Abdelaziz et al., 2009; Green et al., 1993; Wang et al., 2007). After 30 days of system disconnection, the i_{corr} corrosion rate began to decrease over time; however, the steel passivity values were not reached until 575 days after the ECE disconnection ($<0.1\ \mu\text{A}/\text{cm}^2$). When ECE is applied to reinforcing steel with a high precorrosion level, it is not possible to achieve re-passivation (Martinez et al., 2015;

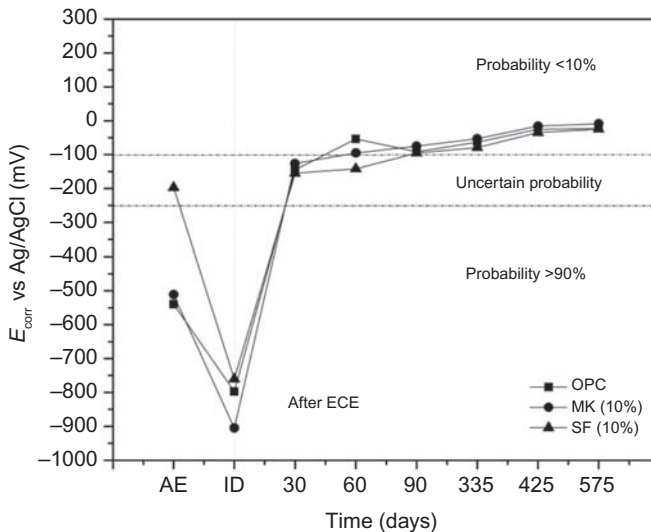


Figure 13.11 Evolution of corrosion potential (E_{corr}) before and after electrochemical chloride extraction (ECE) for ordinary Portland cement (OPC), metakaolin (MK), and silica fume (SF) specimens.

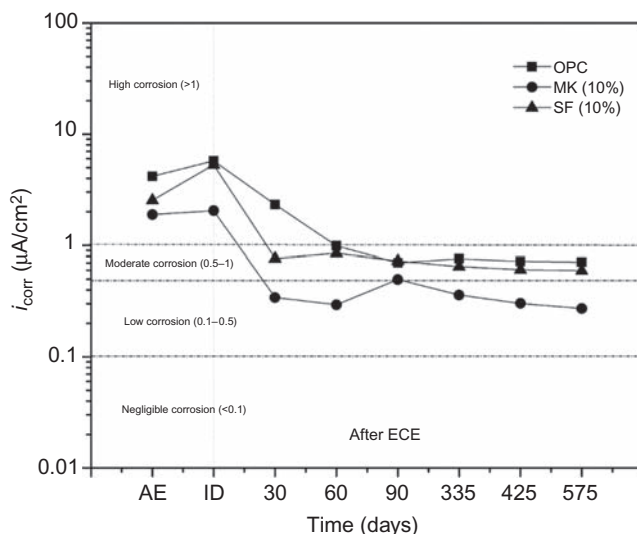


Figure 13.12 Evolution of i_{corr} before and after electrochemical chloride extraction (ECE) for ordinary Portland cement (OPC), metakaolin (MK), and silica fume (SF) specimens.

Miranda et al., 2007; Orellan Herrera et al., 2006; Rodríguez Reyna et al., 2010); nevertheless, ECE decreases the corrosion rate and extends the useful life of a structure. The FHWA (2011) studied the long-term effects of the AE and they observed that the corrosion rates were higher after ECE, however the visual observation of the steel, corrosion potential, and chloride ions concentration shows no evidence of corrosion initiation after ECE. Therefore, the corrosion rate measurements did not accurately reflect the true values. In ECE-treated concrete, the hydroxyl concentration at the steel–concrete interface was much higher, and the generally accepted threshold value of chloride ion concentration for corrosion initiation was not applicable. The re-passivated state is achieved by a combination of lowering the chloride level and increasing the alkali level at the reinforcement (Streicher et al., 2009). ECE can be used for rehabilitation, even though it cannot truly stop the active corrosion of rebar.

For concrete without additions, a higher ECE efficiency can be obtained. The use of mineral additions in concrete, such as MK and SF, reduces the corrosion rate compared to OPC, but the AE reduces the corrosion in OPC concrete. This suggests that ECE is more effective in terms of reducing the corrosion rate compared to the use of mineral additions in reinforced concrete.

13.2.3.2 Geopolymer coating application after electrochemical chloride extraction

There is a consensus that once the ECE technique is applied, a protective coating should be added as a complementary method to limit the re-diffusion of ions into

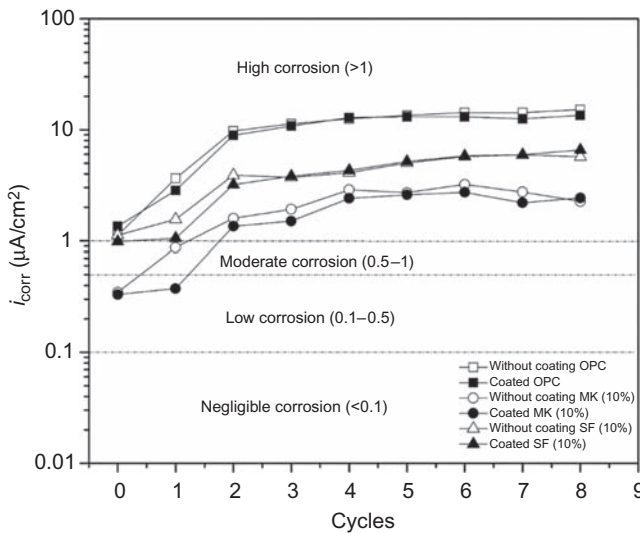


Figure 13.13 Evolution of i_{corr} of ordinary Portland cement (OPC), metakaolin (MK), and silica fume (SF) concretes after treatment electrochemical chloride extraction (ECE) with and without coating FA/10OPC.

the concrete as the structure will remain in the same chloride-contaminated environment. Fig. 13.13 shows the i_{corr} evolution for ECE posttreatment specimens with and without a geopolymer coating, based on FA FA/10OPC exposed to w/d cycles. The coating was applied to OPC concrete without additions and blended concretes with 10% MK and SF. Cycle 0 corresponds to the specimens' corrosion conditions after ECE treatment. The i_{corr} increased for all the specimens from cycle 1, but the coating contributed to a slight reduction in i_{corr} for the first two cycles. However, the values were very similar after cycle 3 for the OPC and SF concrete with and without a coating. The increase in i_{corr} after re-exposure to chloride ions can be attributed to the possible changes in porosity that the cementitious matrix may experience after ECE treatment (Castellote et al., 1999; Miranda et al., 2007; Siegwart et al., 2003).

13.3 Carbonation-induced corrosion

The carbonation process is due to the entry of CO_2 into the concrete from the atmosphere. Urban and industrial environments, and environmental pollution are sources of this phenomenon. The high pH of concrete (approximately 13) provides a natural protection against reinforcing steel corrosion; nevertheless, the carbonation process decreases the pH value of concrete to approximately 9, which destabilizes the passive layer and causes the corrosion of the reinforcing steel (Baccay et al., 2006; Bertolini et al., 2004; El-Reedy, 2008; Han et al., 2013).

For carbonation to take place, the carbon dioxide must encounter water and chemical components of concrete, such as cement hydration products (portlandite C–H and C–S–H gel) (Bertolini et al., 2004; Castellote et al., 2009; Morandea et al., 2014; Šavija and Luković, 2016). The transporting mechanism and advancement of carbonation within concrete are both explained by the diffusion theory, which is described by Fick's first law (El-Reedy, 2008). When the carbonation reaches the reinforcing steel, uniform corrosion is produced that accelerates crack formation (Taffese and Sistonen, 2017).

The penetration rate of CO₂ depends on environmental factors, including relative humidity, and factors related to the concrete; therefore, CO₂ penetration can occur in urban and industrial environments. CO₂ diffusion does not occur in totally dry concrete or totally saturated concrete; a favorable relative humidity for diffusion is between 50% and 70% (Alexander et al., 2007; El-Reedy, 2008). In addition, an increase in temperature can also accelerate the phenomenon. Another critical parameter is the CO₂ concentration, which can be 0.003% in rural environments and approximately 0.1% in urban environments (Bertolini et al., 2004). Other concrete factors that contribute to CO₂ propagation are: an inadequate curing process, poor compaction, and high w/c ratios—which generate more permeable concrete (Cyr, 2013). There are several ways to prevent this deteriorating phenomenon, including the design of the material and control of the construction process. The incorporation of pozzolanic-type minerals that modify the porosity and reduce the permeability can inhibit CO₂ diffusion; however, controversial results have been reported in the literature (Lothenbach et al., 2011; Massazza, 1993; Özbay et al., 2016). Other alternative methods include electrochemical rehabilitation techniques, such as RE and cathodic protection, which can be applied to concrete in service.

13.3.1 *Supplementary cementitious materials*

Mineral additions can lead to a decrease in the diffusion of the surrounding aggressive agents within the cementitious matrix, but the results from evaluating the CO₂ diffusion resistance have been controversial. In general, blended concrete has proven to be more susceptible to carbonation than concrete without mineral additions, and a more demanding curing process is required for the pozzolanic reactions to properly develop (Cyr, 2013). When pozzolanic materials are used in concrete production, they have a lower amount of calcium hydroxide C–H (Lothenbach et al., 2011). Therefore, less calcium hydroxide is available for carbonation, which changes the kinetics and nature of the process (Šavija and Luković, 2016), producing a low resistance to carbonation in some cases.

In concrete with GGBFS, high replacement percentages have shown a low resistance to carbonation. In such cases, a 50% limit (Song and Saraswathy, 2007) and a curing time between 1 month and 3 months (Gruyaert et al., 2013) are recommended to improve carbonation resistance. Concretes with FA have a similar behavior, and high addition percentages reduce the carbonation resistance (Khunthongkeaw et al., 2006; Zhao et al., 2015). However, some researchers have observed that if the w/c ratio is low, the carbonation resistance can be improved

even with high percentages of FA (Pacheco-Torgal et al., 2013). The curing conditions influence the carbonation performance of concrete with FA (Rozière et al., 2009). After 28–90 days of curing, the carbonation resistance markedly improves (Pacheco-Torgal et al., 2013; Siddique, 2011). Low addition percentages, approximately 10%, are recommended to obtain low carbonation coefficients (Khunthongkeaw et al., 2006), but Siddique (2011) observed a decrease in the carbonation coefficient at addition percentages of 25%–35%. A similar behavior was observed for SF, and slight increases in the carbonation depths with respect to concrete without additions were observed (Pacheco-Torgal et al., 2013). Kulakowski et al. (2009) stated that in concrete with SF, and w/c ratios of 0.45–0.50, the carbonation resistance increases. However, higher w/c ratios can have a detrimental effect, which confirmed that the ideal concentration range is 5%–10%. Other researchers have reported different results regarding carbonation (Khan and Siddique, 2011). The performance of MK-concrete in the presence of CO₂ similarly presents controversy (Bai et al., 2002; Kim et al., 2007). Mejía de Gutiérrez et al. (2009) determined the carbonation depth for specimens with MK after curing for 28 days was slightly lower than that of concrete without additions. They confirmed that the carbonation rate is reduced when the curing age is increased; Vejmelková et al. (2010) also verified that concretes with MK have a better performance with respect to carbonation.

Fig. 13.14 shows the carbonation depth and the carbonation coefficient for blended concretes with 10% SF, 10% MK, and without additions (OPC) at a 0.55 w/c ratio with 28 days of curing. The exposure was performed under accelerated conditions in a carbonation chamber (1% CO₂, 65% RH, 25°C) for periods of 1080,

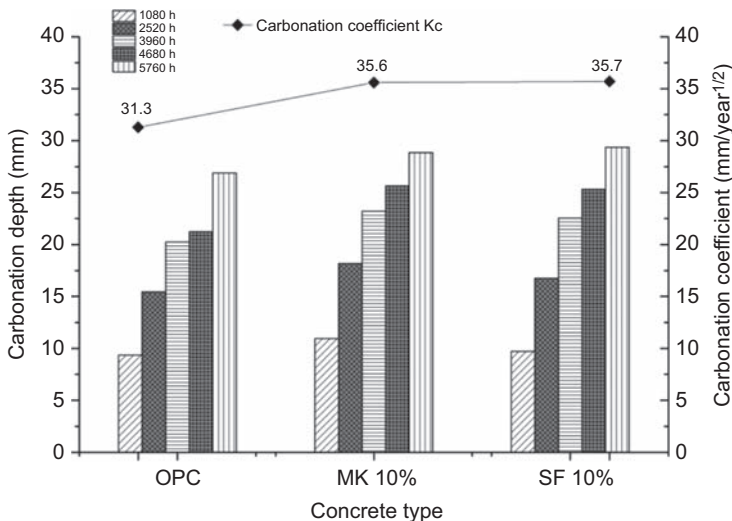


Figure 13.14 Carbonation depth and carbonation coefficient of the ordinary Portland cement (OPC), metakaolin (MK), and silica fume (SF) concrete at different exposure times.

2520, 3960, 4680, and 5760 hours. The behavior of the OPC reference specimen over time, compared to the blended concrete specimens should be noted. The results confirmed that the MK and SF concretes were slightly more susceptible to carbonation than OPC; the carbonation coefficients were similar for all the specimens. The results indicated that the performance of the blended concrete can be improved if the exposure is performed with longer curing periods (approx. 90 days) and using lower w/c ratios (Kulakowski et al., 2009; Mejía de Gutiérrez et al., 2009).

Fig. 13.15 shows the evolution of the OCP for blended concrete with MK and SF, and for OPC without additions. The specimens exposed to carbonation are in the region where the corrosion probability is less than 10%, up to an approximate exposure age of 250 days, after which the corrosion potentials are in the uncertain zone. The carbonation process produces calcium carbonate and water. Calcium carbonate has a low solubility and precipitates within the concrete pores, which reduces the porosity. The precipitation increases the concrete resistance. However, the CO_2 continues to diffuse through the cementitious matrix, and the pH continues to decrease. When the CO_2 reaches the steel, the passive layer is destabilized, which initiates the propagation stage according to the Tutti model (Tutti, 1982). The carbonation coefficients associated with each specimen are shown in Fig. 13.14. Based on these data and the dimensions of the specimens, the time when the carbonation reaches the reinforcement steel surface was obtained for OPC, MK, and SF was 441, 342, and 340 days, respectively. These results match those in Fig. 13.15, where the corrosive process begins at approximately 350 days. Fig. 13.16 shows the evolution of the corrosion current i_{corr} , calculated using the

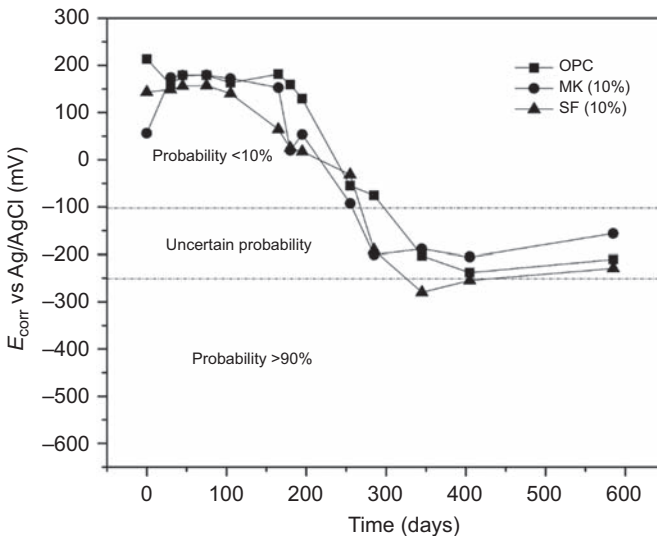


Figure 13.15 Evolution of E_{corr} for ordinary Portland cement (OPC), metakaolin (MK), and silica fume (SF) specimens exposed to CO_2 .

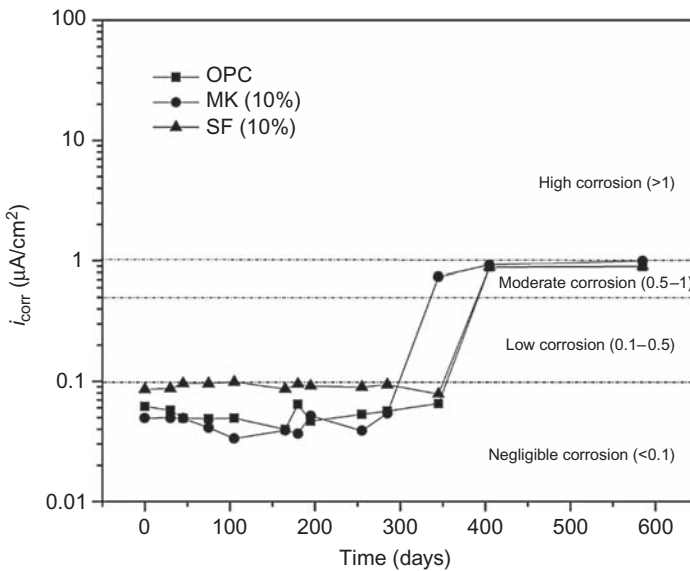


Figure 13.16 Evolution of i_{corr} for ordinary Portland cement (OPC), metakaolin (MK), and silica fume (SF) specimens exposed to CO_2 .

linear polarization resistance (R_p) technique. After 365 days of exposure, the corrosion rate is high, which coincides with the time obtained using the carbonation susceptibility test. Concrete with additions have behaviors very similar to OPC.

13.3.2 Electrochemical realkalisation on blended concretes

To extend the useful life of structures affected by carbonation-induced corrosion, the RE technique can be used. This is similar to ECE and was patented by John Miller in the late 1980s. Its commercialization is attributed to NORCURE in Norway (Banfill, 1997; Bertolini et al., 1996). In RE, a direct current of 1–2 A/m² is applied with respect to the steel surface (cathode), and an electrochemical cell is formed with an auxiliary anode. Sodium carbonate is usually used as an alkaline electrolyte, and the treatment lasts from 3–21 days (Bertolini et al., 2004; Mietz, 1995). During the treatment, electrochemical reactions originate at the cathode surface and generate hydroxyl ions, which increase the pH value near the reinforcing steel. At the same time, the alkaline electrolyte enters the concrete, increases the pH from the surface to the interior and acts as a sink for carbon dioxide in the cementitious matrix (Mietz, 1995; Yeih and Chang, 2005). This technique only has a few application reports compared to the ECE technique (Barrios Durstewitz et al., 2012; Bertolini et al., 1996, 2008; Castellote et al., 2006; González et al., 2011; Marie-Victoire et al., 2014; Mietz, 1995; Miranda et al., 2006; Redaelli and Bertolini, 2011, 2014, 2016; Tong et al., 2012; Yeih and Chang, 2005; Zhang et al., 2013), and only a few of these studies have been performed in blended concrete (Ribeiro et al., 2013).

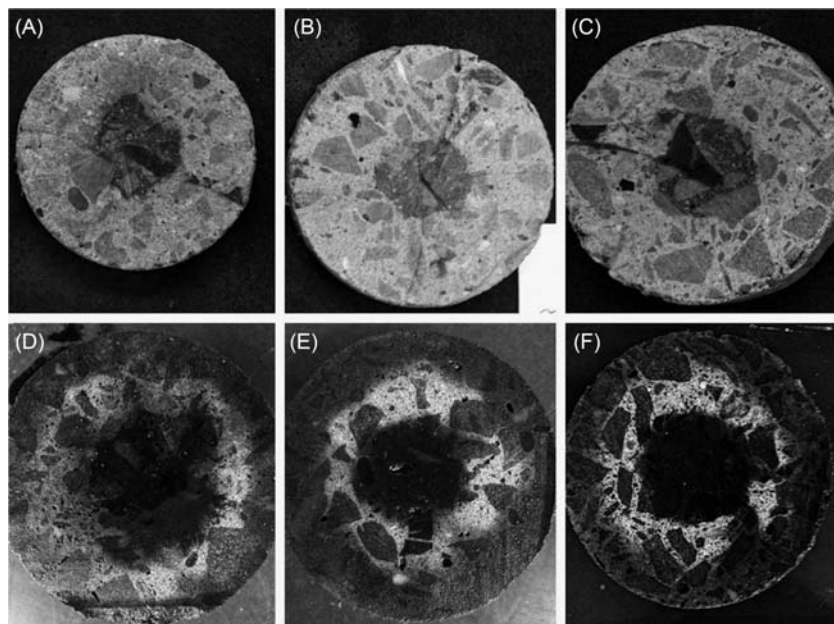


Figure 13.17 Visual monitoring of the evolution of the RE front at 15 days of treatment to specimens with and without addition (A), (B), and (C) ordinary Portland cement (OPC), metakaolin (MK), and silica fume (SF) concrete before electrochemical realkalisation (RE), respectively; (D), (E), and (F) OPC, metakaolin (MK), and silica fume (SF) concrete after electrochemical realkalisation (RE), respectively.

13.3.2.1 Electrochemical realkalisation Application

To analyze the effectiveness of the treatment, a visual inspection was performed by applying 1% phenolphthalein to the concrete before and after RE, to detect an increase in the pH of the carbonated zones. Fig. 13.17 shows the blended concrete with 10% MK, 10% SF, and the concrete reference OPC without additions, before and after applying RE. The application was carried out for a period of 15 days with a single current density of 1 A/m². In general, a recovery of the alkalinity was observed for the concrete, and the OPC concrete had a slightly higher increase in the alkalinity over the other specimens.

The RE occurs in two directions: from the steel to the surface (internal)—due to the alkalinity induced by applying a cathodic current (Castellote et al., 2006; Redaelli and Bertolini, 2011); and from the concrete surface to the steel (external)—due to penetration of the alkaline solution in contact with the anodic system (Castellote et al., 2006). Fig. 13.18 shows the measurements of the RE advance, both internal and external. The OPC concrete had a greater RE advance than the blended concrete, and this was expected because the permeability of the MK and SF concrete is lower. RE obeys electroosmosis (Castellote et al., 2006), in which the aqueous alkaline solution moves through the matrix along an electric field. In this case, the

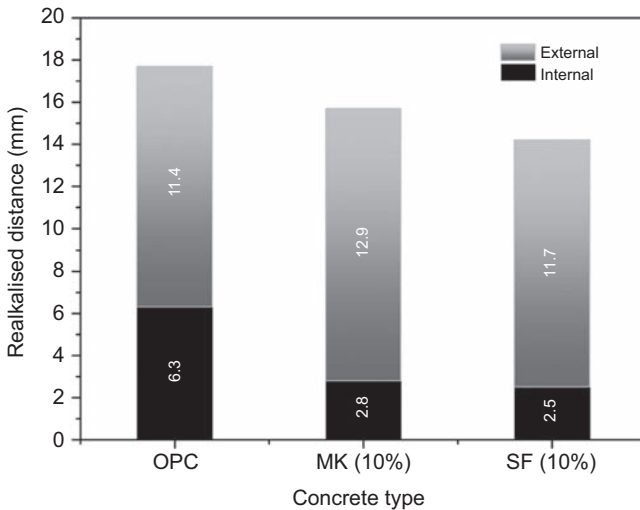


Figure 13.18 Realkalised distance for ordinary Portland cement (OPC), metakaolin (MK), and silica fume (SF) concrete at 15 days of treatment electrochemical realkalisation (RE).

concrete permeability depends on the electrolyte movement inside the matrix and the diffusion of the OH^- generated by the application of the cathodic current to the reinforcing steel (Bertolini et al., 1996). The OPC concrete has a greater advance of internal RE, approximately 2.5 times more than the blended concrete, which indicates greater diffusion of OH^- . This explains why the external diffusion was smaller in comparison to MK and SF. Redaelli and Bertolini (2011) observed the same behavior for concrete with added blast-furnace slag. Ribeiro et al. (2013) stated that an additional electric charge is needed to restore the same level of alkalinity for pozzolanic cement, compared to concrete without additions under the same treatment conditions.

Fig. 13.19 shows the evolution of E_{corr} for blended concrete with MK and SF and OPC before applying RE (AE), immediately after the disconnection of the RE (ID) system, and measurements at 73, 103, 133, 373, 433, and 462 days after RE. Prior to the treatment, all the specimens were in the corrosion probability range $<10\%$. At this point, the carbonation had not reached the reinforcing steel. At the end of the RE period of 15 days, the potential values were below -600 mV, reaching -800 mV. At this point (ID), it was not possible to determine the corrosive state of the reinforcement steel, and it was necessary to allow a depolarization period so the potentials could stabilize. At 133 days, the potentials of the specimens with treatment were in the corrosion probability range of $<10\%$, and these values suggest that the reinforcement steel was in a passive state.

Fig. 13.20 shows the i_{corr} evolution before and after RE. Here, the current density just after the disconnection of the system (ID) was greater than the current density before the application of the treatment (AE). This behavior is similar to the one observed in ECE. After 73 days of system disconnection, the i_{corr} corrosion rate

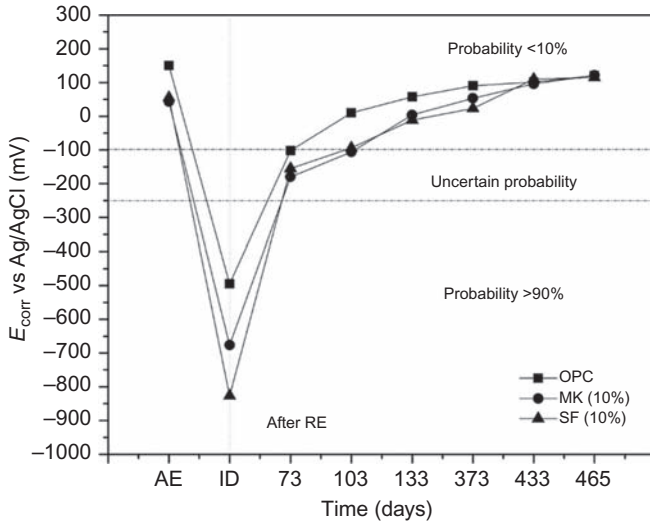


Figure 13.19 Evolution of E_{corr} before and after RE for ordinary Portland cement (OPC), metakaolin (MK), and silica fume (SF) concrete.

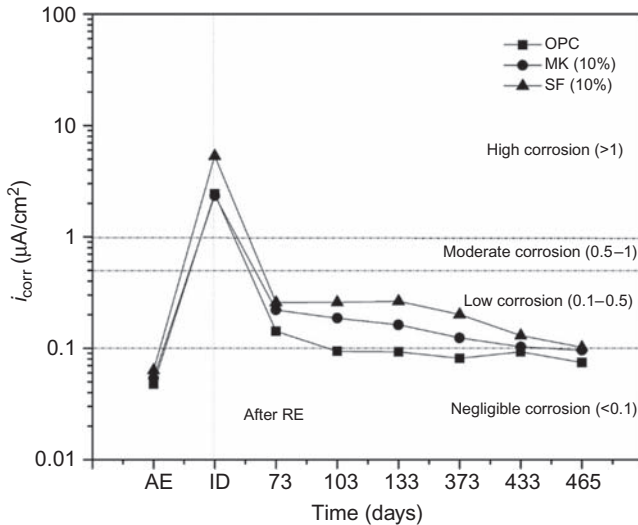


Figure 13.20 Evolution of i_{corr} before and after electrochemical realkalisation (RE) for ordinary Portland cement (OPC), metakaolin (MK), and silica fume (SF) concrete.

began to decrease for all specimens. At 103 days, the OPC reached steel passivity values ($<0.1 \mu A/cm^2$); however, the MK and SF concretes reached the passivation threshold at 465 days. There is a tendency for the current density to decrease over time, but the values before treatment (AE) were slightly lower than those after the

RE treatment at 465 days. After RE application to the blended concrete, the i_{corr} reductions were observed after one year of application, and, in some cases, the values reached steel passivation (Redaelli and Bertolini, 2011; Ribeiro et al., 2013).

The interpretation of electrochemical measurements in treatments such as RE is complex because of the drastic changes in the composition of the pore solution. The conductivity increases due to the increased pH and transport of sodium ions and bicarbonates in the solution, which generates more negative potentials (Elsener, 2001; Martínez et al., 2009). Therefore, in the RE, the steel stabilization process is much slower. Some researchers claim that the linear polarization resistance technique is not an appropriate technique to evaluate corrosion after applying RE (Martínez et al., 2009; Pollet and Dieryck, 2000).

13.3.2.2 Geopolymer coating application after electrochemical realkalisation

Once the RE technique is applied, a complementary method is needed to limit the re-diffusion of CO_2 in the structure. Fig. 13.21 shows the evolution of the current density, i_{corr} , for blended concrete with MK and SF and OPC without additions, with and without GP coatings based on FA/10OPC, after RE exposure to accelerated carbonation conditions (1% CO_2 , 65% RH, 25°C). The time 0 (initial) refers to concrete 30 days after disconnection of the RE system without exposure to carbonation. After approximately 70 days of re-exposure, the uncoated specimens showed an increase in i_{corr} compared to that of the coated specimens, which suggests that the coating goes through a carbonation protection process. Nevertheless,

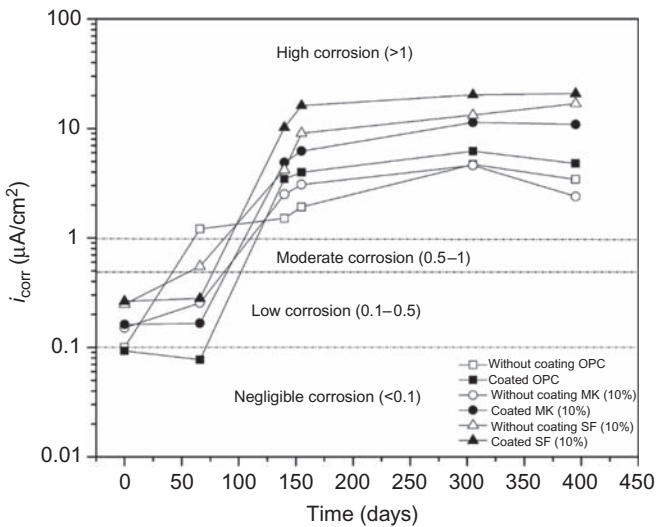


Figure 13.21 Evolution of i_{corr} of the ordinary Portland cement (OPC), metakaolin (MK), and silica fume (SF) concrete after treatment electrochemical realkalisation (RE) with and without coating FA/10OPC.

after 150 days of exposure, all the specimens were in the high corrosion range and exhibited an increase in the i_{corr} of the coated specimens compared to the uncoated specimens. This suggests that the FA/10OPC coating can be a carbonation protective coating, but it has a limited life. At 150 days of accelerated exposure to carbonation, the coating does not have a protective effect.

The performance of geopolymeric or alkaline-activated materials against carbonation is controversial. [Bernal et al. \(2013\)](#) observed a decalcification of the C–A–S–H gel as a carbonation product in GP materials based on FA, with N–A–S–H and C–A–S–H gels, when they were exposed to accelerated carbonation, but no significant changes were observed in the N–A–S–H gel. This suggests that hybrid cementitious materials are equally susceptible to carbonation. Conversely, studies on MK-based geopolymers have shown that these materials show a greater susceptibility to carbonation under accelerated conditions. Still, this is not representative of their performance under natural conditions because the pH of the concrete is reduced and does not reach the levels required to induce depassivation of the reinforcing steel ([Pouhet and Cyr, 2016](#)).

13.4 Conclusions and future trends

Reinforced concrete is susceptible to corrosion of the embedded steel, which affects its durability. The main causes for corrosion are exposure to chloride ions and/or carbonation. There are methods to prevent this phenomenon. The first prevention method requires good quality concrete and design as per standards and regulations during the construction process. In addition, there are prevention and control methods to extend the useful life of structures. The incorporation of additions, such as pozzolan or steel slag, contributes to a permeability reduction and lower chloride ion diffusion, which is an excellent alternative in marine environments. However, in environments with CO₂, mineral additions have yielded controversial results, and positive effects have only been observed under suitable curing conditions. Geopolymer inorganic coatings for concrete surface could be a viable protection alternative for chloride-induced corrosion, because these materials present excellent characteristics, such as mechanical resistance, reduced permeability to chloride ions, and adhesion strength to the concrete surface. Therefore, the coatings have a limited useful lifetime that must be known prior to their application. In studies performed under accelerated conditions, a loss of the protection from the geopolymer coating based on MK was observed after 4 w/d cycles. Because the test conditions were very severe, additional investigations should be performed under natural service conditions to determine the coating performance in different environments.

Electrochemical repARATION techniques, such as ECE and RE, are applied when the structure is in service, but in the case of concrete with mineral additions, their efficiency is lower. For example, in the presence of MK, the bound chloride ions are more difficult to remove than the free chloride ions in the matrix. Additionally, the lower permeability of the MK and SF concrete affects the diffusion of OH[−] into

concrete and RE advance is reduced. These techniques are effective rehabilitation methods. If the initial precorrosion is high, re-passivation of the reinforcing steel is not possible, but it is possible to reduce the corrosion rate and extend the useful life of the structure. The RE technique causes the steel stabilization process to be slower and results in high i_{corr} values after application because of high ion migration in the pore solution. Long-term studies should be conducted because a significant decrease is not observed at 465 days. It is better to prevent than to repair, and demolishing an entire structure because of its deterioration increases costs and generates a greater environmental impact.

References

- Abdelaziz, G.E., Abdelalim, A.M.K., Fawzy, Y.A., 2009. Evaluation of the short and long-term efficiencies of electro-chemical chloride extraction. *Cem. Concr. Res.* 39 (8), 727–732.
- Abdulkareem, O.A., Mustafa Al Bakri, A.M., Kamarudin, H., Khairul Nizar, I., Saif, A.E.A., 2014. Effects of elevated temperatures on the thermal behavior and mechanical performance of fly ash geopolymer paste, mortar and lightweight concrete. *Constr. Build. Mater.* 50, 377–387.
- Abo-El-Enain, S., Abbas, R., Ezzat, E., 2010. Properties and durability of metakaolin blended cements. *Materiales de Construcción.* 60 (299), 21–35.
- Aghaeipour, A., Madhkhan, M., 2017. Effect of ground granulated blast furnace slag (GGBFS) on RCCP durability. *Constr. Build. Mater.* 141, 533–541.
- Aguirre, A.M., de Gutiérrez, R.M., 2013. Durability of reinforced concrete exposed to aggressive conditions. *Materiales de Construcción.* 63 (309), 7–38.
- Aguirre-Guerrero, A.M., Mejía-de-Gutiérrez, R., Montês-Correia, M.J.R., 2016. Corrosion performance of blended concretes exposed to different aggressive environments. *Constr. Build. Mater.* 121, 704–716.
- Aguirre-Guerrero, A.M., Robayo-Salazar, R.A., de Gutiérrez, R.M., 2017. A novel geopolymer application: coatings to protect reinforced concrete against corrosion. *Appl. Clay Sci.* 135, 437–446.
- Ahmad, S., 2003. Reinforcement corrosion in concrete structures, its monitoring and service life prediction—a review. *Cem. Concr. Compos.* 25 (4–5), 459–471.
- Alexander, M.G., Mackechnie, J.R., Yam, W., 2007. Carbonation of concrete bridge structures in three South African localities. *Cem. Concr. Compos.* 29 (10), 750–759.
- Almusallam, A.A., Khan, F.M., Dulaijan, S.U., Al-Amoudi, O.S.B., 2003. Effectiveness of surface coatings in improving concrete durability. *Cem. Concr. Compos.* 25 (4–5), 473–481.
- Alonso, C., Andrade, C., 1987. Corrosion behavior of steel during accelerated carbonation of solutions which simulate the pore concrete solution. *Materiales de construcción.* 37 (206), 5–16.
- Al-Zahrani, M.M., Al-Dulaijan, S.U., Ibrahim, M., Saricimen, H., Sharif, F.M., 2002. Effect of waterproofing coatings on steel reinforcement corrosion and physical properties of concrete. *Cem. Concr. Compos.* 24 (1), 127–137.
- Ampadu, K.O., Torii, K., Kawamura, M., 1999. Beneficial effect of fly ash on chloride diffusivity of hardened cement paste. *Cem. Concr. Res.* 29 (4), 585–590.

- Andrade, C., Buják, R., 2013. Effects of some mineral additions to Portland cement on reinforcement corrosion. *Cem. Concr. Res.* 53, 59–67.
- Angst, U., Elsener, B., Larsen, C.K., Vennesland, Ø., 2009. Critical chloride content in reinforced concrete—a review. *Cem. Concr. Res.* 39 (12), 1122–1138.
- Aponte, D.F., Barra, M., Vázquez, E., 2012. Durability and cementing efficiency of fly ash in concretes. *Constr. Build. Mater.* 30, 537–546.
- Arya, C., Sa'id-Shawqi, Q., Vassie, P.R.W., 1996. Factors influencing electrochemical removal of chloride from concrete. *Cem. Concr. Res.* 26 (6), 851–860.
- Baccay, M.A., Otsuki, N., Nishida, T., Maruyama, S., 2006. Influence of cement type and temperature on the rate of corrosion of steel in concrete exposed to carbonation. *Corrosion.* 62 (9), 811–821.
- Badogiannis, E., Kakali, G., Tsvivilis, S., 2005. Metakaolin as supplementary cementitious material. *J. Therm. Anal. Calorim.* 81 (2), 457–462.
- Badogiannis, E.G., Sfikas, I.P., Voukia, D.V., Trezos, K.G., Tsvivilis, S.G., 2015. Durability of metakaolin self-compacting concrete. *Constr. Build. Mater.* 82 (0), 133–141.
- Bahurudeen, A., Kanraj, D., Gokul Dev, V., Santhanam, M., 2015. Performance evaluation of sugarcane bagasse ash blended cement in concrete. *Cem. Concr. Compos.* 59, 77–88.
- Bai, J., Wild, S., Sabir, B.B., 2002. Sorptivity and strength of air-cured and water-cured PC–PFA–MK concrete and the influence of binder composition on carbonation depth. *Cem. Concr. Res.* 32 (11), 1813–1821.
- Banfill, P.F.G., 1997. Re-alkalisation of carbonated concrete—effect on concrete properties. *Constr. Build. Mater.* 11 (4), 255–258.
- Barrios Durstewitz, C.P., Baldenebro López, F.J., Núñez Jaquez, R.E., Fajardo, G., Almeraya, F., Maldonado-Bandala, E., et al., 2012. Cement based anode in the electrochemical realkalisation of carbonated concrete. *Int. J. Electrochem. Sci.* 7, 3178–3190.
- Batis, G., Pantazopoulou, P., 2000. Advantages of the simultaneous use of corrosion inhibitors and inorganic coatings. Paper presented at the Cement and Concrete Technology in the 2000s. Second International Symposium, Turkey.
- Batis, G., Pantazopoulou, P., Tsvivilis, S., Badogiannis, E., 2005. The effect of metakaolin on the corrosion behavior of cement mortars. *Cem. Concr. Compos.* 27 (1), 125–130.
- Bernal, S.A., Mejía de Gutiérrez, R., Provis, J.L., 2012. Engineering and durability properties of concretes based on alkali-activated granulated blast furnace slag/metakaolin blends. *Constr. Build. Mater.* 33, 99–108.
- Bernal, S.A., Provis, J.L., Walkley, B., San Nicolas, R., Gehman, J.D., Brice, D.G., et al., 2013. Gel nanostructure in alkali-activated binders based on slag and fly ash, and effects of accelerated carbonation. *Cem. Concr. Res.* 53, 127–144.
- Bertolini, L., Bolzoni, F., Elsener, B., Pedferri, P., Andrade, C., 1996. La realcalinización y la extracción electroquímica de los cloruros en las construcciones de hormigón armado. *Materiales de Construcción.* 46 (244), 45–55.
- Bertolini, L., Elsener, B., Pedferri, P., Polder, P., 2004. *Corrosion of Steel in Concrete: Prevention, Diagnosis, Repair.* Wiley-VCH Verlag GmbH & Co. KGaA, Weinheim.
- Bertolini, L., Carsana, M., Redaelli, E., 2008. Conservation of historical reinforced concrete structures damaged by carbonation induced corrosion by means of electrochemical realkalisation. *J. Cult. Herit.* 9 (4), 376–385.
- Boğa, A.R., Topçu, İ.B., 2012. Influence of fly ash on corrosion resistance and chloride ion permeability of concrete. *Constr. Build. Mater.* 31, 258–264.
- Brenna, A., Bolzoni, F., Beretta, S., Ormellese, M., 2013. Long-term chloride-induced corrosion monitoring of reinforced concrete coated with commercial polymer-modified mortar and polymeric coatings. *Constr. Build. Mater.* 48, 734–744.

- Burgos, D., Ángulo, D., Mejía de Gutiérrez, R., 2012. Durabilidad de morteros adicionales con cenizas volantes de alto contenido de carbón. *Revista Latinoamericana de Metalurgia y Materiales*. 32 (1), 61–70.
- Cardenas, H., Kupwade-Patil, K., Eklund, S., 2010. Corrosion mitigation in mature reinforced concrete using nanoscale pozzolan deposition. *J. Mater. Civil Eng.* 23 (6), 752–760.
- Carmona, J., Garcés, P., Climent, M.A., 2015. Efficiency of a conductive cement-based anodic system for the application of cathodic protection, cathodic prevention and electrochemical chloride extraction to control corrosion in reinforced concrete structures. *Corrosion Science*. 96, 102–111.
- Castellote, M., Andrade, C., Alonso, M.C., 1999. Changes in Concrete Pore Size Distribution Due to Electrochemical Chloride Migration Trials. *Mater. J.* 96 (3), .
- Castellote, M., Andrade, C., Alonso, C., 2000. Electrochemical removal of chlorides: Modelling of the extraction, resulting profiles and determination of the efficient time of treatment. *Cem. Concr. Res.* 30 (4), 615–621.
- Castellote, M., Llorente, I., Andrade, C., Turrillas, X., Alonso, C., Campo, J., 2006. In-situ monitoring the realkalisation process by neutron diffraction: Electroosmotic flux and portlandite formation. *Cem. Concr. Res.* 36 (5), 791–800.
- Castellote, M., Fernandez, L., Andrade, C., Alonso, C., 2009. Chemical changes and phase analysis of OPC pastes carbonated at different CO₂ concentrations. *Mater. Struct.* 42 (4), 515–525.
- Chang, C.C., Yeih, W., Chang, J.J., Huang, R., 2014. Effects of stirrups on electrochemical chloride removal efficiency. *Constr. Build. Mater.* 68 (0), 692–700.
- Chao, S., Lin, W., 2013. Effects of silica fume and steel fiber on chloride ion penetration and corrosion behavior of cement-based composites. *Journal of Wuhan University of Technology-Mater. Sci. Ed.* 28 (2), 279–284.
- Chao-Lung, H., Anh-Tuan, B.L., Chun-Tsun, C., 2011. Effect of rice husk ash on the strength and durability characteristics of concrete. *Constr. Build. Mater.* 25 (9), 3768–3772.
- Chen, H.-J., Huang, S.-S., Tang, C.-W., Malek, M.A., Ean, L.-W., 2012. Effect of curing environments on strength, porosity and chloride ingress resistance of blast furnace slag cement concretes: a construction site study. *Constr. Build. Mater.* 35, 1063–1070.
- Cheng, A., Huang, R., Wu, J.-K., Chen, C.-H., 2005. Influence of GGBS on durability and corrosion behavior of reinforced concrete. *Mater. Chem. Phys.* 93 (2–3), 404–411.
- Chindaprasirt, P., Rattanasak, U., 2016. Improvement of durability of cement pipe with high calcium fly ash geopolymer covering. *Constr. Build. Mater.* 112, 956–961.
- Choi, Y.-S., Kim, J.-G., Lee, K.-M., 2006. Corrosion behavior of steel bar embedded in fly ash concrete. *Corros. Sci.* 48 (7), 1733–1745.
- Chousidis, N., Ioannou, I., Rakanta, E., Koutsodontis, C., Batis, G., 2016. Effect of fly ash chemical composition on the reinforcement corrosion, thermal diffusion and strength of blended cement concretes. *Constr. Build. Mater.* 126, 86–97.
- Christodoulou, C., Goodier, C.I., Austin, S.A., Webb, J., Glass, G.K., 2013. Long-term performance of surface impregnation of reinforced concrete structures with silane. *Constr. Build. Mater.* 48, 708–716.
- Courard, L., Darimont, A., Schouterden, M., Ferauche, F., Willem, X., Degeimbre, R., 2003. Durability of mortars modified with metakaolin. *Cem. Concr. Res.* 33 (9), 1473–1479.
- Criado, M., Sobrados, I., Sanz, J., Bastidas, J.M., 2014. Steel protection using sol–gel coatings in simulated concrete pore solution contaminated with chloride. *Surf. Coat. Technol.* 258, 485–494.

- Criado, M., Sobrados, I., Bastidas, J.M., Sanz, J., 2015. Steel corrosion in simulated carbonated concrete pore solution its protection using sol-gel coatings. *Prog. Org. Coat.* 88, 228–236.
- Cyr, M., 2013. 8—Influence of supplementary cementitious materials (SCMs) on concrete durability. In: Pacheco-Torgal, F., Jalali, S., Labrincha, J., John, V.M. (Eds.), *Eco-Efficient Concrete*. Woodhead Publishing, pp. 153–197.
- Damineli, B.L., Pileggi, R.G., John, V.M., 2013. 2 - Lower binder intensity eco-efficient concretes. *Eco-Efficient Concrete*. Woodhead Publishing, pp. 26–44.
- Dang, Y., Xie, N., Kessel, A., McVey, E., Pace, A., Shi, X., 2014. Accelerated laboratory evaluation of surface treatments for protecting concrete bridge decks from salt scaling. *Constr. Build. Mater.* 55, 128–135.
- Davidovits, J., 2002. 30 years of successes and failures in geopolymer applications. Market trends and potential breakthroughs. Paper presented at the Geopolymer 2002 Conference, Melbourne, Australia.
- de Vries, I.J., Polder, R.B., 1997. Hydrophobic treatment of concrete. *Constr. Build. Mater.* 11 (4), 259–265.
- Dhir, R.K., Jones, M.R., 1999. Development of chloride-resisting concrete using fly ash. *Fuel* 78 (2), 137–142.
- Dinakar, P., Sahoo, P., Sriram, G., 2013. Effect of metakaolin content on the properties of high strength concrete. *Int. J. Concr. Struct. Mater.* 7 (3), 215–223.
- Dotto, J.M.R., Abreu, A.Gd, Dal Molin, D.C.C., Müller, I.L., 2004. Influence of silica fume addition on concretes physical properties and on corrosion behavior of reinforcement bars. *Cem. Concr. Compos.* 26 (1), 31–39.
- Duan, P., Yan, C., Zhou, W., 2016. Influence of partial replacement of fly ash by metakaolin on mechanical properties and microstructure of fly ash geopolymer paste exposed to sulfate attack. *Ceram. Int.* 42 (2, Part B), 3504–3517.
- El-Reedy, M., 2008. *Steel-Reinforced Concrete Structures—Assessment and Repair of Corrosion*. Taylor & Francis Group, LLC.
- Elsener, B., 2001. Half-cell potential mapping to assess repair work on RC structures. *Constr. Build. Mater.* 15 (2–3), 133–139.
- Elsener, B., Angst, U., 2007. Mechanism of electrochemical chloride removal. *Corros. Sci.* 49 (12), 4504–4522.
- Fajardo, G., Escadeillas, G., Arliguie, G., 2006. Electrochemical chloride extraction (ECE) from steel-reinforced concrete specimens contaminated by artificial sea-water. *Corros. Sci.* 48 (1), 110–125.
- Fajardo, G., Valdez, P., Pacheco, J., 2009. Corrosion of steel rebar embedded in natural pozzolan based mortars exposed to chlorides. *Constr. Build. Mater.* 23 (2), 768–774.
- Farahani, A., Taghaddos, H., Shekarchi, M., 2015. Prediction of long-term chloride diffusion in silica fume concrete in a marine environment. *Cem. Concr. Compos.* 59, 10–17.
- FHWA, 2011. *Long-Term Effects of Electrochemical Chloride Extraction on Laboratory Specimens and Concrete Bridge Components* (Report No. FHWA-HRT-10-069). Federal Highway Administration.
- Florea, M.V.A., Brouwers, H.J.H., 2012. Chloride binding related to hydration products: Part I: ordinary Portland cement. *Cem. Concr. Res.* 42 (2), 282–290.
- Garcés, P., Sánchez de Rojas, M.J., Climent, M.A., 2006. Effect of the reinforcement bar arrangement on the efficiency of electrochemical chloride removal technique applied to reinforced concrete structures. *Corros. Sci.* 48 (3), 531–545.

- Gastaldini, A.L.G., Isaia, G.C., Saciloto, A.P., Missau, F., Hoppe, T.F., 2010. Influence of curing time on the chloride penetration resistance of concrete containing rice husk ash: a technical and economical feasibility study. *Cem. Concr. Compos.* 32 (10), 783–793.
- González, F., Fajardo, G., Arliguie, G., Juárez, C.A., Escadeillas, G., 2011. Electrochemical realkalisation of carbonated concrete: an alternative approach to prevention of reinforcing steel corrosion. *Int. J. Electrochem. Sci.* 6, 6332–6349.
- Green, W.K., Lyon, S.B., Scantlebury, J.D., 1993. Electrochemical changes in chloride-contaminated reinforced concrete following cathodic polarisation. *Corros. Sci.* 35 (5–8), 1627–1631.
- Gruyaert, E., Van den Heede, P., De Belie, N., 2013. Carbonation of slag concrete: effect of the cement replacement level and curing on the carbonation coefficient – Effect of carbonation on the pore structure. *Cem. Concr. Compos.* 35 (1), 39–48.
- Güneyisi, E., Özturan, T., Gesoğlu, M., 2005. A study on reinforcement corrosion and related properties of plain and blended cement concretes under different curing conditions. *Cem. Concr. Compos.* 27 (4), 449–461.
- Güneyisi, E., Özturan, T., Gesoğlu, M., 2007. Effect of initial curing on chloride ingress and corrosion resistance characteristics of concretes made with plain and blended cements. *Build. Environ.* 42 (7), 2676–2685.
- Güneyisi, E., Gesoğlu, M., Mermerdaş, K., 2008. Improving strength, drying shrinkage, and pore structure of concrete using metakaolin. *Mater. Struct.* 41 (5), 937–949.
- Güneyisi, E., Gesoğlu, M., Algin, Z., 2013a. 9 - Performance of self-compacting concrete (SCC) with high-volume supplementary cementitious materials (SCMs). *Eco-Effic. Concr.*. Woodhead Publishing, pp. 198–217.
- Güneyisi, E., Gesoğlu, M., Karaboğa, F., Mermerdaş, K., 2013b. Corrosion behavior of reinforcing steel embedded in chloride contaminated concretes with and without metakaolin. *Compos. Part B: Eng.* 45 (1), 1288–1295.
- Guo, Y.X., Gong, J.X., 2011. Effect of electrochemical chloride extraction on the bond performance between steel bar and concrete. *Adv. Mater. Res.* 243, 5536–5540.
- Han, S.-H., Park, W.-S., Yang, E.-I., 2013. Evaluation of concrete durability due to carbonation in harbor concrete structures. *Constr. Build. Mater.* 48 (0), 1045–1049.
- Hossain, K.M.A., Lachemi, M., 2004. Corrosion resistance and chloride diffusivity of volcanic ash blended cement mortar. *Cem. Concr. Res.* 34 (4), 695–702.
- Hu, S., Wang, H., Zhang, G., Ding, Q., 2008. Bonding and abrasion resistance of geopolymeric repair material made with steel slag. *Cem. Concr. Compos.* 30 (3), 239–244.
- Irfan Khan, M., Azizli, K., Sufian, S., Man, Z., 2015. Sodium silicate-free geopolymers as coating materials: effects of Na/Al and water/solid ratios on adhesion strength. *Ceram. Int.* 41 (2, Part B), 2794–2805.
- Ismail, M., Muhammad, B., 2011. Electrochemical chloride extraction effect on blended cements. *Adv. Cem. Res.* 23 (5), 241–248.
- Ismail, I., Bernal, S.A., Provis, J.L., San Nicolas, R., Brice, D.G., Kilcullen, A.R., et al., 2013. Influence of fly ash on the water and chloride permeability of alkali-activated slag mortars and concretes. *Constr. Build. Mater.* 48, 1187–1201.
- Kaloari, R.M., Syamsidar, S., Haris, A., Subaer, 2016. Synthesis of geopolymer paste as coating material based on kaolinite and rice husk ash. *Mater. Sci. Forum.* 841, 79–82.
- Karthick, S.P., Madhavamayandi, A., Muralidharan, S., Saraswathy, V., 2016. Electrochemical process to improve the durability of concrete structures. *J. Build. Eng.* 7, 273–280.

- Kayali, O., Zhu, B., 2005. Corrosion performance of medium-strength and silica fume high-strength reinforced concrete in a chloride solution. *Cem. Concr. Compos.* 27 (1), 117–124.
- Keleştemur, O., Demirel, B., 2015. Effect of metakaolin on the corrosion resistance of structural lightweight concrete. *Constr. Build. Mater.* 81 (0), 172–178.
- Kepler, J., Darwin, D., Locke, J., 2000. Evaluation of corrosion protection methods for reinforced concrete highway structures. *Structural Engineering and Engineering Materials SM Report No. 58.*
- Keßler, S., Angst, U., Zintel, M., Gehlen, C., 2015. Defects in epoxy-coated reinforcement and their impact on the service life of a concrete structure. *Struct. Concr.* 16 (3), 398–405.
- Khan, M.I., Siddique, R., 2011. Utilization of silica fume in concrete: review of durability properties. *Resour. Conserv. Recycl.* 57 (0), 30–35.
- Khedr, S., Idriss, A., 1995. Resistance of silica-fume concrete to corrosion-related damage. *J. Mater. Civil Eng.* 7 (2), 102–107.
- Khunthongkeaw, J., Tangtermsirikul, S., Leelawat, T., 2006. A study on carbonation depth prediction for fly ash concrete. *Constr. Build. Mater.* 20 (9), 744–753.
- Kim, H.-S., Lee, S.-H., Moon, H.-Y., 2007. Strength properties and durability aspects of high strength concrete using Korean metakaolin. *Constr. Build. Mater.* 21 (6), 1229–1237.
- Komnitsas, K., Zaharaki, D., 2007. Geopolymerisation: a review and prospects for the minerals industry. *Miner. Eng.* 20 (14), 1261–1277.
- Kong, D.L.Y., Sanjayan, J.G., 2010. Effect of elevated temperatures on geopolymer paste, mortar and concrete. *Cem. Concr. Res.* 40 (2), 334–339.
- Kriven, W.M., Gordon, M., Ervin, B.L., Reis, H., 2009. Corrosion protection assessment of concrete reinforcing bars with a geopolymer coating. *Developments in Porous, Biological and Geopolymer Ceramics: Ceramic Engineering and Science Proceedings*, Vol. 28, Issue 9. John Wiley & Sons, Inc, pp. 373–381.
- Kulakowski, M.P., Pereira, F.M., Molin, D.C.C.D., 2009. Carbonation-induced reinforcement corrosion in silica fume concrete. *Constr. Build. Mater.* 23 (3), 1189–1195.
- Kupwade-Patil, K., Cardenas, H.E., Gordon, K., Lee, L.S., 2012. Corrosion mitigation in reinforced concrete beams via nanoparticle treatment. *ACI Mater. J.* 109, 6.
- Liu, Y., Shi, X., 2012. Ionic transport in cementitious materials under an externally applied electric field: finite element modeling. *Constr. Build. Mater.* 27 (1), 450–460.
- Liu, Q.-f., Xia, J., Easterbrook, D., Yang, J., Li, L.-y., 2014. Three-phase modelling of electrochemical chloride removal from corroded steel-reinforced concrete. *Constr. Build. Mater.* 70 (0), 410–427.
- Lothenbach, B., Scrivener, K., Hooton, R.D., 2011. Supplementary cementitious materials. *Cem. Concr. Res.* 41 (12), 1244–1256.
- Luo, R., Cai, Y., Wang, C., Huang, X., 2003. Study of chloride binding and diffusion in GGBS concrete. *Cem. Concr. Res.* 33 (1), 1–7.
- Madandoust, R., Ranjbar, M.M., Moghadam, H.A., Mousavi, S.Y., 2011. Mechanical properties and durability assessment of rice husk ash concrete. *Biosyst. Eng.* 110 (2), 144–152.
- Marie-Victoire, E., Bouichou, M., Bouteiller, V., Tong, Y.Y., 2014. Realkalisation of a late 19th century bridge. *Concrete Solutions 2014*. CRC Press, pp. 645–654.
- Martínez, I., Andrade, C., Castellote, M., de Viedma, G.P., 2009. Advancements in non-destructive control of efficiency of electrochemical repair techniques. *Corros. Eng., Sci. Technol.* 44 (2), 108–118.

- Martinez, I., Rozas, F., Ramos-Cillan, S., González, M., Castellote, M., 2015. Chloride Electroremediation in reinforced structures: preliminary electrochemical tests to detect the steel repassivation during the treatment. *Electrochim. Acta.* 181, 288–300.
- Massazza, F., 1993. Pozzolanic cements. *Cem. Concr. Compos.* 15 (4), 185–214.
- Medeiros, M.H.F., Helene, P., 2009. Surface treatment of reinforced concrete in marine environment: Influence on chloride diffusion coefficient and capillary water absorption. *Constr. Build. Mater.* 23 (3), 1476–1484.
- Megat Johari, M.A., Zeyad, A.M., Muhamad Bunnori, N., Ariffin, K.S., 2012. Engineering and transport properties of high-strength green concrete containing high volume of ultra-fine palm oil fuel ash. *Constr. Build. Mater.* 30, 281–288.
- Mejía de Gutiérrez, R., Rodríguez, C., Rodríguez, E., Torres, J., Delvasto, S., 2009. Concreto adicionado con metacaolín: Comportamiento a carbonatación y cloruros. *Revista Facultad de Ingeniería Universidad de Antioquia.* 48, 55–64.
- Mietz, J., 1995. Electrochemical realkalisation for rehabilitation of reinforced concrete structures. *Mater. Corros.* 46 (9), 527–533.
- Miranda, J.M., González, J.A., Cobo, A., Otero, E., 2006. Several questions about electrochemical rehabilitation methods for reinforced concrete structures. *Corros. Sci.* 48 (8), 2172–2188.
- Miranda, J.M., Cobo, A., Otero, E., González, J.A., 2007. Limitations and advantages of electrochemical chloride removal in corroded reinforced concrete structures. *Cem. Concr. Res.* 37 (4), 596–603.
- Mohd Basri, M.S., Mustapha, F., Mazlan, N., Ishak, M.R., 2016. Fire retardant performance of rice husk ash-based geopolymer coated mild steel - a factorial design and microstructure analysis. *Mater. Sci. Forum.* 841, 48–54.
- Montemor, M.F., Simões, A.M.P., Salta, M.M., 2000. Effect of fly ash on concrete reinforcement corrosion studied by EIS. *Cem. Concr. Compos.* 22 (3), 175–185.
- Montemor, M.F., Cunha, M.P., Ferreira, M.G., Simões, A.M., 2002. Corrosion behaviour of rebars in fly ash mortar exposed to carbon dioxide and chlorides. *Cem. Concr. Compos.* 24 (1), 45–53.
- Morandea, A., Thiéry, M., Dangla, P., 2014. Investigation of the carbonation mechanism of CH and C-S-H in terms of kinetics, microstructure changes and moisture properties. *Cem. Concr. Res.* 56, 153–170.
- Morozov, Y., Castela, A.S., Dias, A.P.S., Montemor, M.F., 2013. Chloride-induced corrosion behavior of reinforcing steel in spent fluid cracking catalyst modified mortars. *Cem. Concr. Res.* 47, 1–7.
- Nath, P., Sarker, P., 2011. Effect of fly ash on the durability properties of high strength concrete. *Procedia Eng.* 14, 1149–1156.
- Neville, A., 2001. Consideration of durability of concrete structures: past, present, and future. *Mater. Struct.* 34 (2), 114–118.
- Orellan, J.C., Escadeillas, G., Arliguie, G., 2004. Electrochemical chloride extraction: efficiency and side effects. *Cem. Concr. Res.* 34 (2), 227–234.
- Orellan Herrera, J.C., Escadeillas, G., Arliguie, G., 2006. Electro-chemical chloride extraction: influence of C3A of the cement on treatment efficiency. *Cem. Concr. Res.* 36 (10), 1939–1946.
- Özbay, E., Erdemir, M., Durmuş, H.İ., 2016. Utilization and efficiency of ground granulated blast furnace slag on concrete properties—a review. *Constr. Build. Mater.* 105, 423–434.

- Pacheco-Torgal, F., Castro-Gomes, J., Jalali, S., 2008a. Alkali-activated binders: a review. Part 2. About materials and binders manufacture. *Constr. Build. Mater.* 22 (7), 1315–1322.
- Pacheco-Torgal, F., Castro-Gomes, J.P., Jalali, S., 2008b. Adhesion characterization of tungsten mine waste geopolymeric binder. Influence of OPC concrete substrate surface treatment. *Constr. Build. Mater.* 22 (3), 154–161.
- Pacheco-Torgal, F., Jalali, S., 2009. Sulphuric acid resistance of plain, polymer modified, and fly ash cement concretes. *Constr. Build. Mater.* 23 (12), 3485–3491.
- Pacheco-Torgal, F., Miraldo, S., Labrincha, J.A., De Brito, J., 2013. 15 - An eco-efficient approach to concrete carbonation. *Eco-Effic. Concr.*. Woodhead Publishing, pp. 368–385.
- Pan, T., Nguyen, T., Shi, X., 2008. Assessment of electrical injection of corrosion inhibitor for corrosion protection of reinforced concrete. *Transp. Res. Rec. J. Transp. Res. Board.* 2044, 51–60.
- Parande, A.K., Ramesh Babu, B., Aswin Karthik, M., Deepak Kumaar, K.K., Palaniswamy, N., 2008. Study on strength and corrosion performance for steel embedded in metakaolin blended concrete/mortar. *Constr. Build. Mater.* 22 (3), 127–134.
- Pérez, A., Climent, M.A., Garcés, P., 2010. Electrochemical extraction of chlorides from reinforced concrete using a conductive cement paste as the anode. *Corros. Sci.* 52 (5), 1576–1581.
- Polder, R.B., 2012. Effects of slag and fly ash on reinforcement corrosion in concrete in chloride environment—research from the Netherlands. *HERON.* 57 (3), 197–210.
- Pollet, V., Dieryck, V., 2000. Re-alkalisation: specification for the treatment application and acceptance criteria, Annual Progress Report 1999–2000, COST 521 Workshop.
- Poon, C.S., Kou, S.C., Lam, L., 2006. Compressive strength, chloride diffusivity and pore structure of high performance metakaolin and silica fume concrete. *Constr. Build. Mater.* 20 (10), 858–865.
- Pouhet, R., Cyr, M., 2016. Carbonation in the pore solution of metakaolin-based geopolymer. *Cem. Concr. Res.* 88, 227–235.
- Pour-Ali, S., Dehghanian, C., Kosari, A., 2015. Corrosion protection of the reinforcing steels in chloride-laden concrete environment through epoxy/polyaniline–camphorsulfonate nanocomposite coating. *Corros. Sci.* 90, 239–247.
- Ramezaniapour, A.A., Malhotra, V.M., 1995. Effect of curing on the compressive strength, resistance to chloride-ion penetration and porosity of concretes incorporating slag, fly ash or silica fume. *Cem. Concr. Compos.* 17 (2), 125–133.
- Ramezaniapour, A.A., Bahrami Jovein, H., 2012. Influence of metakaolin as supplementary cementing material on strength and durability of concretes. *Constr. Build. Mater.* 30 (0), 470–479.
- Redaelli, E., Bertolini, L., 2011. Electrochemical repair techniques in carbonated concrete. Part I: electrochemical realkalisation. *J. Appl. Electrochem.* 41 (7), 817–827.
- Redaelli, E., Bertolini, L., 2014. Durability aspects of electrochemical realkalisation treatment. Paper presented at the Concrete Solutions—Proceedings of Concrete Solutions, 5th International Conference on Concrete Repair.
- Redaelli, E., Bertolini, L., 2016. Resistance to carbonation of concrete after re-alkalization by absorption of sodium carbonate solution. *Stud. Conserv.* 61 (5), 297–305.
- Reddy, D.V., Edouard, J.-B., Sobhan, K., Rajpathak, S.S., 2011. Durability of reinforced fly ash-based geopolymer concrete in the marine environment. Paper Presented at the 36th Conference on Our World in Concrete & Structures, Singapore.

- Ribeiro, P.H.L.C., Meira, G.R., Ferreira, P.R.R., Perazzo, N., 2013. Electrochemical realkalisation of carbonated concretes—influence of material characteristics and thickness of concrete reinforcement cover. *Constr. Build. Mater.* 40 (0), 280–290.
- Rodríguez Reyna, S.L., Miranda Vidales, J.M., Gaona Tiburcio, C., Narváez Hernández, L., Hernández, L.S., 2010. State of corrosion of rebars embedded in mortar specimens after an electrochemical chloride removal. *Port. Electrochim. Acta.* 28 (3), 153–164.
- Rostami, H., Tovia, F., Masodi, R., Bahadory, M., 2015. Reduction of corrosion of reinforcing steel in concrete using alkali ash material. *J. Solid Waste Technol. Manage.* 41 (2), 136–145.
- Rozière, E., Loukili, A., Cussigh, F., 2009. A performance based approach for durability of concrete exposed to carbonation. *Constr. Build. Mater.* 23 (1), 190–199.
- Sadati, S., Arezoumandi, M., Shekarchi, M., 2015. Long-term performance of concrete surface coatings in soil exposure of marine environments. *Constr. Build. Mater.* 94, 656–663.
- Sakkas, K., Sofianos, A., Nomikos, P., Panias, D., 2015. Behavior of passive fire Protection K-geopolymer under successive severe fire incidents. *Materials.* 8, 6096–6104.
- Sánchez, M., Alonso, M.C., 2011. Electrochemical chloride removal in reinforced concrete structures: Improvement of effectiveness by simultaneous migration of calcium nitrite. *Constr. Build. Mater.* 25 (2), 873–878.
- Saraswathy, V., Song, H.-W., 2007. Corrosion performance of rice husk ash blended concrete. *Constr. Build. Mater.* 21 (8), 1779–1784.
- Saravanan, K., Sathiyarayanan, S., Muralidharan, S., Azim, S.S., Venkatachari, G., 2007. Performance evaluation of polyaniline pigmented epoxy coating for corrosion protection of steel in concrete environment. *Prog. Org. Coat.* 59 (2), 160–167.
- Šavija, B., Luković, M., 2016. Carbonation of cement paste: understanding, challenges, and opportunities. *Constr. Build. Mater.* 117, 285–301.
- Selvaraj, R., Selvaraj, M., Iyer, S.V.K., 2009. Studies on the evaluation of the performance of organic coatings used for the prevention of corrosion of steel rebars in concrete structures. *Prog. Org. Coat.* 64 (4), 454–459.
- Shekarchi, M., Rafiee, A., Layssi, H., 2009. Long-term chloride diffusion in silica fume concrete in harsh marine climates. *Cem. Concr. Compos.* 31 (10), 769–775.
- Shi, C., Jiménez, A.F., Palomo, A., 2011a. New cements for the 21st century: the pursuit of an alternative to Portland cement. *Cem. Concr. Res.* 41 (7), 750–763.
- Shi, X., Yang, Z., Liu, Y., Cross, D., 2011b. Strength and corrosion properties of Portland cement mortar and concrete with mineral admixtures. *Constr. Build. Mater.* 25 (8), 3245–3256.
- Shi, X., Xie, N., Fortune, K., Gong, J., 2012. Durability of steel reinforced concrete in chloride environments: an overview. *Constr. Build. Mater.* 30 (0), 125–138.
- Siddique, R., 2011. Properties of self-compacting concrete containing class F fly ash. *Mater. Des.* 32 (3), 1501–1507.
- Siddique, R., Iqbal Khan, M., 2011. Metakaolin. In: Siddique, R., Khan, M.I. (Eds.), *Supplementary Cementing Materials*. Springer Berlin Heidelberg, Berlin, Heidelberg, pp. 175–230.
- Siddique, R., Klaus, J., 2009. Influence of metakaolin on the properties of mortar and concrete: a review. *Appl. Clay Sci.* 43 (3–4), 392–400.
- Siegwart, M., Lyness, J.F., McFarland, B.J., 2003. Change of pore size in concrete due to electrochemical chloride extraction and possible implications for the migration of ions. *Cem. Concr. Res.* 33 (8), 1211–1221.

- Simčič, T., Pejovnik, S., De Schutter, G., Bosiljkov, V.B., 2015. Chloride ion penetration into fly ash modified concrete during wetting–drying cycles. *Constr. Build. Mater.* 93, 1216–1223.
- Song, H.-W., Saraswathy, V., 2006. Studies on the corrosion resistance of reinforced steel in concrete with ground granulated blast-furnace slag—an overview. *J. Hazard. Mater.* 138 (2), 226–233.
- Song, H.-W., Saraswathy, V., 2007. Corrosion monitoring of reinforced concrete structures—a review. *Int. J. Electrochem. Sci.* 2, 1–28.
- Song, H.-W., Lee, C.-H., Ann, K.Y., 2008. Factors influencing chloride transport in concrete structures exposed to marine environments. *Cem. Concr. Compos.* 30 (2), 113–121.
- Song, H.-W., Pack, S.-W., Nam, S.-H., Jang, J.-C., Saraswathy, V., 2010. Estimation of the permeability of silica fume cement concrete. *Constr. Build. Mater.* 24 (3), 315–321.
- Streicher, P.E., Hoppe, G.E., da Silva, V.A., Kruger, E.J., 2009. The application of electrochemical chloride extraction to reinforced concrete bridge members. In: Alexander, M. G., Beushausen, H.D., Dehn, F., Moyo, P. (Eds.), *Concrete Repair, Rehabilitation and Retrofitting II*. CRC Press.
- Swamy, R.N., Tanikawa, S., 1993. An external surface coating to protect concrete and steel from aggressive environments. *Mater. Struct.* 26 (8), 465–478.
- Swamy, R.N., McHugh, S., 2006. Effectiveness and structural implications of electrochemical chloride extraction from reinforced concrete beams. *Cem. Concr. Compos.* 28 (8), 722–733.
- Taffese, W.Z., Sistonen, E., 2017. Machine learning for durability and service-life assessment of reinforced concrete structures: recent advances and future directions. *Autom. Constr.* 77, 1–14.
- Temuujin, J., Minjigmaa, A., Rickard, W., Lee, M., Williams, I., van Riessen, A., 2009. Preparation of metakaolin based geopolymer coatings on metal substrates as thermal barriers. *Appl. Clay Sci.* 46 (3), 265–270.
- Temuujin, J., Rickard, W., Lee, M., van Riessen, A., 2011. Preparation and thermal properties of fire resistant metakaolin-based geopolymer-type coatings. *J. Non-Cryst. Solids.* 357 (5), 1399–1404.
- Thomas, M., Scott, A., Bremner, T., Bilodeau, A., Day, D., 2008. Performance of slag concrete in marine environment. *ACI Mater. J.* 106 (6), 628–634.
- Thomas, M.D.A., Hooton, R.D., Scott, A., Zibara, H., 2012. The effect of supplementary cementitious materials on chloride binding in hardened cement paste. *Cem. Concr. Res.* 42 (1), 1–7.
- Tittarelli, F., Moriconi, G., 2010. The effect of silane-based hydrophobic admixture on corrosion of galvanized reinforcing steel in concrete. *Corros. Sci.* 52 (9), 2958–2963.
- Tong, Y., Bouteiller, V., Marie-Victoire, E., Joiret, S., 2012. Efficiency investigations of electrochemical realkalisation treatment applied to carbonated reinforced concrete — Part I: sacrificial anode process. *Cem. Concr. Res.* 42 (1), 84–94.
- Topçu, İ.B., Boğa, A.R., 2010. Effect of ground granulate blast-furnace slag on corrosion performance of steel embedded in concrete. *Mater. Des.* 31 (7), 3358–3365.
- Torres, J., Mejía-de-Gutiérrez, R., Puertas, F., 2007. Effect of kaolin treatment temperature on mortar chloride permeability. *Materiales de Construcción.* 57 (285), 61–69.
- Torres-Castellanos, N., Izquierdo, S., Torres-Agredo, J., Mejía de Gutiérrez, R., 2014. Resistance of blende concrete containing an industrial petrochemical residue to chloride ion penetration and carbonation. *Ingeniería e Investigación.* 34 (1), 11–16.

- Toumi, A., François, R., Alvarado, O., 2007. Experimental and numerical study of electrochemical chloride removal from brick and concrete specimens. *Cem. Concr. Res.* 37 (1), 54–62.
- Trithart, J., 1995. Changes in the composition of pore solution and solids during electrochemical chloride removal in contaminated concrete, American Concrete Institute ACI Special Publication, 154, 127–144.
- Tutti, K., 1982. Corrosion of steel in concrete. Swedish Cement and Concrete Research Institute4.
- Ueda, T., Wakitani, K., Nanasawa, A., 2012. Influence of electrolyte temperature on efficiency of electrochemical chloride removal from concrete. *Electrochimica Acta.* 86, 23–27.
- Vaidya, S., Allouche, E.N., 2010. Electrokinetically deposited coating for increasing the service life of partially deteriorated concrete sewers. *Constr. Build. Mater.* 24 (11), 2164–2170.
- Vejmelková, E., Pavlíková, M., Keppert, M., Keřner, Z., Rovnaníková, P., Ondráček, M., et al., 2010. High performance concrete with Czech metakaolin: experimental analysis of strength, toughness and durability characteristics. *Constr. Build. Mater.* 24 (8), 1404–1411.
- Wang, X., Yu, Q., Deng, C., Wei, J., Wen, Z., 2007. Change of electrochemical property of reinforced concrete after electrochemical chloride extraction. *Journal of Wuhan University of Technology-Mater. Sci. Ed.* 22 (4), 764–769.
- Wang, Z., Zeng, Q., Wang, L., Yao, Y., Li, K., 2014. Corrosion of rebar in concrete under cyclic freeze–thaw and chloride salt action. *Constr. Build. Mater.* 53, 40–47.
- Wiyono, D., Antoni, Hardjito, D., 2015. Improving the Durability of Pozzolan Concrete Using Alkaline Solution and Geopolymer Coating. *Proc. Eng.* 125, 747–753.
- Yeau, K.Y., Kim, E.K., 2005. An experimental study on corrosion resistance of concrete with ground granulate blast-furnace slag. *Cem. Concr. Res.* 35 (7), 1391–1399.
- Yeih, W., Chang, J.J., 2005. A study on the efficiency of electrochemical realkalisation of carbonated concrete. *Constr. Build. Mater.* 19 (7), 516–524.
- Yeih, W., Chang, J.J., Hung, C.C., 2006. Selecting an adequate procedure for the electrochemical chloride removal. *Cem. Concr. Res.* 36 (3), 562–570.
- Yeih, W., Chang, J.J., Chang, C.C., Chen, K.L., Chi, M.C., 2016. Electrochemical chloride removal for reinforced concrete with steel rebar cage using auxiliary electrodes. *Cem. Concr. Compos.* 74, 136–146.
- Yiğiter, H., Yazıcı, H., Aydın, S., 2007. Effects of cement type, water/cement ratio and cement content on sea water resistance of concrete. *Build. Environ.* 42 (4), 1770–1776.
- Yuan, Q., Shi, C., De Schutter, G., Audenaert, K., Deng, D., 2009. Chloride binding of cement-based materials subjected to external chloride environment—a review. *Constr. Build. Mater.* 23 (1), 1–13.
- Zeyad, A.M., Megat Johari, M.A., Tayeh, B.A., Yusuf, M.O., 2017. Pozzolan reactivity of ultrafine palm oil fuel ash waste on strength and durability performances of high strength concrete. *J. Cleaner Prod.* 144, 511–522.
- Zhang, Q., Gong, J., 2014. Study on seismic behavior of reinforced concrete columns after ECE treatment. *Constr. Build. Mater.* 50, 549–559.
- Zhang, W., Ba, H., 2012. Effect of ground granulated blast-furnace slag (GGBFS) and silica fume (SF) on chloride migration through concrete subjected to repeated loading. *Sci. China Technol. Sci.* 55 (11), 3102–3108.
- Zhang, Z., Wang, H., 2015. 22 - Alkali-activated cements for protective coating of OPC concrete. *Handbook of Alkali-Activated Cements, Mortars and Concretes.* Woodhead Publishing, Oxford, pp. 605–626.

- Zhang, H.Y., Kodur, V., Wu, B., Cao, L., Wang, F., 2016. Thermal behavior and mechanical properties of geopolymer mortar after exposure to elevated temperatures. *Constr. Build. Mater.* 109, 17–24.
- Zhang, J.X., Jiang, J., Yan, L.C., Lu, J.L., Qian, S.J., Wang, K., et al., 2013. Electrochemical realkalisation and combined corrosion inhibition of deeply carbonated historic reinforced concrete. *Corros. Eng. Sci. Technol.* 48 (1), 28–35.
- Zhang, Z., Yao, X., Zhu, H., 2010a. Potential application of geopolymers as protection coatings for marine concrete: I. Basic properties. *Appl. Clay Sci.* 49 (1–2), 1–6.
- Zhang, Z., Yao, X., Zhu, H., 2010b. Potential application of geopolymers as protection coatings for marine concrete: II. Microstructure and anticorrosion mechanism. *Appl. Clay Sci.* 49 (1–2), 7–12.
- Zhang, Z., Yao, X., Wang, H., 2012. Potential application of geopolymers as protection coatings for marine concrete III. Field experiment. *Appl. Clay Sci.* 67–68 (0), 57–60.
- Zhang, Z., Wang, K., Mo, B., Li, X., Cui, X., 2015. Preparation and characterization of a reflective and heat insulative coating based on geopolymers. *Energ. Buildings.* 87, 220–225.
- Zhao, H., Sun, W., Wu, X., Gao, B., 2015. The properties of the self-compacting concrete with fly ash and ground granulated blast furnace slag mineral admixtures. *J. Cleaner Prod.* 95, 66–74.
- Zhu, H., Zhang, Z., Zhu, Y., Tian, L., 2014. Durability of alkali-activated fly ash concrete: chloride penetration in pastes and mortars. *Constr. Build. Mater.* 65, 51–59.
- Zhu, Y.-G., Kou, S.-C., Poon, C.-S., Dai, J.-G., Li, Q.-Y., 2013. Influence of silane-based water repellent on the durability properties of recycled aggregate concrete. *Cem. Concr. Compos.* 35 (1), 32–38.
- Zhuang, X.Y., Chen, L., Komarneni, S., Zhou, C.H., Tong, D.S., Yang, H.M., et al., 2016. Fly ash-based geopolymer: clean production, properties and applications. *J. Cleaner Prod.* 125, 253–267.

Further reading

- Bernal, S.A., Provis, J.L., 2014. Durability of alkali-activated materials: progress and perspectives. *J. Am. Ceram. Soc.* 97 (4), 997–1008.
- Borges, P.H.R., Costa, J.O., Milestone, N.B., Lynsdale, C.J., Streatfield, R.E., 2010. Carbonation of CH and C–S–H in composite cement pastes containing high amounts of BFS. *Cem. Concr. Res.* 40 (2), 284–292.
- Cañón, A., Garcés, P., Climent, M.A., Carmona, J., Zornoza, E., 2013. Feasibility of electrochemical chloride extraction from structural reinforced concrete using a sprayed conductive graphite powder–cement paste as anode. *Corros. Sci.* 77, 128–134.
- Osborne, G.J., 1999. Durability of Portland blast-furnace slag cement concrete. *Cem. Concr. Compos.* 21 (1), 11–21.
- Topçu, İ.B., 2013. 10 - High-volume ground granulated blast furnace slag (GGBFS) concrete. *Eco-Efficient Concrete*. Woodhead Publishing, pp. 218–240.
- Younsi, A., Turcry, P., Ait-Mokhtar, A., Staquet, S., 2013. Accelerated carbonation of concrete with high content of mineral additions: Effect of interactions between hydration and drying. *Cem. Concr. Res.* 43, 25–33.

This page intentionally left blank

Sulfoaluminate cement-based concrete

14

Kedsarin Pimraksa¹ and Prinya Chindapasirt²

¹Chiang Mai University, Chiang Mai, Thailand,

²Khon Kaen University, Khon Kaen, Thailand

14.1 Introduction

Sulfoaluminate cement (SAC) has been accepted as an environmentally friendly cementitious material because it can be produced at low temperature and low lime saturation factor that consequently lowers the energy consumption and greenhouse gas emission when compared with ordinary Portland cement (OPC) production. Nowadays, the global cement production emits approximately 2 billion tons/year of CO₂ for 2 billion tons of cement. By estimation, in 2025, cement production will emit 3.5 billion tons yearly (Shi et al., 2011). It is a big challenge for cement chemists and civil engineers if SAC can be alternative to replace OPC in the future. Greenhouse gas emissions can be significantly reduced with a use of such alternative. The lower reacting temperature to produce SAC comes from the lower energy requirement to form sulfoaluminate phase. The difference in heat consumption of calcium sulfoaluminate cement and OPC is approximately 805–949 MJ/ton (Gartner and Hirao, 2015). Starting materials such as calcium carbonate and aluminum- and sulfate-bearing materials requires approximately 1250–1350°C to form calcium sulfoaluminate in clinkerization process which is about 100–200°C lower than what is required for the OPC production (Winnefeld and Lothenbach, 2010; Trauchessec et al., 2015). When compared to the alite phase—a main phase of OPC—calcium sulfoaluminate cement emits only one third CO₂ of OPC, which amounts to 1.80 g CO₂/mL and 0.56 g CO₂/mL of the cementing phase for OPC and calcium sulfoaluminate, respectively. Alternative synthesis of SAC, such as the hydrothermal–calcination method, has also been studied for energy saving (Rungchet et al., 2016, 2017). The hydrothermal–calcination method is carried out via an initial dissolution–precipitation step to form intermediate phases then transformation of intermediate phases to required cementitious materials using calcination. The lower transformation temperature is caused by the formation of intermediate submicron- or nano-particles. The lower reaction temperature and the utilization of inorganic waste in the raw mix is feasible (Costa et al., 2016; El-Alfi and Gado, 2016; Rungchet et al., 2016). Concerning the environmental and economic aspects, SAC has recently received much attention. The synthesis of sulfoaluminate cement is explained in Section 14.3.

With regard to its applications, SAC has very promising engineering properties and is considered to be competitive with OPC. For example, setting and hardening

of SAC occurs very rapidly, which is good for repair. Due to the development of swelling phases—such as a tricalcium sulfoaluminate hydrates in the form of ettringite (AFt) after hydration, it is good for special applications such as shrinkage-resistance, self-stress, and self-leveling (Pera and Ambroise, 2004). Its potential to entirely replace OPC is feasible only in terms of workability and strength considerations but will be difficult when applied to reinforced concrete. With SAC, strengths can be obtained which are as high as for standard OPC cured for 28 days (Pera and Ambroise, 2004). The reason for the obstacle in use with steel reinforced concrete is the low pH of sulfoaluminate cement after hydration that can facilitate steel corrosion. There is an attempt to address this issue by producing highly alkaline phases such as tricalcium silicate (C_3S) and dicalcium silicate (C_2S) together with the sulfoaluminate phase. A combination of C_3S is relatively rare because calcium sulfoaluminate phase disappears at the temperature at which C_3S is emerged (Ludwig and Zhang, 2015). Therefore, blending between SAC and OPC might be a solution. Many researchers studied the hydration of a blended system of OPC and calcium SAC (Le Saout et al., 2013) but have not yet investigated the steel corrosion behavior of rebars inside concrete prepared from SAC in the presence of either OPC or such highly alkaline phases. In addition, the expansion mechanism of SACs to obtain positive volume expansion and shrinkage reduction is not well understood (Nocuri-Wczelik et al., 2010). These issues can hamper the practical use of SAC for OPC replacement. Due to its fast setting and hardening, in some applications, the retardation of sulfoaluminate hydration is highly essential to allow better workability. The mechanism of sulfoaluminate hydration in the presence of different retarders is still questionable (Zajac et al., 2016). Therefore, the knowledge with regard to SAC needs to be further developed in order to improve the reliability of its usages for the construction industry.

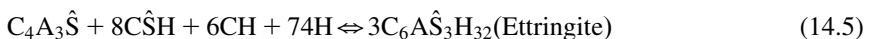
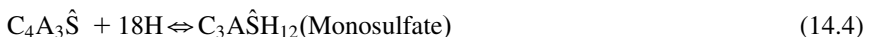
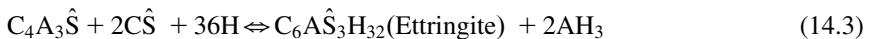
14.2 Definition, type, and usages: sulfoaluminate cement

SAC is any kind of cement containing sulfate and aluminate species in its chemical formula. An example of SAC which is popular are calcium sulfoaluminate phases such as tetracalcium trialuminosulfate or ye'elimite or $C_4A_3\hat{S}$ in which C, A and \hat{S} stand for CaO, Al_2O_3 , and SO_3 , respectively. This cement compound has as mineral name “ye'elimite” or Klein's salt which was introduced in the 1960s by Alexander Klein (Winnefeld and Lothenbach, 2010; Martin-Sedeno et al., 2010). Calcium sulfoaluminate cement is normally found together with other cement phases such as dicalcium silicate, belite or C_2S in which C and S stand for CaO and SiO_2 , respectively. Tetracalcium aluminoferrite or C_4AF in which C, A, and F stand for CaO, Al_2O_3 , and Fe_2O_3 , respectively, is also commonly found when starting materials contain some iron compounds. Ye'elimite has been reported in various forms: orthorhombic, body-centered cubic, or tetragonal crystal structures. Ye'elimite is an end member of sodalite ($Na_8(Al_6Si_6O_{24})Cl_2$), in which Na^+ and Si^{4+} are replaced by Ca^{2+} and Al^{3+} , respectively (Hargis, 2013). The framework

structure of ye'elimite which is more open than that of C_3S and C_2S , resulting in the density of ye'elimite (2.61 g/cm^3) being lower than OPC (3.13 g/cm^3).

Calcium sulfoaluminate-belite (CSAB) cement has been found to be a good combination, as the reaction of $C_4A_3\hat{S}$ and dihydrate calcium sulfate (gypsum) is responsible for rapid setting and hardening due to ettringite (AFt) formation, while C_2S consumes the by-product of the $C_4A_3\hat{S}$ hydration to form useful binding phases for later stages as stated in Eqs. (14.1) and (14.2), respectively. The hydration of $C_4A_3\hat{S}$ takes place very rapidly. The strength which can be obtained with CSA concrete amounts to 65–70 MPa within 1 day which is almost twice the strength which can be obtained with OPC concrete (Ioannou et al., 2015). Use of different forms of calcium sulfate, such as anhydrite, also provides AFt as stated in Eq. (14.3), similar to the use of dihydrate calcium sulfate or gypsum. Without the calcium sulfate compound, the $C_4A_3\hat{S}$ hydration product is monosulfate (AFm) as stated in Eq. (14.4) which does not provide sufficient strength for the requirements at early age (Juenger et al., 2011). The combination between $C_4A_3\hat{S}$ and C_2S in the absence of calcium hydroxide (CH) was recommended by many researchers to obtain highly durable material, due to the formation of stratlingite (CASH) phase incorporating AFt (Winnefeld and Lothenbach, 2010; Juenger et al., 2011). Winnefeld and Lothenbach proposed modeling phase diagrams of hydrated CSA cements as shown in Fig. 14.1, which are in alignment with the above mentioned equations. Two CSA cements were used in comparison. The CSA-1 consisted of 50 wt% of ye'elimite, 15 wt% of gehlenite, 8% of calcium aluminate, and 22 wt% of gypsum. CSA-2 consisted of 54 wt% of ye'elimite, 19 wt% of belite and 21 wt% of anhydrite. The experiment proved that, without C_2S , there was no stratlingite formation.

SAC is named after the existing phases inside SAC. Table 14.1 shows the types of SACs. The coexistence of $C_4A_3\hat{S}$ and C_3S is quite difficult as the reaction temperature of C_3S is high while $C_4A_3\hat{S}$ is unstable at high temperature. Therefore, the main phase of alite-rich CSA is $C_4A_3\hat{S}$ instead of C_3S .



Each phase inside CSA has its own responsibility to enhance the durability of the hardened materials. For example, as stated earlier, C_2S assists to consume AH_3 left over from $C_4A_3\hat{S}$ hydration to form calcium aluminosilicate hydrate in the form of stratlingite. In addition, it helps to take charge of the pH enhancement for $C_4A_3\hat{S}$ due to the generation of $Ca(OH)_2$ for the system. C_3S works in a similar way to

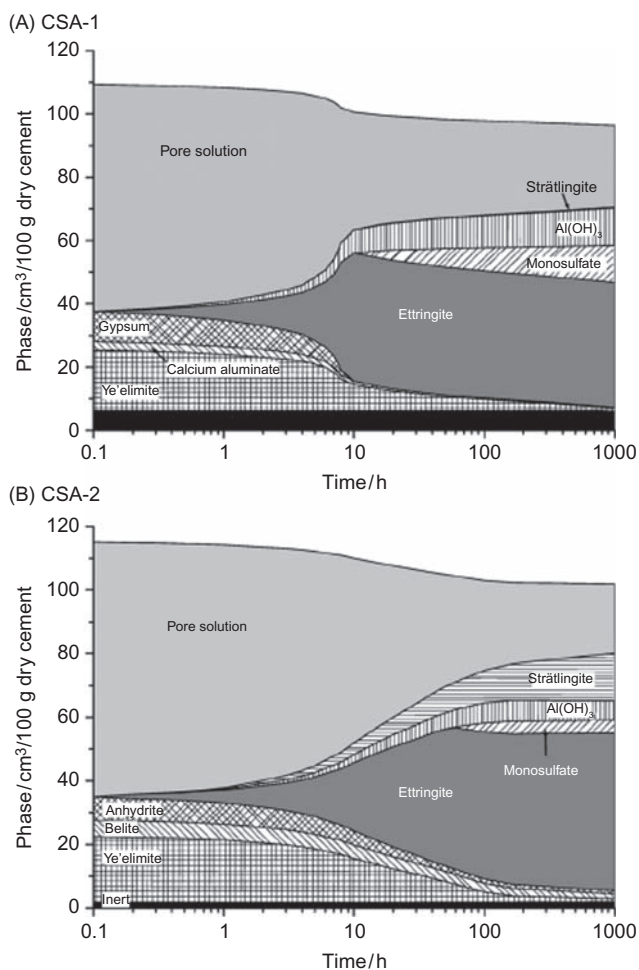


Figure 14.1 Modeled changes of phase volume during hydration of (A) CSA-1 and (B) CSA-2 (Winnefeld and Lothenbach, 2010).

Table 14.1 Type of sulfoaluminate cements (SACs) and their components

Name (Acronym)	Main phase	Minor phases
Calcium sulfoaluminate cement (CSA)	$C_4A_3\hat{S}$	C_2S , C_4AF , $C\hat{S}$, $C_{12}A_7$
Calcium sulfoaluminate-belite cement (CSAB)	$C_4A_3\hat{S}$	C_2S , C_4AF , $C\hat{S}$, $C_{12}A_7$
Belite-rich calcium sulfoaluminate cement (BCSA)	C_2S	$C_4A_3\hat{S}$, C_4AF
Belite-sulfoaluminoferrite cement (BCSAF)	$\alpha-C_2S$, $C_4A_3\hat{S}$ and C_2A_xF ($1-x$)	$C_{12}A_7$
Alite-rich calcium sulfoaluminate cement (ACSA)	$C_4A_3\hat{S}$	C_3S , C_2S

C_2S , and even faster to increase the pH of the system. Not only the increase in pH, but the presence of $Ca(OH)_2$ after C_3S hydration helps to accelerate the hydration of $C_4A_3\hat{S}$. Ettringite obtained from the system with $Ca(OH)_2$ is more substantial than that without $Ca(OH)_2$ as stated in Eq. (14.5). The formation of larger amounts of AFt can cause high expansion. C_4AF and $C_{12}A_7$ are both aluminate phases which can provide additional AFt for the system. Therefore, the amount of calcium sulfate phases to react with those aluminate cement phases ($C_4A_3\hat{S}$, C_4AF , and $C_{12}A_7$) is a very important factor in order to obtain sufficient AFt phase leading to rapid setting and high early strength. For example, a molar ratio of $C_4A_3\hat{S}:CaSO_4 \cdot 2H_2O$ or $C_4A_3\hat{S}:CaSO_4$ of 1:2 is desirable in order to obtain Aft, according to Eqs. (14.1) and (14.3).

For 30 years, CSAs have been intensively used in China in its concrete for constructions such as bridges, pipes, leakage, and seepage prevention materials, precast concrete, repair materials, etc. (Moffatt and Thomas, 2017). Its usage is similar to OPC, more advantageous in term of its early strength development and expansive behavior. Therefore, CSA cement is considered for special applications, such as shrinkage-resistant and self-stressing cements. Self-leveling screed with limited curling and self-leveling repair mortar are also possible due to its expansive property. In addition, CSA cement behaves better than OPC as a matrix for glass fiber reinforcement to secure glass fiber deterioration due to its lower alkalinity (Pera and Ambroise, 2004). Modified CSA with dispersed polymer powders such as vinyl acetate ethylene were also studied in order to improve the adhesion capability of CSA for construction (Brien, 2014). CSA is used as oilwell cement for offshore processing areas instead of OPC because its expansive and low elastic modulus properties decreases the permeability of the set concrete—major requirements for the well construction. Whereas, OPC is more brittle and prone to being more permeable (Liu et al., 2016). Waste encapsulation is also one of the major applications for CSA cement including solidifications of nuclear waste and toxic metal oxides (Luz et al., 2006; Sun et al., 2011).

14.3 Production of sulfoaluminate cement

Production of SAC is more environmental friendly due to its lower firing temperature (less than $1250^\circ C$ for clinkerization process) and lower CO_2 emission when compared to the OPC production (which requires up to $1450^\circ C$) (Winnefeld and Lothenbach, 2010; Trauchessec et al., 2015). Currently, much attention is paid to the synthesis through hydrothermal–calcination process due to many benefits such as lower reaction temperature (less than $1100^\circ C$) and higher reactivity of the cement due to the finer particle size, and better morphology when compared to that from the traditional process such as clinkering. In addition, the utilization of inorganic wastes for CSA production is also feasible in both the clinkerization and the hydrothermal–calcination processes. The estimation of mineralogical phases of cement clinkers is based on the modified Bogue equations for the $CaO-SiO_2-Al_2O_3-Fe_2O_3-SO_3$ system

(Iacobescu et al., 2013). The calculation of cement phases (C_4AF , C_2S , $C_4A_3\hat{S}$, $C\hat{S}$, and C) is performed using Eqs. 14.6–14.10.

$$\%C_4AF = 3.043(\%Fe_2O_3) \quad (14.6)$$

$$\%C_4A_3\hat{S} = 1.995(\%Al_2O_3) - 1.273(\%Fe_2O_3) \quad (14.7)$$

$$\%C_2S = 2.867(\%SiO_2) \quad (14.8)$$

$$\%C\hat{S} = 1.700(\%SO_3) - 0.445(\%Al_2O_3) + 0.284(\%Fe_2O_3) \quad (14.9)$$

$$\begin{aligned} \%C = & 1.000(\%CaO) - 1.867(\%SiO_2) - 1.054(\%Fe_2O_3) \\ & - 0.550(\%Al_2O_3) - 0.700(\%SO_3) \end{aligned} \quad (14.10)$$

14.3.1 Production of calcium sulfoaluminate-belite cement using the clinkerization process

The clinkerization process has been used since many decades and involves solid state reaction between oxides of starting materials. Due to the solid state reaction, high energy is required to allow the diffusion of atoms and molecules of crystals. Raw materials used to produce CSA (ye'elimite or $4CaO \cdot 3Al_2O_3 \cdot SO_3$ or $C_4A_3\hat{S}$) can be any matter that can supply CaO , Al_2O_3 , and SO_3 . Pure reagents such as calcite ($CaCO_3$), alumina (Al_2O_3), and calcium sulfate compounds ($CaSO_4$, $CaSO_4 \cdot 1/2H_2O$, $CaSO_4 \cdot 2H_2O$) are a good choice to produce pure CSA or ye'elimite phases. The required stoichiometry is 4:3:1 for $CaO:Al_2O_3:SO_3$ to obtain $4CaO \cdot 3Al_2O_3 \cdot SO_3$. The ye'elimite phase and the belite phases are unavoidably formed when starting materials contain SiO_2 . This cement is therefore called "CSAB." There were several reports of using various inorganic wastes to produce CSA cement. El-Alfi and Gado (2016) used marble sludge waste from a marble processing factory to prepare CSAB cement via clinkerization. This waste mainly contained only calcite ($CaCO_3$), as identified by X-ray diffraction. To synthesize CSAB, hemihydrates calcium sulfate and kaolin were the sources of sulfate and Al_2O_3 , respectively, to form ye'elimite. This research showed a preference to form ye'elimite when the kaolin (Al_2O_3 source) content was increased. The recommended conditions were 25:20:55 of kaolin:hemihydrate:marble waste and only $1200^\circ C$ of firing temperature. The calculated cement phase using the modified Bogue equations consisted of 22.30% of ye'elimite, 43.6% of C_2S , 1.58% of C_4AF , 18.62% of calcium sulfate and 3.76% of CaO . The strength development after cement hydration was about 36MPa (28 days curing) without additional calcium sulfate compound. Costa et al. (2016) studied the production of CSAB cement using aluminum anodizing sludge as Al_2O_3 source. Aluminum waste contained mainly Al_2O_3 and SO_3 approximately 73.6 wt% and 20.5 wt%, respectively. The raw mix contained 18.5:7.3:72.9 of aluminum anodizing sludge:calcium sulfate:lime stone.

The raw mix was fired at 1250°C for 30 minutes. The resulting CSAB composed of 28.8 wt% of orthorhombic ye'elimite, 6.7 wt% of cubic ye'elimite, 39.1 wt% of belite, 7.4 wt% of brownmillerite (C₄AF), 4 wt% of anhydrite, 8.2 wt% of alite and 5.9 wt% of periclase. The measured belite (C₂S) and alite (C₃S) formations were questionable because starting materials had no SiO₂ content. The compressive strength of hydrated paste at 28 days curing was 41.7 MPa. Viani and Gualtieri (2013) used thermal transformed cement–asbestos to prepare calcium sulfoaluminate cement. The cement–asbestos mineral, which was a CaO and SiO₂ source, composed of 33.1 wt% of SiO₂, 49.2 wt% of CaO, 5 wt% of Al₂O₃, 7.67 wt% of MgO, and 2.12 wt% of Fe₂O₃. β-C₂S, amorphous, C₄AF, mayenite and periclase of this waste were approximately 62 wt%, 13 wt%, 5.5 wt%, 7.3 wt%, and 5.0 wt%, respectively. This waste was used to prepare CSA using 29:25:15:31 of cement–asbestos: gibbsite: gypsum: calcite. The given cement consisted of 41.6 wt% of ye'elimite, 26.3 wt% of β-C₂S, 1.4 wt% of C₄AF, 9.2 wt% of CaO, 8.3 wt% of CaSO₄, and 11 wt% of amorphous phase. There was no report on strength development in this work. Iacobescu et al. (2013) synthesized calcium ferroaluminate belite cements using electric arc furnace steel slag (EAFS) as one of the raw materials. EAFS composed of 32.50 wt% of CaO, 26.30 wt% of FeO, 18.10 wt% of SiO₂, 13.30 wt% of Al₂O₃, 3.94 wt% of MnO, 2.53 wt% of MgO, and 1.38 wt% of Cr₂O₃. Mineralogical compositions of EAFS were 41 wt% of C₂S, 14.7 wt% of gehlenite, 12.0 wt% of wustite, 10.0 wt% of magnetite, 9.4 wt% of C₄AF, 7.2 wt% of C₁₂A₇, 3.7 wt% of merwinite, and 2.0 wt% of spinel. The used raw mix was 62:20:8:10 of lime stone:bauxite:gypsum:EAFS. The obtained cement contained 44.6 wt% of C₂S, 33.0% of C₄AF, 19.7 wt% of ye'elimite, and 3.9 wt% of calcium sulfate calculated by Rietveld X-ray diffraction. The calculated and measured mineralogical compositions were relatively similar. After hydration, the cement with addition of 20 wt% FGD–gypsum (flue-gas desulfurization–gypsum) could gain strength up to 44 MPa at 28 days curing. Katsioti et al. (2006) examined the use of jarosite–alunite precipitates from a stage of a new hydrometallurgical process in order to produce SAC clinker. The jarosite–alunite precipitate consisted of 16.55 wt% of Al₂O₃, 39.66 wt% of Fe₂O₃, 1.20 wt% of SiO₂, and 44.98 wt% of SO₃. The precipitate can be Al₂O₃, Fe₂O₃, and SO₃ sources. The mineralogical compositions were jarosite, goethite, akaganeite, epsomite, and alunite. The raw mix contained 52.4:30.9:5.4:11.3 of lime stone:bauxite:gypsum:jarosite–alunite. The firing temperature was set at 1300°C. As calculated by the modified Bogue equations, the obtained cement clinker consisted of 44.90 wt% of C₂S, 16.37 wt% of C₄AF, 28.35 wt% of C₄A₃Ŝ, and 10.18 wt% of CaSO₄. There was no report of the additional calcium sulfate compound. The strength development of the cement after hydration was approximately 34 MPa at 28 days curing. The strength developed from those several SACs was promising when compared to commercial CSA cement (Trauchessec et al., 2015). The shortage of Al₂O₃-bearing materials to produce CSA cement is now a serious concern worldwide. Looking for alternative inorganic wastes such Al₂O₃-containing materials is inevitable. The previous research lists, as mentioned above, are good examples for substituting the primary Al₂O₃ source. Bauxite residue from Bayer's process (Al₂O₃ manufacturing process) was currently

considered to produce calcium sulfoaluminate cement, due to its great availability all over the world (approximately 2.7 billion tons) (Pontikes and Angelopoulos, 2013). The average chemical compositions of the bauxite residue was 46.1 wt% of Fe_2O_3 , 18.4 wt% of Al_2O_3 , 10.8 wt% of SiO_2 , 9.9 wt% of TiO_2 , 9.7 wt% of CaO , 5.1 wt% of Na_2O . Its mineralogical compositions can be in various forms; hematite ($\alpha\text{-Fe}_2\text{O}_3$), goethite ($\alpha\text{-FeOOH}$), magnetite (Fe_3O_4), boehmite ($\gamma\text{-AlOOH}$), gibbsite ($\gamma\text{-Al(OH)}_3$), diaspore ($\gamma\text{-AlOOH}$), sodalite, crancrinite, quartz, rutile, anatase, calcite, etc. The bauxite residue has been used to produce belite-sulfoaluminoferrite cement (BCSAF) at an industrial scale by Lafarge to obtain $\alpha\text{-C}_2\text{S}$, $\text{C}_4\text{A}_3\hat{\text{S}}$ and $\text{C}_2\text{A}_x\text{F}(1-x)$ solid solution which showed similar performance compared to OPC.

There was a study in the synthesis of alite–ye’elimite cement (Ma et al., 2013). Alite phase was preferred rather than belite in a combination with ye’elimite in terms of its steel corrosion resistance and very high early strength requirement. However, the process to produce alite–ye’elimite cement is more complicated because the formation temperature of alite and ye’elimite is different. As previously mentioned, a suitable temperature for ye’elimite formation is below 1300°C while the alite formation requires heating up to 1300°C . This study proposed different firing profiles compared to previous studies. Two-cycle firing was carried out in order to sustain both phases. A first cycle was at 1450°C for 30 minutes, followed by air-quenching. The second cycle was at 1250°C for 1 hour followed by air-quenching. The subsequent cement clinker consisted of ye’elimite, alite, C_4AF , C_3A , and anhydrite. For one cycle of firing, the cement clinker had lower contents of ye’elimite and alite but larger amounts of C_3A . For two-step firing, the first and second cycles were to form alite (C_3S) and ye’elimite ($\text{C}_4\text{A}_3\hat{\text{S}}$), respectively. With two-cycle firing, C_3A and anhydrite were transformed to $\text{C}_4\text{A}_3\hat{\text{S}}$ and C_4AF during the second step.

The idea to produce belite sulfoaluminate (BSA)–ternesite cement was proposed, in order to study its hydration and strength development (Shen et al., 2015). Ternesite is calcium sulfoasilicate ($\text{C}_5\text{S}_2\hat{\text{S}}$) which can be formed when excess calcium sulfate exists together with belite (C_2S) phase at approximately $1150\text{--}1250^\circ\text{C}$. Above 1250°C , ternesite decomposes. There were many reports indicating a slow hydration of ternesite but providing better hydration at later age. Due to different formation temperatures of $\text{C}_4\text{A}_3\hat{\text{S}}$ and $\text{C}_5\text{S}_2\hat{\text{S}}$, heat treatments of two cycles were used to maintain ternesite in the clinker. The first and second cycles were carried out at 1270°C and $1000\text{--}1200^\circ\text{C}$, respectively. With the use of one cycle, there was no ternesite formation in the clinker. BSA–ternesite cement synthesized with the second cycle heat treatment at 1150°C for 15 minutes, contained 34.5 wt% of $\text{C}_4\text{A}_3\hat{\text{S}}$, 20.3 wt% of C_2S , 8.2 wt% of C_4AF , 5.1 wt% of $\text{C}\hat{\text{S}}$, and 31.9 wt% of $\text{C}_5\text{S}_2\hat{\text{S}}$. For BSA cement, 33.8 wt% of C_2S (33.8 wt%) was formed instead of ternesite together with 38.9 wt% $\text{C}_4\text{A}_3\hat{\text{S}}$. With regard to strength development, BSA cement had better early age compressive strength but BSA with ternesite gained the better strength at later ages while gaining similar heat evolution. The difference between hydration product development of BSA and BSA–ternesite clinkers was the development in stratlingite phase from BSA–ternesite clinker, whereas no stratlingite was formed from BSA clinker. It

was believed that stratlingite was causing the later age strength development (Martin et al., 2017).

14.3.2 Production of calcium sulfoaluminate cement using hydrothermal–calcination process

The hydrothermal–calcination process was developed several years ago by Jiang and Roy (1992). It has several advantages over the clinkerization or firing process. The obtained products have finer particle sizes, greater surface area and a more homogeneous morphology. In addition, the energy required for processing is much lower. However, its drawback is the requirement of a two-step process that can obstruct its final use. Hydrothermal synthesis consists of two reaction steps under high pressure (>1 atmospheric pressure) and temperature; dissolution, and precipitation. The precipitates are commonly in the form of hydrated phases so called “intermediate phases” which would be transformed to the final cement product after heat treatment or calcination. The hydrothermal process was used to synthesize highly reactive belite (C_2S) cement in the first era by Ishida et al. (1992) and Garbev et al. (2014). Ishida et al. (1992, 1993) and Sasaki et al. (1993) showed that the intermediate phases after the hydrothermal process are crucial to obtain various types and characteristics of products after calcinations. From these previous works, the α -dicalcium silicate hydrate ($Ca_2(HSiO_4)(OH)$), hillebrandite ($Ca_2(SiO_3)(OH)_2$), and dellaite ($Ca_6(SiO_4)(Si_2O_7)(SiO_4)(OH)_2$) phases were obtained as intermediate phases by hydrothermal treatment at temperatures between 100–250°C. Hillebrandite phase is recommended to produce more reactive C_2S than α -dicalcium silicate hydrate and dellaite phases.

Only a few works used the hydrothermal–calcination process to synthesize ye’elimite ($C_4A_3\hat{S}$). This is possibly due to the difficulty in processing that requires two main working steps. Rungchet et al. (2016) synthesized calcium sulfoaluminate-belite cement (CSAB) from industrial waste materials such fly ash (FA), aluminum-rich sludge, and FGD–gypsum. Commercial grade hydrated lime ($Ca(OH)_2$) was also used to correct the stoichiometry of the mix. The mix proportion was stoichiometrically weighed by combining the raw materials at 45:20:25:10 of $Ca(OH)_2$:FA:aluminum sludge:FGD–gypsum to obtain a raw mix with 4:3:1 for $CaO:Al_2O_3:SO_3$ and 2:1 for $CaO:SiO_2$ in combination. The hydrothermal treatment was carried out using an autoclave at 130°C. The studied factor was the reaction time under hydrothermal treatment at 1, 3, 6, and 9 hour. The second stage of the synthesis was calcination of the hydrothermal products in an electric furnace at various temperatures between 750°C and 1150°C, with a heating rate of 5°C/min and remaining at the maximum temperature for 1 hour. At 6 hour of hydrothermal treatment, nonalkaline activation hydrothermal treatment (H_2O) led to a complete dissolution of anhydrite containing FA and a precipitation of AFt from the reaction between the dissolved anhydrite and aluminum species present in aluminum sludge (AS) and FA. The formation of cebolite, a calcium aluminum silicate hydroxide ($Ca_5Al_2Si_3O_{12}(OH)_4 \cdot C_5AS_3H_2$) could also be observed. The presence of C–S–H ($Ca_{1.5}SiO_{3.5-x}H_2O$; $C_{1.5}SH_x$) was confirmed by differential scanning calorimetry

(DSC) with an endothermic peak at 160–180°C. The sources of silicon and aluminum for both cebolite and C–S–H formations came from the dissolution of amorphous phases of FA and AS. The alkaline-activated hydrothermal treatment (1 M NaOH) resulted in the formation of new hydration phases called katoite ($\text{Ca}_3\text{Al}_2\text{SiO}_4(\text{OH})_8$; C_3ASH_4). The reflection of portlandite indicated that the pozzolanic reaction of FA under steam pressure and alkaline activation were limited. Whereas the reaction without alkali under the same hydrothermal temperature showed no portlandite leftover. In the alkaline activated system, sulfate available from the dissolution of anhydrite was found as thenardite (Na_2SO_4 ; $\text{N}\hat{\text{S}}$), according to the following reaction: $\text{CaSO}_4 + \text{NaOH} \rightleftharpoons \text{Ca}(\text{OH})_2 + \text{Na}_2\text{SO}_4$ (Kacimi et al., 2010). However, no trace of either AFt or monosulfoaluminate (AFm) was found, even though sulfates were available in the system. This was probably due to the formation of calcium aluminum silicate sulfate gel, as confirmed by the presence of a broad hump around the 10–30 degrees (2θ) region using XRD. Moreover, with the use of water without hydrothermal treatment, phase development was similar to those with hydrothermal treatment, showing the presence of AFt and AFm. The only difference was the higher content of AFt and AFm phases with the hydrothermal treatment. Hydrothermal treatment assisted more rapid precipitation and growth of the products.

After calcination (1050°C), ye'elimite ($\text{C}_4\text{A}_3\hat{\text{S}}$) and $\beta\text{-C}_2\text{S}$ phases were obtained in all conditions, but the intensities or quantities of phases differed depending on the treatment used. Fig. 14.2 shows the formation of ye'elimite and belite phases using

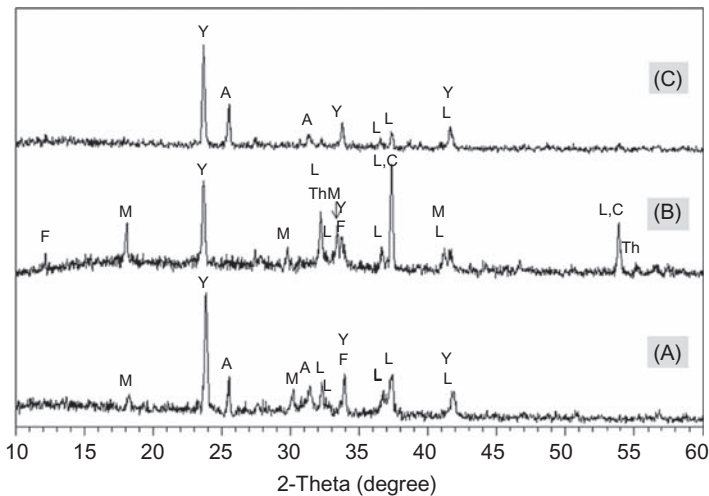
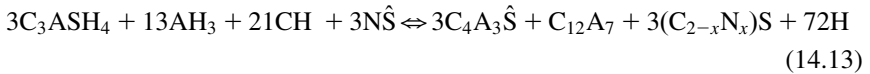
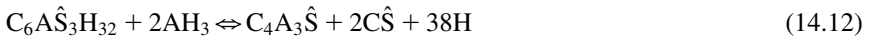


Figure 14.2 XRD pattern of calcinations products after calcining at 1050°C obtained from hydrothermal products (A) under water and hydrothermal treatment, (B) under 1 M NaOH and hydrothermal treatment, and (C) under water with no hydrothermal treatment. Y, Ye'elimite; L, Belite; A, Anhydrite; M, Mayenite; Th, Thernardite; F, Brownmillerite; C, Lime (Rungchet et al., 2016).

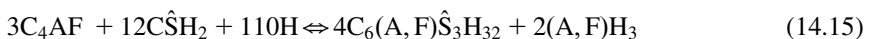
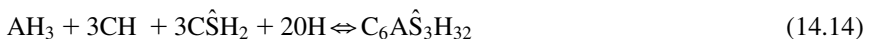
different conditions of synthesis. Mixtures with non-alkaline activation under hydrothermal treatment gave the highest content of $C_4A_3\hat{S}$, but only a small amount of $\beta\text{-}C_2S$. In addition, the calcination products contained anhydrite indicating an incomplete combination of calcium, aluminum and sulfate to form the $C_4A_3\hat{S}$ phase. However, $C_{12}A_7$ —an intermediate phase formed during calcination—reacted further with anhydrite and formed $C_4A_3\hat{S}$, one of the hydraulic phases as shown in Eq. (14.11). Here, an intermediate phase such as AFt played an important role in the conversion reaction to form $C_4A_3\hat{S}$ as shown in Eq. (14.12). It is worth noting that without alkaline treatment, cement mix preferred the formation of $C_4A_3\hat{S}$ instead of C_2S . Alkaline activation with 1 M NaOH conditions led to the complete formation of both $C_4A_3\hat{S}$ and $\beta\text{-}C_2S$ phases. Although no AFt phase was developed under hydrothermal treatment, $C_4A_3\hat{S}$ could be formed via the reaction between katoite, gibbsite, portlandite, and thenardite. In addition, katoite also played an important role in the formation of $\beta\text{-}C_2S$, as shown in Eq. (14.13), where $N = Na_2O$. The alkaline activation also enhanced the formation of $C_{12}A_7$ instead of $C_4A_3\hat{S}$ after calcinations.



After calcinations at 1150°C , $C_{12}A_7$ lost its stability and converted to tricalcium aluminate (C_3A), a new-formed product. At this temperature, the partial melting of aluminate and silicate phases led to the decomposition of $C_4A_3\hat{S}$ and $\beta\text{-}C_2S$. With this method of synthesis, C_3A which is normally formed about $1,300^\circ\text{C}$ using the clinkerization, could be obtained at only 1150°C . To summarize, CSAB cement could be synthesized at temperatures between 950°C and 1050°C , which is about $200\text{--}300^\circ\text{C}$ lower than the temperature used in the traditional CSAB production. Additional 20 wt% of FGD—gypsum ($\text{CaSO}_4 \cdot 2\text{H}_2\text{O}$) was added to observe hydration of the synthesized CSAB cement. The resulting cement set very quickly, with acceptable compressive strengths of 30.0 MPa and 23.0 MPa at 28 days of curing for nonalkaline-activated cement and alkaline activated cement, respectively. The initial setting times of nonalkaline-activated cement and alkaline-activated cement were 15 and 7 minutes, respectively. The faster setting time of nonalkaline-activated cement (lower $C_4A_3\hat{S}$ than alkaline-activated cement) was due to the presence of $C_{12}A_7$ which was more reactive than $C_4A_3\hat{S}$. It is notable that the water to cement ratio used in this research was 0.8 which was more than the one used in previous research works. This was due to the larger surface area of CSAB cement obtained from the hydrothermal—calcination method. In practice, water reducing agent should be added to keep its flow ability as well as higher strength.

14.4 Hydration of sulfoaluminate cement

The hydration of SAC means the chemical reaction to transform SAC to hydrated phases which can set and harden over time. In general, hydration consists of two main stages. The first stage is the dissolution of SAC. The dissolution rate is dependent on the reactivity of each phase in SAC. For example, the reactivity of cementitious materials is as follows; $CA > C_{12}A_7 > C_4A_3\hat{S} > C_4AF > C_2S$. The second stage consists of precipitation of the hydration products. The precipitation rate is dependent on the dissolution rate and other factors such as hydration temperature, the presence of accelerators and retarders, etc. The amount of precipitation is dependent on the water content and additive content such as calcium sulfate and CH, etc. Physical and mechanical properties of the set materials depend on the characteristics of the precipitates such as type, fineness, particle shape, specific surface area, particle–particle interaction or its compactness. Generally, hydration of $C_4A_3\hat{S}$ chemically requires calcium sulfate ($C\hat{S}$) to form new compounds in the form of trisulfoaluminate hydrate or ettringite ($Ca_6Al_2(SO_4)_3(OH)_{12} \cdot 26H_2O$ or $C_6A\hat{S}_3H_{32}$ or $C_3A \cdot 3C\hat{S} \cdot 32H$ or AFt), which can set and harden rapidly according to Eqs. (14.1) and (14.3). Without calcium sulfate, $C_4A_3\hat{S}$ undergoes hydration to form AFm phase ($Ca_4Al_2(SO_4) \cdot 12H_2O$ or $C_3A\hat{S}H_{12}$ or $C_3A \cdot C\hat{S} \cdot 12H$ or AFm) as stated in Eq. (14.4). The formation of AFt results in rapid setting, high early strength, and expansive properties. Shrinkage compensation properties therefore come from the formation of AFt. It is believed that the greater the content of AFt, the larger expansion of the set cement can be obtained. A large amount of AFt can be generated from the hydration of $C_4A_3\hat{S}$ and calcium sulfate with the presence of CH, as stated in Eq. (14.5). Hydration of belite (C_2S) without calcium hydroxide, stratlingite (CASH) can be formed as AH_3 , a by-product of $C_4A_3\hat{S}$ hydration which also plays a role in C_2S hydration as stated in Eq. (14.2). With the presence of CH and sufficient calcium sulfate compound, AH_3 can further react with both of them to generate additional AFt at the early stage as stated in Eq. (14.14). Therefore, C_2S hydration results in the formation of calcium silicate hydrate (C–S–H) instead of stratlingite. C_4AF phase also plays a role with regard to the supply of ettringite as stated in equation by Chen et al. (2012). Major factors generally affecting the hydration of SACs are the type of ye’elimite; the type and amount of the existing major and minor phases; the type and amount of calcium sulfate compounds (anhydrite, bassanite and gypsum); the presence of CH, and the water content.



Expansive behavior is very important in the case of hydration of CSA and cannot be overlooked as it can harm and deteriorate structures of the set cement and concrete. Chen et al. studied the expansion in CSAB cement in order to understand the

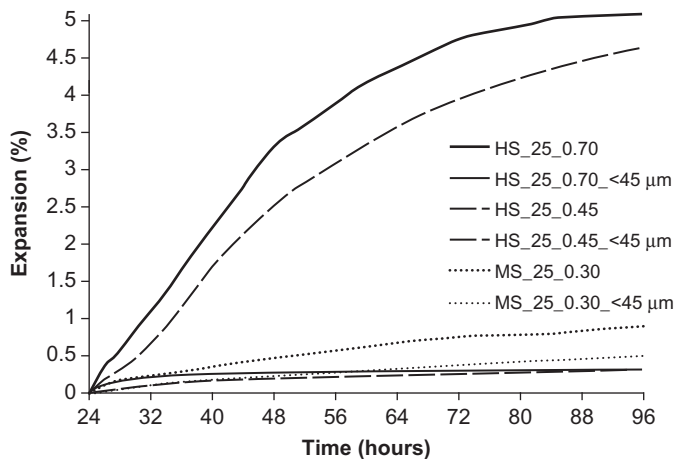


Figure 14.3 Dimensional stability for the HS (High CSA) and MS (Medium CSA) CSAB cement pastes with differing PSDs and w/c cured in ultra-pure water after demolding at 1 day (Chen et al., 2012).

factors affecting expansion (Chen et al., 2012). The factors that played a role on expansion related to the AFt formation. The factors included amount of ye'elimite ($C_4A_3\hat{S}$) in CSAB cement, particle size distribution of CSAB cement, amount of added gypsum, water to cement ratio, and type and content of salts. The study showed that higher amounts of $C_4A_3\hat{S}$ phase tended to result in larger expansion. CSAB cement with $C_4A_3\hat{S}$ content of 65.3 wt% (HS), together with additional 15, 20, and 25% wt of gypsum, encompassed expansion approximately 1.0 wt%, 3.5 wt%, and 3.7 wt%, respectively at three days curing. The gypsum additions of 15–20 wt% and 25 wt% are to generate understoichiometry and overstoichiometry, respectively—as stated by Chen et al. Medium CSAB (MS)—CSAB with lower $C_4A_3\hat{S}$ content (about 42.0 wt% which requires 19.2 wt% of gypsum in theory)—with additional 15% gypsum added, showed a slight expansion of only 0.25% at 3 days curing, as shown in Fig. 14.3. With overstoichiometry of gypsum at 20 and 25 wt%, $C_4A_3\hat{S}$ content of 42.0 wt% expanded very slightly, even less than that with 15 wt% gypsum: only 0.15 and 0.20 wt%, respectively. Therefore, expansive behavior was stronger with high $C_4A_3\hat{S}$ content rather than with high gypsum content. The results also showed that the lower the water to cement ratio, the higher expansion could be obtained due to the dense pore structure. The externally supplied water can cause expansion, due to further hydration, to form expansive AFt in the hardened structures. When CSAB was ground to sizes smaller than 45 μm , the expansion of the cement with $C_4A_3\hat{S}$ content of 65.3 wt% was greatly reduced from 4.5 to 0.25 wt% after 3 days curing and w/c of 0.70. With the lower w/c ratio (0.45), a decrease in particle size of CSAB cement significantly decreased the expansion. The CSAB cement with the lower content of $C_4A_3\hat{S}$ also exhibited the same behavior.

14.4.1 Role of ye'elimite type

As stated before, ye'elimite occurs in various forms; orthorhombic, body-centered cubic, and with tetragonal crystal structures. It is believed that the reactivity of each form is different, due to the difference in crystal lattice energy that results in the difference in dissolubility. Jansen et al. studied the early hydration of two modifications of ye'elimite (Jansen et al., 2017). Orthorhombic (stoichiometric) and cubic (iron containing) phases of ye'elimite were synthesized in this study. In addition to iron, sodium could also work as phase stabilizer to maintain the cubic structure at room temperature, as suggested by Andrac and Glasser (1994). Pure chemicals were used to synthesize stoichiometric $C_4A_3\hat{S}$ (orthorhombic) and $C_4A_{2.7}F_{0.3}\hat{S}$ (cubic), at 1350 and 1250°C, respectively (Jansen et al., 2017). After milling, both clinker powders after milling had the same specific surface area. CA and CF were impurities for orthorhombic and cubic ye'elimite, respectively. Prepared samples consisted of 32 wt% of ye'elimite, 18 wt% of gypsum, and 50 wt% of inert material. During hydration, ettringite could be observed after around 3 hour with the use of orthorhombic ye'elimite and gypsum. No other hydration products besides AFt could be formed. Comparing dissolved ions when ye'elimite reacted with gypsum, Ca and Al ions of cubic ye'elimite were found in a slightly greater amount than for orthorhombic ye'elimite at the beginning of the reaction. After 1 hour hydration, those ions were depleted from the solutions to form AFt. From the heat flow curve, the induction period of cubic ye'elimite was shorter than that of orthorhombic ye'elimite for with and without gypsum additions, as shown in Fig. 14.4. Total heat of hydration for orthorhombic and cubic ye'elimite phases were 515 J/g_{cement} and 469 J/g_{cement}, respectively. Both phases showed similar dissolution and precipitation

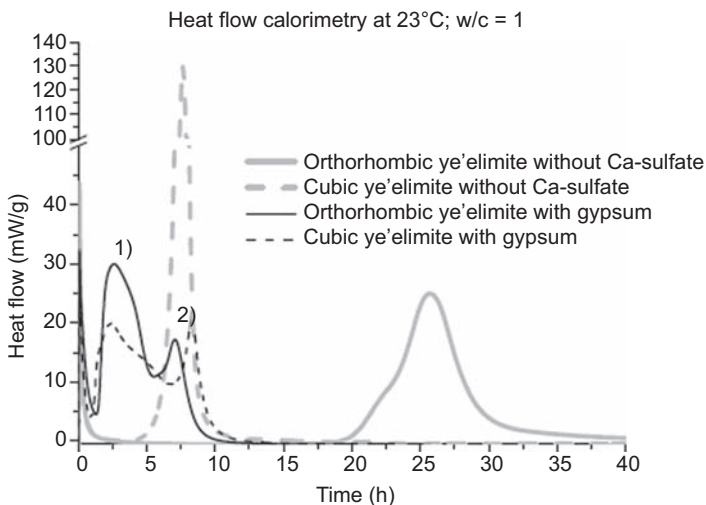


Figure 14.4 Heat flow curves for synthesized ye'elimite with and without gypsum added (Jansen et al., 2017).

rates. A slight difference was found with the slower ye'elimite consumption and less AFt formation in the iron containing system (cubic ye'elimite). It implied that the modification of the ye'elimite phase slightly changed the hydration kinetics.

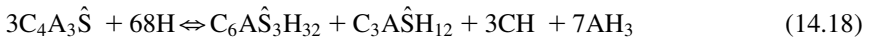
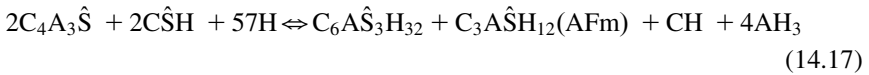
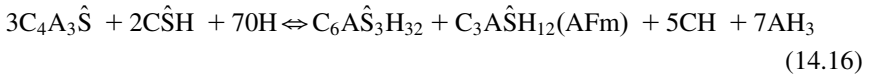
14.4.2 Role of sulfate type and content

As sulfate compounds play a great role in the formation of new phases, which are in charge of strength development according to Eqs. (14.1–14.5) and (14.11–14.15), it is very important to look at the chemistry of sulfate compounds carefully, in order to get the right characteristics and properties of products. Garcia-Mate et al. (2015) investigated the effect of the calcium sulfate source on the hydration of CSA. Calcium sulfoaluminate clinker was mixed with 25% of each calcium sulfate compound (anhydrite, bassanite, gypsum). The rheological behavior of those three different mixes showed shear thinning or pseudoplastic behavior, at which the viscosity decreases with an increase in shear rate. Mixing with bassanite showed the highest viscosity, which corresponded to the fastest initial setting time of ~20 minutes. This was due to the largest dissolubility of bassanite amongst the others. A great reduction in viscosity took place with the use of gypsum and anhydrite; the addition of anhydrite showed the lowest viscosity. It is worth mentioning that anhydrite can be in various forms and their dissolubility is different. In this research paper, anhydrite was prepared from burning gypsum at 700°C. This type of anhydrite, in this stage, is called “anhydrite II” and is more inert than that obtained from the burning at 200°C, which is called “anhydrite III” (Seufert et al., 2009). In addition, adding polycarboxylate-based superplasticizer to the mix containing bassanite at the same water to cement ratio (w/c) could significantly reduce its viscosity (Chen et al., 2012). The amount of AFt formation from the hydration of calcium sulfoaluminate clinker with different sulfate sources is in accordance with the setting time and rheological results. The faster the setting time, the higher the content of AFt. For compressive strength, the added bassanite showed a very low strength—only 5–7 MPa at 7 days, while the mixes with gypsum and anhydrite had a strength of 60 and 65 MPa, respectively at w/c of 0.5. This is similar to the false set at which the AFt crystals cannot grow properly and fail to obtain close contact, leading to deterioration of the structure.

In the authors' current experiment, the effect of calcium sulfate source on the strength development of CSAB cement was also studied. FGD—gypsum from lignite power plants was burnt at 120°C and 200°C to generate hemihydrate calcium sulfate (bassanite) and anhydrite III. The proportion of CSAB and calcium sulfate compound was 70:30 and superplasticizer was added to all mixes (0.15 wt% of cement). In contrast to the previous work (Garcia-Mate et al., 2015), hydration of CSAB with the presence of anhydrite showed the fastest setting time. The setting of the mix with added gypsum was the slowest. The difference was due to the difference in anhydrite structure. The compressive strength at 3 days curing related to the setting time, in that the faster the setting time, the higher strength. The strengths of 39, 30, and 20 MPa could be obtained for the mixes with additions of anhydrite, bassanite, and gypsum, respectively.

The hydration of ye'elimite in different forms in the presences of different calcium sulfate sources was studied by [Cuesta et al. \(2014\)](#). Ye'elimite was synthesized differently as stoichiometric ye'elimite (orthorhombic unit cell) and solid solution ye'elimite (pseudo-cubic unit cell). Gypsum and anhydrite were added in accordance with the stoichiometric ratio as stated in [Eq. \(14.1\)](#). In comparison, the formation of AFt took place earlier in the mix, with the use of orthorhombic ye'elimite and gypsum. It implied that the reactivity of pseudo-cubic ye'elimite was lower, compared to orthorhombic ye'elimite. The formation of AFt was greater when orthorhombic reacted with anhydrite, in comparison with gypsum at the same curing time. However, the formation of AFt from the reaction between pseudo-cubic ye'elimite and anhydrite was lower compared to the AFt formation when using gypsum. Notably, orthorhombic and pseudo-cubic ye'elimite phases preferred anhydrite and gypsum, respectively. These results were in accordance with those reported by [Jansen et al. \(2017\)](#).

The calcium sulfate content plays an important role with regard to the hydration of CSA cement. Hydration product formulation depends on the stoichiometry of CSA and calcium sulfate compounds. For example, according to [Eq. \(14.1\)](#) $C_4A_3\hat{S} + 2C\hat{S}H + 34H \Leftrightarrow C_6A\hat{S}_3H_{32}$ (Ettringite) + $2AH_3$, $C_4A_3\hat{S}$ requires 2 mole of gypsum to generate ettringite and amorphous aluminum hydroxide. When the calcium sulfate compound amount is limited, e.g., with ye'elimite to gypsum ratios of 1.5 and 1.0, the hydration products are a combination of AFt and AFm ($C_3A\hat{S}H_{12}$) as stated in [Eqs. \(14.16\) and \(14.17\)](#), respectively.



The calcium sulfate content is important, providing various properties to the set and hardened materials, ranging from rapid-hardening to shrinkage compensating, and eventually self-stressing ([Carballosa et al., 2015](#)). As is well known, early strength development of CSA cement is mainly caused by the formation of AFt and later strength mainly results from other phases, such as stratlingite and hydrogarnet. Monosulfate (AFm) is also one of the strength developers, but its influence is believed not as strong as that of AFt. [Berger et al. \(2011\)](#) studied the thermal cycle and gypsum content effect on the hydration and mechanical properties of CSA in the long term. That paper proved that AFt formation was feasible in the absence of calcium sulfate. The used CSAB cement consisted of 68.5 wt% of $C_4A_3\hat{S}$, 15.9 wt% of C_2S , 9.5 wt% of $C_{12}A_7$, 2.9 wt% of calcium titanate, 1.5 wt% of MgO, 0.5 wt% of calcium sulfate, 0.5 wt% of quartz, and 2.4 wt% of other compounds. Without gypsum addition at w/c ratio of 0.55, AFt together with AFm phase can be significantly formed at 24 hours and 20°C curing that did not correspond to [Eq. \(14.4\)](#). The

chemical reaction was believed to follow Eq. (14.18). In addition, CAH_{10} could also be formed due to the hydration of C_{12}A_7 together with the by-products (CH and AH_3) of the main reaction, according to Eq. (14.18). By using thermal cycle treatment, however, and in the absence of gypsum, there was no AFt formation, but mainly formation of AFm phase. Similarly, with a use of w/c ratio of 10, there was no AFt formation in the absence of gypsum condition, but AFm phase as majority. With the presence of 10% and 20% gypsum, AFt was formed as major compound at only 5 hours, with a consumption of gypsum. Monosulfate phase was formed as minority. With thermal cycle treatment, AFm was slightly increased. With an increase in gypsum contents from 0–35 wt%, the total cumulated heat evolution was decreased, not only due to the pure dilution effect but also due to the complex chemical reaction of ye'elimite and gypsum. With the addition of 35 wt% gypsum, there was only AFt formation both with and without thermal cycle treatments. When comparing the compressive strength obtained from samples cured under water and in sealed bags with no gypsum addition, the strengths were 46.6 and 55.0 MPa for 1 year curing, respectively. Thermal cycle treatment degraded the strength of the materials at the same conditions, 21.0 and 38.0 MPa for wet curing and sealed bag curing, respectively. With the presence of 20 wt% gypsum and nonthermal cycle treatment, the strength was lowered to 42.1 MPa cured under water, when compared to the sample with the absence of gypsum. It seemed that the strong structures came from the combination of AFt, AFm, and CAH_{10} , instead of pure AFt. The total porosity of the sample with gypsum was lower than that without gypsum but its strength was higher. However, there was no report on the fineness of the developed hydration products that might affect the attractive forces of hydration products.

14.4.3 Role of calcium hydroxide and OPC

As stated in Eq. (14.1), without CH, ye'elimite ($\text{C}_4\text{A}_3\hat{\text{S}}$) reacts with gypsum and water to generate AFt and amorphous aluminum hydroxide. In the presence of CH, according to Eq. (14.5), substantial amounts of AFt are generated. In addition, there is no aluminum hydroxide left behind. Ettringite is a hydration phase which is responsible for very rapid strength development. Early strength can be developed due to the formation of AFt, and a large expansion of the set material can be obtained. Hargis et al. (2013) studied early age hydration of calcium sulfoaluminate in the presence of gypsum and CH. It is believed that the formation of hydration products at the early age directly relates to their final hardened structures. Two different diluted systems: with a small amount and an excess amount of CH solutions, together with calcium sulfoaluminate and gypsum, were prepared and investigated regarding the formation of hydrated phases at the early age using in situ soft X-ray microscopy. The results showed the formation of large acicular crystals with a dimension of $0.5\ \mu\text{m}$ in width and $2\text{--}10\ \mu\text{m}$ in length, for insufficient CH system when observed after 19 minutes hydration. This research confirmed that the growth of acicular crystals expanded outwards from the center of the star, implying the

growth from a single central nucleus. For excess CH system, no well-developed acicular crystals could be observed until 51 minutes hydration. Ettringite crystals with some stellate clusters were similar but much smaller than the insufficient CH system. It is worth noting here that the presence of excess CH initially retards the rate of AFt formation due to the depletion of gypsum and also changes the morphology of the hydration products resulting in the smaller AFt crystals. In addition, Hargis et al. also observed the formation of AFt when CSA was consumed using XRD. Phase development was similar to those from X-ray microscopy but slightly different in the rate of formation, in that, ettringite formation was noticeable in XRD pattern in later age than in X-ray microscopy. This was due to the difference in water to cement ratio. XRD investigation used the lower w/c ratio. It was found that the use of 2–5 wt% CH is suitable to obtain pure AFt while the higher CH addition (5–10 wt%), showed the mixed phases between AFt and AFm as hydration products due to the depletion of gypsum in the system.

Calcium sulfoaluminate can be solely used to replace OPC as the strength which can be developed is as high as OPC. However, its cost is relatively high although the synthesis temperature is lower when compared to OPC due to the high price of alumina-bearing raw materials. The combination of CSA and OPC cements, therefore, becomes more economically attractive to be used in the construction industry. It is more practical to use OPC as majority rather than CSA due to its lower price. There were many researches investigating hydration of cement mixes between CSA and OPC. With these studies, OPC was mostly used as majority, incorporating with CSA as a modifier for specific purposes such as to modify shrinkage behavior, early strength development and heavy metal adsorption capacity of OPC. Pelletier et al. studied the hydration mechanism and mortar properties of a ternary system of Portland cement–calcium sulfoaluminate clinker–anhydrite (Pelletier et al., 2010; Trauchessec et al., 2015). Theoretically, the calcium sulfate phase plays a role in the hydration of OPC in order to retard the early hydration of C_3A by the formation of ettringite. The calcium sulfate phase also reacts with $C_4A_3\hat{S}$ to generate ettringite. Trauchessec studied the hydration of CSA–OPC cements. Anhydrite was used as calcium sulfate source to generate ettringite from CSA hydration. The higher the amount of CSA (46.5 wt% of CSA clinker + 13.5 wt% of anhydrite), the higher the amount of ettringite could be obtained indicated by the water loss at 140°C detected by DTA&TG. The smallest CSA content (9 wt% of CSA clinker + 6 wt% of anhydrite), the ettringite formation could be similar to the medium addition of CSA (21 wt% of CSA clinker + 9 wt% of anhydrite). It was believed that the increased AFt formation was due to the reaction of CH, aluminum hydroxide, and anhydrite according to Eq. (14.14). However, the leftover CH was not all consumed at this rate of addition.

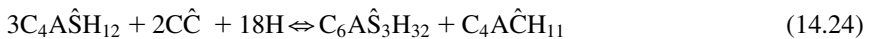
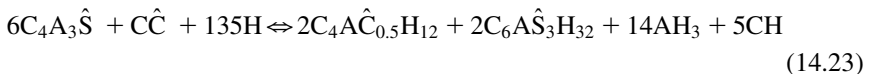
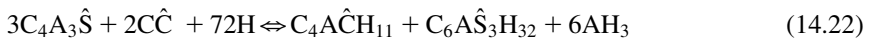
Pelletier studied the blended system of CSA–OPC– $C\hat{S}$ cement. CSA cement consisted of 68.1 wt% of $C_4A_3\hat{S}$, 14.8 wt% of C_2AS , 3.4 wt% of C_3A , 7.8 wt% of CA, 1.2 wt% of CA_2 , and 3.6 wt% of calcium titanate. OPC consisted of 56.1 wt% of C_3S , 15.5 wt% of C_2S , 4.8 wt% of C_3A , 11.5 wt% of C_4AF , 1.0 wt% of MgO, 4.8 wt% of $CaCO_3$, and 4.0 wt% of gypsum. All samples used the same w/c ratio of 0.5. In a series with constant OPC/CSA, the formation of hydration products in the

mix of OPC:CSA:C \hat{S} being 8:3:1 with the presence and absence of citric acid was not significantly different. The presence of citric acid provided only a slight retardation in the hydration. Within 30 minutes, formation of AFt and stratlingite could be found up to 7 days curing. The formation of AFt could be obtained in the maximum level at OPC:CSA:C \hat{S} of 8:3:0.75 (about 22 g/100 g cement). When the OPC/CSA ratio was varied, AFt formation was nearly similar, approximately 18–19 g/100 g cement for OPC:CSA:C \hat{S} ratios of 8:3:1, 7:3:1, and 6:3:1. For investigation of mortar properties, samples with OPC:CSA:C \hat{S} ratios of 8:3:1 showed the highest early strength during 6 h to 1 day. At 7 days, the compressive strength of samples made of either pure OPC or OPC:CSA:C \hat{S} ratios of 8:3:1.25 were superior to that of 8:3:1. At the later age (90 days), samples with larger amount of anhydrite (OPC:CSA:C \hat{S} ratios of 8:3:1.25) could maintain the highest strength among those samples. It is worth nothing here that the maximum level of AFt formation did not correspond to the highest strength development. It might be due to the secondary phase formation assisting packing of the structure. With a decrease in OPC from OPC:CSA:C \hat{S} ratio of 8:3:1 to 6:3:1, the strength could be enhanced from 19 to 24 MPa at 1 day curing. With lower OPC content, the strength development at later age corresponded to the formation of AFt. [Le Saout et al. \(2013\)](#) also studied hydration of mixed cements (Portland cement (PC) and calcium sulfoaluminate cement). OPC used in this research work consisted of 57.5 wt% of C $_3$ S, 16.3 wt% of C $_2$ S, 8.6 wt% of C $_3$ A, 7.3 wt% of C $_4$ AF, 0.7 wt% of MgO, 3.8 of CaCO $_3$, 1.5 wt% of hemihydrates, and 1.7 wt% of gypsum. CSA cement consisted of 22.5 wt% of C $_4$ A $_3$ \hat{S} , 47.7 wt% of anhydrite, 18.6 wt% of free lime and 8.9 wt% of Ca(OH) $_2$. Amorphous calcium aluminate phase (ACA), kind of C $_{12}$ A $_7$ which was also used in this experiment, consisted of 50.9 wt% of C $_{12}$ A $_7$ and 47.6 wt% of anhydrite. The samples were prepared with OPC:CSA:ACA ratios of 100:0:0, 90:10:0, and 80:0:20 with the same w/c ratio of 0.5. Only samples with OPC:CSA:ACA ratios of 80:0:20 were added with 0.8 wt% of retarder. The total accumulated heat of pure OPC was the lowest. When CSA was mixed with OPC, the accumulated heat was higher than for pure OPC. With the addition of ACA, the total heat was greatly increased. Especially at the early hydration, the heat was substantially released due to very fast dissolution of ACA and AFt precipitation. The hydration of C $_{12}$ A $_7$ was even faster than C $_4$ A $_3$ \hat{S} according to [Eq. \(14.19\)](#) showing the highest chemical shrinkage and largest AFt formation among those samples at every curing age. The consumption of calcium sulfate phase took place very rapidly within 1.5 hours. Similar contents of AFm phase were obtained in all mixes. Strength development confirmed the development of AFt in this case due to the great difference in AFt contents. Compressive strength of pure OPC was similar to that of ACA addition at 28 days curing, being approximately 48 MPa. The replacement of OPC with CSA and ACA cements could, therefore, greatly enhance the early strength development.



14.4.4 Role of calcium carbonate

Calcium carbonate in the form of calcite has been used as filler in the construction industry for a very long time. The addition of calcite is beneficial to cement and concrete properties due to the fact that it can chemically react with the tricalcium aluminate (C_3A) phase in PC to form monocarboaluminate ($C_4A\hat{C}H_{11}$ where \hat{C} stands for CO_3) phase, according to Eq. (14.20) (Damidot et al., 2011). Monocarboaluminate is a kind of AFm phase, where sulfate is replaced by carbonate ions. As the formation of monocarboaluminate takes several days, it is thus useful to develop late strength of the hardened structures. Without calcite addition, C_3A that is left behind after OPC hydration would be transformed to monosulfate (AFm) phase, according to Eq. (14.21) (Brown, 1993). This reaction occurs in the system without sufficient gypsum. With the presence of fine calcite as filler, not only $CaCO_3$ ($\hat{C}\hat{C}$) can react with C_3A to form $C_4A\hat{C}H_{11}$ directly, but it also reacts with AFm to form $C_4A\hat{C}H_{11}$ and ettringite, according to Eq. (14.22) (Damidot et al., 2011). Thus, the addition of calcium carbonate in PC cement clinker brings positive results in several terms: The later strength is enhanced and early hydration is accelerated by functioning as nucleating sites for C–S–H to speed up the crystallization (Martin et al., 2015). The role of calcium carbonate on the hydration of calcium sulfoaluminate cement is not yet well understood. Only a few works have been carried out to discover CSA hydration in the presence of calcium carbonate.



Martin et al. (2015) studied the contribution of limestone to the hydration of CSA. The authors proposed the idea of adding limestone in CSA cement for cost reduction, because CSA is more expensive than OPC. The used CSA clinker consisted of 68.1% of $C_4A_3\hat{S}$, 3.2% of CA, 1.4% of $C_{12}A_7$, 0.7% of CA_2 , 1.7% of C_2S , 3.9% of calcium titanate, 19.4% of C_2AS (gehlenite), 0.6% of MgO , and 1.1% of magnesium aluminate. The presence of limestone in CSA clinker using calcium sulfate to $C_4A_3\hat{S}$ ratio of 1.1 ($M = 1.1$) accelerated the hydration of CSA cement. The higher the amount of limestone, the faster the dormant period was. This was due to an increase in nucleating sites for the precipitation of hydration products. At calcium sulfate to $C_4A_3\hat{S}$ ratio of 2.1 ($M = 2.1$), the dormant period of the system with the presence of limestone was longer. This was due to the domination of calcium

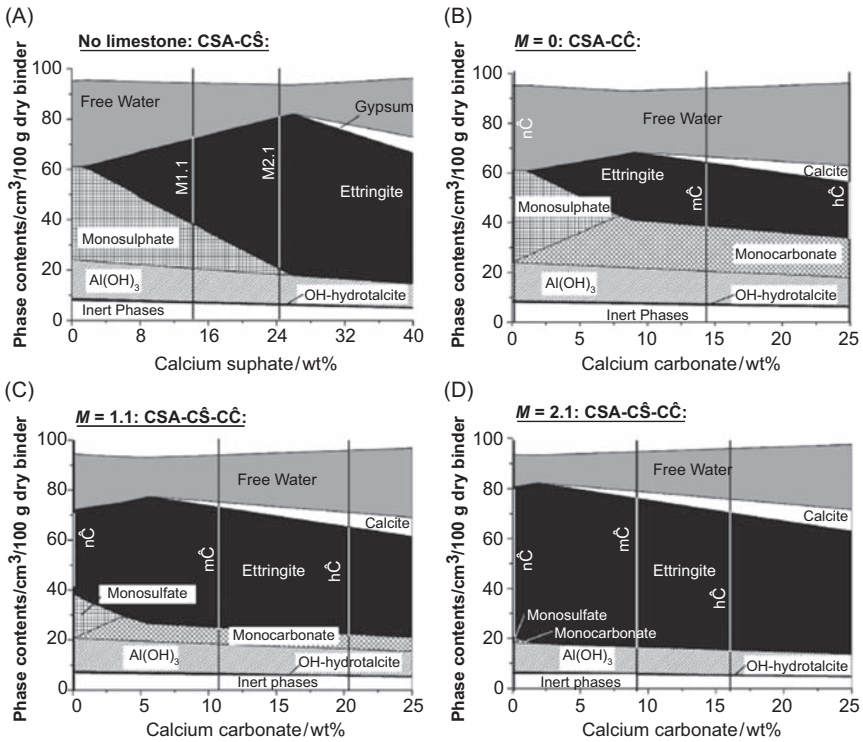


Figure 14.5 Volume change calculated as a function of added sulfate (A) or limestone (B–D), calculated with GEMS-PSI. (A) Systems without limestone. (B) Systems without anhydrite. (C) Systems with calcite and anhydrite at $M = 1.1$. (D) Systems with calcite and anhydrite at $M = 2.1$. The vertical lines indicate the formulations investigated experimentally. Abbreviations: h \hat{C} , high carbonate series; m \hat{C} , medium carbonate series; n \hat{C} , no carbonate series; M, molar ratio of anhydrite to ye’elimitite; CS \hat{C} , calcium sulfate; CC \hat{C} , calcite (Martin et al., 2015).

sulfate governing limestone resulting in the deceleration of hydration. The chemical reaction of limestone and $C_4A_3\hat{S}$ cement resulted in the formation of monocarboaluminate, AFt and amorphous aluminum hydroxide phases, as stated in Eq. (14.22). With the consumption of carbonate instead of sulfate, monocarboaluminate phase could be formed. In addition, AFt could also be formed, although no calcium sulfate was added. In addition, this chapter also reported the formation of hemicarboaluminate instead of monocarboaluminate phase in the absence of calcium sulfate, as stated in Eq. (14.23) and shown in Fig. 14.5.

Hargis et al. (2014) also studied the hydration of CSA in the presence of gypsum, calcite, and vaterite, to prove if calcium carbonate compound can be either reactive with ye’elimitite or enhance the mechanical properties. Vaterite and calcite, the kind of calcium carbonate compounds at which vaterite is less stable, were selected as comparison. The cement used in this experiment was pure $C_4A_3\hat{S}$,

synthesized from pure compounds; alumina, calcium carbonate, and calcium sulfate. The results showed that $C_4A_3\hat{S}$ cement with the presence of 15% of gypsum and 10% of calcite or vaterite exhibited shortened setting times when compared to mixes without calcium carbonate addition. The strength development was also positive—increasing from 39 MPa (without $CaCO_3$) at 28 days curing to 46 and 49 MPa with the presences of calcite and vaterite, respectively. The results also showed that, without gypsum, the reaction of $C_4A_3\hat{S}$ and $CaCO_3$ results in strengths up to 41 and 45 MPa for calcite and vaterite, respectively. The hydration products were found to follow the reaction as stated in Eq. (14.24) as the calcium sulfate used was not sufficient to generate AFt entirely. Therefore, AFm ($C_4A\hat{S}H_{12}$) phase was found incorporating with AFt and afterwards AFm was transformed to monocarboaluminate phase. As mentioned before, vaterite is more reactive than calcite, thus the enhancement in strength due to the formation of monocarboaluminate phase at the same curing time. It was found that the fineness of used vaterite was slightly smaller than calcite that might affect the higher reactivity. The presence of calcium carbonate also reduced expansion because of the formation of monocarboaluminate phase instead of AFt. Thermodynamic modeling also showed the trend of reduced AFt and increased AFm and monocarboaluminate phases with an increase in $CaCO_3$ contents (Damidot et al., 2011).

14.4.5 Role of chemical admixtures

Chemical admixtures are normally used to reduce the limitations of cement hydration, with examples being: water reducer, superplasticizer, retarder, accelerator, shrinkage preventer, segregation reducer, and heat evolution reducer. Interactions between chemical admixtures and cement phases are very important and need to be examined carefully in order to obtain the desired properties and the most durable construction materials. In general, chemical admixtures affect cement particles differently depending on the type of cementitious materials and type of admixture and content. Surface adsorption takes place when organic admixtures meet cement particles due to electrostatic forces between charged particles and ionic groups of admixture molecule (e.g., SO_3^- , COO^-) (Jolicoeur and Simard, 1998). Organic admixtures, e.g., lignosulfonates contains hydrophobic, polar and ionic groups acting very usefully for changing surface chemistry of cement particles. Due to very fast setting of CSA cement thus hindering the workability, chemical admixtures such as retarder are required in order to modify the rheology of cement, mortar and concrete slurries in maintaining high early strength as desired by the construction design. For example, organic chemical admixtures such as carboxylic retarders can adhere to the precipitated hydration products, thus hampering further growth on their surfaces. Zajac et al. (2016) studied the effect of retarders on the early hydration of CSAs. This paper studied the use of different retarders (sodium gluconate, tartrate, and borax) and investigated the developed hydration products. Used CSA clinker consisted of 24.8 wt% of $C_4A_3\hat{S}$, 52.4 wt% of C_2S , 6.6 wt% of C_4AF , 2.1 wt% of C_2F , 1.2 wt% of CA, 1.9 wt% of $CaCO_3$, 0.5 wt% of K_2SO_4 , 1.5 wt% of $C_2K\hat{S}$, and 2.2 wt% of anhydrite. Two cement samples were prepared as ground

clinker, and ground clinker with 10 wt% of anhydrite. To study the hydration and pore solution, a w/c ratio of 2.0 and 2 wt% of each retarder were used. For microstructural analysis, the w/c ratio was 0.5. Without retarder, both samples showed very fast dissolution rate with a huge release of heat during the induction period. CSA cement with the presence of additional anhydrite showed the highest heat release. However, the cumulative heat releases of samples with the presences of sodium gluconate and borax at early hydration (<10 h) were the largest and smallest, respectively, for ground clinker without additional anhydrite. For ground clinkers with additional anhydrite, and tartrate and sodium gluconate, their cumulative heat releases were the highest and about the same values. The cumulative heat release of samples with the presence of gluconate at 100 hours was the smallest. In 30 minutes, 5 wt% of ettringite (AFt) can be formed in samples without additional anhydrite and retarder and the formations were retarded to form 5.7, 4.6, and 0 wt% and of AFt at 8 hours, with the use of tartrate, gluconate and borax, respectively. Thus, borax was the most powerful retarder, according to the heat of hydration experiment. The amount of AFt found at 168 hours from the sample with the presence of gluconate was smallest. Cement clinker with additional anhydrite contained 4.9 wt% of AFt in 30 minutes. When tartrate, gluconate, and borax were used, AFt formations were 3.8, 3.9, and 0.0wt%, respectively at 8 hours. It was suggested that tartrate and gluconate retarded the dissolution of $C_4A_3\hat{S}$ and precipitation of AFt via the adsorption of negatively charged tartrate and gluconate onto AFt surfaces, thus inhibiting its growth while borax acted as pH reducer to retard the dissolution of $C_4A_3\hat{S}$ phase.

Chemical admixture such as superplasticizers are used to reduce the water to cement ratio and to control the setting time, while maintaining the flow ability of cement pastes. SP molecules can stick to cement particle surfaces that change the cement surface charges in order to repel each other. [Ma et al. \(2014\)](#) studied the compatibility between polycarboxylate (PC) superplasticizer and belite-rich SAC, by investigating the setting time and hydration properties. The used cement consisted of 25.4 wt% of $C_4A_3\hat{S}$, 56.2 wt% of C_2S , 6.6 wt% of C_3A , and 11.8 wt% of C_4AF , which was made of raw meal containing limestone, FA, and FGD—gypsum and which was sintered at 1320°C. Cement clinker was mixed with 10 wt% of gypsum, with varying amounts of PC from 0.025%–0.25% (42.83% of active phase). The water to solid ratio was 0.26. Heats of hydration during the induction period for PC-added samples was not significantly different, but total heat releases of samples without PC and with 0.25% PC were relatively different in showing the retardation of hydration. With less than 0.075% PC, total heat releases were not significantly different. Due to the negatively charged PC, it could effectively adsorb onto positively charged cement particles, prolonging initial setting times from 18 minutes (without PC) to 38 minutes (with 0.25% PC). The compressive strengths at 28 days curing of samples without PC and with 0.25% PC were 61.4 MPa and 66.8 MPa, respectively. The maximum strength was at 0.075% PC addition, relating to the largest amount of AFt formation. In addition. Furthermore, the most advantageous effect of PC was a modification of particle–particle interaction, changing from macropores to micropores over time. Another work investigating the addition of

polycarboxylic superplasticizer (25 wt% of active matter) in the range of 0%–0.4% in high SAC was reported by [Garcia-Mate et al. \(2012\)](#). The used CSA cement consisted of 72.3 wt% of $C_4A_3\hat{S}$, 14.5 wt% of C_2S , 6.8 wt% of calcium titanate, and 2.5 wt% of C_4AF , 1.6 wt% of MgO , 1.4 wt% of C_2MS_2 , and 0.9 wt% of calcium sulfate (where M stands for MgO). Gypsum additions were observed at 10, 20, and 30 wt%. Cement pastes were prepared using w/c ratios of 0.4 to 0.5 with the higher content of gypsum. Water to cement ratios of 0.5 and 0.6 were varied, in case of mortar preparation. The rheology of cement pastes showed shear thinning behavior for every amount of gypsum addition (without PC) and became Newtonian fluids when PC was added. At only 0.1 wt%, viscosity was reduced significantly. At 0.4 wt% addition, the viscosity became overdeflocculated showing an increase in the viscosity. The optimum PC content for 10, 20, and 30 wt% of gypsum was 0.2%, 0.15%, and 0.15%, respectively. An increase in gypsum content did not affect the rheology of cement pastes. The ettringite amount was the largest (47.6%) at 7 days in 30% gypsum added sample without PC addition while AFt amounts of 40.6% and 39.4 for samples with w/c ratios of 0.4 and 0.5, respectively at the same content of PC (0.15%) could be obtained. In samples with 10 and 20 wt% gypsum additions, AFt amounts were lower than that with 30% addition at 7 days curing. Without PC, cement paste with 30 wt% of gypsum showed the lowest open porosity, whereas the lowest open porosity could be obtained in paste with 10 wt% of gypsum with the presence of PC. Cement mortars were prepared in order to investigate strength development. At 7 days, mortars with 10 wt% of gypsum and w/c ratio of 0.5 attained the highest compressive strength (50 MPa). The higher w/c ratio degraded the strength in all cases. Significantly, mortar without PC obtained slightly higher strength than that with PC. In addition, compressive strength of CSA mortar was comparable to that of OPC mortar (50.6 MPa) at 7 days curing. The difference in strength development of those two research papers ([Garcia-Mate et al., 2012](#); [Ma et al., 2014](#)) was caused by the water to cement ratio: the lower the w/c ratio, the higher compressive strength—although containing a lower content of ye'elimite phase. In addition, the active phase of polycarboxylate superplasticizer significantly played a role in the different hydration properties.

14.5 Usages of sulfoaluminate cement for repair

Repairing is one of the major challenges for the construction industry, because often it is necessary to do it urgently, for example, repairing airport runways, bridge, dam, and residential buildings, in order to cure cracks or to support more load. Thus, the materials for the repair must set and hardened rapidly (in a few hours). Recent research therefore focuses on developing new kinds of repairing materials, improving the existing repairing materials and developing new assessment methods ([Qian et al., 2014](#); [Bieliatynskiy et al., 2016](#)). In addition to cement-based repairing materials, polymer-modified cement-based materials and resin materials are commonly used. Repair mortars are already available in the market as

readymix (cements, binders, aggregates, and additives) and user-friendly. However, research and development is still necessary to establish the long term service and to develop eco-friendly repair materials (Lopez-Arce et al., 2016). For example, rapid-repair concrete in aggressive marine environment was considered in term of durability such as chloride penetration to prove its corrosion resistance by Moffatt and Thomas (2017).

Cements including PC, SAC, and magnesium phosphate cement (MPC) are often used for repairing the damaged structures. CSA has been recently considered for repairing because of its fast setting and hardening, together with its dense structure due to the combination of ettringite, aluminum hydroxide, and stratlingite. Additionally, chemical and drying shrinkages of CSA cement are relatively low. Strength development properties, as well as durability performances are required for rapid-repair concrete. Moffatt and Thomas studied the chloride penetration of rapid-repair concrete by comparing different cementitious materials; high early strength PC, calcium aluminate cement and calcium sulfoaluminate cement (Moffatt and Thomas, 2017). A combination of CSA and PC showed very promising results with regard to corrosion resistance, due to the ability of calcium silicate hydrate (C-S-H) and monosulfoaluminate (AFm) to bind chloride ions—leading to the formation of Friedel's salt ($C_3A \cdot CaCl_2 \cdot H_{10}$) due to the chemical reaction between AFm and chloride ions while C-S-H phase only physically binds chloride ions. Whereas concrete made of the combination of CSA and belite phase showed a poor corrosion resistance, due to the inability of hydration products such as AFt to chemically bind chloride ions—with the chlorides being physically adsorbed to AFt surfaces instead (Ioannou et al., 2015). Thus, the presence of PC in both calcium aluminate and CSA cements accelerated the early strength development as well as the durability of rapid-repair concrete.

The interface quality, and compatibility between repair material and old concrete or old materials, are also important for repairing, as it is a stress origin—possibly inducing a new crack to the repair zone (Anagnostopoulos and Anagnostopoulos, 2002; Zhou et al., 2016). Therefore, shrinkage of repair materials is one of the crucial factors to be carefully considered. Qian et al. (2014) investigated bond strength and permeability of cement-based materials for repairing. The used cement-based repair materials; being PC, SAC, and MPC, were combined with old concrete to test the old-to-new interface created. The cement-based material to sand ratio was 1:1.5 for all cement types. Setting times of PC, SAC, and MPC were 180, 15, and 22 minutes, respectively. Compressive strength at 7 days of curing was the highest for sulfoaluminate mortar (69.1 MPa). To investigate the old concrete/repairing mortar interface, frustum-shaped specimens were used. PC/concrete and SAC/concrete showed large cracks at the interfaces, whereas there were no cracks from the prism mortars. MPC/concrete interface showed no cracking due to the lower drying shrinkage of MPC for both frustum and prism shaped specimens. The bonding performance order was MPC mortar, then SAC mortar, then PC mortar. The finding from Hu et al. (2017) suggested that hydration products from CSA hydration in a form of AFt likely caused micro-crack and highly porous zones, while aluminum hydroxide (AH_3) showed denser structure resulting in higher indentation modulus

and hardness at AH_3 localized areas. Therefore, crack from SAC/concrete was possibly due to the expansion of AFt crystals whereas PC/concrete contained large shrinkage causing internal stress, leading to micro-crack formation. Chang et al. designed experiments to prove whether AH_3 affected the mechanical properties (Chang et al. 2017). The designed mixes were based on the theoretical chemical reactions between pure $C_4A_3\hat{S}$, $C\hat{S}H_2$, and CH to create specimens with and without CH according to Eqs. (14.1) and (14.5), respectively. The results showed that the higher content of AH_3 after hydration promoted strength enhancement. In fact, amorphous AH_3 —which contained very high surface area—could fill in the pores of AFt structures. The substantial formation of AH_3 was found in the systems without and with small addition of CH. It was reported that belite-rich SAC contains similar durability to PC (e.g., salt resistance, carbonation resistance, and good dimensional stability) but the freeze–thaw resistance is its drawback. The addition of 15 wt% of PC to belite-rich SAC was recommended to reduce the porosity of the hardened structures as the strength and elastic modulus enhancements to resist freeze–thaw cycles (Janotka et al., 2003).

Ultrafine sulfoaluminate cements, mixed with combinations of ultrafine anhydrite and ultrafine quicklime were investigated in terms of heat of hydration and expansion–shrinkage behaviors by Zhang et al. (2017). Ultrafine CSA cements were mixed with ultrafine quicklime and ultrafine anhydrite. The variations of quicklime and anhydrite were at 0–30 wt% of quicklime. Without the addition of quicklime and anhydrite mixture, heat flow at early hydration was very low, whereas the addition of 20 wt% showed the highest heat flow flux corresponding to the greatest compressive strength. Without the mixture of quicklime and anhydrite, cement shrank greatly, yet the presences of quicklime and anhydrite caused expansion up to 1.0%–1.5% at 28 days. With the presence of 30 wt% of the mixture, expansion was about 1.0% at 3 days and remained constant over time. This combination must be further modified and investigated to obtain the zero absolute volume expansion required in order to avoid cracking at the interfacial zone for repair.

Le-Bihan et al. (2012) studied hydration properties of CSA cement to address the cracking or curling of self-leveling screed. The results confirmed that mortar with 60 wt% of CSA cement and 40 wt% of gypsum showed expansive properties with only very slight shrinkage after setting. Pera and Ambroise suggested that higher contents of phosphogypsum provided the promising shrinkage behavior (Pera and Ambroise, 2004). The used CSA cement consisted of 66 wt% of $C_4A_3\hat{S}$, 17 wt% of C_2S , 9.9 wt% of perovskite, and 7.1 wt% of $C_{12}A_7$. With uses of 25 wt% and 30 wt% of phosphogypsum as CSA cement replacement, compressive strength of more than 35 MPa within 24 hours was observed. Moreover, their shrinkages were very small, especially with the highest content of gypsum addition (30 wt%) encompassing the absolute zero volume expansion and shrinkage at 28 days due to the AFt formation. Shrinkage-reducing admixtures such as neopentil glycol were introduced to be combined with CSA cement, in order to reduce shrinkages, especially autogenous shrinkage, as reported by Colleparidi et al. (2005). The shrinkage reduction came from the reduction in surface tension of water, leading to the

reduced capillary tension of cement paste. CSA cement was not responsible for the reduction in drying shrinkage. This finding showed that the curing condition was very important to limit the shrinkage. The length change of concrete with a CSA to CaO ratio of 10:1 with a shrinkage-reducing admixture was investigated. Under water curing, expansion increased greatly, while covering by a plastic sheet provided smaller expansion during 0–36 hours. After 36 hours, the expansion of concrete decreased when cured in air at a relative humidity of 65% and could remain positive volume expansion at 30 days curing. The positive volume expansion was due to the formation of substantial Aft, according to Eq. (14.5). With a smaller content of CaO, the expansion become lowered which would result in zero volume expansion—which is desirable for repair.

CSA has been recommended to combine with MPC in order to enable filling the pores of MPC. Recently, MPC has been found to be very promising for rapid repair. However, its durability is limited, as water is taken up easily due to its high permeability. Zhang et al. (2017) investigated the mechanical properties and water ingress of repair cements—made of a combination of SAC and magnesium potassium phosphate cement (MKPC). MgO in MKOC was partially replaced by CSA cement at 0–40 wt%. With an increase in CSA cement, setting times and compressive strength were not changed significantly. The compressive strength test for water curing showed that mortars with 40 wt% CSA replacement were likely intact with water immersion over time. However, samples with high MgO content also showed higher durability, but had a low compressive strength. Zhou et al. (2016) studied PC hydration and its microstructure especially at the interfacial zone for repair. That paper underlined the importance of moisture exchange between repair cement and concrete substrate. The interfacial quality depended on the water supply from the concrete substrate, as water is a crucial factor for hydration. When the concrete substrate was dry, interfacial hydration products of the repair cement were densely packed, and their degree of hydration was decreased. This was due to the water suction of the concrete substrate from the repair cement layer, leading to a lower w/c ratio. When the concrete substrate was soaked with water prior to application with repair material, the hydration of repair material was improved with additional water, resulting in a denser structure—necessary to obtain a durable repair. CSA cement was also used to modify and limit the length change of OPC concrete in the study of Yan et al. (2004). In this study, delayed ettringite formation was also observed, resulting in cracking after hardening. Mortars with 8 wt% of CSA cement and 92 wt% of OPC were prepared and cured at different conditions. It was found that the formation of AFt was extremely high when the sample was cured under ambient temperature at RH > 90% both, at early age and over time. The formation of AFm of this sample was smaller than for the others cured under high temperature (85°C). Length change of this sample was not significantly changed over time, showing only a slight positive volume expansion (not over 0.01%). Samples cured under water at 85°C during the first 7 days and then exposed to a RH > 95% at ambient temperature showed the largest AFt formation at 200 days. Samples cured at 85°C mostly showed delayed ettringite formation. The results showed that the curing condition and the presence of CSA were very important to avoid cracking in the material. CSA cement is thus a promising cementing material to

fulfill restoration work, showing both compatibility and durability perspectives. The selection of repair material is dependent on the repair conditions; whether they require specific properties such as salt resistance, acid resistance, freeze–thaw resistance and aggressive marine resistance. In general, repair material for rapid setting and hardening purpose can be the mix of CSA and calcium sulfate—with and without smaller additions of hydrated lime or quicklime in order to obtain a combination of Aft and AH_3 . In a repair areas at which old concrete substrate is located, shrinkage–expansion behavior is of serious concern to avoid cracking. The repair material can be a ternary system, such a CSA–OPC– CaCO_3 . From previous studies, combination of CSA and PC provides excellent properties for corrosion resistance in marine areas, as well as from an economic perspective.

References

- Anagnostopoulos, C.A., Anagnostopoulos, A.C., 2002. Polymer-cement mortars for repairing ancient masonries mechanical properties. *Constr. Build. Mater.* 16, 379–384.
- Andrac, O., Glasser, F.P., 1994. Polymorphism of calcium sulfoaluminate ($\text{Ca}_4\text{Al}_6\text{O}_{16}\cdot\text{SO}_3$) and its solid solutions. *Adv. Cem. Res.* 6, 57–60.
- Berger, S., Coumes, C.C.D., Bescop, P., Damidot, D., 2011. Influence of a thermal cycle at early age on the hydration of calcium sulfoaluminate cements with variable gypsum contents. *Cem. Concr. Res.* 41, 149–160.
- Bieliatynskiy, A., Krayushkina, E., Skrypchenko, A., 2016. Modern technologies and materials for cement and concrete pavement's repair. *Proc. Eng.* 134, 344–347.
- Brien, J.V., 2014. Development of Cementitious Materials for Adhesion Type Applications Comprising Calcium Sulfoaluminate (CSA) Cement and Latex Polymer, PhD thesis. University of Kentucky.
- Brown, P.W., 1993. Kinetics of tricalcium aluminate and tetracalcium aluminoferrite hydration in the presence of calcium sulfate. *J. Am. Ceram. Soc.* 76, 2971–2976.
- Carballosa, P., Calvo, J.L.G., Revuelta, D., Sanchez, J.J., Gutierrez, J.P., 2015. Influence of cement and expansive additive types in the performance of self-stressing and self-compacting concretes for structural elements. *Constr. Build. Mater.* 93, 223–229.
- Chang, J., Zhang, Y., Shang, X., Zhao, J., Yu, X., 2017. Effects of amorphous AH_3 phase on mechanical properties and hydration process of $\text{C}_4\text{A}_3\text{S}-\text{C}_2\text{SH}_2-\text{CH}-\text{H}_2\text{O}$ system. *Constr. Build. Mater.* 133, 314–322.
- Chen, I.A., Hargis, C.W., Juenger, M.C.G., 2012. Understanding expansion on calcium sulfoaluminate-belite cements. *Cem. Concr. Res.* 42, 51–60.
- Collepardi, M., Borsoi, A., Collepardi, S., Jacob, J., Olagot, O., Troli, R., 2005. Effects of shrinkage reducing admixture in shrinkage compensating concrete under non-wet curing conditions. *Cem. Concr. Comp.* 27, 704–708.
- Costa, E.B., Rodriguez, E.D., Bernal, S.A., Provis, J.L., Gobbo, L.A., Kirchheim, A.P., 2016. Production and hydration of calcium sulfoaluminate-belite cements derived from aluminum anodizing sludge. *Constr. Build. Mater.* 1, 22, 373–383.
- Cuesta, A., Alvarez-Pinazo, G., Sanfeliix, S.G., Peral, I., Aranda, M.A.G., Torre, A.G., 2014. Hydration mechanisms of two polymorphs of synthetic yeelimite. *Cem. Concr. Res.* 63, 127–136.
- Damidot, D., Lothenbach, B., Herfort, D., Glasser, F.P., 2011. Thermodynamics and cement science. *Cem. Concr. Res.* 41, 679–695.

- El-Alfi, E.A., Gado, R.A., 2016. Preparation of calcium sulfoaluminate-belite cement from marble sludge waste. *Constr. Build. Mater.* 113, 764–772.
- Garbev, K., Beuchle, G., Schweike, U., Merz, D., Dregert, O., Stemmermann, P., 2014. Preparation of a novel cementitious material from hydrothermally synthesized C-S-H phases. *J. Am. Ceram. Soc.* 97, 2298–2307.
- Garcia-Mate, M., Santacruz, I., Torre, A.G., Leon-Reina, L., Aranda, M.A.G., 2012. Rheological and hydration characterization of calcium sulfoaluminate cement pastes. *Cem. Concr. Comp.* 34, 684–691.
- Garcia-Mate, M., Torre, A.G., Leon-Reina, L., Losilla, E.R., 2015. Effect of calcium sulfate source on the hydration of calcium sulfoaluminate eco-cement. *Cem. Concr. Comp.* 55, 53–61.
- Gartner, E., Hirao, H., 2015. A review of alternative approaches to the reduction of CO₂ emissions associated with the manufacture of the binder phase in concrete. *Cem. Concr. Res.* 78, 126–142.
- Hargis, C.W., 2013. *Advances in Sustainable Cements*, Doctoral Dissertation of Civil and Environmental Engineering. University of California, Berkeley.
- Hargis, C.W., Kirchheim, A.P., Monteiro, P.J.M., Gartner, E.M., 2013. Early age hydration of calcium sulfoaluminate (synthetic yeelimite $C_4A_3\hat{S}$) in the presence of gypsum and varying amounts of calcium hydroxide. *Cem. Concr. Res.* 48, 105–115.
- Hargis, C.W., Telesca, A., Monteiro, P.J.M., 2014. Calcium sulfoaluminate (Yeelimite) hydration in the presence of gypsum, calcite, and vaterite. *Cem. Concr. Res.* 65, 15–20.
- Hu, C., Hou, D., Li, Z., 2017. Micro-mechanical properties of calcium sulfoaluminate cement and the correlation with microstructures. *Cem. Concr. Comp.* 80, 10–16.
- Iacobescu, R.I., Pontikes, Y., Koumpouri, D., Angelopoulos, G.N., 2013. Synthesis, characterization and properties of calcium ferroaluminate belite cements produced with electric arc furnace steel slag as raw material. *Cem. Concr. Comp.* 44, 1–8.
- Ioannou, S., Paine, K., Reig, L., Quillin, K., 2015. Performance characteristics of concrete based on a ternary calcium sulfoaluminate-anhydrite-fly ash cement. *Cem. Concr. Comp.* 55, 196–204.
- Ishida, H., Mabuchi, K., Sasaki, K., Mitsuda, T., 1992. Low-temperature synthesis of β -Ca₂SiO₄ from Hillebrandite. *J. Am. Ceram. Soc.* 75, 2427–2432.
- Ishida, H., Yamazaki, S., Sasaki, K., Okada, Y., Mitsuda, T., 1993. α -Dicalcium silicate hydrate: preparation, decomposed phase, and its hydration. *J. Am. Ceram. Soc.* 76, 1707–1712.
- Janotka, I., Krajci, L., Ray, A., Mojumdar, S.C., 2003. The hydration phase and pore structure formation in the blends of sulfoaluminate-belite cement with Portland cement. *Cem. Concr. Res.* 33, 489–497.
- Jansen, D., Spies, A., Neubauer, J., Ectors, D., Goetz-Neunhoeffer, F., 2017. Studies on the early hydration of two modifications of yeelimite. *Cem. Concr. Res.* 91, 106–116.
- Jiang, W., Roy, D.M., 1992. Hydrothermal processing of new fly ash cement. *Ceram. Bull.* 71, 642–647.
- Jolicoeur, C., Simard, M.A., 1998. Chemical admixture-cement interactions: phenomenology and physico-chemical concepts. *Cem. Concr. Comp.* 20, 87–101.
- Juenger, M.C.G., Winnefeld, F., Provis, J.L., Ideker, J.H., 2011. Advances in alternative cementitious binders. *Cem. Concr. Res.* 41, 1232–1243.
- Kacimi, L., Cyr, M., Clastres, P., 2010. Synthesis of α'_1 -C₂S cement from fly-ash using the hydrothermal method at low temperature and atmospheric pressure. *J. Hazard. Mat.* 181, 593–601.

- Katsioti, M., Tsakiridis, P.E., Leonardou-Agatzini, S., Oustadakis, P., 2006. Examination of the jarosite-aluminate precipitate addition in the raw meal for the production of sulfoaluminate cement clinker. *J. Hazard. Mat.* 31, 187–194.
- Le Saout, G., Lothenbach, B., Hori, A., Higuchi, T., Winnefeld, F., 2013. Hydration of Portland cement with additions of calcium sulfoaluminates. *Cem. Concr. Res.* 43, 81–94.
- Le-Bihan, T., Geogin, J.F., Michel, M., Ambroise, J., Morestin, F., 2012. Measurements and modeling of cement base materials deformation at early age: the case of sulfoaluminous cement. *Cem. Concr. Res.* 42, 1055–1065.
- Liu, H., Bu, Y., Nazari, A., Sanjayan, J.G., Shen, Z., 2016. Low elastic modulus and expansive well cement system: the application of gypsum microsphere. *Constr. Build. Mater.* 106, 27–34.
- Lopez-Arce, P., Tagnit-Hammou, M., Menendez, B., Mertz, J.D., Guiavarch, M., Kaci, A., et al., 2016. Physico-chemical stone-mortar compatibility of commercial stone-repair mortars of historic building from Paris. *Constr. Build. Mater.* 124, 424–441.
- Ludwig, H.M., Zhang, W., 2015. Research review of cement clinker chemistry. *Cem. Concr. Res.* 78, 24–37.
- Luz, C.A., Rocha, J.C., Cheriaf, M., Pera, J., 2006. Use of sulfoaluminate cement and bottom ash in solidification/stabilization of galvanic sludge. *J. Hazard. Mater.* B136, 837–845.
- Ma, B., Ma, M., Shen, X., Li, X., Wu, X., 2014. Compatibility between a polycarboxylate superplasticizer and the belite-rich sulfoaluminate cement: setting and the hydration properties. *Constr. Build. Mat.* 51, 47–54.
- Ma, S., Snellings, R., Li, Z., Shen, Z., Scrivener, K.L., 2013. Alite-yeelimite cement: synthesis and mineralogical analysis. *Cem. Concr. Res.* 45, 15–20.
- Martin, L.H.J., Winnefeld, F., Muller, C.J., Lothenbach, B., 2015. Contribution of limestone to the hydration of calcium sulfoaluminate cement. *Cem. Concr. Comp.* 62, 204–211.
- Martin, L., Winnefeld, F., Tschopp, G., Muller, C.J., Lothenbach, B., 2017. Influence of fly ash on the hydration of calcium sulfoaluminate cement. *Cem. Concr. Res.* 95, 152–163.
- Martin-Sedeno, M.C., Cuberos, A.J.M., Torre, A.G., Alvarez-Pinazo, G., Ordonez, L.M., Gateshki, M., et al., 2010. Aluminum-rich belite sulfoaluminate cements: clinkering and early hydration. *Cem. Concr. Res.* 40, 359–369.
- Moffatt, E.G., Thomas, M.D.A., 2017. Performance of rapid-repair concrete in an aggressive marine environment. *Cem. Build. Mater.* 132, 478–486.
- Nocuri-Wczelik, W., Stok, A., Konik, Z., 2010. Heat evolution in hydrating expansive cement systems. *J. Therm. Anal. Calor.* 101, 527–532.
- Pelletier, L., Winnefeld, F., Lothenbach, B., 2010. The ternary system Portland cement-calcium sulfoaluminate clinker-anhydrite: hydration mechanism and mortar properties. *Cem. Concr. Comp.* 32, 497–507.
- Pera, J., Ambroise, J., 2004. New applications of calcium sulfoaluminate cement. *Cem. Concr. Res.* 34, 671–676.
- Pontikes, Y., Angelopoulos, G.N., 2013. Bauxite residue in cement and cementitious applications: current status and a possible way forward. *Resour., Conserv. Recycl.* 73, 53–63.
- Qian, J., You, C., Wang, Q., Wang, H., Jia, X., 2014. A method for assessing bond performance of cement-based repair materials. *Cem. Build. Mat.* 68, 307–313.
- Rungchet, A., Chindapasirt, P., Wansom, S., Pimraksa, K., 2016. Hydrothermal synthesis of calcium sulfoaluminate-belite cement from industrial waste materials. *J. Clean. Prod.* 115, 273–283.
- Rungchet, A., Poon, C.S., Chindapasirt, P., Pimraksa, K., 2017. Synthesis of low-temperature calcium sulfoaluminate-belite cements from industrial wastes and their

- hydration: comparative studies between lignite fly ash and bottom ash. *Cem. Concr. Comp.* 83, 10–19.
- Sasaki, K., Ishida, H., Okada, Y., Mitsuda, T., 1993. Highly reactive β -dicalcium silicate: influence of specific surface area on hydration. *J. Am. Ceram. Soc.* 76, 870–874.
- Seufert, S., Hesse, C., Goetz-Neunhoffer, F., Neubauer, J., 2009. Quantitative determination of anhydrite III from dehydrated gypsum by XRD. *Cem. Concr. Res.* 39 (2009), 936–941.
- Shen, Y., Qian, J., Huang, Y., Yang, D., 2015. Synthesis of belite sulfoaluminate-ternesite cements with phosphogypsum. *Cem. Concr. Comp.* 63, 67–75.
- Shi, C., Jimenez, A.F., Palomo, A., 2011. New cement for the 21st century: the pursuit of an alternative to Portland cement. *Cem. Concr. Res.* 41, 750–763.
- Sun, Q., Li, J., Wang, J., 2011. Solidification of borate radioactive resins using sulfoaluminate cement blending with zeolite. *Nucl. Eng. Des.* 241, 5308–5315.
- Trauchessec, R., Mechling, J.M., Lecomte, A., Roux, A., Rolland, B., 2015. Hydration of ordinary Portland cement and calcium sulfoaluminate cement blends. *Cem. Concr. Comp.* 56, 106–114.
- Viani, A., Gualtieri, A.F., 2013. Recycling the product of thermal transformation of cement-asbestos for the preparation of calcium sulfoaluminate clinker. *J. Hazard. Mater.* 260, 813–818.
- Winnefeld, F., Lothenbach, B., 2010. Hydration of calcium sulfoaluminate cements – experimental findings and thermodynamic modeling. *Cem. Concr. Res.* 40, 1239–1247.
- Yan, P., Zheng, F., Peng, J., Qin, X., 2004. Relationship between delayed ettringite formation and delayed expansion in massive shrinkage-compensating concrete. *Cem. Concr. Comp.* 26, 687–693.
- Zajac, M., Skocek, J., Bullerjahn, F., Haha, M.B., 2016. Effect of retarders on the early hydration of calcium-sulpho-aluminate (C \hat{S} A) type cements. *Cem. Concr. Res.* 84, 62–75.
- Zhang, G., Li, G., He, T., 2017. Effect of sulfoaluminate cement on the strength and water stability of magnesium potassium phosphate cement. *Constr. Build. Mater.* 132, 335–342.
- Zhang, J., Guan, X., Li, H., Liu, X., 2017. Performance and hydration study of ultra-fine sulfoaluminate cement based double liquid grouting material. *Constr. Build. Mater.* 132, 262–270.
- Zhou, J., Ye, G., Breugel, K., 2016. Cement hydration and microstructure in concrete repairs with cementitious repair materials. *Constr. Build. Mater.* 112, 765–772.

Further reading

- Glasser, F.P., Zhang, L., 2001. High performance cement matrices based on calcium sulfoaluminate-belite compositions. *Cem. Concr. Res.* 31, 1881–1886.

This page intentionally left blank

Engineered cementitious composites-based concrete

15

Gürkan Yıldırım¹, Mustafa Şahmaran² and Özgür Anıl³

¹Adana Science and Technology University, Adana, Turkey, ²Hacettepe University, Ankara, Turkey, ³Gazi University, Ankara, Turkey

15.1 The need for sustainable repair of concrete infrastructures

Around the globe, nations struggle with the ever-increasing challenges of unsustainable development. The consequences of this struggle are often most visible in developing nations with rapidly expanding economies. Often, infrastructural development—highways, airports, bridges, underground mass transit facilities, dams, and waste water treatment facilities—creates the backbone of such rapidly expanding economies, supporting trade, and outside investment. In this sense, concrete material can literally be regarded as one of the building blocks of economic development.

While essential for development of economies, the construction and maintenance of infrastructures often necessitates large volumes of Portland cement and aggregates to be incorporated into the production of concrete materials, creating tremendous negative impacts on public health. To illustrate, the production of one ton of Portland cement releases 6.3 mg of particles with diameters less than 10 microns (PM₁₀) into the atmosphere (Marlowe, 2003). Each year, numerous deaths are being attributed to atmospheric PM₁₀ concentration levels being as low as 20 mg/m³ (Ostro, 1994). In addition to direct concerns around public health, production of 1 ton of Portland cement requires 4 GJ of energy and releases approximately 1 ton of CO₂ into the atmosphere. Portland cement production is responsible for 7% of worldwide CO₂ emissions and is a significant contributor to global warming due to ozone depletion (Malhotra, 1999; Mehta, 1998). Furthermore, mining large quantities of raw materials such as limestone and clay for clinkering, and coal for burning in the rotary kilns, often results in extensive deforestation and topsoil loss. Mining of aggregates for concrete production causes significant ecological damage as well. The overall consequence is an inherently unsustainable system measured by economic, environmental, and social indicators.

Sustainability, on the other hand, requires the use of energy efficient materials with a low impact on the environment and improved overall durability. Although sustainability is the ultimate goal, improper design, material selection, and construction practices lead concrete structures to be prone to extensive distresses in a given service environment. In spite of these environmental problems, the global demand

for concrete increases at a very rapid pace, largely driven by the construction boom in developing countries. In less than a century, it has become the most widely used construction material in the world.

European design codes now require a service lifetime of more than 75 years for concrete structures in large public works (Alexander and Stanish, 2005). But, experience has shown that under the combined effects of mechanical loads and severe service conditions—including a wide range of temperature fluctuations and increased use of de-icing materials—many infrastructures begin to deteriorate after only 20 or 30 years (Mehta and Burrows, 2001). The short service life of infrastructures incorporating ordinary Portland cement concrete has significant negative effects, considering the need to produce new materials for repair and replacement of deteriorated infrastructure, along with the related fuel consumption and vehicle emissions from construction-related traffic congestion.

One of the main reasons for the short service life of infrastructures built with ordinary Portland cement concrete is poor durability, which is closely related to concrete cracking (Mindess et al., 2003). Cracking is usually the result of physical, chemical, and mechanical interactions between concrete and its service environment, and it may occur at different stages of the lifetime of a structure. Formation of cracks, coupled with the lack of crack width control in brittle conventional concrete, is primarily responsible for two types of damage: reduced strength and stiffness of the concrete structure and acceleration of ingress of aggressive ions, which leads to other types of deterioration, such as corrosion, alkali–silica reaction (ASR), freeze/thaw damage, and sulfate attack—all resulting in further cracking and disintegration (Mindess et al., 2003; Li and Li, 2007).

A very large number of existing concrete structures worldwide are in a state of deterioration/distress (Vaysburd et al., 2004). Increased CO₂ concentrations in the atmosphere are expected to further weaken the chemical stability of the concrete material in these structures (Engineers Canada, 2008). Repair and maintenance are recurring needs, due to natural degradation of materials and infrastructures under the combined effects of mechanical loads and environmental factors. In the past, the practice was to replace old and deficient structures with the new ones. However, due to today's economic climate and high cost of replacement, emphasis is now placed on repairing existing structures rather than replacing them.

Deterioration of highway pavements, airport runways, bridge decks, marine structures, and other concrete structures poses serious problems and requires huge sums of money for renovation. For example, bridge maintenance costs are higher than \$1 billion per year in Europe (Raupach, 2005). The total cost for maintenance of all types of buildings is assumed to be higher than \$20 billion per year (Raupach, 2005). By some estimates, money spent on the repair of existing structures in recent years has exceeded that spent on new structures (Vecchio and Bucci, 1999). In many countries, the number of new structures being built is declining. However, the market for repair and protection has been growing considerably as the existing infrastructures age. The concrete repair industry is thus facing a major challenge: how do we stop or slow down the decay of the world's infrastructure?

While more and more effective repair materials are being developed, experiences with concrete repair have been mixed. Despite the best efforts of the repair industry, the failure rate for concrete repairs remains unacceptably high; it has been estimated that almost half of all concrete repairs fail in the field (Mather and Warner, 2003). Concrete repairs often lack early age performance and long-term durability. Therefore, it is of utmost importance to develop effective, economical, and durable (ultra-high performance) repair materials to fundamentally address concrete deterioration problems and protect existing concrete from aggressive environments in the long term. In addition to improving the effectiveness and durability of repair materials, it is vital to develop more environmentally benign materials and use by-products and waste materials more effectively in the production of repair materials.

15.2 Holistic model for the design of effective repair materials

Effective and durable concrete repairs require a range of materials with different physical and chemical properties and application techniques. Compatibility with existing construction material (substrate), structural considerations, ease of processing and use in a wide variety of conditions are crucial. A holistic approach should be adopted in the design of repair materials and systems to ensure all potentially influencing parameters are considered on the basis of both design and implementation (Mehta, 1994). A holistic model for the design of a repair material was adopted from the literature and is presented in Fig. 15.1 (Emmons and Vaysburd, 1995; Morgan, 1996). However, before developing innovative materials for the repair and protection of concrete infrastructures, the function of each factor listed in Fig. 15.1 and their interactions must be fully understood. What follows is a discussion of the function of each factor.

15.2.1 Compatibility

Compatibility can be defined as the balance of physical, chemical, and electrochemical properties and dimensions between the repair material and existing substrate phase of a repair system, which ensures that the repair can withstand all anticipated stresses due to volume changes and chemical and electrochemical effects, without distress and deterioration over a designated period of time (Emmons et al., 1993). The importance of installing repair materials and systems with suitable dimensional compatibility, bond compatibility, structural and mechanical (load) compatibility, permeability compatibility, chemical, and electrochemical compatibility is briefly discussed in the following paragraphs.

Dimensional compatibility: Selection of repair materials for concrete structures requires an understanding of material behavior in anticipated service and exposure conditions. Of these considerations, the most important one is dimensional compatibility, which is the ability to withstand volume changes and the ability of the

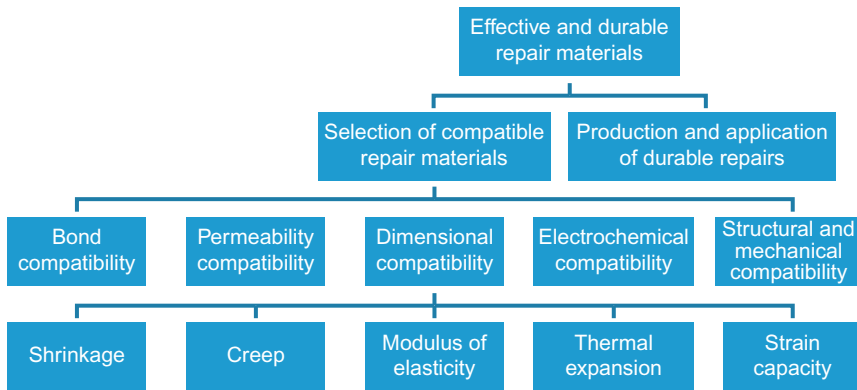


Figure 15.1 A holistic model of repair material design (Emmons and Vaysburd, 1995; Morgan, 1996).

repaired area to carry its share of the applied load without distress. Dimensional changes cause internal stresses within the substrate and repair material itself. High internal stresses may result in tensile cracks, loss of load carrying capacity, delamination, and/or deterioration. Particular attention is required to minimize these stresses and to select materials that properly address the relative dimensional behavior.

Unfortunately, there is limited information on the material properties that affect dimensional compatibility, on the ways in which the various properties interrelate, or on the values that should be specified as performance criteria for individual properties. The notion of the cracking potential of concrete has recently been adopted to help establish a connection among parameters that can influence dimensional compatibility and structural durability of repair materials (Li and Stang, 2004). This newly proposed metric can be used to quantify the likelihood of, or resistance to, early age cracking in repair materials, which can be detrimental to long-term durability. The computation of cracking potential due to shrinkage for restrained concrete at early age is shown in Eq. (15.1):

$$p = \varepsilon_{\text{sh}} - (\varepsilon_e + \varepsilon_i + \varepsilon_{\text{cp}}) \quad (15.1)$$

where p is the cracking potential, ε_{sh} is the concrete shrinkage strain, ε_e is the concrete elastic strain, ε_i is the concrete inelastic strain, and ε_{cp} is the concrete creep strain. A high positive value of p signifies a strong potential for cracking due to restrained shrinkage. The notion of cracking potential is fundamentally a superposition of time-dependent strains within concrete. While the tensile stress development responsible for crack formation also depends on material properties such as elastic modulus according to Hooke's Law, the cracking potential can be seen as a simple value which captures both the "drivers" and "resistors" to early age cracking. It serves as a useful guide for preventing concrete cracking.

Parameters that influence dimensional compatibility and cracking potential include shrinkage (autogenous, plastic, drying, and carbonation), thermal expansion

and contraction, modulus of elasticity (MOE), elastic and inelastic strain capacity, and creep of the repair material. Cracking due to lack of dimensional compatibility of the repair material with the substrate can be reduced/eliminated by one or more of the following factors: low shrinkage, high creep, low MOE, high tensile strength, and high tensile strain capacity of the repair material (Morgan, 1996; Li and Stang, 2004; Li and Li, 2009).

Bond compatibility: Bond compatibility can be defined as the development and maintenance of a satisfactory level of bond (adhesion) between the substrate and repair material (Morgan, 1996). Differences in mechanical properties of two bonded materials can give rise to the development of initial tensile stresses as well as the formation of cracks at or near the interface, leading to debonding and loss of the repair material. Provided that an adequate match of the bonded materials exists, an improvement of bond will lead to an increase in the performance of the repair/substrate system. Therefore, it is fundamental for the success of any concrete repair that an excellent bond is achieved between the repair material and substrate.

Permeability compatibility: Repair materials should have low permeability in order to prevent or reduce the infiltration of aggressive solutions into concrete. In designing repair materials, the permeability compatibility of repair material relative to that of the substrate concrete should also be taken into consideration. There is likely no single recommendation that confirms whether very low permeability or compatible permeability with the existing materials is more effective (Vaysburd and Emmons, 2004). This is important for transport of substances and electrochemical compatibility, as well as the ability of the repair to breathe. Repair materials and systems impermeable to moisture vapor diffusion should be used with caution in situations such as repair of slabs-on-grade, where the subgrade supports rising dampness or hydraulic structures such as dams and reservoirs. Under such conditions, the use of low permeability or impermeability (e.g., polymer-based repair material) could cause saturation of the substrate concrete behind the repair, leading to delamination and loss of material (Morgan, 1996; Emmons et al., 1993).

Chemical and electrochemical compatibility: For chemical compatibility, a repair material must have no adverse effects on the repaired component or structure. For example, the release of chloride ions can interfere with the inhibition of reinforcing steel corrosion in the substrate or surrounding concrete (ring corrosion), and sodium or potassium ions can promote alkali-aggregate reactivity (AAR) in a substrate concrete made with AAR-susceptible aggregates.

Electrochemical compatibility is an important aspect of repair performance that relates to the ability of the repair system to inhibit subsequent corrosion of reinforcement, both within the repair area and in the surrounding, nonrepaired reinforced concrete. There is considerable controversy in the literature as to the most appropriate types of repair materials and systems to provide electrochemical compatibility (Heiman and Koerstz, 1991; Gulikers and van Mier, 1991; Emmons et al., 1994). Previous studies tend to support using repair materials of similar composition, density, and permeability to the surrounding concrete in the repair area to maximize electrochemical compatibility (Emmons et al., 1994). In structures containing embedded ferrous metals, influence of the repair material/system or

electrochemical compatibility must be taken into consideration to avoid corrosion-induced deterioration.

Structural and mechanical compatibility: Structural and mechanical compatibility is also imperative if the repair system is to remain sound. The requirement for this compatibility is that the strength in compression, flexure and tension of the repair material exceed that of the substrate material. This requirement is commonly met with most repair materials. There is, however, one caution: repair materials with excessively high stiffness (MOE) should be avoided as they may cause the repaired area to attract undue load.

15.2.2 Ease of production and application

To ensure satisfactory performance, it is essential that repair materials can easily be mixed in the correct proportions. Repair of concrete infrastructures can involve the casting of concrete in a formwork with complex geometry and in narrow sections, creating difficulties that can hinder the flow of concrete into place. In some cases, repair operations should also secure the architectural surface quality. Given the complexity of the cast elements, mechanical vibration may not be possible in some phases. In addition to compatibility with the original construction material, the ease of production and handling (including self-consolidation casting and shotcreting), makes the repair materials attractive to various civil engineering applications.

15.3 Engineered cementitious composites: a potential repair material solution for sustainable infrastructures

An ideal repair material, therefore, would be volumetrically stable (i.e., it would undergo neither shrinkage nor expansion once installed), and display MOE, strength, creep, shrinkage, thermal expansion, permeability, and electrochemical characteristics compatible with that of the substrate material. Unfortunately, despite the best efforts of material formulators, products with all these properties do not exist. The best that can be hoped for are repair materials with a suitable MOE and volume stability that will neither shrink nor expand until cracking, or impose interfacial shear stress (or direct tensile stress) leading to bond failure.

During the previous several decades, concrete technology has undergone rapid development. Efforts to modify the brittle behavior of plain cement-based materials such as pastes, mortars, and concretes have resulted in modern concepts of high-performance fiber-reinforced cementitious composites (HPFRCC) that exhibit ductile behavior under uniaxial tensile load. In plain concrete, there is no load carrying capacity after the first crack, and cracking immediately leads to failure (Fig. 15.2). In conventional fiber-reinforced cementitious composites, matrix cracking is followed by a reduction in load carrying capacity, known as tension softening (lower curve in Fig. 15.2). In HPFRCC, after the formation of the first

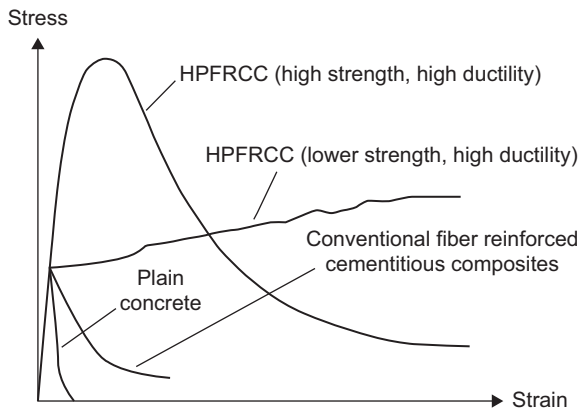


Figure 15.2 Tensile behavior of plain and fiber-reinforced cementitious materials.

crack, the fibers themselves are able to transfer additional load. On further loading, multiple micro-cracks with crack widths less than $100\ \mu\text{m}$ form along the member, leading to a significant increase in tensile strain capacity. The tensile stress–strain curve hence exhibits a postcracking hardening branch similar to that of ductile materials such as aluminum (upper curves in Fig. 15.2). Quantitative criteria for the achievement of ductility (inelastic straining) in terms of various material and geometric parameters (such as properties of fiber, matrix, fiber–matrix interface, fiber geometry, and volume fraction, etc.) were proposed by Li and Leung (1992) and further developed by Li (1993), and Kanda and Li (1999). With the proper selection of parameters to fulfill the criteria, ductile composites with different strength grades can be made with fiber volumes from 1.5% to 5%. The actual ductility of HPFRCC, which can be defined as the strain at maximum tensile stress, depends on the effectiveness of fibers in transferring stresses back into the cementitious matrix, as well as the toughness of the matrix itself (Li, 1998). Normally, the higher the matrix toughness, the lower the ductility achieved with a certain fiber volume fraction. Depending on the particular application, the material design can be varied to produce an optimal tensile stress versus strain relation that satisfies strength and ductility requirements. In the literature, HPFRCCs have been given different names by various researchers. These include multiscale fiber-reinforced cement composite (MSFRCC) (Rossi and Parant, 2005), a type of HPFRCC developed at Cardiff University (CARDIFRC) (Alaee and Karihaloo, 2003) and hybrid fiber composites (Markovic et al., 2004) which are high strength composites with relatively low ductility, as well as Engineered Cementitious Composites (ECC) (Li, 1993), a highly ductile HPFRCC with moderate fiber volume (tensile failure occurs at 2%–5% strain—200–500 times that of conventional concrete or fiber-reinforced concrete) and relatively low strength.

As a new class of HPFRCC materials, ECCs are ductile fiber-reinforced cementitious composites micromechanically designed to achieve high damage tolerance under severe loading and high durability under normal service conditions (Li, 1998,

2003; Li et al., 2001). Fig. 15.3A shows a typical uniaxial tensile stress–strain curve of ECC material containing 2% polyvinyl alcohol (PVA) fibers, by volume. The characteristic strain-hardening behavior after first cracking is accompanied by multiple micro-cracking (Fig. 15.3B). Crack width development during inelastic straining is also shown in Fig. 15.3A. Even at ultimate load, the crack width remains smaller than 100 μm . This tight crack width is self-controlled and, whether the composite is used in combination with conventional steel reinforcement or not, it is a material characteristic independent of rebar reinforcement ratio. In contrast, conventional concrete and fiber-reinforced concrete rely on steel reinforcement for crack width control.

The standard ECC mixture (also known as M45 in the literature) is PVA fiber-based and possesses compressive strength values similar to moderate to high-strength concrete with 30–90 MPa, although the compressive strain capacity is nearly 50% higher. Under severe bending load, ECC beams deform through plastic deformation, similar to a ductile metal plate (Fig. 15.4). Flexural strength and mid-span beam deflection of the standard ECC mixture are in the range of 7–12 MPa and 4–7 mm, respectively, while uniaxial tensile strength and strain capacities are in the range of 4–6 MPa and 3%–5%, respectively. The excessive plastic deformation coupled with multiple micro-cracking behavior is also valid under direct tension. It must be noted that the ranges of different mechanical properties are obtained by modifying the proportions and ingredients of mixtures based on a certain need.

ECC is a material suitable for a wide variety of civil engineering applications, as summarized by the Li (2002), and Kunieda and Rokugo (2006). One of the most promising applications of ECC is in the repair of concrete structures. Several studies described in literature have focused on the advantages of structural repair using HPRCCs. Lim and Li (1997) found mechanical advantages of an interface crack-trapping mechanism within HPRCC/reinforced concrete composites. Li and Li (2009) demonstrated that, to suppress both repair surface cracking and repair/old interface delamination, the repair material needs to exhibit “inelastic straining—tensile ductility” to accommodate its shrinkage deformation, thus relieving the built-up of stresses under restrained drying shrinkage conditions (see Section 15.2.1

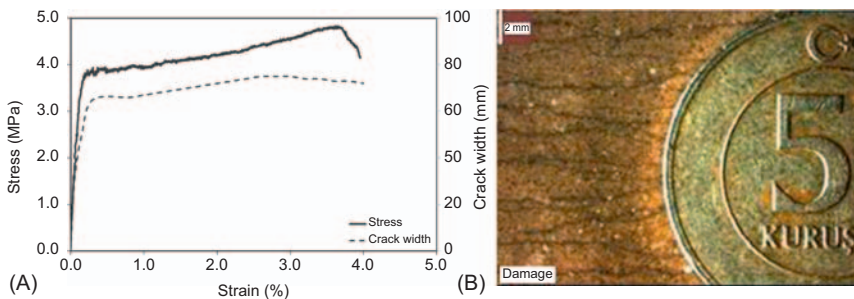


Figure 15.3 (A) Typical tensile stress–strain curve and (B) crack width development of Engineered Cementitious Composites (ECC).



Figure 15.4 (A) Response of Engineered Cementitious Composites (ECC) under flexural loading and (B) typical cracking pattern on positive moment surface of ECC beams.

—“Dimensional compatibility”). This way, surface crack width and interface delamination can both be minimized. Inelastic straining in the form of micro-crack damage has been demonstrated in HPCFRCCs (Li and Li, 2009). Moreover, the self-healing of cracks becomes prominent when crack width is small. If durability—and eventually, sustainability—are the main goals, current construction practices, and codes must undergo a paradigm shift to achieve concrete structures that have tight cracks or are “crack-free” in preference to high strength. The formation of cracks, coupled with no crack width control, in brittle concrete is primarily responsible for distresses that can dramatically reduce the long-term durability performance of concrete. While it is unrealistic to imagine the complete suppression of cracking, using robust self-healing functionality as an autogenous mechanism in areas with tight cracks may lead to the realization of a virtually “crack-free” concrete. Self-healing is generally attributed to the hydration of previously unhydrated cementitious materials, calcium carbonate formation (crystallization), expansion of concrete in the crack flanks, and closing of cracks by solid matter in water, or spalling-off of loose concrete particles as a result of cracking (Ramm and Biscopig, 1998). Self-healing can only be taken into account when crack width is small (generally less than about $150\ \mu\text{m}$ (Yildirim et al., 2014; Şahmaran et al., 2013a, 2014, 2015c) and preferably less than about $50\ \mu\text{m}$ (Snoeck et al., 2014; Snoeck and De Belie, 2015)). Self-healed or very tight cracks (less than 0.1 mm) do not pose a durability problem in concrete structures (Yildirim et al., 2015b, 2015d; Alyousif et al., 2015).

Ductile behavior and self-healing ability of ECCs is associated with many other desirable properties for repair and rehabilitation applications. These include: (1) high energy absorption, impact resistance and inelastic straining; (2) ability to redistribute localized stresses, reducing the sensitivity of the material to stress concentrations; (3) high deformability, passing ability, and resistance to segregation to secure complete filling of the complex formwork and ease of production including self-consolidation casting and shotcreting; (4) high shear strength; (5) high bond strength to steel reinforcement and substrate concrete (high delamination

resistance); and (6) capability to control cracks from opening, preventing the resulting increase of transport properties that would lead to durability problems.

To date, ECCs incorporated with different polymeric fibers such as polyethylene (PE) (Li, 1998), PVA (Şahmaran et al., 2013a, 2014, 2015c; Yıldırım et al., 2014) or high tenacity polypropylene (HTPP) (Felekoğlu et al., 2016) were successfully manufactured without sacrificing the multiple micro-cracking behavior. Moreover, the latest efforts have shown that polymeric fibers (e.g., PVA) in ECCs can alternatively be substituted with eco-friendly natural fibers (e.g., hemp and flax) after chemical surface treatment (Snoeck and De Belie, 2012; Snoeck et al., 2015).

Despite the effectiveness of different fibers on different properties of composite materials, for the time being, PVA is the most successfully used fiber in ECC production (Li, 1998; Rossi and Parant, 2005; Alaei and Karihaloo, 2003; Li et al., 2002). Table 15.1 shows the mixture proportions of a typical PVA–ECC (Li et al., 2002), along with conventional structural concrete. High cement content in ECCs is a consequence of rheological control for easy fiber dispersion and, more essentially, matrix toughness control for strain-hardening behavior. To achieve high ductility (strain-hardening), matrix fracture toughness must be limited so that multiple micro-cracking can occur before reaching maximum fiber-bridging stress. Large aggregates are consequently eliminated in the mixtures, resulting in higher cement content than in normal concrete (NC). In fact, ECC materials use cement paste or mortar with fine sand as a matrix, and typically have cement content in the range of 800–1200 kg/m³. High cement usage results in undesirably high heat of hydration, as well as high material cost and drying shrinkage. In addition, such matrices compromise the sustainability performance of the material, as cement production is responsible for 7% of global greenhouse gas emissions generated by human activities, (Malhotra, 1999; Mehta, 1998) as well as significant levels of nitrogen oxides, particulate matter and other pollutants. Moreover, ECC could generate relatively large shrinkage strains, compared to conventional concrete due to relatively high cement content, low water–cement ratio and lack of coarse aggregates, thus increasing cracking potential. However, the presence of fibers can control crack width so the deterioration is not an issue.

Table 15.1 Typical mixture proportions of concrete and high-performance fiber-reinforced cementitious composites (HPFRCCs)

Material (kg/m ³)	PVA–ECC	Conventional concrete
Cement	558	390
Water	326	166
Fly ash	669	–
Aggregates	446	1717
Fiber	26	–
Superplasticizer	5.1	2

15.3.1 Production of Engineered Cementitious Composites

To ensure satisfactory performance, repair materials should be easy to mix in correct proportions, and the wet mix should have suitable consistency, high deformability, adequate passing ability, and segregation resistance in order to completely fill the complex formwork for repair applications. In manufacturing ECC, normal mixers and mixing procedures are used. For small batches, drum mixers can also be used (Fig. 15.5). All the dry components of the matrix (cement, fly ash, and sand) are blended together, followed by the inclusion of premeasured water and high range water reducing admixture (Li et al., 2003). Finally, fibers are slowly added and dispersed. Normal mixing time for drum mixers is between 8 and 15 minutes, which is sufficient to blend all ingredients homogenously. ECC exhibits excellent workability with self-consolidation capability (Fig. 15.5).

For casting of larger volumes, mobile and central mixers are desirable to ensure accurate proportioning and minimum waste, and maintain quality control of ECC. For large-scale mixing, all dry sand and premeasured water and super-plasticizer are added into the mixer (Li et al., 2003). Once these components are mixed well, all other binders (cement and fly ash) are added, and the entire mortar matrix is mixed until the material is homogenous and sufficiently liquid. After mixing of the mortar phase, fibers are slowly added and mixing continues until the fibers are well-dispersed throughout the composite. This sequence results in an overall mixing time between 9 and 12 minutes, which should be adequate for field applications, but, adjustments can be made in the field if other sequences are found to be more practical. For repair applications, another version of ECC has been designed for shotcrete applications, allowing the material to be pumped through a hose and then sprayed onto a concrete surface with minimal rebound (Kim et al., 2003).



Figure 15.5 (A) Mixing of Engineered Cementitious Composites (ECC) in a 60-L-capacity drum mixer (B) workability of ECC with self-consolidation capability.

15.3.2 Mechanical properties and durability of Engineered Cementitious Composites

Each of the following subsections reviews a specific property and the proportioning variables that influence it.

Compressive strength and MOE: ECC can be developed to achieve a wide range of compressive strength levels from normal to high. Generally, 28-day compressive strength results of standard ECC mixtures (M45) range from 30 to nearly 90 MPa (Wang and Li, 2005). This confirms that it is possible to produce ECC with strength levels to suit nearly all conventional concreting situations. Compressive strength levels are controlled mainly by binder composition, water to cement (w/c) ratio, and applied curing type. ECC mixtures can be produced with any combination of cements and mineral admixtures. If an ECC mixture is developed using a combination of cement and fly ash, as in M45, then compressive strength development may need to be measured after 28 days, as with conventional concrete. Similarly, if high early compressive strength is desired, such as for precast concrete, the replacement level of Portland cement with supplementary cementitious material will need to be limited. For example, in a recent study by Şahmaran et al. (2015a), high-early-strength (HES)—ECC mixtures with saturated lightweight aggregates were designed to achieve low early-age shrinkage. Experimental results revealed that the majority of HES—ECC mixtures attained compressive strength values of more than 20 MPa and a minimum flexural strength of 6 MPa within 6 hours, without sacrificing long-term ductility.

MOE of repair material is important in determining the stress regime in a repair system at the interface between repair and existing substrate. Incompatibility in elastic moduli between repair and substrate materials may lead to a considerable stress concentration when large differential volume changes of the repair material occur in relation with the substrate. Several studies have indicated that the MOE of ECC is lower compared to conventional concrete, as the paste content of mixtures increases and aggregate content decreases with the lack of coarse aggregates. Since a wide range of compressive strength values can be developed, a wide range of MOE values can also be attained in ECC mixtures. MOE is around 20 GPa, as measured at 28 days for the standard ECC mixture (Lepech and Li, 2005).

Fatigue: ECC performance has been investigated in high fatigue scenarios such as rigid pavement overlay rehabilitation or highway repairs. In these overlay applications, reflective cracking through the new overlay is of the greatest concern. Existing cracks and locally reduced load-carrying capacity in the substrate pavement can result in flexural fatigue within the overlay structure. To evaluate ECC performance as a rigid pavement overlay material, ECC/concrete and concrete/concrete overlay systems were tested in flexural fatigue (Zhang and Li, 2002). Test results showed that when ECC was used, the load carrying capacity of ECC/concrete repaired system was double that of concrete/concrete repaired system, deformability of ECC/concrete specimens was significantly higher, and fatigue life was extended by several orders of magnitude. Furthermore, the ability of ECC to display micro-cracking deformation behavior effectively eliminated reflective cracking. Similar advantages in the fatigue resistance of ECC have also been found

in comparison to polymer cement mortars (Suthiwarapirak et al., 2002). Fatigue resistance of ECC for the repair of viaducts subjected to train loading was studied by Inaguma et al. (2006), who reported that application of ECC materials in infrastructures with fatigue-prone concrete may significantly lengthen service life, and reduce maintenance events and life-cycle costs.

Freeze–thaw and salt scaling resistance: It is well-known that freeze–thaw (F/T) cycles and use of de-icing salts in winter are the two major causes of rapid degradation in concrete pavements, bridge decks, parking, and similar structures. ECC used for such structures must be resistant to cyclic freezing and thawing as well as the effects of de-icing agents. A proper air-void system is generally needed in NC to avoid internal cracking due to F/T cycles and scaling due to salt. However, as discussed below, the quality of the hardened air void system is not important for salt scaling and freeze–thaw durability performance of ECC.

Nonair-entrained ECC specimens and nonair-entrained concrete specimens (reference) were tested for F/T durability in accordance with ASTM C666A (Şahmaran et al., 2010). After 110 cycles, the reference concrete specimens had deteriorated severely, requiring removal from the F/T machine, as mandated by the standard. However, all ECC specimens survived the test duration of 300 cycles with no degradation of dynamic modulus. Fig. 15.6 shows the typical surface conditions of ECC specimens after 50 F/T cycles with de-icing salt and after 300 F/T cycles without de-icing salt. Tests showed a durability factor of 10 for concrete and 100 for ECC, computed according to ASTM C666A. In uniaxial tension tests performed on wet-cured and F/T-exposed ECC coupon specimens at the same age, no significant drop in strain capacity occurred after the 300 cycles. Both wet- and F/T-cured specimens exhibited a strain capacity of roughly 3%.

Numerous laboratory test data (in accordance with ASTM C672) indicate that air-entrained concretes incorporating high volumes of fly ash often perform unsatisfactorily when exposed to F/T cycles in the presence of de-icing salts. In standard ECC mixtures, as much as two-thirds of Portland cement is substituted with fly ash. Due to the high fly ash content, it is important to test the performance of ECC exposed to F/T cycles in the presence of de-icing salt. Salt scaling resistance of nonair-entrained sound (uncracked) and mechanically preloaded (cracked) ECC



Figure 15.6 Surface appearance of standard Engineered Cementitious Composites (ECC) after (A) de-icing salt surface scaling after 50 F/T cycles (B) after 300 F/T cycles without de-icing salt.

specimens was evaluated by Şahmaran and Li (2007), in accordance with ASTM C672. Nonair-entrained mortar specimens with and without fly ash were also tested as reference. After 50 F/T cycles with de-icing salt, a visual rating of the surface condition and total mass of scaling residue for ECC specimens showed that even those with high volumes of fly ash remained within the acceptable limits of ASTM C672 (Fig. 15.7). This level of durability holds true even for preloaded ECCs with severe micro-cracking damage. In comparison, reference mortars tested under identical conditions deteriorated severely. Moreover, replacing fly ash with cement in mortar further exacerbated F/T deterioration in the presence of de-icing salt. In a separate test, preloaded and sound ECC coupon specimens were exposed to 25 and 50 F/T cycles in the presence of de-icing salts to compare residual tensile strength and ductility of re-loaded ECC specimens. The re-loaded specimens showed negligible loss of ductility and retained multiple micro-cracking behavior and tensile strain capacity of more than 3%. Micro-cracks due to mechanical loading also healed sufficiently under F/T cycles, with salt solutions nearly restoring the original stiffness. These results confirm that both sound and micro-cracked ECC remains durable despite exposure to F/T cycles in the presence of de-icing salts.

Durability under extremely hot, humid, and alkaline environments: Hot water immersion tests were conducted to simulate the long-term effects of hot and humid environments on ECC. To examine the effects of environmental exposure, individual fibers embedded in ECC matrix and composite specimens were immersed in hot water (Li et al., 2004). Specimens of both individual fiber pull-out and composite ECC material were cured for 28 days at room temperature prior to immersion in hot water at 60°C for up to 26 weeks. After 26 weeks, little change was seen in fiber strength, elastic modulus, and elongation. Tensile strain capacity dropped from 4.5% to 2.75%, still 250 times that of NC.

High alkaline environments can also affect ECC microstructure and composite properties. Although no deleterious expansion is expected due to ASR—thanks to

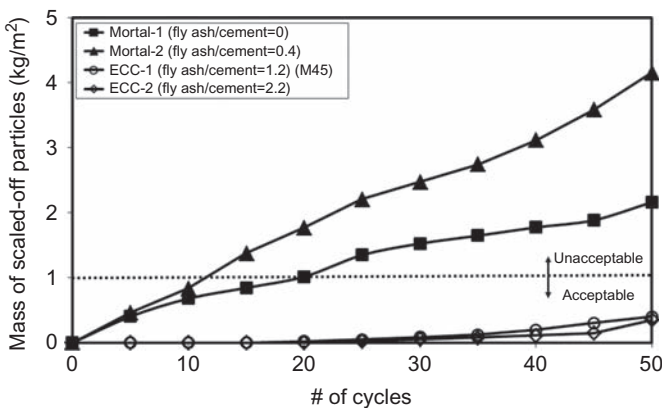


Figure 15.7 Mass of scaled-off particles vs number of Freeze–Thaw (F/T) cycles for virgin mortar and virgin Engineered Cementitious Composites (ECC) prisms in the presence of de-icing salts (Şahmaran and Li, 2007).

high fly ash (HVFA) content, small particle size of sand and micro-fibers in ECC—an extensive study was undertaken to evaluate the performance of HVFA-ECCs under high alkaline environments, in accordance with ASTM C1260 (Şahmaran and Li, 2016). The study considered the possibility of alkali penetration through micro-cracks and/or even in the sound state; length changes of ECC bar specimens were measured at different ages up to 30 days. ECC specimens with different fly ash types (Class-F and Class-C) and amounts were tested. Specimens with reactive sand were also produced and compared. Results and classification ranges from ASTM C1260 are shown by the horizontal gridlines in Fig. 15.8. This figure clearly indicates that, even after 30 days of severe alkaline exposure, ECCs are safe against ASR, regardless of fly ash type (F or C), fly ash to Portland cement ratio (1.2 or 2.2) or reactive sand (R) usage.

In a separate study, Şahmaran and Li (2008) evaluated the mechanical performance of mechanically-loaded and virgin ECC, under high alkaline environments. ECC coupon specimens were initially preloaded under uniaxial tension to different strain levels, then exposed to an alkaline environment at 38°C for up to 3 months and re-loaded up to failure. Re-loaded specimens showed slight loss of ductility and tensile strength, but retained multiple micro-cracking behavior and tensile strain capacity of more than 2% (more than 200 times that of conventional and normal fiber-reinforced concrete). Test results show strong evidence of self-healing of the micro-cracked ECC, which helped re-loaded specimens carry considerable tensile stress and strain, and nearly restore the original stiffness. This observation is also supported by an environmental scanning electron microscope (ESEM) observation of the fractured surface of ECC across a healed crack. Self-healing effectively closed the micro-cracks, even after a month of sodium hydroxide solution exposure (Fig. 15.9).

Corrosion and spalling resistance: Reinforcing steel bars embedded in concrete are usually well-protected against corrosion by the high alkalinity of pore water, since the steel surface is passivated in the presence of oxygen. However, reinforcing steel bars in concrete structures are depassivated when chloride concentration reaches threshold levels on the rebar surface, or when the pH of the concrete cover drops below critical levels due to carbonation (Tuutti, 1982). Some of the most

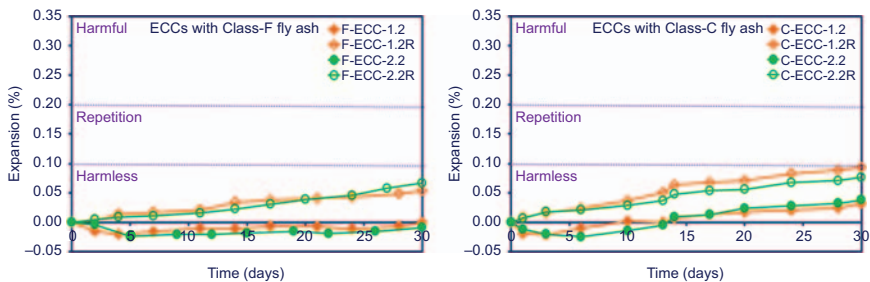


Figure 15.8 Alkali–silica reaction (ASR)-based expansion of Engineered Cementitious Composites (ECC) mixtures produced with different fly ash types (Şahmaran and Li, 2016).

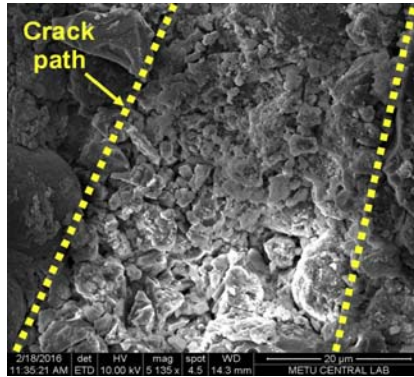


Figure 15.9 Environmental scanning electron microscope (ESEM) micrograph of rehydration products in a self-healed crack after 30-day sodium hydroxide solution exposure period (Şahmaran and Li, 2008).

commonly used methods used to protect steel reinforcement against corrosion include high-quality concrete (low w/c ratio and good consolidation), increased concrete cover thickness, and epoxy coating on steel bars. Generally, low w/c ratio and good consolidation contribute to reduced permeability. A higher cover thickness is intended to provide better physical protection since concrete acts as a barrier, delaying access of chloride ions, carbon dioxide, or moisture into the steel reinforcement. However, due to restrained shrinkage, thermal deformations, chemical reactions, poor construction practices and mechanical loads, concrete unavoidably cracks and the chlorides, carbon dioxide, and moisture can penetrate even high-quality concrete or concrete with good cover thickness over time (ACI 224R, 2001). In addition, greater cover thickness is known to lead to greater crack width. Furthermore, epoxy coatings on the surface of steel bars are sometimes damaged during handling or become brittle and delaminate from the steel under high chloride concentrations so reliability of the coating for steel protection is compromised (Manning, 1996). Consequently, reinforcement corrosion occurs, which can lead to cover spalling, and reduction of steel diameter and therefore load carrying capacity of the reinforced concrete member. The underlying reason for the steel corrosion problem is the brittle nature of conventional concrete. Brittleness inherently results in cracks that allow corrosives to penetrate the cover and fail to resist the expansive force once corrosion starts.

Şahmaran et al. (2008) investigated the cracking behavior and residual flexural load capacities of reinforced ECC (R/ECC) and reinforced mortar (R/mortar) specimens with equal compressive strengths. During accelerated corrosion testing at applied constant voltage, corrosion-induced crack widths of the mortar specimens increased with time as corrosion activity progressed. Larger crack widths up to 2 mm were observed at higher levels of corrosion (Fig. 15.10).

Moreover, the corrosion of reinforced mortar beam specimens resulted in a marked reduction in stiffness and flexural load carrying capacity. After 25 hours of

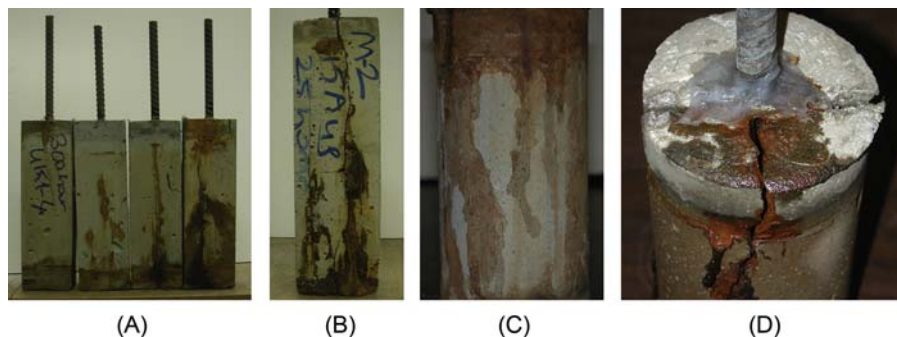


Figure 15.10 (A) Engineered Cementitious Composites (ECC) prismatic specimens after 300 h of accelerated corrosion, (B) mortar prismatic specimen after 25 h of accelerated corrosion, (C) ECC cylindrical specimen after 300 h of accelerated corrosion, (D) mortar cylindrical specimen after 90 h of accelerated corrosion ([Şahmaran et al., 2008](#)).

accelerated corrosion exposure, flexural load carrying capacity was reduced to nearly 34% of the flexural capacity of the control mortar beam. On the other hand, crack widths (~ 0.1 mm) of ECC remained nearly constant with time as corrosion activity progressed, while the number of cracks on the surface of ECC specimens increased. This study also showed that ECC has significant antispalling ability compared with conventional mortar ([Fig. 15.10](#)). In contrast to mortar specimens, after 50 hours of accelerated corrosion exposure, ECC beams retained almost 100% of the flexural capacity of control specimens. Beyond 50 hours, flexural capacity decreased but retained over 45% of that of control specimens, even after 300 hours of accelerated corrosion exposure.

A recent study investigated the effect of different corrosion levels (5%, 10%, 15%, and 20% of mass loss of reinforcing bars) on the shear behavior of reinforced large-scale ECC and NC beam specimens with similar compressive strengths, after testing under four-point bending ([Şahmaran et al., 2015b](#)). The study concluded that ECCs are quite effective in restricting corrosion damage compared to NC, and corrosion does not significantly affect the shear performance of ECC beams. Compared to NC beams, which resulted in spalling ([Fig. 15.11](#)), ECC beams without spalling exhibited significantly higher strength, stiffness and energy absorption capacity, even after high levels of corrosion exposure ([Fig. 15.12](#)).

Water permeability: Low permeability of the repair is necessary because repaired areas are the most vulnerable to attack. For this reason, ECC was tested by various means to ascertain permeability. [Lepech and Li \(2009\)](#) studied the water permeability of mechanically loaded ECC and reinforced mortar. In that study, ECC and reinforced mortar specimens were tensioned to identical deformation of 1.5%, resulting in micro-cracks with different numbers and widths. With applied tensile loading, ECC specimens revealed micro-cracks with widths less than $60\ \mu\text{m}$, regardless of the imposed deformation level. Cracked specimens exhibited nearly the same water permeability as sound concrete. In contrast, cracks larger than $150\ \mu\text{m}$ were easily

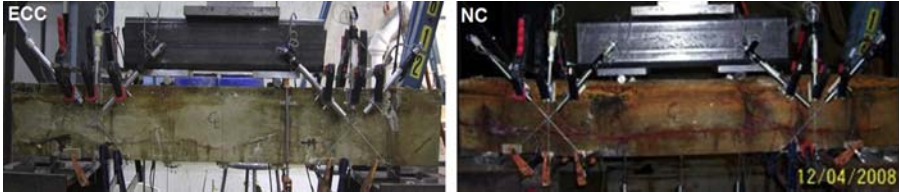


Figure 15.11 Engineered Cementitious Composites (ECC) and normal concrete (NC) specimens after 20% mass loss (Sahmaran and Li, 2008).

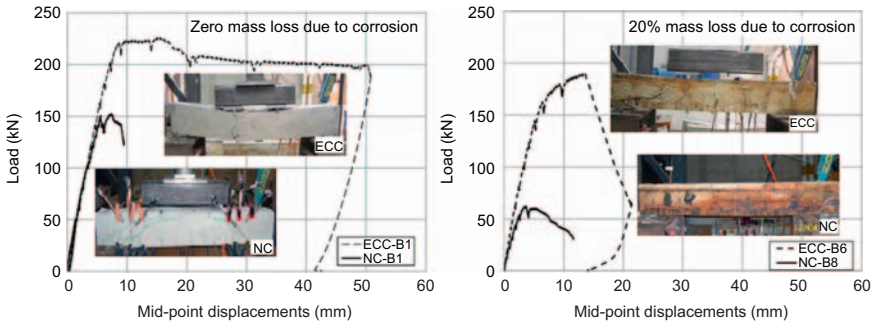


Figure 15.12 Load vs mid-span beam displacement graphs of Engineered Cementitious Composites (ECC) and normal concrete (NC) beams at zero and 20% mass losses due to corrosion (Sahmaran et al., 2015b).

produced in the reinforced mortar specimens under identical imposed uniaxial deformation. Larger crack widths resulted in a significant increase in the water permeability of the reinforced mortar, despite the smaller number of cracks. Further, when normalized by the number of cracks within the specimen, the comparable permeability of cracked ECC with sound material became even more apparent.

Gas permeability: Yildirim et al. (2015e) evaluated the gas permeability (GP) of ECC specimens with different mineral admixtures (Class-F fly ash [F_ECC], Class-C fly ash [C_ECC] and ground granulated blast furnace slag [S_ECC]) in the cracked and uncracked (sound) states, before and after further environmental curing. To create micro-cracking damage, ECC specimens were subjected to different splitting tensile deformation levels (1.25, 1.50, and 1.75 mm). After 28 days of initial curing, the average GPs of F_ECC, C_ECC, and S_ECC were 4.72×10^{-16} , 1.22×10^{-15} , and $9.54 \times 10^{-16} \text{ m}^2$, respectively. Unlike the water permeability results, preloading caused significant increments in the GP results of ECC specimens, irrespective of selected mineral admixtures and preloading levels. It has been reported that crack width is a more decisive parameter on the GP of ECCs than crack number. Although cracking substantially increased the GP of ECC specimens, a further 30 days of continuous curing in air (CA) and under water (CW) caused drops in GP through self-healing effect, although this was much more pronounced for specimens additionally cured under water. As shown in Table 15.2, depending

Table 15.2 Percentage variations in gas permeability (GP) results of different Engineered Cementitious Composites (ECC) mixtures after 30 days of additional conditioning (Yıldırım et al., 2015d, e)

Percent change in GP after 30 days	Mix ID.	Deformation level (mm)	CA-cured	CW-cured
	F_ECC		0	-21
1.25			-8	-93
1.50			-10	-71
1.75			-6	-59
C_ECC		0	-30	-58
		1.25	-8	-87
		1.50	-7	-77
		1.75	-7	-75
S_ECC		0	-40	-51
		1.25	-9	-75
		1.50	-20	-93
		1.75	-16	-78

on initial preloading level and mineral admixture type, it was possible for GP results to recover by 20% and more than 90% with further CA and CW curing, respectively.

Rapid chloride permeability: Rapid chloride permeability test (RCPT) does not actually measure the permeability of concrete materials; the method itself does not represent field conditions, considering there is no structure in the field that has 60 V potential on it. What RCPT measures is chloride ion penetration resistance in the presence of electrical current, with results that can be related to overall permeability. RCPT results can be handy in evaluating corrosion initiation and acceleration in reinforced ECC-based repair materials. In several studies described in literature, 28-day-old RCPT results of standard ECC specimens with Class-F fly ash were categorized in the low (less than 2000 Coulombs) (Özbay et al., 2013) and very low (less than 1000 Coulombs) chloride ion penetrability classes (Yıldırım et al., 2015c; Şahmaran et al., 2017), according to ASTM C1202. All of the cited studies concluded that precracking was quite influential in escalating RCPT results. It must be stated that, although severe precracking caused almost complete failure of specimens, average RCPT results stayed within the acceptable limits, regarded as moderate chloride ion penetrability level (between 2000 and 4000 Coulombs) in accordance with ASTM C1202 (Yıldırım et al., 2015c; Şahmaran et al., 2017). However, after only 15 days of further moist curing of standard ECC specimens at $90 \pm 5\%$ RH and $50 \pm 5^\circ\text{C}$ beyond the initial 28 days, at least 60% recovery in chloride ion penetrability results was achievable (Yıldırım et al., 2015c; Şahmaran et al., 2017). This was attributed to the superior self-healing capability of ECC specimens under moisture-rich conditioning.

Chloride ion diffusion: Corrosion of steel in concrete is one of the major problems affecting durability of reinforced concrete structures, and chloride ion penetration into concrete is one of the main causes of corrosion. Chloride ions in contact with the concrete surface will diffuse through the concrete until a state of equilibrium in ion concentration is achieved. If the concentration of ions at the surface is high, diffusion may lead to concentrations that can cause corrosion of reinforcement.

Miyazato and Hiraishi (2005) were probably the first to show that the penetration depth of chloride ions into ECC cover is substantially lower than that is in concrete cover—using R/C and R/ECC beams preloaded to the same level of flexural deflection and subjected to identical accelerated chloride exposure. In addition, Sahmaran et al. (2007) examined a relationship between flexural deformation levels and effective chloride diffusion coefficient of ECC and reinforced mortar. Effective chloride diffusion was computed based on measured chloride ion concentration profiles fitted to Crank’s solution to Fick’s 2nd Law. Under high-imposed bending deformation, preloaded ECC beam specimens revealed multiple micro-cracks with widths less than 50 μm , and an effective diffusion coefficient significantly lower than that of similarly preloaded reinforced mortar beams, thanks to the tight crack width control in ECC (Table 15.3). In contrast, cracks larger than 150 μm were easily produced in reinforced mortar specimens under the same imposed deformation, producing a significant increase in the effective diffusion coefficient. The effective diffusion coefficient of ECC was found to be linearly proportional to the number of cracks, whereas in reinforced mortar, it was proportional to the square of the crack width. Thus, the effect of crack width on chloride transport was more pronounced than crack numbers. Li et al. (2007) investigated the tensile performances of cracked and uncracked ECC specimens in a marine environment. Apart from slight reductions in ultimate tensile strain and strength capacities, and higher residual

Table 15.3 Diffusion coefficient vs preloading deformation level for Engineered Cementitious Composites (ECC) and mortar (Sahmaran et al., 2007)

Mixture ID.	Beam deformation (mm)	Average crack widths (μm)	Effective diffusion coefficient ($\text{m}^2/\text{s} \times 10^{-12}$)
Mortar	0.00	—	10.58
	0.50	~ 50	33.28
	0.70	~ 150	35.54
	0.80	~ 300	126.53
	0.83	~ 400	205.76
ECC (M45)	0.00	—	6.75
	0.50	~ 0	8.10
	1.00	~ 50	27.99
	1.50	~ 50	37.50
	2.00	~ 50	54.22

crack width, test results largely confirmed the durability performance of ECC material under accelerated aging, even when mechanical loading deformed the material to the strain-hardening stage prior to exposure. Healing of micro-cracks induced by preloading was evident from the recovery of elastic stiffness of exposed precracked specimens on re-loading.

As mentioned previously, the relatively low diffusion coefficient of cracked ECC specimens was not only due to tight crack widths, but self-healing that took place in the cracks with tight widths. According to [Edvardsen \(1999\)](#), and [Reinhardt and Jooss \(2003\)](#), cracks with widths less than $100\ \mu\text{m}$ can be closed by self-healing. In precracked ECC specimens exposed to water or salt solution or wet/dry cycles, micro-cracks closed due to self-healing, slowing further water intake and reducing the rate of water absorption and diffusion ([Lepech and Li, 2009](#); [Sahmaran et al., 2007](#)). [Fig. 15.13](#) shows ESEM observation of the fractured surface of ECC across a healed crack after exposure to salt solution. ESEM observations show that most of the products seen in the cracks were newly formed calcium–silicate–hydrate (C–S–H) gels, which are the basic cementing compound produced by hydration reactions. Formation of C–S–H gels inside the cracks was attributed primarily to the high fly ash content and relatively low water to binder ratio of the ECC mixture. Continued pozzolanic activity of the fly ash was responsible for self-healing of the cracks, further reducing ingress of chloride ions ([Sahmaran et al., 2007](#)).

Absorption: Concrete structures are generally subjected to the drying actions of wind and sun, and thus are rarely fully saturated when in service. Under such conditions, permeability and diffusion may not be the dominant transport processes in concrete. Under dry or partially saturated conditions, water movement into concrete is controlled by the forces of capillary suction in the evacuated capillary cavities in the matrix. Cracking in ECC is fundamentally different from that occurring in concrete or reinforced concrete, and therefore requires special attention regarding its relation to capillary suction. [Şahmaran and Li \(2009\)](#) studied the sorptivity and

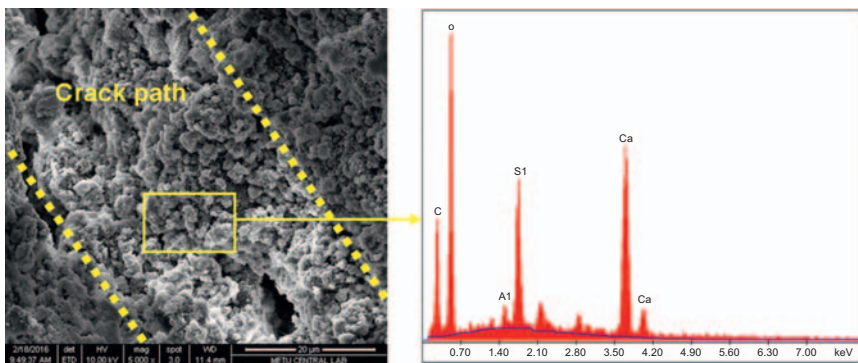


Figure 15.13 Environmental scanning electron microscope (ESEM) micrograph of rehydration products in a self-healed crack after exposure to salt solution ([Sahmaran et al., 2007](#)).

absorption properties of precracked ECC. In that study, water absorption and sorptivity tests were performed on ECC specimens after introducing various numbers of micro-cracks by mechanical preloading. Fig. 15.14 shows the relationship between sorptivity over 6 hours and number of cracks for ECC specimens. Corresponding values for sound ECC specimens (data points with zero number of cracks) are also included in this plot.

The presence of micro-cracking in ECC significantly alters its transport properties, measured as a function of the number of micro-cracks (Fig. 15.14). Water absorption increases steadily as the number of cracks on the surface of ECC specimens increases. Therefore, sorptivity testing shows that micro-cracked ECC specimens would be more vulnerable to attack than sound ones. As the number of cracks increased, sorptivity of ECC increased exponentially. Even so, sorptivity values of ECC specimens preloaded up to strain levels representing 1.5% on the exposed tensile face were not particularly high compared to those of NC, probably due to the higher amount of cementitious materials, lower water-cementitious materials ratio, high fly ash content, and absence of coarse aggregates. Moreover, the same study evaluated the absorption rate in cracked ECCs with water repellent admixture, and found that its use in the production of ECC could easily inhibit water intake through sorptivity, even when mechanical preloading was available (Fig. 15.14) (Şahmaran and Li, 2009).

Wear testing and abrasion: For pavement surface and bridge deck repairs, ECC must provide an adequate surface for driving and braking, while withstanding traffic abrasion. Unlike conventional concrete, abrasion resistance of ECC is not directly related to the compressive strength of composites, which makes normal-strength ECC ideal for abrasive environments. Wearing and abrasion resistance of ECC were evaluated with 28-day-old specimens subjected to both static friction and wear track testing, according to Michigan Test Method 111 (Michigan Department

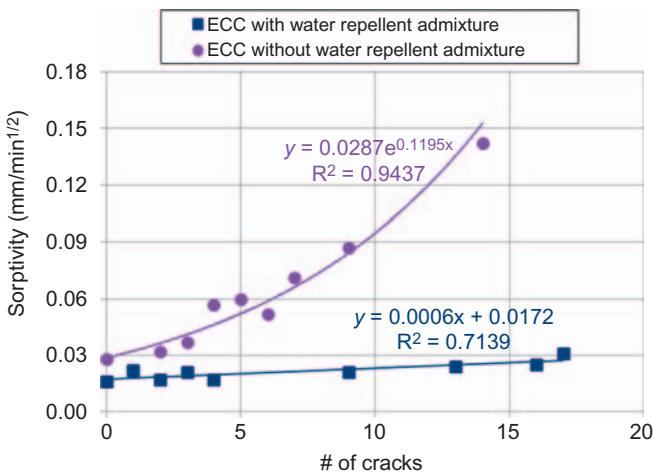


Figure 15.14 Sorptivity vs number of cracks for Engineered Cementitious Composites (ECC) mixtures (Şahmaran and Li, 2009).

of Transportation, 2001). Initial friction forces between vehicle tires operating at 65 kmph and textured ECC specimens were determined using a Michigan Department of Transportation (MDOT) static friction tester. All static friction tests were conducted on a wet pavement surface. Following initial friction testing, ECC specimens were subjected to 4 million tire passes to simulate long-term tire wear. After wearing, friction forces were again determined to assess deterioration or surface polishing during wearing. These final friction forces equate to an Aggregate Wear Index (AWI) used for long-term evaluation of pavement wear; AWI values for the textured ECC samples tested range from 1.6 to 2.3 kN (Li et al., 2003). The established minimum AWI for Michigan trunkline road surfaces is 1.2 kN, significantly lower than all ECC surfaces tested. The superior adhesion performance of normal strength ECC is particularly useful for pavement surface repairs or overlays subjected to heavy or abrasive traffic volumes.

15.3.3 Dimensional stability of Engineered Cementitious Composites

The term “dimensional compatibility” expresses the harmony between properties related to the dimensions of at least two materials. It is a time-dependent phenomenon; dimensions of two materials may be compatible at the time of casting, e.g., but may change with respect to one another with time, causing an incompatibility. Dimensional compatibility is important since the likelihood for one of the two materials to crack is very high when incompatibility is present.

Mass production of ECC is currently limited, due to costly special ingredients and the expertise required for the specialized production technique. On the other hand, ECC has superior properties that cannot be overlooked, and modern structures may benefit from it for greater durability and damage tolerance. Consequently, in most instances, ECC is used partially for certain structural parts including bridge deck link slabs, patch repairs, layered repair systems or overlays, stud connections, shotcrete repair systems, high-early-strength repairs and ductile strips, all of which require the use of ECC along with another material. This makes dimensional compatibility a critical property. However, determining the compatibility of ECC with different materials can be challenging; both materials must be evaluated with respect to the other. Layered or repaired materials used with ECC could include an old concrete/asphalt layer, rock of any origin, or a steel structural member, all of which are more or less dimensionally stable. In this regard, ECC that is dimensionally stable or at least experiences limited time-dependent deformations would also be dimensionally compatible with any of these materials.

On the other hand, like all other cementitious composites, ECC itself is not a dimensionally stable material, although this does not necessarily mean it will eventually crack. If time-dependent strains of ECC can be compensated by the intrinsic strain capacity under mechanical loading, cracking will not occur. Time-dependent strains mainly arise from drying shrinkage, which is the loss of water as a result of exposure to the outside environment. However, measured drying shrinkage may include autogenous or chemical shrinkage, carbonation shrinkage and thermal

shrinkage. In other words, when shrinkage strains develop, differential shrinkage or any restraining condition will result in shrinkage-induced tensile stresses. If the material is capable of bearing these stresses, no cracking will occur. Since stresses are proportional to strains under the proportional limit, a larger elastic modulus will result in larger induced stresses. Although a standard ECC mixture can reach up to 90 MPa of compressive strength, elastic modulus is around 20 GPa, which is lower than that expected from ordinary concrete and offers favorable cracking resistance. Moreover, if the tensile stress-bearing capacity of the material is converted to strain, then cracking potential can be formulated independent of the neighboring material properties. Strain capacity is the sum of instantaneous strains and time-dependent strains, and is also referred to as creep. Instantaneous strains developed may be elastic, or elastic and plastic. In the case of high performance strain-hardening cementitious composites with multiple fine cracks like ECC, strain capacity between first cracking strength and tensile strength may also be added to strain capacity up to first cracking. However, within this region, significantly increased strain capacity is realized through the formation of a number of self-controlled fine cracks. When evaluating the cracking potential of ECC at this point, fine cracks up to 100 μm should not be evaluated; since they originated from incompatibility, they constitute part of the strain capacity of the material when induced tensile stresses exceed cracking strength.

ECC contains significantly high amounts of cementitious materials such as Portland cement, fly ash and ground granulated blast furnace slag. A standard cubic meter of ECC mixture contains around 1200 kg of cementitious materials, with a water to cementitious material ratio of 0.27, which is low enough to make autogenous shrinkage a concern. Autogenous shrinkage results measured at 28 days revealed fairly high values at 442 and 680 μe for mixtures with fly ash and slag, respectively (Keskin, 2012; Keskin et al., 2014). Increasing the amount of sand to around 50% decreased autogenous shrinkage to less than 5%. Replacing Portland cement with a supplementary cementitious material appeared to be a more effective way to lower autogenous shrinkage, as the average results decreased from 442 to 300 μe when fly ash to Portland cement ratio was increased from 1.2 to 2.2. This was not valid for the slag-bearing mixture, as autogenous shrinkage dropped from 680 to only 660 μe for the same replacement level. This phenomenon is attributed to early and faster hydration of slag compared to fly ash, and refined pore sizes of slag-containing ECC matrices, which resulted in higher shrinkage due to increased capillary stresses. Increased autogenous shrinkage in ECC was also augmented by the lack of coarse aggregates, given the insufficient restraining effect of fine aggregates used in ECC production. The effect of sacrificing strain capacity to lower autogenous shrinkage by replacing some of the fine aggregates with coarser ones was also minor, since the contribution of chemical shrinkage is tremendous and can only be compensated by increasing aggregate size. Overall, however, the amounts of supplementary cementitious materials and aggregates can be increased to account for autogenous shrinkage, with only a slight risk to strength and deformability decrements: reducing it to 216 and 510 μe levels for fly ash and slag-bearing mixtures, respectively (Keskin, 2012). Autogenous shrinkage, in terms of dimensional

stability and cracking potential, is relatively important, although its extent is quite limited for conventional and ordinary fiber-reinforced concretes.

Cumulative shrinkage is important for the dimensional stability of ECC. When dealing with shrinkage, the measured change in length of a specimen in a controlled environment is commonly attributed to drying shrinkage. In reality, measured length change is the sum of all shrinkage types including autogenous shrinkage. Thus, drying shrinkage strains, which are greatly influenced by autogenous shrinkage, are sufficient to be used in calculations of cracking potential. Drying shrinkage measurements of different ECC mixtures show similar trends as autogenous shrinkage, revealing the influence of autogenous shrinkage on drying shrinkage, although the dimensions of specimens used for measurements were different for each test. Like autogenous shrinkage, higher values of drying shrinkage attained by slag-containing mixtures showed values up to an average of $1477 \mu\epsilon$, whereas it was $\sim 1157 \mu\epsilon$ for mixtures containing fly ash (Keskin, 2012). Drying shrinkage may also be reduced by employing methods similar to those used to reduce autogenous shrinkage with similar results. Using additional cementitious materials for drying shrinkage mitigation results in a denser structure, which also prevents water loss.

In order to evaluate cracking behavior under drying conditions, mechanical properties should be known (including instantaneous and time-dependent strains developed as a response to induced tensile stresses due to shrinkage). The development of tensile creep strains in ECC specimens is provided in Fig. 15.15 (Keskin, 2012). In this test, seven-day-old ECC specimens were placed into a tensile creep loading frame and subjected to a constant tensile stress corresponding to 30% of their 7-day tensile strength values. At 14 and 28 days, the tensile strengths of the specimens were determined in the same manner, and tensile creep loads were modified to sustain a tensile load at 30% of the ultimate tensile strength until the end of 90 days. As drying and creep simultaneously occurred, drying shrinkage strains were also measured on identical specimens and added to the total strains of loaded specimens. Initial measurements were recorded from unloaded specimens; values on the plot include both instantaneous and creep strains. To calculate cracking potential, tensile creep strains corresponding to a stress level induced by shrinkage are needed, but the plot in Fig. 15.15 can also be used to comment on the general tensile creep behavior of different ECC mixtures. This plot represents data from four different ECC mixtures; two with fly ash and two with slag, with fly ash to Portland cement and slag to Portland cement ratios of 1.2 and 2.2. The mixture containing the higher amount of fly ash (fly ash/Portland cement = 2.2) experienced larger creep deformations, followed by the mixture with a fly ash to Portland cement ratio of 1.2. Slag-bearing mixtures behaved in a similar way, although creep strains were clearly lower than those recorded from fly ash bearing mixtures (Fig. 15.15). This behavior is also similar to the deflection capacities of specimens under bending loads. Specific tensile creep values after 90 days of testing were 301, 502, 146, and 259 ($\mu\epsilon/\text{MPa}$) for mixtures with fly ash/Portland cement = 1.2 and 2.2 and slag/Portland cement = 1.2 and 2.2, respectively. These results therefore indicate that, for each megapascal of tensile stress, the largest creep deformation will be obtained for

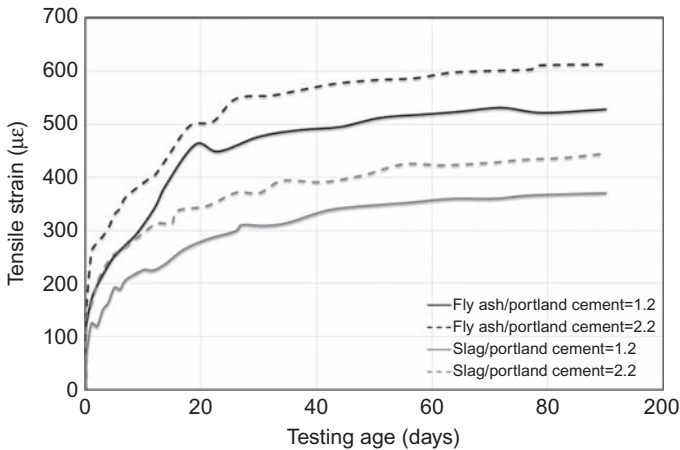


Figure 15.15 Total tensile (instantaneous and creep) strain development with time (Keskin, 2012).

mixtures with high amounts of fly ash, while the smallest creep deformation will be obtained for those containing slag.

In light of the aforementioned shrinkage and creep test results, it is clear that dimensional stability of ECC develops with the use of cement replacement materials (especially fly ash), as they show the lowest shrinkage and the highest total tensile deformation. Cracking tendency can also be measured experimentally using restrained shrinkage rings. In this test, a fresh ECC mixture is cast between two cylindrical steel molds and the outer mold is removed after one day while the inner ring is left in place. The ECC ring is exposed to drying at a relative humidity of 50% from the outer surface and monitored under laboratory conditions for evidence of cracking (Keskin, 2012). Crack numbers and widths are measured daily to evaluate the material's tendency to cracking. As seen in Fig. 15.16, the representative ECC mixture experienced a number of tight cracks with widths smaller than $80\ \mu\text{m}$, which corresponds with the multiple micro-cracking behavior of ECC under loading. The same behavior under restrained conditions was also monitored for all ECC mixtures cast for restrained shrinkage evaluation (Keskin, 2012). Restrained shrinkage results also revealed that crack onset time was delayed and average crack width decreased with the use of large quantities of cement replacement materials. Moreover, conclusions drawn from cracking potential based on drying shrinkage and tensile creep test results, and experimentally determined cracking tendencies by restrained shrinkage testing yielded exactly the same results.

15.3.4 Bond behavior of Engineered Cementitious Composites

The performance of a repaired system is strongly influenced by the quality of bond formed between the repair material and substrate. A variety of methods for

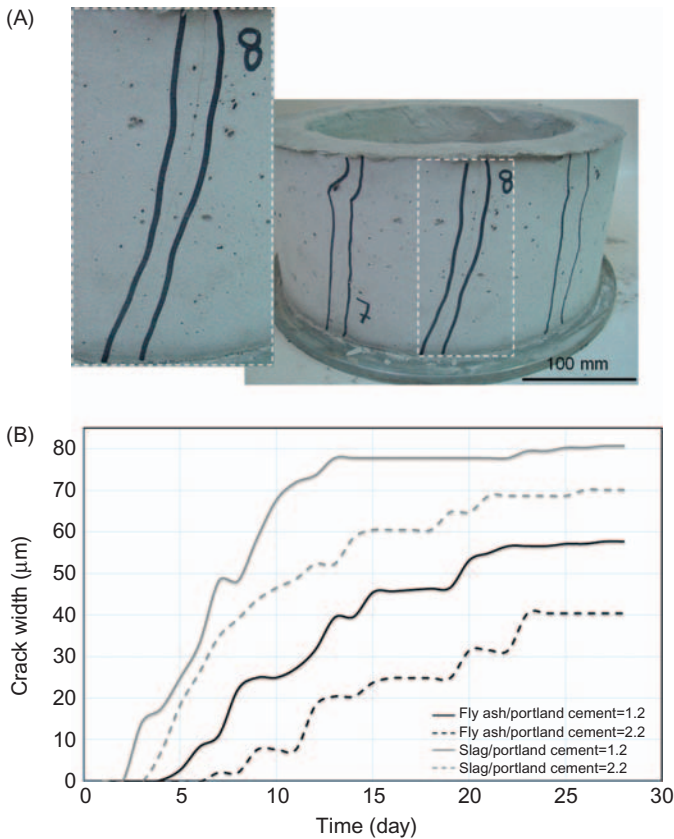


Figure 15.16 (A) Cracking pattern on restrained shrinkage ring, (B) average crack width developments of restrained shrinkage specimens (Keskin, 2012).

evaluating the bond behavior of repair systems have been proposed and reviewed in literature. The most commonly used bond tests can be categorized as direct tension tests, direct shear tests, torsional tests, indirect tension tests (e.g., splitting prism), combined shear, and compression tests (e.g., slant shear test), and pull-off tests (Li et al., 1997; Momayez et al., 2005; Silfwerbrand, 2003; Geissert et al., 1999; Wall and Shrive, 1988; Abu-Tair et al., 1996; Harris et al., 2011; Espeche and León, 2011; Saucier et al., 1991). While some of the methods are inconvenient in practice, slant shear, splitting prism, and pull-off tests appear to be the most advantageous because they have fewer problems and shortcomings, are easy to set up and perform, have a wide range of applications, are inexpensive, and offer greater reliability of results (Li et al., 1997; Silfwerbrand, 2003; Saucier et al., 1991).

Slant shear testing, as described by ASTM C882, is one of the most extensively used methods for measuring bond strength since it is inexpensive, easy to implement and offers results with greater reliability. In this test, repair material is bonded

to a substrate specimen on a slant elliptical plane inclined at an angle of 30 degrees or 45 degrees from the loading axis to form a composite cylinder. Likewise, the pull-off test, done in accordance with ASTM D4541, is one of the simplest and most commonly used tests for bond strength evaluation, and it can easily be performed in both the laboratory and in the field. In the splitting prism test, which is similar to testing explained in ASTM C496, a prism with a rectangular cross-section is loaded along an interface between the repair material and substrate to simulate a tensile load perpendicular to the plane. Tension stresses cause failure in the plane, passing through the upper and lower loading axes and split the specimen into two halves. Along with providing easily calculable measured bond strength values, these test methods are unique in that they provide indications about the level of bonding through monitored failure modes.

Bond strength and behavior of normal strength-ECC applied over substrate concrete (SUBC) with smooth and untreated rough surface textures were studied (Şahmaran et al., 2013b). Bonding performance between micro-silica concrete (MSC)—generally used for overlaying purposes—and ECCs were also compared. According to Şahmaran et al. (2013b), bond strength—which is realized through slant shear and splitting prism tests—is significantly higher in normal strength-ECC mixtures than in MSC with higher compressive strength capacity. Under compression (slant shear test), the bond strength of the ECC–SUBC layered repair system was greater than that of compressive strength of SUBC itself, which was around 30 MPa. However, in the layered MSC–SUBC repair systems, failures consistently occurred at the interface. Moreover, the bond strength of normal-strength ECCs was higher than that of MSC, irrespective of applied surface texturing, which suggests that ECCs have excellent bonding capability with substrate material (Şahmaran et al., 2013b). Splitting prism tests from the same study showed that using ECCs as repair material resulted in bond strength values better than monolithic structures (continuous samples) with no predefined interface plane.

Improved bond performance with ECC suggests that the type of overlay material plays an important role in the performance of the overall repair system, and that increasing the compressive strength of the overlay (repair) material may not necessarily lead to increased bond strength. During the slant shear tests, the tested cylinders were visually observed to see if they failed along the shear plane, due to significant cracking in the repair material or SUBC. Despite the absence of surface roughness, all ECC–SUBC bi-layer specimens failed from the substrate (Fig. 15.17); the high adhesion strength of ECCs kept the interface from failing. It is important to note that failure through the substrate is always desirable since it demonstrates that the existing substrate is the weakest component of the complete repair system.

A different study by Yücel et al. (2013) evaluated the performance of ECCs of different thicknesses (25, 35, and 50 mm) used as overlay material over SUBC with respect to MSC. Performance was analyzed to monitor the flexural performance of overlaid specimens, and to see if the proposed materials were effective in eliminating reflective cracking and delamination failure in repaired systems. The flexural strength of the layered specimens significantly increased (above 100% of the value

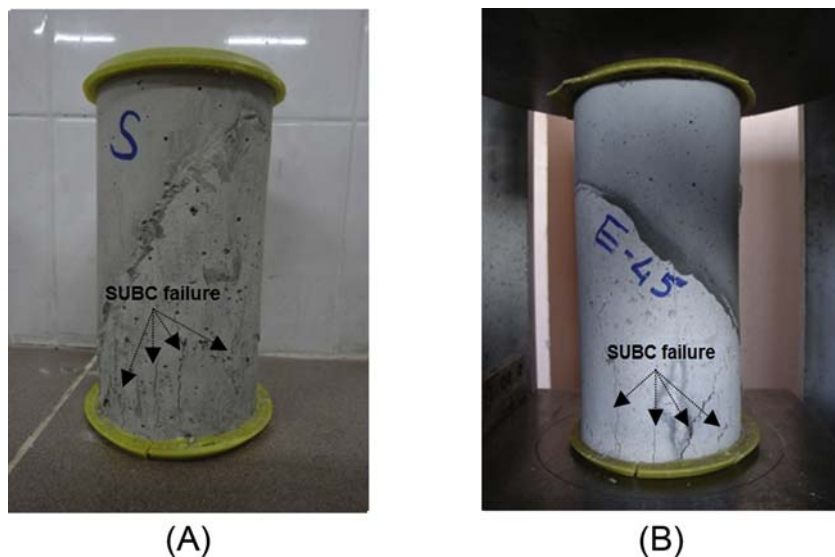


Figure 15.17 Failure examples from slant shear test specimens inclined at an angle of (A) 30 degrees, (B) 45 degrees (Sahmaran et al., 2013b).

obtained from the MSC-overlaid beam) by using ECC as the overlaying material, which was more pronounced with increased thicknesses. Using ECCs as the overlaying material was effective in suppressing the brittle failure of MSC-overlaid systems. ECC-overlaid systems resulted in relatively higher deformability and energy absorption capacities with multiple micro-cracking behavior. The increase in deformability in the form of micro-cracking through the use of ECC totally eliminated the reflective cracking observed in SUBC overlaid with MSC (Fig. 15.18). The ECC-overlaid system was also effective in eliminating delamination. Finally, 35 mm-thick ECC overlays were significantly more effective than 50 mm-thick MSC overlays in prolonging service life under traffic loading and reducing the costs of rehabilitation.

Yildirim et al. (2015a) studied the bond properties of High-Early-Strength–Engineered Cementitious Composites (HES–ECC) characterized by high ductility and low early-age shrinkage. A mixture of commercially-available repair material (REP) used extensively for fast and durable infrastructure repair was included for comparison; slant shear and tensile pull-off tests were performed to evaluate bond properties. Experimental results indicated that HES–ECC mixtures significantly improved the bond properties of a repair assembly in comparison to REP, despite significantly lower differential shrinkage formation of REP specimens. Enhanced bond performance of HES–ECC mixtures over REP was more evident in direct pull-off tests than in slant shear tests, both in bond strength results and failure mode. Depending on the mixture type, 1-day tensile pull-off bond strength results for HES–ECC ranged between 1.83 and 2.45 MPa. As seen in Fig. 15.19, almost all tested HES–ECC specimens failed from the SUBC. Moreover, all mixtures in

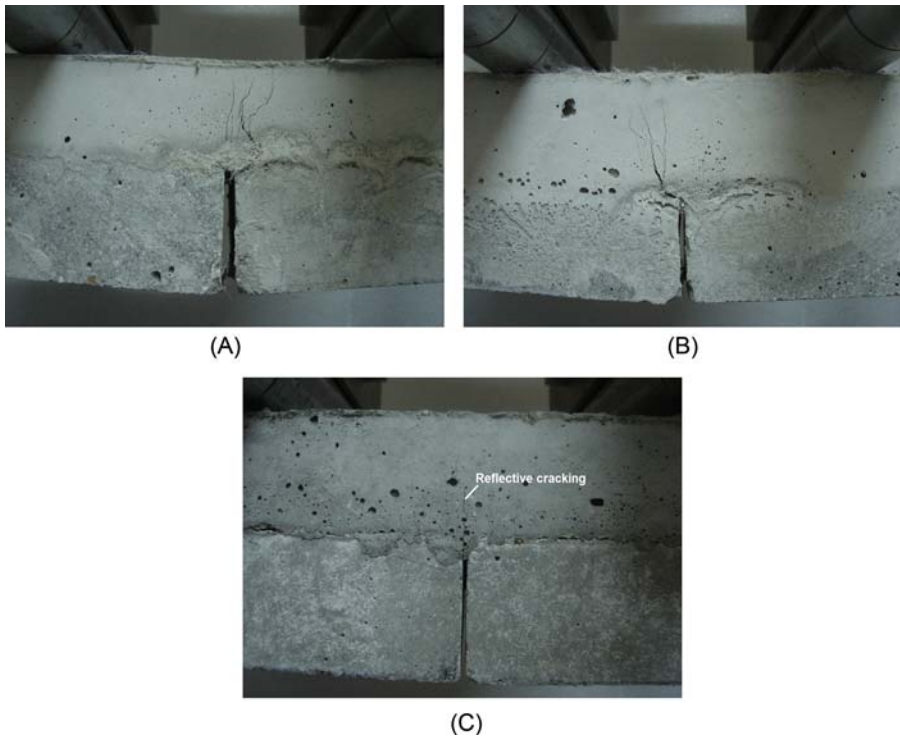


Figure 15.18 Crack patterns at failure of overlay materials after reflective cracking test: (A) F_ECC (ECC with Class-F fly ash), (B) S_ECC (ECC with slag), and (C) micro-silica concrete (MSC) (Yücel et al., 2013).

general showed an increasing trend in bond strength results with time. It should be stressed that the bond strength values of all HES–ECC mixtures fell within the range of very good to excellent levels (Sprinkel and Özyıldırım, 2000). HES–ECC mixtures showed higher bond strength results than REP due to the influence of micro-synthetic fibers on interfaces, along with the higher ductility of HES–ECCs. Fibers play an important role in lowering the total shrinkage-related deformation at the interfaces and lead to a more uniform distribution of micro-cracks by arresting, blunting, deflecting and branching them. As the size of flaws is reduced at the interfaces, repair assembly can resist to a higher tensile loading. It is not the magnitude of total deformation, but the ability to easily bear large strain formations that should be considered when selecting a suitable repair material.

As a follow-up to the earlier study, the authors also focused on freeze/thaw (F/T) durability of layered HES–ECC–SUBC and REP–SUBC repair systems. Layered beam specimens were submerged in water and subjected to temperatures between -18 and $+4^{\circ}\text{C}$, in accordance with ASTM C666A. Six layered specimens from each mixture were tested for frost durability, undergoing 300 F/T cycles. Five out of six REP–SUBC repair system specimens severely deteriorated after 100 to

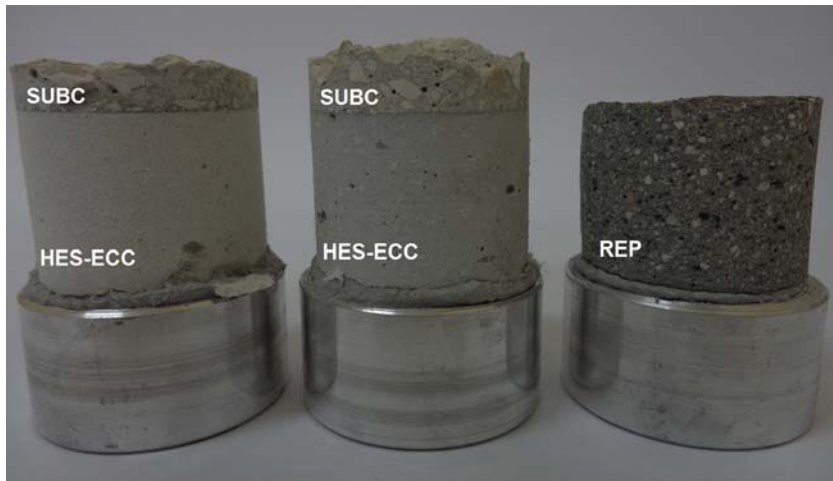


Figure 15.19 Failure modes of High-Early-Strength–Engineered Cementitious Composites (HES–ECC) and repair (REP) specimens after 28 days as a result of direct pull-off tests (Yildirim et al., 2015a).

200 F/T cycles, requiring removal from the F/T. Only one survived the full 300 cycles, with extensive surface scaling. In the case of HES–ECC–SUBC repair systems, on the other hand, all layered specimens survived 300 F/T cycles, with slight scaling restricted entirely to specimen surfaces (Fig. 15.20).

15.3.5 *Intrinsic self-healing of Engineered Cementitious Composites*

Tight micro-cracking behavior—which is a direct outcome of strain-hardening phenomenon in ECCs—is of great importance in achieving superior mechanical properties and the intrinsic autogenous self-healing. Tight micro-cracking is important because of its direct effect on the amount of self-healing products generated by the cementitious system to plug the crack. As might be expected, larger widths require higher volumes of self-healing products to be formed, and this situation is likely to accelerate self-healing kinetics due to higher space availability for newly formed products and easier ingress of necessary substances into the cracks for self-healing occurrence. Although wider cracks accelerate self-healing kinetics, they may result in inadequate plugging of the total crack opening, and may not be sufficient to recover a material’s original durability and mechanical properties. Thus it is more logical to think that narrower cracks would be healed more easily. Considering ECCs with crack widths as low as 30 μm can easily be manufactured nowadays, these materials are highly appealing in terms of intrinsic self-healing in both laboratory and field conditions. As previously mentioned, the superior self-healing capability of ECCs with a great variety of mixture parameters was largely confirmed by mechanical and durability tests under a series of environmental exposures (Yildirim



Figure 15.20 Visual observations of layered repair systems (A) high-early-strength–Engineered Cementitious Composites–substrate concrete (HES–ECC–SUBC) system after 300 F/T cycles, (B) repair–substrate concrete (REP–SUBC) system after 150 F/T cycles.

et al., 2015d). Along with the advanced mechanical, durability, dimensional stability, and bond properties, intrinsic self-healing capability is also a very advantageous property of ECC, making the material an attractive option for a wide array of field applications including repair of infrastructures.

15.3.6 Applications of Engineered Cementitious Composites

To illustrate the versatility of ECC as a durable repair material in field applications, a number of recent/ongoing projects involving the use of ECC are briefly highlighted below.

Fig. 15.21 shows the repair of Mitaka Dam in Hiroshima Prefecture, Japan, which was completed in 2003 (Kojima et al., 2004). By that time, the dam was over 60 years old, with a severely damaged concrete surface. Cracks, spalling, and water leakage were concerns that prompted the use of ECC as a water-tight cover layer. This 20 mm layer was applied by spraying the ECC material directly onto $\sim 600 \text{ m}^2$ of the upstream dam surface.

The second large-scale application in Japan used ECC to repair a concrete gravity, earth-retaining wall (18 m wide, 5 m high) damaged by ASR cracking (Rokugo et al., 2005). The retaining wall was divided into several sections and repair materials including a premixed cement mortar and ECC were used in different sections for performance comparison. The decision to use ECC for the 50–70 mm thick repair was based on the need to prevent reflective cracking from the substrate concrete through the repair layer (Li and Lepech, 2004). After continuous damage-monitoring of the wall at 10 and 24 months following the repair, micro-crack widths in the ECC repair layer remained below $50 \mu\text{m}$ and $120 \mu\text{m}$ respectively, while the maximum crack widths in the premixed mortar repair (used as a control) were 0.2 mm and 0.3 mm, respectively (Kunieda and Rokugo, 2006).

In 2002, in one of the first field applications of ECC in the United States, a concrete bridge deck patch was completed in cooperation with the MDOT (Li and Lepech, 2004). One section of a deteriorated bridge deck was repaired with ECC,



Figure 15.21 Spray repair of the Mitaka Dam with Engineered Cementitious Composites (ECC) for waterproofing (Kojima et al., 2004).



Figure 15.22 Engineered Cementitious Composites (ECC) patch repair placed alongside concrete patch on Michigan bridge deck (Şahmaran and Li, 2016).

Source: This article was originally published in the May/2016 issue of Concrete International, www.concrete.org.

while the remaining portion was repaired with a commercial repair material commonly used by the MDOT (Fig. 15.22). This scenario allowed for a unique ECC/commercial repair material comparison subjected to identical environmental and traffic loads. The concrete repair material used was a prepackaged, commercially available repair mortar. Using a drum mixer, prebatched ECC components were mixed onsite. An ECC with self-consolidating capability was cast without vibration. The repaired bridge deck experienced more than five complete Michigan winter cycles of freezing and thawing, in addition to traffic loads. While the ECC patch repair survived in this combined loading environment with minor micro-cracking of less than 50 μm , the concrete repair portion developed localized cracks in excess of

3.7 mm wide and required re-repair in 2005. From this comparison of adjacent patch sites subjected to identical mechanical and environmental loading, ECC was shown to be superior to the concrete repair material.

Another field application of ECC is a “link slab” in a two-span bridge in the United States, completed in cooperation with MDOT in 2005 (Fig. 15.23). Within this link slab, the material ductility of ECC was leveraged to replace problematic expansion joints within simply supported multi-span bridges with a ductile ECC slab, which links the adjacent simple spans (Lepech and Li, 2005; Li et al., 2005). In this project, about 32 m³ of ECC were cast in place using standard ready-mix concrete trucks to build the first ECC link slab. With a strain capacity exceeding 2%, these composites can be used to replace traditional steel expansion devices and can fully accommodate the thermal deformations of adjacent bridge spans. After 10 years of service, the link slab (Fig. 15.23) continues to function as intended, without any repair or maintenance.

The most recent field application of ECC is the shear keys of bridges with adjacent box beams and voided slabs, completed by Virginia Department of Transportation (VDOT) in 2014 (Özyıldırım and Moruza, 2016). Bridge designs in the United States have grouted shear keys to transfer load between beams. However, shear key cracks frequently occur and leak, even with a waterproofing membrane in place (Miller et al., 1998). To extend the life of reinforced concrete in bridges, VDOT used low-permeability grouts as shear key repair materials. Three different cementitious materials, including nonshrink grout commonly used by VDOT, standard ECC mixture, and ultra-high performance concrete (UHPC) were used in the shear keys of the bridges on different routes; the performance of each material in its respective shear key was investigated. The performances of all grouting materials were recorded during site visits. From this unique comparison, ECC performed the best, even though it had the highest shrinkage among the tested



Figure 15.23 After 10 years of service, Engineered Cementitious Composites (ECC) link slab on Grove Street Bridge, MI (A) immediately after construction in 2005, and (B) in 2015 (Şahmaran and Li, 2016).

Source: This article was originally published in the May/2016 issue of Concrete International, www.concrete.org.



Figure 15.24 (A) Engineered Cementitious Composites (ECC) placement through the joint (B) completed shear keys with ECC.

Source: Courtesy of Çelik Özyıldırım.

composites. As a result of this outstanding performance of ECC in shear keys, it will be selected as a new grout material for VDOT (Fig. 15.24). A VDOT special provision on ECC, including materials, mixture proportions and mixing, placement, curing and testing procedures is available from the VDOT Structure and Bridge Division.

15.4 Conclusions

Despite continuous efforts in new material development, concrete repairs perform inconsistently and failure rates are unacceptably high. It is estimated that nearly half of conventional concrete repairs fail in the field. Concrete repairs are often perceived to lack both early-age performance and long-term durability due to the brittle nature of concrete materials. Rather than focusing on endless repair applications with conventional brittle cement-based materials, a unique solution is to use ECC. Through its ductility and tight crack width, it helps overcome many durability challenges confronting concrete. Criteria for an ideal concrete repair material have been proposed and compared to the properties of ECC; in all cases, ECC meets most demands for high performance repair. Special versions of ECC manufactured with self-consolidating property or spray ability have also been developed and made the material suitable for various types of placement techniques. Furthermore, the capacity of ECC to outperform concrete in real world repair applications verifies its long-term potential. Accordingly, the promise exhibited by ECC offers a potential solution to the worldwide problem of rapidly deteriorating concrete infrastructures. Designed to be easily used with normal construction equipment, this material can readily be adapted to current construction practices.

References

- Abu-Tair, A.I., Rigden, S.R., Burley, E., 1996. Testing the bond between repair materials and concrete substrate. *ACI Mater. J.* 93 (6), 553–558.
- ACI 224R, 2001. *Control of Cracking in Concrete Structures*. American Concrete Institute, Farmington Hills, Michigan.
- Alaee, F.J., Karihaloo, B.L., 2003. Retrofitting of RC beams with CARDIFRC. *ASCE J. Compos. Constr.* 7 (3), 174–186.
- Alexander, M.G., Stanish, K., 2005. Durability design and specification of reinforced concrete structures using a multi-factor approach. In: *3rd International Conference on Construction Materials: Performance, Innovations and Structural Implications*, Vancouver, Canada, N. Banthia, T. Uomoto, A. Bentur and S.P. Shah (Eds.), Compendium of Papers CD ROM, 10 pp.
- Alyouisif, A., Lachemi, M., Yıldırım, G., Şahmaran, M., 2015. Effect of self-healing on the different transport properties of cementitious composites. *J. Adv. Concr. Technol.* 13 (3), 112–123.
- Edvardsen, C., 1999. Water permeability and autogenous healing of cracks in concrete. *ACI Mater. J.* 96 (4), 448–454.
- Emmons, E., Vaysburd, A., McDonald, J.A., 1993. Rational approach to durable concrete repairs. *Concr. Int.* 15, 40–45.
- Emmons E., Vaysburd, A. 1995. Performance criteria for selection of repair materials, Phase I, Technical Report REMR-CS-47, U.S. Army Engineer Waterways Experiment Station, Vicksburg, MS.
- Emmons, P.H., Vaysburd, A.M., McDonald, J.E., 1994. Concrete repair in the future turn of the century—any problems. *Concr. Int.* 16 (3), 42–49.
- Engineers Canada, 2008. *Adapting to climate change: Canada’s first national engineering vulnerability assessment of public infrastructure*, Canadian Council of Professional Engineers (CCPE), Ottawa, Canada.
- Espeche, A.D., León, J., 2011. Estimation of bond strength envelopes for old-to-new concrete interfaces based on a cylinder splitting test. *Constr. Build. Mater.* 25 (3), 1222–1235.
- Felekoğlu, B., Tosun-Felekoğlu, K., Keskinateş, M., Gödek, E., 2016. A comparative study on the compatibility of PVA and HTPP fibers with various cementitious matrices under flexural loads. *Constr. Build. Mater.* 121, 423–428.
- Geissert, D.G., Li, S.E., Franz, G.C., Stephens, J.E., 1999. Splitting prism test method to evaluate concrete-to-concrete bond strength. *ACI Mater. J.* 96 (3), 359–366.
- Gulikers, J.J.W., van Mier, J.G.M., 1991. The effect of patch repairs on the corrosion of steel reinforcement in concrete. In: *Proceedings of 2nd CANMET/ACI International Conference on Durability of Concrete*, Montreal, Canada, V. M. Malhotra (Ed.), pp. 445–460.
- Harris, D.K., Sarkar, J., Ahlborn, T.M., 2011. Characterization of interface bond of ultra-high-performance concrete bridge deck overlays. *Transp. Res. Rec.* 2240 (1), 40–49.
- Heiman, J.L., Koertstz, P., 1991. Performance of polymer-modified cementitious repair mortars in chloride contaminated concrete. *Trans. Inst. Eng., Aust.: Civ. Eng.* 33 (3), 169–175.
- Inaguma, H., Seki, M., Suda, K., Rokugo, K. 2006. Experimental study on crack-bridging ability of ECC for repair under train loading. In: *Proceedings of International Workshop on HPRCC in Structural Applications*, Honolulu, Hawaii, USA, G. Fischer and V.C. Li (Eds.), Rilem Publications, PRO 49, pp. 499–508.

- Kanda, T., Li, V.C., 1999. A new micromechanics design theory for pseudo strain hardening cementitious composite. *ASCE J. Eng. Mech.* 125 (4), 373–381.
- Keskin, S.B., 2012. Dimensional Stability of Engineered Cementitious Composites. Middle East Technical University, PhD Thesis, Ankara, Turkey.
- Keskin, S.B., Şahmaran, M., Yaman, İ.Ö., Lachemi, M., 2014. Correlation between the viscoelastic properties and cracking potential of engineered cementitious composites. *Constr. Build. Mater.* 71, 375–383.
- Kim, Y.Y., Kong, H.J., Li, V.C., 2003. Design of engineered cementitious composite suitable for wet-mixture shotcreting. *ACI Mater. J.* 100 (6), 511–518.
- Kojima, S., Sakata, N., Kanda, T., Hiraishi, T., 2004. Application of direct sprayed ECC for retrofitting dam structure surface-application for Mitaka-Dam. *Concr. J.* 42 (5), 135–139.
- Kunieda, M., Rokugo, K., 2006. Recent progress of HPRCC in Japan—required performance and applications. *J. Adv. Concr. Technol.* 4 (1), 19–33.
- Lepech, M., Li, V.C., 2009. Water permeability of cracked cementitious composites. *Cem. Concr. Compos.* 31 (10), 744–753.
- Lepech, M.D., Li, V.C., 2005. Design and field demonstration of ECC link slabs for jointless bridge decks. In: *Proceedings of the 3rd International Conference on Construction Materials: Performance, Innovations and Structural Implications*, Vancouver, Canada, N. Banthia, T. Uomoto, A. Bentur and S.P. Shah (Eds), pp. 22–24.
- Li, V.C. 2002. Reflections on the research and development of engineered cementitious composites (ECC). In: *Proceedings of the JCI International Workshop on Ductile Fiber Reinforced Cementitious Composites (DFRCC)-Application and Evaluation*, Takayama, Japan, pp. 1–21.
- Li, M., Li, V.C., 2007. Durability of HES-ECC repair under mechanical and environmental loading conditions. In: *Proceedings of High Performance Fiber Reinforced Cement Composites (HPRCC5)*, Mainz, Germany, H. W. Reinhardt and A. E. Naaman (Eds.), pp. 399–408.
- Li, M., Li, V.C., 2009. Influence of material ductility on performance of concrete repair. *ACI Mater. J.* 106 (5), 419–428.
- Li, M., Şahmaran, M., Li, V.C., 2007. Effect of cracking and healing on durability of engineered cementitious composites under marine environment. In: *Proceedings of High Performance Fiber Reinforced Cement Composites (HPRCC5)*, Mainz, Germany, H. W. Reinhardt and A. E. Naaman (Eds.), pp. 313–322.
- Li, S., Geissert, D.G., Li, S.E., Frantz, G.C., Stephens, E.J., 1997. Durability and bond of high-performance concrete and repaired portland cement concrete. Joint Highway Research Advisory Council, Project JHR97-257, University of Connecticut, 232 pp.
- Li, V.C., 1993. From micromechanics to structural engineering—the design of cementitious composites for civil engineering applications. *JSCE J. Struct. Mech. Earthquake Eng.* 10 (2), 37–48.
- Li, V.C., 1998. ECC—tailored composites through micromechanical modeling. In: *Proceedings of Fiber Reinforced Concrete: Present and the Future*, Montreal, Canada, N. Banthia, A. Bentur, and A. Mufti (Eds.), pp. 64–97.
- Li, V.C., 2003. On engineered cementitious composites (ECC)—a review of the material and its applications. *J. Adv. Concr. Technol.* 1 (3), 215–230.
- Li, V.C., Lepech, M., 2004. Crack resistant concrete material for transportation construction. In: *Transportation Research Board 83rd Annual Meeting*, Washington, USA, Compendium of Papers CD ROM, Paper 04-4680.

- Li, V.C., Leung, C.K., 1992. Steady state and multiple cracking of short random fiber composites. *ASCE J. Eng. Mech.* 118 (18), 2247–2264.
- Li, V.C., Stang, H., 2004. Elevating FRC material ductility to infrastructure durability. In: Proceedings of 6th International RILEM Symposium on Fibre Reinforced Concretes (FRC) - BEFIB, Varenna, Italy, M. Di Prisco, R. Felicetti and G. A. Plizzari (Eds.), pp. 171–186.
- Li, V.C., Fischer, G., Kim, Y., Lepech, M., Qian, S., Weimann, M., Wang, S., 2003. Durable Link Slabs for Jointless Bridge Decks Based on Strain-Hardening Cementitious Composites. Michigan Department of Transportation Report no. RC-1438, pp. 1–96.
- Li, V.C., Horikoshi, T., Ogawa, A., Torigoe, S., Saito, T., 2004. Micromechanics-based durability study of polyvinyl alcohol engineered cementitious composite (PVA-ECC). *ACI Mater. J.* 101 (3), 242–248.
- Li, V.C., Lepech, M., Li, M., 2005. Field demonstration of durable link slabs for jointless bridge decks based on strain-hardening cementitious composites. Michigan Department of Transportation (MDOT), Research Report RC-1471, pp 1–147.
- Li, V.C., Wang, S., Wu, C., 2001. Tensile strain-hardening behavior of PVA-ECC. *ACI Mater. J.* 98 (6), 483–492.
- Li, V.C., Wu, C., Wang, S., Ogawa, A., Saito, T., 2002. Interface tailoring for strain-hardening polyvinyl alcohol-engineered cementitious composite (PVA-ECC). *ACI Mater. J.* 99 (5), 463–472.
- Lim, Y.M., Li, V.C., 1997. Durable repair of aged infrastructures using trapping mechanism of engineered cementitious composites. *Cem. Concr. Compos.* 19 (4), 171–185.
- Malhotra, V.M., 1999. Role of supplementary cementing materials in reducing greenhouse gas emissions. In: Proceedings of an International Conference of Infrastructure Regeneration and Rehabilitation - Improving the Quality of Life Through Better Construction, Sheffield, United Kingdom, R. Narayan Swamy (Ed.), pp. 27–42.
- Manning, D.G., 1996. Corrosion performance of epoxy-coated reinforcing steel: North American experience. *Constr. Build. Mater.* 10 (5), 349–365.
- Markovic, I., Walraven, J.C., van Mier, J.G.M., 2004. Tensile behaviour of high performance hybrid fibre concrete. In: Proceedings of the 5th International Symposium on Fracture Mechanics of Concrete and Concrete Structures, Vail Colorado, USA, V.C. Li, C.K.Y. Leung, K.J. Willam and S.L. Billington (Eds.) pp. 1113–1121.
- Marlowe, I., 2003. Emission factors programme Task 4(b): review of cement sector pollution inventory. Report prepared for DEFRA, Reference Number: AEAT/ENV/R/1715/Issue 1, Abingdon, Oxon, United Kingdom.
- Mather, B., Warner, J., 2003. Why do concrete repairs fail? <<http://aec.engr.wisc.edu/resources/rsrc07.html>>.
- Mehta, P.K., 1994. Concrete technology at the crossroads—problems and opportunities. *ACI Spec. Publ.* 144, 1–30.
- Mehta, P.K., 1998. Role of pozzolanic and cementitious material in sustainable development of the concrete industry. *ACI Spec. Publ.* 178, 1–20.
- Mehta, P.K., Burrows, R.W., 2001. Building durable structures in the 21st century. *Concr. Int.* 23 (3), 57–63.
- Michigan Department of Transportation, 2001. Michigan Test Method 111—Determining an Aggregate Wear Index (AWI) by Wear Track Polishing Tests. Michigan Department of Transportation, Lansing, Michigan.
- Miller, R.A., Hlavacs, G.M., Long, T.W., 1998. Testing of Full Scale Prestressed Beams to Evaluate Shear Key Performance. Publication FHWA/OH-98/019. University of Cincinnati, Ohio.

- Mindess, S., Young, J.F., Darwin, D., 2003. *Concrete*. second ed. Prentice Hall, New Jersey.
- Miyazato, S., Hiraishi, Y., 2005. Transport properties and steel corrosion in ductile fiber reinforced cement composites. In: Proceedings of 11th International Conference on Fracture, Turin, Italy, A. Carpinteri (Ed.), CD-ROM, pp. 20–25.
- Momayez, A., Ehsani, M.R., Ramezani-pour, A.A., Rajaie, H., 2005. Comparison of methods for evaluating bond strength between concrete substrate and repair materials. *Cem. Concr. Res.* 35 (4), 748–757.
- Morgan, D.R., 1996. Compatibility of concrete repair materials and systems. *Constr. Build. Mater.* 10 (1), 57–67.
- Ostro, B.D., 1994. *Estimating the Health Effects of Air Pollutants: A Method With an Application to Jakarta*. World Bank Publications, 1301.
- Özbay, E., Şahmaran, M., Lachemi, M., Yücel, H.E., 2013. Self-healing of microcracks in high-volume fly-ash-incorporated engineered cementitious composites. *ACI Mater. J.* 110 (1), 33–43.
- Özyıldırım, H.C., Moruza, G.M., 2016. High-performance grouting materials in shear keys between box beams. *J. Trans. Res. Rec.* 2577, 35–42.
- Ramm, W., Biscop, M., 1998. Autogenous healing and reinforcement corrosion of water-penetrated separation cracks in reinforced concrete. *Nucl. Eng. Des.* 179 (2), 191–200.
- Raupach, M., 2005. Concrete repair according to the new European standard EN 1504. In: International Conference Repair, Rehabilitation and Retrofitting, Cape Town, South Africa, M. G. Alexander, H. D. Beushausen, F. Dehn and P. Moyo (Eds.), pp. 6–8.
- Reinhardt, H.W., Jooss, M., 2003. Permeability and self-healing of cracked concrete as a function of temperature and crack width. *Cem. Concr. Res.* 33 (7), 981–985.
- Rokugo, K., Kunieda, M., Lim, S.C., 2005. Patching repair with ECC on cracked concrete surface. In: 3rd International Conference on Construction Materials: Performance, Innovations and Structural Implications, Vancouver, Canada, N. Banthia, T. Uomoto, A. Bentur and S.P. Shah (Eds.), Compendium of Papers CD ROM, 10 pp.
- Rossi, P., Parant, E., 2005. Mechanical behaviours of a multi-scale fibre reinforced cement composite (MSFRCC) subjected to severe loading conditions. In: 3rd International Conference on Construction Materials: Performance, Innovations and Structural Implications, Vancouver, Canada, N. Banthia, T. Uomoto, A. Bentur and S.P. Shah (Eds.), Compendium of Papers CD ROM.
- Şahmaran, M., Li, V.C., 2007. De-icing salt scaling resistance of mechanically loaded engineered cementitious composites. *Cem. Concr. Res.* 37 (7), 1035–1046.
- Şahmaran, M., Li, V.C., 2008. Durability of mechanically loaded engineered cementitious composites under high alkaline environment. *Cem. Concr. Compos.* 30 (2), 72–81.
- Şahmaran, M., Li, V.C., 2009. Influence of microcracking on water absorption and sorptivity of ECC. *RILEM J. Mater. Struct.* 42 (5), 593–603.
- Şahmaran, M., Li, V.C., 2016. Suppressing alkali-silica expansion. *Concr. Int.* 38 (5), 47–52.
- Şahmaran, M., Li, M., Li, V.C., 2007. Transport properties of engineered cementitious composites under chloride exposure. *ACI Mater. J.* 104 (6), 604–611.
- Şahmaran, M., Li, V.C., Andrade, C., 2008. Corrosion resistance performance of steel-reinforced engineered cementitious composites beams. *ACI Mater. J.* 105 (3), 243–250.
- Şahmaran, M., Lachemi, M., Li, V.C., 2010. Assessing the durability of engineered cementitious composites (ECC) under freezing and thawing cycles. *J. ASTM Int.* 6 (7), 1–13.
- Şahmaran, M., Yıldırım, G., Erdem, T.K., 2013a. Self-healing capability of cementitious composites incorporating different supplementary cementitious materials. *Cem. Concr. Compos.* 35 (1), 89–101.

- Şahmaran, M., Yücel, H.E., Yıldırım, G., Al-Emam, M., Lachemi, M., 2013b. Investigation of the bond between concrete substrate and ECC overlays. *ASCE J. Mater. Civ. Eng.* 26 (1), 167–174.
- Şahmaran, M., Yıldırım, G., Özbay, E., Ahmed, K., Lachemi, M., 2014. Self-healing ability of cementitious composites: effect of addition of pre-soaked expanded perlite. *Mag. Concr. Res.* 66 (7–8), 409–419.
- Şahmaran, M., Al-Emam, M., Yıldırım, G., Şimşek, Y.E., Erdem, T.K., Lachemi, M., 2015a. High-early-strength ductile cementitious composites with characteristics of low early-age shrinkage for repair of infrastructures. *RILEM J. Mater. Struct.* 48 (5), 1389–1403.
- Şahmaran, M., Anıl, O., Lachemi, M., Yıldırım, G., Ashour, A.F., Acar, F., 2015b. Effect of corrosion on shear behavior of reinforced engineered cementitious composite beams. *ACI Struct. J.* 112 (6), 771–782.
- Şahmaran, M., Yıldırım, G., Noori, R., Özbay, E., Lachemi, M., 2015c. Repeatability and pervasiveness of self-healing in engineered cementitious composites. *ACI Mater. J.* 112 (4), 513–522.
- Şahmaran, M., Yıldırım, G., Aras, H.G., Keskin, S.B., Keskin, Ö.K., Lachemi, M., 2017. Self-healing of cementitious composites to reduce high CO₂ emissions. *ACI Mater. J.* 114 (1), 93–104.
- Saucier, F., Bastien, J., Pigeon, M., Fafard, M., 1991. A combined shear-compression device to measure concrete-to-concrete bonding. *Exp. Tech.* 15 (5), 50–55.
- Silfwerbrand, J., 2003. Shear bond strength in repaired concrete structures. *RILEM J. Mater. Struct.* 36 (6), 419–424.
- Snoeck, D., De Belie, N., 2012. Mechanical and self-healing properties of cementitious composites reinforced with flax and cottonised flax, and compared with polyvinyl alcohol fibres. *Biosyst. Eng.* 111 (4), 325–335.
- Snoeck, D., De Belie, N., 2015. Repeated autogenous healing in strain-hardening cementitious composites by using superabsorbent polymers. *ASCE J. Mater. Civ. Eng.* 28 (1), 04015086.
- Snoeck, D., Smetryns, P.A., De Belie, N., 2015. Improved multiple cracking and autogenous healing in cementitious materials by means of chemically-treated natural fibres. *Biosyst. Eng.* 139, 87–99.
- Snoeck, D., Van Tittelboom, K., Steuperaert, S., Dubruel, P., De Belie, N., 2014. Self-healing cementitious materials by the combination of microfibrils and superabsorbent polymers. *J. Intell. Mater. Syst. Struct.* 25 (1), 13–24.
- Sprinkel, M.M., Özyıldırım, C., 2000. Evaluation of high performance concrete overlays placed on Route 60 over Lynnhaven Inlet in Virginia. Final report, Virginia Transportation Research Council, Charlottesville, Virginia.
- Suthiwarapirak, P., Matsumoto, T., Kanda, T., 2002. Flexural fatigue failure characteristics of an engineered cementitious composite and polymer cement mortars. *JSCE J. Mater., Concr. Struct. Pavements.* 718 (57), 121–134.
- Tuutti, K., 1982. Corrosion of Steel in Concrete. CBI Swedish Cement and Concrete Research Institute, pp. 159.
- Vaysburd, A., Emmons, P.H., 2004. Corrosion inhibitors and other protective systems in concrete repair: concepts or misconcepts. *Cem. Concr. Compos.* 26 (3), 255–263.
- Vaysburd, A., Brown, C., Bissonnette, B., Emmons, P., 2004. Realcrete vs. Labcrete. *Concr. Int.* 26 (2), 90–94.
- Vecchio, F., Bucci, F., 1999. Analysis of repaired reinforced concrete structures. *ASCE J. Struct. Eng.* 125 (6), 644–652.

- Wall, J.S., Shrive, N.G., 1988. Factors affecting bond between new and old concrete. *ACI Mater. J.* 85 (2), 117–125.
- Wang, S., Li, V.C., 2005. Polyvinyl alcohol fiber reinforced engineered cementitious composites: material design and performance. In: *Proceedings of International RILEM Workshop on HPFRCC in Structural Applications*, Honolulu, USA, G. Fischer and V. C. Li (Eds.) pp. 65–73.
- Yıldırım, G., Şahmaran, M., Ahmed, H.U., 2014. Influence of hydrated lime addition on the self-healing capability of high-volume fly ash incorporated cementitious composites. *ASCE J. Mater. Civ. Eng.* 27 (6), 04014187.
- Yıldırım, G., Al-Emam, M.K.M., Hameed, R.K.H., Al-Najjar, Y., Lachemi, M., 2015a. Effects of compressive strength, autogenous shrinkage and testing methods on the bond behavior of HES-ECC. *ACI Mater. J.* 112 (3), 409–418.
- Yıldırım, G., Alyousif, A., Şahmaran, M., Lachemi, M., 2015b. Assessing the self-healing capability of cementitious composites under increasing sustained loading. *Adv. Cem. Res.* 27 (10), 581–592.
- Yıldırım, G., Aras, G.H., Banyhussan, Q.S., Şahmaran, M., Lachemi, M., 2015c. Estimating the self-healing capability of cementitious composites through non-destructive electrical-based monitoring. *Ndt & E Int.* 76, 26–37.
- Yıldırım, G., Keskin, Ö.K., Keskin, S.B., Şahmaran, M., Lachemi, M., 2015d. A review of intrinsic self-healing capability of engineered cementitious composites: recovery of transport and mechanical properties. *Constr. Build. Mater.* 101, 10–21.
- Yıldırım, G., Şahmaran, M., Balçıklı, M., Özbay, E., Lachemi, M., 2015e. Influence of cracking and healing on the gas permeability of cementitious composites. *Constr. Build. Mater.* 85, 217–226.
- Yücel, H.E., Jashami, H., Şahmaran, M., Güler, M., Yaman, İ.Ö., 2013. Thin ECC overlay systems for rehabilitation of rigid concrete pavements. *Mag. Concr. Res.* 65 (2), 108–120.
- Zhang, J., Li, V.C., 2002. Monotonic and fatigue performance in bending of fiber-reinforced engineered cementitious composite in overlay system. *Cem. Concr. Res.* 32 (3), 415–423.

This page intentionally left blank

Self-healing concrete with encapsulated polyurethane

16

Kim Van Tittelboom, Philip Van den Heede and Nele De Belie
Ghent University, Ghent, Belgium

16.1 Encapsulation of polymeric healing agents

As polymeric agents are also used for traditional, manual crack injection, multiple polymeric healing agents have already been encapsulated and embedded in concrete to obtain self-healing properties. In order to suit as healing agent for self-healing concrete, several requirements need to be fulfilled. At first, the shelf life of the healing agent is a very important factor: it should be as long as possible. While the healing agent will be embedded inside the cementitious matrix at the time of casting, its reactivity should remain until cracks appear. Not only the reactivity, but also the viscosity of the healing agent at the moment of capsule breakage is of utmost importance. The viscosity should be low enough to allow the agent to flow out of the capsules and to fill narrow micro-cracks. On the other hand, if the viscosity is too low the healing agent will not remain inside the crack as it will be absorbed by the pores of the cementitious matrix or seep out of the crack. A third requirement is that the polymerization reaction should preferably take place without human intervention. Single-component healing agents, which require the application of heat in order to cure, are less suited. Single-component agents which polymerize upon contact with moisture are much more appropriate for encapsulation. In addition, multicomponent agents which harden at room temperature upon contact with a second component can be used. In the latter case, both components will be embedded in separate capsules which may result in an extended shelf life. However, the reaction and the final properties of the cured agent should be insensitive to the mix ratio and should not require proper mixing of both components. Furthermore, the reaction time of the healing agent is an important parameter which needs to be taken into account. When the healing agent reacts too fast, not enough time is left for the agent to fill the crack. Conversely, the reaction time should be limited in order to stabilize the crack and prevent further growth. As a last requirement, it is important that the released healing agent completely fills the cracks, to prevent ingress of aggressive substances. Therefore, expansion of the healing agent upon reaction is a desired property as bigger crack spaces can be filled in this way.

Initial trials to obtain self-healing concrete were performed by [Dry and McMillan \(1996\)](#) with encapsulated methyl methacrylate (MMA) which is a multicomponent healing agent. Later, only limited researchers reported the use of MMA as healing agent ([Yang et al., 2011](#); [Van Tittelboom et al., 2011a](#)). Silicone has also been used as healing agent in self-healing concrete, but the use of this single-component agent

was only reported by Dry et al. (2003). On the other hand, multiple researchers reported the use of single-component cyanoacrylate (Li et al., 1998; Joseph et al., 2010; Sun et al., 2011) and single- or multicomponent epoxy (Nishiwaki et al., 2007; Tran Diep et al., 2009; Mihashi et al., 2000; Feng et al., 2008; Escobar et al., 2013; Dong et al., 2013, 2016; Perez et al., 2015) as healing agent inside self-healing concrete. The encapsulation of single- and multicomponent polyurethane has also been reported as promising healing agent (Van Tittelboom et al., 2011b; Wang et al., 2012; Maes et al., 2014; Araujo et al., 2016; Van den Heede et al., 2016).

The main goal of self-healing concrete is to improve the durability of concrete structures, which requires complete crack filling and expansion of the encapsulated healing agent upon polymerization. As polyurethane is the only of the above mentioned polymeric healing agents which expands upon polymerization, the use of a single- and multicomponent polyurethane-based healing agent is described in this chapter. Both, the single- and multicomponent polyurethane react upon contact with moisture but the reaction of the multicomponent polyurethane is accelerated upon contact with the second component. Moreover, polyurethanes with a very low viscosity were selected to allow the agent to flow easily into the crack. For the multicomponent healing agent, care was taken that the mix ratio and the amount of mixing of both components was of minor importance.

16.2 Suitable encapsulation materials and trigger mechanisms

16.2.1 Glass, ceramic, and polymeric capsules

Suitable encapsulation materials should preferably be able to survive the concrete mixing process, so a certain flexibility and strength of the capsules is required at the time of concrete mixing. In addition, the influence of the capsules on the workability of the fresh concrete needs to remain limited. Once the concrete has hardened, the capsules need to be able to release the healing agent upon crack formation. If the self-healing mechanism should be triggered upon crack formation, this means that once the concrete has hardened, the capsules need to become brittle enough to break as soon as a crack appears. Moreover, the influence of the capsules on the mechanical and physical properties of the hardened concrete need to remain limited. The shape and dimensions of the capsules need to be such that the chance of a crack going through the capsules is maximized and that an optimal release efficiency from the capsules into the crack is obtained. Moreover, the capsules' dimensions need to allow complete filling of the created crack. Although the list of requirements for the encapsulation material is already quite extended, it is also important to notice that capsules can only result in successful self-healing if the encapsulation material can withstand the harsh conditions inside the concrete matrix and is compatible with the healing agent which it should protect against the concrete matrix.

In order to encapsulate polyurethane-based healing agents, the use of glass, ceramic, and polymeric tubular capsules have been reported (Van Tittelboom et al., 2011b; Hilloulin et al., 2015; Gruyaert et al., 2016). Polymeric capsules possess the advantageous possibility of altering their properties and can thus fulfill the contradictory requirements of being flexible at the moment of concrete mixing and become more brittle at the moment of crack formation. However, in order to encapsulate polyurethane, a complete air- and water-tight barrier is needed. In research studies reported until now, polymeric capsules seemed not tight enough and were thus not successful to encapsulate polyurethane. While glass capsules can form an air- and water-tight barrier, it is less likely for glass to survive the concrete mixing process. However, glass is very brittle and will thus ideally fulfill the requirement to break upon crack formation. Because alkali–silica reaction may be feared when glass capsules are used, the use of tubular ceramic capsules was suggested as alternative. The healing efficiency even seemed to increase, as the ceramics are more brittle compared to glass and more easily release the polyurethane-based healing agent upon breakage.

16.2.2 Trigger mechanisms

In order to obtain self-healing concrete, a mechanism is needed to trigger the healing action. While for some self-healing mechanisms, activation through ingress of liquids and gasses or through exertion of heat is mentioned, for self-healing by means of encapsulated polymeric healing agents, the most common trigger mechanism is crack appearance. The big advantage of using crack formation as the trigger mechanism is that the system responds very fast. Crack formation is immediately followed by release of the healing agent into the crack and healing only depends on curing of the agent. As already mentioned, the polymerization reaction of the healing agent is triggered upon contact with moisture (for single-component agents) or upon contact with a second component (for multicomponent healing agents). With regard to polyurethane-based healing agents, the possibility is also explored whether the polymerization reaction can be triggered due to exposure to the high pH environment in cementitious materials once released from the capsules (Araujo et al., 2016). This would be very advantageous to increase the shelf life of the encapsulated polyurethane-based healing agent. However, while the potential of this technique was already assessed through manual crack healing, more research is needed to apply this particular agent as a healing agent in self-healing concrete.

16.3 Crack closure by encapsulated polyurethane

16.3.1 Coverage of the crack surfaces by released polyurethane

One way to evaluate the crack closure efficiency obtained through release of encapsulated polyurethane is to investigate the coverage of the crack surfaces (Vantghem, 2014). Therefore, glass capsules with an inner diameter of 3 mm and

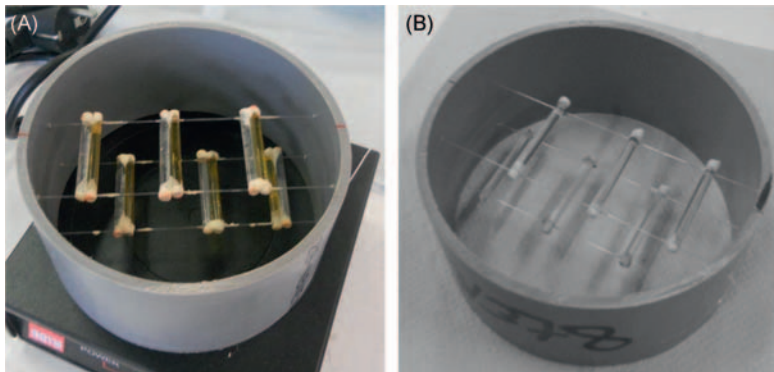


Figure 16.1 PVC mold with attached capsules used to cast cylindrical mortar samples with self-healing properties, (A) capsules filled with polyurethane encoded BASF and (B) capsules filled with polyurethane encoded SLV (Vantygheem, 2014).

a length of 35 mm were used to encapsulate the healing agent. Two commercial polyurethane-based healing agents were tested. The first one, named MEYCO MP 355 1 K, is produced by BASF (code: BASF). This is a single-component polyurethane with very low viscosity of 320 mPa.s (23°C), which reacts upon contact with water. In order to ensure polymerization and to speed up the reaction, this healing agent was applied as a two-component agent with the second component being a mixture of tap water and accelerator (viscosity 70 mPa.s, 23°C). Each component was encapsulated by separate capsules which were attached to each other as shown in Fig. 16.1. The second polyurethane used (code: SLV) has an even lower viscosity of 150-250 mPa.s (25°C) and was used as a single-component healing agent. Cylindrical mortar samples with a height of 50 mm and a diameter of 100 mm were cast. Nylon wires were attached to the PVC molds and capsules were glued on them in order to prevent the capsules from floating during casting. In every sample, six (pairs of) capsules were embedded, which were equally divided along the diameter over two layers, on 12.5 mm and 37.5 mm height as shown in Fig. 16.1.

In addition to the samples with encapsulated polyurethane (CAPS BASF and CAPS SLV), test series without encapsulated healing agent were prepared for manual crack healing (MAN BASF and MAN SLV).

Cracks were created in the cylindrical mortar samples by means of a crack-width controlled splitting test. Two linear variable displacement transducers (LVDT's) were placed on both sides of the samples to control the crack width during the test. Complete failure of the samples was prevented by applying two layers of epoxy coating along the circumference of the mortar cylinders in combination with a clamping screw keeping the parts of the splitted cylinder together. The displacement controlled test was executed until a crack width of 400 μm was obtained. The crack width after unloading amounted to 200 μm for most of the samples.

For the series with encapsulated polyurethane (CAPS BASF and CAPS SLV), the crack was created across the capsules, so crack formation caused capsule breakage.

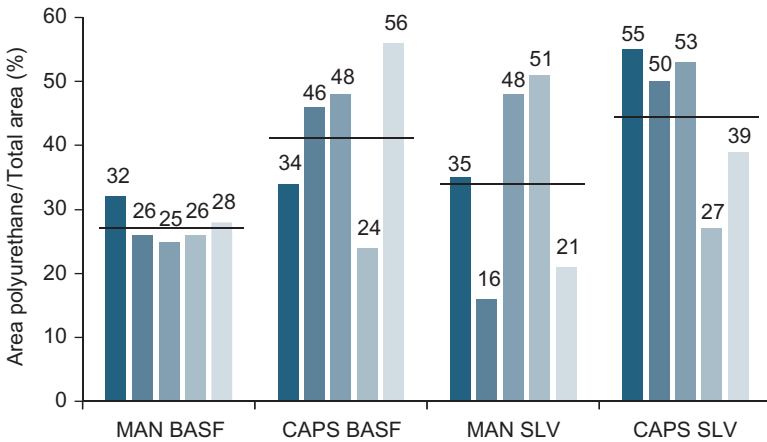


Figure 16.2 Surface ratio of polyurethane on the crack surface. The horizontal black lines indicate the mean per test series (Vantyghem, 2014).

This led to release of the polyurethane into the crack and crack repair. For the two other test series (MAN BASF and MAN SLV) manual healing of the cracks was obtained by injecting the crack with polyurethane by means of a syringe with a needle.

A few days after crack repair, samples were split along the crack in order to study the surface coverage by polyurethane. The polyurethane on the crack surfaces was colored with a red marker. Subsequently, images were taken from the surface and an image analysis was performed to determine the ratio of colored pixels to the total amount of pixels. This ratio is presented in Fig. 16.2 for every test series.

The lowest amount of polyurethane coverage was found for the samples of the series MAN BASF which amounted to 27%. The samples healed with the polyurethane SLV showed more penetration of polyurethane in the crack, for both manually and autonomously healed cracks (34% and 45% coverage, respectively). This may be caused by the lower viscosity of this agent compared to the viscosity of the product BASF. However, the larger amount of polyurethane in the cracks of the samples from series MAN SLV and CAPS SLV, did not result in a better protection against the ingress of chlorides (see Section 16.6.1). It was noticed that the polyurethane SLV was able to penetrate over the whole crack surface, but it was distributed over discontinuous areas in the crack. This can be seen from the reconstructed image in Fig. 16.3A, showing the total coverage by polyurethane on one sample half. As a result, the chlorides were, for some of the samples, still able to penetrate through the crack in between the polymerized agent. For the polyurethane from BASF, almost all areas with polyurethane were connected as a continuous physical barrier inside the crack (Fig. 16.3B). On the other hand, it was noticed that the polyurethane from BASF did not succeed in penetrating further than half of the crack depth in the test series with manually healed cracks. This led to a smaller release of polyurethane in the crack, but also to a more dense polyurethane foam. As a consequence, very good healing of the crack was obtained with test series MAN BASF (see Section 16.6.1).

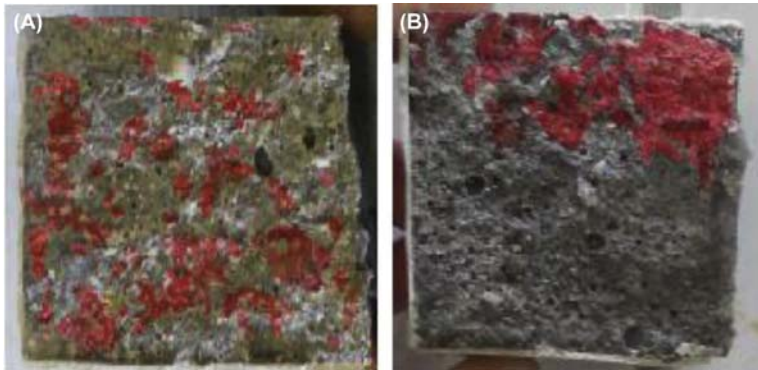


Figure 16.3 Reconstructed images showing the total coverage by polyurethane for a manually injected crack with the polyurethane SLV (A) and the polyurethane BASF (B) (Vantghem, 2014).

16.3.2 Evaluation of the crack filling efficiency by neutron and X-ray tomography

Computed tomography (CT) is a nondestructive test method which allows to visualize the interior of an object in three dimensions (3D) without opening or cutting it. For X-ray or neutron radiography, the radiation passing through a stationary sample is recorded, resulting in two-dimensional (2D) information about the inner structure. Tomography is an extension of radiography and requires a rotating sample so radiographic images can be acquired in different directions. The 2D projections (or radiographs) are consequently back projected to reconstruct the sample in 3D by means of a suitable computer algorithm. As X-ray or neutron CT allows to visualize the internal structure of an object, it is a suitable technique to study the healing efficiency of self-healing materials.

The mortar prisms and cylinders with encapsulated polyurethane which were used to evaluate the regain in mechanical properties (see Section 16.5.1) and the decrease in water permeability (see Section 16.4.1) due to autonomous crack healing were investigated by means of X-ray CT (Van Tittelboom, 2012). The X-ray CT measurements were performed at the Centre for Computed Tomography of Ghent University (UGCT) (Masschaele et al. 2007). Specimens containing glass and ceramic capsules were scanned. Moreover, the healing efficiency for glass samples containing capsules with a diameter of 2 mm and samples containing capsules with a diameter of 3 mm was compared by X-ray CT.

Neutron CT was performed on the samples which were used to visualize the water uptake by means of neutron radiography (see Section 16.4.3) (Van Tittelboom, 2012). Neutron CT was performed at the Paul Sherrer Institute (PSI) in Switzerland (Lehmann et al., 2001). Scans were made of a sample with a manually and an autonomously healed crack after being sized down to 30 mm × 20 mm × 100 mm.

For some of the scanned samples, the healing efficiency was evaluated based on the 2D slices, whereas for others, a 3D render was made in *VGStudio* (Volume

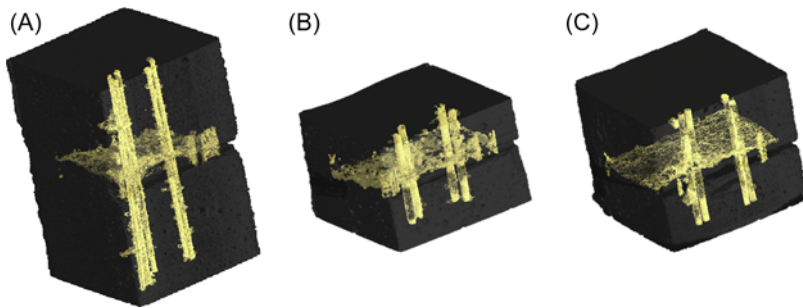


Figure 16.4 3D visualization of X-ray computed tomography (CT) scans of the region of the mortar prism containing the capsules and the crack. As encapsulation material glass capsules with a diameter of 2 mm (A) and 3 mm (B) and ceramic capsules (diameter about 2.6 mm) (C) were used (Van Tittelboom, 2012).

Graphics, 2012). For some scans, the healing agent inside the crack was highlighted through the allocation of a different color. Therefore, the healing agent was selected based on its gray value and the selected range of gray values was replaced in *VGStudio* (Volume Graphics, 2012) by a chosen color.

However, for the samples analyzed by X-ray tomography, it was not so easy to select the polyurethane healing agent based on its gray value. The difference in contrast between polyurethane and air was very low and both gray levels also appeared in the mortar matrix. Therefore, additional treatments were performed in *Morpho*⁺ (Brabant et al., 2011) to clearly visualize the polyurethane released into the crack and left inside the tubular capsules. Fig. 16.4 illustrates the 3D rendered datasets obtained after different processing steps in *Morpho*⁺ (Brabant et al., 2011), showing the part of a mortar prism which contained the broken capsules and the crack.

From Fig. 16.4, it may be concluded that it is possible to visualize polyurethane foam inside a dense mortar matrix. Although polyurethane has a very low X-ray absorption compared to mortar, the remaining polyurethane inside the capsules and filling of the crack with polyurethane were clearly visible. The dark parts that were seen inside the capsules correspond to air bubbles which arose as part of the healing agent leaked out of the capsules into the crack after capsule breakage. Furthermore, it was observed that the released healing agent spread into the crack, which led to sealing of the crack faces.

In order to compare the effectiveness of the three different encapsulation techniques under investigation, cross-sections going through each of the capsules were made. From Fig. 16.5, it becomes obvious that none of the capsules had been completely emptied during crack formation. Unexpectedly, it was seen that in the case of glass capsules with a diameter of 2 mm (Fig. 16.5A), the volume of released healing agent was comparable with the volume released for 3 mm diameter glass capsules (Fig. 16.5B). When comparing these results with the ones obtained when using ceramic capsules (Fig. 16.5C), some difference was observed. In Fig. 16.5C only three out of the four capsules were visible because the fourth capsule was positioned

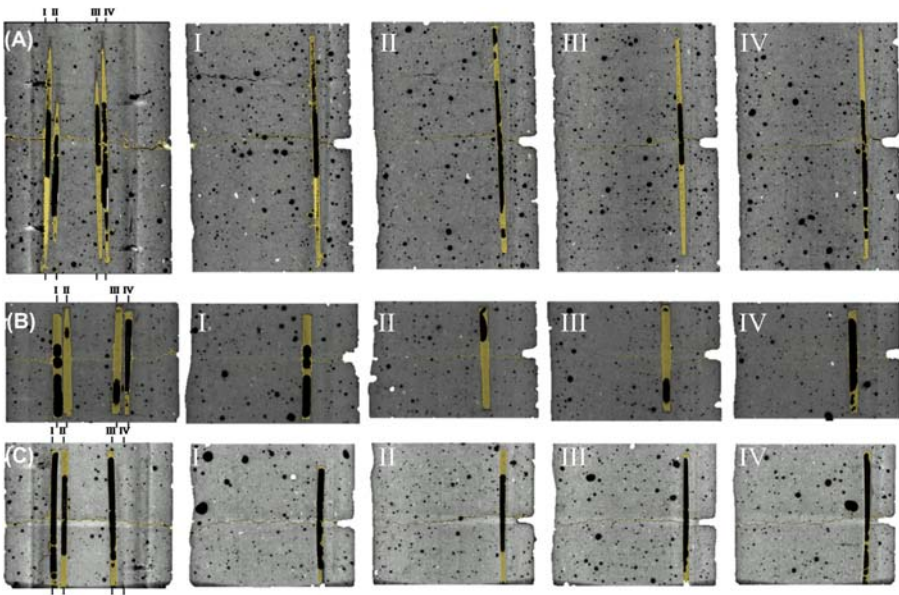


Figure 16.5 X-ray computed tomography (CT) cross-section through the capsules, (A) sample with 2 mm diameter glass capsules, (B) sample with 3 mm diameter glass capsules, and (C) sample with ceramic capsules (diameter about 2.6 mm). I, II, III, and IV denote CT slices through each of the capsules along a perpendicular plane (Van Tittelboom, 2012).

somewhat lower than the others. However, it was noticed that the ceramic capsules seemed to release more healing agent compared to the glass capsules. This may be caused by the difference in surface tension between glass and ceramic.

Although it was possible to visualize the polyurethane left inside the capsules, the accuracy of the scans was not high enough to allow for a quantitative comparison of the release efficiency obtained by each of the considered encapsulation techniques.

In addition to the content of the capsules, filling of the crack with polyurethane was visualized using X-ray CT. It was visible where the polyurethane foam had filled up the crack and where regions were situated where there was no polyurethane (Fig. 16.5). Concerning the crack filling efficiency, no quantitative evaluation could be performed as the dimensions of the crack approached the limits of resolution of the CT scans.

From the 3D rendered images shown in Fig. 16.6, it is noted that for the cylindrical samples which were exposed to a splitting test, part of the polyurethane healing agent remained inside the capsules. Mostly, the remaining polyurethane was attached to the capsule wall and thus it was difficult to see differences between the different encapsulation materials and capsule diameters based on the 3D images.

For the cylindrical samples our main interest was to visualize filling of the crack with healing agent. As these samples were used for the water permeability test

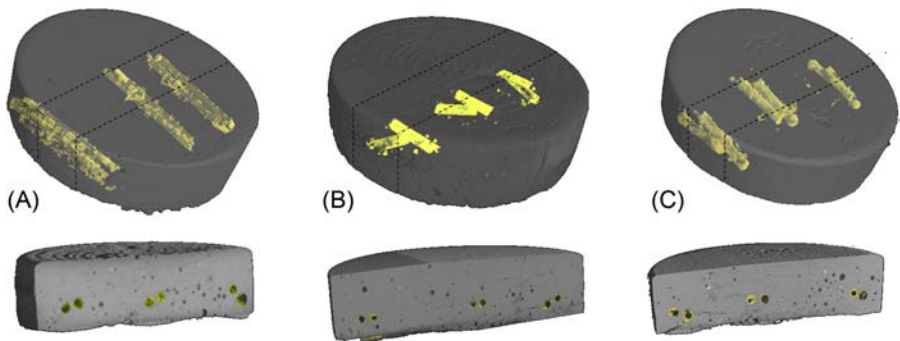


Figure 16.6 3D visualization of X-ray computed tomography (CT) scans of the mortar cylinders with encapsulated polyurethane after performance of the splitting test and thus after release of the healing agent, (A) sample with 2 mm diameter glass capsules, (B) sample with 3 mm diameter glass capsules and (C) sample with ceramic capsules (diameter about 3.3 mm) (Van Tittelboom, 2012).

(see Section 16.4.1), visualization of complete or incomplete crack filling could explain the findings noted from the water permeability test.

For these series, during performance of the CT scans, X-rays had to pass through a mortar layer of about 80 mm (for the prisms mentioned before it was only 60 mm). Therefore, the contrast became too low to visualize the cracks and definitely to visualize the healing agent inside the cracks. Consequently, it was concluded that one sample of each test series would be sized down. The part of the sample containing the crack was sawn out following the lines indicated in Fig. 16.6. When these prisms were positioned straight, during scanning, X-rays only had to pass through a 20 mm thick mortar layer and thus a better contrast was obtained.

The 3D rendered images are shown in Fig. 16.7. For these scans, a distinction could be made between cracks which were filled and cracks which were not filled with healing agent. It was thus possible to discriminate between air and polyurethane inside the crack. Note that different processing steps in *Morpho*⁺ (Brabant et al., 2011) were necessary to allow for this.

For the sample with an untreated crack, it is noted that the crack, which is represented by a dark line, ran over the whole length of the sample. Only at the edges, the crack did not continue.

When the crack was manually healed with polyurethane, it was noted that the healing agent was equally spread over the cracks faces, although, no complete crack filling was noticed. Zones within the crack were seen which were not covered with polyurethane. However, from the water permeability tests (see Section 16.4.1) it was concluded that samples from which cracks were manually healed with polyurethane, were able to resist water leakage as well as uncracked samples and thus complete crack filling would be expected. It is possible that, due to the partial volume effect, misleading conclusions were drawn. As the detector is unable to differentiate

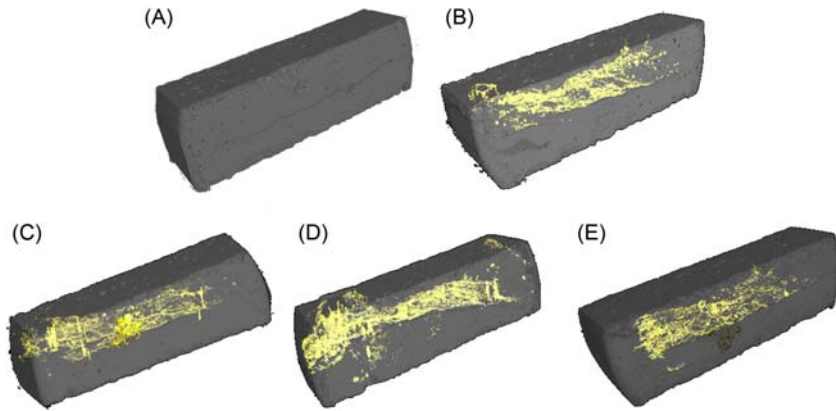


Figure 16.7 3D visualization of X-ray computed tomography (CT) scans of crack filling with polyurethane after prisms were sawn out of the mortar cylinders, (A) untreated crack, (B) manually healed crack, (C, D, and E) autonomously healed crack through release of polyurethane from glass capsules with a diameter of 2 mm (C) or 3 mm (D) or ceramic capsules (diameter about 3.3 mm) (E) (Van Tittelboom, 2012).

between a small amount of low density material (polyurethane inside the crack) and a large amount of high density material (mortar sample) it tries to average out the two densities and information is lost because of “blurring” over sharp edges. When we threshold on the gray value of polyurethane, it is possible that the sides of the crack are not taken into account. As the crack is only a few voxels wide and at some locations, even less. It is possible that not all polyurethane was selected.

When polyurethane was released from embedded capsules, it was seen that the healing agent was spread again over the cracked area. Similarly, as noted for manual crack healing, zones without polyurethane coverage appeared in the rendered images. This could, again, be caused by the partial volume effect or by incomplete crack filling. From the water permeability tests (see Section 16.4.1) it was noted that samples with autonomously healed cracks performed worse than samples with manually healed cracks. So, for these series, incomplete crack filling would correspond to the findings of the water permeability test.

From the obtained results, it was not possible to compare the crack filling efficiency for each of the three encapsulation techniques. As a consequence, it was certainly not possible to perform a quantitative analysis of the crack filling efficiency.

Neutron CT complements X-ray CT due to the specific attenuation characteristics of neutrons by light elements like hydrogen or polymeric materials. This makes the technique more suitable to detect the polymerized healing agent inside the cracks of mortar specimens.

In the rendered 3D neutron CT image (Fig. 16.8A) of the sample manually healed with polyurethane, it is seen that for this specific sample the crack runs over the complete height. This is most clear when the rendered image is cut

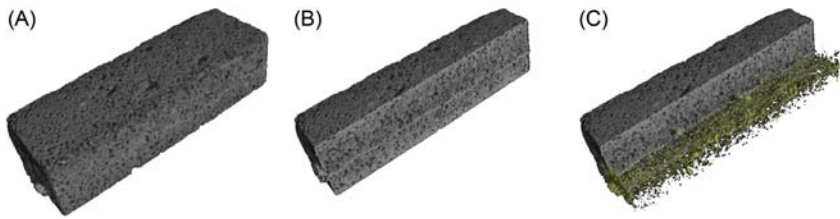


Figure 16.8 3D rendered neutron computed tomography (CT) images of the sample from which the crack was manually healed with polyurethane. Render of the complete sample (A). Render where part of the sample was cut off. The white gray line corresponds with the polyurethane inside the crack (B). Visualization of the polyurethane inside the part of the sample which was cut off in the image (C) (Van Tittelboom, 2012).

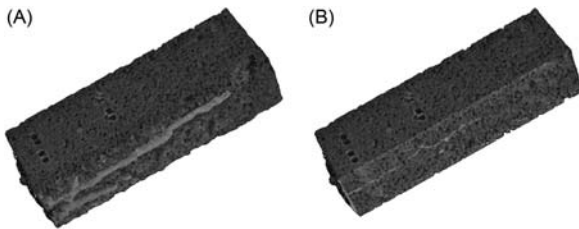


Figure 16.9 3D rendered neutron computed tomography (CT) images of the sample from which the crack was autonomously healed with polyurethane. Render of the complete sample where leakage of the polyurethane out of the crack can be seen. The position of the capsules is also visible (A). Render where part of the sample was cut off. The white gray line corresponds with the polyurethane inside the crack (B) (Van Tittelboom, 2012).

(Fig. 16.8B). Moreover, it is noticed that the complete crack is colored light gray. This proves that the crack was filled completely with the polyurethane healing agent as the polyurethane—which contains lots of hydrogen bonds—is highly attenuated by the neutrons and therefore is colored lighter. From the image shown in Fig. 16.8C it is noted that the polyurethane does not form a continuous layer. However, one must be careful when drawing this conclusion as the resolution of the scans is limited and thus it is possible that a biased view was obtained.

For the sample which was autonomously healed with polyurethane and scanned by means of neutron tomography the crack runs until half height of the sample (Fig. 16.9A and B). Over the whole length of the crack it is colored light gray which proves that also in the case of autonomous crack healing, the crack is completely filled with healing agent. In Fig. 16.9A it is even shown that some healing agent leaked out of the crack and flowed over the surface of the sample. Another interesting notice is that the capsules seem to be completely empty. Due to breakage of the capsules during crack formation both components of the healing agent came out of the capsules and filled the crack where they started to polymerize.

Although a quantitative analysis of the crack healing efficiency by X-ray or neutron radiography seems impossible due to the limited accuracy, these techniques are very relevant to judge whether or to which extent the polyurethane was released from the capsules.

16.4 Regain in impermeability

16.4.1 Water permeability measurements

Cylindrical capsules made from glass and ceramics were used to carry the healing agent and to trigger the healing action upon crack appearance. In order to investigate the effect of the capsule diameter, capsules with a different internal diameter but with the same internal volume of 130 mm^3 were used. As for the ceramic capsules with internal diameter of 3.35 mm, a length of 15 mm was chosen, the length of the glass capsules with internal diameters of 3 mm and 2 mm amounted to 18 mm and 41 mm, respectively.

The commercial polyurethane-based agent BASF was used as healing agent. While half of the capsules was filled with the prepolymer of the polyurethane, the other half was filled with a mixture of accelerator (10%) and water. Inside the mortar specimens, both types of capsules, containing the prepolymer and the accelerator, were positioned next to each other.

To prepare samples for the water permeability tests (Van Tittelboom et al., 2011b), cylindrical molds with a diameter of 76 mm and a height of 20 mm were used. Two steel fibers ($\text{Ø} 1 \text{ mm}$) and three pairs of capsules were placed in the middle of the sample as shown in Fig. 16.10. The test series “UNCR, REF, and MAN BASF” only contained two steel fibers inside the matrix (Table 16.1).

Cracks were created by means of a crack-width controlled splitting test. In order to obtain a similar crack width for each split sample, the crack width was controlled during performance of the splitting test by means of an LVDT attached to each side of the cylindrical specimen at middle height (Fig. 16.11). The crack width was

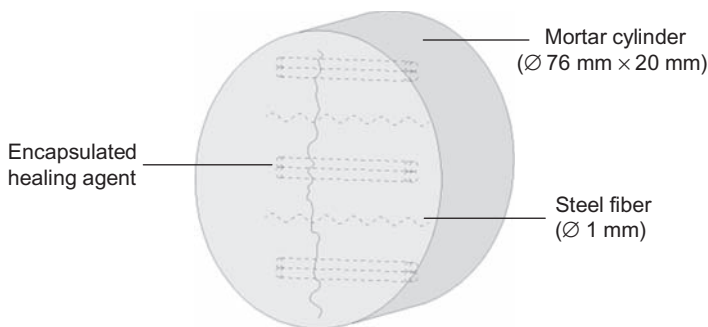
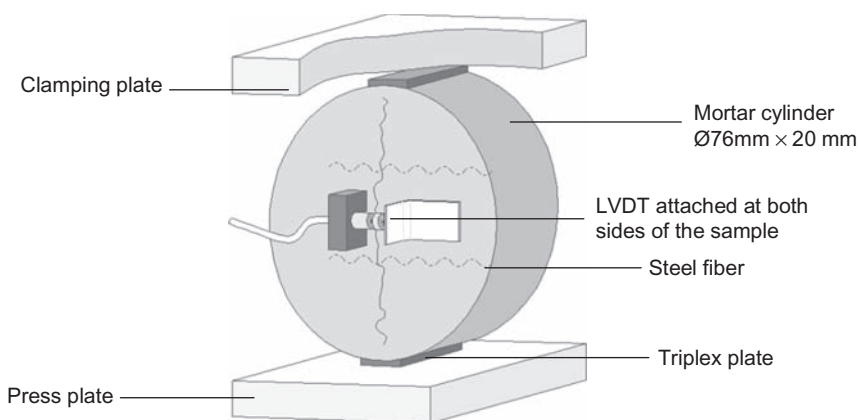


Figure 16.10 Position of the encapsulated healing agent and steel fibers inside cylindrical mortar specimens (Van Tittelboom, 2012).

Table 16.1 Test series used for the water permeability test

Series	Crack	Crack treatment	Encapsulation material
UNCR	No	–	–
REF	Yes	No treatment	–
MAN BASF	Yes	Manual healing	–
CAPS BASF GLA2	Yes	Autonomous healing	Glass capsules (\varnothing 2 mm)
CAPS BASF GLA3	Yes	Autonomous healing	Glass capsules (\varnothing 3 mm)
CAPS BASF CER	Yes	Autonomous healing	Ceramic capsules (\varnothing 3.3 mm)

**Figure 16.11** Performance of a crack width controlled splitting test onto a mortar cylinder with embedded steel fibers (Van Tittelboom, 2012).

increased until a width of 400 μm was reached. Then, specimens were unloaded, giving rise to a decrease in crack width and a final width of approximately 250 μm .

The uncracked and cracked cylindrical specimens were subjected to a water permeability test in order to investigate the efficiency of the (self-)healing mechanism. The test setup used is a slightly modified version of the low pressure water permeability test described by Wang et al. (1997) and Aldea et al. (2000) (Fig. 16.12). By generating water pressure at the top of the samples, by means of a water column, and by following the descent of the water column in time, the water permeability coefficient can be determined.

After being vacuum saturated, the test specimens, glued in PVC rings, were mounted between two cylindrical compartments as shown in Fig. 16.12. The drop in water level in the pipette, due to water flow through the cracked and/or healed specimen, was measured at regular time intervals, normally once a day, depending

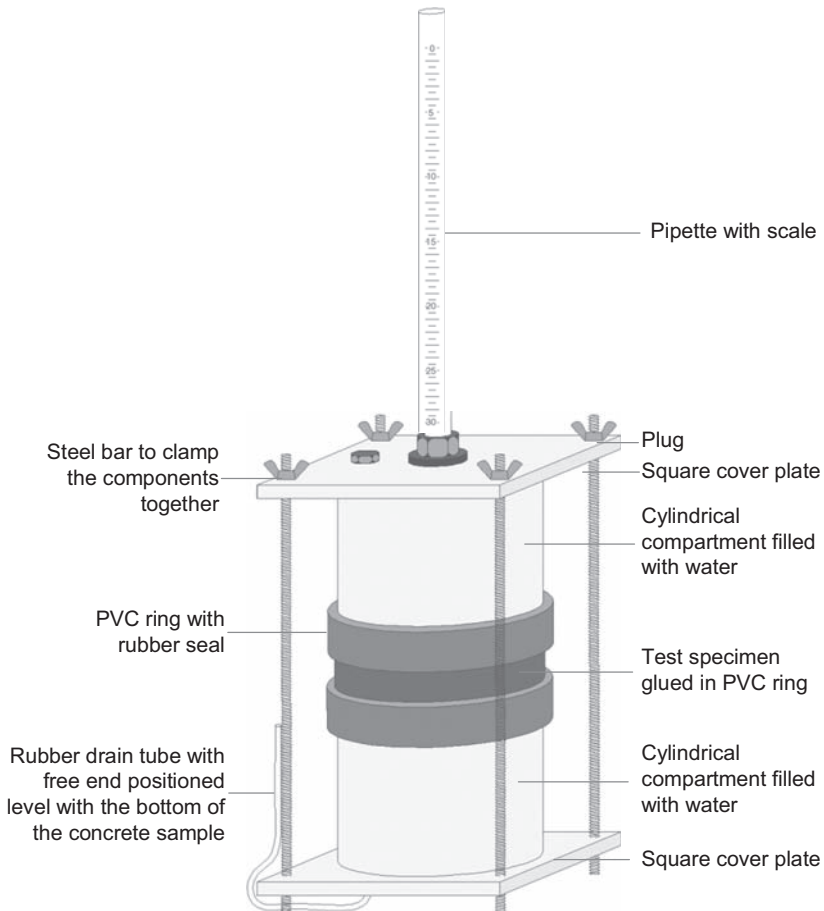


Figure 16.12 Water permeability test setup (Van Tittelboom et al., 2011b).

on the water flow rate through the specimen, and water was restored each time to the original level. Darcy's law (Eq. 16.1) was used to calculate the coefficient of water permeability.

$$k = \frac{a \cdot T}{A \cdot t} \cdot \ln\left(\frac{h_0}{h_f}\right) \quad (16.1)$$

where k = water permeability coefficient (m/s); a = cross-sectional area of the pipette (m^2); A = cross-sectional area of the specimen (m^2); T = specimen thickness (m); t = time (s); and h_0 and h_f = initial and final water heads (cm).

In Fig. 16.13 the water permeability coefficient, k , is plotted against the crack width. To improve the clarity of the graph, the water permeability coefficient is shown on a logarithmic scale.

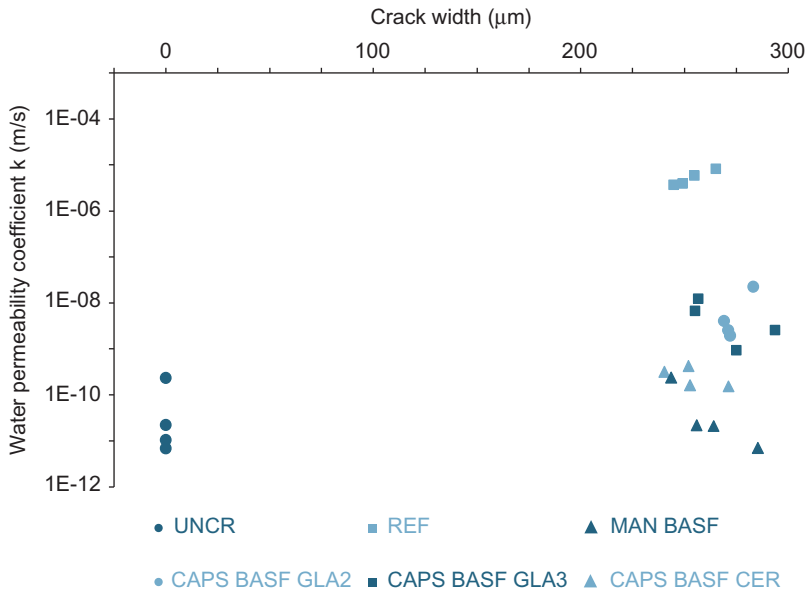


Figure 16.13 Water permeability coefficient in function of the crack width (Van Tittelboom et al., 2011b).

When cracks were created in the specimens and these cracks were left untreated (REF), it was observed that the water permeability coefficient was 10^4 – 10^6 times higher compared to uncracked specimens (UNCR). When these cracks were treated manually (MAN BASF) by means of polyurethane, a similar reduction was noticed. In addition, no significant difference was noticed when comparing the mean water permeability coefficient obtained for specimens with manually healed cracks with the coefficients obtained for uncracked specimens, indicating that the polyurethane healing agent was very effective to make the cracks watertight.

If self-healing properties were built-in by embedding encapsulated polyurethane, the measured water permeability coefficient was slightly higher compared with manually healed cracks, however, it was possible to reduce the water permeability coefficient with a factor of 10^2 – 10^3 when glass capsules were used and even with a factor 10^3 – 10^4 when ceramic capsules were embedded. Here, it was seen that encapsulation of polyurethane by ceramic capsules seemed to result in a significantly better performance.

16.4.2 Gravimetric evaluation of capillary water absorption

Ceramic capsules, with an inner diameter of approximately 3 mm and a length of 75 mm, were used to carry the healing agent. Again, the commercial polyurethane-based healing agent from BASF was used to seal the cracks and each component of the agent was embedded inside separate capsules.

Table 16.2 Test series used in the experiments

Code	Description
UNCR	Uncracked beams
REF	Reference beams (no crack healing)
MAN BASF	Manual crack healing with polyurethane
CAPS BASF	Self-healing of cracks with polyurethane

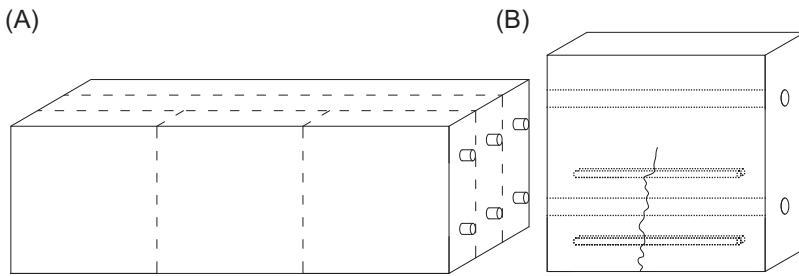


Figure 16.14 Position of the steel reinforcement and the cutting lines (A), resulting specimen on which water sorption was measured (B) (Van Tittelboom et al., 2011c).

Molds with dimensions of 100 mm × 100 mm × 300 mm were used for preparation of four series of mortar beams (Table 16.2). All beams were reinforced with six steel bars having a diameter of 8 mm. Three steel bars were positioned at a height of 25 mm, the remaining three bars were positioned at 75 mm height (Fig. 16.14).

When beams of the test series “CAPS BASF” were made, the molds were filled in several layers. First, a 10 mm mortar layer was brought into the molds. When this layer was compacted by means of vibration, six couples of ceramic capsules were placed on top of it. Afterwards, the molds were further filled with mortar until a layer of approximately 40 mm was obtained. After this layer was vibrated, again six couples of capsules were positioned onto this layer. Finally the molds were completely filled with mortar and vibrated. After curing, the steel reinforced prisms were cut with a diamond saw into three slices along the long axis of the prisms (Fig. 16.14).

All test series, except the series “UNCR,” were cracked by means of a crack-width controlled three-point-bending test. The crack width was measured by means of an LVDT. The crack width was increased until a crack of 400 μm was reached. At that point, the specimen was unloaded causing a decrease in crack width. The resulting crack width amounted to 200 μm. Finally, from the center part of all specimens, slices with a width of 100 mm were sawn (Fig. 16.14A and B).

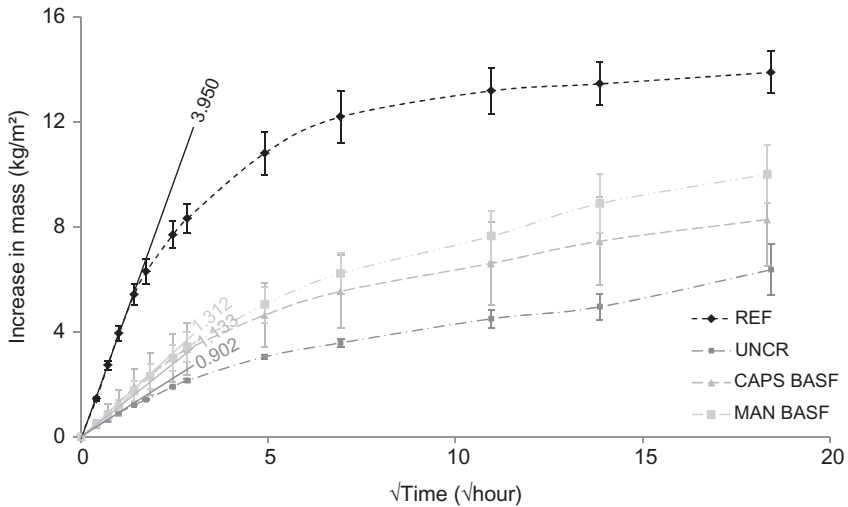


Figure 16.15 Increase in mass due to water sorption (Van Tittelboom et al., 2011c).

The crack healing efficiency was evaluated by capillary water sorption tests (Van Tittelboom et al., 2011c). When the specimens were 1 month old, they were dried in an oven for 1 week. Then, the square surfaces (100 mm × 100 mm) and the two opposite small surfaces (25–30 mm × 100 mm) were covered with self-adhesive aluminum foil in order to impose unidirectional moisture movement during the test. Subsequently, specimens were weighed and afterwards the surface with the crack mouth was placed on two line supports in a container which was filled with water, in such a way that the lower 0.5 cm of the specimens was immersed in water. At regular time intervals, specimens were taken out of the container and placed onto a nonabsorptive support for one minute before they were weighed.

From these measurements the coefficient of initial water sorption (A_i) was determined as the slope of the linear curve fitting the measurements obtained during the first hour. The A_i value measured for the reference specimens (3.950) was very high as the crack was quickly filled with water, whereas the uncracked specimens had much lower A_i (0.902), which characterizes the undamaged cementitious material. The results showed that there is no significant difference between the efficiency of manual and autonomous crack repair (Fig. 16.15). The fact that the A_i values obtained for the manually (1.133) and autonomously (1.312) healed samples were higher than the value measured for the undamaged material is due to the damage induced under the high tensile stress in the zone around the crack before the crack was formed. This led to the conclusion that the autonomous healed cracks were completely water tight and water uptake was due to sorption by the damaged matrix only.

16.4.3 Neutron radiography to evaluate the water uptake

Similar samples and sample series (Table 16.2), as described in Section 16.4.2, were used to evaluate the regain in impermeability by neutron radiography (Van Tittelboom et al., 2013). The only differences were that, in this study, glass instead of ceramic capsules were used, reinforcement bars had a diameter of 2 mm instead of 8 mm and the position of the capsules was fixed inside the specimens by attaching them to the walls of the molds at 10 mm and 40 mm height.

Neutron radiography was performed at the Paul Sherrer Institute (PSI) in Switzerland. Before starting the neutron radiographic experiments, specimens were weighed. During the experiment, two specimens, with their cracked surface downwards, were placed onto two line supports in an aluminum container which was positioned at the highest level of a frame while two more specimens were placed onto line supports at the lower level of a frame in an aluminum container. Before the containers were filled with water, reference images of the samples were taken in the dry state. Subsequently, water was automatically supplied into the containers by means of a water valve which was controlled from the outside of the shielded bunker. When the water level raised ± 4 mm above the bottom of the samples, water supply was turned off. First, 200 radiographs were taken in time steps of approximately 5 seconds. After this, 40 images were taken every 30 seconds. Then, images were taken every 300 seconds until the samples had been in contact with water for 4 hours. At that time, samples were removed from the containers and weighed. After this action, one sample of each test series was immersed again and when they were immersed for 24 hours one more radiographic scan was taken.

In Fig. 16.16 (middle), for one representative sample of each test series, a differential neutron radiographic image is shown, obtained after 30 seconds and 24 hours of contact with water. On the left, a picture of the samples themselves is shown on which the crack location, crack width (w) and the zone used in the quantitative analysis are indicated. In the graphs on the right of Fig. 16.16, the moisture profile is shown when the sample was in contact with water for 30 seconds, 1 minute, 5 minutes, 15 minutes, 30 minutes, 1 hour, 2 hours, 4 hours, and 24 hours. The moisture profile was determined as the average water content over a bandwidth of 160 pixels symmetrically around the crack and perpendicular to the moisture front (see indicated rectangles in Fig. 16.16 left). In the high-resolution radiographic images of samples from the test series with self-healing properties, the positions of the capsules can be noticed. Also in the graphs, the capsule locations and the locations of the reinforcement bars are noticed as positions with reduced water content. These are indicated in the graphs by means of a dot (\bullet reinforcement bar, \circ tubular capsule).

It is noted from the radiographic images, obtained after the samples were in contact with water for 30 seconds, that the untreated crack immediately fills with water. However, when the crack is manually or autonomously healed by means of polyurethane, after 30 seconds no water enters into the crack.

After 24 hours of contact, all samples contain a certain amount of water due to capillary water absorption along the matrix pores of the cementitious matrix. However, the amount of water taken up is dependent on the crack treatment.

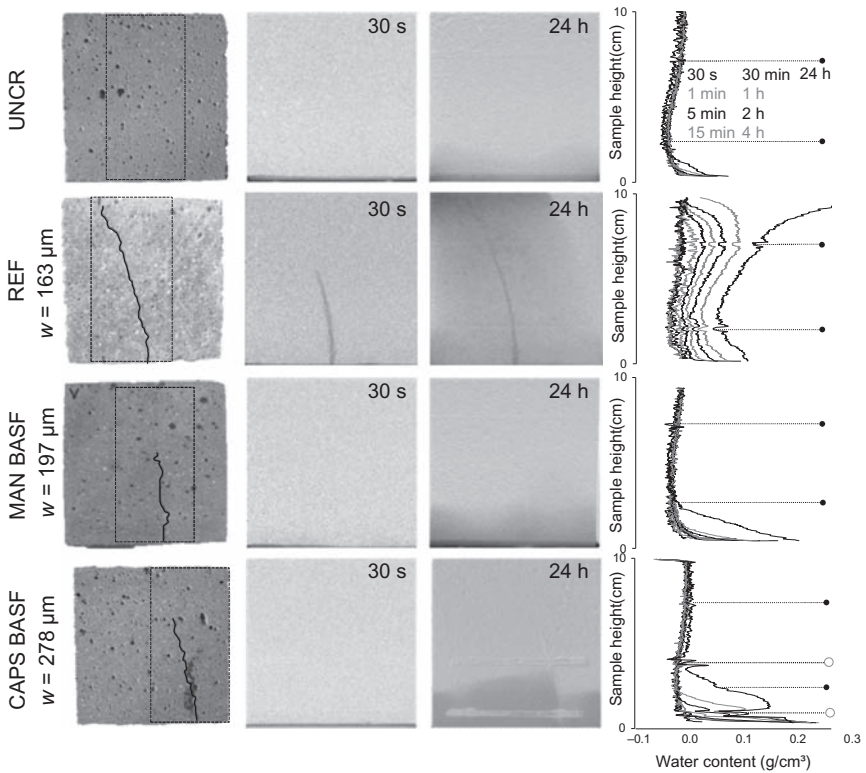


Figure 16.16 Neutron radiographs obtained after 30 s and 24 h of contact with water for one representative sample of each series (field of view measures 100 mm × 100 mm). The moisture profiles determined at different time intervals are shown on the right. Closed dots represent the position of the reinforcement, open dots the position of the capsules. On the left a picture of the considered sample is shown together with the location of the crack, the crack width and the zone in which the water content was calculated (Van Tittelboom et al., 2013).

When the crack has been left untreated, the water front reaches the upper side of the sample. There, the water starts evaporating and an equilibrium arises as the same amount of water evaporates at the top of the sample as is absorbed at the bottom. Moreover, it can be seen that the upper part of the sample is darker than the rest. This means that more water is available at that position. This is due to the fact that, locally, the matrix is more porous due to micro-cracks which formed at the upper part of the beam where the force was located during the bending test. When cracks are manually repaired by polyurethane, after 24 hours of contact with water, an evenly distributed amount of water is absorbed by the matrix. The amount of absorbed water is comparable to the amount absorbed by the uncracked sample.

When encapsulated polyurethane is embedded inside the matrix, water will not enter the crack even after 24 hours of contact with water. However, in comparison with the uncracked sample, a higher amount of water penetrated in the zone just next to the crack.

In order to prevent reinforcement corrosion, it is important that the water front does not reach the reinforcement location. For an uncracked sample the water front does not reach the reinforcement even after 24 hours of continuous contact with water (see curves in Fig. 16.16). For a cracked sample which is left untreated the water front reached the reinforcement already after a few seconds of contact with water and thus at that time corrosion may initiate. When cracks are treated manually with polyurethane, the reinforcement remains in the dry zone even after 24 hours of contact with water. When encapsulated polyurethane is embedded in the matrix, the water front rises above the reinforcement level, although the crack itself is sealed. In this case, water is taken up by the matrix which also increases the risk of reinforcement corrosion.

16.5 Regain in mechanical properties

16.5.1 Regain in strength and stiffness

Again, cylindrical capsules made from glass and ceramic were used to carry the polyurethane healing agent obtained from BASF and to trigger the healing action upon crack appearance. Capsules with a different internal diameter but with the same internal volume were used. An overview of the used capsule dimensions is given in Table 16.3.

Prismatic molds with dimensions of 60 mm × 60 mm × 220 mm, provided with a 5 mm deep notch at the lower side, were used. First, a 10 mm mortar layer was brought into the molds. When this layer was compacted, two reinforcement bars (Ø 2 mm) and two pairs of capsules were placed on top of it. Afterwards, the molds were completely filled with mortar and vibrated (Fig. 16.17). The reference samples (REF) and samples used for manual crack healing (MAN BASF) were prepared in the same way as described earlier, however, samples belonging to these series contained two reinforcement bars only (Table 16.4).

The mortar prisms were cracked, and so, for the prisms containing embedded healing agent, the healing mechanism was triggered by means of a crack-width controlled three-point-bending test. Cracks of the specimens containing encapsulated

Table 16.3 Dimensions of the capsules used for encapsulation of the polyurethane healing agent

Encapsulation material	ϕ_i (mm)	ϕ_o (mm)	Length (mm)	Volume (mm ³)
Glass	2.00	2.20	83	259
Glass	3.00	3.35	37	259
Ceramic	2.57	2.99	50	259

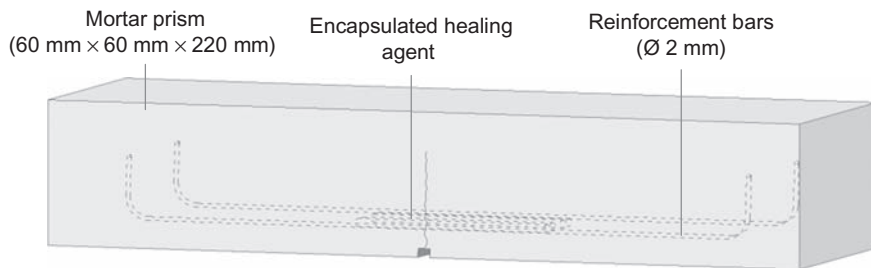


Figure 16.17 Position of the encapsulated healing agent and reinforcement bars inside prismatic mortar specimens (Van Tittelboom, 2012).

Table 16.4 Composition of the specimens

Series	Crack	Crack treatment	Encapsulation material
REF	Yes	No treatment	–
MAN BASF	Yes	Manual healing	–
CAPS BASF GLA2	Yes	Autonomous healing	Glass capsules Ø 2 mm
CAPS BASF GLA3	Yes	Autonomous healing	Glass capsules Ø 3 mm
CAPS BASF CER	Yes	Autonomous healing	Ceramic capsules

healing agent were autonomously healed. Cracks of the samples belonging to the test series “MAN BASF” were treated immediately after crack formation.

One day after crack creation, when the polyurethane inside the cracks of the manually and autonomously healed prismatic specimens was thought to be hardened, all prisms were reloaded in three-point-bending to evaluate the healing efficiency (Van Tittelboom et al., 2011b). Samples were also subjected to a second reloading cycle one day later. Cracks of the test series “MAN BASF” were not injected again with healing agent in between the first and the second reloading cycle.

For the untreated specimens and the specimens for which cracks were manually healed, the curves obtained during crack formation looked similar (Fig. 16.18). In the graph representing the result of a specimen with self-healing properties, some distinct drops in load were observed after the peak load had been reached. These drops in load were related to breakage of the tubular capsules as these drops were accompanied with audible ‘pop’ sounds.

During the first reloading cycle, it was found that, in the case of untreated cracks, the first part of the curve followed the last part of the previous curve. This indicated that no regain in mechanical properties was obtained. The crack just

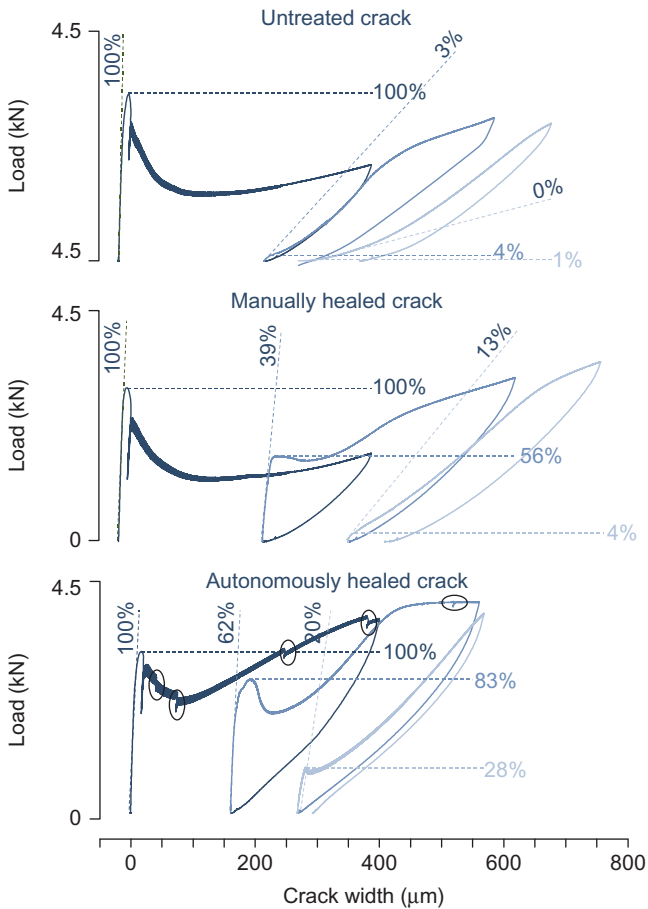


Figure 16.18 Loading curves obtained during crack formation and during the first and second reloading cycle for untreated cracks, manually healed cracks by polyurethane injection and autonomously healed cracks by encapsulated polyurethane. Drops in load due to breakage of the capsules are indicated by means of an ellipse. The amount of regain in strength and stiffness is indicated on the graphs (Van Tittelboom et al., 2011b).

reopened upon reloading. However, when the curve, obtained during the first reloading cycle, of the manually healed and autonomously healed specimens was examined, a new peak load was observed. This indicated that regain in strength was obtained due to crack healing. Additionally, it was also observed that the first part of these curves had a steeper slope compared with the last part of the previous curves. This indicated that there was also regain in stiffness.

For the specimens with self-healing properties, again a small peak was observed during the second reloading cycle. From this, it may be concluded that a second autonomous healing action at the same crack location is feasible, although it is less effective than the first one.

From the obtained loading curves, the strength and the stiffness of the beams was calculated and the mechanical properties after (self-)healing were compared with the original values.

$$\text{Strength regain} = \frac{F_{L2}}{F_{L1}} \text{ or } \frac{F_{L3}}{F_{L1}} \quad (16.2)$$

where F_{L1} = the peak load obtained during crack formation (kN), F_{L2} = the peak load obtained during the first reloading cycle (kN) and F_{L3} = the peak load obtained during the second reloading cycle (kN).

The slope of the curve, joining the points $0 \cdot F_L$ and $0.4 \cdot F_L$ was used to indicate the stiffness. The method used to determine the stiffness is based on the method to calculate the E-modulus according to the standard [NBN EN 1992-1-1 \(2010\)](#) and is given by [Eq. 16.3](#).

$$\text{Stiffness regain} = \frac{0.4 \cdot F_{L2} - 0 \cdot F_{L2}}{0.4 \cdot w_2 - 0 \cdot w_2} \cdot \frac{0.4 \cdot w_1 - 0 \cdot w_1}{0.4 \cdot F_{L1} - 0 \cdot F_{L1}} \text{ or} \quad (16.3)$$

$$\frac{0.4 \cdot F_{L3} - 0 \cdot F_{L3}}{0.4 \cdot w_3 - 0 \cdot w_3} \cdot \frac{0.4 \cdot w_1 - 0 \cdot w_1}{0.4 \cdot F_{L1} - 0 \cdot F_{L1}}$$

where $0 \cdot F_{L1}$, $0 \cdot F_{L2}$ and $0 \cdot F_{L3}$ = the load corresponding to 0 times the peak loads F_{L1} , F_{L2} , and F_{L3} (kN), $0.4 \cdot F_{L1}$, $0.4 \cdot F_{L2}$, and $0.4 \cdot F_{L3}$ = the load corresponding to 0.4 times the peak loads F_{L1} , F_{L2} , and F_{L3} (kN), $0 \cdot w_1$, $0 \cdot w_2$, and $0 \cdot w_3$ = the crack width obtained when the load reaches a value of $0 \cdot F_{L1}$, $0 \cdot F_{L2}$, or $0 \cdot F_{L3}$ (μm), and $0.4 \cdot w_1$, $0.4 \cdot w_2$, and $0.4 \cdot w_3$ = the crack width obtained when the load reaches a value of $0.4 \cdot F_{L1}$, $0.4 \cdot F_{L2}$, or $0.4 \cdot F_{L3}$ (μm).

In [Fig. 16.19A](#) the amount of strength regain is shown. It was observed that, during the first reloading cycle only minimal strength was retrieved for the reference samples (REF), whereas for the samples which cracks were repaired with polyurethane, a higher regain in strength was noticed. In the case where cracks were manually healed (MAN BASF), an average strength regain of 61% was obtained. If encapsulated polyurethane was present inside the mortar matrix, an average regain in strength of 62%, 54%, and 48% was achieved for glass capsules with a diameter of 3 mm (CAPS BASF GLA3) and 2 mm (CAPS BASF GLA2), and for ceramic capsules (CAPS BASF CER), respectively. Compared to the results obtained for the manually healed cracks, no significant difference in strength regain was noticed, during the first reloading cycle, when the cracks were healed autonomously. Moreover, specimens with polyurethane gave evidence of a second healing action. While reference samples and samples with manually healed cracks showed almost no retrieval in strength during the second reloading cycle, specimens with ceramic capsules showed a strength regain of 17% upon second reloading. Samples containing glass capsules with a diameter of 2 mm and 3 mm showed an average regain of 23% and 20%, respectively, during the second reloading cycle.

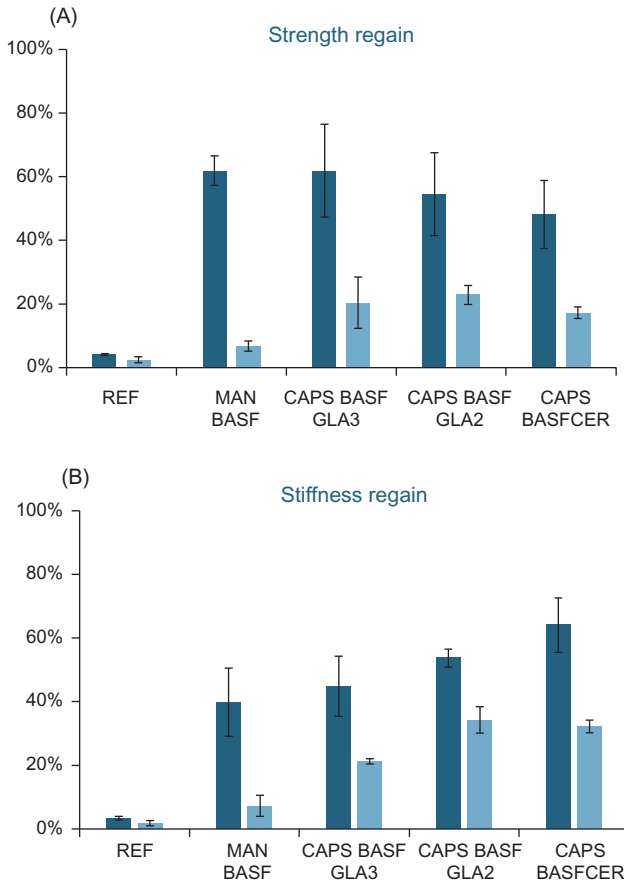


Figure 16.19 Regain in strength and stiffness during the first (dark blue bars) and the second (light blue bars) reloading cycle for untreated, manually and autonomously healed cracks. Error bars represent the standard error.

In Fig. 16.19B the amount of regain in stiffness is shown. During the first reloading cycle, a significant difference in stiffness regain was observed between the reference samples (REF) and the manually (MAN BASF) or autonomously healed samples (CAPS BASF GLA3, GLA2, and CER). While almost no regain in stiffness was obtained for reference samples, an average stiffness regain between 40% and 64% was obtained when cracks were repaired. Again, based on the amount of regain in stiffness, no significant difference was seen between the efficiency of manual and autonomous crack healing. During the second reloading cycle, stiffness regain decreased to an average value of 7% for the manually healed samples, while the specimens with embedded capsules gave evidence of a second healing action and thus a higher stiffness recovery. Specimens with embedded glass capsules, with a diameter of 2 mm and 3 mm and specimens with embedded ceramic capsules showed a second stiffness recovery of 34%, 21%, and 32%, respectively.

Based on these results there is no significant difference between the efficiency of glass capsules and ceramic capsules, nor between glass capsules with an internal diameter of 2 mm and 3 mm. Normally, the efficiency of emptying of the capsules is dependent on the capillary forces inside the capsules, which are reduced when the diameter increases. However, an alteration in the diameter from 2 to 3 mm did not seem to give significant differences in outcome.

16.5.2 Use of acoustic emission analysis to evaluate the regain in mechanical properties

When materials or structures are loaded above their ultimate load capacity, localized zones of cracking develop. Thereby, elastic energy is released, which propagates through the material or structure in the form of elastic waves. These acoustic emissions (AEs) were first observed in metals (crying of tin), but it was soon discovered to be a general phenomenon. This led to the development of a new nondestructive testing method, the so-called AE analysis. In contrast to resonance frequency and ultrasound analysis, where the source emitting the waves is applied to the surface of the material, in AE, the waves are produced by and emitted within the material (Grosse and Ohtsu, 2008). In the following study, AE analysis has been used to evaluate the autonomous crack healing efficiency.

For this study (Van Tittelboom et al., 2012), the earlier-mentioned, polyurethane-based healing agent BASF was used. Ceramic capsules, with an inner diameter of approximately 3 mm and a length of 100 mm, were applied to carry the healing agent. In order to protect the brittle capsules from breakage during preparation of the concrete beams, they were embedded inside mortar bars with dimensions of 600 mm × 20 mm × 20 mm as shown in Fig. 16.20.

Molds with dimensions of 500 mm × 110 mm × 50 mm were used for preparation of concrete beams with and without self-healing properties. Beams with self-healing properties were prepared in different phases. First, a layer of concrete was brought into the molds. When this layer was vibrated, three mortar bars, containing the

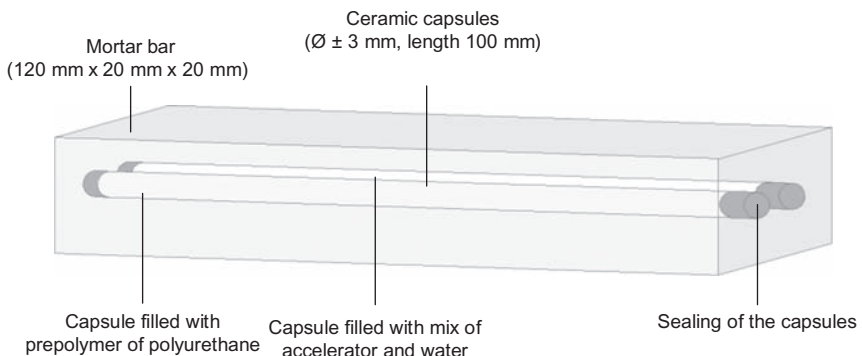


Figure 16.20 Protection of the ceramic capsules by means of mortar bars (Van Tittelboom et al., 2012).

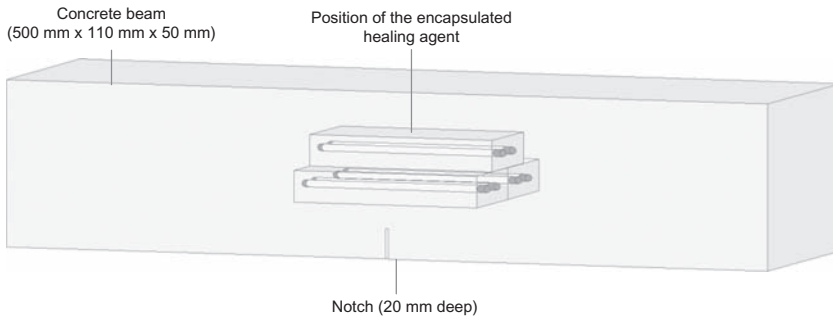


Figure 16.21 Position of the encapsulated healing agent inside the concrete beams (Van Tittelboom et al., 2012).

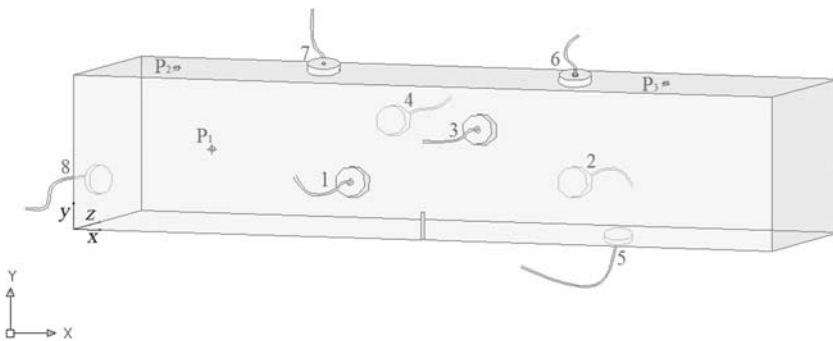


Figure 16.22 Concrete beam with indication of the transducer positions (1–8) (Van Tittelboom et al., 2012).

encapsulated healing agent, were positioned into the mold as shown in Fig. 16.21. Afterwards, molds were completely filled with concrete and vibrated a second time. For beams without self-healing properties, molds were filled at once and vibrated. To enable localized crack formation during the bending tests, a 20 mm deep notch was sawn in each beam at the bottom, in the middle of the specimens (Fig. 16.21).

Cracks were created by means of a crack-width controlled three-point-bending test. An electro-mechanical testing device was used in order to reduce the amount of noise so that the AE measurements were only a little influenced by the test machine. In addition, a Teflon strip was provided between the supports and the beam in order to reduce the contact noise. One day after manual or autonomous crack repair, beams were reloaded using the same setup.

During crack creation as well as during reloading, specimens were instrumented with an AE system. Waves, emitted due to occurrence of cracks and breakage of embedded capsules, are detected by AE transducers, attached to the surface of the beams. Eight piezoelectric transducers with a nominal diameter of 25 mm and a relatively flat frequency response below 1 MHz were used. The transducers were coupled to the concrete beams by means of hot glue on the positions shown in Fig. 16.22. The frequency range of the acquisition of wave forms was set from 1 kHz

Table 16.5 Energy classes used for data analysis of the AE experiments

Class	Energy [–]
1	1–2.5
2	2.5–5
3	5–10
4	10–100
5	100–1000
6	1000–10,000
7	>10,000

to 1 MHz. The slew rate trigger was adjusted to 0.08 V/ μ s and an input range of ± 5 V was chosen. The detected signals were amplified with 54 dB gain amplifiers. Postprocessing of the signals was controlled by the software package *TransOctoAE*, which was developed at the University of Stuttgart (Grosse et al., 2004).

The velocity of the emitted waves (v_p) was determined using ultrasonic wave transmission measurements, similar as done by Kurz et al. (2005). Ultrasonic waves with a frequency of 200 kHz were used. The velocity measurements were performed onto seven arbitrarily chosen concrete beams. As it was found that the sound velocity was similar for these specimens, the mean value (4595×10^{-3} mm/ μ s) was taken as acoustic wave velocity for all beams.

In order to filter out the noise, recorded AE signals were filtered using the *All2SDF* conversion program (Kurz et al., 2003). A band pass filter with a lower cut-off frequency of 35 kHz and a higher cut-off frequency of 300 kHz was chosen. The energy of each filtered signal was calculated as the area under the rectified signal envelope. The energy was calculated for the signals captured by each of the eight transducers. From these eight values, the maximum value was selected and chosen as the energy for the considered event.

The Hinkley picker was used as a picking algorithm to pick the onset times automatically. For further analysis, a selection of the events was made based on their energy and the number of channels for which an accurate onset time determination was possible. Events with a relative energy higher than one and for which more than five channels could be used during localization were selected. Additionally, events were subdivided into arbitrarily chosen classes based onto their energy. Seven energy classes were considered according to Table 16.5.

In Fig. 16.23, a load–displacement curve is shown for one representative beam of each test series (REF, MAN BASF, and CAPS BASF), together with the emitted events recorded during crack creation and reloading. Each event is represented by means of a dot and, based on their energy class, the dots are shown in different levels. Upon reloading of the beams, different phases could be distinguished.

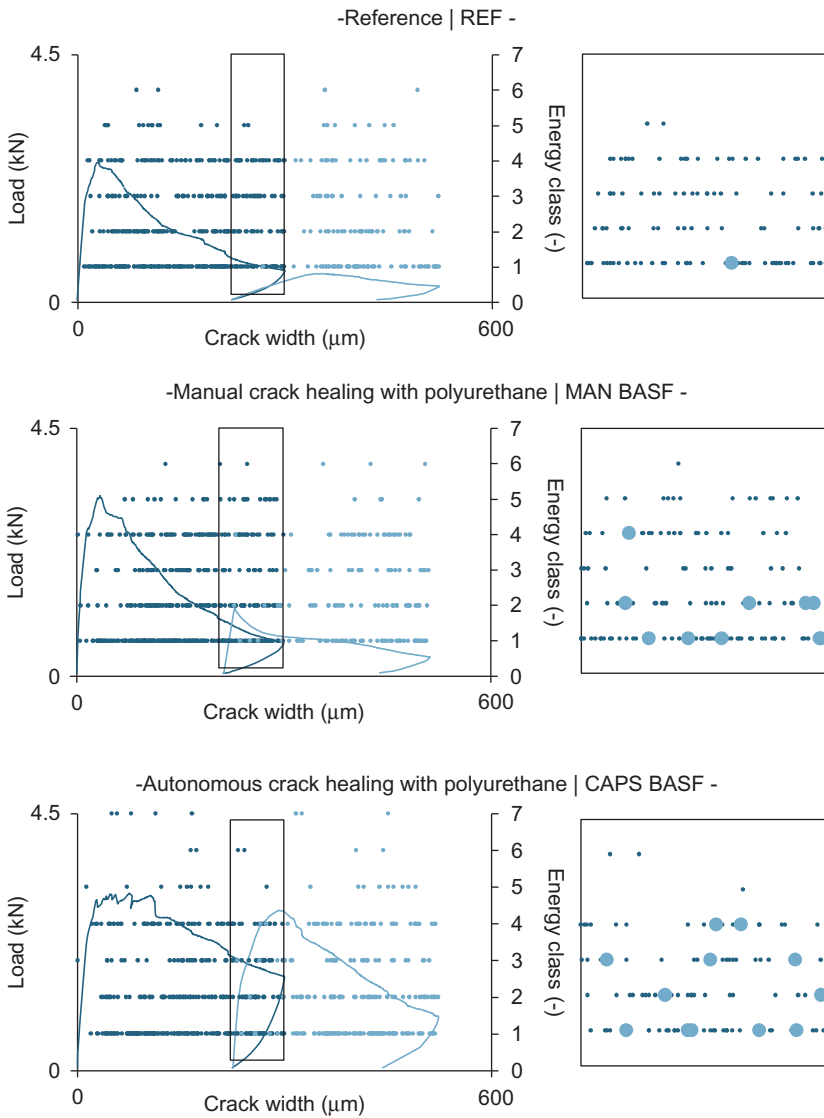


Figure 16.23 Load–displacement curve for one representative beam of each test series in combination with the energy class of the events emitted upon loading and reloading (shown by means of dots). A magnification of the zone indicated in each graph is shown on the right. Smaller dots represent events emitted upon loading while bigger dots represent events recorded upon reloading (Van Tittelboom et al., 2012).

During the first phase, the crack just reopens in the case of reference specimens or the healing agent starts rupturing in the case of beams with healed cracks. When the crack opening which was reached during crack creation is reached again, new cracks starts to form in the concrete matrix. This is the start of the second phase.

The third phase starts at the moment that the adjusted crack width is reached, loading is stopped and the crack width decreases. As the second and the third phase are almost equal for all test series, and many events are produced during the second phase, these events may mask the differences between the first phases of the different test series. As we need to focus on the first phase (indicated with a rectangle in Fig. 16.23) a selected region is magnified at the right of each load–displacement curve in Fig. 16.23. Events which were emitted upon reloading are represented by bigger dots. When looking at these graphs, it can be seen that more events occur upon reloading of beams with healed cracks (MAN BASF and CAPS BASF). However, results need to be interpreted with care: for some test series, the first phase only covers the elastic behavior of the beam, whereas for other test series, the first phase also covers the post peak region. However, from these findings it can be concluded that AE analysis seems a useful instrument to evaluate the self-healing efficiency of cementitious materials.

16.6 Regain in durability

16.6.1 Prevention against chloride ingress

To find out whether self-healing of concrete cracks can help to prevent the ingress of aggressive substances such as chlorides, the chloride ingress of cracked samples with and without self-healing properties was measured and compared to uncracked samples. Samples with dimensions and/or encapsulated healing agents, as described in Section 16.3.1 were used. First, all surfaces of the samples—except the one to be exposed to the chlorides, were coated with epoxy. The chloride diffusion test was performed in accordance with the NT Build 443 test method (1995). The samples were submerged during one week in a saturated $\text{Ca}(\text{OH})_2$ solution. For the next 7 weeks, the samples were submerged in a 2.8 mol/L NaCl solution. Afterwards, some samples were split perpendicular to the crack and sprayed with silver nitrate in order to examine the chloride penetration front. Other samples were used to perform titrations on, so every 2 mm a mortar layer along the crack was ground until a depth of 20 mm. The chlorides were extracted from the powder and this solution was titrated with an automatic titration device. The nonsteady state diffusion coefficient of the crack D_{nssd} was determined by a nonlinear regression analysis in accordance with the least squares method as described in Eq. (16.4), which is mentioned in the NT Build 443 test method:

$$c(x, t) = c_s - (c_s - c_i) \operatorname{erf} \left(\frac{x}{\sqrt{4D_{\text{nssd}}t}} \right) \quad (16.4)$$

With $c(x, t)$ the experimentally obtained chloride concentration at depth x (mm) after a time, t , of 7 weeks, c_s the surface concentration, and c_i the initial concentration in the mortar which was assumed to be zero.

The chloride penetration front obtained from the sample halves which were sprayed with silver nitrate could be categorized in four classes, as indicated in

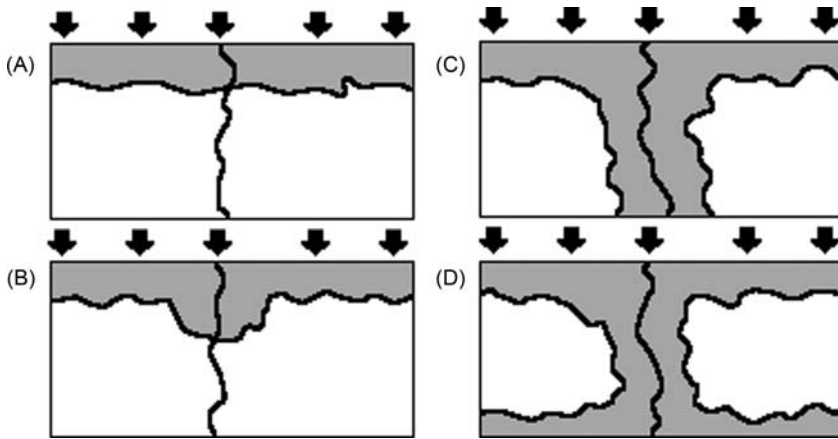


Figure 16.24 Measured chloride profiles: (A) Equal penetration, (B) Additional penetration through crack, (C) Complete penetration through crack, (D) Complete penetration through crack and chlorides accumulate at opposite surface. The gray hatched area corresponds to the zone where chlorides penetrated. Arrows indicate the direction of chloride ingress (Vantygheem, 2014).

Table 16.6 Amount of samples belonging to each of the categories after 7 weeks of exposure to chlorides

	UNCR	REF	MAN BASF	CAPS BASF	MAN SLV	CAPS SLV
Class A	100%	0%	80%	40%	0%	20%
Class B	0%	0%	20%	20%	20%	60%
Class C	0%	40%	0%	40%	60%	20%
Class D	0%	60%	0%	0%	20%	0%

Fig. 16.24. Sample halves which belong to Class A show an equal chloride penetration from the exposed surface. In Class B, additional penetration through the crack can be noticed. Samples of Class C show a full penetration through the crack and, in the case of Class D an accumulation of chlorides at the coated surface was obtained. In [Table 16.6](#) the distribution of the samples per class is presented. The uncracked samples always showed an equal chloride penetration front. Within the test series MAN BASF, 80% of the samples obtained an equal penetration. For these samples, complete crack healing was obtained. The other 20% were only partially healed, since they showed an additional penetration through the crack. When the polyurethane from BASF was released from embedded capsules, it was possible to heal the crack completely for 40% of the samples; 20% showed an additional chloride ingress, and no crack healing (Class C) occurred for 40% of the samples. However, no accumulation of chlorides at the other side of the sample was noticed. This in

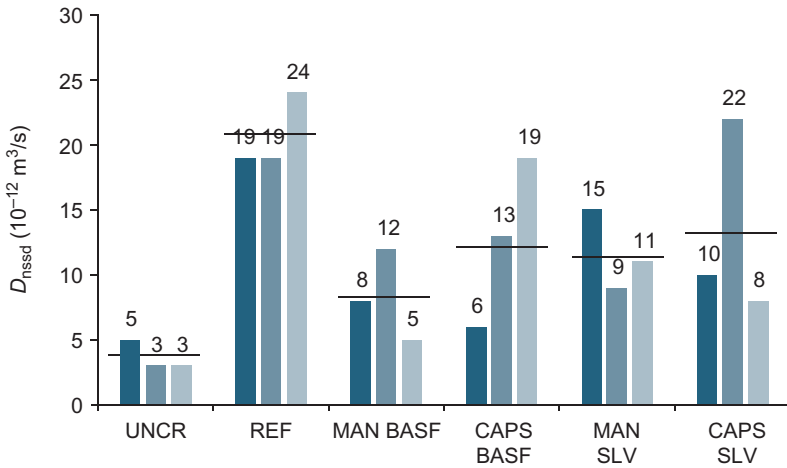


Figure 16.25 Diffusion coefficient measured along the crack for every tested sample. The black horizontal lines indicate the mean per test series (Vantuyghem, 2014).

contrast to the samples of the reference series, where 60% of the samples showed this chloride profile. All other reference samples belonged to Class C.

Within the test series MAN SLV, complete crack closure was obtained for none of the samples. Moreover, for 80% of the samples the crack was not healed at all (Class C or D). On the other hand, the series with encapsulated healing agent performed remarkably better. Only 20% of these samples showed no crack healing. 60% showed partial healing of the crack, whereas 20% showed complete crack healing.

Fig. 16.25 shows the measured diffusion coefficient for every test series. The horizontal black lines indicate the mean diffusion coefficient per test series, where D_{nssd} amounted to $4 \times 10^{-12} \text{ m}^2/\text{s}$ for the uncracked samples. Within the MAN BASF and CAPS BASF test series, one out of three tested samples resulted in a diffusion coefficient of approximately the same magnitude ($5 \times 10^{-12} \text{ m}^2/\text{s}$ and $6 \times 10^{-12} \text{ m}^2/\text{s}$), indicating complete healing of the crack. On the other hand, for one sample of the series CAPS BASF, the crack did not seem to be healed since its diffusion coefficient amounted to $19 \times 10^{-12} \text{ m}^2/\text{s}$, which is about the same as for the reference samples. The other samples of the CAPS BASF test series resulted in partial crack healing, with D_{nssd} varying between $8 \times 10^{-12} \text{ m}^2/\text{s}$ and $13 \times 10^{-12} \text{ m}^2/\text{s}$. The samples of the series where the cracks were healed with the polyurethane SLV only led to partial crack healing. One sample with encapsulated polyurethane (CAPS SLV) was not able to heal the crack at all ($22 \times 10^{-12} \text{ m}^2/\text{s}$). The mean values show a reduction of D_{nssd} by 60%, 39%, 43%, and 35% with respect to the reference samples for respectively the test series MAN BASF, CAPS BASF, MAN SLV, and CAPS SLV.

16.6.2 Prevention against carbonation

Cylindrical cracked mortar samples (diameter 100 mm, height 50 mm) with and without self-healing properties were exposed to a carbonation test. As a healing

Table 16.7 Amount of samples belonging to each of the categories after 9 weeks of exposure to 10% CO₂

	UNCR	REF	MAN BASF	CAPS BASF
Class A	100%	0%	100%	67%
Class B	0%	100%	0%	33%

agent to repair the cracks manually or autonomously, the polyurethane BASF was used. The samples were kept in a carbonation closet (R.H. 65%, CO₂ concentration 10%) during 9 weeks. Afterwards, the samples were split perpendicular to the crack and sprayed with phenolphthalein in order to determine the carbonation front. A comparison was made with uncracked samples which were exposed to the same carbonation test.

The samples could be classified in two categories based on the carbonation front, in a similar way to the chloride diffusion tests (Fig. 16.24). Sample halves showing an equal penetration of CO₂ from the exposed surface are classified as Class A. If an additional penetration is noticed along the crack, the sample belongs to Class B. The penetration of the carbonation front after 9 weeks of exposure was rather low, and consequently for none of the samples carbonation along the whole depth of the crack was noticed. Table 16.7 shows the amount of samples belonging to each of the classes. All uncracked samples were classified as Class A. On the other hand, the carbonation front of all reference samples showed an additional penetration along the crack. The manually healed samples seemed capable to prevent CO₂ ingress along the crack, since all samples have an equal CO₂ penetration depth. Two out of three samples within the CAPS BASF series did also succeed in preventing the penetration of CO₂ through the crack. These results are quite promising, but, additional long term carbonation tests should be carried out in order to confirm the autonomous healing efficiency.

16.7 Extension in service life

16.7.1 Relevance

The most straightforward way of assessing the effectiveness of a self-healing concrete consists of quantifying its extended service life in comparison with ordinary (cracked) concrete. For a given environment and exposure condition, it then immediately shows whether it is indeed worthwhile to invest extra money in the incorporation of encapsulated polyurethane at the production stage in order to minimize the time-dependent maintenance and repair. This kind of information is of utmost importance for contractors who nowadays often have to be able to guarantee a minimum maintenance and repair-free timespan for the structures they build. The latter aspect is a direct consequence of the fact that performance-based design is gaining more and more importance in the construction sector.

16.7.2 First quantification efforts

Unfortunately, until recently, service life prediction models for self-healing concrete were not readily available in the literature. For a long time, service life estimation was done while assuming a total absence of cracks, although they are unavoidable and thus present. This way of working was justified by saying that, if the concrete was designed in accordance with the prescriptions of the Eurocodes for maximum allowable crack width (prestressed concrete: 0.2 mm, reinforced concrete: 0.3 mm, in an aggressive exposure class (XC2, XC3, XC4, XD1, XD2, XD3, XS1, XS2, or XS3)), the concrete would behave as if uncracked. The probabilistic service life prediction models for carbonation- and chloride-induced steel depassivation mentioned in the engineering model codes [DuraCrete \(2000\)](#) and [fib Bulletin 34 \(2006\)](#) were both defined under this premise. However, there is experimental evidence that even cracks with a width of less than 0.2 mm serve as preferential pathways for potentially harmful substances like chlorides ([Van den Heede et al., 2014](#)). The increasing awareness of this fact gradually led to more research efforts specifically dedicated to the modeling of cracked concrete. Among those, a distinction can be made between attempts to modify the existing probabilistic engineering models for uncracked concrete to make them applicable for the cracked condition with limited experimental input, and the development of numerical models that more accurately describe all physical transport phenomena and chemical processes involved. Either way, a thorough understanding of the time-dependent behavior of cracked concrete is needed first, before the effect of polyurethane-based self-healing can be accounted for.

When looking at the first option, i.e., the modification of existing engineering models for carbonation/chloride-induced steel depassivation, the presence of a crack can quite easily be taken into account by assuming a reduced concrete cover at the location of the crack. This approach implies that the corrosion-inducing substances from the surrounding environment, i.e., carbon dioxide/chlorides, reach the full depth of the crack almost immediately and from there on further ingress will proceed slower, in mainly a diffusion-controlled manner. In [Van Belleghem et al. \(2017\)](#), this procedure was followed to estimate the time to chloride-induced steel depassivation for concrete containing an artificially-induced crack with a depth of 25 mm and a width of 0.3 mm. A series of natural and accelerated chloride diffusion tests were performed on both cracked and uncracked concrete to obtain the required experimental input for a probabilistic service life prediction model. The general outlook of this model is shown in [Eq. \(16.5\)](#).

$$C_{\text{crit}} = C_0 + (C_s - C_0) \cdot \left[1 - \operatorname{erf} \left(\frac{d}{\sqrt{4 \cdot \exp \left(b_e \left(\frac{1}{T_{\text{ref}}} - \frac{1}{T_{\text{real}}} \right) \right) \cdot \frac{D_0}{1-n} \cdot \left(\frac{t_0}{t} \right)^n \cdot t}} \right) \right] \quad (16.5)$$

with C_{crit} , the critical chloride concentration (m%/binder); C_0 , the initial chloride concentration (m%/binder); C_s , the chloride surface concentration (m%/binder); $\operatorname{erf}(\cdot)$,

the error function; d , the concrete cover (mm); b_e , a temperature related regression variable (-); T_{ref} , the standard test temperature (K); T_{real} , the actual seawater temperature (K); D_0 , the instantaneous chloride diffusion coefficient (mm^2/years); n , the aging exponent (-); t_0 , the time of reference (0.0767 years); and t , the time (years). The formula is to a large extent based on the one proposed by Visser et al. (2002), yet with additional consideration of the difference in temperature between the laboratory test and the real exposure conditions as also incorporated in the limit state function for chloride-induced steel depassivation of fib Bulletin 34 (2006).

The expected extension in service life made possible with polyurethane-based self-healing concrete was quantified using the very same prediction model. This was done as follows: As the diffusion experiments indicated that the obtained chloride profiles for the tested self-healing concrete did not completely coincide with the profiles obtained for the same concrete without a crack, the same diffusion related transport properties could not be assumed for the former concrete type. To account for this less than 100% self-healing efficiency, chloride profile offset factors were determined with which the fitted D_0 , C_s , and C_0 values for the uncracked concrete could be multiplied in the prediction model, while assuming a full concrete cover of 50 mm. As such, the results obtained for a self-healing concrete with incorporation of an encapsulated high-viscosity polyurethane (code: HV) (CAPS HV) and one containing the formerly-mentioned, super-low viscosity polyurethane (CAPS SLV) in comparison with a cracked concrete (with a reduced concrete cover of 25 mm) and an uncracked concrete reference are presented in Fig. 16.26.

In Van Belleghem et al. (2017), reliability indices (β) and probabilities of failure (P_f) as a function of time were calculated for Eq. 16.5, using the First Order Reliability Method (FORM) available in the probabilistic Comrel software. Cf. fib Bulletin 34 (2006), these parameters need to meet the requirements for the

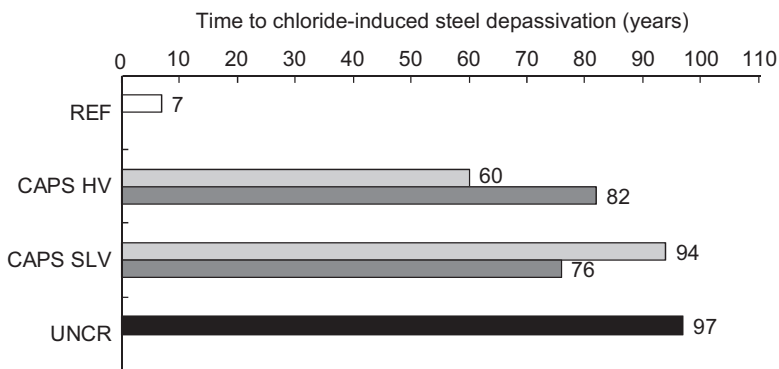


Figure 16.26 Comparison between the estimated time to chloride-induced steel depassivation for cracked concrete (REF), self-healing concrete with high and super low viscosity polyurethane (CAPS HV and CAPS SLV) and uncracked concrete (UNCR) (Van Belleghem et al., 2017).

depassivation limit state ($\beta \geq 1.3$ and $P_f \leq 0.10$) to qualify for use in exposure class XS2. Clearly, the presence of a crack that reduces the concrete cover on top of the reinforcing steel from 50 to only 25 mm, shortens the time to chloride-induced steel depassivation severely from 97 years (UNCR) to only 7 years (REF). Embedding a self-healing mechanism in the concrete through the incorporation of encapsulated polyurethane seems to solve this problem, to a large extent. For the series CAPS HV, the corrosion initiation period can be extended to 60 or 82 years. A slightly better service life performance was obtained for series CAPS SLV. In the latter case, the two chloride diffusion tests seem to indicate that onset of active corrosion would only start after 94/76 years. Although the perfectly uncracked condition could not be reached yet, both healing agents seem to have worked quite effectively. Their presence reduced the repair frequency for the concrete from 14 times to only once within a reference timespan of 100 years. It demonstrates that it is definitely worthwhile to invest extra research time and money in concrete compositions with a pronounced autonomous healing potential.

16.7.3 Remaining challenges

Additional efforts are still needed, however, to confirm this further. Until now, a significant service life extension was only demonstrated using a simplified probabilistic prediction model, similar to those mentioned in engineering model codes. Yet, dedicated numerical modeling describing all physical and chemical processes involved should also be done. The latter approach, although more accurate, is known for being time-consuming because it requires a lot of experimental input. As a consequence, a full service life estimation conducted as such for polyurethane-based self-healing concrete is not available yet. On the other hand, the results of some intermediate numerical modeling steps have been published already. For instance, in [Van Belleghem et al. \(2016\)](#), the results of X-ray radiography experiments were used for modeling the water in uncracked and cracked mortars. Further studies are under way to include the self-healing mechanism in the numerical modeling algorithms and make the transition from mortar to concrete.

Finally, there are still other challenges remaining. Firstly, it should be noted that the currently available service life information reflects only one stage in the chloride-induced corrosion process, i.e., the corrosion initiation period. It does not reveal anything on how the self-healing properties of the concrete will have an effect on the duration of the propagation period once critical chloride concentration is reached at the location of the embedded reinforcing steel. Electrochemical experiments are needed for that. These are currently being conducted on a large scale at the Magnel Laboratory for Concrete Research. Secondly, chloride-induced corrosion represents only one durability problem. For environments subject to other deterioration mechanisms (e.g., carbonation-induced corrosion, freeze-thaw attack, etc.) there are no service life predictions, neither probabilistic or numerical, available yet for polyurethane-based self-healing concrete.

References

- Aldea, C.-M., Ghandehari, M., Shah, S.P., Karr, A., 2000. Combined effect of cracking and water permeability of concrete. Paper presented at the 14th Engineering Mechanics Conference, Austin, Texas, 21–24 Mai 2000.
- Araujo, A., Van Vlierberghe, S., Feiteira, J., Graulus, G., Van Tittelboom, K., Martins, J. C., et al., 2016. Cross-linkable polyethers as healing/sealing agents for self-healing of cementitious materials. *Mater. Des.* 98, 215–222.
- Brabant, L., Vlassenbroeck, J., De Witte, Y., Cnudde, V., Boone, M., Dewanckele, J., et al., 2011. Three-dimensional analysis of high-resolution X-ray computed tomography data with Morpho + . *Microsc. Microanal.* 17 (2), 252–263.
- Dong, B., Cui, H., Han, N., Xing, F., 2013. A microcapsule technology based self-healing system for concrete structures. *J. Earthq. Tsunami.* 7 (3), 11, pages.
- Dong, B., Fang, G., Ding, W., Liu, Y., Zhang, J., Han, N., et al., 2016. Self-healing features in cementitious material with urea-formaldehyde/epoxy microcapsules. *Constr. Build. Mater.* 106, 608–617.
- Dry, C., McMillan, W., 1996. Three-part methylmethacrylate adhesive system as an internal delivery system for smart responsive concrete. *Smart Mater. Struct.* 5 (3), 297–300.
- Dry, C., Corsaw, M., Bayer, E., 2003. A comparison of internal self-repair with resin injection in repair of concrete. *J. Adhes. Sci. Technol.* 17 (1), 79–89.
- DuraCrete, 2000. Probabilistic performance based durability design of concrete structures: general guidelines for durability design and redesign. Document BE95-1347/R15. Gouda: CUR.
- Escobar, M.M., Vago, S., Vázquez, A., 2013. Self-healing mortars based on hollow glass tubes and epoxy-amine systems. *Compos.: Part B.* 55, 203–207.
- Feng, X., Zhuo, N., Ningxu, H., Biqin, D., Xuexiao, D., Zhan, H., et al., 2008. Self-healing mechanism of a novel cementitious composite using microcapsules. Paper presented at the International Conference on Durability of Concrete Structures, Hangzhou, China, 26–27 November 2008, pp. 195–204.
- fib Bulletin 34, 2006. Model code for service life design. Lausanne: fib.
- Grosse, C.U., Finck, F., Kurz, J.H., Reinhardt, H.W., 2004. Improvements of AE technique using wavelet algorithms, coherence functions and automatic data analysis. *Constr. Build. Mater.* 18 (3), 203–213.
- Grosse, C.U., Ohtsu, M., 2008. *Acoustic Emission Testing: Basics for Research—Applications in Civil Engineering*, Springer, 396 pages.
- Gruyaert, E., Van Tittelboom, K., Sucaet, J., Anrijs, J., Van Vlierberghe, S., Dubruel, P., et al., 2016. Capsules with evolving brittleness to resist the preparation of self-healing concrete. *Materiales de Construcción.* 66 (323), 13, pages.
- Hilloulin, B., Van Tittelboom, K., Gruyaert, E., De Belie, N., Loukili, A., 2015. Design of polymeric capsules for self-healing concrete. *Cem. Concr. Compos.* 55, 298–307.
- Joseph, C., Jefferson, A.D., Isaacs, B., Lark, R.J., Gardner, D.R., 2010. Experimental investigation of adhesive-based self-healing of cementitious materials. *Mag. Concr. Res.* 62 (11), 831–843.
- Kurz, J.H., Finck, F., Grosse, C.U., Reinhardt, H.-W., 2003. Automatic analysis of acoustic emission measurements on concrete. Paper presented at the International Symposium (NDT-CE 2003) of Non-Destructive Testing in Civil Engineering, Berlin, Germany, 16–19 September 2003.
- Kurz, J.H., Grosse, C.U., Reinhardt, H.-W., 2005. Strategies for reliable automatic onset time picking of acoustic emissions and of ultrasound signals in concrete. *Ultrasonics.* 43 (7), 538–546.

- Lehmann, E.H., Vontobel, P., Wiesel, L., 2001. Properties of the radiography facility NEUTRA at SINQ and its potential for use as European reference facility. *Nondestr. Test. Eval.* 16 (2-6), 191–202.
- Li, V.C., Lim, Y.M., Chan, Y.-W., 1998. Feasibility study of a passive smart self-healing cementitious composite. *Compos. Part B: Eng.* 29 (6), 819–827.
- Maes, M., Van Tittelboom, K., De Belie, N., 2014. The efficiency of self-healing cementitious materials by means of encapsulated polyurethane in chloride containing environments. *Constr. Build. Mater.* 71, 528–537.
- Masschaele, B., Cnudde, V., Dierick, M., Jacobs, P., Van Hoorebeke, L., Vlassenbroeck, J., 2007. UGCT: New X-ray radiography and tomography facility. *Nucl. Instrum. Methods Phys. Res. Sect. A.* 580 (1), 266–269.
- Mihashi, H., Kaneko, Y., Nishiwaki, T., Otsuka, K., 2000. Fundamental study on development of intelligent concrete characterized by self-healing capability for strength. *Trans. Jpn. Concr. Inst.* 22, 441–450.
- NBN EN 1992 1-1, 2010. Eurocode 2: Design and calculation of concrete constructions—Part 1-1: General rules and rules for buildings.
- Nishiwaki, T., Mihashi, H., Gunji, Y., Okuhara, Y., 2007. Development of smart concrete with self-healing system using selective heating device. Paper presented at the 5th International Conference on Concrete under Severe Conditions Environment and Loading, Tours, France, 4–6 June 2007, pp. 665–672.
- NT Build 443, 1995. Nordtest method, concrete, hardened: accelerated chloride penetration. <<http://www.nordtest.info/index.php/methods/building/item/concrete-hardened-accelerated-chloride-penetration-nt-build-443.html>>.
- Perez, G., Gaitero, J.J., Erkizia, E., Jimenez, I., Guerrero, A., 2015. Characterization of cement pastes with innovative self-healing system based in epoxy-amine adhesive. *Cem. Concr. Compos.* 60, 55–64.
- Sun, L., Yu, W., Ge, Q., 2011. Experimental research on the self-healing performance of micro-cracks in concrete bridge. *Adv. Mater. Res.* 250–253, 28–32.
- Tran Diep, P.T., Tay, J.S.J., Quek, S.T., Pang, S.D., 2009. Implementation of selfhealing in concrete - proof of concept. *IES J. Part A: Civ. Struct. Eng.* 2 (2), 116–125.
- Van Belleghem, B., Montoya, R., Dewanckele, J., Van den Steen, N., De Graeve, I., Deconinck, J., et al., 2016. Capillary water absorption in cracked and uncracked mortar: a comparison between experimental study and finite element analysis. *Constr. Build. Mater.* 110, 154–162.
- Van Belleghem, B., Van den Heede, P., Van Tittelboom, K., De Belie, N., 2017. Quantification of the service life extension and environmental benefit of chloride exposed self-healing concrete. *Materials.* 10 (5), 22 p.
- Van den Heede, P., Maes, M., De Belie, N., 2014. Influence of active crack width control on the chloride penetration resistance and global warming potential of concrete slabs made with fly ash + silica fume concrete. *Constr. Build. Mater.* 67, 74–80.
- Van den Heede, P., Van Belleghem, B., Alderete, N., Van Tittelboom, K., De Belie, N., 2016. Neutron radiography based visualization and profiling of water uptake in (un) cracked and autonomously healed cementitious materials.. *Materials.* 9 (5), 311.
- Van Tittelboom, K., 2012. Self-healing concrete through incorporation of encapsulated bacteria- or polymer-based healing agents. PhD thesis, Department Structural Engineering, Faculty of Engineering and Architecture, Ghent University.
- Van Tittelboom, K., Adesanya, K., Dubruel, P., Van Puyvelde, P., De Belie, N., 2011a. Methyl methacrylate as healing agent for self-healing cementitious materials. *Smart Mater. Struct.* 20 (12), 12 pages.

- Van Tittelboom, K., De Belie, N., Van Loo, D., Jacobs, P., 2011b. Self-healing efficiency of cementitious materials containing tubular capsules filled with healing agent. *Cem. Concr. Compos.* 33 (4), 497–505.
- Van Tittelboom, K., De Belie, N., Zhang, P., Wittmann, F.H., 2011c. Self-healing of cracks in concrete. *ASMES International Workshop*, 28–29 July 2011, Lausanne, Switzerland, 10 p.
- Van Tittelboom, K., De Belie, N., Lehmann, F., Grosse, C., 2012. Acoustic emission analysis for the quantification of autonomous crack healing in concrete. *Constr. Build. Mater.* 28 (1), 333–341.
- Van Tittelboom, K., Snoeck, D., Vontobel, P., Wittmann, F.H., De Belie, N., 2013. Use of neutron radiography and tomography to visualize the autonomous crack sealing efficiency in cementitious materials. *Mater. Struct.* 46 (1–2), 105–121.
- Vantygheem, S., 2014. Tegengaan van wapeningscorrosie door zelfherstel van scheuren in beton. Master thesis, Department Structural Engineering, Faculty of Engineering and Architecture, Ghent University.
- Visser, J.H.M., Gaal, G.C.M., Rooij, M.R., 2002. Time dependency of chloride diffusion coefficients in concrete. *Proceedings of the 3rd international RILEM Workshop on Testing and Modelling the Chloride Ingress into Concrete*, 9–10 September 2002, pp. 423–433.
- Volume Graphics, 2012. <<http://www.volumegraphics.com>>.
- Wang, J., Van Tittelboom, K., De Belie, N., Verstraete, W., 2012. Use of silica gel or polyurethane immobilized bacteria for self-healing concrete. *Constr. Build. Mater.* 26 (1), 532–540.
- Wang, K., Jansen, D.C., Shah, S.P., Karr, A.F., 1997. Permeability study of cracked concrete. *Cem. Concr. Res.* 27 (3), 381–393.
- Yang, Z., Hollar, J., He, X., Shi, X., 2011. A self-healing cementitious composite using oil core/silica gel shell microcapsules. *Cem. Concr. Compos.* 33 (4), 506–512.

Concrete with superabsorbent polymer

17

Hong Seong Wong

Imperial College London, London, United Kingdom

17.1 Introduction

Superabsorbent polymers (SAPs), also known as hydrogels, are cross-linked polymers that have the ability to absorb a disproportionately large amount of fluid relative to their own mass, and expand to form an insoluble gel. This is shown in Fig. 17.1. A unique characteristic of SAP is that its absorption capacity and rate can be altered, depending on a number of factors such as polymer composition, preparation method, and physical characteristics, and properties of the fluid—including composition, ionic concentration, pH, temperature, and pressure. For example, the mass of water absorbed per mass of SAP, i.e., swelling ratio or absorption capacity, can be as high as 1000 g/g in distilled water, but decreases to around 50 g/g in dilute salt solutions such as urine and to about 10–20g/g in concrete pore solution. The rate of swelling ranges from less than a minute to several hours depending on the type, diffusion coefficient, and diffusion path length of the SAP particles (Buchholz and Graham, 1998).

SAPs were first produced during the early 1970s in Japan and the United States. In 2015, the total production capacity of major SAP manufacturers in the world was estimated to be about 3.24 million tons (Nonwovens Industry, 2015). The large absorption capacity and good retention under pressure have enabled SAP to dominate the market for absorbent materials. The main application of SAP is in personal hygiene products such as diapers (Buchholz, 1996). Other applications include biomedical (bandages, surgical sponges, drug release/delivery, tissue engineering, contact lenses) (Caló and Khutoryanskiy, 2015), agricultural (soil conditioning, erosion control, water conservation) (Guilherme et al., 2015), waste treatment, meat packaging, water blocking tapes for undersea cables (Buchholz and Graham, 1998; Stein, 2011) and water purification (Davies et al., 2004).

In construction, several potential applications of SAP in concrete have been suggested. These include waterproof backfilling materials (Moriyoshi et al., 1991), extruded polymeric joint sealants, precooling placement system for concrete (Itou et al., 1994, Takeuchi et al., 1991), enhancing workability (Okamura et al., 1997), strengthening of aluminate concrete (Gao et al., 1997), and preventing drying shrinkage cracking and leakage through cracks (Tsuji et al., 1998, 1999). Jensen and Hansen (2001a,b, 2002) demonstrated that SAPs can be used to create small reservoirs of internal curing water to mitigate self-desiccation and autogenous shrinkage in concretes with low water/binder (w/b) ratio. Since then, research

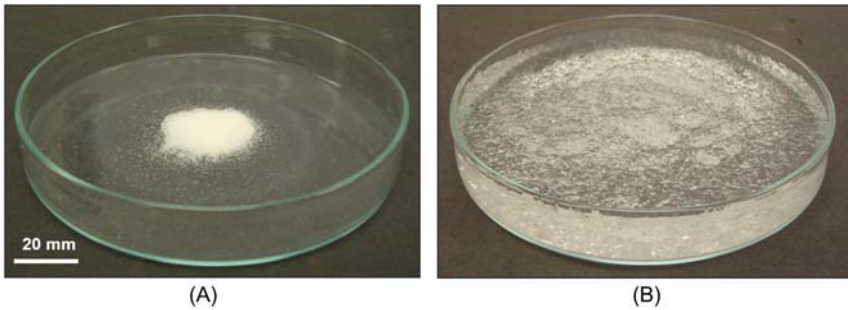


Figure 17.1 Superabsorbent polymers (SAPs) are unique polymers that can absorb large quantity of fluid relative to its own mass and swell to form a gel. (A) Dry SAP. (B) Swollen SAP.

activities examining the influence of SAP on various properties of concrete has grown. A RILEM technical committee was established to look at applications of SAP in concrete and published its state-of-art report in 2012 (TC 225-SAP, 2012).

Over the last few years, the number of scientific publications related to SAP in concrete has increased dramatically. Furthermore, considerable efforts have gone into studying the fundamental mechanisms of SAP and its influence on various properties of concrete. These include understanding the kinetics of water absorption–desorption of SAP in concrete and its effects on rheology, hydration, microstructure development, volumetric changes, mechanical properties, durability, and other properties. The aim of this chapter is to present a broad overview of these issues, emphasizing recent work to identify knowledge gaps and highlight future research needs.

17.2 Types of superabsorbent polymer

SAPs are a subset of a large family of hydrogels and polyelectrolytes polymer gels. The majority of commercially available SAPs are synthetic anionic gels comprised of cross-linked polyacrylic acid partially neutralized with hydroxides of alkali metals, usually sodium or potassium hydroxide. These are referred to as polyacrylates (poly(AA)). Other monomers are also used, such as acrylamide to produce poly(acrylate-co-acrylamide) or poly(AA-co-AM). The acrylamide group is non-ionic, while the carboxylate group is anionic in water due to partial dissociation of the counterions. Poly(AA) and poly(AA-co-AM) are the most commonly used SAPs in cement-based materials.

SAP are typically synthesized through free-radical polymerization either in bulk solution or inverse suspension polymerization (Buchholz and Graham, 1998; Stein 2011). In bulk solution polymerization, the monomers and a small amount of cross-linkers are dissolved in a solvent. An initiator is then added to start the polymerization process, creating a lightly cross-linked network of polymer chains that can

swell or collapse significantly during absorption/desorption. The product is a lump of gel that is subsequently dried, cut, and ground into small particles. The gel is neutralized either before or after the polymerization. Bulk solution polymerization results in granular SAP with a wide particle size range. The particles are irregularly shaped, angular granules or convoluted sheets, with smooth surfaces often appearing like broken glass under the microscope (Fig. 17.2A–C, E).

In suspension polymerization, droplets of aqueous solution containing the monomers are dispersed and suspended in an immiscible inert liquid phase such as a hydrocarbon solvent, e.g., hexane or cyclohexane. Polymerization is initiated at slightly elevated temperatures, the product is subsequently filtered off and dried. This technique allows a good degree of control over the size and shape of the SAP particles. It typically yields spherical particles or raspberry like agglomerates of smaller spherical particles, with rough surface texture and high surface area (Fig. 17.2D, F). However, the suspension process also requires a higher degree of production control, therefore it is costlier and less efficient compared to bulk solution process. As such, the availability of SAP produced by suspension polymerization is relatively small compared to that produced by bulk solution.

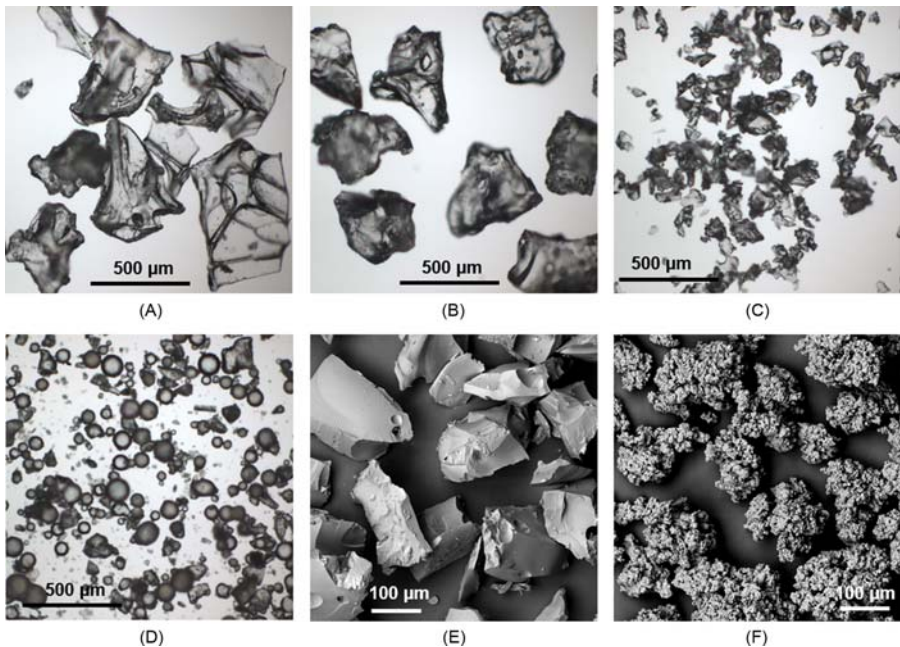


Figure 17.2 Optical transmitted light micrographs (A–D) and scanning electron micrographs (E and F) of dry superabsorbent polymer (SAP) showing a range of particle size and shape.

17.3 Properties of superabsorbent polymer

Commercial SAP come in white granule/powder form with typical particle size ranging from several microns to millimeters. As mentioned earlier, the shape of the SAP particles may be irregular, angular, spherical or agglomerates of spheres, depending on its production process (Fig. 17.2). When swollen, the SAP tends to retain its particle shape. The swelling mechanism of SAP is complex. Essentially, the equilibrium amount and kinetics of absorption depends on properties of the polymer such as ionic groups, degree of cross-linking and particle size as well as properties of the solution such as type of ions present, concentration, ionic strength, pH, pressure, and temperature. Comprehensive treatment of the subject is available elsewhere, e.g., Tanaka et al. (1980), Ricka and Tanaka (1984), Hooper et al. (1990), Buchholz and Graham (1998), Gedde (2001), and Stein (2011), and interested readers are referred to these.

When SAP is exposed to an aqueous solution, a transition in chemical potential occurs between the gel and solution leading to swelling or shrinkage of the SAP. The net effect is a competitive balance between repulsive forces that expand the network chains and attractive forces that shrink the network. Equilibrium is achieved when these are equalized and the net swelling pressure becomes zero. Because SAPs are polyelectrolytes with ionizable groups that dissociate in aqueous solution, this produces a charged polymer containing highly concentrated ions. Water absorption into SAP occurs due to osmotic pressure and the space between polymer chains and cross-links expands. Thus, the swelling of SAP is mainly driven by osmotic pressure arising from a concentration gradient of mobile ions between the gel and solution.

Swelling is balanced and restrained by elastic forces arising from the deformation of the polymer chains, so the amount of deformation depends on elastic modulus of the gel, which in turn depends on its crosslink density. Swelling capacity decreases with an increase in crosslink density. SAP also shrinks under compression by reverse osmosis. Particle size is another factor that influences the amount and rate of absorption. Small particles reach equilibrium swelling much quicker, but absorbs less water in comparison to larger particles of the same chemical composition and synthesis (Jensen and Hansen, 2002; Esteves, 2011).

Characteristics of the solution, such as concentration, type of ions present, ionic strength, pH, pressure, and temperature have important effects on the swelling of SAP. An increase in concentration of the test solution and charge-screening effect due to dissolved ions decrease osmotic pressure, and thus the absorbency of SAP. Furthermore, the type of ions present in the solution can alter the inter- and intramolecular interactions of the polyelectrolytes due to shielding of charges on the polymer chain (Jensen and Hansen, 2001a,b). Multivalent cations such as Ca^{2+} , Mg^{2+} , and Al^{3+} produce a greater reduction in absorption compared to monovalent cations such as Na^+ and K^+ . This is caused by their ability to interact and bind with carboxylate groups from different acrylate chains in the polymer, i.e., complexation, forming additional cross-links that restrain the movement between

acrylate chains and drastically reduce the swelling capacity of the SAP. For example, Ca^{2+} forms a bidentate complex with acrylates of the SAP that limits its swelling capacity (Huber, 1993; Rha et al., 1999; Schweins and Huber, 2001; Horkay et al., 2001; Fantinel, 2004; Schröfl et al., 2012; Lee et al., 2017).

17.4 Superabsorbent polymers in concrete

17.4.1 General behavior

When dry SAP particles are batched with cement, water, and aggregates to produce concrete, they will absorb a portion of the mix water and swell. The swollen SAPs form finely distributed and stable water reservoirs or water-filled inclusions in the hardened cement paste (Fig. 17.3A). However, most of the absorbed water is loosely bound in SAP such that it is subsequently drawn back into the cement paste capillary pores when surrounding humidity drops. A reduction in humidity normally occurs in hardened concrete if exposed to external drying, or if cement hydration consumes mix water to an extent that causes self-desiccation. Therefore, the SAP gradually releases the absorbed water and shrink, leaving behind distributed air-filled cavities (sometimes called macro voids or SAP voids). The collapsed SAP then lie dormant in the macro voids (Fig. 17.3B). If the concrete is subsequently subjected to external wetting, ingress of water causes the surrounding humidity to increase and this could trigger the SAP to re-swell again (Fig. 17.3A).

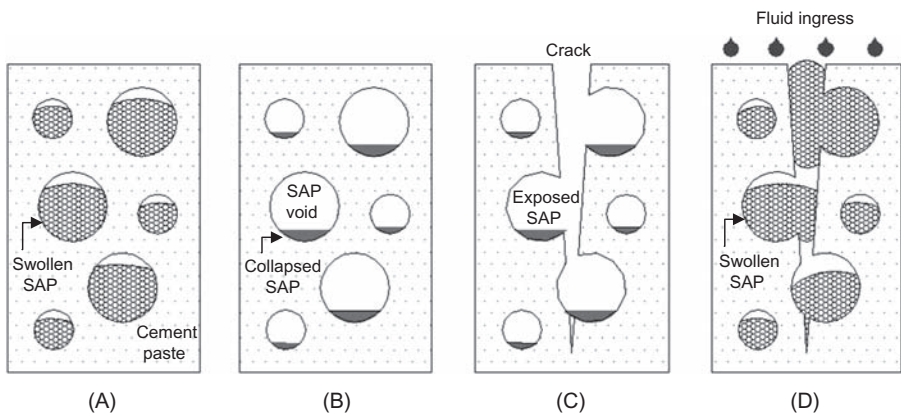


Figure 17.3 Schematic showing the behavior of SAP in hardened cementitious materials and potential applications. (A) Swollen SAP form water-filled reservoirs in freshly mixed or saturated cementitious material. Initial swelling of SAP is confined. (B) On drying, SAP releases absorbed water for internal curing. The polymer shrinks and lies dormant, leaving behind macro voids that may be exploited for frost protection. (C) Subsequent cracking propagates through SAP voids, exposing the polymer to external environment. (D) Ingress of external fluids causes the SAP to swell again, expanding into the crack and restricting further flow.

The schematics of these processes as shown in Fig. 17.3 are based on that of Lee et al. (2010a,b,c, 2016).

As will be discussed later in Section 17.6, this behavior of SAP in concrete can be exploited for a number of applications. For example, the water released by SAP can be used for internal curing to promote further cement hydration and maintain a high internal humidity to mitigate autogenous shrinkage (Jensen and Hansen, 2001a,b). The air-filled SAP macro voids could be exploited to provide frost protection while the re-swelling of SAP may be used to enhance crack sealing/healing (Fig. 17.3C,D).

The amount of SAP used in concrete depends on the intended application. For internal curing and improving freeze–thaw resistance, this is typically around 0.3%–0.6% wt. cement. For crack sealing/healing, a dosage of 1% wt. cement or greater is usually required. As will be discussed in Section 17.5, the SAP dosage has a huge influence on the properties and performance of the concrete (as well as economics). SAP can be added in a dry state or in a pre-saturated (i.e., presoaked) condition prior to concrete batching. However, most researchers tend to dry mix the SAP with cement and aggregates prior to addition of water. This is to achieve a good dispersion of the SAP in concrete. Presoaking the SAP tends to cause the swollen polymers to clump together, creating a less homogeneous distribution that may have undesirable effects on the properties of concrete.

17.4.2 Absorption–desorption kinetics

Understanding the kinetics of water movement into and out of SAP is essential for the design and optimization (cost/performance) of SAP for particular application. The efficiency of SAP in concrete depends critically on its swelling behavior. Furthermore, it influences many other properties of concrete including rheology, hydration, microstructure, strength, and durability (see Section 17.5). As such, understanding this behavior not only helps to optimize SAP usage, but also understand its short and long-term effects on properties of concrete.

For example, the absorption of SAP in fresh concrete affects the free water content and hence the workability and rheology of the mix (Mechtcherine et al., 2015). It also governs the SAP dosage and entrained water required for internal curing, and the amount of residual empty voids available for frost protection. The ionic groups in SAP influences the timing of water release, which is critical for internal curing (Schroefl et al., 2012, 2015). It also influences the re-swelling capacity for crack sealing upon ingress of external fluids (Lee et al., 2010a,b, 2016) and the repeated swelling-shrinkage influences long-term performance. The presence of SAP potentially changes the effective w/b ratio and microstructure development, in particular pore structure, this in turn could impact strength and long-term durability.

However, absorption–desorption kinetics of SAP in concrete is complex. This is because the pore solution in concrete consists of multispecies (mainly Na^+ , K^+ , Ca^{2+} , OH^- , and SO_4^{2-}) and the concentration of each species varies with cement type, the amount of cement and water in the mix. Furthermore, the pore solution composition changes over time due to hydration (dissolution of cement and

precipitation of hydration products) and interactions with the exposure environment (wetting/drying, ingress of external fluids, leaching, etc.).

When batched in concrete, the absorption of SAP is much lower compared to that in fresh water. This is because the concrete mix water achieves a very high ionic concentration ($\sim 150\text{--}700$ mmol/L) and pH ($\sim 12.5\text{--}13$) within minutes of being in contact with cement due to rapid dissolution of cement compounds releasing ions such as Ca^{2+} , K^+ , Na^+ , OH^- , and SO_4^{2-} (Gartner et al., 1985). The charge-screening and complexation effects, as discussed in Section 17.3, drastically limits SAP absorption so the swelling ratio (absorption capacity), defined as mass of water uptake by mass of dry SAP, is only about 10–20 g/g in cement-based materials as opposed to several hundred g/g in deionized water (Jensen and Hansen, 2001a,b, 2002; Lee et al., 2010a,c).

It has also been observed that the swelling ratio in hardened cement-based materials tends to be lower than the “free” swelling ratio measured in synthetic pore solutions (Jensen and Hansen, 2002, Lee et al., 2010c, Schröfl et al., 2012). This discrepancy may be due to the fact that actual pore solution composition is much more complex and variable (compared to synthetic pore solution) because of continuous dissolution and precipitation during cement hydration. The SAP may lose part of the absorbed water before setting because of cumulative binding with Ca^{2+} , and so the measured swelling in hardened paste is lower than that measured in fresh state. Furthermore, mixing and compaction during batching, and the presence of aggregate particles induce physical confinement that reduces the SAP absorption relative to its free swelling.

It is understood that SAP absorption in pore solution is rapid and takes place in the first few minutes after mixing. Esteves (2011) observed that SAP particle size influences the rate of absorption and the maximum absorption capacity, which increases with increasing particle diameter. Desorption occurs in hardened concrete when capillary pores empty, either due to external drying or hydration-induced desiccation, producing a gradient in water activity and capillary pressure (Lura et al., 2007). Changes in pore solution composition with progress of hydration may also alter the SAP osmotic pressure and contribute to desorption. Thus, the kinetics of SAP desorption in hardened concrete depend on the properties of the SAP, progress of hydration and surrounding microstructure, in particular the interface between SAP and cement paste, through which water transport occurs.

In low w/b ratio cementitious systems, it has been observed that SAP desorption starts soon after setting and completes after a couple of days (Nestle et al., 2009; Lura et al., 2012). For example, Nestle et al. (2009) utilized nuclear magnetic resonance relaxometry to monitor hydrating cement pastes containing SAP. They observed that desorption starts during the acceleration period and completes within one or two days, depending on SAP particle size. Trtik et al. (2010) used neutron tomography to visualize and measure water released from SAP into cement paste. They found that desorption kinetics is linked to the progress of cement hydration and that the onset of water release coincided with the transition from dormant to acceleration period. Using neutron radiography, Schroefl et al. (2015) observed that a well-timed release of water is important for mitigating autogenous shrinkage by

internal curing. A better performance was obtained if desorption occurs during the acceleration period and continues into the deceleration period, compared to an early release of water during the dormant period. A premature release of water, i.e., before setting, could increase effective w/b ratio and porosity of the concrete, leading to a decrease in strength (Mechtcherine et al., 2014).

17.4.3 Measuring absorption capacity

As explained in the preceding section, the absorption capacity (swelling ratio) of SAP is a critical parameter for application in cement-based materials. SAP absorbs some amount of the mix water and this not only affects workability of the fresh concrete, but also the effective w/b ratio, which in turn impacts microstructure and many properties of hardened concrete. Therefore, extra water (i.e., “entrained” water) must be added during concrete batching to compensate for SAP absorption and this requires accurate knowledge of the swelling ratio. It is also required to determine the appropriate SAP dosage for a particular application. For example, it defines the amount of entrained water available to mitigate autogenous shrinkage or the amount of air voids for frost protection. Thus, mix design and proportioning of concrete with SAP is only possible when the absorption capacity in concrete is known, and problems occur when this is not done correctly (Esteves, 2011; Craeye et al., 2011; Hasholt et al., 2012).

There is no consensus, however, on how the measurement should be carried out, and few studies have measured the absorption capacity of SAP in hardened concrete directly. The most commonly used method is gravimetric tea-bag method followed by centrifuging or vacuum filtration (Buchholz and Graham, 1998; Lee and Wu, 1996). This is relatively easy to apply, but tends to overestimate absorption because water that is physically held by capillary forces between SAP particles may not be completely removed prior to measurement. To overcome this, Esteves (2011) proposed the use of an optical microscope to observe the swelling of individual SAP and measure only the liquid absorbed into the polymer. In a later study, laser diffraction particle size analysis was used (Esteves, 2015). Jensen (2011) described a method based on measuring the volume increase of loosely packed SAP in a graduated cylinder containing the test solution. Nevertheless, the absorption capacity obtained in a beaker of synthetic pore solution (or cement paste filtrate (Snoeck et al., 2015; Schroefl et al., 2015)) may not be a reliable estimate of actual swelling in concrete. This is because the composition of real pore solution is more complex and variable, and physical constraints from mixing and compaction during batching could further affect absorption capacity.

A number of studies have estimated absorption capacity in cement paste indirectly by observing the difference between total w/b ratio and effective w/b ratio. The effective w/b ratio is estimated by comparing slump flow of the SAP mix to a set of control mixes (without SAP) of known effective w/b (Mönnig, 2005; Reinhardt and Mönnig, 2006), or by adjusting the batch water until the SAP mix has the same slump flow to the control mix of known w/b ratio (Dudziak and Mechtcherine, 2010; Lura et al., 2012). This is sometimes known as the

“consistency” method. It assumes that the swollen SAPs have no influence on rheology of the fresh cementitious mix, which is probably not strictly true (see [Section 17.5.1](#)). Another method for estimating the effective w/b ratio is by measuring the heat of hydration with isothermal calorimetry and matching the data to reference mixes of known w/b ([Johansen et al., 2009](#)). However, a mix containing SAP or any internal curing agents is expected to achieve a higher rate of cement hydration compared to the reference mix.

Absorption capacity may also be estimated by measuring the volume fraction of macro voids produced in hardened cement paste after the SAP dries and shrinks. This can be carried out, e.g., by mercury intrusion porosimetry ([Lee et al., 2010c](#)). The method is quick and allows measurements on bulk samples, but similar to the consistency method, it requires the testing of a companion control sample without SAP at the same effective w/b ratio, hydration degree and air content. This is difficult to achieve in practice. On the one hand, the SAP mix would achieve higher degree of hydration and lower capillary porosity than the control mix due to internal curing ([Section 17.6.1](#)). On the other hand, the swollen SAP affects rheology of the fresh paste such that the additional water required to achieve the same consistency as the control ([Section 17.5.1](#)), is more than the amount needed to compensate for SAP absorption. This increases the effective w/b ratio and capillary porosity of the SAP mix. Hence, swelling ratio is over-estimated.

The volume fraction of SAP macro voids can also be determined by applying image analysis and stereology principles on images of polished cross-sections collected using conventional flatbed scanners, optical microscopy or backscattered electron microscopy ([Pieper, 2016](#); [Lee et al., 2010c](#)). [Laustsen et al. \(2010\)](#) used X-ray computed tomography to measure the distribution of void sizes in hardened concrete containing SAP and showed that this can be used to calculate absorption capacity, which was found to be in reasonable agreement with previous studies. Other methods based on NMR relaxation ([Nestle et al., 2009](#)), neutron tomography ([Trtik et al., 2010](#); [Snoeck et al., 2012](#)) or neutron radiography ([Schroefl et al., 2015](#)), have also been used to study the water absorbed by SAP in fresh cement paste.

Unlike other methods, these do not require comparison with reference control samples. However, they may need access to unique/costly analytical equipment, sample preparation and measurement procedures which are time-consuming, and the reliability of the measurement depends on a number of factors. These include: image resolution, the ability to resolve small SAP voids, contrast between SAP voids and cement paste for accurate segmentation, and the ability to distinguish SAP voids from other voids such as entrapped air, which would be difficult if the SAP are spherical. In some cases, it is difficult to ascertain the original boundary between SAP voids and cement paste, particularly if the polymer has a convoluted shape (see [Fig. 17.2](#)) or when cement grains have infiltrated into the SAP voids, subsequently reacting and precipitating hydration products within the space originally occupied by the swollen SAP (see [Fig. 17.4](#) for example). Therefore, swelling ratio may be under-estimated when MIP or imaging methods are used.

All of the proposed methods for measuring absorption capacity in hardened concrete have their specific advantages and limitations. The results from these methods

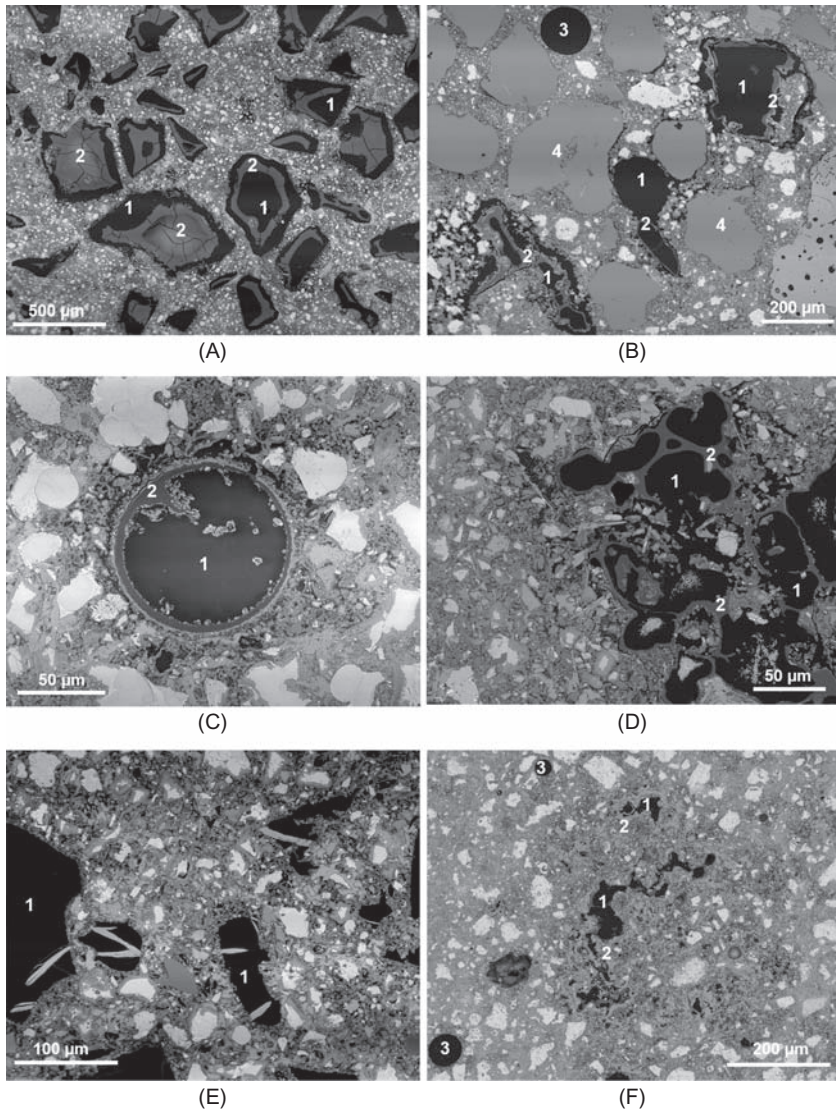


Figure 17.4 Selected examples of backscattered electron images showing typical microstructural characteristics of hardened cementitious materials containing SAP. The micrographs highlight the size, shape and distribution of the SAP voids (1), collapsed SAP particle (2), entrapped air voids (3), aggregate particles (4), and microstructure at the SAP–cement paste interface. (A) Cement paste containing poly(AA) SAP. (B) Mortar containing poly(AA) SAP. (C) Porous interface between SAP and cement paste. (D) Porous interface with infill of small cement grains and hydration products within SAP void. (E) Calcium hydroxide precipitates forming within the SAP macro void. (F) Good bond between SAP (suspension polymerized) and cement paste with relatively dense interface.

tend to be different, but display similar trends or qualitative agreement with each other. The discrepancies are partly due to the underlying assumptions inherent in each method. It is not possible to conclude, however, which method is more accurate since the true absorption capacity of SAP in hardened concrete is unknown. In general, the swelling ratio of poly(AA-co-AM) type SAP tends to be higher compared with poly(AA) type SAP. The swelling ratio measured in hardened cementitious materials also tends to be lower than that measured in free synthetic pore solution (or cement paste filtrate).

17.5 Effects of superabsorbent polymer on properties of concrete

17.5.1 Fresh concrete properties

Since SAP absorbs part of the mix water upon batching in concrete, it lowers the free water content and w/b ratio (Jensen and Hansen, 2002), inevitably changing the workability and rheological properties of fresh concrete. This is important because it influences the ease at which the concrete can be placed, pumped, compacted, and finished. The change in workability can be measured in terms of decrease in consistency, slump and flow, and increase in flow time (e.g., Paiva et al., 2009; Schroefl et al., 2012; Mechtcherine et al., 2014). In addition, the physical presence of swollen SAP will increase the yield stress and plastic viscosity of concrete (Jensen, 2008).

Consequently, extra water (i.e., “entrained” water) must be added during batching in sufficient quantity to compensate for SAP absorption and to mitigate workability loss. Determining the exact amount to add is not straightforward, as discussed in Section 17.4.3, and this aspect of mix design for concretes containing SAP is prone to uncertainties and errors.

For example, some studies have observed reduction in workability with mixes containing SAP, even when additional water was used to compensate SAP uptake (e.g., Dudziak and Mechtcherine, 2010). However, the mix design calculations were based on absorption capacity, measured in synthetic pore solution rather than that measured in the actual mix. In contrast, other studies (e.g., Laustsen et al., 2015) found that SAP addition does not significantly influence slump once its absorption is compensated by increasing the mix water content. Adding too much water will, however, increase the effective w/b ratio and this produces other undesirable effects on the hardened concrete, especially strength and durability.

Mechtcherine et al. (2015) studied the effects of SAP on rheological properties of fresh Portland cement-based mortars. They found that the water uptake kinetics, governed by SAP type, is the major factor influencing rheology. The initial moisture uptake and subsequent release by SAP affects plastic viscosity. The SAP particle-size grading also influences the development of yield stress and plastic viscosity. A finer grading has greater surface for absorption leading to higher yield

stress and plastic viscosity. Other important factors include w/b ratio, dosage of SAP, superplasticizer and silica fume, if present. Increasing w/b ratio increases SAP absorption and this leads to greater changes in rheology.

Addition of SAP tends to increase air content and decrease density of the mixes (Mönnig, 2005; Reinhardt et al., 2008; Paiva et al. 2009; Filho et al., 2012). The round-robin test reported by Mechtcherine et al. (2014) also found a slight decrease in the density of fresh concrete and a general trend of increased setting times. Related to this is the observation by Laustsen et al. (2008, 2015) that suspension polymerized SAP contains a residual air-entraining surfactant that originates from its manufacturing process. This could increase air content, which in turn decrease rheology and strength (Section 17.5.4). Laustsen et al. (2015) cautioned that this may have significant consequences on the interpretation of earlier studies using suspension polymerized SAP. Furthermore, the improved frost resistance (Section 17.6.2) could be due to SAP-generated voids or due to the air-entraining effect of suspension polymerized SAP.

17.5.2 Hydration and microstructure

Addition of SAP has major effects on the hydration process and microstructure development of concrete. This occurs due to a number of reasons. Firstly, the initial SAP absorption could alter the effective w/b ratio and early hydration characteristics. Secondly, the subsequent release of water from SAP promotes further hydration of cement, producing additional hydration products, and pore refinement. Thirdly, the dried and collapsed SAP leaves behind macro voids dispersed throughout the hardened cement paste and this changes total porosity and size distribution, depending on SAP dosage. It also induces an interface between SAP and cement paste matrix with unique microstructure characteristics that may have important consequences.

Mechtcherine et al. (2014) and Justs et al. (2014) observed that SAP caused a slight delay in early hydration, while Hasholt and Jensen (2015) reported a mild accelerating effect. In these cases, extra water was added to compensate for SAP absorption in the fresh mix. Nevertheless, most studies agree that SAP increases the degree of hydration at later ages, particularly from 14 days onwards, due to the additional water made available to react with cement (e.g., Igarashi and Watanabe, 2006; Lura et al., 2006; Justs et al., 2014). Furthermore, the longer term hydration appears to be controlled by total w/b ratio rather than the initial effective w/b ratio (Justs et al., 2014; Reinhardt and Assmann, 2014; Hasholt and Jensen, 2015). In other words, the ultimate degree of hydration depends on the total water available in the system, regardless of the fact that a portion of it was entrained in SAP at early ages.

The improved hydration in systems containing SAP should lead to a reduction in capillary porosity and refinement in pore size distribution, particularly at later ages. However, findings from available studies are not in total agreement. This is because the net effect on pore structure depends on a number of factors, including SAP dosage and absorption capacity, w/b ratio, and whether or not extra water was added

during batching to compensate SAP absorption. The reduction in capillary porosity as a result of improved hydration (internal curing) or decrease in effective w/b ratio due to SAP absorption may or may not be sufficient to counteract the increase in porosity due to macro voids formation. The net effect also depends on w/b ratio because internal curing is only beneficial for systems with very low w/b ratio. This highlights the counteracting effects of SAP on microstructure. The uncertainties in estimating SAP absorption in cementitious materials as discussed in [Section 17.4.3](#) further complicates this issue.

For example, some studies using mercury intrusion porosimetry found higher total porosity in mortars and concretes containing SAP and entrained water. This was attributed to the macro voids that form when the SAP dries ([Mönnig, 2005](#); [Mechtcherine et al., 2009](#)). However, a lower total porosity was observed in systems without entrained water ([Mönnig, 2005](#); [Igarashi and Watanabe, 2006](#)), presumably because effective w/b ratio was decreased by SAP absorption. Using X-ray tomography, [Lura et al. \(2008\)](#) observed a reduction in small capillary pores due to the additional hydration products from internal curing and a reduction of microcracking caused by autogenous shrinkage. Using water vapor sorption, [Snoeck et al. \(2015\)](#) observed that cement pastes with SAP and no entrained water showed a slight decrease in micro (<2 nm) and mesopore (2–50 nm) range. Cement pastes with SAP and entrained water showed no significant change in the micropore range, but a slight increase in the larger mesopore range. [Beushausen et al. \(2014\)](#) also did not find a significant effect of SAP on porosity, which suggests that the higher initial voidage created by SAP is offset by an improved microstructure from internal curing.

[Fig. 17.4](#) shows some examples of backscattered electron images of pastes, mortars, and concretes containing SAP. It can be seen that the SAP particles and macro voids are isolated and well-distributed in the hardened cement paste. The macro voids range from ~10 to more than 500 μm , depending on the initial size of the dry SAP and swelling ([Lam, 2005](#); [Lee et al., 2010a,b,c, 2016](#)). The boundary of the macro voids tend to follow the original shape of the dry SAP, as also observed with X-ray tomography ([Lura et al., 2008](#)). The collapsed SAP particle may appear as solid, porous/cellular or narrow ring-shaped particle. Some samples display a gap between paste and SAP due to shrinkage ([Lam, 2005](#)), while a good bond is retained in samples containing suspension polymerized SAP with rough texture and higher surface area ([Lee et al., 2010a,b,c](#)), as seen, e.g., in [Fig. 17.4F](#). Occasionally, the macro voids contain calcium hydroxide precipitates or small cement grains that have subsequently reacted to form hydration products within the water reservoir, filling up space originally occupied by the swollen SAP ([Fig. 17.4D–F](#)).

The cement paste surrounding SAP exhibits a highly variable microstructure and shares similar characteristics to the aggregate-paste “interfacial-transition zone” and air void-paste interface ([Scrivener et al., 2004](#); [Wong and Buenfeld, 2006](#); [Wong et al., 2011](#)). The interface contains less cement compared to the bulk paste farther away, due to disrupted particle packing. It also tends to be very porous and occasionally contains large calcium hydroxide deposits ([Fig. 17.4C,D](#)). These features can be attributed to the high water content on the surface of swollen SAP, or possibly the early release of absorbed water into the surrounding paste causing

preferential precipitation. Shrinkage of the SAP when it dries may lead to micro-cracking of the surrounding cement paste (Lee et al., 2010a,b,c), but the moisture released by SAP is expected to promote further hydration and microstructure development in the surrounding paste. In mortars and concretes, the SAP voids are of the size of sand grains and they can span between aggregate particles (Lee et al., 2016), e.g., Fig. 17.4B.

17.5.3 Shrinkage

Macroscopic shrinkage affecting concrete can be divided into the following: a) plastic shrinkage that occurs during the first several hours after mixing and prior to setting; b) drying shrinkage in hardened concrete caused by loss of water to the external environment; c) autogenous shrinkage that occurs in a sealed condition caused by cement hydration inducing self-desiccation; and d) carbonation-induced shrinkage. Many studies have collectively shown that addition of SAP and entrained water can significantly decrease autogenous shrinkage, particularly for concretes with low w/b ratios. This effect is more pronounced with higher SAP dosage and higher amount of entrained water. The use of SAP to mitigate autogenous shrinkage is discussed in Section 17.6.1.

Contrary to autogenous shrinkage, the effect of SAP on drying shrinkage is not very clear. Some studies have suggested that drying shrinkage increased in systems containing SAP, but this did not adversely affect total shrinkage (Jensen and Hansen 2002; Reinhardt and Mönnig, 2006). Another study observed that drying shrinkage of high-performance concrete with SAP remained almost the same as the control concrete without SAP (Assmann and Reinhardt, 2014). However, Beushausen and Gillmer (2014) found a slight decrease in drying shrinkage of normal strength mortar containing SAP relative to the control mortar.

Similarly, very little is known at present about the effects of SAP on plastic shrinkage and carbonation shrinkage. Dudziak and Mechtcherine (2010) observed that plastic deformation and capillary pressure decreased in systems containing SAP and entrained water, while settlement deformation increased compared to the control. Clearly, further research on this area is needed.

17.5.4 Mechanical properties

The influence of SAP on mechanical properties of concrete is not straightforward because the same issues that affect workability, hydration and microstructure, as previously discussed, are also at play. On the one hand, improved hydration, densification, and reduced autogenous shrinkage-induced cracking (due to provision of internal curing), should increase strength relative to the control. On the other hand, the macro voids that form when SAP shrinks (Figs. 17.3 and 17.4) could lead to lower strength, similar to the effect of entrained air voids (Jensen and Hansen, 2002; Dudziak and Mechtcherine, 2010; Hasholt et al., 2012). This is particularly the case at high-SAP dosage or high w/b ratio (where the beneficial effect of internal curing is less significant). It is well-known that an increase in entrapped or

entrained air content of 1% in concrete translates into a decrease in compressive strength of around 5% (Popovics, 1998).

The overall effect depends on the SAP dosage and absorption capacity, w/b ratio, and whether or not entrained water was added during batching to compensate SAP absorption. If extra water was not added, then SAP absorption will decrease effective w/b ratio and this will likely lead to strength increase. If extra water was added, and if assuming this was determined accurately for the SAP type and dosage used (see Section 17.4.3), then the net effect depends on whether the benefits gained through further hydration/internal curing can offset the strength loss caused by the SAP voids. These factors should always be considered when interpreting findings from different studies, which are not always consistent.

Studies have generally shown that addition of SAP with entrained water reduces compressive strength at early ages, especially at high-SAP dosages due to the excess macro voids that form (e.g., Jensen and Hansen, 2002; Igarashi and Watanabe, 2006; Piérard et al., 2006; Lura et al., 2006; Esteves et al., 2007; Mechtcherine et al., 2009; Wang et al., 2009; Dudziak and Mechtcherine, 2010; de Sensale and Goncalves, 2014, Beushausen et al., 2014). Kong et al. (2015) observed that addition of presoaked SAP also decreased compressive strength of high-strength concrete, especially at early ages.

At later ages, improvements in hydration through internal curing should compensate, at least in part, the strength loss caused by SAP voids. Therefore, the difference in strength between systems containing SAP and their control should decrease over time (Beushausen et al., 2014). Indeed, some studies have observed similar strengths at later ages and in some cases, the strength of SAP mix even exceeded that of the control (Bentz et al., 2002; Geiker et al., 2004; Esteves et al., 2007; Hasholt et al., 2012). The improvement in strength is notable, particularly for systems containing supplementary cementitious materials where availability of entrained water allows pozzolanic reaction to proceed longer. Gao et al. (1997) also observed an increase in compressive strength in aluminate cement paste containing SAP at w/b ratio of 0.40, however, this was without addition of extra water.

Hasholt et al. (2010, 2012) presented a theoretical analysis of the effect of SAP on compressive strength based on Powers' model (Powers and Brownyard, 1947). For systems with w/b ratio >0.42 , it is expected that strength will decrease with an increase in SAP content, because the SAP creates extra voidage. However, for systems with w/b ratio <0.42 where complete hydration of cement is not possible, provision of additional water by SAP may increase later age hydration degree and thereby counteract the initial strength loss.

Nevertheless, some studies have also reported reduction in compressive strength for mixes containing SAP relative to the control at later ages (e.g., 28 days). For example, Craeye et al. (2011) found 15%–28% loss in 28-day strength with the addition of SAP to a high-performance concrete bridge deck. According to Hasholt et al. (2012), this may be caused by an overestimation of SAP absorption and addition of excess water greater than the amount required, leading to higher w/b ratio in mixes with SAP compared to the reference mix. It should be noted that, the

absorption capacity of SAP in concrete is less than when measured in simulated pore solution, which in turn is much lower than the absorption in water (see [Sections 17.3 and 17.4.2](#)). Therefore, the correct SAP dosage, amount of entrained water, and preparation procedure (mixing, casting and curing) is critical to avoid potential strength loss caused by SAP voids.

Curing condition appears to be another factor that needs consideration. For example, [Esteves et al. \(2007\)](#) observed that mortars containing SAP cured at low humidity had smaller 28-day strength reduction compared to those cured at high humidity. An analysis by [Kovler \(2012\)](#) of data from several investigations found that many studies reported strength reduction at 28 days (up to 35%), but the most severe strength loss came from tests that were carried out on moist-cured samples. In contrast, studies that subjected their samples to sealed curing reported a somewhat lower strength loss or even a slight gain in some cases. Thus, it appears that the application of SAP is more favorable under non-ideal curing conditions because the benefit of internal curing becomes more apparent.

On tensile strength, some studies observed a negative effect of SAP in a similar fashion to compressive strength ([Igarashi and Watanabe, 2006](#); [Mechtcherine et al., 2006](#); [Esteves et al., 2007](#)). Other studies have, conversely, reported a slight improvement in tensile strength with SAP, particularly at later ages ([Lam and Hooton, 2005](#); [Beushausen et al., 2014](#); [Beushausen and Gillmer, 2014](#)). The explanation for this is that because measured tensile strength is sensitive to cracks inherent in the sample, any measures that can mitigate shrinkage-induced cracking would also be expected to improve tensile properties. The elastic modulus of concrete containing SAP is approximately the same as the control concrete ([Dudziak and Mechtcherine, 2010](#)) or lower ([van der Ham et al., 2008](#); [Craeye et al., 2011](#); [Beushausen and Gillmer, 2014](#))

[Mechtcherine et al. \(2014\)](#) reported a large round-robin test and observed that addition of SAP generally produced some losses in compressive and flexural strengths, even though several participants reported contrary effects. The negative effect of SAP was more evident for flexural strength. It was also observed that mixes with small, spherical-shaped SAP performed better than those with larger and irregularly shaped SAP, which probably act as stress inducers. In another interlaboratory investigation, [Mechtcherine et al. \(2017\)](#) also reported a general reduction in compressive and splitting tensile strengths, and elastic modulus in concretes containing SAP and entrained water. The amount of reduction in mechanical properties caused by SAP is approximately equivalent to that obtained by increasing the water/cement ratio, but less than that caused by air entrainment.

The influence of SAP on other mechanical properties of concrete, such as creep and fracture mechanics, has not been widely investigated. However, recent work by [Assmann and Reinhardt \(2014\)](#) indicated that SAP could reduce tensile creep of high-performance concrete by nearly 50% compared to reference concrete of the same total water content, strength, and paste content. Autogenous shrinkage was also considerably lower whereas drying shrinkage remained approximately the same.

17.5.5 Durability

The ability of concrete to resist various degradation mechanisms is often assessed by measuring the penetration rate of aggressive species, i.e., mass transport properties. This is controlled to a large extent by the volume, size, connectivity, and tortuosity of the pore structure. Therefore, the net effect of SAP on durability depends on the way in which it changes the pore structure and other factors discussed in [Sections 17.5.2 and 17.5.4](#). Although the SAP macro voids ([Fig. 17.4](#)) are isolated in the microstructure, they are expected to be interconnected via the smaller capillary pores and/or gel pores. Therefore, the macro voids may be detrimental to some transport properties in a similar manner to that of entrained air voids ([Wong et al., 2011](#)), but capillary pore refinement brought on by an improved hydration could counteract this effect.

Not many investigations have been carried out on transport properties of concrete containing SAP. [Reinhardt and Assmann \(2009, 2012\)](#) reported that the water and oxygen permeability of mixes with SAP were either unaffected or improved compared to the reference mix, despite a decrease in compressive strength. Results from chloride migration testing showed large variations and were inconclusive. [Beushausen et al. \(2014\)](#) also reported an overall positive effect of SAP. They observed that mortars containing SAP generally showed similar or improved durability indexes (porosity, oxygen permeability, chloride conductivity, accelerated carbonation, and bulk diffusion) compared to the reference. Interestingly, they found that the improvement was more evident in mortars at higher w/b ratio (0.55), while mortars with lower w/b ratio (0.45) were not significantly affected by SAP addition.

[Hasholt and Jensen \(2015\)](#) reported the chloride migration coefficient of concretes containing SAP, with and without entrained water. They found an improved degree of hydration in all cases and a reduced chloride migration in fully-saturated concrete. The lower chloride migration was attributed to the decrease in effective w/b ratio (when SAP was added without entrained water), the improved hydration and higher gel/space ratio, resulting in a denser and more tortuous pore structure. Related to the issue of durability is the potential of SAP for improving freeze–thaw resistance and crack sealing/healing ability of concrete. These have been investigated in a number of studies and will be discussed in [Sections 17.6.2 and 17.6.3](#), respectively.

17.6 Applications of superabsorbent polymer in concrete

SAP possesses several unique features that can be exploited to improve the performance, functionality and durability of concretes structures. The main applications include the use of SAP as an admixture for internal curing to mitigate self-desiccation and autogenous shrinkage in low w/b ratio systems, improve freeze–thaw resistance and induce self-sealing/healing of cracks. This chapter presents an overview of these applications and other potential opportunities.

17.6.1 Internal curing and shrinkage reduction

During hydration, cement reacts with water from capillary pore spaces to precipitate hydration products. As the reaction continues, the internal relative humidity (RH) decreases and self-desiccation occurs if the system has no access to external water for curing. Water remaining in capillary pores forms a menisci and exerts hydrostatic tension forces, causing a volumetric reduction known as autogenous shrinkage. If the shrinkage is restrained, tensile stresses will develop in the microstructure causing cracks to form when the stresses exceed local tensile strength. Cement-based materials at low w/b ratios such as high-strength or high-performance concrete are particular prone to early-age cracking induced by autogenous shrinkage.

Jensen and Hansen (2001a,b, 2002) proposed and demonstrated that this problem can be mitigated by adding SAP into fresh concrete, to establish a distributed system of water-filled cavities in the hardened cement paste. The SAP gradually releases its absorbed water (Section 17.4) to the surrounding cement paste and to replace water consumed by cement hydration, thereby maintaining a high internal RH and promoting further hydration. Thus, SAP provides small water reservoirs to cure concrete from the inside, i.e., internal curing. Jensen and Hansen (2002) showed via measurements of internal RH, autogenous deformation, and hydration degree that this approach is very effective for preventing self-desiccation in low w/b ratio systems containing silica fume, where autogenous shrinkage is substantially reduced or completely suppressed.

Since the pioneering work of Jensen and Hansen (2001a,b, 2002), numerous studies have been conducted on different SAP types and cementitious systems. These have, on the whole, substantiated and established SAP as a promising approach to enhance hydration, mitigate autogenous shrinkage, and counteract stress build up due to restrained shrinkage. See, e.g., the work of Geiker et al. (2004), Mechtcherine et al. (2006, 2009), Igarashi and Watanabe (2006), Lura et al. (2006), Friedemann et al. 2006, Nestle et al. (2009), Wang et al. (2009), Schlitter et al. (2010), Craeye et al. (2011), Wyrzykowski et al. (2012), Sensale and Goncalves (2014), Kong et al. (2015), Snoeck et al. (2015) and many others. The state-of-the-art reports by RILEM TC 196-ICC (2007) and TC 225-SAP (2012) presented SAP as an effective internal curing agent for concretes with low w/b ratio. Because of its high absorption capacity, only a small dosage of SAP—typically 0.3%–0.6% wt. cement, plus entrained water, is required to mitigate autogenous shrinkage. The amount of entrained water required can be estimated, for example by using the hydration model of Powers and Brownyard (1947).

Recently, Mechtcherine et al. (2014) presented the results of a round-robin test performed by thirteen research groups on two commercially available SAPs with entrained water for internal curing. The high-performance concretes tested had the same mix design, but made from materials available to participants locally. The data consistently showed that internal curing via SAP produced a considerable decrease in autogenous shrinkage. The work also showed that it is robust in terms of dealing with variation in concrete ingredients, production

process, or measuring techniques. Mechtcherine et al. (2014) also looked at the effects of SAP on other properties of fresh and hardened concrete—these were discussed in Sections 17.5.1 and 17.5.4.

17.6.2 Frost resistance

When SAPs release absorbed water, they shrink and leave behind air-filled voids distributed in the hardened cement paste (Figs. 17.3 and 17.4). These SAP voids could be exploited to provide space to accommodate expansion of pore water on freezing, and thus enhance the resistance against frost damage in a similar manner as air entrained voids (Fig 17.5). This concept has been demonstrated in a number of studies, e.g., Mönnig (2005), Mönnig and Lura (2007), Reinhardt et al. (2008), Laustsen et al. (2008, 2015), Reinhardt and Assmann (2012), Hasholt et al. (2015), Mechtcherine et al. (2017) and others. They collectively show that addition of SAP, whether with or without entrained water, produces a considerable improvement in frost resistance compared to concrete without SAP. When SAP is added without entrained water, the improved resistance may be due to the lowering of effective w/b ratio and/or provision of SAP voids for ice formation. When SAP is added with entrained water, the improved resistance is attributed to SAP voids and further hydration induced by internal curing.

For example, Mönnig (2005), Reinhardt et al. (2008), and Laustsen et al. (2008) found that mixes containing SAP have better resistance to freeze–thaw in the presence of de-icing salts. The results showed that the loss in sample mass to surface scaling after a number of freeze–thaw cycles in de-icing salt solution was significantly lower for samples containing SAP. Hasholt et al. (2015) also reported that concretes with SAP generally performed better than the reference concrete without SAP. Mixes with conventional air entrainment gave the highest resistance to frost.

Laustsen et al. (2008, 2015) also observed that the quantity of scaled material depends on SAP void content, but the void spacing factor seems to have a minor effect. Furthermore, it was reported that suspension polymerized SAP may contain

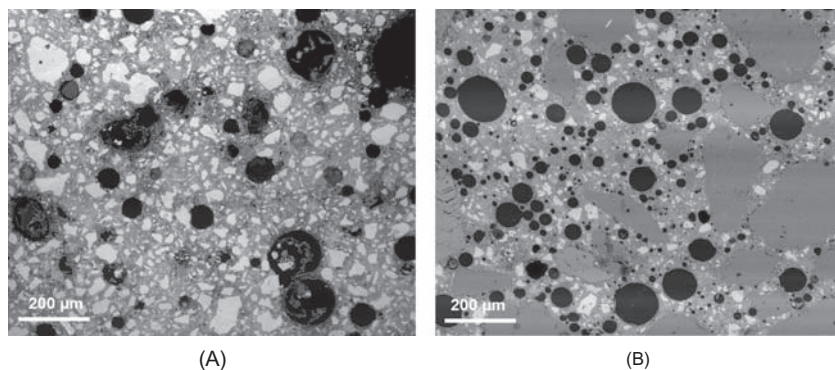


Figure 17.5 Backscattered electron images comparing the microstructure of cementitious materials containing (A) spherical SAP and (B) entrained air voids for frost protection.

a residual surfactant that causes additional air entrainment (see [Section 17.5.1](#)). The residual surfactant can be removed by rinsing with ethanol. Subsequent testing carried out on as-received SAP and rinsed SAP found that both the SAP voids and voids entrained by the surfactant contribute to improving frost resistance/salt scaling. Therefore, SAP voids seem to behave in a similar manner as entrained air.

[Mechtcherine et al. \(2017\)](#) presented an interlaboratory study, performed by 13 research groups as part of RILEM TC 225-SAP on frost resistance of concretes containing two commercially available SAP. The concretes tested had the same mix design, but made from materials locally available to participants. Variables include: w/b ratio (0.45, 0.50), SAP, air entrainment and de-icing salt (NaCl). Furthermore, various accelerated methods were used to test freeze–thaw resistance. Results show that the effect of SAP with entrained water on frost resistance (deduced from mass loss after freeze–thaw cycles in de-icing salt) vary from insignificant to considerably positive, with one participating group reporting a negative behavior. If SAP is added without entrained water, then the results clearly show considerable improvement in frost resistance, as expected. When compared to conventional air entrainment, some participants reported similar performance, but in most cases conventional air entrainment gave better performance compared to SAP. However, the study reported that usage of SAP produced a less detrimental effect on mechanical property (dynamic Young's modulus) compared to air entrainment.

It should be noted that conventional air-entraining admixtures are widely used to produce concretes with good resistance to frost damage and salt scaling. However, problems have sometimes been reported concerning the stability of entrained air voids (against loss during transport, pumping, placement, and compaction, for example) and compatibility with other admixtures such as superplasticizers. Proponents of the SAP approach suggest that SAP is robust and does not suffer from these deficiencies, and that the SAP voids (volume, size, spacing factor) can be accurately engineered to provide a good alternative for achieving frost resistance. More work needs to be carried out to verify these claims. Another issue is the longevity of frost resistance of concrete containing SAP, which may decrease if the SAP re-swells when exposed to a wet environment ([Section 17.6.3](#)) and subsequently freezes, or if the SAP voids become filled with hydration products ([Fig. 17.4D–F](#)) as observed in some studies such as [Lee et al. \(2010a,b,c, 2016\)](#) and [Justs et al. \(2015\)](#). For example, [Justs et al. \(2015\)](#) reported that some hardened cement pastes showed significant portion of SAP voids (>50%) filled with calcium hydroxide precipitates.

17.6.3 Crack healing/sealing

A number of studies have investigated the feasibility of SAP as an admixture to impart an ability to self-seal or self-heal cracks in cement-based materials, e.g., [Tsuji et al. \(1998, 1999\)](#), [Lee et al. \(2010a,b, 2016\)](#), [Snoeck et al. \(2012, 2014, 2016\)](#) and others. The mechanism can be summarized as follows: When SAP is mixed in concrete, its swelling is initially constrained because of the high ionic concentration and pH of the pore solution, coupled with charge-screening/complexation

effects discussed in Sections 17.3 and 17.4.2. If cracks form during the life of the concrete structure, these will likely be attracted to and propagate through the SAP voids (which are essentially defects in the microstructure), thus exposing the SAP to external environment as shown Fig. 17.3C.

Ingress of fluids such as precipitation and groundwater with lower ionic concentration compared to concrete pore solution, together with the reduced physical confinement, will trigger SAP to re-swell to a greater extent. The swollen SAP forms a soft gel that expands beyond its void and into the crack, providing a barrier to reduce or prevent further flow (Fig. 17.3D and Fig 17.6). In addition to direct physical blocking, SAP may promote autogenous healing by narrowing the crack width and trapping fine particulates, or by acting as nucleation sites to encourage precipitation of solid products. During dry periods, the SAP releases absorbed water to promote further hydration and/or carbonation, forming additional products that could provide a more permanent crack healing. These effects would help retain water-tightness and regain mechanical properties of cracked structures.

In Tsuji et al. (1998, 1999), mortars with w/b ratio 0.5 containing up to 3% vol. of SAP (5% wt. cement) were prepared and mechanically loaded to form a single 0.1 mm wide through-crack. The flow rate of water through the crack was monitored. Their results showed that mortars containing SAP had 90% lower initial flow rate than the control, and the flow rate rapidly decreased over time. This concept was further explored by Lee et al. (2010a,b, 2016) in model cracks, and paste, mortar and concrete specimens, as well as by Snoeck et al. (2012, 2014, 2016).

Lee et al. (2016) found that SAP could seal larger cracks (0.1–0.4 mm) that would have limited ability to self-heal naturally. Peak flow rates and total flow of 0.12% NaCl solution at 4 m/m pressure gradient (to simulate groundwater ingress) decreased substantially by up to 85% and 98% respectively, in samples containing SAP (Fig. 17.7B,C). Increasing SAP dosage accelerates crack sealing (Fig. 17.7A), but imparts a strength penalty so this limits practical application. For example,

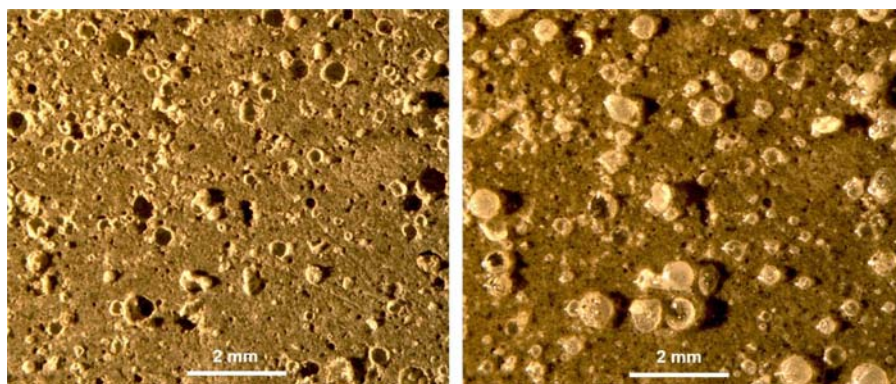


Figure 17.6 Area-matching stereo micrographs of cross-section of hardened cement paste (w/c 0.4, 1.2 wt. % SAP, after drying (left) and wetting (right) with saturated lime solution showing re-swelling of SAP beyond its original void.

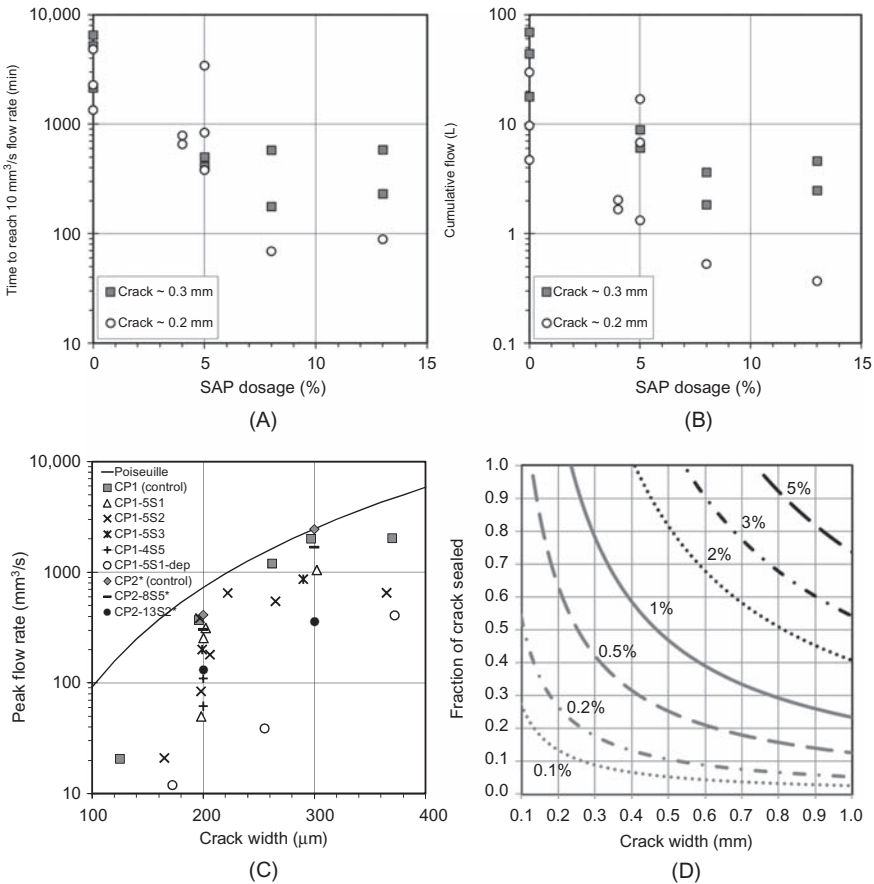


Figure 17.7 Potential for crack sealing. Effect of SAP on: (A) time to reach negligible flow rate; (B) cumulative flow; and (C) peak flow rate of paste, mortar, and concrete samples containing a crack of ~0.2–0.3 mm width. Figure (D) shows example modeling results of fraction of crack sealed as a function of crack width and SAP dosage (wt.% of cement). *Source:* From Lee, H.X.D., Wong, H.S., Buenfeld, N.R., 2016. Self-sealing cracks in concrete using superabsorbent polymers. *Cem. Concr. Res.* 79 194–208.

addition of 5%–13% SAP by weight of cement was found to reduce compressive strength by 80%–87%. Addition of calcium nitrate was found to be beneficial because it depresses initial SAP swelling and enhances autogenous healing. Modeling of crack sealing suggests that the effectiveness of SAP can be enhanced by increasing its re-swelling ratio and particle size, and depressing its initial swelling. These variables increase the SAP exposed in a crack and the gel volume available to seal it (Fig. 17.7D).

Using neutron radiography to study water penetration, Snoeck et al. (2012) found that mortars containing SAP had lower capillary absorption in comparison to the

control sample. [Snoeck et al. \(2014\)](#) also demonstrated the use of SAP to promote self-healing in microfiber-reinforced mortars exposed to wet–dry cycles in water, which facilitated carbonation-induced precipitates on the cracks. They observed that cracks up to 0.13 mm wide were filled with CaCO_3 deposits, which led to decrease in permeability and regain in mechanical properties. Samples exposed to 90% RH environment seemed to show crack healing, but with lower efficiency compared to samples exposed to wet–dry cycles. Using X-ray computed microtomography, [Snoeck et al. \(2016\)](#) observed that the autogenous healing and crack filling with CaCO_3 occurred up to 1 mm depth from the surface exposed to wet/dry cycles, with greater extent of healing when SAP was used.

An advantage of this approach for crack sealing/healing is that the SAP can be widely distributed in the cement paste matrix and that it can undergo many cycles of swelling/de-swelling without apparent degradation. Swelling of SAP remains fairly consistent when exposed to wet–dry cycles ([Lee et al., 2010a,b,c](#)), thus SAP can re-swell after drying with no apparent deterioration, which is obviously desirable for crack sealing. Another attraction of SAP is that the swollen gel is non-rigid and so it should be able to accommodate some crack movements. Methods that are based solely on solid precipitation are less capable of accommodating movements, which would re-open cracks and disrupt autogenous healing.

However, SAP requires external wetting to trigger crack sealing/healing so it is not effective in a dry environment (to prevent gas transport, for example) and less effective in partially saturated conditions. It is also unclear whether it is effective for sealing cracks subjected to high pressure flow, which may decrease the swelling or cause washing out of exposed SAP. The latter was observed in [Lee et al. \(2010a,b,c, 2016\)](#) when cracked samples were subjected to high pressure gradients. This approach is also unlikely to work in a marine environment or in exposure environments where the type of penetrating fluid limits the SAP re-swelling capacity. Furthermore, in a wet environment exposed to freezing, water inside the saturated SAP may expand, induce internal stresses, and cause additional damage. The approach currently requires a fairly high dosage of SAP at 1% wt. cement or greater, and this will limit practical applications due to undesirable effects on strength and cost, and possibly other properties of concrete. The ability to seal large cracks is limited by the SAP dosage and particle size.

17.6.4 Repair

In another application, [Song et al. \(2008, 2009\)](#) described a method to repair leakage in concrete by synthesizing superabsorbent resin in-situ. The precursor polymer (AA-co-AM), initiator and crosslinker are injected into cracks, and then activated with infrared radiation to initialize copolymerization. The synthesized SAP then absorbs water, swells to fill cracks and prevent leakage. Concretes with through-thickness cracks containing large SAP (0.63–1.25 mm) synthesized in-situ were tested before and after being exposed to acid, alkali, salts, wet/dry cycles, and ultraviolet aging. The results show reduction in flow through the repaired crack and

that the efficiency increased with higher SAP absorption capacity and smaller crack widths.

Song et al. (2008) also investigated the potential of SAP synthesized in-situ as a surface treatment method to improve the resistance of concrete against sulfate ingress. Treated samples were subjected to cycles of immersion in 5% sodium sulfate for 16 hours, followed by drying at 80°C. It was found that the surface-treated specimens had lower SO_4^{2-} content, expansion and visible surface damage than nontreated samples. The authors suggested that SO_4^{2-} diffusion was decreased due to static repulsion between SO_4^{2-} and R-COO^- of the ionic groups in SAP.

A common concern in bonded mortar overlays used for concrete repair and lining/levelling concrete members is cracking due to restrained shrinkage. Beushausen and Gillmer (2014) found that the addition of SAP decreases elastic modulus and increases creep and relaxation of bonded mortar overlays, thus improving its resistance to cracking. The effectiveness depends on mix design parameters such as w/b ratio and SAP content. In another study, Beushausen et al. (2014) reported that the use of SAP improved overall performance of repair mortars, including strength, durability, and resistance to cracking when subjected to restrained deformation, particularly when used in combination with silica fume. It should also be noted that there are potential compatibility issues when using SAP as a repair material for existing concrete structures. More research is needed to better understand these issues.

17.6.5 Other applications

A number of other applications of SAP in concrete technology have been proposed and in some cases, supported by limited preliminary studies. These are briefly presented here. As discussed in Sections 17.4.2 and 17.5.2, the addition of SAP presents a new possibility to alter and control the amount of free water in concrete either through purposeful absorption or delayed release (Schroefl et al., 2015). This may be adapted to particular applications. For example, the addition of SAP during concrete batching can be used to induce an abrupt change in rheology, increasing both the yield stress and plastic viscosity. This “thickening” effect of SAP on freshly mixed cementitious materials may be useful in some operations such as pumping and shotcreting, to reduce rebound and allow build-up of thick layers without the need of set-accelerating admixtures (Snashall, 1991; Jensen and Hansen, 2001b; Jensen, 2008).

Harrison (1991) described the use of SAP sheets as an inner liner to conventional formwork to absorb excess water from fresh concrete. During placement and compaction of concrete, some of the mix water is removed by the SAP sheets thereby reducing the effective w/b ratio and improving the durability of the concrete cover zone, similar to controlled-permeability formwork. Jensen and Hansen (2001a,b) suggested the possible use of SAP as micro-reservoirs, containing chemical admixtures that could be released under favorable conditions to induce a change in concrete property or impart a new functionality. In another study, Wyrzykowski and Lura (2013) suggested that, by maintaining a high internal humidity, SAP could

also be used to reduce coefficient of thermal expansion and the amount of thermal deformation during the first few days of hardening. Thus, it appears that SAP can be applied not only to mitigate self-desiccation and autogenous shrinkage, but also control thermal deformation.

17.7 Summary and future research

Superabsorbent polymer is an interesting material with the unique ability to absorb large amounts of fluid, swell and later release the absorbed water when the surrounding humidity drops. The absorption and desorption characteristics of SAP can be controlled via a number of factors. When added to concrete, SAP dramatically alter its fresh and hardened state properties, and this can be exploited to improve the performance of concrete structures. Indeed, there has been a rising interest on the use of SAP in concrete and other cementitious materials. Current main research activities include its use as an admixture for internal curing to mitigate self-desiccation and autogenous shrinkage, improve freeze–thaw resistance and induce self-sealing/healing of cracks, but other potential applications are also being explored.

Clearly, there are many issues that need to be examined before SAP is seen as a viable addition to concrete. Despite the growing research in recent years, fundamental understanding on a number of issues is still lacking. There is much scope for future research, particularly in fundamental understanding of behavior and performance of concrete with SAP, especially long-term durability, optimization of SAP, standardization and design of concrete with SAP, analysis of cost/benefit and commercial viability.

The amount of data concerning the effect of SAP on many properties of concrete is not yet extensive. Furthermore, some findings reported in the literature appear to be inconsistent. To some extent, this is attributable to variation in the materials, mix design and test methods used. For example, it is well-known that the effective w/b ratio controls many properties of concrete. But adding SAP to concrete can drastically change w/b ratio depending on whether extra water is added to compensate SAP absorption and whether this amount, if added, can be determined accurately. However, measuring the absorption of SAP in concrete is not straightforward. This means that in reality, it is difficult to control the effective w/b ratio of mixes containing SAP and be certain that it is the same as the reference mix to enable meaningful comparison.

To date, most investigations have only examined a fairly narrow set of properties of interest within the scope of each study. This is an inevitable nature of empirical research. However, when a new material such as SAP is introduced into concrete and shown to improve some property, it is critical to ensure that it is not detrimental to other properties or leading to other problems. One concern for example, is that the SAP macro voids might negatively impact strength and other properties, particularly in applications that require a high-SAP dosage (e.g., for crack sealing). It is expected that many of these issues will iron out in the near future as more data

become available, together with improvement and standardization in test methods and mix design.

Most investigations have reported findings based on short-term testing, and in some cases under accelerated conditions. Because this is a relative new area of research, there is little data on long-term effects of SAP and performance of concretes containing SAP. But concrete structures are designed to long service lives and are expected to function in a range of exposure environments for many decades. Clearly, more work is required to establish the durability of concretes with SAP, the stability of SAP over time and in various exposure environments, and the longevity of its effect such as for frost protection or crack sealing/healing. For example, the effectiveness of SAP for frost resistant may decrease if the SAP re-swells and freezes, or if the SAP voids become filled with hydration products. Another concern is that the repeated swelling of SAP in concrete and freezing of swollen SAP may cause problems over time.

The SAP used in most studies are commercially available “off-the-shelf” products that have been developed for other applications, and are probably not ideal for concrete. In principle, SAP can be engineered to modify its characteristics and so there should be scope to optimize composition, particle size and shape, absorption–desorption behavior, voidage size, and distribution. This could lead to performance enhancement and/or reduction in the required SAP dosage, to limit strength loss and improve cost effectiveness. Most applications would require SAP that swells rapidly to equilibrium. Slow-swelling SAP is not desirable as it induces a time-dependent effect on fresh concrete properties, disrupts the formation of microstructure, and is less effective for crack sealing. For internal curing, the timing of water desorption is crucial; release that occurs too early/rapid is ineffective and induces negative effects on microstructure. Further research is necessary to establish the feasibility of crack sealing/healing at lower SAP dosages, develop means to limit strength loss, and verify its viability for sealing wider cracks. Finally, more work is needed to establish the commercial viability of SAP for concrete, by carrying out a comprehensive assessment of cost/benefit and comparison with alternative technologies.

References

- Assmann, A., Reinhardt, H.W., 2014. Tensile creep and shrinkage of SAP modified concrete. *Cem. Concr. Res.* 58, 179–185.
- Bentz, D.P., Geiker, M., Jensen, O.M., 2002. On the mitigation of early age cracking. In: Persson, B., Fagerlund, G. (Eds.), *Proc. 3rd International seminar on Self-Desiccation and its Importance in Concrete Technology*. Lund University, Lund, Sweden, pp. 195–204.
- Beushausen, H., Gillmer, M., 2014. The use of superabsorbent polymers to reduce cracking of bonded mortar overlays. *Cem. Concr. Compos.* 52, 1–8.
- Beushausen, H., Gillmer, M., Alexander, M., 2014. The influence of superabsorbent polymers on strength and durability properties of blended cement mortars. *Cem. Concr. Compos.* 52, 73–80.

- Buchholz, F., 1996. Superabsorbent polymers: an idea whose time has come. *J. Chem. Educ.* 73, 512–515.
- Buchholz, F., Graham, A., 1998. *Modern Superabsorbent Polymer Technology*. John Wiley & Sons, 304 pp.
- Caló, E., Khutoryanskiy, V.V., 2015. Biomedical applications of hydrogels: a review of patents and commercial products. *Eur. Polym. J.* 65, 252–267.
- Craeye, B., Geirnaert, M., De Schutter, G., 2011. Super absorbing polymers as an internal curing agent for mitigation of early-age cracking of high-performance concrete bridge decks. *Constr. Build. Mater.* 25, 1–13.
- Davies, L.C., Novais, J.M., Martins-Dias, S., 2004. Detoxification of olive mill wastewater using superabsorbent polymers. *Environ. Technol.* 25, 89–100.
- Dudziak, L., Mechtcherine, V., 2010. Reducing the cracking potential of ultra-high performance concrete by using super absorbent polymers (SAP). In: van Zijl, G., Boshoff, W.P. (Eds.), *Advances in Cement-Based Materials*. Taylor & Francis Group, London, pp. 11–19.
- Nonwovens Industry (2015), An update on the global superabsorbent polymer producers, http://www.nonwovens-industry.com/issues/2015-11-01/view_far-east-report/an-update-on-the-global-superabsorbent-polymer-producers/.
- Esteves, L.P., 2011. Superabsorbent polymers: on their interaction with water and pore fluid. *Cem. Concr. Compos.* 33 (7), 717–724.
- Esteves, L.P., 2015. Recommended method for measurement of absorbency of superabsorbent polymers in cement-based materials. *Mater. Struct.* 48, 2397–2401.
- Esteves, L.P., Cachim, P., Ferreira, V., 2007. Mechanical properties of cement mortars with superabsorbent polymers. In: Grosse, C.U. (Ed.), *Advances in Construction Materials*. Springer, Berlin, pp. 451–462.
- Fantinel, F., 2004. Complexation of polyacrylates by Ca^{2+} ions. Time-resolved studies using attenuated total reflectance Fourier transform infrared dialysis spectroscopy. *Langmuir.* 20 (7), 2539–2542.
- Filho, R.D.T., Silva, E.F., Lopes, A.N.M., Mechtcherine, V., Dudziak, L., 2012. Effect of superabsorbent polymers on the workability of concrete and mortar. In: Mechtcherine, V., Reinhardt, H.-W. (Eds.), *Applications of Super Absorbent Polymers (SAP) in Concrete Construction*. RILEM TC 225-SAP State-of-the-Art Report. Springer, pp. 39–50.
- Friedemann, K., Stallmach, F., Karger, J., 2006. NMR diffusion and relaxation studies during cement hydration—a non-destructive approach for clarification of the mechanism of internal post curing of cementitious materials. *Cem. Concr. Res.* 36 (5), 817–826.
- Gao, D., Heimann, R.B., Alexander, S.D.B., 1997. Box–Behnken design applied to study the strengthening of aluminate concrete modified by a superabsorbent polymer/clay composite. *Adv. Cem. Res.* 9 (35), 93–97.
- Gartner, E., Tang, F., Weiss, S., 1985. Saturation factors for calcium hydroxide and calcium sulfates in fresh Portland cement pastes. *J. Am. Ceram. Soc.* 68 (12), 667–673.
- Gedde, U.W., 2001. *Polymer Physics*. Kluwer Academic Publishers.
- Geiker, M., Bentz, D.P., Jensen, O.M., 2004. Mitigating autogenous shrinkage by internal curing. In: Ries, J.P., Holm, T.A. (Eds.), *High Performance Structural Lightweight Concrete*. ACI SP-218, pp. 143–154.
- Guilherme, M.R., Aouada, F.A., Fajardo, A.R., Martins, A.F., Paulino, A.T., Davi, M.F.T., et al., 2015. Superabsorbent hydrogels based on polysaccharides for application in agriculture as soil conditioner and nutrient carrier: a review. *Eur. Polym. J.* 72, 365–385.

- van der Ham, H.W.M., Koenders, E.A.B., van Breugel, K., 2008. Visco-elastic properties of concrete mixtures including super absorbent polymers. In: Tanabe, T. et al., (Eds.), Proceedings of the 8th International Conference on Creep, Shrinkage and Durability Mechanics of Concrete and Concrete Structures—CONCREEP-8, Ise-shima, Japan, pp. 799–804.
- Harrison, T., 1991. Introducing controlled permeability formwork. Increase concrete durability in the cover zone. *Concrete Construction* 36(2), 198–200.
- Hasholt, M.T., Jensen, O.M., 2015. Chloride migration in concrete with superabsorbent polymers. *Cem. Concr. Compos.* 55, 290–297.
- Hasholt, M.T., Jespersen, M.H.S., Jensen, O.M., 2010. Mechanical properties of concrete with SAP Part 1: Development of compressive strength. International RILEM Conference on Use of Superabsorbent Polymers and other New Additives in Concrete, RILEM Publications SARL, pp. 117–126.
- Hasholt, M.T., Jensen, O.M., Kovler, K., Zhutovsky, S., 2012. Can superabsorbent polymers mitigate autogenous shrinkage of internally cured concrete without compromising the strength? *Constr. Build. Mater.* 31, 226–230.
- Hasholt, M.T., Jensen, O.M., Laustsen, S., 2015. Superabsorbent polymers as a means of improving frost resistance of concrete. *Adv. Civ. Eng. Mater.* 4 (1), 237–256.
- Hooper, H.H., Baker, J.P., Blanch, H.W., Prausnitz, J.M., 1990. Swelling equilibria for positively ionized polyacrylamide hydrogels. *Macromolecules.* 23 (4), 1096–1104.
- Horkay, F., Tasaki, I., Bassar, P., 2001. Effect of monovalent–divalent cation exchange on the swelling of polyacrylate hydrogels in physiological salt solutions. *Biomacromolecule.* 2 (1), 195–199.
- Huber, K., 1993. Calcium-induced shrinking of polyacrylate chains in aqueous solution. *J. Phys. Chem.* 97 (38), 9825–9830.
- Igarashi, S., Watanabe, A., 2006. Experimental study on prevention of autogenous deformation by internal curing using super-absorbent polymer particles. In: Jensen, O.M., Lura, P., Kovler, K. (Eds.), Proceedings of International RILEM conference on Volume Changes of Hardening Concrete: Testing and Mitigation, 20–23 August 2006. Technical University of Denmark, Lyngby, pp. 77–86.
- Itou, Y., Tsuji, M., Kubo, M., 1994. A study on concrete mixed with cooled high absorption polymer. *J. Mater. Concr. Struct. Pavements.* 49 (23), 71–80.
- Jensen, O.M., 2008. Use of superabsorbent polymers in construction materials. In: Sun, W. (Eds.), Proceedings of the First International conference on Microstructure Related Durability of Cementitious Composites, 13–15 October, Nanjing, China, pp. 757–764.
- Jensen, O.M., 2011. Water absorption of superabsorbent polymers in a cementitious environment. In: Leung, C. Wan, K.T. (Eds.), Proc. Int. RILEM Conf. on Advances in Construction Materials through Science and Engineering, RILEM Publications S.A.R.L., Hong Kong SAR, pp. 22–35.
- Jensen, O.M., Hansen, P.F., 2001a. Water-entrained cement-based materials I. Principles and theoretical background. *Cem. Concr. Res.* 31 (4), 647–654.
- Jensen, O.M., Hansen, P.F. 2001b. Water-entrained cement-based materials. PCT Patent Application WO01/02317A1.
- Jensen, O.M., Hansen, P.F., 2002. Water-entrained cement-based materials II. Experimental observations. *Cem. Concr. Res.* 32 (6), 973–978.
- Johansen, N.A., Millard, M.J., Mezencevova, A., Garas, V.Y., Kurtis, K.E., 2009. New method for determination of absorption capacity of internal curing agents. *Cem. Concr. Res.* 39, 65–68.

- Justs, J., Wyrzykowski, M., Winnefeld, F., Bajare, D., Lura, P., 2014. Influence of superabsorbent polymers on hydration of cement pastes with low water-to-binder ratio, A calorimetry study. *J. Therm. Anal. Calorim.* 115, 425–432.
- Justs, J., Wyrzykowski, M., Bajare, D., Lura, P., 2015. Internal curing by superabsorbent polymers in ultra-high performance concrete. *Cem. Concr. Res.* 76, 82–90.
- Kovler, K., 2012. Effect of superabsorbent polymers on the mechanical properties of concrete. In: Mechtcherine, V., Reinhardt, H.W. (Eds.), *Application of Superabsorbent Polymers (SAP) in Concrete Construction*, RILEM TC 225-SAP State-of-the-art report. Springer, pp. 99–114.
- Kong, X.-M., Zhang, Z.-L., Lu, Z.-C., 2015. Effect of pre-soaked superabsorbent polymer on shrinkage of high-strength concrete. *Mater. Struct.* 48, 2741–2758.
- Lam, H., 2005. Effects of internal curing methods on restrained shrinkage and permeability. Portland Cement Association, Research & Development Information Serial No.2620.
- Lam, H., Hooton, R.D., 2005. Effects of internal curing methods on restrained shrinkage and permeability. In: Persson, B., Bentz, D., Nilsson, L.O. (Eds.), *4th International Seminar on Self-Desiccation and Its Importance in Concrete Technology*. Lund University, Lund, Sweden, pp. 210–228.
- Laustsen, S., Hasholt, M.T., Jensen, O.M., 2008. A new technology for air entrainment of concrete. In: Sun, W., Breugel, K., Miao, C., Ye, G., Chen, H. (Eds.), *1st International Conference on Microstructure Related Durability of Cementitious Composites*. Nanjing, China, pp. 1223–1230.
- Laustsen, S., Bentz, D.P., Hasholt, M.T., Jensen, O.M., 2010. CT measurement of SAP voids in concrete. In: Jensen, O.M., Hasholt, M.T., Laustsen, S. (Eds.), *Proc. Int. RILEM Conf. on Use of Superabsorbent Polymers and Other New Additives in Concrete*. RILEM Publications S.A.R.L., Lyngby, pp. 153–162.
- Laustsen, S., Hasholt, M.T., Jensen, O.M., 2015. Void structure of concrete with superabsorbent polymers and its relation to frost resistance of concrete. *Mater. Struct.* 48, 357–368.
- Lee, H.X.D., Wong, H.S., Buenfeld, N.R., 2010a. The potential of superabsorbent polymer for self-sealing cracks in concrete. *Adv. Appl. Ceram.* 5, 296–302.
- Lee, H.X.D., Wong, H.S., Buenfeld, N.R., 2010b. Self-sealing concrete using superabsorbent polymers. *International RILEM Conference on Use of Superabsorbent Polymers and other New Additives in Concrete*, RILEM Publications SARL, pp. 171–178.
- Lee, H.X.D., Wong, H.S., Buenfeld, N.R., 2010c. Estimating the swelling ratio of superabsorbent polymers in cement-based materials. O.M. Jensen, M.T. Hasholt and S. Laustsen (Eds.) *International RILEM Conference on Use of Superabsorbent Polymers and other New Additives in Concrete*. RILEM Publications SARL, pp. 163-170.
- Lee, H.X.D., Wong, H.S., Buenfeld, N.R., 2016. Self-sealing cracks in concrete using superabsorbent polymers. *Cem. Concr. Res.* 79, 194–208.
- Lee, H.X.D., Wong, H.S., Buenfeld, N.R., 2017. Effect of alkalinity and calcium content on the swelling of superabsorbent polymer in cement paste. *Cem. Concr. Compos.* In press.
- Lee, W., Wu, R., 1996. Superabsorbent polymeric materials. I. Swelling behaviors of cross-linked poly(sodium acrylate-co-hydroxyethyl methacrylate) in aqueous salt solution. *J. Appl. Polym. Sci.* 62 (7), 1099–1114.
- Lura, P., Durand, F., Loukili, A., Kovler, K., Jensen, O.M., 2006. Strength of cement pastes and mortars with superabsorbent polymers. In: Jensen, O.M., Lura, P., Kovler, K. (Eds.), *Int. RILEM Conference on Volume Changes of Hardening Concrete: Testing and Mitigation*, RILEM Proceedings PRO 52. RILEM Publications S.A.R.L., Bagneux, France, pp. 117–126.

- Lura, P., Jensen, O.M., Igarashi, S.-I., 2007. Experimental observation of internal water curing of concrete. *Mat. Struct.* 40, 211–220.
- Lura, P., Ye, G., Cnudde, V., Jacobs, P., 2008. Preliminary results about 3D distribution of superabsorbent polymers in mortars. W. Sun, K. van Breugel, C. Miao, G. Ye and H. Chen. (Eds.) 1st International Conference on Microstructure Related Durability of Cementitious Composites. 13–15 October, Nanjing, China, pp. 1341–1348.
- Lura, P., Friedemann, K., Stallmach, F., Mönnig, S., Wyrzykowski, M., Esteves, L.P., 2012. Kinetics of water migration in cement-based systems containing superabsorbent polymers. In: Mechtcherine, V., Reinhardt, H.W., (Eds.), RILEM TC 225-SAP, Application of Superabsorbent Polymers (SAP) in Concrete Construction, RILEM. pp. 21–38.
- Mechtcherine, V., Dudziak, L., Schulze, J., Stähr, H., 2006. Internal curing by superabsorbent polymers—effects on material properties of self-compacting fibre-reinforced high performance concrete. In: Jensen, O.M., Lura, P., Kovler, K., (Eds.), Proceedings of International RILEM conference on Volume Changes of Hardening Concrete: Testing and Mitigation. 20–23 August 2006, Technical University of Denmark, Lyngby, pp. 87–96.
- Mechtcherine, V., Dudziak, L., Hempel, S., 2009. Mitigating early age shrinkage of concrete by using Super Absorbent Polymers (SAP). In: Tanabe, T., et al., (Eds.), Proceedings of the 8th International Conference on Creep, Shrinkage and Durability Mechanics of Concrete and Concrete Structures—CONCREEP-8, Ise-shima, Japan, pp. 847–853.
- Mechtcherine, V., Gorges, M., Schrofl, C., Assmann, A., Brameshuber, W., Ribeiro, A.B., et al., 2014. Effect of internal curing by using superabsorbent polymers (SAP) on autogenous shrinkage and other properties of a high-performance fine-grained concrete: results of a RILEM Round-Robin test. *Mater. Struct.* 47 (3), 541–562.
- Mechtcherine, V., Secieru, E., Schrofl, C., 2015. Effect of superabsorbent polymers (SAPs) on rheological properties of fresh cement-based mortars—development of yield stress and plastic viscosity over time. *Cem. Concr. Res.* 67, 52–65.
- Mechtcherine, V., Schrofl, C., Wyrzykowski, M., Gorges, M., Lura, P., Cusson, D., et al., 2017. Effect of superabsorbent polymers (SAP) on the freeze–thaw resistance of concrete: results of a RILEM interlaboratory study. *Mater. Struct.* 50, 14.
- Moriyoshi, A., Fukai, I., Takeuchi, M., Idota, Y., 1991. The development and characteristics of new bituminous composite material that solidifies even in water-new waterproof backfilling material for underground structures. *J. Mater. Concr. Struct. Pavements.* 43 (15), 157–166.
- Mönnig, S., 2005. Water saturated super-absorbent polymers used in high strength concrete. *Otto-Graf-J.* 16, 193–202.
- Mönnig, S., Lura, P., 2007. Superabsorbent polymers—an additive to increase freeze-thaw resistance of high strength concrete. *Adv. Const. Mater.* 351–358.
- Nestle, N., Kühn, A., Friedemann, K., Horch, C., Stallmach, F., Herth, G., 2009. Water balance and pore structure development in cementitious materials in internal curing with modified superabsorbent polymer studied by NMR. *Micropor. Mesopor. Mater.* 125 (1-2), 51–57.
- Okamura, R., Karibe, S., Hashimoto, S., Harada, H., Uchida, S., Kono, T., 1997. Hydraulic cement composition and its production, JP Patent, JP3273883.
- Paiva, H., Esteves, L.P., Cachim, P.B., Ferreira, V.M., 2009. Rheology and hardened properties of single-coat render mortars with different types of water retaining agents. *Constr. Build. Mater.* 23 (2), 1141–1146.
- Pieper, M.H.G., 2016. Superabsorbent polymers in concrete. MSc Thesis, Imperial College London.

- Piérard, J., Pollet, V., Cauberg, N., 2006. Mitigating autogenous shrinkage in HPC by internal curing using superabsorbent polymers. In: Jensen, O.M., Lura, P., Kovler, K. (Eds.), RILEM Proc. PRO 52 Volume Changes of Hardening Concrete: Testing and Mitigation, RILEM Publications S.A.R.L., Bagnaux, France, pp. 97–106.
- Popovics, S., 1998. *Strength and Related Properties of Concrete: A Quantitative Approach*. Wiley, New York, 535 pp.
- Powers, T.C., Brownyard, T.L., 1947. Studies of the physical properties of hardened Portland cement paste. Bull. 22, Res. Lab. of Portland Cement Association, Skokie, IL, USA, reprinted from J. Am. Concr. Inst. (Proc.) 43, pp. 101–132, 249–336, 469–504, 549–602, 669–712, 845–880, 933–992.
- Reinhardt, H.W., Mönnig, S., 2006. Results of comparative study of the shrinkage behaviour of concretes with different internal water sources. In: Jensen, O.M., Lura, P., Kovler, K., (Eds.), Proceedings of International RILEM conference on Volume Changes of Hardening Concrete: Testing and Mitigation. 20–23 August 2006, Technical University of Denmark, Lyngby, pp. 67–76.
- Reinhardt, H.W., Assmann, A., 2009. Enhanced durability of concrete by superabsorbent polymers. In: Brandt, A.M., Olek, J., Marshal, I.H., (Eds.), Proceedings of the International Symposium on Brittle Matrix Composites 9, Warsaw, Poland, 25–28 October 2009; Woodhead Publishing, pp. 291–300.
- Reinhardt, H.W., Assmann, A., 2012. Effect of superabsorbent polymers on durability of concrete. In: Mechtcherine, V., Reinhardt, H.W., (Eds.), RILEM TC 225-SAP, Application of Superabsorbent Polymers (SAP) in Concrete Construction, pp. 21–38.
- Reinhardt, H.W., Assmann, A., 2014. Time dependent behavior of SAP modified concrete. In: Mechtcherine, V., Schroefl, C. (Eds.), Application of Superabsorbent Polymers and Other New Admixtures in concrete Construction, RILEM Proceedings PRO 95. RILEM Publications S.A.R.L., Bagnaux, France, pp. 235–243.
- Reinhardt, H.W., Assmann, A., Mönnig, S., 2008. Superabsorbent polymers (SAP)—an admixture to increase the durability of concrete. 1st International Conference on Microstructure Related Durability of Cementitious Composites, Nanjing, China, pp. 313–322.
- Rha, C.Y., Seong, J.W., Kim, C.E., Lee, S.K., Kim, W.K., 1999. Properties and interaction of cement with polymer in the hardened cement pastes added absorbent polymer. J. Mater. Sci. 34 (19), 4653–4659.
- Ricka, J., Tanaka, T., 1984. Swelling of ionic gels: quantitative performance of the Donnan theory. Macromolecules. 17 (12), 2916–2921.
- Schlitter, J.L., Barrett, T., Weiss, J., 2010. Restrained shrinkage behaviour and thermal effects in mortars containing super absorbent polymers (SAP). In: Jensen, O.M., Hasholt, M.T., Laustsen, S. (Eds.), Proceedings of International RILEM conference on Use of Superabsorbent Polymers and Other New Additives in Concrete. 15–18 August 2010, Technical University of Denmark, Lyngby, pp. 233–242.
- Schröfl, C., Mechtcherine, V., Gorges, M., 2012. Relation between the molecular structure and the efficiency of superabsorbent polymers (SAP) as concrete admixture to mitigate autogenous shrinkage. Cem. Concr. Res. 42, 865–873.
- Schroefl, C., Mechtcherine, V., Vontobel, P., Hovind, J., Lehmann, E., 2015. Sorption kinetics of superabsorbent polymers (SAPs) in fresh Portland cement-based pastes visualized and quantified by neutron radiography and correlated to the progress of cement hydration. Cem. Concr. Res. 75, 1–13.

- RILEM TC 196-ICC, 2007. State of the Art Report of RILEM Technical Committee on Internal Curing of Concrete. In: Kovler, K., Jensen, O.M., (Eds.), RILEM Publications S.A.R.L., Bagneux, France, 141 pp.
- RILEM TC 225-SAP, 2012. Application of superabsorbent polymers (SAP) in concrete construction. In: Mechtcherine, V., Reinhardt, H.W., (Eds.), State-of-the-art report, Springer, 163 pp.
- Schweins, R., Huber, K., 2001. Collapse of sodium polyacrylate chains in calcium salt solutions. *Eur. Phys. J. E.* 5 (1), 117–126.
- Scrivener, K.L., Crumbie, A.K., Laugesen, P., 2004. The interfacial transition zone (ITZ) between cement paste and aggregate in concrete. *Interface Sci.* 12, 411–421.
- de Sensale, G.R., Goncalves, A.F., 2014. Effects of fine LWA and SAP as internal water curing agents. *Int. J. Concr. Struct. Mater.* 8 (3), 229–238.
- Snashall, H.T., 1991. Cementitious mixes. South African Patent Application ZA9100876 A 19911224.
- Snoeck, D., Steuperaert, S., Van Tittelboom, K., Dubruel, P., De Belie, N., 2012. Visualization of water penetration in cementitious materials with superabsorbent polymers by means of neutron radiography. *Cem. Concr. Res.* 42, 1113–1121.
- Snoeck, D., Van Tittelboom, K., Steuperert, S., Dubruel, P., De Belie, N., 2014. Self-healing cementitious materials by the combination of microfibers and superabsorbent polymers. *J. Intell. Mater. Sys. Struct.* 25 (1), 13–24.
- Snoeck, D., Jensen, O.M., de Belie, N., 2015. The influence of superabsorbent polymers on the autogenous shrinkage properties of cement pastes with supplementary cementitious materials. *Cem. Concr. Res.* 2015 (74), 59–67.
- Snoeck, D., Velasco, L.F., Mignon, A., van Vlierberghe, S., Dubruel, P., Lodewyckx, P., et al., 2015. The effects of superabsorbent polymers on the microstructure of cementitious materials studied by means of sorption experiments. *Cem. Concr. Res.* 77, 26–35.
- Snoeck, D., Dewanckele, J., Cnudde, V., de Belie, N., 2016. X-ray computed microtomography to study autogenous healing of cementitious materials promoted by superabsorbent polymers. *Cem. Concr. Compos.* 65, 83–93.
- Song, X.F., Wei, J.F., He, T.S.H., 2008. A novel method to improve sulfate resistance of concrete by surface treatment with super-absorbent resin synthesised in situ. *Mag. Concr. Res.* 60 (1), 49–55.
- Song, X.F., Wei, J.F., He, T.S.H., 2009. A method to repair concrete leakage through cracks by synthesizing super-absorbent resin in situ. *Constr. Build. Mater.* 23, 386–391.
- Stein, D.B., 2011. Handbook of hydrogels: properties, preparation and applications. Chemical Engineering Methods and Technology Series, Nova Science Publishers Inc., 746 pp.
- Takeuchi, H., Okamoto, T., Demura, K., Ohama, Y., 1991. Fundamental research on superabsorbent polymer as a concrete admixture. *Trans. Jpn. Concr. Inst.* 13, 17–24.
- Tanaka, T., Fillmore, D., Sun, S.T., Nishio, I., Swislow, G., Shah, A., 1980. Phase transitions in ionic gels. *Phys. Rev. Lett.* 45 (20), 1636–1639.
- Trtik, P., Münch, B., Weiss, W.J., Herth, G., Kaestner, A., Lehmann, E., et al., 2010. Neutron tomography investigation of water release from superabsorbent polymers in cement paste. *Int. Conference on Material Science, 64th RILEM Annual Week, Aachen*, pp. 175–185.
- Tsuji, M., Okuyama, A., Enoki, K., Suksawang, S., 1998. Development of new concrete admixture preventing from leakage of water through cracks. *JCA Proc. Cem. Concr.* 52, 418–423.
- Tsuji, M., Shitama, K., Isobe, D., 1999. Basic studies on simplified curing technique and prevention of initial cracking and leakage of water through cracks of concrete by applying superabsorbent polymers as a new concrete admixture. *J. Soc. Mater. Sci., Jpn.* 48, 1308–1315.

- Wong, H.S., Buenfeld, N.R., 2006. Euclidean Distance Mapping for computing microstructural gradients at interfaces in composite materials. *Cem. Concr. Res.* 36, 1091–1097.
- Wang, F., Zhou, Y., Peng, B., Liu, Z., Hu, S., 2009. Autogenous shrinkage of concrete with super-absorbent polymer. *ACI Mater. J.* 106 (2), 123–127.
- Wong, H.S., Pappas, A.M., Zimmerman, R.W., Buenfeld, N.R., 2011. Effect of entrained air voids on the microstructure and mass transport properties of concrete. *Cem. Concr. Res.* 41, 1067–1077.
- Wyrzykowski, M., Lura, P., 2013. Controlling the coefficient of thermal expansion of cementitious materials—a new application for superabsorbent polymers. *Cem. Concr. Compos.* 35, 49–58.
- Wyrzykowski, M., Lura, P., Pesavento, F., Gawin, D., 2012. Modeling of water migration during internal curing with superabsorbent polymers. *ASCE J. Mater. Civ. Eng.* 24 (8), 1006–1016.

This page intentionally left blank

Concrete with self-sensing properties

18

Filippo Ubertini and Antonella D'Alessandro
University of Perugia, Perugia, Italy

18.1 Introduction

Concrete is the leading material in the construction industry worldwide, being used extensively for buildings, infrastructural systems, geotechnical works, industrial plants, road pavements, water dams and more. Among the various features of the material, its low cost, versatility of use and good mechanical properties especially motivate its large use. Concrete civil structures and infrastructural systems are economically vital to our communities, yet they are exposed to ageing and degradation that poses questions about their remaining lifetime and possible performance loss over time. These issues are even enhanced by the increasing complexity of infrastructural networks in western countries and by the current trend towards more and more audacious designs, whereby the maximum height of tall buildings has steadily increased in the last few years, and so the slenderness and span of bridges have done, too. It follows that the definition of appropriate strategies for continuously monitoring the integrity of concrete structures is an urgent priority.

Cost-effective optimization of maintenance activities is especially needed, which would be made possible by automating the monitoring process, resulting in important savings and ensuring users' safety. Structural Health Monitoring (SHM) systems can be conceived to enable such an automated process by linking experimental observations of the in-service response of a structure (e.g., sensor data) to the condition of its integrity (e.g., damage diagnosis and health prognosis). As a matter of fact, SHM is far from being broadly implemented, mainly because off-the-shelf sensors are difficult to apply in the monitoring of large-scale structures, because of their limited durability against environmental actions, and because of transmission issues, difficulty of access, and high costs. In present SHM applications, sensors are externally "attached" to the monitored structure and wired to data acquisition systems, which typically limits the number of sensors that can be deployed in the field. Another bottleneck limiting SHM applications is that permanent monitoring systems often require extensive maintenance as a consequence of the limited durability of traditional sensors and of the limited robustness and exposure to failures of typical SHM architectures.

In order to realize the full potential of SHM solutions for concrete structures, it is critical to develop tailored sensing solutions. In this perspective, an extremely attractive option is the development of multifunctional Self-sensing Concrete (SsC), also called smart concrete, able to work both as structural material and as

distributed sensing system (Han et al., 2014). Extensive research has been carried out in recent years to develop engineered concrete (Mondal et al., 2008; Chuah et al., 2014) by nanoscale modification (Shah et al., 2009) and, among other applications, to develop electrically conductive concrete possessing the functional properties of being strain- and damage-sensitive (Han et al., 2005).

SsC is, in general terms, a concrete engineered at the nanoscale through the addition of functional fillers, enabling strain and damage sensing. It is based on the incorporation of micro- and nano-fillers into cementitious matrices, mostly using carbon nanoinclusions, to provide electrical conductivity. The strain sensitivity of SsC originates from the material's property of exhibiting variations in its internal resistivity and impedance under an applied mechanical deformation or following a damage. At the macroscopic level, SsC can be seen as a two-phase material, whereby phases are matrix and fillers. At the microscopic level, these two phases are not homogeneously distributed one with respect to the other. There is also the interface between fillers and matrix, as well as the interface between fillers themselves. It should be noted that interface areas are typically extremely large because fillers are micro- or nano-scale. This circumstance highly enhances electrical and physical interactions between the fillers and strongly affects the overall behavior of SsC. Fillers typically used in self-sensing concrete can be fibers, particles or other micro- or nanostructured materials. The sensing properties of SsC highly depend upon the structure of the composite concrete and, notably, upon the distribution of the functional fillers, the interfaces between fillers and matrix, as well as on the presence of voids and liquid phases. As it is evident from these preliminary considerations, SsC is a truly multiscale material.

The earliest studies on SsC date back to the 1990s (Chen and Chung, 1993; Fu and Chung, 1996) and, since then, a lot of literature efforts have been devoted to investigating several aspects and practical issues relating to the material. Yet, some of these aspects still need to be solved before SsC can be profitably applied in civil engineering structures. Most of the studies available in the literature have proposed to exploit the piezoresistive properties of SsC for strain sensing, by transducing a mechanical strain into a measurable variation of the electrical resistance and impedance of the material. Other authors have also suggested taking advantage of the electrical conductivity of SsC for direct crack-detection, identifying cracks as interruptions of the conductive paths.

Among the various available particle additives for SsC, Multi Walled Carbon Nanotubes (MWCNTs) have received an increasing attention in recent years (Li et al., 2007; Yu and Kwon, 2009; Azhari and Banthia, 2012; Camacho-Ballesta et al., 2016). The main features of MWCNTs suggests their use in SsC are their excellent mechanical and electrical properties (Heeder et al., 2012; Tamini et al., 2016). Other functional fillers that have been proposed for use in SsC are carbon fibers (Chen and Chung, 1993; Wen and Chung, 2006; Meehan et al., 2010), nanocarbon black (Li et al., 2009), graphene nanoplatelets (Le et al., 2014), nickel powder (Han et al., 2011b), steel slag and magnetic fly ash (Jia, 2009) or hybrid combinations of these fillers (Wen and Chung, 2007b). Luo et al. (2011) for instance proposed the hybrid mixing of MWCNTs and short carbon fibers (CFs) to fabricate SsC.

The main difficulty in limiting applications of strain-sensing cement-matrix materials to large-scale structures is obtaining a uniform dispersion of nanoparticles,

which typically requires sonication of water-nanoparticle emulsions prior to the addition of cement powder and aggregates. This treatment is hardly scalable to large casting volumes but it is often necessary because of the large existing interactions between nanoparticles themselves, leading to their low solubility in water. MWCNTs, for example, tend to form agglomerates and bundles, because of the electronic configuration of tube walls, resulting in a high specific surface area that enhances Van der Waals attraction forces among nanotubes (Konsta-Gdoutos et al., 2010).

A good and uniform dispersion of nanoparticles is necessary in order to achieve a homogeneous, smart concrete without defects, with good mechanical properties, and large strain-sensitivity. A good dispersion of nanoparticles ensures such properties as their interactions with the matrix increase, due to the increase of the interfacial contact area. Moreover, a uniform dispersion of nanoinclusions ensures that an electrically conductive network path develops through the nanoparticles and across the matrix which activates the piezoresistive behavior of the composite.

Electrical conduction through SsC and its strain sensitivity are activated when the amount of properly dispersed functional fillers reaches a critical value called percolation threshold (Xie et al., 1996; Wen and Chung, 2007a). The percolation threshold represents the filler content above which the material becomes really conductive. When a mechanical deformation acts on an SsC specimen, the average distance between nanoparticles changes and so do their electrical interactions. In particular, the tunnel effect, a fundamental mechanism of electrical conduction in the composite material (Kuronuma et al., 2012), is modified, thus inducing macroscopic variations in the electrical resistivity of the material. These changes, measured by means of a proper data acquisition system, can be exploited to infer the state of strain.

This chapter is aimed to give an overview on the current state of development of the technology of SsC, by presenting the state-of-the-art on the topic, as well as the most fruitful research directions for a full development of the potential of such a technology. The chapter is organized as follows: Section 18.2 discusses composition and processing of SsC, including matrix, fillers, dispersion methods and curing. Section 18.3 discusses the topic of strain sensing in SsC starting from available electrical measurement techniques and ending with a discussion on suitable modeling approaches to reproduce the electromechanical behavior of SsC. Section 18.4 presents the main fields of applications of SsC, including, in particular, SHM, traffic detection and its use for concrete structural repairs. Finally, Section 18.5 briefly discusses the main research trends and open problems related to SsC.

18.2 Composition and processing of self-sensing concrete

Fig. 18.1 (Han et al., 2015b) depicts the structure of SsC, where the matrix is the first phase of the material, conductive fillers represent the second phase, and the interface between fillers and matrix represents the third phase. In this section, composition and processing of SsC are illustrated.

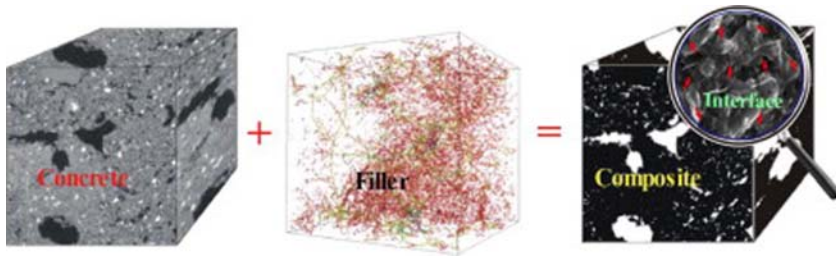


Figure 18.1 Structure of SsC showing the two phases of matrix and filler, as well as the interface between fillers and matrix (Han et al., 2015b).

18.2.1 Matrix and fillers

The matrix is the part of the material that, next to governing the overall mechanical properties and strength of the composite, also has the function of holding the functional fillers in place thus creating the bulk composite concrete. In SsC, the matrix can be concrete, mortar or cement paste. The binder in the matrix can be Portland cement, or other types of cement, but can also be asphalt or polymers to which mineral aggregates are added. Strain sensing asphalt concrete has been, for instance, extensively studied for traffic monitoring (Wu et al., 2003; Liu et al., 2008; Li et al., 2008; García et al., 2009; Liu and Wu, 2009).

Mechanical properties of the matrix, such as its Young modulus, determine the strains developing under mechanical loading conditions and consequently affect the self-sensing ability of SsC. Literature reports on the use of different matrix types, functional fillers and various applications of self-sensing concrete doped with carbon-based additives (Chung, 2012; McEvoy and Cornell, 2015; Han et al., 2015a,b). Strain-sensing ability was demonstrated, in particular, for various carbon-based nanocomposite concretes using impedance and resistance measurements.

As already mentioned, functional fillers used in SsC can be, among others, carbon fibers, carbon nanotubes (CNTs), carbon black (CB), graphene nanoplatelets, nickel powder, or hybrid combinations of these fillers. Chung (2000) proposed piezoresistive concrete for strain sensing by adding carbon fibers to a traditional concrete mixture. Li et al. (2006) dealt with a similar problem by investigating the self-sensing properties of concrete filled with 120 nm CB. Han et al. (2009b) showed that transient loads can be measured by exploiting the smart properties of cement-based materials doped with MWCNTs. Ubertini et al. (2014a) demonstrated that natural frequencies of vibrating concrete structures can be identified by the signal processing of the output of cement-based materials doped with MWCNT. Le et al. (2014) demonstrated the damage detection potential of concrete with dispersed conductive graphene nanoplatelets (GNPs). It is also worth noting that carbon-based fillers, next to providing the material with piezoresistive properties, can also significantly improve mechanical properties (Siddique and Mehta, 2014), strengthening the interest on the concept of multifunctional structural materials doped with carbon-based additives. In this regard, in the study by Abu Al-Rub

et al. (2012) it was reported that the flexural strength and ductility of SsC increase by addition of MWCNTs to the mixture, whereby a low concentration of long MWCNTs was found equivalent to a higher concentration of short MWCNTs, due to a more effective micro-crack bridging in the former case. Similarly, Gdoutos et al. (2016) achieved an increase in flexural strength of cement mortar equal to 87% and 106% by means of well-dispersed MWCNTs and carbon nanofibers (CNFs), respectively. A theoretical multiscale study demonstrating the improvement in mechanical properties of cement-based materials that can be achieved by the incorporation of MWCNTs was performed by Sindu et al. (2014), who highlighted a non-linear strength increase with increasing content of nanotubes.

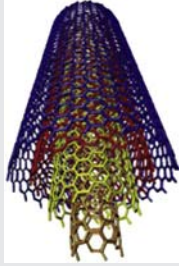

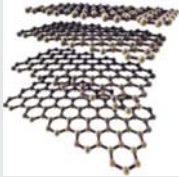

The production cost of the functional fillers has been one of the bottlenecks limiting the diffusion of the technology of SsC in recent years. Nevertheless, for some fillers, such production costs are steadily decreasing, owing to the tremendous increase in their utilization for various purposes. This is the case, for instance, of MWCNTs whose production cost, for a relatively low degree of purity that is nonetheless fully acceptable in application to SsC, is today around 100 USD/kg and further reductions are likely to be expected in the future. This cost is already feasible for fabricating smart nanocomposite concrete strain sensors for embedding into concrete structures at a lower life-cycle cost compared to other off-the-shelf sensing technologies, or for cost-effectively applying SsC in local critical portions of a structure. Among carbon-based fillers, CB is comparatively less expensive than MWCNTs, while GNPs are generally more expensive. The cost of CNFs is, today, intermediate between cost of CB and cost of MWCNTs.

Table 18.1 summarizes the main properties of the most important carbon-based nanofillers used in SsC, while Fig. 18.2 shows Scanning Electron Microscopy (SEM) inspections of the same nanofillers dispersed in hardened cement paste.

18.2.2 *Materials and methods for dispersion*

Literature suggests that there are three different approaches to disperse functional fillers in water (Han et al., 2011a). The former class of methods is represented by so-called mechanical methods, based on the use of mechanical mixers that physically separate the particle or fiber additives. The second class of methods is represented by so-called physical methods, based on the use of special additives, called dispersants, that operate as non-covalent surface modifications on the functional fillers, which facilitate suspension in water. Dispersants or surfactants are widely used in chemistry, whereby their structures are tailored in such a way to develop desired interactions with specific targets (Tiecco et al., 2009, 2013; Di Profio et al., 2010; Corte et al., 2015). Dispersants synthesized for application to carbon nanotubes allow to physically attach the dispersing chemical groups onto the MWCNTs' surface, thus not altering the covalent bonds on the tube lattice. Finally, the third class of dispersion methods is represented by chemical methods, based on a covalent surface modification. Such chemical treatments typically use aggressive chemicals, such as neat acids, in order to operate a functionalization of fillers' surface. When applied to MWCNTs, for instance, nanotubes with attached functional groups are

Table 18.1 Properties of carbon-based nanofillers used in SsC (Pisello et al., 2017)

Nanofiller	Properties		Nanofiller	Properties	
MWCNTs	Outer mean diameter	10–15 nm	Carbon nanofibers	Fiber diameter (average)	150 nm
	Mean agglomerate size	200–500 μm		CVD carbon overcoat on fiber	No
	Weight loss at 105 °C	<1%		Surface area	20–30 m^2/g
	C content	>90 wt%		Dispersive surface energy,	120–140 mJ/m^2
	Free amorphous carbon	Not detectable SEM/TEM		Polyaromatic hydrocarbons:	<1 mg PAH/gm fiber
	Mean number of walls	5–15		Iron	<14,000 ppm
	Apparent density	50–150 kg/m^3		Density	1.0 g/cm^3
	Length	0.1–10 μm		Moisture	<5 wt%
Graphene nano platelets	Diameter (average)	15 μm	Carbon black	Particle size (average):	30 nm
	Purity	97 wt%		Blackness value <i>M</i>	216
	Grade	2		Oil absorption number (OAN)	420
	Surface area	100 m^2/g		Volatile (950°C)	–
	Density	1.8 g/cm^3		Density	1.8 cm^{-3}

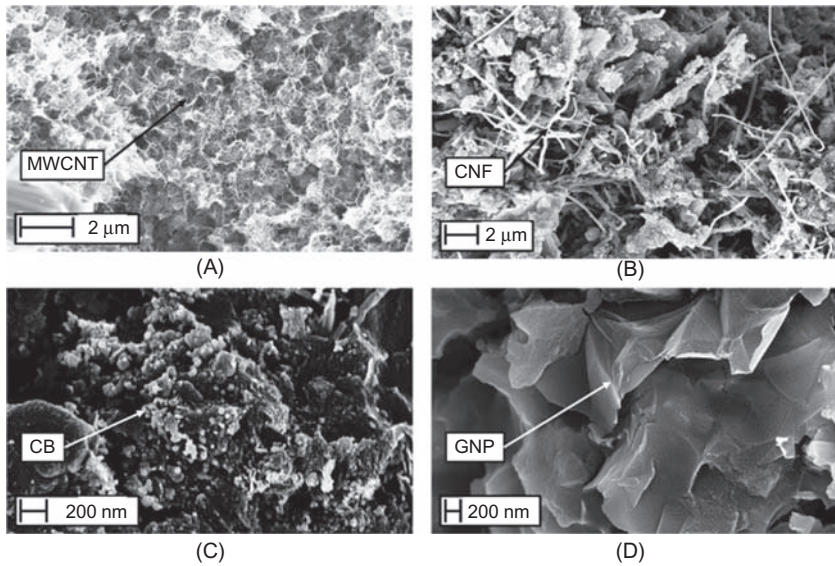


Figure 18.2 SEM images of nanomodified cement paste with MWCNTs (A), CNFs (B), CB (C) and GNPs (D) (Pisello et al., 2017).

less likely to agglomerate. However, they turn out to exhibit defects and alterations due to the chemical treatment itself that result in a poorly performing SsC. A temporary dispersion of nanoparticles can also be effectively achieved by mechanical agitation through ultrasonication (Hilding et al., 2003). For this reason, this sonic treatment often complements chemical or physical methods. As an example, Fig. 18.3 shows a typical fabrication procedure of SsC samples with conductive nanoinclusions (García-Macías et al., 2017b), where a dispersant is used and the water nanoparticle suspension is sonicated prior to the addition of cement and aggregates.

18.2.3 Preparation and curing

The hydration process and the formation of hydration products in SsC are highly affected by curing methods and conditions. Considering that different curing technologies result in different mechanical properties, different interface bonding between filler and matrix, as well as different water contents, it follows that curing also affects the overall electrical and electromechanical properties of smart concretes. Smart concrete was tested with standard curing (i.e., exposure to a temperature of $20 \pm 3^\circ\text{C}$ with a relative humidity higher than 90% or storage in water), hot water curing, and steam curing (Chung, 1998; Wang et al., 2002; Jia, 2009). Jia (2009) investigated how three different curing methods affected the strain sensing behavior of concretes with steel slag and magnetic fly ash. The results showed that the sensitivity of the resulting smart concretes decreased from water curing to

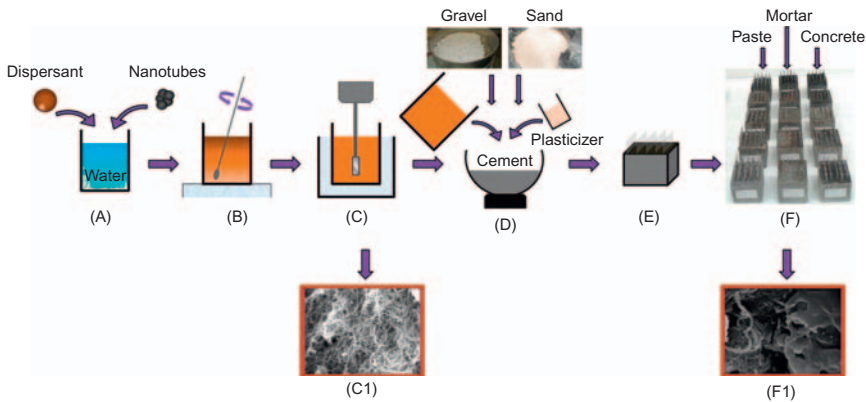


Figure 18.3 Example of preparation procedure of paste, mortar and concrete samples with MWCNTs. (A) Preparation of nanoadded solution; (B) mechanical mixing; (C) sonication; (C1) SEM analysis of suspensions with nanotubes; (D) addition of suspension and aggregates to cement; (E) pouring into oiled molds and embedding of the electrodes; (F) curing of the samples; (F1) SEM analysis of cementitious materials (García-Macías et al., 2017b).

air curing. Overall, increasing the curing age from 1 to 28 days resulted in a decrease in sensitivity (Jia, 2009). Fu and Chung (1997) showed that the electrical resistance of concrete with carbon fibers monotonically increased with increasing compressive strain after 7 days, and 14 days of curing, while the same electrical resistance decreased with compressive loading after 28 days of curing. This peculiar behavior was attributed to some weakening of the fiber-cement interface with curing progress (Fu and Chung, 1997).

18.3 Measurement of sensing data and characterization of self-sensing concrete

18.3.1 Sensing mechanisms

In addition to being electrically conductive, SsC also exhibits dielectric properties that originate from double layer phenomena around electrodes, as well as around nanoparticles. This circumstance highly complicates the electromechanical behavior of SsC. In particular, the material is not simply resistive, but also capacitive, which causes polarization—a charge accumulation under an applied constant electrical field. The main drawback associated with polarization is a time drift of the electrical resistance of the material, measured in both DC and AC configurations, which highly complicates strain sensing and requires appropriate correction and compensation strategies. Fig. 18.4 is an example of a time history of measured electrical resistance versus time of a nanocomposite cement paste doped with MWCNTs,

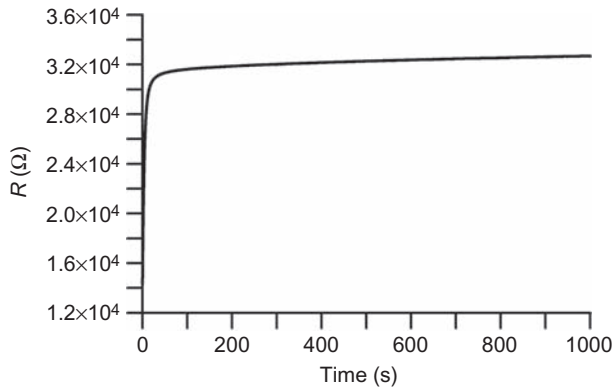


Figure 18.4 Example polarization curve of a SsC specimen.

subjected to a constant DC electrical field. The inherent time drift in the measurement is apparent from this figure.

Many literature works (e.g., [Han et al., 2012](#)) assume that only the internal resistance of the material, and not its capacitive constants, is appreciably influenced by the mechanical deformation. Typically, the resulting relationship between incremental variation in electrical resistance, ΔR , and axial strain, ε (positive in compression), is modeled in analogy with electrical strain gauges as

$$\frac{\Delta R}{R} = -\lambda \varepsilon \quad (18.1)$$

where R is the internal electrical resistance of the material in unstrained conditions and λ is the gauge factor that, for smart concretes, can reach values up to 200–400 and more ([Azhari and Banthia, 2012](#)), so two orders of magnitude larger than gauge factors of typical electric strain gauges. Linearity of [Eq. \(18.1\)](#) is acceptable only under the assumption of sufficiently small deformations.

Although [Eq. \(18.1\)](#) is a drastic simplification of the strain-sensing phenomenon developing within the composites, it has the advantage of highlighting quantities affecting strain sensitivity, S . This last can be defined as the incremental variation of electrical resistance over applied strain and can be derived from [Eq. \(18.1\)](#) as

$$S = \frac{\Delta R}{\varepsilon} = -\lambda R \quad (18.2)$$

[Eq. \(18.2\)](#) suggests that the optimal content of nanoparticles (the one that maximizes S in [Eq. \(18.2\)](#)) represents a trade-off between increasing R and increasing λ . When the content of nanoparticles is larger than this optimal value, the nanoparticles form a continuous network and S decreases because of a drastic reduction of R (electrical conduction is dominated by the percolating path through the nanoparticles). On the contrary, if the content of nanoparticles is smaller than the optimal

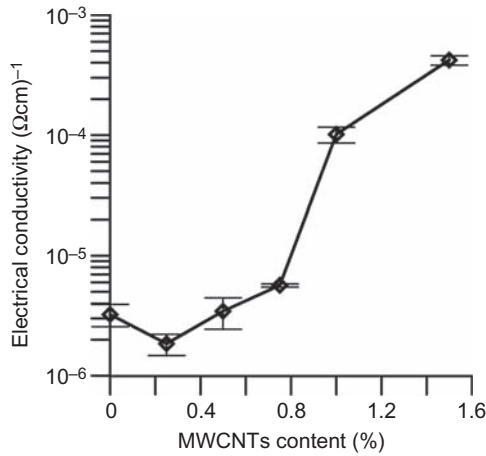


Figure 18.5 Example of a percolation curve of an SsC specimen with error bars representing \pm standard deviation intervals obtained by selecting four different pairs of electrodes.

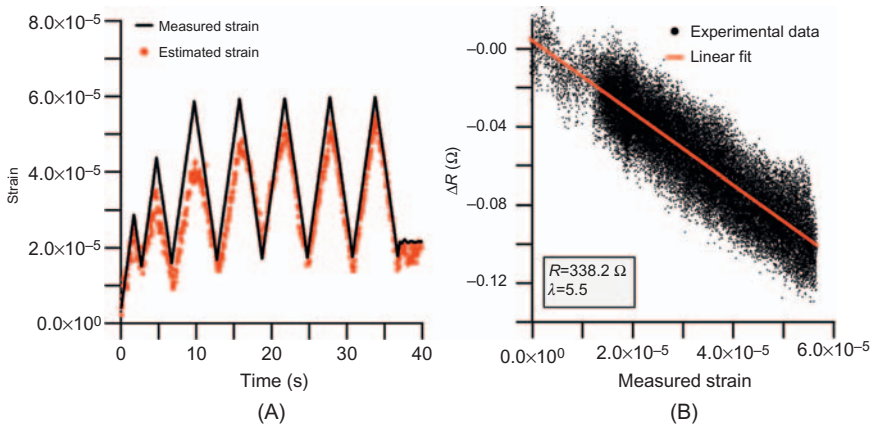


Figure 18.6 Strain sensing test with SsC specimen: time series of applied compression strain measured with resistive strain gauges and strain estimated from material's output using Eq. (18.1) (A); resistance change versus applied strain plot showing validity of the linear assumption of Eq. (18.1) (B).

value, the distance between nanoparticles is too large for strain sensing (the material is electrically isolating) and λ decreases. Literature results suggest that the optimal content of nanoparticles is around the percolation threshold (Han et al., 2015b; García-Macías et al., 2017a,b). An example of a percolation curve of concretes with varying MWCNTs content, expressed in relative terms with respect to the weight of cement, is shown in Fig. 18.5. Validity of Eq. (18.1) is demonstrated in Fig. 18.6 reporting the results of a strain sensing test on a specimen of SsC.

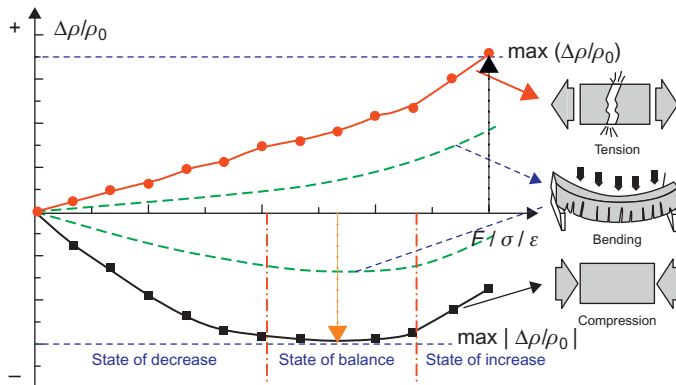


Figure 18.7 Typical sensing behavior of SsC (Han et al., 2015b).

18.3.2 Modeling aspects

Many literature studies have proposed to exploit the strain-induced changes in electrical conductivity of cement-based composites with carbon nanoinclusions for sensing purposes. While many experimental works can be found in this context (Han et al., 2009a,b; Howser et al., 2011; Ubertini et al., 2014a,b; Konsta-Gdoutos and Aza, 2014; D'Alessandro et al., 2016), only a scant number of studies dealt with the theoretically-based design and optimization of the composites.

Fig. 18.7 (Han et al., 2015b) shows the typical sensing behavior of SsC, including sensitivity to damage in compression, bending and tension. In order to reproduce this behavior, the majority of the contributions proposed the use of lumped electrical circuit models, using series and parallel combinations of resistors (Li et al., 2004; Han et al., 2007a, 2009a; D'Alessandro et al., 2014) and capacitors (Han et al., 2012). A very promising alternative to such a modeling approach is represented by micromechanical modeling, that aims at reproducing the electrical behavior of the composites on a physical basis. The two approaches are briefly reviewed in the following subsections.

18.3.2.1 Micromechanics homogenization approaches

The electrical conductivity of cement-based composites doped with carbon inclusions has been extensively studied in recent years, often pointing out its percolation-like nature (Chen et al., 2004; Chiarello and Zinno, 2005; Wen and Chung, 2007a). Overall, many literature studies agree on the two basic mechanisms that originate electrical conduction in such composites, namely electron hopping (or quantum tunneling) and conductive networking (Wen and Chung, 1999; Chen et al., 2004; Li et al., 2006; Chang et al., 2009). When the volume fraction of conductive fillers is below the percolation threshold, conduction is believed to be dominated by intra-fiber or fiber-fiber transfer of electrons and by ionic conduction. On the

contrary, above the percolation threshold, nano- or micro-inclusions start to form a continuous network such that electrons preferably flow through such a network.

The origin of the strain sensing properties of these materials is related to changes in electrical properties associated with geometrical changes in the composites following an applied strain. Literature suggests three major mechanisms enabling strain sensing properties during stretching and compressing (Hu et al., 2011; Feng and Jiang, 2014). These are: (1) composite volume change; (2) change of fillers' orientation; and (3) change in the percolation threshold. The first mechanism can be explained by the circumstance that, in cement-based materials doped with carbon inclusions, volume changes associated with strain are essentially sustained by the matrix, owing to the comparatively larger stiffness of functional fillers. This determines a change in the volume fraction of the functional fillers that, in turn, results into breaking existing and creating new conductive paths, determining an overall change in electrical conductivity (Pham et al., 2008; Feng and Jiang, 2014; Gong and Zhu, 2014). The second mechanism mentioned above consists in the tendency of functional fiber-like fillers to reorient, favoring stretching direction. This mechanism was, for instance, evidenced in the studies performed by Cheng et al. (2009), Wang et al. (2011), and Ameli et al. (2013), highlighting that strain-induced orientation changes of fiber-like fillers determine a certain degree of anisotropy in the electrical behavior of the deformed composite that, at the macroscopic level, results in changes in electrical properties. The third aforementioned mechanism consists of a change in the percolation threshold following an applied strain. Again, this mechanism can be encountered when using fiber-like fillers and can be explained as a change in the likelihood that aligned fibers touch each other and form connecting networks in deformed conditions (Lin et al., 2010; Zeng et al., 2011; Grillard et al., 2012).

Among the literature works attempting micromechanical modeling of the strain-sensing behavior of composites with carbon inclusions, those by Deng and Zheng (2008) and Takeda et al. (2011) deserve special attention. Although in a different context with respect to cement-based materials, those authors employed simplified micromechanical approaches able to model percolation, conductive networking, anisotropy of electrical conductivity, as well as waviness of CNTs achieving a fairly good agreement with literature results. Also notable are the contributions by Seidel and Lagoudas (2009) and by Feng and Jiang (2013), who studied electron hopping (through a conductive interphase surrounding the tubes) and conductive networking (by means of changes of CNT aspect ratios) in CNT-polymer composites, by means of a Mori-Tanaka micromechanical model (Mori and Tanaka, 1973).

The number of literature works attempting to model strain-induced changes in electrical conductivity of carbon-based SsC is very limited. With this regard, Lin et al. (2010) applied Monte Carlo simulations to demonstrate that electrical properties of composites with fiber-like fillers are affected by strain as a consequence of the change in the percolation threshold. Theodosiou and Saravanos (2010) showed that nanotube resistance and tunneling effect govern strain-sensitivity in polymer-based composites doped with CNTs, using a multiscale analysis based on an

atomistic model and a macroscale numerical simulation. A contribution to the explanation of the high level of non-linearity typically exhibited by piezoresistivity of composites is ascribed to [Yasuoka et al. \(2010\)](#), who based their conclusions on the use of a circuit simulator analogous to a percolation network.

The study by [Alamusi and Hu \(2010\)](#), combining a three-dimensional resistor network ([Hu et al., 2008](#)), Simmons tunneling effect ([Simmons, 1963](#)), and a fiber orientation model ([Taya et al., 1998](#)), highlighted that a higher strain-sensitivity can be anticipated when the volume fraction of functional fillers is close to the percolation threshold. Another relevant study is the one performed by [Tallman and Wang \(2013\)](#) who modeled piezoresistivity of CNT-based composites subjected to arbitrary three-dimensional strains, by extending the analytical framework developed by [Takeda et al. \(2011\)](#). The results achieved in that work highlighted, again, the non-linear resistivity-strain behavior, especially for CNT concentrations close to the percolation threshold. Similar conclusions were drawn by [Feng and Jiang \(2014, 2015\)](#).

A very relevant issue in SsC is that the dispersion of functional fillers is never optimal and that fiber-like particle additives tend to change their shape and bend during material processing. As an example, several experiments can be found in the literature showing that most CNTs in composites present a certain degree of waviness ([Vigolo et al., 2000](#)), which is a consequence of their large aspect ratio and low bending stiffness. It follows that non-straightness and agglomeration of fiber-like fillers are essential phenomena to be included in a rigorous theoretical modeling. In this regard, special attention should be devoted to the works of [Weng \(2010\)](#) and [Yang et al. \(2014\)](#), who showed that clustering of nanoparticles inhibits the formation of conductive networks, thus inducing relevant increases in percolation threshold. Non straightness of nanofillers was also considered by [Fisher et al. \(2003\)](#), [Yi et al. \(2004\)](#), and [Berhan and Sastry \(2007\)](#) by assuming a simple sinusoidal shape for CNTs that induced decreases of the overall conductivity of the composites by determining a shift in the percolation threshold. Similar studies were proposed by [Deng and Zheng \(2008\)](#) and [Takeda et al. \(2011\)](#) who introduced a wavy length ratio into an extended micromechanics modeling. [García-Macías et al. \(2017a,b\)](#) applied homogenization theory and micromechanical modeling in order to reproduce the electrical and piezoresistive properties of smart concrete with CNTs, including waviness of the nanotubes and their non-uniform spatial distribution. [Fig. 18.8](#) depicts the representative volume element of SsC, with fiber like conductive nanoinclusions considered in those works, emphasizing the cross-scale nature of the material and of the adopted modeling approach. The studies by [García-Macías et al. \(2017a,b\)](#) allowed to accurately reproduce the experimentally observed behavior of several MWCNT-reinforced cement-based specimens, including specimens made of nanocomposite cement paste, mortar, and concrete. Overall, an analytical micromechanics framework was developed, becoming a helpful tool for understanding of the physical mechanisms that govern the piezoresistivity of MWCNT cement-based composites. Such a framework included both mechanisms contributing to the conductivity of CNT cement-based composites: electron hopping and conductive networks. The strain-induced changes in electrical conductivity were attributed to (1) changes in volume fraction of CNTs; (2) changes in

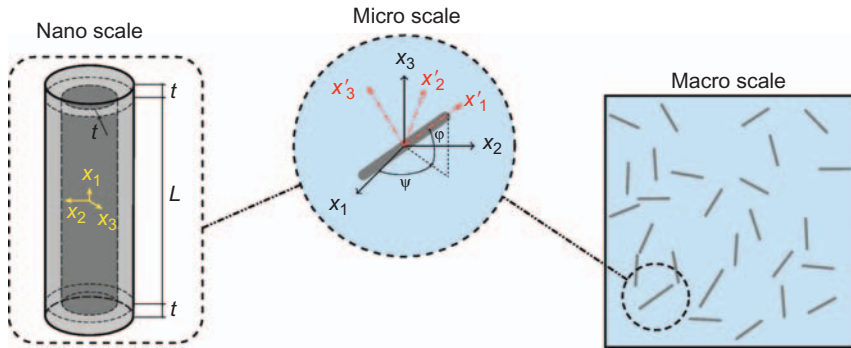


Figure 18.8 Micromechanics modeling approach of SsC with fiber-like conductive nano-inclusions: representative volume element (RVE) including straight nanofibers (García-Macías et al., 2017b).

conductive networks and percolation threshold following reorientation of nanotubes and, finally; (3) changes in tunneling resistance caused by variations of inter-particle distances and height of the potential barrier. The strain-induced variation of the percolation threshold was modeled by means of Komori and Makishima's (1977) stochastic method, allowing an evaluation of the resulting strain-induced orientation distribution function of the CNTs. Moreover, a helical waviness model, and a two-parameter agglomeration approach were proposed to account for imperfect dispersion of nanotubes. Overall, it was theoretically found that the optimum value of gauge factor λ , Eq. (18.1), is attained when the nanofiller content is close to the percolation threshold and that percolating curves can have different shapes, strongly depending upon the quality of nanotube dispersion (see Fig. 18.9).

18.3.2.2 Lumped circuits approaches

Despite the richness of literature studies dealing with the understanding of the electro-chemical and physical mechanisms that govern piezoresistivity of strain-sensing concrete, only a few studies dealt with the problem of modeling the input-output behavior of the materials, duly accounting for the involved dynamic phenomena. In this regard, perhaps the most suitable modeling approach is that of reproducing the behavior of sensors made of SsC by means of equivalent lumped circuits, properly considering that the materials behave as dielectrics. Their dielectric behavior in particular produces a charge accumulation under application of a constant electrical field that, in turn, corresponds to an electrical field opposite to the applied one. The macroscopic consequence of this phenomenon is that the electric current circulating in the material, under application of a constant potential difference, decreases in time (Wen and Chung, 2000; Cao and Chung, 2004). Lumped-circuit models have the advantage that they provide a mathematically tractable, simple tool for signal processing of the output of smart concrete specimens under general mechanical loading conditions.

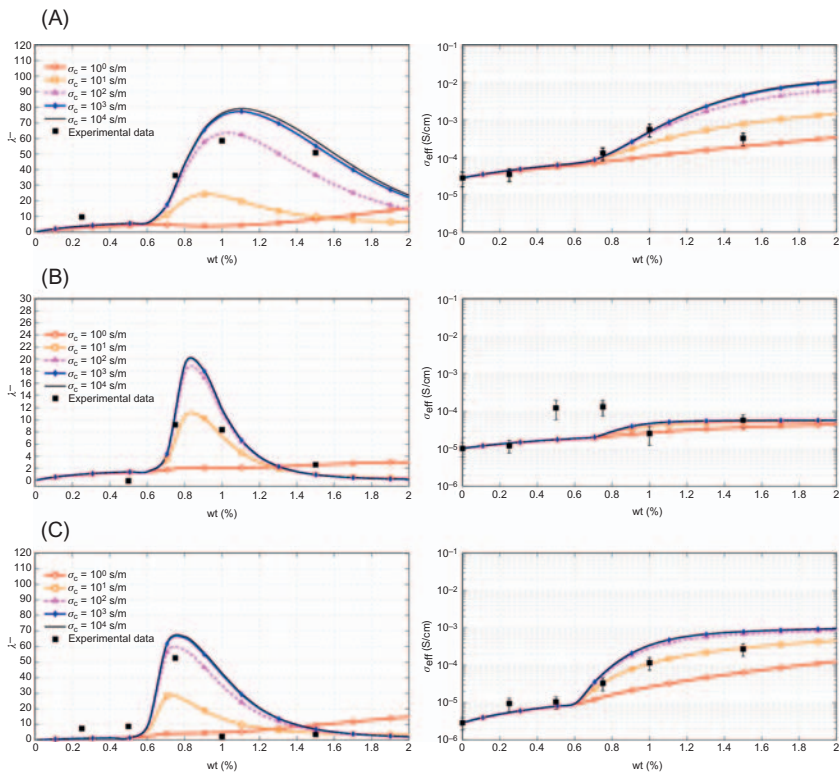


Figure 18.9 Comparison of theoretical predictions and experimental results for gauge factors (left plots) and electrical conductivity (right plots) of cement paste, mortar, and concrete samples (A, B, and C, respectively) doped with varying amounts of MWCNTs by changing parameters related to MWCNTs conductivity and dispersion (García-Macías et al., 2017b).

In the framework presented above, only a few contributions dealt with application in smart concrete, while most of the studies focused on applications in polymers. In that context, notable is the paper of Kang et al. (2006), where the authors proposed the use of a modified Randle's circuit in order to reproduce the dynamic response of CNT/PMMA sensors. As was common in most of the literature works, the authors hypothesized using a simple linear relationship to relate axial strain to relative change in electrical resistance of the sensor, which corresponds to a linearization assumption. This, in particular, limits application of the model to the small deformation range and to the case of filler contents sufficiently different from the percolation threshold. A similar study on CNT/PVA thin films was proposed by Loh et al. (2008), who used an RC-circuit model, based on frequency-domain electrical impedance spectroscopy fitted to experimental data. In that work, a good agreement with experimental results was achieved by assuming some specific analytical representation for contact resistance, double layer capacitance, and bulk resistance. Also interesting is the work of Sanli et al. (2016), who proposed an RC

equivalent circuit to reproduce the impedance responses of sensitive CNT/epoxy films. In that study, the authors showed that, next to internal resistance, internal capacitance of the sensor is also affected by changes in mechanical strain. Application of lumped circuits to model the behavior of SsC was proposed by Wansom et al. (2006), who used a type of universal model, highlighting the different paths through which current flows in SsC, namely matrix paths, particle-matrix paths and—when percolation has been achieved—interparticle paths.

In the context of the application of lumped circuit models to smart concrete materials, Materazzi et al. (2013) experimentally investigated the change in electrical resistance of sensors made from nanocomposite cement paste, subjected to sinusoidal compression loads. The results showed that the amplitude of the electrical response of the sensors increases with the increasing frequency of the mechanical loading, and that the same response contains superharmonic components. In order to shed some light on this behavior, D'Alessandro et al. (2014) proposed to model the electromechanical sensor's response using a Randle's equivalent circuit. The circuit, similar to the one proposed by Han et al. (2012), consisted of two resistors and a capacitor, thus reproducing contact resistance, including cables and electrodes, as well as electric polarization. Experimental and analytical results confirmed that the dynamic response of carbon nanotube cement-based specimens to a sinusoidal mechanical input is not monochromatic, but rather contains superharmonics, and clarified that the origin of these components is not associated to a nonlinear effect, but rather to the differential equation governing the equivalent circuit containing time-varying coefficients. Nevertheless, the proposed circuit model failed at reproducing the increasing amplitude of the response with increasing frequency of the mechanical input.

In summary, it can be stated that all studies published so far in the literature have associated strain-sensitivity of CNT reinforced nanocomposites to a piezoresistive behavior, that is, to a change in internal resistance following an applied strain. Essentially, three mechanisms govern such a change in electrical resistivity: (1) changes in volume fraction of nanofillers due to mechanical strain; (2) reorientation of fiber-like fillers; and (3) changes in tunneling resistance. All lumped circuit models so far proposed for electromechanical characterization of composites with conductive inclusions are based on these principles, with strain sensing being essentially enabled by changes in internal resistance or capacitance.

18.3.3 Electrical measurement methods

The majority of existing literature studies used direct current (DC) for measuring various electrical parameters, such as voltage, resistance and conductivity in SsC specimens. The two typical DC setups are the two-probe and four-probe setup. In the former setup, a single probe is used to source current and measure voltage, while the other probe sinks current and provides a voltage reference. In the latter setup, separate pairs of current-carrying and voltage-sensing probes are used. In comparison, the four-probe method should be regarded as more accurate, because it bypasses the resistance of test cables and of the contact at the signal/sample interface. However, many authors prefer to use the two-probe method as it provides an

easier configuration by requiring only two signal/sample interfaces, also considering that in many cases parasitic contact resistances may be negligible, especially for smart concrete samples having a significant inherent resistivity.

As reported in many literature works (Chung, 2000, 2002; Wen and Chung, 2002; Han et al., 2009a,b; Materazzi et al., 2013; Ubertini et al., 2014a; D'Alessandro et al., 2014, 2016; Qiao et al., 2016), the main shortcoming of the DC measurement approach is that it tends to induce a time-based drift in the electrical response of the composite materials. This drift is typically represented by an increase in resistance during the measurement, without an applied external mechanical load. Many authors tend to attribute the time drift to polarization of the material under the applied electrical field (Turner et al. 1994; Chung, 2002). Other authors attribute it to changes in materials dielectric constant (Wen and Chung, 2002) or to direct piezoelectric effect (Sun et al., 2000). Possible ways of mitigating the effect of the time drift are using a control sample for comparative purposes (Azhari and Banthia, 2012), delaying measurements until the drift levels out (Materazzi et al., 2013), or using a high pass filter in the case of dynamic strain measurements (D'Alessandro et al., 2014). In any case, all these approaches result in loss of information and prevent the evaluation of the absolute values of the mechanical strain, while permitting only to measure strain changes with respect to a static or slowly varying baseline value.

As an alternative to DC measurement approaches, some authors have proposed to perform AC measurements (Fu et al., 1997; Wen and Chung, 2002; Azhari, 2008) seeking relations between mechanical strain and electrical parameters such as reactance, impedance, and phase angle. AC measurement methods appear more suitable to eliminating the time drift, as they continuously charge and discharge the sample, although some residual time drift in electrical characteristics extracted from AC measurement techniques can still be observed in many published results (Wen and Chung, 2002; Hou and Lynch, 2005; Azhari and Banthia, 2012). Another major shortcoming of AC measurements is that the use of multiple LCR meters is incompatible with the need for simultaneous sampling from different sections of a full-scale structure for distributed strain monitoring, which is a consequence of complex interactions between the different LCR's sensing currents and the high level of signal crosstalk that must be expected in practice. Other limitations of AC measurement approaches are the high cost of the electronic equipment that is typically required (Fu et al., 1997), and the need for using fast sampling digitizers and processors that further increase the costs associated with a full-scale deployment of a self-sensing system.

18.4 Applications of self-sensing concrete

18.4.1 Structural health monitoring

SsC is currently used in the form of embedded sensors for concrete structures (embedded form), or as a structural material to build structural components (bulk form), although full-scale applications are still quite scant. Figs. 18.10 and 18.11 show some photographic evidence of these two application modalities in laboratory testing.

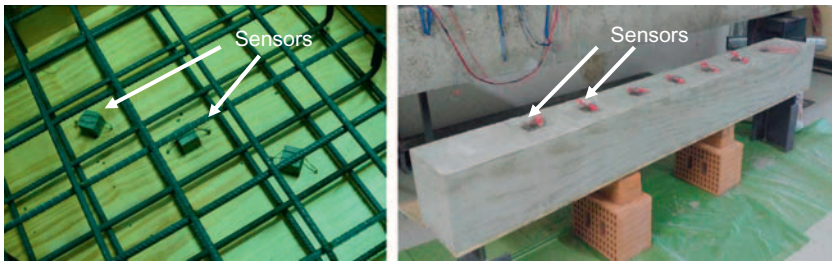


Figure 18.10 Embedding of SsC sensors in RC elements: sensors in rebar cage before casting (left), sensors along a curing beam (right).



Figure 18.11 SsC in bulk form: casting of a scaled-down reinforced SsC beam (left), wiring of the electrodes to the data acquisition system before testing (right).

SsC sensors represent an intelligent solution for embedding in civil engineering reinforced concrete and steel-concrete composite structures, providing effective monitoring of internal strain in the material (Baeza et al., 2013; Ubertini et al., 2014b). One major feature of smart concrete sensors is that they naturally bind with the monitored structure because they are made of the same or a very similar material. When using embedded sensors, the damage detection and SHM task would necessitate of some algorithm that links the local measurement of strain at selected locations to the overall structural state. Within this context, notable is the work by Han and Ou (2007b) who proposed embedded sensors made of cement-based material with carbon fiber and carbon black as promising alternatives to traditional compressive/strain sensors used in concrete structures. Fig. 18.12 (Xiao et al., 2011) shows an experimental setup of a reinforced concrete beam subjected to a four point bending test monitored by means of SsC sensors. Fig. 18.13 (Ubertini et al., 2014a) shows a similar experiment, where the ability of SsC sensors to work as dynamic, vibration-monitoring sensors was demonstrated.

To date, more pioneering work appears, showing the possibility of casting the whole structure with smart concrete or using smart concrete in a spatially distributed fashion, for example, realizing a smart rebar cover layer. Similar applications allow, in

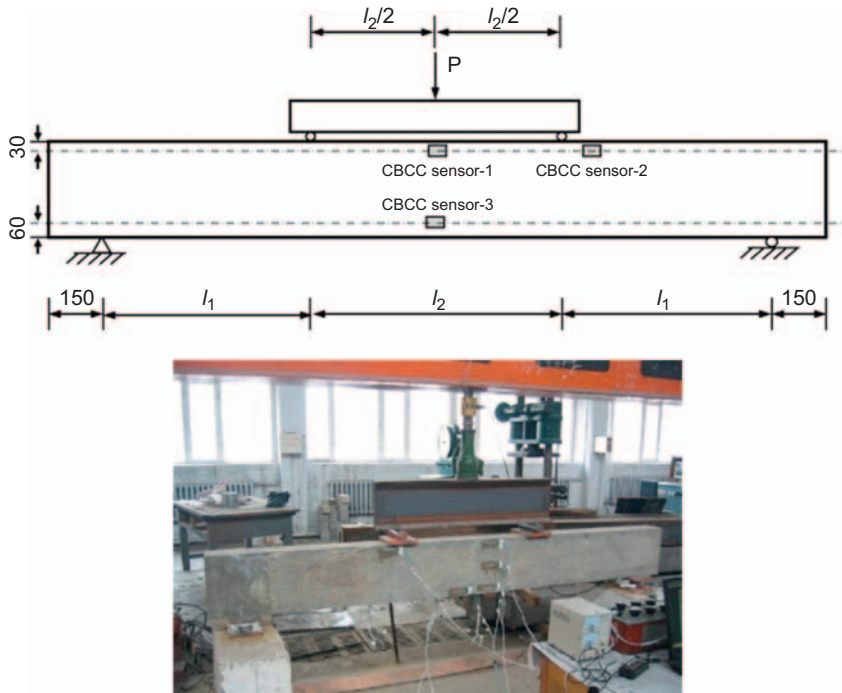


Figure 18.12 Experimental set-up of a bending concrete beam with embedded sensors made of SsC (Xiao et al., 2011).

principle, to detect, localize, and quantify cracks by exploiting electrical conductivity and strain sensitivity of the material. Although proved in various laboratory experiments, applications to full-scale structures have rarely been documented. Similar research has been carried out with reference to different types of conductive cement composites, as literature counts several examples of data-driven damage detection, mostly inferring damage from changes in electrical signal (Fu et al., 1997; Azhari and Banthia, 2012). In this framework, Chen and Liu (2008) proposed a data-driven damage detection method and showed its effectiveness in application to a carbon fiber-reinforced concrete beam subjected to a three-point-bending test. The authors demonstrated that damage could be clearly detected, yet not easily localized. Hou and Lynch (2009) proposed a method for electrical impedance tomography, specifically conceived to be used in concrete structures, allowing damage detection and localization on unreinforced engineered cement-based composites. A limitation of the proposed method was that it required repeated measurements with various applied current distributions, to solve the tomography mapping inverse problem. Another limitation of electrical impedance tomography is that it requires the use of a mathematical model to approximate the solution. Such a model can be either developed in the framework of the finite element method or of the finite difference approach, and its need is related to the circumstance that an analytical solution is generally not feasible (Hou et al.,

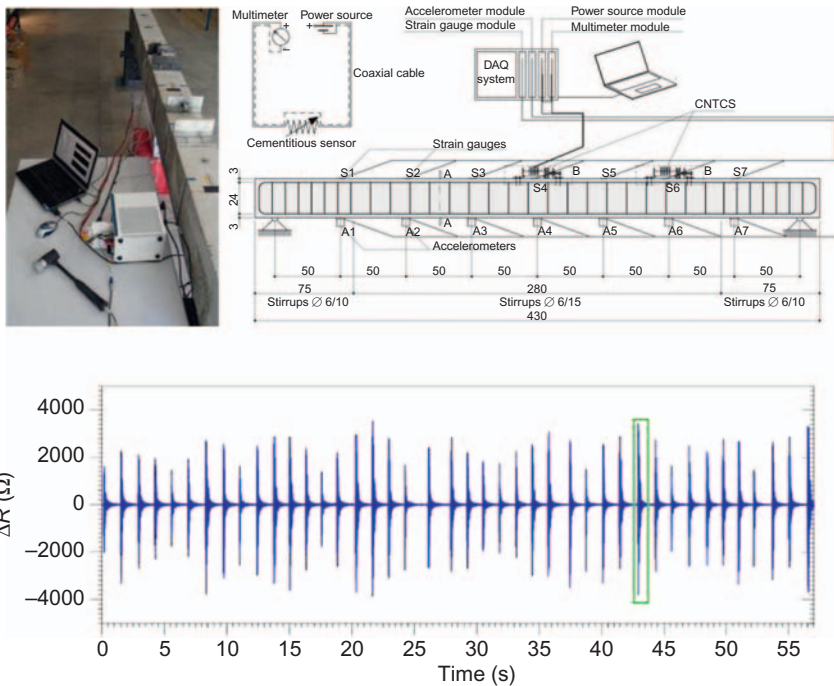


Figure 18.13 Experimental set-up of a reinforced concrete beam vibrating under hammer hits and monitored by means of traditional sensors and sensors made of SsC (Ubertini et al., 2014a).

2007). Howser et al. (2011) proposed to cast reinforced concrete joints using smart concrete doped with carbon nanofibers. Yining et al. (2013) proposed to use nanocarbon black and carbon fiber to fabricate SsC, and carried out an extensive experimental campaign on concrete beams with electric conductive nano inclusions. Clear relationships between fractional change in resistance, strain and damage were evidenced, highlighting the promise of the new nanocomposite material for use in smart structures and sustainable infrastructure management. Galao et al. (2014) investigated the use of smart cement paste with added CNF for SHM applications, showing that, at a curing age of 28 days, the material exhibited a clear strain sensing behavior, though a sufficient current density was necessary to achieve reversibility, as well as clear damage sensing properties.

18.4.2 Vehicle traffic detection

In several management operations and parking automation systems, which are crucial for pedestrians' safety in smart cities, it is necessary to detect traffic conditions. Conventional vehicle detection sensors in concrete pavements are inductive loops,

piezoelectric sensors, or optical fiber sensors embedded in the material. These solutions have the main shortcomings of dramatically reducing the operation life of the pavement and of having limited durability. Smart concrete offers great potential for traffic detection. Among the most significant features of this technology in comparison with traditional sensing systems, one could mention the easier installation and maintenance, the wider sensing area, the lower costs as commented in [Section 18.2.1](#), the higher robustness against traffic jams, the longer sensing life and the improved compatibility with the pavement. A pavement or bridge section made of smart concrete can provide valuable information such as traffic flow rates, traveling speed of vehicles, traffic density and weigh in motion, in the latter case also providing data for SHM, fatigue analysis and, more in general, structural assessment of bridges subjected to repeated loads.

[Shi and Chung \(1999\)](#) carried out a laboratory experiment to show that the electrical resistance of smart concrete doped with short carbon fibers, subjected to a distributed traffic load, decreases consistently with increasing compression, without a strong dependence on the speed, overall showing the feasibility of the material for traffic monitoring and weigh-in motion. Carbon fiber concrete was used for monitoring vehicle speed in the study by [Wei \(2003\)](#) who built a detector made of a strip component from smart concrete. The same material was used to build a weigh-in motion system by [Jian \(2004\)](#), demonstrating the capability of a strip component to detect moving loads from 18 to 100 kN. The traffic detection system proposed by [Wei and Jian](#) was improved by [Gong \(2007\)](#), who proposed the use of a high-sensitivity hybrid carbon fiber and carbon black cement mortar instead of carbon fiber concrete. The capability of SsC doped with conductive carbon-based inclusions, to be heated by flowing currents for ice formation prevention or deicing of pavements, is another notable functional property of the material that has been investigated in the literature ([Galao et al., 2016](#)).

[Han et al. \(2009b\)](#) proposed the use of smart pavements made of cement-based materials doped with carbon nanotubes. The authors found that vehicular loads can be clearly correlated with changes in electrical resistance thus enabling smart traffic monitoring. [Han et al. \(2013\)](#) further extended those results by an extensive road testing campaign, embedding self-sensing carbon nanotube concrete into a controlled pavement test section. The results demonstrated an accurate detection of the passage of different vehicles with different speed values, which allowed a conclusion that the technology is feasible for real time traffic detection at a high rate and with a low probability of false alarms. [Han et al. \(2011b\)](#) also proposed a traffic detection system made of an array of nickel powder cement sensors, demonstrating that the effects of traffic loads on the output signal of the system can be clearly separated from the effects of changes in environmental conditions leveraging the different waveforms associated to the two classes of effects.

18.4.3 Repair of existing structures

The use of smart concrete for structural repairs has not been proposed so far in the literature, due to the developments that the technology still requires to be effectively

used in full scale applications. Smart concrete can be an effective tool for repair interventions whereby it can automatically warn on the re-opening of a crack or on the formation of new damage in a repaired portion of the structure. To be used for structural repairs, the material must be provided with expansion properties, so as to carry local static stresses and to optimally adhere to the repaired structure. Its shrinkage and creep characteristics also need to be properly investigated. If used, for instance, to repair a beam-column joint in an RC-frame structure, smart concrete can give us information of the strain level attained during an earthquake and on the potential lack for lateral confinement. If used in a compressed element, such as a column, it can give us information on the maximum compressive and minimum compressive/tensile stress attained during an earthquake, also indicating potential changes in loading paths allowing for inference on global damage of the structure. Moreover, if used in the critical zone of an RC beam, where the plastic hinge develops during a strong earthquake, SsC can potentially provide information on the level of ductility that has been effectively activated during the earthquake. This would provide a direct indication of the limit state that has been locally reached in the beam, information that is directly related to the residual, vertical load-bearing capacity of the structure. It should also be mentioned that a new structure made of smart concrete or incorporating smart concrete components allows an optimal scheduling of repair activities by enabling a proper condition-based maintenance.

18.5 Trends and future developments

If properly developed, the technology of SsC can potentially enable substantial improvements in the cost-effectiveness of SHM solutions for concrete structures, potentially overcoming the limits of existing sensing solutions. Nevertheless, this technology is not yet applicable at the full-scale, which represents its major weak point. More specifically, existing cement-matrix multifunctional composites require special processing strategies, such as sonication, that are necessary to properly disperse nanoparticles within the cement matrix but are not compatible with large casting volumes. Furthermore, strain sensing has often been carried out using electrodes, while electrode-free sensing strategies need to be developed for an effective large scale deployment of strain-sensing structural composites. Other issues limiting the applications of the technology are: (1) a lack of knowledge of the electromechanical behavior of the composites, a key aspect towards their use in SHM; (2) a lack of signal processing algorithms for interpreting the electrical outputs of the multifunctional composites, especially under dynamically varying loading conditions; and (3) insufficient mechanical properties making the composites unsuitable to be used as structural materials.

Future research will be needed to address the challenge of developing new self-sensing concrete, rather than a sensor, such that the whole structure becomes self-monitoring. To achieve this goal, new smart-structural materials need to be developed, and the lack of scalability of self-sensing composites needs to be overcome, which requires the definition of fabrication procedures suitable for large structures.

Efforts will also need to be devoted to the development of measurement systems able to eliminate sensor drift (polarization) and to achieve stable measurements in time, in multichannel configurations, to enable estimation of absolute values of strain along a structure, and to allow for detection, localization and quantification of cracks by means of suitable electromechanical models of the structure under investigation. Repeatability of measurement results using nominally similar SsC specimens is another issue that must be explored in the same context.

Visionary and pioneering would be the development of distributed (continuous in space) electrode-free, contactless sensing at high sampling rates for smart concrete. This is likely possible in principle, using interference and/or absorption of electromagnetic fields, at least in unreinforced concrete elements. If successful, similar measurement systems would be of extraordinary value and would represent a milestone advance in knowledge, opening the way towards new paradigms in SHM of concrete structures.

Another needed development is broadening the understanding of the electromechanical behavior of smart concrete under dynamic mechanical loading conditions, to allow vibration monitoring and monitoring of structural response under earthquakes. New, tractable mathematical models need to be developed, so as to accurately reproduce the experimentally determined, dynamic response of the material to harmonic mechanical loading conditions of different frequencies, and the related presence of harmonics in the same response.

Application of smart concrete sensors, or of novel sensors made of nanocomposite clay, to enable smart monitoring within masonry buildings, is another research line of extraordinary interest. Such a development would allow highly enlarged fields of application of the presented technologies to the case of cultural heritage structures exposed to earthquake hazard.

Also interesting is the investigation of the beneficial effects of electrical conductivity of smart concretes towards enhancing traditional Non-Destructive Evaluation (NDE) tests, such as those based on electro-magnetic field emissions (e.g. X-rays, eddy current-based devices, rebar scope, etc.) and ultrasonic wave emissions (SONREB method). Being electrically conductive, multifunctional concrete is more permeable to electromagnetic fields. This is expected to improve the damage detection resolution and, perhaps, also the rebar detection resolution, of traditional NDE tests based on electromagnetic field emissions. Furthermore, the presence of the nanoreinforcements might also have a beneficial effect over the results of evaluation tests based on measuring the travel speed of ultrasonic waves within the material.

Acknowledgments

The support of the Italian Ministry of Education, University and Research (MIUR) through the funded Project of Relevant National Interest (PRIN) entitled “SMART-BRICK: Novel strain-sensing nano-composite clay brick enabling self-monitoring masonry structures” (protocol no. 2015MS5L27) is gratefully acknowledged.

The authors would also like to acknowledge all collaborators that have contributed so far to their research in the field of SsC and, in particular, Simon Laflamme and Austin Downey,

from Iowa State University, Rafael Castro-Triguero, from University of Cordoba and Enrique García-Macías, from University of Seville.

References

- Abu Al-Rub, R.K., Ashour, A.I., Tyson, B.M., 2012. On the aspect ratio effect of multi-walled carbon nanotube reinforcements on the mechanical properties of cementitious nanocomposites. *Constr. Build. Mater.* 35, 647–655.
- Alamusi, L.Y., Hu, N., 2010. Numerical simulations on piezoresistivity of CNT/polymer based nanocomposites. *Comput. Mater. Continua.* 20, 101–117.
- Ameli, A., Jung, P., Park, C., 2013. Electrical properties and electromagnetic interference shielding effectiveness of polypropylene/carbon fiber composite foams. *Carbon.* 60, 379–391.
- Azhari, F., 2008. Cement-based sensors for structural health monitoring. Ph.D. Thesis, University of British Columbia.
- Azhari, F., Banthia, N., 2012. Cement-based sensors with carbon fibers and carbon nanotubes for piezoresistive sensing. *Cem. Concr. Compos.* 34, 866–873.
- Baeza, F.J., Galao, O., Zornoza, E., Garcés, P., 2013. Multifunctional cement composites strain and damage sensors applied on reinforced concrete (RC) structural elements. *Materials.* 6 (3), 841–855.
- Berhan, L., Sastry, A., 2007. Modeling percolation in high-aspect-ratio fiber systems. II. the effect of waviness on the percolation onset. *Phys. Rev. E.* 75, 041121.
- Camacho-Ballesta, C., Zornoza, E., Garcés, P., 2016. Performance of cement-based sensors with CNT for strain sensing. *Adv. Cem. Res.* 28 (4), 274–284.
- Cao, J., Chung, D.D.L., 2004. Electric polarization and depolarization in cement-based materials, studied by apparent electrical resistance measurement. *Cem. Concr. Res.* 34, 481–485.
- Chang, L., Friedrich, K., Ye, L., Toro, P., 2009. Evaluation and visualization of the percolating networks in multi-wall carbon nanotube/epoxy composites. *J. Mater. Sci.* 44, 4003–4012.
- Chen, B., Liu, J., 2008. Damage in carbon fiber-reinforced concrete, monitored by both electrical resistance measurement and acoustic emission analysis. *Constr. Build. Mater.* 22 (11), 2196–2201.
- Chen, B., Wu, K., Yao, W., 2004. Conductivity of carbon fiber reinforced cement-based composites. *Cem. Concr. Compos.* 26, 291–297.
- Chen, P.W., Chung, D.D.L., 1993. Carbon fiber reinforced Concrete for smart structures capable of non-destructive flaw detection. *Smart Mater. Struct.* 2, 22–30.
- Cheng, Q., Bao, J., Park, J., Liang, Z., Zhang, C., Wang, B., 2009. High mechanical performance composite conductor: multi-walled carbon nanotube sheet/bismaleimide nanocomposites. *Adv. Funct. Mater.* 19, 3219.
- Chiarello, M., Zinno, R., 2005. Electrical conductivity of self-monitoring CFRC. *Cem. Concr. Compos.* 27, 463–469.
- Chuah, S., Pan, Z., Sanjayan, J.G., Wang, C.M., Duan, W.H., 2014. Nano reinforced cement and concrete composites and new perspective from graphene oxide. *Constr. Build. Mater.* 73, 113–124.
- Chung, D.D.L., 1998. Self-monitoring structural materials. *Mater. Sci. Eng. R. Rep.* 22 (2), 57–78.

- Chung, D.D.L., 2000. Cement reinforced with short carbon fibers: a multifunctional material. *Compos. Part B*. 31 (6), 511–526.
- Chung, D.D.L., 2002. Piezoresistive cement-based materials for strain sensing. *J. Intell. Mater. Syst. Struct.* 13 (9), 599–609.
- Chung, D.D.L., 2012. Carbon materials for structural self-sensing, electromagnetic shielding and thermal interfacing. *Carbon*. 50 (9), 3342–3353.
- Corte, L., Tiecco, M., Roscini, L., De Vincenzi, S., Colabella, C., Germani, R., et al., 2015. FTIR metabolomic fingerprint reveals different modes of action exerted by structural variants of n-alkyltropylium bromide surfactants on *Escherichia coli* and *Listeria innocua* cells. *PLoS One*. 10 (1), e0115275.
- D'Alessandro, A., Ubertini, F., Materazzi, A.L., Porfiri, M., Laflamme, S., 2014. Electromechanical modelling of new nanocomposite carbon cement-based sensors for structural health monitoring. *Struct. Health Monit.* 14 (2), 137–147.
- D'Alessandro, A., Rallini, M., Ubertini, F., Materazzi, A.L., Kenny, J., 2016. Investigations on scalable fabrication procedures for self-sensing carbon nanotube cement-matrix composites for SHM applications. *Cem. Concr. Compos.* 65, 200–213.
- Deng, F., Zheng, Q., 2008. An analytical model of effective electrical conductivity of carbon nanotube composites. *Appl. Phys. Lett.* 92, 071902.
- Di Profio, P., Germani, R., Goracci, L., Grilli, R., Savelli, G., Tiecco, M., 2010. Interaction between DNA and cationic amphiphiles: a multi-technique study. *Langmuir*. 26 (11), 7885–7892.
- Feng, C., Jiang, L., 2013. Micromechanics modeling of the electrical conductivity of carbon nanotube (CNT)–polymer nanocomposites. *Compos. A. Appl. Sci. Manuf.* 47, 143–149.
- Feng, C., Jiang, L., 2014. Investigation of uniaxial stretching effects on the electrical conductivity of CNT-polymer nanocomposites. *J. Phys. D. Appl. Phys.* 47, 405103.
- Feng, C., Jiang, L., 2015. Micromechanics modeling of bi-axial stretching effects on the electrical conductivity of CNT-polymer composites. *Int. J. Appl. Mech.* 7, 1550005.
- Fisher, F., Bradshaw, R., Brinson, L., 2003. Fiber waviness in nanotube-reinforced polymer composites: modulus predictions using effective nanotube properties. *Compos. Sci. Technol.* 63, 1689–1703.
- Fu, X., Chung, D.D.L., 1996. Self-monitoring of fatigue damage in carbon fiber reinforced cement. *Cem. Concr. Res.* 26 (1), 15–20.
- Fu, X., Chung, D.D.L., 1997. Effect of curing age on the self-monitoring behavior of carbon fiber reinforced mortar. *Cem. Concr. Res.* 27 (9), 1313–1318.
- Fu, X., Ma, E., Chung, D.D.L., Anderson, W.A., 1997. Self-monitoring in carbon fiber reinforced mortar by reactance measurement. *Cem. Concr. Res.* 27 (6), 845–852.
- Galao, O., Baeza, F.J., Zornoza, E., Garcés, P., 2014. Strain and damage sensing properties on multifunctional cement composites with CNF admixture. *Cem. Concr. Compos.* 46, 90–98.
- Galao, O., Bañón, L., Baeza, F.J., Carmona, J., Garcés, P., 2016. Highly conductive carbon fiber reinforced concrete for icing prevention and curing. *Materials*. 9 (4), Article No 281.
- García, A., Schlangen, M., Van de Ven, M., Liu, Q., 2009. Electrical conductivity of asphalt mortar containing conductive fibers and fillers. *Constr. Build. Mater.* 23 (10), 3175–3181.
- García-Macías, E., D'Alessandro, A., Castro-Triguero, R., Pérez-Mira, D., Ubertini, F., 2017a. Micromechanics modeling of the electrical conductivity of carbon nanotube cement-matrix composites. *Compos. Part B*. 108, 451–469.
- García-Macías, E., D'Alessandro, A., Castro-Triguero, R., Pérez-Mira, D., Ubertini, F., 2017b. Micromechanics modeling of the uniaxial strain-sensing property of carbon

- nanotube cement-matrix composites for SHM applications. *Compos. Struct.* 163, 195–215.
- Gdoutos, E.E., Konsta-Gdoutos, M.S., Danoglidis, P.A., Shah, S.P., 2016. Advanced cement based nanocomposites reinforced with MWCNTs and CNFs. *Front. Struct. Civ. Eng.* 10 (2), 142–149.
- Gong, S., Zhu, Z.H., 2014. On the mechanism of piezoresistivity of carbon nanotube polymer composites. *Polymer*. 55, 4136–4149.
- Gong, Z.Q., 2007. Research of the traffic monitoring system based on the pressure-sensitivity of CFRM. Ph.D. Thesis, Shantou University, China.
- Grillard, F., Jaillet, C., Zakri, C., Miaudet, P., Derr, A., Korzhenko, A., et al., 2012. Conductivity and percolation of nanotube based polymer composites in extensional deformations. *Polymer*. 53, 183–187.
- Han, B., Wang, Y., Dong, S., Zhang, L., Ding, S., Yu, X., et al., 2005. Smart concretes and structures: a review. *J. Intell. Mater. Syst. Struct.* 26 (11), 1303–1345.
- Han, B., Guan, X., Ou, J., 2007a. Electrode design, measuring method and data acquisition system of carbon fiber cement paste piezoresistive sensors. *Sens. Actuators A. Phys.* 135, 360–369.
- Han, B., Ou, J., 2007b. Embedded piezoresistive cement-based stress/strain sensors. *Sens. Actuators A. Phys.* 138, 294–298.
- Han, B., Han, B., Ou, J., 2009a. Experimental study on use of nickel powder-filled portland cement-based composite for fabrication of piezoresistive sensors with high sensitivity. *Sens. Actuators A. Phys.* 149, 51–55.
- Han, B., Yu, X., Kwon, E., 2009b. A self-sensing carbon nanotube/cement for traffic monitoring. *Nanotechnology*. 20 (44), 445501.
- Han, B., Yu, X., Ou, J., 2011a. Multifunctional and smart nanotube reinforced cement-based materials. *Nanotechnology in Civil Infrastructure: A Paradigm Shift*. Springer-Verlag, Berlin, Heidelberg, pp. 1–48.
- Han, B., Zhang, K., Yu, X., Kwon, E., Ou, J.P., 2011b. Nickel powder-based self-sensing pavement for vehicle detection. *Measurement*. 44 (9), 1645–1650.
- Han, B., Zhang, K., Yu, X., Kwon, E., Ou, J., 2012. Electrical characteristics and pressure sensitive response measurements of carboxyl MWNT/cement composites. *Cem. Concr. Compos.* 34, 794–800.
- Han, B., Zhang, K., Burnham, T., Kwon, E., Yu, X., 2013. Integration and road tests of a self-sensing CNT concrete pavement system for traffic detection. *Smart Mater. Struct.* 22, 015020.
- Han, B., Yu, X., Ou, J., 2014. *Self-Sensing Concrete in Smart Structures*. Butterworth-Heinemann, Oxford, UK.
- Han, B., Sun, S., Ding, S., Zhang, L., Yu, X., Ou, J., 2015a. Review of nanocarbon-engineered multifunctional cementitious composites. *Compos. Part A*. 70, 69–81.
- Han, B., Ding, S., Yu, X., 2015b. Intrinsic self-sensing concrete and structures: a review. *Measurements*. 59, 110–128.
- Heeder, N., Shukla, A., Chalivendra, V., Yang, S., Park, K., 2012. Electrical response of carbon nanotube reinforced nanocomposites under static and dynamic loading. *Exp. Mech.* 52, 315–322.
- Hilding, J., Grulke, E.A., Zhang, Z.G., Lockwood, F., 2003. Dispersion of carbon nanotubes in liquids. *J. Dispers. Sci. Technol.* 24, 1–41.
- Hou, T.C., Lynch, J.P., 2005. Conductivity-based strain monitoring and damage characterization of fiber reinforced cementitious structural components. *Proc. SPIE*. 5765, 419–429.

- Hou, T.C., Lynch, J.P., 2009. Electrical impedance tomographic methods for sensing strain fields and crack damage in cementitious structures. *J. Intell. Mater. Syst. Struct.* 20 (11), 1363–1379.
- Hou, T.C., Loh, K.J., Lynch, J.P., 2007. Spatial conductivity mapping of carbon nanotube composite thin films by electrical impedance tomography for sensing applications. *Nanotechnology*. 18 (31), 315501.
- Howser, R., Dhonde, H., Mo, Y., 2011. Self-sensing of carbon nanofiber concrete columns subjected to reversed cyclic loading. *Smart Mater. Struct.* 20 (8), 085031.
- Hu, N., Karube, Y., Yan, C., Masuda, Z., Fukunaga, H., 2008. Tunneling effect in a polymer/carbon nanotube nanocomposite strain sensor. *Acta Mater.* 56, 2929–2936.
- Hu, N., Fukunaga, H., Atobe, S., Liu, Y., Li, J., 2011. Piezoresistive strain sensors made from carbon nanotubes based polymer nanocomposites. *Sensors*. 11, 10691–10723.
- Jia, X.W., 2009. Electrical conductivity and smart properties of Fe1- σ O waste mortar. Ph.D. Thesis, Chongqin University, China.
- Jian, H.L., 2004. Research of the traffic weighting monitoring system based on the pressure-sensitivity of CFRC. Ph.D. Thesis, Shantou University, China.
- Kang, I., Schulz, M.J., Kim, J.H., Shanov, V., Shi, D., 2006. A carbon nanotube strain sensor for structural health monitoring. *Smart Mater. Struct.* 15, 737–748.
- Komori, T., Makishima, K., 1977. Numbers of fiber-to-fiber contacts in general fiber assemblies. *Text. Res. J.* 47, 13–17.
- Konsta-Gdoutos, M.S., Aza, C.A., 2014. Self sensing carbon nanotube (CNT) and nanofiber (CNF) cementitious composites for real time damage assessment in smart structures. *Cem. Concr. Compos.* 53, 110–128.
- Konsta-Gdoutos, M.S., Metexa, Z.S., Shah, S.P., 2010. Highly dispersed carbon nanotube reinforced cement-based materials. *Cem. Concr. Res.* 40 (7), 1052–1059.
- Kuronuma, Y., Takeda, T., Shindo, Y., Narita, F., Wei, Z., 2012. Electrical resistance-based strain sensing in carbon nanotube/polymer composites under tension: analytical modeling and experiments. *Compos. Sci. Technol.* 72, 1678–1682.
- Le, J.L., Du, H., Pang, S.D., 2014. Use of 2D graphene nanoplatelets (GNP) in cement composites for structural health evaluation. *Compos. Part B.* 67, 555–563.
- Li, G.Y., Wang, P.M., Zhao, X., 2007. Pressure-sensitive properties and microstructure of carbon nanotube reinforced cement composites. *Cem. Concr. Compos.* 29, 377–382.
- Li, H., Xiao, H., Ou, J., 2004. A study on mechanical and pressure-sensitive properties of cement mortar with nanophase materials. *Cem. Concr. Res.* 34, 435–438.
- Li, H., Xiao, H., Ou, J., 2006. Effect of compressive strain on electrical resistivity of carbon black-filled cement-based composites. *Cem. Concr. Compos.* 28, 824–828.
- Li, H., Xiao, H., Ou, J., 2009. Smart concrete, sensors and self-sensing concrete structures. *Key Eng. Mater.* 400–402, 69–80.
- Li, N., Wu, S.P., Liu, C.H., 2008. Investigation of static and dynamic response of graphite and carbon fiber modified conductive asphalt-based composite. *Key Eng. Mater.* 385–387, 469–472.
- Lin, C., Wang, H., Yang, W., 2010. Variable percolation threshold of composites with fiber fillers under compression. *J. Appl. Phys.* 108, 013509.
- Liu, X.M., Wu, S.P., 2009. Research on the conductive asphalt concrete's piezoresistivity effect and its mechanisms. *Constr. Build. Mater.* 23 (8), 2752–2756.
- Liu, X.M., Wu, S.P., Ye, Q.S., Qiu, J., Li, B., 2008. Properties evaluation of asphalt-based composites with graphite and mine powders. *Constr. Build. Mater.* 22, 121–126.
- Loh, K.J., Lynch, J.P., Shim, B., Kotov, N., 2008. Tailoring piezoresistive sensitivity of multi-layer carbon nanotube composite strain sensors. *J. Intell. Mater. Syst. Struct.* 19, 747–764.

- Luo, J., Duan, Z., Zhao, T., Li, Q., 2011. Hybrid effect of carbon fiber on piezoresistivity of carbon nanotube cement-based composite. *Adv. Mater. Res.* 143–144, 639–643.
- Materazzi, A.L., Ubertini, F., D’Alessandro, A., 2013. Carbon nanotube cement-based transducers for dynamic sensing of strain. *Cem. Concr. Compos.* 37, 2–11.
- McEvoy, M.A., Correll, N., 2015. Materials that couple sensing, actuation, computation, and communication. *Science*. 347 (6228), 1261689.
- Meehan, D., Wang, S., Chung, D., 2010. Electrical-resistance-based sensing of impact damage in carbon fiber reinforced cement-based materials. *J. Intell. Mater. Syst. Struct.* 21, 83–105.
- Mondal, P., Shah, S.P., Marks, L.D., 2008. Nanoscale characterization of cementitious materials. *ACI Mater. J.* 105, 174–179.
- Mori, T., Tanaka, K., 1973. Average stress in matrix and average elastic energy of materials with misfitting inclusions. *Acta Metall.* 21, 571–574.
- Pham, G.T., Park, Y., Liang, Z., Zhang, C., Wang, B., 2008. Processing and modeling of conductive thermoplastic/carbon nanotube films for strain sensing. *Compos. B. Eng.* 39, 209–216.
- Pisello, A.L., D’Alessandro, A., Sambuco, S., Rallini, M., Ubertini, F., Asdrubali, F., et al., 2017. Multipurpose experimental characterization of smart nanocomposite cement-based materials for thermal-energy efficiency and strain-sensing capability. *Sol. Energy Mater. Sol. Cells.* 161, 77–88.
- Qiao, B., Xie, N., Meng, J., Yan, T., Feng, L., Zhong, J., 2016. Percolation effect on the piezoresistivity of carbon nanotube/cement composite as a stress self-sensing material. *J. Test. Eval.* 44 (6), 2261–2269.
- Sanli, A., Muller, C., Kanoun, O., Elibol, C., Wagner, M.F.X., 2016. Piezoresistive characterization of multi-walled carbon nanotube-epoxy based flexible strain sensitive films by impedance spectroscopy. *Compos. Sci. Technol.* 122, 18–26.
- Seidel, G.D., Lagoudas, D.C., 2009. A micromechanics model for the electrical conductivity of nanotube-polymer nanocomposites. *J. Compos. Mater.* 43, 917–941.
- Shah, S.P., Konsta-Gdoutos, M.S., Metexa, Z.S., Mondal, P., 2009. Nanoscale modification of cementitious materials. *Nanotechnology in Construction 3*. Springer, Berlin, Heidelberg, pp. 125–130.
- Shi, Z.Q., Chung, D.D.L., 1999. Carbon fiber-reinforced concrete for traffic monitoring and weighing in motion. *Cem. Concr. Res.* 29, 435–439.
- Siddique, R., Mehta, A., 2014. Effect of carbon nanotubes on properties of cement mortars. *Constr. Build. Mater.* 50, 116–129.
- Simmons, J.G., 1963. Electric tunnel effect between dissimilar electrodes separated by a thin insulating film. *J. Appl. Phys.* 34, 2581–2590.
- Sindu, B.S., Sasmal, S., Gopinath, S., 2014. A multi-scale approach for evaluating the mechanical characteristics of carbon nanotube incorporated cementitious composites. *Constr. Build. Mater.* 50, 317–327.
- Sun, M., Liu, Q., Li, Z., Hu, Y., 2000. A study of piezoelectric properties of carbon fiber reinforced concrete and plain cement paste during dynamic loading. *Cem. Concr. Res.* 30 (10), 1593–1595.
- Takeda, T., Shindo, Y., Kuronuma, Y., Narita, F., 2011. Modeling and characterization of the electrical conductivity of carbon nanotube-based polymer composites. *Polymer.* 52, 3852–3856.
- Tallman, T., Wang, K., 2013. An arbitrary strains carbon nanotube composite piezoresistivity model for finite element integration. *Appl. Phys. Lett.* 102, 011909.

- Tamini, A., Hassan, N.M., Fattah, K., Talachi, A., 2016. Performance of cementitious materials produced by incorporating surface treated multiwall carbon nanotubes and silica fume. *Constr. Build. Mater.* 114, 934–945.
- Taya, M., Kim, W., Ono, K., 1998. Piezoresistivity of a short fiber/elastomer matrix composite. *Mech. Mater.* 28, 53–59.
- Theodosiou, T., Saravanos, D., 2010. Numerical investigation of mechanisms affecting the piezoresistive properties of CNT-doped polymers using multi-scale models. *Compos. Sci. Technol.* 70, 1312–1320.
- Tiecco, M., Di Profio, P., Germani, R., Savelli, G., 2009. Synthesis of novel 5'-uridine-head amphiphiles as model for DNA molecular recognition. *Nucleosides Nucleotides Nucleic Acids.* 28 (10), 911–923.
- Tiecco, M., Cardinali, G., Roscini, L., Germani, R., Corte, L., 2013. Biocidal and inhibitory activity screening of de novo synthesized surfactants against two eukaryotic and two prokaryotic microbial species. *Colloids Surf. B. Biointerfaces.* 111, 407–417.
- Turner, R.C., Fuijier, P.A., Newnham, R.E., Shrout, T.R., 1994. Materials for high temperature acoustic and vibration sensors: a review. *Appl. Acoust.* 41 (4), 299–324.
- Ubertini, F., Materazzi, A.L., D'Alessandro, A., Laflamme, S., 2014a. Natural frequencies identification of a reinforced concrete beam using carbon nanotube cement-based sensors. *Eng. Struct.* 60, 265–275.
- Ubertini, F., Laflamme, S., Ceylan, H., Materazzi, A.L., Cerni, G., Saleem, H., et al., 2014b. Novel nanocomposite technologies for dynamic monitoring of structures: a comparison between cement-based embeddable and soft elastomeric surface sensors. *Smart Mater. Struct.* 23 (4), 12 pp.
- Vigolo, B., Penicaud, A., Coulon, C., Sauder, C., Pailler, R., Journet, C., et al., 2000. Macroscopic fibers and ribbons of oriented carbon nanotubes. *Science.* 290, 1331–1334.
- Wang, X., Bradford, P.D., Liu, W., Zhao, H., Inoue, Y., Maria, J., et al., 2011. Mechanical and electrical property improvement in CNT/nylon composites through drawing and stretching. *Compos. Sci. Technol.* 71, 1677–1683.
- Wang, X.F., Wang, Y.L., Jin, Z.H., 2002. Electrical conductivity characterization and variation of carbon fiber reinforced cement composite. *J. Mater. Sci.* 37, 223–227.
- Wansom, S., Kidner, N.J., Woo, L.Y., Mason, T.O., 2006. AC-impedance response of multi-walled carbon nanotube/cement composites. *Cem. Concr. Compos.* 28, 509–519.
- Wei, W.B., 2003. A research of the traffic vehicle-speed measuring system based on the pressure-sensitivity of CFRC. Ph.D. Thesis, Shantou University, China.
- Wen, S., Chung, D.D.L., 1999. Carbon fiber-reinforced cement as a thermistor. *Cem. Concr. Res.* 29, 961–965.
- Wen, S., Chung, D.D.L., 2000. Damage monitoring of cement paste by electrical resistance measurement. *Cem. Concr. Res.* 30, 1979–1982.
- Wen, S., Chung, D.D.L., 2002. Cement-based materials for stress sensing by dielectric measurement. *Cem. Concr. Res.* 32 (9), 1429–1433.
- Wen, S., Chung, D.D.L., 2006. Model of piezoresistivity in carbon fiber cement. *Cem. Concr. Res.* 36, 1879–1885.
- Wen, S., Chung, D.D.L., 2007a. Double percolation in the electrical conduction in carbon fiber reinforced cement-based materials. *Carbon.* 45, 263–267.
- Wen, S., Chung, D.D.L., 2007b. Partial replacement of carbon fiber by carbon black in multi-functional cement-matrix composites. *Carbon.* 45 (3), 505–513.
- Weng, G.J., 2010. A dynamical theory for the Mori-Tanaka and Ponte Castañeda-Willis estimates. *Mech. Mater.* 42, 886–893.

- Wu, S.P., Mo, L.T., Shui, Z.H., 2003. Piezoresistivity of graphite modified asphalt-based composites. *Key Eng. Mater.* 249, 391–396.
- Xiao, H., Li, H., Ou, J., 2011. Strain sensing properties of cement-based sensors embedded at various stress zones in a bending concrete beam. *Sens. Actuators A. Phys.* 167 (2), 581–587.
- Xie, P., Gu, P., Beaudoin, J.J., 1996. Electrical percolation phenomena in cement composites containing conductive fibers. *J. Mater. Sci.* 31, 4093–4097.
- Yang, B., Cho, K., Kim, G., Lee, H., 2014. Effect of CNT agglomeration on the electrical conductivity and percolation threshold of nanocomposites: a micromechanics based approach. *Comput. Model. Eng. Sci.* 103, 343–365.
- Yasuoka, T., Shimamura, Y., Todoroki, A., 2010. Electrical resistance change under strain of CNF/flexible-epoxy composite. *Adv. Compos. Mater.* 19, 123–138.
- Yi, Y., Berhan, L., Sastry, A., 2004. Statistical geometry of random fibrous networks, revisited: waviness, dimensionality, and percolation. *J. Appl. Phys.* 96, 1318–1327.
- Yining, D., Chen, Z., Han, Z., Zhang, Y., Pacheco-Torgal, F., 2013. Nano-carbon black and carbon fiber as conductive materials for the diagnosing of the damage of concrete beam. *Constr. Build. Mater.* 43, 233–241.
- Yu, X., Kwon, E., 2009. A carbon nanotube/cement composite with piezoresistive properties. *Smart Mater. Struct.* 18, 5 pp.
- Zeng, X., Xu, X., Shenai, P.M., Kovalev, E., Baudot, C., Mathews, N., et al., 2011. Characteristics of the electrical percolation in carbon nanotubes/polymer nanocomposites. *J. Phys. Chem. C* 115, 21685–21690.

Bacteria-based concrete

19

Nele De Belie¹, Jianyun Wang¹, Zeynep B. Bundur² and Kevin Paine³

¹Ghent University, Ghent, Belgium, ²Ozyegin University, Istanbul, Turkey,

³University of Bath, Bath, United Kingdom

19.1 Introduction

The presence of microorganisms on concrete and stone structures has been feared in the past, since they can provoke mechanical erosion by growth of hyphae, chemical dissolution, and precipitation reactions due to excreted organic and inorganic acids. Extracellular polymeric substances (EPS) excreted by microorganisms to protect themselves within biofilms may cause discoloration and surface scaling. However, over the last few decades, microorganisms have also been investigated for the positive effects they can exert on mineral construction materials. These research efforts mainly rely on microbially induced calcium carbonate precipitation (MICP) and focus on its application for the consolidation of natural stone and concrete, soil consolidation and sand cementation, as an additive for strength improvement of concrete, for manual crack repair, and self-healing of cracks in concrete.

The positive and negative influences mentioned above have been previously reviewed by De Belie (2010). A review by De Muynck et al. (2010) focused mainly on the different microbial pathways, bacterial strains, and application processes used for biodeposition by different teams around the world, especially the French group including the University of Nantes, the Laboratory for the Research of Historic Monuments (LRMH) and the company Calcite Bioconcept (Le Metayer-Levrel et al., 1999); the research group at the University of Granada, Spain (Rodriguez-Navarro et al., 2003), the Ghent University team (Dick et al., 2006; De Belie et al., 2006; De Muynck et al., 2008a,b); and the Biobrush consortium (BIORemediation for Building Restoration of the Urban Stone Heritage) in the United Kingdom (May, 2005). Techniques that also deviate from the application of bacteria and nutrients to the stone were discussed, such as the application of organic matrix molecules extracted from *Mytilus californianus* shells, to induce the precipitation of calcium carbonate within the pores of the stone (Bioreinforce consortium, Italy; Tiano et al., 1992). However, because of the low yield of this extraction, Tiano et al. (2006) later proposed the alternative use of acid functionalized proteins such as polyaspartic acid.

More recent critical reviews on the application of microorganisms in concrete for strengthening and crack healing purposes include Wang et al. (2016), De Belie and Wang (2016), and De Belie (2016). Mainly bacteria following the pathways of urea decomposition, oxidation of organic acids (aerobic process), or nitrate reduction (anaerobic process) have been studied for these purposes. It was concluded that, for bacteria mixed into fresh concrete, the effects on concrete strength are

variable. Application of bacteria for surface consolidation has been shown to reduce water absorption and increase durability. Microbial self-healing of cracks in concrete shows promising results at the laboratory scale. The use of self-protected mixed cultures especially opens perspectives for practical application. However, their self-healing efficiency needs to be further proven in larger concrete elements, and under non-ideal conditions. The use of denitrifying cultures for concurrent self-healing and corrosion inhibition is a promising new strategy (Ersan et al., 2016; De Belie, 2016).

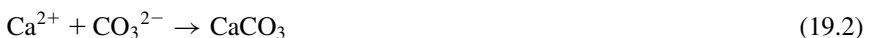
19.2 Production of bacteria suitable for concrete applications

19.2.1 Microbially induced carbonate precipitation through different metabolic pathways

Most bacteria can induce the precipitation of CaCO_3 if given suitable conditions (Boquet et al., 1973). However, the mechanisms of the precipitation of bacterial CaCO_3 are various according to different metabolic pathways. Essentially, different bacteria have different carbonatogenesis. Meanwhile, there are a lot of external factors directly or indirectly governing the biogenic formation, resulting in different carbonate yield under different conditions by the same bacterial strain. The discussion in this section is focused on the three types of bacteria, which have been used for concrete applications.

19.2.1.1 Bacteria involving the nitrogen cycle by degradation of urea (ureolytic strains)

So far, the most commonly used bacteria in cement-based materials are alkali-tolerant ureolytic strains. These types of bacteria can decompose urea into ammonium/ammonia and carbonate ions. With the existence of Ca^{2+} ions, CaCO_3 can be formed (Eqs. 19.1 and 19.2).



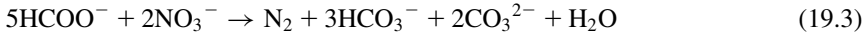
Model strains in this group are *Sporosarcina pasteurii* (also named *Bacillus pasteurii*), *Sporosarcina ureae*, *Bacillus sphaericus*, and *Bacillus megaterium*. Theoretically, 1 mol CaCO_3 can be formed if 1 mol urea is supplied. However, that is not always the case, due to the fact that the bio-chemical reaction process is controlled by an urease enzyme, which is generated through bacterial activities. Therefore, the carbonate productivity relies mostly on bacterial ureolytic activity instead of the concentration of the reactants as in a normal chemical reaction.

A high bacterial urease activity indicates a high carbonate production. Without catalyst, the urea hydrolysis rate is extremely slow ($3 \times 10^{-10} \text{ s}^{-1}$); while urease catalyzed urea hydrolysis is much faster ($3 \times 10^4 \text{ s}^{-1}$), which implies an increase by a factor of 10^{14} . Therefore, the bacterial ureolytic activity (or urease activity) is crucially important for the formation of CaCO_3 . *Bacillus sphaericus* was reported to have a high urease activity of around 40 mM urea hydrolyzed/OD per hour (Wang et al., 2010). At optimal conditions (10^8 cells/mL, 20 g/L yeast extract, 1 M urea and 1 M Ca^{2+} , 28°C), *B. sphaericus* cells can precipitate 60 g/L CaCO_3 within 1 day. Without yeast extract, 800 mM urea was decomposed within 3 days, equivalent to 26 g CaCO_3 /L per day (Wang, 2013). Urea is the substrate of urease. There was an upper limit for the amount of urea that can be used for a certain amount of bacteria. Above this limit, an inhibitory effect was seen and the amount of urea decomposition was decreased. For instance, the upper limit for 10^7 and 2×10^7 cells/mL was 1.5 M and 2 M urea, respectively (Wang et al., 2017a). This indicates that the maximum amount of CaCO_3 can be formed under a specific bacterial concentration. Ca^{2+} also influences bacterial ureolytic activity. High concentrations of Ca^{2+} ions can be toxic for the bacteria since they only need limited amount to regulate their metabolic activities. With a bacterial concentration of 10^8 cells/mL, no significant influence was observed on bacterial ureolytic activity in the presence of 0.9 M Ca^{2+} . With a decreased bacterial concentration (10^7 cells/mL), significant urea decomposition was still obtained at 0.5 M Ca^{2+} (Wang et al., 2017a). At a lower temperature (10°C), CaCO_3 precipitation rate greatly dropped to around 5 g/L per day. *Bacillus sphaericus* spores had a slower CaCO_3 precipitation than vegetative cells, due to the fact that spores are dormant and take time to first become active, while vegetative cells are always in an active state (Wang et al., 2017a). *Bacillus sphaericus* spores (10^8 spores/mL), can decompose 20 g/L urea within 1 day. In the case of 10^7 spores/mL, 3 days were needed for completely hydrolysis of 20 g/L urea, equivalent to 10 g/L per day CaCO_3 . This value was reduced to about 4 g/L per day CaCO_3 at 10°C .

19.2.1.2 Bacteria involving the nitrogen cycle by dissimilation of nitrates

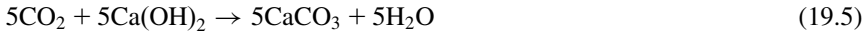
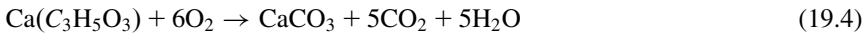
Bacterially-induced CaCO_3 precipitation, through nitrate reduction by different strains such as *Pseudomonas denitrificans* and *Castellaniella denitrificans*, has been investigated for soil consolidation (Karatas, 2008; Van Paassen et al., 2010). Recently, resilient denitrifiers have been used for concrete self-healing due to their suitability for functioning under oxygen-limited conditions (Ersan et al., 2015a). Bacterial urea hydrolysis requires oxygen to initiate bacterial activity (spore germination), which can be a restricting factor for deep crack healing. Under oxygen limited conditions, denitrifiers can use nitrate (NO_3^-) as an alternative electron acceptor for oxidation of organic carbon and generate CO_3^{2-} and HCO_3^- ions, which are necessary for CaCO_3 precipitation (Eq. 19.3). A CaCO_3 precipitation of 7 g CaCO_3 /g $\text{NO}_3\text{-N}$ per day could be achieved by *Diaphorobacter nitroreducens* (Ersan et al., 2015b). Furthermore, the resilience of *D. nitroreducens* enabled

repetitive CaCO_3 precipitation with a constant precipitation rate of $0.72 \sim 1.2$ g/L per day CaCO_3 .



19.2.1.3 Bacteria involving the carbon cycle by oxidation of organic carbon

Another widely used type of bacteria for concrete self-healing are some of the alkaliophilic strains, which can degrade organic compounds into CO_2 and H_2O . In a high pH environment (such as concrete pore solution), CO_2 can be easily converted to CO_3^{2-} , and with the presence of Ca^{2+} , CaCO_3 can be formed. Typical strains in this group are *Bacillus cohnii*, *Bacillus pseudofirmus*, and *Bacillus alkalinitrilicus* (Jonkers et al., 2010; Wiktor and Jonkers, 2011). In this case, calcium lactate was used as the organic carbon source, due to its less negative effect on the mechanical properties of concrete. Therefore, the overall bio-chemical reaction can be the following (Eqs. 19.4 and 19.5). Theoretically, one equivalent of calcium lactate can be converted to six equivalents of CaCO_3 under alkaline pH. Yet, the real precipitate rate was not given in this case. When acetate was used as the carbon source, a CaCO_3 yield of 1.7 g/L per day was obtained by use of *B. cohnii* (Wang, 2013).



Given the relative importance of Eq. (19.5) to the volume of CaCO_3 formed, some research has considered eliminating the addition of extra Ca^{2+} as a precursor. As an example, researchers have utilized self-healing components consisting of glucose, brewer's yeast, and *Bacillus mucilaginosus* (Chen et al., 2016). The healing mechanism consists of the fermentation of the glucose by the yeast to ethanol and CO_2 . The bacteria promote the conversion of CO_2 to CaCO_3 through the reaction, with soluble Ca^{2+} normally present in concrete. The effect of ethanol on the performance of concrete was not discussed. Furthermore, Zhang et al. (2016) have identified that excessive Ca^{2+} in concrete inhibits bacterial-induced CaCO_3 precipitation. They have argued that, due to the poor solubility of $\text{Ca}(\text{OH})_2$, the concentration of free Ca^{2+} is optimum for bacterial-induced CaCO_3 precipitation and that an extra Ca^{2+} source might not be necessary. Nevertheless, as discussed previously, other researchers have shown that addition of an extra Ca^{2+} source is recommended.

In summary, ureolytic strains have the highest carbonate yield compared with the other two types of bacteria. Therefore, more studies were focused on using ureolytic strains. One has to be aware, however, of the related ammonia production, which may raise environmental concerns. Even with a lower CaCO_3 productivity, aerobic oxidation of organic carbon produces less toxic byproducts, and anoxic

oxidation of organic carbon can be used in oxygen limited conditions, which eliminates the disadvantages of the ureolytic strains.

19.2.2 Application of mixed versus pure cultures and industrial scale fermentation of bacteria

With the aim of obtaining a low cost bacterial additive for concrete, Ghent University has partnered with the company Avecom NV (Belgium) in the EC-funded projects SHeMat (Training Network for Self-Healing Materials: from Concepts to Market) and HEALCON (Self-healing concrete to create durable and sustainable concrete structures). [Silva et al. \(2015a\)](#) calculated that the production of axenic ureolytic spores would imply an operational expense (OPEX) cost of more than 400 €/kg of bio-agent. It appeared that axenic production of bacterial spores presents a high cost due to the need for sterile production conditions, which is not compatible with the low material prices in concrete industry. Therefore, a non-axenic production of ureolytic bacterial spores was suggested. [Silva et al. \(2015b\)](#) developed a new selection process to obtain a material that he called “Cyclic EnRiched Ureolytic Powder” or CERUP, containing an efficient ureolytic microbial community.

It is known that sporulation can be induced by several external triggers, such as the lack of essential nutrients, and unfavorable conditions such as extreme pH values, high salt concentrations or large variations in temperature. It is important to determine the timing and quantity of sporulation for experimental purposes and for eventual commercial production. Sporulation in various *Bacillus* species is normally induced by reduced levels of nutrients ([Errington, 2003](#)), but additional elemental Mn^{2+} is required during the active growth phase ([Charney et al., 1951](#)). Recent work has shown that, for typical bacteria used in self-healing concrete, such as *B. pseudofirmus* and *B. cohnii*, 100% sporulation can occur within 24 hours under optimum sporulation conditions ([Sharma et al., 2017](#)). Therefore commercial production of spores could be rapid, reducing production times and cost.

[Silva et al. \(2015b\)](#) decided to expose a mixed bacterial culture, present in a side stream from vegetable processing, to thermal cycles including maxima between 60 and 70°C for a period of 2 hours. In these conditions, some spore-forming bacterial strains have the ability to sporulate fast enough to allow them to survive. In parallel, considerable amounts of urea were added, to stimulate mainly the ureolytic bacteria. Ureolytic activity and calcium carbonate precipitation capability of CERUP produced in 5 and 50 L reactors were proven to be as good as the benchmark *B. sphaericus* (20 g urea/L decomposed in 24 hours). As an additional benefit, self-immobilization and salt encapsulation can be achieved during the production of non-axenic cultures if the appropriate conditions are provided. This means that these cultures are able to protect themselves from harsh conditions, which avoids the need for additional encapsulation. Plain incorporation of CERUP in concrete was found to be efficient at levels of 0.5% and 1% of the cement weight, whereas

the OPEX cost per unit of CERUP is about 40 times lower than the OPEX cost of a *B. sphaericus* axenic culture.

Similarly, special granules called “activated compact denitrifying core” (ACDC) were cultivated by [Ersan et al. \(2015c, 2016\)](#). ACDC is a denitrifying microbial community protected by various bacterial partners and obtained in a sequential batch reactor by applying selective stress conditions. The sequential batch reactor was operated with anoxic/aerobic period sequence, and minimal nutrient solution (COD:N=5:1) was used as feed (4 times/day). The initial pH of the feed solution was set between 9 and 9.5 by using concentrated NaOH solution (10 M). ACDC granules were harvested from the reactor after 2 months and subsequently dried ([Fig. 19.1](#)—left). It was estimated that the OPEX cost range to obtain ACDC would be around 17.4 €/kg. [Ersan et al. \(2015c\)](#) added ACDC granules (0.5–2 mm) consisting of 70% bacteria and 30% inorganic salts into mortar (0.5 w/w cement) without any additional protection, while $\text{Ca}(\text{NO}_3)_2$ and $\text{Ca}(\text{HCOO})_2$ were used as nutrients. After crack creation in 28-day-old mortar specimens and immersion in water for another 28 days, effective crack closure up to 0.5 mm was achieved ([Fig. 19.1](#)—right). Microbial activity during crack healing was monitored through weekly NO_x analysis, which revealed that $92\% \pm 2\%$ of the available NO_3^- was consumed by the bacteria. Another set of specimens were cracked after 6 months curing, and it was proven that cracks occurring in mature specimens were also

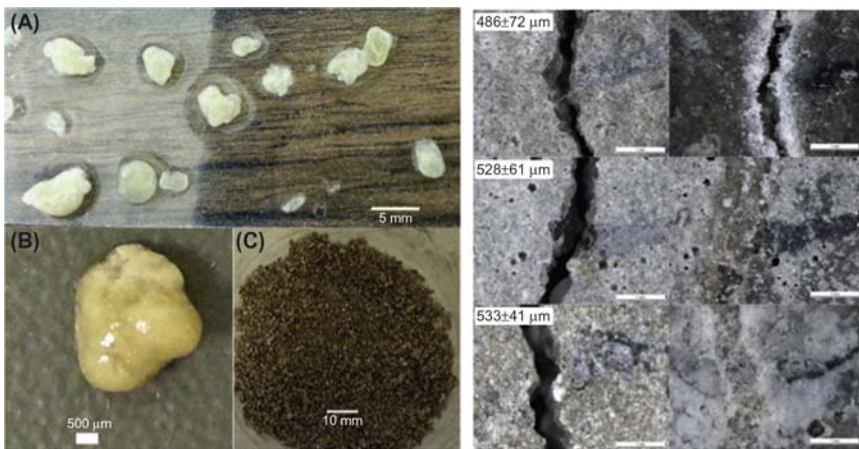


Figure 19.1 Left: appearance of the harvested ACDC granules wet (A, B) and after drying (C); Right: initial (after crack formation) and final (after 28 days incubation) appearance of cracks created in 28-day-old specimens (top: abiotic control (reference + 5% nutrients); middle: specimen with 0.5% ACDC and 5% nutrients; bottom: specimen with 1% ACDC and 5% nutrients; nutrients being 2% $\text{Ca}(\text{HCOO})_2$ + 3% $\text{Ca}(\text{NO}_3)_2$; amounts are in terms of w/w cement; scale bar is 1 mm).

Source: From Erşan, Y.C., January 21, 2016. Microbial nitrate reduction induced autonomous self-healing in concrete. Ph.D. in Bio-Engineering, Ghent University ([Erşan, 2016](#)).

healed. Overall, healed ACDC-containing specimens could be distinguished from the control specimens by the wide range of healed crack widths, the mineral formation at the inner crack surfaces, and up to 70% less capillary water absorption. It was, furthermore, shown that the ACDC induced passivation of steel in corrosive electrolyte solution (0.05 M NaCl) by producing 57 mM NO_2^- in 1 week (Ersan et al., 2016).

19.3 Direct addition of bacteria to concrete

The main challenge in the production of bio-based concrete is to find a way to incorporate microorganisms within the cement-based matrix. Perhaps, the simplest approach is to directly suspend the cells in the mixing water. However, since the microorganisms will be embedded in cement paste, it is important to find a strain that can tolerate these highly alkaline conditions, can survive the mixing process, and can remain viable with limited access to nutrients. It is also possible to add the required nutrients to the mixing water along with the bacterial cells, but it is still questionable whether the cells could resist the stress due to hardening of cement paste. Thus, even though direct addition of the bacteria is a simpler approach compared to other methods—including encapsulation—more challenges rise considering the long-term performance of the cells.

One of the main advantages of incorporating the cells directly into the matrix is reduction in porosity, which leads to improved compressive strength and durability. Ramachandran et al. (2001) studied the influence of *Pseudomonas aeruginosa* and *S. pasteurii* (formerly known as *B. pasteurii*) on compressive strength when they were directly added to mortar mix water. At 7 days there was a compressive strength increase in all mortar samples regardless of the bacterial strain type, concentration, or whether they were incorporated dead or alive. However, at 28 days, the highest compressive strength value was obtained when live *S. pasteurii* cells were incorporated. *Pseudomonas aeruginosa* cells are abundant in nature and could synthesize extracellular polysaccharide (EPS), but the study showed that incorporation of extracellular materials to the mix did not increase the strength of mortar. *Sporosarcina pasteurii* were found to be more efficient, due to their ability to induce biogenic calcium carbonate via urea hydrolysis. Whereas the compressive strength was increasing from 7 to 28 days with addition of live cells, an opposite trend was observed when killed cells were incorporated. This suggests that the increase in compressive strength is directly related to metabolic state of the microorganism. It was stated that the observed strength gain at 7 days with dead cells was due to microorganisms acting as organic fibers. Over time, however, they decomposed and lost their efficiency (Ramachandran et al., 2001).

Even though, *S. pasteurii* was found to be more efficient in improving compressive strength, since it exhibits urease enzyme activity, an increase in compressive strength has also been reported in cases where different types of bacteria were used. Ghosh et al. (2005, 2009) suspended anaerobic *Shewanella* and *Escherichia coli*

species in mixing water without any additional nutrients. Results of their tests suggested that compressive strength could be enhanced due to gehlenite deposition when *Shewanella* cells were added to mortar (Ghosh et al., 2009). Moreover, the increase in compressive strength was found to be related to concentration of cells and reduction in pore diameter. There was not any strength change in samples when only *E. coli* cells were added.

Achal et al. (2011) investigated the possible use of *B. megaterium* cells in fly ash-amended mortar to improve compressive strength and decrease porosity. The cells were grown in a nutrient medium broth containing urea (NBU), and water content of the mix was replaced by the grown bacterial culture. Compared to the control specimen, a 21% increase in 28-day compressive strength was seen when *B. megaterium* culture was added to the concrete without any fly ash. Conversely, this increase was not observed at 7 days (Achal et al., 2011). At 28 days, specimens with 10% fly ash replacement showed 19% strength increase relative to control specimen without microorganisms. Similarly, water permeability in concrete samples was decreased with incorporation of bacterial culture. It was believed that the increase in compressive strength was due to plugging of pores due to calcite precipitation induced by the microorganisms (Achal et al., 2011). Moreover, Achal et al. (2012) examined the impact of bacterial culture on the pullout strength of rebars in reinforced concrete. *Bacillus* sp. CT-5, isolated from commercially available cement, was cultured in two different nutrient media: one containing urea and nutrient broth (NB) and the other one containing urea and corn steep liquor (CSL), which was actually an effluent from the corn wet-milling industry. Subsequently, the mixing water was replaced by the bacterial culture grown in CSL nutrient medium. Then, the specimens were cured in the same nutrient medium. After 7 days, a pullout test was conducted. The pullout strength of the concrete specimen containing the NB medium was 35 kN, and that of the CSL medium was 31 kN, which were both higher than for neat mortar (26 kN). The authors attributed the increase in pullout strength to the bacterial calcium carbonate (CaCO_3) precipitation (Achal et al., 2012).

Jonkers and Schlangen (2006) incorporated the spores of four different strains, including *S. pasteurii*, *B. cohnii*, *Bacillus halodurans*, and *B. pseudofirmus*. The cells were found to be viable up to 10 days and there were no adverse effects on compressive and tensile strength. Jonkers et al. (2010) suspended *B. cohnii* endospores in mixing water. Even though the cell concentration was decreasing with time, viable cells were found in 135-day-old samples. While there was not any change in compressive strength, there was a decrease in pore size diameter. As a related note, the loss of spore viability was attributed to the decrease in matrix pore diameter sizes. Given the well documented resilience of *Bacillus* endospores to adverse conditions and the relatively consistent survival over a long time period (135 days) there is an argument that recovery of spores from the cement matrix is the limiting factor (Sharma et al., 2017).

Even though direct addition of cells was found to be advantageous in decreasing porosity and increasing compressive strength, Portland cement-based systems are challenging due to the complex series of physio-chemical reactions occurring from

the reaction of cement with water. [Achal et al. \(2011\)](#) showed that *B. megaterium* could survive up to 28 days when it is directly added to both mortar and concrete. The concentration of microorganisms was found to be close to initial values when viable plate counts were conducted on 3-day specimens. However, the percent of microorganisms that survived decreased from 7 to 28 days. According to the results obtained, fly ash addition in both mortar and concrete also increased the number of viable microorganisms. [Basaran \(2013\)](#) obtained similar results, showing that *S. pasteurii* cells were found to be viable up to 330 days when the mixing water was replaced by grown bacterial culture. Moreover, only 2% (2×10^3 cells/g of mortar) of the initially mixed vegetative *S. pasteurii* cells were found to be viable, and approximately 40% of these cells were metabolically active within the cement paste matrix. The presence of these cells increased the CaCO_3 content and this led to an increase in compressive strength ([Bundur et al., 2015](#)). Incorporation of the bacterial culture, however, highly influenced the hydration kinetics such that the induction period was exacerbated as long as 10 hours and this effect was more pronounced with increasing cell concentration ([Bundur et al., 2015](#)). This delay was attributed to the presence of yeast extract in the nutrient medium. [Amiri and Bundur \(2016\)](#) used CSL instead of yeast extract in the nutrient medium. Vegetative *S. pasteurii* cells were grown in a nutrient medium containing urea and CSL; the water content of the mix was replaced by this grown bacterial culture. The results suggested that use of CSL decreased the duration of the induction period compared to use of yeast extract, without causing any adverse effect on compressive strength ([Amiri and Bundur, 2016](#)).

Another challenge regarding direct addition of microorganisms is that the addition of certain concrete admixtures could affect the viability of cells. Since they will be exposed to the pore solution, any change in the ingredients might affect the cell viability. Interestingly, it was found that use of 0.2% ammonium salt-based air entraining agents (AEA) by weight, highly influenced the viability of vegetative cells within the first 28 days of mixing ([Bundur et al., 2017](#)). There was a decrease in viable cell concentration with the addition of AEA when the vegetative cells were inoculated with their nutrients. This was attributed to the working mechanisms of AEA, where the non-polar ends of AEA act as a barrier between the nutrients and the bacterial cells. Conversely, the negative impact of AEA on cell viability was not observed when the vegetative cells were suspended in mixing water without any nutrients. Seeing as there were no nutrients added, the addition of AEA would not act like a barrier for the cells to reach the nutrients. Thus, the viable cell concentration at 28 days was found to be similar when the cells were suspended in mixing water, with or without AEA addition.

The key question is whether the remaining low bacterial concentration would be able to remediate cracks in concrete. Even though the cells could be viable up to 330 days in mortar, the remaining cell concentration was as low as 2×10^3 *S. pasteurii* cells per gram of mortar ([Basaran, 2013](#)). [Wang \(2013\)](#) and [Erşan et al. \(2015a\)](#) have shown that the bacterial cell concentration should be at least in the order of 10^6 cells/mL in order to induce biogenic carbonate precipitation. Since there was not any protection of cells, there was a substantial decrease in cell

concentration when the vegetative cells were directly incorporated to mortar, regardless of the strain type (Achal et al., 2011; Basaran, 2013). These results suggested that crack remediation could only be obtained at early ages (i.e., 7 days), when the bacterial concentration was higher than the threshold value. Liu et al. (2016) showed that self-healing of internal microcracks could be triggered in 7-day old mortar samples. The compressive strength of cracked mortar samples could be fully recovered when vegetative cells were directly added to the mortar mix with their nutrient medium and the nutrients were sprayed periodically for further curing. Similarly, Amiri and Bundur (unpublished data) replaced the mixing water with vegetative *S. pasteurii* cells grown in urea-CSL nutrient medium. Flexural cracks were induced in 7-day old mortar samples, and then the beams were submerged in curing solution containing calcium nitrate, urea and CSL for further curing. After 50 days of subsequent curing, flexural cracks as large as 0.3 mm were completely sealed.

Finally, addition of bacterial biofilms to mortar can induce other properties than the ones mainly discussed in this chapter. Grumbein et al. (2016) have added bacterial biofilms, either freshly harvested or as a lyophilized powder, to mortar. They obtained a material that exhibits an increased roughness on the microscale and the nanoscale, and on both the outer and inner surface. Accordingly, the hybrid mortar not only resisted wetting but also suppressed the uptake of water by capillary forces. Contact angles of water droplets on mortar strongly increased from below 30 to 90 degrees. The bacterial strain they used was *Bacillus subtilis* 3610, which robustly forms biofilms with strong hydrophobic surface properties when grown on enriched agar (LB^{plus} agar). Pei et al. (2015) have studied the use of *B. subtilis* cell walls as viscosity modifying agent (VMA). The cell wall of Gram-positive *B. subtilis* is mainly composed of peptidoglycan, which contains long polysaccharide backbone chains and peptide side groups. Incorporation of *B. subtilis* cell walls increased the apparent viscosity of cement paste (Pei et al., 2015), increased the compressive strength, and decreased the porosity (Pei et al., 2013).

In Chapter 20 of this book (Feugeas et al., 2017), the performance of a bio-based admixture was evaluated as a corrosion inhibitor for steel bars used in concrete. The bio-based admixture prepared from bacterial extracellular substances was shown to significantly improve the resistance of steel towards uniform and localized corrosion in simulated pore solutions with added sulphates and chlorides.

19.4 Application of bacteria for surface protection and manual crack repair

19.4.1 Bacteria-based surface protection

Bacteria-based surface protection is realized by a bio-deposition process, in which a bacteria culture and a deposition medium are applied to the surface of the matrix, resulting in the formation of a (continuous) biogenic CaCO₃ layer. This layer has

good cohesion with the surface and works as an extra coating or a barrier to prevent/decrease the intrusion of aggressive substances into the matrix, hence, the surface properties and durability can be improved. The earliest research on bacterial CaCO_3 precipitation for building applications, was aimed at surface protection and consolidation of historical building materials, because the often-used organic coatings have the problems of incompatibility with natural stone and aging, resulting in further degradation (Delgado Rodrigues, 2001; Moropoulou et al., 2003). Regarding the compatibility with building materials, the product first should be inorganic. A good product should have a strong cohesion with the matrix, no peel off, and should be dense enough to prevent/reduce the penetration of corrosive substances. Bacterially induced CaCO_3 precipitation meets all these criteria for surface application on historical stones (Tiano et al., 1999; Rodriguez-Navarro et al., 2003; Qian et al., 2009; De Muynck et al., 2011).

Promising results (surface strengthening, increase of water impermeability and freeze-thaw resistance, etc.) for stone consolidation, both in lab scale and on-site use, have brought along the extensive studies of applying bacterial CaCO_3 precipitation for surface protection of cementitious materials. Most concrete degradation starts from the surface and leads to durability problems. Surface treatment to strengthen concrete surfaces is, therefore, an effective way to enhance concrete durability. The principle of the treatment is the same as for the stones. Yet, due to the special characteristics of concrete, two issues were raised. One is the need for a suitable bacterial source. Many carbonate precipitating bacteria, such as *Bacillus cereus*, *Myxococcus xanthus*, *B. subtilis*, *B. sphaericus*, *S. pasteurii* (*B. pasteurii*), etc., have been utilized for stone surface protection and consolidation. Most pioneer strains were isolated from natural carbonate-producing environments. Consequently they are more used to moderate pH conditions and may not be suitable to be applied on concrete. Compared to historical stones (mostly calcareous stones), cementitious materials have a much higher pH. Normally the surface pH varies from 8 (extremely carbonated surface) to 13.5 (fresh concrete surface). Therefore, only the alkali-tolerant and alkaliphilic strains can be used in this case. So far, the most frequently used are the alkali-tolerant ureolytic strains *S. pasteurii* and *B. sphaericus* (De Muynck et al., 2008a,b; Qian et al., 2009). Bacterial urea hydrolysis is easily controlled and yields high carbonate production within a short period, which facilitates the bio-deposition treatment for a broad range of applications. Recently, an alkaliphilic non-ureolytic strain, *B. cohnii*, was also investigated for the surface treatment of mortar specimens (Xu et al., 2014).

The other aspect to be considered is the treatment procedure. The bio-deposition treatment is often performed by means of immersion, spraying or brushing of a bacteria culture and deposition medium onto the surface (Rodriguez-Navarro et al., 2003; Dick et al., 2006; De Muynck et al., 2008a,b, 2011; Le Metayer-Levrel et al., 1999; Tiano et al., 1999). Among them, immersion has been the most frequently used technique for lab tests due to the fact that bacteria are provided with the most optimal conditions, sufficient water, nutrients, oxygen, and a moderate temperature during immersion, resulting in the formation of a remarkable amount of biogenic CaCO_3 and hence a profound protective effect on the surface. However, immersion

is difficult to realize in practice, so spraying and brushing were adopted for on-site application of the stone surface protection treatments (Le Metayer-Levrel et al., 1999; Tiano et al., 1999). The bacterial culture and deposition media were repeatedly sprayed or brushed on the surface until a considerable amount of bio- CaCO_3 formed. Compared to historical stones, normal concrete has a much denser structure with a low porosity ($\sim 1\%$) and small pore sizes (most pores $< 0.5 \mu\text{m}$), so retention of bio-agents on the surface is quite limited after spraying or brushing. Thus, immersion was most often selected for the laboratory treatment of cementitious materials to ensure a sufficient contact between the surface and the bacterial agents. A two-step immersion-based bio-deposition treatment on mortar and concrete was first applied by De Muynck et al. (2008a,b). The specimens were first immersed into a 1-day-old bacterial culture (*B. sphaericus*) for 24 hours. Subsequently, the specimens were transferred into a deposition medium consisting of urea and Ca source for another 3 days. During the first immersion step, the bacterial cells were expected to penetrate into the surface pores or attach to the surface of the specimen. And hence, biogenic- CaCO_3 was precipitated by the absorbed bacteria after they made contact with the urea and Ca source in the second immersion step. The amount of bio-precipitation largely depends on the amount of the bacteria absorbed onto the specimens, which relies on the pore properties (pore size and porosity) of the matrix. De Muynck et al. (2011) demonstrated that bio-deposition treatment was more effective and feasible for macroporous stones than for microporous stones. For cementitious materials, a higher w/c results in a more porous structure and hence more bacteria absorbed in the matrix. However, no significant difference was found in the amount of bacteria at different depths ($0 \sim 10 \text{ mm}$) in the mortar specimens with w/c of 0.5 and 0.7 (De Muynck et al., 2008a), even if the latter had a higher porosity. The average amount of the absorbed bacteria was only 10^3 cells/g, much less than the expected value (10^6 cells/g). Most of the bacteria were distributed on the surface. The limited penetration depth indicated that the bio-deposition is more a surface phenomenon for cementitious materials. While for porous stones, deep penetration resulted not only in a surface protection effect but also surface layer consolidation (De Muynck et al., 2011). In contrast, Qian et al. (2009) applied a one-step bio-deposition treatment. The specimens were fully immersed in a mixed medium consisting of *S. pasteurii* cells, urea and Ca^{2+} . CaCO_3 formed as a continuous dense layer, mainly on the top surface of the specimen. In order to ensure that plenty of bacteria stay on the surface and realize long-time contact with the deposition agents, Xu et al. (2014) applied a modified immersion procedure by making a pond on the top surface of the specimen.

Promising results were achieved after the bio-deposition treatment on the cementitious matrix. Due to the barrier effect of the formed CaCO_3 layer, the water absorption and chloride diffusion coefficient were greatly decreased by $65\% \sim 90\%$ and $20\% \sim 23\%$, depending on the porosity of the specimens (De Muynck et al., 2008a). The higher contact angle realized by the CaCO_3 layer may also have contributed to the decreased water absorption (De Muynck et al., 2008b). Furthermore, the gas permeability coefficient was found to have dropped, resulting in an improved carbonation resistance. Meanwhile, the freeze-thaw resistance of the

specimens was also improved accordingly. Qian et al. (2009) found that the precipitated bio-CaCO₃ not only decreased the surface permeability (~50%) but also provided a higher acid resistance than normal abiotic CaCO₃. An extra advantage of applying the bio-deposition treatment is that the changes in the chromatic aspect of the surface were quite limited compared to the conventional coatings.

Two aspects should be highlighted in order to achieve a significant treatment efficiency: the quantity of bio-CaCO₃, and its precipitation rate. The former determines the thickness of the layer and hence the plugging effect; while the latter, together with the organic matter, determines the cohesion within the layer and the bond with the matrix (Rodriguez-Navarro et al., 2003). An effective way to yield more bio-CaCO₃ is to increase bacterial concentration. To ensure a sufficient precipitation, a bacterial concentration of at least 10⁶ cells/mL was needed, preferably 10⁸ cells/mL (Wang, 2013). In a two-step immersion system, concentrated bacterial cells (realized by centrifugation) are recommended in the first immersion step, to ensure an enhanced absorption onto the specimens. Okwadha and Li (2010) found that the concentration of carbonate ions was increased more than 30% after the cell concentration was increased from 10⁶ to 10⁸ cells/mL. Urea decomposition rate relied more on bacterial concentration than on initial urea concentration. From a chemical point of view, the amount of Ca²⁺ and urea (source of CO₃²⁻) directly determines the yield of CaCO₃. Though the cementitious matrix itself provides a Ca reservoir, an external Ca source was demonstrated to be necessary for a robust bio-precipitation (De Muynek et al., 2008b). Okwadha and Li (2010) showed that the largest amount of bio-CaCO₃ was obtained with 666 mM urea and 250 mM Ca²⁺, with 2 × 10⁸ cells/mL. Qian et al. (2009) obtained the thickest bio-layer at 200 mM urea and 200 mM Ca²⁺. On the other hand, it was found in Wang et al. (2010) that the optimal concentrations of urea and Ca²⁺ were 0.5 M, at a bacterial concentration of 10⁸ cells/mL. Higher bacterial concentration is often concomitant with higher amount of urea and Ca source, resulting in a larger CaCO₃ productivity. The precipitation rate greatly affects the quality of the CaCO₃ layer. De Muynek et al. (2013) found that the highest and fastest production of CaCO₃ was obtained at a high temperature of 37°C, due to the high ureolytic activity at this temperature. However, the highest weight loss during sonication attack also occurred in this case, compared to treatments performed at lower temperatures (10, 20, and 28°C). The reason is that the bacterial urease enzyme-based reaction proceeds fast at a high temperature, resulting in supersaturation in a short time and hence a rapid precipitation. If CaCO₃ forms too fast, it only loosely accumulates on the surface, with a low cohesion and bond with the matrix. Consequently, it is easily debonded, resulting a low protective effect. The bacteria CaCO₃ formed at low supersaturation had better adhesion with the matrix and higher consolidative effect than the crystals that had been deposited fast at high supersaturation (Rodriguez-Navarro et al., 2003). In most of the studies, the bacteria had already generated urease inside their cells before the start of the bio-deposition treatment and so urea decomposition was immediately triggered. In the study of Qian et al. (2009), in order to slow down the CaCO₃ precipitation rate, the bacteria were grown without urea, and hence, no urease formed in advance in the cells before the immersion of the specimen. The

urease formation was induced with the presence of urea and was decelerated with the presence of Ca^{2+} . Therefore, the overall precipitation rate was slowed down, resulting in a dense and cohesive CaCO_3 layer on the surface. In summary, a lasting moderate (instead of transient high) carbonate production is more favorable to achieve an efficient bio-deposition treatment (Wang et al., 2016).

Furthermore, a novel application of biodeposition for surface consolidation of concrete and stone is found in the consolidation of recycled aggregates for a sustainable concrete production. High water absorption is the main drawback of recycled aggregates, affecting the concrete workability and durability. Biodeposition can be applied to precipitate bacterial CaCO_3 on the surface and in the pores of recycled aggregates, hence function as a barrier against water penetration. Wang et al. (2017b) found that two subsequent immersion treatments for recycled concrete aggregates (CA) and mixed aggregates (MA) in a *B. sphaericus* culture (3×10^8 cells/mL) with urea (0.5 M) and Ca-nitrate (0.5 M), allowed to deposit a layer of biogenic CaCO_3 that had a good cohesion and strong bond with the aggregate surface. The use of these biotreated recycled aggregates in concrete enable an increase to the concrete's compressive strength and decrease its water absorption.

19.4.2 Bacteria-based manual crack repair

Bacteria-based manual crack repair is realized by a bio-cementation process in which bacterial cells, precipitation precursors and filling materials (if needed, depending on the crack size) were mixed beforehand and then were manually plugged or injected into cracks. The cracked specimens were further submerged into a medium consisting of precipitation precursor for 3~28 days. The formed biogenic CaCO_3 solely or together with the filling materials block the cracks. The bio- CaCO_3 functions as a cement gluing loose particles together, which together with the filling material results in a strong repair mortar. Similar as for surface protection application, the most widely used bacteria for this application are the alkali-tolerant ureolytic strains *S. pasteurii* and *B. sphaericus* (Bang et al., 2001; Ramachandran et al., 2001; Ramakrishnan et al., 2001; De Belie and De Muynck, 2009; Van Tittelboom et al., 2010). Bang et al. (2001) were among the first to apply bacterial remediation of concrete cracks (Ramachandran et al., 2001; Ramakrishnan et al., 2001). The artificial cracks (around 3 mm wide) of the specimens were filled with a wet mix of *B. pasteurii* cells, nutrients and sand, and then were immersed in a urea- CaCl_2 medium for 28 days. A significant increase (10%~27%) of compressive strength was obtained (Ramachandran et al., 2001). The sand particles were strongly adhered to each other by bacterial precipitation. The "glue" effect of this bio-cement could be due to the extracellular organic compounds of bacteria (Rodriguez-Navarro et al., 2003). However, it was found that the surface layer was much denser and harder than other parts because most of the precipitation was formed there. The authors assumed the reason could be that the limited amount of oxygen in the deeper part of the crack restricts the bacterial activity. However, Wang et al. (2017a) demonstrated that oxygen has no effect on ureolytic activity of vegetative cells, being an enzyme-controlled bio-reaction. Regarding this, the

proper reason could be that the first deposited CaCO_3 in the surface layer hindered/reduced the ongoing penetration of urea and Ca^{2+} to the deeper part of the crack. One possible solution is to pre-mix everything together before injecting it into the crack: the filling materials, the bacteria, urea and Ca^{2+} . To protect bacterial cells, [Bang et al. \(2001\)](#) first immobilized bacterial cells into polyurethane (PU) foam strips, which were then put inside the cracks of ~ 3 mm in width. The specimens were also submerged in the urea- CaCl_2 medium for 28 days. The advantage of PU is that it has a lot of open pores, resulting in an enhanced penetration of precipitation precursors. The 7-day compressive strength was improved in the specimens with bacterial repair materials compared to those without bacteria. Yet, no regain in tensile strength or stiffness was found. This is attributed to the fact that no chemical bond exists between the PU strips and the crack wall. The PU and the biogenic CaCO_3 purely functioned as a crack filler. A silica sol gel was used in [De Belie and De Muynck \(2009\)](#) and [Van Tittelboom et al. \(2010\)](#) as filling material, to be injected into cracks together with *B. sphaericus* cells. The specimens were then immersed into a medium consisting of urea and Ca-nitrate. Silica sol gel immediately solidified into gel when it met with Ca^{2+} . The gel matrix can entrap most of the bacteria to avoid bacterial loss during the immersion period. A decreased water permeability was observed in both the cracked specimens injected with pure silica sol gel and with silica sol gel-bacteria. The biogenic CaCO_3 in the gel matrix did not contribute too much to the decrease of the water permeability. One drawback of using gel is that it shrinks in a dry condition. In this case, the quantity of the biogenic CaCO_3 should be as high as possible to compensate for the shrinkage effect. Therefore, the ratio between this kind of filling materials and bacterial agents need to be optimized. For some narrow micro cracks, bacterial CaCO_3 can be applied without filling materials. [Sarode and Mukherjee \(2009\)](#) submerged cracked specimens into a bio-mixture consisting of bacterial cells, urea and CaCl_2 for 28 days. It was found that the precipitation was formed in the crack and on the surface, resulting in an enhanced impermeability.

In summary, bacterial-induced CaCO_3 precipitation, together with some suitable filling materials is promising for the repair of the existing cracks. However, much effort is still needed to optimize the composition of the repair agents (bacterial concentration, urea and Ca-salts concentration, the ratio between filling materials and bio-active agents, etc.) to obtain a high quantity of precipitation and a high quality bacteria-based repair. The bond between filling materials and crack surface is of crucial importance and its effect on the durability of the repair cannot be ignored ([Wang et al., 2016](#)).

19.5 Protection strategies for bacteria in concrete

19.5.1 Encapsulation or immobilization of the bacteria

Due to the concerns with limited viability of spores in cement pastes, it is often recommended that the spores should be immobilized prior to their addition to self-

healing concrete. Three general approaches to immobilization have been studied, each with their own distinct advantages and disadvantages: (1) encapsulation in porous solids; (2) microencapsulation in gels; and (3) pellets and flakes.

The most widely used method, due to its simplicity and low cost, is immobilization in lightweight aggregates. Jonkers and his co-workers have immobilized bacterial spores in expanded clay aggregates of 1–4 mm in size (Wiktor and Jonkers, 2011). Impregnation of the spores was carried out twice under vacuum and the resulting expanded clay aggregates contained 1.7×10^5 bacterial spores per gram of aggregate. Calcium lactate (6% by mass of aggregate) and yeast extract (<0.1% by mass of aggregate) were also encapsulated. It was shown that upon cracking these encapsulated particles were capable of providing healing in mortars. There was no significant effect on setting, which demonstrates that there was no leaching of detrimental compounds.

Research at the University of Bath has used a similar approach, in which spores of *B. pseudofirmus* were immobilized in 1–4 mm perlite—a lightweight aggregate commonly used in microbiological applications as a plant growth medium. Unlike Wiktor and Jonkers (2011), the nutrients (calcium acetate and yeast extract) were encapsulated separately from the bacteria spores to minimize the potential for germination before a crack is formed. The perlite was impregnated with the spores by soaking the perlite in the appropriate volume of solution until all solution was absorbed. The resulting perlite contained 4.1×10^9 spores/g of perlite. Due to concerns with spores and nutrients leaching from the perlite in the mix, the perlite was coated with a double layer of sodium silicate and cement powder (Paine et al., 2016).

Erşan et al. (2016) have further investigated the use of expanded clay particles and granular-activated carbon (GAC), both of 0.5–2 mm in size as carriers of bacterial cells. Cell impregnation was carried out under vacuum saturation and the resulting particles contained approximately 10% by mass of cells of *D. nitroreducens* or *P. aeruginosa* and 0.15 M NaCl. No additional protection was considered necessary to prevent leaching of the cells from the particles.

Furthermore, diatomaceous earth, a fine porous powder, has been considered as a carrier of bacterial spores (Wang et al., 2012). Due to the nature of the pores, however, it was observed that the spores sorbed on the surface of the particles and not within the powder itself. This confirms that not all porous particles/lightweight aggregates are necessarily suitable for encapsulation of bacterial spores. Nevertheless, the diatomaceous earth created a protective microenvironment for the bacteria, which allowed them to maintain their ureolytic activity.

A further disadvantage of porous solids, such as lightweight aggregates, is that the strength and stiffness of the concrete is reduced, due to the typical replacement of strong aggregates with a weaker aggregate. Loss of strength occurs because the porous solids break (a key component of their ability to work as a healing carrier) at lower strengths than conventional aggregates. They form the weakest part within the concrete, instead of the cement paste matrix. The loss of strength of the mortar is generally related to the volume of porous solids used. Diatomaceous earth, on the other hand, had a positive effect on strength due to its pozzolanic nature.

Erşan et al. (2015b) have compared the influence of six commercially available protection approaches (diatomaceous earth, metakaolin, expanded clay, granular

activated carbon, zeolite and air entrainment) on mortar setting and compressive strength when combined with either *B. sphaericus* spores or *D. nitroreducens* and their respective nutrients. The influence of two novel, self-protected, bacterial agents (CERUP and ACDC) was also investigated. Their study revealed that, among the tested protection methods for axenic cultures, only zeolite and air entrainment caused a decrease in compressive strength of mortar. However, the protection materials were only added as 5% w/w cement to the mortar (apart from the air entrainment that was added as 1% w/w cement).

As an alternative, researchers at Ghent, in collaboration with the Flemish company Devan, have developed impermeable microcapsules as an encapsulant of spores. In their patented concept, the microcapsule walls were melamine based, flexible in wet environment to enhance resistance during concrete mixing, and more brittle after drying, allowing rupture and release of their contents when cracks appear in the hardened concrete. Research at Bath, in collaboration with the company Lambson, has synthesized gelatin/acacia gum microcapsules to encapsulate spores using complex coacervation. Spores of both *B. subtilis* and *B. pseudofirmus* were homogenized into mineral oil to break up some of the macroscopic aggregates of spores and evenly disperse them through the carrier oil (Fig. 19.2). Both encapsulations went without significant processing problems, giving good yields and sizes of around 180 μm , with no visually identifiable loss of spores from the oil phase. As with those microcapsules developed at Ghent, the microcapsules have been shown to transition between hydrated and dried conditions, converting from a rubbery soft state to a glassy stiff state (Kanellopoulos et al., 2017). This transition enables the microcapsules to survive the wet mixing process but rupture successfully upon crack formation.

Furthermore, researchers at Ghent have pioneered the use of hydrogels as an encapsulant of spores. Hydrogels are hydrophilic gels that have a network of polymer chains created by synthesis of polymer solutions. Spores can be incorporated in the hydrogel to create bio-hydrogels by incorporating a spore suspension into the polymer solution prior to synthesis. Bio-hydrogels investigated by Wang et al. (2014a)

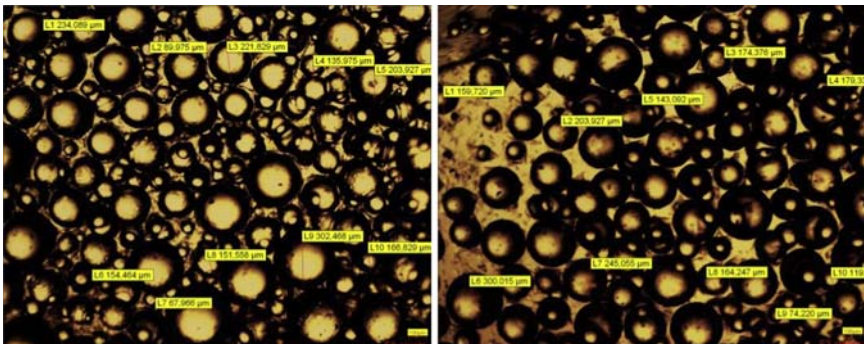


Figure 19.2 Micrograph of encapsulated spores. (Left) Encapsulated spores of a mix of *B. subtilis* and *B. pseudofirmus* and (right) encapsulated spores of *B. pseudofirmus* alone. Source: Courtesy of University of Bath.

incorporated approximately 10^8 cells/mL of hydrogel. These bio-hydrogels were then used in self-healing concrete at a dosage of 5% by mass of cement. They were shown to be a promising carrier due to their ability to both protect spores during mixing and casting, and then their ability to swell and act as a water reservoir for spore germination and bacterial activity once cracking occurs. Wang et al. (2015) have also considered a modified-alginate bio-hydrogel containing around 4×10^9 spores/g of hydrogel, used in mortars at 2% by mass of cement. The bio-hydrogels were shown to have good cell-entrapping capacity and prevented no more than 10% of spores from releasing during the mixing process.

A similar approach has been developed by Palin et al. (2016), where the spores were encapsulated in a bead consisting of calcium alginate and mineral precursors as a bio-composite. The calcium alginate beads were produced by pumping dropwise a precursor solution of magnesium acetate, yeast extract and 7×10^8 of unidentified bacteria spores per liter into a calcium acetate solution. The beads were found to provide considerable crack healing potential, due to a combination of calcite precipitation and swelling of the bead due to interactions between water and the hydrophilic groups of the alginate.

Furthermore, research at Shenzhen has developed a system in which microcrystalline cellulose was mixed with spores and encapsulated in a shell of ethyl cellulose. The survival, viability, and calcium carbonate precipitating capability of the spores after encapsulation has been verified (Han and Xing, 2017).

TU Delft has also proposed a method for producing particles almost fully consisting of active ingredients by roller compaction of powders to sheets, with subsequent milling to flakes in the size range of the sand fraction (1–4 mm) (Jonkers and Mors, 2012). A typical property of the flakes is solubility in water, which is beneficial upon matrix cracking and water ingress, dispersing the healing agent in the crack volume. A challenge, however, is to retain particle integrity during the wet mixing stage of mortar or concrete production. Partial particle dissolution may be prevented by application of a protective coating around the soluble particle. The coating material can be inorganic (e.g., cement paste or geopolymer) or organic (e.g., calcium cross linked polyvinyl alcohol alginate or lactic acid derivatives) (de Koster et al., 2015). In order to retain equal active healing agent content in the mortar or concrete mixture, the addition of particles went from 30% by volume for light weight aggregates to 1% for the proposed flakes.

19.5.2 Effects of nutrients and calcium source on the concrete properties and need for encapsulation

All three major pathways for bacteria-based self-healing: (1) urea hydrolysis, (2) aerobic respiration, and (3) nitrate reduction, rely on the formation of calcium carbonate as the healing compound. Consequently, in almost all research, calcium-based compounds are used as the precursor.

For urea hydrolysis the source of Ca^{2+} for most early research was calcium chloride, although more recent work has tended towards using calcium nitrate

(Wang et al., 2014a,b) to avoid adding chloride ions into the concrete. Calcium nitrate is compatible with concrete and is commonly used as an anti-freeze agent and setting accelerator, and is effective as an anodic inhibitor for defense against chloride induced corrosion in concrete (Østnor and Justnes, 2011). Furthermore, calcium nitrate in concrete is considered to accelerate cement hydration both by the nucleating action of its dissolved ions and through a direct reaction with calcium hydroxide in solution to form calcium hydroxynitrate (Karagöl et al., 2013). Indeed, when added directly to concrete for use in the urea hydrolysis pathway calcium nitrate has been shown to accelerate hydration, reduce setting times (Luo and Qian, 2016a) and increase the degree of hydration (Wang et al., 2014b). In self-healing concrete, Wang et al. (2014b) used a hydrated form of calcium nitrate (containing around 30% by mass of water) at a dosage of 8% by mass of cement—which is equivalent to a dosage of 5.6% of calcium nitrate by mass of cement.

For the aerobic respiration self-healing pathway, a number of organic calcium precursors have been used. Jonkers et al. (2010) have suggested that the only organic calcium precursor that may be added directly to the concrete, in any significant quantity and not cause a loss of strength, is calcium lactate. It has also been shown that calcium lactate may actually increase compressive strength when used at percentages up to 1%–2% by mass of cement (Paine, 2016), and potentially up to 3% by mass of cement and higher (Luo and Qian, 2016a). The effects of calcium lactate on setting of cement are, however, less unclear. Luo and Qian (2016b) have shown that calcium lactate may reduce initial setting time but extend the final setting times by as much as 50%. Elsewhere it has been shown that calcium lactate may increase initial setting times, but accelerate final setting (Paine, 2016).

More recently, it has been considered best practice to encapsulate the calcium precursors prior to addition to concrete (Wiktor and Jonkers, 2011; Paine et al., 2016). Consequently, this could allow for a wider range of calcium salts to be used, as there will be no interaction between the encapsulated salt and the cement matrix—unless there is a failure of the capsules during mixing or casting. For this reason, research is looking at alternatives to calcium lactate, including calcium acetate and calcium formate (Luo and Qian, 2016a). Research with these components is demonstrating that there are few detrimental effects on setting and hardening at the quantities they are ever going to be accidentally released from the capsules. While encapsulation potentially permits a much wider range of materials to be used, it should be noted that compounds that are deleterious to concrete in the hardened state, chloride and sulfate salts for example, should be avoided.

There is evidence that, in addition to the role of the genera of bacteria used, the choice of calcium-based compound has an effect on the morphology of carbonate crystals that precipitate (Seifan et al., 2016). Both calcite and vaterite have been reported in various studies (De Muynck et al., 2010; Amiri and Bundur, 2016). To date there is no evidence that the morphology of the carbonate crystals affects the degree of healing. However, it has been suggested that because the density of vaterite is less than the density of calcite that it will fill more space for a given mass of precipitate (Seifan et al., 2016). Consequently, the efficiency of the self-healing process could, theoretically, be enhanced when vaterite is formed.

The other nutrients added to the cargoes to facilitate precipitation of a healing compound need to play a number of roles, the most significant of which are to: (1) Aid germination of the bacterial spores; (2) Assist in the growth of bacterial cells.

These nutrients need to be compatible with concrete and, as a general rule, known retarders of concrete should be avoided, as well as compounds that may deteriorate concrete in the hardened state. However, it must be recognized that, should the kinetics of germination and precipitation be rapid, then the effect of the nutrients on the properties of concrete may not be important as they will be rapidly consumed and potentially bound in non-reactive forms.

In many self-healing systems, these components are added directly to the concrete during the mixing process; partly due to difficulties with micro-encapsulating water-soluble compounds (Wang et al., 2014b). The effect of these compounds on the setting and hardening of concrete is therefore important. The most important compounds to consider are urea and yeast extract.

In urea hydrolysis, urea is a key component of the nutrient feed-in and is used in dosages up to 4% by mass of cement. Wang et al. (2014b) have suggested that urea (4% by mass of cement) causes a delay in hydration. However, isothermal conduction calorimetry tests undertaken by Bundur et al. (2015) in which urea was used at the lower concentration of 0.5% by mass of cement showed that there was no significant effect on the kinetics of hydration.

Yeast extract (YE) contains amino acids, peptides, water soluble vitamins and carbohydrates. It is widely used as an additive for culture media in general microbiology and as a source of nutrients for bacteria-based self-healing concrete. It is usually added to bacteria-based self-healing concrete in proportions between 0.1% to 1.0% by mass of cement. In addition to being a source of nutrient for bacteria germination and growth, it has also been suggested that the addition of YE improves calcium carbonate precipitation; media with an optimized YE content have been shown to precipitate three times as much as that with a less-optimal YE content (Zhang et al., 2017), although it is not altogether clear that this effect is independent of bacterial growth characteristics. Research shows that YE added directly to concrete delays the setting of cement and hardening of concrete. Bundur et al. (2015) have shown that YE has a significant effect in retarding the hydration of cement. Within a nutrient combination consisting of Tris, urea and YE (1% by mass of cement), it was shown by isothermal conduction calorimetry that YE was the compound with the greatest single effect on the kinetics of hydration (Bundur et al., 2015). Similar results based on isothermal conduction calorimetry have been reported by Wang et al. (2014b) where YE was added at 0.8% by mass of cement. The retarding effect of YE is considered to be due to the presence of carbohydrates within its composition (Amiri and Bundur, 2016).

Furthermore, research by Jonkers et al. (2010) has shown that the addition of YE (1% by mass of cement) leads to a reduction in the strength of concrete. However, elsewhere it has been shown that when used below 0.5% by mass of cement, there is no effect of YE on mortar strength (Paine, 2016).

19.6 Application of encapsulated bacteria for self-healing concrete

A good overview of autogenous and autonomous self-healing systems for crack healing in concrete is provided by [Van Tittelboom and De Belie \(2013\)](#) and by [De Rooij et al. \(2013\)](#). One of the options to obtain engineered self-healing, is the incorporation of encapsulated bacteria. Whereas possible encapsulation strategies have been discussed in the previous section, the focus will now be shifted towards different factors that can affect the self-healing efficiency, the evaluation of self-healing, and the application in large scale tests.

19.6.1 Quantity of cells and nutrients required for self-healing concrete

Essential to self-healing concrete is that a sufficient quantity of Ca^{2+} must be available in the concrete, such that sufficient calcium carbonate can form to fill the crack. The theoretical quantities of calcium carbonate that can be formed are described above ([Section 19.2.1](#)). Clearly, breakdown of the calcium precursor relies on the presence of bacteria cells. Because cells grow and multiply, it has been suggested that healing can be generated initially in the presence of relatively few cells. However, [Zhang et al. \(2017\)](#) have shown that the spore concentration necessary to deliver calcium carbonate precipitation needs to be greater than 4×10^7 spores/mL. Interestingly, the needed spore concentration is, however, independent of calcium precursor content.

The encapsulated clay particles for self-healing developed by [Wiktor and Jonkers \(2011\)](#) included 1.7×10^5 spores and 0.06 g of calcium lactate per gram of aggregate; which equates to approximately 2.8×10^6 spores/g of calcium lactate. Later work by the same team used 10^8 spores/L in combination with 200 g/L of calcium lactate ([Tziviloglou et al., 2016](#)). This equates to a lower ratio of 5×10^5 spores/g of calcium lactate.

In developing self-healing concrete for field trials, [Paine et al. \(2016\)](#) compared a range of ratios of encapsulated spores to encapsulated calcium acetate. It was found that the healing occurred when there was approximately $5 - 9 \times 10^9$ spores/g of calcium acetate. This is a significantly higher quantity than that of [Tziviloglou et al. \(2016\)](#). Higher and lower ratios yielded no healing.

19.6.2 Triggering of self-healing

Bacterial healing has proven useful at recovering the low permeability of concrete when subjected to micro-sized (or smaller) cracks, but, such systems are generally unsuitable for healing macro-scale cracks. [Luo et al. \(2015\)](#) considered healing in cracks ranging from 0.1 to 1 mm in a cement paste, using an unspecified bacterium and set of nutrients for 20 days in wet/dry conditions. It was shown that 50% healing of cracks was achievable in cracks of less than 0.5 mm and that healing was

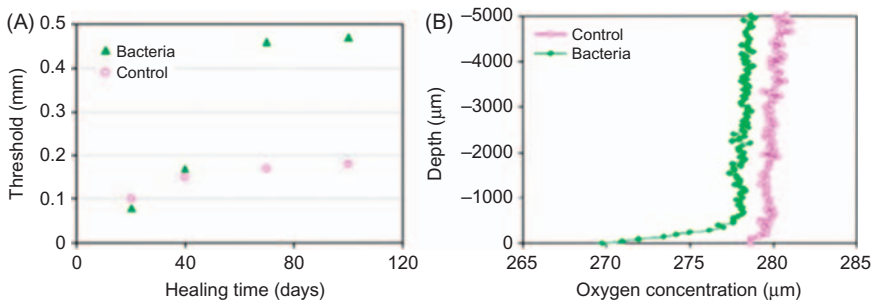


Figure 19.3 (A) Threshold values of maximum crack widths healed after indicated healing time (submersion in water). (B) Measured oxygen concentration microprofiles towards surfaces of submerged control- and bio-chemical agent-based mortar specimens (Wiktor and Jonkers, 2011).

significantly reduced above 0.8 mm. Wiktor and Jonkers (2011) have quantified crack healing over a range of initial crack widths and shown that, over a period of 100 days (immersed in tap water), healing can be achieved in cracks up to 0.46 mm. In this case this was more than twice that which could be achieved by autogenous healing in control specimens (healing of cracks <0.2 mm only) (Fig. 19.3). In the research of Wang et al. (2014a) with hydrogel encapsulated bacteria, the maximum crack width that could be healed was about 0.5 mm while it reached 0.2–0.35 mm in specimens without the bio-hydrogels.

A limiting factor to both the aerobic respiration and urea hydrolysis pathways for self-healing is the lack of availability of oxygen within the cracks at depth. This oxygen-limiting factor means that healing may be restricted to the surface only, which has effects on long-term healing and sealing efficiency. Partially due to the importance of oxygen, healing in wet/dry environments rather than under water has been shown to enhance bacteria growth and calcite precipitation (Wang et al., 2014c; Tziviloglou et al., 2016); the latter most probably also related to the enhanced carbonation of calcium hydroxide in wet/dry environments.

Two approaches to eliminate the oxygen limitation have been investigated. Zhang et al. (2017) have proposed incorporating oxygen within the self-healing agent in the form of an oxygen-releasing tablet made up of calcium peroxide. When the pellet is ruptured the calcium peroxide reacts with water, releasing oxygen that can be used aerobically by the bacteria. A dose of 7.5 g/L of calcium peroxide was shown to improve bacterial calcium carbonate precipitation.

Alternatively, Erşan et al. (2016) have considered biological nitrate reduction. Since nitrate reduction is performed by bacteria that respire NO_3^- , it takes place in oxygen-limiting conditions. The breakdown of calcium nitrate—the precursor—results in calcium carbonate, carbon dioxide, nitrogen and water. Thus, unlike urea hydrolysis, no toxic by-products are formed.

Another potential issue regarding the efficiency of crack healing is the pH of the environment at the time of cracking. Whilst spores are able to remain viable

(survive) at pH values outside their normal growth range, such as the high pH (pH > 13) environment that exists in concrete at very early ages, the bacteria must still be expected to function in an alkaline environment once a crack emerges and germination has proceeded. Therefore, it has been considered that any bacteria used must be alkaliphilic (or at least alkali tolerant).

Generally speaking, alkaliphilic bacteria are those that grow optimally or very well at pH values above 9, often between 10 and 12, but cannot grow or grow slowly at near-neutral pH (Horikoshi, 1999).

Due to the inward diffusion of CO₂ from the surrounding environment, the cement paste carbonates and, subsequently, the pH of concrete, reduces over time. Furthermore, in carbonating concrete the pH at the surface will be lower than that at greater depths. Since the bacteria used in a given self-healing system will have an optimum range of pH, the degree of carbonation that has taken place in the concrete—prior to it cracking—may have an effect on the kinetics and efficiency of the healing process. Consequently, it has been suggested that there is a need in some applications to embed the bacteria with a buffer to maintain the pH at an optimum range of alkalinity (Wiktor and Jonkers, 2015). On the other hand, some alkaliphilic bacteria are known to change external pH to a pH suitable for their growth, or accidentally as a by-product of their metabolism. An example is *B. pseudofirmus* A-57, an alkaliphile, which has a growth range from pH 8 to 10, but which has been shown to change a medium of pH 5 to a pH of 8 by producing an alkaline protease (Horikoshi, 2011). *Bacillus* species are also prolific producers of alkaline proteases (Bhunja et al., 2012) and there is scope to make more use of this in self-healing concrete. Furthermore, in the case of self-healing by urea hydrolysis, the production of the enzyme urease, which splits urea into carbon dioxide and ammonia, significantly increases the pH of the surrounding environment to a value of about 9 (ammonium—ammonia equilibrium) (Achal and Pan, 2011).

19.6.3 Germination and growth aids for bacteria

Experimental research on bacteria-based self-healing concrete in practice has tended to use generic media to obtain organomineralization. As described above, typically the only nutrients added to aid growth and germination of the bacteria in the concrete are those nutrients present in yeast extract. Where greater precipitation has been sought, for example in microbiological experiments, B4 or LB media have been used (Fig. 19.4). However, neither of these media mimics the natural precipitating environment present in concrete, nor are they the ideal media for any particular choice of bacteria used (Marvasi et al., 2012). Consequently, more research is required to produce media that are specific to the bacteria used and the conditions in which the self-healing concrete will be used.

That being said, there have been some limited attempts to add germination and growth aids to the nutrients used in self-healing concrete in order to enhance bacterial growth and maximize calcium carbonate precipitation. For example, Jonkers et al. (2010) added peptone, a partially digested protein that provides a source of amino acids, peptides, proteins and nitrogen, in proportions of 1% by mass of

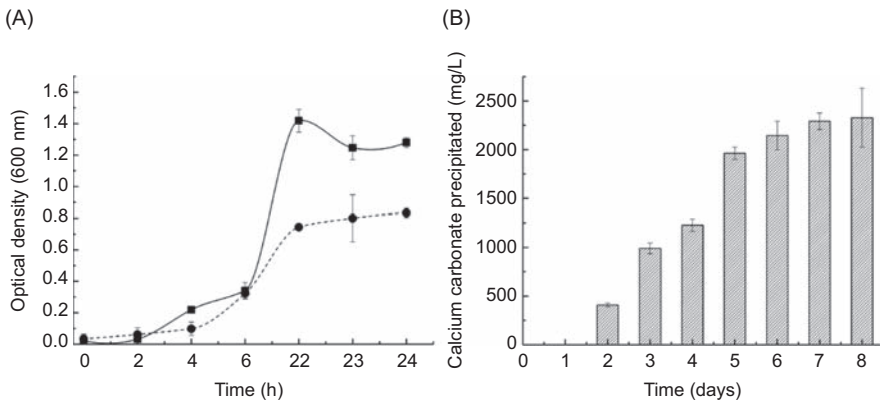


Figure 19.4 (A) Growth of *Bacillus pseudofirmus* DSM 8715 in two calcite inductive media: (●) LB (1/10) and (■) B4. (B) Quantification by atomic absorption spectroscopy of CaCO_3 precipitated during growth of *B. pseudofirmus* DSM 8715. Error bars in both figures show SD (Sharma et al., 2017).

cement to encourage bacteria growth. However, it was observed that peptone reduced the strength of concrete. Bundur et al. (2015) have considered issues arising from use of Tris base ($(\text{HOCH}_2)_3\text{CNH}_2$), an organic compound widely used as a component of buffer solutions. It was found that Tris base increases the rate of hydration of cement, due to impacts on the dissolution of C_3S and/or because it acts as a nucleation point for hydration products.

As bacteria-based self-healing of concrete continues to advance, media more appropriate to the concrete environment and the specific bacteria used will be developed, and consequently the use of germination and growth aids as an integral part of the nutrients is likely to progress.

19.6.4 Activity measurement of bacteria in (cracked) concrete

The bacterial behavior, more specifically the bacterial activity in the crack zone, is of crucial importance, since it essentially governs the biogenic CaCO_3 formation and hence the crack healing efficiency. In most studies, improved healing efficiency was evaluated indirectly by crack closure and water penetration resistance in the specimens with carbonate precipitating bacteria. Yet, CaCO_3 can also be generated from concrete carbonation, and this autogenous healing process also contributes to crack closure. It is difficult to differentiate the biogenic- CaCO_3 from abiotic- CaCO_3 . Measurement of bacterial activity in the crack zone can deliver direct proof of a bacteria-based self-healing. For the bacteria involved in aerobic oxidation of carbon source, oxygen consumption in the crack zone can be a good indicator of bacterial metabolic activity. Wiktor and Jonkers (2011) applied an oxygen micro-sensor to measure oxygen profiles near the crack surface. The specimen was fully immersed in water. As shown in Fig. 19.3B, the oxygen concentration greatly

dropped when the sensor was very close to the surface of the specimen incorporated with bacteria ($0 \sim 200 \mu\text{m}$). This drop was due to the oxygen consumption during bacterial activities.

Wang et al. (2015) utilized the same technique to monitor the *B. sphaericus* spores activity near a mimicked crack surface. *Bacillus sphaericus* is an aerobic ureolytic strain. Though oxygen has no obvious influence on its ureolytic activity (Wang et al., 2017a), oxygen is needed for the germination of *B. sphaericus* spores. Thus, whether the spores become active or not can be deduced from the oxygen consumption at the surface. In this study, an obvious oxygen concentration decrease was seen from the distance of $500 \mu\text{m}$ to the surface. The oxygen consumption in this boundary layer in function of time was monitored in the damaged specimens with and without encapsulated *B. sphaericus* spores. As shown in Fig. 19.5, only the specimens with hydrogel encapsulated spores showed remarkable oxygen consumption. This consumption did not occur in the beginning, but after 24 hours, which indicated that the germination of the spores only started after 1 day. It was noticed that the oxygen consumption varied in the following hours and almost stopped after 3 days. This could indicate that the germinated cells became active to decompose urea, which is an enzymatic reaction and does not consume oxygen.

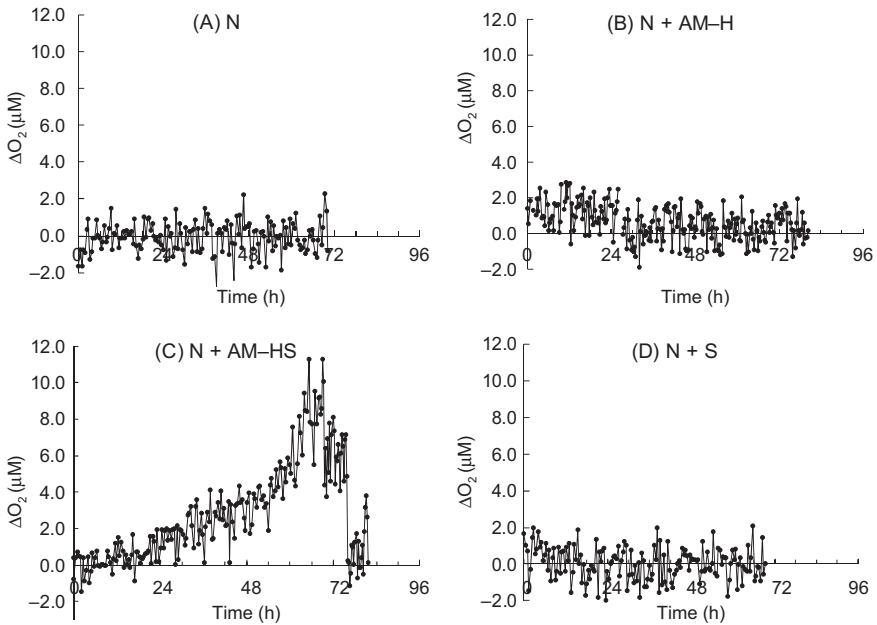


Figure 19.5 Oxygen consumption in the boundary layer as time proceeds. (A) Specimen only containing nutrients; (B) specimen with nutrients and modified alginate hydrogel; (C) specimen with nutrients and hydrogel-encapsulated spores; (D) specimens with nutrients and free spores (Wang et al., 2015).

It should be noted that specimens with free spores did not show any significant oxygen consumption in the whole test period. The reason could be that the non-encapsulated spores had lost their viability after being added into the matrix. This further demonstrated the necessity of the encapsulation of spores to preserve spores viability for a sufficient bacteria-based crack healing.

19.6.5 Evaluation of self-healing efficiency

A good overview of different methods to evaluate self-healing efficiency is provided in the review of Van Tittelboom and De Belie (2013). Methods for the visualization of crack healing, determination of the crack filling and characterization of the healing material, include optical microscopy and image analysis, scanning electron microscopy, thin section analysis, ultrasonic transmission measurements, X-ray radiography, X-ray tomography, digital image correlation, X-ray diffraction analysis, Raman spectroscopy, and infrared analysis. An example of using 3D X-ray tomography to quantify and view the distribution of the healing products in the whole sample is shown in Figs. 19.6 and 19.7 (Wang et al., 2014c). The specimens with hydrogel encapsulated bacteria added had much more precipitation (2.2 vol%) than the reference (0.21 vol%) and the one with pure hydrogel (1.37 vol%). However, it was also noticed that most biogenic precipitation was distributed on/in the surface layer. To check regain in liquid-tightness, water permeability tests can be performed at low or high pressure or by capillary water uptake, and water penetration can be visualized by X-ray or neutron radiography; furthermore air permeability can be measured. Liquid tightness also relates to durability, which can be tested by corrosion tests, frost salt scaling, or chloride diffusion tests. Regain in mechanical properties can be quantified through a compression test, tensile test,

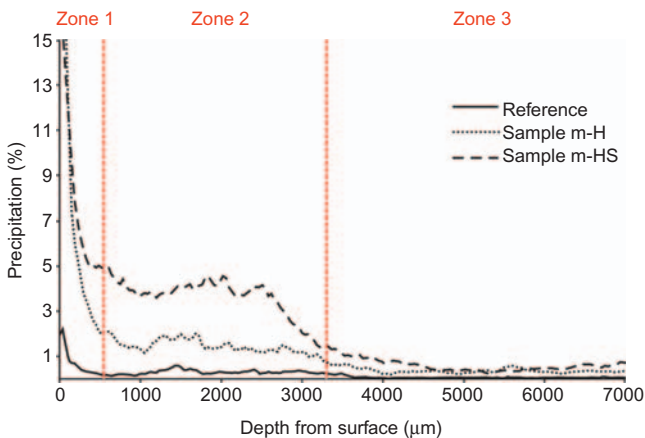


Figure 19.6 The amount of the precipitation in function of the depth of different samples (the reference sample, sample with pure hydrogel (m-H), and sample with hydrogel encapsulated bacteria spores (m-HS) (Wang et al., 2014c)).

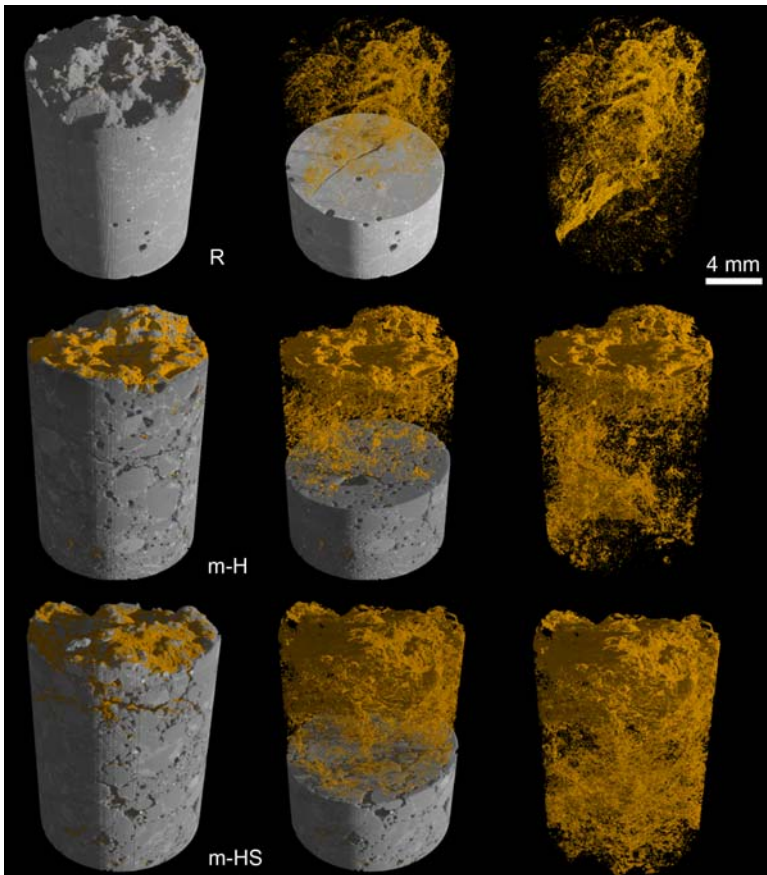


Figure 19.7 3D view of the distribution of healing products (in yellow) in the sample reference (R), the sample with pure hydrogel (m-H), and the sample with hydrogel encapsulated bacterial spores (m-HS) after the self-healing process. Left: samples surface plus the precipitation; middle: distribution of the precipitates inside; Right: the precipitates in the sample (Wang et al., 2014c).

three- or four-point bending test, impact loading, acoustic emission analysis, or resonance frequency analysis. In the EC-funded project HEALCON, two test methods to assess the sealing efficiency were proposed (Gruyaert et al., 2016a,b). The first test method evaluates the absorption of water by the cement matrix in the presence of a healed crack, and compares the sorptivity with the sorptivity of a sound specimen (best case scenario) and the sorptivity of a cracked and unhealed specimen (worst case scenario) in order to calculate the sealing efficiency. The test procedure is based on the standard method according to EN 13057, except that only a small zone of 40 mm wide surrounding the crack is exposed to the water. The second method judges whether a water flow under pressure (0.05–2 bar), supplied via an

inner hole in the specimen crossing the crack, can be withstood by the products sealing the crack. In case the sealing is not perfect, water will flow out of the specimen and the amount will be measured in function of time. Comparing the water flow of the unhealed and healed crack allows to define a sealing efficiency.

19.6.6 Application of self-healing additives in large scale laboratory and in-situ tests

Bacterial self-healing concrete targets crack healing and the recovery of watertightness. This innovative concept has shown promising results at lab-scale tests. But steps have also been taken towards real-scale applications that should prove the functionality of this new technology. An overview of several large scale laboratory and in-situ applications is provided by [Tziviloglou et al. \(2015\)](#).

Since ureolytic mixed self-protected bacterial cultures (CERUP) had been scaled up previously to 50 L scale ([Silva et al., 2015b](#)), this permitted including them (3% versus cement weight) in a concrete beam with the size of $150 \times 250 \times 3000 \text{ mm}^3$. The performed experiments were the same as for beams with an encapsulated polyurethane-based healing agent, and with superabsorbent polymers as described previously by [Van Tittelboom et al. \(2016\)](#). Multiple cracks were created by four-point bending. To facilitate water permeability tests, the beam was loaded in upward direction and was sprayed with water for 1 minute four times per day during 6 weeks, to mimic a realistic condition. It was found, however, that the CERUP provided less crack sealing in the large-scale concrete beam compared with previous tests on small mortar prisms, probably due to the dilution of the healing agent (dosed versus cement weight) and the limited availability of water.

The first field application of bio-based self-healing concrete with light-weight aggregates and natural fibers took place in July 2014 in the Andean highlands in Ecuador. In order to make the local concrete irrigation channels self-healing, a mix including light-weight aggregates with healing agent and a fiber indigenous to Ecuador, Abaca, were chosen. For the trial, three linear meters of concrete linings with bacteria and 3 m without bacteria were cast, using 110 L of concrete. This canal is located at about 2900 m above sea level and the temperature during the casting was around 5°C . The framework was removed after 3 days, and 2 days later the water flow through the canal was reinstalled. One year after casting, the concrete linings showed no signs of cracking or deterioration ([Tziviloglou et al., 2015](#)).

As part of the Materials for Life (M4L) project ([Lark et al., 2013](#)), five vertical walls were cast and deliberately cracked to investigate the capability of a number of combinations of self-healing techniques. One of the walls contained a combination of bacteria-based self-healing concrete and a vascular flow network ([Fig. 19.8](#)). Bacteria-based self-healing concrete was added to the panel at the section where cracking was designed to occur. The self-healing agents (spores of *B. pseudofirmus*, calcium acetate and yeast extract) were encapsulated in perlite and a protective cement/sodium silicate coat. The spores and nutrients were encapsulated separately. Full concrete mix design details are given in [Paine et al. \(2016\)](#). All other parts of

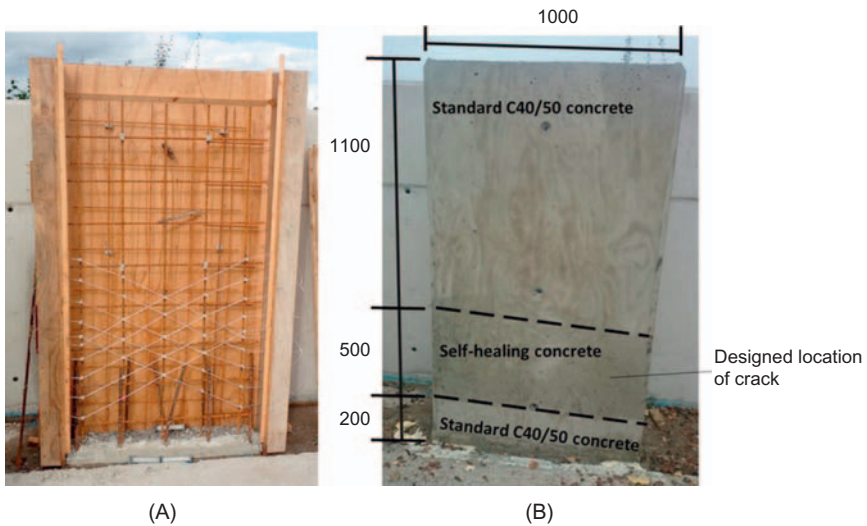


Figure 19.8 M4L wall panels: (A) Embedded capillary network installed prior to casting of the concrete, (B) completed panel containing bacteria-based self-healing concrete (dimensions in mm).

Source: Photos courtesy of University of Bath.

the panel were made of C40/50 ready-mixed concrete. The vascular flow network was created by a 2D network of 4 mm diameter channels, and was designed to permit later addition of further nutrients, bacteria, or oxygen as necessary. The formwork for the wall was struck at 2 days and there was no noticeable delay in setting or early-age hardening of the self-healing concrete, compared with the normal concrete sections. Cubes tested at 7 and 28 days gave mean strengths of 29.1 and 35.1 MPa, respectively. The wall was deliberately cracked at an age of 36 days, leading to residual cracks that ran through the center of the self-healing concrete section as designed (Teall et al., 2016). These residual cracks were approximately 0.1 mm in width and whilst a degree of crack healing was detected for the 6 months that the walls were in service it was not possible to attribute the healing to incorporation of bacteria rather than autogenous healing. Overall the casting and testing of all five panels showed that there are still challenges to the scaling-up of self-healing concrete (Pilegis et al., 2016). Most importantly, however, it was demonstrated that, from a practical aspect, it was possible to mix, place, compact, and strike the formwork of bacteria-based self-healing concrete on site using standard concrete practice.

The self-healing flakey additives developed by Jonkers and Mors (2012) were also tested in outdoor conditions, by adding them to a commercially available repair mortar. A 8 m² degraded concrete wall was pretreated by removing the degraded layer up to or until behind the reinforcement. The healing agent containing mortar was applied by spraying. Observations were made regarding practicality, workability, consistency and visual appearance of the repair mortar. A first visual inspection

indicated a homogenous spread of particles through the matrix. Effective healing agent distribution and crack sealing efficiency for regain of water tightness will be quantified in further outdoor applications.

A bacterial repair system developed at the Technical University of Delft was also tested in 2014, in a parking garage. The system is composed of two solutions: the first one containing sodium-silicate (alkaline buffer), sodium-gluconate (carbon source for bacteria growth), and alkaliphilic bacterial spores, and the second one containing calcium-nitrate and alkaliphilic bacterial spores. The sodium silicate leads to the formation of a gel which rapidly seals the crack. It also provides an optimum environment for bacteria to precipitate CaCO_3 . The system was used to treat a surface area of around 2000 m^2 in a parking garage. Results of leakage tests were encouraging as treated cracks showed significantly less leaking.

The healing agent consisting of *B. cohnii* spores, calcium lactate and yeast extract immobilized in light-weight aggregates was also combined with cement, fly ash, limestone powder, PVA fibers, water and superplasticizer in a repair mortar. Since 2013 this mortar has been applied as patch repair in different locations in the Netherlands, under very diverse weather conditions. The first application took place during May 2013 on a garage where corrosion of the steel reinforcement led to spalling of the concrete. After 1.5 years the patch repair was in good condition without signs of deterioration. The repair mortar has also been applied under extremely moist conditions in an underground parking garage where the retaining walls have had water leaking problems. A month after the repair only a little leakage was still spotted, which did not lead to spalling even after 6 months. Another indoor application took place in a tunnel that was built in the late 1930s. A patch repair of about $250 \times 500 \times 110 \text{ mm}^3$ was applied and no delamination occurred and only very small shrinkage cracks were observed (Tziviloglou et al., 2015).

19.7 Future trends

With regards to bacterial self-healing, several questions remain open for further study (De Belie, 2016). The viability of the self-healing additive in time is yet unknown and will be different for each specific bacterial strain and protection method. It has also not yet been proven whether spores that have germinated and actively contributed to crack healing, will sporulate again and remain in dormant state until their activity is once more needed. Additionally, the self-healing efficiency needs to be proven for concrete elements, since most proof-of-concept tests until now were carried out in mortar specimens. When keeping the dosage of the bacterial additive constant relative to the cement weight when upscaling from mortar to concrete, this results in a significant dilution of the additive. However, when maintaining the same dosage in proportion to the total volume, an unacceptable strength decrease may result.

Significant research has been carried out to isolate spore-forming, aerobic bacteria from environmental conditions that correspond to the conditions present in concrete. A particular problem has been to isolate bacteria that will perform in cool

and/or high-salt conditions, although some progress has been made by [Palin et al. \(2016\)](#). However, it is unlikely that a singular species of bacteria will be found that is able to meet all requirements for self-healing concrete. Therefore, speculatively, there is potential to create synthetic strains that are ideal for self-healing concrete. Indeed, initial research has shown that a genetically-enriched bacterium can be developed that has a biosilification assay, such that nano-calcium aluminum silicate (gehlenite) is formed as the healing compound rather than calcium carbonate ([Sarkar et al., 2015](#)).

As described above, bacterial healing has proven useful at recovering the low permeability of concrete when subjected to micro-sized cracks of less than 0.5 mm. However, it is of limited use should larger cracks appear. To overcome this, there is a scope to use bacteria-based self-healing in combination with other self-healing systems to provide multi-scale healing potential. An example technology is the use of shape-memory polymers, which do not heal cracks but are capable of reducing cracks sufficiently that they may be healed by bacteria-based systems ([Teall et al., 2017](#)).

Recent work has queried whether there really is a need to add an extra source of Ca^{2+} in the aerobic pathway to that already available in the concrete, on the basis that excessive Ca^{2+} inhibits bacterial-induced calcium precipitation ([Zhang et al., 2016](#)). Where significant bacterial-induced calcium precipitation is required there is an argument, therefore, that higher quantities of bacteria should be added. However, there appears to be no consensus on the appropriate quantities of calcium precursor and spores that should be included in the concrete. Further research is required.

References

- Achal, V., Pan, X., 2011. Characterization of urease and carbonic anhydrase producing bacteria and their role in calcite precipitation. *Curr. Microbiol.* 62 (3), 894–902.
- Achal, V., Pan, X., Özyurt, N., 2011. Improved strength and durability of fly ash-amended concrete by microbial calcite precipitation. *Ecol. Eng.* 37, 554–559. Available from: <http://dx.doi.org/10.1016/j.ecoleng.2010.11.009>.
- Achal, V., Mukherjee, A., Goyal, S., Reddy, M.S., 2012. Corrosion prevention of reinforced concrete with microbial calcite precipitation. *ACI Mater. J.* 109 (2), 157–164.
- Amiri, A., Bundur, Z.B., 2016. Impact of biogenic self-healing additive on performance of cement-based mortar. In: *International RILEM Conference on Materials, Systems and Structures in Civil Engineering*, Lyngby, pp. 493–502.
- Bang, S.S., Galinat, J.K., Ramakrishnan, V., 2001. Calcite precipitation induced by polyurethane-immobilized *Bacillus pasteurii*. *Enzyme Microb. Technol.* 28 (4–5), 404–409, [http://dx.doi.org/10.1016/s0141-0229\(00\)00348-3](http://dx.doi.org/10.1016/s0141-0229(00)00348-3).
- Basaran, Z., 2013. *Biom mineralization in Cement Based Materials: Inoculation of Vegetative Cells*. University of Texas, Austin, TX.
- Bhunja, B., Basak, B., Dey, A., 2012. A review on production of serine alkaline protease by *Bacillus* spp. *J. Biochem. Technol.* 3 (4), 448–457.

- Boquet, E., Boronat, A., Ramoscor, A., 1973. Production of calcite (calcium-carbonate) crystals by soil bacteria is a general phenomenon. *Nature*. 246 (5434), 527–529. Available from: <http://dx.doi.org/10.1038/246527a0>.
- Bundur, Z.B., Kirisits, M.J., Ferron, R.D., 2015. Biomineralized cement-based materials: impact of inoculating vegetative bacterial cells on hydration and strength. *Cem. Concr. Res.* 67, 237–245. Available from: <http://dx.doi.org/10.1016/j.cemconres.2014.10.002>.
- Bundur, Z.B., Amiri, A., Erşan, Y.C., Boon, N., De Belie, N., 2017. Impact of air entraining admixtures on biogenic calcium carbonate precipitation and bacterial viability. *Cem. Concr. Res.* 98, 44–49.
- Charney, J., Fisher, W.P., Hegarty, C.P., 1951. Manganese as an essential element for sporulation in the genus *Bacillus*. *J. Bacteriol.* 62, 145–148.
- Chen, H., Qian, C., Huang, H., 2016. Self-healing cementitious materials based on bacteria and nutrients immobilized respectively. *Constr. Build. Mater.* 126, 297–303.
- De Belie, N., De Muynck, W., Verstraete, W., 2006. A synergistic approach to microbial presence on concrete: cleaning and consolidating effects. *Struct. Concr.* 7 (3), 105–109.
- De Belie, N., 2010. Microorganisms versus stony materials: a love-hate relationship—Robert L’Hermite Medal lecture 2010. *Mater. Struct.* 43 (9), 1191–1202.
- De Belie, N., 2016. Application of bacteria in concrete: a critical review. *RILEM Tech. Lett.* 1, 56–61.
- De Belie, N., De Muynck, W., 2009. Crack repair in concrete using biodeposition. In: *Proceedings of the Second International Conference on Concrete Repair, Rehab, Retrofitting*, pp. 291–292.
- De Belie, N., Wang, J., 2016. Bacteria based repair and self-healing of concrete. *J. Sustain. Cem. Based Mater.* 5 (1–2), 35–56. Available from: <http://dx.doi.org/10.1080/21650373.2015.1077754>.
- de Koster, S.A.L., Mors, R.M., Nugteren, H.W., Jonkers, H.M., Meesters, G.M.H., van Ommen, J.R., 2015. Geopolymer coating of bacteria-containing granules for use in self-healing concrete. *Procedia Eng.* 102, 475–484.
- De Muynck, W., Debrouwer, D., De Belie, N., Verstraete, W., 2008a. Bacterial carbonate precipitation improves the durability of cementitious materials. *Cem. Concr. Res.* 38 (7), 1005–1014. Available from: <http://dx.doi.org/10.1016/j.cemconres.2008.03.005>.
- De Muynck, W., Cox, K., De Belle, N., Verstraete, W., 2008b. Bacterial carbonate precipitation as an alternative surface treatment for concrete. *Constr. Build. Mater.* 22 (5), 875–885. Available from: <http://dx.doi.org/10.1016/j.conbuildmat.2006.12.011>.
- De Muynck, W., Belie, N., Verstraete, W., 2010. Microbial carbonate precipitation in construction materials: a review. *Ecol. Eng.* 36 (2), 118–136. Available from: <http://dx.doi.org/10.1016/j.ecoleng.2009.02.006>.
- De Muynck, W., Leuridan, S., Van Loo, D., Verbeken, K., Cnudde, V., De Belie, N., et al., 2011. Influence of pore structure on the effectiveness of a biogenic carbonate surface treatment for limestone conservation. *Appl. Environ. Microbiol.* 77 (19), 6808–6820. Available from: <http://dx.doi.org/10.1128/aem.00219-11>.
- De Muynck, W., Verbeken, K., De Belie, N., Verstraete, W., 2013. Influence of temperature on the effectiveness of a biogenic carbonate surface treatment for limestone conservation. *Appl. Microbiol. Biotechnol.* 97 (3), 1335–1347. Available from: <http://dx.doi.org/10.1007/s00253-012-3997-0>.
- De Rooij, M.R., Van Tittelboom, K., De Belie, N., Schlangen, E. (Eds.), 2013. *Self-Healing Phenomena in Cement-Based Materials*. Springer, Dordrecht, 266 p.

- Delgado Rodrigues, J., 2001. Consolidation of decayed stones. A delicate problem with few practical solutions. In: Loureco, P.B., Roca, P. (Eds.), *International Seminar on Historical Constructions*. University of Minho, Guimarães, Portugal.
- Dick, J., De Windt, W., De Graef, B., Saveyn, H., Van der Meeren, P., De Belie, N., et al., 2006. Bio-deposition of a calcium carbonate layer on degraded limestone by *Bacillus* species. *Biodegradation*. 17 (4), 357–367. Available from: <http://dx.doi.org/10.1007/s10532-005-9006-x>.
- Errington, J., 2003. Regulation of endospore formation in *Bacillus subtilis*. *Nat. Rev. Microbiol.* 1, 117–126.
- Erşan, Y.C., January 21, 2016. Microbial nitrate reduction induced autonomous self-healing in concrete. Ph.D. in Bio-Engineering, Ghent University.
- Erşan, Y.C., de Belie, N., Boon, N., 2015a. Microbially induced CaCO₃ precipitation through denitrification: an optimization study in minimal nutrient environment. *Biochem. Eng. J.* 101, 108–118. Available from: <http://dx.doi.org/10.1016/j.bej.2015.05.006>.
- Erşan, Y.C., Da Silva, F.B., Boon, N., Verstraete, W., De Belie, N., 2015b. Screening of bacteria and concrete compatible protection materials. *Constr. Build. Mater.* 88, 196–203.
- Erşan, Y.C., Gruyaert, E., Louis, G., Lors, C., De Belie, N., Boon, N., 2015c. Self-protected nitrate reducing culture for intrinsic repair of concrete cracks. *Front. Microbiol.* 6, 1228.
- Erşan, Y.C., Hernandez-Sanabria, E., Boon, N., De Belie, N., 2016. Enhanced crack closure performance of microbial mortar through nitrate reduction. *Cem. Concr. Compos.* 70, 159–170.
- Feugeas, F., Tran, M., Chakri, S., 2017. Bio based admixtures with substances derived from bacteria to improve the durability of concrete. In: Pacheco Torgal, F., Melchers, R., Shi, X., Sáez, A., De Belie, N., Van Tittelboom, K. (Eds.), *Eco-Efficient Repair and Rehabilitation of Concrete Structures*. Woodhead Publishing, Cambridge, UK.
- Ghosh, P., Mandal, S., Chattopadhyay, B.D., Pal, S., 2005. Use of microorganism to improve the strength of cement mortar. *Cem. Concr. Res.* 35, 1980–1983. Available from: <http://dx.doi.org/10.1016/j.cemconres.2005.03.005>.
- Ghosh, P., Biswas, M., Chattopadhyay, B.D., Mandal, S., 2009. Microbial activity on the microstructure of bacteria modified mortar. *Cem. Concr. Compos.* 31, 93–98. Available from: <http://dx.doi.org/10.1016/j.cemconcomp.2009.01.001>.
- Grumbein, S., Minev, D., Tallawi, M., et al., 2016. Hydrophobic properties of biofilm-enriched hybrid mortar. *Adv. Mater.* 28, 8138–8143.
- Gruyaert, E., Debbaut, B., Wang, J., Arizo, A., Branco, V., Alakomi, H.L., et al., 2016a. Evaluation of the self-sealing efficiency of cracks in concrete by bioprecipitation or application of hydrogels. In: *HEALCON Conference—Self-Healing Concrete for Prolonged Lifetime*, 28–29 November, Delft, 4 p.
- Gruyaert, E., Debbaut, D., Snoeck, D., Diaz, P., Arizo, A., Tziviloglou, E., et al., 2016b. Self-healing mortar with pH-sensitive superabsorbent polymers: testing of the sealing efficiency by water flow tests. *Smart Mater. Struct.* 25 (084007), 11 p.
- Han, N., Xing, F., 2017. A comprehensive review of the study and development of microcapsule based self-resilience systems for concrete structures at Shenzhen University. *Materials*. 10, 2. Available from: <http://dx.doi.org/10.3390/ma10010002>.
- Horikoshi, K., 1999. Alkaliphiles: some applications of their products for biotechnology. *Microbiol. Mol. Biol. Rev.* 63 (4), 735–750.
- Horikoshi, K., 2011. General physiology of alkaliphiles. In: Horikoshi, K. (Ed.), *Extremophiles Handbook*. Springer, Tokyo and Berlin, pp. 100–118.
- Jonkers, H.M., Schlangen, E., 2007. Self-healing of cracked concrete: a bacterial approach. In: Carpinteri, A., Gambarova, P.G., Ferro, G., Plizzari, G.A. (Eds.), *Proceedings of the*

- 6th International Conference on Fracture Mechanics of Concrete and Concrete Structures, Catania, Italy, 17–22 June 2007, paper 164. Taylor & Francis, Leiden.
- Jonkers, H.M., Thijssen, A., Muyzer, G., Copuroglu, O., Schlangen, E., 2010. Application of bacteria as self-healing agent for the development of sustainable concrete. *Ecol. Eng.* 36 (2), 230–235. Available from: <http://dx.doi.org/10.1016/j.ecoleng.2008.12.036>.
- Jonkers, H.M., Mors, R.M., 2012. Full scale application of bacteria-based self-healing concrete for repair purposes. In: Proceedings Third International Conference on Concrete Repair, Rehabilitation and Retrofitting, 3–5 September 2012, Cape Town, South Africa. Taylor & Francis Group, London, pp. 967–971.
- Kanellopoulos, A., Giannaros, P., Palmer, D., Kerr, A., Al-Tabbaa, A., 2017. Polymeric microcapsules with switchable mechanical properties for self-healing concrete: synthesis, characterisation and proof of concept. *Smart Mater. Struct.* 26 (4), 045025. Available from: <http://dx.doi.org/10.1088/1361-665X/aa516c>.
- Karagöl, F., Demirboğa, R., Kaygusuz, M.A., Yadollahi, M.M., Polat, R., 2013. The influence of calcium nitrate as antifreeze admixture on the compressive strength of concrete exposed to low temperatures. *Cold Reg. Sci. Technol.* 89, 30–35.
- Karatas, I., 2008. Microbiological improvement of the physical properties of soils. Ph.D. Thesis, Arizona State University, Tempe, AZ.
- Lark, R.J., Al-Tabbaa, A., Paine, K., June 2013. Biomimetic multi-scale damage immunity for construction materials: M4L project overview. In: Fourth International Conference on Self-Healing Materials, Ghent, Belgium.
- Le Metayer-Level, G., Castanier, S., Orial, G., Loubiere, J.F., Perthuisot, J.P., 1999. Applications of bacterial carbonatogenesis to the protection and regeneration of limestones in buildings and historic patrimony. *Sediment. Geol.* 126 (1–4), 25–34, doi:10.1016/s0037-0738(99)00029-9.
- Liu, S., Bundur, Z.B., Zhu, J., Ferron, R.D., 2016. Evaluation of self-healing of internal cracks in biomimetic mortar using coda wave interferometry. *Cem. Concr. Res.* 83, 70–78. Available from: <http://dx.doi.org/10.1007/s13398-014-0173-7.2>.
- Luo, M., Qian, C., Li, R., 2015. Factors affecting crack repairing capacity of bacteria-based self-healing concrete. *Constr. Build. Mater.* 87, 1–7.
- Luo, M., Qian, C., 2016a. Influences of bacteria-based self-healing agents on cementitious materials hydration kinetics and compressive strength. *Constr. Build. Mater.* 121, 659–663.
- Luo, M., Qian, C., 2016b. Performance of two bacteria-based additives used for self-healing concrete. *ASCE J. Mater. Civ. Eng.* 28 (12), 1.
- Marvasi, M., Gallagher, K.L., Martinez, L.C., Pagan, W.C.M., Rodriguez Santiago, R.E., Vega, G.C., et al., 2012. Importance of B4 medium in determining organomineralization potential of bacterial environmental isolates. *Geomicrobiol. J.* 29 (10), 916–924.
- May, E., 2005. Biobrush research monograph: novel approaches to conserve our European heritage. EVK4-CT-2001-00055.
- Moropoulou, A., Kouloumbi, N., Haralampopoulos, G., Konstanti, A., Michailidis, P., 2003. Criteria and methodology for the evaluation of conservation interventions on treated porous stone susceptible to salt decay. *Prog. Org. Coat.* 48, 259–270.
- Okwadha, G.D.O., Li, J., 2010. Optimum conditions for microbial carbonate precipitation. *Chemosphere.* 81 (9), 1143–1148. Available from: <http://dx.doi.org/10.1016/j.chemosphere.2010.09.066>.
- Østnor, T.A., Justnes, H., 2011. Anodic corrosion inhibitors against chloride induced corrosion of concrete rebars. *Adv. Appl. Ceram.* 110 (3), 131–136.

- Paine, K., 2016. Bacteria-based self-healing concrete: effects of environment, exposure and crack size. In: RILEM Conference on Microorganisms-Cementitious Materials Interactions, Delft, Netherlands.
- Paine, K., Alazhari, M., Sharma, T., Cooper, R., Heath, A., 2016. Design and performance of bacteria-based self-healing concrete. In: Ninth International Concrete Conference 2016: Environment, Efficiency and Economic Challenges for Concrete, Dundee, pp. 545–554.
- Palin, D., Wiktor, V., Jonkers, H.M., 2016. A bacteria-based bead for possible self-healing marine concrete applications. *Smart Mater. Struct.* 25, 1–6.
- Pei, R., Liu, J., Wang, S., Yang, M., 2013. Use of bacterial cell walls to improve the mechanical performance of concrete. *Cem. Concr. Compos.* 39, 122–130.
- Pei, R., Liu, W., Wang, S., 2015. Use of bacterial cell walls as a viscosity-modifying admixture of concrete. *Cem. Concr. Compos.* 55, 186–195.
- Pilegis, M., Davies, R.E., Lark, R.J., Gardner, D.R., Jefferson, A.D., 2016. Challenges of self-healing concrete scale-up and site trials. In: Ninth International Conference on Fracture Mechanics of Concrete and Concrete Structures, May 29–June 1, 2016, Berkeley, CA.
- Qian, C., Wang, J., Wang, R., Cheng, L., 2009. Corrosion protection of cement-based building materials by surface deposition of CaCO_3 by *Bacillus pasteurii*. *Mater. Sci. Eng. C.* 29 (4), 1273–1280. Available from: <http://dx.doi.org/10.1016/j.msec.2008.10.025>.
- Ramachandran, S.K., Ramakrishnan, V., Bang, S.S., 2001. Remediation of concrete using micro-organisms. *ACI Mater. J.* 98 (1), 3–9.
- Ramakrishnan, V., Ramesh, K.P., Bang, S.S., 2001. Bacterial concrete. In: Wilson, A.R., Asanuma, H. (Eds.), *Smart Materials. Proceedings of Society of Photo-Optical Instrumentation Engineers (SPIE)*, vol. 4234. SPIE, Bellingham, WA, pp. 168–176.
- Rodriguez-Navarro, C., Rodriguez-Gallego, M., Ben Chekroun, K., Gonzalez-Munoz, M.T., 2003. Conservation of ornamental stone by *Myxococcus xanthus*-induced carbonate biomineralization. *Appl. Environ. Microbiol.* 69 (4), 2182–2193. Available from: <http://dx.doi.org/10.1128/aem.69.4.2182-2193.2003>.
- Sarkar, M., Adak, D., Tamang, A., Chattopadhyay, B., Mandal, S., 2015. Genetically-enriched microbe-facilitated self-healing concrete – a sustainable material for a new generation of construction technology. *RSC Adv.* 5, 105363–105371.
- Sarode, D.D., Mukherjee, A., 2009. Microbial precipitation for repairs of concrete structures. In: Grantham, M., Majorana, C., Salomoni, V. (Eds.), *Concrete Solutions*. CRC Press, Boca Raton, FL.
- Seifan, M., Samani, A.K., Berenjian, A., 2016. Induced calcium carbonate precipitation using *Bacillus* species. *Appl. Microbiol. Biotechnol.* 100, 9895–9906.
- Sharma, T.K., Alazhari, M., Heath, A., Paine, K.A., Cooper, R.M., 2017. Alkaliphilic *Bacillus* species show potential application in concrete crack repair by virtue of rapid spore production and germination then extracellular calcite formation. *J. Appl. Microbiol.* 122 (5), 1233–1244. Available from: <http://dx.doi.org/10.1111/jam.13421>.
- Silva, F., Boon, N., De Belie, N., Verstraete, W., 2015a. Industrial application of biological self-healing concrete: challenges and economical feasibility. *J. Commer. Biotechnol.* 21, 31–38.
- Silva, F., Boon, N., De Belie, N., Verstraete, W., 2015b. Production of non-axenic ureolytic spores for self-healing concrete application. *Constr. Build. Mater.* 93, 1034–1041.
- Teall, O., Davies, R., Pilegis, M., Kanellopoulos, A., Sharma, T., Paine, K., et al., 2016. Self-healing concrete full scale site trials. In: 11th Fib International PhD Symposium in Civil Engineering, Tokyo, Japan, ISBN 978-4-9909148-0-6.

- Teall, O., Pilegis, M., Sweeney, J., Gough, T., Thompson, G., Jefferson, A., et al., 2017. Development of high shrinkage polyethylene terephthalate (PET) shape memory polymer tendons for concrete crack closure. *Smart Mater. Struct.* 26 (4), 045006. Available from: <http://dx.doi.org/10.1088/1361-665X/aa5d66>.
- Tiano, P., Addadi, L., Weiner, S., 1992. Stone reinforcement by induction of calcite crystals using organic matrix macromolecules: feasibility study. In: *Seventh International Congress on Deterioration and Conservation of Stone*, Lisbon, pp. 1317–1326.
- Tiano, P., Biagiotti, L., Mastromei, G., 1999. Bacterial bio-mediated calcite precipitation for monumental stones conservation: methods of evaluation. *J. Microbiol. Methods.* 36 (1–2), 139–145.
- Tiano, P., Cantisani, E., Sutherland, I., Paget, J.M., 2006. Biomediated reinforcement of weathered calcareous stones. *J. Cult. Herit.* 7 (1), 49–55.
- Tziviloglou, E., Van Tittelboom, K., Palin, D., Wang, J., Sierra-Beltrán, M.G., Erşan, Y.C., et al., 2015. Bio-based self-healing concrete: from research to field application. In: Hager, M.D., Schubert, U.S., van der Zwaag, S. (Eds.), *Advances in Polymer Sciences, Volume on Self-Healing Materials*. Springer, Cham.
- Tziviloglou, E., Wiktor, V., Jonkers, H.M., Schlangen, E., 2016. Bacteria-based self-healing concrete to increase liquid tightness of cracks. *Constr. Build. Mater.* 122, 118–125.
- Van Paassen, L.A., Daza, C.M., Staal, M., Sorokin, D.Y., van der Zon, W., van Loosdrecht, M.C.M., 2010. Potential soil reinforcement by biological denitrification. *Ecol. Eng.* 36 (2), 168–175. Available from: <http://dx.doi.org/10.1016/j.ecoleng.2009.03.026>.
- Van Tittelboom, K., De Belie, N., De Muynck, W., Verstraete, W., 2010. Use of bacteria to repair cracks in concrete. *Cem. Concr. Res.* 40 (1), 157–166. Available from: <http://dx.doi.org/10.1016/j.cemconres.2009.08.025>.
- Van Tittelboom, K., De Belie, N., 2013. Self-healing in cementitious materials – a review. *Materials.* 6 (6), 2182–2217.
- Van Tittelboom, K., Wang, J.Y., Araújo, M., Snoeck, D., Gruyaert, E., Debbaud, D., et al., 2016. Comparison of different approaches for self-healing concrete in a large-scale lab test. *Constr. Build. Mater.* 107, 125–137.
- Wang, J., 2013. Self-healing concrete by means of immobilized carbonate precipitating bacteria. Ph.D. Thesis, Ghent University, Ghent, Belgium.
- Wang, J., Van Tittelboom, K., De Belie, N., Verstraete, W., 2010. Potential of applying bacteria to heal cracks in concrete. In: *Proceedings of the Second International Conference on Sustainable Construction Materials and Technologies*, Ancona, Italy, pp. 1807–1818.
- Wang, J., De Belie, N., Verstraete, W., 2012. Diatomaceous earth as a protective vehicle for bacteria applied for self-healing concrete. *J. Ind. Microbiol. Biotechnol.* 39, 567–577.
- Wang, J., Snoeck, D., Van Vlierberghe, S., Verstraete, W., De Belie, N., 2014a. Application of hydrogel encapsulated carbonate precipitating bacteria for approaching a realistic self-healing in concrete. *Constr. Build. Mater.* 68, 110–119.
- Wang, J., Soens, H., Verstraete, W., De Belie, N., 2014b. Self-healing concrete by use of microencapsulated bacterial spores. *Cem. Concr. Res.* 56, 139–152.
- Wang, J., Dewanckele, J., Cnudde, V., Van Vlierberghe, S., Verstraete, W., De Belie, N., 2014c. X-ray computed tomography proof of bacterial-based self-healing in concrete. *Cem. Concr. Compos.* 53, 289–304.
- Wang, J., Mignon, A., Snoeck, D., Wiktor, V., Van Vlierberghe, S., Boon, N., et al., 2015. Application of modified-alginate encapsulated carbonate producing bacteria in concrete: a promising strategy for crack self-healing. *Front. Microbiol.* 6, 1088. Available from: <http://dx.doi.org/10.3389/fmicb.2015.01088>.

- Wang, J., Erşan, Y.C., Boon, N., De Belie, N., 2016. Application of microorganisms in concrete: a promising sustainable strategy to improve concrete durability. *Appl. Microbiol. Biotechnol.* 100 (7), 2993–3007. Available from: <http://dx.doi.org/10.1007/s00253-016-7370-6>.
- Wang, J., Jonkers, H.M., Boon, N., De Belie, N., 2017a. *Bacillus sphaericus* LMG 22257 is physiologically suitable for self-healing concrete. *Appl. Microbiol. Biotechnol.* 101 (12), 5101–5114. Available from: <http://dx.doi.org/10.1007/s00253-017-8260-2>.
- Wang, J., Vandevyvere, B., Vanhessche, S., Schoon, J., Boon, N., De Belie, N., 2017b. Microbial carbonate precipitation improves the quality of recycled aggregates for sustainable concrete production. *J. Clean. Prod.* 156, 355–366.
- Wiktor, V., Jonkers, H.M., 2011. Quantification of crack-healing in novel bacteria-based self-healing concrete. *Cem. Concr. Compos.* 33 (7), 763–770. Available from: <http://dx.doi.org/10.1016/j.cemconcomp.2011.03.012>.
- Wiktor, V., Jonkers, H.M., 2015. Field performance of bacteria-based repair system: pilot study in a parking garage. *Case Stud. Constr. Mater.* 2, 11–17.
- Xu, J., Yao, W., Jiang, Z., 2014. Non-ureolytic bacterial carbonate precipitation as a surface treatment strategy on cementitious materials. *J. Mater. Civ. Eng.* 26 (5), 983–991, doi:10.1061/(ASCE)MT.1943-5533.0000906.
- Zhang, J., Mai, B., Cai, T., Luo, J., Wu, W., Liu, B., et al., 2017. Optimization of a binary concrete crack self-healing system containing bacteria and oxygen. *Materials*. 10 (116), 1–11.
- Zhang, J.L., Wu, R.S., Li, Y.M., Zhong, J.Y., Deng, X., Liu, B., et al., 2016. Screening of bacteria for self-healing of concrete cracks and optimization of the microbial calcium precipitation process. *Appl. Microbiol. Biotechnol.* 100, 6661–6670.

Further Reading

- Silva, F., 2015. Up-scaling the production of bacteria for self-healing concrete application. Ph.D. Thesis, Ghent University, Belgium.

This page intentionally left blank

Bio-based admixture with substances derived from bacteria for the durability of concrete

20

Françoise Feugeas¹, Mai Tran² and Sara Chakri²

¹ICube, INSA Strasbourg, Strasbourg, France, ²Paris-Sorbonne University, Paris, France

20.1 Introduction

Cementitious materials are sensitive to many physical, chemical and biological factors responsible for their degradation (Feugeas, 2008; Roux, 2008; Ollivier and Vichot, 2008). One of their most frequent degradation mechanisms is reinforcement corrosion. Although the high-alkaline environment of concrete allows for the formation of a passive and protective oxide film on the surface of carbon steel used in concrete as reinforcement, an abundance of literature can be found concerning problems of concrete structure degradation due to reinforcement corrosion. As a matter of fact, the protective layer can be destroyed by the decrease in alkalinity of concrete (carbonation of the cover concrete) (Chang and Chen, 2006; Johannesson and Utgenannt, 2001; Pade and Guimaraes, 2007) and/or through entrance of chlorides, leading to pitting of passivated reinforcing steel (Ahmad, 2003; Basheer et al., 2001). The environmental conditions, such as CO₂ concentration and presence of chlorides, are not the only phenomena to be taken into account. The physical and chemical nature of concrete is also important, since the aggressive species must penetrate through the concrete pores to reach the reinforcement. Different ways of rebar protection from corrosion have been suggested:

- Increase the concrete cover on the steel rebar in the concrete (standard exposition class Eurocode 2) (Zhang and Lounis, 2006; EN 1992, 1997).
- Cathodic protection of rebars by deposition of a zinc layer on the surface of the steel, or by application of a direct current from a graphite mesh anode to the surface to be protected (Glass et al., 1997; Hassanein et al., 2002; Koleva et al., 2009).
- The use of corrosion inhibitors (Ormellese et al., 2008, 2009). This method can eventually be combined with cathodic protection (Efim, 2002; Whitmore, 2004).

Corrosion inhibitors such as monofluorophosphate (MFP) are sprayed or painted on mature concrete surfaces (Chaussadent et al., 2006), or added to the fresh concrete mix. Many of these inhibitors contain components that are not eco-friendly (Roux et al., 2010).

Corrosion inhibitors have been used successfully to preserve steel structures for many decades. More recently, they have been applied in the field of construction to preserve historical monuments and concrete constructions suffering from rebar corrosion. In their state-of-the-art report, [Sölylev and Richardson \(2008\)](#) focused on the most commonly used inhibitors, such as aminoalcohol, calcium nitrite, and sodium monofluorophosphate. They analyzed the effectiveness of corrosion inhibitors regarding mechanical performances, protection against corrosion in chloride-contaminated and carbonated concrete, penetrability of the inhibitor, influence on workability of fresh concrete and hardened concrete properties, and, finally, long-term behavior for real structures. They made conclusions with regards to the ability of those products to delay the corrosion initiation of rebars exposed to chloride attack and carbonation. The inhibition efficiency appeared to be less significant once corrosion was initiated, mainly due to the difficulty of penetration of the inhibitors through the pores of the concrete. This is why the development of admixtures as corrosion inhibitors has developed as an alternative with higher efficiency. Moreover, the growing demand for corrosion inhibitors that are biodegradable and less toxic than the current formulations turns researchers towards the development of eco-friendly admixtures providing a sustainable protection against corrosion.

This study presents the performance of a bioadmixture, containing bacterial extracellular substances, with regard to the corrosion inhibition efficiency in different solutions representative of concrete. Three interstitial solutions obtained with standard cements CEM I, CEM II, and CEM III were tested with and without bioadmixture. The inhibiting effect of bioadmixture addition in synthetic solutions containing chlorides was also investigated and highlighted the inhibiting effect of the biomolecule against chloride-induced depassivation of steel.

20.2 Types of corrosion inhibitors in concrete

All kinds of corrosion inhibitors used for protection or repair for concrete structures will not be described in this section. These can be classified according to their application methods, or their mechanism of protection, or their content. Here, only corrosion inhibitors that can be used as admixtures or applied on the hardened concrete surface are considered with regard to their content and their ecological impact. These type of corrosion inhibitors can induce an increase in the corrosion potential of the rebar and act as anodic inhibitors. When they act on the oxygen reaction of the reinforcement and reduce the corrosion rate by a decrease in corrosion potential, they are cathodic inhibitors. Mixed inhibitors are able to reduce the corrosion rate without a significant change in the corrosion potential, thanks to their action on both anodic and cathodic sites of the steel.

Admixtures based on alkali metals or on alkaline earth metal nitrates ([Fujita and Kashima, 1982](#); [Kudo and Ibe, 1976](#); [Rosenberg and Gaidis, 1981](#); [Whitaker, 1974](#)) have disadvantages linked to the ecological and toxic risks associated with nitrates.

Admixtures containing alkanolamines and alcohols trihydrates or tetrahydrates have been described (Fellows and Eckler, 1988) for the protection of steel, but their application to mineral building materials like cementitious materials has not been described in the literature. Other water-soluble hydroxylamine-based products (Martin and Miksic, 1987) react with carboxylic acids to reduce their volatility before acting as corrosion inhibitors. As for many migrating corrosion inhibitors, the main problem consists of controlling the concentration of inhibitor needed at the level of the embedded steel. Elsener et al. demonstrated that the inhibitory action of migrating corrosion inhibitors was not detectable by measurements of corrosion currents (Elsener et al., 2000). It is assumed that the inhibitors do not diffuse deep enough into the cement matrix to be active at the metal-cement interface. Another patent (Standke and McGettigan, 2003) discloses the use of organosilane and/or organosiloxane-containing inhibitors as admixture in concrete or to be applied on hardened concrete. No results were found concerning the use of these products as admixture in fresh concretes, particularly with regard to potential modifications in the rheology of these. The same remarks can be made about the patents by Furman et al. (2005) and Miksic et al. (1997, 1998). Their formulas are based on sodium gluconate and sodium molybdate (Miksic et al., 1997, 1998) with aluminum nitrate, cyclohexylammonium benzoate, ethylammonium benzoate, ammonium and dimethyl ethanolamine (Furman et al., 2005) assumed to inhibit possible alkali-reactions in concrete. Some inhibitors were proposed as admixture with rheology-modifying properties of fresh concrete (Miksic et al., 2002). They contain alkaline earth lignosulfates in addition to ammonium benzoates and sodium glucoheptonates which give plasticizer properties to the product. No indication concerning mechanical behavior of these cured concretes was given. One patent (Miksic et al., 2006) describes the composition and method of using fiber-reinforced mortars to repair reinforced concrete structures. Corrosion inhibitors used as admixture in these mortars contain ammonium benzoates, sodium and potassium sebacates. They are assumed to diffuse into the hardened concrete to reach the rebars. Other patents (Arfael et al., 1993; Berke and Hicks, 1997; Berke et al., 1996, 2002) disclose inhibitors containing calcium nitrite and stearate, nitrate or alkaline earth metal nitrite combined with components modifying the rheology of fresh concrete (for instance superplasticizers), or the setting time of the concrete (accelerators or retarders). The 20 patents mentioned offer products that can be used as admixtures in fresh concrete or applied to hardened concretes. Regarding the corrosion inhibitors applied to mature concrete, the main issue concerns the ability of the active ingredient to diffuse from the cover to the reinforcement. This kind of inhibitor mostly acts as a barrier against ingress of aggressive agents in water, rather than through a direct interaction between the inhibitor and the rebars. These products are able to clog the porous network of concrete and consequently decrease the rate of capillary imbibition of the concrete, without having reached the reinforcement located more deeply in the concrete. In the case of mature concrete repair, the solution consisting of the use of mortar with corrosion inhibitors in their composition present the same problem of diffusion control, whatever the chemical composition of the corrosion inhibitor.

Corrosion inhibitors as admixtures present an easily implemented solution to improve the durability of concrete. It could be claimed that a new concrete, correctly designed, should not face problems of rebar corrosion but, with regard to the increasing demands on the time of use and the potential recyclability of concrete, admixtures with corrosion inhibition provide additional safety for concrete to withstand degradation due to aggressive environments.

Concrete is known to bear high compressive stresses but its tensile strength is limited. In the tension zone, concrete will always exhibit cracks. This explains why it has been estimated that, in Europe, 50% of the annual construction budget is spent on the rehabilitation and repair of existing structures (Tittelboom et al., 2011).

Using admixture as a corrosion inhibitor provides the advantage of acting directly on the reinforcement without having to diffuse through the concrete porosity. It is worth pointing out, however, that there are contradictory results in the literature about the influence of such products on concrete properties (Sölylev and Richardson, 2008), depending on their chemical composition, their concentration, their compatibility with other admixtures, their effect on properties of fresh and hardened concrete are susceptible to variation. It is therefore of great importance to check the possibility of harmful effects arising from the use of those admixtures. Furthermore, the majority of inhibitors described in the current patents containing chemical substances, few of them are not eco-friendly with regard to the criteria for Environmental and Health Data Sheets.

20.3 Case study: bio-based admixture from bacterial extracellular substances

20.3.1 Bio surfactant as bio admixture

Many admixtures (chemical admixtures and mineral admixtures) are used to improve the rheological properties of fresh concrete and to influence the behavior of hardened concrete (Palacios and Puertas, 2005; Şahmaran et al., 2006; Černý et al., 2006; Izaguirre et al., 2009).

Bioadmixtures attract increasing scientific interest, as a result of the increasing demand for inhibitors displaying substantially improved environmental properties (Zhor and Bremner, 1996; Plank, 2004; Riedel and Nickel, 2000; Orts et al., 2007). Bioadmixtures generally result from industrial biotechnological processes (e.g., welan gum) (Sonebi, 2006). They are extracted from fermentation processes by culturing fungi or bacteria (e.g., extracellular polysaccharide) (Roux et al., 2010), or include polymers with significant biodegradability (e.g., polyaspartic acid) (Amjad, 2011).

The application of bioadmixtures in the cement-based industry is relatively recent. Kahng used the extracellular production from *Paenibacillus sphaericus* as a viscosity-modifying bioadmixture for cement mortar (Kahng et al., 2001). Khayat and Yahia investigated the effects of combined bioadmixtures of welan gum and naphthalene-based water reducer on the rheological properties of cement grouts

(Khayat and Yahia, 1997). Lignosulfonate is a plasticizer which improves the workability of concrete (Wang et al., 2012). Patural studied the effect of cellulose ethers as bioadmixture on both water retention and rheological properties of cement-based mortars (Patural et al., 2011).

The present study concerns the development of environmentally friendly products to be incorporated into concrete (admixtures) in accordance with REACH requirements and simultaneously fulfilling two conditions: limiting biocontamination of the surface of concrete and improving the corrosion resistance of the reinforcement. The efficiency against biocontamination of cementitious surfaces has been analyzed previously (Chagnot et al., 2015). Furthermore, standardized tests have permitted the validation of this product as admixture for concrete (He et al., 2014), leading to the elaboration of concretes that are more eco-friendly and more resistant to natural environments than traditional Portland cement concrete (CEM I) (Roux et al., 2013). The work presented below focuses on the improvement of durability of concrete structures by protecting their reinforcement from corrosion.

The active ingredients of the admixture consist of bacterial exo-products. They are eco-friendly and in agreement with the criteria for establishing Environmental and Health Data Sheets (SDS).

Many bacteria are able to produce amphipathic substances, i.e., “biosurfactants,” which are potentially interesting compounds in many fields of study, due to having both hydrophilic and hydrophobic moieties in the same molecule (Shubina et al., 2015). Some of them have antimicrobial activity, such as lipopeptides (surfactin, iturin, etc.) produced by *Bacillus* and *Pseudomonas* (Lang, 2002), or amphisin compounds which possess strong antifungal activity (Nielsen et al., 2002). These biomolecules are often controlling plant pathogenic germs (zoospores) and creating ducts in the cytoplasmic membrane of the infectious germ (Raaijmakers et al., 2006). Biosurfactants also have the advantage of being efficient and stable (*Bacillus subtilis* (Joshi et al., 2008)) in a wide range of environmental conditions (pH, temperature, salinity). Some of them are able to maintain their surface activity at temperatures up to 90°C (Kretschmer et al., 1982) or for salinity up to five times higher than those tolerated by chemical surfactants (Donaldson and Staub, 1981). The emulsifying properties of surfactants synthesized by *Serratia marcescens* are also preserved at temperatures in the range of 10–120°C and pH values ranging from 2 to 12 (Pruthi and Cameotra, 1997). Moreover, biosurfactants exhibit good biodegradability and lower toxicity (Nitschke and Costa, 2007).

In this study, a lipopeptide biosurfactant (viscosinamide) derived from *Pseudomonas fluorescens* was used. It was produced on a solid medium, as previously described (Meylheuc et al., 2001). Briefly, plates of King’s B (KB) agar were densely inoculated with two loops of a suspension of *Pseudomonas fluorescens* 495. The inoculated plates were incubated for 4 days at 22°C. The bacterial lawns were scraped from the agar and the cells were resuspended in sterile, demineralized water and dispersed, using a vortex mixer operated at maximum speed. The supernatant containing the biosurfactant was separated from the cells by centrifuging for 30 minutes. The supernatant was then filtered through a 0.22- μm pore-size filter

and stored at 4°C. The surface activity of the biosurfactant and its critical micelle dilution (CMD) were determined by surface tension measurements of the supernatants and dilutions using the Wilhelmy plate method and a tensiometer.

20.4 Corrosion study

Though chloride ion attack and carbonation have been identified as the main mechanisms responsible for the initiation of reinforcing steel corrosion (Cao et al., 1993; Boah et al., 1990; Sagocecrensil et al., 1993; Freire et al., 2009; Albani et al., 1990; Moreno et al., 2004; Abd El Haleem et al., 2010a; Tang et al., 2012), sulfate ions have also been reported to actively participate in the corrosion of reinforcing steel (Abd El Haleem et al., 2010b, 2013; Ghods et al., 2009; Haruna and Komote, 2002; Gui and Devine, 1994; Montemor et al., 1998; Altayyib et al., 1988). The sulfate source for concrete can be external (from water or soil) or internal, when sulfate is initially present in the cement or has been added as gypsum to regulate the hydration reactions of the Portland cement. The presence of sulfates has been reported to have two effects: the first one is related to the resistance of the concrete and the second one to the corrosion resistance of the rebars. When the concentration of sulfates is high enough in the concrete pore solution, it is known to react with tri-calcium aluminates of the cement to form ettringite ($3\text{CaO} \cdot \text{Al}_2\text{O}_3 \cdot 3\text{CaSO}_4 \cdot 32\text{H}_2\text{O}$) which reduces the strength of concrete (Page and Treadaway, 1982). Moreover, according to Abd El Haleem et al. (2013), the presence of sulfates can significantly influence the composition and the thickness of the oxide layer. Comparing the shift of the open-circuit potential of iron in interstitial solutions containing the same amount of chlorides and sulfates, it was concluded that sulfate ions are even more corrosive than chloride ions toward steel rebars.

To follow the stability or the breakdown of the passive film using electrochemical methods, a convenient way is to perform measurements in simulated concrete pore solutions. Corrosion rates, determined by means of experiments involving steel electrodes immersed in simulated solutions, can hardly be extrapolated to the rates measured in concrete, since the diffusion kinetics of the reactants are very different in aqueous solutions than in the solid material. Nevertheless, experiments performed in aqueous solutions provide useful information on the influence of a specific reactant at different concentrations (anions or cations present in the concrete, as well as different additives and inhibitors). Moreover, the pH value of a solution can be easily adjusted.

This approach was used in the present work to check the influence of the presence of the bioadmixture (BA) described above, on the corrosion rate of carbon steel in interstitial solutions with different sulfate concentrations, and in synthetic solutions with different chloride concentrations. The corrosion resistance was evaluated using electrochemical methods such as linear polarization and impedance spectroscopy.

20.4.1 Material

The material studied is a C15 mild steel, generally used as metal reinforcement in concrete, according to EN 10277-2. The composition of the major elements of C15 steel is presented in the Table 20.1.

Table 20.1 Chemical composition (% weight) of the carbon steel C15 (W.NR.: 1.0401) (in accordance with “EN 10227-2”)

C	Si	Mn	P	S	Fe
0.12–0.18	0–0.40	0.30–0.80	0–0.045	0–0.045	Balance

Table 20.2 Majority ions content in the simulated concrete pore solutions (extracted from concrete mixture with w/c = 0.45)

Concrete mixture	Na ⁺ (g/L)	K ⁺ (g/L)	Ca ²⁺ (g/L)	SO ₄ ²⁻ (g/L)	pH
CEM I	2.02	13.65	0.64	18.24	13.6
CEM II	1.38	8.58	0.60	11.52	13.5
CEM III	0.85	7.41	0.76	7.68	13.2

20.4.2 Interstitial solutions obtained from different cements

Interstitial solutions were obtained by adding cement powder to deionized water with a water-cement (w/c) ratio of 0.45. Three Portland cements (CEM I 52.5 N, CEM II/B-S 42.5 N, and CEM III/A 42.5 N-LH with 61% by mass of slag) were used and the cement paste was mixed using a IKA Eurostar 20 mixer with a defloculating blade. After mixing for ~1.5 minutes, the paste was filtered by means of a vane pump, using two filters of 11 and 20 μm, then using a 1.0 and 0.2 μm filter syringe. The elemental concentrations of Ca²⁺, Na⁺, K⁺, and SO₄²⁻ in the pore solutions extracted shortly after mixing were then monitored as follows: concentrations in alkali (sodium and potassium) were assayed by atomic absorption spectrometry, whereas sulfate and calcium concentrations were determined respectively by turbidimetry and by potentiometry using a calcium ion-selective electrode. The pH value and the concentrations obtained for the various cements are shown in Table 20.2. Similar calcium concentrations and similar pH values were observed for the three cements (as expected), since the interstitial solution of the concrete is usually saturated with lime. CEM I cement, which contains higher amount in clinker than CEM II and CEM III cements, also shows the higher sulfate and alkali (Na⁺ and K⁺) contents. In all solutions used for electrochemical measurements, the pH value was systematically adjusted to a fixed value of 13.0, in order to avoid the effect of small pH differences between the solutions. At the end of each experiment, the pH was measured again and its value was found to be always greater than or equal to 12.5. This small pH variation due to the carbonation of the solution is assumed to have no effect on the corrosion behavior of the steel.

In order to obtain interstitial solutions with BA, 10% by volume of the bioadmixture (BA) was added.

To study the influence of BA on the corrosion behavior of the C15 steel sample in the presence of chlorides, a synthetic solution was prepared, containing 0.1 mol/L (4 g/L) of NaOH (pH = 13). Two chloride concentrations were investigated: 0.5 and 1 mol/L (17.75 and 35.50 g/L).

20.4.3 Corrosion inhibition of bio-based admixture in interstitial solutions without chlorides

Anodic polarization curves obtained in the interstitial solutions of CEM I and CEM III are presented in Fig. 20.1, after 60 hours of immersion of the steel sample at the open-circuit potential. The shape of all polarization curves is similar, showing a passivity plateau extended over several hundreds of millivolts. This passive step is followed by an increase in the current, corresponding to the trans-passive domain for potentials $E > 0.1$ V/MSE (saturated mercury sulfate electrode $E = +0.645$ V/SHE).

Since the behavior in interstitial solutions obtained with CEM II and CEM III are identical, only the results obtained in the latter case are here reported and discussed.

20.4.3.1 Without bio-based admixture (BA)

In the absence of BA (curves a and c) the amplitude of the stationary passive current density is 15 times higher in the CEM solution I compared with that obtained in the CEM III solution. Since sodium and potassium ions are not likely to influence the corrosion rate, and since the pH of the solution was adjusted to the same value in the two solutions, the difference in the amplitude of the passive plateau was attributed to the difference in sulfate concentration, with a significant increase in the stationary passive current density when the concentration of sulfates increases. A higher sulfate content in the CEM I solution is not surprising since CEM I has a higher clinker content than CEM III.

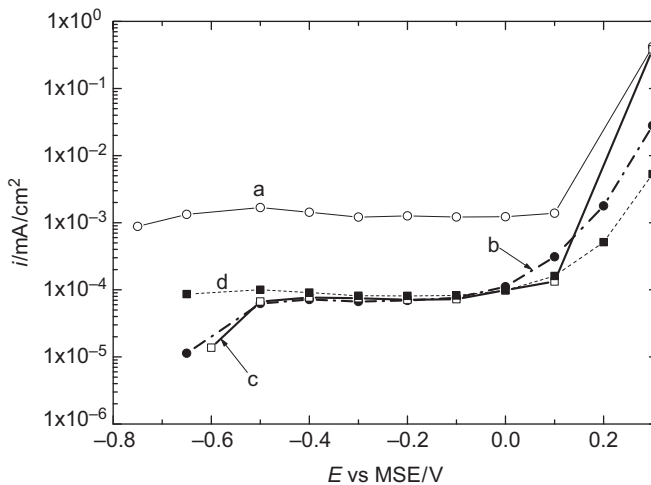


Figure 20.1 Stationary anodic curves of a C15 steel electrode after 60 h of immersion in interstitial solution: (a) CEM I; (b) CEM I with bioadmixture; (c) CEM III; (d) CEM III with bioadmixture.

The results in the present work are in agreement with those obtained by Haruna and Komote (2002), Abd El Haleem et al. (2010a, 2010b), Ghods et al. (2009), and Gui and Devine (1994), who have demonstrated the detrimental effect of sulfate ions on the protective oxide layer of reinforcing steel. Using XPS surface analyses, Montemor et al. (1998) have highlighted the influence of the chemical composition on the interstitial solution on the composition of the passive oxide layer. The presence of sulfates in the interstitial solution has been shown to lead to the formation of a hydrated passive film of mainly oxyhydroxide (FeOOH), in accordance with the results of Altayyib et al. (1988) who concluded that corrosion of steel in concrete in the presence of sulfates is induced by the modification of the protective oxide layer.

20.4.3.2 In the presence of bio-based admixture (BA)

The open-circuit potential of the C15 mild steel sample immersed during 60 hours in the two different interstitial solutions shows roughly the same value in the presence and absence of BA, as shown in Fig. 20.1 (compare curves a and c to curves b and d). The shapes of the anodic curves are similar with and without BA, showing a passive behavior characteristic of the presence of a passive oxide layer on the surface of the C15 mild steel. A clear effect of BA addition was observed in the CEM I solution, for which the amplitude of the passive current density decreased significantly in the presence of BA. Indeed, the passive current density of 1.2×10^{-6} A/cm² in absence of the BA is 17 times larger than that recorded in the presence of the BA (7×10^{-8} A/cm²), thereby evidencing the BA's inhibiting effect towards corrosion. On the contrary, in the CEM III solutions no significant influence of BA addition could be deduced from the anodic curves. The passive currents in these two solutions did not differ significantly and are very low in the two cases (in the range of 0.08 μ A/cm²). Since the current density plateau starts in the vicinity of the open-circuit potential, its value can provide a good estimation of the corrosion current density. This approach was used in Table 20.3 for estimating the corrosion rates from Fig. 20.1. The impedance diagrams obtained at the open-circuit potential in CEM I solutions with and without BA are shown in Fig. 20.2. The low

Table 20.3 Corrosion rate of C15 in the different interstitial solutions: i_{passive} is the passive current density, Δm the mass loss calculated from Faraday's law, Δe is the loss of thickness

Solution	CEM I	CEM I with BA	CEM III	CEM III with BA
i_{passive} (μ A/cm ²)	1.2	0.07	0.08	0.08
Δm (mg/cm ² per year)	11	0.64	0.73	0.73
Δe (μ m/year)	14	0.82	0.94	0.94

frequency limit of the real part of the diagram (R_p) is inversely proportional to the corrosion current density. In the CEM I solution, the low frequency limit is significantly higher in the presence of BA, thus reflecting the inhibiting effect of the bioadmixture added to the solution CEM I. On the contrary, the modification of the impedance diagrams in the presence of BA is negligible for CEM II and CEM III solutions (results not shown). These results are in agreement with that obtained from the anodic polarization curves where the corrosion current in the presence of BA is 17 times less than without addition of BA for the solution CEM I. In the other solutions, the difference in the electrochemical behavior with and without BA was not very obvious. However, the addition of BA in solution CEM I demonstrated the good inhibition efficiency of the bioadmixture towards corrosion in the presence of sulfates.

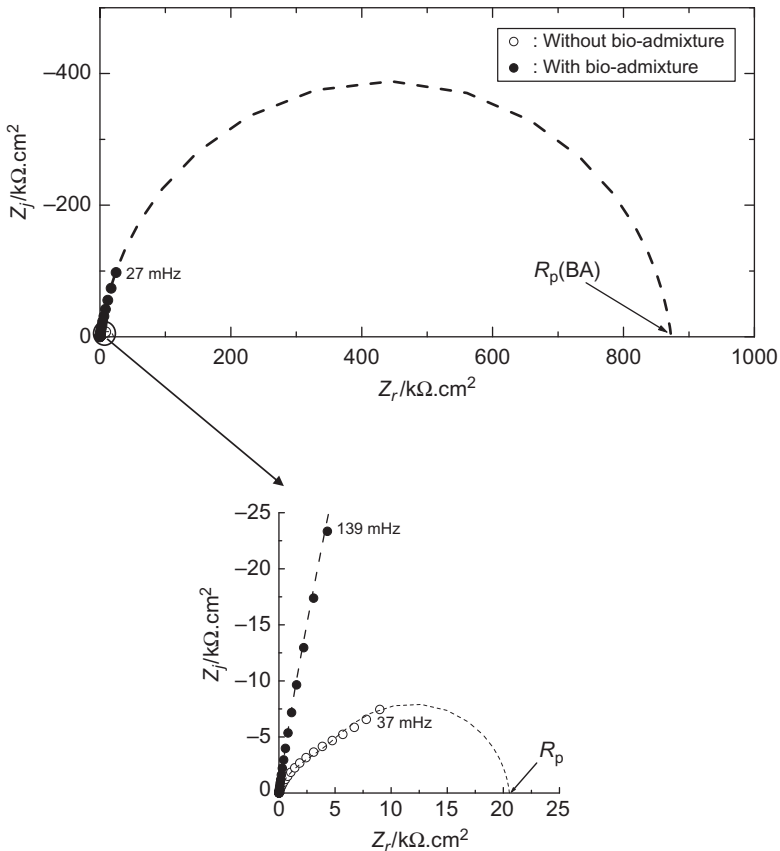


Figure 20.2 Impedance diagrams of C15 steel electrode at corrosion potential E_{corr} after 60 h of immersion in interstitial CEM I solution with and without bioadmixture.

20.4.4 Corrosion inhibition of bio-based admixture (BA) in synthetic solutions containing chlorides

The anodic polarization curves of the C15 mild steel obtained after 60 hours of immersion at the corrosion potential in different solutions are presented in Fig. 20.3.

In the presence of chloride ions, the curves have the same shape, with a passivity plateau extending over few-hundred millivolts, depending on the concentration of

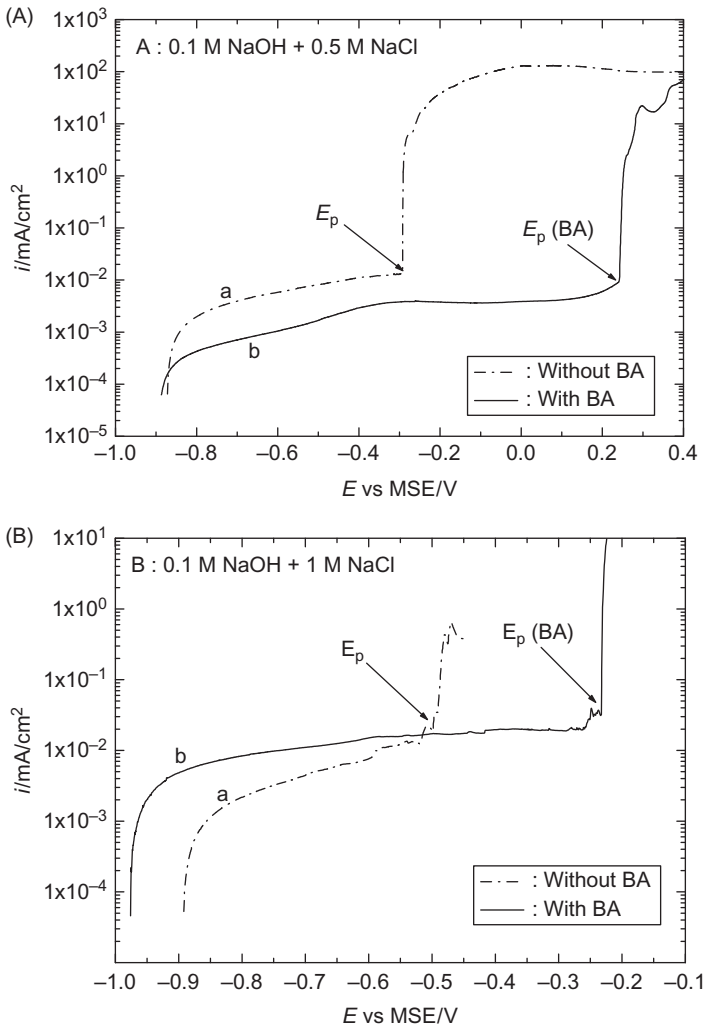


Figure 20.3 Anodic polarization curves ($v = 0.5$ mV/s) of a C15 steel electrode after 60 h of immersion in 0.1 M NaOH solution (pH = 13) containing 0.5 (A) or 1 M NaCl (B) with and without bioadmixture.

chloride ions. The value of the passive current is similar with and without chlorides, with an amplitude of several microampere. The value of the corrosion potential E_{corr} is about -0.9 V/MSE in the presence of chlorides—slightly more negative than the value obtained in the absence of chlorides (-0.7 V/MSE) (Fig. 20.1). This is in agreement with numerous studies reported in the literature, and in particular with the work of Abd El Haleem et al. (2010a, 2010b), for which the corrosion potential becomes less and less noble, when the chloride concentration increases.

20.4.4.1 Effect on pitting potential

An abrupt increase in the current density is observed at $E = -0.3$ V/MSE for the solution with 0.5 mol/L NaCl, and at $E = -0.5$ V/MSE for the solution with 1 mol/L NaCl. This potential corresponds to the pitting potential and its value gets less and less anodic when the chloride concentration increases. Simultaneously, the passive plateau gets shorter and the susceptibility to pitting is enhanced. This result is in agreement with the literature which reports that the risk of corrosion increases when the ratio $[\text{Cl}^-]/[\text{OH}^-]$ increases (Page and Treadaway, 1982; Wasime and Hussain, 2015).

The shape of the curves is the same with and without BA. Nevertheless, the influence of the addition of BA clearly modifies the value of the pitting potential which moves ~ 500 mV towards more anodic potentials for 0.5 M NaCl and 300 mV for 1 M NaCl. These results demonstrate the good corrosion-inhibiting effect of the bioadjuvant towards pitting. It is also noted that the efficiency of BA on the current of passivity is comparable in the presence and absence of chloride ions in solution.

Impedance diagrams were plotted at the open-circuit potential with and without addition of BA and are shown in Fig. 20.4.

The diagrams in Nyquist representation show a capacitive loop. The diameter of this capacitive loop increases considerably in the presence of BA, corroborating the protective character of the layer of oxides, which is in agreement with the results obtained from the polarization curves.

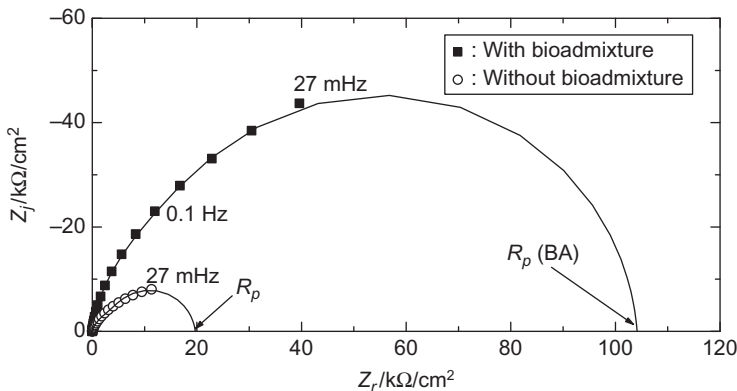


Figure 20.4 Impedance diagrams of C15 steel in representation of Nyquist at E_{corr} after 60 h of immersion in chloride solution with and without addition of BA.

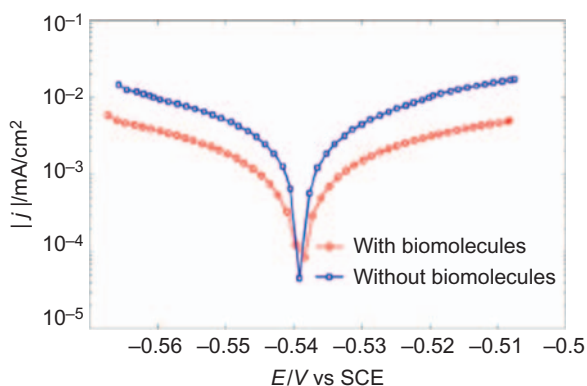


Figure 20.5 Polarization curves of carbon steel in aggressive simulated concrete pore solution with and without biomolecules (Shubina et al., 2016).

20.4.4.2 Corrosion inhibiting mechanism of bioadmixture (BA)

The efficiency of BA as a corrosion inhibitor was studied by Shubina et al. (2016) in chloride containing solutions. The current potential curves in the anodic and the cathodic potential range are presented in Fig. 20.5. It clearly appears that the presence of the biomolecules decrease both the anodic current (metal oxidation through the passive layer) and the cathodic current (oxygen or water reduction). Such a behavior is characteristic of a mixed inhibitor and is in agreement with previous observations (Fig. 20.1) that BA addition into the interstitial solution has no influence on the value of the open-circuit potential.

In order to get further insights into the corrosion inhibiting mechanism of BA, the authors Shubina et al. (2016) performed XPS analyses of the surface of carbon steel samples immersed in the BA containing alkaline solution (Fig. 20.6). The presence of a nitrogen peak on the survey spectrum is assumed to be the fingerprint of an adsorbed layer of biomolecules at the steel surface.

In the present case, the BA molecules are likely to be adsorbed at the passivated steel surface, via a nitrogen containing group. This behavior is usually observed in the case of organic inhibitors, which possess at least one functional group containing a heteroatom (like N, O, S) able to interact with the metallic substrate.

20.5 Conclusions

Electrochemical measurements clearly showed the beneficial influence of BA addition towards corrosion of a reinforced steel sample in interstitial concrete solutions.

In the absence of chlorides and of any carbonation, the corrosion rate is already very low in solutions with low sulfate addition. In this case, addition of BA has no influence on the corrosion rate. In the presence of higher sulfate concentrations, for

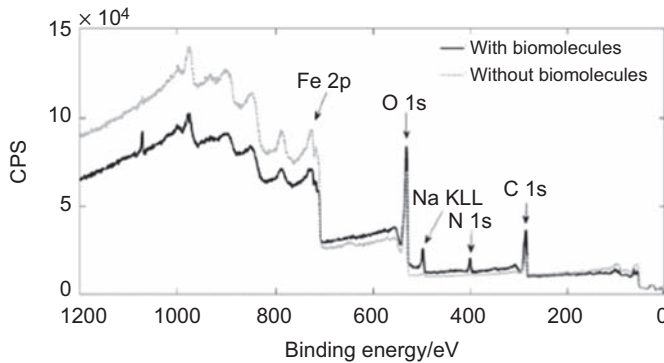


Figure 20.6 XPS survey spectra for the carbon steel specimens after corrosion tests in simulated concrete pore solution: without (dashed line) and with biomolecules (full line) (Shubina et al., 2016).

instance in the solutions obtained with CEM I cement, the presence of BA is able to compensate the detrimental effect of sulfates on the corrosion rate.

In the case of chloride uptake by the concrete, the chloride-induced depassivation of steel is clearly inhibited in the presence of BA. In summary, biomolecule addition to the interstitial solution has a beneficial effect on the stability of the passive film on mild steel, improving its resistance against damage caused by uniform attack, as well as by pitting process.

The product prepared from bacterial extracellular substances, validated as bioadmixture with composition and dosage determined for the most common concretes (CEM I) proved its effectiveness as a corrosion inhibitor on young concrete (pH 13).

Original experimental procedures have been developed to provide a better understanding of:

- Modifications of the films formed on the steels subjected to different electrolytes representative of the interstitial fluids present in different types of concretes.
- The inhibitory capacities of these films.

The effectiveness of the bioadmixture in real conditions still needs to be tested with respect to the corrosion of reinforcement within different concrete mixtures subjected to different environmental conditions (sea water, alpine environment ...). The bioadmixture developed thus proves to be an eco-friendly and innovative solution with a high potential in the field of the market for agents protecting concrete.

References

- Abd El Haleem, S.M., Abd El Aal, E.E., Abd El Wanees, S., Diab, A., 2010a. Environmental factors affecting the corrosion behaviour of reinforcing steel: I. The early stage of passive film formation in $\text{Ca}(\text{OH})_2$ solutions. *Corros. Sci.* 52 (12), 3875–3882.
- Abd El Haleem, S.M., Abd El Wanees, S., Abd El Aal, E.E., Diab, A., 2010b. Environmental factors affecting the corrosion behavior of reinforcing steel II. Role of some anions in

- the initiation and inhibition of pitting corrosion of steel in $\text{Ca}(\text{OH})_2$ solutions. *Corros. Sci.* 52 (2), 292–302.
- Abd El Haleem, S.M., Abd El Wanees, S., Bahgat, A., 2013. Environmental factors affecting the corrosion behaviour of reinforcing steel. V. Role of chloride and sulphate ions in the corrosion of reinforcing steel in saturated $\text{Ca}(\text{OH})_2$ solutions. *Corros. Sci.* 75, 1–15.
- Ahmad, S., 2003. Reinforcement corrosion in concrete structures, its monitoring and service life prediction--a review. *Cem. Concr. Compos.* 25, 459–471.
- Albani, O.A., Gassa, L.M., Zerbino, J.O., Vilche, J.R., Arvia, A.J., 1990. Comparative study of the passivity and the breakdown of passivity of polycrystalline iron in different alkaline-solutions. *Electrochim. Acta.* 35 (9), 1437–1444.
- Altayyib, A.J., Somuah, S.K., Boah, J.K., Leblanc, P., Almana, A.I., 1988. Laboratory study on the effect of sulfate-ions on rebar corrosion. *Cem. Concr. Res.* 18 (5), 774–782.
- Amjad, Z., 2011. Effect of surfactants on gypsum scale inhibition by polymeric inhibitors. *Desalin. Water Treat.* 36, 270–279.
- Arfael, A., Berke, N.S., Jardine, L.A., 1993. Additifs inhibiteurs de la corrosion pour ciments hydrauliques et compositions les contenant. European Patent Office, W.R. Grace & Co., USA.
- Basheer, L., Kroppb, J., Clelandc, D.J., 2001. Assessment of the durability of concrete from its permeation properties: a review. *Constr. Build. Mater.* 15, 93–103.
- Berke, N.S., et al., 1996. Composés améliorés d'inhibition de la corrosion à bas de nitrite de calcium. World Intellectual Property Organization, W.R. Grace & Co., USA.
- Berke, N.S., Hicks, M.C., 1997. Inhibiteurs de corrosion à base de nitrite, à performance améliorée d'inhibition de la corrosion anodique et cathodique. European Patent Office, W.R. Grace & Co., USA.
- Berke, N.S., Hicks, M.C., Malone, J., 2002. Composition d'adjuvant entraîneur d'air. World Intellectual Property Organization, W.R. Grace & Co., USA.
- Boah, J.K., Somuah, S.K., Leblanc, P., 1990. Electrochemical-behavior of steel in saturated calcium hydroxide solution containing Cl^- , SO_4^{2-} , and CO_3^{2-} ions. *Corrosion.* 46 (2), 153–158.
- Cao, H.T., Bucea, L., Sirvivatnanon, V., 1993. Corrosion rates of steel embedded in cement pastes. *Cem. Concr. Res.* 23 (6), 1273–1282.
- Černý, R., Kunca, A., Tydlitát, V., Drchalová, J., Rovnaníková, P., 2006. Effect of pozzolanic admixtures on mechanical, thermal and hygric properties of lime plasters. *Constr. Build. Mater.* 20, 849–857.
- Chagnot, C., Shen, C., Munzer, C., Deschamps, J., Feugeas, F., Meylheuc, T., 2015. Méthode d'évaluation de la biocontamination de surface des matériaux cimentaires par microscopie confocale à balayage laser. *Mater. Tech.* 103 (2), 205.
- Chang, C.-F., Chen, J.-W., 2006. The experimental investigation of concrete carbonation depth. *Cem. Concr. Res.* 36, 1760–1767.
- Chaussadent, T., Nobel-Pujol, V., Farcas, F., Mabile, I., Fiaud, C., 2006. Effectiveness conditions of sodium monofluorophosphate as a corrosion inhibitor for concrete reinforcements. *Cem. Concr. Res.* 36, 556–561.
- Donaldson, E.C., Staub, H.L., 1981. Comparison of methods for measurement of oil saturation. In: Symposium of Enhanced Oil Recovery, San Antonio, TX.
- Efim, Y.L., 2002. Cathodic protection of reinforced concrete with impregnated corrosion inhibitor. WO/2002/033147, Northern Technologies International Corporation, World Intellectual Property Organisation.
- Elsener, B., et al., 2000. Migrating corrosion inhibitor blend for reinforced concrete: Part 2. Inhibitor as repair strategy. *Corrosion.* 56 (7), 727–732.

- EN 1992, 1997. Eurocode 2: Calcul des structures en béton. AFNOR.
- Fellows, L.A., Eckler, E.P., 1988. A corrosion inhibitor for mild steel comprising the combination of trimethylolethane or trimethylolpropane with a disclosed alkanolamine. United States Patent and Trademark Office, International Minerals & Chemical Corp., USA.
- Feugeas, F., 2008. Bétons: Bioaltération et Biodétérioration. In: Biodétérioration des matériaux: Action des microorganismes de l'échelle nanométrique à l'échelle macroscopique. ELLIPSES, collection Technosup, pp. 85–100.
- Freire, L., Novoa, X.R., Montemor, M.F., Carmezim, M.J., 2009. Study of passive films formed on mild steel in alkaline media by the application of anodic potentials. *Mater. Chem. Phys.* 114 (2–3), 962–972.
- Fujita, T., Kashima, T., 1982. Corrosion-inhibiting method for steel materials in concrete. Kiresuto Kagaku Kabushiki Kaisha (Ed.), United States Patent and Trademark Office, Kiresuto Kagaku Kabushiki Kaisha, USA.
- Furman, A., et al., 2005. Corrosion inhibiting materials for reducing corrosion in metallic concrete reinforcements. United States Patent and Trademark Office, Cortec Corporation, USA.
- Ghods, P., Isgor, O.B., McRae, G., Miller, T., 2009. The effect of concrete pore solution composition on the quality of passive oxide films on black steel reinforcement. *Cem. Concr. Compos.* 31 (1), 2–11.
- Glass, G.K., Hassanein, A.M., Buenfeld, N.R., 1997. Monitoring the passivation of steel in concrete induced by cathodic protection. *Corros. Sci.* 39, 1451–1458.
- Gui, J., Devine, T.M., 1994. The influence of sulphate ions on the surface enhanced Raman spectra of passive films formed ions. *Corros. Sci.* 36 (3), 441–462.
- Haruna, T., Komote, K., 2002. Effect of sulfate ion on corrosion of carbon steel in carbonate/bicarbonate solutions. *Corros. Eng.* 51, 485–494.
- Hassanein, A.M., Glass, G.K., Buenfeld, N.R., 2002. Protection current distribution in reinforced concrete cathodic protection systems. *Cem. Concr. Compos.* 24, 159–167.
- He, H., Serres, N., Meylheuc, T., Feugeas, F., 2014. Workability tests on fresh concrete formulated with eco-friendly admixture. *J. Civ. Eng. Archit.* 8 (3), 98–104.
- Izaguirre, A., Lanas, J., Álvarez, J., 2009. Effect of water-repellent admixtures on the behavior of aerial lime-based mortars. *Cem. Concr. Res.* 39, 1095–1104.
- Johannesson, B., Utgenannt, P., 2001. Microstructural changes caused by carbonation of cement mortar. *Cem. Concr. Res.* 31, 925–931.
- Joshi, S., Bharucha, C., Desai, A.J., 2008. Production of biosurfactant and antifungal compound by fermented food isolate *Bacillus subtilis* 20B. *Bioresour. Technol.* 99, 4603–4608.
- Kahng, G.G., Lim, S.H., Yun, H.D., Seo, W.T., 2001. Production of extracellular polysaccharide, EPS WN9, from *Paenibacillus* sp. WN9 KCTC 8951P and its usefulness as a cement mortar admixture. *Biotechnol. Bioprocess. Eng.* 6, 112–116.
- Khayat, K., Yahia, A., 1997. Effect of welan gum-high-range water reducer combinations on rheology of cement grout. *ACI Mater. J.* 94, 365–372.
- Koleva, D.A., Guo, Z., Van Breugel, K., De Wit, J.H.W., 2009. Conventional and pulse cathodic protection of reinforced concrete: electrochemical behavior of the steel reinforcement after corrosion and protection. *Mater. Corros.* 60, 344–354.
- Kretschmer, A., Bock, H., Wagner, F., 1982. Chemical and physical characterization of interfacial-active lipids from *Rhodococcus erythropolis* grown on n-alkanes. *Appl. Environ. Microbiol.* 44, 864–870.
- Kudo, N., Ibe, H., 1976. Process for inhibiting corrosion of iron or steel placed in cement products. United States Patent and Trademark Office, Onoda Cement Company, Ltd., USA.

- Lang, S., 2002. Biological amphiphiles (microbial biosurfactants). *Curr. Opin. Colloid Interface Sci.* 7, 12–20.
- Martin, P., Miksic, B.A., 1987. Inhibition de la corrosion dans un béton renforcé. European Patent Office, S.A. Corp., USA.
- Meylheuc, T., Van Oss, C.J., Bellon-Fontaine, M.-N., 2001. Adsorption of biosurfactant on solid surfaces and consequences regarding the bioadhesion of *Listeria monocytogenes* LO28. *J. Appl. Microbiol.* 91, 822–832.
- Miksic, B.A., et al., 1997. Inhibiteur de la corrosion pour réduire la corrosion de l'armature du béton. European Patent Office, Cortec Corp., USA.
- Miksic, B.A., et al., 1998. Corrosion inhibitor for reducing corrosion in metallic concrete reinforcements. United States Patent and Trademark Office, Cortec Corporation, USA.
- Miksic, B.A., Bjegovic, D., Furman, A., 2002. Migrating corrosion inhibitors combined with concrete and modifiers. United States Patent and Trademark Office, Cortec Corporation, USA.
- Miksic, B.A., Furman, A., Jackson, J., 2006. Composition and method for repairing metal reinforced concrete structures. United States Patent and Trademark Office, Cortec Corporation, USA.
- Montemor, M.F., Simoes, A.M.P., Ferreira, M.G.S., 1998. Analytical characterization of the passive film formed on steel in solutions simulating the concrete interstitial electrolyte. *Corrosion.* 54 (5), 347–353.
- Moreno, M., Morris, W., Alvarez, M.G., Duffo, G.S., 2004. Corrosion of reinforcing steel in simulated concrete pore solutions: effect of carbonation and chloride content. *Corros. Sci.* 46 (11), 2681–2699.
- Nielsen, T., Sørensen, D., Tobiasen, C., Andersen, J.B., Christophersen, C., Givskov, M., et al., 2002. Antibiotic and biosurfactant properties of cyclic lipopeptides produced by fluorescent *Pseudomonas* spp. from the sugar beet rhizosphere. *Appl. Environ. Microbiol.* 68, 3416–3423.
- Nitschke, M., Costa, S., 2007. Biosurfactants in food industry. *Trends Food Sci. Technol.* 18, 252–259.
- Ollivier, J.P., Vichot, A., 2008. La durabilité des bétons—bases scientifiques pour la formulation de bétons durables dans leur environnement. Presses de l'école nationale des Ponts et Chaussées, Paris.
- Ormellese, M., Bolzoni, F., Lazzari, L., Pedferri, P., 2008. Effect of corrosion inhibitors on the initiation of chloride-induced corrosion on reinforced concrete structures. *Mater. Corros.* 59, 98–106.
- Ormellese, M., Lazzari, L., Goidanich, S., Fumagalli, G., Brenna, A., 2009. A study of organic substances as inhibitors for chloride-induced corrosion in concrete. *Corros. Sci.* 51, 2959–2968.
- Orts, W.J., Espinosa, A.R., Sojka, R.E., Glenn, G.M., Imam, S.H., Erlacher, K., et al., 2007. Use of synthetic polymers and biopolymers for soil stabilization in agricultural, construction, and military applications. *J. Mater. Civ. Eng.* 19, 58–66.
- Pade, C., Guimaraes, M., 2007. The CO₂ uptake of concrete in a 100 year perspective. *Cem. Concr. Res.* 37, 1348–1356.
- Page, C.L., Treadaway, K.W.J., 1982. Aspects of the electrochemistry of steel in concrete. *Nature.* 297 (5862), 109–115.
- Palacios, M., Puertas, F., 2005. Effect of superplasticizer and shrinkage-reducing admixtures on alkali-activated slag pastes and mortars. *Cem. Concr. Res.* 35, 1358–1367.
- Patural, L., Marchal, P., Govin, A., Grosseau, P., Ruot, B., Devès, O., 2011. Cellulose ethers influence on water retention and consistency in cement-based mortars. *Cem. Concr. Res.* 41, 46–55.

- Plank, J., 2004. Applications of biopolymers and other biotechnological products in building materials. *Appl. Microbiol. Biotechnol.* 66, 1–9.
- Pruthi, V., Cameotra, S., 1997. Rapid identification of biosurfactant-producing bacterial strains using a cell surface hydrophobicity technique. *Biotechnol. Tech.* 11, 671–674.
- Raaijmakers, J.M., De Bruijn, I., De Kock, M.J., 2006. Cyclic lipopeptide production by plant-associated *Pseudomonas* spp.: diversity, activity, biosynthesis, and regulation. *Mol. Plant Microbe Interact.* 19, 699–710.
- Riedel, U., Nickel, J., 2000. Natural fibre-reinforced biopolymers as construction materials—new discoveries. *Macromol. Mater. Eng.* 272, 34–40.
- Rosenberg, A.M., Gaidis, J.M., 1981. Corrosion inhibiting concrete composition. United States Patent and Trademark Office, W.R. Grace & Co., USA.
- Roux, S., 2008. Evaluation des risques de biodégradation des bétons en contact avec des eaux naturelles. Ph.D. Thesis, Université Louis Pasteur, Strasbourg, France.
- Roux, S., Bur, N., Ferrari, G., Tribollet, B., Feugeas, F., 2010. Influence of a biopolymer admixture on corrosion behavior of steel rebars in concrete. *Mater. Corros.* 61, 1026–1033.
- Roux, S., Tribollet, B., Serres, N., Lecomte, A., Feugeas, F., 2013. Use of biopolymers to improve the reinforced concrete sustainability. *Restor. Build. Monum.* 19 (2/3), 163–170.
- Sagocecentsil, K.K., Yilmaz, V.T., Glasser, F.P., 1993. Corrosion inhibition of steel in concrete by carboxylic-acids. *Cem. Concr. Res.* 23 (6), 1380–1388.
- Şahmaran, M., Christianto, H.A., Yaman, İ.Ö., 2006. Effect of chemical admixtures and mineral additives on the properties of self-compacting mortars. *Cem. Concr. Compos.* 28, 432–440.
- Shubina, V., Gaillet, L., Ababou-Girard, S., Gaudefroy, V., Chaussadent, T., Farcas, F., et al., 2015. The influence of biosurfactant adsorption on the physicochemical behavior of carbon steel surfaces using contact angle measurements and X-ray photoelectron spectroscopy. *Appl. Surf. Sci.* 351, 1174–1183.
- Shubina, V., Gaillet, L., Chaussadent, T., Meylheuc, T., Creus, J., 2016. Biomolecules as a sustainable protection against corrosion of reinforced carbon steel in concrete. *J. Clean. Prod.* 112, 666–671.
- Sölylev, T.A., Richardson, M.G., 2008. Corrosion inhibitors for steel in concrete: state-of-the-art report. *Constr. Build. Mater.* 22, 609–622.
- Sonebi, M., 2006. Rheological properties of grouts with viscosity modifying agents as diutan gum and welan gum incorporating pulverised fly ash. *Cem. Concr. Res.* 36, 1609–1618.
- Standke, B., McGettigan, E., 2003. Corrosion inhibitor for steel-reinforced concrete. United States Patent and Trademark Office, Degussa AG, USA.
- Tang, Y.M., Miao, Y.F., Zuo, Y., Zhang, G.D., Wang, C.L., 2012. Corrosion behavior of steel in simulated concrete pore solutions treated with calcium silicate hydrates. *Constr. Build. Mater.* 30, 252–256.
- Tittelboom, K.V., De Belie, N., Van Loo, D., Jacobs, P., 2011. Self-healing efficiency of cementitious materials containing tubular capsules filled with healing agent. *Cem. Concr. Compos.* 33, 497–505.
- Wang, X., Pang, Y., Lou, H., Deng, Y., Qiu, X., 2012. Effect of calcium lignosulfonate on the hydration of the tricalcium aluminate–anhydrite system. *Cem. Concr. Res.* 42, 1549–1554.
- Wasim, M., Hussain, R.R., 2015. Passive film formation and corrosion initiation in light-weight concrete structures as compared to self compacting and ordinary concrete structures at elevated temperature in chloride rich marine environment. *Constr. Build. Mater.* 78, 144–152.

- Whitaker, G., 1974. Cement additives. United States Patent and Trademark Office, Fosroc AG, USA.
- Whitmore, D., 2004. Cathodic protection of steel within a covering material. WO2004057056 (A3), Ade & Company, World Intellectual Property Organisation.
- Zhang, J., Lounis, Z., 2006. Sensitivity analysis of simplified diffusion-based corrosion initiation model of concrete structures exposed to chlorides. *Cem. Concr. Res.* 36, 1312–1323.
- Zhor, J., Bremner, T., 1996. Influence of new environmentally beneficial lignin-based superplasticizer on concrete performance. In: Dhir, R.K., Hewlett, P.C. (Eds.), *Radical Concrete Technology*, Scotland, UK. E & FN Spon, London and New York, pp. 295–308.

Further reading

- Rosenberg, A.M., Gaidis, J.M., 1978. Method for corrosion inhibition of reinforced bridge structures. United States Patent and Trademark Office, W.R. Grace & Co., USA.

This page intentionally left blank

Part III

Design, LCC, LCA, and case studies

This page intentionally left blank

Eco-efficient design of concrete repair and rehabilitation

21

Rachel Muigai

University of Johannesburg, Johannesburg, South Africa

21.1 Introduction

From the mid-20th Century and into the 21st century, there has been an increased uptake of concrete as a structural material. The worldwide consumption of concrete is estimated to have increased from 6.4 billion m³ in 1997 (Aïtcin, 2000) to about 8 billion m³ in 2009 (CEMBUREAU, 2009), a 25% increase in only 12 years. This volume will continue to increase, particularly in developing countries, due to an exponential increase in population growth, urbanization and economic growth (Scheubel and Nachtwey, 1997; Humphreys and Mahasenan, 2002). While concrete production continues to grow and contribute towards economic development around the world, evidence suggests, however, that this growth is also associated with escalating impacts on the environment and society. Firstly, cement production and aggregate extraction and processing may lead to loss of arable/forest land coupled with the loss of biodiversity, waste generation, and resource depletion. (Uher, 1999; Alexander and Mindess, 2006; Cheng et al., 2006). Secondly, quarrying, construction, and repair activities may affect society negatively, due to the noise and air pollution that arise during blasting at quarry/construction sites, transportation of materials, and repair activities which also lead to user inconveniences. Thirdly, cement—the key constituent in concrete—is energy-intensive and accounts for 5%–8% of global anthropogenic CO₂ emissions (WBCSD, 2002; Damtoft et al., 2008), as well as significant levels of SO_x, NO_x, particulate matter, and other pollutants (USEPA, 1999). Lastly, concrete produces massive amounts of inert waste through construction, repair, rehabilitation, and demolition activities. It is clear that if no action is taken, an increase in concrete production with time will cause an escalation of concrete’s environmental damage through depletion of the natural resource base, and pollution.

Sustainable development is a key concept that is seen as contributory towards solutions to environmental degradation, as well as economic and social conditions that have an influence on the environment. The concept requires interdisciplinary efforts to deal with environmental problems, such as natural resource depletion, pollution, and loss of biodiversity caused by economic activities and social conditions, which include both poverty and affluence. The term “sustainable development” has a wide range of definitions, though it is commonly defined as “. . . *development that meets the needs of the present without compromising the ability of future generations to meet their own needs*” (WCED, Brundtland Commission, 1987).

This definition has been purposefully put in a general manner to allow the involvement of a multiplicity of persons, institutions, governments and practitioners—including civil engineers—to include the sustainable development concept in decision making.

Transference of the concept of sustainable development to the concrete construction industry gives rise to the associated concept of “eco-efficient concrete structures.” Furthermore, concrete is invariably used in construction, implying some form of structure or infrastructural expression. However, there remains a lack of definition of the term “eco-efficient concrete structure” to allow for its operationalization. One of the contributions of this study is to give a working definition of the term “eco-efficient concrete structure.”

This study first reviews sustainable development principles that can be applied to the concrete construction industry. Sustainable development principles range from those given by international organizations such as the United Nations, to ones given by environmental groups and individuals. Finally, a comprehensive definition of an “eco-efficient concrete structure” is given, based on the underlying principles of sustainable development.

The responsibility of achieving an eco-efficient concrete structure lies on the industry stakeholders, including the material producers, and those involved in the design and specification, construction, maintenance and repair, and the demolition and recycling of a structure. There is a potential area(s) of the life-cycle of the structure within which each of the industry stakeholders can influence. Of importance and focus of this study is the potential of structural engineers in reducing the environmental impacts of concrete structures through selecting repair and rehabilitation systems which consume less natural raw materials and induce less CO₂ emissions, while providing the same reliability with a much longer durability.

As is evidenced in current design practice, the practitioner in structural engineering is increasingly required by the client to synthesize a solution, which includes sustainability requirements of the structure as a whole. However, in structural design there is a lack of grasp of materials aspects, and environmental aspects of construction. Hence, the main contribution of this study will be to develop a framework for the design of reinforced concrete (RC) structures which structural and materials engineers can use to consistently and rationally consider “sustainability” in their repair and rehabilitation systems design.

21.2 Eco-efficient design of concrete structures

21.2.1 Background

The sustainable development concept can be applied to the concrete construction industry attempting to ensure that activities within the industry are carried out within the ecological capacity of the earth. While there is little consensus about the definition for “sustainable development,” there are certain commonly accepted principles and practices that can nonetheless be used to guide sustainable development.

“Principle,” as defined by the Oxford Dictionary refers to “a fundamental truth or a general doctrine that is used as a basis for reasoning or action.” Sustainable development principles range from those of international organizations such as the [United Nations, as detailed in international agreements such as Agenda 21 \(1992\)](#)—agreed upon at the United Nations Conference on Environment and Development held in 1992; to those put forward by environmental groups and individuals, such as the “cradle-to-cradle” principles for sustainable design, which were formulated by Michael Braungart and William McDonough ([Braungart and McDonough, 2002](#)). This set of principles can be used to operationalize the concept of sustainable development on different scales and levels, from the government level when passing legislation and formulating policies, to practitioners at local level institutions or businesses during decision making.

This study reviews sustainable development principles that can be applied to the concrete construction industry in general. These principles are detailed in the subsequent sections and include: (1) The circular materials design model; (2) Dematerialization; (3) Increased production and operational efficiency; and (4) Durability design.

The circular materials model draws from the “cradle-to-cradle” approach for sustainable design ([Braungart and McDonough, 2002](#)). The model advocates for the design of materials and products in ways that can relieve the environmental burden from waste disposal and also reduce the extraction of virgin materials.

Dematerialization is defined as the reduction of the quantities of materials needed to serve an economic function, or the decline over time in the mass of materials used in industrial end products ([Wernick et al., 1996 as cited in Kibert et al., 2002](#)). This implies delivering the same performance with less volume of raw materials, hence minimizing the generation of wastes and eliminating problems associated with waste disposal ([Peng et al., 1997](#)).

Improving the production and operational efficiency of a product can lower the energy requirements and emissions associated with its production and functioning.

Durability design, in the context of construction, refers to the ability of a structure to resist deterioration during its intended service life. Suffice to say, products designed for durability will lead to the conservation of resources that could have otherwise been expended in repair actions.

In summary, these set of principles can be used to operationalize the concept of sustainable development in the concrete construction industry. As such, a definition of an “eco-efficient concrete structure” is important, as it would ideally incorporate the various sustainable development principles and assist in defining the roles of the key players in the concrete construction industry, establishing their potential in contributing towards the overall sustainability of the industry.

21.2.2 Circular materials design model

Some anthropogenic activities which impact negatively on the physical environment, such as resource depletion, can be attributed to the current economic system model which follows a linear structure ([Doppelt, 2003](#)) as illustrated in [Fig. 21.1](#).

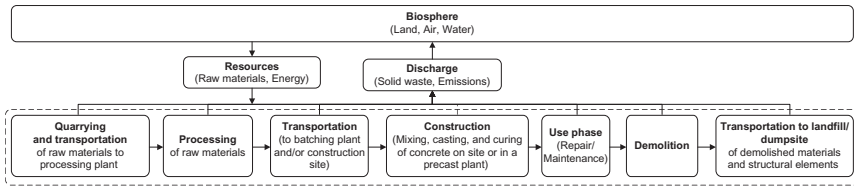


Figure 21.1 Linear model applied in the life-cycle of concrete construction material.

Source: Adapted from Turner, K.R., Pearce, D., Bateman, I., 1993. Environmental Economics: An elementary introduction. The John Hopkins University Press, Baltimore.

This economic system model views the production of products and services as a linear progression, from extraction of materials to their final disposal into landfills. Using the linear model, natural resources are extracted from the physical environment and refined into raw or constituent materials that are then remanufactured into consumer products, based mainly on cost and time-efficiency considerations, and occasionally on quality. The latter point in this case refers to construction management skills that control the workmanship and curing of a concrete structure. Such construction practices determine partly whether additional materials will be consumed for repair and maintenance during the structure's service life. Notwithstanding, high quality construction may result in overconsumption of resources (materials and labor costs). Thus, a balance must be struck between the three bases of the economic systems model: time, cost, and quality, in order to avoid over- or under-consumption of resources.

The linear model makes an assumption of infinite natural resources and so may lead to their over-exploitation and inequality in resource distribution between current and future generations. In addition, the linear model gives little thought, if any, to the discharge of waste products and emissions to the biosphere. In particular, the generation of construction and demolition waste (C&DW) has increased substantially in recent decades. C&DW refers to the nonhazardous waste resulting from the construction, remodeling, repair and demolition of structures (Macozoma, 2006). Developed and developing countries both generate considerable amounts of C&DW, which are mostly disposed of in landfill sites. For example, South Africa produces approximately 4 million tons/year of C&DW (Department of Environmental Affairs (DEA), 2012). Of the total C&DW generated per year, only 16% is recycled and the rest is disposed of by land (landfill sites, illegal dumps, or backfills) (DEA, 2012). Australia generates 13.7 million tonnes of C&DW per year, 81% of which is concrete waste, whereas Japan generates only 0.75 million tonnes of C&DW annually, of which 98% is recycled (Tam, 2009). In the global setting, approximately 1 billion tons of C&DW are generated yearly (Katz, 2004).

Growing demands for resource conservation and recycling due to scarcity of landfill capacity or sites, present considerable challenges not only to the concrete construction industry but to all large solid waste emitting industries. These challenges can be partially addressed through the adoption of the circular model, illustrated in Fig. 21.2. The circular model is a biomimetic (life-imitating) approach that

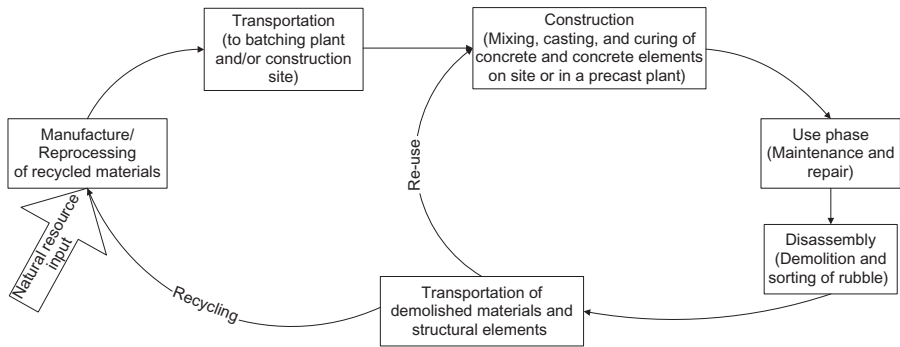


Figure 21.2 Circular (or closed-loop) model applied in the life-cycle of concrete construction material.

Source: Adapted from: Allenby, B.R., 1992. Industrial ecology: the materials scientist in an environmentally constrained world. *MRS Bull.* 17(3), 46–51 (Allenby, 1992).

borrowed from ecosystem cycles which operate off solar energy, and allow for the flow of energy and matter from the physical environment, and the release of wastes back to the physical environment.

The circular model is also referred to as the “cradle-to-cradle” approach to design (Braungart and McDonough, 2002). The model encourages the designer to rethink ways the design product can relieve the environmental burden from waste disposal and also reduce the extraction of virgin materials. Following the circular model, economic activities including construction aim at utilizing wastes produced from all production processes as substitutes for natural resources and as inputs to construction activities. Waste management mechanisms that are available in a circular model include the biodegradation, reuse and/or recycling of wastes. Biodegradation of wastes, as explained in Braungart and McDonough (2002), involves the design of materials for the purpose of biodegradation and the absence of toxic substances after their useful life. A product can also be designed for adaptive reuse. In this case, the reuse of a structural component or material can be achieved if the structural engineer considers beforehand the possible changes in use of the structure, and designs the structure for adaptability. For example, a building may be designed to have a flat slab that avoids the use of beams to make it adaptable to functions in the future other than the one for which it was originally designed. Furthermore, C&DW can be recycled using two different processes (Calkins, 2009): (1) Up-cycling—which occurs when C&DW is remanufactured to produce value added products, e.g., the use of demolished waste for cement manufacture (Schepper et al., 2013) or as aggregates in concrete (Hansen, 1992; Olorunsogo and Padayachee, 2002; Kutegeza and Alexander, 2004). (2) Down-cycling—which occurs when a material is used in low-grade applications, due to its low durability or strength properties, and since demolished concrete has a lower quality compared to natural aggregates (NA) due to mortar and cement paste which remains adhered after the recycling process (Marinkovic et al., 2010). Consequently,

recycled aggregates are currently used in the construction of road base and subbase layers instead of concrete production for high strength applications. Recycling promotes resource conservation and creates value in the economy by reducing the input of virgin raw materials, reducing the need for landfills, and increasing use of labor through sorting of demolished waste on site or at dump sites.

In summary, a circular model limits the use of virgin materials for economic activity and also minimizes the use of the environment as a sink for discharged solids and emissions. The adoption of such a model in economic activities requires product developers to design products that facilitate recycling, both within the economy and via natural ecosystem cycles (biodegradability) (Daly, 1990). Through the use of a circular model, the concrete practitioner is able to take on a life-cycle perspective to the design of a concrete structure. This is a conscious process that requires the designer to plan the life-cycle flow of resources and wastes of a structure.

21.2.3 Dematerialization

Concrete construction is marked by activities related to the quarrying and processing of raw materials, which consist largely of NA. NA are nonrenewable as their geological processes of formation take a long time (millions of years) and their continuous and increased consumption decreases their reserves. Currently, high-grade reserves of the earth's NA have been exploited in construction activities to a point where the availability of NA is now scarce, if not practically unrealizable in some regions or countries, particularly in urban areas. As a result, materials are transported for long distances, and this in turn elevates the energy consumed and construction project costs, both leading to a number of environmental problems such as greenhouse gas (GHG) emissions and resource depletion. Environmental concerns over the excessive mining of NA compared to other aggregate types, such as recycled aggregates, can be addressed by changing raw material consumption patterns in concrete construction through dematerialization.

The application of dematerialization in concrete construction can be partially achieved through the use of recycled concrete aggregates and through the structural optimization of a structural component to reduce the volume of materials used, which in turn leads to a reduction in pollution generation.

21.2.4 Increased production and operational efficiency

Improved efficiency in all the manufacturing processes of a product, including the extraction of raw materials for its production and processing of these materials, can lower the energy requirements and emissions associated with their production.

For example, current solutions to aid in reducing the 5%–8% global anthropogenic CO₂ emissions from cement manufacture (WBCSD, 2002; Damtoft et al., 2008) include improving the efficiency of cement kilns. Optimizing kiln processes and plant efficiencies during cement production results in the reduction of CO₂ emissions and also brings down the cost of production. Modern cement kilns should

use the dry process of raw materials, as opposed to the wet process. The former refers to the process whereby raw materials are first ground and heated before being fed into the kiln, whereas in the wet process, the raw materials are crushed, ground, and mixed as slurry.

The most efficient dry-process kilns use approximately 2.9 GJ of energy per ton of clinker (<http://www.energyefficiencyasia.org/docs/industrysectorscementdraftMay05.pdf>). Wet-process kilns are more energy-intensive and can consume more than twice the amount used by dry process kilns (Gartner, 2004). However, there is a thermodynamic limit where it is not possible to increase production efficiency and hence limit GHG emissions. Further reductions in energy used in materials production can then be achieved through the substitution of renewable energy sources for fossil fuels. For example, waste tyres can help reduce the amount of coal energy used in cement kilns. In addition, the use of blended cements can improve the efficiency of concrete production. Blended cements are produced by inter-grinding Portland cement clinker (Clinker is the main product of Portland cement manufacture and is generated by heating raw materials (limestone, iron ore, and aluminosilicates such as clay) together at temperatures of about 1400–1500°C.) with supplementary cementitious materials (SCMs) or by blending Portland cement with SCMs such as fly ash from coal combustion in electricity-producing plants or blast furnace slag from iron-making plants. The use of blended cements reduces the amount of clinker that needs to be produced, also lowers the GHG emissions, and diverts wastes from landfills, as SCMs are by-products of other industries that would otherwise have been disposed.

In addition to the production efficiency considerations above, there are operational efficiency considerations that are specific to the type of structure, e.g., civil engineering structure or building, and relate to the use-phase of the structure. This includes the use of efficient heating and ventilating systems in buildings so as to reduce their operational energy. In addition, the thermal performance of alternative construction materials should not be ignored by the designer, as they have a role to play in reducing the operation energy losses in heating and/or cooling a building. In particular, concrete has a higher thermal mass than other building materials, and its use in the fabric of a building can reduce the cooling and/or heating energy needs of a building.

21.2.5 Durability design

Durability refers to the ability of a structure to resist deterioration during its intended service life. Construction products are marked by a long life-time and can consume large resources in their life-cycle if they do not have adequate durability. The durability design of concrete structures is concerned with ensuring the ability of concrete, inter alia, to resist the penetration of aggressive agents during its intended service life. Most approaches to concrete durability design and specification rely on the so-called “prescriptive method,” i.e., the design and specification “rules” are intended to provide for durability by prescribing limiting values for material properties and proportions, depending on the environmental conditions and life span of the structure.

The specified parameters are usually the concrete cover to reinforcement, 28-day compressive strength, maximum water-cement (w/c) ratio, and minimum cement content. For example, design standards such as [BS 8500-1: 2006](#), give the limiting values of the concrete cover to be provided to all reinforcement, 28-day compressive strength and cement content in order to achieve a durable concrete for a range of w/c ratios. Beside the fact that these requirements can sometimes be mutually contradictory, this approach does not explicitly address rational, quantitative durability design, nor does it address sustainability issues. Regarding this latter point, prescriptive specifications are generally restricted to conventional materials and do not have the flexibility to address “new” and marginal concrete materials such as recycled and site-derived materials. These materials may, in certain circumstances, be adequately durable but also bring reductions in raw material resource use, and also possible cost savings. Furthermore, by using the prescriptive method there is a danger of over-specification, since the prescriptive approach is inherently conservative and results in resource waste. Lastly, the approach assumes that the as-built quality of concrete is what has been specified, without the means to check actual as-built quality. It also does not account for variability in as-built quality that may occur due to material variability and variable site practices, including poor workmanship and inadequate curing in as-built quality. Such practices may result in poor quality concrete which will require additional repair and maintenance during the structure’s service life, resulting in additional unanticipated material consumption, social disruptions, and costs. Thus, the present prescriptive approach to durability specifications should be phased out, since it contributes, in many cases, directly to un-sustainability.

On the other hand, performance-based approaches to durability design, such as those put forth by the fib (2010) (fédération internationale du béton) Model Code for Service Life Design, are specifically intended to limit the environmental consequences on the structure, to defined acceptable levels or targets during the structure’s service life. The approach advocates the use of service life prediction models that quantify environmental deterioration and provide an output in terms of the required material quality. From this requirement, the designer is left with the choice of selecting a suitable material (conventional, new or marginal) that will meet the requirements within the predefined acceptable level. The specified material quality is then verified on site, using suitable tests that characterize that quality. Considerations of sustainability of concrete structures should consequently relate to service life and performance requirements of the structure, in which durability considerations are embedded.

21.2.6 Definition of an “eco-efficient concrete structure”

Based on the principles of sustainable development given in the previous sections, a definition of an “eco-efficient concrete structure” is suggested here as ([Muigai, 2014](#)):

a concrete structure that is designed to meet case-specific needs of the users, that minimizes life-cycle costs and environmental impacts through (i) use of efficient production, construction operational, repair and rehabilitation technologies (ii) selection of materials that have a minimal negative environmental impact and

which give optimized properties for long-term durability (iii) selection of an appropriate structural layout and form, and optimized volume, and (iv) is designed for deconstruction and recycling

The definition of an “eco-efficient concrete structure” assists in establishing the roles of the key players in the concrete construction industry, in a bid to show their potential in contributing towards the overall environmental performance of the cement and concrete industry. This information is summarized in Fig. 21.3.

The key players in the industry consist of the material producers and the design and construction team which includes: the architect, structural and materials engineer, geotechnical engineer, mechanical and electrical engineer, the quantity surveyor, the project manager and the contractor and the client.

Fig. 21.3 shows the potential areas in which these key players can influence (in order to improve) the overall environmental performance of the industry. For example, from Fig. 21.3, it is noted that the structural and materials engineer is faced with a major role in ascertaining the probable service life of the repaired structure and in selecting appropriate materials and methods for concrete repair and rehabilitation, which not only contribute to the durability performance of a concrete structure but additionally reduce the recurring environmental impacts due to deterioration.

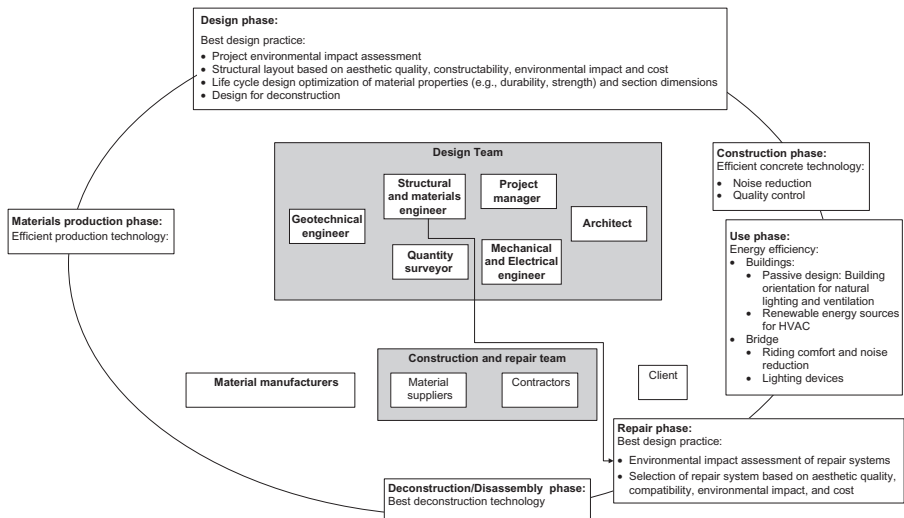


Figure 21.3 Roles of the key players in the concrete construction industry.

21.2.7 Proposed framework for the eco-efficient design of concrete repair methods and materials

21.2.7.1 Introduction

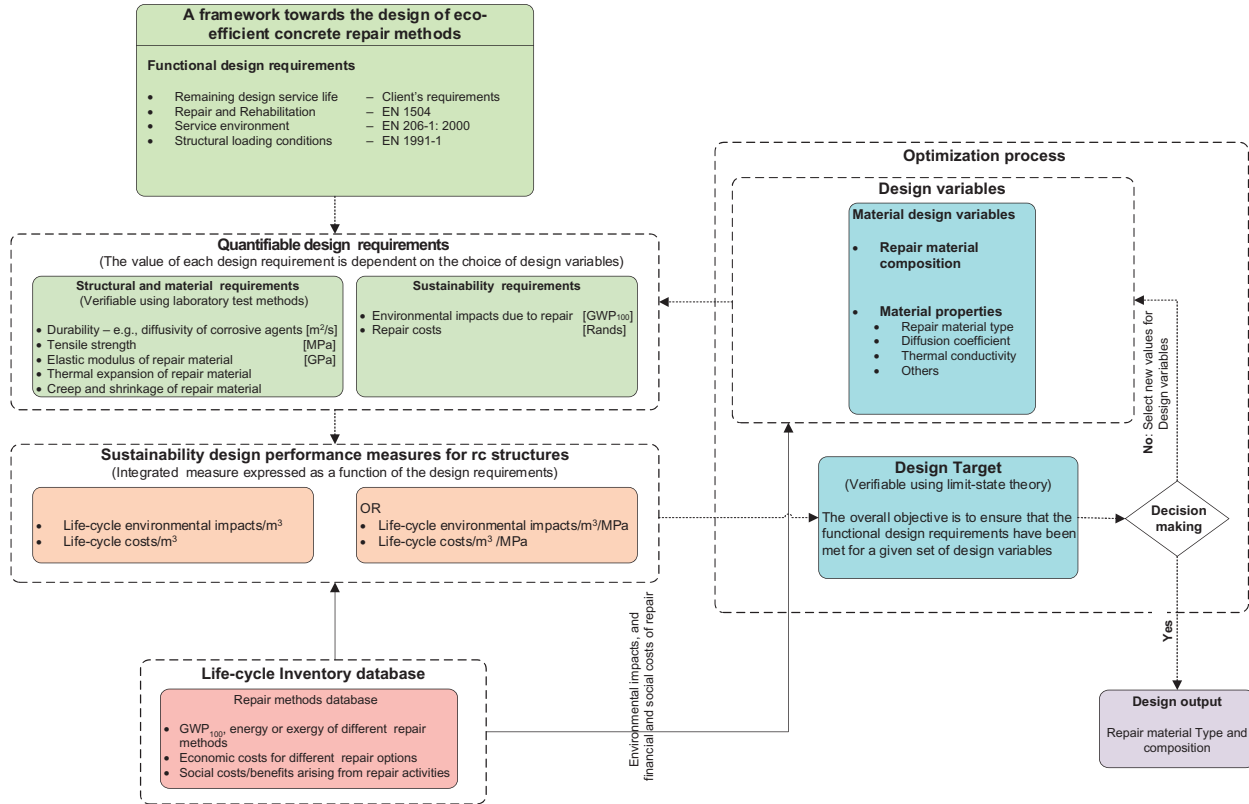
Concrete repairs may be broadly classified as “nonstructural” or cosmetic repairs, in which stress-carrying is not a major consideration for the repair, and “structural” repairs where the repair is required to carry stress (Morgan, 1996). Both types of concrete repairs can be carried out using protective surface treatments and/or patch repairs, among other repair methods. Protective surface treatments mainly use polymeric resins based on epoxy, silicone, acrylics, polyurethanes, or polymethacrylate. Patch repairs are mortars that can be grouped into three categories (Emberson and Mays, 1990): (1) resin mortars; (2) plain cementitious mortars; or (3) polymer-modified cementitious mortars. In addition to ensuring the structural performance of a repair system, the practitioner in structural engineering is increasingly required by the client to synthesize a solution, which includes sustainability requirements of the structure as a whole. This can be made possible through the development of a framework for design which structural and materials engineers can use to consistently and rationally consider “sustainability” in their designs.

The current key driver to the design of eco-efficient repair and rehabilitation methods has been the need to minimize resource use of natural resources and GHG emissions over the life-cycle of concrete. This involves GHG-emission reduction through the design of durable repaired structures, by ensuring adequate resistance to environmental effects and providing adequate structural capacity and safety under the expected loading. The durability of the repaired structure depends on the interactions with the service environment, in which penetration of deleterious substances is highly significant. The ingress of various ions, liquids, and gases from the environment is responsible for the deterioration of the original concrete and/or repair material directly or indirectly (Basheer et al., 2001). When the loading and environmental conditions to which a repaired structure would be exposed to during its remaining service life are well defined, it is the responsibility of the Engineer to tailor the design of eco-efficient repair methods and materials. An eco-efficient repair method/material is one that attains specified performance levels in terms of strength, durability, costs, and carbon footprint to respond to the design requirements.

21.2.7.2 Design framework

The concept of designing for eco-efficient concrete repairs, calls for the design team to adopt a different approach to thinking about the decisions regarding the choice of repair materials and their long-term effects on the environment and cost. To facilitate this process, a framework for design is proposed as shown in Fig. 21.4 that consists of key criteria that should be taken into consideration for concrete repair design. These are:

1. *A set of quantifiable design parameters and variables*—consisting of the repair material constituents and concrete hardened properties that have an influence on the life-cycle sustainability of concrete. The framework is limited to quantifiable parameters and variables. However, there are other qualitative parameters that have an influence on the overall sustainability of concrete, e.g., construction site practices such as curing, compaction,



Design output

Repair material Type and composition

Figure 21.4 Proposed framework for the eco-efficient design of concrete repair methods and materials.

and good workmanship. These qualitative factors also play a major role in the long-term structural performance of the repaired concrete. They are excluded from this study as they cannot be quantified in physical units. Suffice to say, the best practice in these aspects is necessary to realize eco-efficient concrete structures.

2. *Performance measures*—that consist of quantitative indicators that allow for the selection of appropriate design variables and parameters.
3. A *database*—of alternative materials for concrete repair methods and end-of-life strategies for concrete, and their associated unit environmental life-cycle impacts and costs/benefits to the user and owner of the structure.

21.2.7.3 Description of the design framework

The framework (Fig. 21.4) consists of the following processes:

1. A set of functional design requirements of an RC structure, as specified by the client and/or the design codes and standards. For example, European Standards EN 1504 gives guidelines for the repair and protection of RC structures.

Other functional requirements include the remaining service-life of the structure, which may be specified by the client/owner of the structure. To ensure that the remaining design service life is met, the designer should take into consideration the service environment of the structure and classify it based on the requirements of EN 206-1: 2013. In essence, the designer is required to establish the environmental actions, i.e., those chemical and physical actions to which the RC structure is exposed and that result in deterioration of the concrete or reinforcement. Deterioration of RC results from reinforcement corrosion, alkali–silica reaction, chemical attack, leaching by nonbasic (and nonalkaline) solutions, and high temperatures generated in case of fire (EN 1992-1-1: 2004). The main environmental action on an RC structure is frequently related to corrosion caused by ingress of chlorides or CO₂ gas.

2. The functional design requirements are translated into measurable design requirements which consist of structural and material requirements, and sustainability performance requirement in terms of the life-cycle environmental impact of the repaired structure. The latter requires knowledge of the quality of the material at the end of its service life.
3. A set of measurable design variables which have an influence on the sustainability of RC structures.
4. The design requirements have different measurement units. Consideration should be given to the selection of a suitable integrated unit for comparing the performance of different materials with respect to the design requirements. The selected integrated performance measure is expressed as a function of the design requirements.
5. A reliable database of the unit environmental impact and costs of repair materials and construction activities. The current study includes the global warming potential (GWP₁₀₀) (kg CO₂-eq) metric as a measure of the environmental impact and the unit costs are expressed in Rands.
6. The design verification is an optimization process seeking to ensure that the selected design variables satisfy the performance requirements and result in minimum life-cycle environmental/cost impact. This assessment involves a limit-state approach.
7. The outputs of the framework are the optimal repair material properties for the selection of eco-efficient repair concrete methods and materials.

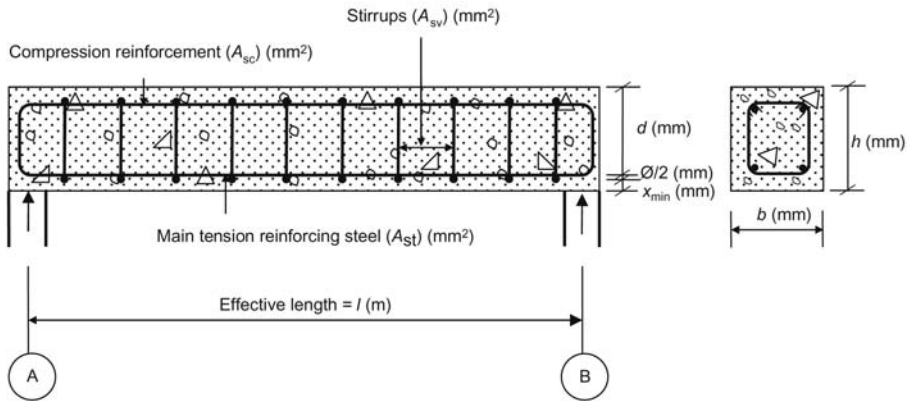


Figure 21.5 Design example of a simply-supported RC beam. Where d (mm) is the effective depth of the beam; b (mm) is width of the beam; l (m) = 6 m is the span of the beam; \varnothing (mm) is the diameter of the tension steel (A_{st}) and is assumed to be 25 mm; x_{min} (mm) is the minimum cover to reinforcement; and h (mm) is the total height of the beam; b , h , x_{min} , and A_{st} are the structural design variables in the optimization problem. A_{sc} and A_{sv} are taken as nominal reinforcement.

21.2.8 Case study

The design framework guides a designer in finding the geometry and materials specifications for structural components that result in the lowest environmental impact while meeting design requirements for serviceability and safety. To demonstrate the application of the proposed framework to design, the study uses a hypothetical simplified RC beam idealized in Fig. 21.5.

The span (l) of the RC beam is determined a priori at the conceptual phase of design and is indicated in Fig. 21.5. While the example below is ideally simplistic, it should be noted that more complex geometries and shapes could easily be adopted for further refinement.

The hypothetical RC beam is assumed to be part of a structure located in a marine environment. For this example, it is assumed that the environmental condition corresponds to the exposure class $XS1$ in EN 206-1:2013. For the $XS1$ marine zone, the concrete is exposed to airborne salts, but not in direct contact with sea water. The design service life of the structure is specified as 30 years. In addition to its self-weight, the RC beam is expected to support uniformly distributed loads of: 30 kN/m live load; 60 kN/m dead load.

21.2.8.1 Design variables

This study utilizes a vector of design variables $[X]$ represented as:

$$[X] = \{x_1, x_2, x_3, x_4, x_5, x_6, x_7\} = \{b, h, x_{min}, A_{st}, w/b, M_w, M_a\} \quad (21.1)$$

where b (mm) is the width of the beam; h (mm) is the overall depth of the beam; x_{\min} (mm) is the minimum concrete cover; A_{st} (mm²) is the area of tension steel reinforcement; w/b (-) is the water/binder ratio of the concrete design mix (which depends on the choice of the binder system); M_w (kg/m³) is the water content; and M_a (kg/m³) is the mass of fine and coarse aggregates. In addition, there are response variables describing the resultant material properties represented by a vector $[Y]$ as follows:

$$[Y] = \{y_1, y_2\} = \{D_o, f_{ck}\} \quad (21.2)$$

where, D_o (m²/s) is the chloride diffusion coefficient of the concrete; and f_{ck} (MPa) is the concrete characteristic compressive strength. The two variables are dependent on: the binder system, w/b ratio, and aggregate/binder ratio (Papadakis et al., 1996; Papadakis and Tsimas, 2002).

21.2.8.2 Design parameters

Other than the design variables, there are particular design parameters which have an influence on the sustainability of concrete. These design parameters relate to: (1) The span (l); (2) Reinforcing steel bar diameter; and (3) Unit environmental impacts of the constituent materials indicated in units of greenhouse warming potential (GWP100) (kg CO₂-eq).

21.2.8.3 Objective function

The optimization problem in this study considers the nonlinear objective function $f(X, Y)$ (Eq. (21.3)) that represents the life-cycle environmental impacts of the structural component as a function of selected design variables. The aim is to select a vector of material variables, $[X]$ and $[Y]$ that gives the minimum environmental impact for the concrete section.

$$\text{Minimize } f(X, Y) \quad (21.3)$$

where, X and Y represents vectors of design variables (see $[X]$ and $[Y]$ in Eq. 21.1 and Eq. 21.2, respectively); $f(X, Y)$ represents the environmental impact per-unit length of the structural component. Eq. (21.4) gives the expanded form of $f(X, Y)$, and includes the environmental impacts of concrete and steel. The environmental impacts of the formwork and placing of concrete have been excluded as these are assumed to be similar for all the concrete mixes to be compared.

$$f(X, Y) = \left[\rho_s A_s \text{Env}_{\text{steel}} + \left(b \left(d + \frac{\phi}{2} + x_{\min} \right) - A_s \right) \text{Env}_{\text{concrete}} \right] \quad (21.4)$$

where,

X, Y	:	Vector of material design variables (in Eqs. (21.1) and (21.2)) which optimize the value of the objective function
ρ_s (kg/m ³)	:	Density of steel
A_s (mm ²)	:	Reinforcement area for a unit length of beam (consists of tension steel— A_{st} , nominal compression steel— A_{sc} , and nominal shear links— A_{sv}). A_s is a function of ϕ and the number of steel bars in the beam section
b (mm)	:	Width of the concrete component
d (mm)	:	Effective depth of the concrete component
ϕ (mm)	:	Diameter of the steel reinforcement
x_{min} (mm)	:	Minimum concrete cover to reinforcing steel
Env_{steel} (kg CO ₂ -eq/ton)	:	Unit environmental impact of steel per unit mass
$Env_{concrete}$ (kg CO ₂ -eq/m ³)	:	Unit environmental impact of concrete per unit volume as given by Eq. (21.5)

Eq. (21.4) gives the quantified cradle-to-gate environmental impacts of materials in the RC beam (i.e., the concrete and steel) in units of kg CO₂-eq per unit length of the beam. The cradle-to-gate environmental impacts cover all material processing activities until the factory gate.

Further, Eq. (21.5) gives the environmental impact of concrete per unit volume (kg CO₂-eq/m³), needed for Eq. (21.4), and is computed as a function of its compressive strength.

$$\begin{aligned}
 Env_{concrete} = & \left[M_w \left(\frac{f_{ck}}{K_B} + a \right) - kM_P \right] Env_{binder} + \left[M_w \left(\frac{f_{ck}}{K_B} + a \right) - M_c \right] \frac{Env_{binder}}{k} \\
 & + 2650Env_a - \frac{2.65}{RD_{binder}} \left[M_w \left(\frac{f_{ck}}{K_B} + a \right) - kM_P \right] Env_a \\
 & - \frac{2.65}{RD_{binder}} \left[M_w \left(\frac{f_{ck}}{K_B} + a \right) - M_c \right] \frac{Env_a}{k} - 2.65 \left[\frac{M_c + kM_P}{\left(\frac{f_{ck}}{K_B} + a \right)} \right] Env_a \\
 & - 2.65w_aEnv_a + \left[\frac{M_c + kM_P}{\left(\frac{f_{ck}}{K_B} + a \right)} \right] Env_w + M_{Adm}Env_{Adm}
 \end{aligned}
 \tag{21.5}$$

where,

K_B (MPa)	:	Bolomey coefficient that depends on the aggregate and cement type, and is assumed to be 21.3 MPa for all concrete types
f_{ck} (MPa)	:	characteristic compressive strength of concrete, at 28-days
a (-)	:	a parameter that depends on the time and curing of the concrete and is estimated as 0.5 for f_{ck} at 28 days (Papadakis and Tsimas, 2002)
w_a (%)	:	air content in fresh concrete
k (-)	:	efficiency factor of the respective supplementary cementitious material
M_c (kg/m ³)	:	mass of Portland cement per cubic meter of concrete
M_w (kg/m ³)	:	mass of water per cubic meter of concrete
M_P (kg/m ³)	:	mass of supplementary cementitious materials per cubic meter of concrete. This is expressed as a percentage of the mass of Portland cement, e.g., 30% M_c
M_{Adm} (kg/m ³)	:	mass of admixture (superplasticizer) per cubic meter of concrete
RD_{binder} (-)	:	relative density of the binder
Env_a (kg CO ₂ -eq/ton)	:	environmental impact of aggregates per unit mass
Env_{binder} (kg CO ₂ -eq/ton)	:	environmental impact of the binder per unit mass
Env_{Adm} (kg CO ₂ -eq/ton)	:	environmental impact of admixture (superplasticizer) per unit mass
Env_w (kg CO ₂ -eq/1000 L)	:	environmental impact of water per 1000 liter

The form of Eq. (21.5) was chosen so as to be able to quantify the variables involved in the problem, rather than using purely empirical relationships. The parameters in Eq. (21.5) represent the mix-design composition and the resultant concrete property (compressive strength) which have an influence on the life-cycle environmental performance of concrete.

21.2.8.4 Design constraints

The design constraints relate to the ultimate limit states (ULS) and serviceability limit states (SLS) for RC given in EN 1992-1-1: 2004. The constraints include: (1) the ultimate-limit state of bending resistance of the structural component; (2) the durability of the structural component in its service environment; (3) deflection in the member due to service loads. In addition, the optimization problem includes two side constraints: (1) the upper and lower boundaries of the area of steel reinforcement; and (2) the upper and lower boundaries of the geometry of the cross-section of the structural member.

21.2.8.5 Results and discussion

The member section and material design involves the selection of optimum cross-section dimensions and concrete mix-design properties for the RC beam. This is

achieved by optimizing the objective function (Eq. (21.4)), subject to the given design constraints. Due to the nonlinear nature of the objective and constraint functions, the optimization problem is solved using a nonlinear programming technique based on the generalized reduced-gradient optimization algorithm (Drud, 1994).

21.2.8.6 *Optimized concrete mix-design and structural geometry for the RC beam*

The following procedure is used to evaluate and select the optimum concrete mix-design, material properties, and geometry of the RC beam:

1. A set of commonly used binder types is selected. In general, this selection will depend on binder types available in the locality of concern, and a measure of judgement. The binder types chosen for the present example are: CEM I 52.5 N, CEM II/B-V 42.5 N, CEM II/A-V 52.5 N, CEM III/A-S 42.5 N, and CEM I 52.5 N with a superplasticizing admixture. The corresponding compositions of the binder types are indicated in the third row of Table 21.1.
2. A common concrete grade of C30/37 was selected for all concrete made using the four binder types.
3. Using MATLAB[®] software, a generalized, reduced-gradient optimization algorithm was written and used to solve the optimization problem, to give optimized values for the design variables and response variables represented by Eq. (21.1) and Eq. (21.2), respectively.
4. A comparative analysis of the optimum design variables for the different binder types was then carried out.

Using the optimization procedure given above, the optimum design variables for the different concretes made using the four binder types with similar binder contents are given in Table 21.1. Also in Table 21.1, it can be seen that the water content is selected to vary with binder type in order to give a constant slump for all concrete mixes.

From Table 21.1, it can be seen that concrete made using CEM III/A-S 42.5 N has the lowest environmental impact compared to other concrete types. This is followed by CEM II/B-V 42.5, CEM II/A-V 52.5, CEM I 52.5 N with admixture, and finally CEM I 52.5 N.

In comparison to conventional, prescriptive-based design, the minimum cover depth design provisions for CEM III/A-S 42.5 N and CEM II/B-V 42.5 concretes for the optimized RC beam are lower than the recommended value of 40 mm by BS 8500-1: 2006 at a w/b ratio of 0.4, due to better chloride resisting properties of these binders. The latter comparison shows that the design provisions by current design codes are conservative for certain binder types. The latter comparison also shows that the design provisions by current design codes are conservative for certain binder types.

Note: in this case the comparison is not strictly correct, since BS8500-1:2006 allows for a 50-year design life, while the example given was for a 30-year design life. The principles however still apply, noting that codes normally prescribe

Table 21.1 Optimized material and structural design variables for a C30/37 RC beam

Variables [X] and [Y]	Units	Optimized solutions				
		Mix I	Mix II	Mix III	Mix IV	Mix V
		CEM II/B-V 42.5 N (30%:70% FA:PC)	CEM II/A-V 52.5 N (20%:80% FA:PC)	CEM III/A-S 42.5 N (50%:50% GGBS:PC)	CEM I 52.5 N (100% PC)	CEM I 52.5 N (100% PC with admixture)
M_{binder} (Mass of binder)	(kg/m ³)	425	350	450	370	320
M_{water} (Mass of water)	(kg/m ³)	170	175	180	185	160
w/b ratio	(-)	0.4	0.5	0.4	0.5	0.5
M_a (Mass of aggregates)	(kg/m ³)	1805	1750	1780	1848	1848
b (width)	(mm)	170	185	175	180	180
d (effective depth)	(mm)	680	730	685	720	720
x_{min} (minimum cover depth)	(mm)	20	40	25	75	75
h (overall depth)	(mm)	715	785	740	810	810
n_b (number of 25 \varnothing bars)	(mm)	6	5	6	5	5
$A_{\text{st, required}}$	(mm ²)	2792	2489	2676	2477	2477
Diffusion coefficient (D_0)	m ² /s	6.7×10^{-13}	3.0×10^{-12}	1.3×10^{-12}	4.5×10^{-12}	4.5×10^{-12}
$f(X,Y)$	(kg CO ₂ – eq/m)	66	67	60	78	69

minimum cover values. However, the proposed method can be used to modify code values in selected cases.

Generally, the following deductions can be made from [Table 21.1](#):

1. It is important to select an appropriate binder content for a binder system, and vice-versa, as the choice of binder system is based on its environmental impact at a particular binder content.
2. The use of SCMs allows the designer to select optimized values of concrete cover and hence leads to reduced cross-sectional dimensions, which translates to reduced volume of materials.
3. The use of a chemical admixture in concrete made using CEM I 52.5 results in a 12% reduction in the unit environmental impact of concrete, despite the relatively high unit environmental impact of superplasticizers. This shows that the use of chemical admixtures is beneficial to the environment as it leads to resource conservation i.e. chemical admixtures lead to a reduction in the water content of the mix-design and hence the binder content in order to maintain the original w/b ratio.

In conclusion, the optimization enables the selection of the optimum section dimensions, binder content, and type and strength of binder that meet the required performance in terms of characteristic compressive strength (f_{ck}) and durability requirements of concrete, and in addition minimizes the environmental impact.

21.3 Conclusions

Increased concrete repair activities due to durability failure are associated with escalating impacts on the environment and society worldwide. Concrete repair and rehabilitation activities contribute to natural resource depletion and produce massive amounts of CO₂ emissions and inert waste. In addition, the repair activities affect society negatively due to noise and air pollution and lead to user inconveniences. It is clear that if no action is taken, an increase in concrete repair activities with time will cause an escalation of concrete's environmental damage through depletion of the natural resource base, and pollution. Engineers have a role to play in designing eco-efficient repair systems that attain specified performance levels in terms of strength, durability, costs, and carbon footprint to respond to the design requirements.

References

- Aïtcin, P.C., 2000. Cements of yesterday and today: concrete of tomorrow. *Cem. Concr. Res.* 30 (9), 1349–1359.
- Alexander, M.G., Mindess, S., 2006. *Aggregates in Concrete*, 2005. Taylor and Francis, p. 432.
- Allenby, B.R., 1992. Industrial Ecology: the materials scientist in an environmentally constrained world. *MRS Bull.* 17 (3), 46–51.

- Basheer, L., Kropp, J., Cleland, D.J., 2001. Assessment of the reliability of concrete from its permeation properties: a review. *Constr. Build. Mater.* 15 (2001), 93–103.
- Braungart, M., McDonough, W., 2002. *Cradle to Cradle: Remaking the Way we Make Things*. Northpoint press, New York, 208 pp.
- BS 8500-1, 2006. Concrete. Complementary British Standard to BS EN 206-1. Method of specifying and guidance for the specifier, London BSI.
- Calkins, M., 2009. *Materials for Sustainable Sites: A Complete Guide to the Evaluation, Selection, and Use of Sustainable Construction Materials*. Wiley, United States.
- CEMBUREAU, 2009. CEMBUREAU, 2009 Available at: <<http://www.cembureau.be/about-cement/key-facts-figures>> (Accessed on 08.12.2010).
- Cheng, E.W.L., Chiang, Y.H., Tang, B.S., 2006. Exploring the economic impact of construction pollution by disaggregation the construction sector of the input-output table. *Build. Environ.* 4 (2006), 1940–1955.
- Daly, H.E., 1990. Towards some operational principles of sustainable development. *Ecol. Econ.* 2 (1990), 1–6.
- Damtoft, J.S., Lukasik, J., Herfort, D., Sorrentino, D., Gartner, E.M., 2008. Sustainable development and climate change initiatives. *Cem. Concr. Res.* 38 (2), 115–127.
- Department of Environmental Affairs (DEA), 2012. National Waste Information Baseline Report, Department of Environmental Affairs, Pretoria.
- Doppelt, B., 2003. *Leading Change toward Sustainability: A Change-Management Guide for Business*. Government and Civil Society, Sheffield: Greenleaf Publishing.
- Drud, A.S., 1994. CONOPT—a large scale GRG Code. *ORSA J. Comput.* 6 (2), 207–216.
- Emberson, N.K., Mays, G.C., 1990. Significance of property mismatch in the patch repair of structural concrete Part 1: Properties of repair systems, *Magazine of Concrete Research*, 42(152), 147–160.
- EN 1504, 2015. Repair and protection of RC structures. European Committee for Standardization (CEN).
- EN 206-1, 2013. Concrete-Part 1: specification, performance, production and conformity. British Standards Institution, p. 70.
- EN 1992-1-1, 2004. Design of concrete structures - Part 1-1: general rules and rules for buildings. European Committee for Standardization (CEN).
- fib Model code for concrete structures, 2010. Ernst & Sohn, 402 p.
- Gartner, E., 2004. Industrially interesting approaches to “low-CO₂” cements. *Cem. Concr. Res.* 34 (2004), 1489–1498.
- Hansen, T.C., 1992. *Recycling of Demolished Concrete and Masonry*. Taylor & Francis, London and New York.
- http://www.energyefficiencyasia.org/docs/industrysectorscement_draftMay05.pdf (Accessed 17.12.2010).
- Humphreys, K., Mahasenan, M., 2002. “Towards a Sustainable Cement Industry”, Climate Change Sub-study 8, World Business Council for Sustainable Development.
- Katz, A., 2004. Treatments for the improvement of recycled aggregate. *J. Mater. Civ. Eng.* 16 (6), 597–603.
- Kutegeza, B., Alexander, M.G., 2004. The Performance of Concrete Made with Commercially Produced Recycled Coarse and Fine Aggregates in the Western Cape. In: Limbachiya, M.C., Roberts, J.J. (Eds.), *Construction Demolition Waste Conference Proceedings*. Thomas Telford, pp. 235–244.
- Macozoma, D.S., 2006. *Developing a Self-Sustaining Secondary Construction Materials Market in South Africa*. Masters Dissertation, University of the Witwatersrand, South Africa.

- Marinković, S., Radonjanin, V., Malešev, M., Ignjatović, I., 2010. Comparative environmental assessment of natural and recycled aggregate concrete. *Waste management*. 30 (11), 2255–2264.
- Morgan, D.R., 1996. Compatibility of concrete repair materials and systems. *Constr. Build. Mater.* 10 (1), 57–67.
- Muigai, R., 2014. A Framework Towards The Design Of More Sustainable Concrete Structures, PhD Thesis. University of Cape Town.
- Olorunsogo, F.T., Padayachee, N., 2002. Performance of recycled aggregate concrete monitored by durability indexes. *Cem. Concr. Res.* 32 (2), 179–185.
- Papadakis, V.G., Tsimas, S., 2002. Supplementary cementing materials in concrete. Part I: efficiency and design. *Cem. Concr. Res.* 32 (2002), 1525–1532.
- Papadakis, V.G., Roumeliotis, A.P., Fardis, M.N., Vagenas, C.G., 1996. Mathematical modeling of chloride effect on concrete durability and protection measures. In: Dhir, R.K., Jones, M.R. (Eds.), *Concrete Repair, Rehabilitation and Protection*. E&FN Spon, London, pp. 165–174.
- Peng, C.L., Scorpio, D.E., Kibert, C.J., 1997. Strategies for successful construction and demolition waste recycling operations. *J. Constr. Manage. Econ.* 15 (1), 49–58.
- Schepper, M., Buysser, K., Driessche, I., De Belie, N., 2013. The regeneration of cement out of completely recyclable concrete: clinker production evaluation. *Constr. Build. Mater.* 38, 1001–1009.
- Scheubel, B., Nachtwey, W., 1997. Refra Kolloquium. Development of Cement Technology and Its Influence on the Refractory Kiln Lining. World Cement, Berlin, Germany, pp. 55–62. As cited in: Aitcin, P.C. (2000). Cements of yesterday and today: concrete of tomorrow, *Cem. Concr. Res.* 30(9), pp. 1349–1359.
- Tam, V.W.Y., 2009. Comparing the implementation of concrete recycling in the Australian and Japanese construction industries. *J. Cleaner Prod.* 17 (2009), 688–702.
- Turner, K.R., Pearce, D., Bateman, I., 1993. *Environmental Economics: An elementary introduction*. The John Hopkins University Press, Baltimore.
- Uher, T.E., 1999. Absolute indicators of sustainable construction. Royal Institution of Chartered Surveyors (RICS) series 1999.
- United Nations Conference on Environment and Development (UNCED), 1992. Agenda 21.
- USEPA, 1999. United States Environmental Protection Agency.
- WBCSD, 2002. World Business Council on Sustainable Development, 2002.
- WCED (World Commission on Environment and Development), 1987. *Our Common Future*. Oxford University Press, Walton Street, Oxford.
- Wernick, I.K., Herman, R., Govind, S., Ausubel, J.H., 1996. Materialization and dematerialization: measures and trends. *Daedalus*. 25, 171–198. As cited in: Kibert, C.J., Sendzimir, J., Guy, G.B., 2002. *Construction Ecology: Nature as the Basis for Green Buildings*, London and New York, Spon Press.

Further reading

- EN 1991. Eurocode 1: Actions on Structures.
- EN 1990-1, 2002. Basis of Structural Design. European Committee for Standardization (CEN).
- Fulton's Concrete Technology 2001. In: Addis, B.J., Owens, G., (Eds.), *Midrand: Portland Cement Institute*, pp.135.

This page intentionally left blank

Cost-effective design to address climate change impacts

22

Emilio Bastidas-Arteaga¹ and Mark G. Stewart²

¹University of Nantes, Nantes, France,

²The University of Newcastle, Newcastle, NSW, Australia

22.1 Introduction

22.1.1 Background

Concrete is the predominant construction material for buildings, bridges, wharves, and other infrastructure worldwide. A potentially important factor for asset management is the possible influence of climate change (Chapter 3: Impact of climate change on the service life of concrete structures). This may alter the environment to which infrastructure is exposed and, in turn, may alter the factors known to affect the corrosion of reinforcing steel, including atmospheric CO₂ concentration, temperature, humidity, ocean acidification, airborne pollutants, etc.

A rise in temperature will increase the rate of infiltration of deleterious substances (increased material diffusivity) and increase the corrosion rate of steel. Changes in relative humidity levels may also increase the rate of infiltration of deleterious substances (Nguyen et al., 2017; Stewart et al., 2011). Typically these parameters must be considered as random variables or stochastic processes, and their statistical characteristics will gradually change with time. An appropriate framework for dealing with this, and other climate adaptation problems, is structural reliability and risk-based decision analysis, taking into account the updating with inspection data (Stewart and Deng 2015; Tran et al., 2016a,b).

Several studies have used probabilistic or deterministic methods to assess climate change effects on the durability of RC structures placed in several countries (Bastidas-Arteaga et al., 2010, 2013; de Larrard et al., 2014; Stewart et al., 2011; Talukdar et al., 2012; Wang et al., 2012). These researchers found that the temporal and spatial effects of a changing climate can increase current chloride ingress or carbonation-induced damage risks and justify the need for comprehensive adaptation. Thus, Stewart and Peng (2010) used a simplified carbonation model and global IPCC (2007) CO₂ concentration and temperature change data to assess the cost-effectiveness of increasing design cover as an adaptation measure. This preliminary analysis found that increasing design cover may not be cost-effective. Nevertheless, the results were based on an oversimplified carbonation model and the authors highlighted that the reported preliminary results cannot be generalized, that further

research is needed to better characterize the cost-effectiveness of adaptation strategies. [Stewart et al. \(2012\)](#) considered the effect of climate adaptation strategies, including increases in cover thickness, improved quality of concrete, and coatings and barriers on damage risks. It was found that increases in design cover ameliorate the RC durability under a changing climate. However, such a study does not include cost-benefit assessment of climate adaptation strategies, and later work in this area proved inconclusive ([Peng and Stewart, 2015](#)).

22.1.2 *Aims and scope*

Within this context, the main objectives of this chapter are:

- to propose a framework for probabilistic cost-benefit analysis of adaptation measures to ameliorate chloride-induced corrosion in new and existing structures
- to apply the methodology to structures subjected to various environmental conditions and/or located in specific locations in France.

These challenges require the consideration of time-dependent damage risks and costs that differ as a function of the construction time and particular geographical conditions. Time-dependent damage risks depend mainly on exposure (climate change projections) and technical considerations (design standards at the time of construction, properties of the construction and repair materials, inspection and maintenance strategies, implementation (or not) of standards updating, etc.). The assessment of cost-effectiveness of adaptation strategies is mainly related to economic aspects (discount rate, repair, adaptation costs, etc.) and the level of use of structures (remaining lifetime, assessment time, adaptation times, etc.). This study includes many of the above-mentioned aspects.

[Section 22.2](#) poses the problem of adaptation of deteriorating RC structures. [Section 22.3](#) describes the proposed framework for evaluating the cost-effectiveness of adaptation measures. It accounts for deterioration models, probabilistic methods, and cost-benefit analysis. [Section 22.4](#) presents the repair and adaptation strategy that will be used in the illustrative example ([Section 22.5](#)). The example focuses on adaptation of existing RC structures placed in the coastal French cities of Saint-Nazaire and Marseille.

22.2 Adaptation of RC structures

Climate adaptation, in terms of the enhancement of adaptive capacity, can be done by developing new technologies and materials to counter the impact of increasing corrosion risk under a changing climate. From a practical point of view, three questions about the problem of adaptation of structures emerge:

- which measure could be used to adapt?
- when is the best time to implement adaptation measures?
- what is the best way to measure the cost and effectiveness of adaptation measures?

22.2.1 Adaptation measures

There is a wide range of existing and “low-tech” options that can enhance the durability of concrete structures, and these can be applied to reduce the adverse effects of climate change. The design options generally include the selection of cover, concrete mix, surface coating barriers, extraction, and cathodic protection. In addition to reducing environmental exposure as much as possible, practical adaptation solutions in a new design may come from increasing cover and strength grade, or any approaches that reduce the material diffusion coefficient without compromising the reliability and serviceability of concrete. Adaptation measures for new and existing concrete structures may include:

- Surface treatments
- Realkalization
- Extra design cover
- Increase concrete durability
- Stainless or galvanized steel reinforcement
- Corrosion inhibitors
- Cathodic protection
- Replace existing cover with new concrete.

22.2.2 Adaptation time

The time of adaptation is highly variable and dependent on the extent and location of corrosion damage. Some adaptation strategies could be applied at time of construction (coatings/surface treatments, reinforcement), and others at time of corrosion initiation (realkalization, chloride extraction). Clearly, it is preferable to use adaptation strategies that are implemented during design and construction rather than in-service (e.g., when corrosion damage occurs) as the latter will be much more costly in terms of direct costs and inconvenience/user delays and other indirect costs (Stewart et al., 2012).

22.2.3 Cost-effectiveness of adaptation strategies

Adaptation strategies will have varying degrees of effectiveness and cost. Some will require regular maintenance over the life of the structure, such as surface treatments, which will increase their lifecycle cost. Given that there are many millions of new and existing concrete infrastructure in many countries the cost of adaptation can be immense. For this reason, a risk-based approach is needed to assess the optimal level, if any, of adaptation measures. This includes the cost, location, timing, and extent of adaptation measures.

An increase in cover thickness can increase the time of carbonation and chloride ingress to reach concrete reinforcement and, in turn, delay carbonation and chloride-induced corrosion. It is therefore one of the most obvious and simplest adaptation options in the design of concrete infrastructure under a changing climate to maintain structural durability and serviceability. While the change of cover is

considered as the most straightforward design approach to reduce the impact of changing climate, other options may also include the selection or design of concrete materials to reduce the diffusion coefficient of deleterious substances—i.e., slow the ingress of those substances and so delay corrosion of concrete reinforcement. In practice, selection of a higher strength grade of concrete is one approach to reduce the diffusion coefficient, in addition to enhancing its mechanical properties.

Stewart and Peng (2010) have conducted a preliminary lifecycle cost assessment to assess the cost-effectiveness of increasing design cover as an adaptation measure to mitigate the effects of carbonation of concrete. The lifecycle cost analysis considered costs associated with extra design cover and expected maintenance/repairs for typical RC structures and elements over the next 100 years—taking into account several IPCC atmospheric CO₂ emission scenarios. The preliminary analysis found that lifecycle costs for the current situation (“do nothing”—use existing covers) are lower than those for proposed increases in design cover. This suggests that, although enhanced greenhouse conditions will lead to increased carbonation-induced corrosion of RC structures, it may not be cost-effective to increase design covers. However, a more detailed assessment of risks, costs, benefits of adaptation measures and environmental impact may reveal a different conclusion. Further work considered the effects of spatially variable corrosion damage, and the costs and benefits of adaptation measures (Peng and Stewart 2014, 2015). What is important is the need to estimate time-dependent changes in damage risks, the effectiveness and cost of one or more adaptation measures, costs of repairing damage, and other criteria needed to assess the optimal level of adaptation measures both now and into the future.

22.3 Proposed adaptation framework

The main practical problem concerning adaptation of structures lies in evaluating its costs and effectiveness. Fig. 22.1 shows the proposed framework for dealing with this problem that combines:

- general methods that could be applied to any structure: deterioration models, stochastic approaches, and cost-benefit analysis
- information specific to each structure: climate change predictions and structural characteristics

The following sections focus on describing the general methods that are employed in the proposed framework. Information specific to each structure will be detailed in the numerical application (Section 22.5).

22.3.1 Deterioration models

As mentioned in Bastidas-Arteaga et al. (2010), de Larrard et al. (2014), and Stewart et al. (2014), the assessment of climate change consequences on RC durability requires deterioration models that account for the influence of surrounding

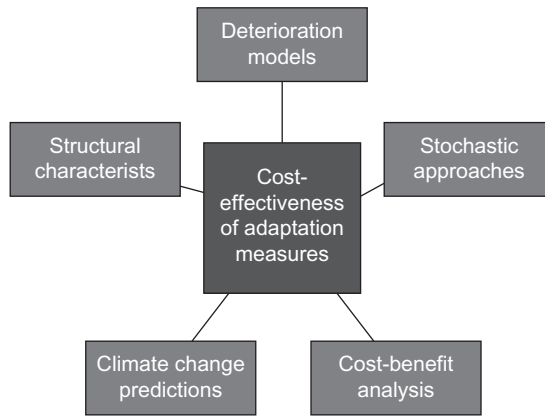


Figure 22.1 Proposed framework for determining the cost-effectiveness of adaptation measures.

Table 22.1 Main characteristics of deterioration models considered in this study

Deterioration stages	Physical phenomena	Influencing environmental factors
Corrosion immunity	Diffusion and convection	Temperature, relative humidity
Active corrosion	Electrochemistry	Temperature
Corrosion until severe cracking	Electrochemistry and mechanics	Temperature

environmental actions (temperature, relative humidity, rain, etc.). Table 22.1 summarizes the characteristics of the models considered in this study. We will focus on modeling deterioration since construction (or repair) until severe concrete cracking. Thus, the whole lifetime will be divided into three stages (Table 22.1) that are modeled on the basis of different principles. For the stage of corrosion immunity (i.e., before corrosion initiation), we use a finite element model that accounts for chloride ingress into concrete by diffusion and convection (Bastidas-Arteaga et al., 2011; Saetta et al., 1993). This model takes into account the influence of temperature and relative humidity variations on the chloride penetration process. The stage of active corrosion is modeled on the basis of electrochemical principles and considers only the effects of temperature (Duracrete, 2000). The stage of corrosion until severe concrete cracking is assessed by two models. The former concerns the time since corrosion initiation until the appearance of a first crack on the concrete surface (El Maaddawy and Soudki, 2007). The second represents the time until reaching a threshold crack width w_{lim} (Mullard and Stewart, 2011). Both models combine mechanical and electrochemical principles. The corrosion propagation models

considered in the second stage, influenced by temperature variations, drive both models. Although corrosion propagation is widely influenced by relative humidity, there is not a current model that accounts for this factor in a comprehensive manner.

22.3.2 Stochastic assessment of time-dependent damage risks

The cumulative distribution function for the time of first damage (corrosion initiation, severe concrete cracking, failure) T_{dam} in the period $[0, t]$ for original concrete is:

$$p_s(0, t) = \Pr[t \geq T_{\text{dam}}] \quad (22.1)$$

where, depending on the asset maintenance policy, the owner can specify the limit criteria for repair: threshold chloride content, limit crack width, etc. However, after repair, the time-dependent damage risks of the repaired structure will not be the same as the original one $p_s(0, t)$ due to changed temperature and RH at the time of repair. Hence, the damage risk for repaired structures exposed to the environment for the first time at time of repair, $t_{\text{rep}} = i\Delta t$, will change depending on the new climatic conditions and time of repairs (Bastidas-Arteaga and Stewart, 2013, 2015; Nguyen et al., 2017; Stewart et al., 2014):

$$p_{s,i}(i\Delta t, t) = \Pr[t \geq T_{\text{dam},i}] \quad (22.2)$$

where $T_{\text{dam},i}$ is the time to damage when the repaired structure is exposed to the environment for the first time after repair and Δt is the inspection length.

Fig. 22.2 presents a conceptual description of the time-dependent probability of damage for a structure subjected to chloride-induced deterioration under various

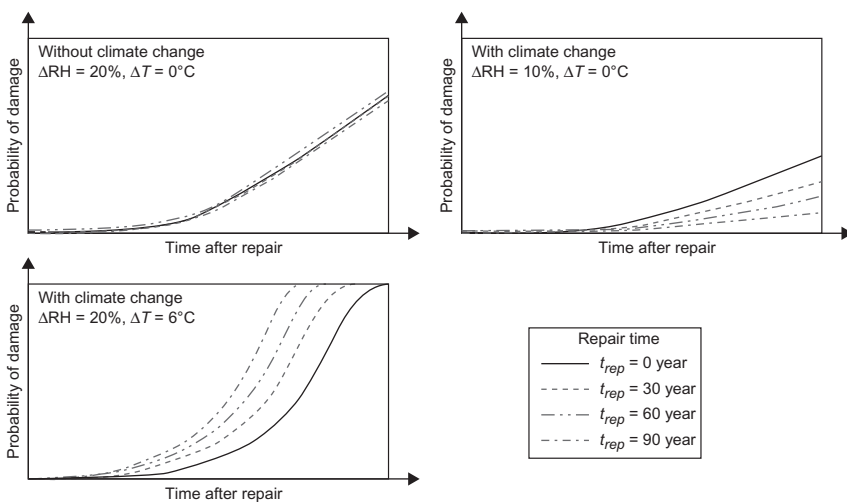


Figure 22.2 Conceptual description of the probability of damage for various climate change scenarios and repair times.

climate change scenarios. The climate change scenarios are simply represented as relative changes with respect to current climate conditions of a given location after 100 years. The overall trend indicates that the deterioration processes increase probability of damage with time. Fig. 22.2 clearly shows that the rate of damage risk is highly dependent on climate change effects. If there is no change in climate ($\Delta RH = 0\%$ and $\Delta T = 0^\circ\text{C}$), the probability of damage increases with time and remains constant, irrespective of time of repair. However, if climate change reduces the environmental relative humidity, i.e., $\Delta RH = -10\%$ in 100 years, the chloride ingress mechanism slows down, and consequently, the probability of severe cracking decreases. In this case, climate change has a “positive effect” on RC durability by reducing corrosion damage risk. An opposite behavior is observed when climate change increases the temperature and relative humidity ($\Delta RH = 20\%$ and $\Delta T = 6^\circ\text{C}$). In this case, the probability of damage increases if the structure is new or repaired at time t_{rep} . Therefore, the time-dependency of damage risks should be considered for a comprehensive cost-benefit analysis of adaptation measures.

22.3.3 Cost-benefit analysis

22.3.3.1 General framework

Costs and benefits may occur at different times, so, in order to obtain consistent results, it is necessary for all costs and benefits to be discounted to a present value. The proposed cost-benefit framework could be applied to both new and existing structures. Costs and benefits are measured from the time of the cost-benefit assessment, t_{assess} . For example, for an existing structure, if a decision-maker is making a decision in $t_{\text{assess}} = 2013$ about predicted costs and benefits of adaptation measures for a structure built in $t_{\text{construct}} = 1970$, then damage costs incurred prior to $t_{\text{assess}} = 2013$ are not considered in the benefit-to-cost ratio as the decision-maker is only concerned with costs and benefits that arise after 2013. For a new structure $t_{\text{assess}} = t_{\text{construct}}$. If a structure is built in the calendar year $t_{\text{construct}}$, and if it is assumed that corrosion damage is always detected when the structure is inspected, then the expected damage cost measured from year of assessment t_{assess} to end of service life, is $E_{\text{damage}}(T_t)$ and is the product of probability of corrosion damage and damage costs, i.e.,

$$E_{\text{damage}}(T_t) = \sum_{n=1}^{T_t/\Delta t} \sum_{i=n}^{T_t/\Delta t} [p_{s,n}(i\Delta t) - p_{s,n}(i\Delta t - \Delta t)] \frac{C_{\text{damage}}}{(1+r)^{t_{\text{construct}}+i\Delta t-t_{\text{assess}}}}$$

with $i\Delta t > t_{\text{assess}} - t_{\text{construct}}, t_{\text{construct}} \leq t_{\text{assess}}$

(22.3)

where T_t is the service life (typically $T_t = 100$ years), Δt is the time between inspections, n is the number of damage incidents, i is the number of inspections, $p_{s,n}(t)$ the probability of the n^{th} damage incidence before time t , r is the discount rate and

C_{damage} is the cost of damage including maintenance and repair costs, user delay and disruption costs, and other direct or indirect losses arising from damage to infrastructure. For example, an asset owner should be able to quantify the unit repair cost ($\text{€}/\text{m}^2$), and if the area of damage is known then repair cost can be estimated.

Eq. (22.3) can be generalized for costs arising from multiple limit states, such as flexural failure, shear failure, etc. Corrosion damage (severe corrosion-induced cracking) is considered herein as the most influential mode of failure for the estimation of benefits. Eq. (22.3) can be re-expressed as:

$$E_{\text{damage}}(T_t) = \sum_{i=1}^{T_t/\Delta t} \Delta P_{s,i} \frac{C_{\text{damage}}}{(1+r)^{t_{\text{construct}}+i\Delta t-t_{\text{assess}}}} \quad (22.4)$$

$$\text{with } i\Delta t > t_{\text{assess}} - t_{\text{construct}}, t_{\text{construct}} < t_{\text{assess}}$$

where $\Delta P_{s,i}$ is the probability of damage incident between the $(i-1)^{\text{th}}$ and i^{th} inspections which is a function of time since last repair which is turn is affected by damage risks for original and repaired concrete $p_s(0,t)$ and $p_{s,i}(i\Delta t,t)$, respectively. The repaired concrete may have the same durability design specifications as the original concrete, or may be repaired to a higher standard (e.g., increased concrete cover). The risk reduction caused by an adaptation measure is thus:

$$\Delta R(T_t) = \frac{E_{\text{damage-BAU}}(T_t) - E_{\text{damage-adaptation}}(T_t)}{E_{\text{damage-BAU}}(T_t)} \quad (22.5)$$

where $E_{\text{damage-BAU}}(T_t)$ and $E_{\text{damage-adaptation}}(T_t)$ are the cumulative expected damage cost (economic risk) for no adaptation measures (business as usual (BAU) or existing practice) and adaptation measures, respectively. If an adaptation measure is cost-effective then $E_{\text{damage-adaptation}}(T_t)$ will be significantly lower than $E_{\text{damage-BAU}}(T_t)$ resulting in high risk reduction $\Delta R(T_t)$. In other words, $\Delta R(T_t)$ represents the proportional reduction in expected repair costs, due to an adaptation measure.

The cost of adaptation, in this case the additional repair costs associated with increased cover, will occur at the same time as the damage (repair) costs are incurred. It follows that the expected cost of adaptation is directly proportional to damage costs

$$E_{\text{adapt}}(T_t) = \sum_{i=1}^{T_t/\Delta t} \Delta P_{s,i} \frac{C_{\text{adapt}}}{(1+r)^{t_{\text{construct}}+i\Delta t-t_{\text{assess}}}} \text{ with } i\Delta t > t_{\text{adapt}} - t_{\text{construct}}, t_{\text{construct}} < t_{\text{assess}} \quad (22.6)$$

where C_{adapt} is the cost of adaptation measures that reduces risk by ΔR and t_{adapt} is the adaptation year.

The “benefit” of an adaptation measure is the reduction in damages associated with the adaptation strategy, and the “cost” is the cost of the adaptation strategy. The benefit-to-cost ratio $BCR(T_t)$ is:

$$BCR(T_t) = \frac{E_{\text{damage-BAU}}(T_t)\Delta R(T_t)}{E_{\text{adapt}}(T_t)} \quad (22.7)$$

Clearly, an adaptation measure that results in a benefit-to-cost ratio exceeding unity is a cost-effective adaptation measure. Since costs and benefits are time-dependent, then it follows that the benefit-to-cost ratio is time-dependent. Thus, an adaptation measure may not be cost-effective in the short-term, due to high adaptation cost for example, but the benefits may accrue over time, resulting in improved cost-effectiveness in the longer-term. Note that the additional cost of repair (such as increasing cover on repaired concrete) is treated herein as an adaptation cost, and not as a reduced benefit.

Since the proposed adaptation framework considers uncertainties (Section 22.3.2), the output of the analysis (BCR) is also variable. This allows the mean BCR and the probability that an adaptation measure is cost-effective $\Pr(BCR > 1)$ to be calculated. These criteria are used to evaluate the cost-effectiveness of adaptation strategies. Monte-Carlo simulation analysis will be used as the computational tool to propagate uncertainties through the cost-benefit analysis, although analytical methods could also be used—e.g., Stewart and Melchers (1997).

For all adaptation options, construction and repair cost data are needed, and such cost data is country-, site-, and structure-specific, so it is difficult to make generalizations about these costs. In this chapter, costs are expressed in 2013 Euros. Note, however, that Eqs. (22.3)–(22.7) show that BCR is not dependent on the monetary units, but it is a function of the ratio of damage that is related to adaptation costs. It is assumed that design and inspection costs are similar for different adaptation measures and so are not needed for this comparative analysis. Consequently, adaptation strategies will only affect the expected damage costs. As we are concerned about outdoor exposures then the external RC structural elements of interest are slabs, beams and columns. Corrosion damage is assumed to occur on one (exposed) face of a slab and beam, and all faces of a column.

22.3.3.2 Discount rates

There is some uncertainty about the level of discount rate, particularly for climate change economic assessments (e.g., Dasgupta, 2008). France used a discount rate of 8% to evaluate public investments from 1985 to 2005. However, following the 2005 Lebègue Report (Lebègue et al., 2005), the Commissariat Général au Plan has recommended a 4% discount rate for short-term investments and a lower discount rate of 2% for cash flows occurring after more than 30 years (Gollier, 2012). These discount rates were revised in 2013 by the Commissariat Général à la Stratégie et à la Prospective recommending 2.5% and 1.5% discount rates for short-term (lifetime lower than 70 years) and long-term investments, respectively (Quinet, 2013).

Quinet (2013) also recommends carrying out a sensitivity analysis with a 4.5% discount rate to compare new and old approaches. Countries and institutions worldwide use other discount rates. The European Commission recommends a 5% discount rate (Harrison, 2010). Infrastructure Australia recommends discount rates of 4%, 7% and 10% for infrastructure projects (IA, 2008). Other discount rates vary from 3% (Germany) to over 10% (World Bank) (Harrison, 2010).

Discount rates are generally assumed constant with time. However, this may not be appropriate when considering intergenerational effects often associated with climate change policy decisions (Boardman et al., 2011). Projects with significant effects beyond 30–50 years are considered intergenerational. The British Treasury, for example, recommends the following time-declining discount rates: 3.5% (0–30 years), 3.0% (31–75 years), 2.5% (76–125 years), 2.0% (126–200 years), 1.5% (201–300 years), and 1.0% (300+ years) (HM Treasury, 2003). However, there is some controversy about time-declining discount rates (Viscusi, 2007), and the Australian Office of Best Practice and Regulation (OBPR) states that ‘there is no consensus about how to value impacts on future generations’ and ‘Rather than use an arbitrarily lower discount rate, the OBPR suggests that the effects on future generations be considered explicitly’ (OBPR, 2010). Nonetheless, the 2006 UK Stern Review adopted a discount rate of 1.4% (Stern, 2006), and the Australian Garnaut Review adopted discount rates of 1.35% and 2.65% (Garnaut, 2008). These relatively low discount rates were selected to not underestimate climate impacts on future generations. However, others suggest higher discount rates when assessing economic impacts of climate change (Nordhaus, 2007).

The quantification of discount rates above relates mainly to public-sector investments in infrastructure. Private investments in infrastructure, such as the owners of a port, power station, airport, etc., tend to include a risk premium which leads to a higher discount rate (BTRE, 2005). The marginal rate of return on private investments is suggested as one method to derive discount rates for private investments (Boardman et al., 2011). According to Boardman et al. (2011), the best “proxy” for marginal rate of return on private investments is the before-tax rate of return on corporate bonds – approximately 4.5%.

In this chapter, discount rates of 2%, 4% and 8% are considered. These discount rates represent the range of discount rates in several countries, and the lower (2%) discount rate is also representative of values used to consider intergenerational and climate change effects.

22.4 Considered repair and adaptation measures

22.4.1 Definition

For illustrative purposes, this study considers patch repair as the most common technique to repair corrosion damage in RC structures—e.g., (BRE, 2003; Canisius and Waleed, 2004). For a patch repair, the concrete cover is typically removed to

approximately 25 mm past the steel bars (which are then cleaned of corrosion products) and a repair material is installed. The maintenance strategy assumes that (Stewart, 2001):

- concrete is inspected at time intervals of Δt
- patch repair is carried out immediately after corrosion damage has been discovered at time of i^{th} inspection at time $i\Delta t$
- damage limit state exceedance results in the entire RC surface being repaired
- repair provides no improvement in durability performance of the repaired structure (i.e., it is repaired with the same cover and concrete quality as the original design specification)

Damage may re-occur during the remaining service life of the structure, i.e., multiple repairs may be needed. The maximum possible number of damage incidents is $n_{max} = T_r/\Delta t$, where T_r is the total lifetime.

We consider increase in design cover as the climate adaptation measure aimed at reducing the impact of chloride-induced corrosion damage. Increasing the strength grade of concrete, which reduces the diffusion rate, is another possible climate adaptation measure. For more details of this adaptation measure see Bastidas-Arteaga and Stewart (2015, 2016) and Peng and Stewart (2015).

22.4.2 Repair and adaptation costs

22.4.2.1 Cost of damage (C_{damage})

The cost of repair or replacement, and associated user losses, etc. are considerable and, for some structures, user losses are often much greater than direct repair, replacement and maintenance costs. Val and Stewart (2003) assumed that the cost of RC bridge deck-replacement is double the construction cost, based on cost data for removal and replacement costs. However, this is likely to over-estimate the repair costs for most corrosion damage. The estimated cost for concrete patch repair using ordinary Portland cement is 286 €/m² (BRE, 2003; Mullard and Stewart, 2012; Yunovivh et al., 2001). User losses and other user disruption costs are site- and structure-specific, but for many RC structures such costs will be minimized if the RC element to be repaired is an external structural member such as walls, columns or facade panels. For bridges, however, closure of one lane of a four lane bridge can cause user delay costs of 39,650€ per day (Yunovivh et al., 2001). To allow for a minor user disruption cost, Bastidas-Arteaga and Stewart (2013, 2015) assumed that the total failure cost was $C_{damage} = 325 \text{ €/m}^2$ (approximately \$450–500 per m²).

On a more detailed cost analysis, Bastidas-Arteaga and Stewart (2016) considered costs estimated for the repair of RC slabs and beams of the Agri-foodstuffs terminal of the Nantes Saint-Nazaire Port (Srifi 2012). Table 22.2 summarizes the costs of damage which include costs of damage reports, preparation of the building site, repair (removal and reconstruction of the cover) and operating losses. These costs were computed considering recent maintenance operations for three repair alternatives.

Table 22.2 Repair strategies and corresponding costs of damage of the agri-foodstuffs terminal at the Port of Nantes Saint-Nazaire

Description of repair strategy	Type of cost in €/m ²					
	Reports and site installation	Concrete removal	Repair	operating loss	Other costs	Total
<i>Repair 1:</i> Preventive Maintenance, where the structure is repaired before corrosion initiation. Actions: 4 cm concrete removal without replacement of corroded bars.	65	62.7	111.6	12.5	11.4	263.2
<i>Repair 2:</i> Corrective Maintenance, where repair takes place after severe concrete cracking but the loss of cross-sectional area of rebars is not significant. Actions: 6 cm concrete removal without replacement of corroded bars.	76.1	71.8	134.3	29.4	11.4	323
<i>Repair 3:</i> Corrective Maintenance where repair takes place after severe concrete cracking and therefore the loss of cross-sectional area of rebars is significant. Actions: 6 cm concrete removal and replacement of corroded bars.	76.3	71.8	135	58.9	11.4	353.4

Table 22.3 Adaptation costs for slabs

Structural element	D (mm)	$\Delta c_{\text{adapt}} 5 \text{ mm}$ (€/m ²)	$\Delta c_{\text{adapt}} 10 \text{ mm}$ (€/m ²)
Slabs	100	4.23	8.45
Slabs	300	2.44	4.88

It is noted from [Table 22.2](#) that most of the costs are related to concrete removal and repair operations, followed by the costs of studies and preparation of the building site and operation losses. For the alternative 3, the replacement of corroded steel requires a longer repair time and so increasing operational losses.

22.4.2.2 Cost for the adaptation strategy

The baseline case for construction cost per unit volume (C_{cv}) including forms, concrete, reinforcement, finishing and labor is approximately 490–850 €/m³, 910–1010 €/m³ and 780–1560 €/m³ for RC slabs (4.6–7.6 m span), RC beams (3.0–7.6 m span), and RC columns (300 mm × 300 mm to 900 mm × 900 mm), respectively ([RSMeans, 2012](#)). These values will therefore be used to estimate the costs of the two adaptation strategies.

It is assumed that an increase in design cover Δc_{adapt} would increase the cost of forms, concrete, reinforcement, finishing and labor by an amount proportional to the extra volume of concrete needed. Since C_{damage} units are €/m² of surface area, but C_{cv} is given as per unit volume, then cost of construction (C_c) and C_{adapt} should be converted to cost per surface area exposed to deterioration, and so is corrected for structural member dimension such as slab depth or beam or column width (D). [Table 22.3](#) provides the adaptation costs for various structural elements (per mm of extra cover). The relationships used to evaluate the adaptation costs are provided in [Bastidas-Arteaga and Stewart \(2016\)](#). This table also presents the adaptation costs for $\Delta c_{\text{adapt}} = 5$ and 10 mm increase in extra cover.

22.5 Illustrative example: Adaptation of existing RC structures

22.5.1 Problem description

22.5.1.1 Concrete cover and exposure

This example illustrates the probabilistic assessment of the cost-effectiveness of adaptation strategies for existing RC structures placed in two coastal cities in France (Saint-Nazaire and Marseille) under splash and tidal exposure. Since this application deals with existing structures, it is important to determine which were the standards at the construction time. There was an evolution over time of the minimum concrete cover recommended by French design standards for maritime exposure. These standards were published as circulars of the official diary in France.

The first circular on October 20, 1906, recommended a minimum concrete cover varying between 15 and 20 mm for the main reinforcement without distinction of the kind of exposure. In 1934, a new circular recommended 35 mm cover for structures close to the sea and 20 mm for structures in land. Concrete cover was increased to 40 and 50 mm in 1964 and 1992, respectively for structures close to the sea. Finally, the Eurocode 2 (European Standard, 2004), which is mandatory after 2010 in France, suggests concrete covers for different exposure conditions. For example, there are three exposure zones for marine structures: atmospheric XS1, submerged XS2, and splash and tidal XS3. For the XS3 exposure the recommended concrete cover is 55 mm.

This example considers two adaptation strategies implemented at a given adaptation time (e.g., $t_{\text{adapt}} = 2030$) defined as follows:

- *Adaptation 1*: increase existing (Eurocode) design covers by $\Delta c_{\text{adapt}} = 5$ mm for XS3 exposure
- *Adaptation 2*: increase existing (Eurocode) design covers by $\Delta c_{\text{adapt}} = 10$ mm for XS3 exposure.

It is assumed that, if severe concrete cracking is detected when there is an evolution of the construction standard, the concrete cover is increased according to standard recommendations at the time of repair. For example, a 1970 structure (40 mm design cover) damaged in 2015 is repaired to the 2015 specified design cover of 55 mm.

This study does not focus on a specific structure. Therefore, there is not information about the characteristics of the concrete used to build the existing structures. Besides, there is no information about the repair materials that will be used in the future. For simplicity, this example assumes that the same concrete was used for the construction and repair of all structures during their lifetime. This concrete has a characteristic compressive strength, $f'_{ck} = 35$ MPa, as recommended by the Eurocode 2 for XS3 exposure (European Standard, 2004).

Other assumptions are summarized as follows:

- the structural lifetime is $T_t = 100$ years
- the limit crack width for repair is $w_{lim} = 1$ mm
- rebar diameter is $d_0 = 16$ mm
- the environmental chloride concentration, C_{env} , corresponds to a XS3 exposure
- all structural components will be subjected to the same environmental conditions
- the chloride ingress is one-dimensional
- the time of adaptation will vary between 2020 and 10 years before the end of the structural lifetime
- the adaptation strategy consists of increasing concrete cover by 5 or 10 mm with respect to standard recommendations
- the time for assessment of costs is $t_{\text{assess}} = 2013$
- the costs of damage are: $C_{\text{damage}} = 263.2$ €/m², $C_{\text{damage}} = 323$ €/m², and $C_{\text{damage}} = 353.4$ €/m² for Repairs 1, 2 and 3 (Table 22.2)
- the adaptation costs are defined according to Table 22.3
- the discount rates are 2%, 4% and 8%

The probabilistic models used to estimate damage probabilities ($p_{s,i}$) are given in Table 22.4. $p_{s,i}$ (Eq. 22.2) corresponds herein to the probability of severe concrete

Table 22.4 Probabilistic models of the random variables

Variable	Units	Distribution	Mean	COV	References
Reference chloride diffusion coefficient, $D_{c,ref}$	m^2/s	Log-normal	3×10^{-11}	0.20	Duracrete (2000); Saetta et al. (1993); Val and Trapper (2008)
Environmental chloride concentration, C_{env}	kg/m^3	Log-normal	7.35	0.20	Duracrete (2000), Vu and Stewart (2000)
Concentration threshold for corrosion initiation, C_{th}	wt% cem.	Normal ^a	0.5	0.20	Bastidas-Arteaga and Schoefs (2012), Duracrete (2000)
Cover thickness, c_r	mm	Normal ^b	55	0.25	European Standard (2004), Val and Stewart (2003)
Reference humidity diffusion coefficient, $D_{h,ref}$	m^2/s	Log-normal	3×10^{-10}	0.20	Saetta et al. (1993), Val and Trapper (2008)
Thermal conductivity of concrete, λ	W/($m^\circ C$)	Beta on [1.4;3.6]	2.5	0.20	Neville (1981)
Concrete specific heat capacity, c_q	J/($kg^\circ C$)	Beta on [840;1170]	1000	0.10	Neville (1981)
Density of concrete, ρ_c	kg/m^3	Normal ^a	2400	0.04	JCSS (Joint committee of structural safety) (2001)
Reference corrosion rate, $i_{corr,20}$	$\mu A/cm^2$	Log-normal	6.035	0.57	Duracrete (1998)
28 day concrete compressive strength, $f_c(28)$	MPa	Normal ^a	$1.3(f'_{ck})$	0.18	Pham (1985)
Concrete tensile strength, f_{ct}	MPa	Normal ^a	$0.53 (f_c)^{0.5}$	0.13	Mirza et al. (1979)
Concrete elastic modulus, E_c	MPa	Normal ^a	$4600 (f_c)^{0.5}$	0.12	Mirza et al. (1979)

^aTruncated at 0.

^bTruncated at 10 mm.

cracking until reaching the limit crack width w_{lim} . This serviceability limit state allows us to generalize the results. It is assumed that all the random variables are statistically independent. Monte-Carlo simulations were used for the assessment of damage probabilities and the propagation of uncertainties throughout the cost-benefit analysis. For more details of the deterioration models used herein see Bastidas-Arteaga et al. (2011, 2013) and Nguyen et al. (2017).

22.5.1.2 Climate change scenarios

The economic assessment of adaptation measures is widely influenced by time-dependent changes in environmental parameters (temperature, relative humidity (RH)) that are site-specific. This work focuses on the study of the cost-effectiveness of climate change adaptation strategies for two port locations in France: Saint-Nazaire and Marseille. These cities correspond to different types of climate. Saint-Nazaire is close to the Atlantic Ocean in the Northern part of the country and it has a temperate oceanic climate. Marseille is placed in the South-East of France (Mediterranean coast) and it has a Mediterranean climate that is hot and dry.

The overall impact of climate change on the future weather of the selected locations was estimated by using data computed by the French general circulation model CNRM-CM5. Fig. 22.3 presents the yearly projections of temperature and RH for Saint-Nazaire and Marseille for the selected climate change scenarios

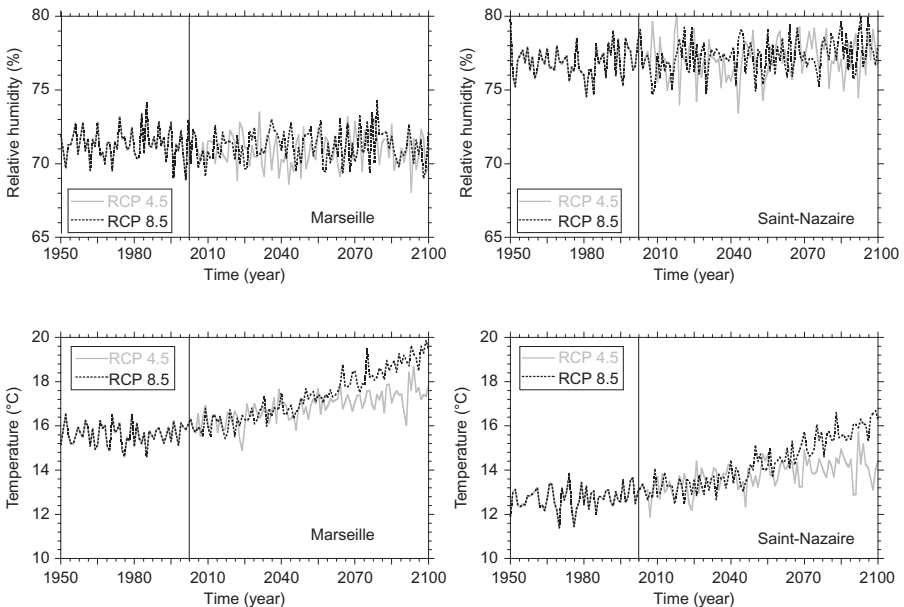


Figure 22.3 Yearly temperature and relative humidity projections for Saint-Nazaire and Marseille for RCP 4.5 and 8.5 climate change scenarios.

(RCP 4.5 and RCP 8.5) since 2005. By comparing climate (before 2005) in both cities, it is noted that Marseille is hotter and dryer than Saint-Nazaire. Climate change projections mainly predict temperature increase without significant changes in RH for both cities until the end of this century. By comparing mean temperatures over the periods (2001–10) and (2091–00) for both places, it was found that climate change could increase temperature by approximately 1.5°C and 3.5°C for RCP 4.5 and RCP 8.5 scenarios, respectively. Although climate change effects are relatively similar for both cities, the kinematics of chloride ingress and corrosion propagation is affected by the climate specific to each location. Comprehensive deterioration models are therefore useful tools for estimating the effects of specific climate conditions on RC durability.

Climate projections are subjected to considerable uncertainty and are dependent on CO₂ emission scenarios and accuracy of general circulation models (GCM). A comprehensive model of weather (RH and temperature) should be integrated with deterioration models to assess the effects of a changing climate. Given the difficulties of integrating a GCM with deterioration models, a simplified approach for modeling climate is considered in this study (Teodorescu et al., 2017). It accounts for influence of climate change, seasonal variations, and random nature of weather within a season. The formulation of this model is detailed in Bastidas-Arteaga et al. (2011, 2013).

22.5.2 Results

22.5.2.1 Damage probabilities and climate change effects

Fig. 22.4 depicts the time-dependent probability of severe cracking for the RCP 4.5 and RCP 8.5 climate change scenarios and structures built under different construction standards in Saint-Nazaire and Marseille. Although the concrete properties and cover are the same for both cities, the probabilities of severe cracking are larger for structures built in Saint-Nazaire. As indicated in Section 22.5.1.2, RH is ~8% higher in Saint-Nazaire than Marseille by increasing water content in the capillary pores and chloride diffusion rate. This higher RH will, therefore, shorten the time

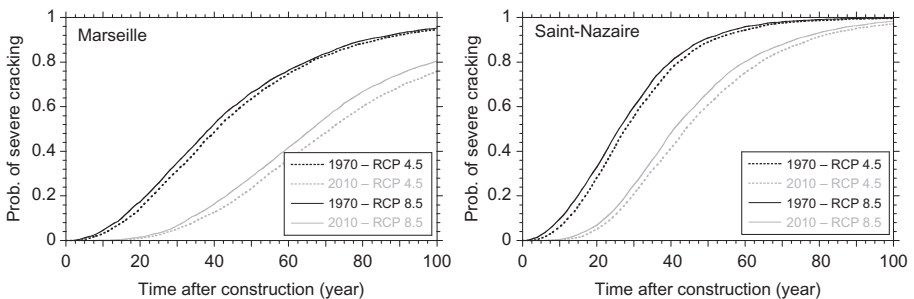


Figure 22.4 Probability of severe cracking for structures built in Saint-Nazaire and Marseille under the RCP 4.5 and RCP 8.5 scenarios.

to corrosion initiation by increasing the probability of severe cracking. It is also observed that the effects of the evolution of construction standards (in 1990 and 2010), for a given time after construction, decrease the probabilities of damage. These results indicate that, although increasing design cover is an effective protection for reducing damage induced by chloride ingress, the effectiveness of this measure depends on specific exposure conditions.

For both places, climate change projections show increases of temperature with respect to year 2000 levels for the RCP 4.5 and RCP 8.5 climate change scenarios, respectively. The effects of these climate change scenarios on the probability of severe cracking is also illustrated in Fig. 22.4. As expected, probabilities of severe cracking are larger for RCP 8.5 exposure because higher temperatures accelerate chloride ingress and corrosion propagation (Bastidas-Arteaga et al., 2011; Nguyen et al., 2017). The effects of the RCP 8.5 scenario are larger for recent structures because the differences in temperatures between both climate change scenarios announced by general circulation models increase after 2050 (Fig. 22.3). As a consequence, for structures built in 1970 the difference of temperature between both climate change scenarios is about 0.7°C (in 2070) whereas for recent structures (built in 2010), this difference is 1.7°C (in 2110). From an engineering point of view, RCP 8.5 and RCP 4.5 climate change scenarios could be interpreted respectively as upper and lower bounds for carrying out sensitivity studies. This point is illustrated later in the assessment of the cost-effectiveness of adaptation measures.

22.5.2.2 Cost-effectiveness of damage adaptation strategies

This section illustrates the probabilistic assessment of the cost-effectiveness of adaptation strategies for existing RC structures. These results were computed for a discount rate $r = 4\%$ and a damage cost $C_{\text{damage}} = 323 \text{ €/m}^2$ (Repair 2). According to Table 22.2, this damage cost corresponds to a medium damage extent that does not require replacement of corroded steel. A sensitivity study about the effects of discount rate will be presented in Section 22.5.2.3.

Fig. 22.5 presents the mean BCR for RC slabs in Marseille and Saint-Nazaire under the RCP 4.5 scenario. These results were obtained for slabs built in 2010 and $t_{\text{adapt}} = 2020$. Time of adaptation is taken as 2020 to represent the shortest practical time for a national standard (e.g., Eurocode 2 (European Standard, 2004)) to consider changes to existing specification, recommend changes, and have changes implemented in future standards. The overall behavior indicates that the mean of BCR is highly dependent on both the location and the slab size. The mean BCR is lower for Marseille and small slabs. For slabs with $D = 100 \text{ mm}$ in Marseille, the mean BCR is lower than 1, indicating that the adaptation strategies are not cost-effective. Therefore, for the studied material, current design cover (55 mm) is cost-efficient for Marseille. Conversely, adaptation strategies are cost-effective for all slab sizes in Saint-Nazaire. Thus, recommendations of current standards and adaptation measures could be more or less adapted to local climate conditions. For both locations, increasing extra cover by 10 mm is less cost-effective than a 5 mm increase in cover. Even if risk reduction ΔR should be higher for $\Delta c_{\text{adapt}} = 10 \text{ mm}$,

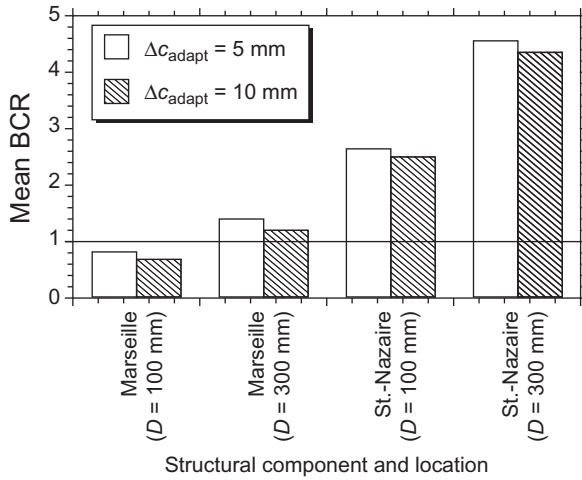


Figure 22.5 Mean BCR for RC slabs in Marseille and Saint-Nazaire under a RCP 4.5 climate change scenario, for structures built in 2010 and $t_{\text{adapt}} = 2020$.

Table 22.5 Mean BCR for slabs ($D = 300 \text{ mm}$) built in several years in Saint-Nazaire and $t_{\text{adapt}} = 2020$

Construction year	RCP 4.5		RCP 8.5	
	$\Delta c_{\text{adapt}} = 5 \text{ mm}$	$\Delta c_{\text{adapt}} = 10 \text{ mm}$	$\Delta c_{\text{adapt}} = 5 \text{ mm}$	$\Delta c_{\text{adapt}} = 10 \text{ mm}$
1970	0.81	0.71	0.82	0.71
1990	3.76	3.41	3.85	3.58
2010	4.57	4.34	4.74	4.5

the costs associated to this adaptation strategy are larger, by reducing the mean BCR. Thus, it is possible to conclude that the mean BCR for the whole structure could be maximized by performing different actions for individual components: optimizing the extra cover, considering different types of adaptation strategies, and/or business as usual (or do nothing).

The mean BCR is also influenced by the year of construction. To explain this relationship, Table 22.5 provides the mean BCR as a function of the construction year for slabs built in Saint-Nazaire and $t_{\text{adapt}} = 2020$. It is noted that the BCR is lower than one for older structures and increases for recent ones. A $\text{BCR} < 1$ implies that the adaptation measure is not cost-effective for old structures and that the existing standard recommendations are most cost-effective during the structural lifetime. The increment of BCR is due, on the one hand, to the increase of concrete cover recommended by the standards and/or considered by the adaptation measures. This means that larger concrete cover is more effective for this kind of exposure. On the other hand, larger BCR values are also related to the increase of climate

change effects on deterioration rates that justify the implementation of adaptation measures. As mentioned in previous results, the adaptation strategy $\Delta c_{\text{adapt}} = 10$ mm is less cost-effective for all adaptation years. The following results will therefore focus on the repair strategy $\Delta c_{\text{adapt}} = 5$ mm.

Table 22.5 also gives the effects of the climate change scenario. It is noted that higher mean BCRs are expected for the RCP 8.5 scenario which announces more important changes with respect to actual climate. The differences between results for both scenarios are larger for recent structures because they will be exposed to the largest climate variations that are more pronounced after 2050 (Fig. 22.3). These climate variations will induce more corrosion damage by increasing the cost-effectiveness of adaptation strategies.

The effect of the time of adaptation on the mean BCR and $\text{Pr}(\text{BCR} > 1)$ for slabs ($D = 300$ mm) in Saint-Nazaire, $\Delta c_{\text{adapt}} = 5$ mm and the RCP 4.5 scenario is shown in Table 22.6. It is noted that both the mean BCR and the $\text{Pr}(\text{BCR} > 1)$ decrease when the adaptation year is close to the end of the structural lifetime. Of interest is that the $\text{Pr}(\text{BCR} > 1)$ is close to 60% when mean BCR exceeds 4. This illustrates the high variability of damage risks caused by uncertainties of climate projections, and variabilities of material, dimensional, and deterioration parameters. These results could be used by an owner/stakeholder to evaluate the benefits and the risks of implementing adaptation strategies at various years. For example, it is observed that mean BCR and $\text{Pr}(\text{BCR} > 1)$ are small for older structures and therefore the owner/stakeholder could prioritize investments in adaptation measures for recent structures. These results could also be used to evaluate the impact of the adaptation year. For example, for structures built in 1990, if the owner/stakeholder decides to postpone the adaptation actions until 2040 the mean BCR is about 1.4 which is still interesting. However, the $\text{Pr}(\text{BCR} > 1)$ for this adaptation time is less than 11% indicating that the risks of having no benefits are larger.

22.5.2.3 Effect of discount rate

Table 22.7 describes the influence of discount rates (r) on both the mean BCR and the $\text{Pr}(\text{BCR} > 1)$ for slabs ($D = 300$ mm) built in several years in Saint-Nazaire and

Table 22.6 Mean BCR and $\text{Pr}(\text{BCR} > 1)$ (within brackets) for various adaptation years (slabs ($D = 300$ mm) built at several years in Saint-Nazaire, RCP 4.5 scenario and $\Delta c_{\text{adapt}} = 5$ mm)

Construction year	Adaptation year			
	2020	2040	2060	2080
1970	0.83 (6.1%)	0.05 (0.2%)	0 (0.0%)	0 (0.0%)
1990	3.64 (43.5%)	1.38 (10.2%)	0.2 (0.7%)	0 (0.0%)
2010	4.63 (59.0%)	3.85 (44.7%)	1.69 (13.1%)	0.29 (0.9%)

Table 22.7 Mean BCR and $\Pr(\text{BCR} > 1)$ (within brackets) for various discount rates and construction years (slabs ($D = 300$ mm) built at several years in Saint-Nazaire, RCP 4.5 scenario and $\Delta c_{\text{adapt}} = 5$ mm)

Construction year	$r = 2\%$	$r = 4\%$	$r = 8\%$
1970	1.32 (5.9%)	0.81 (5.9%)	0.29 (5.4%)
1990	5.8 (44.6%)	3.76 (43.4%)	1.58 (39.8%)
2010	7.15 (64.2%)	4.61 (62.3%)	2.15 (53.6%)

$t_{\text{adapt}} = 2020$. It is observed that the mean BCR and $\Pr(\text{BCR} > 1)$ are very sensitive to r and both parameters are larger for small discount rates. This is explained by the fact that small discount rates imply that future costs are larger at present cost by increasing the cost-effectiveness of adaptation measures for repairs close to the end of the structural lifetime. As discussed in Section 22.3.3.2, various governments recommend lower discount rates of $\sim 2\%$ for long-term investments. The BCR analysis therefore shows that the adaptation strategies are more cost-effective according to these recommendations.

22.6 Conclusions

The kinematics of the chloride ingress and corrosion propagation mechanisms is highly influenced by the surrounding environmental conditions, including climate change, that could accelerate or decelerate these processes, depending on specific exposure and environmental conditions. Therefore, the results presented in this chapter highlight that a comprehensive probabilistic cost-benefit analysis of adaptation strategies should combine general methods (deterioration models able to account for climate variations, stochastic methods to propagate uncertainties, and cost-benefit analysis) with factors specific to each structure (structural characteristics and climate change predictions). The numerical results focused on climate adaptation for existing RC structures built at different years (and therefore under different durability standards), and subjected to two different types of climate in France. The adaptation strategies consisted of increasing the cover recommended in the standards by 5 or 10 mm.

The assessment of the mean BCR and the $\Pr(\text{BCR} > 1)$ indicated that, although increasing design cover is an effective protection for reducing damage induced by chloride ingress, the cost-effectiveness of this measure depends on specific exposure conditions. An adaptation strategy consisting of increasing design cover by 5 mm was cost-effective for Saint-Nazaire but it was not cost-effective for Marseille. The probabilistic analysis also indicated that the mean BCR and $\Pr(\text{BCR} > 1)$ are dependent on type of structural element, age of construction,

adaptation time, damage costs and discount rates. The overall results indicate that the probabilistic framework is well suited to assessing the impact of climate change on RC corrosion damage, and assessing the cost-effectiveness of climate adaptation strategies. Future work will consider other adaptation strategies, such as improved concrete quality and coatings.

References

- Bastidas-Arteaga, E., Chateauneuf, A., Sánchez-Silva, M., Bressolette, P., Schoefs, F., 2010. Influence of weather and global warming in chloride ingress into concrete: a stochastic approach. *Struct. Saf.* 32 (4), 238–249.
- Bastidas-Arteaga, E., Chateauneuf, A., Sánchez-Silva, M., Bressolette, P., Schoefs, F., 2011. A comprehensive probabilistic model of chloride ingress in unsaturated concrete. *Eng. Struct.* 33 (3), 720–730.
- Bastidas-Arteaga, E., Schoefs, F., 2012. Stochastic improvement of inspection and maintenance of corroding reinforced concrete structures placed in unsaturated environments. *Eng. Struct.* 41, 50–62.
- Bastidas-Arteaga, E., Schoefs, F., Stewart, M.G., Wang, X., 2013. Influence of global warming on durability of corroding RC structures: a probabilistic approach. *Eng. Struct.* 51, 259–266.
- Bastidas-Arteaga, E., Stewart, M.G., 2013. Probabilistic cost-benefit analysis of climate change adaptation strategies for new RC structures exposed to chloride ingress. In: Deodatis, G., Ellingwood, B.R., Frangopol, D. (Eds.), 11th International Conference on Structural Safety & Reliability. CRC Press, New York, USA, pp. 1503–1510.
- Bastidas-Arteaga, E., Stewart, M.G., 2015. Damage risks and economic assessment of climate adaptation strategies for design of new concrete structures subject to chloride-induced corrosion. *Struct. Saf.* 52, 40–53.
- Bastidas-Arteaga, E., Stewart, M.G., 2016. Economic assessment of climate adaptation strategies for existing RC structures subjected to chloride-induced corrosion. *Struct. Infrastruct. Eng.* 12 (4), 432–449.
- Boardman, A.E., Greenberg, D.H., Vining, A.R., Weimer, D.L., 2011. *Cost-Benefit Analysis: Concepts and Practice*. Pearson, Boston.
- BRE, 2003. Residual life models for concrete repair - assessment of the concrete repair process. Building Research Establishment, UK.
- BTRE, 2005. *Report 110: Risk in Cost-Benefit Analysis*. Bureau of Transport and Regional Economics. Australian Government, Canberra.
- Canisius, T.D.G., Waleed, N., 2004. Concrete patch repairs under propped and unpropped implementation. *Struct. Build.* 157 (SB2), 149–156.
- Dasgupta, P., 2008. Discounting climate change. *J. Risk Uncertainty.* 37 (2–3), 141–169.
- Duracrete, 1998. Modelling of degradation, duracrete - probabilistic performance based durability design of concrete structures. EU - Brite EuRam III, Contract BRPR-CT95-0132, Project BE95-1347/R4-5.
- Duracrete, 2000. Statistical quantification of the variables in the limit state functions, duracrete - probabilistic performance based durability design of concrete structures. EU - Brite EuRam III, Contract BRPR-CT95-0132, Project BE95-1347/R9.
- El Maaddawy, T., Soudki, K., 2007. A model for prediction of time from corrosion initiation to corrosion cracking. *Cem. Concr. Compos.* 29 (3), 168–175.

- European Standard, (2004). Eurocode 1 and 2: Basis of design and actions on structures and design of concrete structures.
- Garnaut, R., 2008. The Garnaut Climate Change Review: Final Report. Commonwealth of Australia, Cambridge University Press, U.K.
- Gollier, C., 2012. Pricing the Planet's Future: The Economics of Discounting in an Uncertain World. Princeton University Press, New Jersey.
- Harrison, M., 2010. Valuing the Future: The Social Discount Rate in Cost-Benefit Analysis. Visiting Researcher Paper, Productivity Commission, Canberra.
- IA, 2008. Outline of Infrastructure Australia's Prioritisation Methodology. Infrastructure Australia, Australian Government, Canberra, September 24, 2008.
- JCSS (Joint committee of structural safety), 2001. *Probabilistic model code*.
- de Larrard, T., Bastidas-Arteaga, E., Duprat, F., Schoefs, F., 2014. Effects of climate variations and global warming on the durability of RC structures subjected to carbonation. *Civil Eng. Environ. Syst.* 31 (2), 153–164, Taylor & Francis.
- Lebègue, D., Hirtzman, P., and Baumstark, L., 2005. *Révision du taux d'actualisation des investissements publics*. Commissariat Général au Plan (In French), Paris, France.
- Mirza, S.A., Hatzinikolas, M., MacGregor, J.G., 1979. Statistical descriptions of strength of concrete. *J. Struct. Div.* 105, 1021–1037.
- Mullard, J.A., Stewart, M.G., 2011. Corrosion-induced cover cracking: new test data and predictive models. *ACI Struct. J.* 108 (1), 71–79.
- Mullard, J.A., Stewart, M.G., 2012. Life-cycle cost assessment of maintenance strategies for RC structures in chloride environments. *J. Bridge Eng. ASCE.* 17 (2), 353–362.
- Neville, A., 1981. *Properties of Concrete*. third ed. Longman Scientific & Technical, Harlow.
- Nguyen, P.-T., Bastidas-Arteaga, E., Amiri, O., El Soueidy, C.-P., 2017. An efficient chloride ingress model for long-term lifetime assessment of reinforced concrete structures under realistic climate and exposure conditions. *Int. J. Concr. Struct. Mater.* In Press.
- Nordhaus, W.D., 2007. A review of the stern review on the economics of climate change. *J. Econ. Lit.* XLV, 686–702.
- OBPR, 2010. Best Practice Regulation Handbook. Canberra.
- Peng, L., Stewart, M.G., 2014. Spatial time-dependent reliability analysis of corrosion damage to RC structures with climate change. *Mag. Concr. Res.* 66 (22), 1154–1169, Thomas Telford.
- Peng, L., Stewart, M.G., 2015. Damage risks and cost-benefit analysis of climate adaptation strategies of RC structures in Australia. *Concr. Aust.* 41 (3), 36–47.
- Pham, L., 1985. Reliability analysis of reinforced concrete and composite column sections under concentric loads. *Civil Eng. Trans.* 1, 68–72.
- Quinet, E., 2013. L'évaluation socioéconomique des investissements publics. Commissariat Général à la Stratégie et à la Prospective (In French), Paris, France.
- RSMeans, 2012. *RSMeans Building Construction Cost Data*. RSMeans, Kingston, MA.
- Saetta, A., Scotta, R., Vitaliani, R., 1993. Analysis of chloride diffusion into partially saturated concrete. *ACI Mater. J.* 90 (5), 441–451.
- Srifi, H., 2012. Gestion, surveillance et pertinence des méthodes de réparation des ouvrages maritimes. Master's report for the Nantes Saint-Nazaire Port. University of Limoges (In French).
- Stern, N., 2006. The Economics of Climate Change: The Stern Review. Cabinet Office - HM Treasury, London.
- Stewart, M.G., 2001. Spalling risks, durability and life-cycle costs for RC buildings. International Conference on Safety, Risk and Reliability – Trends in Engineering. IABSE, Malta, Zurich, pp. 537–542.

- Stewart, M.G., Melchers, R.E., 1997. Probabilistic Risk Assessment of Engineering Systems. Chapman & Hall, London.
- Stewart, M.G., Peng, J.X., 2010. Life-cycle cost assessment of climate change adaptation measures to minimise carbonation-induced corrosion risks. *Int. J. Eng. Uncertainty*. 2, 35–46.
- Stewart, M.G., Val, D.V., Bastidas-Arteaga, E., O'Connor, A., Wang, X., 2014. Climate adaptation engineering and risk-based design and management of infrastructure. In: Frangopol, D., Tsompanakis, Y. (Eds.), *Maintenance and Safety of Aging Infrastructure*. CRC Press, pp. 641–684.
- Stewart, M.G., Deng, X., 2015. Climate impact risks and climate adaptation engineering for built infrastructure. *ASCE-ASME J. Risk Uncertainty Eng. Syst., Part A: Civil Eng.* 1 (1), 4014001.
- Stewart, M.G., Wang, X., Nguyen, M.N., 2011. Climate change impact and risks of concrete infrastructure deterioration. *Eng. Struct.* 33 (4), 1326–1337.
- Stewart, M.G., Wang, X., Nguyen, M.N., 2012. Climate change adaptation for corrosion control of concrete infrastructure. *Struct. Saf.* 35 (0), 29–39.
- Talukdar, S., Banthia, N., Grace, J.R., Cohen, S., 2012. Carbonation in concrete infrastructure in the context of global climate change: Part 2, Canadian urban simulations. *Cem. Concr. Compos.* 34 (8), 931–935.
- Teodorescu, I., Țăpuși, D., Erbașu, R., Bastidas-Arteaga, E., Aoues, Y., 2017. Influence of the climatic changes on wood structures behaviour. *Energy Proc.* 112, 450–459.
- Tran, T.B., Bastidas-Arteaga, E., Schoefs, F., 2016a. Improved Bayesian network configurations for random variable identification of concrete chlorination models. *Mater. Struct.* 49 (11), 4705–4718.
- Tran, T.B., Bastidas-Arteaga, E., Schoefs, F., 2016b. Improved Bayesian network configurations for probabilistic identification of degradation mechanisms: application to chloride ingress. *Struct. Infrastruct. Eng.* 12 (9), 1162–1176.
- Treasury, H.M., 2003. *The Green Book: Appraisal and Evaluation in Central Government*.
- Val, D.V., Stewart, M.G., 2003. Life-cycle analysis of reinforced concrete structures in marine environments. *Struct. Saf.* 25, 343–362.
- Val, D.V., Trapper, P.A., 2008. Probabilistic evaluation of initiation time of chloride-induced corrosion. *Reliab. Eng. Syst. Saf.* 93, 364–372.
- Viscusi, W.K., 2007. Rational discounting for regulatory analysis. *Univ. Chicago Law Rev.* 74 (1), 209–246.
- Vu, K.A.T., Stewart, M.G., 2000. Structural reliability of concrete bridges including improved chloride-induced corrosion. *Struct. Saf.* 22, 313–333.
- Wang, X., Stewart, M.G., Nguyen, M., 2012. Impact of climate change on corrosion and damage to concrete infrastructure in Australia. *Clim. Change*, 110. Springer, Netherlands, pp. 941–957. 3–4.
- Yunovich, M., Thompson, N.G., Balvanyos, T., Lave, L., and CC Technologies Laboratories Inc., 2001. *Corrosion Costs and Preventive Strategies in the United States*. Washington, D.C.

Lifecycle cost and performance analysis for repair of concrete tunnels

23

Jian Hong Wang

Nippon Koei Co., Ltd, Tsukuba, Ibaraki, Japan

23.1 Introduction

Many concrete tunnels have been constructed to serve as the important infrastructures, e.g., railway, subway, road transportation tunnels, water supply, sanitary/drainage, and gas supply piping systems, as shown in Fig. 23.1. Such concrete tunnels inevitably degrade due to the material aging, aggressive condition and extreme loads and etc., in the forms of concrete cracking, delamination and spalling, water leakage, and steel or reinforcement corrosion (Richards,1998; Mashimo, 2002; Asakura and Kojima, 2003; Muto and Kawabata, 2011). As a public facility tunnel it is always necessary to maintain satisfactory serviceability and safety, because any failure would affect its operation, even bringing in a substantial damage to the economy and society, e.g., the ceiling collapse accident in the Sasako road tunnel in 2012 (MLIT, 2012). Consequently, the appropriate maintenance for tunnels is required in order to maintain the normal operation of facility with less cost, in consideration of the increasing maintenance cost, is of great concern to stakeholders.

On infrastructure maintenance, much research (e.g., Dekker, 1996; Frangopol et al., 1997, 2004; Frangopol and Liu, 2007; Furuta, et al., 2004; Biondini et al., 2006; Biondini and Frangopol, 2008; Wang et al., 2015, 2016a,b) has been carried out. Dekker (1996) clearly indicated that a maintenance plan should be made to solve the real problem rather than a mathematical application. Frangopol et al. (1997, 2004, 2007) and Furuta, et al. (2004) presented the important concept and approach to manage infrastructure, based on the performance and lifecycle cost (LCC) as benchmark indices. Biondini et al. (2006), Biondini and Frangopol, (2008) discussed the general approach to probabilistic predication of service life of concrete structure. Wang et al. (2015, 2016a,b) discussed the necessity of maintenance in developing a sustainable tunnel infrastructure, and presented the practical solution to help planning maintenance for old tunnels. On the other hand, eco-efficiency was proposed by the World Business Council for Sustainable Development (WBCSD, 2000) as an effective management tool to promote transformation from unsustainable to sustainable development. This management tool can help to create more value through technology and process changes, while reducing the resource use and environmental impact throughout the whole life. In recent years, the eco-efficiency has been widely studied and applied to various

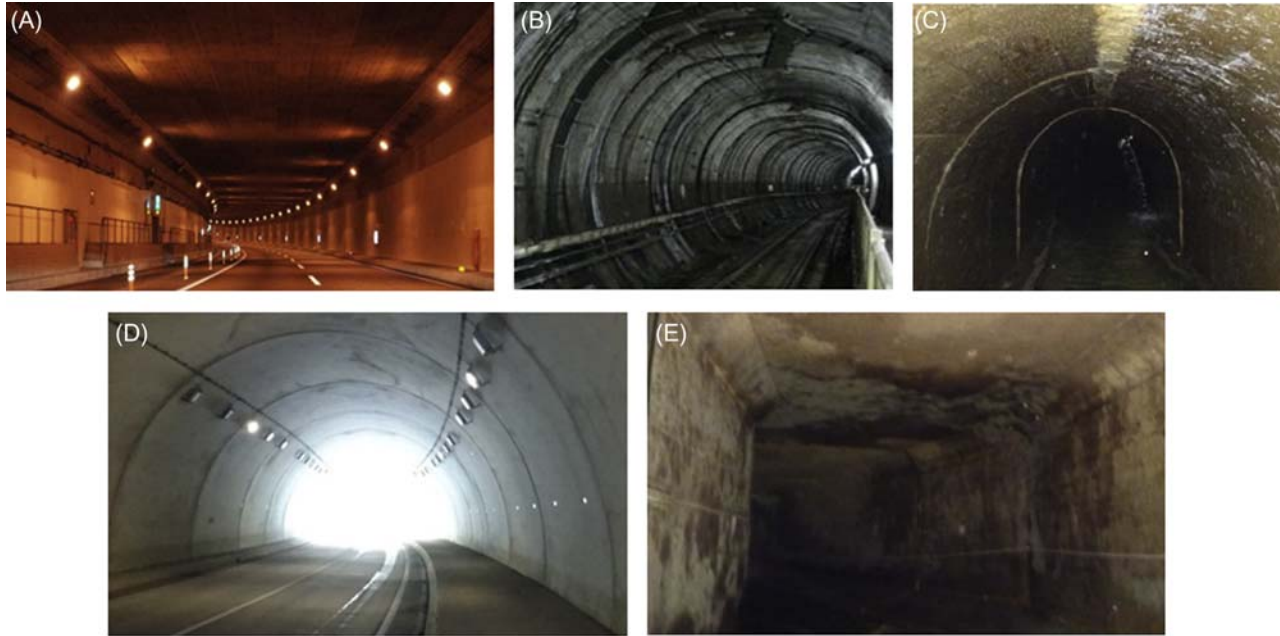


Figure 23.1 Examples of concrete tunnels: (A) immersed tube tunnel for road, (B) shield driven tunnel for railway, (C) ribbed system tunnel for sanitary infrastructure, (D) NATM tunnel for road, and (E) cut and cover tunnel for drainage.

engineering fields (e.g., Kicherer, et al., 2007; Pacheco-Torgal et al., 2013a). As for maintenance of tunnel infrastructure, the eco-efficiency should be considered, in order to realize the maximum utilization of a facility with the minimum LCC and environmental impact. In other words, an eco-efficient maintenance should be implemented to ensure the tunnel is in good performance with less cost, through using eco-efficient technologies.

As a buried structure, the tunnel has many aspects varying from an aboveground one, e.g., the structure characteristics, loading condition, environmental condition, and deterioration pattern. In addition, the maintenance of a tunnel involves the facility function, its operation, management policy, related technologies of inspection and repair or rehabilitation, and so on (JRB, 2014; FHWA, 2015). A preventative maintenance is generally considered prior to a corrective one with respect to safe operation; however, the tunnel maintenance practice should balance the two maintenance strategies, e.g., preventative maintenance for a transportation tunnel (e.g., road or railway) and corrective maintenance for a pipeline tunnel. Accordingly, the basic knowledge on tunnel and degradation should firstly be make clear, as well as the current maintenance practice. Furthermore, regarding the eco-efficiency of maintenance, the approaches for evaluating the structural performance and LCC of a tunnel should be discussed, as well as the related eco-efficient repair technologies.

This chapter first introduces the background for the eco-efficient maintenance of infrastructure tunnels. Then, basic information on the tunnel construction and structure is briefly introduced in Section 23.2. In Section 23.3, tunnel degradation is discussed in terms of concrete deteriorations and their causes, as well as the maintenance practice. In the following section, tunnel repair is discussed, with respect to the methods and technology for concrete repair, waterproofing work, tunnel rehabilitation, and eco-efficient repair. In Section 23.5, the approaches for tunnel performance evaluation are discussed in terms of the reliability analysis and the stochastic process. Meanwhile, a lifecycle costing method is discussed and a stochastic approach-based framework are proposed. At the end of this section, an application example of a deteriorating tunnel is given to illustrate how to decide on an eco-efficient maintenance plan. Finally, the summaries of this chapter are made, and some useful findings are suggested, as well as future prospects for tunnel maintenance.

23.2 Tunnel construction and structure

23.2.1 Construction method

Concrete tunnels can be constructed using various tunneling methods, e.g., the cut and cover method in soft ground, tunnel boring machine (TBM) method for a rock tunnel or shield-driven tunnel in soil ground, new Austrian tunneling method (NATM) for sound ground, and immersed tube method for underneath a river or sea (JSCE, 2006a,b,c; Chapman, et al., 2010; Kuesel et al., 2012). The cut and cover method is popular to use for constructing shallow tunnels because of its relative lower cost. It involves excavating an open trench, installing in-situ concrete

linings, and subsequently covering the tunnel with compacted soil to design ground level. For excavation, piles and lagging, tie back anchors, or slurry wall systems are usually used as temporary support systems, depending on the ground condition and surrounding situation in an urban area. The immersed tube tunnel method is usually used to cross a river, sea bay, etc. A trench is first dug in the bed under the water, and then, prefabricated tunnel segments are placed in the design positions and connected to adjacent segments. Finally, the trench is usually backfilled to cover the tunnel for preventing from the entry of water-borne traffic. The shield tunnel is excavated with a TBM or shield, and immediately a temporary or permanent lining system is installed to support the surrounding ground and provide a foundation for advancing the machine. Depending on the condition of the excavated ground, the boring machine can be designed as an open or a closed type, a slurry or earth pressure balanced type, using a roller or teeth cutter, etc. NATM is often considered the most cost-efficient tunneling method, because it is able to effectively integrate the surrounding ground into an overall ring-like support system. The tunnel is excavated gradually, and a composite lining (e.g., a flexible combination of rock bolts, wire mesh, steel ribs, and sprayed concrete (shotcrete) is installed immediately after the tunnel face advances, to stabilize the surrounding ground. Finally, the invert is installed to create a closed ring system for load bearing. Generally, the construction of NATM tunnel requires real-time, on-site measurement and monitoring to help determining the support system. In addition, the jacked tunnel method is often used to construct a short tunnel underneath certain obstructions, or a long pipe tunnel with a small diameter. The drill and blast method is usually applied as an alternative of the TBM method in rock situations.

23.2.2 Support systems and linings

A tunnel support system is rather complicated; it may be the surrounding ground itself, a lining system, or a composite system of ground and linings. For tunnel maintenance, the support systems of a tunnel should be analyzed and clarified first. In general, infrastructure tunnels are lined with lining systems as shown in Fig. 23.2 (ICE, 2004; JSCE, 2006a,b,c; Chapman, et al., 2010). The support systems vary with the construction method; ground reinforcement and ribbed systems are commonly applied to mountain tunnels (e.g., rock TBM and NATM tunnels), and cast-in-place or precast concrete linings to urban tunnels (e.g., shield tunnels and cut and cover tunnels). As shown in Fig. 23.2A, ground reinforcement systems that usually utilize rock bolts, wire mesh, metal straps, mine ties and shotcrete, are often applied in NATM tunnels to supplement the strength and stability of the surrounding ground. Ribbed support systems are typically used as two-pass lining systems for a drill-and-blast or TBM rock tunnels. The first pass provides the structural integrity of support lings with timber or steel girders, while the second pass typically places concrete to furnish the tunnel. A recent application of this system involves the formation of ribs using prefabricated reinforcing bar cages embedded in multiple layers of shotcrete. Precast linings (Fig. 23.2B and C) are widely used in tunnel construction, accounting for their high manufacture quality and easy installation. The precast segmental

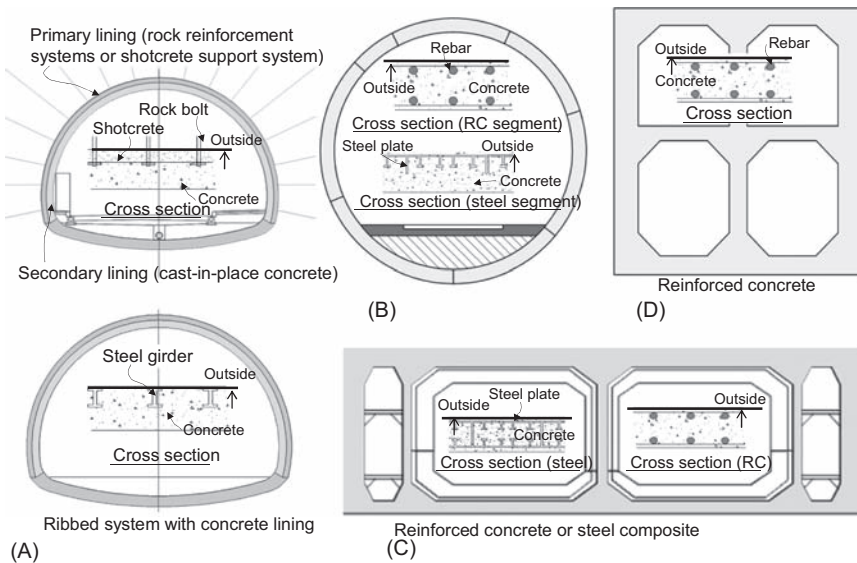


Figure 23.2 Support system and composition: (A) NATM or rock tunnel, (B) shield tunnel, (C) immersed tube tunnel, and (D) cut and cover tunnel.

linings are primarily used for TBM tunnels, and precast tube segments for immersed tunnel. They are fabricated with steel, steel-reinforced concrete, or concrete steel composite in a factory, and both are installed in-situ through bolting the adjacent segments together and using gaskets for joint waterproofing. In addition, cast-in-place concrete linings are usually used for the support systems because of their easy adaptability to site conditions. Placed concrete linings can be used as a structural support system of reinforced concrete (RC) or as a nonstructural one of plain concrete, depending on the ground condition and the tunneling method. A cut and cover tunnel (Fig. 23.2D) usually employs RC to form the structural linings.

Furthermore, for a lining system, its composition and function should be distinctly clarified, with respect to the primary linings, secondary linings, or composite linings. A secondary lining is usually installed in the tunnel, in order to form a smooth internal surface, satisfy the functional requirement, protect the primary lining, etc. The cast-in-place concrete is used, accounting for its low cost, high durability, and workability, to easily obtain a smooth surface. The secondary lining is generally considered as a nonstructural furnish lining; however, in special cases it may be looked as a part of the composite lining depending on the construction method. In engineering practice, only the primary linings are considered the structural lining for most urban tunnels (e.g., cut and cover, shield, immersed tube tunnels), while the composite linings for the rock or NATM tunnels (JSCE, 2006a,b,c). However, inspecting and diagnosing of the primary lining need to be considered as of great concern for the maintenance of urban tunnels with secondary linings (Wang et al., 2016a).

23.3 Tunnel degradation and maintenance practice

23.3.1 Degradation and deterioration

Concrete tunnel inevitably degrades over time, in the forms of leakage, deformation and concrete deterioration, owing to initial defects, material aging, aggressive operation condition, extreme loads, and etc. (JRB, 2014; FHWA, 2015). The initial defects produced by inappropriate construction practices often initiate the concrete deterioration. The aggressive operation condition easily induces the serious deterioration to a tunnel. An undesirable event such as traffic, fires, and earthquakes can seriously degrade tunnel with excessive deformation, leakage, concrete deterioration, and even a structural failure. In general, tunnel degradation causes aesthetic, serviceable, or structural problems, sometimes may lead to the closure of the facility if appropriate repairs are not made.

23.3.1.1 Concrete deterioration

The concrete deteriorates in forms of cracking, delamination, spalling, scaling, staining, honeycombing, steel corrosion, etc., although concrete material is typically expected to be durable (Emmons, 1993; Mays, 2002). These typical deteriorations of concrete are shown in Fig. 23.3. Cracking may occur as a result of material shrinkage, steel corrosion, extreme force. The influence of a crack on tunnel integrity varies, depending on its activity characteristics, location and dimension. An active crack should be cautioned as an important sign of the

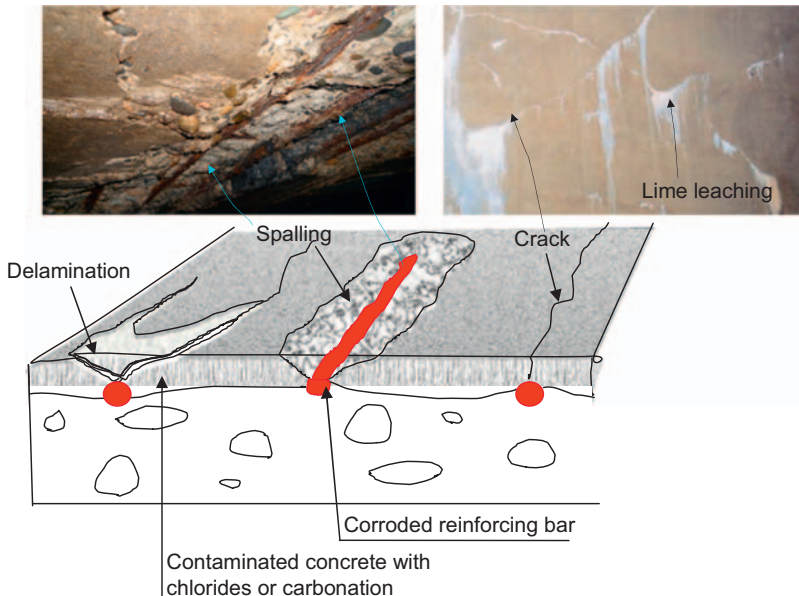


Figure 23.3 Concrete tunnel deteriorations.

structural degradation of a tunnel; its propagation in length, width, or depth must be monitored for urgent measures. In contrast, a dormant crack may be considered to have been caused by improper construction or material shrinkage, but an early repair should be carried out to prevent further deterioration. Delamination often occurs during concrete curing, as water and air trapped below the surface form subsurface voids. The reaction of coarse aggregate or steel corrosion may also cause concrete delamination. Concrete spalling often occurs as a result of delamination when the delaminated surface layer completely detaches. Spalling and delamination should be considered as a decline in structural integrity, in terms of the reduction of the cross-sectional area.

The corrosion of steel reinforcements can substantially decrease the structural integrity of a RC tunnel. The corrosion mechanism and the steel corrosion example in a tunnel is shown in Fig. 23.4. The corrosion progresses, depending on many aspects—such as the available moisture and oxygen, temperature, acid situation, and bacteria (e.g., sulfate-reducing bacteria in sewage tunnels). Commonly, the access of deleterious factors cause the steel or reinforcement bars in concrete corroding. After it begins, the steel corrosion continually progresses, with the subsequent problems of cracking, delamination, and spalling of the cover concrete. Therefore, the earlier detection of corrosion and appropriate repair are important to prevent the tunnel degradation.

Otherwise, concrete scaling initially occurs as a local flaking or peeling of a concrete surface, which eventually results in the gradual and continual loss of mortar and aggregate. Severe scaling is judged by the exposure of the coarse aggregate below the surface. Staining is a discoloration of the concrete surface due to the passage of water with dissolved materials. Staining is useful for signifying interior deterioration, e.g., the corrosion of steel or reinforcement.

Conclusively, the cracking, delamination, and spalling of concrete and corrosion of steel or reinforcements can severely degrade the structural integrity of a tunnel and shorten its service life. In addition, concrete deterioration should be of more concern for its impacts on the use of a facility, and particularly the safety of users (e.g., users can be injured by falling concrete).

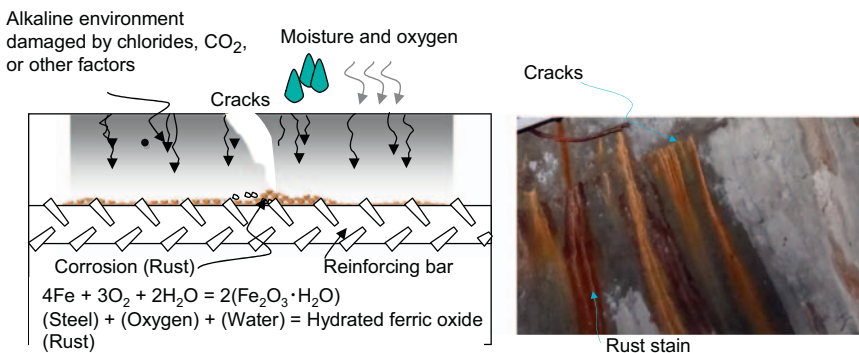


Figure 23.4 Steel reinforcement corrosion and tunnel deterioration example.

23.3.1.2 Leakage

For many tunnels, leakage—as the most common and troubling problem—occurs with water intrusion in regions with penetrating cracks or joints (see Fig. 23.5). Water intrusion has little direct impact on structural integrity of a tunnel, but it can cause problems to mechanical and electrical utilities, and promote the deterioration of concrete. The typical problems of a tunnel due to water leakage include (1) steel or reinforcement corrosion, especially when the groundwater is acidic; (2) concrete cracking, spalling, and delamination; (3) freeze thaw damage in colder climates; (4) the deterioration of protective finishes and coatings; (5) ground loosening or voids around a tunnel; and (6) the drainage system clogging. Accordingly, leakage should be considered the one of vital factors that substantially degrades tunnels. Similarly, the intrusion of rainwater or snow from the opening should also be considered to have the same impacts as leakage.

23.3.1.3 Degradation causes

A ground movement such as landslide, ground heave, and subsidence can easily degrade the structural integrity of a tunnel, as well as the voids in ground (Meguid and Dang, 2009; JRB, 2014). In Japan, several tunnels suffering serious damage due to ground movement have been reported (Saitoh et al., 1994). The structural degradation caused by ground movement appears as transverse or longitudinal cracks and crushing at the inside surface of a tunnel, as well as sudden leakage (see Fig. 23.6). Once one of these signs is observed, the tunnel integrity must be reevaluated in terms of the loading condition and structural strength of the support lining. Furthermore, the surrounding ground condition of a leaking tunnel should be carefully investigated to identify the ground loosening or voids. In addition, a fire or earthquake event may bring great damage to the utilities and structural integrity. Difference of temperature along a tunnel which causes the concrete to expand and contract, may induce transverse cracks. Such concrete cracks are usually limited to areas near portals because of a relatively uniform environment within a tunnel. Moreover, erosive environment can easily cause concrete deterioration, e.g., the concrete disintegrates when is exposed to certain chemicals like acids, alkaline solutions, or salt solutions. Despite this, the workmanship may be the most critical

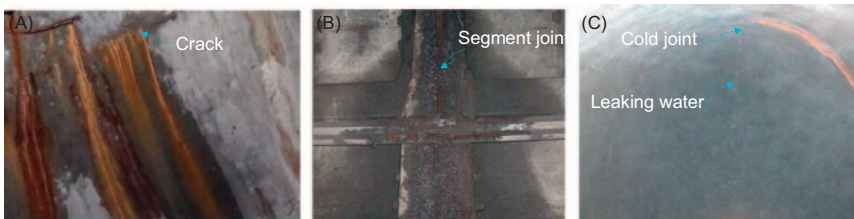


Figure 23.5 Examples of leaks in tunnel: (A) at cracks, (B) at segment joint, and (C) at cold joint.

factor affecting concrete deterioration; the poor concrete and the inherent defects may be due to the improper placement of reinforcement steel, insufficient vibration to consolidate the concrete, or improper concrete curing.

23.3.2 Maintenance strategy

Generally, the maintenance strategy is classified into two categories, based on the repair timing: corrective maintenance and preventative maintenance (DoD, 2008), as shown in Fig. 23.7. In corrective maintenance, the repair or retrofiting activities are only performed after the facility fails to meet the requirement of operation. Preventative maintenance tends to prevent the incipient failure of a facility through previous interventions at periodic or predicated times. For a tunnel, the maintenance plan is usually made during construction stage; however, during operation stage its adjustment should be periodically conducted, based on the degradation condition.

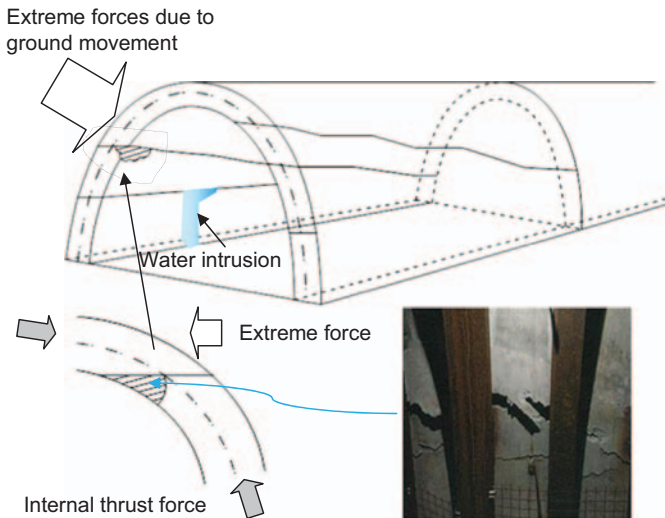


Figure 23.6 Example of tunnel failure due to ground movement.

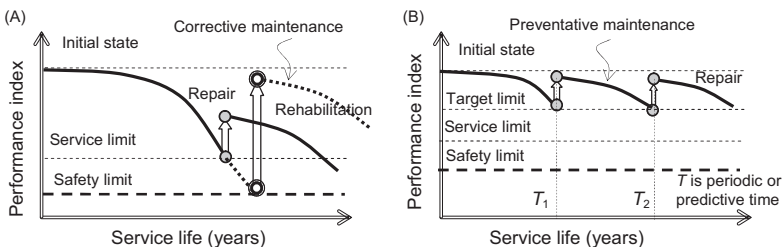


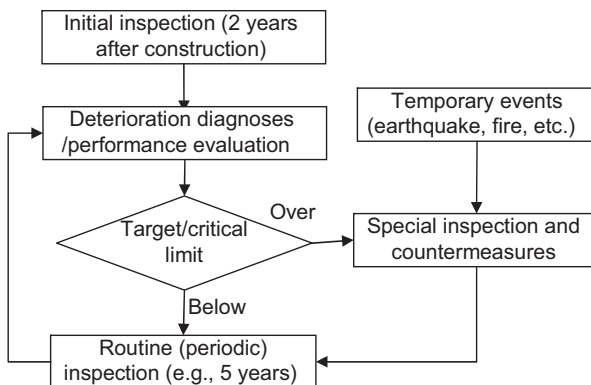
Figure 23.7 Maintenance philosophies: (A) corrective maintenance and (B) preventative maintenance.

In addition, the maintenance strategy should strike a balance between preventative and corrective maintenance, according to the facility function and operation conditions (FHWA, 2015). For a pipeline tunnel under desirable conditions, corrective maintenance may be effective. In contrast, for a transportation tunnel, preventative maintenance should be performed within a safer limit designed in advance.

In practice, tunnels deteriorate in various ways, depending on the material used, the support system, the operation condition, and etc. One tunnel may degrade slightly over a long period, whereas the another one under serious operation conditions may deteriorate to the serviceability limit over several years. Additionally, the influence of deteriorations on a concrete tunnel varies depending on its type, location, and size. Accordingly, the deterioration tendency over years of a similar tunnel should be referenced to make and modify a maintenance plan. If the tunnel is vulnerable to severe deterioration, the preventative maintenance should be considered, otherwise, the corrective maintenance may be more desirable. Nevertheless, the maintenance strategy should also take into consideration the LCC.

23.3.3 Maintenance procedure

Preventative maintenance mostly adopted for the infrastructure tunnels involves the activities of periodic inspection, performance evaluation, and repair. The general program used for preventative maintenance is shown in Fig. 23.8 (e.g., JRB, 2014; FHWA, 2015). In general, based on the schedule or conditional requirement, tunnel maintenance is performed with routine (periodic) inspection, special inspection, performance evaluation, countermeasures (e.g., repair and rehabilitation). All maintenance activities must obey the related specifications on the health and safety, inspection equipment and so on. Routine inspection mainly involves checking the mechanical and electrical utilities, visually inspecting for deterioration conditions, and qualitatively grading the tunnel performance based on the related criteria listed in Table 23.1.



Target/critical limit is set in advance using performance index or deterioration state, depending on the performance requirement.

Figure 23.8 Chart of preventative maintenance procedure.

Table 23.1 Definitions of deterioration states

Deterioration	Rebar	Concrete		Others
	Corrosion	Cracking	Delamination/spalling	
State I	Fresh or slightly corroded; no intervention is required.	No cracks or cracks so minor that countermeasures are not needed.	No delamination/spalling due to cracks, etc., or there is no possibility of concrete failure.	
State II	Slight corrosion at superficial or small areas; further monitoring or intervention is required for preventative maintenance	Fine cracks; because the future function of the structure is likely to decrease, monitoring and measures are required for preventative maintenance.	Signs of delamination/spalling due to cracks, etc.; because of possible failure in the future, monitoring or measures are required for preventative maintenance.	Leakage, stain, coloring, etc.
State III	Corrosion-induced cross-sectional loss in the rebar; slightly reduced structural capacity; measures need to be taken as soon as possible.	Cracks concentrated along the steel reinforcement or some shear cracks; because the structural integrity is reduced, intervention measures should be taken as soon as possible.	Delamination/spalling; because of possible failure, intervention measures must be taken as soon as possible.	Leakage, stain, coloring, etc.
State IV	Corrosion-induced cross-sectional loss and significant functional impairment of the rebar; intervention urgently required.	Large-scale crack concentration or shear cracks; because the function of the structure is severely degraded, urgent measures must be taken.	Large-scale delamination/spalling; because of possible early failure, urgent intervention measures must be taken.	Leakage, stain, coloring, etc.

The potential causes for deterioration are also analyzed and reported. When a tunnel is judged having serious deterioration over the critical limit, a special inspection is performed. In addition, the tunnel must be specially investigated after an event such as an earthquake, traffic, or a fire. The special inspection commonly involves a detailed concrete survey and on-site testing to obtain quantitative information on the deterioration or damage. Based on the inspection results, the structural performance evaluation is usually conducted using methods such as structural analysis, load rating, and risk-based assessment.

The technologies related to inspection and testing are listed in [Table 23.2](#) (Bungey et al., 1996; Malhotra and Carino, 2003). For instance, deterioration such

Table 23.2 Inspection and testing techniques

	Target	Technique
Tunnel geometry	Dimension, deflection	<ul style="list-style-type: none"> • Measurer, • 3D laser scanner • Others
Concrete quality and strength	Quality of concrete	<ul style="list-style-type: none"> • Ultrasonic pulse velocity • Others
	Compressive strength	<ul style="list-style-type: none"> • Core testing • Rebound hammer • Others
	Tensile strength	<ul style="list-style-type: none"> • Pull off testing • Splitting tensile strength • Others
Concrete deterioration	Concrete cracks/delamination/spalls	<ul style="list-style-type: none"> • Hammer sounding • Infrared thermography • Impact echo • Pulse velocity • Exploratory removal • Others
	Steel or reinforcement	<ul style="list-style-type: none"> • Tachometer • Radiography • Ground penetrating radar • Exploratory • Others
Deterioration causes	Carbonation	<ul style="list-style-type: none"> • Tachometer • Radiography • Ground penetrating radar • Exploratory • Others
	Chloride content	<ul style="list-style-type: none"> • Petrographic analysis • X-ray diffraction • Infrared spectroscopy • Others
	Ground voids	<ul style="list-style-type: none"> • Ground penetrating radar • Subsurface interface radar • Others

as the spalling and delamination of the concrete can be diagnosed using the hammer sound, impact echo, pulse velocity, and infrared thermography methods. Nondestructive methods such as radiography and ground penetrating radar are used for the steel or steel reinforcement. A leakage investigation can use infrared thermography. The carbonation can be simply examined using a phenolphthalein solution and petrographic analysis.

23.4 Tunnel repairs

Tunnel repair or rehabilitation is taken following the flow chart shown in Fig. 23.9 (JRB, 2014; FHWA, 2015). The measures need to be feasible, durable, easy to install, environmentally friendly, and cost-effective; therefore, appropriate material and technology should be primarily considered. In addition, based on the effects and cause of the deterioration, the repair or rehabilitation should be determined. If a tunnel severely degrades as a result of critical environmental conditions or increasing external forces, the rehabilitation of tunnel should be implemented by installing a new cast-in-place concrete or precast concrete lining, or trenchless methods; otherwise, only a general concrete repair is applied to restore the tunnel. Other related factors such as the deterioration scale and location and leaking condition are also taken into account in the selection of repair or rehabilitation. Moreover, the decision of tunnel rehabilitation or repair is often made according to the maintenance strategy and financing capacity of the stakeholder.

For most urban tunnels with the cast-in-place concrete or precast concrete linings, their repairs are carried out for mainly remedying concrete cracking, spalling, and steel reinforcement corrosion. However, the shield tunnel and immersed tunnel may face the deterioration of joints and gaskets, resulting in the leakage and the

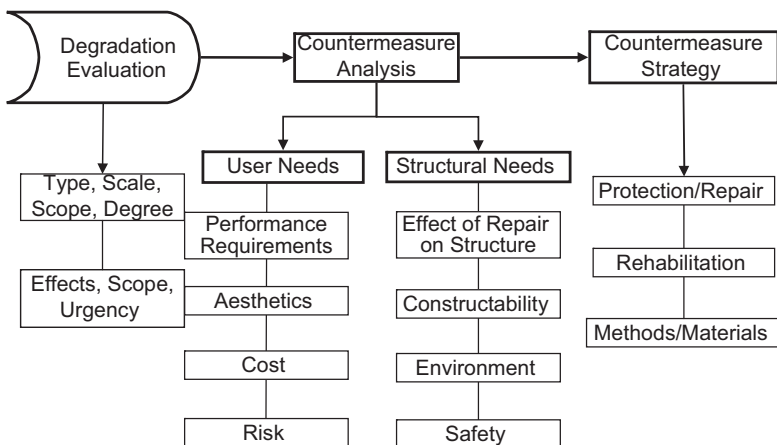


Figure 23.9 Flow chart of tunnel repair.

void in the surrounding ground; their repairs should also be considered. Repairs for a dry tunnel can use the concrete repair methods; however, for a leaking tunnel, the additional countermeasures, e.g., water rerouting and ground grouting is required to take. In addition, concrete tunnels are commonly furnished inside with a decorative or anticorrosive material (e.g., ceramic tile); the tunnel investigation requires the special consideration.

23.4.1 Concrete repair

The repair method should be selected after clarifying the cause of the concrete deterioration (Emmons, 1993; RTRI, 2000; Grantham, 2011). Concrete deterioration may result from the exposure condition, thermal effects, loading effects, and poor concrete quality. Based on the cause of concrete deterioration, the corresponding material and repair method can be appropriately selected to prevent the future deterioration (e.g., JSCE, 2013). Moreover, the eco-efficient material and technology should be extensively applied for concrete repair.

23.4.1.1 Crack repair

The crack repair should account for the presence of water presence and the crack activity. In practice, epoxy resins is usually used to fill dry cracks without further active propagation. Because the cracks in a tunnel are commonly vertical and overhead, the crack repair uses syringes to inject resin into the crack, after sealing the surface of the crack with a paste gel or seal sheet, as shown in Fig. 23.10. For active cracks, a structural retrofit should primarily be implemented, to prevent a subsequent crack occurring along or near the original one. In addition, for the cracks under leakage, the waterproofing discussed below should be performed in advance.

23.4.1.2 Delamination and spall repair

Delamination and spalls generally occur with irregular shapes, which vary depending on whether the concrete is reinforced. For RC, delamination typically occurs

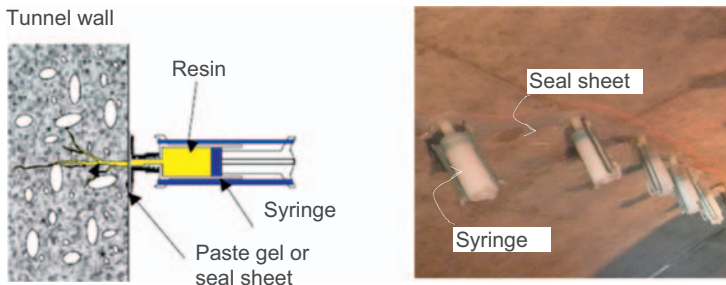


Figure 23.10 Tunnel crack repairs.

along reinforcement bars and eventually results in the spalling of the concrete cover. The delaminated concrete should be removed immediately when it is identified as spalled. Spall repair depends on the size and effects; a deep spall must be repaired early, while a shallow one may be repaired later for aesthetic reasons. In consideration of the durability and structural integrity of the tunnel lining, delamination and spalling should be repaired by completely removing the deteriorating concrete and replacing the corroded steel. The repair procedure is illustrated in Fig. 23.11, involving: (1) remove the loosened or delaminated concrete to completely expose the reinforcement; (2) clean deleterious materials or replace the reinforcement if corroded seriously; (3) protect the reinforcement with an anticorrosion coating; (4) place concrete and coat the surface with a durable coating material such as a polymer mortar.

23.4.2 Waterproofing

Water leakage as a troubling problem to tunnel, often occur at a concrete crack or joint. The waterproofing method can be determined based on the water intrusion passage and volume (RTRI, 2000; JSCE, 2009; JRB, 2014). Fig. 23.12 presents several waterproofing methods. In general, the waterproofing methods can be classified into crack or joint sealing, according to the passage of water infiltration. Crack sealing and coating are useful for repairing a slight leak at a crack but are not suitable for a

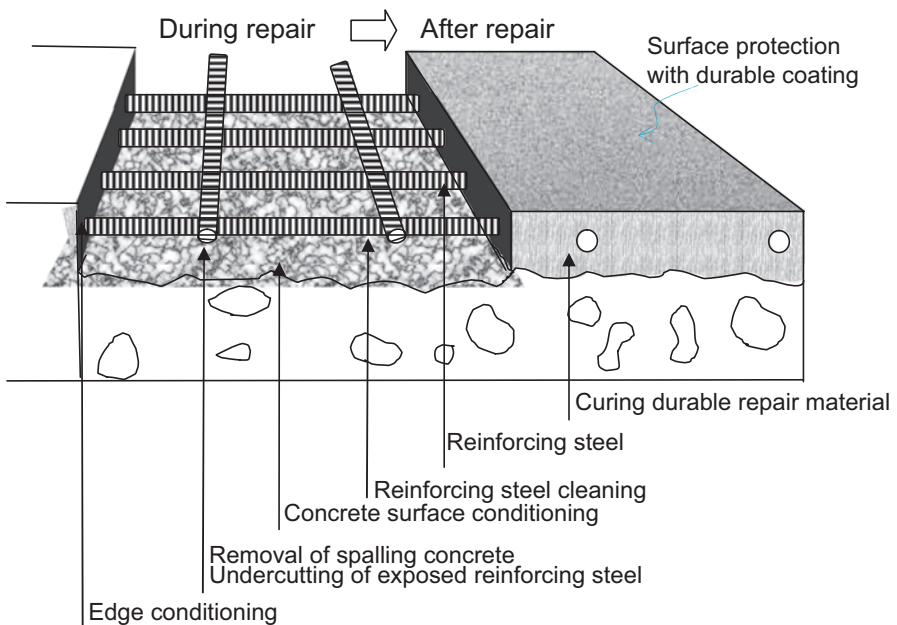


Figure 23.11 Repair of deteriorating concrete (delamination, spalling, and steel corrosion).

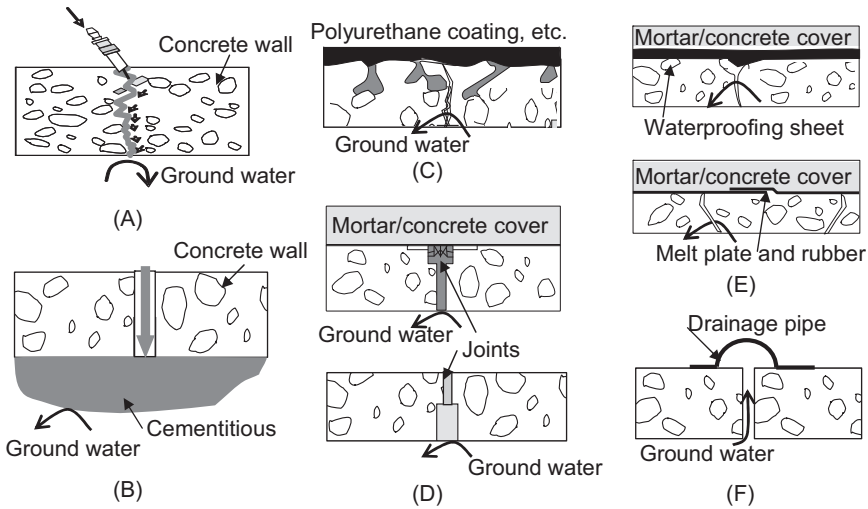


Figure 23.12 Tunnel waterproofing methods. (A) Crack seals, (B) ground grouting, (C) surface coatings, (D) joints seals, (E) membranes, and (F) rerouting.

torrential leak. In the case of a leak through a joint, a joint sealing method should be considered. In addition, for a shield tunnel or immersed tunnel, repacking the joint with a new gasket and new bolts may be required, depending on the deterioration condition of the gasket and bolts. Furthermore, the underground grouting, rerouting, and membrane methods should be considered as the effective waterproofing methods for the intense and mass invasion of groundwater. The final waterproofing countermeasure should be determined through optimization of two or more methods, in terms of the costs, service lives, aesthetics, functional effects, and constructability.

23.4.3 Rehabilitation and retrofitting

When the structural integrity of a tunnel has substantially declined, tunnel rehabilitation may be considered. Many rehabilitation technologies have been developed in recent years, e.g., trenchless approaches for urban pipelines and additional lining method for a large tunnel (RTRI, 2000; Asakura and Kojima, 2003; Najafi and Gokhale, 2005). For instance, spiral wound pipe method and pipe-in-pipe method, as shown in Fig. 23.13, are typically used for the trunk sewer and the water supply pipe, respectively, through installing a new pipe inside to improve the serviceability and strength of the existing tunnel. The additional lining method is used to enhance the stiffness and strength of a large tunnel, with a new structural lining installed inside. However, if a local region or a member is under severe degradation, a local retrofitting should be used, through placing an additional strengthening sheet (e.g., a carbon or polyaramide glass fiber sheet or grid). Such retrofitting can only improve the structural strength, but not the stiffness, and the effects greatly depend on the fiber sheets

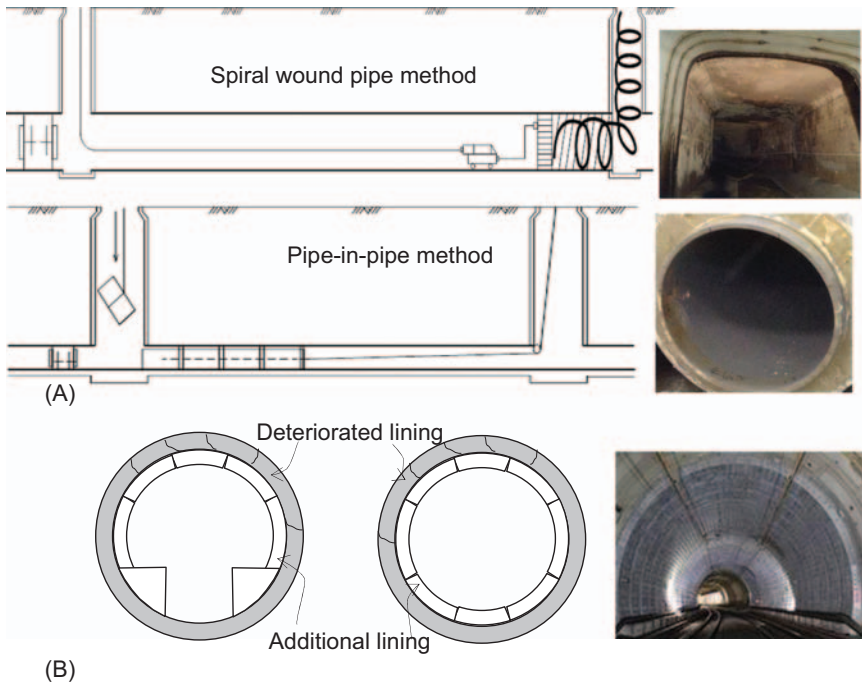


Figure 23.13 Tunnel rehabilitation: (A) trenchless approach (spiral wound pipe method and pipe-in-pipe method) and (B) secondary lining method.

placement, which must be placed in the transverse and longitudinal layers with an high strength adhesive. Special caution should be paid when installing fiber sheets in a tunnel with the potential for fires or members subjected to water infiltration.

23.4.4 Eco-efficient repairs

Rapid global warming and climate change explicitly indicates the urgency of environmental protection. However, until the present, tunnel construction, repair or rehabilitation mainly use the traditional cementitious material, which not only consumes natural sources and energy but also emits a large quantity of greenhouse gas, e.g., carbon dioxide (CO_2). For the whole concrete industry, the demand for Portland cement is expected to increase almost 200% by 2050 from 2010 levels, reaching 6000 million tons/year (Pacheco-Torgal et al., 2013a). Regarding these environmental concerns, tunnel maintenance should consider the eco-materials and environment-friendly technologies.

The materials used for tunnel repair or rehabilitation should have high strength and durability. In addition, the material should be of an extremely low permeability. High-performance concrete has been suggested to use for realizing the eco-efficient repair of concrete structure (Tayeh et al., 2013; Pacheco-Torgal et al., 2013b).

Particularly, high performance fiber concrete is useful for retrofitting severely deteriorating members. Accordingly, a tunnel repair using the high-performance concrete can be expected to extend its service life with less further maintenance, eventually resulting in the less consumption of material and energy. In addition, as the minimally processed natural material, geopolymer should be considered for the construction or repair of infrastructure due to its high eco-efficiency (Davidovits, 2013). Particularly, fly ash-based geopolymer cement or concrete is recommended as an eco-efficient material, because fly ash, as an industrial byproduct, can significantly reduce the Portland cement usage and carbon emission while improving the concrete workability, acid and fire resistance, impermeability and long-term durability (Hardjito et al., 2004; Rangan, 2008; Pacheco-Torgal et al., 2012).

Meanwhile, advanced repair technology should also be considered for tunnel maintenance, regarding eco-efficiency. For example, a biomineralization technology may be the most eco-efficient solution to repair cracks, because it make the cracks self-healed with just biologically induced precipitation (De Muynck et al., 2008; Jonkers et al., 2010; Pacheco-Torgal and Labrincha, 2013). Briefly, this technology involves using a special bacteria to create a microenvironment, in which the chemical precipitation of mineral phases produces and fills micropores to reduce the permeability. However, the practical application of such technology still has a long way to go, in consideration of the several problems indicated by Pacheco-Torgal and Labrincha (2013), e.g., it is difficult to reliably provide the calcite-producing bacteria which are able to live more efficiently in a highly alkaline environment, as well as to explicitly clarify the health and environmental conditions and clear air-entraining agents to prevent bacteria loss. In addition, it is required to present an eco- and cost-efficient encapsulation and biomineralization method. As another highlighted technology, nanotechnology is highly expected to contribute to eco-efficient tunnel repairs. Via the mixing of nanoparticles, concrete can be dramatically improved in mechanical strength and durability, because nanoparticles fill the voids in the microstructure and contribute to the development of hydration in the Portland cement (Sanchez and Sobolev, 2010; Pacheco-Torgal et al., 2013b). However, the optimal proportions of different nanoparticles needs to be clarified quantitatively, since its effects on concrete largely depends on their types and dimensions. In addition, further investigations are required to determine the most effective nanoparticles for enhancing the durability and strength of concrete.

Furthermore, the surface coating technology should also be considered as an effective solution to prevent the concrete deterioration through using an impervious material, e.g., epoxy, polyurethane, acrylic, or chlorinated rubber, geopolymer cement (Almusallam et al., 2003).

23.5 Eco-efficient maintenance

Eco-efficiency generates more value through technology and process changes whilst reducing resource use and environmental impact throughout the product or

service's life (WBCSD, 2000). Since then, the eco-efficiency has been widely applied in various projects, as a powerful support tool for strategy decision-making (Kicherer et al., 2007). Accordingly, the eco-efficiency should be applied to tunnel maintenance, in order to help generating more value while reducing the resource use and environmental impact. In other words, an eco-efficient maintenance should be considered to ensure the tunnel facility in good performance for longer time with less LCC, through using the eco-efficient technologies.

With respect to the structural performance and LCC in infrastructure maintenance, many studies have been carried out, (e.g., Furuta, et al., 2004; Frangopol et al., 1997, 2004; Frangopol and Liu, 2007; Akiyama et al., 2014; Wang et al., 2015, 2016a,b). The evaluation of the structural performance and LCC is generally based on two methods: reliability-based method and stochastic process-based one (Mori and Ellingwood, 1993; van Noortwijk and Frangopol, 2004; Frangopol, et al., 2004; Biondini, et al., 2006; Biondini and Frangopol, 2008). Anyway, the former method may be considered only suitable to evaluate the locally conditional performance of a tunnel, because the failure model is assumed for the locally deteriorated member while disregarding the most part in good condition. On the other hand, the stochastic process-based method has been used extensively in the field of infrastructure management to forecast the both local and overall performance (Abraham and Wirahadikusumah, 1999; Micevski et al., 2002; Baik et al., 2006; Agrawal et al., 2010; Kaito and Kobayashi, 2015; Chikata et al., 2015). Meanwhile, the lifecycle costing has been applied as an effective method to optimize the maintenance plan (Kleiner, 2001; Rebitzer et al., 2004; Frangopol et al., 1997; Frangopol and Liu, 2007). An integrated probability-based approach is required, as the rational basis for understanding the effect of technological, environmental, economical, social and political interactions on the lifecycle performance and cost of engineering infrastructure (Frangopol, 2011). Therefore, firstly, the approach to integrate LCC and structural performance should be developed to assist in formulating eco-efficient maintenance.

23.5.1 Reliability-based performance evaluation

23.5.1.1 Reliability analysis approach

Ideally, the structural performance of a tunnel should be evaluated using reliability analysis, based on the probabilistic variables associated with the deterioration, geometry, material, and load effects. However, for an infrastructure tunnel, the deteriorations vary from different time and location in longitudinal and transverse direction, and its failure mode is unclear. This make the collection of filed date rather difficult. As a result, the reliability analysis of a deteriorating tunnel is hardly performed, and the reliability-based structural performance is limited to the partial member. The reliability analysis can be performed by the first-order reliability method (FORM), second-order reliability method (SORM), point estimation method, and Monte Carlo simulation method (MC) (e.g., Melchers, 1987; Tee et al., 2013). To illustrate the engineering application, the procedure of basic

FORM is given as: (1) set the conditional variables (X_1 to X_n) associated with deterioration, dimensions, materials, and load effects, and define their probabilistic models; (2) define the failure function $Z(X_1, X_2, \dots, X_n)$ based on the structural or mechanical failure model and conduct the reliability analysis. The mean value and standard deviation of the failure function can be expressed as,

$$\bar{Z} \approx Z(\bar{X}_1, \bar{X}_2, \bar{X}_3, \dots, \bar{X}_n) \quad (23.1)$$

$$\sigma^2(Z) \approx \sum_{i=1}^n \left[\sigma_{X_i}^2 \left(\frac{\partial Z}{\partial X_i} \right)_{X_i=\bar{X}_i}^2 \right] \quad (23.2)$$

Thus, the reliability index (β) and failure probability (P_f) can then be obtained as follows:

$$\beta = \frac{\bar{Z}}{\sigma(Z)} \quad (23.3)$$

$$P_f = P[Z \leq 0] = 1 - \Phi(\beta) \quad (23.4)$$

where Φ is the cumulative distribution function for the standard normal distribution. Moreover, the contribution of the variable X_i to the failure or reliability can be evaluated as follows:

$$\alpha_i^2 = \frac{\frac{\partial Z}{\partial X_i} \sigma(X_i)}{\sigma^2(Z)} \quad (23.5)$$

where α_i^2 is the sensitivity coefficient.

23.5.1.2 Deterioration model

The reliability analysis of a tunnel should consider the factors of the deterioration, dimensions, materials, and load effects. The dimensions, material properties, and load effects can adopt the normal (Gaussian) distribution defined in structural design. However, the deteriorations require an appropriate model, to account for its continually or gradually variation over time.

As for an aging tunnel, the deterioration model usually plays a vital role in the estimation of the structural performance and prediction of the residual life. The successful modeling of the deteriorations depend on the selection of the major deterioration and the description of its effects (e.g., Wang et al. 2016a). The major deterioration should be selected based on the comprehensive consideration of the deterioration condition, tunnel structure, used material, repair history, etc. The deterioration model needs to correctly describe the deteriorating effect and its variation over time. In particular, repair interventions must be reflected in the

deterioration model, because of its direct effects on the degradation of a tunnel. The typical deterioration models associated with structural performance are discussed below.

23.5.1.3 Concrete deterioration

For a RC structure, the crack is generally disregarded in terms of its effects on the structural strength. However, recent research (e.g., Wang et al., 2013) indicates that cracks may significantly decrease the shear strength of a cracked member due to the cross-sectional area reduction. Accordingly, the deterioration model should reflect the effect of crack, with a variable to describe the dimensional size of the cracked cross section. Similarly, large-scale spalls or delamination in a tunnel under severe hydrogen sulfide or chloride attacks should be considered, with the variable of the cross section. The model of the aforementioned concrete deterioration can use a variable (C_r) to reduce the area of deteriorated cross section, as follows:

$$C_r = 0(T < T_1) \text{ or } \alpha(T)(T \geq T_1) \quad (23.6)$$

where T_1 is the initiation time of the concrete deterioration, and α is the of time-depended reduction factor for the deteriorated cross section. The above deteriorations model is only suitable for the reliability analysis of structural lining.

23.5.1.4 Steel and steel reinforcement corrosion

Steel corrosion may process as a local pitting or a wide area corroding surface, and generally experiences initiation and propagation nonlinear with time. (Romanoff, 1957; Tuutti, 1982; Alamilla et al., 2009; Ricker, 2010). In engineering practice, the corrosion loss of steel is commonly estimated, using an simplified expression (e.g., Ricker, 2010; JSCE, 2013):

$$A_c = k_c T^n \quad (23.7)$$

where A_c is the corrosion loss in dimensions (thickness, diameter or area), k_c is the annual corrosion loss ratio, T is the service years, and n is the exponential corrosion constant. The corrosion constants k_c and n varying depending on the many factors, e.g., corrosion pattern, environmental condition, should be determined based on the field data. However, if in any cases the field data is unavailable, the related design specifications can be referenced. For example, the corrosion of steel segment of shield tunnel adopts a simply liner relationship with time for a safe design, with the larger exponential corrosion constant $n = 1.0$ for safety (JSCE, 2009; Ricker, 2010). The steel corrosion loss ratio (k_c) is set as follows: $k_c = 0.02$ and 0.03 mm/year for land tunnels below and above the groundwater level, respectively, and $k_c = 0.1$ mm/year for exposed tunnels. The other model of steel corrosion can

reference the related studies (Romanoff 1957; Ahammed and Melchers, 1994; Alamilla et al., 2009; Caleyo et al., 2009). Moreover, although the corrosion commonly occurs nonuniformly and in various patterns, the mostly corroded section should be considered for safety.

On the other hand, for the corrosion of embedded steel or steel reinforcement, the appropriate modeling is rather difficult, because its deterioration effects involves serious concrete damage, the corrosion loss, and the bond strength weakening (Tuutti, 1982; Ahmad, 2003; JSCE, 2013; Akiyama et al., 2014). In engineering practice, the modeling of embedded material corrosion, is briefly performed for its four stages: (1) initiation stage (before corrosion initiation), (2) propagation stage (corrosion propagates stable), (3) acceleration stage (after cracking of concrete cover), and (4) deterioration (completely exposed to air).

23.5.2 Stochastic process-based performance evaluation

Stochastic processes are often applied to infrastructure management as mathematical models of systems that appear to vary in a random manner. (e.g., Micevski et al., 2002; Kallen, 2007; Agrawal et al., 2010). In general, a stochastic process is defined as a collection of random variables that is indexed by some mathematical set. According to the relation with time and their properties, stochastic processes are classified into the discrete-time and continuous-time categories, e.g., the Markov chain process, random walks, Bernoulli process, Lévy process and Poisson process (Bass, 2011).

Because a tunnel may suffer various deterioration or disorders over lifetime, its performance is rather difficult to appropriately evaluate. In maintenance practice, the discrete-time stochastic Markov process (Markov, 1971, Madanat et al., 1995) is usually used, in consideration of the deterioration with the feature of one-way transition from the previous state. The Markov chain is described using a sequence of random variables X_t ($t = 0, 1, \dots, n$), thus the conditional probability of moving to state j at time $t + 1$ from current state i at time t can be given as follows:

$$\begin{aligned} P_{ij} &= \Pr\{X_{t+1} = j | X_0 = i_0, X_1 = i_1, \dots, X_t = i\} \\ &= \Pr\{X_{t+1} = j | X_t = i\} \end{aligned} \quad (23.8)$$

State j is accessible from state i by defining $P_{ij} \geq 0$ in the Markov chain. The determination of the Markov chain involves assessing the transition probabilities between all possible condition state pairs. For a state space with N states, the transition probability is given by an $N \times N$ matrix:

$$P = \begin{bmatrix} P_{11} & P_{12} & \dots & P_{1N} \\ P_{21} & P_{22} & \dots & P_{2N} \\ \dots & \dots & \dots & \dots \\ P_{N1} & P_{N2} & \dots & P_{NN} \end{bmatrix} \quad (23.9)$$

where the probability of moving from one state to any other state (including itself) must satisfy $\sum_{j=1}^N P_{ij} = 1$ ($i = 1, \dots, N$). In addition, the probability of moving from state i to state k in m time steps can be evaluated by

$$P_{ik} = \Pr\{X_{t+m} = k | X_t = i\} = P_{ij}^m \tag{23.10}$$

For Markov process, the evaluation of the transition probability is key work. As for the tunnel deterioration, the transition of two states generally obeys the rules shown in Fig. 23.14, but the transition time may vary from each other. The transition probabilities can be evaluated with the minimum error model, hazard model or average model, based on the inspected data (Mishalani and Madanat, 2002; Chikata et al., 2015). Meanwhile, referring to the practical specifications (JRB, 2014; JSCE, 2013), the deterioration states of an RC tunnel can be defined with four states (I–IV), as listed in Table 23.1, based on the visual inspection results of concrete cracking, spalling, steel bar corrosion, and leakage. Many old concrete tunnels have not had adequate inspected data and the transition probability varies with the different deterioration state; a analytical method is considered for calculating the transition probabilities ($p_1, p_2,$ and p_3), based on the two selected deterioration conditions (Wang et al., 2016b). A basic transition matrix is assumed as following:

$$P_B = \begin{bmatrix} 1 - p_1 & p_1 & 0 & 0 \\ 0 & 1 - p_2 & p_2 & 0 \\ 0 & 1 - p_3 & p_3 & 0 \\ 0 & 0 & 0 & 1 \end{bmatrix} \tag{23.11}$$

where $p_1, p_2,$ and p_3 are the transition probabilities from state I to II, II to III, and III to IV, respectively. The current deterioration state space, X_m moving from the base state space, X_0 in m time steps is evaluated as follows:

$$X_m = X_0(P_B)^m \tag{23.12}$$

The future deterioration state in n time steps is then predicted by the following:

$$X_{m+n} = X_m(P_B)^n = X_0(P_B)^{m+n} \tag{23.13}$$

Substituting the inspected deterioration states into Eq. 23.12 or 23.13 and solving them, the basic probability transition matrix can be obtained. Thus, any

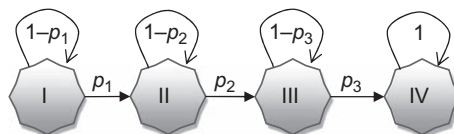


Figure 23.14 Deterioration state transition of RC tunnel.

deterioration state can be evaluated with Eq. 23.13. More accurately, the deterioration state should be evaluated with respect to different small areas set according to the structural components. Fine division of the each area is also required to account for the localization of deteriorations.

The tunnel performance can be evaluated by considering a performance index for each deterioration state (I–IV). Referring to the Japanese code (JRB, 2014), the performance indices $\alpha = 5.0, 4.0, 2.5,$ and 1.0 are used for deterioration states I, II, III, and IV, respectively. Thus, the structural performance at time t ($Gd(t)$) can be estimated as follows:

$$Gd(t) = \sum_{i=1}^4 X_i \alpha_i \quad (23.14)$$

Depending on the deterioration states for an individual area or the overall tunnel, the local or overall structural performance can be obtained. The structural performance is ultimately judged, based on the assumption of a sound state for grade A ($Gd \geq 4.5$), fair state for grade B ($4.5 > Gd \geq 3.5$), poor state for grade C ($3.5 > Gd \geq 2.5$), and unacceptable state for grade D ($Gd < 2.5$).

However, for use of the Markov process there are some critical issues, such as the transition probability being difficult to assess subjectively. As an alternative, the structural performance of an RC tunnel may also be evaluated by analyzing the rebar corrosion based on a schematic of the relationship between the performance and rebar corrosion shown in Fig. 23.15 (Akiyama et al., 2014; JSCE, 2013; Wang et al., 2016b).

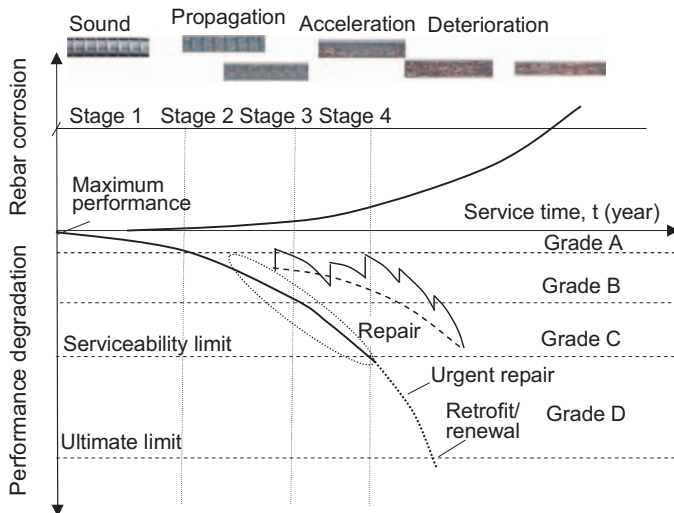


Figure 23.15 Rebar corrosion and performance degradation.

23.5.3 Lifecycle costing

The whole-life cost rigorously includes the expenditure in financing, planning, design, construction, acquisition, operation, maintenance, depreciation, replacement or disposal, and environmental and social costs (Rebitzer et al., 2004; Gluch and Baumann, 2004). Generally, the LCC adopts a net present value method to calibrate the cost at different times, by which future payments are discounted while past ones are compounded. LCC, as an economic criterion, is used to optimize the alternative plans for tunnel construction and maintenance. A tunnel plan is often determined by the initial construction cost, because the construction cost is rather high. In addition, the environmental and social costs are still hardly quantified appropriate for an infrastructure tunnel (Richards, 1998; Muto et al., 2011).

The lifecycle costing may be more helpful if it could account for all possible factors during planning phase; however, for optimization of maintenance plan it can be simplified by only considering the factors related to the maintenance activities (Frangopol et al., 1997; Frangopol and Liu, 2007). The LCC can adopt the sum of the initial construction cost, maintenance costs of periodic inspections, repair costs, rehabilitation costs, and replacement or disposal costs. For a relatively old tunnel, the consideration of asset depreciation may be reasonable to decide a large-scale rehabilitation or replacement, through evaluating an appropriate residual value (Falls et al., 2004). Furthermore, the costing should consider the structural performance and the failure risk. Thus, the net present value of LCC (C_t) can be calculated as

$$C_t = C_{in} + \int_0^t \left(\sum_{i=1}^{IV} x_i C_m^i / (1+r)^t \right) + \left(\sum_{n=1}^N C_r / (1+r)^{t_n} \right) + C_f P_f^t / (1+r)^t \tag{23.15}$$

where C_t is also the expected total cost over t years; C_{in} is the initial cost; C_m^i is the maintenance cost (annual expenditure) depending on the deterioration condition; C_r is the repair or rehabilitation cost; C_f is the failure cost; $P_f (=1-NORMSDIST(Gd(t)-2.5))$ is the failure probability evaluated from the normalized performance indicator, $Gd(t) \in [0,5]$, as shown in Fig. 23.16; r is the discount rate; x_i is the proportion of each deterioration state; N is the repair or rehabilitation times; and t is the year. Where, the maintenance cost includes the expenditures of routine inspection, surface cleaning and minor repairs.

23.5.4 Maintenance planning

Maintenance planning should account for all the related factors, e.g., the time-variant deterioration, structure type, functional requirements, and maintenance strategies (Frangopol et al., 2004; JSCE, 2013; JRB, 2014). Importantly, the lifecycle performance should be predicted for the existing tunnel. Based on the results, the corrective or preventative maintenance plans are made through scheduling the

ordinary maintenance and the repair or rehabilitation for a critical limit. The critical limit in the preventative maintenance is usually set to ensure a tunnel within a fair performance, whereas corrective maintenance adopts the failure limit state of serviceability or structural safety, depending on the operation requirement of the facility. The performance evaluation for a tunnel before and after intervention can use the aforementioned stochastic process method or reliability analysis. Finally, with respect to all the maintenance plans, the corresponding structural performance and the LCC are estimated, and the optimal plan is determined.

An example of the corrective and preventative maintenance plans is illustrated in Fig. 23.17, in terms of the structural performance and LCC. Whereby, for the preventative maintenance plans, besides the traditional preventive repair, an eco-

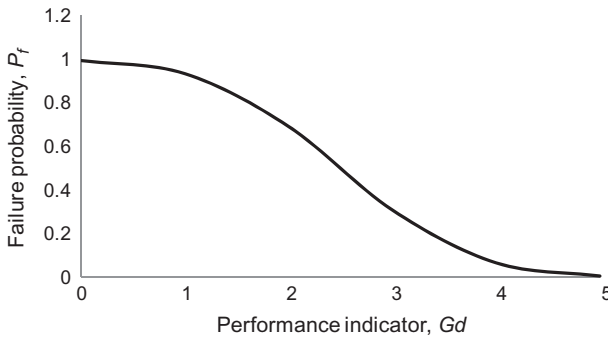


Figure 23.16 Relation of failure probability and performance indicator.

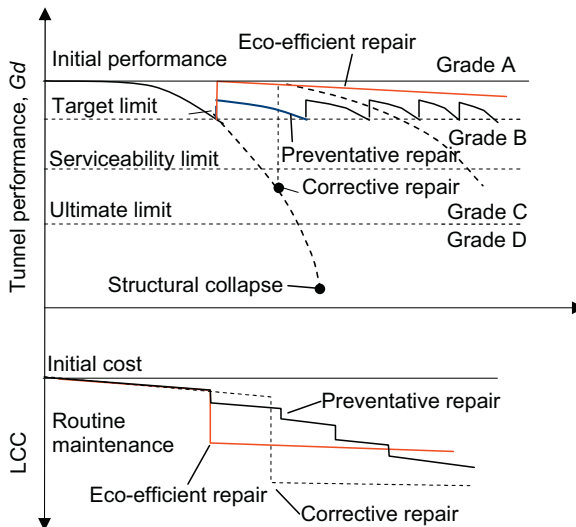


Figure 23.17 Illustration of maintenance plans developed based on performance and LCC.

efficient repair able to realize the maintenance free is considered. Fig. 23.17 clearly shows that the plan using eco-efficient repair is the most reasonable in the economy and the structural performance, while the corrective maintenance plan is worst. Consequently, the eco-efficient maintenance of a tunnel can be achieved if the maintenance-free after repair could be realized.

Regarding the eco-efficient maintenance that could help ensure tunnel is in good performance with less LCC over a life time, a framework for optimizing maintenance plan is proposed, as shown in Fig. 23.18. The performance and LCC are used as the criteria to optimize the maintenance plans. The detailed procedure includes (1) collecting conditional information of structure and deteriorations; (2) predicting the performance of the tunnel over a designed service life (e.g., 100 years); (3) planning maintenance scenarios based on the predicted performance; (4) evaluating the performance and LCC of the tunnel under each maintenance plan; and (5) optimizing and determining the final maintenance plan with the maximum performance and minimum LCC.

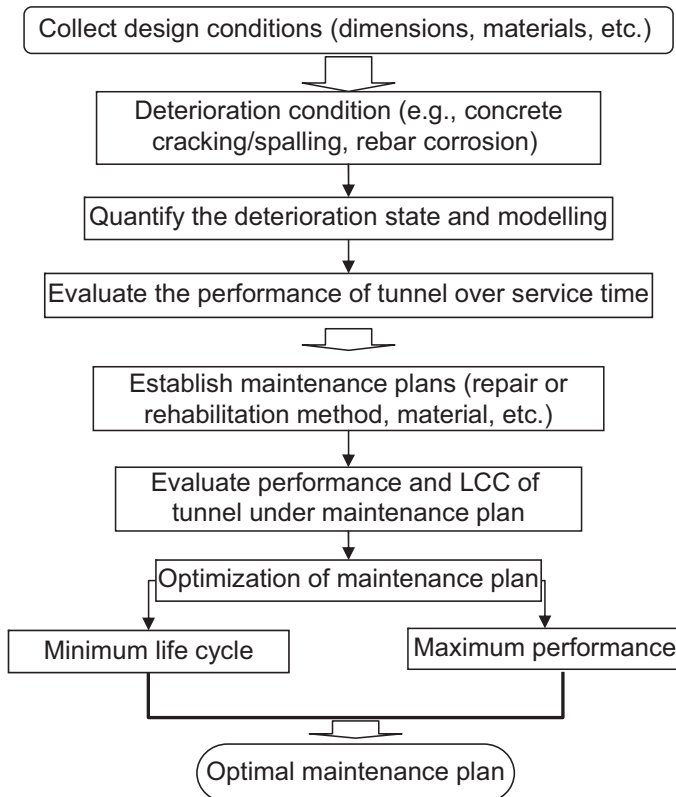


Figure 23.18 Framework for optimizing maintenance plan.

For the application for a tunnel, the target can be the whole tunnel or a part of tunnel. In addition, the critical limit should be set specially considering whether the failure results in a high risk to users.

23.5.5 Example of tunnel maintenance

A 40-year-old immersed tube tunnel in a highway network was discussed using the proposed approach for the decision-making of a maintenance plan. The cross sectional profile of the tunnel is shown in Fig. 23.19. The rainwater mixed with seawater causes a severe chloride-induced deterioration occurring in the floor slab of the middle inspection room. The RC slab consists of the concrete with a compressive strength of 45 N/mm^2 and 13 mm diameter rebar spaced at 125 mm. The deterioration condition was inspected and evaluated according to the criteria listed in Table 23.3, in terms of the concrete cracking, spalling, and steel corrosion. The evaluated deterioration states in years 20 and 40 (Fig. 23.20A), are selected to compute the basic transition matrix of the Markov process, and the deterioration state process over 100 year is evaluated as shown in Fig. 23.20B.

Three maintenance plans are considered, with respect to the corrective plan ($P1$), the ordinary preventative plan ($P2$), and the eco-preventative plan ($P3$) as shown in Table 23.3A. The critical limit state in the preventative maintenance adopts the performance index $Gd = 4.0$ in grade B ($4.5 > Gd \geq 3.5$), while that in the corrective maintenance is set to prevent the tunnel from degrading into grade D, with the upper performance index $Gd = 2.5$. Meanwhile, the various costs are considered for the routine maintenance, which generally includes the inspection, cleaning, special inspection (in-depth survey), and emergency measure, but the implementation work varies from the deterioration states I, II, III, and IV. The repair cost is considered for completely replacing the deteriorated concrete and reinforcing bar. The basic

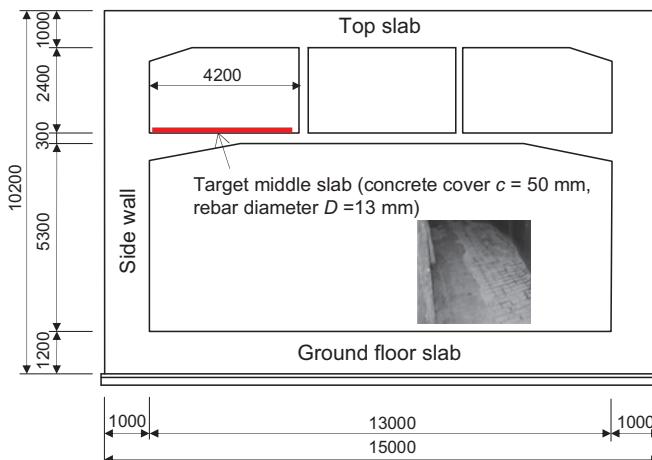


Figure 23.19 Cross section profile and target slab.

Table 23.3 Maintenance plans and cost setting

<i>(A) Repair plan and costs</i>			
Plans	Repair activity	Repair	
		Time	Cost (million/whole slab)
P1-Corrective repair	Restore deterioration states II, III, and IV to I	in year 40	50
P2-Preventative repair	Restore deterioration states III and IV to I	in year 20	50
P3-Eco-preventative repair	Restore deterioration states III and IV to I and coat with high-performance material	in year 20	55
<i>(B) Routine maintenance costs</i>			
Deterioration	Maintenance activities	Cost (million/whole slab)	
State I	Routine inspection	0.15	
State II	Routine inspection + Surface Cleaning	1.26	
State III	Routine inspection + special inspection + temporary protection	3.33	
State IV	Routine inspection + special inspection + emergency measures	11.95	

The costs listed below are those for the whole slab; the money spent is calculated by multiplying by the area ratio for each action.

costs for whole slab are set, as listed in [Table 23.3](#), by referring to a similar project in Sekan tunnel ([Obata and Sugawara, 1999](#)). The initial cost is set as $C_i = 100$ million Japanese yen; the annual maintenance costs are $C_m = 0.15, 1.26, 3.33,$ and 11.95 million for deterioration states I, II, III, and IV, respectively; and the repair cost is $C_r = 50$ million. In addition, the failure cost, $C_f = 100$ million, is assumed to be the same as the initial cost, accounting for serious damage due to the failure of the ceiling slab of the road tunnel. The total costs of routine maintenance and repair are computed through multiplying the basic cost listed in [Table 23.3](#) with the corresponding area proportion to the whole slab.

The structural performance and LCC are evaluated with the aforementioned Markov process-based method, and the results are presented in [Fig. 23.21](#). From [Fig. 23.21A](#) it is clearly indicated that the middle slab of the tunnel degrades to grade B in year 10, grade C in year 28, and grade D in year 40, if the repair intervention is not implemented. Considering the critical limit for the corrective

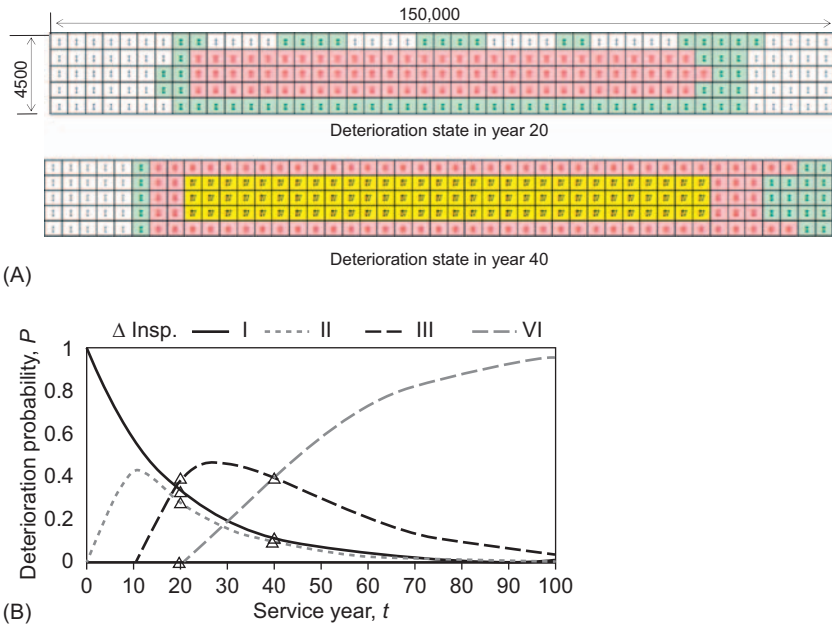


Figure 23.20 Deterioration states and transmission over 100 years: (A) inspection results and (B) deterioration state transition condition.

maintenance is the upper performance of grade D, the slab must be repaired in year 40. In addition, from Fig. 23.21A, it can be observed that all of the repair plans can assist the slab to achieve a performance of grade A at the end of the service life (100 years). However, if the general preventative plan ($P2$) is applied, the slab will experience about 40 years in a fair state of grade B performance. The eco-preventative plan ($P3$) is decisively superior to the other two plans, considering it can ensure the slab in a sound condition (grade A) for all of its service years.

On the other hand, an economic comparison of the three plans can be made using the LCC, as shown in Fig. 23.21B. In general, it is easy to find that the eco-preventative plan ($P3$) can ensure the slab in the highest structural performance with the least cost from year 20. If the eco-preventative plan ($P3$) is used, the slab can be maintained in grade A, and a great reduction of the LCC can be expected by year 100: about 25 million and 14 million less than that of the corrective repair plan ($P1$) and the general preventative repair plan ($P2$), respectively. The corrective maintenance plan ($P1$) is relatively costly because of the higher failure risk and the large-scale repair.

Conclusively, the eco-preventative plan can significantly improve the performance and reduce the LCC. However, the eco-efficiency greatly depend on the used material and the technology. In this example, the high-performance geopolymer concrete and coating material are considered to have a conditional durability over 80 years when used in the room. The durability verification for such material may be required for a long term.

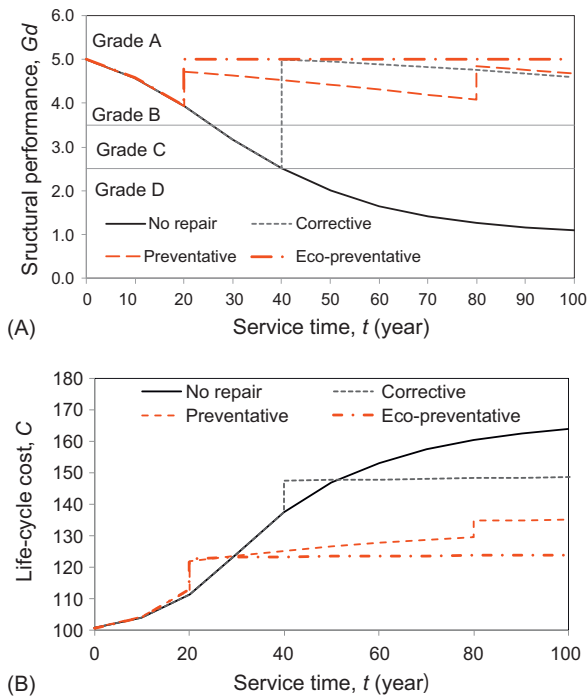


Figure 23.21 Results of performance and life cycle cost with respect to corrective, preventative, and eco-preventative maintenance: (A) performance and (B) life cycle cost.

23.6 Recommendations and future trends

Many concrete tunnels have been constructed with different tunneling methods and serve as important infrastructure facilities; their normal operation requires appropriate maintenance using the sophisticated technologies on the evaluation of performance and LCC, inspection, repair, and rehabilitation, based on scientific knowledge on the tunnel structure, used material and deterioration. This chapter comprehensively discussed tunnel maintenance, from tunnel construction to degradation, along with related methods or technologies for repair, performance, LCC evaluation, and eco-efficient maintenance planning. A framework to help achieve eco-efficient maintenance was proposed with the performance and LCC as the benchmarks for the decision-making of the maintenance plan, and was successfully applied to a road tunnel.

In general, the maintenance of an infrastructure tunnel needs to account for its use and function as a facility, the structure of the support system, the exposed environmental condition, the deterioration condition, etc. Eco-efficient maintenance should be implemented in order to realize the maximum utilization of the facility with the minimum LCC and environmental impact. The proposed framework, using

the performance and LCC, may be an effective solution to help achieving eco-efficiency of tunnel maintenance, with respect to ensuring the tunnel in a good condition with less cost. In addition, high-performance materials and advanced repair technologies (e.g., biomineralization, nanotechnology) is highly expected to assist in realizing maintenance-free tunnels, ultimately achieving the eco-efficiency of maintenance in the future.

However, the quantitative effects of maintenance activities on environment is still unclear. Further study works should be carried out, in terms of integrating the economical and environmental effects with maintenance. In addition, the high-performance materials and eco-efficient repair technologies should be developed for early realizing of the maintenance-free tunnel. Moreover, the more field data should be collected to clarify the deterioration propagation and durability of repair materials, as well as to verify the performance evaluation methods

References

- Abraham, D.M., Wirahadikusumah, R., 1999. Development of prediction models for sewer deterioration. *Durability Build. Mater. Compon.* 8.
- Agrawal, A.K., Kawaguchi, A., Chen, Z., 2010. Deterioration rates of typical bridge elements in New York. *J. Bridge Eng.* 15 (4), 419–429.
- Ahamed, M., Melchers, R.E., 1994. Reliability of underground pipelines subject to corrosion. *J. Transport. Eng.* 120 (6), 989–1002.
- Ahmad, S., 2003. Reinforcement corrosion in concrete structures, its monitoring and service life prediction—a review. *Cem. Concr. Compos.* 25 (4), 459–471.
- Akiyama, M., Frangopol, D.M., Matsuzaki, H., 2014. Reliability-based durability design and service life assessment of concrete structures in a marine environment. *Maint. Saf. Aging Infrastruct.* 1–26.
- Alamilla, J.L., Espinosa-Medina, M.A., Sosa, E., 2009. Modelling steel corrosion damage in soil environment. *Corros. Sci.* 51, 2628–2638.
- Almusallam, A.A., Khan, F.M., Dulaijan, S.U., Al-Amoudi, O.S.B., 2003. Effectiveness of surface coatings in improving concrete durability. *Cem. Concr. Compos.* 25 (4), 473–481.
- Asakura, T., Kojima, Y., 2003. Tunnel maintenance in Japan. *Tunnel. Underground Space Technol.* 18 (2), 161–169.
- Baik, H.S., Jeong, H.S., Abraham, D.M., 2006. Estimating transition probabilities in Markov chain-based deterioration models for management of wastewater systems. *J. Water Resour. Plan. Manage.* 132 (1), 15–24.
- Bass, R.F., 2011. *Stochastic Processes*, Vol. 33. Cambridge University Press.
- Biondini, F., Frangopol, D.M., 2008. Probabilistic limit analysis and lifetime prediction of concrete structures. *Struct. Infrastruct. Eng.* 4 (5), 399–412.
- Biondini, F., Bontempi, F., Frangopol, D.M., Malerba, P.G., 2006. Probabilistic service life assessment and maintenance planning of concrete structures. *J. Struct. Eng.* 132 (5), 810–825.
- Bungey, J.H., Millard, S.G., Grantham, M., 1996. *Testing of Concrete in Structures*. Blackie Academic & Professional, New York, NY, USA.

- Caleyo, F., Velázquez, J.C., Valor, A., Hallen, J.M., 2009. Probability distribution of pitting corrosion depth and rate in underground pipelines: a Monte Carlo study. *Corros. Sci.* 51 (9), 1925–1934.
- Chikata, Y., Suzuki, S., Ogawa, F., 2015. A consideration on calculation process of Markov transition probability for deterioration prediction based on inspection results. *J. Struct. Eng.* Vol. 61A, P70–80, In Japanese.
- Chapman, D., Metje, N., Stärk, A., 2010. *Introduction to Tunnel Construction*, Vol. 3. CRC Press.
- Davidovits, J., 2013. Geopolymer cement. a review. *Geopolym. Inst. Tech. Pap.* 21, 1–11.
- De Muynck, W., Debrouwer, D., De Belie, N., Verstraete, W., 2008. Bacterial carbonate precipitation improves the durability of cementitious materials. *Cem. Concr. Res.* 38 (7), 1005–1014.
- Dekker, R., 1996. Applications of maintenance optimization models: a review and analysis. *Reliab. Eng. Syst. Saf.* 51 (3), 229–240.
- Department of Defense (DoD), 2008. *Condition Based Maintenance Plus DoD Guidance*. Deputy Under Secretary of Defense for Logistics and Material Readiness, Washington, DC.
- Emmons, R.H., 1993. *Concrete Repair and Maintenance Illustrated. Problem Analysis. Repair Strategy. Techniques.*
- Falls, L.C., Haas, R., Tighe, S., 2004. A comparison of asset valuation methods for civil infrastructure. In *Presentation at the Coordinating Pavement and Maintenance Management with Asset Management Session of the 2004 Annual Conference of the Transportation Association of Canada.*
- Federal Highway Administration (FHWA), 2015. *National Tunnel Inspection Standards (NTIS)*. Federal Highway Administration.
- Frangopol, D.M., 2011. Life-cycle performance, management, and optimisation of structural systems under uncertainty: accomplishments and challenges 1. *Struct. Infrastruct. Eng.* 7 (6), 389–413.
- Frangopol, D.M., Liu, M., 2007. Maintenance and management of civil infrastructure based on condition, safety, optimization, and life-cycle cost. *Struct. Infrastruct. Eng.* 3 (1), 29–41.
- Frangopol, D.M., Kallen, M.J., Van Noortwijk, J.M., 2004. Probabilistic models for life-cycle performance of deteriorating structures: review and future directions. *Progr. Struct. Eng. Mater.* 6 (4), 197–212.
- Frangopol, D.M., Lin, K.Y., Estes, A.C., 1997. Life-cycle cost design of deteriorating structures. *J. Struct. Eng.* 123 (10), 1390–1401.
- Furuta, H., Kameda, T., Fukuda, Y., Frangopol, D.M., 2004. Life-cycle cost analysis for infrastructure systems: life-cycle cost vs. safety level vs. service life. *Life-cycle Performance of Deteriorating Structures. Assessment, design and management*, pp. 19–25.
- Gluch, P., Baumann, H., 2004. The life cycle costing (LCC) approach: a conceptual discussion of its usefulness for environmental decision-making. *Build. Environ.* 39 (5), 571–580.
- Grantham, M.G. (Ed.), 2011. *Concrete Repair: A Practical Guide*. CRC Press.
- Hardjito, D., Wallah, S.E., Sumajouw, D.M., Rangan, B.V., 2004. On the development of fly ash-based geopolymer concrete. *ACI Mater. J.-Am. Concr. Inst.* 101 (6), 467–472.
- Institution of Civil Engineers (ICE), 2004. *Tunnel Lining Design Guide*. Thomas Telford Ltd.

- Japan Road Bureau (JRB), 2014. Road tunnel routine inspection manual. Tokyo, Japan Road Bureau of Ministry of Land, Infrastructure, Transport and Tourism. (In Japanese).
- Japan Society of Civil Engineers (JSCE), 2009. Segment Design (2nd version). Tunnel Library No. 23, pp 108. Tokyo: Japan Society of Civil Engineers. (In Japanese).
- Japan Society of Civil Engineers (JSCE), 2013. Standard Specifications for Concrete Structure (Maintenance and Repair). Japan Society of Civil Engineers, Tokyo.
- Japan Society of Civil Engineers (JSCE), 2006a. Standard Specifications for Tunneling—Mountain Tunnels. Japan Society of Civil Engineers, Tokyo.
- Japan Society of Civil Engineers (JSCE), 2006b. Standard Specifications for Tunneling—Shield Tunnels. Japan Society of Civil Engineers, Tokyo.
- Japan Society of Civil Engineers (JSCE), 2006c. Standard Specifications for Tunneling—Cut and Cover Tunnels. Japan Society of Civil Engineers, Tokyo. (In Japanese).
- Jonkers, H.M., Thijssen, A., Muyzer, G., Copuroglu, O., Schlangen, E., 2010. Application of bacteria as self-healing agent for the development of sustainable concrete. *Ecol. Eng.* 36 (2), 230–235.
- Kaito, K., Kobayashi, K., 2015. Big — data based infrastructure management: towards asset-metrics. *Journal of Japan Society of Civil Engineers, Ser. D3 Infrastructure Planning and Management*, Vol. 70 (5), I_21-I_30. (In Japanese).
- Kallen, M.J., 2007. Markov processes for maintenance optimization of civil infrastructure in the Netherlands (Doctoral dissertation, TU Delft, Delft University of Technology).
- Kicherer, A., Schaltegger, S., Tschochohei, H., Pozo, B.F., 2007. Eco-efficiency. *Int. J. Life Cycle Assess.* 12 (7), 537.
- Kleiner, Y., 2001. Scheduling inspection and renewal of large infrastructure assets. *J. Infrastruct. Syst.* 7 (4), 136–143.
- Kuesel, T.R., King, E.H., Bickel, J.O., 2012. *Tunnel Engineering Handbook*. Springer Science & Business Media.
- Madanat, S., Mishalani, R., Ibrahim, W.H.W., 1995. Estimation of infrastructure transition probabilities from condition rating data. *J. Infrastruct. Syst.* 1 (2), 120–125.
- Malhotra, V.M., Carino, N.J., 2003. *Handbook on Nondestructive Testing of Concrete*. second ed. CRC press.
- Markov, A.A., 1971. Extension of the limit theorems of probability theory to a sum of variables connected in a chain. In: Howard, R. (Ed.), *Dynamic Probabilistic Systems*, volume 1: Markov Chains. John Wiley and Sons, reprinted in Appendix B.
- Mashimo, H., 2002. State of the road tunnel safety technology in Japan. *Tunnel. Underground Space Technol.* 17 (2), 145–152.
- Mays, G.C. (Ed.), 2002. *Durability of Concrete Structures: Investigation, Repair, Protection*. CRC Press.
- Meguid, M.A., Dang, H.K., 2009. The effect of erosion voids on existing tunnel linings. *Tunnel. Underground Space Technol.* 24, 278–286.
- Melchers, R.E., 1987. *Structural Reliability Analysis and Prediction*. Ellis Horwood, Chichester, Wiley.
- Micevski, T., Kuczera, G., Coombes, P., 2002. Markov model for storm water pipe deterioration. *J. Infrastruct. Syst.* 8 (2), 49–56.
- Ministry of Land, Infrastructure, Transport and Tourism of Japan (MLIT), 2012. Sasago Tunnel Ceiling Collapse on the Chuo Expressway on the Chuo Expressway. Retrieved from: https://www.mlit.go.jp/road/road_e/03key_challenges/1-2-1.pdf.
- Mishalani, R.G., Madanat, S.M., 2002. Computation of infrastructure transition probabilities using stochastic duration models. *J. Infrastruct. Syst.* 8 (4), 139–148.

- Mori, Y., Ellingwood, B.R., 1993. Reliability-based service-life assessment of aging concrete structures. *J. Struct. Eng.* 119 (5), 1600–1621.
- Mutou, Y., Kawabata, M., 2011. Maintenance of railroad shield tunnel. In *Proceeding of the 6th Japan–China conference on shield-driven tunnelling*, Nagaoka. (In Japanese).
- Najafi, M., Gokhale, S., 2005. *Trenchless Technology: Pipeline and Utility Design, Construction, and Renewal*. McGraw Hill Professional.
- Obata, T., Sugawara, S., 1999. Maintenance and management of the undersea section of the Seikan tunnel. *Jpn. Railway Eng.* 39 (1), 16–20, 1999. (In Japanese).
- Pacheco-Torgal, F., Abdollahnejad, Z., Miraldo, S., Baklouti, S., Ding, Y., 2012. An overview on the potential of geopolymers for concrete infrastructure rehabilitation. *Construct. Build. Mater.* 36, 1053–1058.
- Pacheco-Torgal, F., Labrincha, J.A., 2013. Biotech cementitious materials: some aspects of an innovative approach for concrete with enhanced durability. *Construct. Build. Mater.* 40, 1136–1141.
- Pacheco-Torgal, F., Miraldo, S., Ding, Y., Labrincha, J.A., 2013b. Targeting HPC with the help of nanoparticles: an overview. *Construct. Build. Mater.* 38, 365–370.
- Pacheco-Torgal, F., Jalali, S., Labrincha, J., John, V.M. (Eds.), 2013a. *Eco-efficient Concrete*. Elsevier.
- Railway Technical Research Institute(RTRI), 2000. *Design Manual of countermeasure to deteriorated tunnel*. Railway Technical Research.
- Rangan, B.V., 2008. Fly ash-based geopolymer concrete.
- Rebitzer, G., Ekvall, T., Frischknecht, R., Hunkeler, D., Norris, G., Rydberg, T., Pennington, D.W., 2004. Life cycle assessment: Part I: Framework, goal and scope definition, inventory analysis, and applications. *Environ. Int.* 30 (5), 701–720.
- Richards, J.A., 1998. Inspection, maintenance and repair of tunnels: international lessons and practice. *Tunnel. Underground Space Technol.* 13 (4), 369–375.
- Ricker, R.E., 2010. Analysis of pipeline steel corrosion data from NBS (NIST) studies conducted between 1922–1940 and relevance to pipeline management. *J. Res. Natl. Inst. Stand. Technol.* 115 (5), 373.
- Romanoff, M., 1957. *Underground Corrosion*. US Government Printing Office, Washington, DC.
- Saitoh, M., Furuta, M., Yamamoto, M., 1994. Study on deformation of shield tunnels constructed in alluvial ground. In *Proceedings of Tunnel Engineering, JSCE*, Vol. 4, pp. 55–62. (In Japanese).
- Sanchez, F., Sobolev, K., 2010. Nanotechnology in concrete—a review. *Construct. Build. Mater.* 24 (11), 2060–2071.
- Tayeh, B.A., Bakar, B.A., Johari, M.M., Voo, Y.L., 2013. Utilization of ultra-high performance fibre concrete (UHPFC) for rehabilitation—a review. *Proc. Eng.* 54, 525–538.
- Tee, K.F., Khan, L.R., Chen, H., 2013. Probabilistic failure analysis of underground flexible pipes. *Struct. Eng. Mech.* 47, 167–183.
- Tuutti, K., 1982. *Corrosion of steel in concrete*.
- van Noortwijk, J.M., Frangopol, D.M., 2004. Two probabilistic life-cycle maintenance models for deteriorating civil infrastructures. *Prob. Eng. Mech.* 19 (4), 345–359.
- Wang, J., Shi, Z., Nakano, M., 2013. Strength degradation analysis of an aging RC girder bridge using FE crack analysis and simple capacity-evaluation equations. *Eng. Fract. Mech.* 108, 209–221.
- Wang, J., Koizumi, A., Tanaka, H., 2016a. Framework for maintenance management of shield tunnel using structural performance and life cycle cost as indicators. *Struct. Infrastruct. Eng.* 13 (1), 44–54.

- Wang, J.H., Tanaka, H., Koizumi, A., 2015. Tunnelling technology for developing sustainable infrastructure: Part 1 - Maintenance and management. In Proceedings of the 8th Japan—China conference on shield—driven tunnelling, Nanjing. (In Japanese).
- Wang, J.H., Nakano, M., Matsuyama, K., Sugiyama, H., Tanaka, H., Koizumi, A., 2016b. Performance evaluation of reinforced concrete tunnel suffering chloride attack. In Proceedings of The Fifth International Symposium on Life - Cycle Civil Engineering, IALCCE2016. CRC Press.
- World Business Council for Sustainable Development, 2000. Eco-efficiency: creating more with less impact. Published online: www.wbcsmotability.org.

Life cycle analysis of strengthening concrete beams with FRP

24

Sebastian George Maxineasa and Nicolae Taranu
"Gheorghe Asachi" Technical University of Iasi, Iasi, Romania

24.1 Introduction

The climate change phenomena registered in recent years has fueled a growing public awareness of the effects that humanity's daily activities have over the natural environment, but also of their impact on the current and future generations. In this context, considering and fulfilling the primary dimensions of sustainability can be thought of as one of the most important challenges of the 21st century. In order to achieve this global goal, we first need to grasp the primary reasons that have led to the present environmental crisis, by analyzing and interpreting the impact of various industrial sectors over the Earth's ecosystem.

Over the years, improving quality of life has been one of the primary reasons for creating new technologies and manufacturing activities that, although having a critical role in the economic and social development, exerted a negative impact over the environment. Since an enormous volume of natural resources has already been depleted and are continuously being consumed, the recorded evolution of the past and present generations will negatively influence the life conditions for the future ones. The European industrial revolution of the late 18th century can be regarded as the point from which human activities started to massively influence the environment.

Technological innovations and medical breakthroughs have provided a solid ground for the improvement of living conditions and the increase of life expectancy, being one of the primary factors of the massive population growth recorded in the last 200 years. In order to sustain the needs of an increasing number of people who do not, in general, embrace rational consumption, the level of depleted raw materials has been enlarged yearly, putting in danger the resource stock needed in the future to offer an equitable chance at development for next generations. Alarming levels of greenhouse gas emissions and the amount of water consumed are among other significant negative environmental effects resulting from our daily activities.

Out of all economic activities, the construction industry has one of the most important social and economic influences at the global scale. Taking into account the amount of raw materials and nonrenewable resources used in this sector, the built environment also has a significant impact over the natural one. It is worth

mentioning that this negative influence is recorded in both the developed countries and in the developing ones. In the latter case, the environmental impact is a direct result of the construction processes needed to complete a new building stock that will satisfy the necessities of an increasing population. In recent years, in the developed nations, the negative ecological effects of the construction sector are more and more influenced by the situation of the existing building stock, this problem shaping into a serious environmental issue. In these countries, a significant number of structures have exceeded the life span considered in the design stage and are failing to satisfy the current structural requirements. Therefore, in order to provide a proper level of safety for the user, the existing constructions need to be replaced, upgraded or strengthened—operations that will put additional pressure over the environmental performances of the industry.

These facts provide valid reasons for considering the construction sector as one of the key actors in the global stage of sustainability. In order to protect and improve the Earth's ecosystem in the near future, all the industrial fields should put into action different policies with the goal of satisfying the primary dimensions of sustainability. Thus, in order to improve the ecological performances of the construction sector, civil engineering specialists and researchers should analyze, promote, and make use of specific applications, systems and techniques that help achieve a reduced environmental load and that could bring this industry one step closer to achieving the global sustainable development goals. Reusing the existing structures by considering different fiber-reinforced polymer (FRP) strengthening systems could represent a solution to diminishing the impact of the built environment over the natural one, by minimizing the amount of traditional building materials used, therefore reducing the level of the natural resources consumed and the volume of environmental burdens resulted from the life cycle of these products.

24.2 Sustainability in civil engineering

In 1972, a group of researchers from the Massachusetts Institute of Technology completed the report "The Limits to Growth." This study was published at the request of the international association The Club of Rome, which wanted to bring to public attention the alarming situation regarding the challenges that humankind will face in the next years with respect to preserving the natural environment. One of most important remarks of the analysis was the fact that, in the 21st century, the Earth's ecosystem will not be able to properly sustain humanity's daily activities, thus the very existence of the race is being put in danger (Meadows et al., 1972; Turner, 2008; Berardi 2013; Pacheco-Torgal, 2014). Twenty years later, the report was updated, and the new analysis showed that some of the predicted consumption rates have already been exceeded (Meadows et al., 1992; Pacheco-Torgal, 2014).

Even if part of the scientific community did not consider these reports as a piece of valuable and consistent research, the analysis published in the early 1970's is regarded as being the starting point of the sustainability concept at a global scale.

The alarming facts on the present and future state of the natural environment has created the necessary momentum for the United Nations (UN) to coordinate, the first meeting on sustainable development in 1972, having the “Human Environment” as the main topic. During the conference, the framework for creating the United Nations Environment Programme (UNEP) was established, an organization handling global environmental problems (Drexhage and Murphy, 2010; Berardi, 2013; Pacheco-Torgal, 2014).

After creating the UNEP agency, global efforts have been made in order to define the sustainable development and to understand how the existing industries and consumption habits would affect the global stock of natural resources and their impact over future generations. Therefore, in 1983, the UN initiated the World Commission on Environment and Development (WCED)—also known as the Brundtland Commission—with the goal of addressing the concerns regarding the “accelerating deterioration of the human environment and natural resources and the consequences of that deterioration for economic and social development” (Drexhage and Murphy, 2010). Four years later, the work group published the “Our Common Future” report (or the Brundtland Report), which was almost instantaneously recognized as the landmark manuscript for the global sustainability. The worldwide-accepted definition for sustainable development is present in this report, i.e., the “development that meets the needs of current generations without compromising the ability of future generations to meet their own needs” (WCED, 1987; Drexhage and Murphy, 2010). This definition is also used at the present time, for example in the international standard ISO 15392:2008 which deals with the use of the sustainability concept in construction sector (ISO, 2008a).

The Brundtland Report is considered to be one of the main driving forces behind the 1992 UN summit in Rio de Janeiro. Also known as the “Earth Summit,” the conference established the international recognition and institutionalization of sustainability. During the summit, two important documents were adopted: the “Rio Declaration on Environment and Development” and “Agenda 21.” These reports established a series of principles as well as a plan regarding the consideration and implementation of sustainability on a global scale (UN, 1992a, b; Drexhage and Murphy, 2010). Throughout the years, an impressive number of summits and international conferences having sustainable development as their main topic have been held with notable results. We can mention the 1997 Earth Summit + 5 in New York, the 1997 United Nations Climate Change Conference in Kyoto, which resulted in the treaty known as the “Kyoto Protocol” and which has been adopted with the goal of reducing greenhouse gas emissions, and last but not least, the 2015 United Nations Climate Change Conference in Paris, which concluded with the adoption of the famous “Paris Agreement,” establishing various policies to be implemented in 2020 with the goal of reducing climate change phenomena.

Even if the concept gained more and more recognition globally, substantial action is still needed to be taken. For example, it is common knowledge that the current rates of natural resources consumption are approximately 60% higher than the Earth’s capacity of renewing the raw materials stock, thus, the present values are unsustainable (Ewing et al., 2010; Tautsching and Burtscher, 2013;

WWF, 2016). The Global Footprint Network announced August 8 to be the “Earth Overshoot Day” for the year 2016 (i.e., the day of the year when the resource consumption rates have exceeded the stock renewing capacity of planet Earth for that year) (Global Footprint Network, 2016). It is estimated that the quantity of extracted raw materials ranges between 47 and 59 billion metric tons per year (Krausmann et al., 2009). All facts considered, all industrial sectors must implement consistent environmental policies in order to diminish their impact over the natural environment. Out of these, the construction sector is one of the most far-reaching with regards to the ecological, economic, and social impact it exerts over the environment.

24.2.1 Sustainable development and the built environment

At the global scale, out of all economic activities, the construction industry is considered to be one of the most pollutant. Taking into account the substantial amounts of nonrenewable natural resources consumed, the issue regarding the consideration and fulfilment of the sustainability aspects in the built environment has become more and more debated in recent decades (Ortiz et al., 2009; Miller and Ip, 2013; Yeh and Haller, 2013; Ingrao et al., 2014). In the current context of global sustainable development, aside from the environmental effects, the construction sector also has an important socio-economic impact, since this industry is responsible for approximately 7% of the total number of jobs (Tautsching and Burtscher, 2013).

It is estimated that the construction industry annually depletes between 40% and 60% of the total amount of natural resources used worldwide, making it the biggest consumer (Bribian et al., 2011; Messari-Becker et al., 2013; Tautsching and Burtscher, 2013). This sector is also responsible for producing approximately 40% of the total greenhouse gas emissions, and almost 25% of global waste. At the same time, the processes specific to this field consume over 40% of the total primary energy, and nearly 15% of the total freshwater resources (Ramesh et al., 2010; Mokhlesian and Holmen, 2012; Simion et al., 2013; Ding, 2014; Pacheco-Torgal, 2014). It must also be mentioned that out of the total amount of materials consumed globally, between 40% and 50% are represented by building materials (Miller and Ip, 2013; Pacheco-Torgal and Labrincha, 2013; Blankendaal et al., 2014; Pacheco-Torgal, 2014). In the European Union, the construction sector is accountable for using about 40% of the total amount of energy and materials, and for producing nearly 40% of the total volume of waste (Ferreira et al., 2014; Marinkovic et al., 2014; Rossi, 2014; Solis-Guzman et al., 2014).

Taking into account the impact of the construction sector over the Earth’s ecosystem, the International Organization for Standardization has published the ISO 15392:2008 standard, which clarifies the way the sustainability concept could be applied in the construction sector. This international standard defines sustainability as the “state in which components of the ecosystem and their functions are maintained for the present and future generations,” where sustainability is “the goal of sustainable development.” In the same norm, sustainable development is defined as “development that meets the needs of the present without compromising the ability

of future generations to meet their own needs,” also stating that “addressing sustainability in buildings and other construction works includes the interpretation and consideration of sustainable development in terms of its three primary aspects—economic, environmental, and social aspects—while meeting the requirements for technical and functional performance of the construction works” (ISO, 2008a). Therefore, in order to consider a product or service specific to the construction sector as sustainable, the main dimensions of the concept must be considered and interpreted. However, due to the alarming state of the Earth’s ecosystem, the environmental aspect has been regarded as the most important one in the last few years.

In the future, it is expected that the level of the construction sector’s environmental burdens will significantly increase. As stated above, the negative impact of the built environment over the natural one can be noticed in both the developed and in developing countries. The present research is focused on analyzing the implications resulted from considering the environmental dimension of sustainability in the first case. In these countries, the ecological performances of the construction industry will be massively influenced by the condition of the existing built stock. A significant part of the constructions that exceeded the life span considered in their design stage will present difficulties in providing an acceptable level of structural safety to the users (Hollaway, 2011). Resolving this problem with a minimum negative environmental output will represent one of the most important tasks for civil engineers. A viable solution could be represented by the strengthening and reusing of the existing structures, considering different materials and techniques. By making allowance for FRP materials in these applications, it is possible to take significant steps in minimizing the environmental footprint of the sector.

24.2.2 Environmental impact of traditional building materials

The impact of the construction industry is highly affected by the impact of the specific products (i.e., materials and structures) used in this sector. The environmental performances of the built environment can be greatly influenced by the preoperation and postoperation phases of a structure—the considered structural solutions adopted in the design stage, and the building materials consumed. Therefore, we will try to clarify what the environmental implications resulted from the manufacturing stage of traditional building materials.

24.2.2.1 Concrete

Concrete is the most utilized product in the construction sector; the total quantity of concrete used is two times larger than the amount of other materials used in this sector. 25 billion tons of concrete are produced each year, which equals to 3.8 tons processed for every person. In the last 60 years, the levels of concrete consumption have multiplied 10-fold, an alarming situation given that concrete is the second most consumed resource, the first one being water (EPC, 2009; Gursel et al., 2014; Marinkovic et al., 2014).

It is estimated that, for the production of the amount of concrete used worldwide, between 8 and 12 billion tons of natural aggregates are consumed annually (Shafiqh et al., 2014), while the manufacturing stage processes around 80 L of water per ton of concrete (MPA, 2015). From the concrete mix, cement is the component material with the most important influence on the overall environmental impact. In the last 60 years, the amount of cement produced and consumed worldwide has increased from 0.5 to ~3 billion tons (Estrada et al., 2012; Gursel et al., 2014; Habert, 2014). It is also estimated that, considering the current consumption trends, the quantity of cement used at the global level will reach between 3.69 and 4.40 billion tons (WBCSD, 2009). Probably the most important fact related to the environmental impact of cement, and therefore of concrete, is that 1 kg of CO₂ is released as a result of the production of 1 kg of cement (Estrada et al., 2012; Habert, 2014). Taking into account the significant amount of concrete consumed each year and its overall environmental impact, concrete represents an important component in achieving sustainability (its environmental dimension, at least) in the construction sector.

24.2.2.2 Steel

The processes specific to steel manufacturing are responsible for approximately 9% of the total amounts of global CO₂ emissions (Moynihan and Alwood, 2012). It is estimated that in the last 40 years, the amount of steel produced globally has increased about 2.5 times, from 595 million tons in 1970 to approximately 1600 million tons in 2013 (WSA, 2013a, b). The impact of this material is very important in assessing the environmental footprint of the built environment, due to the fact that about 50% of the total volume of steel produced worldwide is consumed in the construction sector (Wang et al., 2007; Moynihan and Alwood, 2012).

The environmental performances of steel are highly influenced by the producing technique. Two methods are generally used: the basic oxygen furnace (BOF) process and the electric arc furnace (EAF) process (Estrada et al., 2012; Strezov et al., 2013). Taking into account that the EAF process uses electricity and the BOF method coal and natural gas, and also considering that in the first manufacturing method, larger amount of recycled material is utilized, it can be concluded that the steel produced by using the EAF method has a lower environmental impact. Compared with other traditional construction materials, steel has an important environmental advantage in that it can be 100% recycled numerous times without any quality loss (Estrada et al., 2012).

It must be mentioned that, in recent decades, the steel industry has made significant progress with respect to its environmental impact. For example, in the United States of America since 1975, greenhouse gas emissions resulted from the manufacturing process have decreased by approximately 45%; the carbon footprint from steel is also smaller by 47%, compared with the one from 1990 (AISC, 2016). Even if the environmental footprint has decreased, the steel industry must take supplementary actions in order to produce a material with a nearly zero impact over the Earth's ecosystem.

24.2.2.3 *Masonry*

The level of environmental burdens characteristic to these elements is highly influenced by the type of material used in the manufacturing stage of masonry units. Fired clay bricks have a level of embedded energy higher than the one corresponding to concrete masonry units (or concrete bricks). Being a fired material, during the production stages of clay bricks, significant amounts of energy are consumed, which has a direct effect over the carbon footprint of the manufactured products (Volz and Stonver, 2010a; Estrada et al., 2012). In order to produce fired clay bricks, temperatures have to reach and be maintained between 900°C and 1050°C. Another important fact that influences the impact of clay units is represented by the time consumed during the heating and cooling processes, that can last up to 150 hours (Bingel and Bown, 2010; Volz and Stonver 2010a; Lourenco și Vasconcelos, 2015).

As in the case of concrete, the environmental performances of masonry concrete blocks are highly influenced by the amount of cement used in the manufacturing stage (Bingel and Bown, 2010; Volz and Stonver, 2010a). In order to improve the environmental performances of these type of bricks, the masonry industry has decided to use complementary materials, like fly ash. This type of material has been used to replace a volume of cement in the case of concrete masonry units, or to produce a new type of brick, the fly ash brick, resulting in a type of unit with a lower environmental footprint than fired clay bricks concrete bricks, due to the amount of energy consumed in the manufacturing processes. The embodied energy of fly ash bricks is approximately 2 times lower than the one of classic concrete masonry blocks (Bingel and Bown, 2010; Volz and Stonver, 2010b; Estrada et al., 2012).

24.2.2.4 *Timber*

It is well known that forests are Earth's most proficient tool for enhancing air quality by sequestering an important volume of carbon dioxide (CO₂) and replacing it with oxygen (O₂). A well-managed wood plantation has the ability of sequestering approximately 670 g of CO₂, releasing at the same time up to 490 g of O₂, which makes timber a carbon negative material (DeStefano, 2009; Estrada et al., 2012). Forests also provide a natural habitat for a significant part of the wildlife, having probably one of the most important roles in the global efforts of achieving the environmental dimension of sustainability. Another benefit of wood, with respect to the Earth's ecosystem, is that this material is biodegradable and can also be recycled as bio fuel (Estrada et al., 2012; Hafner et al., 2014).

One of the most important environmental disadvantages of wood as a building material is the vulnerability to insect attacks and decay (Estrada et al., 2012). This means timber elements must be protected in order to ensure a long-term durability by using preservatives, which usually are chemical solutions with a negative influence over the natural environment. Even if the use of timber products made by processing trees from sustainable wood plantations (known as certified forests) is

encouraged, there is still another major problem: illegal deforestation. Being a widely used material in the built environment, the consumption rates of timber in this sector have an important effect over the overall state of the Earth's ecosystem.

24.2.3 Environmental impact of fiber-reinforced polymer composites constituent materials

In the last few years, the number of FRP applications specific to the construction sector have significantly increased. Composite materials are mainly used for strengthening the existing structures but they are also used for constructing new structural members. Currently, these types of materials present a certain level of concern regarding their environmental performances and the way in which they can be used in the present global context of sustainability. Therefore, in order to properly use composite materials with respect to the sustainable development of the construction sector, we must first analyze their environmental performances. The following section introduces the implications resulting from using the most common fibers and polymers in different construction applications.

24.2.3.1 Glass fibers

Due to their favorable mechanical properties and low production costs, glass fibers are one of the most popular solutions used as reinforcement in composite applications specific to the construction sector. In order to produce this type of fiber, the constituents must be mixed and melted at temperatures reaching 1400°C (Hollaway, 2011; Lee et al., 2012). In order to produce glass fibers, a significant amount of nonrenewable energy is utilized. It is estimated that approximately 54.7 MJ of energy is consumed for producing 1 kg of glass fibers (Joshi et al., 2004; Lee et al., 2012). The analysis of the environmental footprint of the fibers also has to consider that, during their production, large amounts of dust that can have a significant negative effect over the Earth's ecosystem are emitted in the air.

24.2.3.2 Carbon fibers

The quality of this type of fiber is highly influenced by the processes used during the manufacturing stage and also by the raw materials utilized. The carbon fibers or the graphite fibers are produced by using two precursors: polyacrylonitrile (PAN) and the petroleum pitch (Barbero, 2011; Hollaway, 2011). The production process is quite complex, the temperature reaching between 2500°C and 3000°C (fib, 2007; Campbell, 2010). Compared to the other types of fibers used as reinforcement in composite applications, it is considered that the carbon fibers have the highest environmental impact due to the consumption of a significant amount of nonrenewable energy in order to reach the high temperatures required during the manufacturing stages. Their high mechanical properties allow for decreasing the amount of reinforcement needed in different composite applications, which significantly reduce their overall environmental impact.

24.2.3.3 *Aramid fibers*

This type of fiber is considered to be organic, and in order to produce them, liquid crystal polymers are used (Barbero, 2011; Hollaway, 2011). Compared to the glass and carbon fibers, the manufacturing process of aramid fibers does not require high temperatures; the maximum value reached during the production stage is around 200°C. One of the most important environmental disadvantages is that in order to produce fibers, very strong chemical substances are used. Taking into account the needed amount of nonrenewable energy during the manufacturing process, it can be concluded that aramid fibers have the lowest impact over the natural environment compared with glass and carbon fibers.

24.2.3.4 *Polyester resins*

Due to their mechanical performances/cost ratio, these type of resins are a very popular alternative in applications specific to build environment. Their main disadvantage is represented by the impact over the human health. The negative effects are determined by the use of peroxide as a polymerization catalyst, and styrene as a crosslinking agent. These substances can produce eye and skin irritation or even brain damage. It is considered that, compared to the epoxy and vinyl ester resins, the polyester resins have the biggest important environmental impact (Lee et al., 2012).

24.2.3.5 *Epoxy resins*

Due to their good mechanical properties and versatility, epoxy resins are a very common choice in construction applications. An epoxy system is formed by using, beside the resin, a hardener or an accelerator in order to set up the crosslinking process between the molecules. It is known that the toxicity level of an epoxy system decreases by increasing the molecular weight (Barbero, 2011; Lee et al., 2012). The hardeners used in an epoxy mix can have a serious impact over human health. Being a thermoset system, the recycling of the epoxy matrix represents another important environmental issue.

24.2.3.6 *Vinyl ester resins*

This type of resin is an intermediary product, between the polyester and epoxy resins. The vinyl ester matrices are formed by using an epoxy resin and an acrylic or methacrylic acid (GangaRao et al., 2007). The vinyl esters are produced by handling a combination of epoxy and polyester resins production methods (GangaRao et al., 2007; Lee et al., 2012). Therefore, it can be stated that the environmental impact of the vinyl ester resins combines the negative effects of the other two resins mentioned earlier.

24.2.4 *Life cycle assessment methodology*

It is considered that the Life Cycle Assessment (LCA) studies are the most powerful tools that can be used to evaluate and interpret the environmental impact of a

product or service. The methodology of this type of analysis is legislated by the international standards ISO 14040:2006 and ISO 14044:2006. The LCA is defined as the “compilation and evaluation of the inputs, outputs, and the potential environmental impacts of a product system throughout its life cycle” that can be used for “identifying opportunities to improve the environmental performance of products at various points in their life cycle; informing decision-makers in industry, government or nongovernment organization; the selection of relevant indicators of environmental performance, including measurement techniques and marketing” (ISO, 2006a, b). Fig. 24.1 shows the stages that, according to ISO 2006a, b must be considered in order to analyze a system by using the LCA methodology.

There are different types of LCA studies, depending on the period of the product’s life cycle under analysis. Therefore, in order to assess the environmental

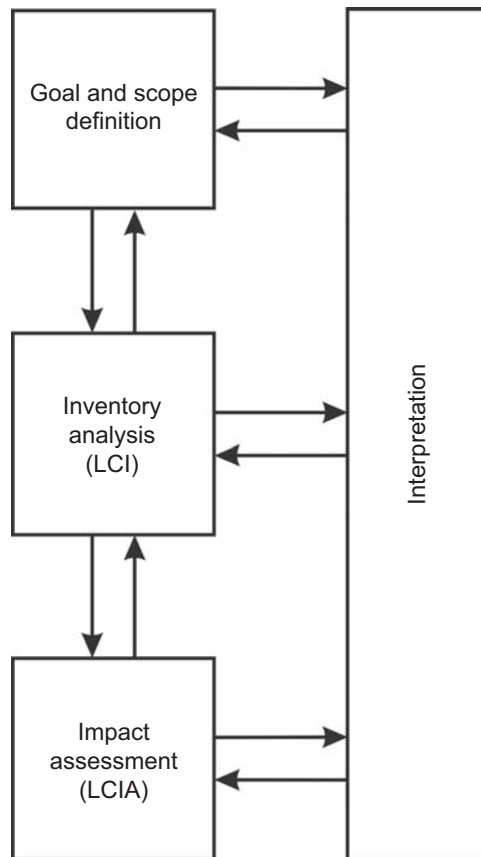


Figure 24.1 Phase of a Life Cycle Assessment (LCA) study (SR EN ISO, 2007) “This reproduction was done according to ASRO—Romanian Standards Association Agreement no. LUI/17/ 580-1/11.05.2017. Any infringement of copyright on standards is an offense and can be punished under Law No.8/1996 on copyright and related rights.”

impact, the following categories of analysis can be used (Nebel, 2006; Tundrea et al., 2014): Gate-to-Gate, Cradle-to-Gate, Cradle-to-Grave, and Grave-to-Grave. In order to simplify and get a better understanding on the environmental impact of a building, the European Norm EN 15804:2012 + A1:2013 has divided the life cycle of an analyzed product in four stages, covering 16 modules: from the raw material supply, named module A1, to the disposal of demolition wastes, known as module C4 (EN, 2013).

24.2.5 Assessing the environmental performances of different construction materials

In order to better understand the differences between the environmental impact of traditional construction materials and FRP composites, a series of cradle-to-gate LCA studies are presented in the following section. The goal of the analyses was to assess and compare the environmental performances over the production stage (A1) from the life cycle of the following materials: concrete (C 20/25), fired clay brick, structural steel, timber, glass fiber, carbon fiber, epoxy resin, and polyester resin. It must be noted that the analyzed concrete C 20/25 mix is one of the most used mixes in Romania; the values used have been worked up in another LCA study dealing with different concrete mixes (Taranu et al., 2016).

The assessment has been made by using the GaBi software; it considers 1 kg of material as functional unit. In order to quantify the effects over the natural environment, the impact categories presented in Table 24.1 have been considered. The environmental parameters have been selected from the recommended methods list of the European Commission's Joint Research Centre (2011), and from the index of parameters provided by the European Norm EN 15804:2012 + A1:2013.

Analyzing Fig. 24.2, it can be observed that the considered FRP materials have the highest impact over the climate change phenomena, the highest carbon footprint being attributed to carbon fibers and epoxy resins. We can also see that, of all traditional building materials considered, steel has the highest impact in the case of the global warming potential (GWP) parameter. It must be mentioned that if biogenic

Table 24.1 Considered impact categories

Impact category	Parameter	Unit	Methodology
Global warming (climate change)—excluding the biogenic carbon	Radiative forcing global warming potential (GWP)	kg CO ₂ -eq.	IPCC
Human toxicity, cancer effects	Human toxicity potential, cancer (HTPc) effects	CTUh	USEtox
Ozone depletion	Depletion potential of the stratospheric ozone layer/ ozone depletion potential (ODP)	kg CFC-11 eq.	ReCiPe

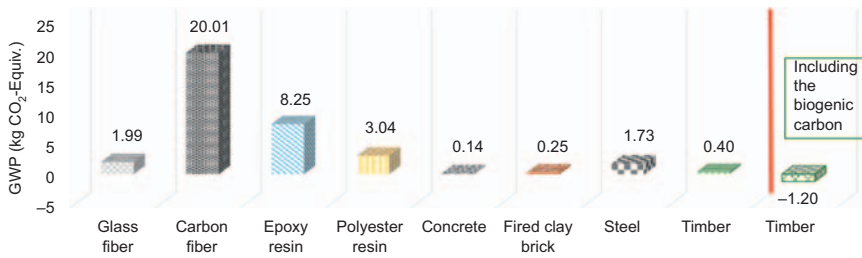


Figure 24.2 Results for the global warming potential (GWP) parameter.

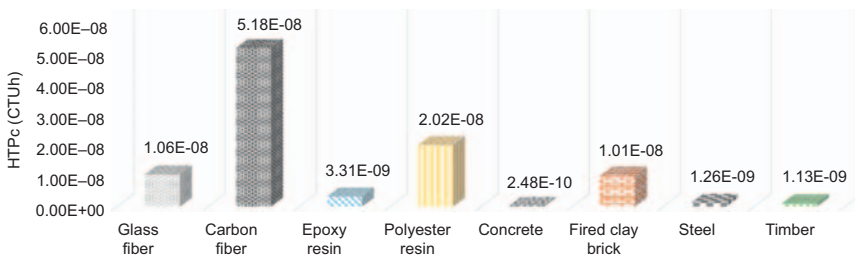


Figure 24.3 Results for the Human toxicity potential, cancer (HTPc) parameter.

carbon is included in the analysis, the timber elements have a negative carbon footprint. Taking into account that, at the moment, there is an outgoing debate regarding the consideration of the biogenic carbon in the analysis of wood products by using the GWP parameter, the authors have decided to present the resulted values in both cases. Excluding biogenic carbon from the assessment equates with timber having a higher negative effect compared with concrete and fired clay bricks.

In the case of the Human Toxicity impact category (Fig. 24.3), the carbon fiber and the polyester resin have the highest impact. Also, it can be observed that, from the considered traditional building materials, the fired clay bricks present the most significant level of negative effects over human health. The same situation is met in the case of the Ozone depletion potential (ODP) parameter (Fig. 24.4), the fired clay bricks having the most negative effect from the materials commonly used in this sector. At the same time, their impact over the stratospheric ozone layer is lower than the one of the glass fiber and epoxy resin.

At first glance, analyzing the resulting values for the production phase may lead to the conclusion that composite materials are of no use in the sustainable development of the construction sector. Notwithstanding, it must be considered that by using a small amount of FRP materials in specific construction applications, a significant volume of traditional materials can be successfully replaced, therefore improving the environmental performances of the construction sector.

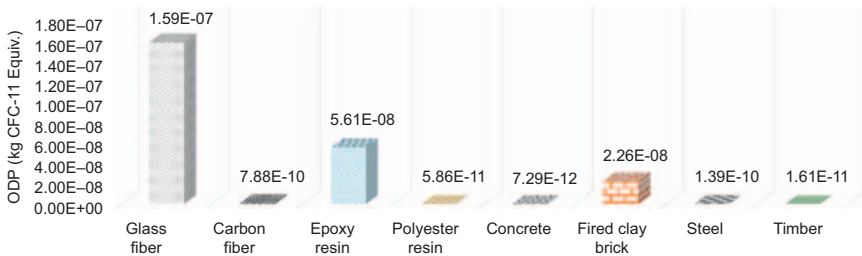


Figure 24.4 Results for the Ozone depletion potential (ODP) parameter.

24.3 Fiber-reinforced polymers for the rehabilitation of reinforced concrete members

Fiber-reinforced polymer composite materials consist of strong and stiff fibers embedded and bonded to a low modulus continuous polymeric matrix. The individual phases, fibers and matrix, are separated by a clear interface, retaining their identities and producing a combination that cannot be provided by any constituent acting individually (Agarwal et al., 2006). The reinforcing fibers constitute the backbone of the material, determining its strength and stiffness in the direction of the fibers. The polymeric matrix binds together the fibers and protects their surfaces from damage during handling, fabrication, and service life. The interface has an important role in controlling the overall stress–strain behavior of the composites, determining the failure mechanisms and the fracture toughness, as well as the resistance of the FRP composite to corrosive environments.

Many FRP composites provide a combination of physical properties (low density, thermal insulation) and mechanical properties (strength/weight and stiffness/weight ratios) that are superior to those offered by metallic materials. The properties of an FRP composite depend on the direction of measurement: the strength and elastic modulus of a unidirectional fiber-reinforced polymer are maximum along the fibers and minimum in the direction perpendicular to fibers, with intermediate values at any other angle of measurement. Other properties such as thermal conductivity, coefficient of thermal expansion, or impact strength exhibit similar angular dependences (Mallick, 2008).

The anisotropic nature of FRP composites enables the tailoring of their properties according to the design requirements. Composite structures can be reinforced in the directions of maximum stresses, thus increasing the stiffness in the preferred directions. Most FRP composite materials behave elastically under tensile loading; however, depending on the type and magnitude of the load, FRP composite laminates with various stacking may undergo gradual deterioration, thus avoiding a catastrophic failure. Corrosion resistance is an important advantage of FRP composites. However, some FRPs absorb moisture from the environment, creating dimensional changes or internal stresses (Mallick, 2008). The degradation of FRP

composites may be caused by UV radiation, elevated temperature, and corrosive fluids, therefore appropriate protection by paint or coating should be provided.

24.3.1 Fibers

Fibers are used in polymeric composites because they are strong, stiff, and lightweight. These constituent materials are stronger than the original bulk material that constitutes the fibers, due to their filamentary form in which there are less surface flaws than in the bulk form. However, in the filamentary form, their strength data show a larger scattering. The selection of the fiber type, fiber volume fraction, and fiber orientation strongly influences the design characteristics of FRP composites and their costs. Table 24.2 shows the main types of fibers utilized to reinforce polymeric matrices that are commonly utilized in the strengthening solutions for traditional building materials.

Table 24.2 Typical properties of fibers for fiber-reinforced polymer (FRP) composites (fib, 2007)

Fiber Type	Density	Tensile strength	Young modulus	Ultimate tensile strain	Thermal expansion coefficient	Poisson's coefficient
	(kg/m ³)	(MPa)	(GPa)	(%)	(10 ⁻⁶ /°C)	
E-glass	2500	3450	72.4	2.4	5	0.22
S-glass	2500	4580	85.5	3.3	2.9	0.22
Alkali-resistant glass	2270	1800-3500	70-76	2.0-3.0	—	—
Carbon (high modulus)	1950	2500-4000	350-650	0.5	- 0.1... - 1.2	0.20
Carbon (high strength)	1750	3500	240	1.1	- 0.2... - 0.6	0.20
Kevlar 29	1440	2760	62	4.4	- 2.0 longitudinal	0.35
Kevlar 49	1440	3620	124	2.2	- 2.0 longitudinal	0.35
Kevlar 149	1440	3450	175	1.4	- 2.0 longitudinal	0.35
Technora H	1390	3000	70	4.4	- 6.0 longitudinal	0.35
Basalt (Albarrie)	2800	4840	89	3.1	59 radial 8	—

Fibers are used as continuous reinforcements in unidirectional composites by aligning them in an elementary layer called lamina or ply. A unidirectional lamina has maximum values of mechanical properties (strength and modulus) along the fibers' direction and minimum values in the direction normal to the fibers' orientation. When balanced properties are required in two perpendicular directions, orthogonal bidirectional reinforcement is used, and when the same properties are needed in every direction on the plane of lamina, randomly oriented fibers are used.

The desirable structural and functional requirements of the fibers in composite elements are: high elastic modulus for an efficient use of reinforcement; high ultimate strength and convenient elongation at tensile fracture; low variation of strength between individual fibers; stability of properties during handling and fabrication; uniformity of fiber diameter and surface; high toughness; durability; availability in suitable forms and acceptable cost (fib, 2007; Taranu et al., 2013).

The most common fibers used to make FRP reinforcing elements are glass, carbon aramid, and basalt (Chang 2001; Hollaway, 2011). Carbon and aramid fibers are anisotropic, with different values for their mechanical and thermal properties in the main directions, whereas glass fibers and basalt fibers are isotropic (Gay and Hoa, 2007; Gibson, 2012). All these fibers exhibit a linear elastic behavior under tensile loading up to failure (Fig. 24.5).

24.3.1.1 Glass fibers

Glass fibers are the most commonly used reinforcing fibers for polymeric matrix composites. The main advantages that enable the widespread of glass fibers in composites are high strength, good chemical resistance, availability, good handleability, ease of processing, and competitive price, while the chief disadvantages are low stiffness, sensitivity to abrasion during handling, and low fatigue resistance.

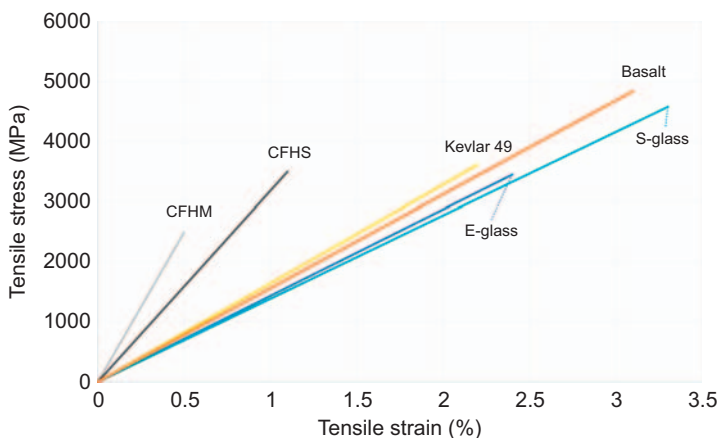


Figure 24.5 Tensile stress–strain diagrams for various reinforcing fibers.

The structure of glass is a three-dimensional network of silicon, oxygen and other atoms, randomly distributed, making glass fibers amorphous and isotropic (Mallick, 2008). The fabrication process of glass fibers requires the following phases: the ingredients of the glass formulation are dry mixed and melted in a furnace, after which this molten material is pushed through a bushing and drawn into filaments. A protective size is then applied on the filaments until they are gathered together into a strand and wound on a drum. The protective size is a mixture of lubricants, antistatic agents, and a coupling agent to improve the wetting of fibers by the matrix and provide better adhesion between the composite constituents. Coating the glass fibers with a coupling agent will provide a flexible layer at the interface, while also improving the strength of the bond the reducing the number of voids in the material.

The most common glass fibers are made of E- and S-glass. E-glass is the least expensive of all glass types and has a wide application in the fiber-reinforced plastic industry. S-glass has higher tensile strength and higher modulus than E-glass. However, the higher cost of S-glass fibers makes them less popular than E-glass. Alkali-resistant glass fibers contain an amount of zirconium which helps prevent corrosion by alkali attacks in cement matrices. The main properties of E-glass, S-glass, and Alkali-resistant glass are summarized in Table 24.2.

The original tensile strength of freshly drawn fibers decreases due to surface damage caused by abrasion. The tensile strength of glass fibers lowers at elevated temperatures but can be considered constant for the range of temperatures at which FRP composites can be exposed to. Tensile strength also reduces with chemical corrosion and with time under sustained loads that accelerate the growth of surface flaws and induce static fatigue.

To facilitate the fabrication of glass fiber-reinforced polymer membranes, strips and plates for structural rehabilitation of concrete members, the glass fibers are incorporated into the architectural forms illustrated in Figs. 24.8–24.11.

24.3.1.2 Carbon fibers

Carbon and graphite fibers can be fabricated with a large variety of tensile strengths and tensile moduli. Graphite fibers have carbon contents exceeding 99% and exhibit high elastic moduli, while carbon fibers have carbon contents between 93% and 95% (Campbell, 2010). The main advantages of carbon fibers are high strength-weight ratios, high modulus-weight ratios, very good fatigue strength, and excellent corrosion resistance. The tensile modulus and strength of carbon fibers are stable as temperature rises; they are also highly resistant to aggressive environmental factors.

The key disadvantages of carbon fibers are: they behave elastically to failure and fail in a brittle manner, while also being 10–30 times more expensive than E-glass. The high cost of these fibers is caused by the high price of raw materials and the long process of carbonization and graphitization. Moreover, graphite fibers cannot be easily wetted by the matrix, therefore sizing is necessary before embedding them in the matrix.

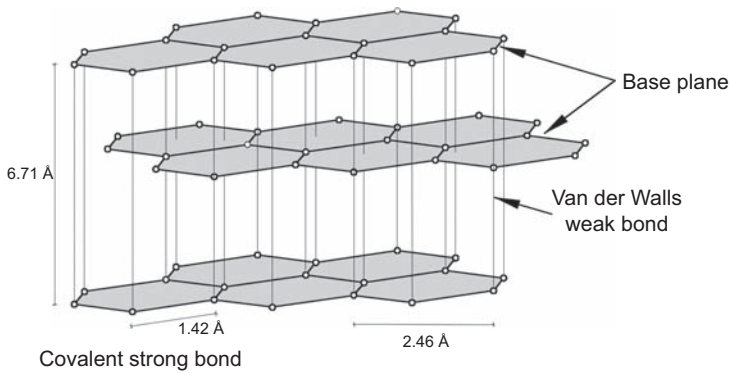


Figure 24.6 Crystal structure of graphite (Matthews and Rawlings, 2008)

Carbon fibers include amorphous carbon and graphitic carbon; their high modulus is given by the graphitic form in which carbon atoms are arranged in a regular crystallographic structure of parallel layers (Fig. 24.6).

The basal planes, with strong covalent bonds between the carbon atoms, are aligned along the fiber axis, while the bonds between the planes due to van der Waals forces are much weaker. This arrangement results in highly anisotropic properties for the carbon fibers with large differences between elastic moduli in the longitudinal and transverse directions (Gay and Hoa, 2007).

As presented in the previous section, in order to produce carbon and graphite fibers, different precursors are used; it is known that the most of these fibers are made from polyacrylonitrile (PAN). The fabrication process is divided into the following stages (Campbell, 2010): stretching the PAN copolymer to obtain a fiber; stabilization and oxidation at 200–300°C under tension; carbonisation in an inert atmosphere at 1000–1600°C; graphitization 1980–3040°C; surface treatment, and sizing. At about 1600°C, the filaments have the highest tensile strength but a relatively low tensile modulus. When the temperature of the heat treatment exceeds 2000°C, the structure of the filaments turns into a graphitic form (Mallick, 2008). As shown in Fig. 24.7, at this stage, the graphitized filaments reach a high modulus whilst the tensile strength decreases.

Two types of PAN carbon fibers, namely high strength (HS) and high modulus (HM), are commonly utilized to make FRP composites for the structural rehabilitation of civil engineering structures (Table 24.2). Carbon fibers are commonly available for structural strengthening in the architectural forms illustrated in Figs. 24.8–24.11.

24.3.1.3 Aramid fibers

Among the fibers currently utilized in FRP composites, these type of fibers can exhibit the highest tensile strength to weight ratio and the best resistance to impact damage. Aramid fibers have a level of strength and stiffness intermediate between glass fibers and carbon fibers. These fibers absorb a large amount of energy during

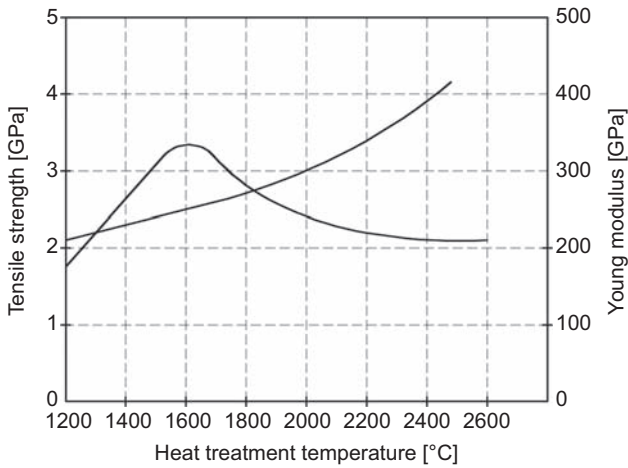


Figure 24.7 Effect of heat treatment temperature on strength and modulus of carbon fibers produced from PAN (Mathews and Rawlings, 2008).

fracture, undergo plastic deformation in compression, and defibrillate during tensile fracture. Aramid fibers have excellent toughness and are resistant to most solvents, but have a strong tendency to absorb moisture. They are degraded by UV radiation and are prone to stress rupture under static loading (Campbell, 2010).

Aramid fibers are fabricated by extruding a precursor through a spinneret. During the filament drawing process, the aramidic molecules become highly oriented in the direction of the filament axis. In the transverse direction, the molecules are held together by weak hydrogen bonds. As a result, the filament has much better properties in the longitudinal direction than in the radial direction.

Aramid fibers are currently produced by DuPont (Kevlar), Teijin (Technora), and Akzo Nobel (Twaron). Kevlar fibers are produced by extruding the liquid crystalline solution of the polymer with partially oriented molecules. Kevlar is an aromatic polyamide with rigid aromatic rings. There are several types of Kevlar fibers: Kevlar 29 (for composites with maximum impact and damage tolerance), Kevlar 49 (used in reinforced plastics), and Kevlar 149 (with the highest tensile modulus among all available aramid fibers). The compressive strength of Kevlar fibers is less than 20% of their tensile strength. Kevlar 49 has brittle behavior under tension, but under compressive load it is ductile, metal-like, and absorbs a large amount of energy. It also shows a large degree of yielding on the compression side when subjected to bending. This type of behavior, not observed in glass or carbon fibers, gives Kevlar composites better impact resistance. Kevlar has very good tension fatigue resistance, low creep, and can withstand relatively high temperatures. The strength and modulus of Kevlar fibers decrease linearly when the temperature rises, but they retain more than 80% of their original strength at 180°C. The typical properties of aramid fibers are given in Table 24.2 and fiber reinforcements are shown in Figs. 24.8–24.11.

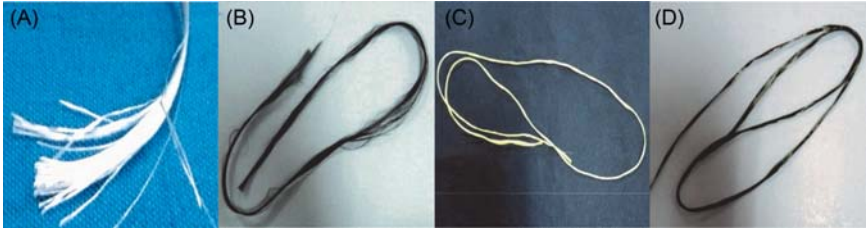


Figure 24.8 Strands of fibers. (A) Glass strand, (B) Carbon tow, (C) Aramid strand, (D) Basalt strand (Taranu et al., 2013).

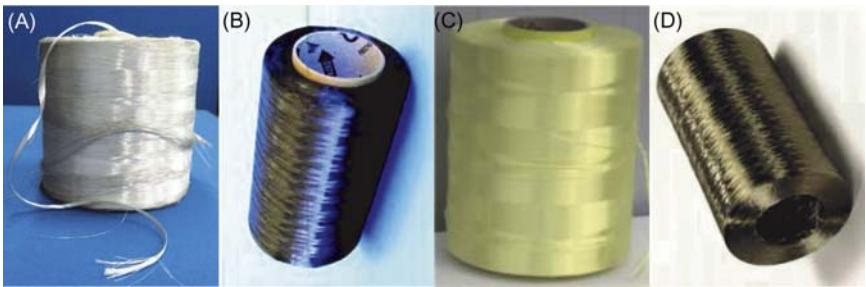


Figure 24.9 Rovings. (A) Glass roving, (B) Carbon roving, (C) Aramid roving, (D) Basalt roving (Taranu et al., 2013).

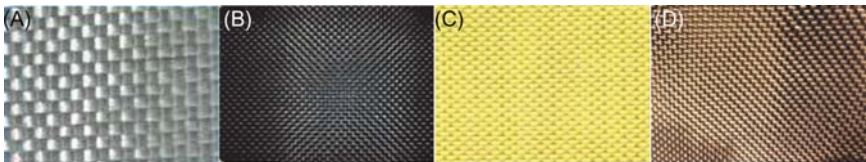


Figure 24.10 Woven fabrics. (A) Glass fabric, (B) Carbon fabric, (C) Aramid fabric, (D) Basalt fabric (Taranu et al., 2013).

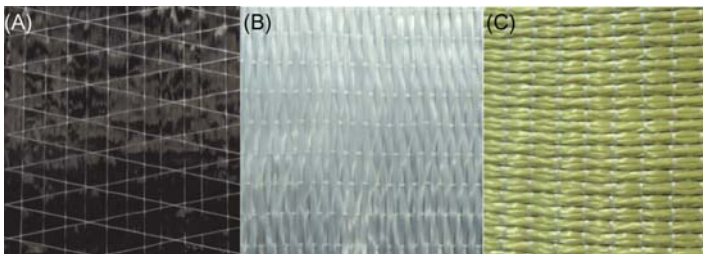


Figure 24.11 Unidirectional fabrics. (A) Carbon fabric, (B) Glass fabric, (C) Aramid fabric (Taranu et al., 2013).

24.3.1.4 Basalt fibers

Basalt fibers are fabricated by melting crushed basalt rocks at 1400°C and drawing the molten material. Basalt fibers have better mechanical and physical properties than glass fibers, their main advantages being: fire resistance, good resistance to chemically active environments, vibration and acoustic insulation capacity (fib, 2007). The improved production facilities and quality control capacity enable fabrication of basalt fibers with high quality and low variability of properties (Matthys, 2014). Basalt fibers are more expensive than E-glass fibers, but much cheaper than carbon fibers. Some typical properties of basalt fibers are given in Table 24.2, while the architectural forms of these fibers are illustrated in Figs. 24.8–24.11.

24.3.1.5 Forms of reinforcement for fiber-reinforced polymer composites

All fiber types are available in a number of forms and fiber architectures, corresponding to manufacturing procedures, but also depending on the requirements of FRP composites for structural rehabilitation. A short description of the various forms of fiber reinforcements is given in the following sections.

The smallest unit of fibrous reinforcement is the filament, which is an individual fiber as drawn during fabrication. Individual filaments cannot be used as reinforcement, so they are gathered into strands of fibers for use in composites. Strands are bundles of individual untwisted filaments made of glass, aramid or basalt (Fig. 24.8A,C,D) while in the case of carbon fibers, the bundle is called a tow (Fig. 24.8B). Yarns are closely associated bundles of twisted filaments, continuous strands of fibers, or strands in a form suitable for weaving or other textile processes (Balaguru et al., 2009).

Roving is a loosely assembled bundle of untwisted parallel strands or tows without twisting (Fig. 24.9). Rovings are preferred for many reinforcements because they have higher mechanical properties than twisted yarns.

Woven fabrics are two-dimensional assemblies that have the form of flat sheets of one or more layers of fibers (Fig. 24.10). The layers are held together by mechanical interlocking or with secondary materials that bind fibers together and hold them in place. The fibers are oriented at 0 degrees and 90 degrees. Most weaves contain similar numbers of fibers and use the same material in both directions. Another solution is represented by the hybrid fabrics that can be used to obtain specific properties, e.g., mixing carbon with aramid combines the stiffness provided by carbon fibers with the toughness of aramid, while mixing glass with carbon fibers reduces the cost of reinforcement.

Unidirectional fabrics, shown in Fig. 24.11, are made with a weave pattern designed for strength and stiffness in only one direction. A high strength modulus material like carbon/graphite fiber is sometimes utilized in this form for specific applications, such as the strengthening of reinforced concrete (RC) members. Unidirectional fibers are commonly manufactured in narrow rolls.

24.3.2 Polymeric matrices

In general, a polymer is called a resin system during processing and a matrix after the polymer has cured (fib, 2007). The matrix in FRP composites can be regarded as a structural or a protection component. The selection of a polymer matrix is mainly based on its basic mechanical properties such as strength, modulus of elasticity, and fracture toughness. Other characteristics such as resistance to moisture, as well as dimensional stability at exploitation temperatures may be considered in the case of FRP composites used in structural rehabilitation.

The main functions of a matrix in an FRP composite are: binding the reinforcements together; transferring stresses to the fibers; protecting the reinforcements from environmental and mechanical abrasion; providing the composite with a solid form, which aids handling during manufacture and is typically required in a finished part; having a decisive influence on the compressive strength, interlaminar shear, and in plane shear properties; controlling the transverse properties; enabling the strength of the fibers to be used to their full potential by providing effective load transfer from external forces to the reinforcement; holding reinforcing fibers in the proper orientation; distributing the loads more or less evenly among the fibrous reinforcement; enabling the redistribution of the internal stresses from broken fibers; determining the thermal stability and maximum temperature use of the FRP composite. There are two basic classes of polymeric matrices used in FRP composites: thermosetting and thermoplastics resins. The thermosetting polymers are those which form the matrix material of FRP composites used in the rehabilitation of structures (Hollaway, 2011).

Thermosetting resins are polymers which are irreversibly formed from low molecular weight precursors of low viscosity. In thermosetting polymers, the molecules are chemically linked by cross-links that form a three-dimensional network. These polymers have strong bonds both in and between the molecules. If they are heated after the curing process, they do not melt and will retain their shape until they begin to thermally decompose at high temperature. The most common thermosetting resins for FRP composites are epoxies, polyesters, and vinyl esters; their typical properties are given in Table 24.3.

Thermosetting resins have initial low viscosity, allowing for high fiber volume fractions to be incorporated. The three-dimensional network of thermosets results in less flow under stress, better dimensional stability, lower coefficient of thermal expansion, and greater resistance to solvents. However, thermosetting polymers have a limited storage life, require long fabrication time, and low failure strain which results in low impact resistance. The cure cycles can take place at room temperature or at high temperature. The reactions are exothermic and gelation is usually rapid. Once cured, the mixture thickens, releases heat, solidifies, and shrinks. The volumetric shrinkage upon curing varies between 1% and 4% for epoxy and 5%–15% for polyester, with intermediate values for vinyl ester (Mallick, 2008). The fiber reinforcement does not shrink, therefore internal stress can be induced, causing cracking, fiber misalignment, and dimensional inaccuracy.

Table 24.3 Typical properties for thermosetting matrices (fib, 2007)

Property	Matrix		
	Polyester	Epoxy	Vinyl ester
Density (kg/m ³)	1200—1400	1200—1400	1150—1350
Tensile strength (MPa)	34.5—104	55—130	73—81
Longitudinal modulus (GPa)	2.1—3.45	2.75—4.10	3.0—3.5
Poisson's coefficient	0.35—0.39	0.38—0.40	0.36—0.39
Thermal expansion coefficient (10 ⁻⁶ /°C)	55—100	45—65	50—75
Moisture content (%)	0.15—0.60	0.08—0.15	0.14—0.30
Service temperature (°C)	155	185	120

24.3.2.1 Epoxy matrix

Epoxy resins define a family of matrices that provide better performances compared to other polymeric resins (Balaguru et al., 2009). Epoxies are the dominant resins used for low and moderate temperatures (Campbell, 2010). The term refers to a class of thermosetting resins prepared by the ring-opening polymerization of compounds containing an average of more than one epoxy group per molecule.

The primary advantages of epoxy resins are: a wide range of material characteristics, high mechanical properties, easy processing, low shrinkage during cure, and good adhesion to all types of fibers. Epoxies have high corrosion resistance and are less affected by water and heat than other polymeric matrices. The main disadvantage of epoxy resins are their relatively high cost, long curing time, and handling difficulties. The representative properties of the epoxy matrix are given in Table 24.3.

24.3.2.2 Polyester matrix

Polyester resins are the most economical resin systems used in engineering applications, but with limited use in high performance composites. They can be produced for a large variety of properties, from soft and ductile to hard and brittle (Balaguru et al., 2009). The principal advantages of polyesters are: low cost, low viscosity, and a relatively short curing period. However, polyesters have lower mechanical properties than other thermosets, inferior weathering resistance, and high shrinkage. This volumetric shrinkage can be reduced by adding a thermoplastic component. Polyester resins can be formulated to cure at either room or elevated temperatures and can enable great versatility in processing operations (Campbell, 2010). Table 24.3 gives some of the typical properties of a polyester matrix.

24.3.2.3 Vinyl ester matrix

Vinyl esters are similar to polyesters, but due to their chemical structure, these resins have fewer cross links, they are more flexible, and have a higher fracture

toughness than polyesters. They also have very good wet-out and good adhesion features when reinforced with glass fibers. The properties of vinyl esters are a good combination of those given by epoxy resins and polyesters. They combine some of the good characteristics of epoxies, such as chemical resistance and tensile strength, with those of polyesters, such as viscosity and fast curing. However, their volumetric shrinkage (4%–12%) is higher than that of epoxy, and they have only moderate adhesive strength compared to epoxy resins. Vinyl ester resins are highly resistant to acids, alkalis, solvents, and peroxides. Their main properties are given in [Table 24.3](#).

24.3.3 Manufacturing techniques of Fiber reinforce polymer composites for strengthening reinforced concrete beams

There are various manufacturing options of FRP composites available and they have been developed to suit the variety of production parameters. However, two basic techniques are available for the manufacturing of FRP polymer composites used in the external reinforcing of RC beams: the manual production process (hand lay-up) and the automated process (pultrusion). Each technique has an important effect on the performance of the composite product. The choice of a manufacturing process depends on the type of matrix and fibers, the temperature required to form the part and cure the matrix, and the cost effectiveness of the process. The following operations are involved in any manufacturing process of a FRP composite element: fiber placement along the required orientation; impregnation of the fiber with the resin; consolidation of the impregnated fibers to remove excess resin, air, and volatiles; solidification of the polymer; extraction from the mold (in case of pultrusion); finishing operations ([Barbero, 2011](#)).

24.3.3.1 The manual procedure

This is the simplest procedure used for the manufacturing of fiber-reinforced polymeric composite components; it consists of the following steps ([Hollaway, 2011](#)):

- applying a first layer of polymeric resin plus curing agent (acting as an adhesive and as the matrix of the FRP composite) on the prepared concrete surface;
- laying a first layer of fibrous reinforcement, cut to size, over the thermosetting resin and pressing down onto the surface with the aid of a brush and a roller to eliminate the entrapped air between the fibers and the polymer;
- applying subsequent layers of resin and reinforcement until the required thickness of the FRP composite membrane is reached;
- curing the lay-up at ambient temperature, seeing as the procedure is an on-site operation.

This process has the advantage of using minimum equipment, but the labor cost is high and the quality of the composite product depends to a large extent on the workers' skill. For composite parts manufactured in the field, the fiber volume fractions range from 25% to 40%. The tensile strength of composites made using unidirectional carbon fibers could vary from 800 to 1000 MPa ([Balaguru et al., 2009](#)).

24.3.3.2 *The pultrusion technique*

Pultrusion is a continuous fully automated manufacturing process, which allows the production of long, straight constant section structural shapes made of fiber-reinforced polymeric composites. The FRP plates for bonding to the soffit of the element (for the plate bonding solution of flexural strengthening), the rods, or other shapes for near surface mounted (NSM) composite reinforcing elements, are fabricated using a hot-cure resin.

The constituent materials are: a liquid resin mixture (containing resin, fillers, and specialized additives), and flexible textile reinforcing fibers. The process involves pulling these raw materials through a heated, steel forming die, by using continuous fiber forms such as rolls of roving or rolls of mats. As the reinforcements are preimpregnated and saturated with the resin mixture in the resin bath and pulled through the die, the hardening phase of the resin is initiated by heat from the mold. On exiting the die, the cured profile is pulled to the saw in order to be cut to the desired length. In general, pultrusion is dominated by the use of unidirectional reinforcement, which lends itself most appropriately to the process and gives maximum strength and stiffness in the axial direction of the composite product.

When the FRP pultruded plates are used for the rehabilitation of RC beams, a roughened surface is required on the side of the pultruded element to be bonded to the concrete surface. This roughened surface can be provided by using a peel-ply on the bonding side (Hollaway, 2011). The peel-ply is stripped from the pultruded surface prior to bonding to the adherent, thus ensuring a clean surface to the composite plate. Pultruded products for the plate bonding are currently reinforced with carbon, glass, aramid, and basalt fibers embedded in epoxy, vinyl ester, and polyester polymeric resins. Fiber volume fraction for factory-made composite elements varies from 60% to 70%. For factory-produced sheets, the tensile strength of polymer composites reinforced with unidirectional carbon fibers can reach 3500 MPa. For glass fiber composites, the tensile strength of unidirectional sheets ranges from 500 to 1400 MPa, and for aramid fibers the range of strength is 700–1700 MPa (Balaguru et al., 2009).

24.4 **Strengthening solutions for reinforced concrete beams**

RC beams may become structurally deficient and in need of strengthening to enable their continuous use. The structural deficiency of RC beams, in terms of flexural capacity, may occur due to structural degradation (corrosion of the internal reinforcing steel, carbonation of the concrete, design, or construction errors, inappropriate alterations during maintenance) or changes in the use (increased dead and live load, change in load path, new loading requirements, and application of modern design practice) (De Lorenzis et al., 2008).

To increase the flexural capacity of RC beams, the FRP composite oriented laminates are installed along the longitudinal axis of the load bearing element. The

composite laminates are bonded to the most-tensioned face of the beam. The externally bonded reinforcement (EBR) made of FRP composites is a supplementary strengthening in tension (Bolsamo et al., 2012). The process of attaching the EBR made of FRP composite to a prepared concrete surface consists of several phases (GangaRao et al., 2007):

- preparing the concrete surface to achieve a proper bondable surface between the adherents. The concrete substrate should be uniform and even; in the case of excessive cracking or uneven surfaces, a high viscosity polymer putty can be utilized as a filler;
- applying a primer (a low-viscosity polymer) coat to obtain a uniform bondable substrate. The primer bonds to both the resin applied on the FRP fabric and to the concrete surface;
- applying a polymeric resin layer to the concrete substrate. The resin wets the fabric and chemically bonds to the primer applied on the concrete substrate and the fabric.

A protective coating may be applied over the composite laminate to protect the EBR from environmental exposure effects and to enhance the fire ratings of the FRP strengthening solutions. Three main techniques are utilized to attach FRP composite materials to RC beams for strengthening purposes (Bank, 2006). One method, known as wet lay-up, consists of in-situ forming of the FRP composite on the surface of the RC beam, using flexible dry fiber fabrics, or sheets and liquid polymers (Fig. 24.12).

The wet lay-up systems are commonly utilized in the field. In this system, the fibers are impregnated and saturated with resin at the site and cured in-situ, at ambient temperatures, resulting in an FRP composite laminate. The fiber reinforcement can be in the form of unidirectional or multidirectional fabrics. As stated previously, the fiber fabric is placed on top of the primer, then impregnated with polymeric resin by spreading it over the fabric. Compaction is performed with an aluminum roller to remove entrapped air and excess resin. The entire length of the laminate is checked for defects during and after placement (Lee, 2011).

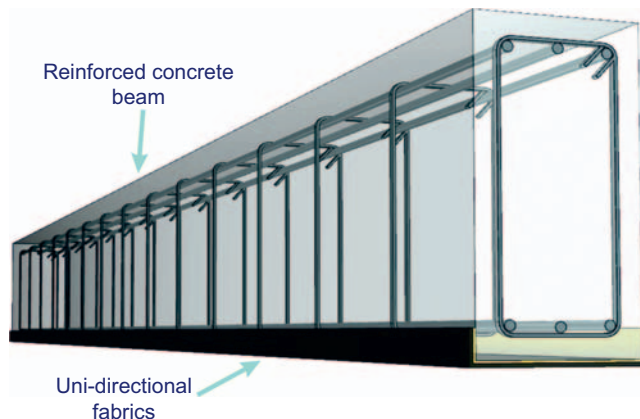


Figure 24.12 The wet lay-up strengthening technique of reinforced concrete (RC) beams.

Another method, known as plate bonding, employs FRP composite pultruded plates or strips bonded to the most-tensioned side of the strengthened element (Fig. 24.13). As in the wet lay-up system, the concrete substrate must be properly prepared in order to obtain a bondable surface before the installation of the pultruded composite plate. A two-component epoxy adhesive is mixed and applied to the surface of concrete and prefabricated composite plate. The composite plate is bonded by applying pressure in a continuous manner from one end of the pultruded plate to the opposite, in the fiber direction. Typically, uniform pressure is applied on the composite plate using a roller, and excess adhesive is removed using a squeegee edge (Lee, 2011). The application of FRP composite pultruded plates for the strengthening of RC beams has been extensively researched in the past 25 years, the results of which are found in many well-known works (Teng et al., 2001; Taljsten, 2003; Bank, 2006; GangaRao et al., 2007; Hollaway and Teng, 2008; Karbhari and Lee, 2011).

An alternative method to the externally bonded techniques mentioned above is the NSM technique, presented in Fig. 24.14. In this method, narrow FRP strips, or

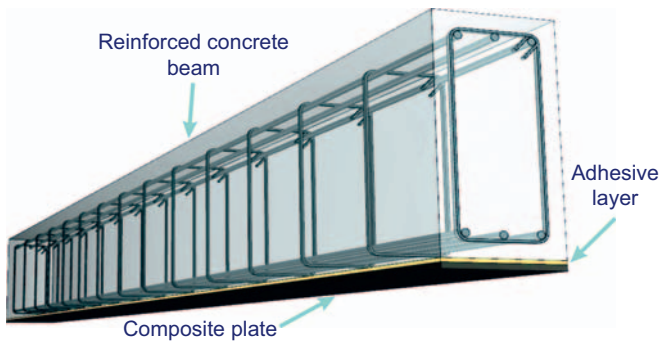


Figure 24.13 The plate bonding strengthening technique of reinforced concrete (RC) beams.

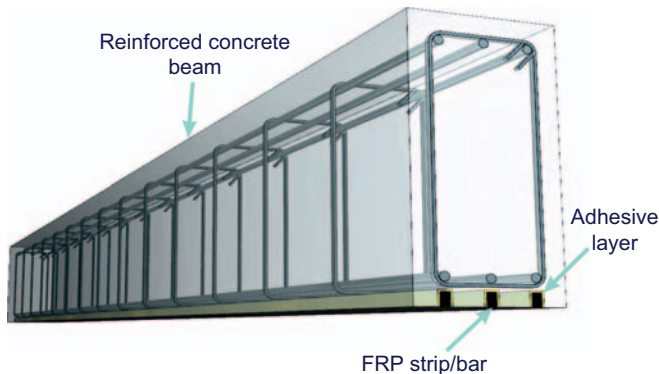


Figure 24.14 The near surface mounted strengthening technique of reinforced concrete (RC) beams.

small-diameter round FRP bars are inserted into precut grooves in the soffit of flexural beams. The grooves are then filled with a high viscosity adhesive. The NSM technique offers some important advantages (Hollaway, 2011; Kotynia, 2012): minimum installation time compared to the FRP plate bonding, since no surface preparation work other than growing is required; the grooves can be cut in one pass if customized growing tools are utilized; the technique is recommended when strengthening in the negative moment region; a significant decrease of the fire damage risk, vandalism, and aging effects compared with the plate bonding method; the embedded system requires minimal intervention and provides protection from the external environment; this technique does not change the aesthetics of the structural member; a significant increase in the load bearing capacity, sectional stiffness, and FRP strain utilization is obtained; the enlarged contact surface of NSM FRP and concrete improves the FRP efficiency and delays the concrete debonding.

However, this technique has some disadvantages that should not be neglected: the danger of cutting the shear link rods or the longitudinal steel reinforcement; the possibility of debonding at the ends of the rods or strips; the bonding between concrete and FRP strips/rods is located in the concrete cover (the weakest part of RC beams).

24.5 Life cycle analysis of carbon fiber-reinforced polymer strengthening solutions

As stated before, in the developed countries, the situation of the existing building stock will represent a major environmental issue. The entire life cycle of a structure, presented in Fig. 24.15, has an important impact over the natural environment. Consequently, in the case of an existing construction that surpassed the designed life span and/or no longer presents a certain structural safety to the users,

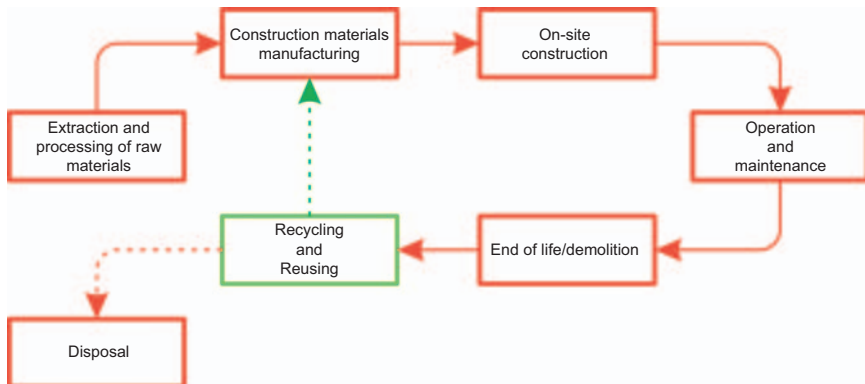


Figure 24.15 Life cycle of a structure (Maxineasa et al., 2015).

demolishing and replacing this structure with a new one will result in wasting all the environmental investments (i.e., the cumulative impact over the natural environment over the life cycle of the product) of the old building. Furthermore, this impact will affect the performances of the new construction by increasing its environmental output in an artificial way.

Taking into account all that mentioned previously, the LCA studies presented in the following section had the primary goal of assessing the environmental implications resulting from using FRP composites, by determining what is the most environmentally friendly solution in the case of an existing RC beam that does not present a proper level of safety (i.e., to strengthen and reuse the existing beam or to demolish the element and construct a new one). In order to fulfill this aim, the environmental impact of a new, unstrengthened RC beam has been assessed and compared with the impact of different carbon fiber-reinforced polymer (CFRP) flexural strengthening solutions. This assessment represents an updated and more complex examination of the research conducted during the PhD programme by [Maxineasa \(2015\)](#), also briefly discussed in [Maxineasa et al. \(2015\)](#).

The examined products have been assessed by using the cradle-to-gate with options LCA type of study, considering the following life cycle stages/modules, according to EN 15804 ([EN, 2013](#)):

- A1—raw material extraction and processing of secondary material input
- A2—transport to the manufacturer
- A3—manufacturing
- A4—transport to the building site
- A5—installation into the building.

The primary reason behind choosing this type of LCA study is the lack of accurate information regarding the operation and postoperation stages from the life cycle of the FRP materials used in different construction applications (e.g., the recycling of the thermoset matrices still represents a big challenge). Taking into account the fact that one of the most important goals of an LCA study is to analyze and consider data with a low level of uncertainties, the authors have decided to only consider the preoperation stage from the life cycle of the analyzed products.

24.5.1 Case studies

Six case studies have been considered, each assessing the following construction products:

- Case study 1: Unstrengthened RC beam cast of C20/25 concrete;
- Case study 2: First scheme of the EBR strengthening technique, consisting of one $1.4 \times 36 \times 2600$ mm CFRP strip;
- Case study 3: Second scheme of the EBR strengthening technique, made of one $1.4 \times 72 \times 2600$ mm CFRP strip;
- Case study 4: First scheme of the NSM strengthening technique, consisting of two $1.4 \times 18 \times 2600$ mm CFRP strips;

- Case study 5: Second scheme of the NSM strengthening technique, consisting of three $1.4 \times 12 \times 2600$ mm CFRP strips;
- Case study 6: Third scheme of the NSM strengthening technique, consisting of three $1.4 \times 24 \times 2600$ mm CFRP strips.

The behavior of the assessed products has been analyzed during an experimental programme developed at the Faculty of Civil Engineering and Building Services, Gheorghe Asachi Technical University of Iasi, Romania. The amounts of the constituent materials considered for assessing the environmental performances of the unstrengthened RC beam and FRP strengthening solutions are presented in Table 24.4. In the analyzes, the epoxy adhesive used for applying the carbon elements has been replaced with epoxy resin. The transportation stages were simulated by using a EURO 6 diesel truck with 3.3 tons payload capacity; the transport distances are presented in Table 24.5. Different electricity consumption values have been considered in the analyses in order to take into consideration the pultrusion process and the surface preparation life cycle stages corresponding to the FRP strengthening schemes.

Table 24.4 Amount of component materials used in the studies (Maxineasa, 2015; Maxineasa et al., 2015)

Component material	Quantity (kg)					
	Case no. 1	Case no. 2	Case no. 3	Case no. 4	Case no. 5	Case no. 6
Fine aggregate (<3 mm)	122.4	—	—	—	—	—
Coarse aggregate (> 3 mm)	228.6	—	—	—	—	—
Cement (CEM II 32.5)	54	—	—	—	—	—
Steel reinforcement	16.39	—	—	—	—	—
Water	27	—	—	—	—	—
Carbon fibers	—	0.1434	0.2868	0.1434	0.1434	0.2868
Epoxy resin	—	0.0675	0.135	0.0675	0.0675	0.135
Epoxy adhesive paste	—	0.328	0.655	0.882	0.772	1.544

Table 24.5 Distances considered in the transportation stages (Maxineasa, 2015; Maxineasa et al., 2015)

Component material	Distances (km)	From→To
Fine aggregate (<3 mm)	30	Quarry—concrete mixing plant
Coarse aggregate (> 3 mm)	30	Quarry—concrete mixing plant
Cement (CEM I 52.5)	165	Quarry—concrete mixing plant
Steel reinforcement	10	Steel mill—concrete mixing plant
Concrete	15	Concrete mixing plant—construction site
CFRP strips	1850	Manufacturing unit—construction site
Epoxy adhesive paste	1850	Manufacturing unit—construction site

The environmental analyses have been performed by using the GaBi software, operating the Ecoinvent v3.3 and GaBi databases. The environmental performances of the assessed construction products have been quantified by using the impact categories (using the midpoint approach) presented in Table 24.6. Aside from the “Land use” and “Ionizing radiation, ecosystems,” the study considers all indicators listed in the recommended methods list of the European Commission—Joint Research Center—Institute for Environment and Sustainability (2011). In addition, the nonlegislative act L124 2013/179/EU has been taken into account in the analysis. In order to have a better understanding of the impact of different life cycle phases of the overall product’s environmental performances for every considered impact category, the resulted values are presented in a tabular format.

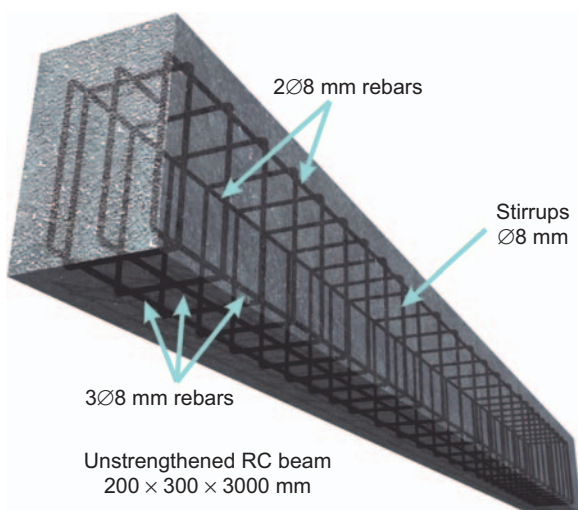
Table 24.6 Considered impact categories

Impact category	Parameter	Unit	Methodology
Acidification	Accumulated exceedance (AE)/Acidification potential	mole of H ⁺ eq.	Accumulate exceedance model/ ILCD 2011
Global warming (climate change)—excluding the biogenic carbon	Radiative forcing global warming potential (GWP)	kg CO ₂ – eq.	IPCC
Ecotoxicity for aquatic freshwater	Ecotoxicity potential	CTUe	USEtox
Aquatic eutrophication, freshwater	Potentially disappeared fraction of species (PDF)	kg P eq.	ReCiPe
Aquatic eutrophication, marine	Expression of the degree to which the emitted nutrients reaches the marine end compartment	kg N eq.	ReCiPe
Terrestrial eutrophication	AE	mole of N eq.	Accumulate exceedance model/ ILCD 2011
Human toxicity, cancer effects	Human toxicity potential, cancer (HTPc) effects	CTUh	USEtox
Human toxicity, noncancer effects	Human toxicity potential, noncancer effects (HTPnc)	CTUh	USEtox
Ionizing radiation, human health	Ionizing radiation potential (IRP)	kBq U-235	ReCiPe
Ozone depletion	Depletion potential of the stratospheric ozone layer/ Ozone depletion potential (ODP)	kg CFC-11 eq.	ReCiPe

(Continued)

Table 24.6 (Continued)

Impact category	Parameter	Unit	Methodology
Particulate matter/ Respiratory inorganics	Intake fraction for fine particles/Particulate matter potential	kg PM 2.5 eq.	RiskPoll
Photochemical ozone formation, human health	Photochemical ozone creation potential (POCP)/ Maximum incremental reactivity (MIR)	kg NMVOC	ReCiPe
Resource depletion, water	Freshwater scarcity/Biotic resource depletion potential	m ³ eq.	Swiss Ecoscarcity
Resource depletion, mineral, fossils and renewables	Scarcity of mineral resources/Abiotic resource depletion	kg Sb-eq.	CML2002

**Figure 24.16** Assessed product in Case study 1 (Maxineasa, 2015; Maxineasa et al., 2015).

24.5.2 Assessing the environmental impact of the analyzed products

24.5.2.1 Environmental performances in Case study 1

The first case study assesses the environmental impact of an unstrengthened RC beam with a rectangular cross-section of 200 × 300 mm and a length of 3000 mm (Fig. 24.16).

The resulted values of the analysis are presented in Table 24.7. Considering all the environmental impact categories, cement can be said to have the most important

Table 24.7 Environmental impact in Case study 1

Impact category	Life cycle stages								
	Cement	Coarse aggregate	Fine aggregate	Water	Steel reinforcement	Mixing	Vibrating of concrete	Diesel	Transport
Acidification (mole of H ⁺ eq.)	0.0725	0.0038	0.0021	2.85E-05	0.0640	0.0683	0.0006	0.0010	0.0032
Global warming (climate change)— excluding the biogenic carbon (kg CO ₂ -eq.)	45.1835	0.5262	0.2848	0.0095	20.7781	7.0551	0.0644	0.1543	3.2898
Ecotoxicity for aquatic freshwater (CTUe)	0.6106	0.0770	0.0312	0.0025	5.0821	0.3045	0.0028	0.1706	8.86E-08
Aquatic eutrophication, freshwater (kg P eq.)	2.57E-05	5.63E-06	2.59E-06	7.23E-07	2.16E-05	1.14E-06	1.04E-08	6.12E-06	0
Aquatic eutrophication, marine (kg N eq.)	0.0010	0.0001	3.04E-05	3.59E-06	0.0001	9.88E-05	9.01E-07	0.0001	0.0016
Terrestrial eutrophication (mole of N eq.)	0.1947	0.0156	0.0082	0.0001	0.1218	0.0553	0.0005	0.0024	0.0180
Human toxicity, cancer effects (CTUh)	2.38E-08	3.37E-09	1.79E-09	8.37E-11	3.68E-08	6.33E-09	5.78E-11	6.77E-09	4.11E-13
Human toxicity, noncancer effects (CTUh)	1.69E-06	2.13E-07	9.27E-08	1.04E-09	3.95E-06	3.25E-07	2.97E-09	9.11E-08	1.04E-13
Ionizing radiation, human health (kBq U-235)	0.6471	0.0876	0.0469	0.0005	0.0359	0.9997	0.0091	0.0042	0
Ozone depletion (kg CFC-11 eq.)	3.35E-10	1.44E-10	7.70E-11	6.33E-13	1.82E-07	1.90E-09	1.73E-11	6.95E-12	0
Particulate matter/Respiratory inorganics (kg PM 2.5 eq.)	0.0022	0.0003	0.0002	1.92E-06	0.0050	0.0050	4.58E-05	4.16E-05	6.11E-05
Photochemical ozone formation, human health (kg NMVOC)	0.0570	0.0041	0.0022	2.03E-05	0.0432	0.0171	0.0002	0.0006	0.000622
Resource depletion, water (m ³ eq.)	0.0640	0.0031	0.0017	0.0045	-0.0115	0.1017	0.0009	0.0005	0
Resource depletion, mineral, fossils, and renewables (kg Sb-eq.)	1.98E-05	8.59E-07	4.39E-07	8.16E-10	-6.79E-05	1.31E-05	1.19E-07	4.02E-07	0

negative effect over the natural environment, being responsible for the highest values for six environmental parameters. Another component material with a great influence over the natural environment is represented by the steel reinforcement, though it must be noticed that it has a positive impact over the natural environment considering the last two parameters. Overall, the environmental performance of the unstrengthened RC beam is mainly influenced by the amount of cement and steel used, these materials having the highest impact in 11 out of 14 indicators.

24.5.2.2 Environmental performances in Case study 2

In the second case study, the environmental performances of the first EBR scheme presented in Fig. 24.17 have been evaluated. The analyzed strengthening solution consists of applying a carbon strip with 1.4×36 mm cross-section and a length of 2600 mm on the soffit of the RC beam by using epoxy adhesive.

Table 24.8 presents the values that describe the impact of the CFRP strengthening solution over the natural environment. It can be observed that the overall performances of the analyzed scheme are highly influenced by only three life cycle categories. The epoxy resin has the most important impact in seven of the considered categories, followed by the pultrusion process, with peak values for four parameters, and carbon fibers with maximum values in the case of three indicators.

24.5.2.3 Environmental performances in Case study 3

Case study 3 assesses the environmental impact of the second EBR strengthening technique scheme, presented in Fig. 24.18, consisting of bonding a carbon strip with a length of 2600 mm and a rectangular cross-section of 1.4×72 mm.

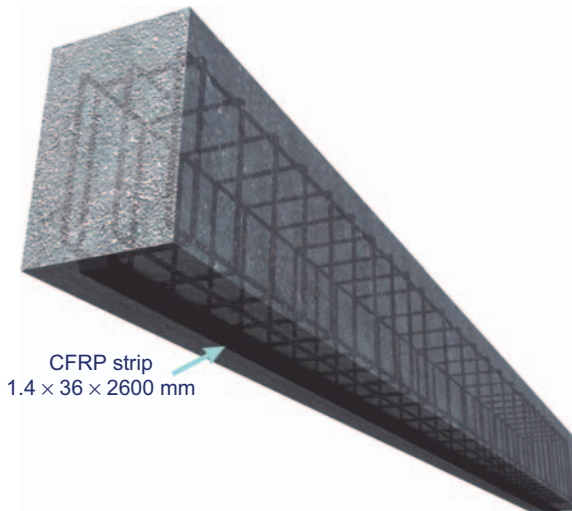


Figure 24.17 Assessed product in Case study 2 (Maxineasa, 2015; Maxineasa et al., 2015)

Table 24.8 Environmental impact in Case study 2

Impact category	Life cycle stages					
	Carbon fibers	Epoxy resin	Pultrusion process	Surface preparation	Diesel	Transport
Acidification (mole of H ⁺ eq.)	0.0063	0.0101	0.0172	0.0064	0.0002	0.0001
Global warming (climate change)—excluding the biogenic carbon (kg CO ₂ -eq.)	2.8689	3.2626	1.7823	0.6562	0.0231	0.1252
Ecotoxicity for aquatic freshwater (CTUe)	0.1674	0.0238	0.0769	0.0283	0.0256	3.36E-09
Aquatic eutrophication, freshwater (kg P eq.)	8.83E-06	7.09E-05	2.89E-07	1.06E-07	9.17E-07	0
Aquatic eutrophication, marine (kg N eq.)	0.0003	0.0021	2.49E-05	9.19E-06	1.79E-05	2.53E-05
Terrestrial eutrophication (mole of N eq.)	0.0213	0.0226	0.0140	0.0051	0.0004	0.0003
Human toxicity, cancer effects (CTUh)	7.43E-09	1.31E-09	1.60E-09	5.89E-10	1.02E-09	1.56E-14
Human toxicity, noncancer effects (CTUh)	5.55E-08	1.10E-07	8.22E-08	3.02E-08	1.37E-08	3.95E-15
Ionizing radiation, human health (kBq U-235)	0.2089	0	0.2525	0.0930	0.0006	0
Ozone depletion (kg CFC-11 eq.)	1.13E-10	2.22E-08	4.79E-10	1.77E-10	1.04E-12	0
Particulate matter/Respiratory inorganics (kg PM 2.5 eq.)	0.0002	0.0011	0.0013	0.0005	6.23E-06	1.10E-06
Photochemical ozone formation, human health (kg NMVOC)	0.0058	0.0062	0.0043	0.0016	9.01E-05	2.07E-05
Resource depletion, water (m ³ eq.)	0.0198	0.0178	0.0257	0.0095	7.16E-05	0
Resource depletion, mineral, fossils, and renewables (kg Sb-eq.)	5.18E-06	5.81E-06	3.30E-06	1.22E-06	6.03E-08	0

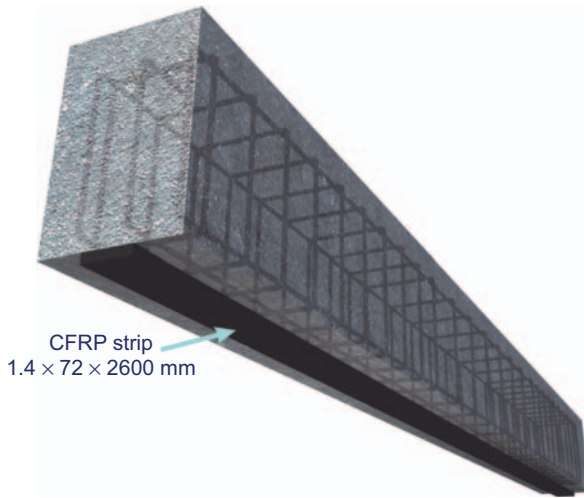


Figure 24.18 Assessed product in Case study 3 (Maxineasa, 2015; Maxineasa et al., 2015).

As shown in Table 24.9, the component materials of the carbon strip have the most important influence over the environmental performance of the strengthening application. As in the previous case, the epoxy resin has the highest negative ecological effect, followed by the carbon fibers. The resulting values show that the matrix and the adhesive are responsible for the highest impact in 10 categories, while the fibers have reached peak values in four considered indicators. Compared with the previous case study, the influence over the total environmental impact given by increasing the dimensions of the carbon strip is quite large.

24.5.2.4 Environmental performances in Case study 4

The present case study assesses the impact over the natural environment of the CFRP strips and epoxy adhesive utilized for setting up the first NSM strengthening technique scheme. This application is formed by bonding two $1.4 \times 18 \times 2600$ mm carbon strips in the precut grooves of the RC beam (Fig. 24.19).

Table 24.10 presents the resulting values, describing the environmental impact of the assessed CFRP strengthening solution. It can be observed that the amounts of epoxy resin and adhesive have the most significant influence over the total performance in eight impact categories. The negative environmental effect of these component materials is followed by the impact resulted for the surface preparation phase, with peak values for five parameters, and lastly by the fibers, which have the highest cancerogenic impact over human health. Compared with the results for the EBR strengthening schemes, in the present case the surface preparation phase has a much more important influence over the overall environmental performances. This fact is a direct result of the increased volume of surface preparation works needed to complete the NSM scheme.

Table 24.9 Environmental impact in Case study 3

Impact category	Life cycle stages					
	Carbon fibers	Epoxy resin	Pultrusion process	Surface preparation	Diesel	Transport
Acidification (mole of H ⁺ eq.)	0.0126	0.0202	0.0172	0.0064	0.0003	0.0001
Global warming (Climate change)—excluding the biogenic carbon (kg CO ₂ -eq.)	5.7378	6.5169	1.7823	0.6562	0.0462	0.2501
Ecotoxicity for aquatic freshwater (CTUe)	0.3349	0.0476	0.0769	0.0283	0.0511	6.72E-09
Aquatic eutrophication, freshwater (kg P eq.)	1.77E-05	0.0001	2.89E-07	1.06E-07	1.83E-06	0
Aquatic eutrophication, marine (kg N eq.)	0.0006	0.0041	2.49E-05	9.19E-06	3.58E-05	5.05E-05
Terrestrial eutrophication (mole of N eq.)	0.0426	0.0452	0.0140	0.0051	0.0007	0.0006
Human Toxicity, cancer effects (CTUh)	1.49E-08	2.62E-09	1.60E-09	5.89E-10	2.03E-09	3.12E-14
Human Toxicity, noncancer effects (CTUh)	1.11E-07	2.20E-07	8.22E-08	3.02E-08	2.73E-08	7.90E-15
Ionizing radiation, human health (kBq U-235)	0.4178	0	0.2525	0.0930	0.0013	0
Ozone depletion (kg CFC-11 eq.)	2.26E-10	4.43E-08	4.79E-10	1.77E-10	2.08E-12	0
Particulate matter/Respiratory inorganics (kg PM 2.5 eq.)	0.0004	0.0022	0.0013	0.0005	1.25E-05	2.20E-06
Photochemical ozone formation, human health (kg NMVOC)	0.0115	0.0124	0.0043	0.0016	0.0002	4.13E-05
Resource depletion, water (m ³ eq.)	0.0395	0.0356	0.0257	0.0095	0.0001	0
Resource depletion, mineral, fossils and renewables (kg Sb-eq.)	1.04E-05	1.16E-05	3.30E-06	1.22E-06	1.21E-07	0

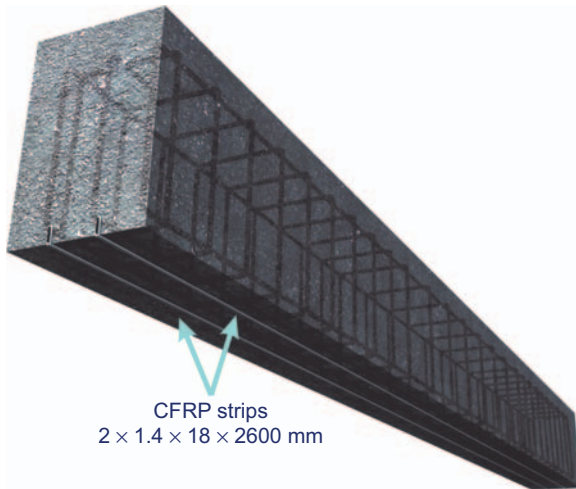


Figure 24.19 Assessed product in Case study 4 (Maxineasa, 2015; Maxineasa et al., 2015)

24.5.2.5 Environmental performances in Case study 5

Case study 5 evaluates the impact of the second NSM strengthening scheme. The composite solution is set up by bonding three carbon pultruded elements in the beams' prepared grooves. The composite strips, presented in Fig. 24.20, are 1.4×12 mm in cross-section and have a length of 2600 mm.

Analyzing the resultant values shown in Table 24.11, we can observe that the required RC beam surface preparation works have the most significant impact in eight environmental parameters. These operations are followed by the ecological effects resulting from using the epoxy resin and adhesive, with peak values for five impact categories, and carbon fibers, which have the highest value in the case of the HTPc indicator. Compared with the values in the previous case study, where the same amount of FRP component material is used, it can be concluded that the processes needed for cutting and preparing a supplementary groove have a sensitive effect over the entire environmental performance.

24.5.2.6 Environmental performances in Case study 6

The last case study analyzes the environmental impact of the third NSM strengthening solution, formed by using three carbon strips with a length of 2600 mm and a cross-section of 1.4×24 (Fig. 24.21). The composite elements are mounted by utilizing epoxy adhesive.

The resulting values that describe the environmental impact of the last CFRP strengthening technique scheme are presented in Table 24.12. As in the previous case studies that involve composite elements, the amount of epoxy resin and adhesive used for manufacturing and bonding the carbon strips has the most important impact over the overall environmental performances of the composite solution. The

Table 24.10 Environmental impact in Case study 4

Impact category	Life cycle stages					
	Carbon fibers	Epoxy resin	Pultrusion process	Surface preparation	Diesel	Transport
Acidification (mole of H ⁺ eq.)	0.0063	0.0243	0.0343	0.0403	0.0003	0.0001
Global warming (Climate change)—excluding the biogenic carbon (kg CO ₂ -eq.)	2.8689	7.8368	3.5468	4.1649	0.0469	0.2540
Ecotoxicity for aquatic freshwater (CTUe)	0.1674	0.0572	0.1531	0.1798	0.0519	6.82E-09
Aquatic eutrophication, freshwater (kg P eq.)	8.83E-06	0.0002	5.74E-07	6.74E-07	1.86E-06	0
Aquatic eutrophication, marine (kg N eq.)	0.0003	0.005	4.96E-05	5.83E-05	3.64E-05	5.13E-05
Terrestrial eutrophication (mole of N eq.)	0.0213	0.0543	0.0278	0.0326	0.0007	0.0006
Human toxicity, cancer effects (CTUh)	7.43E-09	3.15E-09	3.18E-09	3.74E-09	2.06E-09	3.17E-14
Human toxicity, noncancer effects (CTUh)	5.55E-08	2.65E-07	1.63E-07	1.92E-07	2.77E-08	8.02E-15
Ionizing radiation, human health (kBq U-235)	0.2089	0	0.5026	0.5902	0.0013	0
Ozone depletion (kg CFC-11 eq.)	1.13E-10	5.33E-08	9.54E-10	1.12E-09	2.11E-12	0
Particulate matter/Respiratory inorganics (kg PM 2.5 eq.)	0.0002	0.0027	0.0025	0.003	1.27E-05	2.23E-06
Photochemical ozone formation, human health (kg NMVOC)	0.0058	0.0149	0.0086	0.0101	0.0002	4.19E-05
Resource depletion, water (m ³ eq.)	0.0198	0.0428	0.0511	0.06	0.0001	0
Resource depletion, mineral, fossils, and renewables (kg Sb-eq.)	5.18E-06	1.40E-05	6.57E-06	7.72E-06	1.22E-07	0

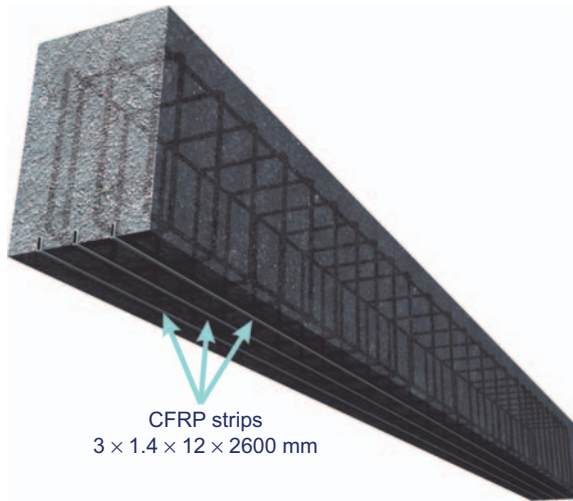


Figure 24.20 Assessed product in Case study 5 (Maxineasa, 2015; Maxineasa et al., 2015).

surface preparation operations have registered the highest values for three parameters, while the carbon fibers have maximum values in two impact categories. Taking into account the fact that the same volume of surface preparation works is required, analyzing the resultant values from the present and previous case study, the environmental influence given by modifying the cross-section of the carbon strips can be clearly observed.

24.5.3 Comparing the environmental performances

In order to determine the most environmentally friendly solution from the evaluated products, the LCA results will be compared. Table 24.13 presents the values that describe the environmental impact over all considered life cycle stages. In order to have a better understanding of, and take the best decision regarding, the environmental benefits of using CFRP strengthening solutions, this final comparison stage of the analysis has also considered the values for the load carrying capacity of the unstrengthened and strengthened RC beams.

Analyzing the resulting values, it can be observed that the RC beam assessed in Case Study 1, and the last evaluated CFRP strengthening scheme (Case study 6) have the most significant impact over the natural environment. Compared with the rest of the assessed products, the unstrengthened element has registered the biggest impact in eight categories, while the last case study has recorded six peak values. Taking into account the fact that, by using the CFRP solution which consists in applying three pultruded $1.4 \times 24 \times 2600$ mm carbon strips, the load capacity of an existing beam is increased by approximately 207% (Table 24.14), and also considering that in the case of almost all environmental parameters where the composite solution had the highest impact there are slight differences between these values

Table 24.11 Environmental impact in Case study 5

Impact category	Life cycle stages					
	Carbon fibers	Epoxy resin	Pultrusion process	Surface preparation	Diesel	Transport
Acidification (mole of H ⁺ eq.)	0.0063	0.0214	0.0476	0.0597	0.0003	0.0001
Global warming (Climate change)—excluding the biogenic carbon (kg CO ₂ -eq.)	2.8689	6.9252	4.9168	6.1709	0.0422	0.2283
Ecotoxicity for aquatic freshwater (CTUe)	0.1674	0.0505	0.2122	0.2663	0.0467	6.13E-09
Aquatic eutrophication, freshwater (kg P eq.)	8.83E-06	0.0002	7.96E-07	9.99E-07	1.67E-06	0
Aquatic eutrophication, marine (kg N eq.)	0.0003	0.0044	6.88E-05	8.64E-05	3.27E-05	4.61E-05
Terrestrial eutrophication (mole of N eq.)	0.0213	0.048	0.0385	0.0483	0.0007	0.0005
Human toxicity, cancer effects (CTUh)	7.43E-09	2.78E-09	4.41E-09	5.54E-09	1.85E-09	2.85E-14
Human toxicity, noncancer effects (CTUh)	5.55E-08	2.34E-07	2.27E-07	2.84E-07	2.49E-08	7.21E-15
Ionizing radiation, human health (kBq U-235)	0.2089	0	0.6967	0.8744	0.0011	0
Ozone depletion (kg CFC-11 eq.)	1.13E-10	4.71E-08	1.32E-09	1.66E-09	1.90E-12	0
Particulate matter/Respiratory inorganics (kg PM 2.5 eq.)	0.0002	0.0023	0.0035	0.0044	1.14E-05	2.01E-06
Photochemical ozone formation, human health (kg NMVOC)	0.0058	0.0132	0.0119	0.0149	0.0002	3.77E-05
Resource depletion, water (m ³ eq.)	0.0198	0.0378	0.0708	0.0889	0.0001	0
Resource depletion, mineral, fossils and renewables (kg Sb-eq.)	5.18E-06	1.23E-05	9.11E-06	1.14E-05	1.10E-07	0

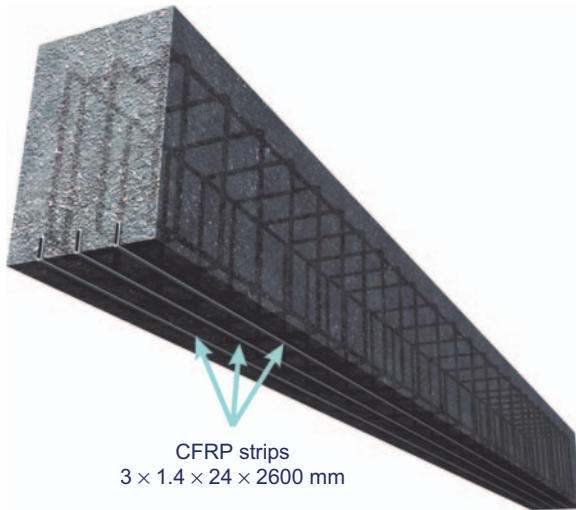


Figure 24.21 Assessed product in Case study 6 (Maxineasa, 2015; Maxineasa et al., 2015).

and the negative effects resulted in the case of the RC beam, it can be stated that using this strengthening application represents a more sustainable solution than building a new beam.

The resultant values show beyond doubt the importance of LCA studies in the design stage of a product. It can be observed that, depending on the needed level of structural safety in the case of an existing RC beam, various CFRP solutions with different environmental performances are available. For example, specialists may decide to use the composite solution assessed in the second case study which will increase the load capacity of the unstrengthened element by approximately 0.6 times, with a lower load over the environment in 12 impact categories. It is also worth mentioning that the RC beam has a lower impact compared with the CFRP solutions only in two environmental parameters: freshwater aquatic eutrophication and mineral, fossils, and renewable resources depletion. One can also notice that the surface preparation phase has a significant influence over the environmental performances of the FRP strengthening schemes. Thus, the overall impact of the composite applications can be reduced by considering different approaches/solutions regarding the operations needed during the surface preparation of the unstrengthened construction element (e.g., renewable energy, like wind and solar energy, may be used, thus providing electricity with a nearly zero environmental footprint).

Also taking into account the fact that, in the case of strengthening an existing beam, all environmental effects of the old element over its entire life span will increase the impact of the new RC element, strengthening and reusing the existing product represents a solution with a significantly lower environmental footprint. Overall, it can be concluded that FRP materials can have a significant role in minimizing the impact of the built environment over the natural one, being one of the most important factors in achieving global sustainability.

Table 24.12 Environmental impact in Case study 6

Impact category	Life cycle stages					
	Carbon fibers	Epoxy resin	Pultrusion process	Surface preparation	Diesel	Transport
Acidification (mole of H ⁺ eq.)	0.0126	0.0429	0.0476	0.0597	0.0006	0.0002
Global warming (Climate change)—excluding the biogenic carbon (kg CO ₂ -eq.)	5.7378	13.8505	4.9168	6.1709	0.0844	0.4566
Ecotoxicity for aquatic freshwater (CTUe)	0.3349	0.1011	0.2122	0.2663	0.0933	1.23E-08
Aquatic eutrophication, freshwater (kg P eq.)	1.77E-05	0.0003	7.96E-07	9.99E-07	3.35E-06	0
Aquatic eutrophication, marine (kg N eq.)	0.0006	0.0088	6.88E-05	8.64E-05	6.54E-05	9.22E-05
Terrestrial eutrophication (mole of N eq.)	0.0426	0.0960	0.0385	0.0483	0.0013	0.0011
Human toxicity, cancer effects (CTUh)	1.49E-08	5.56E-09	4.41E-09	5.54E-09	3.71E-09	5.69E-14
Human toxicity, noncancer effects (CTUh)	1.11E-07	4.68E-07	2.27E-07	2.84E-07	4.98E-08	1.44E-14
Ionizing radiation, human health (kBq U-235)	0.4178	0	0.6967	0.8744	0.0023	0
Ozone depletion (kg CFC-11 eq.)	2.26E-10	9.42E-08	1.32E-09	1.66E-09	3.80E-12	0
Particulate matter/Respiratory inorganics (kg PM 2.5 eq.)	0.0004	0.0047	0.0035	0.0044	2.27E-05	4.02E-06
Photochemical ozone formation, human health (kg NMVOC)	0.0115	0.0263	0.0119	0.0149	0.0003	7.54E-05
Resource depletion, water (m ³ eq.)	0.0395	0.0756	0.0708	0.0889	0.0003	0
Resource depletion, mineral, fossils, and renewables (kg Sb-eq.)	1.04E-05	2.47E-05	9.11E-06	1.14E-05	2.20E-07	0

Table 24.13 Comparing the environmental performances of the assessed construction products

Impact category	Case study 1	Case study 2	Case study 3	Case study 4	Case study 5	Case study 6
Acidification (mole of H ⁺ eq.)	0.2155	0.0403	0.0568	0.1056	0.1354	0.1636
Global warming (Climate change)—excluding the biogenic carbon (kg CO ₂ -eq.)	77.3457	8.7183	14.9895	18.7183	21.1523	31.217
Ecotoxicity for aquatic freshwater (CTUe)	6.2813	0.3220	0.5388	0.6094	0.7431	1.0078
Aquatic eutrophication, freshwater (kg P eq.)	6.35E-05	8.1E-05	0.0002	0.0002	0.0002	0.0003
Aquatic eutrophication, marine (kg N eq.)	0.003	0.0025	0.0048	0.0055	0.0049	0.0097
Terrestrial eutrophication (mole of N eq.)	0.4166	0.0637	0.1082	0.1373	0.1573	0.2278
Human toxicity, cancer effects (CTUh)	7.9E-08	1.19E-08	2.17E-08	1.96E-08	2.2E-08	3.41E-08
Human toxicity, noncancer effects (CTUh)	6.37E-06	2.92E-07	4.71E-07	7.03E-07	8.25E-07	1.14E-06
Ionizing radiation, human health (kBq U-235)	1.831	0.5550	0.7646	1.3030	1.7811	1.9912
Ozone depletion (kg CFC-11 eq.)	1.84E-07	2.3E-08	4.52E-08	5.55E-08	5.02E-08	9.74E-08
Particulate matter/Respiratory inorganics (kg PM 2.5 eq.)	0.0129	0.0031	0.0044	0.0084	0.0104	0.013
Photochemical ozone formation, human health (kg NMVOC)	0.1250	0.0180	0.03	0.0396	0.046	0.064975
Resource depletion, water (m ³ eq.)	0.1649	0.0729	0.1104	0.1738	0.2174	0.2751
Resource depletion, mineral, fossils, and renewables (kg Sb-eq.)	− 3.3E-05	1.56E-05	2.66E-05	3.36E-05	3.81E-05	5.58E-05

Table 24.14 The values of the load capacity resulted through experimental program (Maxineasa et al., 2015)

Case study	Number 1	Number 2	Number 3	Number 4	Number 5	Number 6
Load capacity (kN)	60	95	116.3	155.2	151.7	184.3

24.6 Conclusions and future trends

The state of the natural environment will most likely continue to represent the most important issue that humankind has to provide an answer for in the near future. As mentioned in this chapter, the construction industry is one of the most polluting economic activities at a global scale, having a tremendous influence over global sustainable development. Therefore, improving the environmental performances of the built environment represents a mandatory task for all players and decision-makers involved in this sector.

Arguably, the most important contributors to the environmental footprint of the industry are the utilized construction materials. Thus, in order to improve the performances of this sector, we must consider minimizing the level of environmental burdens resulting from the preoperation stage of a structure. Even if composite materials have a decisive effect on the Earth's ecosystem, they can nonetheless be considered as a viable solution. As shown in the LCA studies put forth, by using a small amount of FRP materials, a higher volume of concrete can be replaced, leading to better environmental performances. Thus, the strengthening solutions taken under analysis can be successfully used for strengthening, retrofitting or upgrading old structures from the existing building stock, with a lower environmental footprint compared with the one resulted from demolishing the existing constructions and building new ones.

One of the most significant future trends, if not the most far-reaching, is represented by the fact that researchers and producers of FRP constituent materials must find solutions to the problem of recycling composite materials. Aside from the environmental benefit, this matter is also highly important for the future cradle-to-cradle LCA studies, in order to obtain results with a low level of uncertainties that can be used with a high level of credibility by final users. Considering the information available at the moment and the studies presented in this chapter, we can conclude that—if used properly—FRP materials will have an important role in satisfying the most important dimension of sustainable development—the environmental one.

References

- Agarwal, B.D., Broutman, L.J., Chandrashekhara, K., 2006. *Analysis and Performance of Fiber Composites*. third ed. Wiley-Interscience, New York.

- AISC, 2016. Structural steel: the premier green construction material. Sustainable manufacturing process. American Institute of Steel Construction, Chicago. <<https://www.aisc.org/why-steel/sustainability/#29351>>.
- Balaguru, P., Nanni, A., Giancaspro, J., 2009. FRP composites for reinforced and prestressed concrete structures. A Guide to Fundamentals and Design for Repair and Retrofit. Taylor & Francis, New York.
- Bank, L.C., 2006. Composites for construction: structural design with FRP materials. John Wiley & Sons, Inc., New Jersey.
- Barbero, E.J., 2011. Introduction to Composite Materials Design. second ed. CRC Press, Boca Raton.
- Berardi, U., 2013. Clarifying the new interpretations of the concept of sustainable building. *Sustainable Cities and Society*. 8, 72–78.
- Bingel, P., Bown, A., 2010. Sustainability of masonry in construction. In: Khatib, J.M. (Ed.), *Sustainability of Construction Materials*. Woodhead Publishing Limited, Cambridge, pp. 82–119.
- Blankendaal, T., Schuur, P., Voordijk, H., 2014. Reducing the environmental impact of concrete and asphalt: a scenario approach. *J. Cleaner Prod.* 66, 27–36.
- Bolsamo, A., Di Ludovico, M., Lignona, G.P., Prota, A., Manfredi, G., Cosenza, E., 2012. Composites for structural strengthening. In: *second ed.* Nicolais, L., Borzacchiello, A. (Eds.), *Encyclopedia of Composites*, vol. 1. Wiley, New Jersey, pp. 393–417.
- Bribian, I.Z., Capilla, A.V., Uson, A.A., 2011. Life cycle assessment of building materials: comparative analysis of energy and environmental impacts and evaluation of the eco-efficiency improvement potential. *Build. Environ.* 46 (5), 1133–1140.
- Campbell, F.C., 2010. *Structural Composite Materials*. ASM International, Ohio.
- Chang, K.K., 2001. Aramid fibers. In: Miracle, D.B., Donaldson, S.L. (Eds.), *ASM Handbook, Volume 21: Composites*. ASM International, the Materials Information Society, Material Park, Ohio.
- De Lorenzis, L., Stratford, T.J., Holloway, L.C., 2008. Structurally deficient civil engineering infrastructure: concrete, metallic, masonry and timber structures. In: Holloway, L.C., Teng, J.G. (Eds.), *Strengthening and Rehabilitation of Civil Infrastructures Using Fiber-Reinforced Polymer (FRP) Composites*. Woodhead Publishing Limited, Cambridge.
- DeStefano, J., 2009. Building green with wood construction. *Struct. Mag.* 16 (8), 17–19.
- Ding, G.K.C., 2014. Life cycle assessment (LCA) of sustainable building materials: an overview. In: Pacheco-Torgal, F., Cabeza, L.F., Labrincha, J., de Magalhaes, A. (Eds.), *Eco-efficient Construction and Building Materials. Life Cycle Assessment (LCA) Eco-labelling and Case Studies*. Woodhead Publishing Limited, Cambridge, pp. 38–62.
- Drexhage, J., Murphy, D., 2010. *Sustainable Development: From Brundtland to Rio 2012*. United Nations Headquarters, New York.
- EN, 2013. Sustainability of construction works—environmental product declarations—core rules for the product category of construction products (EN 15804:2012 + A1:2013), European Committee for Standardization, Brussels.
- EPC, 2009. Sustainable benefits of concrete structures. European Concrete Platform. <http://www.europeanconcrete.eu/images/stories/publications/ECP_Book_Sustainable_Benefits_of_Concrete.pdf?phpMyAdmin=16bbb563ca43adfed14bd78eb7d8cd8a>.
- Estrada, H., Borja, D.H., Lee, L., 2012. Sustainability in infrastructure design. In: Jain, R., Lee, L. (Eds.), *Fiber Reinforced Polymer (FRP) Composites for Infrastructure Applications*. Springer Science + Business Media B.V, Dordrecht, pp. 23–52.
- European Commission – Joint Research Centre – Institute for Environment and Sustainability, 2011. *International Reference Life Cycle Data System (ILCD) Handbook*

- Recommendations for Life Cycle Impact Assessment in the European context, EUR 24571 EN, Publications Office of the European Union, Luxembourg.
- Ewing, B., Moore, D., Goldfinger, S., Oursler, A., Reed, A., Wackernagel, M., 2010. Ecological footprint atlas 2010. Global Footprint Network, Oakland. <http://www.footprintnetwork.org/images/uploads/Ecological_Footprint_Atlas_2010.pdf>.
- Ferreira, J., Pinheiro, M.D., de Brito, J., 2014. Portuguese sustainable construction assessment tools benchmarked with BREEA and LEED: an energy analysis. *Energ. Build.* 69, 451–463.
- fib, 2007. FRP reinforcement in RC structures. Technical report on the design and use of fibre reinforced polymer reinforcement (FRP) in reinforced concrete structures. Fédération internationale du béton/International Federation for Structural Concrete, Lausanne.
- GangaRao, H.V.S., Taly, N., Vijay, P.V., 2007. Reinforced Concrete Design with FRP Composites. CRC Press, Boca Raton.
- Gay, D., Hoa, S.V., 2007. Composite materials: Design and applications. second ed. CRC Press, Boca Raton.
- Gibson, R.F., 2012. Principles of Composite Material Mechanics. third ed. CRC Press, London.
- Global Footprint Network, 2016. Press Release: August 8th is Earth Overshoot Day this year. <<http://www.overshootday.org/newsroom/press-release-english/>>.
- Gursel, A.P., Masanet, E., Horvath, A., Stadel, A., 2014. Life-cycle inventory analysis of concrete production: a critical review. *Cem. Concr. Compos.* 51, 38–48.
- Habert, G., 2014. Assessing the environmental impact of conventional ‘green’ cement production. In: Pacheco-Torgal, F., Cabeza, L.F., Labrincha, J., de Magalhaes, A. (Eds.), *Eco-efficient Construction and Building Materials. Life Cycle Assessment (LCA), Eco-labelling and Case Studies*. Woodhead Publishing Limited, Cambridge, pp. 199–238.
- Hafner, A., Ott, S., Winter, S., 2014. Recycling and end-of-life scenarios for timber structures. In: Aicher, S., Reinhardt, H.-W., Garrecht, H. (Eds.), *Materials and Joints in Timber Structures, RILEM Bookseries 9*. Springer, Dordrecht, pp. 89–98.
- Hollaway, L.C., 2011. Key issues in the use of fibre reinforced polymer (FRP) composites in the rehabilitation and retrofitting of concrete structures. In: Karbhari, V.M., Lee, L.S. (Eds.), *Service Life Estimation and Extension of Civil Engineering Structures*. Woodhead Publishing Limited, Cambridge, pp. 3–74.
- Hollaway, L.C., Teng, J.G., 2008. Preface. In: Hollaway, L.C., Teng, J.G. (Eds.), *Strengthening and Rehabilitation of Civil Infrastructures Using Fibre-Reinforced Polymer (FRP) Composites*. Woodhead Publishing Limited, Cambridge.
- Ingrao, C., Lo Giudice, A., Tricase, C., Mbohwa, C., Rana, R., 2014. The use of basalt aggregates in the production of concrete for the prefabrication industry: environmental impact assessment, interpretation and improvement. *J. Cleaner Prod.* 75, 195–204.
- ISO, 2006a. Environmental management – life cycle assessment – principles and framework (ISO 14040:2006). The International Organization for Standardization (ISO), Geneva.
- ISO, 2006b. Environmental management – life cycle assessment – requirements and guidelines (ISO 14044:2006). The International Organization for Standardization (ISO), Geneva.
- ISO, 2008a. Sustainability in building construction – general principles (ISO 15392:2008). The International Organization for Standardization (ISO), Geneva.
- Joshi, S.V., Drzal, L.T., Mohanty, A.K., Arora, S., 2004. Are natural fiber composites environmentally superior to glass fiber reinforced composites? *Compos. Part A: Appl. Sci. Manuf.* 35 (3), 371–376.

- Karbhari, V.M., Lee, L.S. (Eds.), 2011. *Service Life Estimation and Extension of Civil Engineering Structures*. Woodhead Publishing Limited, Cambridge.
- Kotynia, R., 2012. Bond between FRP and concrete in reinforced concrete beams strengthened with near surface mounted and externally bonded reinforcement. *Constr. Build. Mater.* 32, 41–54.
- Krausmann, F., Gingrich, S., Eisenmenger, N., Erb, K.H., Harbel, H., Fischer-Kowalski, M., 2009. Growth in global materials use, GDP and population during the 20th century. *Ecol. Econ.* 68 (10), 2696–2705.
- L 124, 2013. Commission Recommendation of 9 April 2013 on the use of common methods to measure and communicate the life cycle environmental performance of products and organisations (2013/179/EU). Official Journal of the European Union, Publications Office of the European Union, Luxembourg.
- Lee, L., Jain, R., Stephenson, L., Ramirez, C., 2012. Introduction. In: Jain, R., Lee, L. (Eds.), *Fiber Reinforced Polymer (FRP) Composites for Infrastructure Application*. Springer Science + Business Media B.V., Dordrecht, pp. 1–21.
- Lee, L.S., 2011. Rehabilitation and service life estimation of bridge superstructures. In: Karbhari, V.M., Lee, L.S. (Eds.), *Service Life Estimation and Extension of Civil Engineering Structures*. Woodhead Publishing Limited, Cambridge, pp. 117–144.
- Lourenco, P.B., Vasconcelos, G., 2015. The design and mechanical performance of high-performance perforated fired masonry bricks. In: Pacheco-Torgal, F., Lourenco, P.B., Labrincha, J.A., Kumar, S., Chindaprasirt, P. (Eds.), *Eco-efficient Masonry Bricks and Blocks. Design, Properties and Durability*. Woodhead Publishing, Cambridge, pp. 13–44.
- Mallick, P.K., 2008. *Fiber Reinforced Composites. Materials, Manufacturing and Design*. CRC Press, London.
- Marinkovic, S.B., Malesev, M., Ignjatovic, I., 2014. Life cycle assessment (LCA) of concrete made using recycled concrete or natural aggregates. In: Pacheco-Torgal, F., Cabeza, L. F., Labrincha, J., de Magalhaes, A. (Eds.), *Eco-efficient Construction and Building Materials. Life Cycle Assessment (LCA) Eco-labelling and Case Studies*. Woodhead Publishing Limited, Cambridge, pp. 239–266.
- Matthews, F.L., Rawlings, R.D., 2008. *Composite Materials: Engineering and Science*. CRC Press, Woodhead Publishing Limited, Cambridge.
- Matthys, S., 2014. Material characteristics. In: Zoghi, M. (Ed.), *The International Handbook of FRP Composites in Civil Engineering*. CRC Press, Taylor & Francis Group, London, New York, pp. 359–387.
- Maxineasa, S.G., 2015. *Composite and hybrid solutions for sustainable development in constructions*. PhD. Thesis (in Romanian).
- Maxineasa, S.G., Taranu, N., Bejan, L., Isopescu, D., Banu, O.M., 2015. Environmental impact of carbon fiber-reinforced polymer flexural strengthening solutions of reinforced concrete beams. *Int. J. Life Cycle Assess.* 20, 1343–1358.
- Meadows, D.H., Meadows, D.L., Randers, J., Behrens III, W.W., 1972. *The Limits to Growth*. Universe Books, New York.
- Meadows, D.H., Meadows, D.L., Randers, J., 1992. *Beyond the Limits: Confronting Global Collapse, Envisioning a Sustainable Future*. Chelsea Green Publishing Company, White River Junction, Vermont.
- Messari-Becker, L., Bollinger, K., Grohmann, M., 2013. Life-cycle assessment as a planning tool for sustainable buildings, In: Strauss, A., Frangopol, D.M., Bergmeister, K., (Eds.), *Life-Cycle and Sustainability of Civil Infrastructure Systems. Proceedings of the Third International Symposium on Life-Cycle Civil Engineering (IALCCE 2012)*, Taipei, pp. 1558–1562.

- Miller, A., Ip, K., 2013. Sustainable construction materials. In: Yao, R. (Ed.), *Design and Management of Sustainable Built Environments*. Springer-Verlag, London, pp. 341–358.
- Mokhlesian, S., Holmen, M., 2012. Business model changes and green construction processes. *Constr. Manage. Econ.* 30 (9), 761–775.
- Moynihan, M.C., Alwood, M.J., 2012. The flow of steel into the construction sector. *Resour., Conserv. Recycl.* 68, 88–95.
- MPA, 2015. Concrete industry sustainability performance report. 8th report: 2014 Performance Data, MPA The Concrete Centre, London.
- Nebel, B., 2006. White paper—life cycle assessment and the building and construction industry. Prepared for Beacon Pathway Limited, Auckland.
- Ortiz, O., Castells, F., Sonnemann, G., 2009. Sustainability in the construction sector industry: a review of recent developments based on LCA. *Constr. Build. Mater.* 23, 28–39.
- Pacheco-Torgal, F., 2014. Introduction to the environmental impact of construction and building materials. In: Pacheco-Torgal, F., Cabeza, L.F., Labrincha, J., de Magalhaes, A. (Eds.), *Eco-efficient Construction and Building Materials. Life Cycle Assessment (LCA) Eco-labelling and Case Studies*. Woodhead Publishing Limited, Cambridge, pp. 1–10.
- Pacheco-Torgal, F., Labrincha, J.A., 2013. The future of construction materials research and the seventh UN Millennium. Development goal: a few insights. *Constr. Build. Mater.* 40, 729–737.
- Ramesh, T., Prakash, R., Shukla, K.K., 2010. Life cycle energy analysis of buildings: an overview. *Energy Build.* 42 (10), 1592–1600.
- Rossi, B., 2014. Discussion on the use of stainless steel in constructions in view of sustainability. *Thin-Walled Struct.* 83, 182–189.
- Shafiqh, P., Mahmud, H.B., Jumaat, M.Z.B., Ahmad, R., Bahri, S., 2014. Structural lightweight aggregate concrete using two types of waste from the palm oil industry as aggregate. *J. Cleaner Prod.* 80, 187–196.
- Simion, I.M., Ghinea, C., Maxineasa, S.G., Taranu, N., Bonoli, A., Gavrilescu, M., 2013. Ecological footprint applied in the assessment of construction and demolition waste integrated management. *Environ. Eng. Manage. J.* 12 (4), 779–788.
- Solis-Guzman, J., Martinez-Rocamora, A., Marrerro, M., 2014. Methodology for determining the carbon footprint of the construction of residential buildings. In: Muthu, S.S. (Ed.), *Assessment of Carbon Footprint in Different Industrial Sectors*, vol. 1. Springer Science + Business Media, Singapore, pp. 49–83.
- SR EN ISO, 2007. Environmental management. Life cycle assessment. Principles and framework, in Romanian (SR EN ISO 14040:2007). This standard is identical with the European Standard EN ISO 14040:2006, Romanian Standards Association (ASRO), Bucharest.
- Strezov, V., Evans, A., Evans, T., 2013. Defining sustainability indicators of iron and steel production. *J. Cleaner Prod.* 51, 66–70.
- Taljsten, B., 2003. FRP Strengthening Existing Concrete Structures. Design Guideline. Lulea University Press, Lulea.
- Taranu, N., Bejan, L., Cozmanciuc, R., Hohan, R., 2013. *Composite Materials and Elements I. Lectures and Applications (in Romanian)*. Editura Politehniun, Iasi.
- Taranu, N., Maxineasa, S.G., Mihai, P., Entuc, I.S., Oprisan, G., 2016. The environmental impact of different concrete mixes. Proceedings of the 15th International Multidisciplinary Scientific Geoconference SGEM 2015. Ecology, Economics, Education and Legislation, Albena, Book 5, Vol. I, pp. 707-714.
- Tautsching, A., Burtscher, D., 2013. Has sustainability become the norm in the planning and execution of building projects? In: Strauss, A., Frangopol, D.M., Bergmeister, K., (Eds.),

- Life-cycle and Sustainability of Civil Infrastructure Systems. Proceedings of the Third International Symposium on Life-Cycle Civil Engineering (IALCCE 2012), Taipei, pp. 1579–1585.
- Teng, J.G., Chen, J.F., Smith, S.T., Lam, L., 2001. FRP Strengthened RC Structures. John Wiley & Sons Limited, Chichester.
- Tundrea, H., Maxineasa, S.G., Simion, I.M., Taranu, N., Budescu, M., Gavrilesco, M., 2014. Environmental impact assessment and thermal performances of modern earth sheltered houses. *Environ. Eng. Manage. J.* 13 (10), 2363–2369.
- Turner, G., 2008. A Comparison of the Limits to Growth with Thirty Years of Reality. CSIRO Sustainable Ecosystems, Canberra.
- UN, 1992a. Report of the United Nations conference on environment and development, annex I: Rio declaration on environment and development. The United Nations Conference on Environment and Development, United Nations, Rio de Janeiro. <<http://www.un.org/documents/ga/conf151/aconf15126-1annex1.htm>>.
- UN, 1992b. Agenda 21, The United Nations Conference on Environment and Development. United Nations, Rio de Janeiro. <<https://sustainabledevelopment.un.org/content/documents/Agenda21.pdf>>.
- Volz, V., Stovner, E., 2010a. Reducing the embodied energy in masonry construction. Part 1: understanding embodied energy in masonry. *Struct. Mag.* 17 (5), 8–10.
- Volz, V., Stovner, E., 2010b. Reducing embodied energy in masonry construction. Part 2: evaluating new masonry materials. *Struct. Mag.* 17 (9), 42–45.
- Wang, T., Müller, D.B., Graedel, T.E., 2007. Forging the anthropogenic iron cycle. *Environ. Sci. Technol.* 41 (14), 5120–5129.
- WBCSD, 2009. Cement Technology roadmap 2009. Carbon emissions reductions up to 2050. World Business Council of Sustainable Development, Geneva. <http://wbcسدservers.org/wbcسدpublications/cd_files/datas/business-solutions/cement/pdf/CementTechnologyRoadmap.pdf>.
- WCED, 1987. Report of the World Commission on Environment and Development: Our Common Future. World Commission on Environment and Development, United Nations Headquarters, New York.
- WSA, 2013a. World steel in figures 2013. World Steel Association, Brussels.
- WSA, 2013b. Crude steel production—December 2013, world steel in figures 2013. World Steel Association, Brussels.
- WWF, 2016. Living Planet Report 2016. Risk and resilience in a new era, World Wide Fund for Nature International, Gland, Switzerland.
- Yeh, Y., Haller, P., 2013. LCA of multi-storey timber buildings and comparative estimation with alternative building materials. In: Strauss, A., Frangopol, D.M., Bergmeister, K., (Eds.), Life-Cycle and Sustainability of Civil Infrastructure Systems. Proceedings of the Third International Symposium on Life-cycle Civil Engineering (IALCCE 2012), Taipei, pp. 1593–1600.

This page intentionally left blank

Life-cycle analysis of repair of concrete pavements

25

Hao Wang

Rutgers, The State University of New Jersey, Piscataway, NJ, United States

25.1 Introduction

Pavements pose a particular challenge to achieving the goal of sustainable transportation infrastructure because construction and maintenance of roadway requires large economic investments and consumption of non-renewable materials, creating significant energy and environmental impacts. With the limited budget constraints and the focus of environmental sustainability, agencies and contractors desire to adopt cost-effective and environment-friendly products, processes and technologies associated with design, construction, and maintenance of pavement.

There are three primary pavement types in the paved roadway: asphalt pavement, concrete pavement, and composite pavement. The asphalt pavement is composed of asphalt course over aggregate base and subgrade. The composite pavement is composed of asphalt overlay on concrete slabs that are mainly resulted from pavement rehabilitation. The concrete pavement is composed of concrete slabs placed over stabilized based and subgrade. Concrete pavements are widely used to carry heavy load and provide long-lasting solutions in highways, airports, and bridge decks. Compared to asphalt pavement, concrete pavement may require less maintenance and has more rigorous requirements on construction and curing time.

It is important to conduct appropriate pavement repairs at the right timing to extend concrete pavement life. The common repair activities of concrete pavement usually include joint resealing, slab stabilization, partial-depth repairs, full-depth repairs, load transfer restoration, and diamond grinding and grooving. These treatments are mainly used to preserve or maintain pavement condition and retard further deterioration, which can be considered in the category of pavement preservation and routine maintenance. The selection of maintenance treatment type is determined by the specific distress type in the existing pavement.

On the other hand, major rehabilitation treatments of concrete pavements mainly include crack and seat, rubblization, concrete overlay, or asphalt overlay. Compared to routine maintenance, rehabilitation treatments are usually conducted towards the end of pavement service life, can restore pavement structure capacity, and therefore they are much more costly. The most expensive option would be remove and replace, which means reconstruction of pavement section without utilizing existing pavement.

Transportation agencies need to use a systematic approach for disseminating limited funds and decide the timing to conduct maintenance and repairs. In order to establish a cost-effective budget plan and achieve the optimum utilization of

available resources, the agencies need to decide which maintenance treatment to use and where and when to apply it in the pavement lifecycle. The economic and environmental impacts of different pavement maintenance and rehabilitation activities are important for the selection of pavement repair.

25.2 Lifecycle cost analysis of concrete pavement repair

Lifecycle cost analysis (LCCA) can be used to evaluate the overall and long-term economic worth of pavement, by calculating initial costs and discounted future costs. Agency costs and user costs are two major parts in LCCA. Agency costs are defined as all the costs related to the owning organizations over the life of pavement, such as initial construction costs and maintenance costs etc. User costs are including travel time, vehicle operation, accidents, and discomfort costs paid by the road users (FHA, 2004). The activity flow of pavement LCCA is shown in Fig. 25.1.

Analysis period and discount rate are the two most significant parameters affecting pavement lifecycle cost. The analysis period should be chosen to be reasonably long enough to include major rehabilitation treatments (Walls and Smith 1998). Pavement LCCA with different analysis periods, discount rates and repair strategies were considered in the sensitivity analysis part.

According to National Cooperative Highway Research Program (NCHRP) Guide for Pavement-Type Selection, an analysis period of at least 40 years was suggested for new construction or reconstruction of pavements, while an analysis period of at least 30 years was suggested for the rehabilitation of pavements. A respectively longer analysis period should be selected for long-life pavements. A discount rate is

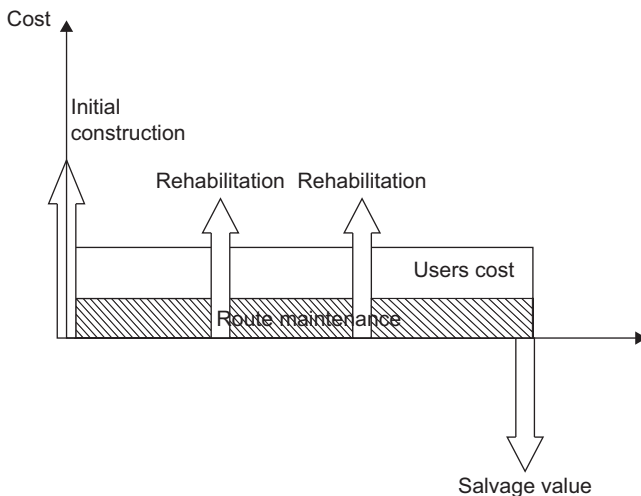


Figure 25.1 Activity flow of pavement Lifecycle cost analysis (LCCA).

used to convert future costs to present year costs. The discount rates vary in the range of 2%–5%. The long-term real discount rate values supplied in the Office of Management and Budget (OMB) Circular A-94, Appendix C—*Discount Rates for Cost-Effectiveness, Lease Purchase, and Related Analyses*, is suggested to be used in LCCA.

There are several economic indicators used in the LCCA such as benefit/cost (B/C) ratios, internal rate of return (IRR), net present value (NPV), and equivalent uniform annual costs (EUAC). The IRR is a return rate which makes net present value of all cash flows from a certain project investment equal to zero. The NPV converts all costs to a single base year costs; while converts all projects to a recurring yearly cost. After converting to NPV or EUAC, the costs of various pavement design and repair alternatives can be compared.

The agency costs of maintenance and rehabilitation significantly affect the result of LCCA (USDOT, 2003). The difference between pavement maintenance and rehabilitation cost was defined by American Concrete Pavement Association (2002). Maintenance costs are daily costs related to maintaining a certain level of service of pavement which are difficult to obtain and itemize; whereas rehabilitation costs are large, future periodic costs that keep pavement in the usable condition. It is noted that the difficulty of collecting maintenance costs has been mentioned in previous studies due to an absence of record keeping, since the daily maintenance cost is difficult to obtain and itemize (Babashamsi et al., 2016; American Concrete Pavement Association, 2002). The available data of maintenance cost is relatively limited compared to initial construction costs and major rehabilitation costs.

One of the available data sources for maintenance costs of concrete pavement can be found from a study entitled as “Life-Cycle Cost Comparison of Asphalt and Concrete Pavements on Low-Volume Roads; Case Study Comparisons” by Embacher and Snyder (2001). The study collected nine years’ maintenance costs for two counties in Minnesota from 1991 to 1999. The age of pavement sections ranged from new to 25 years old. The study report summarized several findings: (1) as the pavement was getting older, the maintenance cost would get higher; (2) Hot-mix asphalt (HMA) maintenance cost was higher than portland cement concrete (PCC) pavement; (3) the cost curve might vary due to different maintenance activities. The report also indicated that the maintenance costs are critical in LCCA for small agencies/projects while it might be insignificant in comparison to initial construction costs and major rehabilitation costs for large projects.

Another maintenance cost data source is the report “Guidelines for Routine Maintenance of Concrete Pavement” by Jung et al. (2008). The authors discussed the visual identification distress types of concrete pavement and nondestructive testing (NDT) evaluation techniques. The report summarized the routine maintenance repairs data including repair stage, repair type, repair object, limitations, unit repair cost, typical repair work time, and the expected life extension after the repair. The data can be used as comparison in life cycle cost estimations. The original cost data is from the National Highway Institute training course 131062, “PCC Pavement Evaluation and Rehabilitation” (Hoerner et al., 2001).

In addition to agency cost, user cost is another significant factor affecting LCCA results. The LCCA guidance of [American Concrete Pavement Association \(2002\)](#) indicated that the user delay cost due to major rehabilitations should be considered in LCCA study. The user delay cost is mainly due to reduced traffic capacity through work zones. From the examples provided in the report, the value of time lost for cars is \$0.25/minute and \$1.00/minute for trucks (in 2002 dollar). Information that should be collected for calculation of delay cost includes the dimension and number of closed lanes, speed reduction, restricted traffic flow length, restricted flow time, normal flow for 5 miles, overall increased travel time, average daily traffic for truck and cars, and the value of time lost for cars and trucks. The report indicated that concrete pavements are often quicker to construct. For example, for 5 miles of highway rehabilitation, the paving for concrete can be finished in less than 20 work days; while asphalt need more than 60 work days.

The LCCA study conducted by [Zhang et al. \(2008\)](#) considered traffic delay due to overlay construction and maintenance as well as vehicle operation cost (VOC) due to pavement deterioration. The VOC due to surface deterioration is measured by the increase of fuel consumption because of the increasing surface roughness in long run. In the study, the values of additional time for vehicles passing the congesting work zone or detouring are shown in [Fig. 25.2](#). These were compared to \$0.13/VMT traveled in the work zone and \$0.09/VMT traveled in detour in the state of Michigan. The authors indicated that user delay costs related to congestion were significant in user costs that contribute over 80% of total life cycle cost.

The activities and schedules of concrete pavement maintenance and rehabilitation have critical effects on LCCA results. [American Concrete Pavement Association \(2002\)](#) introduced several rehabilitation activities for concrete pavements and the timing of rehabilitations. The authors indicated that the early

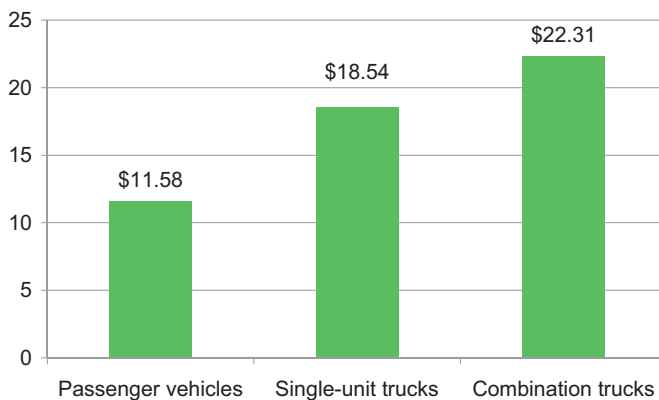


Figure 25.2 Value of vehicles passing congested work zone (/veh-hr).

Source: After Zhang, H., Keoleian, G., Lepech, M., 2008. An integrated life cycle assessment and life cycle analysis model for pavement overlay systems. Paper presented at the Proc., 1st Int. Symp. on Life-Cycle Civil Engineering.

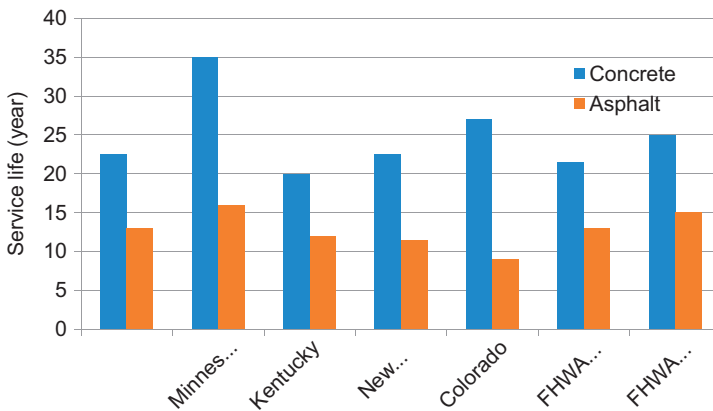


Figure 25.3 Average pavement service life for heavy duty highways.

Source: American Concrete Pavement Association, 2002. Life Cycle Cost Analysis: A Guide for Comparing Alternate Pavement Analysis. EB 220P.

rehabilitation activities have greater impact on the LCCA result since they were less discounted. Fig. 25.3 shows the pavement service life for heavy-duty highways reported by ACPA. The report summarized that the service life of concrete pavement was typically 20–30 years; while the rehabilitation activities normally provided additional 7–10 years of service.

It is noted that most of the studies have been focused on building the model and the procedures, while only a few have accessed the performance measurement of LCCA. Chan (2007) evaluated the accuracy of a LCCA model used by Michigan DOT. The resulting difference between the estimated cost of LCCA and the actual cost was mainly from the uncertainties of installation and maintenance costs of concrete pavements. Two conclusions related to maintenance and rehabilitations were drawn: (1) for all LCCA cost-estimation modules reviewed, none of them considered special construction conditions such as intersections, underpasses, or cross-overs which had different requirements of maintenance activities and construction techniques; (2) the estimated maintenance schedules in the LCCA model failed to meet actual maintenance events.

25.3 Lifecycle assessment of concrete pavement repair options

Lifecycle Assessment (LCA) is a technique to assess environmental effects associated with the life cycle of product with flexibility and comprehensiveness (ISO 14044). The life cycle of pavement can be divided into different stages including raw material extraction, material processing and manufacturing, transportation, construction, maintenance, and end-of-life.

As defined by the International Standards Organization (ISO), the frame of LCA includes three basic stages: goal and scope definition, inventory analysis, and impact assessment (ISO 14044). There are three major types of LCA models. The first is Economic Input-Output model (EIO), known as EIO-LCA, which is developed by Carnegie Mellon University. The second is process-based LCA which disaggregate the project or product production into individual processes or activities independently. Hybrid LCA is the third method, in which an EIO model is combined with process-based inventory data to produce comprehensive representations for environmental effects. Fig. 25.4 shows the flowchart of process-based LCA for pavement.

Portland Cement Association (2007) conducted a lifecycle inventory (LCI) study on Portland cement concrete (PCC). The system boundaries included the raw material manufacturing stage, the transportation of raw materials to the processing facility, and the mixing stage to produce PCC. The energy use and emission from aggregate production were estimated using the data from the US Census Bureau and EPA AP-42 emission factors. The energy and emission information for cement was retrieved from PCA's 2006 cement LCI report. The plant energy was calculated from confidential LCI surveys of ready-mix concrete plants. It is noted that the life inventory data of raw material and manufacturing processes from literature vary between multiple data sources. These discrepancies may exist due to different geographic locations, technologies, and system boundaries. Table 25.1 summarizes the LCI data related to concrete pavement from literature and a wide range of variation is observed.

The rehabilitation strategies of concrete pavement mainly include asphalt and concrete overlays. Weiland and Muench (2010) conducted a study on the LCA of concrete pavement on interstate highways with focus on rehabilitation and replacement stages. Three repair options were considered to replace the old PCC pavement and

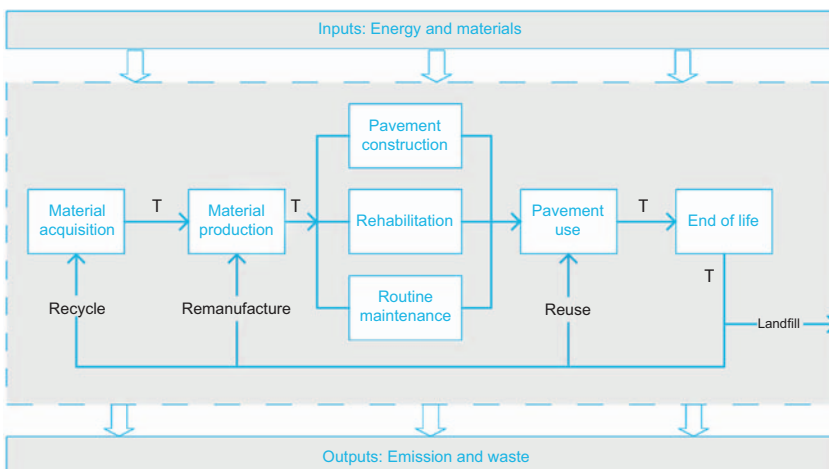


Figure 25.4 Flowchart of process-based pavement life cycle assessment.

Table 25.1 Lifecycle inventory (LCI) data of concrete pavement

Material/process	LCI data from literature		Data Sources
	Energy consumption (MJ/t)	Emissions CO ₂ eq. (kg/t)	
Portland cement	4340–5350	670–928	Hakkinen and Makela (1996); Stipple (2001); Choate (2003); Anthena (2005); Marceau et al. (2006)
Sand or gravel	6–68.6	0.07–6.1	
Crushed stone	32–52	1.42–6	
PCC manufacturing	18–110	0.7–9.5	

the expected service life after reconstruction is 50 years with regular maintenance. The three repair options are: remove and replace with concrete overlay; remove and replace with asphalt overlay; and crack and seat with asphalt overlay. For the first option, a 13-in. slab—which is 4 in. thicker than the old pavement and is designed to provide sufficient strength—and diamond grinding is planned at 20, 40, and 50 years after reconstruction. For asphalt overlay, a total of 13-in. asphalt overlay is designed with complete removal of existing concrete pavement. For the last option, 5-in. asphalt overlay is placed on the top of 9-in. concrete after crack and seat. Milling and paving were scheduled at 16, 32, and 48 years after reconstruction with asphalt overlay. The LCA results show that concrete overlay generated the highest CO₂ emission while it was the second high in terms of total energy consumption. The largest contribution to the LCA results came from production of paving material (PCC and Hot Mix Asphalt (HMA)), especially for asphalt overlay.

It is noted that most studies did not include minor or routine maintenance treatments in the LCA of concrete pavement, such as joint resealing, crack sealing, patch repairs, diamond grinding, and load transfer restoration. Since the material required for minor repair is small and difficult to estimate, it was usually assumed that there was no critical effect on the total environmental impact of pavement life cycle. Additionally, manual operation, short duration, and small equipment are usually used in minor maintenance activities, which validate the fact that it might be insignificant in comparison to the construction activities in the initial construction and rehabilitation of concrete pavement.

Meil (2006) compared asphalt pavements with jointed plain concrete (JPCP) pavements in Canada for an analysis period of 50 years. The major rehabilitation for high traffic volume rigid concrete pavement was 80 mm asphalt overlay at year 40. Results show that concrete pavement with one major rehabilitation of HMA overlay has lower energy consumption than HMA pavement in the 50-year study period. The feedstock energy was found to have the highest contribution to the total energy for asphalt pavements. However, the greenhouse gas (GHG) emission of concrete pavement is 11% higher than HMA pavement.

Wang et al. (2016) quantified lifecycle energy and environmental impact of concrete and asphalt pavement designs at the airfield. The case study was conducted

for Runway 132R-31L at John F. Kennedy (JFK) International Airport in New York. The runway rehabilitation alternatives include rigid overlay and flexible overlay. The analysis period was 40 years with lifecycle stages of material production, transportation, construction, and major rehabilitations. The study did not include use stage and end-of-life stages. The environmental assessment included energy consumption and GHG emission for both upstream value and direct combustion value. For concrete overlay, only minor repair is required for every 8 years and no major rehabilitations during the 40-year period. The concrete repair treatments mainly include patching and partial-depth repair. The contribution of minor repairs in the LCA was assumed, based on the cost percentage of minor repairs in the LCCA. Under this assumption, the study results are shown in Fig. 25.5. It was found that the maintenance activities of the PCC overlay account for 8%–10% of the total life cycle GHG emission and energy consumption. The results indicate that the expected pavement service life and maintenance treatments significantly affect the comparison between HMA and PCC pavements. The consideration of energy and emissions resulted from the production of process fuels and electricity in the upstream process cannot be neglected in the LCA.

Due to the uncertainty of pavement deteriorating rates, the estimated repair technologies and schedule are not always the same (Chan, 2007). To increase the accuracy of LCA results and reduce the difference between the estimated and actual environmental impact, it is important to carefully assume the types and timings of maintenance and rehabilitation treatments in LCA. Several studies followed the standard specifications for construction from state Department of Transportation or other agencies (Zhang et al., 2008; Chan, 2007; Wang et al., 2016), while a study from

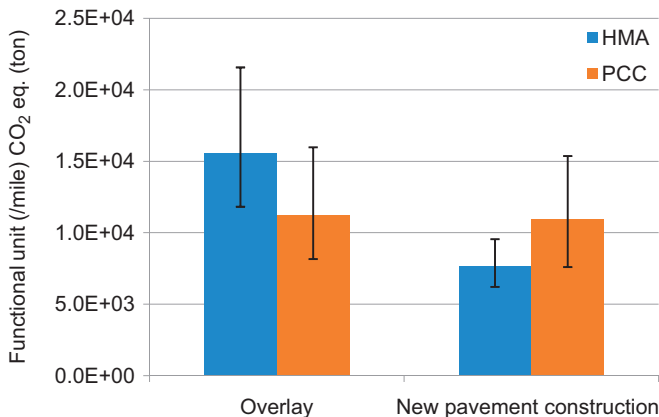


Figure 25.5 Functional unit CO₂ emission of overlay and new pavement construction of runway.

Source: After Wang, H., Thakkar, C., Chen, X., Murrel, S., 2016. Life-cycle assessment of airport pavement design alternatives for energy and environmental impacts. *J. Cleaner Prod.* 133, 163–171.

Milachowski et al. (2011) considered two maintenance scenarios with minimum and maximum maintenance efforts. The study compared concrete and asphalt pavement for one-km motorway construction and maintenance in Germany. A usage period of 30 years was considered for the pavement with normal traffic conditions. For the concrete pavement, the maintenance activities included complete renovation of joints for 2–3 times, repair of 5%–20% edges and corners, lifting and fixing of 1%–3% slabs, and replacement of 1%–3% slabs. The results of impact assessment showed that the environmental impact from maintenance activities of concrete pavement was much less than that of asphalt pavement. To reduce the environmental impact of concrete maintenance, the authors suggested increasing the durability of concrete slab joint filers. The overall result showed that both concrete and asphalt pavements have similar environmental impacts on global warming potential (GWP). The largest reduction of potential impact lay in lowering fuel consumption in the use stage, since the estimated impact due to traffic is 100 times more than the combined impact from construction and maintenance stages.

While the material and construction stages of concrete pavement have obvious effects on LCA results, user delay due to major rehabilitations is another significant factor but often neglected in many studies. From the perspective of LCA, the environmental impact from user delay is primarily the increased fuel consumptions and emissions due to reduced speeds or increase idling when passing work zones, or the extra mileage traveled due to detour.

Chan (2007) indicated that the road capacity and traffic volume was critical for environmental impact from traffic delay through work zones. An LCA model was developed to investigate and compare the environmental impact of asphalt and concrete pavements for 13 Michigan DOT projects. The system boundary of LCA included material production and waste treatment, transportation, construction, and maintenance phases. For maintenance and rehabilitation activities, the study used NONROAD2005 from EPA for construction equipment data and SimPro 6.0 (commercial software) for the upstream fuel production data. The environmental impact due to traffic delay caused by construction was from the KyUCP model developed by Kentucky Transportation Center. The results showed that the emissions associated with construction equipment operation were not the major source of emissions except for PM₁₀.

Zhang et al. (2008) concluded that the GHG emission occurred in traffic delay due to construction and maintenance was about 20%–30% of the total lifecycle emission. The energy consumption due to traffic delay was about 15%–40% of total energy consumption in the life cycle. The LCA study included three alternatives: unbonded concrete overlay, asphalt overlay, and engineered cementitious composite (ECC) overlay. The LCA model relies on four external models: SimaPro (Pre Consultants) for material production, MOBILE 6.2 (EPA) for vehicle emissions, NONROAD (EPA) for construction equipment, and a traffic flow model. The maintenance strategies for overlays followed the historical maintenance and management records of Standard Specifications for Construction from Michigan DOT. The maintenance schedule is shown in Table 25.2. The results showed that the main contributions are from material production, congestion, and use stage.

Table 25.2 Maintenance and rehabilitation schedules of three alternatives

	Reconstruction	Major maintenance events	Minor maintenance events
Concrete overlay	21	11, 31	None
HMA overlay	20	8, 28	6, 12, 26, 32
ECC overlay	None	None	None

Source: From Zhang, H., Keoleian, G., Lepech, M., 2008. An integrated life cycle assessment and life cycle analysis model for pavement overlay systems. Paper presented at the Proc., 1st Int. Symp. on Life-Cycle Civil Engineering.

At the usage stage of pavement after treatments, fuel consumptions, and vehicle emission vary significantly depending on tire rolling resistance that is affected by pavement surface roughness, macro-texture, and deflection (Chatti and Zaabar, 2012). Although the relationship between vehicle emission and pavement surface characteristics are complicated and depends on vehicle type and operation condition, the usage stage of pavement should not be neglected in the LCA study of concrete pavement.

Two models related to construction equipment and traffic vehicles have been commonly used in pavement LCA in the United States; namely the Greenhouse Gases, Regulated Emissions, and Energy Use in Transportation (GREET) model developed by Argonne National Laboratory and the NONROAD2005 developed by Environmental Protection Agency (EPA). The NONROAD2005 is used to calculate energy consumption of off-road equipment after knowing the equipment type and horse power (EPA, 2005). GREET model is used to quantify energy consumption and emission in the life cycle of different fuel types (Argonne, 2007).

Santero et al. (2011) suggested reducing the GHG emission by four options. They include: the use of fly ash, the use of white aggregate to reduce albedo, stockpiling at end-of-life for carbonation, and extra rehabilitation for better pavement–vehicle interaction (PVI). The substitution of cement with 10%–30% fly ash is allowable for five state DOT practices, which have shown to increase the rate of carbonation by 5% and 10%. The use of white aggregate—both fine and coarse—was experimentally proved to achieve higher albedo which contributes to negative GHG emission. The end-of-life stockpiling of concrete pavement for 1 year is assumed to sequester 28% initial CO₂ released from carbonation, which is about 310 lb CO₂ per ton of cement in the mix. Finally, extra rehabilitation to reduce pavement roughness can provide greater fuel economic improvement during the pavement–vehicle interaction phase, indirectly reducing the GHG emission through the pavement life cycle.

The application of supplementary cementitious materials (SCMs) and ECC has shown that they have smaller life cycle environmental impacts (Weiland and Muench, 2010; Zhang et al., 2008), but it is difficult to accurately estimate the service life of concrete pavements with SCMs or ECC due to the short history of practice.

Table 25.3 summarizes the LCA studies of concrete pavement repair that considers different stages of pavement life cycle, and uses different impact assessment metrics.

25.4 Integration of economic and environmental analysis

LCA evaluates environmental impact of all phases in the pavement life cycle from raw material to the end of life. At the same time, LCCA quantifies the discounted cost in the pavement life cycle. The integration of LCA and LCCA enable the incorporation of sustainability metrics into economic decision making process.

To incorporate LCA and LCCA results, one of the practices is to quantify the agency cost and user cost of LCCA and the emission cost of LCA in an equivalent way. It must be noted that large uncertainty exists in estimation of emission cost. For example, the marginal cost of carbon was obtained from the climate framework for uncertainty, negotiation, and distribution (FUND) mode, in which the cost of emission reduction was estimated considering different scenarios in climate change, human health impacts, and emissions (Tol et al., 2003). The marginal cost of carbon can be converted to the equivalent cost of GHG that includes carbon dioxide (CO₂), methane (CH₄), and nitrous oxide (N₂O) based on carbon content and global warming potential. In this case, the different objectives from LCCA and LCA are combined to form a single objective in terms of cost.

Kendall et al. (2008) combined LCA–LCCA to analyze the sustainability metrics of a concrete bridge deck. Two different bridge decks were used in their study: conventional design of steel expansion joint, and link slab using ECC. When these bridge decks were evaluated over the entire life cycle, the study concluded that the slab design resulted in the reduction in both lifecycle cost and environmental impact. Due to traffic delay caused by construction, costs to the funding agency include less than 3% and 0.5 % of total costs and environment-related costs, respectively. The integrated model; LCA–LCCA; can be applied to other infrastructure assets including pavements.

Similarly, Zhang et al. (2010) developed an integrated LCA and LCCA model to evaluate environmental impact and costs of rigid pavement overlay designs over a period of 40 years. The LCCA model included user cost on traffic delay due to overlay construction, maintenance, and deterioration. The integrated model considered environmental cost from LCA of an overlay system as the impacts to human health from air pollutions and global warming potential. Since air pollutions are a regional impact, cost is separated into three categories: urban, urban fringe, and rural areas. The global costs are used for conversion of GHG cost responsible for global warming potential.

Santero et al. (2011) introduced the cost-effectiveness analysis to quantify the benefits and cost of GHG emission-reduction of concrete pavement with alternative and base case. The estimate price of the market value of carbon mainly comes from European Union Emissions Trading Scheme of \$17/ton in 2011, and a national

Table 25.3 Summary of LCA practices for concrete pavement repair

Reference	Analysis period	Application	Maintenance activities	Rehabilitation activities	Traffic delay	Construction	Output
Meil (2006)	50 years	Arterial roadways, high; volume highways in Canada	Not included	80 mm asphalt overlay at the year of 40	Not included	SimaPro Database 1998; Canada's Greenhouse Gas Inventory 1990-02	Energy, global warming potential (GWP)
Chan (2007)	–	Four-lane highway	–	–	KyUCP, MOBILE6	NONROAD2005, SimaPro 6.0	Energy, GHG, air pollutants
Zhang et al. (2008)	40 years	Two directions freeway	Major maintenance at year 11 and 31	Reconstruction at year 21	MOBILE 6.2 KyUCP	NONROAD2005	Energy, GWP
Weiland and Muench (2010)	50 years	Highway	Dowel bar retrofit	Diamond Grind at year 20, 40, 50	Not included	NONROAD2005 GREET	GWP, acidification, HH criteria air, Eutrophication, photochemical smog
Cass and Mukherjee (2011)	–	Interstate highway	–	Concrete overlay	Not included	e-Clac SimaPro 7.0	GWP
Milachowski et al. (2011)	30 years	Motorway in Germany	Renovation of joints, repair of broken edges and corners, lifting and fixing of slabs, replacement of slabs	Not included	Not included	Swiss database "ecoinvent," SimaPro	GWP, depletion of the stratospheric ozone, photo-oxidant formation, acidification, eutrophication
Wang et al. (2016)	40 years	Airport runway overlay	Patching and partial-depth repair	Not included	Not included	NONROAD2005 GREET2013	Energy, GWP

carbon tax of \$25/ton placed by Australian government in 2012. The social cost of carbon price reviewed ranged from to \$23/ton to \$77/ton with different scenarios. The study assumed five scenarios to capture the different GHG emission reduction strategies. The results showed that a wide range from $-\$540/\text{ton CO}_2$ saved for urban interstates to more than $-\$910/\text{ton CO}_2$ saved on rural arterials.

Yu et al. (2013) developed a methodology to incorporate environmental damage cost (EDC) in the total cost evaluation. In general, the researchers combined LCA to LCCA models to optimize a pavement maintenance strategy using EDC. Three overlay systems were used in a case study, which is HMA overlay, PCC overlay, and crack, seat, and overlay (CSOL). The optimized maintenance plans a reduction between 9% and 13% energy/GHGs and 6%–10% regarding holistic costs compared to the previous optimization plans.

It has been argued, however, that the relatively large scale of user cost and the high levels of uncertainty of emission cost compared to agency cost cause inconsistency in the total cost and it is not feasible to unify all the costs with summation. The ideal goal is to reduce costs, while at the same time maintaining good pavement surface conditions for fewer user costs and emission from traffic. However, these two objectives are directly contradictory as the reduction in costs will likely cause the increase in pavement roughness and thus user cost and emission. In such cases, all proposed solutions will inevitably compromise one objective for the benefit of another. As such, the goal is to find feasible solutions that are acceptable and balanced between different objectives. Therefore, the agencies seek solutions to consider the tradeoffs between economic and environmental factors make multiobjective decision making.

Lidicker et al. (2012) extended the continuous-time to solve the multiobjective decision problem, based on two criteria; minimum cost and emission. Two case studies in California with two different traffic volumes (high and light) were used in their study. The researchers concluded that minimum achievable roughness and traffic loadings had a significant role to increases or decrease total GHG emissions. For the same, smoother rehabilitated pavement, the low traffic volume produced lower emission than heavy traffic. Heavy traffic sections forced more frequent overlays, while the smoother pavement created more emissions. In this study, the emission is quantified in tons instead of equivalent cost and the Pareto frontier was used for bi-objective optimization.

It is not an easy task to solve multiobjective decision making problems in the lifecycle analysis of pavement repair. While there are several methods of resolving these issues, they can be broadly classified as either the converted single objective approach or the Pareto nondominant solutions approach (Messac et al., 2003). The former aims to create single objective function by treating other objectives as the constraints. The latter approach, on the other hand, generates Pareto optimal solutions and the decision maker then determines which is most suitable in light of their own preferences or requirements. The solution space provides for tradeoffs among different feasible solutions and can be used to identify the optimal solution based on the user-defined weighted criteria.

25.5 Recommendations to future research

Most previous studies focused on LCA of concrete pavement with different rehabilitation treatments such as overlays. Although routine concrete pavement repairs might be insignificant in comparison to initial construction and rehabilitation for large projects, it can be critical in LCCA study for small agencies/projects. To overcome the limited cost data for routine maintenance of concrete pavement, a lump-sum cost of routine maintenance can be added to the LCCA result, based on the practices from agencies. In addition, future studies can improve LCCA model by using site-specific data. For example, urban streets or sidewalks, highway intersections, underpasses, and crossovers have different requirements of maintenance activities and construction techniques compared to typical highway sections. It is important to conduct periodic review of LCCA results compared to actual cost in the feedback process, which would also accelerate the implementation of LCCA practices.

In the current practice of LCA, the consumed energy and the released emission at different timings in the pavement life cycle are not discounted in the way as used by LCCA. With different treatment costs and timings of pavement repair alternatives, future LCA study should consider the time-value of environmental impact such as emissions and energy usage in the time-horizon of pavement life cycle. For example, it is not clear about the differences of environmental impact if the same amount of total GHG emission is generated every year (due to routine maintenance) or only at the specific year (due to major rehabilitation). This also affects the consideration of traffic delay due to pavement repair activities in the LCA, which has been recognized as one of the critical factors affecting LCA results.

It is important to select concrete pavement maintenance and rehabilitation options that have the highest benefit-cost ratio and the least impact on energy consumption and environment. The optimal pavement maintenance and repair strategies may vary depending on various objectives and constraints and agency practice. Therefore, both LCCA and LCA should be considered in pavement lifecycle management framework. A multiobjective decision making process is needed to incorporate sustainability metrics into infrastructure management system, including economic cost, energy consumption, carbon footprint, etc.

References

- American Concrete Pavement Association, 2002. Life Cycle Cost Analysis: A Guide for Comparing Alternate Pavement Analysis. EB 220P.
- Argonne National Laboratory, 2007. GREET 2.7 Vehicle Cycle Model. Argonne National Laboratory.
- Athena Sustainable Materials Institute, 2005. Cement and Structural Concrete Products: Life Cycle Inventory Update #2. Athena Sustainable Materials Institute (Athena), Ottawa, Canada.

- Babashamsi, P., Yusoff, N.I.M., Ceylan, H., Nor, N.G.M., Jenatabadi, H.S., 2016. Evaluation of pavement life cycle cost analysis: review and analysis. *Int. J. Pavement Res. Technol.* 9 (4), 241–254.
- Cass, D., Mukherjee, A., 2011. Calculation of greenhouse gas emissions for highway construction operations by using a hybrid life-cycle assessment approach: case study for pavement operations. *J. Constr. Eng. Manage.* 137 (11), 1015–1025.
- Chan, A.W.C., 2007. *Economic and Environmental Evaluations of Life Cycle Cost Analysis Practice: A Case Study of Michigan DOT Pavement Projects*. University of Michigan.
- Chatti, K., Zaabar, I., 2012. Estimating the Effects of Pavement Condition on Vehicle Operating Costs. NCHRP 720, Transportation Research Board, Washington, D.C.
- Choate, W.T., 2003. Energy and emission reduction opportunities for the cement industry. Office of Energy Efficiency and Renewable Energy, U.S. Department of Energy.
- Embacher, R., Snyder, M., 2001. Life-cycle cost comparison of asphalt and concrete pavements on low-volume roads; case study comparisons. *Transp. Res. Rec.* 1749, 28–37.
- EPA, 2005. User's Guide for the final NONROAD2005 model.
- Federal Highway Administration, 2004. *Life-Cycle Cost Analysis RealCost User Manual*. RealCost Version 2.1. Office of Asset Management, FHWA, U.S. Department of Transportation.
- Hakkinen, T., Makela, K., 1996. Environmental Impact of Concrete and Asphalt Pavements in Environmental Adaptation of Concrete. Technical Research Center of Finland.
- Hoerner, T.E., Smith, K.D., Yu, H.T., Peshkin, D.G., Wade, M.J., 2001. PCC Pavement Evaluation and Rehabilitation. Reference Manual, NHI Training Course, 131062.
- Jung, Y.U., Freeman, T.J., Zollinger, D.G., 2008. Guidelines for Routine Maintenance of Concrete Pavement. Texas Transportation Institute.
- Kendall, A., Keoleian, G.A., Helfand, G.E., 2008. Integrated life-cycle assessment and life-cycle cost analysis model for concrete bridge deck applications. *J. Infrastruct. Syst.* 14 (3), 214–222.
- Lidicker, J., Sathaye, N., Madanat, S., Horvath, A., 2012. Pavement resurfacing policy for minimization of life-cycle costs and greenhouse gas emissions. *J. Infrastruct. Syst.* 19 (2), 129–137.
- Marceau, M.L., Nisbet, M.A., Vangeem, M.G., 2006. *Life Cycle Inventory of Portland Cement Manufacture (No. SN2095b)*. Portland Cement Association, Skokie, Illinois.
- Meil, J., 2006. *A Life Cycle Perspective on Concrete and Asphalt Roadways: Embodied Primary Energy and Global Warming Potential*. Athena Research Institute.
- Messac, A., Ismail-Yahaya, A., Mattson, C.A., 2003. The normalized normal constraint method for generating the pareto frontier. *Struct. Multidiscipl. Optim.* 25 (2), 86–98.
- Milachowski, C., Stengel, T., Gehlen, C., 2011. *Life Cycle Assessment for Road Construction and Use*. European Concrete Paving Association, Brussels.
- Santero, N., Loijos, A., Akbarian, M., Ochsendorf, J., 2011. Methods, Impacts, and Opportunities in the Concrete Pavement Life Cycle. MIT Concrete Sustainability Hub.
- Stripple, H., 2001. *Life Cycle Assessment of Road, a Pilot Study for Inventory Analysis*. second revised ed. IVL Swedish National Road Administration, Gothenburg, Sweden.
- Tol, R.S.J., Heintz, R.J., Lammers, P.E.A., 2003. Methane emission reduction: an application of FUND. *Clim. Change.* 57 (1–2), 71–98.
- U.S. Department of Transportation, 2003. *Life-Cycle Cost Analysis Primer*. U.S. Department of Transportation, Federal Highway Administration, Office of Asset Management, Washington, DC.
- Walls, J., Smith, M.R., 1998. *Life-cycle Cost Analysis in Pavement Design-Interim Technical Bulletin*. Federal Highway Administration, FHWA-SA-98-079.

- Wang, H., Thakkar, C., Chen, X., Murrel, S., 2016. Life-cycle assessment of airport pavement design alternatives for energy and environmental impacts. *J. Cleaner Prod.* 133, 163–171.
- Weiland, C.D., Muench, S.T., 2010. Life Cycle assessment of Portland Cement Concrete Interstate Highway Rehabilitation and Replacement. Washington State Department of Transportation.
- Yu, B., Lu, Q., Xu, J., 2013. An improved pavement maintenance optimization methodology: integrating LCA and LCCA. *Transp. Res. Part A: Policy Practice.* 55, 1–11.
- Zhang, H., Keoleian, G., Lepech, M., 2008. An integrated life cycle assessment and life cycle analysis model for pavement overlay systems. F. Biondini and D.M. Frangopol (Eds.), *Proceedings of the International Symposium on Life-Cycle Civil Engineering 2008*, 907–912.
- Zhang, H., Lepech, M., Keoleian, G., Qian, S.Z., Li, Victor, 2010. Dynamic life-cycle modeling of pavement overlay systems: capturing the impacts of users, construction, and roadway deterioration. *J. Infrastruct. Syst.* 16 (4), 209–309.

Further reading

- EPA, 2010. Emissions Factors & AP 42, Compilation of Air Pollutant Emission Factors.
- Horvath, A., Hendrickson, C., 1998. Comparison of environmental implications of asphalt and steel-reinforced concrete pavements. *Transportation Research Record No. 1626*. Transportation Research Board. 1626, 105–113.
- Marceau, M.L., Nisbet, M.A., Vangeem, M.G., 2007. Life Cycle Inventory of Portland Cement Concrete (No. SN2011). Portland Cement Association, Skokie, Illinois.
- Tol, R.S.J., 1999. The marginal costs of greenhouse gas emissions. *Energy.* 20 (1), 61–81.
- Zapata, P., Gambatese, J.A., 2005. Energy consumption of asphalt and reinforced concrete pavement materials and construction. *J. Infrastruct. Syst.* 11 (1), 9–20.

Index

Note: Page numbers followed by “*f*” and “*t*” refer to figures and tables, respectively.

A

- Absorption–desorption kinetics, 472–474
- Acoustic emission (AE), 177–178, 177*f*, 221, 453–457
 - structural health monitoring through, 123
 - background and general application, 124–127
 - intensity analysis of AE signal, 135
 - intensity category of beam, 140–142
 - intensity of precast beam specimen, 139–140
 - monitoring and analysis, 127–131
 - precast reinforced concrete beam, damage assessment of, 131–132
 - principles of AE technique, 127*f*
 - sample and experimental set up, preparation of, 132–134
 - signal strength, AE parameter analysis based on, 135–139
 - typical AE parameters, 126*f*
- Acoustic impact methods, 191
- Activated compact denitrifying core (ACDC), 536–537
- Admixtures, 570–572
 - air-entraining, 486
 - bio-based. *See* Bio-based admixture
 - chemical, 376–378
 - shrinkage-reducing, 380–381
- Aerosol, 47, 49, 52
- Agency cost, 724–725
- Aggregate Wear Index (AWI), 408–409
- Air entraining agents (AEA), 539
- Alite-rich calcium sulfoaluminate cement (ACSA), 358*t*
- Alite–ye’elimite cement, 362
- Alkali-activated binders, 264, 276–277, 282–283
 - Alkali-activated materials (AAM), 264–265, 267, 273–276, 280*f*, 281, 285
 - Alkali-activated mortars, 265–267, 273–286, 275*t*, 276*f*
 - compositions of, for the sulfate resistance experiment, 279*t*
 - efflorescence of, 274–276, 276*f*
 - fly ash-based repair mortars, 278–282
 - metakaolin-based repair mortars, 282–284
 - properties of, 285*t*
 - repair mortars based on mixtures of different precursors, 284–285
 - slag-based repair mortars, 273–278
- Alkali-aggregate reactions (AAR), 19
- Alkaline earth lignosulfates, 570–571
- Alkalinity of the concrete, 19
- Alkaliphilic bacteria, 553
- Alkali-silica reaction (ASR), 7, 19, 44, 196, 198–200, 199*f*, 223
- Alumino-silicate materials,
 - geopolymerization of, 293
- Aluminosilicates, geopolymer mortars based on. *See* Geopolymer mortars based on aluminosilicates
- Ambient vibration test, 241, 243, 252–253
 - acquisition equipment for, 240*f*
- Amorphous calcium aluminate phase (ACA), 372–374
- Amplitude, 48, 126
- Anhydrite II, 369
- Anhydrite III, 369
- ANSYS, 238, 252
- Aramid fibers, 681, 689–691
- Aramid Fiber Reinforced Polymers (AFRP), 162–163
- Arctic sea ice, 50–51
- Asphalt pavement, 723, 729–730

- ASTM FRP pull-off test, 174–175, 174f
 Atmosphere-related deterioration, 19–20
 Auto-calibration, 128
 Autogenous shrinkage, 410–411, 480, 484
 Auto-regressive models, 242–243
- B**
- Bacillus alkalinitrilicus*, 534
Bacillus cohnii, 534–535, 538, 541, 560
Bacillus halodurans, 538
Bacillus megaterium, 532–533, 538–539
Bacillus mucilaginosus, 534
Bacillus pseudofirmus, 534, 538, 546–547, 554f
Bacillus sphaericus, 532–533, 535–536, 546–547, 555
Bacillus subtilis, 540, 547
- Bacteria-based concrete, 531
 carbon cycle, bacteria involving
 by oxidation of organic carbon, 534–535
 direct addition of bacteria to concrete, 537–540
 future trends, 560–561
 manual crack repair, bacteria-based, 544–545
 mixed versus pure cultures and industrial scale fermentation of bacteria, 535–537
 nitrogen cycle, bacteria involving
 by degradation of urea, 532–533
 by dissimilation of nitrates, 533–534
 protection strategies, 545–550
 effects of nutrients and calcium source on concrete properties, 548–550
 encapsulation/immobilization of bacteria, 545–548
 self-healing concrete, application of encapsulated bacteria for, 551–560
 activity measurement of bacteria in (cracked) concrete, 554–556
 germination and growth aids for bacteria, 553–554
 in large scale laboratory and in-situ tests, 558–560
 quantity of cells and nutrients required, 551
 evaluation of self-healing efficiency, 556–558
 triggering of self-healing, 551–553
 surface protection, bacteria-based, 540–544
- Bacterial exo-product, 573
 Bacterial extracellular substances, bio-based admixture from, 572–574
 bio surfactant as bio admixture, 572–574
- Basalt fibers, 692
- Basic oxygen furnace (BOF) process, 678
- Bayesian framework, 111
- Belite-rich calcium sulfoaluminate cement (BCSA), 358r
- Belite sulfoaluminate (BSA), 362–363
 BSA–ternesite cement, 362–363
- Belite-sulfoaluminoferrite cement (BCSAF), 358r, 360–362
- Bioadmixtures, 570, 572–574, 577–578
 corrosion inhibiting mechanism of, 581
- Bio-based admixture, 540
 from bacterial extracellular substances, 572–574
 bio surfactant as bio admixture, 572–574
 corrosion inhibitors, types of, 570–572
 corrosion study, 574–581
 corrosion inhibition in interstitial solutions without chlorides, 576–578
 corrosion inhibition in synthetic solutions containing chlorides, 579–581
 interstitial solutions obtained from different cements, 575
 material, 574
- Bio-CaCO₃, 541–545
 Bio-hydrogels, 547–548
 Biomineralization technology, 654
 Biosurfactants, 573–574
 Bond compatibility, 391
 Bond strength, 158–159, 264–265, 299–300, 414
- Brazilian coast, corrosion of reinforcements on, 54–64
 chloride penetration, models for predicting, 57–64
 data and scenario definition
 relative humidity, 56–57
 temperature, 55–56
 hypotheses, 54
 study area, 54–55

- Brillouin optical time domain analysis (B-OTDA), 103
- Brillouin optical time domain reflectometry (B-OTDR) technique, 103, 104*f*
- Brillouin scattering, 100, 102–103
- Brundtland Commission, 675
- Brundtland Report, 675
- C**
- Calcium alginate beads, 548
- Calcium-based compound, 549
- Calcium carbonate, 19, 22–23, 335–336, 374–376, 548, 551
- Calcium hydroxide, 34–35, 160, 295–297, 324, 479
- and ordinary Portland cement (OPC), 371–373
- Calcium nitrate, 487–488, 548–549
- Calcium silicate hydrate, 366
- Calcium sulfate, 357, 369–371
- Calcium sulfoaluminate-belite (CSAB) cement, 357, 358*t*, 360–367
- Calcium sulfoaluminate cement (CSA), 356–357, 358*t*, 359, 372, 380–382
- production of, using
 - hydrothermal–calcination process, 363–365
- CAPS BASF test series, 459
- Carbonation, 315
- in concrete infrastructure, 53
 - of metakaolin mortars, 283
 - prevention against, 459–460
 - shrinkage, 480
 - testing, 281–282
- Carbonation-induced corrosion, 3–4, 53, 332–341
- electrochemical realkalisation on blended concretes, 336–341
 - application, 337–340
 - geopolymer coating application after, 340–341
- of reinforcement, 22–25
- supplementary cementitious materials, 333–336
- Carbon-based nanofillers, properties of
- used in Self-sensing Concrete (SsC), 506*t*
- Carbon black (CB), 504–505, 518
- Carbon cycle, bacteria involving
- by oxidation of organic carbon, 534–535
- Carbon dioxide emissions, 51, 53
- Carbon dioxide in water, 24–25
- Carbon fiber reinforced polymer (CFRP), 130, 250–251, 264–265, 700
- Carbon fiber-reinforced polymer strengthening solutions, life cycle analysis of, 699–715, 699*f*
- case studies, 700–702
 - environmental impact assessment of analyzed products, 703–711
 - environmental performances, comparing, 711–715
- Carbon fibers, 159–160, 504–505, 521, 680, 688–689
- Carbon nanofibers (CNFs), 504–505, 518
- Carbon nanotubes (CNTs), 504–505
- Carbon-reinforced FRP, 160
- Castellaniella denitrificans*, 533–534
- Cathodic protection, 15, 316
- Cebolite, 363–364
- Cement-based composites, electrical conductivity of, 511–512
- Cementitious materials, 318, 333–336, 410–411, 541, 569
- Chemical admixtures, 376–378
- Chemical compatibility, 391
- Chloride attack, 315
- Chloride deposition, 48–49
- Chloride-induced corrosion, 26, 35, 317–332
- electrochemical chloride extraction on blended concretes, 328–332
 - application, 328–331
 - geopolymer coating application, 331–332
 - geopolymer coatings, 323–328
 - of reinforcement, 25–26
 - supplementary cementitious materials, 318–323
- Chloride ingress, 45, 58, 70–71, 633
- prevention against, 457–459
- Chloride ion diffusion, 406
- Chloride penetration, 57
- models for predicting, 57–64
- Chlorides, 74
- and corrosion, 21–22
 - electrochemical chloride extraction application, 328–331

Chlorides (*Continued*)

- electrochemical chloride extraction on
 - blended concretes, 328–332
- embeddable chloride sensors, 74–75
- rapid chloride permeability test (RCPT), 405
- recent research on the effects of, 32–35
- Chloride sensors, embeddable, 74–75
- Chloride threshold, 26
- Chlorination-induced corrosion, 3–4
- Circular materials design model, 593–596
- Climate, intentional modification of, 49–50
- Climate change, 2–4, 43
 - Brazilian coast, corrosion of
 - reinforcements on, 54–64
 - chloride penetration, models for predicting, 57–64
 - hypotheses, 54
 - relative humidity, 56–57
 - study area, 54–55
 - temperature, 55–56
 - climate projection, 51–52
 - concrete durability, impact on, 52–54
 - damage probabilities and, 629–630
 - on the mechanisms of degradation of
 - concrete structures, 43–49
 - chloride deposition, 48–49
 - precipitation, 46–47
 - relative humidity, 45–46
 - temperature, 44–45
 - waves and tides, 47–48
 - wind, 47
- Clinkerization process, 355
 - production of calcium sulfoaluminate-belite cement using, 360–363
- The Club of Rome, 674
- CO₂ emission reductions, 592, 596–597
- Coatings
 - geopolymer, 323–328
 - types of, 316
- Coin tap test demonstration, 177*f*
- Cold-cured epoxy matrix, 155
- Cold-cured epoxy resins, 153–155, 157, 159
- Cold-cured thermosetting (epoxy) resins, 152–155
- Compatibility, 389–392
 - bond, 391
 - chemical and electrochemical, 391
 - dimensional, 409
 - electrochemical, 391–392
 - permeability, 391
 - structural and mechanical, 392
- Compressive strength testing, 297–298, 302–303
- Computed tomography (CT), 434
- Concrete, 677–678
- Concrete deterioration, 2, 202*f*, 320, 639, 642–643, 657
- Concrete durability, 2, 45–46, 52–54, 541, 597–598
- “Consistency” method, 474–475
- Constitutive Relation Error (CRE), 111–112
- Construction and demolition waste (C&DW), 594–596
- Construction Products Directive (CPD), 5–6
- Construction Products Regulation (CPR), 5–6
- Construction sector, 673–678
- Corn steep liquor (CSL), 538–539
- Corrosion, 21–22, 150
 - carbonation-induced, 3–4, 22–25
 - chloride-induced, 25–26, 35
 - chlorination-induced, 3–4
 - protecting steel reinforcement against, 15
 - rebar corrosion, 70–73
 - reinforcement corrosion, 20–22
 - of steel reinforcements, 643, 657–658
- Corrosion inhibition of bio-based admixture
 - in interstitial solutions without chlorides, 576–578
 - in the presence of bio-based admixture, 577–578
 - without bio-based admixture, 576–577
 - in synthetic solutions containing chlorides, 579–581
 - corrosion inhibiting mechanism of bioadmixture, 581
 - pitting potential, effect on, 580
- Corrosion inhibitors, 569–570, 572
 - types of, 570–572
- Corrosion monitoring, 70–71, 74–75, 81–82, 90
- Corrosion of reinforcements on the Brazilian coast, 54–64
 - chloride penetration, models for predicting, 57–64
 - data and scenario definition
 - relative humidity, 56–57

- temperature, 55–56
 - hypotheses, 54
 - study area, 54–55
 - Corrosion protection methods for reinforced concrete, 315
 - carbonation-induced corrosion, 332–341
 - electrochemical realkalisation on blended concretes, 336–341
 - supplementary cementitious materials, 333–336
 - chloride-induced corrosion, 317–332
 - electrochemical chloride extraction on blended concretes, 328–332
 - geopolymer coatings, 323–328
 - supplementary cementitious materials, 318–323
 - future trends, 341–342
 - Cost-benefit analysis, 619–622
 - discount rates, 621–622
 - general framework, 619–621
 - Cost-effective design to address climate change impacts
 - aims and scope, 614
 - background, 613–614
 - existing RC structures, adaptation of, 625–633
 - climate change scenarios, 628–629
 - concrete cover and exposure, 625–628
 - cost-effectiveness of damage adaptation strategies, 630–632
 - damage probabilities and climate change effects, 629–630
 - effect of discount rate, 632–633
 - proposed adaptation framework, 616–622
 - cost-benefit analysis, 619–622
 - deterioration models, 616–618
 - stochastic assessment of time-dependent damage risks, 618–619
 - reinforced concrete (RC) structures,
 - adaptation of, 614–616
 - adaptation measures, 615
 - adaptation strategies, cost-effectiveness of, 615–616
 - adaptation time, 615
 - repair and adaptation costs, 623–625
 - cost for the adaptation strategy, 625
 - cost of damage, 623–625
 - repair and adaptation measures, 622–623
 - Cost-effectiveness analysis, 733–735
 - Cost-effectiveness of damage adaptation strategies, 630–632
 - Cost savings, through field assessment, 224–228
 - Count, 127
 - Cracked concrete, 461
 - activity measurement of bacteria in, 554–556
 - Crack filling efficiency, evaluation of by neutron and x-ray tomography, of, 434–440
 - Crack formation, 139–140, 431
 - micro-crack formation, 379–380, 431
 - Crack healing/sealing, effect of SAP on, 486–489
 - Cracking potential, 390, 409–412
 - Cracks in concrete, 18–19, 124–125, 539–540
 - Crack surfaces by released polyurethane, 431–433
 - Creep, 409–410
 - Critical micelle dilution (CMD), 573–574
 - Crystalline zeolites, 278–280
 - Crystallization of soluble salts, 274–276
 - Cyclic loading protocol, 208–209
- D**
- Damage adaptation strategies, cost-effectiveness of, 630–632
 - Damage identification methods, 97, 105–106
 - Damage probabilities and climate change effects, 629–630
 - Data driven monitoring using only optical fibers, 107–109
 - Decision-making cost, 223–228
 - cost savings, 224–228
 - replacement cost, 223–224
 - Degradation of concrete structures, 43–44
 - effect of climate on the mechanisms of, 43–49
 - chloride deposition, 48–49
 - precipitation, 46–47
 - relative humidity, 45–46
 - temperature, 44–45
 - waves and tides, 47–48
 - wind, 47

- Dematerialization, 593, 596
of concrete construction, 596
- Destructive field assessment, 173–176
ASTM pull-off test, 174–175, 174f
differential scanning calorimetry, 175
witness panel test, 175–176
- Deterioration assessment, 237
field tests and monitoring for, 238–242
finite element model for. *See* Finite element (FE) models
modal-based, 242–243
of the Molinos Bridge, 250–257
- Deterioration ratios, 242–243
- Diagnostic load tests, 195
- Diaphorobacter nitroreducens*, 533–534, 546–547
- Dielectric spectroscopy, 184
measurement set up, 184f
- Differential scanning calorimetry, 175
- Dihydrate calcium sulfate (gypsum), 357
- Dilatation wave, 127
- Dimensional compatibility, 389–391, 409
- Discount rates, 621–622, 632–633
- Dispersion, materials and methods for, 505–507
- Distortion wave, 127
- Distributed fiber optic sensor, 99f
- Distributed optical fiber sensors, 107–114
data driven monitoring, 107–109
model-based monitoring, 110–114
pre-stressed concrete beams in a viaduct, 113
reinforced concrete beam in the laboratory, 110–112
reinforced concrete slab in the laboratory, 113–114
- Distributed sensors, 98, 100
optical frequency domain reflectometry (OFDR) based, 104–105
optical time-domain reflectometry (OTDR) based, 101–103
- Drying shrinkage, 411, 480
- Durability, 315, 318, 597–598
concrete construction, durability design of, 597–598
effect of SAP on, 483
impact on, 52–54
regain in, 457–460
- Durability problems of concrete structures, 43, 147
durability of fiber reinforced polymer, 155–163
fibers, durability of, 159–160
matrix/adhesive resins, durability of, 157–159
standard tests, traditional and alternative methods of assessing, 163–165
whole system, durability of, 163–165
- fiber reinforced polymer components, 149–155
cold-cured thermosetting (epoxy) resins, 152–155
peculiarities of fiber reinforced polymer used in constructions, 150–152
- fiber reinforced polymer composites, application of, 148–149
- further research and future trends, 165–166
- Duration, 126–127
- Dynamic test, 239
- E**
- Earth Summit, 6, 675
- Eco-efficiency, concept of, 6
- Eco-efficient concrete structure, 592–609
background, 592–593
case study, 603–609
design constraints, 606
design parameters, 604
design variables, 603–604
objective function, 604–606
optimized concrete mix-design and structural geometry for RC beam, 607–609
results and discussion, 606–607
- circular materials design model, 593–596
definition of, 598–599
dematerialization, 596
durability design, 597–598
increased production and operational efficiency, 596–597
repair methods and materials, 600–602, 601f
design framework, 600–602

- Eco-efficient maintenance, of tunnel.
See Tunnel; eco-efficient maintenance
- Economic costs, 223–225, 227–228
- Economic Input-Output model (EIO), 728
- Eddy Current Test (ET), 182–183
- Efflorescence, 274–276, 276*f*, 281, 283–286
- E-glass, 688
- Electrical conductivity sensor, embeddable, 78
- Electrical measurement methods, 516–517
- Electrical resistivity (ER), 75, 78
- Electric arc furnace (EAF) process, 678
- Electrochemical chloride extraction (ECE), 316
 on blended concretes, 328–332
 application, 328–331
 geopolymer coating application, 331–332
- Electrochemical compatibility, 391–392
- Electrochemical impedance spectroscopy (EIS), 71, 81–82
- Electrochemical reactions, 20
- Electrochemical realkalisation (RE), 316
 on blended concretes, 336–341
 application, 337–340
 geopolymer coating application after, 340–341
- Electrochemical techniques, 316
- Electromagnetic techniques, 182–185, 191
- Electro-mechanical impedance (EMI) technique, 70–71
- Embeddable chloride sensors, 74–75
- Embeddable electrical conductivity sensor, 78
- Embeddable moisture sensor, 77–78
- Embeddable oxygen sensors, 78
- Embeddable pH sensors, 75–76
- Embeddable sensors, accelerated testing of, 79–90
 accelerated weathering test, procedure of, 81–82
 results and discussion, 82–89
 sensors and sensing units tested, 79–81
- Embedded fiber reinforced polymer rebars, rehabilitation with, 172–173
- Embedded multiring-electrode (MRE) sensor, 77–78, 77*f*
- Embedded sensor, 74–75
 for real time structure health monitoring, 190
- Encapsulated bacteria, application of
 for self-healing concrete. *See* Self-healing concrete, application of encapsulated bacteria for
- Encapsulation/immobilization of bacteria, 545–548
- Engineered cementitious composites (ECC)-based concrete, 387
 after 20% mass loss, 404*f*
 alkali–silica reaction (ASR)-based expansion of, 401*f*
 applications of, 418–421
 bond behavior of, 412–417
 dimensional stability of, 409–412
 holistic model for the design of effective repair materials, 389–392
 compatibility, 389–392
 ease of production and application, 392
 intrinsic self-healing of, 417–418
 load vs mid-span beam displacement graphs of, 404*f*
 mechanical properties and durability of, 398–409
 absorption, 407–408
 chloride ion diffusion, 406
 compressive strength and MOE, 398
 corrosion and spalling resistance, 401–402
 durability under extremely hot, humid, and alkaline environments, 400
 fatigue, 398–399
 freeze–thaw and salt scaling resistance, 399
 gas permeability, 404–405
 rapid chloride permeability, 405
 wear testing and abrasion, 408–409
 micro-cracking damage in, 404–405, 408
 mixing of, 397*f*
 need for sustainable repair, 387–389
 placement through the joint, 421*f*
 production of, 397
 spray repair with, 419*f*
 for sustainable infrastructures, 392–421
 tight micro-cracking behavior, 417–418
- Enhanced Frequency Domain Decomposition method, 252–253
- Environment, defined, 157

- Environmental costs, 223–224, 733
 Environmental damage cost (EDC), 735
 Environmental footprint, 678–680, 713, 716
 Environmentally friendly products, 573
 Environmental performances assessment of
 different construction materials,
 683–684
 Epoxy coating on steel bars, 401–402
 Epoxy matrix, 694
 Epoxy resins, 150, 152, 158, 650, 681, 694
 Equivalent uniform annual costs (EUAC),
 725
 Ettringite, 355–359, 363–364, 368–369,
 371–372
 European design codes, 388
 Extended Finite Element Method (X-FEM),
 117
 External fiber reinforced polymer fabric
 wrapping, rehabilitation with, 173
 Externally-applied FRP laminates, 171
 Externally-bonded FRP (pre-cured) plates,
 148
 Externally bonded reinforcement (EBR),
 696–697
 Extracellular polymeric substances (EPS),
 531
 Extracellular polysaccharide (EPS), 537
 Extrinsic optical fiber sensors, 100
- F**
 Failure domain, 16–17
 Failure probability, 656
 Fatigue, 123, 131, 398–399
 Fatigue loading, 124
 damage assessment of precast reinforced
 concrete beam subjected to, 131–132
 increasing, 131–132, 136f
 Fatigue load range
 intensity category of beam under various
 phases of, 140–142
 intensity of precast beam specimen under
 various phases of, 139–140
 FEMtools, 248
 Fiber-reinforced polymers (FRP), 6, 147,
 149–155, 163, 171–173, 175,
 685–696
 application of, for rehabilitation of
 concrete structures, 148–149
 aramid fibers, 689–691
 basalt fibers, 692
 carbon fibers, 688–689
 cold-cured thermosetting (epoxy) resins,
 152–155
 durability of, for rehabilitation of concrete
 structures, 155–163
 fibers, durability of, 159–160
 matrix/adhesive resins, durability of,
 157–159
 whole system, durability of, 163–165
 environmental impact of FRP composites
 constituent materials, 680–681
 aramid fibers, 681
 carbon fibers, 680
 epoxy resins, 681
 glass fibers, 680
 polyester resins, 681
 vinyl ester resins, 681
 forms of reinforcement for, 692
 functions of a matrix in, 693
 glass fibers, 687–688
 manufacturing techniques of FRP
 composites, 695–696
 manual procedure, 695
 pultrusion technique, 696
 peculiarities of fiber reinforced polymer
 used in constructions, 150–152
 polymeric matrices, 693–695
 epoxy matrix, 694
 polyester matrix, 694
 vinyl ester matrix, 694–695
 rehabilitation with embedded fiber
 reinforced polymer rebars, 172–173
 rehabilitation with external fiber
 reinforced polymer fabric wrapping,
 173
 standard tests, traditional and alternative
 methods of assessing, 163–165
- Fibers, durability of, 159–160
 Fiber under test (FUT), 104
 Fick's laws, 59–60
 Fick's second law of diffusion, 25–26
 Field assessment, 195
 cost of decision-making based on,
 223–228
 cost savings, 224–228
 replacement cost, 223–224
 destructive, 173–176
 execution of, 208–214

- load testing procedures, 208–209
 - sensor plan, 209–214
 - future trends, 228–229
 - postprocessing of, 215–223
 - discussion and comparison to
 - international guidelines, 221–222
 - repair recommendations, 223
 - test results, 215–221
 - preparation of, 200–208
 - damage identification, 200–202
 - shear and bending moment positions, 203–208
 - viaduct Zijlweg, 196–200
 - alkali-silica reaction monitoring, 198–200
 - history, 196–197
 - Field assessment of concrete structures
 - rehabilitated with FRP, 171
 - destructive field assessment, 173–176
 - ASTM pull-off test, 174–175, 174*f*
 - differential scanning calorimetry, 175
 - witness panel test, 175–176
 - embedded fiber reinforced polymer rebars, rehabilitation with, 172–173
 - external fiber reinforced polymer fabric wrapping, rehabilitation with, 173
 - future trends, 191–192
 - nondestructive assessment, 176–190
 - Acoustic Emission (AE), 177–178
 - electromagnetic techniques, 182–185
 - embedded sensors for real time structure health monitoring, 190
 - Ground Penetrating Radar (GPR), 185–186
 - load testing, 189
 - mechanical and acoustic vibration, 176–177
 - optical methods, 186–188
 - real time radiography (RTR), 180–182
 - thermographic imaging, 188
 - ultrasonic methods, 178–180
 - visual inspection, 176
 - relative assessment of available techniques, 190–191
 - Field tests, 241–242
 - for deterioration assessment, 238–242
 - Fillers, 504–505
 - Finite element (FE) models, 235, 237–238
 - application example, 250–257
 - with critical position for shear, 206*f*
 - field tests and monitoring, 238–242
 - future trends, 258
 - iterative updating method based on global optimization, 249*f*
 - modal identification, 239–240
 - updating, 236, 243–250
 - basics, 244–246
 - preliminary manual tuning and establishing a search domain, 248–249
 - process, 249–250
 - residual selection, 247–248
 - sensitivity analysis and parameter selection, 248
 - First-order reliability method (FORM), 655–656
 - Flaw detection, 186–188
 - Flexible textile reinforcing fibers, 696
 - Fly ash (FA), 266, 295–297, 318–319
 - Fly ash-based repair mortars, 278–282
 - Force balance accelerometer, 240*f*
 - Forced vibration test, 239
 - Fourier transform infrared (FTIR), 300
 - FTIR spectra, 307
 - Free vibration tests, 241
 - Freeze–thaw cycles, 399
 - Freeze–thaw exposure, 162
 - Frequency, 127
 - Friedel’s salt, 317, 320, 328–329, 379
 - Frost attack, 53
 - Frost resistance, effect of SAP on, 485–486
- G**
- GaBi software, 683, 702
 - Gabor distribution, 242–243
 - Genetic algorithms, 253–255
 - Geoelectrical Imaging methods, 74
 - Geopolymer coatings, 323–328, 331–332
 - application
 - after electrochemical chloride extraction, 331–332
 - after electrochemical realkalisation, 340–341
 - Geopolymer mortars based on aluminosilicates, 261
 - alternative repair mortars for concrete repair, 264–267
 - future trends, 285–286

- Geopolymer mortars based on
 aluminosilicates (*Continued*)
 performance of alkali-activated repair mortars, 273–285
 fly ash-based repair mortars, 278–282
 metakaolin-based repair mortars, 282–284
 repair mortars based on mixtures of different precursors, 284–285
 slag-based repair mortars, 273–278
 standard requirements for, 267–272
 application of repair mortars and concretes, 272
 basic requirements, 268–270
 special requirements, 270–272
- Geopolymers mortars based on low reactive clay, 293
 experimental work, 293–301
 adhesion strength and flexural strength of Portland cement concrete rehabilitated beams, 299–300
 compressive strength testing, 297–298
 Fourier transform infrared, 300
 materials, 293–294
 mix proportioning and synthesis, 295–297
 modulus of elasticity, 299
 scanning electron microscopy (SEM), 301
 unrestrained shrinkage, 297
 workability, 297
 future trends, 311
 results and discussion, 301–311
 adhesion strength and flexural strength of rehabilitated beams, 304–305
 compressive strength, 302–303
 hydration products of mortars, 305–311
 modulus of elasticity, 303–304
 unrestrained shrinkage, 301–302
 workability, 301
- Germination and growth aids for bacteria, 553–554
- Gibbs free energy requirements, 21
- Glass, ceramic, and polymeric capsules, 430–431
- Glass fiber reinforced polymer (GFRP), 160, 162–163
- Glass fibers, 150, 160, 680, 687–688
- Glass FRP (GFRP), 182–183
- Glass transition temperature, 152–153
- Global algorithms, 246
- Global Footprint Network, 675–676
- Global sustainability, 1
- Global warming potential (GWP), 683–684, 684*f*, 730–731
- Good quality concretes, 19, 25, 341
- Granular-activated carbon (GAC), 546
- Graphene nanoplatelets (GNPs), 504–505
- Graphite, crystal structure of, 689*f*
- Graphite fibers, 688
- Gravimetric effect, 49
- Greenhouse gas (GHG) emissions, 355, 596
- Greenhouse Gases, Regulated Emissions, and Energy Use in Transportation (GREET) model, 732
- Ground-granulated blast furnace slag (GGBFS), 273–274, 277*f*, 318
- Ground-granulated blast slag (GGBS), 329
- Ground Penetrating Radar (GPR), 185–186, 185*f*, 191
- Gypsum, 357, 366–367, 369–371
- H**
- HadCM3 model, 56
- Handrails at Arbroath, Scotland, 29
- High-Early-Strength-Engineered Cementitious Composites (HES-ECC), 415–416
 failure modes of, 417*f*
- High-performance fiber-reinforced cementitious composites (HPFRCC), 263, 392–393, 396*t*
- High quality concretes, 23–24, 34
- Hinkley picker, 455
- Historical index, 128–130
- Holographic interferometry, 186–188, 187*f*
- Hooke's Law, 390
- Hornibrook Bridge, Brisbane, 27–29
- Human toxicity potential, cancer (HTPc) parameter, 684*f*
- Hydration products of mortars, 305–311
 Fourier transform infrared (FTIR) spectra, 307
 scanning electron microscopy, 308–311
 thermal analysis (TGA/DSC), 305
 X-ray diffractograms, 305–307

Hydrogels, 467, 547–548
 bio-hydrogels, 547–548
 Hydrothermal—calcination process, 355,
 359–360
 production of calcium sulfoaluminate
 cement using, 363–365
 “Hygrothermal” aging, 157

I

Impact echo, 179
 “Impressed current” system, 15
 Inelastic straining—tensile ductility,
 394–395
 Infrared camera, 188, 188*f*
 Infrared Thermography technique, 188, 189*f*
 Inorganic coatings, 316
 Inspection, 235
 Integrated sensors, 98
 Intensity analysis of AE signal, 135
 Intergovernmental Panel of Climatic Change
 (IPCC), 51
 Internal rate of return (IRR), 725
 Intrinsic distributed optical fiber sensors,
 100–101
 Intrinsic optical fiber sensors, 100, 101*f*
 Inverse problem, solving, 111, 117
 Ion selective electrode (ISE), 75–76
 Iterative techniques, 244

K

Katoite, 363–365
 Kevlar 149, 690
 Kevlar fibers, 690
 Klein’s salt, 356–357
 Kyoto Protocol, 675

L

“Law of Fives”, 4–5
 Lifecycle analysis (LCA), of repair of
 concrete pavements, 723, 734*t*
 Economic Input-Output model (EIO), 728
 future research, 736
 integration of economic and
 environmental analysis, 733–735
 lifecycle cost analysis (LCCA), 724–727,
 724*f*
 options, 727–733
 Life cycle analysis (LCA), of strengthening
 concrete beams with FRP, 673

aramid fibers, 689–691
 basalt fibers, 692
 carbon fiber-reinforced polymer
 strengthening solutions, 699–715,
 699*f*
 assessing the environmental impact of
 the analyzed products, 703–711
 case studies, 700–702
 environmental performances,
 comparing, 711–715
 carbon fibers, 688–689
 environmental impact of FRP composites
 constituent materials, 680–681
 aramid fibers, 681
 carbon fibers, 680
 epoxy resins, 681
 glass fibers, 680
 polyester resins, 681
 vinyl ester resins, 681
 environmental performances assessment,
 683–684
 forms of reinforcement for FRP
 composites, 692
 future trends, 716
 glass fibers, 687–688
 Life Cycle Assessment (LCA)
 methodology, 681–683, 682*f*
 manufacturing techniques of FRP
 composites, 695–696
 manual procedure, 695
 pultrusion technique, 696
 polymeric matrices, 693–695
 epoxy matrix, 694
 polyester matrix, 694
 vinyl ester matrix, 694–695
 reinforced concrete beams, strengthening
 solutions for, 696–699
 sustainable development and built
 environment, 676–677
 traditional building materials,
 environmental impact of, 677–680
 concrete, 677–678
 masonry, 679
 steel, 678
 timber, 679–680
 Life Cycle Assessment (LCA) methodology,
 6, 681–683, 682*f*
 Lifecycle cost (LCC), 17, 637–639, 646,
 655, 661–663, 665–668

- Lifecycle inventory (LCI) study, 728
 Lignosulfonate, 376–377, 572–573
 Linear polarization resistance (LPR) sensor, 71
 Linear variable differential transformer, 189, 210–212, 214
 for measuring strains, 213f
 for measuring the crack widths, 213f
 Linear variable displacement transducers, 432
 Lipopeptide biosurfactant, 573–574
 Liquid resin mixture, 696
 Literature studies, 511–512, 514, 516–517
 Load-displacement diagram, 210–212, 214–215
 for the shear test, 219f
 Load testing, 189, 208–209
 Load vs mid-span beam displacement graphs of, 405
 Local and global optimization algorithms, 246
 Long-term continuous monitoring, 241–242
 Low-permeability grouts, 420–421
 Low reactive clay, geopolymers mortars
 based on. *See* Geopolymers mortars
 based on low reactive clay
 Lumped circuits approaches, 514–516
- M**
- Macroscopic shrinkage, 480
 Macro voids, 471–472
 Magnesium phosphate cement (MPC), 263, 379
 Maintenance, measures of, 235
 Maintenance costs, 725
 Masonry, environmental performances of, 679
 Material degradation, 195–196, 228
 Material-related deterioration, 19
 Materials for Life (M4L) project, 558–559, 559f
 Matrix, 504–505
 Matrix/adhesive resins, durability of, 157–159
 Mazer's model, 60
 Mechanical and acoustic vibration, 176–177
 Mechanical Transfer Function (MTF), 114
 Mercury-intrusion porosimetry (MIP), 266
 Metakaolin (MK), 264–265, 295–297, 319–321
 -based geopolymers, 341
 -based repair mortars, 274–276, 282–284
 carbonation of metakaolin mortars, 283
 Metallic coatings, 316
 Metal–metal oxide (MMO)-activated titanium, 76–77
 Methyl methacrylate (MMA), 429–430
 Michigan Department of Transportation (MDOT) static friction tester, 418–420
 Microbially induced calcium carbonate precipitation (MICP), 531
 Microbially induced carbonate precipitation, 532–535
 bacteria involving carbon cycle by oxidation of organic carbon, 534–535
 bacteria involving nitrogen cycle by degradation of urea, 532–533
 by dissimilation of nitrates, 533–534
 Microclimate, 44
 Micromechanics homogenization approaches, 511–514
 Micro-silica concrete (MSC), 414–415
 Microwave-based electromagnetic technique, 183–184
 Mineral additions, 316, 318, 331, 333
 MK/100PC coated concretes, 325–328
 MOBILE 6.2, 731
 Modal-based deterioration assessment methods, 242–243
 Module C4, 682–683
 Modulus of elasticity (MOE), 299, 303–304, 390–392
 compressive strength and, 398
 Moire interferometry, 186–188, 186f
 Moisture sensor, embeddable, 77–78
 Molinos Bridge, deterioration assessment of, 250–257
 Monocarboaluminate, 374–375
 Monofluorophosphate (MFP), 569
 Monosulfoaluminate (AFm), 363–364, 370–371, 374
 Monte Carlo simulation method (MC), 655–656

- Multi-electrode array sensor (MAS)
corrosion current sensor, 79
- Multielectrode Array Sensor (MAS) sensor,
72–73
- Multiobjective function approach, 245–246
- Multiplexed sensors, 98
- Multiring-electrode (MRE) sensor,
embedded, 77–78
- Multiscale fiber-reinforced cement
composite (MSFRCC), 392–393
- Multi Walled Carbon Nanotubes
(MWCNTs), 502, 504–505
- Mytilus californianus*, 531
- N**
- Natural clay (NC) fractions, chemical
composition of, 294*t*
- Natural environment, 673–674, 679–681,
703–705
- Near surface mounted (NSM) composite,
696
- Near surface mounted strengthening
technique of reinforced concrete
beams, 698*f*
- NEN-EN 1990:2002, 205
- NEN-EN 1991-2:2003, 203–204, 204*f*
- Net present value (NPV), 725
- Neutron radiography, 434, 473–474
to evaluate the water uptake, 446–448
- New Austrian tunneling method (NATM),
639–640
- Nickel powder, 504–505
- Nitrates, bacteria involving nitrogen cycle
by dissimilation of, 533–534
- Nitrogen cycle, bacteria involving
by degradation of urea, 532–533
by dissimilation of nitrates, 533–534
- Noise test, 128
- Nonair-entrained mortar specimens,
399–400
- Noncarbonated concrete, 315
- Non-destructive evaluation (NDE) tests,
523
- Nondestructive testing (NDT) techniques,
124, 176–190, 181*f*
Acoustic Emission (AE), 177–178
electromagnetic techniques, 182–185
embedded sensors for real time structure
health monitoring, 190
- Ground Penetrating Radar (GPR),
185–186
load testing, 189
mechanical and acoustic vibration,
176–177
optical methods, 186–188
real time radiography (RTR), 180–182,
182*f*
thermographic imaging, 188
ultrasonic methods, 178–180
visual inspection, 176
- Nonlinear ultrasonic, 179–180
- NONROAD2005, 732
- Nuclear Magnetic Resonance (NMR),
184–185
- Nutrients and calcium source, effects of
on concrete properties, 548–550
- O**
- Open circuit potential (OCP), 321, 335–336
- Operational modal analysis (OMA),
239–241, 243
- Optical backscattered reflectometry (OBR)
measuring technology, 113
- Optical fiber sensors (OFSs), monitoring
with, 75, 97, 190
distributed optical fiber sensors, 107–114
data driven monitoring, 107–109
model-based monitoring, 110–114
future trends, 117–118
intrinsic distributed optical fiber sensors,
100–101
optical frequency domain reflectometry
(OFDR) based distributed sensor,
104–105
optical time-domain reflectometry
(OTDR) based distributed sensor,
101–103
structural health monitoring purposes,
classifications of, 105–106
technical guide, 114–117
- Optoelectronic technology, 98
- Ordinary Portland cement (OPC), 320–321,
337–338
adhesion test for, 324*f*
production, 355, 372–374
- Oregon Department of Transportation
(ODOT), 69
- Organic carbon, oxidation of, 534–535

- Organic coatings, 316
- Oxygen and corrosion, 21–22
- Oxygen sensors, embeddable, 78
- Oxyhydroxide, 577
- Ozone depletion potential (ODP) parameter, 684, 685*f*
- P**
- Paenibacillus sphaericus*, 572–573
- Pareto frontier, 735
- Pareto optimal front, 245–246
- Paris Agreement, 675
- Pavement LCCA, 724–727
process-based, 728*f*
- Pavements, 723
- Peel-ply, 696
- Pencil lead fracture (PLF), 128
- Permeability compatibility, 391
- Petroleum pitch, 680
- pH sensors, embeddable, 75–76
- Physical damage of concrete, 18–19
- Piezoceramic lead zirconate (PZT)
transducer, 70–71
- Piezoelectric wafer active sensors (PWAS), 190
- Piles in storage after demolition, 27, 27*f*
- Pitting corrosion, 21, 26
- Plain cement-based materials, 392–393
- Plastic shrinkage, 480
- Plate bonding, 698, 698*f*
- Point estimation method, 655–656
- Point sensors, 97
- Polarization optical time domain
reflectometry (P-OTDR), 101
- Polyacrylonitrile, 689
- Polyacrylates (poly(AA)), 468
- Polyacrylonitrile, 680
- Polyester matrix, 694
- Polyester resins, 681
- Polymeric healing agents, encapsulation of, 429–430
- Polymeric matrices, 693–695
epoxy matrix, 694
polyester matrix, 694
vinyl ester matrix, 694–695
- Polyurethane, encapsulated, 429
crack closure by, 431–440
coverage of crack surfaces, 431–433
crack filling efficiency, evaluation of, 434–440
- durability, regain in, 457–460
prevention against carbonation, 459–460
prevention against chloride ingress, 457–459
- encapsulation materials and trigger
mechanisms, 430–431
glass, ceramic, and polymeric capsules, 430–431
trigger mechanisms, 431
- extension in service life, 460–463
challenges, 463
first quantification efforts, 461–463
relevance, 460
- impermeability, regain in, 440–448
capillary water absorption,
gravimetric evaluation of, 443–445
neutron radiography to evaluate water uptake, 446–448
water permeability measurements, 440–443
- mechanical properties, regain in, 448–457
acoustic emission analysis, use of, 453–457
regain in strength and stiffness, 448–453
- Polyvinyl alcohol (PVA) fibers, 393–394
- Portland cement (PC), 293
- Portland cement-based systems, 538–539
- Portland cement concrete (PCC), 728
adhesion strength and flexural strength of
PCC rehabilitated beams, 299–300, 304–305
- Pourbaix diagram, 21
- Precast reinforced concrete beam, damage
assessment of, 131–132
- Precipitation on concrete, 46–47
- Pre-stressed concrete beams in a viaduct, 113
interaction between the optical fiber and
the model, 113
mechanical model, 113
optical fiber measurement, 113
- Printed circuit board (PCB)-based corrosion
potential sensor, 72
- Prismatic molds, 448
- Probability of failure, 16–17

Proof load test, 195–196, 208–209,
222–223
preparation of, 203–208
Pseudomonas aeruginosa, 537
Pseudomonas denitrificans, 533–534
Pseudomonas fluorescens, 573–574
Pultrusion technique, 696
PVC mold, 431–432, 432*f*

Q

Quasi-distributed/multiplexed sensors, 98

R

Radio frequency identification (RFID) tags,
74–75
Raman scattering, 100, 102–103
Random variables, probabilistic models of,
627*t*
Rayleigh scattering, 99, 113
Rayleigh wave, 127
Real time radiography (RTR), 180–182,
182*f*
Real time structure health monitoring,
embedded sensors for, 190
Rebar corrosion, online monitoring of,
70–73
Reduced basis, 117
Reference electrode, 75, 78
Reference probe, 76–77
Rehabilitation cost, 293, 725
Rehabilitation of concrete structures
application of fiber reinforced polymer
composites for, 148–149
Rehabilitation strategies of concrete
pavement, 728–729
Reinforced concrete (RC), 15
corrosion protection methods for.
See Corrosion protection methods for
reinforced concrete
infrastructure deterioration, causes of,
18–22
atmosphere-related deterioration,
19–20
effect of seawater, 20
material-related deterioration, 19
physical damage, 18–19
reinforcement corrosion, 20–22
Reinforced concrete beam, 110–112, 125,
131, 133*f*

near surface mounted strengthening
technique of, 698*f*
plate bonding strengthening technique of,
698*f*
strengthening solutions for, 696–699
wet lay-up strengthening technique of,
697*f*
Reinforced concrete corrosion, monitoring
of, 69
embeddable chloride sensors, 74–75
embeddable electrical conductivity sensor,
78
embeddable moisture sensor, 77–78
embeddable oxygen sensors, 78
embeddable pH sensors, 75–76
embeddable sensors, accelerated testing
of, 79–90
accelerated weathering test, procedure
of, 81–82
results and discussion, 82–89
sensors and sensing units tested, 79–81
embedded MRE sensor, 77–78, 77*f*
future research needs, 90–91
rebar corrosion, online monitoring of,
70–73
Reinforced concrete slab, 113–114
interaction between the optical fiber and
the model, 114
mechanical model, 114
optical fiber measurement, 113
Reinforced concrete structures, 123–125,
128–130, 592, 614–616
adaptation measures, 615
adaptation time, 615
cost-effectiveness of adaptation strategies,
615–616
problem description, 625–629
climate change scenarios, 628–629
concrete cover and exposure, 625–628
results, 629–633
cost-effectiveness of damage adaptation
strategies, 630–632
damage probabilities and climate
change effects, 629–630
effect of discount rate, 632–633
Reinforcement
carbonation-induced corrosion of,
22–25
chloride-induced corrosion of, 25–26

- Reinforcement corrosion, 17–18, 20–22, 52, 69, 401–402
- Reinforcement drawing, 201*f*
- Relative humidity (RH), 45–46, 56–57
RH sensor, 77–78
- Reliability index, 656
- Repair, measures of, 235
- Repair and rehabilitation of concrete
infrastructures on the context of
sustainable development, 1–6
- Repair material design, holistic model of, 390*f*
- Repair mortars, 263
based on mixtures of different precursors,
284–285
- Replacement cost, 223–224
- Residuals, 244
selection, 247–248
- Rovings, 691*f*, 692
- S**
- Scaling Subtraction Method (SSM),
179–180
- Scanning electron microscopy (SEM), 301,
308–311, 505
- Scattering phenomena, 99
optical spectrum of, 100*f*
- Seawater, effect of, 20
- Second-order reliability method (SORM),
655–656
- Self-healing additives, application of
in large scale laboratory and in-situ tests,
558–560
- Self-healing concrete, application of
encapsulated bacteria for, 551–560
activity measurement of bacteria in
(cracked) concrete, 554–556
application of self-healing additives in
large scale laboratory and in-situ
tests, 558–560
germination and growth aids for bacteria,
553–554
quantity of cells and nutrients required,
551
self-healing efficiency, evaluation of,
556–558
triggering of self-healing, 551–553
- Self-healing concrete with encapsulated
polyurethane. *See* Polyurethane,
encapsulated
- Self-healing efficiency, evaluation of,
556–558
- Self-sensing concrete (SsC), 501, 504*f*
applications of, 517–522
repair of existing structures, 521–522
Structural Health Monitoring, 517–520
vehicle traffic detection, 520–521
in bulk form, 518*f*
composition and processing of, 503–508
materials and methods for dispersion,
505–507
matrix and fillers, 504–505
preparation and curing, 507–508
electrical conduction through, 503
embedding of, 518*f*
measurement of sensing data and
characterization of, 508–517
electrical measurement methods,
516–517
modeling aspects, 511–516
sensing mechanisms, 508–510
micromechanics modeling approach of,
514*f*
properties of carbon-based nanofillers
used, 506*t*
trends and future developments, 522–523
typical sensing behavior of, 511*f*
- Sensor plan, 209–214
- Serratia marcescens*, 573
- Service life estimation of concrete
infrastructures, 13
carbonation-induced corrosion of
reinforcement, 22–25
chloride-induced corrosion of
reinforcement, 25–26
chlorides, recent research on the effects
of, 32–35
practical experience, observations and
investigations, 26–32
Handrails at Arbroath, Scotland, 29
Hornibrook Bridge, Brisbane, 27–29
synthesis of observations, 30–32
reinforced concrete infrastructure
deterioration, causes of, 18–22
atmosphere-related deterioration,
19–20
effect of seawater, 20
material-related deterioration, 19
physical damage, 18–19

- reinforcement corrosion, 20–22
 - service life assessment, practical
 - implications for, 35–36
- Severity index, 128–130
- S-glass, 688
- Shearographic imaging, 187*f*
- Short-time Fourier transform, 242–243
- Shrinkage, 480
 - autogenous, 480
 - carbonation-induced, 480
 - drying, 480
 - macroscopic, 480
 - reducing admixtures, 380–381
 - reduction, 484–485
- Signal strength, AE parameter analysis based
 - on, 135–139
- Silica fume (SF), 319
- SimaPro, 731
- Single-objective function approach, 245–246
- Slag-based repair mortars, 273–278
- Slant shear testing, 413–414
- Smart concrete, 501–502, 507–508, 513–516, 518, 520–523
- Social cost, 223–224
- Sodium bicarbonates, 281–282
- Sodium silicate, 280–281, 560
- Sol-gel/trinitrobenzenesulfonic acid (TNBS)
 - composite film, 75–76
- Spontaneous Brillouin scattering, 103
- Sporosarcina pasteurii*, 532–533, 537–538
- Spray repair, 419*f*
- Square root of time, 61
- Static test, 239, 241–242, 257
- Steel, environmental performances of, 678
- Steel rebar, 172–173
- Steel reinforcement protect against
 - corrosion, 15
- Steel reinforcing bars, 28
- Stimulated Brillouin scattering, 103
- Stochastic process-based performance
 - evaluation, 658–660
- Stochastic variables, 16–17
- Stratlingite, 357, 366
- Strength regain, 451
- Structural and mechanical compatibility, 392
- Structural assessment, 235
 - activities required for, 236
 - conducting, causes for, 236
- Structural health monitoring (SHM), 74–75, 97, 501
 - embedded sensors for, 190
 - purposes, classifications of, 105–106
 - through acoustic emission. *See* Acoustic emission (AE); structural health monitoring through
- Substrate concrete (SUBC), 414
 - failure, 415*f*
- Sulfate attack, 45
- Sulfate resistance, 277–278, 282
- Sulfoaluminate cement (SAC)-based
 - concrete, 355, 358*t*
 - definition, type, and usages, 356–359
 - hydration of, 366–378
 - role of calcium carbonate, 374–376
 - role of calcium hydroxide and OPC, 371–373
 - role of chemical admixtures, 376–378
 - role of sulfate type and content, 369–371
 - role of ye’elimite type, 368–369
 - production of, 359–365
 - using clinkerization process, 360–363
 - using hydrothermal–calcination process, 363–365
 - usages of sulfoaluminate cement for
 - repair, 378–382
- Superabsorbent polymers (SAPs), 467
 - applications of, 483–491
 - crack healing/sealing, 486–489
 - frost resistance, 485–486
 - internal curing and shrinkage reduction, 484–485
 - repair, 489–490
 - in concrete, 471–477
 - absorption–desorption kinetics, 472–474
 - general behavior, 471–472
 - measuring absorption capacity, 474–477
 - effects of, on properties of concrete, 477–483
 - durability, 483
 - fresh concrete properties, 477–478
 - hydration and microstructure, 478–480
 - mechanical properties, 480–482
 - shrinkage, 480
 - future research, 491–492

- Superabsorbent polymers (SAPs)
 (*Continued*)
 properties of, 470–471
 types of, 468–469
- Superplasticizer, 369, 377–378
- Supervised learning, 106
- Supplementary cementitious materials
 (SCM), 264, 318–323, 333–336,
 597, 732
- Surface washing effect, 46
- Sustainability in civil engineering, 674–684
 construction materials, environmental
 performances assessment of,
 683–684
 definition, 676–677
 fiber-reinforced polymer composites
 constituent materials, environmental
 impact of, 680–681
 aramid fibers, 681
 carbon fibers, 680
 epoxy resins, 681
 glass fibers, 680
 polyester resins, 681
 vinyl ester resins, 681
- Life Cycle Assessment (LCA)
 methodology, 681–683, 682*f*
 sustainable development and built
 environment, 676–677
 traditional building materials,
 environmental impact of, 677–680
 concrete, 677–678
 masonry, 679
 steel, 678
 timber, 679–680
- Sustainability Index for Bridges, 223–224
- Sustainable development, 591–593,
 676–677
 and the built environment, 676–677
 principles, 593
- Sustainable repair, need for, 387–389
- T**
- Ternesite, 362–363
- Tetracalcium aluminoferrite, 356–357
- Textile Reinforced Concrete (TRC), 263
- Thermal analysis (TGA/DSC), 305
- Thermographic imaging, 188
- Thermosetting matrices, typical properties
 for, 694*t*
- Thermosetting polymers, 693
- Thermosetting resins, 693
- Threshold, defined, 126
- Tides, 47–48
- Tight micro-cracking, 417–418
- Tikhonov and Constitutive Relation Error-
 based techniques, 111
- Timber, environmental performances of,
 679–680
- Time-dependent damage risks, 614
 stochastic assessment of, 618–619
- Time-frequency domain methods, 242–243
- Time-temperature superposition principle,
 165
- TNO DIANA, 203
- Traditional building materials,
 environmental impact of, 677–680
 concrete, 677–678
 masonry, 679
 steel, 678
 timber, 679–680
- Transformation techniques, 242–243
- Tricalcium aluminate, 317, 365
- Trigger mechanisms, 431
- Tunable laser source (TLS), 104
- Tunnel, 639–649
 concrete deterioration, 642–643, 642*f*
 construction method, 639–640
 degradation causes, 644–645
 deterioration states, 647*t*
 eco-efficient maintenance, 654–666
 concrete deterioration, 657
 deterioration model, 656–657
 example, 664–666
 lifecycle costing, 661
 planning, 661–664
 reliability analysis approach, 655–656
 reliability-based performance
 evaluation, 655–658
 steel and steel reinforcement corrosion,
 657–658
 stochastic process-based performance
 evaluation, 658–660
 examples of, 638*f*
 inspection and testing techniques, 648*t*
 leakage, 644
 maintenance procedure, 646–649, 646*f*,
 647*t*
 maintenance strategy, 645–646

- recommendations and future trends, 667–668
- support systems and linings, 640–641
- Tunnel boring machine (TBM) method, 639–640
- Tunnel repairs, 649–654
 - concrete repair, 650–651
 - crack repair, 650, 650*f*
 - delamination and spall repair, 650–651
 - eco-efficient repairs, 653–654
 - flow chart of, 649*f*
 - rehabilitation and retrofitting, 652–653, 653*f*
 - waterproofing, 651–652, 652*f*
- U**
- Ultrafine sulfoaluminate cements, 380
- Ultra-High Frequency (UHF) RFID technology, 77–78
- Ultrasonic pulse velocity (UPV) tests, 178–180, 178*f*
- Ultrasonic sensors, 190
- Ultrasonic tomography method, 179, 180*f*
- Ultraviolet radiations, 159
- Unidirectional fabrics, 691*f*, 692
- United Nations Environment Programme (UNEP), 51, 674–675
- Urban human population, 2
- Urea, 550
 - bacteria involving nitrogen cycle by degradation of, 532–533
- User costs, 724, 726, 735
- V**
- Vehicle operation cost (VOC), 726
- Vehicle traffic detection, 520–521
- Viaduct Zijlweg, 196–200, 223, 225, 229
 - alkali-silica reaction monitoring, 198–200
 - history, 196–197
 - structural system of, 198*f*
- Vinyl ester matrix, 694–695
- Vinyl ester resins, 681
- Virginia Department of Transportation (VDOT), 420–421
- Viscosinamide, 573–574
- Viscosity modifying agent (VMA), 540
- Visual inspection, 97, 123–124, 176
- Volkersen's theory, 114–115
- W**
- Water permeability measurements, 440–443, 441*t*, 442*f*
- Waterproofing, 651–652
- Wavelet transform, 242–243
- Waves and tides, 47–48
- Weathering, 147, 164–165
- Weathering test, 81–82
- Wet lay-up FRP application, 151
- Wet lay-up strengthening technique of reinforced concrete (RC) beams, 697*f*
- Wet lay-up systems, 697
- “Whole of life” analysis, 17
- Whole system, durability of, 163–165
- Wigner-Ville distribution, 242–243
- Wind, 47
- Witness panel test, 175–176
- World Commission on Environment and Development (WCED), 675
- World Meteorological Organization (WMO), 51
- Woven fabrics, 691*f*, 692
- X**
- X-ray computed tomography (CT), 436*f*
 - 3D visualization of, 435*f*, 437*f*, 438*f*
 - cross-section through the capsules, 436*f*
- X-ray diffractograms, 305–307
- X-ray tomography, 434–440
- Y**
- Yeast extract (YE), 550
- Ye'elimite, 356–357, 360–362, 368–369
- Young's modulus, 111–112, 253–254

"It is a must-have for all engineers and researchers dealing with design and maintenance of concrete structure like roads, bridges, tunnels, dams and coastal defence works"

Erik Schlangen, Civil Engineering Professor at Delft University of Technology and the Chair of Experimental Micromechanics

Concrete infrastructure is crucial to services and economic activities of modern civilization. Unfortunately concrete deteriorates due to several causes including mechanical deterioration, like impact or excessive loading or deterioration due to physical causes like erosion or shrinkage. More frequently, however, it deteriorates by chemical detrimental reactions when it is exposed to environmental conditions containing chlorides from seawater or from de-icing salts and other aggressive media. Climate change is also being increasingly responsible for premature deterioration of concrete infrastructure. As a consequence, worldwide concrete infrastructure repair rehabilitation needs are enormous and the costs are staggering.

This book provides an updated state-of-the-art review on eco-efficient repair and rehabilitation of concrete infrastructure. Presented over three parts; the first part reviews service life estimation, monitoring of concrete structures, durability performance, and field assessment. Part II focuses on innovative materials for repair and rehabilitation including geopolymers, ECC, and materials with self-sensing properties. Part III addresses eco-efficient and cost-effective design, accountability of climate change impacts, and includes case studies using life cycle analysis and life cycle cost analysis.

This book is an essential reference resource for materials scientists, civil and structural engineers, architects, contractors, designers, and other professionals working in construction on the repair and rehabilitation of concrete infrastructures.

Fernando Pacheco-Torgal is a Senior Researcher in the C-TAC Research Centre at the University of Minho, Portugal. **Robert E. Melchers** is Professor of Civil Engineering at The University of Newcastle, Australia. **Xianming Shi** is an Associate Professor of Civil and Environmental Engineering at Washington State University, United States. **Nele De Belie** is Professor in Durability and Sustainability of Cement Bound Materials at Ghent University, Belgium. **Kim Van Tittelboom** is an Assistant Professor within the Department of Structural Engineering at the Faculty of Engineering and Architecture of Ghent University, Belgium. **Andrés Sáez** is a Professor in the Department of Continuum Mechanics and Structural Analysis at the University of Seville, Spain.



WP
WOODHEAD
PUBLISHING
An imprint of Elsevier
elsevier.com/books-and-journals

ISBN 978-0-08-102181-1



9 780081 021811